

**INTERNATIONAL JOURNAL OF MODERN
ENGINEERING RESEARCH (IJMER)**

ISSN : 2249-6645



Volume 2 - Issue 2

Web : www.ijmer.com

Email : ijmer.editor@gmail.com

International Journal of Modern Engineering Research (IJMER)

Editorial Board

Executive Managing Editor

Prof. Shiv Kumar Sharma
India

Editorial Board Member

Dr. Jerry Van
Department of Mechanical, USA

Dr. George Dyrud
Research centre dy. Director of Civil Engineering, New Zealand

Dr. Masoud Esfal
R& D of Chemical Engineering, Australia

Dr. Nouby Mahdy Ghazaly
Minia University, Egypt

Dr. Stanley John
Department of Textile Engineering, United Kingdom

Dr. Valfitaf Rasoul
Professor and HOD of Electromechanical, Russian

Dr. Mohammed Ali Hussain
HOD, Sri Sai Madhavi Institute of Science & Technology, India

Dr. Manko dora
Associate professor of Computer Engineering, Poland

Dr. Ahmed Nabih Zaki Rashed
Menoufia University, Egypt

Ms. Amani Tahat
Ph.D physics Technical University of Catalonia-Spain

Associate Editor Member

Dr. Mohd Nazri Ismail
University of Kuala Lumpur (UniKL), Malaysia

Dr. Kamaljit I. Lakhtaria
Sir Padmapat Singhaniya University, Udaipur

Dr. Rajesh Shrivastava
Prof. & Head Mathematics & computer Deptt. Govt. Science & commerce College Benazir. M.P

Dr. Asoke Nath
Executive Director, St. Xavier's College, West Bengal, India

Prof. T. Venkat Narayana Rao
Head, CSE, HITAM Hyderabad

Dr. N. Balasubramanian
Ph. D (Chemical Engg), IIT Madras

Jasvinder Singh Sadana
M. TECH, USIT/GGSIPU, India

Dr. Bharat Raj Singh

Associate Director, SMS Institute of Technology, Lucknow

DR. RAVINDER RATHEE

C. R. P, Rohtak, Haryana

Dr. S. Rajendran

Research Supervisor, Corrosion Research Centre Department of Chemistry, GTN Arts College, Dindigul

Mohd Abdul Ahad

Department of Computer Science, Faculty of Management and Information Technology, Jamia Hamdad, New Delhi

Kunjai Mankad

Institute of Science & Technology for Advanced Studies & Research (ISTAR)

NILANJAN DEY

JIS College of Engineering, Kalyani, West Bengal

Dr. Hawz Nwayu

Victoria Global University, UK

Prof. Plewin Amin

Crewe and Alsager College of Higher Education, UK

Dr. (Mrs.) Annifer Zalic

London Guildhall University, London

Dr. (Mrs.) Malin Askiy

Victoria University of Manchester

Dr. ABSALOM

Sixth form College, England

Dr. Nimrod Nivek

London Guildhall University, London

Data Mining for Prediction of Clothing Insulation

M.Martin Jeyasingh¹, Kumaravel Appavoo², P.Sakthivel³

¹Research Scholar, ²Dean & Professor,

^{1&2}Bharath Institute of Higher Education and Research, Chennai-73, Tamilnadu, India.

³Associate Professor, ³Anna University, Chennai-25, Tamilnadu, India.

ABSTRACT

Owing to difficulties of gathering large volumes of textile domain data in a context of less mining research, predicting the characteristics of garments becomes an important open problem which receives more and more attention from the textiles research community. In this research work, the field of Data mining attempts to predict clothing insulation factors with the goal of understanding the computational character of learning. Characteristics of clothing learning is being investigated as a technique for making the selection and usage of training data and their outcomes. It is observed from the results obtained by experimentation that the Linear Regression is quite appealing because of effectiveness in terms of high prediction rate and Linear Regression is able to discover the clothing insulation performance in a most efficient manner in comparison to all other learning algorithms experimented. Data mining Classifiers has showed spectacular success in reducing classification error from learned classifiers like Linear regression, LeastMedSq and AdditiveRegression functions have been analyzed for improving the predictive power of classifier learning systems.

Keywords : - Classifiers, Clothing Insulation, Data Mining, Garment layers, Linear Regression, Manikins

I. INTRODUCTION

Just as the diet is critical to survival, so too is the clothing. It is used to protect the wearer from the most extreme conditions. Clothing is all the more important for people who travel or live in a variety of conditions and temperatures. One never wants to be in a position of being inadequately protected!

There are three essential layers in the modern clothing system. The inner-most layer is "moisture control." The key to warmth and comfort is to have a dry layer next to your skin — this is absolutely essential. This first layer is made of a fabric which carries away or "wicks," the perspiration from the body, keeping the wearer dry. The second layer is the "temperature control" layer. This layer is for comfort and warmth and is where insulation is the key factor. Different thicknesses of polar fleece, which keeps the wearer warm, breathes, and dries quickly, are used most often in this layer. Finally, the third layer is for "element protection." This outer layer protects the wearer from wind, precipitation, and extreme temperature [1].

Industry standards are often rules of thumb, developed over many years, that offset many conflicting goals: what people will pay, manufacturing cost, local climate, traditional building practices, and varying standards of comfort. Both heat transfer and layer analysis may be performed in large industrial applications, but in household situations (appliances and building insulation), air tightness is the key in reducing heat transfer due to air leakage (forced or natural convection). Once air tightness is achieved, it has often been sufficient to choose the thickness of the insulating layer based on rules of thumb. Diminishing returns are achieved with each successive doubling of the insulating layer. It can be shown that for some systems, there is a minimum insulation thickness required for an improvement to be realized.

The type of clothing worn by people directly affects the heat loss from the human body to the environment. Clothing blocks conduction losses by trapping still air within fabric structures and between garment layers. Clothing also reduces radiant heat loss since each fabric layer serves as a thermal radiation barrier. Clothing impedes evaporative heat loss by restricting the evaporation of sweat that may be produced by the body. Dry or sensible heat loss refers to the first three types of heat loss; latent heat loss refers to the evaporative form. Only dry heat loss is addressed in this clothing study[1]. This research work explores and studies the Clothing insulation in various stages and uses the clothing dataset to find the prediction of accuracy in clothing insulation with the help of data mining techniques. Besides storing information concerning the properties of datasets, this database must also store information about the performance of base classifiers on the selected datasets. Data quality is an important aspect in clothing learning as in any machine learning task.

II. METHODS AND DATA DESCRIPTION

A. Description of Dataset

Data processing : The data types like nominal(text), numeric or mixed attributes and classes, and the missing data has been filled with meaningful assumptions in the database. Specification of database with description and table structure as shown in Table 1.

B. Description of Data Mining

Data mining is the process of extracting patterns from data and it is becoming an increasingly important tool to transform these data into information. It is commonly used in a wide range of profiling practices, such as sales marketing, surveillance and scientific discovery [6].

B.1. The Function of Data Mining

The primary function of data mining is to assist in the analysis of collections of observations of behaviour Knowledge Discovery in Databases is used to describe the process of finding interesting, useful data [3]. Data mining commonly involves five classes of tasks:

- Classification: to arrange the data into predefined groups. Common algorithm include Decision Tree Learning, Nearest neighbour, naive Bayesian classification and Neural network.
- Clustering: to classify the groups while the groups are not predefined. The algorithm should try to group similar items together.
- Regression: to find a function which models the data with the least error.
- Association rule learning: to searches for relationships between variables.
- Predictive analytic: to exploit patterns found in historical and transaction data to identify risks and opportunities, and analyse current and historical facts to make predictions about future events[4].

B.2. The Application of Data Mining

Data mining can be used to uncover patterns. The increasing power of computer technology has increased data collection and storage. Automatic data processing has been aided by computer science, such as neural networks, clustering, genetic algorithms, decision trees and support vector machines. Data mining is the process of applying these methods to the intention of uncovering hidden patterns [5]. It has been used for many years by businesses, scientists to sift through volumes of data. The application of data mining in fashion product development for detection analysis, forecasting by using classification and prediction methods by algorithms as shown in Fig. 1.

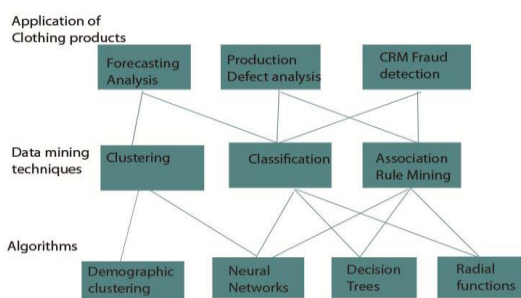


Fig. 1 Application of data mining in fashion Products

B.3. Steps of Data Mining

Data Mining process involved in various steps as follows:

- Data Integration: First of all the data are collected and integrated from all the different sources.
- Data Selection: We may not all the data we have collected in the first step.

- Data Cleaning: The data we have collected are not clean and may contain errors, missing values, noisy or inconsistent data.
- Data Transformation: The data even after cleaning are not ready for mining as we need to transform them into forms appropriate for mining. The techniques used to accomplish this are smoothing, aggregation, normalization etc.
- Data Mining: Now we are ready to apply data mining techniques on the data to discover the interesting patterns.
- Pattern Evaluation and Knowledge Presentation: This step involves visualization, transformation, removing redundant patterns etc. from the patterns we generated.
- Decisions / Use of Discovered Knowledge: This step helps user to make use of the knowledge acquired to take better decisions[9].

TABLE 1. SPECIFICATION OF DATABASE

Field No.	Field Name	Description	Data Type
1	Garment Code	To refer the garment type according to their category	Numeric
2	Design Description	The type of garment (eg. Shirts, Trousers, Sweatersetc)	Nominal (Text)
3	Fabric type	the particular garment construction style features	Nominal (Text)
4	Garment Weight	weight of the garment which is used as an predictor of insulation. The present study garment weight ranged from 0.03 to 1.54 kg.	Numeric
5	Body Surface Area	The amount of body surface area covered by garments which is given in (%) for clothing insulation, It is also used as a predictor of the insulation.	Numeric
6	Fcl	Clothing area factor – the increased surface area for heat loss, and the number of fabric layers in the garment (e.g., pockets, lining)	Numeric
7	IT	Total insulation (Total thermal insulation of clothing plus air layer, clo) $IT = (k(T_s - T_a) A_s) / Q$	Numeric
8	Icle	Effective clothing & insulation $I_{cle} = IT - I_a$	Numeric
9	Icl	Basic or intrinsic clothing insulation (amount of body surface area) $I_{cl} = IT - (I_a / F_{cl})$	Numeric

III. CLOTHING INSULATION

A. Factors for Clothing Insulation

Dependent upon specific clothing design the insulation will be provided by individual garments, which in turn, affects the amount of body surface area covered by the garment, and the fit (loose or tight), the increased surface area for heat loss (i.e., F_{cl}), and the number of fabric layers in the garment (e.g., pockets, lining). Garment insulation is also related to characteristics of fabric—particularly the thermal resistance or thickness of the fabric. In addition to other fabric properties such as stiffness can affect the increase in surface area for heat loss, and extensibility can change garment fit (i.e., skin contact vs. air gap).

The insulation provided by a clothing system is usually expressed in clo units, with $1 \text{ clo} = 0.155 \text{ m}^2 \text{ K/V}$ [2]. The insulation provided by clothing ensembles is related to the characteristics of the component garments including their insulation values, the amount of body surface area covered by clothing, the distribution of the insulation over the body (i.e., number of fabric layers on different parts of the body), looseness or tightness of fit, and the increased surface area for heat loss. Several of these factors can be varied for a given ensemble by changing the way the garments are worn on the body (i.e., degree of garment closure, sequence of garment layering) [1].

B. Heated Manikins

Electrically-heated manikin in an environmental chamber is always recommended method measuring for clothing insulation. The manikin is a constant temperature method of. It would be heated internally to simulate the skin temperature distribution of a human being. The amount of power that it takes to keep the manikin's average skin temperature at the proper level (i.e. approximately 33°C) in a cooler environment is recorded. The power level will vary in proportion to the amount of insulation provided by the clothing worn by the manikin. Manikins in use today are designed primarily for measuring the resistance to dry heat transfer. However, some researchers have determined the resistance to evaporative heat transfer provided by clothing using a "sweating" manikin [7].

C. Selection of Garments

A variety of garment designs were made into summer and winter seasons using different fabrics. The designs were selected by considering the following

- variation in the amount of body surface area covered,
- longevity of style with regard to fashion obsolescence,
- looseness or tightness of fit, and
- fabric overlap.

Nightwear (i.e., robes, nightgowns, and pajamas), common work garments, (i.e., coveralls and overalls), and special garments (i.e., sweatshirt and sweatpants) also were representative knits for these garments are not available in the fabric market. Sweater design comparisons for sleeve length were made by shortening the sleeves of additional long-sleeve sweaters that were purchased. The undergarments were also purchased ready-made because it would be difficult if not impossible to construct

representative items in a clothing laboratory (e.g., bra), and these items were inexpensive and readily available in retail outlets. Miscellaneous garments were purchased readymade because they were not directly compared to one another. Clothing items for the head and hands were not included because these garments cover only a small amount of body included since clo values for these types of garments are not listed in the dataset. Some of the garments such as long trousers were constructed into summer (cool) and winter (warm) seasons. Others are worn only during one season (e.g., short shorts), or they are worn all year round with no seasonal fabric variation (e.g., sweatshirt). These types of garments were constructed or purchased in only one characteristic fabric. According to the seasons different types of garments would be used by consumers, this analysis examined by Clothing merchandisers. The sweaters were purchased ready-made because surface area and are rarely worn by people in indoor environments [1].

D. Measurement of the Body Surface Area

The manikin's surface will be modified so that the body surface area covered by a garment could be determined from photographs. A stylus was used to etch the manikin's surface into a grid of small areas, most of which measured $3 \times 3 \text{ cm}$. The body was also divided into a grid of small areas, most of which measured $3 \times 3 \text{ cm}$. The body was also divided into 17 major segments as shown in Fig 2. The location and surface area of each square and segment was recorded. White tape was then used to cover the markings etched into the anodized copper to make them more visible Fig 3.

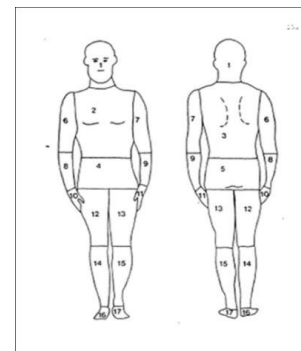


Fig. 2. Segments of manikin [1]

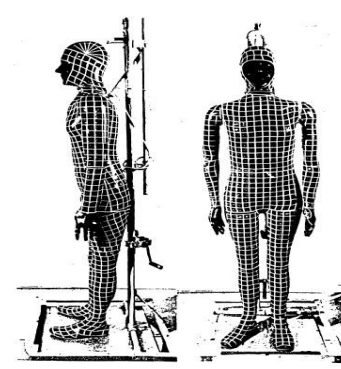


Fig. 3. Anodized copper manikin [1]

IV. EXPERIMENT AND RESULTS

A. Distribution of Classes

The main reason to use this dataset is that the relevant data that can easily be shared with other researchers, allowing all kinds of techniques to be easily compared in the same baseline. The data-set might have been criticized for its potential problems, but the fact is that it is the most widespread dataset that is used by many researchers and it is among the few comprehensive datasets that can be shared in clothing insulation. Like the test dataset, 302 different types of garments that are broadly categorized in nine groups of Shirts, Sweaters, Sleepwear, Dresses, Robes, Skirts, Suit Jackets and Vests, Trousers and Coveralls, Underwear/Footwear. The Distribution of Classes in the actual training data for classifiers evaluation and the occurrences as given in Table II. The percentage of Garment Design Categories using Pie chart as shown in Fig.4.

The clothing information in the original Database files were summarized into associations. Therefore, each instance of data consists of garment features and each instance of them can be directly mapped and discussed in classifiers algorithms. Due to the huge number of audit data records in the original database, 302 instances have been extracted as datasets for this experiments.

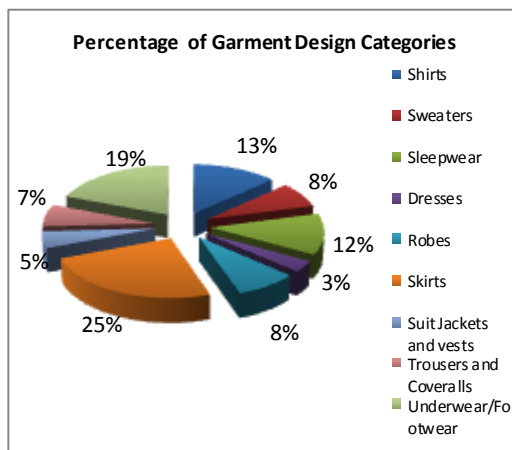


Fig. 4 Percentage of Garment Design Category

TABLE II. DISTRIBUTION OF CLASSES IN THE ACTUAL TRAINING SET

Garment Design Category (Class)	No. of Records	Percentage of Class Occurrences (%)
Shirts	40	13
Sweaters	23	8
Sleepwear	37	12
Dresses	10	3
Robes	25	8
Skirts	74	25
Suit Jackets and vests	15	5
Trousers and Coveralls	20	7
Underwear/Footwear	58	19
Total	302	100

B. Data Mining Process

For the experimental setup the collected data preprocessed for data cleaning, transformation, pattern evaluation and knowledge discovery using the data mining software called weka 3.6.4 which has been implemented in Java with latest windows 7 operating system, These dataset has been applied and then evaluated for accuracy by using 10-fold CrossValidation strategy[8]. The predicted result values of various classifiers with prediction accuracy as given Table III.

TABLE III. DATA MINING CLASSIFIERS WITH PREDICTION ACCURACY

Functions	Correlation coefficient	Mean absolute error	Root mean squared error
Linear Regression	0.9663	0.0094	0.0545
Leastmedsq	0.8936	0.0437	0.1059
Multilayerperceptran	0.9984	0.0024	0.012
RBFNetwok	0.5566	0.1288	0.1745
Additive Regression	0.9676	0.0422	0.0548

C. Regression Analysis

This comprehensive dataset to develop equations for predicting clothing insulation. Consequently, regression analyses were conducted using data collected. The garment data set are representative of the types of clothing worn by a people in indoor environments. Therefore, the regression equations reported here should be applicable to most types of clothing. When a particular equation does not work well for certain types of clothing (i.e., as evidenced by a few data points located way of the regression line on the graph), the exceptions will be noted and explained. Removal of any data has not done from garment set because of an effort to strengthen or improve the predictive ability of an equation. A number of variables that could be related to garment insulation were used to develop a series of linear and quadratic regression equations. The equations were developed with the Y intercept equal to zero (or whatever the origin should theoretically be) and with the actual Y intercept based on the data set. Both types of equations were developed so that trade-offs in the simplicity and, accuracy of the equations could be evaluated. Surprisingly, none of the quadratic forms of the equations offered any significant improvement in predictability over the linear equations with a Y intercept.

D. Experimental Outcomes

This section presents experimental results using data mining function classifiers LeastMedSq, Linear Regression with different base classifiers along with the results obtained from various existing algorithms. Data

mining classification result for current regression equations as given in Table IV. and comparisons of existing dataset regression measures are shown in Table V. Performance of classifier instances with highest prediction accuracy as correlation coefficient and mean absolute error as shown in Fig. 5.

TABLE IV. DATA MINING CLASSIFICATION RESULT OF CURRENT EQUATIONS

Method	Equation	Slope	Intercept
Linear Regression	$F_{cl} = 0.448 * I_{cl} + 1.01$	0.448	1.01
Linear Regression When y intercept 1.00	$F_{cl} = 0.458 * I_{cl} + 1.00$	0.458	1.00

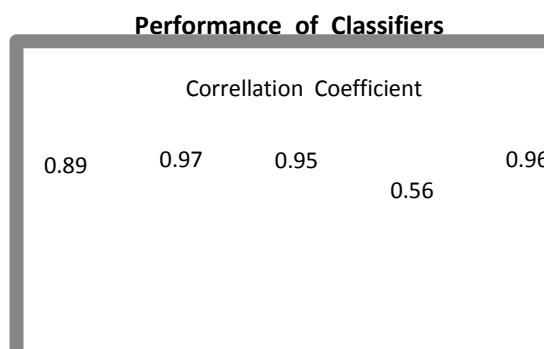


Fig.5.Performance of Classifiers with Prediction Errors

TABLE V. COMPARISON OF RESULT MEASURES WITH EXISTING REGRESSION EQUATIONS

Method	Equation	Slope	Intercept
LeastMedSq	$F_{cl} = 0.584 * I_{cl} + 0.981$	0.584	0.981
Linear Regression	$F_{cl} = 0.480 * I_{cl} + 1.002$	0.480	1.002

V. CONCLUSION AND DISCUSSION

It is observed from the results obtained by experimentation is that the Linear Regression is quite effective in terms of high prediction performance rate. Linear Regressions are able to discover the clothing insulation performance in a most efficient manner in comparison to all other learning algorithms discussed in this work. Thus resulting effects on clothing insulation is derived with remarkable prediction accuracy by using the data mining classification technique. More work is needed to relate manikin data on clothing insulation to human subject data for thermal comfort, particularly in factory environments. Clothing insulation has been done on stitched garments with manikin or human subjects the same could be applied in simulated computer model with changes in clothing system by using various design

software's. Classifiers have shown comparable performance in reducing classification error from selected classifiers. Therefore this study reinforces that, Data mining is the perfect and prevailing technological tool to implement the clothing insulation factors to reveal the prediction rapidly for the accurate result that would facilitate to make the precise clothing products in the apparel sector.

REFERENCES

- [1] Elizabeth A., McCullough and Byron W. Jones., A Comprehensive database For Estimating Clothing Insulation, 32-5620, 1984.
- [2] M. Kantardzic Data Mining: Concepts, Models, Methods and algorithms. John Wiley & Sons, pp.62-81, 2003,
- [3] Jiao Licheng and Liu Fang, Data Mining and Knowledge Discovery. Xian University of Electric Technology Publishing, pp.25-7., 2006.
- [4] L. Devroye, L. Györfi and G. Lugosi, A Probabilistic Theory of pattern Recognition. Springer- Verlag, pp.112-149, 1996.
- [5] Liang Xun, Data Mining: Algorithms and Application. Beijing university Press: pp.22-42, 2006.
- [6] <http://dataminingwarehousing.blogspot.com/2008/10/data-mining>.
- [7] McCullough, E.A.; Arpin, E.J.; Jones, B.; Konz, S.A.; and Rohles, F.E., Jr. Heat transfer characteristics of clothing worn in hot industrial environments ASHRAE Transactions, Vol.88, Part 1, pp.1077-1094, 1982.
- [8] H. Dai, R. Srikant, and C. Zhang (Eds.) Evaluating the Replicability of Significance Tests for comparing learning algorithms, PAKDD 2004, LNAI 3056, pp. 3-12 2004

STABILIZATION OF LINEAR SYSTEMS

Vanita Jain

Bharati Vidyapeeth College of Engineering, New Delhi

ABSTRACT

Simultaneous stabilization is recognized as one of the open issues in linear system theory, arises for instance in many applications such as reliable control, robust control and nonlinear control. This paper deals with designing a constant output feedback controller for the stabilization of given M linear systems. The design equations are functions of the state and control weighting matrices.

Keywords- controller, linear, time-invariant, simultaneous stabilization

I. INTRODUCTION

The problem of simultaneously stabilizing a family of linear continuous systems by an output controller is considered here. The simultaneous stabilization problem (SSP)

can be formally stated as given an r-tuple $G_1(s), \dots, G_r(s)$ of proper distinct transfer functions for plants, find a compensator $C(s)$ (if it exists) such that all closed-loop

systems $\frac{C(s)G_i(s)}{1+C(s)G_i(s)}, (i=1,2,\dots,r)$ are internally

stable [1, 2, 3]. If the compensator $C(s)$ is further restricted to be stable, i.e. it has no unstable poles, then the simultaneous stabilization problem (SSP) is referred to as a strong simultaneous stabilization problem (SSSP). The requirement for a stable compensator arises in certain cases where the instability of the compensator appears to result in poor overall system sensitivity are to variations in plant parameters as is shown in [4].

The motivation behind the simultaneous control problem is to control a nonlinear system, represented by linear models at different operating points, using one controller. In this case, each linear model represents an operating point. The parameter variations of the system model form a low-frequency upper bound on the singular values of the loop gain transfer function. Some of the robust controller design methods, LQG/LTR for example, have no mechanism for dealing with this upper bound. On the other hand, the simultaneous control technique can make gain scheduling easier to implement by reducing the number of operating points to be scheduled. This is accomplished by grouping the total number of pre-specified operating points into classes. A different controller is then designed for each of these classes [5]. Another use of the simultaneous control is in the design

of controllers that are robust against sensor or actuator failures. When a sensor or an actuator fails during operation, the system characteristics change, effectively generating a new system. Simultaneous control design can be used to design a single controller that gives good performance for both the original system and the new system generated by the failure.

The simultaneous control problem has attracted many researchers over the last many years. Some of the results for single-input single-output (SISO) transfer functions were reported in [6,7]. Peterson [8] obtained a nonlinear state feedback controller that quadratically stabilized a set of single-input linear systems simultaneously. Schmitendorf [9] acquired a sufficient condition for the existence of a stabilizing linear state feedback for a collection of single-input linear systems. Miller [10,11] employed linear periodically time-varying controllers for the simultaneous stabilization and disturbance rejection for a set of linear systems. Suryanarayana et al. [12] have also addressed the problem of simultaneously stabilizing controllers for automated vehicles. Strong simultaneous stabilization of linear systems is addressed in [15,16]. Wang et al. [17] and, subsequently, Cai et al. [18] have also addressed the problem of simultaneous stabilization of nonlinear systems. In this paper a design technique for the stabilization of M continuous systems by a single output feedback controller has been developed.

II. METHODOLOGY

Consider the system:

$$\dot{x} = A(q)x + B(q)u$$

(1)

$$y = C(q)x$$

Where q is a vector of dimension v , and the value of q determines the system matrices. The above system may represent a linear approximation of a non linear system at different operating points. It may also represent an uncertain plant. In the first case, q is used as an index for identifying operating points while in the second case q may represent intervals of uncertainties of system's parameters.

Definition 1. The region of operation of the above system is the domain of q .

Definition 2. The linear systems

$$\dot{x} = A_i x + B_i u$$

$$y = C_i x$$

(2)

$i = 1, \dots, M$, represent the system in (1) if the stabilization of the M systems in (2) guarantees the stabilization of (1).

Assume that the M systems in (2) represent the system in (1). We also assume that each of the M systems in (2) is stabilizable by output-feedback controller, and we seek an output-feedback controller K which stabilizes the system in (1) for some values of q . The following theorem shows how to construct such a controller.

Theorem. An output feedback controller $u(t) = Ky(t)$ which stabilizes the system in (1) exists if there exist Q_i 's and R_i 's such that

$$Q_i + C_i' K_i' R_i K_i C_i + C_i' \sum_{j \neq i} K_j' B_j' P_j + P_j B_j \sum_{j \neq i} K_j C_j > 0, i=1, \dots, M$$

(3)

Where K_i is given by

$$K_i = R_i^{-1} B_i' P_i N_i C_i' (C_i N_i C_i')^{-1}$$

(4)

P_i is given by

$$(A_i - B_i K_i C_i)' P_i + P_i (A_i - B_i K_i C_i) + Q_i + C_i' K_i' R_i K_i C_i = 0$$

(5)

And N_i is the solution of

$$N_i (A_i - B_i K_i C_i)' + (A_i - B_i K_i C_i) N_i + I = 0$$

(6)

Proof

Define Lyapunov function $V_i = x^t P_i x$

Where P_i is a positive definite matrix. Using the controller in (4), system (1) is stable if the derivatives of V_i with respect to time

$$\dot{V}_i = x [A_i^t P_i + P_i A_i] x + u B_i^t P_i x + x P_i B_i u$$

are negative for all $i = 1, \dots, M$. Choose P_i as the solution of (5), the derivative of V_i will be negative if and only if (3) is satisfied.

III. EXAMPLE

Consider the stabilization of the short-period longitudinal modes of the McDonnell Douglas F4-E aircraft. This is a three-state model. The states are normal acceleration, pitch

rate, and elevator angle. Consider two operating points representing (1) Mach 0.5, altitude 5000ft., and (2) Mach 9, and altitude 35,000 ft. The system matrices corresponding to these flight conditions are:

$$A_1 = \begin{bmatrix} -0.9896 & 17.41 & 96.15 \\ 0.2648 & -0.8512 & -11.39 \\ 0.0 & 0.0 & -30.0 \end{bmatrix},$$

$$A_2 = \begin{bmatrix} -0.6607 & 18.11 & 84.34 \\ 0.08201 & -0.6587 & -10.81 \\ 0.0 & 0.0 & -30.0 \end{bmatrix},$$

$$B_1 = \begin{bmatrix} -97.78 \\ 0.0 \\ 30.0 \end{bmatrix}, B_2 = \begin{bmatrix} -272.2 \\ 0.0 \\ 30.0 \end{bmatrix},$$

and

$$C_1 = C_2 = \begin{bmatrix} 1 & 0 & 0 \\ 0 & 1 & 0 \end{bmatrix}.$$

Using the result, the output-feedback controller is

$$K = [-4.141 \quad -2.923],$$

which is found using (3) – (6). The designed controller stabilizes both operating points. The eigen values of first operating point are $-4.33.02 - 1.86 \pm 7.48j$ and the second operating point has eigenvalues -135.3, -1.8 and -20.3. Figs 1 and 2 show the impulse responses of the uncontrolled and controlled system with the designed controller for first as well as for second operating point.

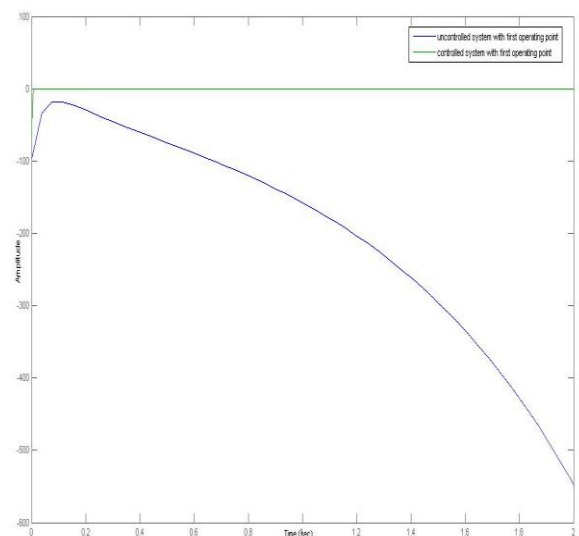


Figure1. Impulse responses of the uncontrolled system and the controlled system with the designed controller at first operating point

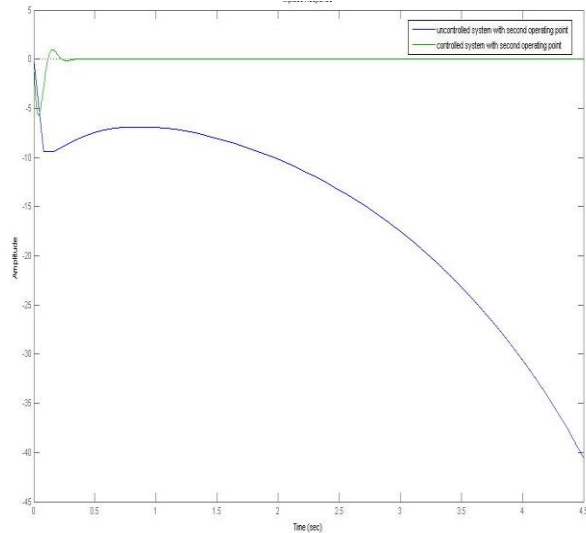


Figure2. Impulse responses of the uncontrolled system and the controlled system with the designed controller at second operating point

IV. CONCLUSION

The paper has utilized the state and control weighing matrices of the LQR output-feedback controller for solving the problem of stabilization more than one system by a fixed controller. The stabilization of aircraft at two different operating points is presented.

REFERENCES

- [1] V. Blondel , *Simultaneous stabilization of Linear Systems* (Lecture Notes in Control and Information Sciences 191, Springer-Verlag, Berlin, 1994).
- [2] J.Ackermann, *Uncertainty and Control*, (Lecture Notes in Control and Information Sciences 70, Springer-Verlag, Berlin, 1985).
- [3] Alos , Stabilization of A Class of Plants with Possible Loss of Outputs or Actuator Failures, *IEEE Trans. Automatic Control*, 28(2), 1983, 231-233.
- [4] J. Ackermann, Parameter Space Design of Robust Control Systems, *IEEE Trans. Automatic Control*, 25(6), 1980, 1058-1082.
- [5] Al. F. Sunni, and F. L. Lewis, Gain scheduling simplification by simultaneous stabilization, *Trans. ASME: J. Guidance, Control, and Dynamics*, 16(3), 1993,602-603.
- [6] B.Ghosh and C. Byrns, Simultaneous stabilization and pole placement by nonswitching dynamic compensation, *IEEE Trans. Automat. Control*, 28, 1983, 735-741.
- [7] D.Looze, A dual optimization procedure for linear quadratic robust control problems, *Automatica*, 19, 1983, 299-302.
- [8] I.Peterson, A procedure for simultaneously stabilizing a collection of single input linear systems using nonlinear state-feedback control, *Automatica*, 23, 1987,33-40.
- [9] W. Schimitendorf, and C.Holot, Simultaneous stabilization via state feedback control, *IEEE Trans. Automat. Control*, 34(9), 1989, 1001-1005.
- [10] D. E. Miller, and Chen T.W., Simultaneous stabilization with near-optimal H performance, *IEEE Trans. on Automatic Control*, 47(12), 2002, 1986-1998.
- [11] D. E. Miller, and M. Rossi, Simultaneous stabilization with near-optimal LQR performance, *IEEE Transactions on Automatic Control*, 46(10), 2001, 1543-1555.
- [12] S. Suryanarayanan ,M. Tomizuka , and T. Suzuki , Design of Simultaneously Stabilizing Controllers and Its Application to Fault-Tolerant Lane –Keeping Controller Design for Automated Vehicles, *IEEE Trans. Automatic Control*, 12(3), 2004, 329-339.
- [13] M.Jing, and M.Kun, Simultaneous stabilization for a class of generalized linear systems, *Ninth International Conference on Hybrid Intelligent Systems*, 3, 2009, 499-503.
- [14] S.K. Korovin, A.V. Kudritskii and A.S. Fursor, A remark on the simultaneous α -stabilization of linear plants, *Differential Equations*, 45(5), 2009, 713-720.
- [15] Y.Z. Wang, G.Feng, and D.Z. Cheng, Simultaneous stabilization of a set of nonlinear port-controlled Hamiltonian systems, *Automatica*, 43(3), 2007, 403-415.
- [16] X.S. Cai, Z.Z.Han and W.Zhang, Simultaneous stabilization for a collection of multi-input nonlinear systems with uncertain parameters, *Acta Automatica Sinica*, 35(2), 2009, 206-209.

Theoretical Model of Absorber for Miniature LiBr-H₂O Vapor Absorption Refrigeration System

¹Manu.S

Dept.of Mech. Engg.,
Sri Siddhartha Institute of Technology, Tumkur

³T.B.Prasad

Dept. of Mech. Engg.,
Sri Siddhartha Institute of Technology, Tumkur

²T.K.Chandrashekar

Dept.of Mech.Engg.,
Sri Siddhartha Institute of Technology, Tumkur

⁴Nagendra

Dept.of Mech.Engg.,
Sri Siddhartha Institute of Technology, Tumkur

ABSTRACT

Convective air cooling techniques are facing difficulties in removing high heat flux under limited space for thermal management. In order to overcome this problem the researchers are developing new technologies like microchannel heat sink, heat pipes and miniature refrigeration system. Among all the methods, refrigeration is the promising technology to overcome the problem. The absorption based heat pump system pressurizes the fluid by chemical compressor and consumes less power compared with the mechanical compressor. The coefficient of performance of this system is more compared with the other systems. In absorption based refrigeration system the absorber is widely acknowledged as the bottle neck which defines the performance and cost of the system. On account of these drawbacks, the present study aims to design the absorber for miniature LiBr-H₂O Vapor Absorption Refrigeration for cooling electronic devices.

Keywords - : Absorber; LiBr-H₂O; Miniature

I. INTRODUCTION

Recent advances in semi conductor technologies are accompanied by rapid increase in the power density levels from high performance chips such as microprocessors, IC chips etc.. Convective air cooling techniques are facing difficulties in removing high heat flux under limited space for thermal management. The researchers are developing new technologies like microchannel heat sink, heat pipes, miniature refrigeration system and etc... Among all the methods of cooling, refrigeration is the promising technology to overcome the problem. In this aspect, small miniature vapor compression system for electronics cooling

which remove 50W of heat from central processing unit having Coefficient of Performance of 2.25 [Mongia et.al, (2006)]. [Drost and Friedrich, (1997)] developed the mesoscale water lithium bromide absorption based heat pump system for portable and distributed space conditioning applications with 350W of cooling capacity. The merit of system is, it uses the chemical compressor which is driven by heat [A.Beutler et.al (1997), Yoon Jo Kim et.al (2008)].

In the chemical compressor the power consumption for liquid compression is less compared to mechanical compression. LiBr (Lithium-Bromide)/water pair absorption

system possesses several advantages over the other types of absorption systems such as highest Coefficient of Performance compared to other absorption units operating under same conditions. The system works efficiently without the need of rectification columns and a basic generator is sufficient to vaporize the water, as the absorbent is non-volatile and having higher evaporating temperature. This will be beneficial for the cooling of electronic device operating under room temperature.

In absorption refrigeration system the absorber is widely acknowledged as the bottle neck which defines the viability of the entire absorption cycle and also it is the most critical component in absorption heat pump system in terms of cycle performance and system cost [A.Beutler et.al (1997), J.D Killion and Garimella (2001)]. The different models of absorber were analyzed based on working fluid pair like ammonia/water and water/LiBr. The LiBr is non volatile and the water vapor will be in pure state as such there is no resistance to mass transfer in the vapor phase during the absorption process [Killion and Garimella (2001)].

The appropriate relations for describing the properties of the working fluid for different operating conditions were mentioned in design and construction of the vapor absorption system [G.A Florides et.al, (2003)]. The series of experimental studies on falling film absorber for smooth horizontal tubes were carried out. The results reveal that, effect of cooling water inlet temperature on absorber performance is significant as the cooling water inlet temperature decreases; there is an enhancement in the heat transfer coefficient. In addition to that, inlet solution concentration of LiBr has a critical impact on heat transfer coefficient. As the inlet concentration increases there is an increase in the heat transfer coefficient [S.M Deng and W.B.Ma (1999)]. From the numerical model of the vertical absorber provides relation between inlet temperature of coolant and size of the absorber [A. Yigit, (1999)]. By providing the flow guidance medium between the falling film and the coolant tube results in the reduction of the absorber size without affecting the vapor and coolant side pressure drop [Nitin Geol and D.Yogi Goswami (2005)].

The series of experiments by [William Miller and Majid Keyhani(2001)] on simultaneous heat and mass transfer on a vertical falling film absorber showed that local heat and mass transfer rates are linear along the length of the

absorber. The correlation of Nusselt and Sherwood Number provides the simple calculation for load and mass absorber under given inlet conditions of the absorber. The experiments on the adiabatic vapor absorption into aqueous LiBr solution for three different arrangements like mono-disperse droplets, unstable jets breaking into Poly-disperse droplets and film falling ramps by [D.Arzo et.al (2005)]. The results showed that falling film can handle higher flows per unit of disperse area and simultaneously, offer more contact area with water vapor pre-unit length. [Vinod Naryan and Jeromy Jenks, (2008)] have found that as the channel depth increases there is decrease in the overall heat transfer coefficient for weak solution and increases for vapor refrigerant in the Micro scale-Film Ammonia-water bubble. In the light of the above, the present work is focussed on systematic miniature absorber for vapor absorption refrigeration system working under minimum load.

II. CYCLE DESCRIPTION

A single effect LiBr water absorption refrigeration system is shown in the Fig.1. The water was used as a refrigerant and LiBr used as absorbent in the present system. The heat was added to the weak solution in generator which boils the refrigerant and flows into the condenser. The refrigerant rejects the heat as it condenses in the condenser and flow restrictor reduces the pressure and temperature of the refrigerant. The low pressure and temperature liquid refrigerant enters into the evaporator. In the evaporator liquid refrigerant evaporates by absorbing the heat and flows to the absorber. The vapor refrigerant (water) is absorbed by the strong LiBr solution forming the weak solution in the absorber and this process is exothermic. The weak solution is pumped to the generator through the liquid heat exchanger. The remaining strong solution in the generator flows to the absorber through the liquid heat exchanger and flow restrictor. In liquid heat exchanger, heat flows from the strong solution to weak solution and temperature, pressure were reduced in the flow restrictor.

Improving the performance of the absorber directly increases the efficiency of the system. The absorber is the largest part of the system. The literature reveals the different design of the absorber by changing the configuration such as tube spacing, tube diameter, tube length, tube material and different operating conditions. Since the absorption is associated with heat and mass transfer. The vapor flow mechanism divides the absorber into two broad categories namely, falling film absorption and bubble absorption mode. The falling film mode was widely accepted because of its simplicity and effectiveness with respect to heat and mass transfer. The absorber is also been categorized as counter flow and co current flow based on the direction of the flow. Since The counter flow is an attractive approach in which rate of heat and mass transfer is more compared with the other.

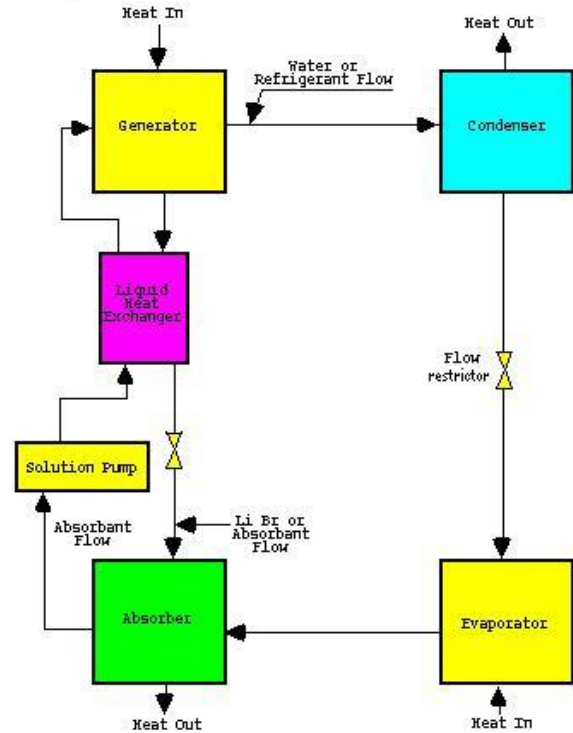


Figure 1: Description of LiBr Absorption Refrigeration Cycle

One of the disadvantage of vapor absorption refrigeration was its large size of components especially the absorber which is the most critical component and its characteristics have significant effect on the overall system performance. So in order to miniaturize the absorption system, it is necessary to miniaturize the absorber. In this context the paper aims in the efficient design of the miniature absorber having high heat and mass transfer coefficients by providing minichannel.

III. CONCEPTUAL DESIGN

Since the absorption process is associated with heat and mass transfer, the various system parameters are included in the designing a miniature absorber. The main parameters that can be grouped are as follows:- 1) Operating parameters, 2) Geometric parameters & 3) Thermal/Fluid parameters based on Weilin and Issam Mudwar for the heat sink.

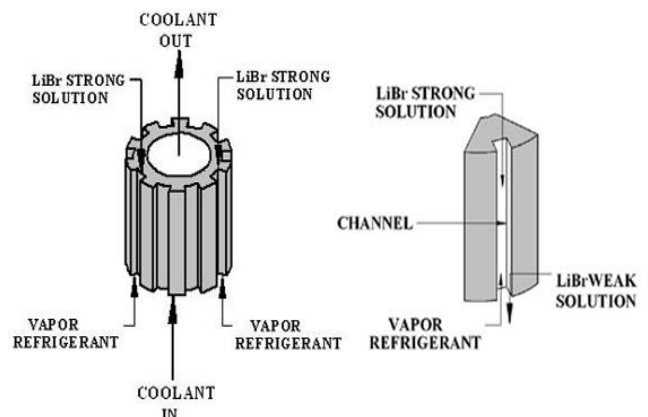


Figure 2: Miniature of Absorber

The Fig. 2 illustrates the construction of a minichannel absorber like minichannel heat sink with a coolant system. The absorber was made by high thermal conductivity material such as aluminum. In order to obtain the compactness, series of vertical parallel mini-slots of different ranges hydraulic diameters were cut on the circumference and centre hole was drilled at the centre for the coolant.

The Fig 2 shows the conceptual diagrams of the liquid cooled counter flow falling film absorber. It is shown that the refrigerant vapor flows through outer channels and the aqueous LiBr solution counter-currently flow along the outer channel walls which are cut on the circumference. All the heat generated during the absorption process is rejected to the coolant through the cylinder wall. A liquid cooling scheme provides higher heat transfer coefficient and lower coolant temperature than air cooling leads to improve the absorber performance.

IV. SOLUTION SIDE

4.1 OPERATING PARAMETERS

The operating parameters represent the condition under which the absorber is expected to operate. They are inlet strong solution concentration (x_{ss}) and outlet weak solution concentration (x_{ws}), inlet mass flow rate of strong solution (m_{ss}), inlet mass flow rate of refrigerant (m_r) and outlet mass flow rate of weak solution (m_{ws}), inlet strong solution temperature (T_{ss}) and inlet refrigerant temperature (T_r) and outlet weak solution temperature (T_{ws}). One of the important considerations in designing absorber is the absorber temperatures (T_{ws}), Generator temperatures/ Bubble pump temperature (T_g), Condenser temperatures (T_c) and Evaporator temperatures (T_e) and their pressures. [F.L Lansing] provided the systematic model for determination of the operating parameters and it as follows.

Temperature of the strong solution enters in to the absorber is given by:

$$T_{ss} = T_g - z(T_g - T_{ws}) \quad 1$$

Based on generator and condenser temperature the concentration of strong solution is given by:

$$x_{ss} = \frac{49.04 + 1.25T_g - T_c}{134.65 + 0.47T_g} \quad 2$$

In consideration of absorber and evaporator temperature the concentration of weak solution is given by:

$$x_{ws} = \frac{49.04 + 1.25T_a - T_e}{134.65 + 0.47T_a} \quad 3$$

Based on the heat load the mass flow rate of refrigerant is given by

$$m_r = \frac{Q_e}{h_{eout} - h_{cout}} \quad 4$$

Where, h_{eout} outlet enthalpy of refrigerant which is coming out of evaporator

$$h_{eout} = (572.8 + 0.417T_e)4.187 \quad 5$$

Where, h_{cout} outlet enthalpy of refrigerant which is coming out of condenser

$$h_{cout} = (T_c - 25)4.187 \quad 6$$

Mass flow rate of strong solution is given by:

$$m_{ss} = m_r \left(\frac{x_{ws}}{x_{ss} - x_{ws}} \right) \quad 7$$

Mass flow rate of weak solution weak solution is given by:

$$m_{ws} = m_r \left(\frac{x_{ss}}{x_{ss} - x_{ws}} \right) \quad 8$$

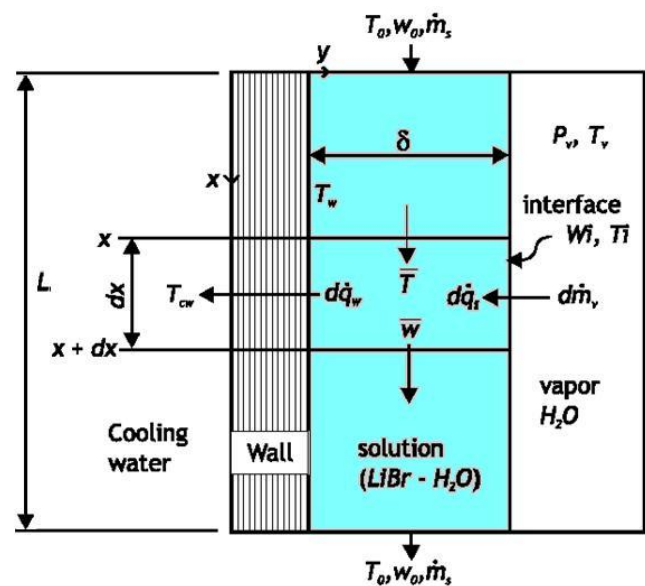


Fig 3: Schematic of the Model (Khalid, 2001)

The properties of solution were determined by average temperature of inlet and outlet of absorber but refrigerant properties are found at the evaporator temperature.

4.2 Thermal/Fluid Parameters and geometric parameters

The parameters are dependent transport parameters that determine the performance of absorber under given operating and geometric parameters. Geometric parameters includes length, diameter, width of channel, depth of channel, thickness of the fin and the thermal parameters include heat and mass transfer coefficient, pressure drop etc... Due to the negligible frictional losses the pressure drop is neglected. The absorber model started with following assumptions and the procedure of Wassenaar, Reinderhette (2008).

- The liquid is Newtonian has constant physical properties. The values of the properties based on the liquid entry conditions.
- The film flow may be considered laminar and one dimensional.
- Momentum effects and shear stress at the interface are negligible.
- The absorbed mass flow is small relative to the film mass flow.
- At the interface, thermodynamic equilibrium exists between the vapor and liquid. The relation between surface temperature and mass fraction is linear with constant coefficient at constant pressure.
- All the heat of absorption is released at the interface.
- The liquid is a binary mixture and only one of the components is present in the vapor phase
- There is no heat transfer from the liquid to vapor and no heat transfer because of radiation, viscous dissipation, pressure gradient or gravitational effects.
- There is no diffusion because of pressure gradient, temperature gradient or chemical reactions.
- Diffusion of heat and mass in the flow direction is negligible relative to the diffusion perpendicular to it.

Under the above assumption, the equations of momentum, energy and diffusion of mass and their specific boundary are represented in four dimensionless combined ordinary differential equations [19-11] as below. These equations describe the average mass fraction of water in the solution, the average solution temperature, the heat transfer to the cooling medium across the plate wall per unit width (dq_w), and the mass fraction of the water vapor to the film per unit width (dm_v), in one infinitesimal part of the film with length (dx) as shown fig 3.

Change of average mass fraction of water is given by [Wassenaar, Reinderhette (2008)]:

$$d\gamma = \frac{-A}{m_s (T_{eq} - T_o)} \left[1 - (w_{eq} - w_o) \bar{\gamma} - w_o \right] dm_s \quad 9$$

Where, $m_s = \rho_s \Gamma_v$

The change in the Mass transfer of the water vapor to film is given by [Wassenaar, Reinderhette (2008)]:

$$dm_v = \frac{m_s dFo (w_{eq} - w_o) (1 - \bar{\gamma} - \bar{\theta})}{\frac{1}{Le} \left[\frac{A(1 - w_o)}{Nu_i} - \frac{1}{Sh} \right]} \quad 10$$

The average solution temperature change is given by [Wassenaar, Reinderhette (2008)]:

$$d\theta = \frac{1}{m_s C_p (T_{eq} - T_o)} \left\{ \left[h_m + \phi_w (w_{eq} - w_o) \bar{\gamma} \right] dm_v - dq_w \right\} \quad 11$$

Heat transfer to cooling medium across the plate is given by [Wassenaar, Reinderhette (2008)]:

$$dq_w = \frac{C_p m_s dF_h (T_{eq} - T_o) (\bar{\theta} - \theta_c)}{\left[\frac{1}{Nu_w} + \frac{1}{Nu_c} \right]} \quad 12$$

Dimensionless temperature is given by [Wassenaar, Reinderhette (2008)]:

$$\theta = \frac{(T - T_o)}{(T_{eq} - T_o)} \quad 13$$

Dimensionless mass fraction is given by [Wassenaar, Reinderhette (2008)]:

$$\gamma = \frac{(w - w_o)}{(w_{eq} - w_o)} \quad 14$$

Sherwood number (Sh) is given by [Wassenaar, Reinderhette (2008)]:

$$Sh = 0.69 (Fo Le)^{-0.5} \quad 15$$

A good estimation for Nusselt, found analytically [Khalid A. Joudi, and Ali H.Lafta, (2001), Wassenaar, Reinderhette (2008)]

These numbers are

$$Nu_i = 2.67$$

$$Nu_w = 1.6$$

Constant in interface thermodynamic equilibrium [Wassenaar, Reinderhette (2008)]:

$$A = \frac{-\rho_s D_s h_m}{[(1-w_o)k_s C_1]} \quad 16$$

Lewis number is given by [Wassenaar, Reinderhette (2008)]:

$$Le = \frac{D_s}{\alpha_s} \quad 17$$

Heat of absorption is given by [Wassenaar, Reinderhette (2008)]:

$$h_m = h_v - [h_{ss} + (1-w_o)\phi_w] \quad 18$$

Dimensionless x (heat transfer Fourier number) is given by Wassenaar, Reinderhette (2008)]:

$$Fo = \frac{x\alpha_s}{\delta_s \Gamma_v} \quad 19$$

Volumetric flow rate per wetted length is given by [Wassenaar, Reinderhette (2008)]:

$$\Gamma_v = \frac{m_{ss}}{2L\rho_s} \quad 20$$

Wassenaar, Reinderhette (2008) provides Solution film thickness based on volumetric flow rate per wetted length is given by

$$\delta_s = \left(\frac{3v_s \Gamma_v}{g} \right)^{\frac{1}{3}} \quad 21$$

The Equilibrium temperature and Equilibrium mass fraction of water are defined under the above assumption, by a linearization of the thermodynamic equilibrium equation of LiBr-H₂O solution at a fixed pressure. The equilibrium equation is expressed in the solution temperature T_s as a function of the LiBr concentration (X) in the solution and the vapor pressure (P) or refrigerant temperature $T_e=f(X, P)$ or $T_s=f(X, T_r)$. [Khalid, (2001)]

$$T_s = C_1 w_{eq} + C_2 \quad 22$$

Where

$$C_1 = -21.8789 - 0.58527T_r$$

$$C_2 = 0.0436688 + 1.407T_r$$

Equilibrium temperature is given by Wassenaar, Reinderhette (2008)

$$T_{eq} = C_1 w_o + C_2 \quad 23$$

Equilibrium mass fraction of water is given by [Wassenaar, Reinderhette (2008)]

$$w_{eq} = \frac{1}{C_1} (T_o - C_2) \quad 24$$

By integrating the differential equations and by assuming the length and width of the absorber until the equation are balanced. The obtained width of the absorber is converted into circular dimension. The circumference of the cylinder is same as the perimeters of a rectangular wall by this the diameter of the circle is determined. And the complete channel geometry can be determined by assuming the aspect ratio, hydraulic diameter and fin spacing ratio of the channel.

Aspect ratio is given by:

$$\beta_s = \frac{a_s}{b_s} \quad 25$$

Fin spacing ratio is given by

$$FA_s = \frac{t_s}{b_s} \quad 26$$

Hydraulic diameter is given by

$$D_{hs} = \frac{2a_s b_s}{a_s + b_s} \quad 27$$

No of channels is given by:

$$N_s = \frac{\pi d_s}{a_s + t_s} \quad 28$$

By assumed the cooling plate is fully wet by the liquid film so that there is no direct contact or heat exchange between the refrigerant vapor and cooling plate is allowed and thermal equilibrium exist at the interface between the aqueous LiBr solution and refrigerant vapor and also mass transfer driven by thermal and pressure difference is regarded to be negligible [Yoon Jo Kim et.al (2008),W.Wilke (1962)] developed the correlation for heat

transfer coefficient between the cooling plate and liquid film solution is determined by:

$$h_s = 1.88 \frac{k_s}{\delta}$$

Where, δ is the film thickness

$$\delta = \left[\frac{3\mu\Gamma}{\rho_s^2 g} \right]^{1/3}$$

Mass transfer coefficient for the range $40 < \text{Re}_{\text{film}} < 280$ and $\text{Sc} < 2.13 \times 10^5 / \text{Re}_{\text{film}}^{1.6}$, is given by [Yoon Jo Kim et.al (2008)]

$$k_m = 3.7522 \text{Re}_{\text{film}}^{1/3} \cdot \frac{D_{AB}}{S_r}$$

Where, Re_{film} Reynolds number of the film

$$\text{Re}_{\text{film}} = \frac{4\Gamma}{\mu}$$

To account for heat and mass transfer at the interface, the modified heat transfer coefficient is given by [Yoon Jo Kim et.al (2008)]

$$h_s^* = \frac{N \cdot c_{ps}}{1 - e^{-\left(\frac{N \cdot c_{ps}}{h_s}\right)}}$$

The wall temperature at the solution side can be determined by [Yoon Jo Kim et.al (2008)]

$$\frac{d(m_s \cdot h_s)}{dz} = h_s \cdot p_s (T_w - T_s) + h_s^* \cdot p_s (T_i - T_s) + \frac{d m_{ss}}{dz} h_{si}$$

Liquid vapor interface temperature by [Yoon Jo Kim et.al (2008)]

$$T_i = \frac{q_{\text{sen.l}}}{h_s^* p_s L} + T_s$$

Perimeter of the solution

$$P_s = [2[\delta] + a_s]$$

Perimeter of refrigerant

$$P_r = [2[b_s - \delta] + a_s]$$

The mean of inlet and outlet wall temperature at solution side of the absorber determines the final wall temperature of solution side.

V. COOLANT SIDE

5.1 Operating Parameters

The operating parameters represent condition under which the Absorber coolant side is expected to operate. They include material, type of coolant, Inlet temperature (T_{ci}), Outlet temperature (T_{co}), Mass flow rate of coolant (m_c), total heat (Q_a) represents the heat absorbed by the coolant. By assuming coolant only absorbs the heat and the complete surface is insulated and temperature rise is limited to 10°C .

$$m_c = \frac{C_{p,c}(T_{c,o} - T_{c,i})}{Q_a}$$

5.2 Thermal/Fluid Parameters

The parameters are dependent transport parameters that determine the performance of Absorbers under given operating and geometric parameters. Thermal parameters includes heat transfer coefficient, pressure drop etc...

5.3 Heat transfer coefficient for coolant side

[Satis G. Kandlikar et.al (2006)] provides the Nusselt number for fully developed laminar flow in ducts,

$$\text{Nu} = 3.66$$

Heat transfer coefficient (h_c) in coolant side is given by:

$$h_c = \frac{\text{Nu}_c k_c}{D_c}$$

By neglecting the conductive resistance, the Overall heat transfer coefficient is given by:

$$\frac{1}{U} = \frac{1}{h_s} + \frac{1}{h_c}$$

Logarithmic mean temperature difference is given by:

$$\text{LMTD} = \frac{(T_a - T_{c,i}) - (T_a - T_{c,o})}{\ln \left(\frac{T_a - T_{c,i}}{T_a - T_{c,o}} \right)}$$

Number of channels in coolant side is given by:

$$Q = UA_c \text{LMTD}$$

5.4 Geometric Parameters

The geometric parameters include miniature Absorber are illustrated in Fig.3. The overall Absorber dimensions are length (L), Diameter (d_c).

The thickness of wall between solution side and coolant side is proportional to the thermal conduction resistance between the solution side and the coolant side due to this, the thickness always should less so that all the heat will be absorbed by the coolant. Surface area of the coolant side (A_c) is given by

$$A_c = \pi d_c L_c \quad 43$$

VI. THEORETICAL RESULTS

The thermodynamic properties of solution and refrigerant are determined by relations given by G.A Florides et.al, (2003).The above model theoretically designed and the results are tabulated as below:-

Table 1:Thermal/ Fluid Parameters

Parameter	Values
Heat transfer coefficient between the cooling plate and liquid film in W/m^2K	25453
Average wall temperature between inlet and outlet in $^{\circ}C$	38
Coolant side heat transfer coefficient W/m^2K	1050
Overall heat transfer coefficient W/m^2K	1008

Table 2:Operating parameters for solution

Parameter	Values
Fluid	Steam and LiBr
Generator Temperature in $^{\circ}C$	70.88
Condenser Temperature in $^{\circ}C$	49
Evaporator Temperature in $^{\circ}C$	24
Absorber Outlet Temperature in $^{\circ}C$	32.35
Evaporator Load in W	100
Absorber Load in W	108
Refrigerant flow rate in kg/s	4.2×10^{-5}
Strong Solution Concentration in kg LiBr	0.475
Weak Solution Concentration in kg LiBr	0.41
Mass flow rate of strong solution in kg/s	2.69×10^{-4}
Mass flow rate of weak solution in kg/s	3.120×10^{-4}
Operating Pressure in Pa	3000

Table 3:Geometric Parameter for Solution and Refrigerant

Parameter	Values
Length in m	0.08
Width in m	0.075
Diameter in m	0.05
Hydraulic Diameter in m	0.003
Fin spacing ratio (α)	0.16
Material	Aluminum
Channel Geometry	
Depth in m	0.002
Width in m	0.01
Thickness in m	0.00095
No. of channel (N)	13

Table 4:Geometric parameters for Coolant

Parameter	Values
Length in m	0.08
Hydraulic Diameter in m	0.003
Material	Aluminum

Table 5:Operating parameters for coolant

Parameter	Values
Temperature rise in $^{\circ}C$	10
Inlet temperature in $^{\circ}C$	26
Mass flow rate in kg/s	2.58×10^{-3}

VII. Conclusion

The paper concludes with following results:-

- The design procedure developed for miniature based is simple and systematic.
- The design procedure based on different parameters like operating, geometric and thermal/fluid.
- The theoretical results showed the enhancement in the heat transfer coefficient $25453 W/m^2K$ and mass transfer coefficient $6.78 \times 10^{-5} m^2/s$ which leads to improve the performance of the system.

References

1. Beutler,; F.Ziegler;G.Alfed.(1996):Falling film absorption with solutions of a hydroxide mixture, International Absorption Heat Pump Confrence,Monteral,Cannada, pp.303-309.
2. R.Mongia,;K.Masahiro,;E.Distefano,;J.Barry,;W.Chen,; M.Izenson,;F.Possasami,;A.Zimmermann,;M.Mochizuki.(2006):Small scale refrigeration system for electronic cooling within note book computer, Proc.Tenth Intersociety confrence on Thermal and Thermomechanical Phenemenon in Electronics system,San Diego, USA, pp.751-758.
3. Drost,;Friedrich.(1997):Miniature heat pump for portable and distributed space conditioning application: Proc. Thirty-Second Intersociety Energy Conversion Engineering Confrence,Honolou, Hawaii,USA, pp.1227-1274.
4. Yoon Jo Kim,;Yogendra K.Joshi,;Andrei G.Fedrov.(2008): Performance Analysis of air-cooled microchannel absorber in absorption-based miniature electronic cooling system, Journal of Mechanical Science and Technology, 22, pp.338-349.
5. J.D Killon,; S.Garimella.(2001): A critical review of models coupled heat and mass transfer in falling film absorption, 24, pp.755-797.
6. S.M Deng,;W.B.Ma. (1999): Experimental studies on the characterstics of an absorber using LiBr/H2O solution as working fluid, International Journal of Refrigeration, 22, pp.1999.
7. Yigit.(1999):A Numerical Study of Heat and Mass Transfer in Falling Film Absorber, International Communication Heat Mass Transfer, 26(2), pp.269-278.

8. Nitin Geol.;D.Yogi Goswami. (2005):A Compact Falling Film Absorber,Journal of Heat Transfer,127, pp.957-1013.
9. G.A. Florides,; S.A. Kalogiroua,; S.A. Tassoub,; L.C. Wrobelb. (2003):Design and construction of a LiBr–water absorption machine, 44(15),pp.2483-2508.
10. William Miller,;Majid Keyhani.(2001):The Correlation of Simulataneous Heat and Mass Transfer Experimental Data for Aqueous Lithium Bromide Falling Film Absorption, 123, pp30-42.
11. D. Arzoz,; P. Rodriguez,; M. Izquierdo. (2005): Experimental study on the adiabatic absorption of water vapor into LiBr–H₂O solutions, 25, pp.797-811.
12. Vinod Naryan,; Jeromy Jenks. (2008); Effect of Channel Geometry variations on the performance of a constrained Microscale-Film Ammonia-Water Bubble Absorber, 130, pp. 1-9.
13. Wassenaar,;Reinderhette (2008): Simultaneous heat and mass transfer in a horizontal tube absorber: Numerical tools for present and future absorber designs (Ph.D. Thesis), Delft University of Technology,1994.
14. W.Wilke, 1962:Warmeubergang and riselfime,VDI-Forschungsheft 490,B28.
15. Satish G. Kandlikar,; Srinivas Garimella,; Dongqing Li, Stéphane Colin,; Michael R. King,2006: Heat Transfer and Fluid Flow in Minichannels and Microchannels, Elsevier publication, 1st Edn.
16. F.L Lansing,
http://ipnpr.jpl.nasa.gov/progress_report2/42-32/32AA.PDF, pp.1-11.
17. Khalid A.Joudi,;Ali H.Lafta.(2001):Simulation of a simple absorption refrigeration system, Energy Conversion and Management 42, pp.1575-1605.

w Mass fraction of the volatile component
X concentration
h_{si} Interface enthalpy
x Distance along co-ordinate axis in m
Z Effectiveness

Subscript

* Modified
a Absorber
c condenser, coolant
e Evaporator
eq Equilibrium
g Generator
i inlet
l Liquid
m mixing
o Entrance or outlet
r Refrigerant
s solution
sen Sensible
ss strong solution
ws Weak Solution

Greek words

γ Activity Coefficient / dimensional less mass fraction
A Constant in interface thermodynamic equilibrium
 α Thermal diffusivity in m²/s
 β Aspect ratio
 δ Film Thickness
 Γ Mass flow per wetted perimeter.
 μ Dynamic viscosity in pa-s
 ν Kinematic viscosity in m²/s
 θ Non dimensional less temperature
 ρ Density in kg/m³
 Γ_v Volume flow per wetted length

Nomenclature

A_c Area in m²
C1 Constant
C2 Constant
C_p Specific heat in kJ/kg
d Diameter
D_{hs} Hydraulic diameter in m
D_s Mass diffusivity in m²/s
FA_s Fin spacing ratio
Fo Heat transfer Fourier no
g Acceleration due to gravity in m²/s
h Enthalpy in kJ/kg
h Heat transfer coefficient in w/m²k
k Thermal conductivity in w/m.k
L Length in m
Le Lewis no
m Mass flow rate in kg/s
N No of Channel, Mass flux at the phase interface
Nu Nusselt number
P Perimeter in m
Q Heat load in W
Sh Sherwood number
T Temperature in °C
t thickness

Enhanced RSA Combined with DWT Domain Watermarking

Saira Varghese¹, Leda Kamal²

*(Department of Computer Science, Toc H Institute of Science & Technology, India)

** (Department of Computer Science, Toc H Institute of Science & Technology, India)

ABSTRACT

This paper presents a framework of combining enhanced RSA algorithm with watermarking techniques for hiding secret information in digital images. RSA algorithm is one of the widely used public key algorithms. Considering increment of security requirements, size of the keys has been larger. With key length growing, delay of exponentiation computation has changed into major problem in selecting longer keys. With enhanced RSA cryptosystem, delay in exponentiation calculation is reduced substantially. Encryption and watermarking are two major tools that can be used to prevent unauthorized consumption and duplications. Enhanced RSA encrypted data and watermark is embedded inside an HSV (Hue Saturation Value) color image using Discrete Wavelet Transform (DWT) algorithm. The accuracy of the wavelet transform is determined after reconstruction by calculating the Mean Square Error (MSE), Correlation and Peak Signal to Noise Ratio (PSNR) of the signal. The invisible robust watermarking using DWT leave the original data unchanged. The original plain text can be obtained by applying enhanced RSA decryption algorithm over the extracted cipher text.

Keywords - DWT, HSV, RSA, Watermarking.

1 INTRODUCTION

Information security is a fundamental requirement for an operational information society. Although issues considered as information security, such as secrecy of messages, privacy of communication, and reliable authentication, to name a few, have been important throughout history, developments in digital computing and information technology have set new requirements and challenges for them. The importance of information security has grown because new technologies have made accessing and misusing confidential information easier and more profitable.

Cryptography is defined as the science of using mathematics to encrypt and decrypt data that enables the storage and transmission of sensitive data in a secure manner. Cryptography has two processes; the first process is the encryption where the original data is converted into secured form using certain specified steps. The second process is the decryption, where the encrypted data is restored to the original form by applying the inverse to the steps applied in the encryption process. RSA (which stands for Rivest, Shamir and Adleman who first publicly described it) is an algorithm for public-key cryptography. It is the first algorithm known to be suitable for signing as well as encryption, and was one of the first great advances in public key cryptography. RSA is widely used in electronic

commerce protocols, and is believed to be secure given sufficiently long keys and the use of up-to-date implementations. Because of wide uses of networks during the last decade and growing security requirements in communication, public-key cryptosystems have been regarded highly. Nowadays choosing a key with 1024-bit length to apply in RSA is a good way to prevent analyses predictions, but in the near future 2048-bit and even 4096-bit key lengths will become available. Increasing number of multiplication operations is a problem that appears due to public-key growing and more operations means more delay in case of encryption and decryption in RSA. The modulo exponentiation in RSA has $2(k-1)$ multiplications in worst case and $(k-1)$ multiplications in best case where k is the number of bits in key[1]. In this context an enhanced RSA algorithm is used to increase the speed of exponentiation operation.

Watermarking represents an efficient technology for ensuring data integrity and data-origin authenticity. A watermarking algorithm consists of the watermark structure, an embedding algorithm, and an extraction, or a detection algorithm [2][3]. In multimedia applications, embedded watermarks should be invisible, robust, and have a high capacity. Invisibility refers to the degree of distortion introduced by the watermark. The literature survey explains robustness is the resistance of an embedded watermark against intentional attacks such as noise. DWT is any wavelet transform for which the wavelets are discretely sampled. As with others wavelet transforms, a key advantage it has over Fourier transforms is temporal resolution: it captures both frequency and location information (location in time) The Discrete Wavelet Transform (DWT), which is based on sub-band coding is found to yield a fast computation of Wavelet Transform. It is easy to implement and reduces the computation time and resources required. The basic idea of discrete wavelet transform (DWT) in image process is to multi-differentiated decompose the image into sub-image of different spatial domain and independent frequency district [3][4]. Then transform the coefficient of sub-image. After the original image has been DWT transformed, it is decomposed into 4 frequency districts which is one low-frequency district(LL) and three high-frequency districts(LH,HL,HH). Daubechies (db1) derives a family of wavelets, the first of which is the Haar wavelet. The db1 wavelet is same as Haar wavelet. The dwt2 performs single-level two-dimensional wavelet decomposition with respect to either a particular wavelet and computes the approximation coefficients matrix cA and details coefficients matrices cH , cV , and cD (horizontal, vertical, and diagonal, respectively). Single level inverse discrete 2D wavelet transform $idwt2$ performs a single-level two-dimensional wavelet reconstruction with respect to either a particular wavelet.

2 IMPROVED TECHNIQUES

3.1 Encryption and Watermark Embedding

2.1 Enhanced RSA Algorithm

The purpose of modular exponentiation is computing $M^e \pmod{n}$ to achieve the result with the least multiplication operation and memory requirements. The classical method to do modular exponentiation is binary method or square-and-multiply method. In binary method, exponentiation result can be achieved by squaring or squaring and multiplying depended on exponent's bits. The binary algorithm calculates exponentiation with $(k-1)$ to $2(k-$

1) multiplications according to Hamming weight of the exponent. To solve this problem, in improved exponentiation algorithm $M^e \pmod{n}$ is considered as a collection of 2^1 modular multiplications. ie squaring and multiplication is done in parallel. TABLE 1 presents the parallel computation[1]. The enhanced RSA algorithm uses this method for modular exponentiation.

Parallel Computation

Step	Squaring	Final Result(multiplication)
Initial	$M := M \pmod{n}$	If $(e_0=1)$ then $C := M \pmod{n}$ else $C := 1$
Parallel algorithm	for $j=1$ to l $M_j := M_{j-1} \times M_{j-1} \pmod{n}$	for $i=1$ to l if $(e_i \neq 0)$ $C := C \times M_i \pmod{n}$

2.2 Embedding encryption in Watermarking

The data encrypted using enhanced RSA algorithm is used for watermarking. In DWT-based watermarking, the DWT coefficients are modified to embed the watermark data [3]. Because of the conflict between robustness and transparency, the modification at a given level is usually made in HL, LH, and HH sub-bands[3]. To measure distortion and similarity between the original watermark (W) and the extracted watermark (W'), Peak Signal to Noise Ratio, Mean Square Error and Correlation are computed. These metrics will help the user decide if a watermark can be consistently recovered with the given method [5].

3 PROPOSED ALGORITHM

This paper proposes a new implementation of embedding enhanced RSA encrypted data in watermarking digital images. This architecture is presented using enhanced RSA algorithm and Discrete Wavelet Transform (DWT) for performing encryption and watermarking respectively. In watermarking Discrete Wavelet Transform(DWT) technique is used for achieving robustness.

1. Apply enhanced RSA encryption on plaintext to produce cipher text.
2. Read cover image and secret image.
3. Combine secret image and cipher text to generate the watermark.
4. Apply DWT on original image and watermark.
5. Add the watermark in original image using IDWT.

3.2 Watermark Distilling and Decryption

1. Obtain watermarked and encrypted image.
2. Recover watermark by taking the difference of watermarked and encrypted RGB image and the value part of HSV image.
3. Recover secret image by applying DWT.
4. Recover cover image by taking the difference between watermarked and encrypted RGB image and recovered watermark.
5. Recover cipher text from recovered watermark.
6. Calculate PSNR, MSE and Correlation Coefficient.
7. Apply enhanced RSA decryption to recover plaintext.

4 ANALYSIS

Nowadays choosing a key with 1024-bit length to apply in RSA is a good way to prevent analyses predictions, but in the near future 2048-bit and even 4096-bit key lengths will become available. Increasing number of multiplication operations is a problem that appears due to public-key growing and more operations means more delay in case of encryption and decryption in classical RSA. Enhanced RSA which uses improved exponentiation algorithm provides a solution to this problem.

The parameters such as Peak Signal to Noise Ratio (PSNR) for the host image, Correlation Coefficient (CC) and the Mean Square Error (MSE) for the watermark can be used to evaluate the performance of the watermarking technique used.

5 CONCLUSION

In this paper we have proposed a method for embedding encrypted messages in watermarked images. In the first phase encryption is performed using enhanced RSA algorithm and in the second phase watermarking is done using Discrete Wavelet Transform. This design combines the computational speed of enhanced RSA algorithm and robustness of DWT based watermarking technology. By combining these efficient techniques information security can be achieved. Peak Signal to Noise Ratio(PSNR), Correlation coefficient and Mean Square Error (MSE) metrics can be computed for the extracted watermark and the original watermark to examine the degree of distortion.

The proposed method grants the authenticity of the transmitted data, thanks to the watermarking technique, and the privacy, obtained through the encryption procedure.

Finally, the proposed method can be used for exchanging highly secret messages most likely for defense departments.

REFERENCES

- [1] S.Sepahvandi, M. Hosseinzadeh and K. Navi and A.jalali "An Improved Exponentiation Algorithm for RSA Cryptosystem "DOI 10.1109/ICRCCS, IEEE 2009.
- [2] Rawa I. Zaghoul, Enas F. Al-Rawashde. "HSV Image Watermarking Scheme Based on Visual Cryptography", *Proceedings of World Academy of Science, Engineering and Technology 44*, 2008.
- [3] Anumol T.J ,P Karthigaikumar, "DWT based Invisible Image Watermarking Algorithm for color Images," IJCA Special Issue on "Computational Science –New Dimensions and Perspectives," NCCSE 2011, pp 76-79.
- [4] Mei Jiansheng, Li Suleang and Tan Xiaomei, "A Digital Watermarking Algorithm Based On DCT and DWT," in *Proceedings of the 2009 International Symposium on Web Information Systems and Applications*, May 2009, pp 104-107 .
- [5] Emir Ganic ,Ahmet M Eskicioglu, "Robust DWT-SVD Domain Image Watermarking Embedding Data In All Frequencies," in *Proceedings of MM&SEC'04, 2004*, pp 166-174.

Security of Embedded Systems Applied in a Green-House Environment For Monitoring and Controlling Physical Parameters

Trailokya Oraon

Faculty, Master of Computer Application Department
Jorhat Engineering College
Jorhat, Assam, India

Nelson R Varte

Faculty, Master of Computer Application Department
Jorhat Engineering College
Jorhat, Assam, India

Abstract— Embedded systems are extensively use in the field of pervasive computing. These systems are use to such an extent that embedded systems are now controlled and monitored from remote locations. Both intranet and internet now extensively used to control embedded systems used in most areas of our life. With the introduction of Internet Protocol version 6 (IPv6) on the web, peer-to-peer communication between internet-enabled devices helped web services to make performance improvement. On the worse side, it created new attacks on the components used in the embedded systems. The paper discusses the details of security vulnerabilities of both stand-alone and web-enabled embedded systems used in greenhouse environment. To ensure the correctness of working of these devices monitored and controlled by different hardware and software components, security of the components is a major concern. Various vulnerabilities are introduced during entire development process of the greenhouse environment. The problem is to search the real threats, then define security policies and implement them during development process. The paper tries to find out possible security techniques to deal with the vulnerabilities. It shows to introduce security policies at various levels of life-cycle, be it before development or during development or after development.

Keywords- IPv6;Cryptography;System vulnerabilities; Security analysis ;Sockets;Threat Model

I. INTRODUCTION

Our lives and our businesses depend unavoidably on computing systems and, increasingly, on embedded systems in particular. Applications of embedded systems to monitor and control the greenhouse environment has become a notion of pervasive computing and now these computing devices can be applied and are available anywhere and anytime. Embedded systems are generally hidden from the user [1]. For example, its proper use in a greenhouse environment helps the crop-growers to maximize the productivity and better the quality of crops and seeds. Embedded products and tools that growers have at their disposal to control the environment are manipulated with respect to the important environmental influences on plant growth and development, for the actual optimization of the greenhouse environment. These embedded systems, which are ubiquitously used to sense, capture, store, process and transmit vital data used for control of the environment to maximize the photosynthetic process in the crop. Security observation is a basic requirement when an embedded system performs any of these tasks. As more and more embedded systems came to be accessed from remote

locations, security became a major concern. Security of embedded systems employed in greenhouse environment provided new business opportunities and also prevents dangers of economical loss. For example, it prevents undue change of environmental changes and should help preserve grower's expectations. Examples of new business opportunities are secure embedded devices that are applied for use in timely production of crops. With the adoption of Internet Protocol version 6 (IPv6), network solutions for embedded devices, peer-to-peer communication is now possible and thereby giving easy access and control of such devices from remote locations. This has resulted an increasing number of security breaches, which have been detected in embedded systems in recent years, which also reveals the importance of fundamental security solutions. Security solutions, which are basically applied to embedded systems that also incorporate the concept of network model, are specific cryptographic algorithms, adding security functionality to the network security protocols or adding one more security layer to the embedded device [2]. In general, most developers apply security 'patches' only at the beginning of implementation phase or only if a security faults is detected. The embedded system data processing itself is vulnerable to its own system. The paper discusses the various embedded system security issues with reference to systems employed in greenhouse environment.

It is often argued for giving too much importance to security of embedded systems [3]. Security policies should be implemented to tackle real threats. Vulnerabilities arises when a system is connected to network and also when working as a single system. Mere encryption and decryption of incoming and outgoing data does not provide a complete integrated solution of security. Security should not be on short term benefits, but long-term benefits should be taken keeping the cost factors into account.

II. LIFE-CYCLE OF EMBEDDED SYSTEM FOR GREENHOUSE ENVIRONMENT

In general, there are three phases of any embedded system: development, use and disposal.

- Development of the system for the environment
- Deployment and use of the system in the environment
- Disposal / Removal/ Transfer of the system from the environment

The "Development of the system for the environment" incorporates all activities starting from system requirement specification to acceptance testing. It also includes the

activities until the final system is delivered. All activities are carried out only after proper study of the environment and various climatic factors that are going to affect the system. The various activities of this phase are Requirement specification, Design, Production, Product Shipment and Support/ Maintenance. The “*Deployment and use of the system in the environment*” starts when the system passes user’s acceptance testing and the system is deployed in the environment. Deployment activities consist of installation of the system and configuring the system to match and create the greenhouse environment. Use phase consists of educating the users of the system, alternating periods of correct service delivery, service outage, service shutdown and maintenance. The “*Disposal / Removal/ Transfer of the system from the environment*” phase starts when the system no longer performs its activities. In such as case, the system may not be able to monitor and control the environment according to the requirement or the system may start malfunction under specific climatic changes. It can also start when the climate undergoes an abrupt change or the device is transferred from one person to another. Activities of this phase include removal of the storage media, software, components and data stored on the device. The significant aspect of this phase is that it prevents release of vulnerable data, information or software. In maintaining greenhouse environment, this phase will prevent flow or usage of data when the system is moved from one location to another. The security is needed to be considered in this phase to preserve and adhere to copyright, statutory and regulatory requirements, verify the authenticity, confidentiality and integrity of the system.

III. SOURCES OF VULNERABILITIES IN LIFE-CYCLE

It is important to analyze the vulnerabilities of each phase of life-cycle. Vulnerabilities and security threats can rise in every process and entities associated with processes created before, during or end of life-cycle of embedded system.

A. Vulnerabilities in Development Phase

The correct physical world phenomenon cannot be predicted at the start of a greenhouse environment project. Poor analysis of the environment conditions can be a source of vulnerability. In the development phase, the system and environment analyst who does not processes enough knowledge are a source of vulnerabilities. There may be some ‘harmful’ developers, who assist in this phase, whose aim is to harm the development phase with the available development tools, production tools and test tools, thus damaging hardware and software process and these can be the source vulnerabilities.

B. Vulnerabilities in Deployment and Use Phase

When system was brought to the environment, the persons responsible for installation and configuration, the administrators, users responsible for providing service, service providers, entities associated with the service, climatic conditions, natural disasters of the environment and adversaries from other living things of the environment are the source of the vulnerabilities. Improper handling of the system by users and lack of proper manual of running the system can be a source of vulnerability during the use phase. Though the basic source of new vulnerability during this phase is forcing the system to create the requisite environment even during the abrupt environmental climatic changes and conditions.

C. Vulnerabilities in Disposal/Removal/Transfer Phase

Security is not a major concern in design phase when the system is removed from the environment. A major source of vulnerability in this phase is when the system is transferred to another location with the information and data used in the previous location and the users are unaware about this fact. Available vulnerabilities and threats are ignored during security analysis when there is a complete discard of the system from the environment.

IV. SECURITY IN PRODUCT DESIGN METHODOLOGY

Our requirement defines the embedded system design, what product we are going to apply, whom we are asking for a solution. It may range from a least expensive thermostat to computer that uses microprocessors that controls variety of equipments used to perform specific task. For some, it is analog device that considers multiple sensors in a single environment when it performs control actions. But it is always a device with some RAM, ROM, storage media and some peripheral device performing some desired input and output. Design should support development process so that the result is outcome-oriented. Developers have enough flexibility to adopt new tools so that they can deliver the best to meet the governance criteria and schedule tasks according to the design. Design methodology helps to analyze the requirements, conceptualizing, planning, developing, testing and supporting the components, products and solutions that respond to those requirements. So a product design advances through various levels down the completion and final delivery.

At the *Business level*, design process develops preliminary specifications for the proposed product and helps to enable investment risk. At the *operational level*, the product requirements are drawn in detail with adherence to plans and checkpoints. At the *schedule assignment, design, testing and debugging and delivery levels*, peer design reviews are conducted. The most critical stage in this process is testing and debugging where the test plans are executed. This is one area where the development process moves back to design. So the information assets need to be protected and the products developed to acceptable quality tolerance. At the *final release level*, the user manual and documentation are developed before taken to the deployment site. Here, the checkpoints help to test the quality of the product to acceptable conditions. Initial approaches to support security in product design methodology are described in [4, 5, 6, 7].It is necessary to know the threat(s) of a product under consideration and then devise security policies. Threats help to define policies and a secure product is designed based on those policies.

The embedded product design is a combination of hardware and software. The hardware is generally selected based on current availability. The most critical module is the software module selection. Most system vulnerability arises from this module, and even more, if it uses the concept of network model, hence this is one area where security is a major concern. The existence of hardware and software on a common platform is an area of vulnerability. There are certain vulnerabilities that exist side-by-side. For example the information gained from power consumption, electromagnetic leaks, timing, sound, physical implementation of cryptosystem that can make the system vulnerable[8, 9].Vulnerability assessment in design process is mostly done in software. Vulnerabilities arises when the *scope is too big for software* (software modules are written for existing software), when

there is *too much interaction between software modules* (execution of a sub-function which never really belongs to the main executing function), *when software modules are not clearly defined* (there is no cleanly defined interfaces and function use different schemes to achieve results), when there is *no establishment of communication protocols* (lack of usage of proper global variables and not adhering to module development rules) and *inflexible platform* (modules calling the remote procedures of different platform and presence of security loopholes on the executing platform).

Embedded software products that are designed on client-server paradigm are highly vulnerable to network threats. Designing the software around sockets and messages opens up potential security holes in the system to the network. We require high degree of security in software module design as the users of the system always thinks the network as secure and thus forgets to apply security policies. Applying the network security policies in modular design, like client-server, will take the developer and other users quite some time to be aware of security functionalities.

No system is ever 100 percent secure. Security is not a mixture of cryptographic algorithms and security protocols to the system. Security is a process, not a product. It changes from time to time depending on requirement. Why we require security in embedded products varies from user to user and depends on what we are going to use, where we are going to use and who will use it. The basic requirement of security for most users is to preserve the identity of the system and authenticate the system so that others cannot access it. Different security responses of analyst, developers, administrators, maintenance personnel, authorize users of system are required to be generated during product design at any time, be it before development, during development, after development, during the use phase and during disposal phase. Good security policies will help the investors invest in the product confidently, thus making sure that their revenue is properly protected.

To remove some of the above vulnerabilities and threats of an embedded product, there is a need to enforce security to product design.

V. REQUIREMENTS FOR A SECURE PRODUCT DESIGN

The Security in the design should be considered from the beginning. In the previous sections, vulnerabilities in different phases in life-cycle and the requirement of security in design has been emphasized, now we see the possible security solutions for the threats[10, 11, 12].

Security analysis is an initial requirement in designing a secure embedded system. Most threats and their counter-measures are studied for a long time [13]. Security threats of and from both internal and external components should be considered. This will help to build a protected security policy. Generally, the security consideration of a system is frozen at the start, as development process for most products goes through adhoc approaches. There is always a need to hire a security specialist.

Security threats are analyzed by building threat models. A threat model is necessary to analyze the threats, assess the probability of potential harm and attack priorities. A hierarchical arrangements of threats in threat model helps to know the different attack goals of the attacker to the system.

A few basic points that should be taken in security requirements are:

- Hardware and software involvement in an embedded system design incurs cost. Securing an embedded product on heterogeneous platforms still incurs bigger cost; so only the real threats of the system should be considered.
- External sources of power needed by an embedded product should undergo change or recharge. Powerless systems open-up disposal security threats and loss of data.
- There should be a requirement to hire a experienced security specialist as most developers use tools they apply generally to all products without knowing the real threats.
- Too much security is harm to the product design itself [14]. So, equilibrium should be maintained between flexibility and security, thus saving resources.
- Violation of integrity should be checked so that components of the system do not behave abruptly under normal conditions.
- A system should learn to secure by itself. A self-adaptive, self-configuring or self-restoring techniques preserves security.
- Present security solutions should pave the way for new security solutions with less computational requirements, smaller size and lower energy consumption.
- Applying security policies should not cause the development process to cross the deadline in delivering the final product. Time-to-market is an essential which increases the value the product. So organizations should make to invest more money on right security practices to deliver the product within specified deadlines.
- A mandate for continuous security improvement in technology and manufacturing drives accountability and action.
- A community of hardware and software engineers that innovate and share practices and tools for secure product development.
- Integration across products that is achieved through client use cases, scenarios, and end-to-end usage threads in concert with an architectural framework that enables componentization.
- Consumability analysis that looks beyond product defects to the client experience of using the offerings.
- Organizations should be responsible for implementing security awareness programs for their development teams. Persons working in development teams should have different roles to create *security awareness programs* so that they deliver the right information to each other and the impact of security issues on the clients. The key concern on the technical details on security issues lies in the hands of developers.

Security standards, security practices and security compliance criteria play an important role in supporting the product development process of organizations. In the overall requirement, hardware, software and services development are governed by four necessary factors: assets security, check points in product development, security and quality plans, product testing[15].

Resources used in development projects are always required by an organization. In fact, they are never isolated. “*Security of assets*” aims in protecting disclosure of user’s privacy, location and personal information and other proprietary information. “*Checkpoints Product in Development*” help to review the development when the project moves from one level to the next. These checkpoints can be used as control points for assessing project risk, expense control, product quality, security issue review, and for synchronization of a secure project plan. The project development team should define and remove the vulnerabilities for the prior work before transition to the next level. If there is any change in scope or content, it should prove the change from a security level. Though this paper highlights most of the security issues of embedded system with a special attention towards systems employed in greenhouse environment, but “*quality plans*” are also required. A *quality plan* highlights the technical and audit requirements for asset control, along with the standards and practices for quality engineering to be applied in the development process. The development checkpoint plan should help to review all of the security and quality plans, practices, and findings in the development phase. “*Product testing*” is required to verify the functionality of the various components of the product and whether it secures from the vulnerabilities in the product. It should go through all official design specifications of component, product, or solution. Security mechanisms and services included into the component, product, or solution should be verified.

VI. CONCLUSION

A very specific concept of life-cycle of embedded products and the vulnerabilities is discussed and why secure design is needed. The security philosophy of almost all greenhouse embedded systems is quite same. Some basic points that should be taken in security requirement are discussed and how the hardware security, software security and security of services are governed. To design a highly secure system, different design strategies are proposed. Further research is needed on strategies such as prevention, tolerance, removal and forecasting. Prevention and tolerance are basic security strategies while removal and forecasting are strategies for security assurance.

REFERENCES

- [1] Peter Marwedel, "Embedded System Design", 1st edition, Kluwer Academic Publishers: Hardbound, pp.1-8, 2003.
- [2] Rita C. Summers, "Secure Computing: Threats and Safeguards", pp. 3-11, McGraw-Hill, 1997.
- [3] Paar, C., Weimerskirch, A. "Embedded security in a pervasive world", Inf. Secur. Tech. Rep. 12,3, pp.155-161. Jan.2007.
- [4] Eric Uner, "A Framework for Considering Security in Embedded Systems", Embedded.com, Sept. 2005.
- [5] Wayne Jansen, Serban Gavrilă, Vlad Korolev, Thomas Heute, Clément Séveillac, "A Unified Framework for Mobile Device Security", Proceedings of the International Conference on Security and Management (SAM'04), pp. 9-14, June 2004.
- [6] Ingrid Verbauwhede and Patrick Schaumont, "Design methods for Security and Trust", Design, Automation & Test in Europe Conference & Exhibition, pp. 1-6, DATE '07, 2007.
- [7] Divya Arora, Srivaths Ravi, Anand Raghunathan and Niraj K. Jha, "Architectural Enhancements for Secure Embedded Processing", NATO Workshop on Security and Embedded Systems, VOL 2, pp. 18-25, August 2005.
- [8] Weingart S., "Physical Security Devices for Computer Subsystems: A Survey of Attacks and Defenses", Workshop on Cryptographic Hardware and Embedded Systems, 2000.
- [9] J. J. Quisquater, D. Samide, "Side channel cryptanalysis", In proceedings of the SECI 2002, pp. 179-184.
- [10] Srivaths Ravi, Anand Raghunathan, Paul Kocher, Sunil Hattangady, "Security in embedded systems: Design challenges", ACM Transactions on Embedded Computing Systems (TECS), Volume 3, Issue 3, Pages: 461 - 491, 2004.
- [11] David Hwang, Patrick Schaumont, Ingrid Verbauwhede, Shenglin Yang, "Multilevel Design Validation in a Secure Embedded System", IEEE Transactions on Computers archive, Pages: 1380 - 1390, 2006.
- [12] Joe Grand, "Practical Secure Hardware Design for Embedded Systems", Proceedings of the 2004 Embedded Systems Conference, San Francisco, California.
- [13] Ravi, S., Raghunathan, A., and Chakradhar, S. "Tamper Resistance Mechanisms for Secure Embedded Systems", In Proceedings of the International Conference of VLSI Design. pp 605-611, 2004.
- [14] Srivaths Ravi, Paul Kocher, Ruby Lee, Gary McGraw, Anand Raghunathan, "Security as a new dimension in embedded system design", In Proc. ACM/IEEE Design Automation Conf., pp. 753-760, June 2004.
- [15] D. Allan, T. Hahn, A. Szakal, J. Whitmore and A. Buecker, Security in Development: The IBM Secure Engineering Framework. Available online: <http://www.redbooks.ibm.com/redpapers/pdfs/redp4641.pdf>

Study of the wear and friction behavior of immiscible as cast-Al-Sn/Graphite composite

S.Srivastava^{1*}, S. Mohan², Yogesh Srivastava¹ and Aman J. Shukla³

¹Materials Science & Metallurgical Engineering

¹Maulana Azad National Institute of Technology, Bhopal M.P. (India)-462051

²Institute of Technology, Banaras Hindu University, Varanasi-221005

³Research & Technology Development Centre
Sharda University, G. Noida U.P. (India)-201306

Abstract:

In this paper we investigate the tribological properties of Al-Sn-based alloy with different amount of graphite at different normal loads and sliding speed. A modified impeller mixing coupled with chill casting technique was used for the preparation of immiscible alloys. In this paper Al-Sn binary alloys was chosen for this study. This binary system shows the miscibility gap at different concentration and temperature. Graphite was chosen as reinforcing element which was reinforced in the Al-Sn matrix. The graphite content in the composite varied from 1.6 to 8.4 wt%. The presence of graphite in the matrix not only improves the mechanical properties but also improve the tribological properties due to lubricating action. The ductility of composite materials showed the adverse effect with increase of the graphite content in the matrix. Pin-on-disc sliding wear tests were conducted in an ambient condition to examine the tribological behavior of the aluminum-based graphite composite. The experiment was commenced at different sliding distance, speed and using normal load. Having finished the tests, the weight losses of the specimen were measured, wear and friction characteristics were calculated with respect to time, depth of wear track, sliding speed and bearing load. Friction coefficient and wear volume have shown large sensitivity to the applied normal load and the testing time (or sliding distance). The XRD and SEM analysis were used to analyze the wear debris and track.

Key words: Aluminum alloy, Friction coefficient, Pin-on-Disc, SEM, Sliding velocity, Tribometer, Wear, and XRD.

1. Introduction

Aluminum alloys and other lightweight materials have growing applications in the automotive industry, with respect to reducing the fuel utilization and shielding the environment, where they can successfully reinstate steel and cast iron parts. There are a number of elements which have a limited solubility in the aluminum matrix. Therefore they

exhibit two immiscible liquid phases within a certain temperature range. However, the different densities of these liquid phases lead, to the formation of two different layers. This prevents the homogeneous distribution of particles in a matrix using simple and inexpensive casting processes. The development of immiscible alloys has been largely constrained by the conventional equilibrium processing, which generally results in gross segregation due to the wide miscibility gap, and high disparity in the densities and melting temperatures between the immiscible elements [1, 2]. The idea is to obtain aluminum matrix with finely distributed particles of *e.g.* indium, bismuth or lead as a soft phase or iron, nickel or cobalt as a hard phase with lubricating function. However this is still far from the practical application because the miscibility phenomenon poses problems during solidification [3-5]. A miscible gap in the liquid state is found in metal-metal systems such as Al-Bi, Al-Pb, Al-In, Al-Sn, Cu-Pb, and Zn-Pb, Ga-Pb etc. For this study Al-Sn was selected as basic materials in which small amount of the graphite was added for improving the wear and seizure properties of the materials. A typical equilibrium phase diagram is shown in Fig.1. The solid solubility is of the order of 0.10% Sn at approximately 900. °K, decreasing to reach a probable value of 0.05-0.07% Sn at eutectic temperature, and much smaller values at lower temperatures. The density increased is approximately 0.06% for every 0.1% Sn added. Liquid gas surface tension and ratio solid-liquid /solid-solid surface tension decreases, and this affect the shape of phase. Fluidity is greatly reduced, and electric conductivity is decreased. There is practically no change in hardness, strength or elongation of commercial aluminium, high purity aluminium is slightly strengthened. Strength and especially elongation drop rapidly with temperature at 500°K the strength of a 10% tin alloy is halved and the elongation has dropped from 60% at room temperature to less than 5% at 900°K the alloy are brittle. Plastic deformation to break the tin network, followed by annealing to spheroidized the tin improve the properties [6].

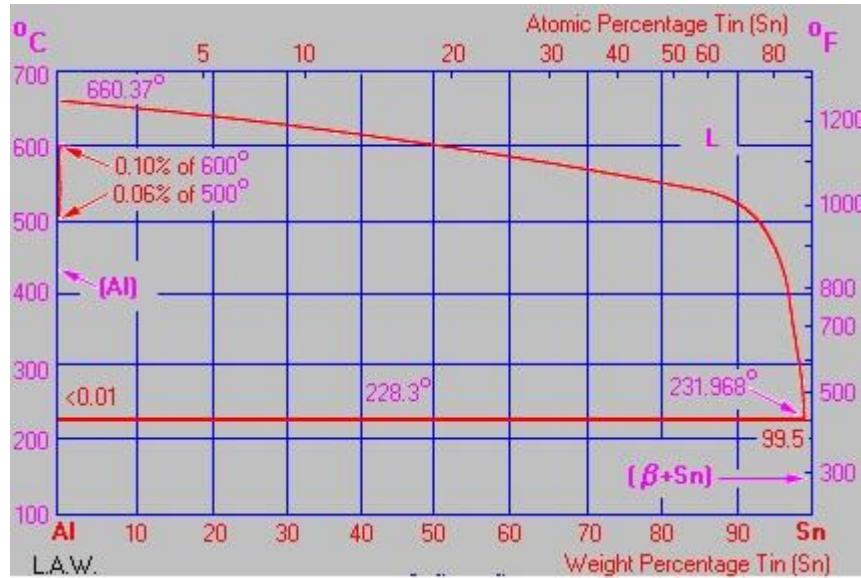


Fig. 1. Phase diagram of Al-Sn

With solid lubricant particle like graphite or MoS_2 dispersion in the matrix of aluminum alloy this material exhibits good potential for resistant to wear and consequently becomes more suitable for tribological applications [7-9]. Considerable efforts have been put into incorporating lubricating particles in aluminum alloy matrices to improve resistant to wear. Earlier researcher [9-12] has reported graphite as a suitable solid lubricating material for the preferred applications. Aluminum alloy–Graphite particulate composite exhibits its potential to act as a self lubricating material with improved resistance to wear, machinability, delayed on set of severe wear and seizure. P.R. Gibson et al [13, 14] and S. Das et al [15] investigated that a solid lubricating film can be formed on the wearing surface with addition of graphite particulate in the aluminum alloy. It helps in reducing the friction coefficient and to increase the anti seizing quality and also improve tribological behavior of the base alloy. Jha et al [7] have observed that the porosity encountered during the production of aluminum-graphite composite material embrittles the material with crack nucleation and reduction in fracture toughness and elongation of the matrix alloy leading to increased wear. However addition of appropriate level of graphite particulate can reduce it. Also at increased sliding speeds the wear rate decreases with addition of graphite content [16-20].

The present article aims to contribute to a better understanding of the interrelation between presence of the graphite particles in the matrix and the corresponding mechanical properties and wear behavior. In the present work, Al-Sn composite with different amount of graphite are being produced by liquid metallurgical route. Experimental quantitative expressions, which correlate the ultimate tensile strength (UTS), yield tensile strength, elongation, wear

volume and frictional coefficients to the presence of graphite in the matrix, have been determined.

2. Experimental investigation

2.1 Selection of materials

Commercially pure aluminium (99.8%) and tin-metal were selected for the preparation of Al-Sn composites with different content of graphite.

2.2 Procedure for preparation

The experimental set-up used for mixing and casting of composites is shown in Fig 2. It comprises of a cylindrical sillimanite crucible of 150mm diameter and 250mm depth with attachment of four baffles to its sidewalls for proper dispersion of second phase in melt during stirring. The crucible was placed in an electric heated muffle furnace. It was also equipped with a bottom pouring attachment, which could be closed or opened by graphite stopper with a lever system. A steel mould was placed beneath the furnace to cast the molten metal. In the top cover suitable opening was provided to charge materials and insert thermocouples. The temperature of the furnace could be controlled with an accuracy of about $\pm 5^\circ\text{C}$. Metallic bath temperature was measured continuously by chromel/alumel thermocouple. The agitator system could be raised or lowered with the help of the hanger and steel frame structure. After adjusting the mixer in a central position and required height from the bottom of the crucible, the motor was bolted and locked while mixing of melt. Three-blade impeller was used for effective mixing. This design provides very high rates of shear and only axial and radial flow currents are utilized for mixing without any significant vortex formation due to the presence of baffles. The Al-Sn-graphite composites were prepared employing liquid metallurgical route. The required

amount of commercial pure aluminum was charged into the crucible and aluminum was heated to a temperature 200°C above its melting point i.e. 662°C . A mechanical stirrer was inserted into the melt, and agitation was started at a speed of 35 s^{-1} . The $50\text{-}\mu\text{m}$ -size electrolytic grade graphite powder was charged into the melt during stirring and the addition of the particulate into the melt was facilitated by vortex created

2.3 Evaluation of as-cast Properties of the Composite

The wet chemical analysis was used to determine the percentage of iron in the bulk. The metallographic specimens were prepared using standard technique and studied under SEM for different feature present. The densities of the composite were determined using Archimedes' principle by weighing in water and air. The hardness of the entire composite was measured using a Vickers hardness testing machine. The hardness of the entire composite was measured using a Vickers hardness testing machine. The hardness was measured using Vickers hardness instrument Leitz Welzlar at a load of 5Kg . At least 3 indentations have been taken for each point. Tensile testing of all the Al-alloy-graphite composite was performed stress along with percentage elongation and reductions in area were computed from the results.

by stirring action. Mixing was done for a period of 60 seconds. The emulsion was poured into the chilled cylindrical mould placed beneath the crucible. The same procedure was adopted for different compositions. Cylindrical casting of length 20cm and dia. 2cm were obtained.

2.4 Wear test

Pin-on-disc machine was used for evaluating the wear properties under dry sliding condition. The cylindrical test pin of 8mm diameter and 40mm length were used against a hardened steel disc of 120 mm diameter. Wear tests were conducted with variable applied pressure $3.9 \times 10^{-1}\text{ Mpa}$ and a sliding speed of 0.5 m/s with a constant sliding distance of 10000 meters . Wear test were also conducted with selected varying speeds and sliding distance ranging up to 1000 meters . The initial weight of the specimen was determined in a digital balance with a precision of $\pm 0.1\text{ mg}$. The pin was kept pressed against a rotating steel disc of hardness 58 HRC under loaded condition. The frictional traction en-counted by the pin in sliding is measured by a PC based data logging system. On completion of the running through the required sliding distance the specimen pins were cleaned with acetone, dried and their weight were again determined for ascertaining the weight loss. Wear debris were analyzed by XRD.

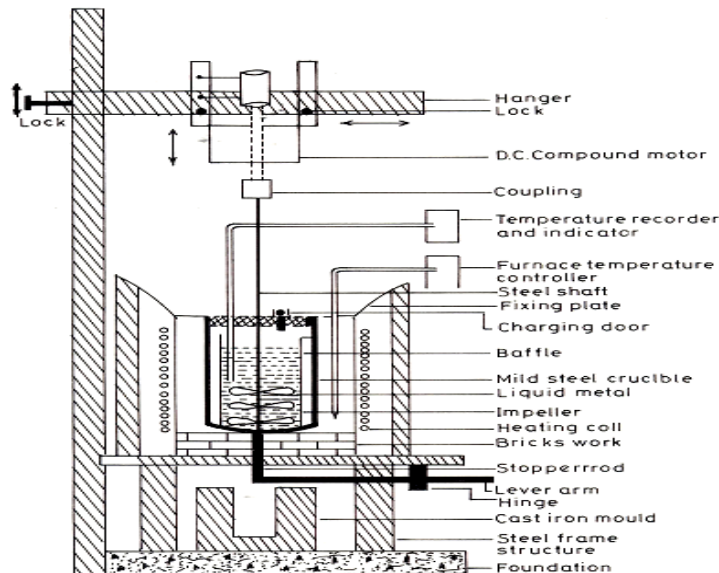


Fig 2.-Schematic diagram of casting set-up

3. Result and Discussion

3.1 Physical investigation

The liquid metallurgy methods were used to synthesize the composite materials with different amount of the graphite content in the matrix. The theoretical density of the composite materials varies from 2.88 g/cc to 2.84 g/cc with graphite content. But the experimental density of the composite

materials was found to vary from 2.72 g/cc to 2.70 g/cc along with porosity varies from 5.2% to 4.9% . The XRD methods were used to investigate the different phase/element present in the prepared composite materials. Fig 3 shows the XRD pattern of $\text{Al-6.3\%Sn-3.4\%Gr}$ composite. The XRD scanning from 10° - 80° shows the lines (200), (101), (400), (220), (511), (211) for tin (111), (101)(110) (222) (112) for graphite, small peak of Al_2O_3 {(110) and

(005)}, along with aluminum peak aluminum {(111) (200), etc} at $2\theta = 30.62^\circ, 32.09^\circ, 43.9^\circ, 44.9^\circ, 62.6^\circ$ for tin, 26.7, 43.5, 46.4 and 56.68 for graphite 15.45, 18.99° for alumina, 38.86° , for aluminum respectively.

3.2 Study of the mechanical properties

The resistance to indentation or scratch is termed as hardness. Among various instruments for measurement of hardness, Brinell's, Rockwell's and Vickers's hardness testers are significant. Theoretically, the rule of mixture of the type $H_c = v_r H_r + v_m H_m$ (suffixes 'c', 'r', and 'm' stand for composite, reinforcement and matrix respectively and v and H stand for volume fraction and hardness respectively) is valid for composites materials which helps in approximating the hardness values. Among the variants of reinforcements, the low aspect ratio particle reinforcements are of much significant in imparting the hardness of the material in which they are dispersed. Table 1 shows a comparison of the mechanical properties of Al-Sn/graphite composite samples produced by the liquid metallurgy methods. Fig.4 shows the variation of mechanical properties with the graphite content in the Al-Sn alloys. It is observed that the hardness of the composite materials decrease with increasing the graphite content in the matrix. Graphite is a very brittle materials and it is responsible factor for decreasing the hardness of the materials.

The uniform distribution and the nature of the interfacial bonding between graphite particles and matrix have an important relationship on the

mechanical properties of a composite material. It has been suggested that graphite particles, being very weak compared to the aluminum matrix, may be treated as non-load-bearing constituents [21]. With a view to extending their applications to structural components, these materials should have a good combination of strength and ductility. The Al-Sn/graphite composites with different graphite content show an increase in the tensile elongation together with an increase in the ultimate tensile strength of the material, resulting from the better dispersion of the particles. The magnitudes of these increases are observed to average approximately 18%. A strong bond between the reinforcement and matrix helps in the load transfer from the latter to the former. As a result, fracture takes place in the composite via the reinforcement and not along the interface [22, 23]. Although the graphite is a non-load bearing constituent, a strong particle/matrix interface helps graphite particles embed themselves into the matrix properly, improving the fracture resistance.

3.3 Wear study

3.3.1 Effect of sliding distance and load

The variation of bulk wear with sliding distance was studied at different combinations of loads and sliding velocities. Almost a linear relationship in bulk wear and sliding distance i.e. steady state wear is observed after an initial running-in period of 500–1000 m in almost all the cases irrespective of load or sliding velocity used.

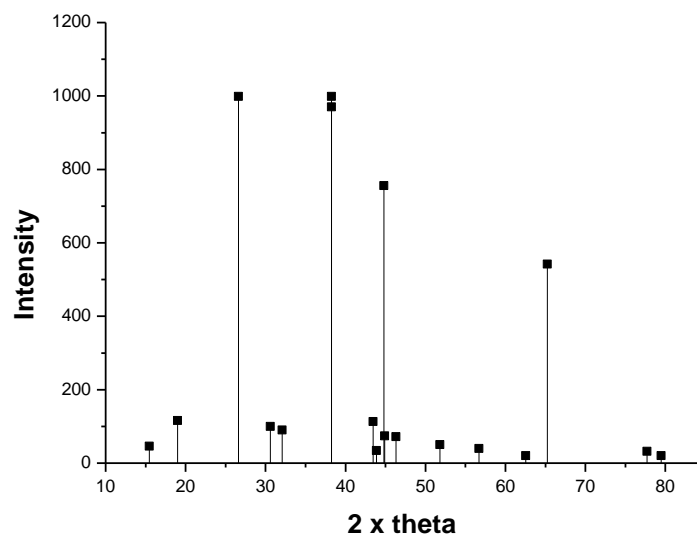


Fig 3. XRD graph of Al-6.3%Sn-3.4%Gr composite

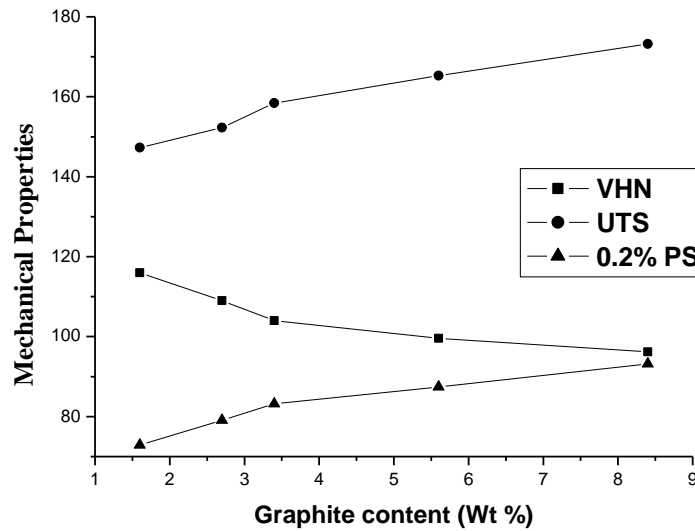


Fig 4. Variation of hardness with varying graphite content

Table 1- Mechanical properties of the Al-Sn/ Graphite composite

S.No.	Composite	VHN	UTS (MPa)	0.2%PS(MPa)	% elongation
1	Al-6.3%Sn-1.6%Gr	116	147.3	72.9	16.3
2	Al-6.3%Sn-2.7%Gr	109	152.3	79.1	16.9
3	Al-6.3%Sn-3.4%Gr	104	158.4	83.2	17.3
4	Al-6.3%Sn-5.6%Gr	99.6	165.3	87.4	18.1
5	Al-6.3%Sn-8.4%Gr	96.2	173.2	93.2	19.3

Fig. 5 shows results for a test conducted at 2 kg load and 0.5m/s sliding velocity. In running in period, the Al-Sn/graphite composite shows large wear rates. The relation found here is in accordance with the pattern for most metallic materials derived theoretically as well as observed experimentally [18,19]. But irrespective of variables used, bulk wear is large with large graphite content in Al-Sn/graphite composite. The self-lubricated role of graphite reinforcing particles was significant in dry sliding conditions, as well as in conditions of lubricated sliding. The free graphite particles are released from the composite material during dry sliding of mating surfaces form a lubricant film at the interface. Fig.6 shows the variation of rise in temperature of the test specimen during experiment with sliding distance. The maximum rise in temperature is found in Al-6.3%Sn-1.6%Gr and minimum in Al-6.3%Sn-8.4%Gr. This type of the behavior can be explained on the basis of thermal conductivity. Al-6.3%Sn-1.6%Gr shows less conductivity as Al-6.3%Sn-8.4%Gr. Fig. 7 shows the SEM micrographs of wear

tracks of Al-Sn/graphite composites (Al-6.3%Sn-3.4%Gr) for 2 kg applied load and 0.5 m/s sliding velocity at 10,000 m sliding distances. This micrograph was taken at the higher magnification. This figure is clearly revealed the presence of the oxide layer which might be adhered on the rubbing surface.

3.3.2 Effect of applied load

The studies conducted to see the effect of applied load on wear rate revealed that wear rate increases continuously with load in a linear manner irrespective of the sliding velocity used as it is evident from Fig. 8 for a particular velocity. But in all the cases wear rate first decreases with increase in graphite content for all combinations of loads and sliding velocities used in the present investigation and then increase with increase the graphite content. Corresponding temperature curve shown in Fig.9, clearly reveal that temperature continuously increases with increase in load but with increase in iron percentage in composite a decrease in temperature rise is observed

which is indicative of larger heat dissipation capability of iron.

Fig. 8 shows the variation of temperature and micro hardness of the test specimen with the variation of load. With increase the load on the test specimen, the composite material bears maximum rise in temperature. The materials at the contacting surface

on the pin-on-disc become soften, which is responsible factor for decreasing the micro hardness of the contacting surface. As expected, the high wear resistance of Al-graphite composites is primarily due to the presence of graphite particles which act as a solid lubricant.

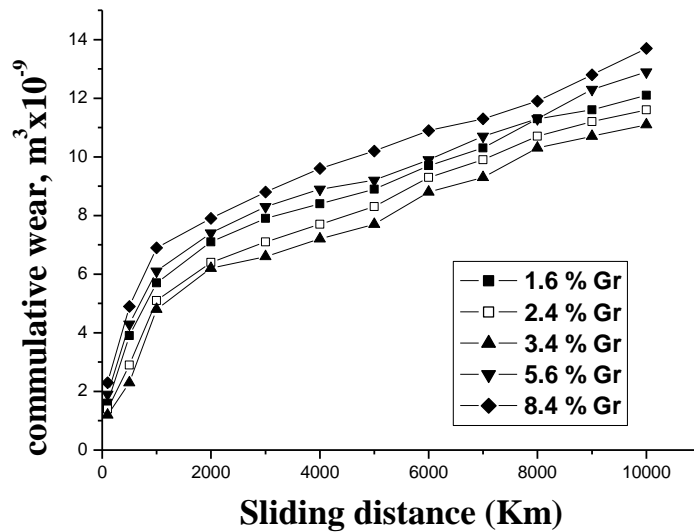


Fig 5. Variation of bulk wear with sliding distance at 2 kg load and 0.5 m/s sliding velocity for as-cast Al-Sn/graphite composites.

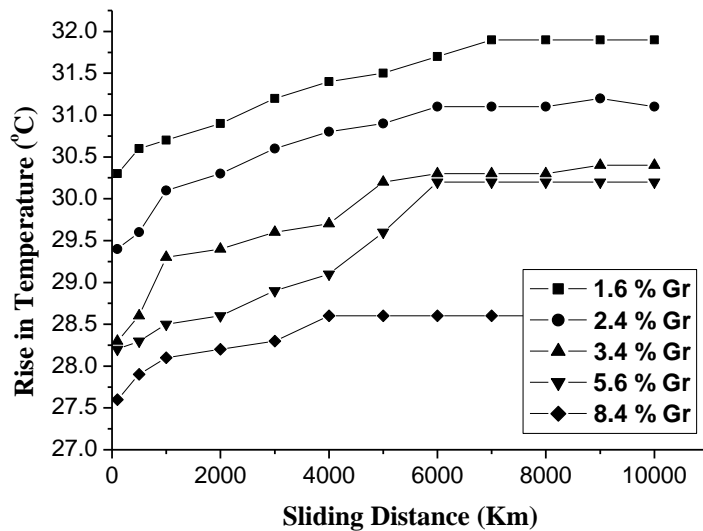


Fig 6. Variation of rise in temperature of the test specimen with sliding distance at 2 kg load and 0.5 m/s sliding velocity for as-cast Al-Sn/graphite composites.

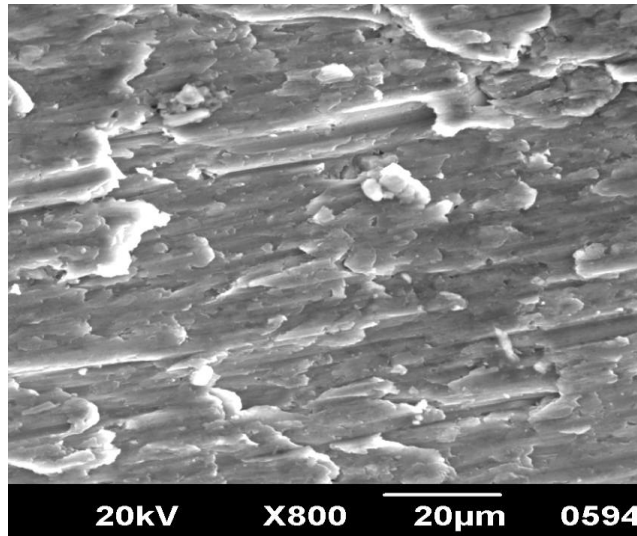


Fig 7. SEM micrographs of wear tracks of Al-Sn/graphite composites (Al-6.3%Sn-3.4%Gr) for 2 kg applied load and 0.5 m/s sliding velocity at 10,000 m sliding distances.

Fig. 11 shows the SEM micrographs of wear tracks of Al-Sn/graphite composites (Al-6.3%Sn-3.4%Gr) at the higher magnification for 2 kg applied load and 0.5 m/s sliding velocity at 3000 m sliding distances. The oxides layer with small amount of the graphite particles are adhered on the material surface. Fig. 12 a and b : SEM micrographs of wear tracks of Al-Sn/graphite composites (Al-6.3%Sn-3.4%Gr) for 15 kg applied load and 0.5 m/s sliding velocity at 3000 m sliding distances (a) worn surface (b) crack surface. Worn surface topographies of the investigated compacts indicate that the dominant wear mechanism was plowing. The degree of surface damage (i.e. depth and width of the grooves) depended on the applied load and microstructure of the material. At the higher load, generally metallic failure is observed as shown in Fig. 12 (a). For observing the mechanistic phenomenon at the higher load, the SEM micrograph was taken at the higher magnification, as shown in Figure 12b. While studying the wear tracks at different loads for a particular velocity (from 2 to 15 Kg) the operating modes changes from oxidative-to oxidative-metallic to metallic as load applied is increased and wear track observes broken oxide film, deep grooves and delamination of surface as evident from Fig. 12 (b). in this SEM micrograph some small crack was found

at the oxide surface. With increase the load, the produce cracks within the material by sliding action easily propagate and the form oxidative film at lower load are ruptured as shown in Figure 12b at 15 Kg load and 0.7m/sec sliding velocity.

3.3.3 Effect of sliding velocity

Self-lubricating role of graphite in sliding contact is provided by layered-lattice structure. Namely, graphite is characterized by hexagonal layered structure. The bonds between the parallel layers are relative weak (Vander Waals type). Except that, graphite reacts with gases (such as water vapor) forming strong chemical bonds. The adsorbed water vapor and other gases from environment onto the crystalline edges weaken the interlayer bonding forces. It results in easy shear and transfer of the crystalline platelets on the mating surfaces. Fig. 13 shows the variation of wear rate with sliding velocity at 2 kg load, 3000m running distance. Like all other aluminum alloys/ composites, Al-Sn/graphite composites also show an initial decrease in wear rate followed by a sharp increase in wear rate after attaining minima with increase of sliding velocity for all composites at different loads. But in all the cases wear rate decreases with increase in graphite content for (say up to 3.4 %graphite in the matrix) all combinations of loads and sliding velocities used.

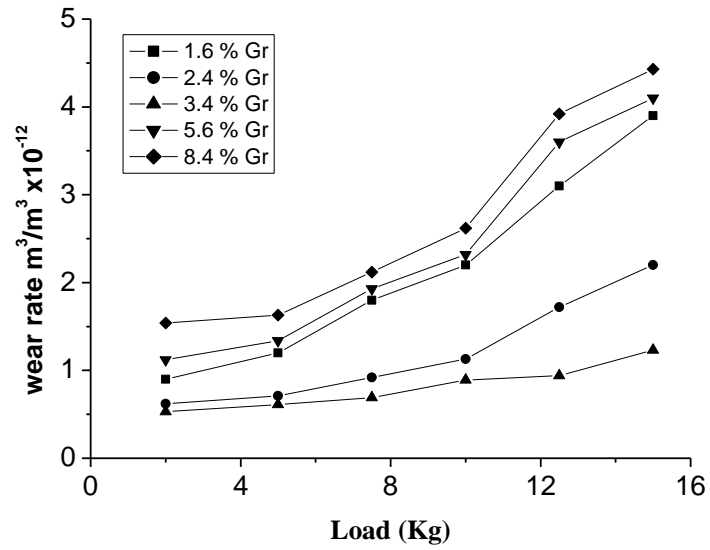


Fig 8. Variation of wear rate with load at 0.5 m/s sliding velocity and running distance 3000 m for as-cast Al-Sn/graphite composites.

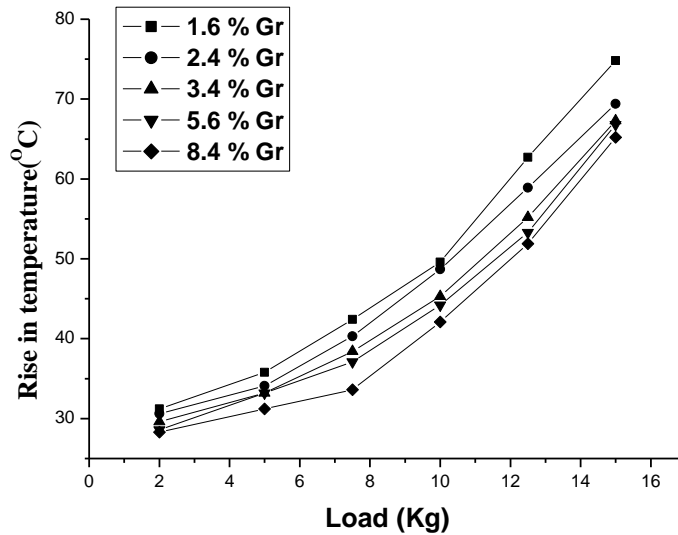


Fig 9. Variation of rise in temperature of the test specimen with load at 3000 running distance and 0.5 m/s sliding velocity for as-cast Al-Sn/graphite composites.

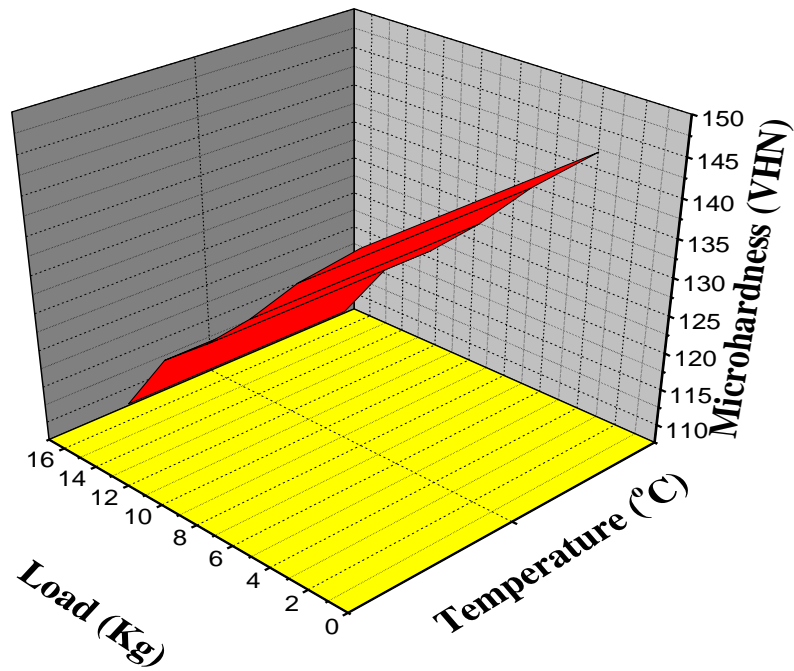


Fig 10. Variation of rise in temperature & micro hardness of the test specimen with load at 3000 running distance and 0.5 m/s sliding velocity for as-cast Al-Sn/graphite composites.

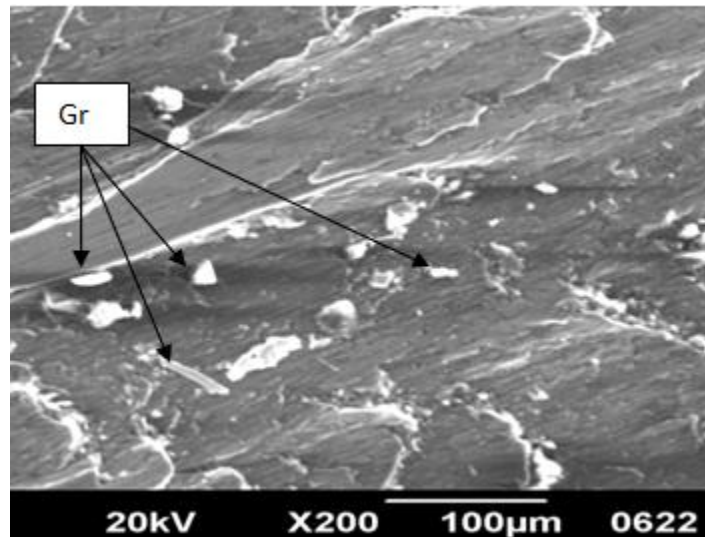


Fig 11. SEM micrographs of wear tracks of Al-Sn/graphite composites (Al-6.3%Sn-3.4%Gr) for 2 kg applied load and 0.5 m/s sliding velocity at 3000 m sliding distances.

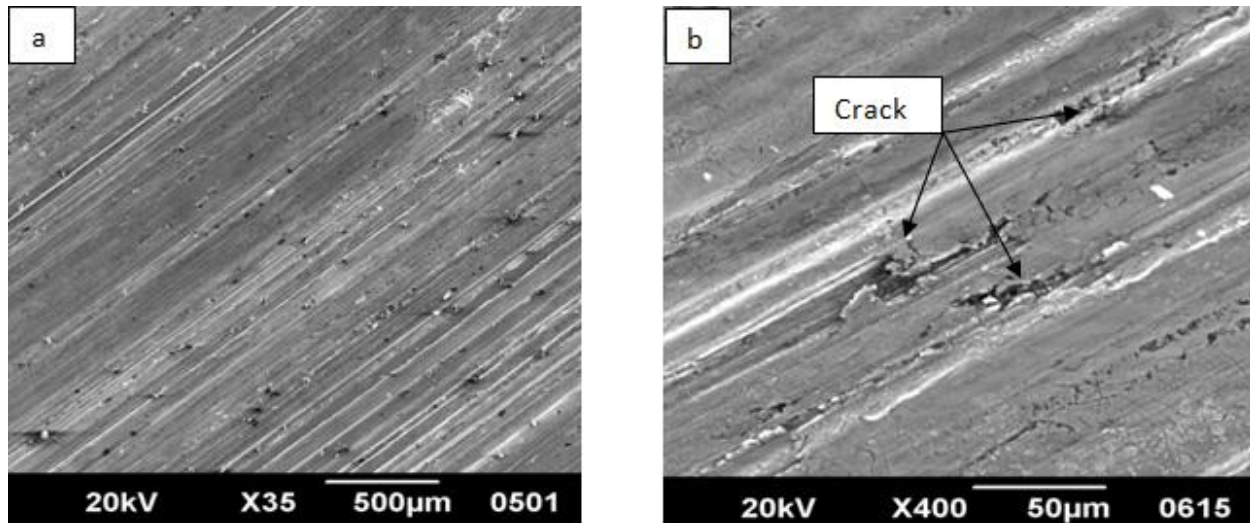


Fig 12. SEM micrographs of wear tracks of Al-Sn/graphite composites (Al-6.3%Sn-3.4%Gr) for 15 kg applied load and 0.5 m/s sliding velocity at 3000 m sliding distances (a) worn surface (b) crack surface

While that wear rate again increase with increase the graphite content in the matrix. Further, variation of wear rate and hardness of worn wear track surface is shown in Fig. 14. It clearly shows highest hardness at minima in wear rate, which is clearly indicative of the presence of hard oxide particles. With increase in sliding velocity, oxides particles are removed from the mating surface, due to decrease the hardness of the composite materials and hence increases the wear rate. Fig. 15 for temperature increase with sliding velocity follows the same trend as observed in the case of variation of temperature with applied load. Higher velocity gives higher amount of wear loss due to fast rubbing of the contacting surface. Therefore maximum rise in temperature in the test specimen at the contacting surface occurs. The SEM observations of the wear tracks at 2.0 Kg load for different sliding velocities are shown in Fig.16 (a-b) and 17(a-c). In Fig. 16 (a-b) shows the SEM observation at the lower and the higher velocity and Fig. 17(a-c) show SEM result at the optimized velocity. SEM micrograph of the wear track in Fig. 16(a) was mainly comprised of oxide particles and the wear track surface is seen to have more pronounced layer of oxide particles adhered at the surface of the materials. But at the higher velocity, metallic particles come out during wear processes and wear track is seen clear and smooth as shown in Fig. 16(b). The minima in the wear rate was found at 1.22 m/sec. Fig. 17 show SEM micrographs of wear tracks of Al-Sn/graphite composites (Al-6.3%Sn-3.4%Gr) for 2 kg applied load and 1.22 m/s sliding velocity at 3000 m sliding distances (a) worn surface (b) crack observation (c) observation of the oxide layer. Wear rate continuously decreases with increase the sliding

velocity due to formation of thin film of oxide layers along with metallic layer at the mating surface as shown in Fig. 17(a). This is confirmed from the SEM observation of the wear track taken at the higher magnification as shown in Fig. 17(b). The oxide layer of the respective metals adhered on the mating surface is clearly visible in this micrograph. The failure of the materials from the wear process is due to formation and propagation of the crack within the materials as shown in Fig. 17(c). The cracks are formed at the adjacent surface of the materials. An examination of the three micrographs shows the formation of severe patches and grooves resulting from plastic deformation of the aluminum graphite composite and relatively small groves and mild patches on 3.4 wt % graphite composite. This reduction in severity of the worn surface of the composite material is due to the formation of a Graphite lubricating film which prevents the direct contact of the specimen with the rotating steel disc surface. This formation of the lubricating layer at the sliding surface becomes thicker with more graphite as the addition of graphite content to the base alloy increases and it is this graphite lubricating layer that is responsible for playing an effective role for keeping the wear behavior of the composite low.

3.4 Study of the surface particles and its mechanistic approach

Fig. 18 a-b shows the SEM micrograph of wear debris for 2 kg applied load and 1.22 m/s sliding velocity at 3000 m sliding distances (a) collecting particles (b) examination of the graphite particles. This observation has been also confirmed by XRD observation as shown in Fig. 19. Debris in all figures

was mainly comprised of oxide particles of aluminum and tin. But it also be contained some small amount of graphite as shown in Fig. 18 b. In the XRD observation, the aluminum oxide, tin and its oxides (from EDAX observation) and graphite are found as the main peak. Tin and lead are weak and ductile and hence they decrease the strength property of aluminum alloys under study. Further, Sn/Pb, being a ductile material, deforms in preference to the stronger matrix. This reduces the stress concentration in the matrix and makes it more deformable. It is also found that the alloys containing tin have slightly more strength and hardness but low ductility values compared to the alloys containing lead. Al wear particles on the worn surfaces are laminated by the pin on the contact area, forming plough. Because wear particles contain some aluminum oxide, Zhou et al believed that the oxidation wear was the main wear mechanism of composites [24]. However, according to the SEM observation of worn surfaces of the composite and the study of delamination theory of wear, it can be concluded that the delamination wear could be the main wear mechanism. Dislocations at the mating surface, subsurface crack and void are

induced due to the repeated plastic deformation between the test pin and disc. The cracks extend later and cause break and split of the hardened surface layer by shear deformation mechanism [25].

4. Friction studies

The characterization of friction behaviour of Al-Sn/graphite base composite with sliding at the specific load (i.e. 10N) is illustrated in Fig. 20. The Figure show is graphically representation of the results obtained from the friction experiment at a fixed load and sliding velocity. It is evident from the Fig. 20 the friction coefficient drastically decreases during the running in period. During the steady state period the friction coefficient is being stabilized. In dry sliding, the reason for decreasing the wear rate and the coefficient of friction of Al-Sn/graphite composite as compared with the base alloy is the presence of smeared graphite layer at the sliding surface which acts as the best solid lubricant. The friction behaviour also varies with applied load. The average value of the friction coefficient at normal load is shown in Fig. 21.

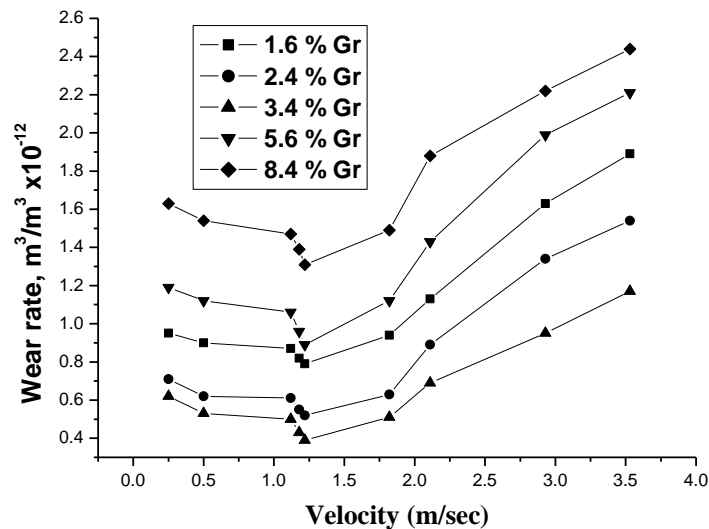


Fig 13. Variation of wear rate with sliding velocity at 2 kg load for Al-Sn/graphite composites.

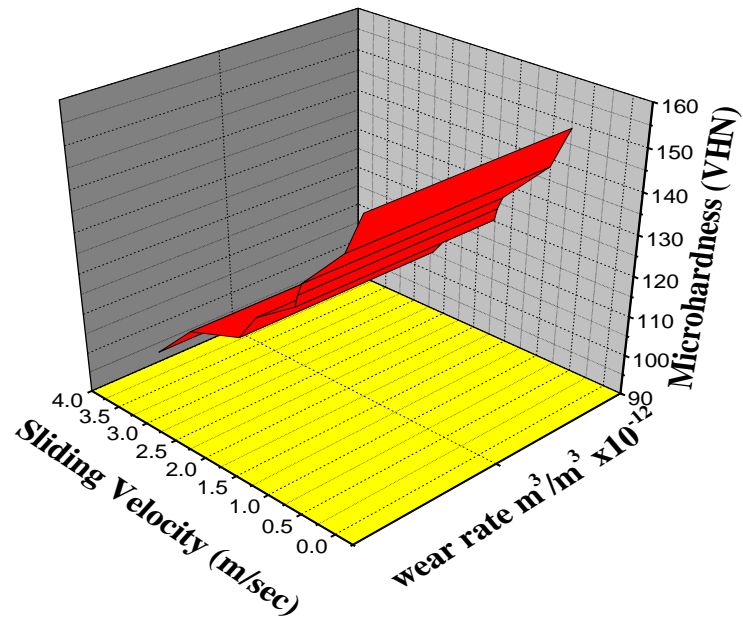


Fig 14. Variation of micro-hardness and wear rate of worn surface with sliding velocity at 2 kg load.

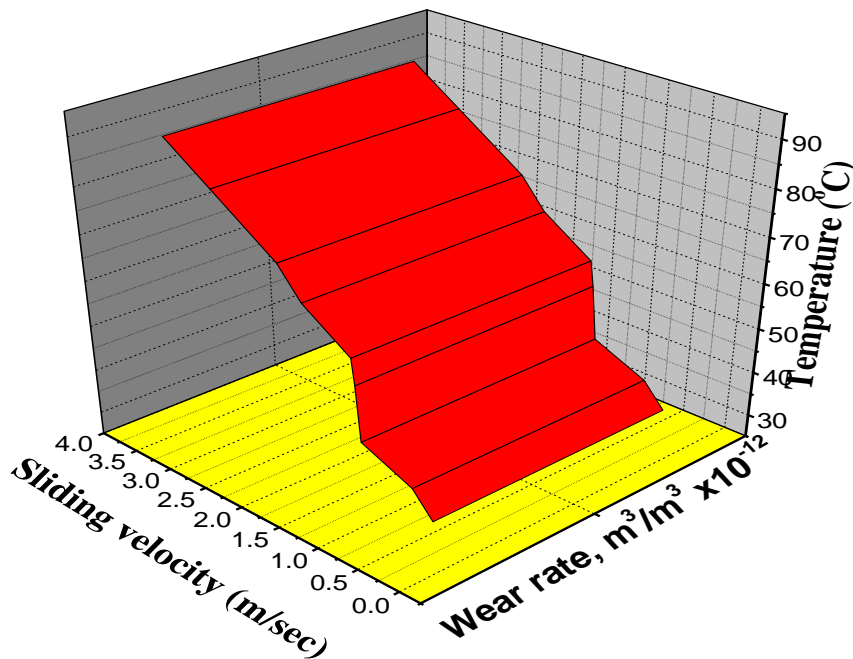


Fig 15. Variation of micro-hardness and wear rate of worn surface with sliding velocity at 2 kg load.

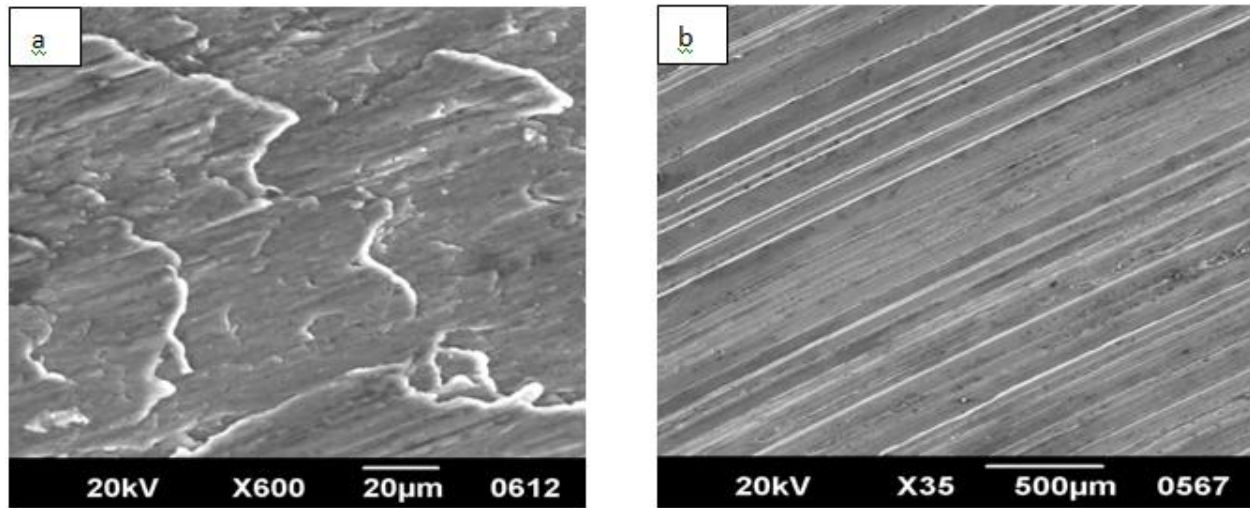
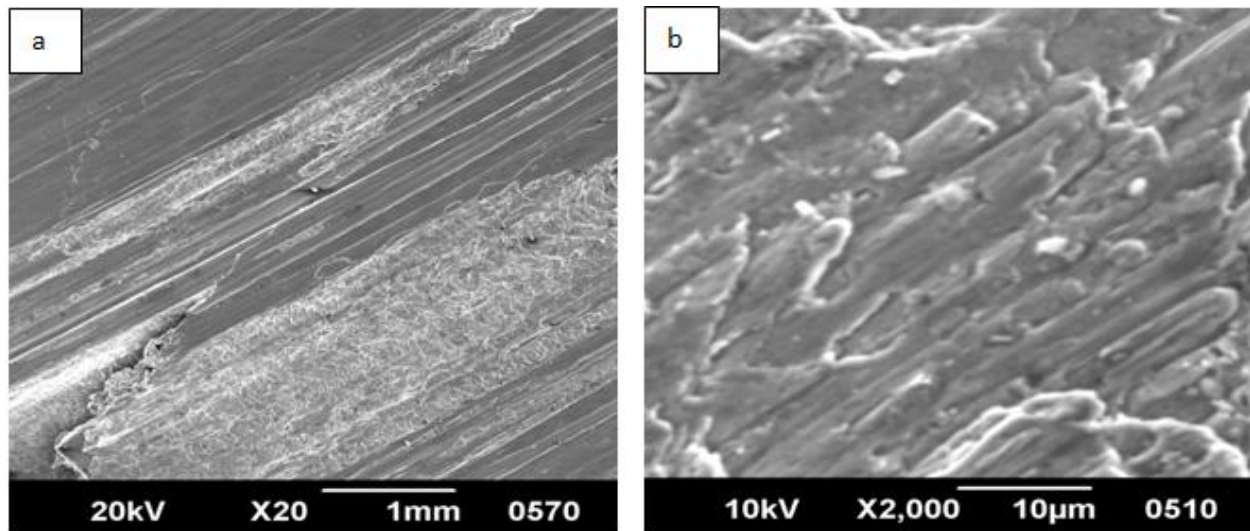


Fig 16. SEM micrographs of wear tracks of Al-Sn/graphite composites (Al-6.3%Sn-3.4%Gr) for 2 kg applied load and 0.5 m/s sliding velocity at 3000 m sliding distances (a) worn surface at 0.25m/sec (b) worn surface at 3.53m/sec



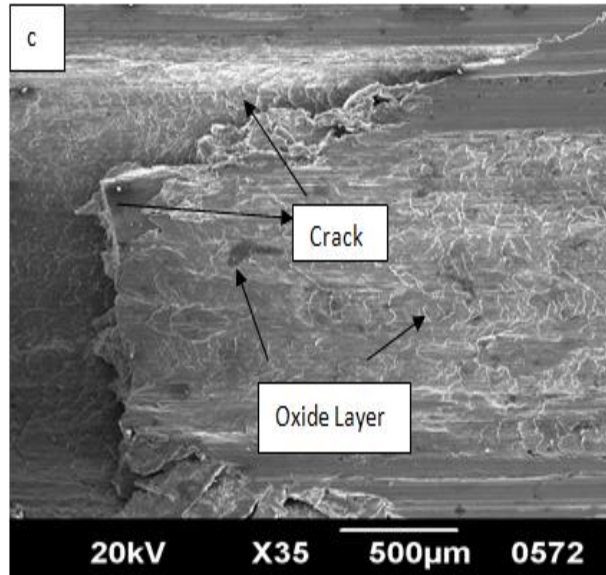


Fig 17. SEM micrographs of wear tracks of Al-Sn/graphite composites (Al-6.3%Sn-3.4%Gr) for 2 kg applied load and 1.22 m/s sliding velocity at 3000 m sliding distances (a) worn surface (b) observation of the oxide layer (c) Crack propagation in oxide layer

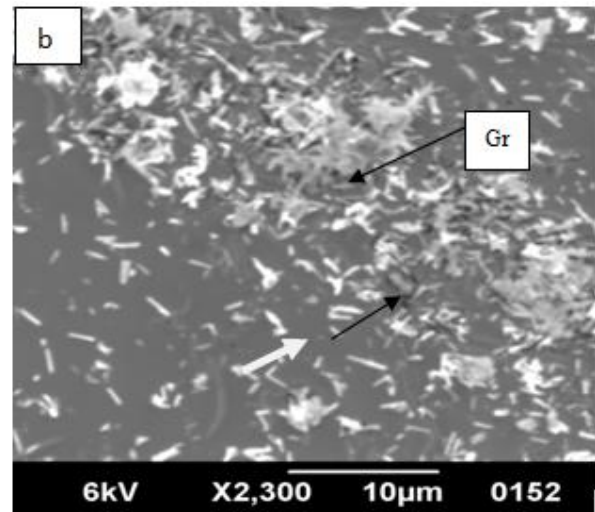
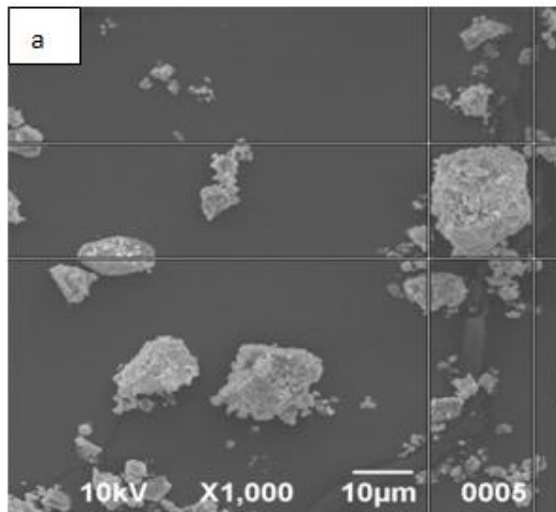


Fig 18. SEM micrographs of wear debris of Al-Sn/graphite composites (Al-6.3%Sn-3.4%Gr) for 2 kg applied load and 1.22 m/s sliding velocity at 3000 m sliding distances (a) collecting particles (b) examination of the graphite particles. In Fig 18(a) X=17.0µm, Y=21.6µm and D=27.5µm

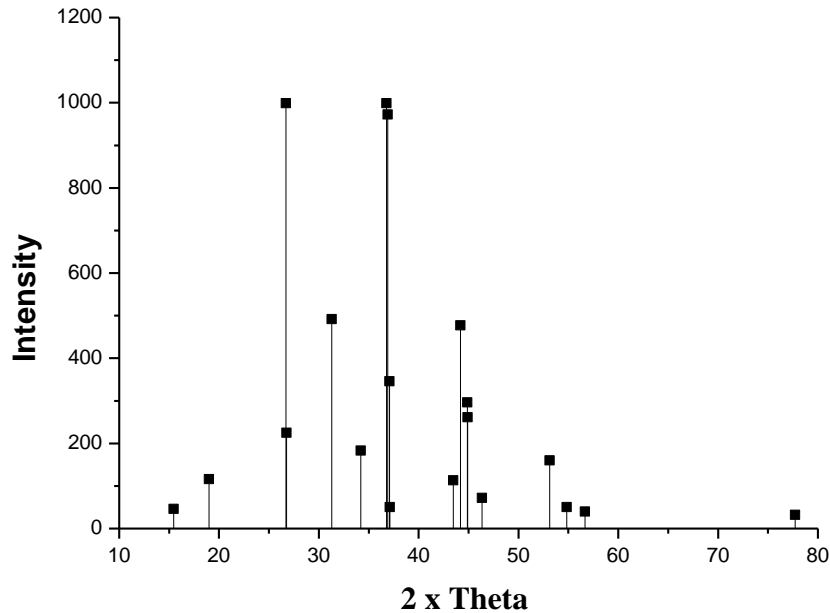


Fig 19. XRD of the wear debris.

In accordance with the figure the increase of the friction coefficient corresponds to increase the normal load. The increase rate is especially evident for load change from 10 to 50 kg. On increasing the applied load, lubricating condition of the graphite deteriorates; the alloy composition starts to play its role in determining the running ability of the test under friction. Fig. 22 shows the variation of coefficient of friction with wt % of graphite content in the matrix. The friction coefficient of the test materials decreases with increase the graphite content in the matrix. With increasing the graphite content, the thickness of the lubricating film and the amount the graphite in the lubricating film increases. The graphite comes more and more contact with sliding surface and results in lowering the frictional coefficients of the composite materials. The worn surfaces of the samples from the SEM examination

are shown in Fig. 23. The worn surfaces of the (Al-6.3%Sn-3.4%Gr) samples were noticed to be smoother than those of the (Al-6.3%Sn-8.4%Gr). Generally, the parallel ploughing grooves and scratches can be seen over all the surfaces in the direction of sliding. These grooves and scratches resulted from the ploughing action of asperities on the counter disc of significantly higher hardness. The worn surfaces of the samples from the SEM examination are shown in Figure 23 a-b. The worn surfaces of the test sample were noticed to be smoother at the higher load than at the lower load as shown in Fig 23. Generally, the parallel ploughing grooves and scratches can be seen over all the surfaces in the direction of sliding. These grooves and scratches resulted from the ploughing action of asperities on the counter disc of significantly higher hardness.

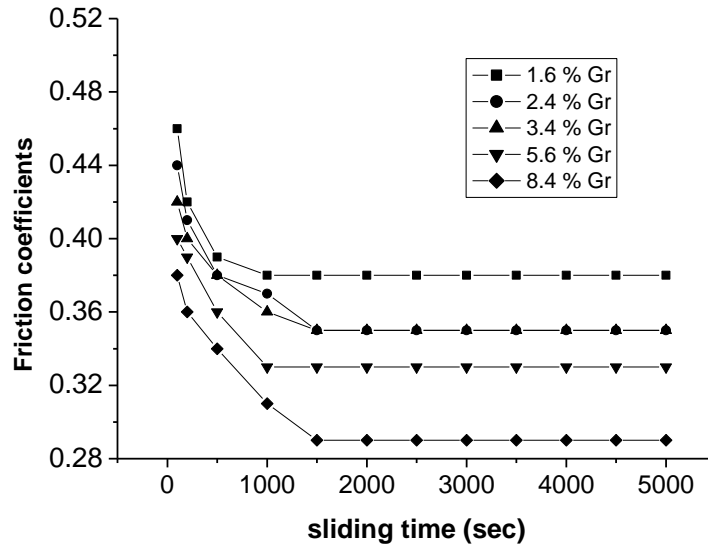


Fig 20. Friction coefficient variation of (Al-Sn/Gr) composite during sliding time at fixed specific loads (i.e. 10N) and sliding speeds (1.22 m/sec)

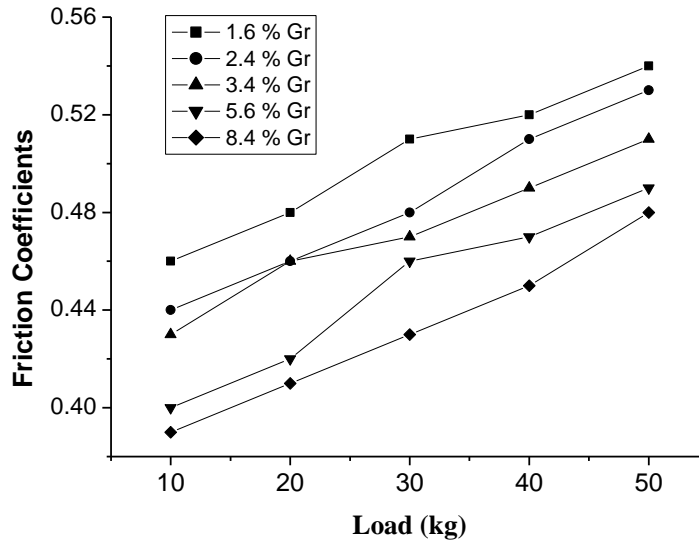


Fig 21. Coefficient of friction vs. applied load for (Al-Sn/Gr) composite at 0.932m/sec

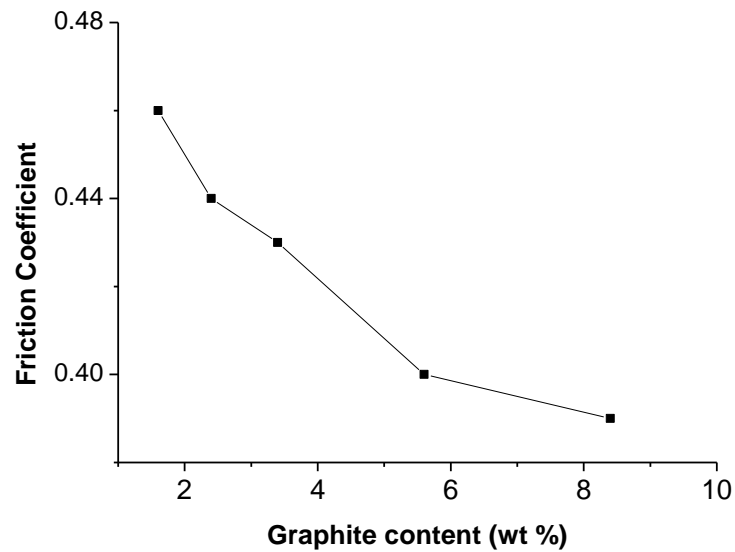


Fig 22. variations in the coefficient of friction with the wt % of graphite in the matrix.

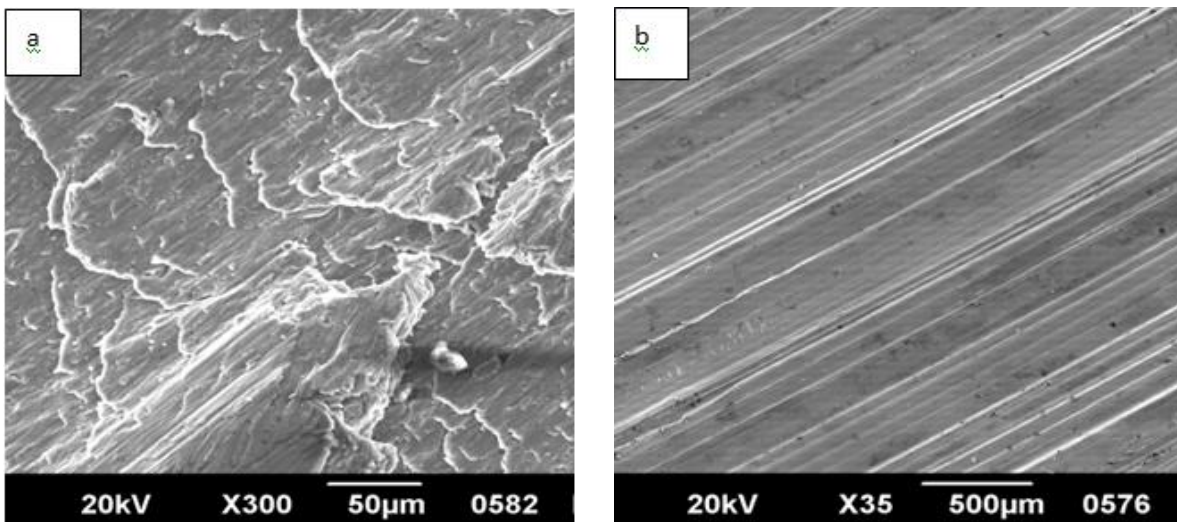


Fig 23. SEM micrographs of wear debris of Al-Sn/graphite composites (Al-6.3%Sn-3.4%Gr) for 2 kg applied load and 1.22 m/s sliding velocity at 3000 m sliding distances (a) at lower loads (b) at higher loads.

5. Conclusion

1. The Al-Sn/Graphite composite is being prepared from liquid metallurgical methods. It can be observed from the present investigation that graphite could be successfully and uniformly distributed in aluminium-tin base matrix using impeller mixing chill casting technique.
2. UTS, 0.2%PS and VHN increased with decreases with increases the volume fraction of the graphite in the matrix.
3. The Al-6.3%Sn-8.4%Gr composite showed higher percentage of elongation while compared to Al-6.3%Sn-1.6%Gr
4. From the present investigation we have also observed that the ductility of composite increase with increase the percentage of graphite.
5. The hardness is another affecting parameter which affects the rate of wear, decreases with increase the percentage of graphite in the matrix.
6. At higher contents, a graphite agglomeration is presented, and this effect reduces the mechanical resistance. This variation is related to the graphite dispersion / agglomeration into aluminum alloy matrix.

7. Wear rate with sliding distance shows almost a linear relationship for all combinations of loads and sliding velocities and composites.
8. Wear rate increases continuously with applied load for all the sliding velocities and composites studied.
9. Wear rate initially decreases with increase in sliding velocity attains a minima in wear rate and then increases with further increase in sliding velocity for all the loads and composites.
10. Low loads and sliding velocities are dominated by oxidative debris whereas higher loads and sliding velocities are dominated by metallic debris..
11. At low loads and sliding velocities wear track surface is largely covered with oxide layer and smooth in nature but at higher loads or sliding velocities surface is highly deformed with deep grooves and gross delamination occurs leading to larger wear rate.
12. The coefficient of friction decreases with increase the graphite content in the matrix.

Reference

- [1] **A. N. Patel** and **S Diamond.**, Mater. Sci. Eng. **98**, 329 (1988).
- [2] **J. P. Pathak, V Singh.**, and **S. N. Tiwari, J.** Mater. Sci. Lett. **11**, 639 (1992).
- [3] **T. B. Massalki**, *Binary Alloy Phase Diagrams* (American Society for Metals, Metals Park, OH, 1986).
- [4] **L. Ratke**, and **S. Diefenbach**, Mat. Sci. Eng. **R15**, 263 (1995).
- [5] **R. N. Singh** and **F. Sommer**, Rep. Prog. Phys. **60**, 57 (1997).
- [6] **L. F. Mandolfo**, Aluminum Alloys, structure and properties, Butterworth's London (1976), 8585
- [7] **A.K. Jha, S.V Prasad., G.S. Upadhyaya**, Dry sliding wear of sintered 6061 aluminium alloy / graphite particle composite, Tribology International, (1989) p 321-327.
- [8] **A.K. Jha, S.V. Prasad, G.S. Upadhyaya**, Sintered 6061 aluminium alloy – Solid lubricant particle composites: Sliding wear and Mechanism of lubrication, Wear 133 (1989) p 163-172.
- [9] **R.C Prasad., and P. Ramakrishnan** Composites Science & Technology, New Age International Publishers, (2009).
- [10] **F. Akhlaghi**, and **A. Zare-Bidaki**, Influence of graphite content on the dry sliding and oil impregnated sliding wear behavior of aluminium 2024 – graphite composites produced by in situ powder metallurgy method. Wear 266 (2009) 37-45.
- [11] **P.K. Rohatgi** and **B.C. Pai**, Seizure Resistance of Cast Aluminum Alloys Containing Dispersed Graphite Particles of Various Sizes, Wear, 1980, 59, p 323–332
- [12] **S.V Prasad.** and **R Asthana.**, Aluminum Metal Matrix Composites for Automotive Applications: Tribological Considerations, Tribol. Lett., 2004, 17(3), p 445–453
- [13] **P.R Gibson.**, **A. J Clegg.** and **A.A. Das**, Mater. Sci. Technol. 1 (1985), p 559-567.
- [14] **P.R Gibson.**, **A. J Clegg.** and **A.A. Das**, Wear of cast Al-Si alloys containing graphite: Wear, vol 95(1984) p193-198.
- [15] **S. Das, S.V. Prasad, T.R. Ramachandran**, Wear 133 (1989) p 173-187.
- [16] **C.B. Lin, R.J. Chang, W.P. Weng.**, A study on process and Tribological behavior of aluminum alloy / Graphite particle composite, Wear 217 (1998), p 167-174.
- [17] **T. Savaskan, and A. Aydiner** Effects of silicon content on the mechanical and tribological properties of monotectoid-based zinc-silicon-silicon alloys, Wear 257(2004) ,p 377-388,.
- [18] **B. K Prasad** Effects of microstructure on the sliding wear performance of Zn-Al-Ni alloy, Wear 240(2000), p100-112.
- [19] **G. Purcek, T. Kucukomeroglu, T. Savaskan., and S. Murphy.**: Dry sliding friction and wear properties of zinc-based alloy, Wear 252(2002), p 894 – 901,
- [20] **S. Mohan.** and **S. Srivastava** Surface behaviour of as-Cast Al-Fe intermetallic composites. Tribology Letters, Vol. 22, No. 1, April (2006).
- [21] **B.S. Majumdar, A.H. Yegneswaran, and P.K. Rohatgi**, Strength and Fracture Behavior of Metal Matrix Particulate Composites, Mater. Sci. Eng., (1984), 68, p 85–96
- [22] **K.K Chawla.**, Composite Materials, 2nd ed., Springer, New York, 1998, p 3–5
- [23] **T.W Clyne.** and **P.J .Withers.**, An Introduction to Metal Matrix Composites, 1st ed., Cambridge University Press, Cambridge, (1993), p 1–10.
- [24] **Sheng-ming Zhou, Xiao-bin Zhang, Zhi-peng Ding, Chun-yan Min, Guo-liang Xu, Wen-ming Zhu.** Fabrication and tribological properties of carbon nanotubes reinforced Al composites prepared by pressureless infiltration technique [J]. Composites Part A: Applied Science and Manufacturing, (2007), 38(2): 301–306.
- [25] **N. P. Suh** The delamination theory of wear [J]. Wear, (1973), 25(1): 111–124.–13

Synthesis and Characterization of BaTiO₃ Nano particles by Organic Precursor Method

R.Sengodan¹, B.Chandar Shekar^{2*} S.Sathish²

¹Department of Physics, Kumaraguru College of Technology, Coimbatore, Tamil Nadu.

²Department of Physics, Kongunadu Arts and Science College, G.N- Mills, Coimbatore, Tamil Nadu.

Abstract

BaTiO₃ nano powders prepared by using organic acid method. IR spectrum and EDS were used to identify the composition of the nano particles. XRD spectrum indicated the polycrystalline nature of the particles. Surface morphology of the particle was studied by scanning electron microscope (SEM). No pits and pin holes were found in the surface.

Keywords: BaTiO₃, EDS, XRD, SEM, etc.,

1. INTRODUCTION

Ferroelectric thin films are very promising for a wide range of application such as high dielectric capacitors, insulating surface layer, non volatile memories with low switching voltage, infrared sensors and electro optic devices. BaTiO₃ family ceramic thin films are receiving extensive investigation as the charge- storage dielectric for G-bit dynamic random access memory(DRAM), on-chip components such as de-coupling capacitors and positive temperature coefficient of resistance (PTCR) thermistors due to high dielectric constant, low dielectric loss, low leakage current, low temperature coefficient of dielectric constant and thermal stability[1].

Synthesis of BaTiO₃ nanopowders and thin films has attracted great attention over the last few decades due to the desirable properties and applications. BaTiO₃ particles could be produced by employing various chemical methods such as sol-gel technique[2], metal-organic processing [4], co-precipitation[3], hydrothermal treatment [5,6] and mechanochemical synthesis[7]. Organic acid precursor is a promising method that offer relative low cost, uniform size, homogeneous powder and high purity of the ceramics.

This films of BaTiO₃ could be prepared by different technique like r.f sputtering [8], pulsed laser ablation [9] and metal- organic chemical vapour deposition [10] etc. Despite that several technique have been explored to deposit thin film of BaTiO₃ less attention has been devoted to thermal evaporation. In the present study, we have reported about the BaTiO₃ nanopowder prepared by using organic acid precursor method using titanium dioxide TiO₂ as a source of titanium and oxalic acid as organic acid..

2. EXPERIMENTAL

2.1 Synthesis of BaTiO₃ nanopowder

BaTiO₃ nanopowders were synthesized using organic acid precursor method. The starting materials used were barium chloride BaCl₂·2H₂O, TiO₂ powder and Oxalic acid. A solution of Ba: Ti : Oxalic acid mole ratio 1: 1: 1 was stirred and evaporated at 70°C till a clear, viscous resin was obtained, then dried at 110°C for 20 hours. The precursor formed was heated at 900°C for 2 hours to form BaTiO₃ nanopowder.

2.2 Characteristics of BaTiO₃ nanopowder

FTIR and Energy Dispersive X-ray micro analyzer (EDX) were used for the identification of the chemical composition. The XRD patterns of the resulting products were obtained from X- ray powder diffraction with CuK α radiation. The micrograph of BaTiO₃ was examined by direct observation via scanning electron microscope (SEM).

3. RESULT AND DISCUSSION

Fig.1 shows infrared spectra of the prepared BaTiO₃ nanopowder. A strong absorption feature at 3205cm⁻¹ has been identified as the stretching mode of OH ions interpreted in the film and is commonly found in pervoskite films grown at low temperature by more conventional techniques.

This absorption referred to as hydroxyl defects because of the high mobility of hydrogen in pervoskite materials and is usually annealed out at temperatures near the phase transformation temperatures. The peaks at 809 cm⁻¹, 1290 cm⁻¹, 1663 cm⁻¹, 2357 cm⁻¹, 2521cm⁻¹ and 2646 cm⁻¹ are characteristics of the CO₃²⁻ group. The band at 3205 cm⁻¹ assigned to bulk hydrogen impurities [11].

It is well known that hydrogen impurities can penetrate several ternary oxides with perovskite structure as H^+ bonded to lattice oxygen in the form of an OH^- [12]. These protons can compensate for the cation charge defect due either to reduced centers such as Ti^{3+} or to cation vacancies in nonstoichiometric samples. The weak shoulder near 2900 cm^{-1} , 1958 cm^{-1} and 1042 cm^{-1} which are characterized by the absorption of CH_2 groups. The broad bands at 557 cm^{-1} and 400 cm^{-1} are due to Ti-O vibrations in $BaTiO_3$. FTIR analysis suggested that defects of negligible percentage are present in the lattice of $BaTiO_3$ nano powder.

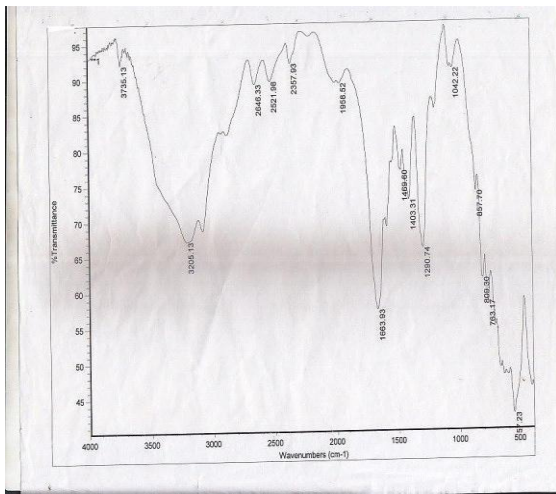


Fig. 1 FTIR spectrum of $BaTiO_3$ nano powder

Fig.2 shows the EDS spectrum of as prepared $BaTiO_3$ nano powder. Elemental composition analysis indicated the presence of Ba, Ti and O in the synthesized $BaTiO_3$ nano powder.

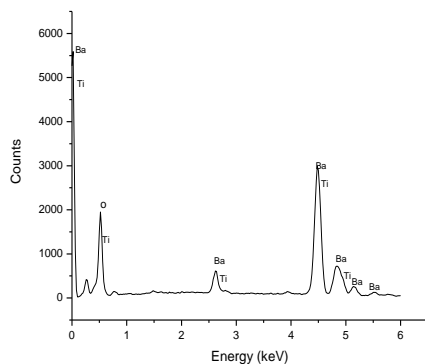


Fig.2 EDS spectrum of $BaTiO_3$ nano powder

A typical X-ray diffraction (XRD) pattern of $BaTiO_3$ powder as shown in the Fig.3.

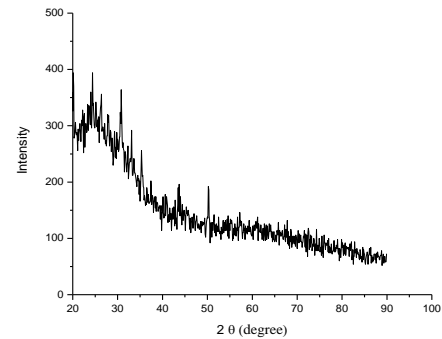


Fig. 3 XRD pattern of $BaTiO_3$ nano powder.

The crystallite size of $BaTiO_3$ for the most intense peak determines from the X-ray diffraction data using the Debye-Scherrer formula.

$$d_{RX} = kd/\beta \cos \theta$$

Where d_{RX} is the crystallite size to account for particle size $k = 0.9$ is a correction factor to account for particle shapes, F is the full width at half maximum (FWHM) of the most intense diffraction peak, λ is the wavelength of Cu target = 1.5406 \AA , and θ is the Bragg's angle. The small peaks are observed at $2\theta=24.4^\circ$ with a d value of 3.64 \AA , at $2\theta=30.712^\circ$ with a d value of 2.908 \AA , at $2\theta=35.34^\circ$ with a d value of 1.81 \AA . The peaks at $2\theta = 24.4^\circ$, 30.71° , 35.34° and 44° are respectively results from (001), (101), (110) and (002)/(200) planes of $BaTiO_3$. The resulting XRD and lattice parameters exactly match $BaTiO_3$ pattern (JCPDS 31-174).

A typical scanning electron micrographs of $BaTiO_3$ nano powder as shown on Fig. 4. The particulate phase in the micrograph is the $BaTiO_3$ grains and the voids seen in the micrograph. The micrograph indicates that the average grain size of $BaTiO_3$ nano powder varies from 90.68 nm to 133 nm .

REFERENCE

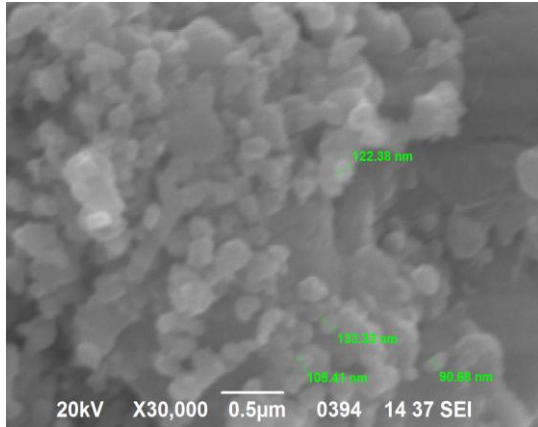


Fig.4 SEM micrograph of BaTiO₃ nano powder.

The grain size of vacuum evaporated BaTiO₃ thin films are relatively large compared to as prepared BaTiO₃ nano powder. Arlt.et.al [13] have reported that BaTiO₃ exists predominantly in the tetragonal structure for grain size of 1.5 µm and above and that, for an average grain size below 1.5 µm, tetragonal and orthorhombic phases coexist. Therefore, it seems that BaTiO₃ films prepared in this study also exists as a mixed system of tetragonal and orthorhombic or pseudocubic structure. Our X-ray studies also support this conclusion, because the peaks corresponding to the (002) and (200) planes are not well resolved.

4. CONCLUSION

We have successfully synthesized nano powder of BaTiO₃ by low cost organic acid precursor method using commercially available chemicals such as oxalic acid, TiO₂ and BaCl₂. The composition of BaTiO₃ nanopowder were confirmed by IR and EDX analysis. XRD indicated the predominantly amorphous nature of the film. The presence of small peaks indicated the presence of crystallites of very low dimension in the amorphous region. No pits, pin holes and dendritic features are found on the surface in SEM micrographs.

1. Scott, J.F., Annu. Rev. Mater. Sci., 28(1998)79.
2. Tangwiwat, S. and Milne, S.J., J. Non. Crystalline Solids, 351 (2005) 976.
3. Kirby, K.W., Mater. Res. Bull, 12 (1998) 881.
4. Shaikh, A.S. and Vest, G.M., J. Am. Ceram. Soci., 69 (1986) 682.
5. Boulos, M., Fritsch, S., Mathieu, F., Durand, B., Lebey, T., and Bley, V., Solid State Ionics, 176 (2005) 1301.
6. Tsumara T., Matsnoka K. and Toyoda M., J. Mater. Sci. Technol., 26(1) (2010) 33.
7. Stojanovic, B.D., Simowes, A.Z., Santos, C.O., Jovalekic, C., Mitic, V.V., and Varela, J.A., J. Euro. Ceram. Soci., 25(2005)1985.
8. Bhattachariya,P., Komeda,T., Park,D. and Nishioka,Y., Japan J. Appl. Phys., 32(1993)4103.
9. Yoon, S.G., Lee, J. and Safari, A., Integrated Ferroelectrics., 7(1995)329.
10. Tahan, D., Safari, A. and Klin, L.C., J. Am. Ceram. Soci., 79(1996)1593.
11. Kapphan, S. and Weber, G.R., Ferroelectrics, 37(1981) 673.
12. Baikov, Y.M. and Shalkona, E.K., J. Solid State Chem., 4(1994)1875.
13. Arlt, G., Hennings, D. and Dewith, G., J. Appl. Phys., 58(4)(1985)1619.

THE FINITE ELEMENT ANALYSIS OF THE HUMAN RIB CAGE

ROSHAN P. GHODKHANDE.

Department Of Mechanical Engg.
Yeshwantrao Chavan College Of Engineering Nagpur,
Maharashtra, India

Prof .AJINKYA P. EDLABADKAR

Department Of Mechanical Engg.
Yeshwantrao Chavan College Of Engineering Nagpur,
Maharashtra, India.

Abstract

In this paper, finite element analysis of the rib cage model is applied to, recognize stress distributions and to determine the rate of bone fractures (especially for pathologically changed bones). Also to determine the load and stress to occurs on the human rib cage at any accident.

Key words: finite element model, thorax, rib cage, Nuss implant, pectus Excavatum, fail chest.

Introduction

Generally, frontal impacts are considered to be the most common vehicle collisions causing injuries. This paper describes development and validation of a thorax finite element model of a 15-25 years old child. The thorax model is developed in order to perform more detailed investigation of the human rib cage responses and injuries subject to impact loads. Anthropometric data of thorax is obtained from measurements and from drawings of crosssections found in atlases of the human anatomy. Let us begin first from a brief description of the rib cage anatomy. The skeleton of thorax or chest is an Osseo-cartilaginous cage containing and protecting principal organs of respiration and circulation. The *posterior surface* is formed by twelve thoracic vertebrae and posterior parts of the ribs. It is convex from the above downwards, and presents (on either side of the middle line) a deep groove, in consequence of the lateral and backward direction taken by the ribs from their vertebral extremities to their angles. The *anterior surface*, formed by the sternum and costal cartilage, is flattened or slightly convex, and inclined from the above downwards and forwards. The *lateral surfaces* are convex. They are formed by the ribs, separated from each other by the intercostal spaces, eleven in number, which are occupied by the intercostal muscles and membranes. Ribs (1-7) either increase in length or decrease (7-12). Ribs 1-7 (called TRUE) are attached directly to sternum (sternal joints or interchondral joints) via strips or bars of hyaline cartilage, called the costal cartilage. Ribs 5-12 are called FALSE, since the costal cartilage is not attached directly to the sternum. Cartilage of ribs 8, 9, 10 are attached to each other and then to the cartilage of rib 7, and they form the costal margins. The left and right costal margins form costal arch. Ribs 11 and 12 are called FLOATING, because anterior ends are not attached to the sternum and posterior ends. The

latter are attached to thoracic vertebrae (see Fig. 1). The ribs and the sternum contain red bone marrow capable of hematopoiesis.

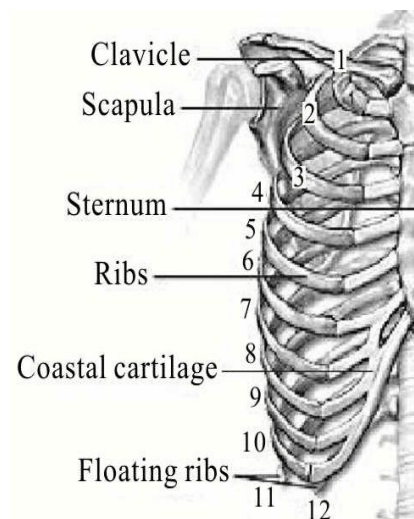


Fig. 1. Thorax anatomy

Let us now introduce description of joints of the thorax.

Costovertebral joints: head of each typical rib articulates with demifacets of two adjacent vertebrae and the crest of the head is attached by a ligament to the intervertebral disk.

Costotransverse joint: the tubercle of a typical rib articulates with the facet on the tip of the transverse process of its own vertebra to form a synovial joint.

Sternocostal joints: the point of articulation between the costal cartilages and the sternum (costal notches). The lower joints are strengthened anteriorly and posteriorly by radiate sternocostal ligaments.

Costochondral joints: a joint between the costal cartilage and a rib. No movement normally occurs at these joints.

Interchondral joints: articulation between costal cartilages from adjacent ribs.

2. Materials and methods

2.1. Thorax model

Anthropometric data of thorax is obtained from measurements and from drawings of crosssections found in atlases of the human anatomy . Note that the rib cage is difficult to model due to complex curves of the ribs. After reviewing descriptions and diagrams of the ribs, when lungs inhale and exhale, it had been discovered that they are rotated around the costovertebral joints (the joints that are attached to the spine). The pivot points are moved into this position and the ribs are rotated to test their movement. The root bones are placed in the centre of the spine where the pivot points are placed. Figure 2 shows the axis which the ribs rotate around. The root bones are placed to get an accurate representation of ribs movement during breathing.

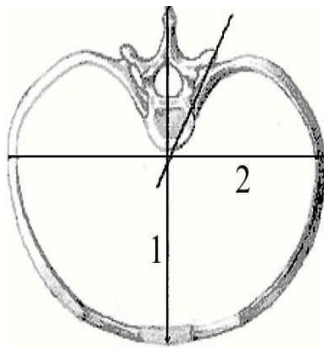


Fig. 2. Thorax joints

The created FE model of thorax has a few important simplifications:

- the costochondral, intercostals, interchondral joints are neglected;
- natural complex curves of ribs are simplified;
- heterogeneous, anisotropic, non-linear material properties of bones and cartilage are approximated by a homogeneous, isotropic and linear elastic material.

2.2. Method

All computations are carried out using the commercial FEM (Finite Element Method) program ANSYSR. Static and linear strain-displacement relation analysis are performed. To create a finite element representation of a structure, it is first divided into simple parts called elements. Consider a single element: forces and displacements at the nodes are linked by the stiffness matrix for the element. Each element has nodes which are joined by the nodes of adjacent elements to re-create the total structure. The

stiffness terms for a node are then a sum of all stiffness terms composed of the elements joined at that node. In this way, the global stiffness matrix for the whole structure is obtained by re-assembly of individual elements.

Model environment

The thorax model is cylindrically supported in place, where in a real rib cage the costovertebral joints are placed (see Fig. 3). In the internal surface of ribs and sternum a pressure of 0.04MPa is applied in order to simulate interaction of internal organs. A force of 5000N is applied to the sternum, which is generated by a car-to-car frontal collision .

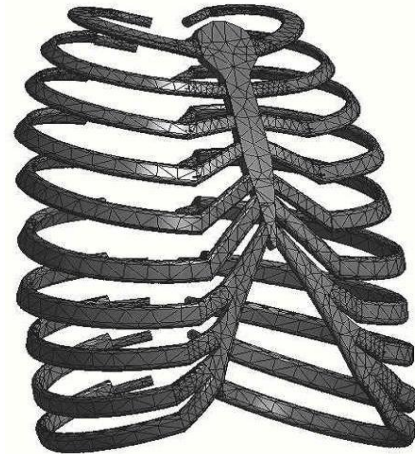


Fig. 3. Meshed model, applied loads and support

2.4. Model verification

The model is verified for correct movement of each rib in inhale and exhale periods . Bochenek and Reicher found from measurements the range of displacement for each rib. Our simulation of the rib cage model is in a good agreement with Bochenek's observation. carried out a series of cadaver tests for the thoracic frontal impacts. Their test included cadavers of anthropometric data and was similar to our model. The simulation result showed a good agreement with the test data. Figure 4 demonstrates that the model can predict a bone fracture in the ribs and sternum, which is in agreement with observation in the cadaver tests.

3. Model

Two thorax models are considered. The first model is designed to investigate stress distribution in a healthy human rib cage. The second one taken into account is a numerical model of the chest after the Nuss pectus excavatum repair procedure. Pectus excavatum, or the funnel chest, is one of the finite element model of the human rib cage 29

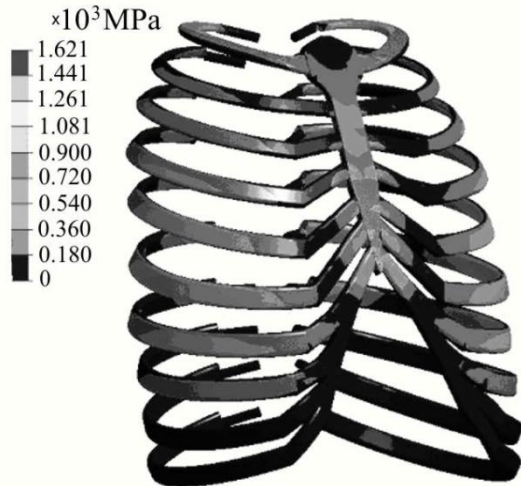


Fig. 4. Equivalent stress distribution without implant

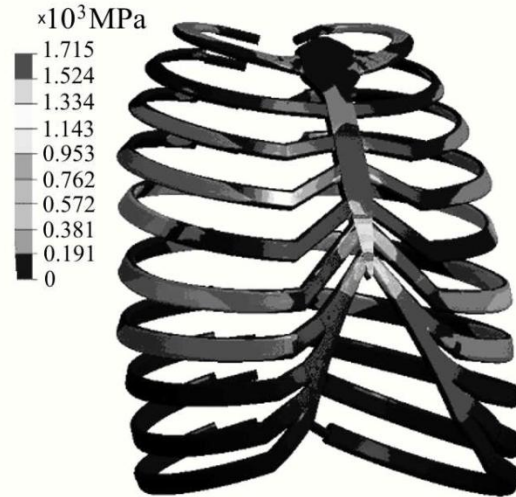


Fig. 5. Equivalent stress distribution with implant

most common major congenital anomalies occurring in approximately one in every 400 births. The Nuss procedure is a new and minimally invasive technique of repair of pectus excavatum. The Nuss procedure avoids any cartilage resection and sternal osteotomy by placing a carefully preformed convex steel bar under the sternum through bilateral thoracic incisions, and then by turning it over to elevate the deformed sternum and costal cartilages to a desired position. The bar is secured to the lateral chest wall muscles with heavy sutures. If the bar is unstable, a 2 up to 4 cm stabilizing cross bar is attached to one or both ends of the sternal bar. The bar is left in such a position for two or more years, depending on patient's age and severity of deformation, when re-modeling of the deformed cartilages and sternum has occurred. It is to be remembered that the nuss implant is left in the human organism for two or even more years. It can happen that during such a long period of time the patient may participate in a road accident. Therefore, investigation of the rib cage responses to impact loads is being carried out. Comparison of stress distributions in skeleton parts for these two cases is expected to be useful for further developments of appropriate implant designs.

4. Conclusion

Careful analysis of Fig. 4 and Fig. 5 leads to the following conclusions:

- in the model with the implant, a fracture of the 5-th rib appears faster and is caused by a smaller force, and the implant may damage lungs or heart,
- it is easy to recognize that the stress distribution is violated by the implant,
- in healthy thorax, ribs (1-7) transfer a large majority of the load.

Comparing Fig. 6 and Fig. 7, one can conclude that the sternum displacement in the model with the implant is smaller. However, this could be an illusion since the implant causes faster fracture of the 5-th rib, and the thorax stiffness becomes weaker. When a human body is exposed to an impact load, soft tissues of internal organs can sustain large stress and strain rates. To investigate mechanical responses of the internal organs, further development of the model should include modelling of the organs as well. Homogenous and linear elastic properties of incorporated materials are assigned to each part of the model, whereas the human cartilages and bones may exhibit different material properties. In order to create a more realistic representation, more complex tissue material properties should be reflected in the study.

The finite element model of the human rib cage 31

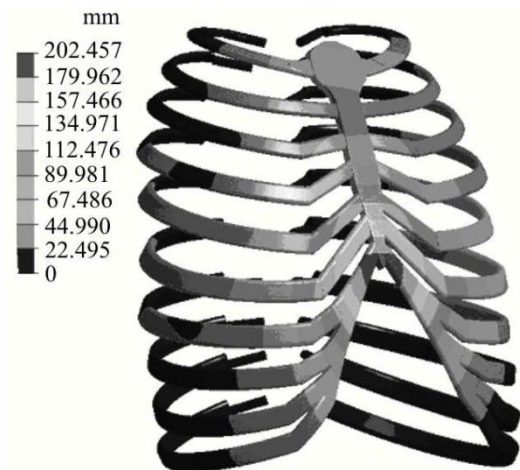


Fig. 6. Equivalent displacements distribution without implant

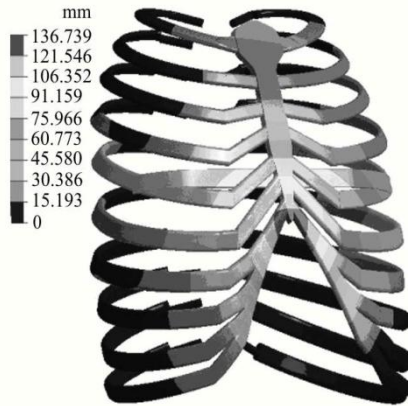


Fig. 7. Equivalent displacements distribution with implant

References

- **Art of Human Anatomy : Frank H. Netter MD**
Publisher: Saunders,
Published: 2010-05-03 ASIN: 1416059512
- **The finite element method in engineering :-S.S. Rao**
,Butterworth Heinemann, 1999
- **Introduction to finite elements in engineering :-**
Tirupathi R. Chanrupatla & Ashok D. Belegundu
,Prentice Hall, 2002
- Będziński R., 1997, *Engineers Biomechanics, Technical University of Wroclaw Press, Wroclaw* [in Polish].
- Łaczek S., 1999, *Introduction to the Finite Element Method ANSYS, Technical University of Krakow* [in Polish].
- Harrigan T.P., Hamilton J.J., 1994, Necessary and sufficient conditions for global stability and uniqueness in finite element simulations of adaptive bone,*Int. J. Solids Structures*, 31, 1, 97-107.
- Oshita F., Omori K., Nakahira Y., Miki K., 2001, Development of a finite element model of the human body, *7-th International a LS-DYNA Users Conference*
- Harrigan T.P., Hamilton J.J., 1994, Necessary and sufficient conditions for global stability and uniqueness in finite element simulations of adaptive bone,*Int. J. Solids Structures*, 31, 1, 97-107
- . Kowalewski J., Brocki M., Sapiezko J., Dancewicz M., 1997, *Chirurg-*

Design of Integral Controller for SSSC and TCPS based AGC of hydrothermal System under Deregulated Environment

K.Subbaramaiah¹, V.C Jagan Mohan², V.C Veera Reddy³

*(EEE Department, Yogananda Institute of technology and Science, Tirupathi, India)

** (Research Scholar, S.V University, Tirupathi, India)

** (Department of Electrical Engineering, S.V.University, Tirupathi)

ABSTRACT

This paper presents the design of integral controller for Automatic Generation Control (AGC) of hydrothermal system under deregulated environment employing simulated annealing (SA). Static Synchronous Series Compensator (SSSC) has also been proposed to further increase the dynamic performance of the system in terms of peak time, overshoot and settling time. The concept of soft computing techniques greatly helps in overcoming the disadvantages posed by the conventional controllers. Open transmission access and the evolving of more socialized companies for generation, transmission and distribution affects the formulation of AGC problem. So the traditional AGC system is modified to take into account the effect of bilateral contracts on the dynamics. Simulation results show that the simulated annealing based system employing Static Synchronous Series Compensator has better dynamic performance over the system without SSSC.

Keywords - Automatic Generation Control, Static Synchronous Series Compensator, Simulated annealing, Hydrothermal system

I. INTRODUCTION

Successful operation of a power system is the process of properly maintaining several sets of balances. Two of these balances are between load-generation and scheduled and actual tie line flows. These two balances are predominant factors to keep frequency constant. Constant frequency is identified as the primary index of healthy operation of system and the quality of supplied power to consumer as well. Both of these balances are maintained by adjusting generation keeping load demand in view. If frequency is low, generation is increased and if the actual outflow is greater than the scheduled outflow, generation is decreased. Since system conditions are always changing as load constantly varies during different hours of a day, precise manual control of these balances would be impossible. Automatic Generation Control (AGC) was developed to both maintain a (nearly) constant frequency and to regulate tie line flows [1-3].

Under open market system (deregulation) the power system structure changed in such a way that would allow the evolving of more specialized industries for generation (Genco), transmission (Transco) and distribution (Disco). A

detailed study on the control of generation in deregulated power systems is given in [4]. The concept of independent system operator (ISO) as an unbiased coordinator to balance reliability with economics has also emerged [5-6]. The assessment of Automatic Generation control in a deregulated environment is given in detail in [7] and also provides a detailed review over this issue and explains how an AGC system could be simulated after deregulation.

In recent years intelligent methods such as simulated annealing (SA) have been applied to various problems of electrical engineering. The salient feature of these soft computing techniques are that they provide a model-free description of control systems and do not require any model identification. SA is a search and optimization method developed by mimicking the principle of annealing of molten metals. For comparison, the considered power system is controlled by using both simulated annealing based integral controller and SSSC. The results obtained show that the system with SSSC and SA based integral controller gives good dynamic response with respect to conventional controller.

The remainder of the paper is organized as follows: Section (II) focuses on Automatic Generation Control under restructured scenario. Section (III) emphasizes on modelling and implementation of SSSC. The concept of SA applied to AGC is discussed in Section (IV) and results and discussions are carried out in Section (V).

II. DYNAMIC MATHEMATICAL MODEL

The Automatic Generation Control (AGC) system investigated is composed of an interconnection of two areas under deregulated scenario. Area 1 comprises of a reheat system and area 2 comprises of hydro system. Three generators in each area have been considered for this study. Fig. 1 is the block diagram of two-area hydrothermal system under open market scenario where ACE of each area is fed to the corresponding controller. The accurate control signal is generated for every incoming ACE at that particular load change. In order to compare the performance of both the systems a performance index has been considered and the performance index which has been considered is given by

$$J = \int_0^t (\alpha \cdot \Delta f_1^2 + \beta \cdot \Delta f_2^2 + \Delta P_{tie12}^2)$$

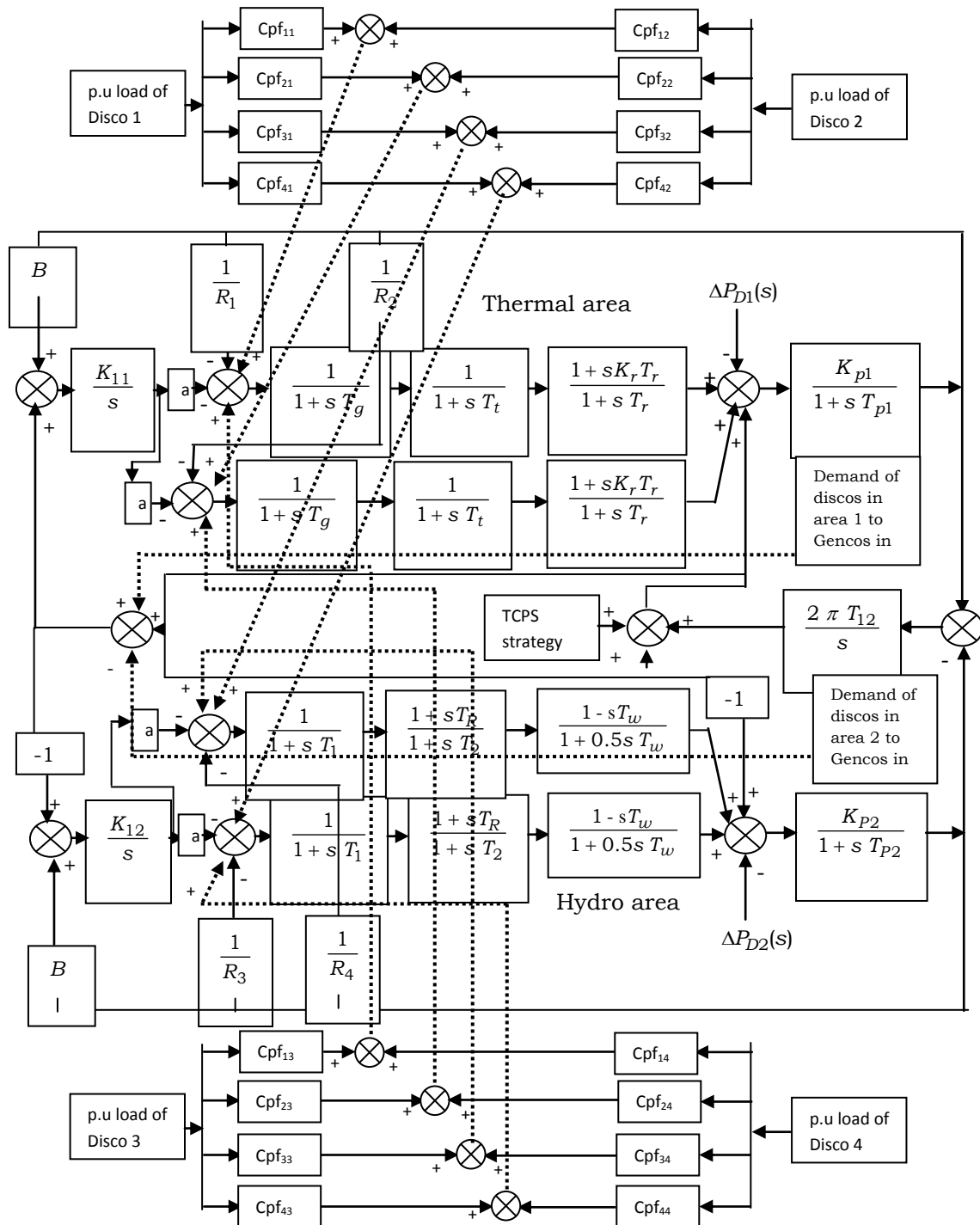


Figure. 1. Two area hydrothermal AGC block diagram under deregulated scenario

III. MODELING OF SSSC

A SSSC employs self-commutated voltage-source switching converters to synthesize a three-phase voltage in quadrature with the line current, emulates an inductive or a capacitive reactance so as to influence the power flow in the transmission lines. The compensation level can be controlled dynamically by changing the magnitude and polarity of injected voltage, V_s and the device can be operated both in capacitive and inductive mode. The schematic of an SSSC, located in series with the tie-line between the interconnected areas, can be applied to stabilize

the area frequency oscillations by high speed control of the tie-line power through interconnection as shown in Figure. 2. The equivalent circuit of the system shown in Figure 2 can also be represented by a series connected voltage source V_s along with a transformer leakage reactance X_s . The SSSC controllable parameter is V_s , which in fact represents the magnitude of injected voltage. Figure 3 represents the phasor diagram of the system taking into account the operating conditions of SSSC.

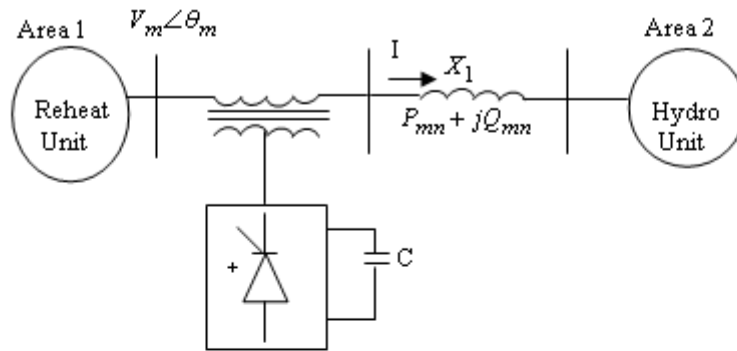


Figure 2: Schematic of SSSC applied to AGC

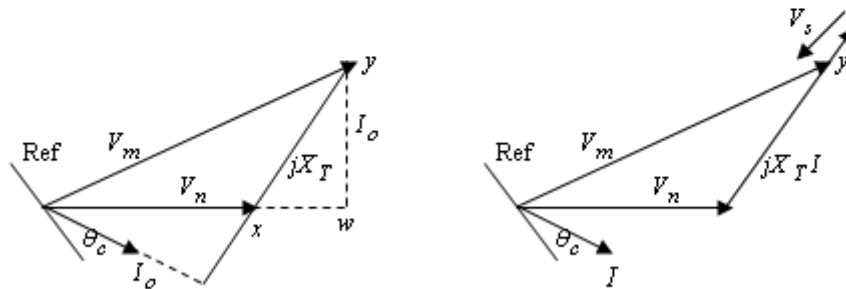


Figure 3: Phasor diagram at $V_s=0$ and V_s lagging I by 90°

Based on the above figure when $V_s = 0$, the current I_o of the system can be written as

$$I_o = \frac{V_m - V_n}{jX_T} \quad (1)$$

Where $X_T = X_L + X_S$. The phase angle of the current can be expressed as

$$\theta_c = \tan^{-1} \left[\frac{V_n \cos \theta_n - V_m \cos \theta_m}{V_m \sin \theta_m - V_n \sin \theta_n} \right] \quad (2)$$

But Eqn (1) can be expressed in a generalized form as

$$I = \frac{V_m - V_s - V_n}{jX_T} = \left[\frac{V_m - V_n}{jX_T} \right] + \left[\frac{-V_s}{jX_T} \right] = I_o + \Delta I \quad (3)$$

The term ΔI is an additional current term due to SSSC voltage V_s . The power flow from bus m to bus n can be written as $S_{mn} = V_m I^* = S_{mno} + \Delta S_{mn}$ which implies

$$P_{mn} + jQ_{mn} = (P_{mno} + \Delta P_{mn}) + j(Q_{mno} + \Delta Q_{mn}) \quad (4)$$

Where P_{mno} and Q_{mno} are the real and reactive power flow respectively when $V_s = 0$. The change in real power flow caused by SSSC voltage is given by

$$\Delta P_{mn} = \frac{V_m V_s}{X_T} \sin(\theta_m - \alpha) \quad (5)$$

When V_s lags the current by 90° , ΔP_{mn} can be written as

$$\Delta P_{mn} = \frac{V_m V_s}{X_T} \cos(\theta_m - \theta_c) \quad (6)$$

From Eqn (2) the term $\cos(\theta_m - \theta_c)$ can be written as

$$\cos(\theta_m - \theta_c) = \frac{V_n}{V_m} \cos(\theta_n - \theta_c) \quad (7)$$

Referring to Fig 3 it can be written as

$$\cos(\theta_n - \theta_c) = \frac{yw}{xy} \quad (8)$$

And it can be seen as $yw = V_m \sin \theta_{mn}$ (9)

$$\text{Also } xy = \sqrt{V_m^2 + V_n^2 - 2V_m V_n \cos \theta_{mn}} \text{ and } \theta_{mn} = \theta_m - \theta_n \quad (10)$$

Using these relationships Eqn (6) can be modified as follows

$$\Delta P_{mn} = \frac{V_m V_n}{X_T} \sin \theta_{mn} \times \frac{V_s}{\sqrt{V_m^2 + V_n^2 - 2V_m V_n \cos \theta_{mn}}} \quad (11)$$

From Eqn (4) it can be written as $P_{mn} = P_{mno} + \Delta P_{mn}$ which implies

$$P_{mn} = \frac{V_m V_n}{X_T} \sin \theta_{mn} + \left(\frac{V_m V_n}{X_T} \sin \theta_{mn} \times \frac{V_s}{\sqrt{V_m^2 + V_n^2 - 2V_m V_n \cos \theta_{mn}}} \right) \quad (12)$$

Linearizing Eqn (12) about an operating point it can be written as

$$\Delta P_{mn} = \frac{V_m V_n}{X_T} \cos(\theta_m - \theta_n) (\Delta \theta_m - \Delta \theta_n) + \left(\frac{V_m V_n}{X_T} \sin \theta_{mn} \times \frac{\Delta V_s}{\sqrt{V_m^2 + V_n^2 - 2V_m V_n \cos \theta_{mn}}} \right) \quad (13)$$

$\Delta P_{mn} = \Delta P_{tie} + \Delta P_{SSSC}$ which implies

$$\Delta P_{SSSC} = \left(\frac{V_m V_n}{X_T} \sin \theta_{mn} \times \frac{\Delta V_s}{\sqrt{V_m^2 + V_n^2 - 2V_m V_n \cos \theta_{mn}}} \right) \quad (14)$$

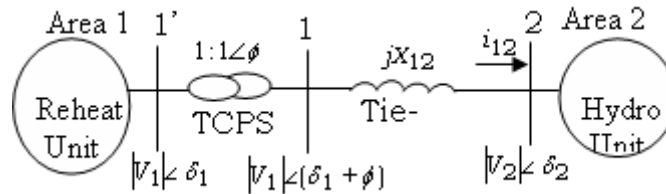


Figure.4. Schematic of TCPS in series with Tie line

The phase shifter angle $\Delta \phi(s)$ can be written as

$$\Delta \phi(s) = \frac{K_\phi}{1 + sT_{ps}} \Delta Error_1(s) \quad (15)$$

Where K_ϕ and T_{ps} are the gain and time constants of the TCPS and $\Delta Error_1(s)$ is the control signal which controls the phase angle of the phase shifter. Thus, it can be written as

$$\Delta P_{tie12}(s) = \frac{2\pi T'_{12}}{s} [\Delta F_1(s) - \Delta F_2(s)] + T'_{12} \frac{K_\phi}{1 + sT_{ps}} \Delta Error_1(s) \quad (16)$$

$\Delta Error_1$ can be any signal such as the thermal area frequency deviation Δf_1 or hydro area frequency deviation Δf_2

IV. SA APPLIED TO AGC

SA is a point by point method. The algorithm begins with an initial point, $x_t = (x_1, x_2)$ where x_1, x_2 correspond to the gains of integral controllers of both areas in Fig 1 and a high temperature, T . A second point is created in the vicinity of

Based on Eqn (14) it can be observed that by varying the SSSC voltage ΔV_s , the power output of SSSC can be controlled which will in turn control the frequency and tie line deviations. The structure of SSSC to be incorporated in the two area system in order to reduce the frequency deviations is provided in Figure 4 shown below. The frequency deviation of area 1 can be seen as input to the SSSC device.

Modelling of TCPS

Figure 5 shows the schematic of the two-area interconnected hydrothermal system considering a TCPS in series with the tie-line. TCPS is placed near area 1. Area 1 is the thermal area comprising of three reheat units and area 2 is the hydro area consisting of three hydro units. With TCPS, the incremental tie-line power flow from area 1 to area 2 under open market system can be expressed as (16)

the initial point with the help of increment vector, Δ and the difference in the function values Δf at these two points is calculated. If the second point has a smaller function value, the point is accepted otherwise the point is accepted with a probability given by $\exp\left(\frac{-\Delta f}{T}\right)$. In order to do this a random point, r is created and checked whether $r \leq \exp\left(\frac{-\Delta f}{T}\right)$. If the condition is satisfied and the termination criteria is not met, the temperature, T is lowered and the procedure continues till the termination criteria is met. The algorithm is terminated when sufficiently small temperature and small enough change in function values are obtained. In order to simulate the thermal equilibrium at every temperature, a number of iterations 'n' are tested at a particular temperature before reducing the temperature by using temperature reduction parameter.

V. RESULTS AND DISCUSSIONS

The proposed system is modeled in MATLAB/SIMULINK environment and the results have been presented. A load change of 0.04 p.u M.W in each area has been considered to study the comparison between SSSC based system with SA controller and system with conventional integral controller and without SSSC. Due to application of SA to the system, optimal values of $k_{i1} = 1.35$ and $k_{i2} = 0.267$ have been obtained. The

Discos contract with the Gencos as per the following Disco participation matrix. The Disco participation matrix (DPM) in this work is taken as follows:

$$DPM = \begin{bmatrix} 0.1 & 0.0 & 0.3 & 0.4 \\ 0.0 & 0.1 & 0.0 & 0.2 \\ 0.3 & 0.4 & 0.1 & 0.0 \\ 0.2 & 0.0 & 0.2 & 0.1 \\ 0.2 & 0.3 & 0.0 & 0.1 \\ 0.2 & 0.2 & 0.4 & 0.2 \end{bmatrix}$$

Figure 5 shows the various frequency deviations and tie line power deviations in both the areas during a load change of 0.04p.u MW. Figure 6-7 show the generations of various Gencos in both the areas. It can be observed that the system with SSSC is far superior to the system without SSSC in terms of peak time, overshoot and settling time in both the areas. Three generators in each area have been considered for the study. Each Genco participates in AGC as defined by following area participation factors (apfs):

$apf_1 = 0.5, apf_2 = 0.25, apf_3 = 0.25, apf_4 = 0.5, apf_5 = 0.25, apf_6 = 0.25$. Coefficients that distribute ACE to several Gencos are termed as “ACE participation factors” (apfs). It should

be noted that $\sum_{j=1}^m apf_j = 1$, where m is the number of

Gencos. Figure 8 shows the comparison of performance index of both the systems.

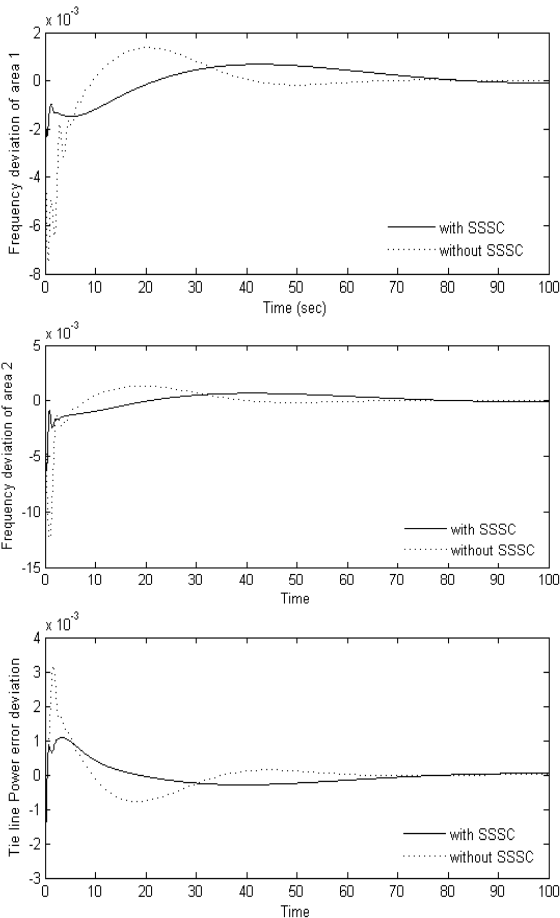


Figure 5: Frequency and tie line power deviations for both areas

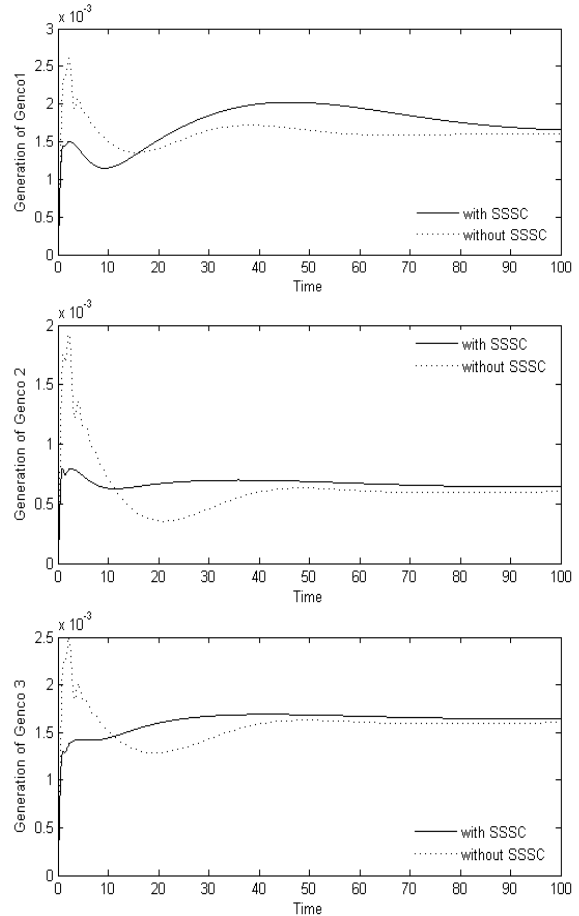


Figure 6: Generation of Gencos in area 1

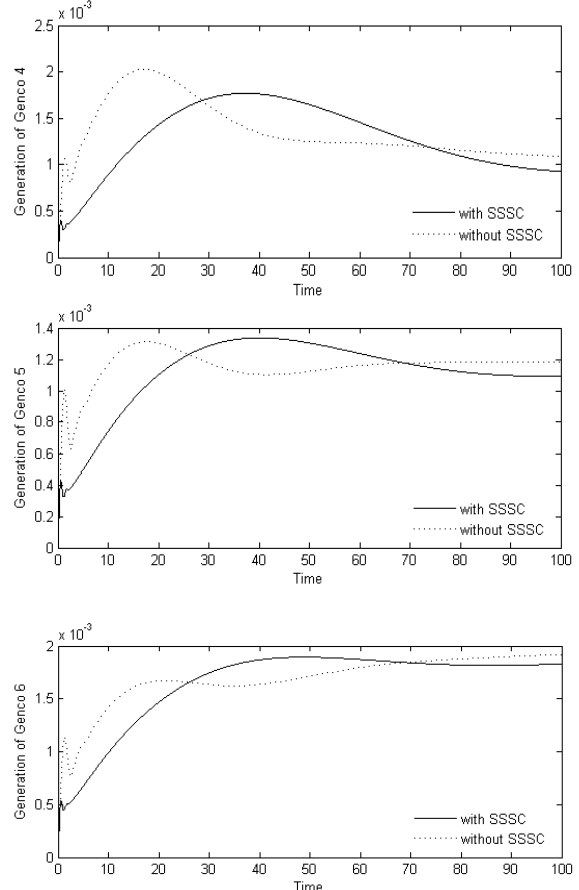


Figure 7: Generation of Gencos in area 2

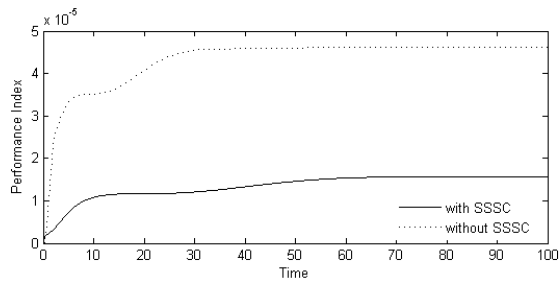


Figure 8: Comparison of performance Index

VI. CONCLUSIONS

A systematic method has been suggested for the design of a static synchronous series compensator and TCPS for a two-area hydrothermal system under deregulated scenario. This paper has also investigated the design of integral controller through Simulated Annealing technique. Effort has been made to study the performance of the system with SSSC-TCPS and integral controller tuned with the help of SA with respect to reduction of frequency deviations and tie line power deviations during a load change on a two area hydrothermal system under deregulated scenario. The simulation results indeed show that the proposed method indeed successfully mitigates the frequency and tie line power deviations during a load change and also it can be seen that the performance index of the system with SSSC-TCPS-SA based integral controller is less than the system without SSSC-TCPS-Integral controller which indicates the superiority of the proposed method.

REFERENCES

- [1] C. Concordia and L.K.Kirchmayer, *Tie-Line Power and Frequency Control of Electric Power System - Part II*, *AIEE Transaction*, vol. 73, Part- 111-A, pp. 133-146, April 1954.
- [2] M.L.Kothari, B.L.Kaul and J.Nanda, *Automatic Generation Control of Hydro-Thermal system*, *journal of Institute of Engineers(India)*, vol.61, pt EL2, pp85-91, Oct 1980.
- [3] J.Nanda, M.L.Kothari, P.S.Satsangi, *Automatic Generation Control of an Interconnected hydrothermal system in Continuous and Discrete modes considering Generation Rate Constraints*, *IEE Proc.*, vol. 130, pt D, No.1, pp 455- 460, Jan. 1983
- [4] Robert P. Schulte, "Automatic generation Control modification for present demands on interconnected power systems", *IEEE Trans. On Power Systems*, August 1996,pp. 1286- 1291.
- [5] Jayant Kumar, Kah-Koeng and Gerald Sheble, "AGC simulator for price based operation Part1", *IEEE Transactions on Power Systems*, vol.12,no.2, May 1997,pp. 527-532.
- [6] Jayant Kumar, Kah-Hoeng and Gerald Sheble, "AGC simulator for price based operation part- 2", *IEEE Transactions on Power Systems*, Vol.12, no. 2, May1997, pp 533-538.
- [7] Bjorn H.Bakken and OvesGrande, "Automatic generation control in a deregulated environment", *IEEE*

Transactions on Power Systems, vol.13, no.4, Nov1998,pp. 1401-1406.

- [8] David Goldberg. *Genetic algorithms in search, optimization and machine learning*. Addison-Wesley, 1989.
- [9] J. H. Holland. *Adaptation in nature and artificial systems*. Michigan, 1975.
- [10] Dynamic Models for steam and Hydro Turbines in Power system studies, *IEEE committee report. Transactions in Power Apparatus & Systems*, Vol.92, No.6,pp.1904-915,Nov./Dec.1973.

Performance comparison of Dynamic Source Routing with Weight Based Reliable Routing method

S.Dhanalakshmi¹, Mrs.V.Seethalakshmi²

*(Department of Electronics and Communication Engineering,Anna University,India

** (Department of Electronics and Communication Engineering,Anna University,India

ABSTRACT

Mobile ad hoc networks (MANET) are infrastructure less networks. The network topology may change rapidly because of high mobile nodes. Link failures are common because of the same reason. In this paper, Weight-Based Reliable Routing Method for MANETs is proposed. This method includes features that improve routing reliability, defined as the ability to increase packet delivery rate and throughput and uses the weight-based route strategy to select a stable route. Some parameter are assumed, like Node Remaining Energy, Route Expiration Time, No of Errors and No of Hops. Experimental results shows that the proposed WBRR performs better than DSR in the high mobility environment. Finally ensuring security in the weight based reliable routing method.

Keywords- AODV, DSR, MANET, RREQ, WBRR

I. INTRODUCTION

A wireless ad hoc network is a dynamic network consisted of a group of mobile device in which communicate with each other by wireless media. Communication can be done when a node is in the wireless transmission region of another node. A source can send data to a destination which is not in its communication region through a group of nodes that willing to forward its packets. The determination of which nodes forward data is made dynamically based on the network connectivity. This is in contrast to wired networks in which routers perform the task of routing .It is also in contrast to managed wireless networks, in which a special node known as an access point manages communication among other nodes [1].

The other type of mobile wireless network is then on-infrastructure network commonly known as Mobile Ad hoc Network (MANET). Mobile ad hoc networks are a heterogeneous mix of different wireless and mobile devices, ranging from little hand-held devices to laptops. Such devices rely on on-board batteries for energy supply; hence energy efficiency of mobiles is an important issue[2]. Examples of MANET's applications are communication in remote or hostile environments, management of emergencies, and disaster recovery. Given the limited range of wireless communication, the network is generally multi hop, since direct communication between mobiles is generally not available. For this reason, a distributed routing protocol is required in order to provide communication between arbitrary pairs of nodes.

A major problem arises from the mobility of nodes causing the network topology to be variable and to some extent unpredictable. In fact, linkage break probability of nodes will be high, when stability of routing path is not

considered. Best criteria's that are used for reliability in routing are:

- Route Expiration Time
- Node Remaining Energy
- No of Errors
- No of Hops

These criteria gives weight of the path. Procedures of path discovery usually find several path from source node to destination node then select path with maximum weight path as optimal path.

In this paper, it is aimed at how to enhance the stability of the network. A weight-based on demand reliable routing method (WBRR) is proposed to achieve this objective. The proposed scheme uses the weight-based route strategy to select a reliable route in order to enhance system performance.

II.RELATED WORK

In recent years, many routing protocols have been proposed for MANETs. Key routing protocols in MANETs is first reviewed in three broad categories: proactive routing protocols, reactive routing protocols, and location based routing protocols [2].

The proactive routing protocols maintain routing information independently of need for communication. The Update messages send throughout the network periodically or when network topology changes. It continuously try to maintain up-to-date routing information on every node in the network. It has Low latency which is suitable for real-time traffic. In proactive routing protocols bandwidth might get wasted due to periodic updates[3]. There are many proactive routing protocols, such as destination sequenced distance vector DSDV), wireless routing protocol (WRP), cluster head gateway switch routing (CGSR), fisheye state routing (FSR), and optimized link state routing (OLSR).

The reactive routing protocols determine route if and when needed. The Source initiates route discovery. The source node will issue a search packet and transmit the packet using the flooding technique to look for the destination node. This flooding technique will consume a large amount of time because of many redundant retransmissions. Hence significant delay might occur as a result of route discovery[3]. There are also many reactive routing protocols, such as ad hoc on-demand distance vector (AODV), dynamic source routing (DSR), temporally order routing algorithm (TORA), associativity-based routing (ABR), signal stability-based adaptive (SSA) and relative distance micro discovery ad hoc routing (RDMAR).

The location-based protocols, utilize the location information of sensor nodes to achieve scalability [21] in large-scale sensor networks. Location service systems

also justify the use of these location-based routing protocols. Among them, stateless routing protocols do not require a node to memorize past traffic/paths, thus maintain almost no state information. These protocols that have been proposed are based on a geographic model[3]. Recent examples of this approach are GPS zone routing protocol (GZRP), location-aided routing (LAR), fully location-aware routing protocol (GRID), and zone-based hierarchical link state (ZHLS).

In this section, DSR is introduced, most general on-demand routing protocols. DSR is an on-demand routing protocol based on source routing. The Dynamic Source Routing protocol (DSR) is a simple and efficient routing protocol designed specifically for use in multi-hop wireless ad hoc networks of mobile nodes. DSR allows the network to be completely self-organizing and self-configuring, without the need for any existing network infrastructure or administration[4]. An important criterion in this algorithm is shortest path between source and destination. In the other hand minimum number of Hop between source and destination is important. Although shortest path may have minimum durability[5].

III.ROUTE DISCOVERY

1. Dynamic Source Routing

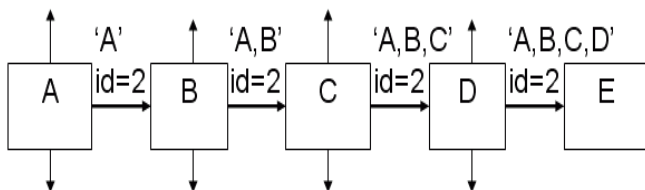


Fig 1. Route discovery

Node A (initiator) sends a Route Request packet by flooding the network. If node B has recently seen another RouteRequest from the same target or if the address of node B is already listed in the Route Record, Then node B discards the request. If node B is the target of the Route Discovery, it returns a RouteReply to the initiator. The RouteReply contains a list of the “best” path from the initiator to the target. When the initiator receives this RouteReply, it caches this route in its Route Cache for use in sending subsequent packets to this destination. Otherwise node B isn't the target and it forwards the Route Request to his neighbors (except to the initiator). In DSR every node is responsible for confirming that the next hop in the Source Route receives the packet. Also each packet is only forwarded once by a node (hop-by-hop routing). If a packet can't be received by a node, it is retransmitted up to some maximum number of times until a confirmation is received from the next hop[6].

Only if retransmission results then in a failure, a RouteError message is sent to the initiator that can remove that Source Route from its Route Cache. So the initiator can check his Route Cache for another route to the target. If there is no route in the cache, a RouteRequest packet is broadcasted.

error message

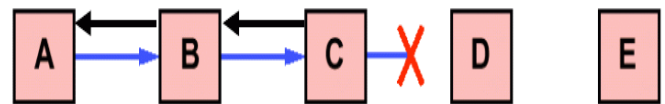


Fig 2. Route maintenance

If node C does not receive an acknowledgement from node D after some number of requests, it returns a RouteError to the initiator A. As soon as node receives the RouteError message, it deletes the broken-link-route from its cache. If A has another route to E, it sends the packet immediately using this new route. Otherwise the initiator A is starting the Route Discovery process again.

2. Weight-Based Reliable Routing Method

The proposed WBRR is an on-demand routing protocol and the route discovery process is similar to that of the DSR. However, WBRR, when a source node wants to select path to destination it first calculates the required energy (REQ) for the packets to be sent, then searches for an available path to the destination node from its own node information table. If the source node does not have an available path that can meet the energy constraint with maximum RET, minimum HC and EC, in this case it put REQe (minimum energy that nodes needed for sending whole of file) in route request packet and then initiates a route discovery procedure by sending the RREQ message to its neighbor nodes. If remaining energy of intermediate node is greater than requested energy for sending of file or data then the node automatically is selected and calculate LET and EC of a link if value of Calculated LET is smaller than value of pervious link then it is replaced in RREQ packet else it uses pervious LET. Then intermediate node that has all condition broadcast packets to its neighborhoods. Reversely if the remaining energy of node is smaller than requested energy for sending data in RREQ packet, then intermediate node, discard the packet and do not send it to neighborhood nodes. Therefore it prevent from broadcasting of discovery path from this node to its neighbors.

With considering this condition, intermediate node sends route discovery packet along the reverse path to the source node. Otherwise, the node increments the hop count by one and rebroadcasts the route discovery packet. Note that a node may receive multiple copies of the same RREQ packet from various neighboring nodes. When an intermediate node receives a RREQ packet with the same source ID and routing list ID, it discards the redundant RREQ packet and does not rebroadcast it. When the destination node finds a suitable path, it sends back a RREP packet to the source node[7].

When a node receive a RREQ message if it has enough remaining energy for supporting resource after calculating and changing broadcast packet to it's neighbors. This procedure is continued until RREQ packet find destination node. In other on demand routing algorithm route discovery packet is passed from all neighborhoods but in our method rout discovery packet is passed only from neighborhood nodes which have enough energy for supporting resource, therefore it prevent flooding of unnecessary packet like DSR which increase the consuming of energy.

By the time a broadcast packet arrives at a node that can supply a route to the destination node, a reverse path has been established to the source node of the route request. As the RREP packet travels back to the source node, each node along the path sets up a forward pointer to the node from which the route reply came, updates its timeout information for route entries to the source node and the destination node, and records the latest destination sequence number for the requested destination node[8].

IV.ROUTE SELECTION

In this section, the factors of the weight function is defined. Then the weight function of proposed method is introduced.

1. The Factors of the Weight Function

The weight function includes four factors: the route expiration time, residue energy of node, error count and hop count. The four factors are described as below;

1.1. Route Expiration Time (RET)

The RET is the minimum of the set of link validation times (LETs) for the feasible path. The LET represents the duration of time between two nodes. So first we obtain minimum value of LET in each path and then select the maximum number of RET witch represents the more reliable routing path.

$$RET = \text{Min}\{LET\}$$

The LET can be obtained by the principle that two neighbours in motion will be able to predict future disconnection time. Such a prediction can be accomplished by the following method[9]. The motion parameters of two neighbouring nodes can be obtained by using global positioning system (GPS). A free space propagation model is designed[9] in which the signal strength solely depends on the distance to the transmitter. It is assumed that all nodes have their clocks synchronized by using the GPS clock. If the motion parameters of two nodes are known, then the duration of time for which these two nodes remained connected is calculated. These parameters include speed, direction, and radio range and can be obtained from GPS.

For the sake of simplicity, we assume that nodes n1 and n2 have equal transmission radius r and that they are initially within hearing range. Let (x, y) and (x, y) denote the (x, y) position for node n and n, respectively. Also, let v_i and v_j denote their speeds along the directions q1 and q2 respectively. Then the duration of time between n1 and n2 is given by the following equation:

$$D_t = \frac{-(ab+cd) + \sqrt{(a^2+c^2)r^2 - (ad-cd)^2}}{(a^2+c^2)}$$

$$a = v_1 \cos \theta_1 - v_2 \cos \theta_2 \quad b = x_1 - x_2$$

$$c = v_1 \sin \theta_1 - v_2 \sin \theta_2 \quad d = y_1 - y_2$$

The LET between two nodes in the feasible path by the Equation (2) is obtained. Then the RET is equal to the minimum value between set of LETs for the feasible path.

1.2. Node Remaining Energy

In this parameter, the total energy required to transfer the entire file is calculated, and it is named as requested energy. All data packets are send through the path which has the requested energy. In reliable path selecting, must consider the estimation of total energy for sending all of packet.

When a mobile node performs power control during packet transmission, the transmitting energy for one packet relative to the node distance is given as:

$$E_{tx} = Kd^\alpha$$

Where k is the proportionality constant, d is the distance between the two neighbouring nodes, and α is a parameter that depends on the physical environment (generally between 2 and 4).

The shorter distance between the transmitter and the receiver, the smaller amount of energy required. At each node, the total required energy is given by

$$REQ_e = n \times (E_{tx} + E_{Proc})$$

Where n is the number of packets. The energy required for packet processing (E) is much smaller than that required for packet transmitting. There is an Energy field (ECD) in RREQ packet that shows needed data transfer energy. Each node which receive RREQ packet, compare value of its own REQ value in own table with packet ECD, then two cases occur::

1. If $ECD \geq REQ$ and the node is not destination node then it broadcast packet to all.
2. It does not pass RREQ and drop it.

1.3.No of Errors(EC)

The error count is used to indicate the number of link failures caused by a mobile node. When an intermediate node receives a RREQ packet, it compares the error count in the route record of the packet with the error count in its route cache, and assigns the larger one as the new error count in the packet. The process continues until the RREQ packet reaches the destination node. The destination node eventually takes record of the error count values along all feasible routes. The smaller EC represents the more reliable routing path.

1.4.No of Hops(HC)

If each intermediate host has a larger roaming area, and the MANET has many nodes (and hops), then a feasible path with less hop is the preferred choice. The smaller HC presents the more reliable and less cost of routing path.

2. Route weight function

An algorithm which effectively combines all the four parameters with certain weighing factor C1, C2, C3 & C4 were proposed .Larger Route Expiration time(RET) and node energy(ECD) represents higher reliability and so do lower error count and lower hop count. The weight function is defined as an empirical mean value, where first normalization

of each item is done and then combination of these four quantities is performed. More precisely:

$$W_i = C_1 \times \left(\frac{RET_i}{MaxRET} \right) + C_2 \times \left(\frac{ECD_i}{MaxECD} \right) + C_3 \times \left(\frac{EC_i}{MaxEC} \right) + C_4 \times \left(\frac{HC_i}{MaxHC} \right)$$

C1 , C2, C3 ,C4 are the values which can be chosen according to the system needs. For example, route expiration time is very important in MANETs, thus the weight of C1 factor can be made larger[10].

The flexibility of changing the factors helps to select routing path.

$$|C_1| + |C_2| + |C_3| + |C_4| = 1$$

V. EXPERIMENTAL RESULTS

1. Route Expiration Time

PATH	RET
I	22.2349
II	18.0202
III	32.222
IV	11.6574

Third path is having maximum RET and hence it is the feasible path.

2. Node Remaining Energy

PATH	ECD
I	889573
II	1.35E+06
III	6.17E+06
IV	4.89E+06

Third path is having maximum ECD and hence it is the feasible path.

3. No of Errors

PATH	EC
I	1.25
II	1
III	0.8
IV	1.6

Third path is having minimum EC and hence it is the feasible path.

4. No of Hops

First path is having minimum number of nodes and hence it is the feasible path.

In this section, the performance of the proposed WBRR with DSR is compared. First some assumptions on the parameters of the system architecture in the simulations are made. The simulation modelled a network with 12 nodes.

The radio transmission range was assumed to be 250 m. The speed of each mobile node was assumed to be 15 m/s. The random waypoint mobility model was employed. Each node randomly selects a position and moves toward that location with a speed between the minimum and the maximum speed. Once it arrives at that position, it stays for a predefined time e.g. 2 second (pause time). After that time, it re-selects a new position and repeats the process.

Simulation shows the packet delivery ratio, throughput and packet loss of proposed method and DSR with different mobility speeds.

5.Packet Delivery Rate

The packet delivery ratio is the ratio of the number of data packets received by the destination to the number of data packets transmitted by the corresponding source. It is observed that proposed method transmits and receives more data packets than DSR .

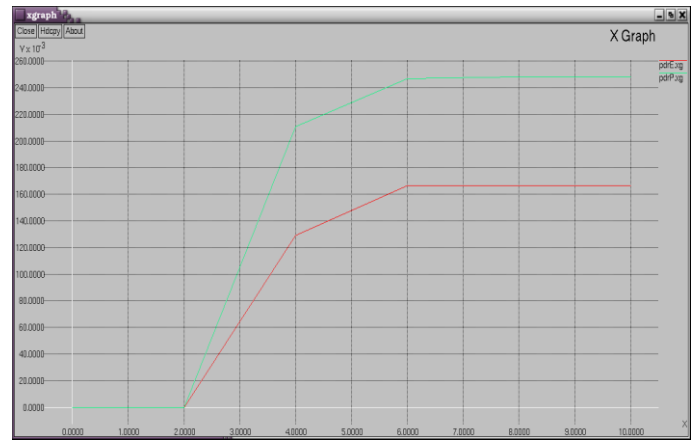


Fig 3: Packet Delivery Rate

The packets have been transmitting for ten seconds which can be seen from the figure 3. The x axis indicates the duration of time taken for transmitting the packets in which it takes two seconds to send hello packets and check whether the nodes in a particular range and from third second onwards the transmission starts and it ends by tenth second. The y axis indicates PDR.

6. Packets Throughput

The number of packets successfully received by the destination node.



Fig 4: Packets throughput

The packets have been transmitting for ten seconds which can be seen from the figure 4. The x axis indicates the duration of time taken for transmitting the packets in which it takes two seconds to send hello packets and check whether the nodes in a particular range and from third second onwards the transmission starts and it ends by tenth second. The y axis indicates throughput. It is clear from the above graph that the proposed WBRR is better than the existing method.

7.Number of packet drop

The total number of packets dropped while transmitting the packets from source node to destination node.

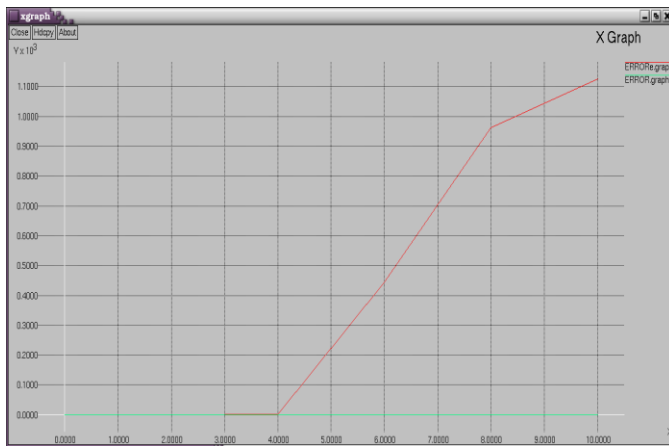


Fig 5: Packets drop error

The graph shows the dropping of packets while transmitting the packets from source node to destination node. The packets have been transmitting for ten seconds which can be seen from the figure 5. The x axis indicates the duration of time taken for transmitting the packets in which it takes two seconds to send hello packets and check whether the nodes in a particular range and from third second onwards the transmission starts and it ends by tenth second. The y axis indicates the number of packets. It is clear from the above graph that the proposed WBRR is better than the existing method.

VI. ACKNOWLEDGEMENT

The third path is the feasible path using reliable routing method and hence the next aim is to ensure security over that path. To ensure whether the path is still alive and transmissions are taking place, it is necessary to send acknowledgement. Ensuring security is done by transmitting a set of packets from source node to the destination node and the destination node in turn should reply the source node by means of an acknowledgement packet. The retrieval of the acknowledgment packet by the source node make sure that the feasible path is completely secure for transmitting the data.

Fig.6 shows that the third path is the feasible path, after substituting the results of all the four factors in the weight function and here by sending acknowledgement from destination to source, we have sent acknowledgement over that path.

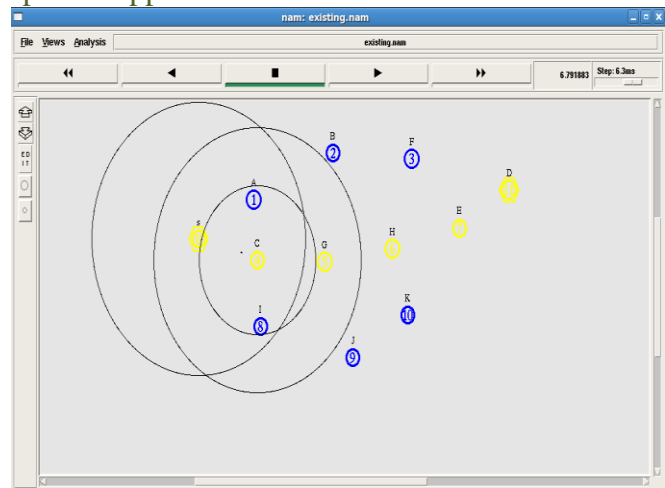


Fig 6: Acknowledgement

VII. CONCLUSION

In this paper, a routing algorithm with high stability is proposed, this method maximizes the weight among the feasible path in order to select a stable routing path. The route selection is based on the weight value of each feasible path. In a feasible path, the high weight value represents good reliability. It also represents higher mobility of each node in the path. It also represents that the feasible path is secured. The results shows that in the high mobility environment the proposed WBRR method outperforms DSR and also the security has been ensured for the feasible path.

Research on new simulation environments similar to ns2 could also be done, resulting in the development of new features such as more detailed graphs. In addition to this, improving packet delivery efficiency is the challenging area to be explored more. Moreover, due to the dynamically changing topology and infrastructure less property, secure and power aware routing is hard to achieve in mobile adhoc networks. An attempt will be made to cope up these issues in our future research work by proposing a solution for secure and power aware routing. Ad-hoc networks are highly vulnerable to security attacks and dealing with this is one of the main challenges of developers of these networks today.

REFERENCES

- [1] Performance Evaluation of *Stable Weight-Based on Demand Routing Protocol for Mobile Ad Hoc Network* by Oon Chong Hsi and Azizol Abdullah, 2009 Science Publications
- [2] *A Framework for Reliable Routing in Mobile AdHoc Networks* by Zhenqiang Ye and Srikanth V. Krishnamurthy, Satish K. Tripathi.
- [3] *Analysis of Delay & Throughput in MANET for DSR Protocol* by Kumar Manoj, Ramesh Kumar, Kumari Arti, World Academy of Science, Engineering and Technology 77 2011
- [4] *Introduction to Wireless Ad-Hoc Networks Routing* by Michalis Faloutsos, PPT slides
- [5] *Mobile Ad Hoc Networks* by Sridhar Iyer, IIT Bombay
- [6] Aggelou, G., R. Tafazolli, 1999. RDMAR: a bandwidth-efficient routing protocol for mobile ad hoc networks, Proceedings of the Second ACM International Workshop on Wireless Mobile Multimedia (WoWMoM), August, pp: 26–33.

- [7] Johnson, D.B., D.A. Maltz, 1996. "*Dynamic Source Routing in Ad Hoc Wireless Networks*", Kluwer,
- [8] Sonal, P., S. Arun, A. Tyagi, 2002. "*A reliable protocol for processing within IP-routed networks*",
- [9] Wang, Nen-Chung, Chen. Jhu-Chan, 2006. "*A Stable On-Demand Routing Protocol for Mobile Ad Hoc Networks with Weight-Based Strategy*" Department of Computer Science and Information Engineering National United University, Miao-Li 360, Taiwan, R.O.C. IEEE
- [10] Dube, R., C.D. Rais, K.Y. Wang, S.K. Tripathi, 1997. "*Signal stability-based adaptive routing (SSA) for ad hoc mobile networks*", IEEE Personal Communications, pp: 36

ANALYSIS OF SAFETY MEASURES AND QUALITY ROUTING IN VANETS

Vedha Vinodha.D*, Mrs.V.Seethalakshmi**

*II M.E CS, Sri Shakthi Institute of Engineering and Technology, Coimbatore

**Assistant professor ECE Dept, Sri Shakthi Institute of Engineering and Technology, Coimbatore

Abstract- Vehicle to vehicle communication (V2V) systems, where vehicles exchange information's with each other, become an important need in order to decrease traffic accidents and improve capacity of highways traffic and also road side infrastructure (V2I) communication from transportation operation center. The security could indeed be increased if the communication between the vehicles is established and maintained, this enables the driver of a car to be aware at an early time of the emergency breaking of the preceding vehicle and so eventually avoid a collision. Two efficient algorithms are proposed. Distributed-fair power adjustment for vehicular environments (D-FPAV) is a transmit power control approach for periodic messages based on a strict fairness criterion that can maximize the minimum value over all transmission power levels assigned to nodes that form the vehicular network under a given constraint on the Maximum Beaconsing Load. Emergency message dissemination for vehicular environments (EMDV), for fast and effective multihop information dissemination of event-driven messages with respect to both probability of reception and latency. Synergy is gained when using both protocols together because D-FPAV can ensure the channel load is kept at a level where EMDV can successfully operate with the help of nearby base station. Analysis and Simulation is carried using NS-2.

Keywords- Active safety, contention, fairness, information dissemination, power control, vehicle-to-vehicle communication.

1 INTRODUCTION

DIRECT vehicle-to-vehicle communication plays an important role for improving road safety based on radio technologies. Many organizations worldwide are funding national and international initiatives that are devoted to vehicular networks, such as the Internet ITS Consortium [1] in Japan, the Vehicle Infrastructure Integration (VII) Initiative [2] in the U.S., the Car2Car Communication Consortium (C2CCC) [3] in Europe, and the Network on Wheels (NoW) Project [4] in Germany. Currently, the IEEE 802.11p Working Group [5] is developing a standard. The effort is assisted by initiatives from various parts of the globe. There are two types of messages in safety-related communication that can be identified: 1) periodic and 2) event driven. Periodic messages which refers the vehicle's position, speed, etc can be used by safety applications to detect potentially dangerous situations. A distributed fair power adjustment for vehicular environments (D-FPAV) that controls the beaconsing load under a strict fairness criterion is used for safety reasons. D-FPAV gives more priority for event-driven over periodic messages. A contention-based strategy called emergency message dissemination for vehicular environments (EMDV) for event driven messages ensures a fast effective dissemination of alerts in a target geographical area along with D-FPAV.

2. CHALLENGES IN SAFETY MEASURES

Safety applications can be achieved by two types of messages: 1) periodic and 2) event driven. Periodic status messages are mainly used to exchange state information to the sending vehicle, like position,

direction, speed, etc. Through this beaconsing activity, safety applications acquire an accurate knowledge of the surroundings and therefore smart cars are used as shown in Fig. 1. The main factor related to this beaconsing activity is to control the channel load to avoid channel congestion. Beacon messages decreases when generation rate of the probability of successful reception of each of them is increased. When transmission power is increased for greater distance it leads to congested wireless medium, and also leads to packet collisions.

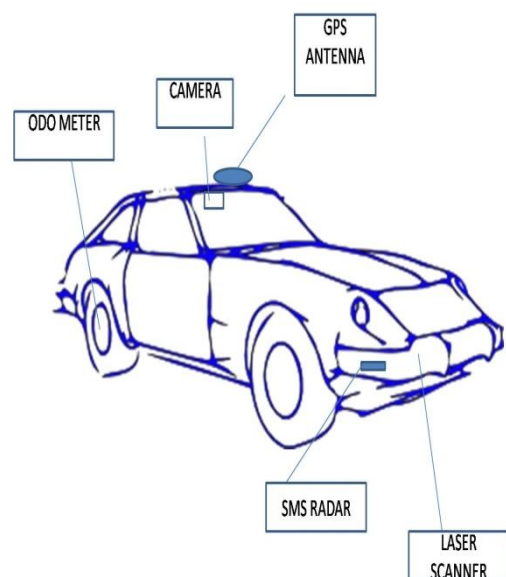


Fig. 1 Smart Cars

The packet generation rate should be at the minimum to adjust the transmission power of beacons in case of congestion. This mechanism should keep the load on the wireless medium below a certain level, called the maximum beaconing load (MBL). Fig. 2 shows the reception probability between periodic and event driven messages. The desired performance can be achieved at close distances as periodic messages experience a high reception probability, and event-driven emergency messages achieve an enhanced performance at reducing dissemination delay and improving reliability in high channel load conditions.

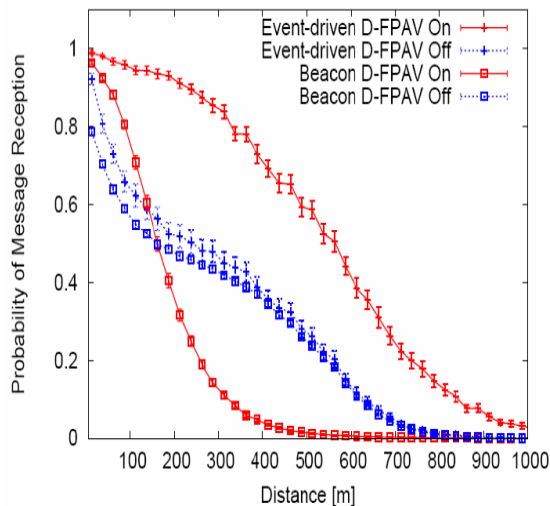


Fig. 2 Reception Probability between Periodic and Event Driven Messages

3 CONGESTION CONTROL

The D-FPAV algorithm to achieve the following design goals makes use of transmit power control.

- 1) Congestion control. Limit the load on the medium produced by periodic beacon exchange.
- 2) Fairness. Maximize the minimum transmit power value over all transmission power levels assigned to nodes that form the vehicular network under Constraint 1.
- 3) Prioritization. Give event-driven emergency messages higher priority compared to the priority of periodic beacons.

The congestion control requirement (Constraint 1) is applied only to beacon messages to control the channel bandwidth assigned to periodic safety-related messages. Prioritization is achieved through the EDCA mechanism by Constraint 3 available in the IEEE 802.11p and by always sending an event-driven emergency message using the maximum possible transmit power.

D-FPAV is based on the following factors:

- 1) Executing the FPAV algorithm at each node with the information gathered from received beacons;
- 2) Exchanging the locally computed transmit power control values among surrounding vehicles; and
- 3) Selecting the minimum power level among the one locally computed and those computed by the surrounding vehicles.

Algorithm D-FPAV: (algorithm for node u_i)

INPUT: geographical positions of all nodes in $CS_{MAX}(i)$

OUTPUT: a power setting $PA(i)$ for node u_i , such that the resulting power assignment is an optimal solution to BMMTxP

1. Based on the geographical positions of all nodes in $CS_{MAX}(i)$, use FPAV to compute the maximum common transmit power level P_i s.t. the MBL threshold is not violated at any node in $CS_{MAX}(i)$
- 2a. Disseminate P_i to all nodes in $CS_{MAX}(i)$
- 2b. Collect the power level values computed by nodes u_j such that $u_j \in CS_{MAX}(j)$ and store the received values in P_j
3. Assign the final power level:

$$PA(i) = \min \{P_i, \min_{j: u_j \in CS_{MAX}(j)} \{P_j\}\}$$

Fig. 3 DFP AV Algorithm

The D-FPAV algorithm (conventional) is summarized in Fig. 3 [7]. A perfect information accuracy from *all* nodes inside $CS_{MAX}(i)$ is required to *guarantee* strict fairness, achieving such a perfect knowledge is very difficult in a fully distributed fast-moving scenario as given by vehicular ad hoc networks. D-FPAV is expected to operate in situations in which nodes have incomplete knowledge about the environment.

4 EMERGENCY RESPONSE

The second main goal is the dissemination of event-driven messages within a geographical area as in Fig. 4. A certain vehicle issues a hazard warning message (also called emergency message in the following) in case a dangerous situation is detected (e.g., obstacle on the road, airbag explosion, malfunctioning of the braking system, and so on). This emergency message should be propagated backward on the road as quickly and reliably as possible, in order to enable the drivers of approaching vehicles to undertake adequate countermeasure in Fig. 5.

An effective strategy that offers short delay is required to deliver a message that contains information about an existing threat.

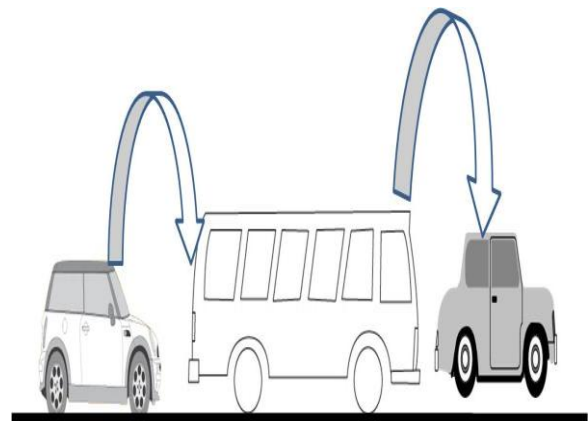


Fig. 4 Car2Car Communications

This dissemination strategy is to select the appropriate nodes to efficiently forward the message in the direction of dissemination to cover the dissemination area. The proposed strategy deals with uncertainties that result from node mobility, fading phenomena, and packet collisions. In order to cover the destination area, some intermediate nodes (forwarders) will be selected by the contention mechanism to forward the message in the direction of dissemination.

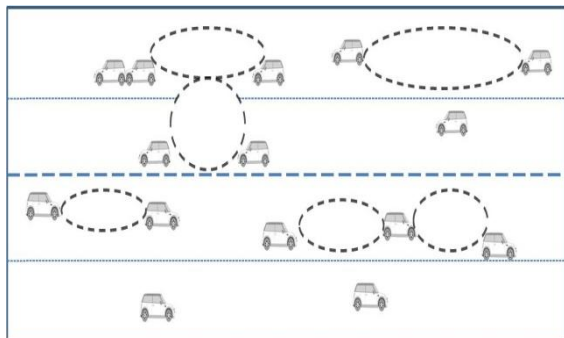


Fig. 5 Relevant area for dissemination of emergency information after an accident detection in a highway.

Cars in the opposite direction are also included. A wireless channel is utilized for periodic beacon exchange. Thus, relatively busy medium can be encountered by event-driven emergency messages in dense vehicular traffic situations.

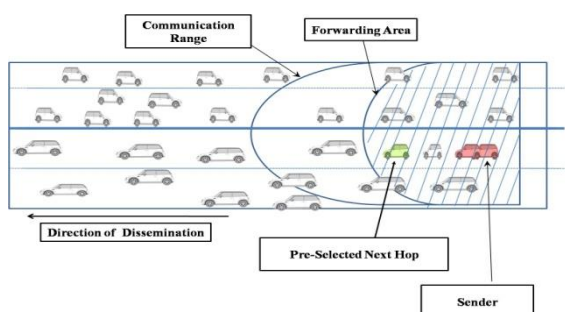


Fig. 6. Sender perspective when utilizing the EMDV protocol.

EMDV is based on the following three design principles.

- 1) A contention scheme is used message to deal with uncertainties like node mobility, fading phenomena, and collisions after the broadcast transmission.
- 2) To minimize the delay, the contention strategy is complemented with the selection of one specific forwarder made at transmission time, referred to as the next hop which immediately forwards the message.
- 3) The reliability of the dissemination process is increased by the following factors:

a) Assuming a forwarding range shorter than the communication range and b) a controlled message retransmission scheme within the dissemination area.

Fig. 6 shows a sketch of conventional figure of a sender perspective, which must preselect a next hop among known nodes and then broadcast the message [9]. The forwarding area identifies the area where the next

forwarders can be located. EMDV is composed of four main procedures, as shown by the conventional pseudocode description of the protocol as shown in Fig.7 [8]. A node that transmits an emergency message invokes the *PrepareMessage()* procedure. This procedure first checks whether the message has already been transmitted for the maximum number of times (*maxMessages*) within the node's forwarding area. If not, the *FindNextHop()* procedure is invoked to determine the message's destination node.

Once the message has been transmitted, the message counter is increased, and a contention period is started to verify that at least one neighbor forwards the message. The *FindNextHop()* procedure essentially scans the neighbor table of the sender to find (if any) the neighbor in the sender's forwarding area with the highest progress in the direction of dissemination. If no neighbor in the dissemination direction can be found or if the sender's forwarding area is at the border of the dissemination area, no specific forwarder is selected, and *NextHop* is set to *broadcastAddress*.

The *ReceiveMessage()* procedure is invoked when a node receives an emergency message and first ensures that the node lies inside the dissemination area to proceed. Then, it is checked whether the received message has been sent by a node that is farther in the direction of dissemination and lies inside its own *forwardingArea*. In this case, the message can be considered to be a sort of "implicit ack" of message forwarding, and the corresponding message counter is increased so that contention for forwarding the message can be canceled if enough "implicit acks" have already been received.

If the aforementioned conditions are not satisfied and the receiving node is located inside the *forwardingArea* of the sender, the dissemination criteria are used to determine whether immediate or contended forwarding will be performed: If the receiving node is indicated as the intended forwarder in the *NextHop* field, then the message is forwarded with no contention by invoking the *PrepareMessage()* procedure; otherwise, a contention period is started by invoking the *PrepareContention()* procedure.

Finally, the protocol has to be adjusted with respect to two specific situations. First, the contention period after delivering the message to lower layers (*PrepareMessage()*) must take into account the time that the message needs to access the channel and transmission. The contention time is set to $maxContentionTime + maxChannelAccessTime$ when $flag = sent$. Second, nodes located within *forwardingRange* from the border of the *disseminationArea* will act a little differently, because the message must not travel farther distances than *borderDisseminationArea*. Therefore, the following cases hold:

- 1) They will not select a nextHop; instead, the *broadcastAddress* will be utilized, and

- 2) they will increment countMessages when receiving a message from any node that is also located within forwardingRange of borderDisseminationArea instead of only counting the ones that come from their forwardingArea.

```

Procedure: PrepareMessage()
if countMessages < maxMessages then
    nextHop ← FindNextHop()
    TransmitEMDVMessage(nextHop)
    countMessages ++
    PrepareContention(sent)

Procedure: FindNextHop()
nextHop ← broadcastAddress
if borderDisseminationArea ∈ myForwardingArea then
    return nextHop
progress ← 0
for each neighbor ∈ myNeighborTable do
    if neighborPosition ∈ myForwardingArea and
       neighborProgress > progress
    then
        progress ← neighborProgress
        nextHop ← neighborAddress
return nextHop

Procedure: ReceiveMessage()
if myPosition ∈ disseminationArea then
    if senderPosition ∈ myForwardingArea or
       borderDisseminationArea
       ∈ myForwardingArea ∩ senderForwardingArea
    then
        countMessages ++
        if countMessages ≥ maxMessages then
            CancelContention()
        else if messageDestinationAddress = myAddress then
            if contending then
                CancelContention()
            PrepareMessage()
        else if myPosition ∈ senderForwardingArea and
            not contending
        then
            PrepareContention(received)

Procedure: PrepareContention(flag)
if flag = sent then
    time ← maxContentionTime + maxChannelAccessTime
else time ← maxContentionTime × (1 - myProgress/forwardingRange)
contending ← true
Contend(time)
    
```

Fig. 7 EMDV protocol for emergency message dissemination.

5 RESULTS AND DISCUSSION

5.1 D-FPAV Performance and EMDV Performance
 To evaluate D-FPAV performance, two main simulation setups are consider: 1) D-FPAV On and 2) D-FPAV Off as shown in Fig. 8.

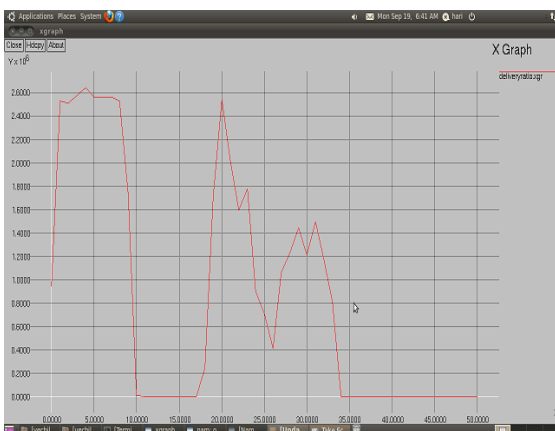


Fig.8 D-FPAV-ON/OFF

The main metrics considered to evaluate D-FPAV's performance are given as follows: 1) the probability of successful reception of a beacon message with respect to the distance and 2) the average channel access time (CAT). The CAT is computed for all nodes and it is used to achieve fairness. The probability of reception is used to prioritize a safety-related message which is obtained by ensuring a high probability of correctly receiving beacons at close distances from the sender. It also increases the probability of successful reception of event-driven messages at all distances.

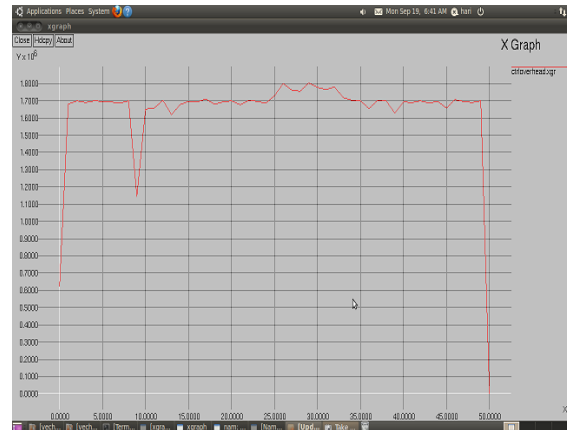


Fig.9 EMDV-ON/OFF

The performance of the EMDV protocol is shown in Fig.9. With a lower MBL, the EMDV protocol achieves a more efficient performance due to the lower channel load.

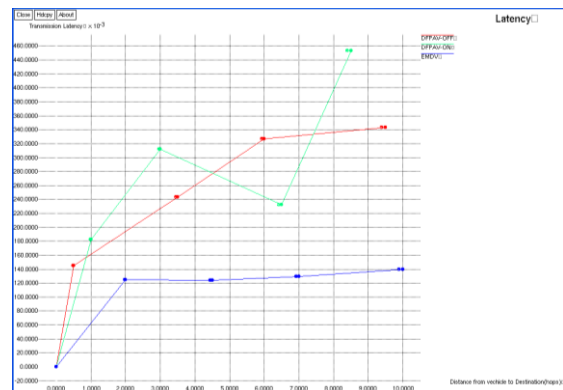


Fig.10 Comparison of Latency

Latency time (L) is defined as the time needed to propagate generated data between two vehicles positioned D meters from each other and the comparison graph is shown in Figure 10.

6 CONCLUSION

In this paper, a new efficient system for safety measures in VANETs. The vehicular networks which uses the IEEE 802.11p and active-safety communication will consist of two types of messages: 1) periodic beacon messages and 2) event-driven emergence messages. The

channel saturation can “easily” occur due to the load caused by beacon message transmissions. Simply increasing the rate or power will just make the channel conditions worse. In these conditions, both types of messages might not be received where they are needed. D-FPAV is a transmit power control approach based on a strict fairness criterion that can maximize the minimum value over all transmission power levels. The EMDV approach provides for robust and effective information dissemination of emergency information with help of nearby base station. For EMDV, the idea of contention-based forwarding that can very well deal with the unreliability of the channel and with node mobility is used. The emergency dissemination model is evaluated using latency time metric.

For the reduction of the dissemination delay, use of beacon information and forwarding techniques in combination with the contention-based approach is used. Efficient Performance is obtained when using both protocols together. The performance of the proposed protocols has been analyzed via ns2 tool. As future work, the selection criteria that decides whether a car should participate in broadcasting or not will be considered. These criteria will depend on several factors such as traffic density and car speeds.

REFERENCES

- [1] Internet ITS Consortium. [Online]. Available: <http://www.Internetits.org>
- [2] Vehicle Infrastructure Integration (VII) Project. [Online]. Available: <http://www.its.dot.gov/vii/>
- [3] Car2Car Communication Consortium. [Online]. Available: <http://www.car-to-car.org/>
- [4] The NOW: Network on Wheels Project. [Online]. Available: <http://www.network-on-wheels.de>
- [5] IEEE P802.11p/D0.21, Draft Amendment for Wireless Access in Vehicular Environments (WAVE), Jan. 2006.
- [6] Network Simulator ns-2. [Online]. Available: <http://www.isi.edu/nsnam/ns/>.
- [7] M. Torrent-Moreno, P. Santi, and H. Hartenstein, “Distributed fair transmit power assignment for vehicular ad hoc networks,” in Proc. 3rd Annu. IEEE Conf. Sens., Mesh Ad Hoc Commun. Netw. SECON, Reston, VA, Sep. 2006, vol. 2, pp. 479–488.
- [8] Torrent-Moreno, M, Mittag, J., Santi, P. Hartenstein, “Vehicle-to-Vehicle Communication: Fair Transmit Power Control for Safety-Critical Information”, in IEEE Transaction on Vehicular Technology, Vol 58, No. 7, Sep 2009.
- [9] M . Torrent - Moreno, “ Intervehicle comm.-unications: Assessing information dissemination under safety constraints,” in Proc. 4th IEEE/IFIP Conf. WONS, Obergurgl, Austria, Jan. 2007, pp. 59–64.

PERFORMANCE EVALUATION OF DATABASE MANAGEMENT SYSTEMS BY THE ANALYSIS OF DBMS TIME AND CAPACITY

Aparna Kaladi¹ and Priya Ponnusamy²

¹M.E Computer Science and Engineering, Sri Shakthi Institute of Engineering and Technology, Coimbatore, India

²Asst.Professor, Computer Science and Engineering, Sri Shakthi Institute of Engineering and Technology, Coimbatore, India

ABSTRACT

Performance evaluation of database systems are made difficult by the existence of different database management systems, which serves different requirements. As DBMSes are limited in speed, they need to be highly efficient through its performance. A DBMS provides facilities for controlling data access, enforcing data integrity, managing concurrency control, recovering the database after failures and restoring it from backup files, as well as maintaining database security. It is a set of software programs that controls the system organization, storage, management, and retrieval of data in a database. That is why they need to be efficient in storage and speed. This is the same reason why DBMSes need to be evaluated based on their performances. Different DBMSs performs differently in different environment. This paper, evaluate the performance of Three different database management systems(MySql, Sqlite, PostgreSQL). Based on that, comparison of different DBMSs in the same environment is possible. This performance evaluation is done based on response time and memory capacity.

KEYWORDS

PostgreSQL, SQLite, MySQL, Response time, Memory

1. INTRODUCTION

A database management system (dbms) is a complicated set of software programs which controls the organization, storage, management, and retrieval of data in a database. Database management is no longer limited to "monolithic entities". Many solutions have been developed to satisfy the individual needs of users. The development of numerous database options has created flexibility in database management. There are several ways database management has affected the field of technology. Because organizations' demand for directory services has grown as they expand in size, businesses use directory services that provide prompted searches for company information. Mobile devices are able to store more than just the contact information of users, and can cache and display a large amount of information on smaller displays. Search engine queries are able to locate data within the World Wide Web. Online transactions have become tremendously popular for e-business

The last few decades has seen huge transformations in the way businesses are conducted. The growth and diversity of the market has greatly profited consumers through higher availability, better quality and lower prices. The same factors however has made it more difficult for businesses to maintain their competitive edge over one another and hence has forced them to think beyond their product portfolio and look at other means to gain higher visibility and customer satisfaction, maintaining all the while their core advantages on pricing and product through improved and more efficient methods of manufacturing and distribution. Database management systems now form the core of almost all enterprise logic and business intelligence solutions.

Database Systems are one of the key enabling forces behind every business transformations. Apart from supporting enterprise logic they also enable business intelligence. Information is the key to success in today's businesses. However, maintaining information in logically consistent and feasibly retrievable format is a daunting task. More so with the added complications of transaction consistency management, synchronization across multiple repositories spread geographically across the globe, failover management and redundancy management, today's database systems are truly state-of-the-art high performance software systems.

Database management systems need to be efficient in terms of storage and speed. Dynamic addition and deletion of data from the database poses a challenge to maintaining an efficient data retrieval mechanism. Though, limited in speed, database systems need to achieve full throttle through efficient storage and retrieval techniques.

Reliability, availability and fault-tolerance is a huge concern for database systems. Reliability of a system is generally improved through redundancy. Modern businesses cannot afford to lose data or present wrong data. Modern business activities are highly cantered around and dependant on electronic data. Modern database systems thus need to build in high reliability mechanisms in their designs. High level view of database management systems

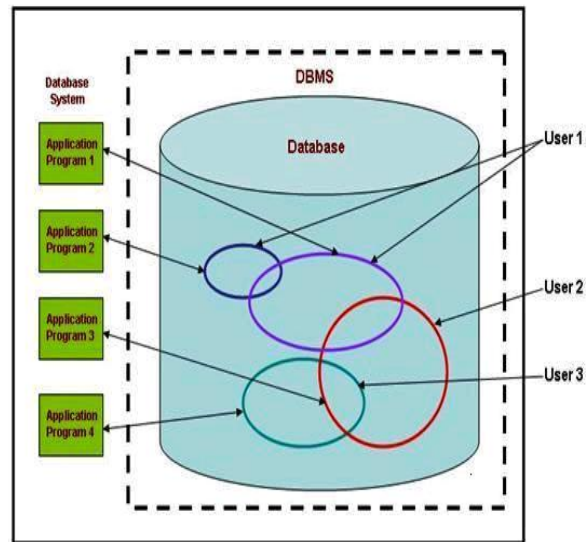


Figure 1 - a generic high level view of a database management system

Performance evaluation of database systems is thus an important concern. However, easier said than done, performance evaluation of database system is a non-trivial activity, made more complicated by the existence of different flavours of database systems fine tuned for serving specific requirements.

2. RELATED WORKS

2.1 General approaches to database management system performance evaluation:

The word "general" means that the approaches mentioned here are generally true for "systems" with a special focus on database systems. Performance analysis of database systems serves two basic purposes:

1. For the evaluation of the best configuration and operating environment of a single database system, and
2. Studying two or more database systems and providing a systematic comparison of the systems.

Accordingly, some of the analytical modelling methods for evaluating systems that are applicable for database systems too are:

2.1.1 Queuing Models:

These models are effective to study the dynamics of a database system when it is modelled as a multi-component system with resource allocation constraints and jobs moving around from one component to another. Examples of such dynamic studies are concurrent transaction control algorithms, data allocation and management in distributed database systems etc.

2.1.2 Cost Models:

Cost Models are useful in studying the cost in terms of Physical storage and query processing time. The cost model gives some real insight into the actual physical structure and performance of a database system.

2.1.3 Simulation Modelling:

A simulation modelling is more effective for obtaining better estimates since it not only analyses the database system in isolation but can effectively analyze the database system with the application program running on top of it and the database system itself operating within the constrained environment of an operating system on a real physical hardware.

2.1.4 Benchmarking:

Benchmarking is the best method when multiple database systems need to be evaluated against each other but suffer the inherent setback that it assumes all systems to be fully installed and operational. Benchmarking relies on the effectiveness of the synthetic workloads. Real workloads are non repeatable and hence not good for effective benchmarking.

A set of methods for database performance evaluation assuming the system to be operating in a multi-user environment. Accordingly the three factors that affect the performance of a database system in a multi-user environment are:

1. Multi-programming level
2. Query Mix
3. Extent of data sharing

Data sharing is the condition of concurrent access of a data object by multiple processes. The interesting factor here is that of the query mix. A proper query mix needs to test the appropriate levels of CPU and disk utilization required to serve a particular query.

The query mix needs to properly represent a true multi-user environment. Also, the query mix may be designed to represent a certain percentage of data sharing. Once these have been figured out, the query-mix forms a representative benchmark program and multiple copies of the bench-mark program are issued concurrently to simulated multi-programming effects. Also, different query-mixes allow diversity in the experimental design conditions. The response variable studied is system throughput and response time.

3. PERFORMANCE EVALUATION CONCEPT

Two approaches have been taken to early performance analysis of dbms. The first approach is a qualitative analysis in terms of possible impacts of system aspects on product qualities such as performance.. The second approach is quantitative, using models. Smith developed an approach to building a queuing model based on scenario-like “execution graphs” that are specially built for performance analysis.

difficulties posed by early analysis, are:

- incompleteness of the specification, because it is so abstract. This includes open choices of design approaches, algorithms and components to be used, and lack of definition of the final execution environment
- lack of knowledge of the computational effort required
- other aspects such as ignorance of the workload intensity

Factors affecting performance: There are mainly 4 factors affecting the performance of database management systems.

3.1. Response time

Response time is defined as the time interval from the instant a command is input to the system to the instant the corresponding reply begins to appear at the terminal.

3.2 Throughput

Throughput is the overall capability of the computer to process data. It is the combination of IO speed, CPU speed, parallel capabilities of the machine and efficiency of the operating system and system software.

3.3. Resources

Hardware and software tools, which include memory, disk speed, cache controller etc.

3.4. Memory

The total space required by a query to complete its execution. The values it takes for the completion of its execution

The workload parameters are partly specifications that must be taken as assumptions (such as the number of clients, types of query, query response time, execution time etc.) and partly predictions (such as CPU time for the operations to be implemented, the number of disk accesses and their cache hit ratio).

4. PERFORMANCE ANALYSIS OF DATABASE MANAGEMENT SYSTEMS

The development of systems that could adapt gracefully and opaquely to changing data and environment are the need of time. Query optimization, is one of the most happening fields in different areas of computer systems. In the last few years, researchers have been exploring the design of systems that are adaptive to operate in unpredictable and changeable environments.

Nowadays, different types of database are available, like ORACLE dbms, MS Access and SQL server from Microsoft, DB2 from IBM, open Source DBMS MySQL etc.

In my paper, I am analyzing the Performance of three databases management systems. They are,

4.1 mysql

MySQL is a relational database management system (RDBMS) that runs as a server providing multi-user access to a number of databases. MySQL database is used for this project because it supports Linux and Java. For administrative purpose MySQL administrator is used. MySQL Administrator is a program for performing administrative operations, such as configuring your MySQL server, monitoring its status and performance, starting and stopping it, managing users and connections, performing backups, and a number of other administrative tasks. You can perform most of those tasks using a command line interface such as that provided by mysqladmin or mysql

4.2. Postgresql

PostgreSQL, often simply Postgres, is an object-relational database management system (ORDBMS) available for many platforms including Linux, FreeBSD, Solaris, Windows and Mac OS X.^[6] It is released under the PostgreSQL License, which

is an MIT-style license, and is thus free and open source software. As with many other open-source programs, PostgreSQL is not controlled by any single company — a global community of developers and companies develops the system.

4.3. sqlite

SQLite implements most of the SQL-92 standard for SQL but it lacks some features. For example it has partial support for triggers, and it can't write to views (however it supports INSTEAD OF triggers that provide this functionality). While it supports complex queries, it still has limited ALTER TABLE support, as it can't modify or delete columns.

The time and memory capacity taken by different databases is different, because each and every database have its own specifications..Applications can make use of any of these databases according to users choice. This project aims to identify, time and memory capacity taken by different databases. That is instead of randomly selecting any one of the databases for each applications, it is possible to give provision to the user to select a database which take less time and less memory capacity . Evaluation of the response time of each query must be done. The result can be formulated by combining them. By comparing the results formed from different databases, it will be possible to identify which database take less time and less memory capacity.

Performance evaluation of database systems is an important concern. This is the same reason why Database management systems need to be evaluated based on their performances. Different Database management systems perform differently even in the same environment. There are multiple ways to measure the performance of a system. The most commonly used performance metrics are response time (R) and throughput (X). The response time is defined as the time interval from the instant a command is input to the system to the instant the corresponding reply begins to appear at the terminal. The throughput is generally considered as a measure of the system's productivity, that is, the number of programs or transactions processed during the measurement period. Essentially, they are the same aspect of the system viewed from different perspectives.

Users are interested in the response time while system managers are interested in throughput. Given infinite resources, the expected quality of service can always be provided, but with limited resources, capacity planning and resource management is needed. This project, evaluate the performance of different database management system. Based on that comparison of different DBMSs in the same environment is possible. This performance evaluation is done based on various parameters such as execution time, throughput etc.

5. ANALYSIS

Performance evaluations of database systems are made difficult by the existence of different database management systems (DBMS), which serves different requirements. Even though database management systems are limited in speed due to many limitations, they need to achieve full throttle through its efficient performance. Database management systems perform many complicated jobs. That is why they need to be efficient in storage and speed. This is the same reason why database management systems need to be evaluated based on their performances. Different database management systems performs differently even in the same environment.

5.1. Response time calculation:

Query response time is the total time a query takes to complete its execution. It depends on the complexity of the query type. Database time is calculated by aggregating the CPU time and wait time of all user sessions not waiting for idle wait events. The figure shows the number of queries used, type of query, the checkout time across the database time.

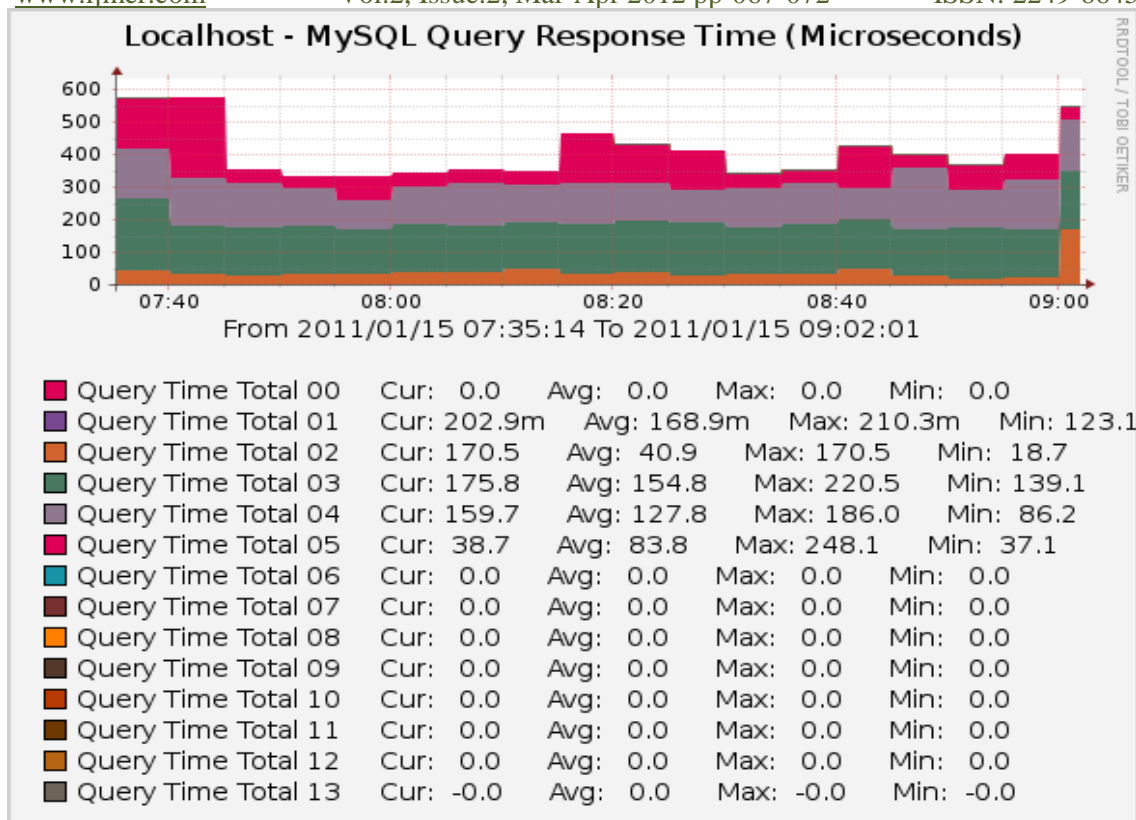


Figure 2: Response time calculate inaccordance with the queries

Figure 2 displays a histogram of the query response time distribution. Because the time units are user-configurable, exact unit labels are not displayed; rather. There are 13 entries on the graph. The graph actually displays the amount of response time spent on queries of various lengths. The units are in microseconds on the graph. When the processor speed changes from 1 GHz to 2 GHz, the modeled response time also increases.

5.2. Memory capacity calculation:

The total space required by a query to complete its execution. The values it takes for the completion of its execution. By combining the space, each query takes for execution together gives the total memory space required by that application

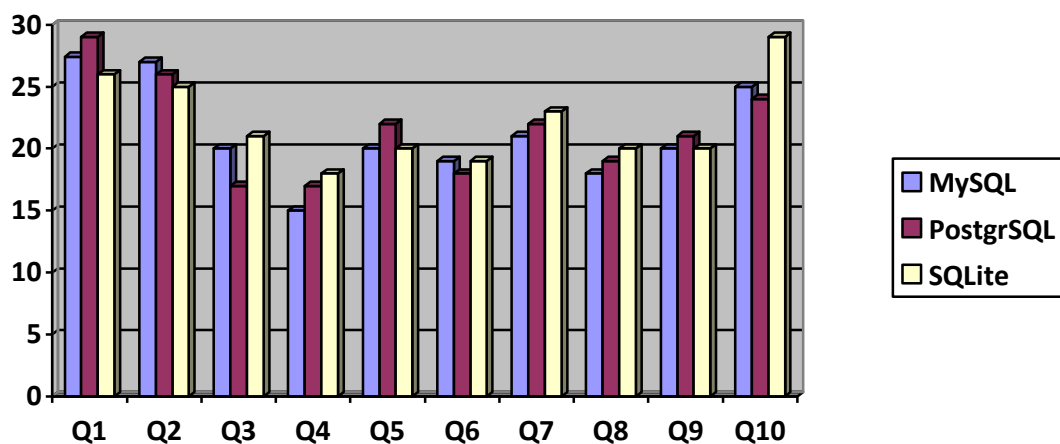


Figure 3: Performance comparison of MySQL,PostgreSQL and Sqlite against different query types

The response time and memory for executing every single operation may be different. It depends upon the current system conditions also. That is whether the system is in ideal state, or multiple processes are running concurrently etc. The analysis is performed against each query type and ,the response time and the memory to execute those query is calculated. By combining the result obtained by these calculations analysis can be done. The analysis is performed against various system conditions also. The graph shows response time of these database management systems which is taken for different queries. Memory capacity taken by different dbms can also be shown in the same way the response time is calculated in milli seconds.

6. CONCLUSION

This paper evaluates the performance of three different database management systems They are MySQL, SQLite, PostgreSQL. Based on that, comparison of different database management systems in the same environment is possible. This performance evaluation is done based on parameters such as response time, memory capacity etc. The results obtained by evaluating time and memory capacity of different database management systems are stored within a DBMS. These values are compared with each other, to get the specific database management system which gives better performance than the others. Different database management systems works differently even in a unique environment. That is why analysis of the database management system which shows better performance is an important issue. . By comparing the performance of different database management system, selection of the database management system which took less time and less memory in that environment is possible

REFERENCES

- [1] Amol deshpande, Zachary ives and Vijayshankar raman. "Database Performance Evaluation Techniques for Specialized Databases" vol. 1, no. 1 (2007) 1–140c2007
- [2] Xilin cui, "A capacity planning study of database management systems with Olap workloads", tcset'2008, february 19-23, 2009, lviv-slavsko, Ukraine
- [3] Jian pei, Runying mao, Kkan hu and Hua zhu," Multiple approaches for Query Analysis", sigmod '00: proceedings of the 2000 ACM sigmod international conference on Management of Data, pp 592,2000
- [4] Nurul husna mohd saad and Hamidah Ibrahim,"Multilingual Database Management System: A performance evaluation" , 43400 upm, serdang, selangor, Malaysia-2011
- [5] Kyoung-Don Kang and Phillip H. Sin and Jisu Oh, A Real-Time Database Testbed and Performance Evaluation, Proceedings of the 13th IEEE International Conference on Embedded and Real-Time Computing Systems and Applications, Pages 319-326 , 2007
- [6] Amol Deshpande, Zachary Ives and Vijayshankar Raman. "Adaptive Query Processing" -Foundations and Trends R in Databases Vol. 1, No. 1 (2007) 1–140c2007
- [7] N. Bruno and S. Chaudhuri, "Exploiting statistics on query expressions for optimization," in SIGMOD '02: Proceedings of the 2002 ACM SIGMOD international conference on Management of data, (New York, NY, USA), pp. 263– 274, ACM Press, 2002. international conference on Management of data, pp 592,2000
- [8] Piotr Mazur,Jan Marlewki,Marek Kamiski. "Universal database repository model for use in near real-time database warehouse environment":TCSET'2008, February 19-23, 2009, Lviv-Slavsko, Ukraine

Authors

APARNA KALADI received B.Tech degree in Computer Science and Engineering from the Mahathma Gandhi University, Kerala in 2010 and pursuing ME degree in Computer Science and Engineering in Sri Shakthi Institute of Engineering and Technology under Anna University, Coimbatore. Her research interests include Data mining and computer networks.

MRS. PRIYA PONNUSAMY is working as an Assistant Professor in Sri shakthi institute of engineering and technology. She is a research scholar under Anna University of Technology- Coimbatore. She did her ME in Anna University of Technology- Coimbatore and her BE in Tamilnadu College of Engineering, Coimbatore. Her area of interest includes networking and hardware.

A Hybrid Mechanism For Dominating Set Based Power Aware Routing In MANET

Sowmyadevi Kanagasabapathy¹, Malini Anbumani², Reha Subbiyan³

*(Department of Computer Science Engineering, CIET/ Anna University, India)

** (Department of Information Technology, SNS/ Anna University, India)

*** (Department of Information Technology, Anna University Coimbatore, India)

ABSTRACT

Many researches are going on to improve the routing, control the topology, reduce the energy consumption, improve quality of service and to establish a secured routing. Among these energy conservation is one of the vital factor deciding up the life time of the network. There are many existing works carried out for power-aware routing. Each of them is concentrating on individual factors like controlling transmission range, reducing power distribution among nodes, using directional antennas and controlling mobility topology. But no work is done that covers all the above factors. The proposed work is based on the idea of combining the important factors of energy aware routing like controlling topology, reducing power distribution and adapting variable transmission range. So it is a hybrid approach for saving power in the mobile ad hoc networks. The proposed model of MANET first insists on identifying the dominating set of nodes and based on the controlled topology, power aware routing is carried on. In this case the node mobility is completely neglected. Then a dynamic topology is considered and the dominating set is identified for the same. Then the power distribution is taken into account to carry on the routing. Finally a variable transmission range of the nodes is considered to implement the power-aware routing. In each of the cases the network parameters like throughput, bandwidth, number of hops, distance-hop energy are evaluated and analyzed.

Keywords – Ad hoc network, MANET, Nodes, router, topology.

I. INTRODUCTION

Ad hoc networks are multi-hop wireless networks where all nodes cooperatively maintain network connectivity. These types of networks are useful in any situation where temporary connectivity is needed, such as in disaster relief. Building such ad hoc network poses a significant technical challenge because of the many constraints imposed by the environment. A Mobile Ad hoc NETWORK (MANET) as shown in Fig.1.1, is a kind of wireless ad hoc network, and is a self-configuring network of mobile routers (and associated hosts) connected by wireless links – the union of which form an arbitrary topology. The routers are free to move randomly and organize themselves arbitrarily; thus, the network's wireless topology may change rapidly and unpredictably. Such a network may operate in a standalone fashion, or may be connected to the larger Internet. Recently the introduction of new technologies such as the Bluetooth, IEEE 802.11 and HIPERLAN are helping enable eventual commercial MANET deployments outside the military domain. These

recent evolutions have been generating a renewed and growing interest in the research and development of MANET. Applications include emergency management, security, helping vulnerable people to live independently, traffic control, warehouse management, and environmental monitoring.

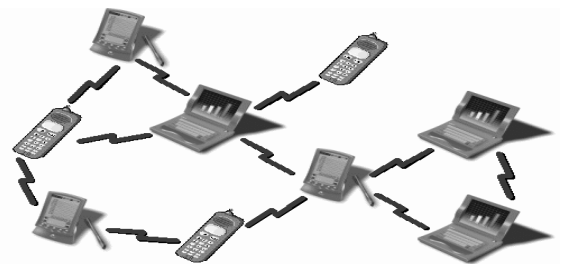


Figure 1.1 Mobile Ad hoc NETWORK (MANET)

II. ENERGY CONSERVATION

Energy use is a crucial design concern in wireless ad hoc networks since wireless terminals are typically battery operated. The devices used in the MANET must be light weight. Furthermore, since they are battery operated, they need to be energy conserving so that battery life is maximized. Energy management strategies need to consider the node and its local applications. Nodes are interdependent and must cooperate to provide routing and other services, to maximize the network lifetime. When Greedy strategies are taken over by the nodes, it results in frequent network failure, since each node seeks only to minimize its own energy consumption.

III. POWER-AWARE ROUTING

Recent studies have stressed the need for designing protocols to ensure longer battery life. The design objectives of energy-aware routing are two folds: selecting energy-efficient paths and minimizing the protocol overhead incurred for acquiring such paths. Examining the existing MAC protocols and network protocols, indicates a clear need for improvement: in all of the current protocols, nodes are powered on most of the time even when they are doing no useful work. Intuitively, it is best to route packets through nodes that have sufficient remaining power. Similarly, routing packets through lightly loaded nodes is also energy-conserving because the energy expended in contention is minimized.

Two classes of power-saving protocols:

- Network layer
- Medium Access Control layer

3.1 Network layer

Network layer protocols make up the largest class of power-save protocols. Scheduling of the interface is driven by network layer traffic which is buffered at the MAC layer for sleeping neighbors or routed so as to take advantage of non sleeping ones. The power-save protocols are based upon three basic strategies outlined below:

First approach:

- Simplest synchronized power-save mechanism
- Nodes periodically wake up to listen to announcement of pending traffic, till the work is over.
- Phase synchronization problem in a dynamic network is present.
- Restricted windows for announcing and forwarding traffic can result in high latencies.

Second approach:

- Based on the network topology.
- Covering set of network that provides connection equivalent to that of the full network.
- Other nodes remain in sleep state with minimal impact on network performance.
- Protocols may be either synchronous or asynchronous.

Third approach:

- Fully asynchronous operation.
- Nodes maintain independent and dissimilar sleep-wake schedule.
- Scheduling rules are defined.
- Retransmission rules are defined.

3.2 Medium Access Control layer

MAC layer power-save protocols use information derived from the media-access control process to find intervals during which the network interface does not need to be awake. While a packet is being transmitted, nearby nodes whose transmissions might interfere with the ongoing transmission must remain silent. These nodes can sleep with little or no impact on throughput.

IV. RELATED WORKS

4.1 FEED BACK POWER CONTROL

Distributed power control schemes are extensively employed in the cellular networks and are capable of improving the capacity of the network. However the power control schemes from the cellular networks suffer from performance degradation due to self and direct-interference and hidden-terminal problems when directly employed in ad hoc networks. Most of the existing channel reservation-based power control protocols for ad hoc networks employ incremental power allocation rather than global allocation of the power to the incoming links; thus they may not effectively utilize the spatial frequency reuse in the network. So a distributed channel access protocol that couples the channel reservation and the iterative/global transmission power control schemes in ad hoc networks is proposed. The designed protocol considers the convergence problem of the

global power control in ad hoc networks. The designed access criteria employ the local transmission control based on the sufficient criteria for admissibility and global power control for balancing the SIR (signal to interference ratio) of the links.

4.2 CORRELATIVE POWER CONTROL

The correlations that exist between the required transmission power of RTS (Request To Send), CTS (Clear To Send), DATA and ACK frames to guarantee a successful 4-way handshake in wireless ad hoc networks based on the IEEE 802.11 distributed coordination function (DCF) are examined. From these correlations, and starting from a set of different initial conditions, a class of power controlled media access control (MAC) algorithms for single channel ad hoc networks based on the existing IEEE 802.11 DCF is derived. From substantial simulations of the different algorithms and comparison to prominent alternatives, a conclusion that contradicts the intuitively sound, commonly held belief which states that sending control frames at maximum power to reduce interference on the long data frames-then, the ensuing long data frames at a lower, yet sufficient power level decreases power consumption per carried bit was arrived.

4.3 VARIABLE-RANGE TRANSMISSION POWER CONTROL

Effective transmission power control is a critical issue the design and performance of wireless ad hoc networks. Today, the design of packet radios and protocols for wireless ad hoc networks is primarily based on common range transmission control. Power control affects the performance of the physical layer in two ways. First, power control impacts the traffic carrying capacity of the network. On the one hand, choosing too high a transmission power reduces the number of forwarding nodes needed to reach the intended destination, but as mentioned above, this creates excessive interference in a medium that is commonly shared. In contrast, choosing a lower transmission power reduces the interference seen by potential transmitters, but packets require more forwarding nodes to reach their intended destination. The impact of variable-range transmission power control on the physical and network connectivity, on network capacity, and on power savings in wireless multihop networks are taken into account. The average range is half the range obtained when common-range transmission control is used. An expression for the average traffic carrying capacity of variable-range-based multihop networks is derived. A model that approximates the signaling overhead of a routing protocol as a function of the transmission range and node mobility for both route discovery and route maintenance is derived. There is an optimum setting for the transmission range, not necessarily the minimum, which maximizes the capacity available to nodes in the presence of node mobility.

4.4 FAIR COALITIONS FOR POWER-AWARE ROUTING

Several power-aware routing schemes have been developed for wireless networks under the assumption that the nodes are willing to sacrifice their power reserves in the interest of the network as a whole. But, in several applications of practical utility, nodes are organized in groups, and as a result, a node is willing to sacrifice in the interest of other nodes in its

group but not necessarily for nodes outside its group. Such groups arise naturally as sets of nodes associated with a single owner or task. Here, considering the premise that groups will share resources with other groups only if each group experiences a reduction in power consumption. Then, the groups may form a coalition in which they route each other's packets. The sharing between groups has different properties from sharing between individuals and investigates fair, mutually beneficial sharing between groups. A pareto-efficient condition for group sharing based on max-min fairness called fair coalition routing is given. The fair coalition routing allows different groups to mutually beneficially share their resources.

4.5 ENERGY-AWARE ADAPTIVE ROUTING

An energy-aware traffic-adaptive routing strategy for large-scale mobile ad hoc network is done. Energy-Aware GEolocation-aided Routing (EAGER) protocol optimally blends proactive and reactive strategies for energy efficiency. In proactive routing, the network topological information is maintained at every node. Such a strategy avoids the need for establishing routes for each message and is especially efficient when the network topology is relatively static and traffic is relatively heavy. Reactive routing, on the other hand, does not maintain global topological information. When a message arrives, the source floods a request packet over the network, searching for the destination. Such strategy avoids the need for frequent topological updates and, therefore, substantially reduces energy consumption when the traffic is light or the topological variation is high. EAGER partitions the network into cells and performs intracell proactive routing and intercell reactive routing. The cell size and the transmission range are optimized analytically. By adjoining cells around hot spots and hot routes in the network, EAGER is capable of handling time varying and spatially heterogeneous traffic conditions.

4.6 SELFISH NODE BEHAVIOUR

The problem of topology control is to assign per-node transmission power such that the resulting topology is energy efficient and satisfies certain global properties such as connectivity. The conventional approach to achieve these objectives is based on the fundamental assumption that nodes are socially responsible. Here, considering nodes to behave in a selfish manner and its impact on the overall connectivity and energy consumption in the resulting topologies is examined. The above problem is established as a non-cooperative game and game-theoretic analysis is used to address it. It shows that even when the nodes have complete information about the network, the steady-state topologies are suboptimal. An algorithm based on a better response dynamic is derived and this algorithm is guaranteed to converge to energy-efficient and connected topologies. Moreover, the nodes transmit power levels are more evenly distributed, and the network performance is comparable to that obtained from centralized algorithms.

V. PROPOSED HYBRID APPROACH

The proposed system contributes a solution for the energy efficient routing in the mobile ad hoc networks. The topology of the network, power distribution among the nodes and the transmission range of the nodes are combined to get a well-organized model for the MANET.

5.1 DOMINATING SET

The first module of the proposed system is based on the topology of the networks. The dominating set of nodes can be identified and the topology of the network can be decided based upon it. A dominating set of a network is a subset of nodes such that each node is either in the dominating set (the minimum number of nodes that are sufficient to establish energy efficient routing) or is a neighbor of a node in the dominating set. In a connected dominating set as shown in Fig.5.1, the dominating nodes form a connected sub graph of the network.

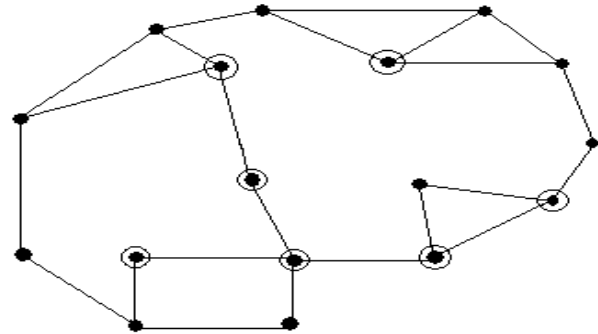


Figure 5.1 Connected dominating sets

5.1.1 ALTERED PRIORITY BASED SELECTION ALGORITHM

- Step 1:** Send neighbor list to all neighbors
Step 2: Receive neighbor list from all neighbors
Step 3: Determine status:

If the node's status is INT CANDIDATE:

- Change status to DOMINATEE if at least one neighbor has DOMINATOR status
- Change status to DOMINATOR if

* the node has the highest priority among its 1-hop INT CANDIDATE neighbors and the neighbors of these INT CANDIDATE nodes, which are two hop away from the original node.

* the node has a leaf INT CANDIDATE neighbor, i.e., an INT CANDIDATE neighbor node with degree 1.

* a DOMINATOR neighbor reported fully connected status.

• If the node's status is DOMINATEE or EXT CANDIDATE:

- Change status to DOMINATOR if
 - * the node has the highest priority among its 1-hop INT CANDIDATE neighbors and their two hop neighbors.
 - * the node has a leaf INT CANDIDATE neighbor.
 - * at least one DOMINATOR neighbor reported fully connected status.

• If the node's status is DOMINATOR:

- Change status back to DOMINATEE if there is another DOMINATOR node with lower node ID covering the same set of DOMINATEE nodes.

With the dominating sets identified the energy efficient routing in the network is carried on.

5.2 TOPOLOGICAL CONTROL METHOD

The second module of the proposed system is based upon the effects caused by the dynamic topological changes of the above model of the mobile ad hoc networks. The topological control methods are applied to find out the energy efficient routing in this case. The transmit power of the nodes is controlled to have power over the mobility of the nodes.

5.2.1 COMMON POWER LEVEL

Network nodes executing COMPOW operate on the smallest power level to reach maximum network connectivity. COMPOW maintains a routing table at different power levels. Each routing table exchanges link state updates at different powers to generate the route information. The optimum power of a node is the smallest power level whose routing table has the same number of entries as that of a routing table at the maximum power level. COMPOW reduces the transmission power redundancy and interference by selecting the maximum operational power settings to reach the furthest neighbour node. In the worst case scenario the algorithm will incur a cost of $O(PN)$, where P are the number of power levels and N are the number of network nodes. In this module by controlling the transmission controlling the transmission stabilizes power the node mobility and power aware routing is implemented for the mobile ad hoc networks.

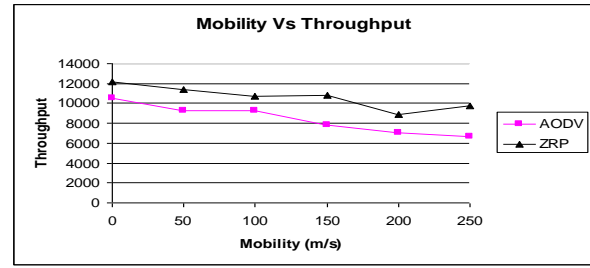
5.3 VARIABLE RANGE TRANSMISSION TECHNIQUE

The third module of the proposed system concentrates on the transmission range of the mobile nodes in the network. A variable transmission range is taken up for the nodes leaving of the common transmission range, since the former increases the network connectivity. Routing protocols can take advantage of fully connected networks to provide multiple routes for a given source-destination pair in cases where some nodes or links fail. However, it results in reducing network capacity and energy-savings (Javier Gomez 2007). To improve the power minimum energy routing is implemented along with the variable transmission range technique. The minimum energy routing minimizes the total energy consumed in forwarding a packet from source to destination. In each of the modules after finding the energy efficient routing, the network parameters like distance per hop, overall hop count, per-node energy consumption, residual energy, distance-hop energy and throughput are evaluated and compared with the earlier results as specified in the reference papers.

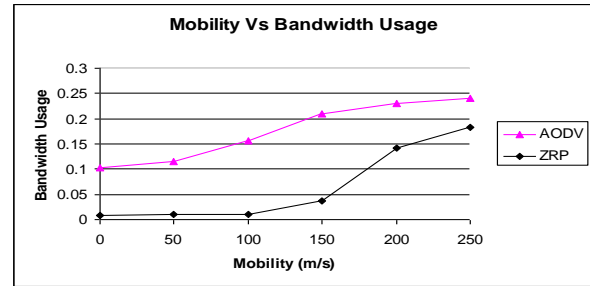
CONCLUSION

Minimum energy routing is combined with the variable range transmission technique and the network parameters like distance per hop, overall hop count, per-node energy consumption, residual energy, distance-hop energy and throughput are evaluated in both AODV and ZRP routing techniques. The results and analysis shows this energy efficient routing setup, works efficiently with ZRP rather than AODV. The minimum energy routing minimizes the total energy consumed in forwarding a packet from source to destination.

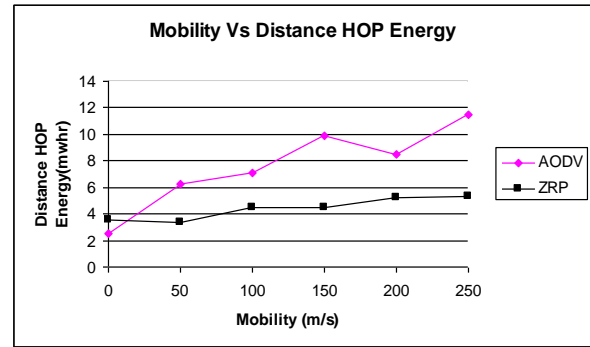
RESULTS



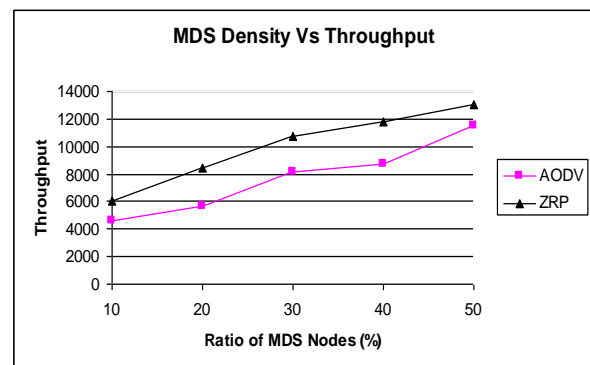
Performance Analysis chart for Mobility Vs Throughput



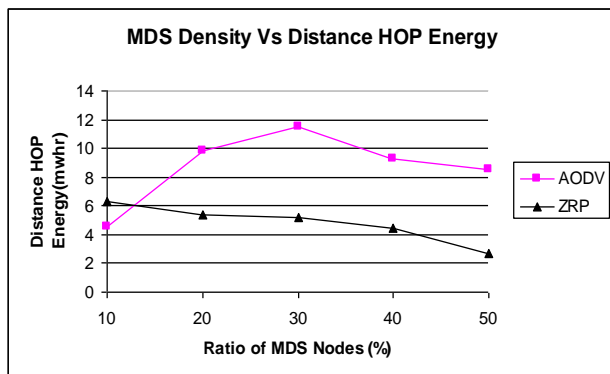
Performance Analysis chart for Mobility Vs Bandwidth Usage



Performance Analysis chart for Mobility Vs Distance Hop Energy



Performance Analysis chart for MDS Density Vs Throughput



Performance Analysis chart for MDS Density Vs Distance Hop Energy

AUTHORS



Sowmyadevi Kanagasabapathy B.Tech., (M.E.), Currently pursuing Master of Engineering in Coimbatore Institute of Engineering and technology, Anna university Coimbatore. As completed B.Tech Information technology in Coimbatore Institute of Engineering and technology, Anna university chennai. Her research work is in the Computer Networking.



Malini Anbumani B.Tech., (M.Tech.), Currently pursuing Master in Technology in S.N.S College of Technology, As completed B.Tech Information Technology in Coimbatore Institute of Engineering and technology, Anna university chennai. Her research work is in the Cloud computing and Networking.



Reha Subbiyan B.Tech., (M.Tech.), Currently pursuing Master in Technology in Anna University Coimbatore, As completed B.Tech Information Technology in Coimbatore Institute of Engineering and technology, Anna university chennai. Her research work is in the Data Mining and Networking.

ACKNOWLEDGEMENTS

An acknowledgement section may be presented after the conclusion, if desired.

REFERENCES

This heading is not assigned a number.

References

- [1] Chao Liang and Kapil R. Dandekar, (2007) 'Power Management in MIMO Ad Hoc Networks: A Game-Theoretic Approach' IEEE Transactions on Wireless Communications, Vol. 6, No 4.
- [2] Hasan Raza.S Naqvi and Patnaik.L.M, (2006) 'A Distributed Channel Access Protocol for Ad Hoc Networks with Feedback Power Control' IEEE Transactions on Mobile Computing, Vol. 5, No. 10.
- [3] Javier Gomez and Andrew T. Campbell, (2007) 'Variable-Range Transmission Power Control in Wireless Ad Hoc Network' IEEE Transactions on Mobile Computing, Vol. 6, No. 1.
- [4] Jun Zhang and Brahim Bensaou, (2007) 'Core-PC: A Class of Correlative Power Control Algorithms for Single Channel Mobile Ad Hoc Networks' IEEE Transactions on Wireless Communications, Vol. 6, No. 9.
- [5] Michael Olsen.C and Chandra Narayanaswami, (2006) 'PowerNap: An Efficient Power Management Scheme for Mobile Devices' IEEE Transactions on Mobile Computing, Vol. 5, No. 7.
- [6] Qing Zhao, Lang Tong and David Council, (2007) 'Energy-Aware Adaptive Routing for Large-Scale Ad Hoc Networks: Protocol and Performance Analysis' IEEE Transactions on Mobile Computing, Vol. 6, No. 9
- [7] Ramakant S. Komali, Allen B. MacKenzie and Robert P. Gilles, (2008) 'Effect of Selfish Node Behavior on Efficient Topology Design' IEEE Transactions on Mobile Computing, Vol. 7, No. 9.
- [8] Ratul K. Guha, Carl A. Gunter and Saswati Sarkar, (2007) 'Fair Coalitions for Power-Aware Routing in Wireless Networks' IEEE Transactions on Mobile Computing, Vol. 6, No. 2.
- [9] Redi.J, Kolek.S, Manning.K, Partridge.C, Rosales-Hain.R, Ramanathan.R and Castineyra.I (2008) 'JAVeLEN – An ultra-low energy ad hoc wireless network' ELSEVIER, Ad Hoc Networks 6.

Efficient MAC Protocol for Heterogeneous Cellular Networks (HC-MAC)

¹Y V Adi Satyanarayana, ²Dr. K Padma Raju

¹ Y V Adi Satyanarayana, Assoc. Professor, Dr. Samuel George Inst. of Engg. & Tech., Markapur, A.P, India

² Dr. K Padma Raju, Professor of Electronics & Communications Engineering & Director, Industry Institute Interaction and Placement & Training JNT University Kakinada Andhra Pradesh India

Abstract: This paper details the efficient MAC protocol for heterogeneous Cellular network. Present 3G-cellular radio access network cannot support many concurrent high data rate unicast (or) flows due to limited radio resources. We proposed Mac protocol for heterogeneous cellular network (HC-MAC). The heterogeneous network uses a proprietary protocol for communication within the network and TCP/IP for connection with other networks. Here we study here how the 802.11 medium access control (MAC) protocol can be applied and how it performs in the Heterogeneous cellular network (HC-MAC). By exploiting the fact that timeout intervals are not explicitly specified, without modifying the standard, we propose a new timing structure for the distribution coordination function (DCF) and the handshake of request-to-send (RTS) and clear-to-send (CTS) to handle increased signal propagation delay in Heterogeneous cellular network (HC-MAC). We find that the DCF and RTS/CTS protocols as specified in the standard continue to work properly for a link distance up to 6 km. Our analysis reveals that the DCF performance degrades slightly in the 802.11 network with cell size of 6 km when compared with the 600 m WLAN. Thus, as far as the MAC protocol is concerned, the Heterogeneous cellular network (HC-MAC), with 8 km cell size is feasible.

Keywords:- Heterogeneous networks, IEEE 802.11, 3G/4G, Cellular network, Quality of service.

I. Introduction

Today the development of Cellular communication technologies is actively developing, testing and deploying third generation (3G) wireless networks, customers are expecting services with data rate higher than that to be provided by 3G networks. To meet such demand for better quality of service (QoS) [1] and security [2]. Many companies have started to provide high-speed data services using wireless local-area-networks (WLAN) in places such as airports and hotels. Such an approach is particularly attractive due to the maturity and low cost of the IEEE 802.11b technology [199b, VAM99]. The 802.11b network provides data rates up to 11 Mbps, far exceeding that to be offered by, for example, EDGE [SAE98, CQW99] and W-CDMA networks [HT00].

Besides high data rates, 802.11b networks offer several advantages over 3G network: The cost of 802.11b equipment is much lower than that for 3G equipment because of the simple design of the former networks, coupled with competition among WLAN vendors. Second,

802.11b networks operate in the 2.4 GHz ISM band, which is free spectrum. In contrast, the 3G spectrum is licensed and very expensive. Thus, both reasons make the operating cost of the 3G network higher than that of WLAN.

Similarly, each WLAN can serve only a small area, up to a few hundred meters, where a cell radius of 10 kilometers is supported in the 3G networks. In addition, future 3G networks are expected to provide ubiquitous coverage and availability. In contrast, public WLAN service is available only in isolated places such as airports and hotels. Users will use both types of networks, one for excellent coverage while the other for enhanced data rates.

In this research, we explore the following question: Is it possible to design HC-MAC, cellular network based on the existing 802.11 air-interface standard for wireless data services? If the answer is affirmative, then users can use the same air-interface mechanism to obtain wireless services from indoor WLAN and outdoor 802.11 networks. There are many technical issues pertinent to the design of an 802.11 cellular network.

Recall that 802.11 as well as its extension 802.11b [199b] and 802.11a [199a] standards were developed specifically for WLAN with the transmission range up to a few hundred meters in indoor environment. First, the signal propagation delay increases when applying the 802.11 to outdoor networks relative to the indoor WLAN, which in turn may affect the applicability of the medium access control (MAC) protocol. Second, the outdoor environment has increased delay spread that causes intersymbol interference. Further, Doppler effects due to mobility may require sophisticated processing for channel estimation and QoS.

We focus this paper on the MAC protocol design and performance when using the 802.11 specification for HC-MAC cellular networks, while radio issues will be addressed in our subsequent papers. Much work related to the 802.11 MAC protocol has been published; see e.g., [B00], [CCG00] and [VCM01].

The rest of the work is organized as follows in section II. We provide an overview of the IEEE802.11 standards in section III. We provide how the protocols may or may not work properly in the heterogeneous network, we estimate the maximum cell radius in heterogeneous cellular networks due to consideration of MAC protocols. In section IV we analyze the MAC protocol performance for heterogeneous cellular networks and finally in section V we conclude the results.

Overview of IEEE 802.11

IEEE 802.11 is the leading standard for wireless LAN [3]. It adopts the standard 802 logic link control (LLC Protocol) but provides optimized physical layer (PHY) and medium access control (MAC) sub layers for wireless communications. 802.11 specifies two physical layers. 1. Direct Sequence Spread Spectrum (DSSS) and 2. Frequency Hopping spread spectrum (FHSS). Based on transmission technologies and operating spectrum the next generation will propose 802.11 can be classified into three categories: 802.11a (orthogonal frequency division multiplexing, OFDM, 5GHz), 802.11b (High rate DSS, HR/DSSS, and 2.4 GHz), and 802.11g (OFDM, 2.4 GHz). 802.11b is based on HR/DSSS and operates at 2 GHz industrial, scientific, Medical (ISM) bandwidth transmission rate from 1 to 11 MBPS. 802.11a is based on OFDM and use 5 GHz and licensed national information infrastructure (U-NII) band in America with a transmission rate of 6-54 MBPS. 802.11g is also based on OFDM but uses 2.4 GHz ISM Band and was formally ratified by the IEEE standards associations' standard board in June 2003. This specifies maximum transmission rate of 54 MBPS. The same as 802.11a. The family IEEE 802.11 standards are as shown in Table 1.

The 802.11 MAC supports two medium access protocols: Contention based distributed co ordination function (DCF) and optional point co ordination function (PCF). When the PCF is enabled, the wireless channel is divided into super frames. Each super frame consists of a contention free period (CFP) for PCF and a contention period for DCF. From the beginning of CFP the point coordinator (usually the access point (AP)) contends for access to the wireless channel. Once it acquires the channel, it cyclically polls high priority stations and grants them the privilege of transmitting. Also the optional PCF is designed for delay bounded services, and also it is centralized and also used for network infrastructure mode.

A The PCF Protocol

In IEEE 802.11 specification [197] the PCF protocol, an AP polls its associated mobile stations one after another by sending polling messages. If the AP has data to send to a mobile station being polled, the data can be included in the polling message. If the polled station has data for the AP, it is sent in the response message. When applicable, an acknowledgment (which acknowledges receipt of a previous data frame from the AP) can also be included in the response message.

As an illustrative example in Figure 1, the AP first sends the polling message and data, if any, to mobile station 1 (denoted by S1). Station 1 should immediately send an acknowledgment or a data frame, if any, to the AP within the SIFS interval. After receiving an ACK or data from station 1, the AP polls mobile station 2 within the SIFS interval. In this illustration, station 2 does not respond, either because the polling message is lost or station 2 has no data to send to the AP. In this case, as a response is not received from station 2 before the SIFS expires, the AP moves on to poll station 3 within the PIFS interval, which starts from the end of the last polling message for station 2.

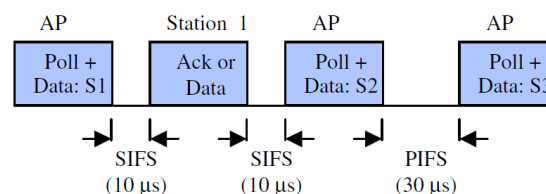


Figure 1. The PCF of the 802.11 MAC Protocol

Task Group	Responsibility
802.11a – OFDM in 5 GHz band	Specification enabling up to 54 MBPS to be achieved in the 5 GHz and licensed radio band by utilizing OFDM.
802.11b – HR/DSSS in 2.4 GHz Band	Specification enabling up to 22 MBPS to be achieved in the 2.4 GHz and licensed radio band by utilizing HR/DSSS.
802.11c – Bridge operation procedures	Provides required information to ensure proper bridge operations, which is required when developing access points.
802.11d – Global Harmonization	Covers additional regulatory domains, which is important for operation in the 5 GHz band.
802.11 e – MAC Enhancements for QoS	Covers use of MAC Enhancements for quality of service such as EDCF service differentiation and coordination function (HCF).
802.11f - Inter access point protocol(IAPP)	Provides inter operability for users roaming from one access point to another of different vendor.
802.11g – OFDM in 2.4 GHz band	Specification enabling high data rates (36 or 54 MBPS) to be achieved in the 2.4 GHz unlicensed radio band.
802.11h – Dynamic frequency selection (DFS)Dynamic channel selection and transmission power control.	
802.11i – Security	Specification for WLAN security to replace the Weak Wired Equivalent Privacy (WEP).

Table1: The family of IEEE 802.11 standards

B. The DCF Protocol

The DCF employs the CSMA/CA mechanism and works as follows. A station (including the AP) with a new packet ready for transmission senses whether or not the channel is busy. If the channel is detected idle for a DIFS interval (i.e., 50 μs for 802.11b networks), the station starts packet transmission. Otherwise, the station continues to monitor the channel busy or idle status. After finding the channel idle for a DIFS interval, the station: a) starts to treat channel time in units of slot time, b) generates a random backoff interval in units of slot time, and c) continues to monitor whether the channel is busy or idle. In the latter step, for each slot time where the channel remains idle, the backoff interval is decremented by one. When the interval value reaches zero, the station starts packet transmission. During this backoff period, if the channel is sensed busy in a slot time, the decrement of the backoff interval stops (i.e., is frozen) and resumes only after the channel is detected idle continuously for the DIFS interval and the following one slot time. Again, packet transmission is started when the backoff interval

reaches zero the backoff mechanism helps avoid collision since the channel has been detected to be busy recently. Further, to avoid channel capture, a station must wait for a

backoff interval between two consecutive new packet transmissions, even if the channel is sensed idle in the DIFS interval. This is depicted in Figure 2.

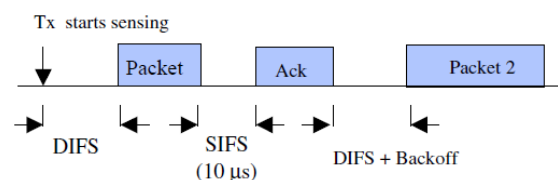


Figure 2. The DCF of the 802.11 MAC Protocol

The backoff mechanism for the DCF is an exponential one. For each packet transmission, the backoff time in units of slot time (i.e., an integer) is uniformly chosen from 0 to n-1, where n depends on the number of failed transmissions for the packet. At the first transmission attempt, n is set to a value of CW_{min}=32, the so-called minimum contention window. After each unsuccessful transmission, n is doubled, up to a maximum value of CW_{max}=1024.

The 802.11 specification requires a receiver to send an ACK for each packet that is successfully received. Furthermore, to simplify the protocol header, an ACK

contains no sequence number, and is used to acknowledge receipt of the immediately previous packet sent. That is, stations exchange data based on a stop-and-go protocol. As shown in Figure 2, the sending station is expected to receive the ACK within the 10 μ s SIFS interval after the packet transmission is completed. If the ACK does not arrive at the sending station within a specified ACK_timeout period, or it detects transmission of a different packet on the channel, the original transmission is considered to have failed and is subject to retransmission by the backoff mechanism.

In addition to the physical channel sensing, the 802.11 MAC protocol implements a network allocation vector (NAV), whose value indicates to each station the amount of time that remains before the channel will become idle. All packets contain a duration field and the NAV is updated according to the field value in each packet transmitted. The NAV is thus referred to as a virtual carrier sensing mechanism. The MAC uses the combined physical and virtual sensing to avoid collision.

The protocol described above is called the two-way handshaking mechanism. In addition, the MAC also contains a four-way frame exchange protocol. Essentially, the four-way protocol requires that a station send to the AP a special, Request-to-Send (RTS) message, instead of the actual data packet, after gaining channel access through the contention process described above. In response, if the AP sees that it is appropriate, it sends a Clear-to-Send (CTS) message within the SIFS interval to instruct the requesting station to start the packet transmission immediately. The main purpose of the RTS/CTS handshake is to resolve the so-called hidden terminal problem.

III. MAC PROTOCOLS IN HETEROGENIOUS CELLULAR NETWORKS

A. The PCF Protocol Infeasible

It is important to emphasize that the SIFS and PIFS timing requirements for the PCF in Figure 1 are clearly defined in the standard. In particular, the most stringent requirement is that the ACK has to be received from the polled station to the AP within the SIFS interval, which is 10 μ s for 802.11b networks. When the standard is used for heterogeneous cellular networks, the distance between a mobile station and its AP is expected to be longer than that in the WLAN. Consider a link distance of 1.5 km as an example. The round-trip signal propagation delay for the 1.5 km distance requires 10 μ s. Since at least several μ s are needed for signal processing at the receiver, the link distance is likely to be limited to hundreds of meters, as in WLAN environments. In fact, this is the intention of the 802.11 specification. Thus, it is unrealistic to expect that the PCF can be supported for 802.11 heterogeneous cellular networks with cell radius of several km.

B. Applicability of the DCF Protocol

Let us consider the DCF in the heterogeneous cellular networks. It is worth noting that as far as the MAC protocol is concerned, the major difference between 802.11 heterogeneous cellular networks and their

WLAN counterparts is increased signal propagation delay. As shown in Figure 2, the major constraint for the applicability of the DCF in heterogeneous cellular networks is that the ACK is expected to be received within the SIFS interval (10 μ s) after packet transmission. That is, the 10 μ s includes the round-trip signal propagation and processing at the receiver. However, in order to be useful, we aim at having an heterogeneous cellular cell size of several km. Thus, the one-way signal propagation delay can be more than 10 μ s, even neglecting the return propagation and processing time. Evidently, this would not be practical without violating the protocol specification. Our solution is based on the following key observation: Typically, there is no consequence if the ACK is received later than the SIFS interval. This is because, after a station transmits a packet, it starts an ACK_timeout period, which is not specified in the standard and is usually chosen to be a value much larger than 10 μ s by vendors. Thus, as long as the ACK is received before the timeout expires, the MAC protocol responds properly.

As in typical implementations, we assume that the ACK_timeout period is longer than the DIFS interval of 50 μ s. Then, we argue that as long as the ACK arrives at the sending station within the DIFS interval following a packet transmission, the DCF operates properly in the heterogeneous cellular network environment where the link distance can reach as much as several km. The reasoning is as follows. First, because the ACK is received within the DIFS interval, the ACK_timeout has not expired so that the protocol can respond upon receipt of the ACK as if it were received within the SIFS interval, as originally specified in the protocol standard. Second, since the DCF protocol requires any station to sense the channel being idle for at least the DIFS interval before transmitting, the return of the ACK within the DIFS interval following the previous packet transmission by the sending station prevents any stations other than the receiving one from gaining access to the channel. Consequently, the channel is implicitly "reserved" for the receiving station to send the ACK. In addition, the pairing of a packet transmission and its ACK transmitted in sequence for any pair of sending and receiving stations remains intact, as required by the specification.

Extending the arrival delay of ACK from the SIFS to the DIFS interval comes with a penalty. That is, the computation of the NAV assumes that the ACK returns within the SIFS interval. So, the delay extension causes an erroneous determination of the NAV, thus incorrect virtual sensing. Nevertheless, since protocol operations are based on both physical and virtual channel sensing, as long as the former works properly, the malfunctioning of the virtual sensing due to incorrect NAV value causes no apparent, negative impacts.

Actually, the extension of the ACK arrival delay from the SIFS interval to the DIFS interval can also be applied to the RTS and CTS handshake for resolving the hidden terminal problem. Specifically, a sending station starts a CTS_timeout period after sending an RTS. The MAC protocol specifies that the CTS, if any, is supposed to arrive from the receiving station within the SIFS interval

(10 μ s). However, similar to the ACK_timeout, the CTS_timeout period is typically chosen to be much longer than 10 μ s by equipment manufacturers. Therefore, by the same arguments discussed above, the arrival delay for the CTS can be extended to the DIFS interval.

C Maximum Cell Size for the DCF Protocol

With the arrival delay for the ACK and CTS extended to the DIFS interval, let us consider its limit on the maximum cell size (i.e., link distance) in heterogeneous cellular 802.11 networks.

Recall that the ACK and CTS arrival delay consists of a round-trip signal propagation delay and signal processing time. As shown in Figure 3, one reasonable allocation of the 50 μ s DIFS delay is: a one-way signal propagation delay of 20 μ s and a processing time of 10 μ s at the receiving station. The latter should not cause a processing burden for the receiver because the original delay of the SIFS interval is 10 μ s. For the 20 μ s propagation delay, the maximum cell size is about 6 km. In other words, with the cell size of 6 km or less, the DCF protocol operates properly in 802.11 cellular networks.

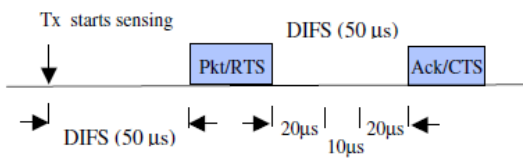


Figure 3. Allocation of ACK/CTS delay

IV. DCF PERFORMANCE IN 802.11 HETEROGENIOUS CELLULAR NETWORKS

We present an approximate analysis of the DCF throughput for heterogeneous cellular networks and WLAN. As shown in Figure 3, if a station with a packet for transmission senses the channel idle for the DIFS interval (denoted by d in μ s in the following), it starts to transmit. Following the packet transmission, the channel remains idle for the DIFS interval and then the ACK is transmitted by the receiver. If the sending station senses the channel busy, it goes through the backoff mechanism discussed above. For simplicity, we do not model the details of the backoff algorithm. Instead, it is assumed that the aggregated traffic, which includes new packets and transmission reattempts, from all stations forms a Poisson process with an intensity of G packets/ μ s. This assumption is reasonable if the backoff period is sufficiently long so that new transmission and reattempts become independent sources. For simplicity, assume that the signal propagation delay a in μ s is identical between any pair of stations. Thus, the *vulnerable period* is also given by a , during which a new packet transmission cannot be sensed by other stations. As a result, these stations under the CSMA protocol can possibly start their own transmissions and cause collisions. Each station senses the channel idle for d μ s (DIFS interval) before transmitting. The packet transmission time is assumed to be constant L μ s. Consider the channel activity for a successful packet transmission. The channel is idle for d μ s and followed by packet transmission of L μ s. As Figure 3 shows, the transmitter waits for d μ s (DIFS

interval) for the ACK. Let the ACK transmission time be c μ s. The channel is sensed idle again by all stations a μ s after the ACK transmission.

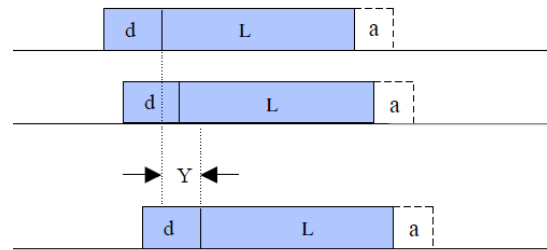


Figure 4. Busy period with Collided Transmissions

Figure 4 shows a typical busy period with collided transmissions due to the vulnerable period for the CSMA protocol, where Y denotes the time span between the first and the last packet transmissions in the busy period. Using the result in [K76], the average duration of Y is given by

$$\bar{Y} = a - \frac{1 - e^{-aG}}{G} \tag{1}$$

The average length of a busy period (which contains a successful transmission or collisions) is given by

$$\bar{B} = d + \bar{Y} + L + a + (d + c)e^{-aG} \tag{2}$$

Where the last term accounts for the waiting and transmission time of the ACK for successful transmission with probability e^{-aG} , based on the Poisson assumption of aggregated traffic. By the same assumption, the average cycle time, consisting of a busy period and the following idle period, is given by

$$\bar{T} = d + \bar{Y} + L + a + (d + c)e^{-aG} + \frac{1}{G} \tag{3}$$

The channel throughput S is defined as the fraction of time at which data is successfully transmitted. Thus, we have

$$S = \frac{Le^{-aG}}{T} \tag{4}$$

Where the numerator is the average amount of time when data is transmitted without collision and T is obtained from (3). Three common packet sizes of 60 bytes (e.g., TCP ACK), 576 bytes (typical size for web browsing) and 1500 bytes (the maximum size for Ethernet) plus a 34 byte 802.11 MAC header are considered. For an 802.11 network with a 1 Mbps data rate, the corresponding transmission time L is 0.75, 4.88 and 12.27 msec, respectively. The sensing idle time of the DIFS interval of 50 μ s and the transmission time c for the 112-bit ACK is 0.112 μ s. Based on our discussions above, the link distance is assumed to be 6 km, and thus the one-way propagation delay a is 20 μ s. For comparison, we also consider a WLAN with a service radius of 600 m with a signal propagation delay of 2 μ s. In this WLAN, after packet transmission, a station waits for the SIFS interval of 10 μ s as in the standard, instead of the DIFS interval as shown in Figure 3, for the arrival of the associated ACK.

Applying these parameters to (1) to (4), we obtain in Figure 5 the MAC throughput as a function of the aggregated traffic load for selected packet lengths. As expected, when the link distance increases from 600 m to 6 km for a given packet length, the maximum throughput decreases because of the increased signal propagation

delay and thus the vulnerable period. For the 576-byte packet size, the maximum throughput drops from 92.9% to 84.8%, when the link distance increases from 600 m to 6 km. Nevertheless, since a 576-byte size is typical for popular web applications, the throughput of 84.8% is still satisfactory. For 1500-byte packets, the channel throughput for the 6 km cell can reach a maximum of 90.8%. Even for the short TCP ACKs of 60 bytes long, the channel throughput is about 60%. In summary, the MAC throughput is still satisfactory despite the increase of cell size to 6 km.

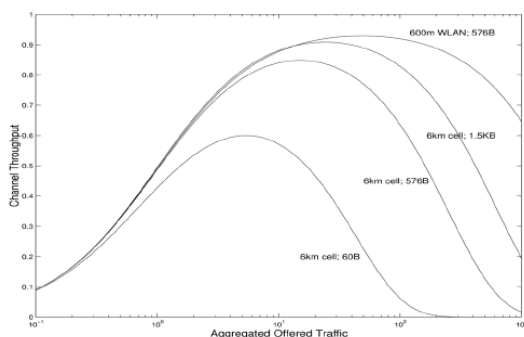


Figure 5. MAC Throughput Comparison.

CONCLUSION AND FUTURE WORK

We have studied how the 802.11 MAC can be applied and how it performs in heterogeneous cellular networks. By exploiting the fact that timeout intervals are not explicitly specified, without modifying the standard, we have proposed a new timing structure for the distribution coordination function (DCF) and the handshake of request-to-send (RTS) and clear-to-send (CTS) to handle increased signal propagation delay in the 802.11 heterogeneous cellular networks. It was found that the DCF and RTS/CTS protocols as specified in the standard continues to work properly if the cell radius is less than 6 km. Our analysis reveals that the DCF performance degrades slightly for a cell size of 6 km when compared with the 600 m WLAN. Thus, as far as the MAC protocol is concerned, the 802.11 cellular network with a cell size of 6 km is feasible.

In terms of future work, a major issue is to examine and enhance the 802.11 radio design so that it performs properly in the cellular environment. In a companion paper [CLMK01], we shall address the issue of radio link performance in the 802.11 cellular networks. We also plan to investigate techniques such as advanced equalizers, smart antennas and call admission control to further improve the performance of the heterogeneous cellular 802.11 cellular networks.

References

1. S.Chakrabarti and A.Mishra. Qos issues in ad hoc wireless networks. IEEE personal Communication Magazine, pages 142-148, Feb 2001
2. Z.Zhou and Z.hass. Secure ad hoc networks. IEEE networks, 13(6):24-30, 1999
3. M.Li, B.Prabhakaran, and S. Sathyamurthy, "On flow Reservation and Admission Control for Distributed Scheduling Strategies in IEEE802.11 Wireless LAN." Proc. 6th ACM Int'l. Wksp. Modeling, Anal and Sim. Wireless and Mobile Sys, Sept. 2003

[199b] IEEE 802.11b, "Part 11: Wireless LAN Medium Access Control (MAC) and Physical Layer (PHY) Specification: High-Speed Physical Layer Extension in the 2.4 GHz Band," 1999.

[VAM99] R. van Nee, et. al., "New High-Rate Wireless LAN Standard," IEEE Commun. Mag., Dec. 1999, pp. 82-88.

[SAE98] P. Schramm, et. al., "Radio Interference Performance of EDGE, a Proposal for Enhanced Data Rates in Existing Digital Cellular Systems," Proc. of IEEE VTC, Ottawa, Canada, May 1998, pp. 1064- 1068.

[CQW99] J. Chuang, X. Qiu and J. Whitehead, "Data Throughput Enhancement in Wireless Packet Systems by Improved Link Adaptation with Application to the EDGE System," Proc. of IEEE VTC'99, Sept. 1999.

[199a] IEEE 802.11a, "Part 11: Wireless LAN Medium Access Control (MAC) and Physical Layer (PHY) Specification: High-Speed Physical Layer Extension in the 5 GHz Band," 1999.

[199b] IEEE 802.11b, "Part 11: Wireless LAN Medium Access Control (MAC) and Physical Layer (PHY) Specification: High-Speed Physical Layer Extension in the 2.4 GHz Band," 1999.

[VCM01] M. Veeraraghavan, N. Cocker and T. Moors, "Support of Voice Services in IEEE 802.11 Wireless LANs," Proc. of IEEE Infocom 2001, Anchorage, Alaska, April 2001, pp. 488-497.

[B00] G. Bianchi, "Performance Analysis of the IEEE 802.11 Distributed Coordination Function," IEEE J. Selected Areas in Commun., Vol. 18, March 2000, pp. 535-547.

[CCG00] F. Cali, M. Conti and E. Gregori, "Dynamic Tuning of the IEEE 802.11 Protocols to Achieve a Theoretical Throughput Limit," IEEE/ACM Trans. On Networking, Vol. 8, Dec. 2000, pp. 785-799.

[K76] L. Kleinrock, Queueing Systems, Vol. 2: Computer Applications, John Wiley & Sons, 1976, p. 398.

[CQW99] J. Chuang, X. Qiu and J. Whitehead, "Data Throughput Enhancement in Wireless Packet Systems by Improved Link Adaptation with Application to the EDGE System," Proc. of IEEE VTC'99, Sept. 1999.

WEB SERVICE BASED E-LOGISTICS APPLICATION

S. Chinchu Krishna *, G. Selvakumar**

*II MECSE, Sri Shakthi Institute of Engineering and Technology, Coimbatore, India

**Assistant Professor (CSE), Sri Shakthi Institute of Engineering and Technology, Coimbatore, India

Abstract — The paper describes the approach for developing e-commerce applications from web services. The applications implemented in heterogeneous platforms and areas can collaborate through Web Services. Presentation layer communicates with database systems through services interface layer. The legacy system layer consists of the existing data sources and information technology systems available for each organization involved in the integrated application. The service interface layer enables the functionality of the legacy systems to be available as Web Services, abstracting from the implementation details. The methodology for building an application using web services illustrates the approach through a use case on e-logistics. The e-logistics platform is integrated with the GPS/GIS technology for efficient logistics distribution management information platform for tracking purpose.

General Terms: E-commerce, web service, tracking, E-logistics

Keywords: SOAP, UDDI, WSDL, service interface layer, connection layer, GPS/GIS technology

I. INTRODUCTION

With the intent of Web Services as part XML-based distributed computing, the integration of business applications on the Web became an easier task. Web Services enable business organizations to provide services by exposing process functionalities through a standard interface description, keeping implementation of computing systems. Thus, applications in diverse areas such as e-commerce and e-governance can interoperate through Web Services implemented in heterogeneous platforms.

The standards used are Web Service description (e.g. WSDL, Web service description language) and publishing (e.g. UDDI, Universal Description Discovery and Integration). XML plays a role of trivializing the exchange of business data among organizations by providing cross-platform approach in the areas of data encoding and data formatting for most integration architecture which is a platform and language neutral content representation technology. For example, SOAP, built on XML, defines a simple way to package information for information exchange across system boundaries between different business applications. UDDI Registries, on the other hand, allow programmable elements to be placed on Web Sites where others can access remotely. Making use of the above technologies, we get interoperability for applications our customers and can use our multi-platform approach to provide better offerings and solutions with the help of which any organization can accomplish their transactions efficiently and profitably.

Logistics management is the process of strategically managing the procurement, movement and storage of materials, parts and finished inventory and the related information flows through the organizations and its marketing channels in such a way that current and future profitability are maximized through the cost-effective fulfillment of orders. The tracking of moving entities can be performed by the integration of GPS/GIS in the logistics platform. GPS (Global Positioning System) and GIS (Geographic Information System) performs pinpointing of specific locations and complex mapping technologies that is connected to a particular database.

II. E-LOGISTICS FRAMEWORK

The business to business (B2B) transactions is performed through different application platforms. Here many logistics service providers are taken into consideration. Although, the applications are developed in diverse platforms, they can provide services through unique interfaces. The communication between the user and the applications is done through different layers.

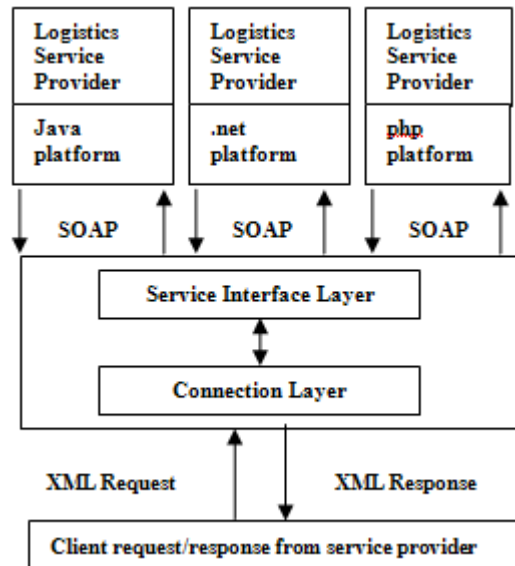


Fig 1: Framework of the system

The client request is placed in connection layer and through the service interface layer, the request is placed to appropriate service provider by SOAP messages. The logistics service provider integrates the response with the information in the request and produces SOAP response. The response will pass through the layers and then delivered to requestor as XML responses. According to the Council of Logistics Management (CLM), logistics is the process of planning, implementing, and controlling the efficient effective flow and storage of goods, services, and related information from point of origin to point of consumption for the purpose of conforming to customer requirements.

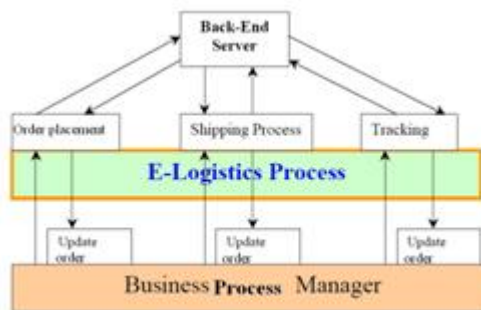


Fig 2: E-logistics working flow

Large numbers of companies now view for their own websites for e-commerce purposes. Logistic management is the management process which integrates the flow of supplies into, through and out of organizations. Logistics Management is that part of a Management Solution that plans, implements, and controls the efficient, effective forward flow and storage of goods, services and related information between the point of origin and the point of consumption in order to meet customers' requirements. The transactions must be integrated with the business process manager and the back end server.

III. LAYERS AND SERVICES

A. Service interface layer

A set of common interfaces are available to carriers, and provides more flexibility to service requestor. Requestor can place the order through standard interface instead of multiple requests. Application developing involves coding once for service providers. By increasing reliability and availability, quality of service can be improved. Easier adaptation to new services makes the system more flexible.

B. Connection Layer

The connection between the Web Services and the legacy system is provided by this layer. This is the service broker between service requestor and service provider response. Transportation broker communicates with UDDI register.

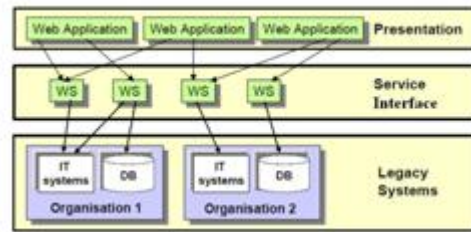


Fig 3: Application architecture

When the request for the web service generated, it is forwarded to the connection layer. The authentication involves signature mapping between requestor and Web Services methods, protocol transformation (e.g. from SOAP to HTTPS). After, the server is invoked. Response from the server is aggregated by connector layer and is sent to the client. Aggregation functionality involves splitting service request to multiple service providers and integrating the responses according to dynamic data.

C. Presentation and legacy systems

Presentation layer holds the applications developed in diverse platforms. Presentation layer communicates with legacy systems through connection layer and service interface layer which is build on XML technology. Legacy systems built for different organizations.

IV. WEB SERVICES

XML manages the exchange of business data between different applications by platform-neutral approach for encoding and formatting. For example, SOAP, built on XML, defines a simple way to exchange messages across applications.

A. Order web service

The application can send an order request to the order Web Services. Then the order will be mapped to a XML message and will send to the connector layer. After the order creation, it will be embedded to the SOAP message. Based on the order information, the order processing is done and forms transportation planning. Here transportation web service is invoked and communicates with database servers. Then the response formed by these processes is sent back to requestor as SOAP.

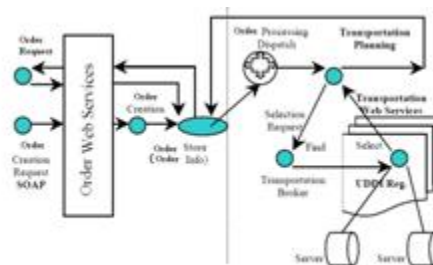


Fig 4: Services and processes

The service interface layer directs the request to the service providers and aggregates response from the servers, binds the data received from the service provider with the response XML and send to the requestor application. The flexibility to choose the best services according to the quality of service is provided to clients. The authentication based in username and password is required for secure transaction. For example, the XML request is

```
<? xml version="1.0">
<LicenseNum>123</LicenseNum> <Username>John</Username>
<Password>kinng</Password> <transport>
<Source>
<City>Kochin</City>
<State>Kerala</State>
<PIN>577664</PIN>
<Country>India</Country> </Source>
<Destination>
<City>Coimbatore</City>
<State>Tamil Nadu</State>
<PIN>678654</PIN>
<Country>India</Country>
</Destination>
```

```
<Weight>500</Weight>
  <Unit>kilogram</Unit>
</transport>
```

The service request will be sent to the server and the response will be given to the requestor .The Response XML template can have followingstructure:

```
<?xml version="1.0">
  <Response>
<Weight>500</Weight>
<Unit>kilogram</Unit>
<Rate>
<Charge>
<Currency>Indian Rupees</Currency> <Value>1200</Value>
</Charges>
<DaysToDeliever>1</DaysToDeliever>
  <DelieveryTime>10:00AM</DelieveryTime>
</Rate>
</Response>
```

B. GPS tracking Web Service

This gives instantaneous position of the vehicle to the clients and thus provides the information about the progress in transportation. The authenticated user can request the GPS location of the vehicle. The alarm function is used in emergency. When the driver was robbed on the way, can press the car's GPS alarm device to alert the monitoring center. The status of the shipment corresponding to a specific order can be monitored by the client. After the map server gets the transport status from the Tracking Web Services, the connector layer can communicate with other layers and services.

C. Transport Web Service

After selecting the transport medium and order processing, the data should bind dynamically with destination, weight, and source with connector layer. The connector layer then sends the request to the appropriate service provider and gets response from the service provider. The server binds the data with the request with the response. The client will get a response containing transportation information. The processes are authenticated through username and password.

V. SYSTEM DESIGN

Combining GIS and GPS technology, platform is formed based on the analysis of the latest computer technology and Logistics business. Focused on the mobile users Logistics information requirement, the system architecture, workflow and functional modules is put forward and designed.The system consist of map server which stores and manipulates all identified locations, local monitoring GPS server, GIS server and the GSM network for vehicle to server communication. Map server and the GIS server collectively provide the information for decision making which is essential for the supply chain management. Effective routing can be done by locations in the map server. Most transportation services require spatial and temporal information.

However, traffic monitoring detectors described above are localized and lack spatial coverage. Remote sensing imagery from satellites cannot provide time continuous transportation information.

VI. GPS/GIS INTEGRATION

The functionality provided by the system is accurate information supporting, graphical display enhancing analysis, wireless communications makes the logistics platform controlled. The stored information contains property and time characteristics and uniform geographical coordinates. Thereby it can able to display, express, analysis all information accurately, in a comprehensive manner which distributed continuously in time and space to support a variety of analysis and decision making. In Logistics platform management, it is used in spatial information management, such as the change of goods spatial location, the reasonable choice of transportation routes, the warehouse layout, the distribution center layout, etc. The GIS functions as a graphical user interface. The functionalities are storage, analysis, forming analytical maps according to the positions. The GIS spatial analysis function, which does different spatial analysis against point, line, surface and body, has a unique role in Logistics analysis, such as the shortest path, network analysis, distribution region segmentation, etc. We can calculate the optimum Logistics route to the destination with the help of GPS real-time road information. The instantaneous route tracking, communication with the central server, proposes the idea of just-in time delivery of the products. As shown in Figure 5, basic components of data system can be divided into two parts: field-based and office-based components. Recording and reporting of coordinates are involved in the first part followed by the second part of data storage, data retrieval, data analysis, and information distribution system to perform the transactions and thereby we can build an integrated E-logistics system.

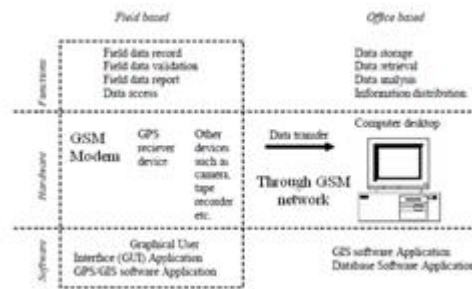


Fig 5: The proposed data system

The instantaneous route tracking and analysis system, proposes an integration of core technologies, which GPS and GIS and map server in which database software application and GIS software application is running, the office based system. In this framework, the GSM receiver device and GSM modem are integrated to a single device, communicate with attention commands. In the map server, there will be another GSM modem which will communicate with the GSM modem placed in field based system. So with the existing infrastructure,(GSM network) the data transmission can be performed with little effort. After the non-spatial and spatial data are gathered, GIS would be a versatile database management tool for other tasks including data retrieval, data analysis, and information distribution.

VII. CONCLUSION AND FUTURE SCOPE

Through the effective integration of web services in different e-logistics platforms, the client can select the appropriate services. The implementation details are abstracted in the developing section and business transactions is done across these heterogeneous applications by SOAP and UDDI. The web service develops a communication framework for legacy systems with existing data sources and information technology systems. The order web services, tracking web services and transport web services makes the request-response scenario more flexible. The current system is only for acquiring the web services to get the information regarding the logistics service provider as per user preferences. As a future scope, we can extend the

REFERENCES

- [1] Geert Van de Putte, Joydeep Jana, Martin Keen, Sandhya Kondepudi, Roberto Mascarenhas, Satish Ogirala, Daniela Rudrof, Ken Sullivan, Peter Swithinbank "Using Web Services for Business Integration"
- [2] Tung-Hsiang Chou, Yu-Min Lee," Integrating E- services with a Telecommunication E-commerce using Service-Oriented Architecture" Journal of Software, Vol.3, No.9, December 2008
- [3] Christopher.M.Judd,"Consuming and producing Web services with web tools"
- [4] Carreker,L.E.Bachman,W.(2000) Geographic Information System Procedures to Improve Speed and Accuracy in Locating Crashes, Transportation Research Record 1719, TRB, National Research Council, Washington D.C., 215- 218
- [5] Y.Xue, A.Cracknelland, H.Guo,"Telegeoprocessing: the integration of remote sensing, Geographic Information Systems (GIS), Global Positioning System (GPS) and telecommunication", International Journal of Remote Sensing, Vol. 23, 2002, pp. 1851-1893.
- [6] N. Uno, F. Kurauchi, H. Tamura and Y. Iida,"Using Bus Probe Data for Analysis of Travel Time Variability", Journal of Intelligent J.-C Thill, "Geographic information systems for Transportation in perspective", Transportation Research Part C, Vol. 8, 2000, pp. 3-12
- [7] Zhirong Chen, Ling Zhu, Yu Teng College of Science, Ningbo University of Technology Ningbo, China."Application of GIS/GPS Technology in Mobile Logistics Public Information Platform", Logistics Engineering and Intelligent Transportation Systems (LEITS), 2010 IEEE International Conference.
- [8] Z. R. Chen and C. J. Xu, "Application of Mobile GIS in Special Equipment Inspection Based on PDA,"

Ecology push: a novel methodology in product design

Nikolaos Efkolidis¹, Dr Ing. Panagiotis Kyratsis²

Department of Industrial Design Engineering,
Technological Educational Institution of West Macedonia, Kila Kozani, GR50100, Greece.

ABSTRACT

Product design is a function that aims to the satisfaction of the customer needs. Nowadays, that the environmental issues become more and more important, product design should address not only economical issues but environmental and social as well. The present research focuses on the development of a novel methodology called Ecology Push and proposes a step by step approach utilizing this method. Although, it takes into consideration the economical and environmental aspects of product design, it also stresses the importance of its social aspect. Additionally, a case study is presented, which validates the proposed methodology. At the same time a new role for the product designer becomes apparent. The designer through his work is able to educate his customers and motivate them towards a more sustainable way of life.

Keywords - assessment tool, product design, sustainable design.

I. INTRODUCTION

Nowadays, all over the world there are signs of severe stress on the interdependent economic, environmental and social systems. Population is rising, while excessive consumption and poverty continue to put enormous pressure on the environment. Societies want to achieve economic development, in order to secure higher standards of living, together with the protection and enhancement of the environment for the future generations. Sustainable development reconciles these two objectives, in order to provide development that meets the needs of the present generation, without compromising the ability of future generations, to meet their own needs as well.

During the early design stages of a product development cycle, all decisions taken contribute to over 70 per cent of the overall product's cost. Although the pieces of information available are limited at the beginning of the product design, appearance, material selection, innovation, performance, environmental impact and perception of quality have to be dealt with at this early stage [1, 2]. As a result, designers have the opportunity to influence the impact that products have on both the environment and the society. Their decisions can have at the same time positive and negative social and environmental impacts. Designers can influence the decisions that people make about what they buy and why they do. These decisions reflect peoples' perceptions of lifestyle and their associated status in the world. Lifestyle is about identity choices, about how individuals wish to be and how they wish to be seen by others. This is expressed through their consumer habits regarding the material, aesthetic and symbolic perspective of the items they buy or consume. Lifestyles are patterns of actions that differentiate between people. They map onto conventional social

categories of class, income, age, gender and ethnicity and often transcend them [3].

With the right point of view, designers have the opportunity to influence attitudes and aspirations, in order to achieve a cultural transformation on customer demands. They can easily promote a new, more environmental friendly, culture and lifestyle. In addition, they should understand how to make the required changes, in order to develop products with more sustainable values. However, many of these values are openly considered under a range of other factors, such as ergonomics and styling [4]. Sustainable product design faces three major challenges [5]:

- Economic: this can be tackled by creating products and services that are less expensive to produce, transport and use, and better adapted to the customer needs in a variety of countries around the globe.
- Environmental: it reduces the use of non-renewable resources and minimizes the environmental impact. Principal rules are: using low-impact materials, smaller consumption of natural resources, creation of longer-lasting and better-functioning products, which can be reused, recycled or composted after their initial use, and
- Social: it allows for increased usability, user-friendliness and safety. It targets users from minorities (disabled and elderly individuals, children and individuals from cultural or linguistic minorities). It plays a key role for some individuals' ability, to enjoy basic human rights like housing, employment, education e.tc.

Park and Seo developed a knowledge based approximate life cycle assessment system in order to assess the environmental impacts of product design alternatives. They aimed at improving the environmental efficiency of a product using artificial neural networks, which consisted of high-level product attributes and LCA results. The framework allows the users to access the product data and other related information on a wide variety of applications [6].

Jeong and Lee proposed an assessment method for eco design improvement options using global warming and economic performance indicators. A reduction in the greenhouse gases (GHG) emissions in the entire life cycle stages of a product was chosen as the global warming performance indicator of the product. The life cycle cost of the product was chosen as the economic performance indicator to measure the performance of its life cycle cost reduction. The assessment method based on the two performance indicators was applied to a liquid crystal display panel [7].

Donnelly et al. presented Lucent's wireless business unit, Mobility Solutions, that pioneered a product based environmental management system to formally address the impact of wireless hardware products on the environment throughout the entire product life cycle, regardless of where

products are developed. Their approach looks beyond the environmental impacts of manufacturing, to include conceptual design, development, customer use and final product disposal [8].

Aoe proposed eco-efficiency indicators and has actually utilized them since 2001 in companies. He has conducted many case studies of eco efficiency using these indicators [9]. Munoz et al. presented a cradle-to-grave life cycle assessment of a toy, incorporating electric and electronic components following the ISO 14044 standard, aiming to identify the environmental hotspots and suggesting eco design measures to the manufacturer. The toy was designed by a Spanish company, but manufactured entirely in China, being exported to Europe, America and Africa. The assessment includes production of all components in China, maritime and road distribution, and considerations of use phase and end-of-life [10].

Ljungberg reviewed current methods on how to develop sustainable products. Different methods for achieving products with the lowest possible environmental impact and principles for product development with special regards to materials selection, design, the product in use and recycling are presented [11]. Fuller and Ottman demonstrated how sustainable product design can affect ecosystems degradation. As the natural capital conversions that underlie product making are the source of the waste that is polluting ecosystems, it makes sense for the researchers to tackle the source of the problem itself [12].

Luttrupp and Lagerstedt started with the hypothesis that there is a strong need for a tool to facilitate the integration of reasonable environmental demands into the product development process. The presented tool 'The Ten Golden Rules', can be helpful in this effort, because it adapts to the task and as a result, the individual product developer/designer is able to develop personal versions of products from the generic guidelines [13].

Although different researchers have come up with different ideas and proposals about sustainability design methodologies, most of them have dealt mainly with the

financial and environmental aspects of product design. The present paper contributes towards the development of a novel methodology, named ecology push, which can lead designers to apply the principles of sustainability in a formal manner. The main novelty incorporated is that except from the financial and environmental issues of a product design, its social aspect is greatly considered. The outcome is to upgrade the role of the designers and make them educators of their own customers.

II. THE CONCEPT OF ECOLOGY PUSH

In the innovative design literature, there is a distinction between the technology-push and the market-pull approaches (Fig. 1). A technology push approach implies that a new invention is pushed through research and development, production and sales functions onto the market, without proper consideration of whether or not it satisfies the customer's needs. In contrast, an innovative product or service based on market-pull can be developed in response to an identified customer need. In a 'pull' strategy, the customer requests a new product/service and 'pulls' it through the delivery channel. A 'push' strategy in marketing is used, when a new product/service, unknown to the customer, has been developed or improved. As there is no customer demand in the product/service launch, the product and the information are 'pushed' to the consumer by distribution and promotion [14].

The concept of ecology push is generated by the need of ecological consciousness to the majority of people and the rising importance of recycling, especially on children, teenagers and young adulthoods (Fig. 2). The reason that the concept is focused on young ages is that, today's children are tomorrow customers, managers and most important parents. According to this approach, a push strategy in marketing is used, when a new environmental friendly product is developed or redesigned based on a more ecological conscious culture. The term product design implies that the product has been developed in order to satisfy customer needs and desires.

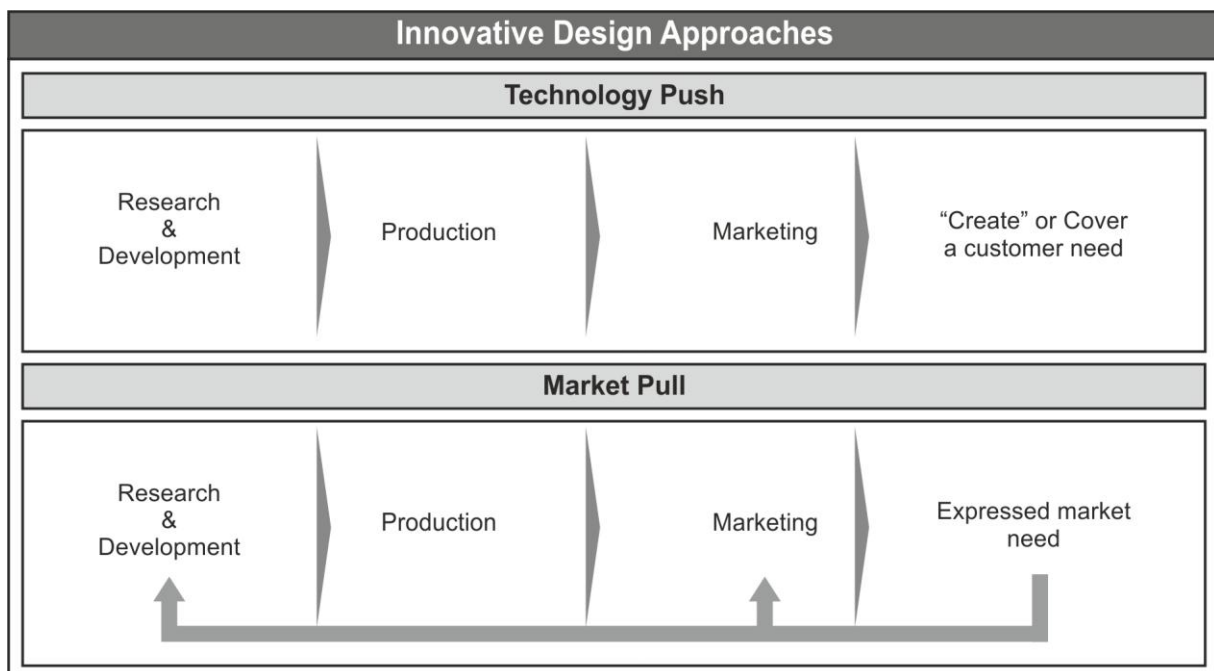


Figure 1. The Technology-Push and Market-Pull approaches

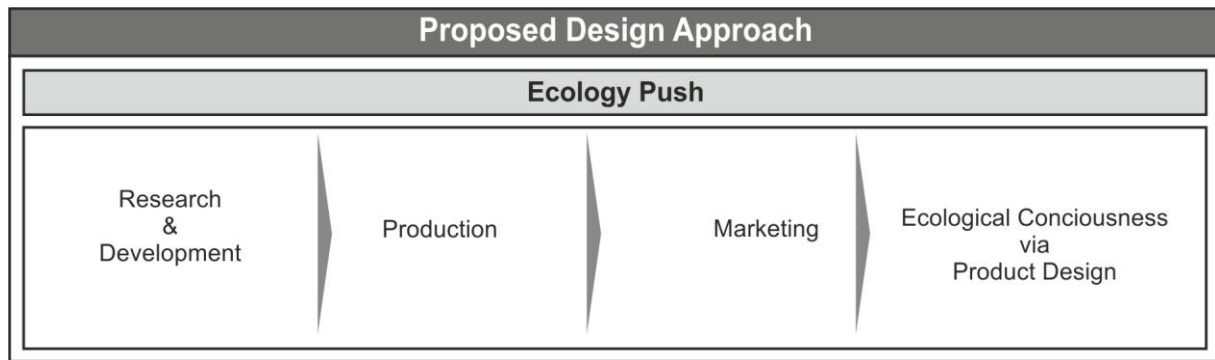


Figure 2. The Ecology-Push approach

Designing for sustainability requires awareness of both short and long-term consequences of any transformation of the environment. Sustainable product design is the conception and realization of environmentally sensitive and responsible expression as a part of the evolving matrix of nature. Moreover product design can encourage recycling and propose solutions. Fingerprinting materials by color or emblem or barcodes allow recognition. Design for disassembly and the avoidance of mutually contaminating combinations, allow economic separation. Clever chemistry (strippable paints, soluble glues) helps with decontamination. Finally design to bypass the need to recycle, longer primary life and more thought, at the initial design stage, towards a possible secondary usage.

Ecology Push can be used as a new model for product design. These products should aim to spread the meaning of sustainable development to consumers in all over the world while at the same time encourage the act of recycling.

III. THE PROPOSED FRAMEWORK

The proposed framework that incorporates the ecology push approach aims in developing a new eco tool which could emphasize the principles of the social impact that a product might have, when it is promoted in the market. The concept of ecology-push was generated by the need of ecological consciousness to the majority of people and the increasing importance of recycling. These concepts suggest that environmental problems in society should not only be addressed via technological innovations (i.e. cleaner production), but also require social changes in the way of living, consumption patterns/levels etc. If such approach is achieved, the most important element of creating a fruitful interaction between technical and social innovation could be found, and place an even greater focus on social innovations when sustainable design is applied.

Based on the need for a new approach in the product design cycle, the proposed ecology-push framework incorporates new roles for both the designer and the customer (Fig. 3). The designer should design or redesign the products keeping in mind their impact to the environment, while the customer offers its feedback during the design process. It is the designers' responsibility to educate their future end-users in order to promote a more environmental friendly thinking.

Further to the feasibility study, designers proceed to the conceptual design of the product. They should incorporate eco-design principles and by the end of that phase, customers come into the picture and assess the designs (stage A). The assessment is based on a questionnaire which has two aims. First, the customers express their idea about the product functionality, worthiness, aesthetics, ergonomics etc, and the feedback is concentrated on traditional issues. Second, the designers are trying to examine, if the ecology issues have been identified from the customers' point of view. The main goal, at this level, is for the customer to understand the eco-messages based on sustainability design, while adapting their way of living and activities accordingly. Together with the questionnaire several interview sessions are taking place, in order to capture the customer perception on the ecological message that the product incorporates. At that stage it is crucial to adjust the product's design and achieve a message transfer through the product's appearance and functionality. It is not enough to design a nice looking or even very handy product, if the ecological message is not clearly defined in a direct manner. In the next step, the product which proved to clearly prompt the customers towards sustainability in their lives is undergoing the proposed changes and then a detail design, testing and prototype building phase follows. It is then that a new customer assessment (stage B) is performed, in order to provide evidence that the expected product is according to the customer needs and at the same time promotes the sustainability principles. Both the assessment activities result in redesigning the product in order to take into account the customer feedback.

The customer assessment tool targets to the customer satisfaction through innovation and cultural transformation, in order to promote the sustainability principles as a way of life. It was developed to support the newly proposed ecology push model. The key issue is the change on customer perception about the product, with an emphasis on eco design and the principles of sustainability. The new designs have to motivate the end-users to change their lifestyle towards a more environmental friendly way. The development of the product could be done in a variety of ways, but the emphasis should be given on the customer perceptions. The main idea is to educate future customers towards sustainability and not actually design eco products in the traditional way.

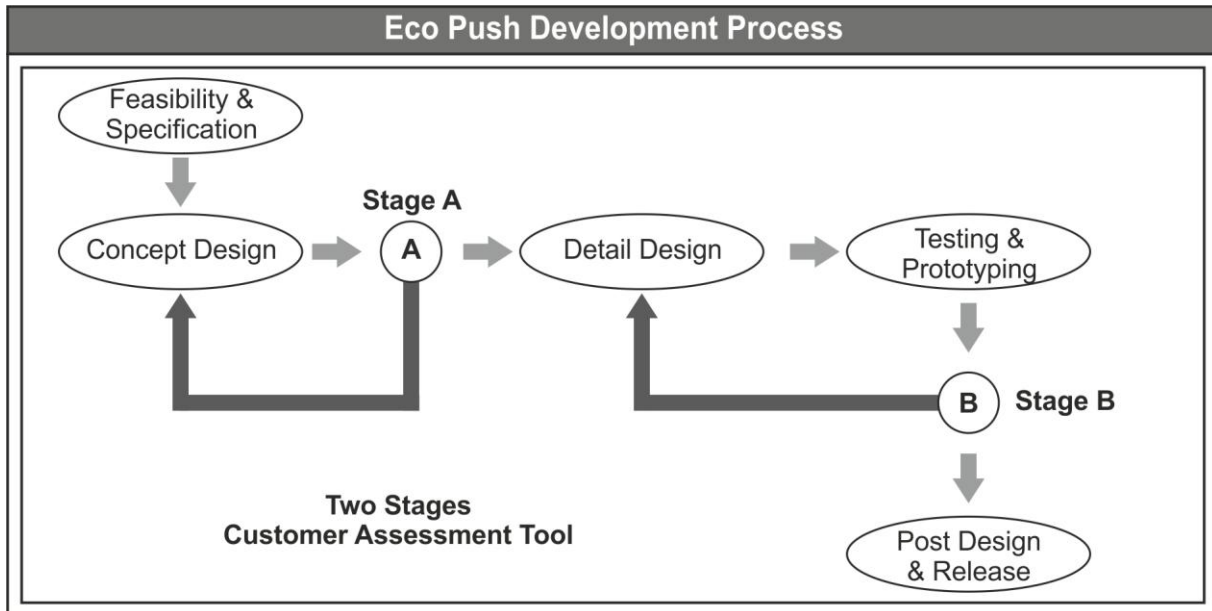


Figure 3. The Eco push framework based on customer assessments

IV. CASE STUDY

A number of different products can be developed based on the proposed ecology push framework. The product under study is called 'Eco-Maniac Bin' (Fig. 4). It consists of a basic bin together with a number of additional parts such as bottle-like, can-like, book-like and tetrapack-like slots. Moulded pulp recycled paper is proposed for all these items because it can be moulded to the desired shape since its fiber is relatively soft and absorbs impacts. It is only recently, that moulded pulp has emerged as the interior packaging material of choice for many electronic and consumer products. It is 100% recyclable, 100% biodegradable, light in weight, safe, sanitary, non-toxic, acid-proof, alkali proof, water proof and finally is easy shaped and practical.

The most important difference, from the material point of view, between traditional toys and the Eco-Maniac bin is the substitution of all plastic components with recycled moulded pulp paper ones. Molded pulp paper is a sustainable product in compliance to ISO 14000 and the European Green Dot standards. The change of the material is targeting to the reduction of the environmental impact during the toy's life cycle.

The development of the product was completed in accordance to design for sustainability within the aforementioned methodology. There was an effort to reconsider the product and its functions. The similar existing toys are targeting to the development of children wit spark and all toy-pieces should be entered successfully based on their shape through the correct slots. Traditionally, the shapes used are cylindrical, conical, cubical, pyramidal etc. Eco-maniac bin, transforms these simple solids to existing products geometry and try to teach the action of recycling:

- The Eco Maniac Bin tries to introduce the children-users in a more sustainable way of life. More specifically, it creates a culture towards recycling and promotes the social aspect of the sustainable design methodology (the child learns to recycle by playing in a very young age with the Eco Maniac Bin).

- Moreover, the use of recycled moulded pulp paper instead of plastic aims to reduce energy and material consumption throughout a product's life cycle and replace harmful substances with more environmentally friendly alternatives. The product may be used more effectively and as a result a reduction of energy can be achieved.
- The designed toy is simple and works manually without the need for external source of energy (i.e. battery).
- The product presents no need for packaging. The main material which is used is from recycled paper and can be recycled again. The principles of design for assembly and disassembly were extensively used in order to be able to be recycled without problems.
- The main bin of the toy could be reused after its main use, as an office bin or as a flower pot. Finally, the toy was designed based on the principle of repairing components instead of replacing the whole product.

The main target for businesses is to design and develop profitable products, which are both environmentally friendly and socially acceptable. Further to the concept design stage, the Eco Maniac Bin went through the first customer assessment procedure based on the proposed framework. An appropriate questionnaire was given to 47 families in order to receive their feedback. The key idea was for the participating families to understand the messages dealing with the social issues of sustainable development. That means, that apart from the traditionally perceived issues (recycled material, pulp paper etc.) the children should be able to discover the importance of separating materials. In such a way, they learn from a very young age the recycle activity and a cultural transformation can be achieved in a very early stage of their life. Studying the results from the first assessment, modifications were made and finally, based on the detailed design a prototype was built and used for a second customer assessment.

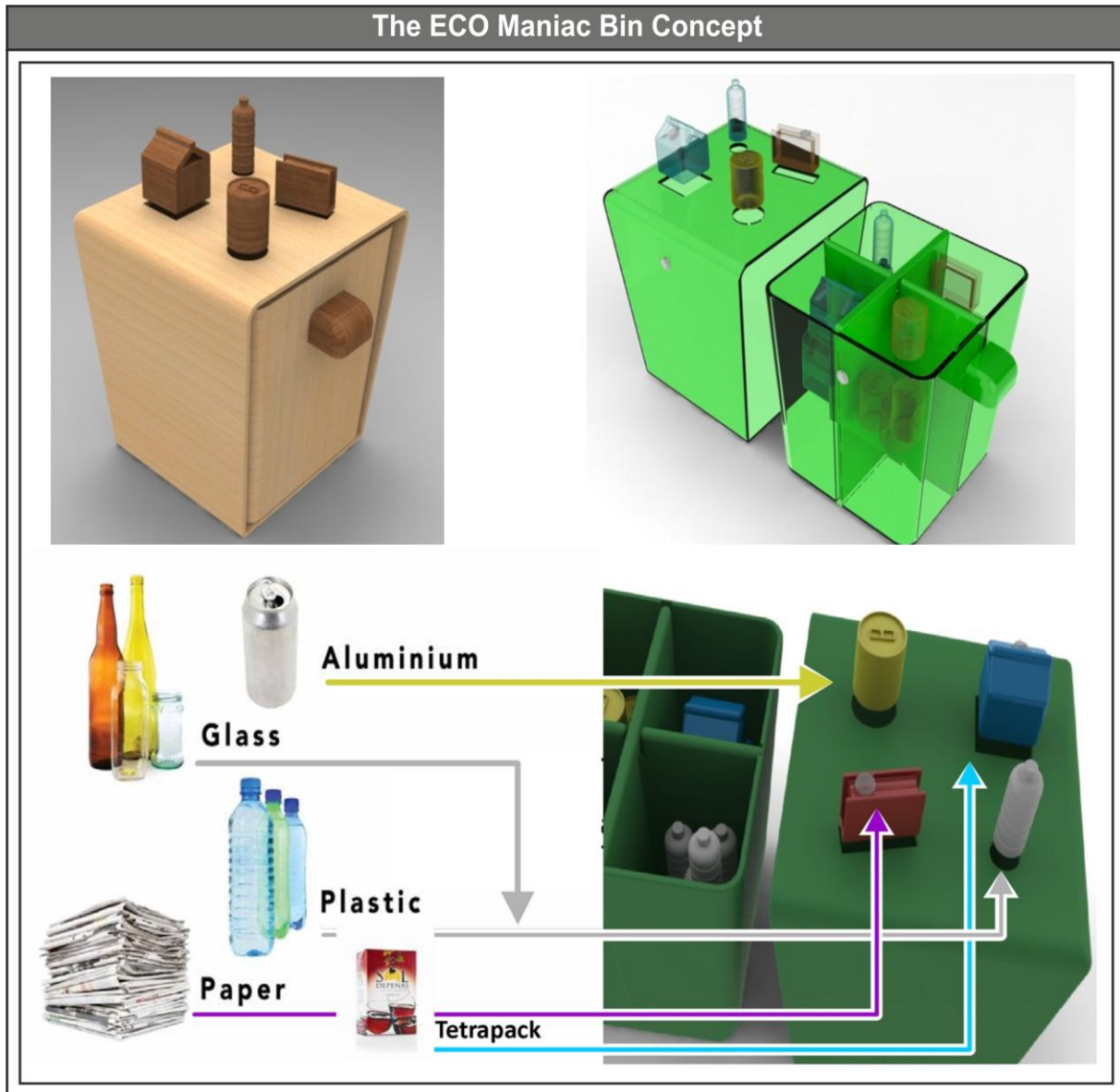


Figure 4. The Eco-Maniac Bin Concept

The results from both the customer assessments can be summarized as follows:

- although the two thirds of the participants were not sure about what sustainable development means, more than 90% understood the aim for the children cultural transformation,
- 75.6% of the family members mentioned that they are willing to purchase the product, even if its price was greater than the similar traditionally designed toys,
- 82.4% of the family members liked the fact that they can participate in the design of a product early enough and thus contribute to its future,
- 64.1% of the participants recognize the need for ecologically designed products, acknowledging the need to become environmentally educated customers.
- When measuring their perception about the importance of the three sustainable development pillars, the results were 65%, 69% and 45% acceptance of environmental, social and economic issues respectively.
- 73.6% of the family members would definitely purchase other redesigned toy which would be based

on existing one, even if that means that must pay 30% more for its acquisition.

Further to the questionnaires, the design team conducted a number of interviews with the participants, in order to have a more direct contact with them and analyse their thoughts and perceptions directly. In addition to that, designers were brought together in brainstorming sessions, in order to consolidate the outcome of the customer participation. The Eco Maniac Bin affects sustainable development to its three pillars but emphasizes its social impact. Furthermore, it motivates young people to learn about sustainable development. The designer can become a kind of sustainable development teacher.

V. CONCLUSIONS

With all the environmental issues people facing in today's world (i.e. the pollution coming either from industrial or from public wastes, the energy consumption of non renewable resources), it is important to grasp the need for a change in our consuming culture and start thinking the promotion of environmental friendly way of life. Product design with environmental friendly techniques and technologies cannot by itself be the solution towards better

resources management. There is a need for cultural transformation, and that need should be addressed to the young people, in order to promote the appropriate culture early enough.

The concept of ecology push aims to spread the sustainable development, especially to children and young people, in order to create the new environmental culture of the young generations. The ecology push strategy via designing environmental friendly products aims in developing ecological consciousness to young consumers. The role of the designer becomes more important because, in addition to the product design issues, he/she is shaping the required attitude of the customers. The customers from their point of view clearly understand the environmental messages and learn how to recycle from a very young age.

REFERENCES

- [1] J. Fiksel, J., *Design for environment – A guide to sustainable product development, 2nd ed.* (McGraw Hill, 2009, ISBN: 978-0071605564).
- [2] P. Trott, *Innovation Management and New Product Development, 5th ed.* (Prentice Hall, 2011, ISBN: 978-0273736561).
- [3] T. Bhamra, and V. Lofthouse, *Design for sustainability- practical approach* (Ashgate Publishing, 2007, ISBN: 978-0566087042).
- [4] M.F. Ashby, *Materials Selection in Mechanical Design, 4th ed.* (Butterworth-Heinemann, 2010, ISBN: 978-1856176637).
- [5] G. Howarth, and M. Hadfield, A sustainable product design model, *Materials and Design*, 27, 2006, 1128-1133.
- [6] J.H. Park, and K.K. Seo, A knowledge-based approximate life cycle assessment system for evaluating environmental impacts of the product design alternatives in a collaborative design environment. *Advanced Engineering Informatics*, 20, 2006, 147-154.
- [7] I.T. Jeong, and K.M. Lee, Assessment of the ecodesign improvement options using the global warming and economic performance indicators, *Journal of Cleaner Production*, 17, 2009, 1206-1213.
- [8] K. Donnelly, Z. Becket-Furnell, S. Traeger, T. Okrasinski, and S. Holman, Eco-design implemented through a product-based environmental management system, *Journal of Cleaner Production*, 14, 2006, 1357-1367.
- [9] T. Aoe, Eco-efficiency and ecodesign in electrical and electronic products, *Journal of Cleaner Production*, 15, 2007, 1406-1414.
- [10] I. Munoz, C. Gazulla, A. Bala, and R. Puig, LCA and ecodesign in the toy industry: case study of a teddy bear incorporating electric and electronic components, *International Journal of Life Cycle Assessment*, 14, 2009, 64-72.
- [11] L.Y. Ljungberg, Materials selection and design for development of sustainable products, *Materials and Design*, 28, 2007, 466-479.
- [12] D.A. Fuller, and J.A. Ottman, Moderating unintended pollution: the role of sustainable product design, *Journal of Business Research*, 57, 2004, 1231-1238.
- [13] C. Luttrupp, and J. Lagerstedt, Ecodesign and The Ten Golden Rules: generic advice for merging environmental aspects into product development, *Journal of Cleaner Production*, 14, 2006, 1396-1408.
- [14] B. Hollins, and S. Pugh, *Successful Product Design* (Butterworth-Heinemann Publishing, 1990, ISBN: 978-0408038614).

Collaborative Trust-based Secure Routing based Ad-hoc Routing Protocol

¹Abdalrazak T. Rahem, ²H K SAWANT

^{1, 2} Department of Information Technology,
Bharati Vidyapeeth Deemed University
College Of Engineering, Pune-46

ABSTRACT:

The current existing Authenticated Routing for Ad Hoc Networks (ARAN) secure routing protocol is capable of defending itself against most malicious nodes and their different attacks. However, ARAN is not capable of defending itself against any authenticated selfish node participating in the network. Therefore, the objective of my thesis is to make the Authenticated Routing for Ad Hoc Networks secure routing protocol capable of defending itself against authenticated selfish nodes participating in the mobile ad hoc network. The resulting new protocol is called Reputed-ARAN. This work is done by integrating a reputation-based scheme, to detect, punish and isolate selfish nodes, to currently existing ARAN protocol and then measuring the effectiveness of that integration.

1. INTRODUCTION

To understand routing principles in a MANET, it is a good idea to take a look at conventional routing algorithms such as distance vector, link state, flooding and source routing. This is because many of the routing protocols for a MANET have roots in traditional routing concept as underlying algorithm.[4]

1.1 Distance vector

The distance vector technique is based on that every node maintains a forwarding table with the best route to every node in a network. In a certain time interval the information is sent to every neighboring node in the network. These nodes then conduct a comparison between their own routing table and the received one. If the distance between any nodes in the received table is smaller compared to the one at hand, the node updates the routing table with the new value. If the value that is in the forwarding table is from the node that now is sending a new value, the node updates the forwarding table regardless of if the value is bigger than the existing one. This procedure is continuous so that each and every node has an updated forwarding table with the shortest path to all nodes in the network.

1.2 Flooding

With this technique every packet is sent to every node in the network and is broadcasted by the receiving nodes exactly once. Each node receiving the packet broadcasts it to every neighboring node, except the one it received it from. These, neighboring nodes, in term do the same and so on. To avoid retransmitting the same packet twice every packet is tagged with a source address and a sequence number which serve as a unique identifier. With these identifiers each node keeps track of which packets they have transmitted.

This approach has a very high consumption of network resources since every packet is sent to every possible node to ensure that the packet arrives to its destination. On the other hand it results in an extremely high delivery ratio [4].

1.3 Link state routing

Link state routing works almost like distance vector when it comes to the usage of a forwarding table. What differentiates them is how the table is updated. Link state generates its

table so that every node keeps a map over the nodes in the network. From this map every node can use a shortest path algorithm to decide which way is the shortest to each destination and hence know what the next hop should be in the forwarding table. When there is a change in the network, for example a node connects or disconnects, a message is sent throughout the network to announce the change [1]. The message is called a link state advertisement (LSA) and is passed through the network by flooding. All nodes receive the message and update their maps accordingly. If this method is compared with the method used in distance vector, it makes link state routing more reliable, easier to detect errors and consume less bandwidth. This is because link state routing uses event-triggered updates instead of periodic updates as in distance vector [4].

2. LITERATURE REVIEW

Security in MANET is an essential component for basic network functionalities like packet forwarding and routing. Network operation can be easily jeopardized if security countermeasures are not embedded into basic network functions at the early stages of their design. In mobile ad hoc networks, network basic functions like packet forwarding, routing and network management are performed by all nodes instead of dedicated ones. In fact, the security problems specific to a mobile ad hoc network can be traced back to this very difference. Instead of using dedicated nodes for the execution of critical network functions, one has to find other ways to solve this because the nodes of a mobile ad hoc network cannot be trusted in this way [2].

There are basically two types of security threats to a routing protocol, external and internal attackers. An external attacker can be in the form of an adversary who injects erroneous information into the network and cause the routing to stop functioning properly [2]. The internal attacker is a node that has been compromised, which might feed other nodes with incorrect information. Fig. 3.1 illustrates the different attacks that can be made towards a network. [3,6].

2.1 Active and Passive Attacks

Security exposures of ad hoc routing protocols are due to two different types of attacks: active and passive attacks. In active attacks, the misbehaving node has to bear some energy costs in order to perform some harmful operation. In passive attacks, it is mainly about lack of cooperation with the purpose of energy saving. Nodes that perform active attacks with the aim of damaging other nodes by causing network outage are considered to be malicious while nodes that perform passive attacks with the aim of saving battery life for their own communications are considered to be selfish.

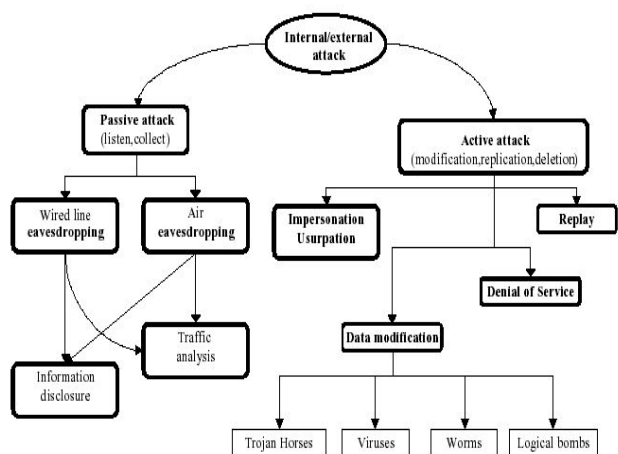


Fig.1: Different sorts of attacks

2.2 Malicious and Selfish Nodes in MANETs

Malicious nodes can disrupt the correct functioning of a routing protocol by modifying routing information, by fabricating false routing information and by impersonating other nodes. On the other side, selfish nodes can severely degrade network performances and eventually partition the network by simply not participating in the network operation. In existing ad hoc routing protocols, nodes are trusted in that they do not maliciously tamper with the content of protocol messages transferred among nodes. Malicious nodes can easily perpetrate integrity attacks by simply altering protocol fields in order to subvert traffic, deny communication to legitimate nodes (denial of service) and compromise the integrity of routing computations in general. As a result the attacker can cause network traffic to be dropped, redirected to a different destination or to take a longer route to the destination increasing communication delays. A special case of integrity attacks is spoofing whereby a malicious node impersonates a legitimate node due to the lack of authentication in the current ad hoc routing protocols. The main result of spoofing attacks is the misrepresentation of the network topology that possibly causes network loops or partitioning.

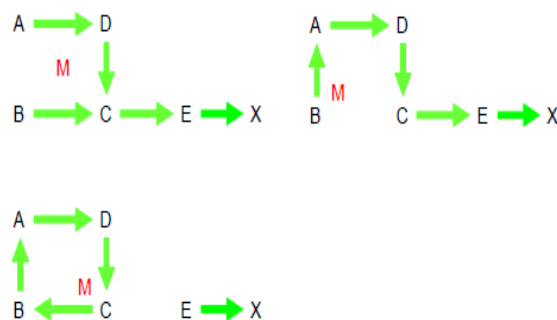


Fig. 2: Impersonation to create loops

In the above figure, a malicious attacker, M, can form a routing loop so that none of the four nodes can reach the destination. To start the attack, M changes its MAC address to match A's, moves closer to B and out of the range of A. It then sends an RREP to B that contains a hop count to X that is less than the one sent by C, for example zero. B therefore changes its route to the destination, X, to go through A. M then changes its MAC address to match B's, moves closer to C and out of range of B, and then sends to C an RREP with a hop count to X lower than what was advertised by E. C then routes to X through B. At this point a loop is formed and X is unreachable from the four nodes. Lack of integrity and authentication in routing protocols can further be exploited through "fabrication" referring to the generation of bogus routing messages. Fabrication attacks cannot be detected without strong authentication means and can cause severe problems ranging from denial of service to route subversion. A more subtle type of active attack is the creation of a tunnel (or wormhole) in the network between two colluding malicious nodes linked through a private connection bypassing the network. This exploit allows a node to short-circuit the normal flow of routing messages creating a virtual vertex cut in the network that is controlled by the two colluding attackers.

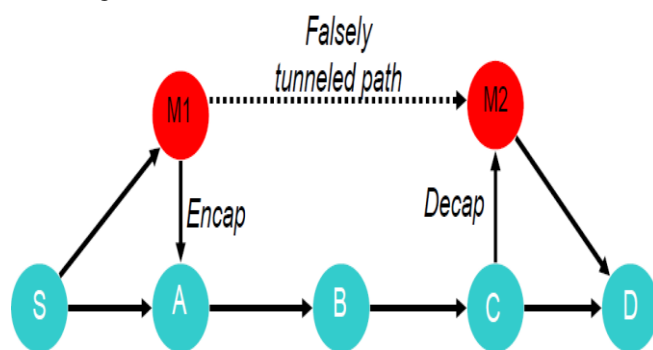


Fig. 3: Wormhole Attack

In the above figure, M1 and M2 are malicious nodes collaborating to misrepresent available path lengths by tunneling route request packets. Solid lines denote actual paths between nodes, the thin line denotes the tunnel, and the dotted line denotes the path that M1 and M2 falsely claim is between them. Let us say that node S wishes to form a route to D and initiates route discovery. When M1 receives a RDP from S, M1 encapsulates the RDP and tunnels it to M2 through an existing data route, in this case {M1->A->B->C->M2}. When M2 receives the encapsulated RDP, it forwards the RDP on to D as if it had only traveled {S->M1-

>M2->D}. Neither M1 nor M2 update the packet header to reflect that the RDP also traveled the path {A->B->C}. After route discovery, it appears to the destination that there are two routes from S of unequal length: {S->A->B->C->D} and {S->M1->M2->D}. If M2 tunnels the RREP back to M1, S would falsely consider the path to D via M1 a better choice (in terms of path length) than the path to D via A.

Another exposure of current ad hoc routing protocols is due to node selfishness that results in lack of cooperation among ad hoc nodes. A selfish node that wants to save battery life, CPU cycles and bandwidth for its own communication can endanger the correct network operation by simply not participating in the routing protocol or by not forwarding packets and dropping them whether control or data packets. This type of attack is called the black-hole attack. Current Ad Hoc routing protocols do not address the selfishness problem and assumes that all nodes in the MANET will cooperate to provide the required network functionalities [2,4,5].

2.3 Routing Protocols' Security Requirements

To solve the security issue in an ad hoc network and make it secure we have to look at a number of requirements that have to be achieved. These requirements are: availability, confidentiality, integrity, authentication and non-repudiation [7].

The network must at all times be available to send and receive messages despite if it is under attack. An attack can be in the form of a denial of service or an employed jamming to interfere with the communication. Other possible threats to the availability are if an attacker disrupts the routing protocol or some other high-level service and disconnects the network. The node itself can also be the problem to availability. This is if the node is selfish and will not provide its services for the benefit of other nodes in order to save its own resources like, battery power. Confidentiality provides secrecy to sensitive material being sent over the network. This is especially important in a military scenario where strategic and tactical information is sent. If this information would fall into enemy hands it could have devastating ramifications. Integrity ensures that messages being sent over the network are not corrupted. Possible attacks that would compromise the integrity are malicious attacks on the network or benign failures in the form of radio signal failures. Authentication ensures the identity of the nodes in the network. If A is sending to B, A knows that it is B who is receiving the message. Also B knows that it is A who is sending the message. If the authentication is not working, it is possible for an outsider to masquerade a node and then be able to send and receive messages without anybody noticing it, thus gaining access to sensitive information. Non-repudiation makes it possible for a receiving node to identify another node as the origin of a message. The sender cannot deny having sent the message and are therefore responsible for its contents. It is particularly useful for detection of compromised nodes. However, because there are so many threats to protect from, there can not be a general solution to them all. Also different applications will have different security requirements to take into consideration. As a result of this diversity, many different approaches have been made which focus on different parts of the problems. In the coming section, a comparison of some of the existing secure mobile ad hoc

routing protocols with respect to most of the fundamental performance parameters will be given [8].

3. PROPOSED REPUTATION BASED AUTHENTICATION SCHEME

Performance of Mobile Ad Hoc Networks is well known to suffer from free-riding, selfish nodes, as there is a natural incentive for nodes to only consume, but not contribute to the services of the system. In the following, the definition of selfish behavior and the newly designed reputation-based scheme, to be integrated with normal ARAN routing protocol ending up having Reputed-ARAN, are presented.

3.1 Problem Definition

Whereas most of the attacks performed by malicious nodes can be detected and defended against by the use of the secure routing ARAN protocol, as was explained earlier, there remain the attacks that an authenticated selfish node can perform.

There are two attacks that an authenticated selfish node can perform that the current ARAN protocol cannot defend against. To illustrate these two possible attacks that a selfish node can use to save its resources in a MANET communication that allows the categorization of attacks that lead an attacker to reach a specific goal is used. In the below table, the attack tree that cannot be detected by current ARAN protocol is shown:

Attack tree: Save own resources OR 1. Do not participate in routing 1. Do not relay routing data OR 1. Do not relay route requests 2. Do not relay route replies 2. Do not relay data packets 1. Drop data packets
--

Table 1: Attack Tree: Save own resources

All the security features of ARAN fail to detect or defend against these attacks, as they focus only on the detection of malicious nodes' attacks and not the authenticated selfish nodes' attacks. ARAN protocol assumes that authenticated nodes are to cooperate and work together to provide the routing functionalities.

3.2 Proposed Reputation-based Scheme

3.2.1 Introduction

As nodes in mobile ad hoc networks have a limited transmission range, they expect their neighbors to relay packets meant for far off destinations. These networks are based on the fundamental assumption that if a node promises to relay a packet, it will relay it and will not cheat. This assumption becomes invalid when the nodes in the network have tangential or contradictory goals. The reputations of the nodes, based on their past history of relaying packets, can be used by their neighbors to ensure that the packet will be relayed by the node. In the upcoming subsections, a discussion of a simple reputation-based scheme to detect and defend against authenticated selfish nodes' attacks in MANETs built upon the ARAN protocol is presented. Sometimes authenticated nodes are congested and they cannot fulfill all control packets broadcasted in the MANET so they choose not to reply to other requests in order to do their own assigned load according to their battery,

performance and congestion status. My scheme do not forward control packets, by considering the reputation value of the node asking others to forward its packets. If the packet has originated from a low-reputed node, the packet is put back at the end of the queue of the current node and if the packet has originated from a high-reputed node, the current node sends the data packet to the next hop in the route as soon as possible. This scheme helps in encouraging the nodes to participate and cooperate in the ad hoc network effectively. Moreover attacks in which authenticated nodes promise to route data packets by replying to control packets showing their interest in cooperation in forwarding these data packets but then they become selfish and start dropping the data packets. This is done by giving incentives to the participating nodes for their cooperation. The proposed scheme is called Reputed-ARAN. Different from global indirect reputation-based schemes like Confidant and Core, the proposed solution uses local direct reputations only like in Ocean reputation-based scheme. Each node keeps only the reputation values of all direct nodes it dealt with. These reputation values are based on the node's firsthand experience with other nodes. My work is partially following the same methodology about reputation systems for AODV.

3.2.2 Design Requirements

The following requirements are set while designing the reputation-based scheme to be integrated with the ARAN protocol:

- ➔ The reputation information should be easy to use and the nodes should be able to ascertain the best available nodes for routing without requiring human intervention.
- ➔ The system should not have a low performance cost because low routing efficiency can drastically affect the efficiency of the applications running on the ad hoc network.
- ➔ Nodes should be able to punish other selfish nodes in the MANET by providing them with a bad reputation.
- ➔ The system should be built so that there is an injection of motivation to encourage cooperation among nodes.
- ➔ The collection and storage of nodes' reputation values are done in a decentralized way.
- ➔ The system must succeed in increasing the average throughput of the mobile ad hoc network or at least maintain it.

3.2.3 Main Idea of the Reputation System

In the proposed reputation scheme, all the nodes in the mobile ad hoc network will be assigned an initial value of null (0) as in the Ocean reputation-based scheme. Also, the functionality of the normal ARAN routing protocol in the authenticated route setup phase will be modified so that instead of the destination unicasts a RREP to the first received RDP packet of a specific sender only, the destination will unicast a RREP for each RDP packet it receives and forward this RREP on the reverse-path. The next-hop node will relay this RREP. This process continues until the RREP reaches the sender. After that, the source node sends the data packet to the node with the highest

reputation. Then the intermediate node forwards the data packet to the next hop with the highest reputation and the process is repeated till the packet reaches its destination. The destination acknowledges the data packet (DACK) to the source that updates its reputation table by giving a recommendation of (+1) to the first hop of the reverse path. All the intermediate nodes in the route give a recommendation of (+1) to their respective next hop in the route and update their local reputation tables. If there is a selfish node in the route, the data packet does not reach its destination. As a result, the source does not receive any DACK for the data packet in appropriate time. So, the source gives a recommendation of (-2) to the first hop on the route. The intermediate nodes also give a recommendation (-2) to their next hop in the route up to the node that dropped the packet. As a consequence, all the nodes between the selfish node and the sender, including the selfish node, get a recommendation of (-2). The idea of giving (-2) to selfish nodes per each data packet dropping is due to the fact that negative behavior should be given greater weight than positive behavior. In addition, this way prevents a selfish node from dropping alternate packets in order to keep its reputation constant. This makes it more difficult for a selfish node to build up a good reputation to attack for a sustained period of time [23]. Moreover, the selfish node will be isolated if its reputation reached a threshold of (-40) as in the Ocean reputation-based scheme. In the following table, the default Reputed-ARAN parameters are listed:

Initial Reputation	0
Positive Recommendation	+1
Negative Recommendation	-2
Self fish Drop Threshold	-40
Re-induction Time out	5 Minutes

Table 2: Reputed-ARAN Default parameters

The proposed protocol will be structured into the following four main phases, which will be explained in the subsequent subsections:

- Route Lookup Phase
- Data Transfer Phase
- Reputation Phase
- Timeout Phase

3.2.3.1 Route Lookup Phase

This phase mainly incorporates the authenticated route discovery and route setup phases of the normal ARAN secure routing protocol. In this phase, if a source node S has packets for the destination node D, the source node broadcasts a route discovery packet (RDP) for a route from node S to node D. Each intermediate node interested in cooperating to route this control packet broadcasts it throughout the mobile ad hoc network; in addition, each intermediate node inserts a record of the source, nonce, destination and previous-hop of this packet in its routing records. This process continues until this RDP packet reaches the destination. Then the destination unicasts a route

reply packet (RREP) for each RDP packet it receives back using the reverse-path. Each intermediate node receiving this RREP updates its routing table for the next-hop of the route reply packet and then unicasts this RREP in the reverse-path using the earlier-stored previous-hop node information. This process repeats until the RREP packet reaches the source node S. Finally, the source node S inserts a record for the destination node D in its routing table for each received RREP.

In the below fig., the route lookup phase is presented in details, illustrating the two phases of it, the authenticated route discovery phase and the authenticated route setup phase.

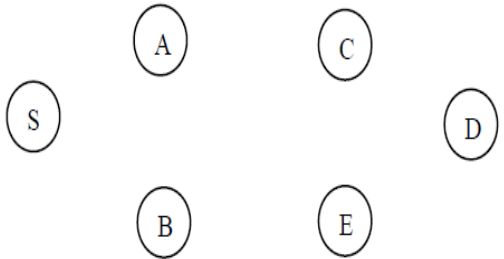


Fig. 4: A MANET Environment

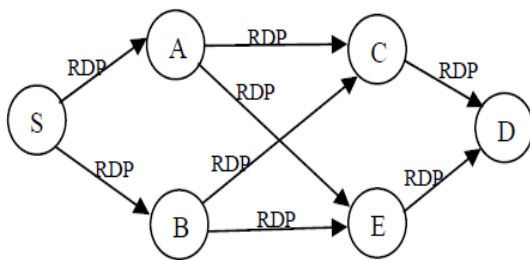


Fig. 5: Broadcasting RDP

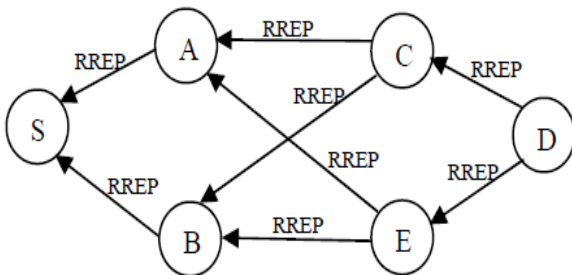


Fig. 6: Replying to each RDP

3.2.3.2 Data Transfer Phase

At this time, the source node S and the other intermediate nodes have many RREPs for the same RDP packet sent earlier. So, the source node S chooses the highly-reputed next-hop node for its data transfer. If two next-hop nodes have the same reputation, S will choose one of them randomly, stores its information in the sent-table as the path for its data transfer. Also, the source node will start a timer before it should receive a data acknowledgement (DACK) from the destination for this data packet. Afterwards, the chosen next-hop node will again choose the highly-reputed next-hop node from its routing table and will store its information in its sent-table as the path of this data transfer. Also, this chosen node will start a timer, before which it should receive the DACK from the destination for this data packet. This process continues till the data packet reaches the destination node D. And of course in this phase, if the data packet has originated from a low-reputed node, the

packet is put back at the end of the queue of the current node. If the packet has originated from a high-reputed node, the current node sends the data packet to the next highly-reputed hop in the route discovered in the previous phase as soon as possible. Once the packet reaches its destination, the destination node D sends a signed data acknowledgement packet to the source S. The DACK traverses the same route as the data packet, but in the reverse direction.

In the following fig., the data transfer phase is illustrated:

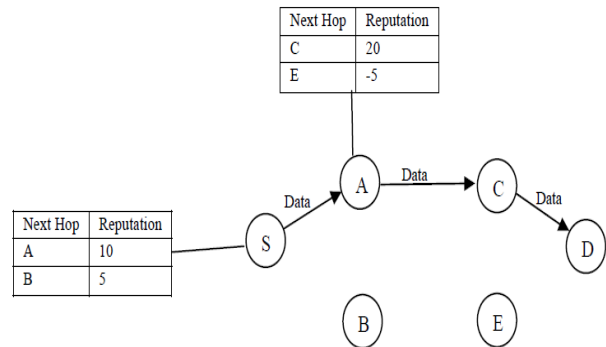


Fig. 7: Choosing the highly-reputed next-hop node

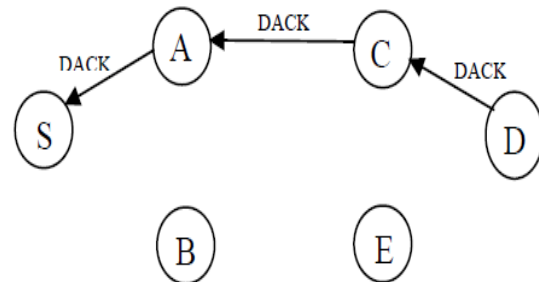


Fig.8: Sending Data Acknowledgement for each received data packet

3.2.3.3 Reputation Phase

In this phase, when an Intermediate node receives a data acknowledgement packet (DACK), it retrieves the record, inserted in the data transfer phase, corresponding to this data packet then it increments the reputation of the next hop node. In addition, it deletes this data packet entry from its sent-table. Once the DACK packet reaches node S, it deletes this entry from its sent-table and gives a recommendation of (+1) to the node that delivered the acknowledgement.

3.2.3.4 Timeout Phase

In this phase, once the timer for a given data packet expires at a node; the node retrieves the entry corresponding to this data transfer operation returned by the timer from its sent-table. Then, the node gives a negative recommendation (-2) to the next-hop node and deletes the entry from the sent-table. Later on, when the intermediate nodes' timers up to the node that dropped the packet expire, they give a negative recommendation to their next hop node and delete the entry from their sent-table. As a consequence, all the nodes between the selfish node and the sender, including the selfish node, get a recommendation of (-2). Now, if the reputation of the next-hop node goes below the threshold (-40), the current node deactivates this node in its routing table and sends an error message RERR to the upstream nodes in the route. Then the original ARAN protocol handles it. Now, it is the responsibility of the sender to reinitiate the route discovery again. In addition, the node whose reputation

value reached (-40) is now temporally weeded out of the MANET for five minutes and it later joins the network with a value of (0) so that to treat it as a newly joined node in the network.

Conclusion

Throughout this thesis, a discussion of existing mobile ad hoc networks' routing protocols' types and their advantages and disadvantages was given and a list of existing proactive, reactive and secure MANET routing protocols was compiled. Then, the different types of attacks targeting MANET routing protocols' security were explored. Also, the difference between malicious and selfish nodes and their associated attacks were discussed and a presentation of the fundamental requirements for the design of a secure routing protocol to defend against these security breaches was given. Furthermore, a comparison between some the existing secure mobile ad hoc routing protocols was presented. Then, an in-depth talk about the Authenticated Routing for Ad Hoc Networks protocol (ARAN) as one of the secure routing protocols built following the fundamental secure routing protocols design methodology was given. Afterwards, a discussion of how ARAN defends against most of the attacks that are conducted by malicious nodes such as spoofing, fabrication, modification and disclosure ones was presented. That resulted in proving that the currently existing specification of the ARAN secure routing MANET protocol does not defend against attacks performed by authenticated selfish nodes. Thus, I moved on discussing the different existing MANET cooperation enforcement schemes by stating their types: the virtual currency-based and the reputation-based schemes. In this proposal, the different phases of the proposed reputation-based scheme were explained. Then, an analysis of the various forms of selfish attacks that the proposed reputation-based scheme defends against was presented. Also, some time was invested in surveying the different simulation packages that are used in mobile ad hoc networks. The solution presented in this thesis only cover a subset of all threats and is far from providing a comprehensive answer to the many security problems in the MANETs field. Last but not least, according to the many simulations that were performed, the newly proposed reputation-based scheme, built on top of normal ARAN secure routing protocol, achieves a higher throughput than the normal ARAN in the presence of selfish nodes. Thus, the proposed design, Reputed-ARAN, proves to be more efficient and more secure than normal ARAN secure routing protocol in defending against both malicious and authenticated selfish nodes.

References

- [1] R.PushpaLakshmi and Dr.A.Vincent Antony Kumar, "Security aware Minimized Dominating Set based Routing in MANET", IEEE 2010 Second International conference on Computing, Communication and Networking Technologies. Dept. of Inf. Technol.,PSNA Coll. of Eng. & Technol., India,pp. 1 – 5, July 2010.
- [2] G. LAVANYA, C.KUMAR and A. REX MACEDO AROKIARAJ, "SECURED BACKUP ROUTING PROTOCOL FOR AD HOC NETWORKS", IEEE International Conference on Signal Acquisition and Processing. Bangalore, India , pp.45-50, 2010.
- [3] YongQing Ni, DaeHun Nyang and Xu Wang, "A-Kad: an anonymous P2P protocol based on Kad network", IEEE 2009. Inf. Security Res. Lab., Inha Univ., Incheon, South Korea , pp. 747 – 752, 2009.
- [4] N.Bhalaji,Dr.A.Shanmugam,"ASSOCIATION BETWWEN NODES TO COMBAT BLACKHOLE ATTACK IN DSR BASED MANET", Wireless and Optical Communications Networks,WOCN., IEEE 2009 IFIP International Conference on Cairo ,pp.1-5 ,2009 .
- [5] Sohail Jabbar, Abid Ali Minhas, Raja Adeel Akhtar, Muhammad Zubair Aziz, "REAR: Real-Time Energy Aware Routing for Wireless Adhoc Micro Sensors Network", Eighth IEEE International Conference on Dependable, Autonomic and Secure Computing pp. 825-830, 2009.
- [6] D.Suganya Devi and Dr.G.Padmavathi, "Performance Efficient EOMCT Algorithm for Secure Multicast Key Distribution for Mobile Adhoc Networks", IEEE International Conference on Advances in Recent Technologies in Communication and Computing. pp 1-25, 2009.
- [7] Jian Ren and Yun Li and Tongtong Li, "Providing Source Privacy in Mobile Ad Hoc Networks", IEEE, Macau SAR, P.R.China,PP. 12-15 ,2009.
- [8] Matthew Tan Creti, Matthew Beaman, Saurabh Bagchi, Zhiyuan Li, and Yung-Hsiang Lu, Multigrade Security Monitoring for Ad-Hoc Wireless Networks", IEEE 6th International Conference on Mobile Adhoc and Sensor Systems , Pages: 342-352,2009.
- [9] S. Zhong, J. Chen, and Y. Yang. Sprite: A simple, Cheat-proof, Credit-based System for Mobile Ad hoc Networks. Proceedings of IEEE Infocom, , pages 1987-1997, April 2003.
- [10] L. Zhou and Z. Haas. Securing Ad Hoc Networks. IEEE Networks Special Issue on Network Security. Vol. 13, no. 6, pages 24-30 ,December 1999.
- [11] Wenchao Huang, Yan Xiong, Depin Chen, "DAAODV: A Secure Ad-hoc Routing Protocol based on Direct Anonymous Attestation", IEEE 2009 International Conference on Computational Science and Engineering, pp 809-816,2009.
- [12] A.H Azni, Azreen Azman, Madihah Mohd Saudi, AH Fauzi, DNF Awang Iskandar, "Analysis of Packets Abnormalities in Wireless Sensor Network", IEEE 2009 Fifth International Conference on MEMS NANO, and Smart Systems, pp 259-264,2009.
- [13] Cuirong Wang, Shuxin Cai, "AODVsec: A Multipath Routing Protocol in Ad-Hoc Networks for Improving Security", IEEE 2009 International Conference on Multimedia Information Networking and Security, pp 401-404,2009.
- [14] A Nagaraju and B.Eswar, "Performance of Dominating Sets in AODV Routing protocol for MANETs", IEEE 2009 First International Conference on Networks & Communications, pp 166-170,2009.
- [15] Sheng Cao and Yong Chen, "AN Intelligent MANet Routing Method MEC", 2009 Eighth IEEE International Conference on Dependable, Autonomic and Secure Computing, pp 831-834.
- [16] WANG Xiao-bo ,YANG Yu-liang, AN Jian-wei, "Multi-Metric Routing Decisions in VANET", 2009

Author Profile

Eighth IEEE International Conference on Dependable, Autonomic and Secure Computing, PP 551-556,2009.

- [17] Zeyad M. Alfawaer and Saleem Al_zoubi, "A proposed Security subsystem for Ad Hoc Wireless Networks", IEEE 2009 International Forum on Computer Science-Technology and Applications, Volume 02, pp 253-256, 2009.
- [18] Shayesteh Tabatabaei, "Multiple Criteria Routing Algorithms to Increase Durability Path in Mobile Ad hoc Networks", IEEE 2009 by the Institute of Electrical and Electronics Engineers. PP. 1 – 5, Nov.2009.
- [19] Cuirong Wang, Shuxin Cai, and Rui Li, "AODVsec: A Multipath Routing Protocol in Ad-Hoc Networks for Improving Security", IEEE 2009 International Conference on Multimedia Information Networking and Security, Northeastern Univ. at Qinhuangdao China ,Volume: 2, pp 401-404,2009.
- [20] A Nagaraju and B.Eswar, "Performance of Dominating Sets in AODV Routing protocol for MANETs", IEEE 2009 First International Conference on Networks & Communications, pp 166-170,2009.
- [21] Tirthankar Ghosh, Niki Pissinou, Kia Makki, "Collaborative Trust-based Secure Routing Against Colluding Malicious Nodes in Multi-hop Ad Hoc Networks", 29th Annual IEEE International Conference on Local Computer Networks (LCN'04). pp.224-231,USA,2009.
- [22] M. F. Juwad, and H. S. Al-Raweshidy, "Experimental Performance Comparisons between SAODV & AODV", IEEE 2008 Second Asia International Conference on Modelling & Simulation, pp 247-252,2008.
- [23] Wei Ren, Yoohwan Kim, Ju-Yeon Jo, Mei Yang³ and Yingtao Jiang, "IdSRF: ID-based Secure Routing Framework for Wireless Ad-Hoc Networks", IEEE 2007 International Conference on Information Technology (ITNG'07) , pp.102-110,2007.
- [24] Anand Patwardhan and Michaela Iorga, "Secure Routing and Intrusion Detection in Ad Hoc Networks", 3rd IEEE Int'l Conf. on Pervasive Computing and Communications (PerCom 2005). University of Maryland - Baltimore County, pp.191-199,2005.

Abdalrazak T. Rahem persuing Mtech from Information Technology Department at Bharati Vidyapeeth Deemed University College of Engineering, Dhankawadi, Pune India. His areas of interest are Software Engineering and networks .

Mr. H K Sawant is working as an Professor in Information Technology Department at Bharati Vidyapeeth Deemed University College of Engineering, Dhankawadi, Pune India. He was awarded his Master of Technology Degree from IIT Mumbai. He is persuing his PhD from JJTU. His areas of interest are Computer Network, Software Engineering and Multimedia System. He has nineteen years experience in teaching and research. He has published more than twenty research papers in journals and conferences. He has also guided ten postgraduate students.

Design and Development of ACK-Based Scheme Using FSA for Ad-hoc Networks

¹Mustafa Sadeq Jaafar , ² H K Sawant

^{1, 2} Department of Information Technology,
Bharati Vidyapeeth Deemed University
College Of Engineering, Pune-46

ABSTRACT:

Ad hoc network is a group collection of mobile node. During the last few years we have all witnessed steadily increasing growth in the deployment of wireless and mobile communication networks. Mobile ad hoc networks consist of nodes that are able to communicate through the use of wireless mediums and form dynamic topologies. The basic characteristic of these networks is the complete lack of any kind of infrastructure, and therefore the absence of dedicated nodes that provide network management operations as do the traditional routers in fixed networks. In order to maintain connectivity in a mobile ad hoc network all participating nodes have to perform routing of network traffic. The cooperation of nodes cannot be enforced by a centralized administration authority since one does not exist. Therefore, a network-layer protocol designed for such self-organized networks must enforce connectivity and security requirements in order to guarantee the uninterrupted operation of the higher layer protocols. Unfortunately all of the widely used ad hoc routing protocols have no security considerations and trust all the participants to correctly forward routing and data traffic.

1. INTRODUCTION

The network that uses wires is known as a wired network. Initially the networks were mostly wired networks. When there is a use of wire in a network, definitely it also requires network adapters, routers, hubs, switches if there are more than two computers in a network. The installation of a wired network has been a big issue because the Ethernet cable should be connected to each and every computer that makes a network. Definitely this kind of connection takes time, in fact more time than expected, because when we connect wires with computers we have to take care of lot of things like wire should not come under the feet, it should be under ground or it should be under the carpet if computers are in more than one room. However in new homes nowadays, the wiring is being done in such a way that it will look like as it is a wireless connection, greatly simplifying the process of cables. Similarly the wiring of a wired network depends on lot of things like what kind of devices are being used in a wired network, whether the network is using external modem or is it internal, the type of internet connection and many other issues. As we know making a wired network is not an easy task, but still there are many other tasks that are more difficult than making a wired network, but we are not going to discuss these tasks here. In configuring the wired network, the hardware implementation is a main task. Once the hardware implementation is finished in a wired network, the remaining steps in a wired network do not differ so much from the steps in a wireless network. There are some advantages of wired network that include cost, reliability and performance. While making a wired network, Ethernet cable is the most reliable one because the makers of Ethernet cable continuously improving its technology and always produces a new Ethernet cable by removing the drawbacks of previous one. That is why Ethernet cable is the most preferable in making a wired network, as its reliability is kept on growing

from the past few years. In terms of performance, wired networks can provide good results. In the category of Ethernet, there is Fast Ethernet too, that provides enormous performance if a wired network is built in home for some features like data sharing, playing games and for the sake of high speed internet access. Still it is not false to say that Fast Ethernet can fulfill the need of network that is built in home for these kinds of purposes, till many years in future. Security in wired LANs can be a little problem because a network that is wired and is connected with internet must have firewall also in it, but unfortunately wired network does not have tendency to support firewalls, which is a big issue. However this problem can be solved by installing firewall software on each individual computer in a network.

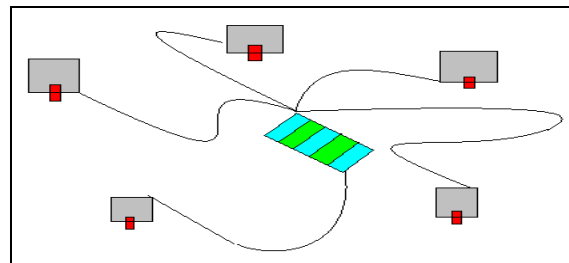


Figure 1 Wired Networks

The nodes of wired network does require power, as they get that power from the alternating current (AC) source that is present in that particular network.

1.1 Wireless Networks

On the other hand, wireless network is such kind of network that does not use wires to build a network. It uses radio waves to send data from one node to other node. Wireless networks lie under the category of telecommunications field. It is also known as wireless local area network (WLAN). It

uses the Wi-Fi as a standard of communication among different nodes or computers. There are three types of Wi-Fi communication standard.

802.11b

802.11a

802.11g

802.11b was the oldest standard that was being used in WLAN. After 802.11b, the standard being introduced was 802.11a. It offers better speed than previous one and is mostly used in business networks. The latest standard is 802.11g that removes the deficiencies of previous two standards. Since it offers best speed from other two standards, also it is the most expensive one.

The installation of this kind of network can be done by two ways. First one is ad-hoc mode and the second one is infrastructure mode. Ad-hoc mode allows wireless devices in a network to communicate on the logic of peer to peer with each other. However the second mode is the most required mode as it allows wireless devices in a network to communicate with a central device which in turn communicates with the devices that are connected with central device through wire. But both these modes have one similarity that they use wireless network adapters, termed as WLAN cards.

Wireless LAN costs more than the wired network as it requires wireless adapters, access points that makes it three or four times expensive than Ethernet cables, hubs/switches for wired network. Wireless network faces reliability problem also as compared to wired networks, because while installing the wireless network it may encounter the interference that can come from the household products like microwave ovens, cordless phone etc. Wi-Fi communication standard's performance is inversely proportional to the distance between the computers and the access points. Larger the distance between the computers and access point, smaller will be Wi-Fi performance and hence smaller will be performance of wireless network. Similarly, security wise it is less secure than the wired network because in wireless communication data is sent through the air and hence there are more chances that data can be intercepted.

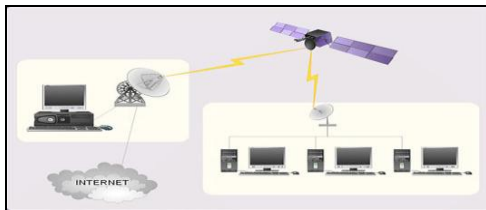


Figure 2 Wireless Networks

1.2 Advantages and Application of Ad-Hoc Networks

Ad hoc networks are wireless connections between two or more computers and/or wireless devices (such as a Wi-Fi enabled smart phone or tablet computer). A typical wireless network is based on a wireless router or access point that connects to the wired network and/or Internet. An ad hoc network bypasses the need for a router by connecting the

computers directly to each other using their wireless network adapters.

Router Free

Connecting to files on other computers and/or the Internet without the need for a wireless router is the main advantage of using an ad hoc network. Because of this, running an ad hoc network can be more affordable than a traditional network---you don't have the added cost of a router. However, if you only have one computer an ad hoc network won't be possible.

Mobility

Ad hoc networks can be created on the fly in nearly any situation where there are multiple wireless devices. For example: emergency situations in remote locations make a traditional network nearly impossible, but "The medical team can utilize 802.11 radio NICs in their laptops and PDAs and enable broadband wireless data communications as soon as they arrive on the scene."

Speed

Creating an ad hoc network from scratch requires a few settings changes and no additional hardware or software. If you need to connect multiple computers quickly and easily, then an ad hoc network is an ideal solution.

2. COMMON ROUTING IN MANETS

There is possibility of common protocols to be implemented in Mobile Ad-hoc networks. These protocols are commonly known as link state or distance vector kind of protocols. The major disadvantage of using these protocols in mobile Ad-hoc networks is that they are basically manipulated for static topology not for steady conditions in mobile Ad-hoc networks with great dynamic changing. Dynamic and Link state routing can be applied efficiently with low mobility. But these routing techniques depend on messages with periodic control. Thus it shows its static nature, when the number of nodes is large, the potential destination may also be large, which can create problem. The requirement of frequent and abrupt change of data within network increases. Therefore these routing techniques should be operated in low mobility scenarios. One of the attribute of these common protocols is that they are bidirectional, for instance the transfer of data will be in both the directions between two hosts or clients. As mobile Ad-hoc networks has their own conventional routing protocols, to understand the difficulties and problems for the usage of common protocols it is necessary to develop the concept of following terms .

2.1 Link State Routing

In this state, every node develops the consistency to analyze complete topology and show the cost of each link. For the persistence of costs, every node periodically spreads costs of output links to other nodes by using the process of flooding. Flooding is the process to transfer updated version of packets to all nodes within network without any obstacle. When the node gets the information, it upgrades the network

policy and utilize shortest path to select the next hop for every target i.e. the path that delivers the lowest cost. There may be some problems may arise to view the node due to long spreader delays, distributed networks, such undetermined network topology may result into loop formation, but these loops are temporary they are vanished when the message is transferred to network.

2.2 Distance Vector Routing

In this routing scheme, every node views the cost of outgoing link. It disseminates periodically information to its neighbors and helps out to find the shortest path to every other node in the network, instead of promulgating information to all the nodes. The information received by nodes estimate routing table again through shortest path algorithm. Distance vector routing is more reliable, feasible to implement and short storage space is required for this routing, but one of the drawback of distance vector is the creation of short and large routing loops. Due to these loops nodes have to select their next hops in full distributed way depends on the information that should be refreshed.

2.3 Source Routing

In case of source routing, every packet has complete route information to the target or destination. This phenomenon or technique has the ability to remove the presence of routing loops. As source determines the routing path and information about the packet which travels through specified route, this technique is called as source routing technique. Moreover the addition of overhead in this approach is actually the larger packets which contain complete path information .

2.4 Flooding

The basic phenomenon to distribute routing or control information by usage of spreading or disseminating method, in which source nodes have the responsibility to send packets to all nodes in the network. Flooding is basically the implementation of broadcast method in wireless scenario. The source node sends the information to all neighbor nodes in wireless network. The neighbor nodes then forward this information to the entire node within their approach. So in this way, all the packets spread or flood within entire network. The packets are sequenced in number form to avoid staling information and loops.

3. PROPOSED ACK-BASED SCHEME

Proposed Modified Ack-Based scheme for node authentication with AODV existing protocol in MANET. Ack-Based scheme also provide facility for the detection of wormhole attack and node misbehaviors in ad hoc network. Different researcher proposed different scheme for Ack_Based for providing security in mobile ad hoc network. But all technique suffered common problem that problem is generation of huge amount of pack overhead and node ambiguity. Due to this problem the given scheme is not used in generalize form. So we proposed the Ack-Based scheme with the help of finite state machine for controlling a

generation of packet and also improve performance of AODV protocol. Here first we discuss basic Ack-Based scheme and then we discuss finite state machine and finally we discuss combine approach for Ack-Based scheme.

ACK based scheme overcome the limitation of passive-feedback technique when power control transmission is used. To implement this scheme, an authentication mechanism is used to prevent the next hop from sending a forged Ack packet on behalf of the intended two hop neighbor. The main drawback of this scheme is the huge overhead. In order to reduce the overhead, the authors have proposed in that each node asks its two hop neighbor to send back an ACK randomly rather than continuously. Likewise, this extension also fails when the two hop neighbor refuses to send back an Ack. In such situation, the requester node is unable to distinguish who is the malicious node, its next hop or the requested node. To overcome the previous ambiguity in determining the true malicious node, focuses on detecting malicious links instead of malicious nodes. The authors propose the 2Ack scheme to detect malicious links and to mitigate their effects. This scheme is based on 2Ack packet that is assigned a fixed route of two hops in the opposite direction of the received data traffic's route. In this scheme, each packet's sender maintains the following parameters; (i) list of identifiers of data packets that have been sent out but have not been acknowledged yet, (ii) a counter of the forwarded data packets, (iii) and a counter of the missed packets. According to the value of the acknowledgement ratio (Rack), only a fraction of data packets will be acknowledged in order to reduce the incurred overhead. This technique overcomes some weaknesses of the Watchdog/path rater such as: ambiguous collisions, receiver collision and power control transmission. Both of the previous works remain vulnerable to the attacks launched by group of nodes. To counter these attacks, provides a framework to mitigate the damage caused by the colluding black hole attack in AODV. The proposed technique has a moderate overhead induced by the ACK sent back by the destination during selected intervals of data transfer period. Throughout the data packets transmission, a flow of special packets is transmitted at random intervals along with the data. The reception of these special packets invokes the destination to send out an ACK through multiple paths. The ACK packets take multiple routes to reduce the probability that all ACK s being dropped by the malicious nodes, and also to account for possible loss due to broken routes or congestion in certain nodes. If the source node does not receive any ACK packet, then it becomes aware of the presence of attackers in the forwarding path. As a reaction, it broadcasts a list of suspected malicious nodes to isolate them from the network

All the nodes running a solution based on acknowledgment need to maintain a timeout (To) value. This timeout represents an upper bound of the time that the sender node has to wait for the ACK to arrive. The determination of this timeout value is critical since a small value induces a large number of false accusations and a large value increases the memory required to store the outgoing packets for further comparisons. Figure (3) depicts an

example of the lower bound of the timeout value maintained by node A for the reception of two hops ACK from node C. The timeout value should be greater than the estimated threshold (Th) value which can be calculated as follows

$$Th = T_1 - T_2$$

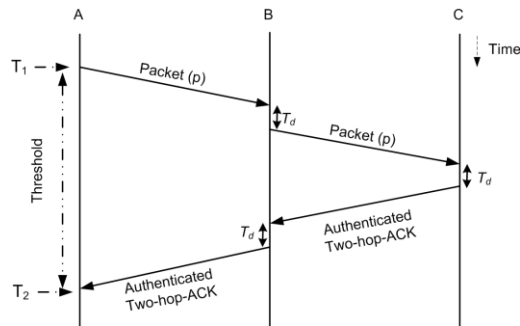


Figure 3: shows that state diagram of ack scheme

Where T_1 and T_2 are the sending (reception) time of the packet (Ack), respectively this threshold is estimated for a successful transmission at MAC layer without any retransmission, which is not a realistic assumption in MANETs, thus the timeout value should satisfy the following condition

$$T_o > T_h + (\text{avg } r_t \times \text{hop delay})$$

Where $AVG RT$ is the average number of retransmissions of a packet at MAC layer, and hop delay is the one hop transmission delay which includes packet transmission delay, random backoff delay at the MAC layer and the processing delay.

4. IMPLEMENTATION

The main code is implemented in aodv.cc and the functions are declared in aodv.h. In aodv_packet.h, the AODV message formats (RREQ, RREP, RERR and HELLO) are defined. Moreover the new message format FSAPAC (Finite state automata) has been added and defined in this file.

The main modifications have been done in aodv.cc.

- When a mobile node is to send a data packet to a destination, it tries to find a route to the destination (FSARt_resolve).
- If the mobile node does not have any valid route to the destination it broadcasts a RREQ message (send Request).
- The RREQ message is eventually received by the destination or another node which knows a route to the destination (recvRequest).
- The node sends a RREP/RREP_I message back to the originator of the RREQ (send Reply).
- The originator of the RREQ receives the RREP/RREP_I message (recvReply) and starts sending data packets to the destination (find_send_entry if the destination is a fixed node).

Simulation is run for 100 seconds of simulated time. 10 of the 25 mobile nodes are constant bit rate traffic sources.

They are distributed randomly within the mobile ad hoc network.

The time when the ten traffic sources start sending data packets is chosen uniformly distributed within the first ten seconds of the simulation. After this time the sources continue sending data until one second before the end of the simulation. The destination of each of the sources is one of the two hosts, chosen randomly.

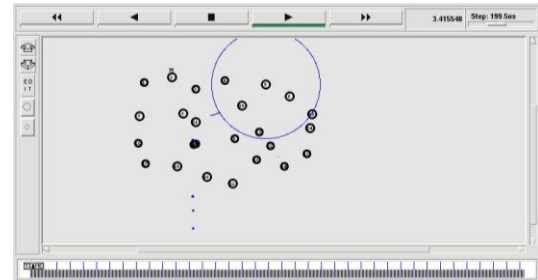


Figure 4: Simulation scenario of ACK-Based scheme on pause time 10 s

Figure 4 shows that the simulation scenario of ACK-Based scheme on pause time 10s that means node mobility starting on this time and flow of control packet started.

5. CONCLUSION AND FUTUREWORK

Without infrastructure and node mobility in adhoc network is a great challenge as concern to the security. For security concern various method are used for node authentication in mobile adhoc network. The authentication scheme of leader agent and member surveillance greatly reduces the relative calculating overheads and communication costs. Generally speaking, when leader agent node and surveillance nodes are not destroyed, the united nodes can ensure the reliability, the authentication result is reliable.

Suggestion of future work is to apply modified Ack-Based FSA add with other protocol to requirement of memory. During path discovery and path establishment it take much time in comparison of normal Ack-Based schemes in future minimized route calculation with finite state machine.

REFERENCES

- [1] Soufiene Djahel, Farid Na'it-abdesslam, and Zonghua Zhang "Mitigating Packet Dropping Problem in Mobile Ad Hoc Networks: Proposals and Challenges" in IEEE Communication and survey 2010.
- [2] S. Marti, T. J. Giuli, K. Lai and M. Baker, Mitigating routing misbehavior in mobile ad hoc networks, In Proc. 6th annual international conference on Mobile computing and networking (MOBICOM '00), Boston, Massachusetts, USA, August 2000
- [3] Y. C. Hu, A. Perrig and D. B. Johnson, Ariadne: A secure On-Demand Routing Protocol for Ad Hoc Networks, In Proc. 8th ACM International Conference on Mobile Computing and Networking, Westin

- Peachtree Plaza, Atlanta, Georgia, USA, September 2002.
- [4] D. Djenouri and N. Badache, New Approach for Selfish Nodes Detection in Mobile Ad hoc Networks, In Proc. Workshop of the 1st International Conference on Security and Privacy for Emerging Areas in Communication Networks (SecurComm'05), Athens, Greece, September 200
- [5] E. Gerhard's-Padilla, N. Aschenbruck, P. Martini, M. Jahnke and J. Tolle. Detecting Black Hole Attacks in Tactical MANETs using Topology Graphs, In Proc. of the 33rd IEEE Conference on Local Computer Networks (LCN), Dublin, Ireland, and October 2007.
- [6] Y. Zhang, W. Lou, W. Liu and Y. Fang, A secure incentive protocol for mobile ad hoc networks, Wireless Networks journal, 13(5): 569-582, October 2007.
- [7] S. Kurosawa, H. Nakayama, N. Kato, A. Jamalipour and Y. Nemoto, Detecting Blackhole Attack on AODV-based Mobile Ad Hoc Networks by Dynamic Learning Method, International Journal of Network Security, 5(3): 338-346, November 2007.
- [8] P. Agrawal, R. K. Ghosh and S. K. Das, Cooperative black and gray hole attacks in mobile ad hoc networks, In Proc. of the 2nd International Conference on Ubiquitous Information Management and Communication (ICUIMC 2008), SKKU, Suwon, Korea, Jan/Feb 2008.
- [9] M. Amitabh, Security and quality of service in ad hoc wireless networks, Cambridge University Press; 1st edition, March 2008.
- [10] Z. H. Zhang, F. Na'it-abdesselam, P. H. Ho and X. Lin, RADAR: a ReputAtion-based scheme for Detecting Anomalous nodes in wireless mesh networks, In Proc. IEEE Wireless Communications and Networking Conference (WCNC2008), Las Vegas, USA, March 2008.
- [11] B. Kannhavong, H. Nakamaya, Y. Nemoto, N. Kato and A. Jamalipour, SA-OLSR: Security Aware Optimized Link State Routing for Mobile Ad Hoc Networks, In Proc. International Conference of Communication (ICC 2008), Beijing, China, May 2008.
- [12] S. Djahel, F. Na'it-Abdesselam and A. Khokhar, An Acknowledgment- Based Scheme to Defend against Cooperative Black Hole Attacks in Optimized Link State Routing Protocol, In Proc. of the International Conference on Communication (ICC 2008), Beijing, China, May 2008.
- [13] Z. Li, C. Chigan and D. Wong, AWF-NA: A Complete Solution for Tampered Packet Detection in VANETs, In Proc. Global Communications Conference (IEEE GLOBECOM 08), New Orleans, LA, USA, NOV/DEC 2008
- [14] www.cs.montana.edu/webworks

Author Profile

Mustafa Sadeq Jaafar persuing Mtech from Information Technology Department at Bharati Vidyapeeth Deemed University College of Engineering, Dhankawadi, Pune India. His areas of interest are Software Engineering and networks .

Mr. H K Sawant is working as an Professor in Information Technology Department at Bharati Vidyapeeth Deemed University College of Engineering, Dhankawadi, Pune India. He was awarded his Master of Technology Degree from IIT Mumbai. He is persuing his PhD from JJTU. His areas of interest are Computer Network, Software Engineering and Multimedia System. He has nineteen years experience in teaching and research. He has published more than twenty research papers in journals and conferences. He has also guided ten postgraduate students.

Design, Fault Detection and Mitigation in Cascaded H-Bridge STATCOM

VAMSI MULPURI

M-Tech Student, Power Electronics & Electrical Drives,
Department Of Electrical And Electrical Engineering,
Koneru Lakshmaiah University(A.P)

B.KRISHNAVENI

Assistant Prof, Power systems,
Department Of Electrical & Electrical Engineering,
Koneru Lakshmaiah University(A.P)

Abstract-The concept of multilevel inverters, introduced about 20 years ago entails performing power conversion in multiple voltage steps to obtain improved power quality, lower switching losses, better electromagnetic compatibility, and higher voltage capability. The benefits are especially clear for medium-voltage drives in industrial applications and are being considered for future naval ship propulsion systems. This dissertation is dedicated to a comprehensive study of static synchronous compensator (STATCOM) systems utilizing cascaded-multilevel converters (CMCs). Among flexible AC transmission system (FACTS) controllers, the STATCOM has shown feasibility in terms of cost effectiveness in a wide range of problem-solving abilities from transmission to distribution levels. Referring to the literature reviews, the CMC with separated DC capacitors is clearly the most feasible topology for use as a power converter in the STATCOM applications. The controls for the CMC-based STATCOM were, however, very complicated. The intricate control design was begun without well-defined system transfer functions. The control compensators were, therefore, randomly selected. The stability of the system was achieved by trial and error processes, which were time-consuming and ineffective. To be able to operate in a high-voltage application, a large number of DC capacitors are utilized in a CMC-based STATCOM. All DC capacitor voltages must be balanced in order to avoid over-voltages on any particular link. Not only do these uneven DC voltages introduce voltage stress on the semiconductor switches, but they also lower the quality of the synthesized output waveforms of the converter. A SIMULINK based model is developed and Simulation results are presented.

Keywords-Cascaded H-Bridge, Multilevel Converter, PWM

I. INTRODUCTION

With the advancement of power electronics and emergence of new multilevel converter topologies, it is possible to work at voltage levels beyond the classic semiconductor limits. The multilevel converters achieve high-voltage switching by means of a series of voltage steps, each of which lies within the ratings of the individual power devices. Among the multilevel Converters [1-4], the cascaded H-bridge topology (CHB) is particularly attractive in high-voltage applications, because it requires the least number of components to synthesize the same number of voltage levels.

Additionally, due to its modular structure, the hardware implementation is rather simple and the maintenance operation is easier than alternative multilevel converters. The multilevel voltage source inverter is recently applied in many

industrial applications such as ac power supplies, static VAR compensators, drive systems, etc. One of the significant advantages of multilevel configuration is the harmonic reduction in the output waveform without increasing switching frequency or decreasing the inverter power output [5-11]. The output voltage waveform of a multilevel inverter is composed of the number of levels of voltages, typically obtained from capacitor voltage sources. The so-called multilevel starts from three levels. As the number of levels reach infinity, the output THD approaches zero. The number of the achievable voltage levels, however, is limited by voltage unbalance problems, voltage clamping requirement, circuit layout, and packaging constraints.

As higher level converters are used for high output rating power applications, a large number of power switching devices will be used. Each of these devices is a potential failure point. Therefore, it is important to design a sophisticated control to produce a fault-tolerant STATCOM. A faulty power cell in a cascaded H-Bridge STATCOM can potentially cause switch modules to explode [10] leading to the fault conditions such as a short circuit or an overvoltage on the power system resulting in an expensive down time [11]. Subsequently, it is crucial to identify the existence and location of the fault for it to be removed. Several fault detection methods have been proposed over the last few years [10]-[18]. Resistor sensing, current transformation, and V_{CE} sensing are some of the more common approaches. For example, a method based on the output current behavior is used to identify IGBT short circuits [12]. The primary drawback with the proposed approach is that the fault detection time depends on the time constant of the load. Therefore, for loads with a large RL time constant, the faulty power cell can go undetected for numerous cycles, potentially leading to circuit damage. Another fault detection approach proposed in [13] is based on a switching frequency analysis of the output phase voltage. This method was applied to flying capacitor converters and has not been extended to cascaded converters. AI-based methods proposed to extract pertinent signal features to detect faults in [14]. In [15], sensors are used to measure each IGBT current and to initiate switching if a fault is detected. A fault-tolerant neutral point-clamped converter was proposed in [16]. In [17], a reconfiguration system based on bidirectional switches has been designed for three-phase asymmetric cascaded H-bridge inverters. The fundamental output voltage phase shifts are used to rebalance a faulted multilevel cascaded converter in [18].

In this paper, the method we propose requires only that the output dc link voltage of each phase be measured. This measurement is typically accomplished anyway for control purposes. If a fault is detected, the module in which the fault occurred is then isolated and removed from service. This approach is consistent with the modular design of cascaded converters in which the cells are designed to be interchangeable and rapidly removed and replaced. Until the module is replaced, the multilevel STATCOM continues to operate with slightly decreased, but still acceptable, performance. In summary, this approach offers the following advantages:

- No additional sensing requirements;
- Additional hardware is limited to two by-pass switches per module;
- Is consistent with the modular approach of cascaded multilevel inverter; and
- The dynamic performance and THD of the STATCOM is not significantly impacted.

II. PROPOSED NOVEL CONVERTER

III. DESIGN OF MULTILEVEL BASED STATCOM

A. Principle of STATCOM

A STATCOM, which is schematically depicted in Figure-1, consists of a two-level VSC, a dc energy storage device, a coupling transformer connected in shunt to the DS. The VSC converts the dc voltage across the storage device into a set of three-phase ac output voltages. These voltages are in phase and coupled with the ac system through the reactance of the coupling transformer. Suitable adjustment of the phase and magnitude of the STATCOM output voltages allows effective control of active and reactive power exchanges between the STATCOM and the ac system. Such configuration allows the device to absorb or generate controllable active and reactive power.

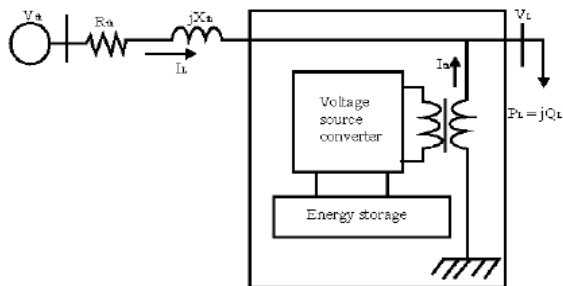


Figure –1 Schematic Diagram of a STATCOM

Here, such device is employed to provide continuous voltage regulation using an indirectly controlled converter. As shown in Figure-1 the shunt injected current I_{sh} corrects the voltage sag by adjusting the voltage drop across the system impedance Z_{th} . The value of I_{sh} can be controlled by adjusting the output voltage of the converter. The shunt injected current I_{sh} can be written as,

$$I_{sh} = I_L - I_S = I_L - (V_{th} - V_L) / Z_{th} \tag{1}$$

$$I_{sh} / _ \eta = I_L / _ - \theta \tag{2}$$

The complex power injection of the STATCOM can be expressed as,

$$S_{sh} = V_L I_{sh}^* \tag{3}$$

B. Control for Reactive Power Compensation

The main aim of the control scheme is to maintain constant voltage magnitude at the load point. The control system only measures the rms voltage at the load point, i.e., no reactive power measurements are required.

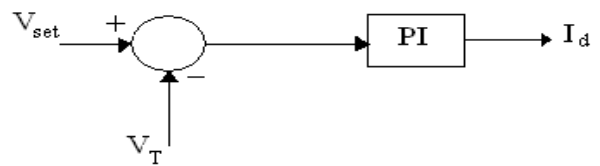


Figure-2 PI control for reactive power compensation

The controller input is an error signal obtained from the reference voltage and the rms terminal voltage measured. Such error is processed by a PI controller; the output is the I_d , which is provided to the PWM signal generator as shown in figure-2. The PI controller processes the error signal and generates the required active power component to drive the error to zero, i.e. the load rms voltage is brought back to the reference voltage.

C. Control for Harmonics Compensation

The Modified SRFT method is presented in [7]. It is called the instantaneous current component (i_d - i_q) method. This is similar to the SRFT method. The transformation angle ' θ ' is now obtained with the voltages of the ac network. The major difference is that, due to voltage harmonics and imbalance, the speed of the reference frame is no longer constant. It varies instantaneously depending of the waveform of the three phase voltage system. In this method the compensating currents are obtained from the instantaneous active and reactive current components of the nonlinear load. In the same way, the mains voltages $V_{(a,b,c)}$ and the available currents $i_{(a,b,c)}$ in α - β components must be calculated as given by (4), where C is Clarke Transformation Matrix. However, the load current components are derived from a SRF based on the Park transformation, where ' θ ' represents the instantaneous voltage vector angle (5).

$$\begin{bmatrix} I_{l\alpha} \\ I_{l\beta} \end{bmatrix} = [C] \begin{bmatrix} I_{la} \\ I_{lb} \\ I_{lc} \end{bmatrix} \tag{4}$$

$$\begin{bmatrix} I_{ld} \\ I_{lq} \end{bmatrix} = \begin{bmatrix} \cos\theta & \sin\theta \\ -\sin\theta & \cos\theta \end{bmatrix} \begin{bmatrix} I_{l\alpha} \\ I_{l\beta} \end{bmatrix}, \theta = \tan^{-1} \frac{V_{\beta}}{V_{\alpha}} \tag{5}$$

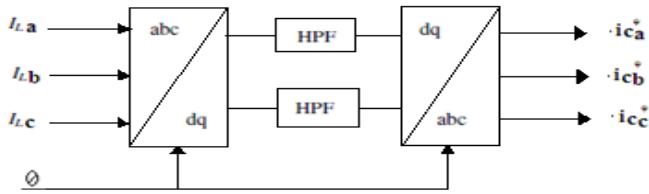


Figure-3 Block diagram of SRF method

Fig-3 shows the block diagram SRF method. Under balanced and sinusoidal voltage conditions angle θ is a uniformly increasing function of time. This transformation angle is sensitive to voltage harmonics and unbalance; therefore $d\theta/dt$ may not be constant over a period. With transformation given below the direct voltage component is

$$\begin{bmatrix} i_{ld} \\ i_{lq} \end{bmatrix} = \frac{1}{\sqrt{V_\alpha^2 + V_\beta^2}} \begin{bmatrix} V_\alpha & V_\beta \\ -V_\beta & V_\alpha \end{bmatrix} \quad (6)$$

$$\begin{bmatrix} i_{ca} \\ i_{cb} \end{bmatrix} = \frac{1}{\sqrt{V_\alpha^2 + V_\beta^2}} \begin{bmatrix} V_\alpha & -V_\beta \\ V_\beta & V_\alpha \end{bmatrix} \begin{bmatrix} i_{cd} \\ i_{cq} \end{bmatrix} \quad (7)$$

$$\begin{bmatrix} I_{Comp,a} \\ I_{Comp,b} \\ I_{Comp,c} \end{bmatrix} = [C]^T \begin{bmatrix} i_{ca} \\ i_{cb} \end{bmatrix} \quad (8)$$

D. Cascaded H-Bridge Multilevel Inverter

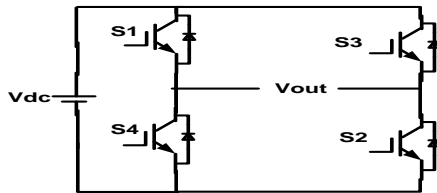


Figure-4 Circuit of the single cascaded H-Bridge Inverter

Fig.4 shows the circuit model of a single CHB inverter configuration. By using single H-Bridge we can get 3 voltage levels. The number of output voltage levels of CHB is given by $2n+1$ and voltage step of each level is given by $V_{dc}/2n$, where n is number of H-bridges connected in cascaded. The switching sequence is given in Table-I.

E. PWM Techniques for CHB Inverter

The most popular PWM techniques used for CHB inverter are 1. Phase Shifted Carrier PWM (PSCPWM), 2. Level Shifted Carrier PWM (LSCPWM)

Case-1:- Phase Shifted Carrier PWM (PSCPWM)

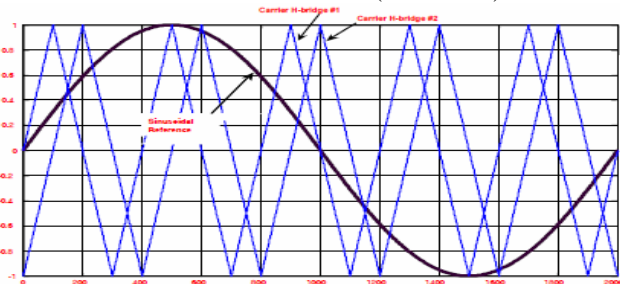


Fig-5 phase shifted carrier PWM

Figure-5 shows the PSCPWM. In general, a multilevel inverter with m voltage levels requires $(m-1)$ triangular carriers. In the PSCPWM, all the triangular carriers have the same frequency and the same peak-to-peak amplitude, but there is a phase shift between any two adjacent carrier waves, given by $\phi_{cr} = 360^\circ / (m-1)$. The modulating signal is usually a three-phase sinusoidal wave with adjustable amplitude and frequency. The gate signals are generated by comparing the modulating wave with the carrier waves. It means for five-level inverter, four triangular carriers are needed with a 90° phase displacement between any two adjacent carriers. In this case the phase displacement of $V_{cr1} = 0^\circ$, $V_{cr2} = 90^\circ$, $V_{cr3} = 180^\circ$ and $V_{cr4} = 270^\circ$.

Case-2:- Level Shifted Carrier PWM (LSCPWM)

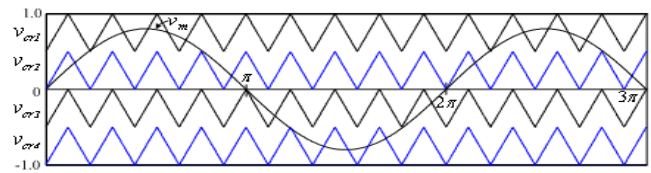


Figure-6 Level shifted carrier PWM (IPD)

Figure-6 shows the LSCPWM. The frequency modulation index is given by $m_f = f_{cr} / f_m$, (34)

where f_m is modulating frequency and f_{cr} are carrier waves frequency. The amplitude modulation index ' m_a ' is defined by $m_a = V_m / V_{cr}$ for $0 \leq m_a \leq 1$ (35)

Where V_m is the peak value of the modulating wave and V_{cr} is the peak value of the each carrier wave [1]. The amplitude modulation index, m_a is 1 and the frequency modulation index, m_f is 6. The triggering circuit is designed based on the three phase sinusoidal modulation waves V_a , V_b , and V_c . The sources have been obtained with same amplitude and frequency but displaced 120° out of the phase with each others. For carriers signals, the time values of each carrier waves are set to $[0 \ 1/600 \ 1/300]$ while the outputs values are set according to the disposition of carrier waves. After comparing, the output signals of comparator are transmitted to the IGBTs. Figures 9, 10 and 11 show the waveforms based on three schemes of LSCPWM: (a) in phase disposition (IPD) fig-9, where all carriers are in phase; (b) alternative phase opposite disposition (APOD) fig-10, where all carriers are alternatively in opposite disposition; and (c) phase opposite disposition (POD) fig-11, where all carriers above zero reference are in phase but in opposition with those below the zero reference [1]. Out of IPD, APOD and POD; the authors studied that, IPD give better harmonic performance.

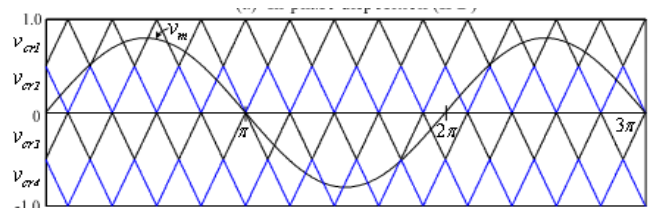


Fig. 7 Alternative phase opposite disposition (APOD)

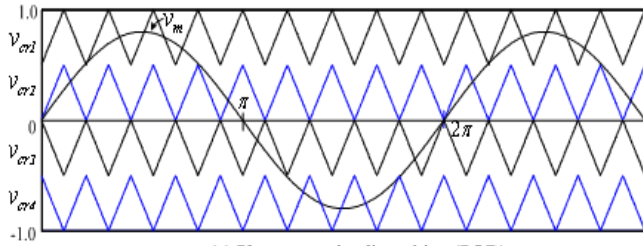


Fig.8phase opposite disposition (POD)

IV. DESIGN OF SINGLE H-BRIDGE CELL

A Device Current

The IGBT and DIODE currents can be obtained from the load current by multiplying with the corresponding duty cycles. Duty cycle, $d = \frac{1}{2}(1 + K \sin \omega t)$

Where, m = modulation index $K = +1$ for IGBT, -1 for Diode.

$$i_{ph} = \sqrt{2}I \sin(\omega t - \phi)$$

Where i = RMS value of the load (output) current,
 ϕ = Phase angle between load voltage and current.
 Then the device current can be written as follows.

$$\therefore i_{device} = \frac{\sqrt{2}}{2}I \sin(\omega t - \phi) * (1 + km \sin \omega t)$$

The average value of the device current over a cycle is calculated as

$$i_{avg} = \frac{1}{2\pi} \int_{\phi}^{\pi+\phi} \frac{\sqrt{2}}{2}I \sin(\omega t - \phi) * (1 + km \sin \omega t) d\omega t$$

$$= \sqrt{2}I \left[\frac{1}{2\pi} + \frac{Km}{8} \cos \phi \right]$$

The device RMS current can be written as

$$i_{rms} = \sqrt{\int_{\phi}^{\pi+\phi} \frac{1}{2\pi} (\sqrt{2}I \sin(\omega t - \phi))^2 * \frac{1}{2} * ((1 + km \sin \omega t))^2 d\omega t}$$

$$= \sqrt{2}I \sqrt{\left[\frac{1}{8} + \frac{Km}{3\pi} \cos \phi \right]}$$

B IGBT Loss Calculation

IGBT loss can be calculated by the sum of switching loss and conduction loss. Where conduction loss can be calculated by,

$$P_{on(IGBT)} = V_{ceo} * I_{avg(igbt)} + I_{rms(igbt)}^2 * r_{ceo}$$

$$I_{avg(igbt)} = \sqrt{2}I \left[\frac{1}{2\pi} + \frac{m}{8} \cos \phi \right]$$

$$I_{rms(igbt)} = \sqrt{2}I \sqrt{\left[\frac{1}{8} + \frac{m}{3\pi} \cos \phi \right]}$$

Values of V_{ceo} and r_{ceo} at any junction temperature can be obtained from the output characteristics (I_c vs. V_{ce}) of the IGBT as shown in Fig .9.

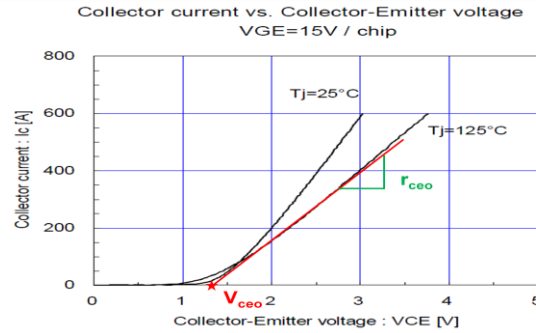


Figure9 IGBT output characteristics

The switching losses are the sum of all turn-on and turn-off energies at the switching events

$$E_{sw} = E_{on} + E_{off} = a + bI + cI^2$$

Assuming the linear dependence, switching energy $E_{sw} =$

$$(a + bI + cI^2) * \frac{V_{DC}}{V_{nom}}$$

Here V_{DC} is the actual DC-Link voltage and V_{nom} is the DC-Link Voltage at which E_{sw} is given. Switching losses are calculated by summing up the switching energies.

$$P_{sw} = \frac{1}{T_o} \sum_n E_{sw} (i)$$

Here ‘n’ depends on the switching frequency.

$$P_{sw} = \frac{1}{T_o} \sum_n (a + bI + cI^2)$$

$$= \frac{1}{T_o} \left[\frac{a}{2} + \frac{bI}{\pi} + \frac{cI^2}{4} \right]$$

After considering the DC-Link voltage variations switching losses of the IGBT can be written as follows.

$$P_{sw(IGBT)} = f_{sw} \left[\frac{a}{2} + \frac{bI}{\pi} + \frac{cI^2}{4} \right] * \frac{V_{DC}}{V_{nom}}$$

So, the sum of conduction and switching losses gives the total losses.

$$P_{T(IGBT)} = P_{on(IGBT)} + P_{sw(IGBT)}$$

C Diode Loss Calculation

The DIODE switching losses consists of its reverse recovery losses and the turn-on losses are negligible.

$$E_{rec} = a + bI + cI^2$$

$$P_{sw(DIODE)} = f_{sw} \left[\frac{a}{2} + \frac{bI}{\pi} + \frac{cI^2}{4} \right] * \frac{V_{DC}}{V_{nom}}$$

So, the sum of conduction and switching losses gives the total DIODE losses.

$$P_{T(DIODE)} = P_{on(DIODE)} + P_{sw(DIODE)}$$

The total loss per one switch (IGBT+DIODE) is the sum of one IGBT and DIODE loss.

$$P_T = P_{T(IGBT)} + P_{T(DIODE)}$$

D. Thermal Calculations

The junction temperatures of the IGBT and DIODE are calculated based on the device power losses and thermal resistances. The thermal resistance equivalent circuit for a module is shown in Fig 5. In this design the thermal calculations are started with heat sink temperature as the reference temperature. So, the case temperature from the model can be written as follows.

$$T_c = P_T R_{th(c-h)} + T_h$$

Here $R_{th(c-h)}$ = Thermal resistance between case and heat sink

P_T = Total Power Loss (IGBT+DIODE)

IGBT junction temperature is the sum of the case temperature and temperature raise due to the power losses in the IGBT.

$$T_{j(IGBT)} = P_{T(IGBT)} R_{th(j-c)IGBT} + T_c$$

DIODE junction temperature is the sum of the case temperature and temperature raise due to the power losses in the DIODE.

$$T_{j(DIODE)} = P_{T(DIODE)} R_{th(j-c)DIODE} + T_c$$

The above calculations are done based on the average power losses computed over a cycle. So, the corresponding thermal calculation gives the average junction temperatures. In order to make the calculated values close to the actual values, transient temperature values are to be added to the average junction temperatures.

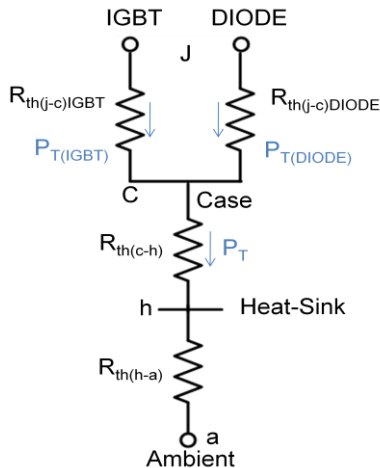


Figure. 10 Thermal resistance equivalent circuit

A. DC-Capacitor Selection

The required capacitance for each cell depends on the allowable ripple voltage and the load current. The rms ripple current flowing into the capacitor can be written as follows and the ripple current frequency is double the load current frequency (Novel Hybrid H-Bridge).

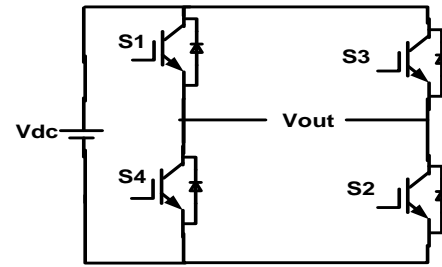


Fig. 11 H-Bridge converter

$$I_c = -\frac{I}{V_{dc}} \frac{1}{2} (|U_{ac}| * K + I\omega L) \sin(2\omega t)$$

Since the value of ‘L’ is very small, the above equation can be written as below.

$$I_c = -\frac{I}{V_{dc}} \frac{1}{2} (|U_{ac}| * K) \sin(2\omega t)$$

$$I_c = -K \frac{1}{2} \frac{|U_{ac}|}{V_{dc}} * \sin(2\omega t)$$

$$= -K \frac{m}{2} \sin(2\omega t)$$

Here ‘m’ is the modulation index.

Here $I_{cp} = C \frac{du_{pp}}{dt}$

$$\frac{m}{2} I \sqrt{2} = C 2\omega * \Delta V V_{dc}$$

$$C = \frac{m}{4\omega} \frac{1}{\Delta V V_{dc}} \sqrt{2} I$$

V. MATLAB/SIMULINK MODELING AND SIMULATION RESULTS

Figure-12 shows the Matab/Simulink power circuit model of DSTATCOM. The system parameters chosen are source voltage (V_s) as 11kv, 50Hz AC supply, DC bus capacitance 1550 μ F, Inverter series inductance 10mH, Source resistance of 0.1 Ω and inductance of 0.9mH. Nonlinear loads with resistance and inductance are chosen as 30mH and 60 Ω respectively.

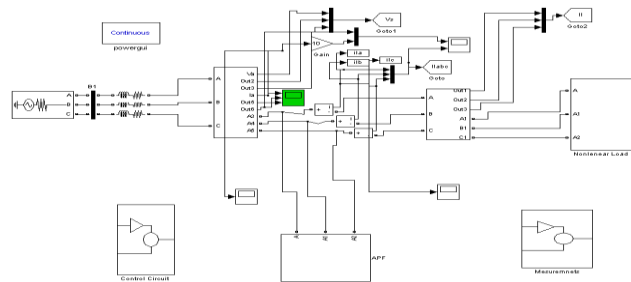


Fig-12 Matlab/Simulink power circuit model of DSTATCOM

Case-1 STATCOM without Fault in Gate Driver

Fig. 13 shows the phase-A voltage of five level output of phase shifted carrier PWM inverter.

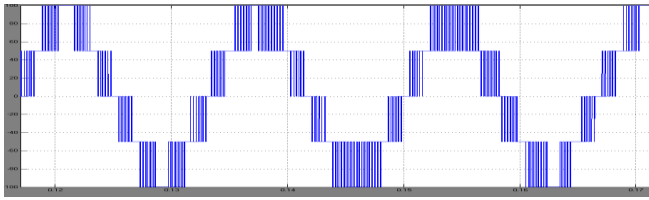


Fig. 13 five-level PSCPWM output

Fig. 14 shows the three phase source voltages, three phase source currents and load currents respectively without DSTATCOM. It is clear that without DSTATCOM load current and source currents are same.

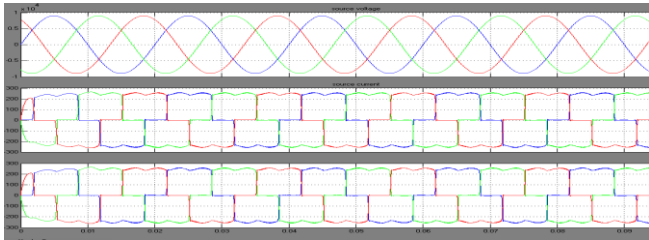


Fig. 14 Source voltage, current and load current without DSTATCOM

Fig. 15 shows the three phase source voltages, three phase source currents and load currents respectively with DSTATCOM. It is clear that with DSTATCOM even though load current is non sinusoidal, source currents are sinusoidal.

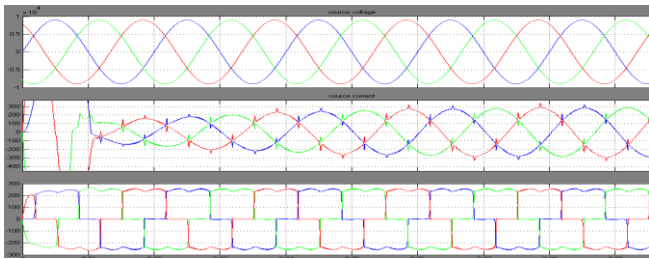


Fig. 15 Source voltage, current and load current with DSTATCOM

Fig. 16 shows the DC bus voltage is regulated to 11kv by using PI regulator.

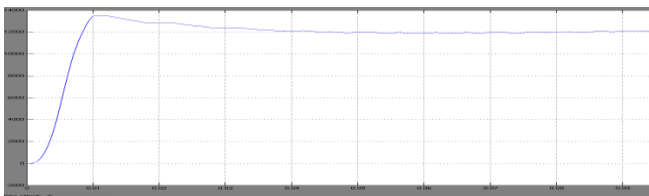


Fig. 16 DC Bus Voltage for PSCPWM

Fig. 17 shows the phase-A source voltage and current, even though the load is non linear RL load the source power factor is unity.

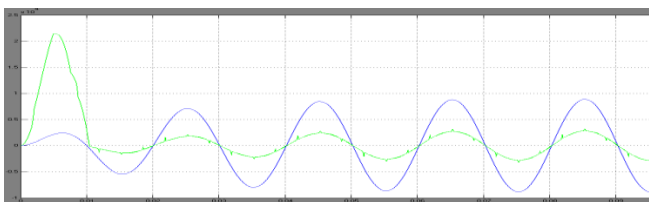


Fig. 17 Phase-A source voltage and current

Fig. 18 shows the harmonic spectrum of Phase –A Source current without DSTATCOM. The THD of source current without DSTATCOM is 36.89%.

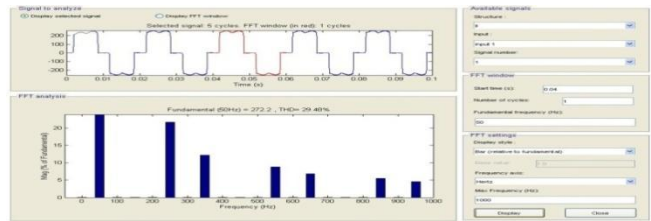


Fig. 18 Harmonic spectrum of Phase-A Source current without DSTATCOM

Fig. 19 shows the harmonic spectrum of Phase –A Source current with DSTATCOM. The THD of source current with DSTATCOM is 5.05%.

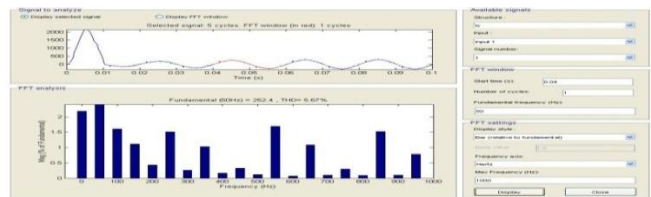


Fig. 19 Harmonic spectrum of Phase-A Source current with DSTATCOM

Case-2 STATCOM with Fault in Gate Driver

Fig. 20 shows the phase-A voltage of five level output of phase shifted carrier PWM inverter with fault in the gate driver. The fault is applied between 0.1 and 0.2 sec. Here one voltage level is missing during the period of fault.

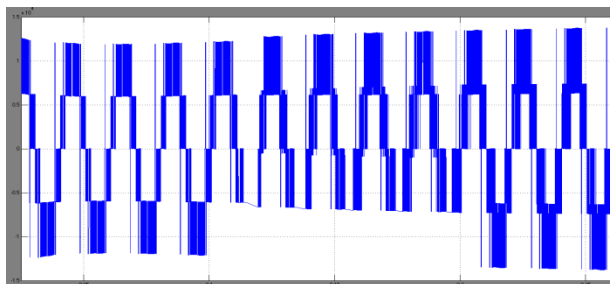


Fig.20 output waveform with fault

Figure 21 shows the filtered waveform by using the filter. The fall in the voltage is clearly observed during the fault.

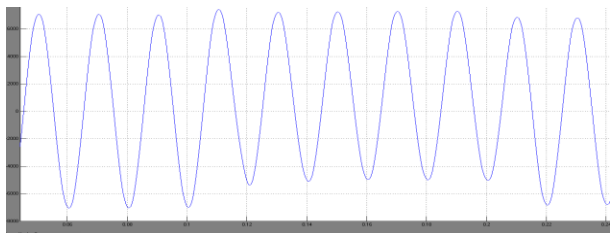


Fig.21 Filtered waveform

Fig 22 shows the dc capacitor voltage which clearly shows the fall in voltage during the fault and regain after mitigation.

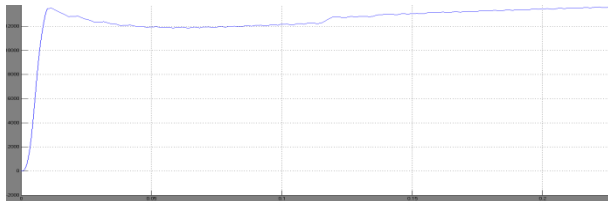


Fig:22 DC capacitor voltage

Fig 23 shows the source voltage, source current and load current before, during and after the fault.

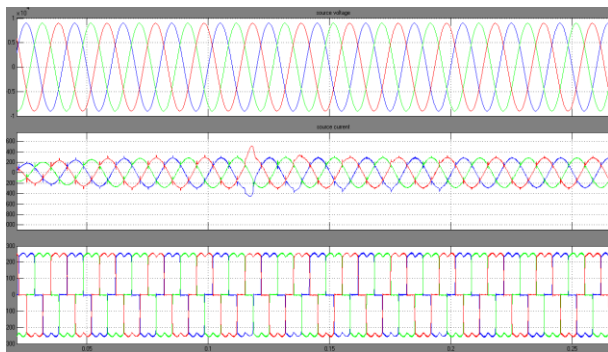


Fig:23. Source voltage, sourcecurrent, load current before, during and after fault

VI. CONCLUSION

This paper presents Novel Hybrid H-Bridge multilevel converter. The proposed converter produces more voltage levels with less number of switches compared to H-bridge configuration. This will reduce number of gate drivers and protection circuits which in turn reduces the cost and complexity of the circuit. In this paper, the design procedure for single cell based on cost and losses optimization is carried out. The selection of a single cell is based on SSOA (safe operating Area) and Thermal Rating .The selection of capacitor and heat sink is also carried out. A SIMULINK based model is developed and Simulation results are presented.The total harmonic distortion is also calculated.THd before fault is 0.64%,THd during fault is 1.28% and THd after the fault is 0.64%.

VII. REFERENCES

- [1] J. S. Lai and F. Z. Peng, "Multilevel converters – A new breed of power converters", *IEEE Trans. Ind. Appl.*, V32, No. 3, pp. 509-517, May/June, 1996.
- [2] José Rodríguez, Jih-Sheng Lai, FangZhengPeng "Multilevel Inverters: A Survey of Topologies, Controls, and Applications" *IEEE Trans. Ind. App.*, VOL. 49, NO. 4, August 2002.
- [3] K.A Corzine, and Y.L Familant, "A New Cascaded Multi-level H-Bridge Drive," *IEEE Trans. Power.Electron.*, vol.17, no.1, pp.125-131. Jan 2002.
- [5] Manjrekar, M. D., Lipo, T. A. "A hybrid multilevel inverter topology for drive applications". in Proc. of APEC, 1998, p. 523–529.
- [6] R. Schnell, U. Schlapbach, "Realistic benchmarking of IGBT – modules with the help of a fast and easy to use simulation tool".

- [7] Jean-Philippe Hasler, "DC Capacitor Sizing for SVC Light Industrial Application".
- [8] G.Carrara, S.Gardella, M.Marchesoni, R.salutari,and G.scitutto, "A New Multilevel PWM Method; A theoretical analysis," *IEEE Trans. Power.Electron.*, vol.7, no.3, pp.497-505. Jul.1992.
- [9] L.M.Tolber, T.G.Habetler, "Novel Multilevel inverter Carrier based PWM Method," *IEEE Ind.Appli.*, vol.35. pp.1098-1107. Sep/Oct 1999.
- [10] Holmes, D. G. and Lipo, T. A., Pulse width modulation for power converters: principles and practice, IEEE.
- [11] V. Dinavahi, R. Irvani, and R. Bonert, "Design of a real-time digital simulator for a D-STATCOM system," *IEEE Trans. Ind. Electron.*, vol. 51,no. 5, pp. 1001–1008, Oct. 2004.
- [12] B. Singh, S. Murthy, and S. Gupta, "STATCOM-based voltage regulator for self-excited induction generator feeding nonlinear loads," *IEEE Trans. Ind. Electron.*, vol. 53, no. 5, pp. 1437–1452, Oct. 2006.
- [13] D. Soto and T. C. Green, "A comparison of high-power converter topologies for the implementation of FACTS controllers," *IEEE Trans. Ind.Electron.*, vol. 49, no. 5, pp. 1072–1080, Oct. 2002.
- [14] S. Khomfoi and L. Tolbert, "Fault diagnosis and reconfiguration for multilevel inverter drive using AI-based techniques," *IEEE Trans. Ind. Electron.*, vol. 54, no. 6, pp. 2954–2968, Dec. 2007.
- [15] M. Ma, L. Hu, A. Chen, and X. He, "Reconfiguration of carrier-based modulation strategy for fault tolerant multilevel inverters," *IEEE Trans. Power Electron.*, vol. 22, no. 5, pp. 2050–2060, Sep. 2007.
- [16] S. Ceballos, J. Pou, E. Robles, I. Gabiola, J. Zaragoza, J. L. Villate, and D. Boroyevich, "Three-level converter topologies with switch breakdown fault-tolerance capability," *IEEE Trans. Ind. Electron.*, vol. 55, no. 3,pp. 982–995, Mar. 2008.

Authors Profile



M.VAMSI is currently pursuing M.Tech (power electronics and drives), in K L University, Andhra Pradesh. He completed his b.tech in Electrical And Electronics Engineering at Sri Sunflower College Of Engineering And Technology in 2010. His areas of interest are Power Electronics, Multilevel inverters, FACT devices.



Mrs.B.KRISHNAVENI is currently working as assistant professor in electrical and electronics engineering department at K L University (A.P). She completed her M.Tech (power systems) in 2009 at Koneru Lakshmaiah College Of Engineering. she received B.E in 2003 from LBRCE. Her research areas include FACT devices, Power systems.

Pondering of Fundamental Search Methods and Protocols for Unstructured Peer To Peer NETWORKS

Shanmukha Babu.kotha¹, Anilkumar.talasila², Venkata vara Prasad.padyala³, Sahitya.Kandimalla⁴

¹PG Scholar, CSE, K L University , Andhrapradesh, India,

²PG Scholar, CSE, K L University, Andhrapradesh, India,

³Assit.Professor, CSE, K L University, Andhrapradesh, India,

⁴Assit Professor, CSE RVR&JC college of engineering and technology, AP,India,

Abstract

Designing proficient search algorithms is a major aspect in unstructured peer-to-peer networks, because Search algorithms offer the capabilities to trace the queried resources and to route the message to the target node. Different techniques can be used to trace resources on the network. If the network is small, no intricate search techniques are needed. We can use simple broadcasting or multicasting for querying. Centralized systems with a small number of servers also do not have need of intricate query propagation techniques. However, if we want to sustain intricate queries in decentralized networks, such as unstructured P2P overlays, complicated search techniques have to be applied to query propagation to attain scalability. In this paper, we discuss the most general search algorithms and example protocols that make use of these methods and hence we illustrate the importance of search algorithms in unstructured P2P networks.

Index Terms: Search algorithm, peer-to-peer, Unstructured networks.

1 INTRODUCTION

Peer-to-peer networks are widely used for file sharing purposes. This type of usage tends to favor resilient, decentralized architectures over centralized solutions. However this comes at a penalty in ease of searching. At first, peer-to-peer systems addressed this shortcoming by incorporating a flooding mechanism for resource discovery. A node in the peer-to-peer network broadcasts a query message to its neighbours. The neighbors in turn are responsible for reporting any matches as well as forwarding the message to its neighbors, if necessary. This mechanism has been proven effective in practice for finding items which are prevalent across the peer-to-peer network, but otherwise ineffective and resource consuming. Previous works about search algorithms in unstructured P2P networks can be classified into two categories: breadth first search (BFS)-based methods, and depth first search (DFS)-based methods. These two types of search algorithms tend to be inefficient, either generating too much load on the system [1], [2], or not meeting users' requirements [3]. Flooding, which belongs to BFS-based methods, is the default search algorithm for Gnutella network [4], [5]. By this method, the query source sends its query messages to all of its neighbors. When a node receives a query message, it first checks if it has the queried resource. If yes, it sends a response back to the query source to indicate a query hit. Otherwise, it sends the query messages to all of its neighbors, except for the one the query message comes from. The drawback of flooding is the search cost. It

produces considerable query messages even when the resource distribution is scarce. On the other hand, random walk (RW) is a conservative search algorithm, which belongs to DFS-based methods [6], [7], [8], [9], [10]. By RW, the query source just sends one query message (walker) to one of its neighbors. If this neighbor does not own the queried resource, it keeps on sending the walker to one of its neighbors, except for the one the query message comes from, and thus, the search cost is reduced.

Different techniques can be used to discover resources on the network. If the network is small no complex search techniques are needed. One can use simple broadcasting or multicasting for querying. Centralized systems with few servers also do not require complex query propagation methods. However, if we want to support complex or free-form queries in decentralized networks, such as unstructured P2P overlays, sophisticated search techniques have to be applied to query propagation to achieve scalability and efficient operation. Below we give an overview of the most common search algorithms and example protocols that utilize these methods. Search in a graph is defined as finding a path from a start node to a destination node. In our context the destination node is the node that contains the service searched. The cost of a search can be defined in various ways, for example as the number of edges traversed in locating the destination node or the number of packets sent into the network during the search process. A simple scenario of P2P network is shown in Fig.1.

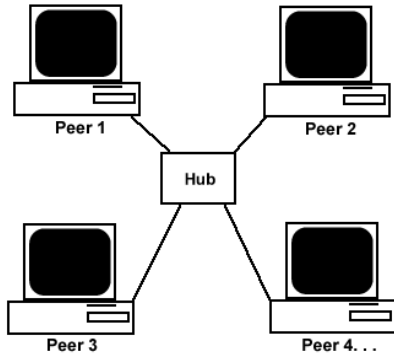


Fig. 1 P2P network

In the next section we will thrash out fundamental search methods in unstructured peer-to-peer networks.

2. BASIC SEARCH METHODS AND PROTOCOLS FOR UNSTRUCTURED NETWORKS

The search algorithms are classified into uninformed [11], where sending nodes know nothing of the surrounding networks, and informed [12] that rely on the partial network information discovered previously. Informed and probabilistic methods significantly reduce the overhead in the system, but they suffer from the partial coverage problem, in extreme cases showing very poor performance.

2.1 Uninformed search methods and related protocols

Uninformed search methods [11] can be further divided into systematic and random search algorithms. Systematic search methods typically explore the searched tree or graph according to some predefined rules. There is no place for probabilistic or random choice in such methods. Often systematic methods conduct a complete or almost complete search of the studied graph. The theoretical evaluation of the considered uninformed systematic search methods is given in Table 1, where the notation established in [13] is used: b is the branching factor; d is the depth of the shallowest solution; m is the maximum depth of the search tree; l is the depth limit. Superscript caveats are used as follows: a complete if b is finite; b complete if step costs $\geq \epsilon$ for positive ϵ ; c is optimal if step costs are all identical; d is optimal if both directions use breadth-first search.

TABLE 1

Evaluation of Uninformed Systematic Search Methods [11]

Criterion \ Name	Breadth-first	Depth-first	Depth-limited	Iterative-deepening	Uniform cost
Complete?	Yes ^a	No	No	Yes ^a	Yes ^{a,b}
Time	$O(b^{d+1})$	$O(b^m)$	$O(b^l)$	$O(b^d)$	$O(b^{l+1} \lceil C/\epsilon \rceil)$
Space	$O(b^{d+1})$	$O(bm)$	$O(bl)$	$O(bd)$	$O(b^{l+1} \lceil C/\epsilon \rceil)$
Optimal	Yes ^c	No	No	Yes ^c	Yes

A. Breadth-first search and flooding: The most well known search algorithms in this category are Breadth-first (BFS) and Depth-first (DFS) searches. BFS first explores all neighboring nodes of the sender and, if the solution is not found, proceeds to explore all the two-hop neighbors. The depth of the search is further increased until either a solution is found or all nodes of the network have been searched. Flooding [14], [15] is one of the basic search protocols. Its foundation lies on the BFS search algorithm. The query is propagated to all nodes in the network. The number of query packets typically increases exponentially further the query travels from the source node, causing huge overhead. The basic solution is to introduce a time-to-live field that limits the query propagation to a certain hop depth.

B. Depth-first search, related methods and protocols: Depth-first search explores one neighbor of the sender. If solution is not found it increases the depth of the search, i.e. explores one neighbor of the previously searched node. The search continues in depth: each new node searched is situated at the increased hop distance from the requester. If maximum depth is reached than the search path is traced back until it can branch and go again in depth. Depth-limited search is a special case of the depth-first search, where only nodes with depth less than some bound are considered. Famous time-to-live (TTL) field is means for implementing this principle. Iterative deepening depth-first repeatedly applies the depth-limited search. In each iteration the maximum search depth is increased and the search is re-run. During the iteration BFS algorithm is applied.

C. Uniform-cost search: The search starts with a root node and all the neighboring nodes are explored. The neighbor connected to the root node with the lowest path cost link is chosen. Then all possible neighbors of the nodes, that already were chosen, are searched again and the node with the lowest path cost is preferred. The process continues until the searched object is found. Uniform cost is always optimal (since at any stage the cheapest solution is chosen). Dijkstra's algorithm is an example of uniform cost search.

D. Random search methods and protocols: These methods are governed by random variables. Good performance is expected, but not guaranteed by these algorithms. The random walk is one of popular random search methods [12]. This strategy is a formalization of the intuitive idea of taking successive steps, each in a random direction. A random walk is a simple stochastic process. The mathematical properties of random walks are quite well known for a long time, one of the celebrated examples being the Brownian motion. Random Walk (RW) protocol implements the random walk search technique described above. It is one of the basic and most widely used networks protocols. Its properties are discussed in detail by Q. Lv et al. in [15]. The source node sends a query to a fixed number of neighboring nodes.

The number of query replicas does not increase with the hop distance. The method allows in many cases

considerably reduce the overhead imposed on the network with a tradeoff of the reduction in hit rate, increased round-trip time, and highly variable performance.

Probabilistic forwarding [16] is another of the random search methods. For each node where the query might be forwarded a random number in range [0, 1] is generated. If this number exceeds a threshold then the node is searched, otherwise it is skipped.

Probabilistic Flooding protocol [17] is based on flooding, but the query replicas are forwarded here only to a certain percentage (p) of the node's neighbors. Normal flooding is an extreme case of the probabilistic flooding with $p = 1$. If $p = 0$ then the query is, of course, not propagated anywhere. Probabilistic flooding is one of the often proposed techniques to be used in large dense wireless networks. There the propagation via standard flooding, besides leading to huge overhead, also increases the collision rate and leads to the degradation of the network performance. Careful choice, maybe even an adaptive adjustment, of the probability of further packet propagation leads to a drastic increase in the protocol efficiency and at the same time keeps high the probability of the packet delivery to the destination. Use of this method in sparse networks is not justified, as there the sufficient probability of the packet delivery cannot be ensured.

Gossip-based protocols [18] are based on probabilistic flooding. A node forwards a message to a certain number of its neighbors if it believes that they have not already received a certain amount of the message replicas. The protocol is especially suited to the large-scale distributed systems with limited mobility and high node failure level, i.e., when the connection between nodes rarely change, but the nodes themselves are often unavailable.

2.2 Informed search methods

Informed search methods [12] make extensive use of heuristics. A heuristic is a method that does not guarantee the solution found to be optimal, but usually finds an acceptably good solution in a reasonable time.

Best-first search goes through a list of possible nodes to explore and chooses the most promising ones to be explored first. Heuristic is used to rank the neighboring nodes based on the estimated cost from the current node to the solution. There are several variations of this algorithm. Greedy search algorithm chooses the node that appears to be closest to the goal node from the current node. The algorithm makes the locally optimal choice at each stage with the hope of finding the global optimum. Beam search is similar to the best-first search, however it unfolds not one, but the first m most promising nodes at each depth.

A* search falls into the category of best-first searches. The algorithm takes into account both the cost from the root node to the current node (function $g(n)$) and estimates the path cost from the current node (function $h(n)$). Function $F(n) = g(n) + h(n)$ represents the path cost of the most efficient estimated path towards the goal and is

continuously re-evaluated while the search runs in order to arrive at the minimal cost to the goal. A* is monotonic, it is complete and optimal on graphs that are locally finite and where the heuristics are admissible and monotonic.

Backtracking, falling in the class of constraint searches is used to find solutions to problems specified by a set of constraint variables. Backtracking in the worst case tries all possible combinations in order to obtain a solution. The method's strength is that many implementations avoid trying many partial combinations, thus speeding up the running-time. The term "backtrack" was coined by American mathematician D. H. Lehmer in the 1950s [19].

Hill climbing falls in the class of Iterative improvement methods. The method extends the search path with a node which brings the path closer to the solution than it was before attaching the node. Two major modifications of the algorithm are used. In simple hill climbing the first node that brings the user closer to the solution is chosen. In steepest ascent hill climbing all possible nodes are compared and the closest to the solution successor is chosen. Finding of only local maximum (in the case that heuristic is not good enough) is the main problem with hill climbing. Several methods exist to overcome this drawback, including iterated hill climbing, stochastic hill climbing, random walks, and simulated annealing.

Lately, simulated annealing, a generic probabilistic meta-heuristic for global optimization problems, was tried successfully as a possible search algorithm for unstructured P2P networks [20], [21]. With this algorithm a fair approximation to the global optimum of a given function in a large search space can be achieved. Simulated annealing allows the system to move consistently toward lower energy states, yet still jump out of local minima due to the probabilistic acceptance of some upward moves during the first few iterations.

Tabu search is a local search algorithm that uses memory structures, tabu-lists, forbidding the use of certain values of attributes in the search. Tabu lists containing the prohibited values are very effective, though a very good solution that just happens to have this value might be missed. To overcome this problem aspiration criteria are introduced. They allow overriding the tabu state of a solution and including the solution in the allowed set.

Ant colony optimization [22] is a meta-heuristic inspired by the behavior of ants in finding paths from the colony to food sources. It uses many ants (or agents) to traverse the solution space and find locally productive areas. The strategy usually does not perform as well as simulated annealing and other forms of local search, but it can solve tasks where no global or up-to-date perspective can be obtained, and therefore the other, in general more effective methods cannot be applied. Ant colony optimization outperforms simulated annealing, tabu search and genetic algorithms in dynamic environments, as it can adapt continuously to the changes in real time.

Genetic algorithms [23] try to solve problems using techniques inspired by biological evolutionary mechanisms, such as yielding successive generations of possible solutions using reproduction, "survival of the fittest" and mutation methods. In genetic programming, the above approach is extended to algorithms, by regarding the algorithm itself as a "possible solution" to a problem. The genetic algorithm approach is used in Immune Search [24].

Neural search algorithms are based on the use of artificial neural networks (ANN) [25], that imitate the structure of the brain. Artificial neurons, modeling brain cells, are interconnected with each other to form a network using both forward and feedback links. The links connecting the neurons can have different weights, possibly changing during the run-time, thus producing an adaptive system. Based on these elements ANN creates a mapping between inputs and outputs, either deterministically or probabilistically. Neural search algorithms are widely used for speech and image recognition systems, pattern matching and search engines.

3. PROTOCOLS BASED ON INFORMED SEARCH ALGORITHMS

We now consider several search protocols that are based on informed algorithms. Most of them utilize the best-first approach. Many protocols are also using history-based metrics, to determine the destination or the next forwarding node.

Intelligent-BFS [26] and Directed-BFS [27] are informed versions of probabilistic flooding. The neighbors to which the query is to be forwarded are chosen judging from the success rate of the neighboring nodes for the queries of the same type. The answer packet, while traveling to the source node, updates the local indices on the bypassing nodes, increasing the probability that these nodes will forward these types of queries in the future. Hybrid flooding [28] is a further development of this approach. The algorithm uses probabilistic flooding to forward the query only to a subset of the current node's neighbors. Multiple weighted metrics are used to select these neighbors.

Degree-based random walk was first proposed by Adamic et al. in 2001 [29]. The algorithm is based on random walk and it issues a number of walkers (queries) that are forwarded to the highest-degree neighbors that have not seen the query. The neighbor connectivity is learned via the exchange of "Hello" messages. The algorithm shows a very good performance for power-law random networks when resources are concentrated in the high-degree nodes. However, if resources are not concentrated in the most-connected nodes, then the heuristic fails and can even perform worse than the basic random walk.

Distributed resource location [30] protocol makes nodes to listen listens to the bypass traffic and cache the information from the relevant search-related packets: the locations of the answer to the query as well as the description of the resource. Later, if the node receives a query searching for the resource the location of which is cached, then the query

is forwarded directly to the relevant node, thus saving network resources and time. This technique is aimed for large and fairly static networks, where the initial discovery-caused overhead is compensated by saving in later requests. In a very dynamic network due to the outdated of the cached information the effectiveness of the method drastically decreases. The method exhibits increasing accuracy as the object popularity drops, as the less popular objects are less likely to be reallocated.

Adaptive probabilistic search (APS) [31] uses k random walkers and tracing messages to update supplementary information on nodes. The method employs distributed resource location mechanism. To choose the direction of packet forwarding a combination of probabilistic forwarding, historic learning and best-first technique is used. The supplementary information on the nodes is updated using both positive and negative feedback. The nodes estimate using the history of previous requests the direction for the query to travel. However, a non-zero probability exists that a packet will be send to non-best fitting neighbor, thus enabling the protocol to explore new routes. A single entry is kept for each type of the resource for precise targeting. Compared to random walk, APS is rather a bandwidth efficient protocol and with additional adaptive techniques used [31] it achieves much higher hit rates. It is said that APS does suffer from partial coverage problem due to the use of random walk and informed propagation techniques. Routing Indices [32], Query Routing Protocol [33], [34] and Local Indices [36], [35] are examples of other protocols that extensively use metadata to exchange information between nodes.

Local Minima Search [37] is another search algorithm for unstructured networks based on greedy search and local minimum. It is somewhat similar to the mechanism used in DHT-based systems and suffers from the same inability to conduct complex searches. Each item is assigned a key, for example via hashing. Replicas of the (key, value) pair are propagated through the network looking for the local minimum between the key and the node ID. At the local minimum the replica is stored. The propagation method is a combination of random walk and greedy deterministic forwarding; this way the wide spread of the (key, value) pairs is ensured. The query for the item is propagated in the same fashion: first the key corresponding to the searched item is determined and then the search is started using random walk followed by the deterministic forwarding. Additional methods are employed by the protocol to improve its performance, such as dynamic adjustment of the number of replicas or use of bloom filters.

Immune search method as well as Genetic routing [38] falls into the class of protocols based on genetic algorithms. The protocol consists of two parts: query propagation through the network and the topology evolution initiated as a result of search. The originating node issues a query that is forwarded to its neighbors via random walk until the packet arrives to a node where similarity metric between the information profile and the message content exceeds the

threshold. Then the message packet undergoes proliferation (more messages are issued) in order to be able to find more nodes with similar information in the neighborhood. Some of the proliferated packets are also mutated. Due to mutation the chance of message packets to meet similar items increases, which in turn helps in packet proliferation. Clustering is introduced in the system to bring similar node together. The distance a node moves towards the query originating node depends on the similarity between them, their distance and the number of times (age) the node moved before.

NeuroSearch [39] makes use of neural search algorithms and correspondingly neural networks to decide to which neighbor to forward the query. The decision whether to propagate a query to a certain neighbor is based on the output neuron of three layer perceptron neural network. Each neighbor is evaluated using seven parameters, such as was the neighbor connectivity or acknowledgment of the fact that a certain message was received before. Prior to the deployment the protocol needs to be trained on test networks to adjust neural network weights. A genetic algorithm is used during the training. With current array of input parameters the protocol performs well compared to flooding with low TTL on the network built after power-law distribution. The authors in [39] expect considerable performance improvement with introduction of history-based inputs.

3.1 Common exchange metrics

Nodes employing informed search methods exchange different types of information in order to predict the location of the searched resource. The examples of these metrics are a list of known services and their location, topology information, traffic load, power capacity, computational resources, communication channel quality, available bandwidth, historical feedback (e.g. number of successful queries forwarded) and node uptime. For the latter parameter it is generally assumed [40] that the longer the node stays without failure in the network the higher the chances are that it will be connected to the network in the future. In the next section we discuss a dynamic search algorithm [41] for unstructured P2P networks.

4. DYNAMIC SEARCH ALGORITHM [41]

Designing efficient search algorithms is a key challenge in unstructured peer-to-peer networks. Flooding and random walk (RW) are two typical search algorithms. Flooding searches aggressively and covers the most nodes. However, it generates a large amount of query messages and, thus, does not scale. On the contrary, RW searches conservatively. It only generates a fixed amount of query messages at each hop but would take longer search time. We discuss the dynamic search (DS) algorithm, which is a generalization of flooding and RW. DS takes advantage of various contexts under which each previous search algorithm performs well. It resembles flooding for short-term search and RW for long-term search. Moreover, DS

could be further combined with knowledge-based search mechanisms to improve the search performance.

4.1 Operation of Dynamic Search Algorithm

```

Algorithm: The pseudo-code of dynamic search DS
Input: query source  $s$ , queried resource  $f$ , transmission probability  $p$ 
Output: the location information of  $f$ 
DS( $s, f, p$ )
/* the operation of  $s$  */
 $h \leftarrow 0$ 
if ( $h \leq n$ )
     $h \leftarrow h + 1$ 
     $s$  choose  $p$  portion of its neighbors
     $m_i$  carrying  $h$  visits these chosen neighbors
elseif ( $h > n$ )
     $h \leftarrow h + 1$ 
     $m_i$  carrying  $h$  visits one neighbor of  $s$ 
/* the operation of  $r$  */
foreach ( $r$ )
    if ( $r$  has the location information of  $f$ )
         $r$  returns the information to  $s$ 
         $m_i$  stops
    elseif ( $h > TTL$ )
         $m_i$  stops
    elseif ( $h \leq n$ )
         $h \leftarrow h + 1$ 
         $r$  choose  $p$  portion of its neighbors
         $m_i$  carrying  $h$  visits these chosen neighbors
    elseif ( $h > n$ )
         $h \leftarrow h + 1$ 
         $m_i$  carrying  $h$  visits one neighbor of  $r$ 

```

Fig. 2 The DS Algorithm [41]

DS is designed as a generalization of flooding, MBFS, and RW. There are two phases in DS. Each phase has a different searching strategy. The choice of search strategy at each phase depends on the relationship between the hop count h of query messages and the decision threshold n of DS.

1) Phase 1. When $h \leq n$

At this phase, DS acts as flooding or MBFS. The number of neighbors that a query source sends the query messages to depends on the predefined transmission probability p . If the link degree of this query source is d , it would only send the query messages to $d \cdot p$ neighbors. When p is equal to 1, DS resembles flooding. Otherwise, it operates as MBFS with the transmission probability p .

2) Phase 2. When $h > n$

At this phase, the search strategy switches to RW. Each node that receives the query message would send the query message to one of its neighbors if it does not have the queried resource. The pseudo code is shown in Figure 2.

5. CONCLUSION

In this paper we have explicated Fundamental search methods and protocols for unstructured peer-to-peer network, hence the importance of these algorithms and the need of dynamic algorithm. Next, we have discussed the DS algorithm, which is a generalization of the flooding, MBFS, and RW. DS overcomes the disadvantages of flooding and RW, and takes advantage of various contexts under which each search algorithm performs well. It resembles flooding or MBFS for the short-term search and RW for the long-term search. Finally, we conclude that this work may be useful to design a new algorithm or to modify the existing algorithms for better performance.

ACKNOWLEDGEMENTS

We like to express our gratitude to all those who gave us the possibility to carry out the paper. We would like to thank Mr.K.Satyanarayana, chancellor of K.L.University, Dr.K.Raja Sekhara Rao, Dean, and K.L.University for stimulating suggestions and encouragement. We have further more to thank Prof.S.Venkateswarlu, Dr.K.Subrahmanyam, who encouraged us to go ahead with this paper.

REFERENCES

- [1] K. Sripanidkulchai, The Popularity of Gnutella Queries and Its Implications on Scalability, white paper, Carnegie Mellon Univ.,Feb. 2001.
- [2] M. Jovanovic, F. Annexstein, and K. Berman, "Scalability Issues in Large Peer-to-Peer Networks: A Case Study of Gnutella," technical report, Laboratory for Networks and Applied Graph Theory, Univ. of Cincinnati, 2001.
- [3] B. Yang and H. Garcia-Molina, "Improving Search in Peer-to-Peer Networks," Proc. 22nd Int'l Conf. Distributed Computing Systems(ICDCS '02), pp. 5-14, July 2002.
- [4] G. Kan, "Gnutella," Peer-to-Peer Harnessing the Power of Disruptive Technologies, O'Reilly, pp. 94-122, 2001.
- [5] RFC-Gnutella 0.6, <http://rfc-gnutella.sourceforge.net/developer/testing/index.html>, 2008.
- [6] C. Gkantsidis, M. Mihail, and A. Saberi, "Random Walks in Peer-to-Peer Networks," Proc. IEEE INFOCOM '04, pp. 120-130, 2004.
- [7] L.A. Adamic, R.M. Lukose, A.R. Puniyani, and B.A. Huberman, "Search in Power-Law Networks," Physical Rev., E, vol. 64, 046135, 2001.
- [8] L.A. Adamic, R.M. Lukose, and B.A. Huberman, "Local Search in Unstructured Networks," Handbook of Graphs and Networks. pp. 295-317, Wiley-VCH, 2003.
- [9] C. Gkantsidis, M. Mihail, and A. Saberi, "Hybrid Search Schemes for Unstructured Peer-to-Peer Networks," Proc. IEEE INFOCOM '05, pp. 1526-1537, 2005.
- [10] N. Bisnik and A. Abouzeid, "Modeling and Analysis of Random Walk Search Algorithm in P2P Networks," Proc. Second Int'l Workshop Hot Topics in Peer-to-Peer Systems (HOT-P2P '05), pp. 95-103, 2005.
- [11] S. Russel and P. Norvig, Artificial Intelligence A Modern Approach, 2nd ed. Upper Saddle River, New Jersey 07458, USA: Pearson Education, 2003, pp. 73-81.
- [12] ———, Artificial Intelligence A Modern Approach, 2nd ed. Upper Saddle river, New Jersey 07458, USA: Pearson Education, 2003, pp. 95-136.
- [13] M. Handley, H. Schulzrinne, E. Schooler, and J. Rosenberg, "SIP: Session Initiation Protocol," Request for Comments, vol. 2543, March 1999.
- [14] D. Tsoumakos and N. Roussopoulos, "A Comparison of Peer-to-Peer Search Methods," in Proceedings of the WebDB'03, June 2003, pp. 61-66, San Diego, USA.
- [15] Q. Lv, P. Cao, E. Cohen, K. Li, and S. Shenker, "Search and Replication in Unstructured Peer-to-Peer Networks," in Proceedings of the 16th ACM International Conference on Supercomputing (ICS), June 2002, pp. 84-95, New York, USA
- [16] K. Birman, M. Hayden, O. Ozkasap, Z. Xiao, M. Budiu, and Y. Minsky, "Bimodal multicast," ACM Transactions on Computer Systems (TOCS), vol. 17, no. 2, pp. 41-88, 1999.
- [17] V. Kalogeraki, D. Gunopulos, and D. Zeinalipour-Yazti, "A local search mechanism for peer-to-peer networks," in Proceedings of the 11th International Conference on Information and Knowledge Management, McLean, VA, USA, November 2002, pp. 300-307.
- [18] A. Ganesh, A. Kermarrec, and L. Massoulie, "Peer-to-peer membership management for gossip-based protocols," IEEE Transactions on Computers, vol. 52, no. 2, pp. 139-149, February 2003.
- [19] S. Golomb and L. Baumert, "Backtrack programming," Journal of the ACM (JACM), vol. 12, no. 4, pp. 516-524, October 1965.
- [20] S. Kirkpatrick, C. Gelatt Jr, and M. Vecchi, "Optimization by Simulated Annealing," Science, vol. 220, no. 4598, p. 671, 1983.
- [21] C. C. H. Wang, T. Lin and Y. Shen, "Dynamic Search in Peer-to-Peer Networks," in Proceedings of the 13th international World Wide Web Conference, May 2003, pp. 332-333, New York, USA.
- [22] M. Dorigo, Ant Colony Optimization. MIT Press, 2004.
- [23] J. Koza, Genetic programming: on the programming of computers by means of natural selection. Cambridge, Mass. : MIT Press, December 1992.
- [24] A. D. N. Ganguly, G. Canright, "Design Of An Efficient Search Algorithm For P2P Networks Using Concepts From Natural Immune Systems," in Proceedings of the 8th International Conference on Parallel Problem Solving from Nature, September 2004, pp. 491-500, Birmingham, UK.
- [25] S. Haykin, Neural Networks: A Comprehensive Foundation, 2nd ed., M. Horton, Ed. Prentice Hall International, Inc., 1999.

- [26] I. Clarke, "Freenet home page." <http://www.freenetproject.org/>, [last visited on 02.07.2007].
- [27] B. Yang and H. Garcia-Molina, "Improving search in peer-to-peer networks," in Proceedings of 22nd International Conference on Distributed Computing Systems (ICDCS), Vienna, Austria, July 2002, pp. 5-14.
- [28] L. X. Z. Zhuang, Y. Liu and L. Ni, "Hybrid Periodical Flooding in Unstructured Peer-to-Peer Networks," in Proceedings of the International Conference on Parallel Processing (ICPP 03), April 2003, pp. 171-178, Kaohsiung, Taiwan.
- [29] L. A. Adamic, R. M. Lukose, A. R. Puniyani, and B. A. Huberman, "Search in power-law networks," Physical Review, vol. 64, no. 4, pp. 46135-46 143, Sep 2001.
- [30] D. Menascé and L. Kanchanapalli, "Probabilistic scalable p2p resource location services," in Proceedings of the ACM SIGMETRICS Performance Evaluation Review, vol. 30, no. 2, Marina del Rey, CA, USA, September 2002, pp. 48-58
- [31] N. R. D. Tsoumakos, "Adaptive Probabilistic Search (APS) for Peer- to-Peer Networks," in Proceedings of the International Conference on Parallel Processing (ICPP 03), Linkoping, Sweden, September 2003.
- [32] A. Crespo and H. Garcia-Molina, "Routing indices for peer-to-peer systems," in Proceedings of the The 22nd International Conference on Distributed Computing Systems (ICDCS), Vienna, Austria, July 2002.
- [33] M. W. G. Sakaryan and H. Unger, "Search Methods in P2P Networks: a Survey," in Proceedings of the Innovative Internet Community Systems (I2CS 2004), June 2003, Guadalajara, Mexico.
- [34] C. Rohrs, "Query routing for Gnutella network," May 2002, http://www.limewire.com/developer/query_routing/keyword%20routing.htm [last time visited on 15.02.2008].
- [35] B. Yang and H. Garcia-Molina, "Improving Search in Peer-to-Peer Networks," in Proceedings of the 22nd International Conference on Distributed Systems, Vienna, Austria, July 2002, p. 5.
- [36] S. Helal, N. Desai, and V. Verma, "Konark-a service discovery and delivery protocol for ad-hoc networks," in Proceedings of the Third IEEE Conference on Wireless Communication Networks (WCNC), vol. 3, 2003, NOT FINISHED.
- [37] R. Morselli, B. Bhattacharjee, M. Marsh, and A. Srinivaran, "Efficient Lookup on Unstructured Topologies," IEEE Journal on selected areas in communications, vol. 25, no. 1, pp. 62-72, January 2007.
- [38] M. Iles and D. Deugo, "A Search for Routing Strategies in a Peer-to- Peer Network Using Genetic Programming," in Proceedings of the 21st IEEE Symposium on Reliable Distributed Systems (SRDS'02), Suita, Japan, October 2002, p. 341.
- [39] M. Vapa, N. Kotilainen, A. Auvinen, H. Kainulainen, and J. Vuori, "Resource Discovery in P2P Networks Using Evolutionary Neural Networks," in Proceedings of the AISTA, November 2004, Luxembourg
- [40] Z. Zhuang, Y. Liu, and L. Xiao, "Dynamic layer management in super-peer architectures," in Proceedings of the 2004 international Conference on Parallel Processing (ICPP 04), Montreal, Quebec, Canada, August 2004.
- [41] Tsungnan Lin, Pochiang Lin, Hsinping Wang, and Chiahung Chen," Dynamic Search Algorithm in Unstructured Peer-to-Peer Networks " IEEE TRANSACTIONS ON PARALLEL AND DISTRIBUTED SYSTEMS, VOL. 20, NO. 5, MAY 2009



Shanmukhababu.kotha, presently I am doing M tech in department computer science and engineering in K L University.



Anilkumar.talasila, presently I am doing M tech in department computer science and engineering in K L University.



P.V V Prasad, presently working as a assistant professor in department computer science and engineering in K L University.

Fuzzy Soft Matrix Theory And Its Decision Making

Manash Jyoti Borah¹, Tridiv Jyoti Neog², Dusmanta Kumar Sut³

¹Deptt. of Mathematics, Bahona College, Jorhat, Assam, India

²Deptt. of Mathematics, D.K. High School, Jorhat, Assam, India

³Deptt. of Mathematics, N.N.Saikia College, Titabor, Assam, India

ABSTRACT

The purpose of this paper is to put forward the notion of fuzzy soft matrix theory and some basic results. Finally we have put forward a decision making problem using the notion of product of fuzzy soft matrices.

Keywords – Fuzzy set, Soft set, Fuzzy soft set, Fuzzy soft matrix.

1. INTRODUCTION

In order to deal with many complicated problems in the fields of engineering, social science, economics, medical science etc involving uncertainties, classical methods are found to be inadequate in recent times. Molodtsov [1] pointed out that the important existing theories viz. Probability Theory, Fuzzy Set Theory, Intuitionistic Fuzzy Set Theory, Rough Set Theory etc. which can be considered as mathematical tools for dealing with uncertainties, have their own difficulties. He further pointed out that the reason for these difficulties is, possibly, the inadequacy of the parameterization tool of the theory. In 1999 he proposed a new mathematical tool for dealing with uncertainties which is free of the difficulties present in these theories. He introduced the novel concept of Soft Sets and established the fundamental results of the new theory. He also showed how Soft Set Theory is free from parameterization inadequacy syndrome of Fuzzy Set Theory, Rough Set Theory, Probability Theory etc. Many of the established paradigms appear as special cases of Soft Set Theory. In 2003, P.K.Maji, R.Biswas and A.R.Roy [2] studied the theory of soft sets initiated by Molodtsov. They defined equality of two soft sets, subset and super set of a soft set, complement of a soft set, null soft set, and absolute soft set with examples. Soft binary operations like AND, OR and also the operations of union, intersection were also defined. In 2005, Pei and Miao [3] and Chen et al. [4] improved the work of Maji et al. [2]. In 2008, M.Irfan Ali, Feng Feng, Xiaoyan Liu, Won Keun Min, M.Shabir [5] gave some new notions such as the restricted intersection, the restricted union, the restricted difference and the extended intersection of two soft sets along with a new notion of complement of a soft set.

In recent times, researches have contributed a lot towards fuzzification of Soft Set Theory. Maji et al. [6] introduced some properties regarding fuzzy soft union, intersection, complement of a fuzzy soft set, DeMorgan Law etc. These results were further revised and improved by Ahmad and Kharal [7]. They defined arbitrary fuzzy soft union and intersection and proved De Morgan Inclusions and De Morgan Laws in Fuzzy Soft Set Theory. In 2011, Neog and Sut [8] put forward some more propositions regarding fuzzy soft set theory. They studied the notions of fuzzy soft union, fuzzy soft intersection, complement of a fuzzy soft set and

several other properties of fuzzy soft sets along with examples and proofs of certain results.

Matrices play an important role in the broad area of science and engineering. However, the classical matrix theory sometimes fails to solve the problems involving uncertainties, occurring in an imprecise environment. In [9], Yong Yang and Chenli Ji initiated a matrix representation of a fuzzy soft set and successfully applied the proposed notion of fuzzy soft matrix in certain decision making problems. In this paper, we extend the notion of fuzzy soft matrices put forward in [9]. In our work, we are taking fuzzy soft sets with different set of parameters whereas in [9], notion of fuzzy soft matrix was put forward considering a single set of parameters, which is not the case in actual practice. Throughout our work, we are using t - norm and t - conorm as intersection and union, respectively, of fuzzy sets.

2. PRELIMINARIES

Definition 2.1 [1]

A pair (F, E) is called a soft set (over U) if and only if F is a mapping of E into the set of all subsets of the set U .

In other words, the soft set is a parameterized family of subsets of the set U . Every set $F(\varepsilon), \varepsilon \in E$, from this family may be considered as the set of ε - elements of the soft set (F, E) , or as the set of ε - approximate elements of the soft set.

Definition 2.2 [6]

A pair (F, A) is called a fuzzy soft set over U where $F : A \rightarrow \tilde{P}(U)$ is a mapping from A into $\tilde{P}(U)$.

Definition 2.3 [7]

Let U be a universe and E a set of attributes. Then the pair (U, E) denotes the collection of all fuzzy soft sets on U with attributes from E and is called a fuzzy soft class.

Definition 2.4 [6]

A soft set (F, A) over U is said to be null fuzzy soft set denoted by φ if $\forall \varepsilon \in A, F(\varepsilon)$ is the null fuzzy set $\bar{0}$ of U where $\bar{0}(x) = 0 \forall x \in U$.

Definition 2.5 [6]

A soft set (F, A) over U is said to be absolute fuzzy soft set denoted by \tilde{A} if $\forall \varepsilon \in A, F(\varepsilon)$ is the null fuzzy set $\bar{1}$ of U where $\bar{1}(x) = 1 \forall x \in U$.

Definition 2.6 [6]

For two fuzzy soft sets (F, A) and (G, B) in a fuzzy soft class (U, E) , we say that (F, A) is a fuzzy soft subset of (G, B) , if

(i) $A \subseteq B$

(ii) For all $\varepsilon \in A, F(\varepsilon) \subseteq G(\varepsilon)$ and is written as

$(F, A) \subseteq (G, B)$.

Definition 2.7 [6]

Union of two fuzzy soft sets (F, A) and (G, B) in a soft class (U, E) is a fuzzy soft set (H, C) where $C = A \cup B$ and $\forall \varepsilon \in C$,

$$H(\varepsilon) = \begin{cases} F(\varepsilon), & \text{if } \varepsilon \in A - B \\ G(\varepsilon), & \text{if } \varepsilon \in B - A \\ F(\varepsilon) \cup G(\varepsilon), & \text{if } \varepsilon \in A \cap B \end{cases}$$

And is written as $(F, A) \cup (G, B) = (H, C)$.

Definition 2.8 [6]

Intersection of two fuzzy soft sets (F, A) and (G, B) in a soft class (U, E) is a fuzzy soft set (H, C) where $C = A \cap B$ and $\forall \varepsilon \in C, H(\varepsilon) = F(\varepsilon) \cap G(\varepsilon)$ (as both are same fuzzy set) and is written as $(F, A) \cap (G, B) = (H, C)$.

Ahmad and Kharral [7] pointed out that generally $F(\varepsilon)$ or $G(\varepsilon)$ may not be identical. Moreover in order to avoid the degenerate case, he proposed that $A \cap B$ must be non-empty and thus revised the above definition as follows -

Definition 2.9 [7]

Let (F, A) and (G, B) be two fuzzy soft sets in a soft class (U, E) with $A \cap B \neq \emptyset$. Then Intersection of two fuzzy soft sets (F, A) and (G, B) in a soft class (U, E) is a fuzzy soft set (H, C) where $C = A \cap B$ and $\forall \varepsilon \in C$,

$$H(\varepsilon) = F(\varepsilon) \cap G(\varepsilon)$$

We write $(F, A) \cap (G, B) = (H, C)$.

Definition 2.10 [10]

The complement of a fuzzy soft set (F, A) is denoted by $(F, A)^c$ and is defined by $(F, A)^c = (F^c, A)$ where $F^c : A \rightarrow \tilde{P}(U)$ is a mapping given by $F^c(\alpha) = [F(\alpha)]^c, \forall \alpha \in A$.

Definition 2.11 [11]

A binary operation $*$: $[0,1] \times [0,1] \rightarrow [0,1]$ is continuous t -norm if $*$ satisfies the following conditions.

- (i) $*$ is commutative and associative
- (ii) $*$ is continuous
- (iii) $a * 1 = a \quad \forall a \in [0,1]$
- (iv) $a * b \leq c * d$ whenever $a \leq c, b \leq d$ and $a, b, c, d \in [0,1]$

An example of continuous t -norm is $a * b = ab$.

Definition 2.12 [11]

A binary operation \diamond : $[0,1] \times [0,1] \rightarrow [0,1]$ is continuous t -conorm if \diamond satisfies the following conditions:

- (i) \diamond is commutative and associative
- (ii) \diamond is continuous
- (iii) $a \diamond 0 = a \quad \forall a \in [0,1]$
- (iv) $a \diamond b \leq c \diamond d$ whenever $a \leq c, b \leq d$ and $a, b, c, d \in [0,1]$

An example of continuous t -conorm is $a \diamond b = a + b - ab$.

Definition 2.13 [9]

Let $A = [a_{ij}]_{m \times n}, B = [b_{ij}]_{m \times n}$ be two fuzzy soft matrix. Then A is a fuzzy soft sub matrix of B , denoted by $A \subseteq B$, if $a_{ij} \leq b_{ij}, \forall i, j$,

Definition 2.14 [9]

The $m \times n$ fuzzy soft matrix whose elements are all 0 is called the fuzzy soft null matrix (or zero matrix). It is usually denoted by $\tilde{0}$ or $\tilde{0}_{m \times n}$

Definition 2.15 [9]

The $m \times n$ fuzzy soft matrix whose elements are all 1 is called the fuzzy universal soft matrix. It is usually denoted by $\tilde{1}$ or $\tilde{1}_{m \times n}$

Definition 2.16 [9]

Let $A = [a_{ij}]_{m \times n}, B = [b_{ij}]_{m \times n}$ be two fuzzy soft matrix. Then A is equal to fuzzy soft matrix B , denoted by $A = B$, if $a_{ij} = b_{ij}, \forall i, j$,

Definition 2.12 [9]

Let $A = [a_{ij}] \in FSM_{m \times n}$. Then we define

$$A^T = [a_{ij}^T] \in FSM_{n \times m}, \text{ where } a_{ij}^T = a_{ji}$$

Definition 2.13 [9]

Let $A_k \in FSM_{m \times n}, k = 1, 2, 3, \dots, l$, their product is $\prod_{k=1}^l A_k = [c_i]_{m \times l}$. Then the set $O_s = \{j : c_j = \max\{c_i : i = 1, 2, 3, \dots, m\}\}$ is called the optimum subscript set, and the set $O_d = \{u_j : u_j \in U \text{ and } j \in O_s\}$ is called the optimum decision set of U .

3. FUZZY SOFT MATRICES

Definition 3.1

Let $U = \{c_1, c_2, c_3, \dots, c_m\}$ be the universal set and E be the set of parameters given by $E = \{e_1, e_2, e_3, \dots, e_n\}$. Let $A \subseteq E$ and (F, A) be a fuzzy soft set in the fuzzy soft class (U, E) . Then we would represent the fuzzy soft set (F, A) in matrix form as

$$A_{m \times n} = [a_{ij}]_{m \times n} \text{ or simply by } A = [a_{ij}]$$

$$i = 1, 2, 3, \dots, m ; j = 1, 2, 3, \dots, n$$

$$\text{where } a_{ij} = \begin{cases} \mu_j(c_i) & \text{if } e_j \in A \\ 0 & \text{if } e_j \notin A \end{cases}$$

Here $\mu_j(c_i)$ represents the membership of c_i in the fuzzy set $F(e_j)$. We would identify a fuzzy soft set with its fuzzy soft matrix and use these two concepts interchangeable. The set of all $m \times n$ fuzzy soft matrices over U would be denoted by $FSM_{m \times n}$.

Example 3.1

Let $U = \{c_1, c_2, c_3, c_4\}$ be the universal set and E be the set of parameters given by $E = \{e_1, e_2, e_3, e_4, e_5\}$.

Let $P = \{e_1, e_2, e_4\} \subseteq E$ and (F, P) is the fuzzy soft set $(F, P) = \{F(e_1) = \{(c_1, 0.7), (c_2, 0.6), (c_3, 0.7), (c_4, 0.5)\}, F(e_2) = \{(c_1, 0.8), (c_2, 0.6), (c_3, 0.1), (c_4, 0.5)\}, F(e_4) = \{(c_1, 0.1), (c_2, 0.4), (c_3, 0.7), (c_4, 0.3)\}\}$

The fuzzy soft matrix representing this fuzzy soft set would be represented in our notation as

$$A = \begin{bmatrix} 0.7 & 0.8 & 0.0 & 0.1 & 0.0 \\ 0.6 & 0.6 & 0.0 & 0.4 & 0.0 \\ 0.7 & 0.1 & 0.0 & 0.7 & 0.0 \\ 0.5 & 0.5 & 0.0 & 0.3 & 0.0 \end{bmatrix}_{4 \times 5}$$

Proposition 3.1

Let $A = [a_{ij}]_{m \times n}$, $B = [b_{ij}]_{m \times n}$, $C = [c_{ij}]_{m \times n}$ be three fuzzy soft

matrix. Then

- (i) $\tilde{0} \subseteq A$
- (ii) $A \subseteq \tilde{U}$
- (iii) $A \subseteq A$
- (iv) $A \subseteq B, B \subseteq C \Rightarrow A \subseteq C$

Proof: The proof is straight forward and follows from definition.

Definition 3.2

Let $A = [a_{ij}] \in FSM_{m \times n}$, where $a_{ij} = \mu_j(c_i)$. If $m \neq n$, then A is called a fuzzy soft rectangular matrix.

Definition 3.3

Let $A = [a_{ij}] \in FSM_{m \times n}$, where $a_{ij} = \mu_j(c_i)$. If $m = n$, then A is called a fuzzy soft square matrix.

Definition 3.4

Let $A = [a_{ij}] \in FSM_{m \times n}$, where $a_{ij} = \mu_j(c_i)$. If $m = 1$, then A is called a fuzzy soft row matrix.

Definition 3.5

Let $A = [a_{ij}] \in FSM_{m \times n}$, where $a_{ij} = \mu_j(c_i)$. If $n = 1$, then A is called a fuzzy soft column matrix.

Definition 3.6

Let $A = [a_{ij}] \in FSM_{m \times n}$, where $a_{ij} = \mu_j(c_i)$. Then A is called fuzzy soft diagonal matrix if $m = n$ and $a_{ij} = 0$ for all $i \neq j$.

Definition 3.7

Let $A = [a_{ij}] \in FSM_{m \times n}$, where $a_{ij} = \mu_j(c_i)$. Then A is called fuzzy soft scalar matrix if $m = n, a_{ij} = 0$ for all $i \neq j$ and $a_{ij} = \lambda \in [0, 1] \forall i = j$.

Definition 3.8

Let $A = [a_{ij}] \in FSM_{m \times n}$, where $a_{ij} = \mu_j(c_i)$. Then A is called fuzzy soft upper triangular matrix if $m = n, a_{ij} = 0$ for all $i > j$.

Definition 3.9

Let $A = [a_{ij}] \in FSM_{m \times n}$, where $a_{ij} = \mu_j(c_i)$. Then A is called fuzzy soft lower triangular matrix if $m = n, a_{ij} = 0$ for all $i < j$.

A fuzzy soft matrix is said to be triangular if it is either fuzzy soft lower or fuzzy soft upper triangular matrix.

Definition 3.10

Let $A = [a_{ij}] \in FSM_{m \times m}$, where $a_{ij} = \mu_j(c_i)$, then the elements $a_{11}, a_{12}, \dots, a_{mm}$ are called the diagonal elements and the line along which they lie is called the principal diagonal of the fuzzy soft matrix.

Definition 3.11

Let $A = [a_{ij}], B = [b_{ij}] \in FSM_{m \times n}$. Then union of A, B is defined by $A_{m \times n} \tilde{\cup} B_{m \times n} = C_{m \times n} = [c_{ij}]_{m \times n}$, where $c_{ij} = a_{ij} \diamond b_{ij} = a_{ij} + b_{ij} - a_{ij}b_{ij}$ for all i and j .

Example 3.2

Let $A = \begin{bmatrix} 0.1 & 0.2 & 0.3 \\ 0.2 & 0.5 & 0.7 \\ 0.0 & 1.0 & 0.3 \end{bmatrix}$ and $B = \begin{bmatrix} 0.5 & 0.2 & 0.6 \\ 0.1 & 0.3 & 0.2 \\ 0.2 & 0.7 & 0.0 \end{bmatrix}$.

Then

$$A_{3 \times 3} \tilde{\cup} B_{3 \times 3} = C_{3 \times 3} = \begin{bmatrix} 0.55 & 0.36 & 0.72 \\ 0.28 & 0.65 & 0.76 \\ 0.20 & 1.00 & 0.30 \end{bmatrix}$$

Definition 3.12

Let $A = [a_{ij}], B = [b_{ij}] \in FSM_{m \times n}$. Then intersection of A, B is defined by $A_{m \times n} \tilde{\cap} B_{m \times n} = C_{m \times n} = [c_{ij}]_{m \times n}$, where $c_{ij} = a_{ij} * b_{ij} = a_{ij}b_{ij}$ for all i and j .

Example 3.3

For the fuzzy soft matrices cited in **example 3.2**, we have

$$A_{3 \times 3} \tilde{\cap} B_{3 \times 3} = C_{3 \times 3} = \begin{bmatrix} 0.05 & 0.04 & 0.18 \\ 0.02 & 0.15 & 0.14 \\ 0.00 & 0.70 & 0.00 \end{bmatrix}$$

Proposition 3.2

Let $A, B \in FSM_{m \times n}$. Then

- (i) $A \tilde{\circ} \tilde{0} = A$
- (ii) $A \tilde{\circ} \tilde{1} = \tilde{1}$
- (iii) $A \tilde{\circ} B = B \tilde{\circ} A$
- (iv) $(A \tilde{\circ} B) \tilde{\circ} C = A \tilde{\circ} (B \tilde{\circ} C)$

Proof: Let $A = [a_{ij}]_{m \times n}$, $B = [b_{ij}]_{m \times n}$, $C = [c_{ij}]_{m \times n}$ be three fuzzy soft matrices.

- (i) $A \tilde{\circ} \tilde{0} = [a_{ij} + 0 - a_{ij} \times 0] = [a_{ij}] = A$
- (ii) $A \tilde{\circ} \tilde{1} = [a_{ij} + 1 - a_{ij} \times 1] = [1] = \tilde{1}$
- (iii) $A \tilde{\circ} B = [a_{ij} + b_{ij} - a_{ij} \times b_{ij}]$
 $= [b_{ij} + a_{ij} - b_{ij} \times a_{ij}]$
 $= B \tilde{\circ} A$
- (iv) $(A \tilde{\circ} B) \tilde{\circ} C = [a_{ij} + b_{ij} - a_{ij} \times b_{ij}] \tilde{\circ} [c_{ij}]$
 $= [(a_{ij} + b_{ij} - a_{ij} \times b_{ij}) + c_{ij}]$
 $- (a_{ij} + b_{ij} - a_{ij} \times b_{ij}) c_{ij}]$
 $= [a_{ij} + b_{ij} + c_{ij} - a_{ij} \times b_{ij}$
 $- a_{ij} \times c_{ij} - b_{ij} \times c_{ij} + a_{ij} \times b_{ij} \times c_{ij}]$

$$A \tilde{\circ} (B \tilde{\circ} C) = [a_{ij}] \tilde{\circ} [b_{ij} + c_{ij} - b_{ij} \times c_{ij}]$$

$$= [a_{ij} + (b_{ij} + c_{ij} - b_{ij} \times c_{ij})$$

$$- a_{ij} \times (b_{ij} + c_{ij} - b_{ij} \times c_{ij})]$$

$$= [a_{ij} + b_{ij} + c_{ij} - a_{ij} \times b_{ij}$$

$$- a_{ij} \times c_{ij} - b_{ij} \times c_{ij} + a_{ij} \times b_{ij} \times c_{ij}]$$

Hence $(A \tilde{\circ} B) \tilde{\circ} C = A \tilde{\circ} (B \tilde{\circ} C)$.

Remark

Let $A = [a_{ij}]_{m \times n}$, $B = [b_{ij}]_{m \times n}$ be two fuzzy soft matrices.

If we consider $C_{m \times n} = A_{m \times n} \tilde{\circ} B_{m \times n} = [c_{ij}]_{m \times n}$,

where $c_{ij} = \max\{a_{ij}, b_{ij}\}$, for all i and j , then $A \tilde{\circ} A = A$.

Proposition 3.3

Let $A, B \in FSM_{m \times n}$. Then

- (i) $A \tilde{\sim} \tilde{0} = A$
- (ii) $A \tilde{\sim} \tilde{1} = A$
- (iii) $A \tilde{\sim} B = B \tilde{\sim} A$
- (iv) $(A \tilde{\sim} B) \tilde{\sim} C = A \tilde{\sim} (B \tilde{\sim} C)$

Proof: Let $A = [a_{ij}]_{m \times n}$, $B = [b_{ij}]_{m \times n}$, $C = [c_{ij}]_{m \times n}$ be three fuzzy soft matrices, for all i and j .

$$(i) A \tilde{\sim} \tilde{0} = [a_{ij} \times 0] = [0] = \tilde{0}$$

$$(ii) A \tilde{\sim} \tilde{1} = [a_{ij} \times 1] = [a_{ij}] = A$$

$$(iii) A \tilde{\sim} B = [a_{ij} \times b_{ij}]$$

$$= [b_{ij} \times a_{ij}]$$

$$= B \tilde{\sim} A$$

$$(iv) (A \tilde{\sim} B) \tilde{\sim} C = [a_{ij} \times b_{ij}] \tilde{\sim} [c_{ij}]$$

$$= [(a_{ij} \times b_{ij}) \times c_{ij}]$$

$$= [a_{ij} \times (b_{ij} \times c_{ij})]$$

$$= [a_{ij}] \tilde{\sim} [b_{ij} \times c_{ij}]$$

$$= A \tilde{\sim} (B \tilde{\sim} C)$$

Remark

Let $A = [a_{ij}]_{m \times n}$, $B = [b_{ij}]_{m \times n}$ be two fuzzy soft matrices. If we consider $C_{m \times n} = A_{m \times n} \tilde{\sim} B_{m \times n} = [c_{ij}]_{m \times n}$, where $c_{ij} = \min\{a_{ij}, b_{ij}\}$, for all i and j , then $A \tilde{\sim} A = A$.

Definition 3.13

Let $A = [a_{ij}]_{m \times n}$, then complement of A is denoted by $A^C = [c_{ij}]$, where $c_{ij} = 1 - a_{ij}$ for all i and j .

Example 3.4

$$\text{Let } A = \begin{bmatrix} 0.9 & 0.8 & 0.0 \\ 0.8 & 0.5 & 0.0 \\ 1.0 & 0.0 & 0.0 \end{bmatrix}$$

Then

$$A^C = \begin{bmatrix} 0.1 & 0.2 & 1.0 \\ 0.2 & 0.5 & 1.0 \\ 0.0 & 1.0 & 1.0 \end{bmatrix}$$

Proposition 3.4

- (i) $(A^C)^C = A$
- (ii) $(\tilde{0})^C = \tilde{1}$

Proof

(i) Let $A = [a_{ij}]_{m \times n}$ be a fuzzy soft matrix. Then

$$A^C = [1 - a_{ij}] \text{ for all } i \text{ and } j$$

$$\therefore (A^C)^C = [1 - (1 - a_{ij})] = [a_{ij}] = A$$

$$(ii) (\tilde{0})^C = [1 - 0] = [1] = \tilde{1}$$

Proposition 3.5

Let $A = [a_{ij}]_{m \times n}$, $B = [b_{ij}]_{m \times n}$ be two fuzzy soft matrices. $s(tA) = s(t[a_{ij}]_{m \times n})$

Then De Morgan's Laws are valid, for all i and j .

(i) $(A \tilde{\cup} B)^C = A^C \tilde{\cap} B^C$

(ii) $(A \tilde{\cap} B)^C = A^C \tilde{\cup} B^C$

$$\begin{aligned} &= s([ta_{ij}]_{m \times n}) \\ &= s[ta_{ij}]_{m \times n} \\ &= [s(ta_{ij})]_{m \times n} \\ &= [(st)a_{ij}]_{m \times n} \\ &= (st)[a_{ij}]_{m \times n} = (st)A \end{aligned}$$

Proof:

(i) $(A \tilde{\cup} B)^C = ([a_{ij}] \tilde{\cup} [b_{ij}])^C$
 $= [a_{ij} + b_{ij} - a_{ij}b_{ij}]^C$
 $= [1 - a_{ij} - b_{ij} + a_{ij}b_{ij}]$
 $= [(1 - a_{ij})(1 - b_{ij})]$
 $= [1 - a_{ij}] \tilde{\cap} [1 - b_{ij}]$
 $= A^C \tilde{\cap} B^C$

(ii) $(A \tilde{\cap} B)^C = ([a_{ij}] \tilde{\cap} [b_{ij}])^C$
 $= [a_{ij}b_{ij}]^C$
 $= [1 - a_{ij}b_{ij}]$
 $A^C \tilde{\cup} B^C = [1 - a_{ij}] \tilde{\cup} [1 - b_{ij}]$
 $= [1 - a_{ij} + 1 - b_{ij} - (1 - a_{ij})(1 - b_{ij})]$
 $= [1 - a_{ij}b_{ij}]$

Hence $(A \tilde{\cap} B)^C = A^C \tilde{\cup} B^C$

Definition 3.14

Let $A = [a_{ij}] \in FSM_{m \times n}$ and k , $0 \leq k \leq 1$ any number called scalar. The scalar multiple of A by k is denoted by $kA = [ka_{ij}]_{m \times n}$.

Example 3.5

Let $A = \begin{bmatrix} 0.1 & 0.2 & 0.3 \\ 0.2 & 0.5 & 0.7 \\ 0.0 & 1.0 & 0.3 \end{bmatrix}$
 $\therefore 0.5A = \begin{bmatrix} 0.05 & 0.10 & 0.15 \\ 0.10 & 0.25 & 0.35 \\ 0.00 & 0.50 & 0.15 \end{bmatrix}$

Proposition 3.6

If s and t are two scalars such that $0 \leq s, t \leq 1$ and $A = [a_{ij}]_{m \times n}$ is any fuzzy soft matrix, then

(i) $s(tA) = (st)A$

(ii) $s \leq t \Rightarrow sA \subseteq tA$

(iii) $A \subseteq B \Rightarrow sA \subseteq sB$

Proof

We only prove (i) and others follow the similar lines.

Let $A = [a_{ij}]_{m \times n}$

Definition 3.15

Let $A = [a_{ij}]_{m \times m}$ be a fuzzy soft square matrix. Then

$t\tilde{r}A = \sum_{i=1}^m a_{ii} = a_{11} + a_{22} + a_{33} + \dots + a_{mm}$

Example 3.6

Let $A = \begin{bmatrix} 0.1 & 0.2 & 0.3 \\ 0.2 & 0.5 & 0.7 \\ 0.0 & 1.0 & 0.3 \end{bmatrix}$

$\therefore t\tilde{r}A = 0.1 + 0.5 + 0.3 = 0.9$

Proposition 3.8

Let A and B be two fuzzy soft square matrices of order m and k be a scalar. Then $t\tilde{r}(kA) = kt\tilde{r}A$

Proof: Let $A = [a_{ij}]_{m \times m}$

We have, $kA = [ka_{ij}]_{m \times m}$

$\therefore t\tilde{r}(kA) = \sum_{i=1}^m ka_{ii} = k \sum_{i=1}^m a_{ii} = kt\tilde{r}A$

Proposition 3.7

If A be a fuzzy soft matrix of order $m \times n$, then $(kA)^{\tilde{t}} = kA^{\tilde{t}}$, k being any scalar.

Proof

Let $A = [a_{ij}]_{m \times n}$ be fuzzy soft matrix.

We have $kA = [ka_{ij}]_{m \times n}$

$\therefore (kA)^{\tilde{t}} = [ka_{ji}]_{n \times m} = k[a_{ji}]_{n \times m} = kA^{\tilde{t}}$

Proposition 3.8

Let $A, B \in FSM_{m \times n}$. Then

(i) $(A \tilde{\cup} B)^{\tilde{t}} = A^{\tilde{t}} \tilde{\cup} B^{\tilde{t}}$

(ii) $(A \tilde{\cap} B)^{\tilde{t}} = A^{\tilde{t}} \tilde{\cap} B^{\tilde{t}}$

(iii) $(A^C)^{\tilde{t}} = (A^{\tilde{t}})^C$

Remark

Let $A, B \in FSM_{m \times n}$. Then the following distributive laws are valid for *max* and *min* operations only.

(i) $A \tilde{\cup} (B \tilde{\cap} C) = (A \tilde{\cup} B) \tilde{\cap} (A \tilde{\cup} C)$

(ii) $A \tilde{\cap} (B \tilde{\cup} C) = (A \tilde{\cap} B) \tilde{\cup} (A \tilde{\cap} C)$

4. T - PRODUCT OF FUZZY SOFT MATRICES

(ii) The proof is similar to that of (i).

Definition 4.1

Let $A_k = [a_{ij}^k] \in FSM_{m \times n}, k = 1, 2, 3, \dots, l$.

Then the T - product of fuzzy soft matrices, denoted by

$\prod_{k=1}^l A_k = A_1 \times A_2 \times A_3 \times \dots \times A_l$, is defined by

$\prod_{k=1}^l A_k = [c_i]_{m \times 1}$, where

$$c_i = \sum_{j=1}^n \prod_{k=1}^l a_{ij}^k, i = 1, 2, 3, \dots, m$$

While defining T-Product in [9], c_i is calculated by the formula -

$$c_i = \frac{1}{n} \sum_{j=1}^n \prod_{k=1}^l a_{ij}^k, i = 1, 2, 3, \dots, m$$

This requires more computational time. Our method requires less computational time and we obtain the same result as was obtained in [9]. In our work, we will take $T = *$ or $T = \diamond$ according to the type of the problems.

Example 4.1

We assume that $A_1, A_2, A_3 \in FSM_{4 \times 2}$ are given as follows

$$A_1 = \begin{bmatrix} 0.2 & 0.7 \\ 0.6 & 0.4 \\ 0.3 & 0.6 \\ 0.1 & 0.9 \end{bmatrix}, A_2 = \begin{bmatrix} 0.6 & 0.2 \\ 0.1 & 0.6 \\ 0.8 & 0.5 \\ 0.8 & 0.2 \end{bmatrix}, A_3 = \begin{bmatrix} 0.4 & 0.3 \\ 0.3 & 0.1 \\ 0.3 & 0.2 \\ 0.5 & 0.7 \end{bmatrix}.$$

Then the * product is

$$\begin{aligned} & \prod_{k=1}^3 A_k \\ &= A_1 \times A_2 \times A_3 \\ &= \begin{bmatrix} 0.2 * 0.6 * 0.4 + 0.7 * 0.2 * 0.3 \\ 0.6 * 0.1 * 0.3 + 0.4 * 0.6 * 0.1 \\ 0.3 * 0.8 * 0.3 + 0.6 * 0.5 * 0.2 \\ 0.1 * 0.8 * 0.5 + 0.9 * 0.2 * 0.7 \end{bmatrix} \\ &= \begin{bmatrix} 0.090 \\ 0.042 \\ 0.132 \\ 0.166 \end{bmatrix} \end{aligned}$$

Proposition 4.1

Let $A, B \in FSM_{m \times n}$. Then

- (i) $A \times B = B \times A$
- (ii) $(A \times B) \times C = A \times (B \times C)$

Proof

(i) Let $A = [a_{ij}]$, $B = [b_{ij}]$ be two fuzzy soft matrices. Then

$$A \times B = \left[\sum_{j=1}^n a_{ij} T b_{ij} \right] = \left[\sum_{j=1}^n b_{ij} T a_{ij} \right] = B \times A, \text{ where } T = * \text{ or } \diamond$$

Proposition 4.2

Let $A, B, C \in FSM_{m \times n}, B \subseteq C$. Then $A \times B \subseteq A \times C$

Proof: The proof follows similar lines as above.

5. FUZZY SOFT MATRICES IN DECISION MAKING

In this section, we put forward a fuzzy soft matrix decision making method by using fuzzy soft “*” product.

ALGORITHM

Input: Fuzzy soft sets with m objects, each of which has n parameters.

Output: An optimum set.

- Step1: Choose the set of parameters
- Step2: Construct the fuzzy soft matrices for each set of parameters.
- Step3: Compute “*” product of the fuzzy soft matrices
- Step4: Find the optimum subscript set O_s
- Step5: Find the optimum decision set O_d

Suppose $U = \{c_1, c_2, c_3, c_4, c_5\}$ be the five candidates appearing in an interview for appointment in managerial level in a company and

$$E = \{e_1(\text{enterprising}), e_2(\text{confident}), e_3(\text{wiling to takerisk})\}$$

be the set of parameters. Suppose three experts, Mr. A, Mr. B and Mr. C take interview of the five candidates and the following fuzzy soft matrices are constructed accordingly.

$$A = \begin{bmatrix} 0.3 & 0.2 & 0.1 \\ 0.5 & 0.4 & 0.2 \\ 0.6 & 0.5 & 0.7 \\ 0.4 & 0.6 & 0.8 \\ 0.8 & 0.6 & 0.3 \end{bmatrix}, B = \begin{bmatrix} 0.7 & 0.2 & 0.5 \\ 0.6 & 0.4 & 0.9 \\ 0.7 & 0.8 & 0.6 \\ 0.5 & 0.6 & 1.0 \\ 0.4 & 0.5 & 0.7 \end{bmatrix} \text{ and}$$

$$C = \begin{bmatrix} 0.5 & 0.4 & 0.6 \\ 0.4 & 0.7 & 0.6 \\ 0.6 & 0.5 & 0.5 \\ 0.8 & 0.6 & 0.4 \\ 0.5 & 0.6 & 0.5 \end{bmatrix}$$

We have,

$$A \times B \times C$$

$$= \begin{bmatrix} 0.3 * 0.7 * 0.5 + 0.2 * 0.2 * 0.4 + 0.1 * 0.5 * 0.6 \\ 0.5 * 0.6 * 0.4 + 0.4 * 0.4 * 0.7 + 0.2 * 0.9 * 0.6 \\ 0.6 * 0.7 * 0.6 + 0.5 * 0.8 * 0.5 + 0.7 * 0.6 * 0.5 \\ 0.4 * 0.5 * 0.8 + 0.6 * 0.6 * 0.6 + 0.8 * 1.0 * 0.4 \\ 0.8 * 0.4 * 0.5 + 0.6 * 0.5 * 0.6 + 0.3 * 0.7 * 0.5 \end{bmatrix}$$

$$= \begin{bmatrix} 0.151 \\ 0.340 \\ 0.662 \\ 0.696 \\ 0.445 \end{bmatrix}$$

It is clear that the maximum score is 0.696, scored by c_4 and the decision is in favor of selecting c_4 .

6. CONCLUSION

In this work, we have put forward the notions related to fuzzy soft matrices. Our work is in fact an attempt to extend the notion of fuzzy soft matrices put forward in [9]. Future work in this regard would be required to study whether the notions put forward in this paper yield a fruitful result

7. REFERENCES

- [1] D. A. Molodtsov, "Soft Set Theory - First Result", Computers and Mathematics with Applications, Vol. 37, pp. 19-31, 1999
- [2] P. K. Maji and A.R. Roy, "Soft Set Theory", Computers and Mathematics with Applications 45 (2003) 555 – 562
- [3] D. Pei and D. Miao, "From soft sets to information systems," in *Proceedings of the IEEE International Conference on Granular Computing*, vol. 2, pp. 617–621, 2005.
- [4] D. Chen, E.C.C. Tsang, D.S. Yeung, and X.Wang, "The parameterization reduction of soft sets and its applications," *Computers & Mathematics with Applications*, vol. 49, no.5-6, pp. 757–763, 2005.
- [5] M.I Ali, F. Feng, X.Y. Liu, W. K. Min, M. Shabir (2009) "On some new operations in soft set theory". *Computers and Mathematics with Applications* 57:1547–1553
- [6] P. K. Maji, R. Biswas and A.R. Roy, "Fuzzy Soft Sets", *Journal of Fuzzy Mathematics*, Vol 9, no.3, pp.-589-602, 2001
- [7] B. Ahmad and A. Kharal, *On Fuzzy Soft Sets*, *Advances in Fuzzy Systems*, Volume 2009.
- [8] T. J. Neog, D. K. Sut, "On Union and Intersection of Fuzzy Soft Sets" *Int.J. Comp. Tech. Appl.*, Vol 2 (5), 1160-1176

- [9] Yong Yang and Chenli Ji "Fuzzy Soft Matrices and Their Applications" AICI 2011, Part I, LNAI 7002, pp. 618–627, 2011.
- [10] T. J. Neog, D. K. Sut, "On Fuzzy Soft Complement and Related Properties", Accepted for publication in *International Journal of Energy, Information and communications (IJEIC)*, Japan.
- [11] B. Schweirer, A. Sklar, "Statistical metric space", *Pacific Journal of Mathematics* 10(1960), 314-334.

PFC Circuit for Wind Generator with PWM Controller

Mohanraj.M, Dr.Rani Thottungal, Nithyashree.R.B

Department of Electrical and Electronics Engineering
Kumaraguru College of Technology, Coimbatore.

ABSTRACT-The single-stage converters (SSC's) with power-factor-correction (PFC) feature is implemented in the wind generator is presented in this paper. The wind induction generator(IG) feeding an isolated load through the PWM controller with the power factor correction circuit. In this circuit, the power factor is improved by using an auxiliary winding coupled to the transformer of a cascade dc/dc flyback converter. The topology of this converter is derived by combining a boost circuit and a forward circuit in one power stage. To improve the performance of the ac-dc converter (i.e., good powerfactor correction, low total harmonic distortion (THD) and low dc bus voltage), two bulk storage capacitors are adopted. The output voltage and frequency of the wind generator can be varied according to random fluctuation of wind-speed variation.Due to its simplified power stage and control circuit, this converter presents a better efficiency, lower cost and higher reliability.

Index Terms— Single-stage converters (SSC's), Induction generator (IG),Total harmonic distortion (THD),Power-factor-correction (PFC), AC/DC converter,Input Current Sharper (ICS).

I. INTRODUCTION

Power-Factor-Correction (PFC) techniques have become attractive since several regulations have been effected recently. Many PFC converters have been presented. They usually can be divided into two categories: the two-stage and single-stage approaches [1]. In order to reduce the cost, the single-stage approach, which integrates the PFC stage with a dc/dc converter into one stage (base).The additional discharge path in the PFC inductor and DC-bus voltage feedback effectively suppresses the DC-bus voltage and increases the overall efficiency [2]. Traditionally, to improve power factor of a given power electronic system, normally a power factor correction (PFC) circuit is designed and placed in front end of the system, which in turn interfaced with the load. This PFC circuit may be an independent unit followed by a dc-dc converter, or an inseparable part of circuit incorporated into the power supply of the load, namely two-stage PFC power supply and single-stage PFC power supply, respectively[3].

For high-power levels, the PFC stage is operated in the continuous-conduction mode (CCM), while the discontinuous-conduction-mode (DCM) operation is commonly used at lower power levels due to a simpler control[4]. For single stage PFC rectifiers, the performance measures, such as efficiency, hold up time, component count, component voltage and current stress, input current quality, etc., are largely dependent of the circuit topology[5].

The performance of IG supplying various static loads using different control schemes are studied and analysed in various papers. An interleaved converter with a coupled winding is proposed to provide a lossless clamp. Moreover, the proposed converter design reduces the volume and weight of the magnetic material by almost half compared to existing boost-based single-stage PFC converters.

A common approach to improving the power factor is a two-stage approach. In this approach, an active power-factor-correction (PFC) stage, which is usually realized by a dc/dc converter, is adopted at the input of electronic equipment to force the line current tracking the line voltage. A PFC converter is adopted at the front-end to force the line current tracking the line voltage and another conventional DC/DC converter is cascaded after the PFC stage to obtain the desired tightly regulated output voltage[2].

The voltage across the DC-bus capacitor varies with the variation of the input voltage and the load, especially while the PFC part operates in discontinuous conduction mode (DCM) and the DC/DC part is in continuous conduction mode (CCM). The secondary winding is added in the PFC boost inductor, some input power is directly transferred to the output. In this paper, a review of the most interesting solutions for single phase and low power applications is carried out.

II. POWER FACTOR CORRECTION CIRCUIT

A single power stage with dual outputs produces both the desired DC output and a boosting supply in series with the input. In fig.1. the function of the circuit is illustrated. This circuit is original but the component count is high. Another way to realize single stage PFC is by cascading a boost ICS with a dc-dc converter using one switch.

Both pulse width modulation (PWM) and frequency modulation (FM) were applied in the control circuitry. In a single-stage approach, power-factor correction, isolation, and high-bandwidth control are performed in a single step, i.e., without creating an intermediate dc bus. Generally, these converters use an internal energy-storage capacitor to handle the differences between the varying instantaneous input power and a constant output power.

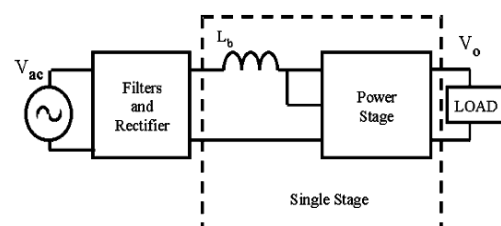


Fig. 1. General circuit diagram for single stage AC/DC PFC Converter.

In this family a boost circuit accompanied by a dc/dc converter was introduced to form the so-called single stage single-switch ac/dc converters. The family circuits have PFC function, as illustrated in Fig. 1. This concept successfully simplifies a conventional power-factor corrector by changing it from two stages to one stage. However, this concept employs a bulk inductor in the boost section, which occupies significant volume and weight.

A boost circuit accompanied by a dc/dc converter was introduced to form the so-called single-stage single-switch ac/dc converters. Single-stage PFC converters meet the regulatory requirements regarding the input current harmonics, but they do not improve the power factor and reduce the THD as much as their conventional two-stage counterpart. The power factor could be as low as 0.8, however, they still meet the regulation. In addition, although the single-stage scheme is especially attractive in low cost and low power applications due to its simplified power stage and control circuit, major issues still exist, such as low efficiency and high as well as wide-range intermediate dc bus voltage stress.

This concept successfully simplifies a conventional power-factor corrector by changing it from two stages to one stage. The implemented values in simulation of power factor circuit is shown in Table I. Table II indicates the performance of the ac/dc converter. However, this concept employs a bulk inductor in the boost section. Moreover, the proposed converter design reduces the volume and weight of the magnetic material by almost half compared to existing boost-based single-stage PFC converters.

Furthermore, the voltage across the bulk capacitor can be reduced to a reasonable value by adjusting the turns ratio of the windings N_1 and N_3 . Therefore, this design can adapt to significant line voltage variation. Experimental results for a 60W converter at a constant switching frequency of 70 kHz are obtained to show the performance of the proposed converter.

III. QUASI ACTIVE PFC CIRCUIT

The proposed quasi-active PFC circuit is analyzed in this section. As shown in Fig. 2, the circuit comprised of a bridge rectifier, a boost inductor L_B , a bulk capacitor C_a in series with the auxiliary windings L_3 , an intermediate dc-bus voltage capacitor C_B , and a discontinuous input current power load, such as flyback converter. The flyback transformer has three windings N_1, N_2 and N_3 . The secondary winding $N_2 = 1$ is assumed. In the proposed PFC scheme, the dc/dc converter section offers a driving power with high-frequency pulsating source.

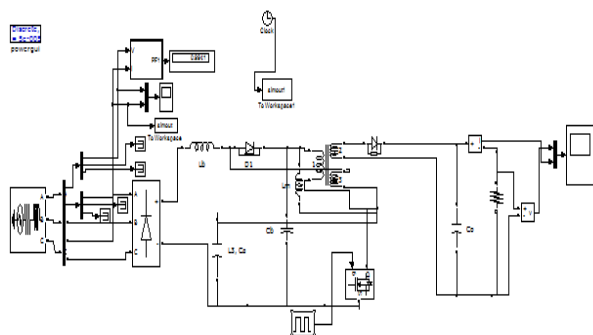


Fig. 2. Simulation diagram for Quasi-active power factor circuit

TABLE I

Technical data for the Quasi active power Factor Circuit

Transformer Turns Ratio:	$N_1 = 30, N_2 = 10, N_3 = 15$
Magnetizing Inductor, L_m	200 μH
Energy Buffer, L_b	80 μH
Voltage capacitor, C_b	47 μF
Bulk Capacitor, C_a	22 MF
Capacitance, C_o	470 MF
Input Voltage, V_{in}	230V
Line Voltage, V_{rms}	(100-240)V
Switching Frequency	100kHz

The capacitor voltage can be maintained below 450 V by properly designing the turns ratio N_3/N_1 and the inductors ratio L_m/L_b .

TABLE II

Performance of the Circuit

Semiconductor	2 diodes, 1 switch, 1 bridge rectifier
Passive components	1 inductor, 3 capacitors, 3- winding transformer
Switch current	$(N_3/N_1) I_{LB} + I_{Lm}$, where $N_3/N_1 < 1$
Efficiency at full load	>90%
Capacitor voltage V_{CB} (for constant input voltage)	Controlled by the ratio L_m/L_B and the winding ratio N_3/N_1
THD of the input current	<10%

IV. WIND MODEL

The generation system is designed with IG. The block diagram of the wind model with PFC circuit is shown in Fig. 3. The stator winding terminals of the IG are connected to the load through the rectifier, DC link, PFC circuit, and inverter. The closed loop PWM signal generates proper PWM signals to switch the two power electronics devices of the Interleaved Boost Converter (IBC). The wind turbine rotates the IG. The IG generates power when the speed of the turbine is above the rated speed. The power generated from the IG is converted to DC with a diode bridge rectifier. The obtained DC voltage will not be in a pure DC signal. A filter circuit is used to filter out the ripple current and a pure DC voltage is obtained. This DC voltage is then boosted to the required DC level and then converted to phase AC signal with IGBT which is driven by PWM signal. To regulate the AC output voltage the IBC is controlled by close loop PWM signals. A load is connected at the output of the inverter.

Pulse-width modulation (PWM) is a very efficient way of providing intermediate amounts of electrical power between fully on and fully off. A simple power switch with a typical power source provides full power only when switched on.

The term duty cycle describes the proportion of on time to the regular interval or period of time; a low duty cycle corresponds to low power, because the power is off for most of the time. Pulse-width modulation uses a

rectangular pulse wave whose pulse width is modulated resulting in the variation of the average value of the waveform. If we consider a pulse waveform $f(t)$ with a low value y_{min} , a high value y_{max} and a duty cycle D , the average value of the waveform is given by

$$\bar{y} = T \int_0^T f(t) dt$$

$$\bar{y} = \frac{1}{T} \left(\int_0^{DT} y_{max} dt + \int_{DT}^T y_{min} dt \right)$$

$$= \frac{D.T.y_{max} + T(1-D)y_{min}}{T}$$

$$\bar{y} = D.y_{max} + (1-D)y_{min}$$

The simplest way to generate a PWM signal is the interceptive method, which requires only a sawtooth or a triangle waveform and a comparator. When the value of the reference signal is more than the modulation

waveform, the PWM signal is in the high state, otherwise it is in the low state.

V. OPERATION OF WIND MODEL

In this the integrated single-stage power factor correction (PFC) converters usually use a boost converter to achieve PFC with discontinuous current mode (DCM) operation. Usually, the DCM operation gives a lower total harmonic distortion (THD) of the input current compared to the continuous current mode (CCM).

However, the CCM operation yields slightly higher efficiency compared to the DCM operation. In the DCM operation of the ICS inductor, low line-current harmonic distortions are achieved because of the inherent property of the DCM boost converter to draw a near sinusoidal current if its duty cycle is held relatively constant during a half line.

When the switch (SW) is turned on at $t = t_1$, diodes D_1 and D_0 are OFF, then the value of i_m can be calculated.

$$i_m = \frac{V_{CB}}{L_m} (t_0 - t_1)$$

V_{CB} – DC Bus voltage

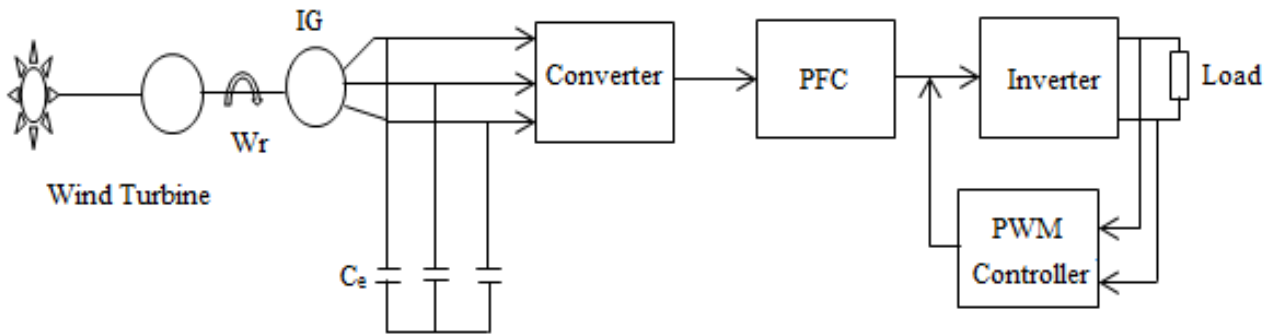


Fig. 3. Block Diagram of wind model

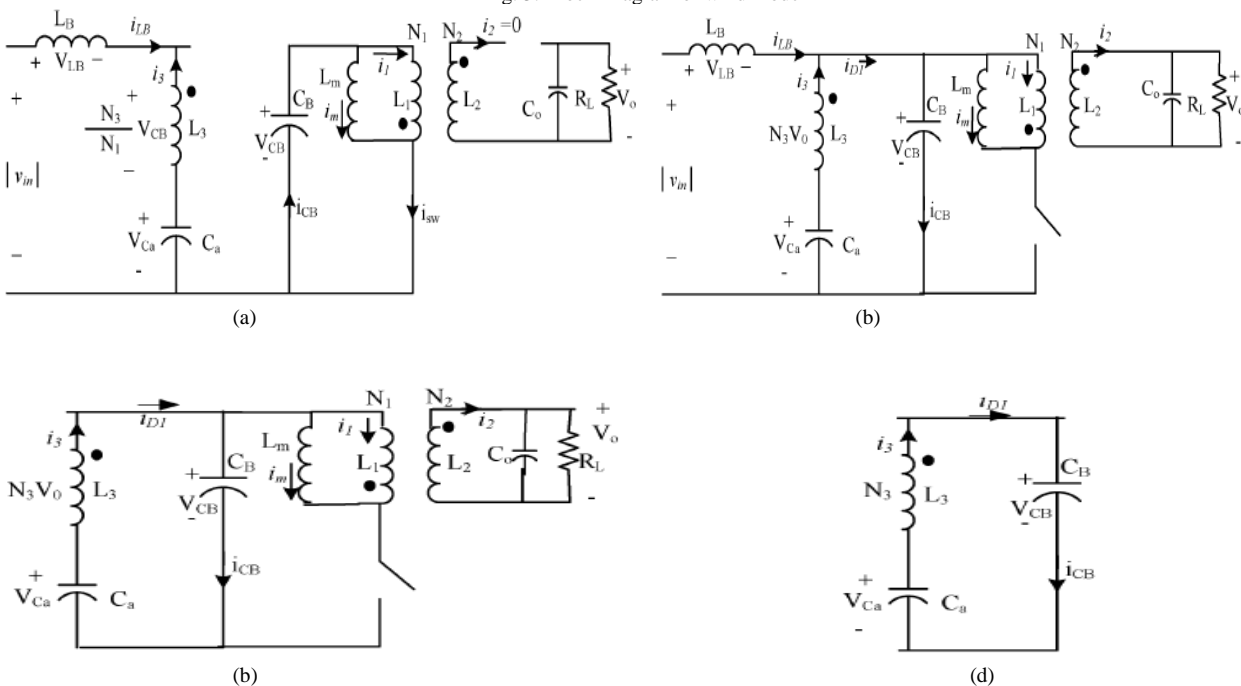


Fig. 4. Equivalent circuit operation of power factor correction circuit for the corresponding switching period. (a) At the switching period $(t_0 - t_1)$; (b) At the switching period $(t_1 - t_2)$; (c) At the switching period $(t_2 - t_3)$; (d) At the switching period $(t_3 - t_4)$;

A. OPERATION OF POWER FACTOR CORRECTION CIRCUIT

In the fig. 4(a),the diode D_1 is OFF, the input inductor L_B is charged by input voltage, therefore, the inductor current i_{LB} is linearly increased. On the other hand, D_0 is reversed biased and there is no current flow through the secondary winding.

$$i_{SW} = i_m + i_{LB}$$

At $(t_1 - t_2)$ the switch is turned OFF at $t_1 = t_2$ output diode D_0 begins to be forward biased as shown in fig 5 (b). Therefore, the energy stored in the transformer magnetizing inductor is delivered to the load through the secondary winding. Similarly, the diode D_1 is also forward biased and the voltage across L_B now, $V_{in} - V_{CB}$.

Therefore, the current i_{LB} is linearly decreased to zero at $t = t_2$ (DCM operation), and the energy stored in L_B is delivered to the dc bus capacitor C_B . The capacitor (C_a) is also discharging its energy to the dc bus capacitor C_B and the current i_3 reverse its direction. Therefore, the capacitor current is given by

$$i_{D1} = i_{CB} = i_{LB} + i_3$$

In fig. 4(c).that is in the stage $(t_2 - t_3)$, the input inductor current i_{LB} reaches zero and the capacitor C_a continues to discharge its energy to the dc bus capacitor C_B .Therefore, $i_{D1} = i_{CB} = i_3$. At $t = t_3$, the magnetizing inductor releases all its energy to the load and the currents i_m and i_2 reach to zero level because a DCM operation is assumed.

In the stage 4,at $(t_3 - t_4)$ the currents i_m and i_2 reach to zero as shown in fig.5(d). Diode D_1 still forward biased, therefore, the capacitor C_a still releasing its energy to the dc bus capacitor C_B . This stage ends when the capacitor C_a is completely discharged.

The energy absorbed by the circuit from the source during a half switching cycle is given by

$$P_{in} = \frac{1}{\pi} \int_0^{\pi} V_m \sin(t) I_{in} dt$$

$$P_{in} = \frac{1}{\pi} \frac{V_m}{2L_B} d^2 T_S(A) \int_0^{\pi} \sin(t) B dt$$

Here,

$$A = \left[\left(1 + \frac{N_3}{N_1} \right) V_{CB} - V_{Ca} \right]$$

$$B = \frac{V_m \sin(t) + \frac{N_3}{N_1} V_{CB} - V_{Ca}}{V_{CB} - V_m \sin(t)}$$

The turns ratio N_3/N_1 and the dc bus voltage V_{CB} can be optimized in order to reduce the dead time and improve the quality of the input current.

Usually, the DCM operation gives a lower total harmonic distortion (THD) of the line current compared

to the CCM operation. However, the CCM operation yields a slightly higher efficiency compared to the DCM operation. Regarding the power factor correction stage, the boost converter is widely used because of its advantages: grounded transistor, small input inductor, simplicity and high efficiency (around 95%). The main drawback is that the output voltage is higher than the peak input voltage, causing switching losses in the transistor and in the diode, due to its reverse recovery.

VI. SIMULATION RESULTS

The wind model is simulated by using Matlab software.

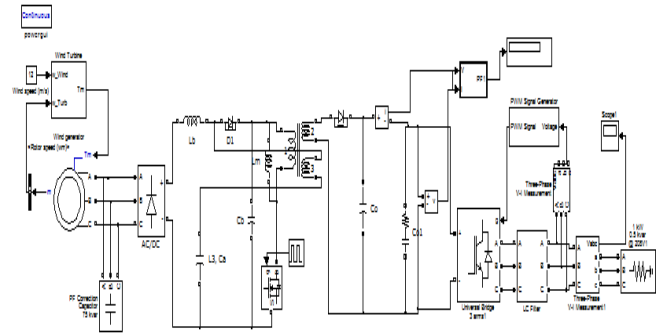


Fig. 5. Simulation diagram for the wind turbine.

The IG design is made with the calculated value of resistance, flux linkage of the stator and rotor windings and with the torque equation and the number of poles. The generated power is rectified. The generated power varies with the wind speed. The power converter converts the three phase AC to DC and then the filter circuit is used for obtaining smooth DC voltage across it.

The project module is simulated using MATLAB 7.7.0(R2008b). The simulation is executed under ode23tb (stiff/TR-BDF2) state which is used to fasten the execution speed and the Zero-crossing control is disabled. The solver method is set to fast. The voltage is measured at different points in the simulation circuit. The simulated output is shown below. The system is tested with different load and wind speed. The designed system generates AC power with asynchronous generator (215HP;400V50Hz).

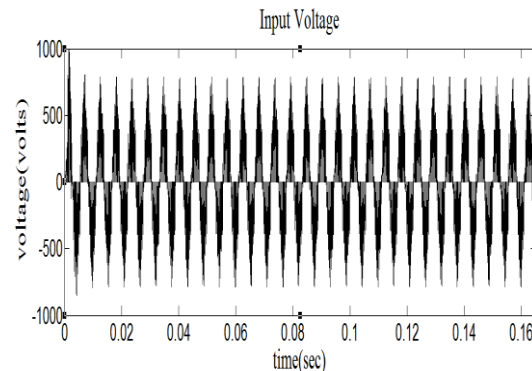


Fig. 6. Input Voltage for power factor circuit.

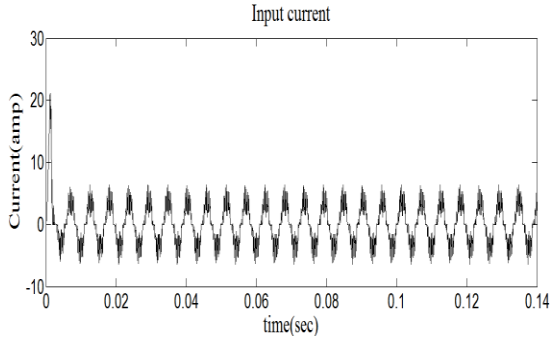


Fig. 7. Input Current for power factor circuit.

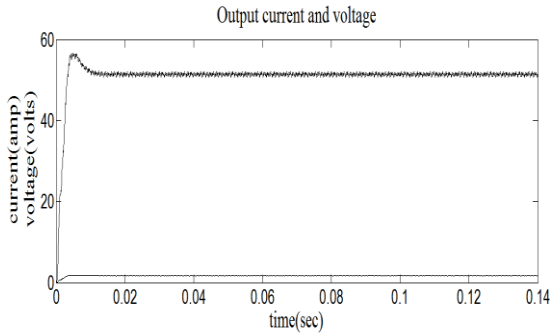


Fig. 8. Output Voltage and Current for power factor circuit.

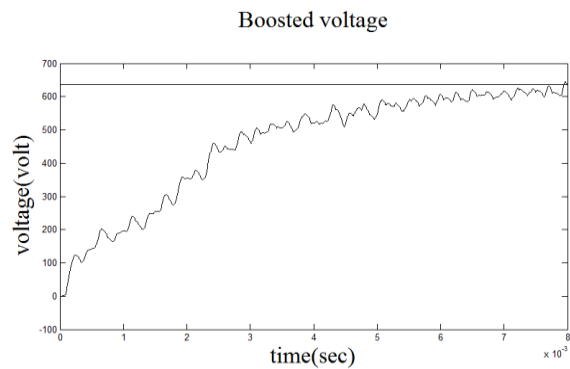


Fig. 9. Boosted voltage from PFC circuit.

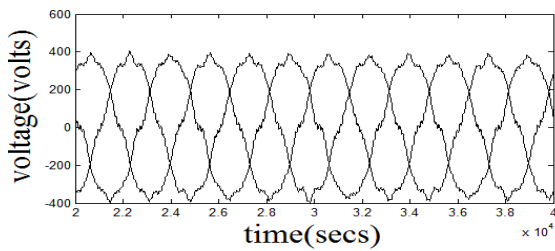


Fig. 10. Output Voltage of Wind model.

The turns ratio N_3/N_1 and the dc bus voltage VCB can be optimized in order to reduce the dead time and improve the quality of the input current. In the Fig. 6. the input current for the power factor circuit. Note that, in order to improve the visibility of the higher order harmonics, class A limits are scaled down by a factor of 5 (class A limits/5). The measured THD = 6.70% and the power factor is 0.994 for the closed loop wind power generation circuit.

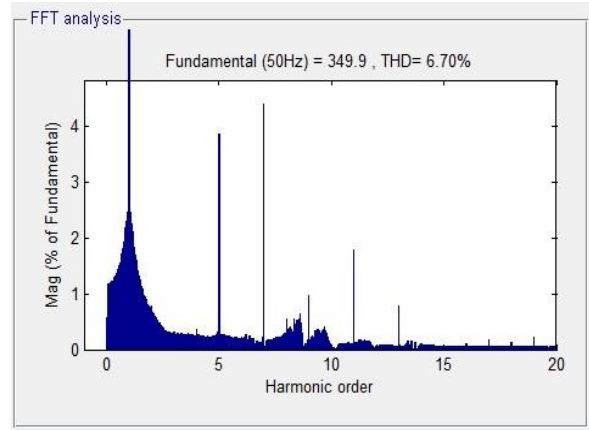


Fig. 11. THD for input current in the closed loop circuit

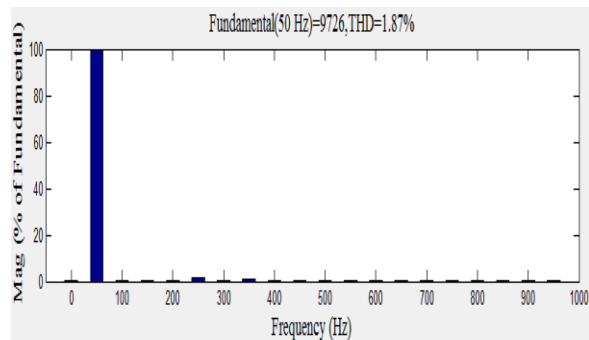


Fig. 12. THD for input current in open loop circuit.

VII. CONCLUSION

A ac/dc converter based on a quasi-active PFC scheme has been presented and simulated in this paper. The proposed method produces a current with low harmonic content to meet the standard specifications and the high efficiency. This circuit is based on adding an auxiliary winding to the transformer of a cascade dc/dc DCM flyback converter. The main advantage of the system is that the minimum wind speed is required for the power generation. The simulated results of output voltage shows the performance of the proposed wind model. The input inductor can operate in DCM to achieve lower THD and high power factor. By properly designing the converter components, the relation between efficiency and harmonic content can be established to obtain the proper regulation and efficiency as high as possible.

REFERENCE

- [1] J. Qian, Q. Zhao, and F. C. Lee, "Single-stage single-switch power factor correction ac/dc converters with dc-bus voltage feedback for universal line applications," *IEEE Trans. Power Electron.*, vol. 13, no. 6, pp. 1079–1088, Nov. 1998.
- [2] H. L. Do, "Single-stage single-switch power factor correction AC/DC converter," *Inst. Electr. Eng. Proc. Electr. Power Appl.*, vol. 152, no. 6, pp. 1578–1584, Nov. 2005.
- [3] H. Wei, I. Batarseh, G. Zhu, and K. Peter, "A single-switch AC-DC converter with power factor correction," *IEEE Trans. Power Electron.*, vol. 15, no. 3, pp. 421–430, May 2000.
- [4] K. Zhou, J. G. Zhang, S. Yuvarajan, and D. F. Weng, "Quasiactive power factor correction circuit for switching power supply," *IEEE Trans. Power Electron.*, vol. 23, no. 3, pp. 1410–1414, May 2008.
- [5] Qian and K. Smedley, "A topology survey of single-stage power factor with a boost type input-current-shaper," *IEEE Trans. Power Electron.*, vol. 16, no. 3, pp. 360–368, May 2001.
- [6] S.S. Murthy, O.P. Malik, and A.K. Tandon, "Analysis of self-excited induction generators," *IEE Proceedings, Part C—Generation, Transmission, and Distribution*, vol. 129, no. 6, pp. 260-265, 1982.
- [7] Singh and L.B. Shilpakar, "Analysis of a novel solid state voltage regulator for a self-excited induction generators," *IEEE Proceedings, Generation Transmission and Distribution*, vol. 145, no.6, pp. 647-655, 1998.
- [8] E.G. Marra and J.A. Pomilio, "Induction-generator-based system providing regulated voltage with constant frequency," *IEEE Trans. Industrial Electronics*, vol. 47, no. 4, pp. 908-914, 2000.
- [9] E.G. Marra and J.A. Pomilio, "Self-excited induction generator controlled by a VS-PWM bidirectional converter for rural applications," *IEEE Trans. Industry Applications*, vol. 35, no. 4, pp.877-883, 1999.
- [10] S. Wekhande and V. Agarwal, "Simple control for a wind-driven induction generator," *IEEE Industry Applications Magazine*, vol. 7, no. 2, pp. 45-53, 1999.

BIOGRAPHIES



M. Mohanraj, received B.E degree in Electrical and Electronics Engineering from Bharathiar University in the year 2001 and M.E (Power System) from Annamalai University in 2005. Currently he is pursuing Ph.D research work under Anna University of Technology, Coimbatore. He is a senior Assistant Professor of EEE department in Kumaraguru College of Technology, Coimbatore. He is having one year of industrial and ten years in teaching experience. He has published twelve papers in National conferences and one journal. He is a Life member in Indian Society for Technical Education (India). His research area includes Wind Energy Conversion, Solar Energy, Machines and Power Quality issues.



Rani Thottungal, obtained her B.E and M.E degrees from Andhra University and Doctorate from Bharathiar University. She is currently working as Professor and Head in EEE department, Kumaraguru College of Technology, Coimbatore. Her research interest includes Power System, Power Inverter and Power Quality Issues.



R.B. NITHYASHREE, finished her UG in M. Kumarasamy College of Engineering, Karur and pursuing her final year M.E. in Power Electronics and Drives in Kumaraguru College of Technology, Coimbatore.

Policy Measures for Improving the Imageability in the City of Mysore

Dr. Shankar B¹, Dr. Chidambara Swamy²

¹(Associate Professor in Urban and Regional Planning, Institute of Development Studies, University of Mysore, Mysore)

²(Professor and Head, Adhiyamaan College of Engineering, Hosur)

ABSTRACT

Mysore city is an ancient, historical, cultural capital and heritage city. The city is known as the 'city of palaces'. The city has both natural and built heritage and it has retained its studiously built character of a native princely city. The most imposing and majestic building in Mysore is the Ambavilas Palace, which is the landmark of the city. The architectural and urban design elements like vistas, focal points, landmarks, avenues, plazas etc., make it undoubtedly the most important tradition city in India. Albert – Victor road is beautifully laid down street, has a pathway beautifully laid within the Curzon park which and hugging the palace gate and fort with a moat on northern side of the palace as a landmark, represents the vista with edges. The townscape of the city viewed from Chamundi hills present a skyline of clock tower, statues, palaces, mansions depicts the beauty of the city. The paper attempts to identify the urban design elements which contributed to *image of the city* and suggest policy measures for conserving the elements of urban design in the City of Mysore.

Key Words: Built Heritage, Imageability and Policy Measures.

I. INTRODUCTION

Mysore is the third largest city in the State of Karnataka and it had a population of 7,85,800 as per 2001 census. The name of Mysore was derived from *mahisha* (a demon). Formerly, the city was the state capital and head quarters of the Princely State of Mysore. It is situated at a distance 140kms from Bangalore, on the southern part of Karnataka State at 12° 18' North latitude and 76° 12' East longitude, and at an altitude of 770 mts above mean sea level. The city lies in a saucer shaped basin flanked by Chamundi hills on the south-east and a raised platform near Hinakal village on the west. The city has a salubrious climate and the temperature varies from 12° C to 35° C. It has an average annual rainfall of about 798mm. The city spreads across an area of 128.42sq.kms. The literacy rate is 82.8 percent. A majority of the city's population speaks Kannada language, while other languages such as Tulu, Tamil and Hindi are also spoken.

II. HERITAGE OF MYSORE

Mysore is a cultural and prime heritage city and it exhibits both tangible and intangible elements. It combines the historical facts and anecdotes with a harmonious combination of natural and built heritage. The city is known as 'cultural capital' of Karnataka. It

was the capital of Wodeyar Kings who ruled Mysore Kingdom for many centuries and contributed significantly to make the city as a cultural centre including art, poetry and music. The city is as known city of palaces and the museums, art galleries and the festivities that take place during the period of *Dasara* which attract worldwide audience. The total harmony of buildings, sites, lakes, parks and open spaces including backdrop of Chamundi hill adds to the city's aesthetics with different cultures and different styles of architecture. The heritage buildings have four distinct architectural styles viz. Indo-Saracenic, Traditional Hindu Style, Greaco-Roman and Gothic (Pearl). Thus, the city exhibits both tangible and non tangible elements of heritage character, and therefore, the Government of Karnataka recognized the city as Heritage city and Government of India has selected the city for Urban Renewal Project under cultural and heritage tag.

III. BUILT HERITAGE OF MYSORE

Mysore city has both natural and built heritage. The city has retained its studiously built character of a native princely city. The most imposing and majestic building in Mysore is the Ambavilas Palace, which is the focal point of the city. It was built in an Indo-Saracenic style. The city is characterized by buildings, gardens, boulevards, and planned markets all these were the contributions of Maharajas, Dewans, and their talented workmanship. Their architectural and urban design elements like vistas, focal points, landmarks, avenues, plazas etc., make it undoubtedly the most important tradition city in India. Albert – Victor road is beautifully laid down street, has a pathway beautifully laid within the Curzon park which and hugging the palace gate and fort with a moat on northern side of the palace as a landmark, represents the vista with edges. The townscape of the city viewed from Chamundi hills present a skyline of clock tower, statues, palaces, mansions depicts the beauty of the city.

IV. DEFINITION OF IMAGEABILITY

Imageability is a participative technological installation investigating the relationships between special conceptions of the city, historical memory, and the continuous dynamic emergence of cultural identity. It is a tool for expressing one's own vision of the city, exploring its history, and constructing a collective. Kevin Lynch introduced the concept of *imageability*, which he defined as that quality in a physical object which gives it a high probability of evoking a strong image in any given observer. It is that shape, colour, or arrangement which facilitates the making of vividly identified, powerfully structured, highly useful mental images of the environment. It might also be called legibility, or perhaps

visibility in a heightened sense, where objects are not only able to be seen, but are presented sharply to their senses. Kevin Lynch's *The Image of the City* of 1961 was also seminal to the movement, particularly with regards to the concept of legibility, and the reduction of urban design theory to five basic elements - *paths, districts, edges, nodes, and landmarks*.

V. IMAGEABILITY OF MYSORE

Mysore is designed studiously as a princely city, has an established urban form to include urban design elements, imageability of the city and built structures that contributed to the aesthetics and architecture. The city is characterized by the towering presence of Amba Vilas Palace, which is the landmark and focal point of the city. Mysore is a city of long boulevards radiating from well defined central axis with well recessed public buildings balanced on either side can be a model for any town planner. The city planning can be identified as a combination of grid iron pattern residing on the radially expanding city. It has both architectural and urban design elements namely vistas, focal points, landmarks, avenues, and plazas made it undoubtedly the prominent heritage city. Mysore is characterized by heritage buildings, gardens, boulevards, and planned markets all these are the contributions of Maharajas, Dewans, and their talented workmanship. The architectural growth in Mysore occurred from 1805 and was completed by 1940. This marvel gave the city a skyline which is proclaimed a powerful aristocracy. Though, a large number of buildings were deliberately made in Hindu style or in Indo-Saracenic style, and European classical remained the major style of the period. Chamarajendra Wodeyar and the Maharani Regent commissioned many distinguished buildings including some remarkable buildings in European Classical style between 1881- 1902. However Krishnaraja Wodeyar IV, who stands out among the great builder's of Mysore city and creators of its remarkable aesthetics. Mysore also witnesses a blend of various styles. The balanced treatment of architectural composition with a blend of man-made structures of natural features, have given the city a rare and captive beauty. The combination of different styles applied in statues, clock towers and fountains are so well executed in terms of purity of style and located in right places with the right proportion of open spaces incorporated in it. The townscape of the city viewed from Chamundi hills present a skyline of clock tower, statues, palaces, mansions, etc., which exists with its beauty. The treatment given to the public buildings are reasons of admiration inspiring state of thought about the rich past. The maintenance of beautiful gardens in the premises enhanced the appearance of the city.

The imageability of city's aesthetics of urban design elements are expressed through the following elements:

- | | |
|-----------------------------|---------------------|
| 1. Land Marks | 8. Edges |
| 2. Focal Point | 9. Path |
| 3. Precinct | 10. Juxtaposition |
| 4. Public Square | 11. Urban Imagery |
| 5. Public and Private Realm | a. Street Furniture |
| 6. Vista and Axis | b. Gateways |
| 7. Nodes | c. Railings |
| | d. Hoardings |

A. Landmarks

"The position of a prominent or well-known object in a particular landscape is called the landmark, which attracts attention". There are two important landmarks in the City of Mysore and they are Ambavilas Palace and Chamaraja Circle.

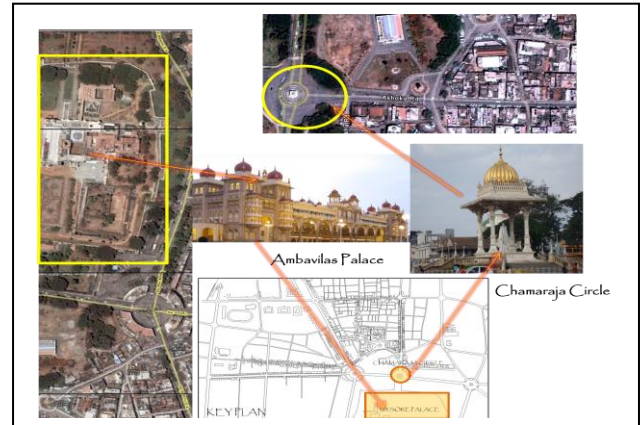


Fig. 1 Land Marks of Mysore

Ambavilas Palace is a prominent landmark, a three storied structure having the tallest tower with the gilded dome rising to a level of 145 ft from the ground. It was built in Indo-saracenic architecture style. The domes and the external elements are of Islamic architecture. But the interior of the palace is a fine example of Hindu architecture. Together, it is an aesthetic blend of Hindu and Muslim architectures. Illuminated palace stands in its full grandeur and splendour posing the majestic image to the city. The palace exhibits the following characters namely (a) most renowned Palace, (b) innermost landmark (c) reveal the strength and power of the place, (d) monumental scale (e) most visited tourist place and derives income from tourist (f) architectural style, domes, arches, decorations, carvings etc., makes it significant and (g) draws people's attention. Chamaraja Circle is another landmark in the city and it has straight axis to the K.R.Circle. The circle also acts as a focal point from the Ashoka road and Harding circle. It has square in composition with Dilwara-style carved brackets of elaborate design and Maharaja Chamaraja Wodeyar's statue erected in 1920. The gold plated dome and intricate carvings makes it important.

B. Focal point

'Focal point is a critical point of a distance function. Focal point focuses specifically a point of interest which makes a place unique in streets, market places of town. Focal point will be column, cross, clock tower which crystallises the situation and confirms this in the spot'. Silver Jubilee Clock Tower has been built to commemorate the Silver Jubilee of the then king Krishnaraja Wodeyar IV. Seventy Five (75'0) feet square tower topped with Indo Saracenic style and vertical symbol of congregation. It is located in the centre of the city and acts as a main focal point, located on the old procession street. The Krishna Rajendra circle which has the statue of the then king Krishnaraja Wodeyar as a focal point is located in the intersection of Sayyaji Rao road, Albert Victor Road and Devaraja Urs Road. Surrounding

structures respond to the circle in circular form, integrating the character and stylistic unity.

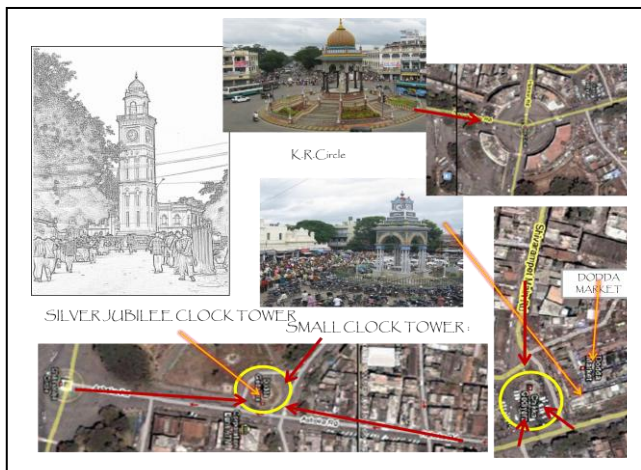


Fig. 2 Focal Point

C. Precinct

'A subdivision or district of a city or town forming a particular part of an urban area is precinct. When a group of buildings placed together having different or varied styles of architecture, then the area around it forms a precinct'. Krishnarajendra Hospital is an example of an entire building having a typical architectural style, thereby forming the precincts around it. The central dome, built in Vatican model, dominates the elevation. Tuscan, Ionic and Corinthian columns and Greek architecture presents a grand look, thereby providing area surrounding it a precinct. The hospital complex consisting of group of buildings with different specialization, like Cheluvamba hospital, K.R.hospital, Ophthalmology block and surrounded by Medical College together form a precinct. The Ambavilas Palace and its group of building, temples, landscape and public space within fort forms another relevant example of a precinct due to its distinct style of architecture within the premises. The other precincts are Devaraja market along with the 'small clock tower' (Chikka Ghadiyara), Town Hall Precincts, Gandhi Square Precincts, Old and Present Procession Street-Precincts and many more.



Fig. 3 K.R. Hospital Precincts

D. Public Square

'Public Square is a space used by the public. A public square can acts as the focal point, land mark and enclosure'. Harding Circle commemorates the Viceroy's visit to Mysore city in 1913. The circle is geometrically designed with six gateways facing each other. The roads split into six deviations, all of which are flanked with ornamental gateways, which in turn add to the aesthetic part of the circle. Vasavi circle in front of the Devaraja market including the Chikka Ghadighara form a public square. In an intersection wherein the JLB road and Irwin road meets near railway station, the Statue of Dr.Babu Jagajeevanram is installed in this intersection by replacing the beautiful water fountain circle with landscaped traffic rotaries which with urban form. Railway station is also a public square and it is the rendezvous point of all who board and disembark the train at this point.

E. Vista and Axis

'Foreground linked by background through different elements like landscape, water bodies or pathways etc., closed by a mass of building and it produces a sense of power and omnipresence'. The stretch of buildings on either side of the road creates a vista, with the foreground circle. Albert Victor Road leading from Harding circle to DC office via Chamaraja circle and Krishnaraja circle forms a vista. The street axis has avenue of trees and beautiful architectural landmarks on the same street. The pathway leading from Ashoka circle is a very good example of vista.

F. Nodes and Edges

'Nodes are strategic points in a city which the observer can enter. Primary junctions, transport transit, terminals and convergence of path. The circles and junctions forms the nodes. There are many nodes and the buildings or open spaces around them form the edges'. Krishna Rajendra Circle is a node, and four roads converge at this junction. The buildings at the edges respond to the node. A large number of vehicles moving towards the nodes because of proximity of location of city bus resulted in greater volume of traffic, congestion and delay. Traffic signals are installed to regulate the vehicular and pedestrian movement. Vishweswaraiah circle is also a node with four roads converging at this intersection. This junction is functioning as self operating rotary without traffic signals. Harding Circle is a self operating rotary with six roads converging at this rotary and all the roads have gateways. It is installed with water fountain and traffic signals. One of the interesting characters of Mysore city is that the building responds to the road edges in K.R.Circle, Ashoka circle and other prominent places. At all these points, the buildings respond to geometry of curvilinear pattern by converging towards the focal point which can either be a fountain, statue, and island. Even though, the buildings differ in their functions, the building styles follow the pattern of uniqueness.

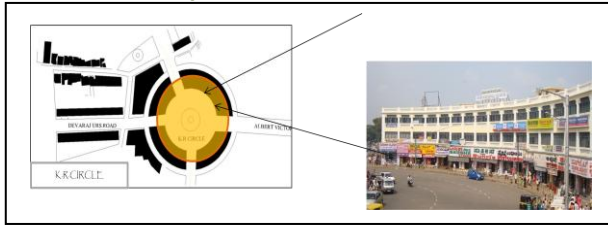


Fig. 4 Edges-K.R.Circle

G. Path

'Paths are the channels along which the observer customarily moves. Paths are nothing but pedestrian networks, which links the town together in a viable pattern. Continuity and access are always maintained'. All main roads in city core have pathways and are well regulated for the movement of traffic and pedestrians with signal synchronisation in the central area. Paths were provided with street furniture like lamp post, railings, ornamented sign boards etc.

H. Juxtaposition

'Juxtaposition is an act or instance of placing close together or side by side, especially for comparison or contrast. The unequal character of both is sharply brought together. It demonstrates a mixture of different elements'. Mysore has many heritage structures and these are vital for their architectural style. But due to the change in trend and demand for more commercial spaces, people started glass façade buildings by replacing old traditional architectural buildings. This change in urban form is seen more in the heritage area. Many buildings, which have come up in the recent past in the heritage area are not compatible and harmonious with the existing architecture.



Fig. 5: Juxtaposition

I. Public and Private Realm

'Public realm refers to the level of comfort of the public. Private realm refers to the view or perception which a person has, by looking at the exterior of the private building'. The streets used by people, their ease in using them are the public realm. The Albert Victor Road an example for this and creates a safe, attractive and accessible town at central environment. Avenue of trees, which gives a soothing view for the people who drive or walk on that way. The treatment of these areas of public realm is as important as the built development for vision.

J. Urban Imaginary: Gateways, Railings, Signage and Hoardings Gateways: Gateways are one of the prominent urban imaginary features of Mysore acting as the

welcoming element denoting power and traditional access to the Fort Area in the central. The gateways are diminishing in importance with every passing day due to lack of maintenance and roads widening.



Fig. 6 Gateways of Mysore City

Railings: The railings in Mysore city are traditional in style with different patterns made out of cast iron. There were varieties of railings found in different roads with floral and other patterns and these railings are damaged, misplaced and even stolen due to lack of maintenance and security.

Signages: Signages are symbols or words whose functions are to provide directions, identification, information and orientation. Signages are not addressed properly to establish harmony to outfit the heritage area due to absence of certain prototype designs which depicts some style of architecture of the place.

Hoardings: It is a large outdoor signboard structure erected for displaying advertisements. Hoardings are not compatible with the heritage area; either obstruct the view or cover the architectural characteristics of the buildings. In many places street names and valuable information about the buildings are covered by the hoardings.

VI. PROPOSED POLICY MEASURES

Mysore city is rich with built heritage structures of architectural, historical, cultural importance, but, built heritage character of Mysore city is dominated by urban design elements like, landmarks, vistas, nodes, axis, focal point elements, streetscapes, water bodies and parks and open spaces. Lack of control and insensitive approach by recent developments urban design elements are facing threats and due to excessive demand for commercial developments the existing architectural buildings/areas are undergoing architectural transformation, massing, modern materials with juxtaposition, deterioration, etc., are all incompatible with the existing architecture in the core area. Landmarks, nodes, focal elements, vista, skylines, have been affected by insensitive and intrusive developments in addition to 195 signage and hoardings which are incompatible with the existing areas in the palace surroundings. The following are the suggestions for improving the imageability in Mysore city.

- 1) Comprehensive urban design guidelines are to be introduced to protect and preserve the built structures in the heritage zones of Mysore city. The existing built-form, massing, setbacks, scale and architectural style are to be strictly monitored and maintained. Urban design elements which exist in the core area need to be protected to enhance the aesthetic quality.
 - 1) Architectural control in terms of height, bulk, facade style, character, elements, building materials, etc, to be strictly imposed in core area.
 - 2) Architectural control in relation to building height, facades treatment, building style, character, colour, materials usage, etc., may be imposed in the palace surrounding buildings/areas of primary zone.
 - 3) Architectural control to be imposed on Sayyaji rao road, Albert victor road, Ashoka road, Deavaraja Urs road, Irwin road, New Sayyaji rao road and Palace surroundings, so that architectural character of the street to be maintained in harmony with the heritage area
 - 4) All signages, hoardings, heritage plaque, information signs, to be compatible and designed to suite the existing architecture of the place.
 - 5) Street furniture to be designed to suite the heritage areas and placed at appropriate intervals.
 - 6) All the railings, sitting benches, compound wall details and sign boards should conformity with the heritage area.
 - 7) Electric light poles and fixtures must be consistent with the existing architecture of the place.
- Vol.3, No.5, International Journal on Recent Trends in Engineering and Technology (IJRTET), ISSN 2158-5563, May 2010.
 - [2]. Chidambara Swamy and Dr. B. Shankar, Reprising the Eternal Glory of Udaipur: Issues and Strategies for Heritage Conservation, Vol. 54, World Academy of Science and Engineering, Technology (WASET), June-2009
 - [3]. Eishas, Simon and Arthor, Gallion (1986), *The Urban Pattern*, CBS Publishers, New Delhi.
 - [4]. Feilden M Bernard (2000), *Conservation of Historic Buildings*, Architectural Press.
 - [5]. Government of India, Heritage Tool Kit for Preparation of City Development Plan under JNNURM, Ministry of Urban Development, New Delhi, November 2006.
 - [6]. Issar, T.P. (1991), *The Royal City - A Celebration of the Architectural Heritage and City Aesthetics of Mysore*, My tech Process Pvt. Ltd., Bangalore.
 - [7]. Lynch Kevin (1991), *The Image of the City*, Mc Graw-Hill, New York.
 - [8]. Madanipour, Ali (2003), *Public & Private Spaces of the city*, Rout ledge, New York.
 - [9]. Shibley, Plattus and Watson (2003), *Time - Saver Standards for Urban Design*, Mc Graw - Hill Companies, Inc.
 - [10]. Shirley, Peter and Moughti, Cliff (2005), *Urban Design: Green Dimensions*, Second Edition, Architectural Press.
 - [11]. Spirokostof (1992), *The City Assembled - The Elements of Urban Form Through History*, Thames & Hudson.
 - [12]. Tiesdell, Steven, Taner and Moughtin, Cliff (1999), *Urban Design: Ornament and Decoration*, Second Edition, Architectural Press.

VII. CONCLUSIONS

Mysore City is a royal city, and it has strong roots of urban design elements viz. landmarks, path, nodes, axis and urban imaginary which contributed significantly for good imageability of the city. The major heritage buildings, precincts and areas are located in the core area of the city. The development from 1860 to 1930 has contributed to the city's aesthetics, architecture, and beatification of the city and cultural heritage of the city. The development of architectural built heritage structures of Mysore city lead by Ambavilas palace as landmark and focal point of city's elements indicate that the city is meticulously planned and accompanied by distinctive monuments, royal mansions and other built forms; gardens, lakes and water bodies, boulevards and urban design elements like, focal points, vista, axis, landmarks, water fountains, statues, etc., make it undoubtedly the most important heritage components of the city and worth conserving it.

REFERENCES

- [1]. Chidambara Swamy and Dr. B. Shankar, Conservation Strategies for Heritage City: Mysore,

BIOGRAPHIES



Dr. B. Shankar received the B.E. degree in Civil Engineering in 1984, M.U.R.P degree in Urban and Regional Planning in 1989 and Ph.D degree in Urban and Regional Planning in 1997 from the University of Mysore, Mysore. He is working as Associate Professor in Urban and Regional Planning at the Institute of Development Studies, University of Mysore, Mysore. His research interests to include Urban Planning, Urban Poverty, Community Development, Heritage Conservation, and Planning Legislation



Dr. Chidambara Swamy received the Bachelor degree in Architecture in 1994 and M.U.R.P degree in Urban and Regional Planning in 1999 from the University of Mysore, Mysore. He is working as the Professor and Head, Department of Architecture, Adhiyamaan College of Engineering-Hosur.. His research interest includes, heritage planning and conservation, city planning.

Architecture and Heritage Resources of Mysore City

Dr. Chidambara Swamy¹ and Dr. B. Shankar²

¹(Professor and Head, Adhiyamaan College of Engineering, Hosur)

²(Associate Professor in Urban and Regional Planning, Institute of Development Studies, University of Mysore, Mysore)

ABSTRACT

Mysore city is known as the 'city of palaces'. It is an ancient, historical, cultural capital and a heritage city in India. The city has been recognised as a heritage city under the cultural tag both by the state and national governments. The total harmony of architectural buildings, sites, lakes, parks and open spaces and the back drop of Chamundi hills adds to the city's attraction. The city has long boulevards radiating from a well defined central axis, with well recessed public buildings balanced on either side, can be a model for any town planner. Architectural heritage includes not only individual buildings of exceptional quality and their surroundings or group of buildings providing a special setting by virtue of uniqueness of their architectural style, but also all areas and settings of cities which have historic or cultural interests. The city has both tangible and intangible heritage elements; with many urban design elements of built structure to include monuments, heritage buildings, precincts/ heritage areas and natural areas. A very few building have been identified by the State Archaeology Department and Mysore Urban Development Authority. This paper attempts to identify the heritage resources in the City of Mysore for conservation.

Key Words: Heritage Resources, Architectural Buildings, Tangible and Intangible elements.

I. INTRODUCTION

Mysore is the third largest city in the State of Karnataka and it had a population of 7,85,800 as per 2001 census. The name of Mysore was derived from *mahisha* (a demon). Formerly, the city was the state capital and head quarters of the Princely State of Mysore. It is situated at a distance 140kms from Bangalore, on the southern part of Karnataka State at 12° 18' North latitude and 76° 12' East longitude, and at an altitude of 770 mts above mean sea level. The city lies in a saucer shaped basin flanked by Chamundi hills on the south-east and a raised platform near Hinakal village on the west. The city has a salubrious climate and the temperature varies from 12° C to 35° C. It has an average annual rainfall of about 798mm. The city spreads across an area of 128.42sq.kms. The literacy rate is 82.8 percent. A majority of the city's population speaks Kannada language, while other languages such as Tulu, Tamil and Hindi are also spoken.

II. HERITAGE OF MYSORE

Mysore is a cultural and prime heritage city and it exhibits both tangible and intangible elements. It combines the historical facts and anecdotes with a harmonious combination of natural and built heritage. The city is known as 'cultural capital' of Karnataka. It was the capital of Wodeyar Kings who ruled Mysore Kingdom for many centuries and contributed significantly to make the city as a cultural centre including art, poetry and music. The city is as known city of palaces and the museums, art galleries and the festivities that take place during the period of *Dasara* which attract worldwide audience. An image of the Goddess Chamundeshwari is placed on a golden mantapa on the back of a decorated elephant and taken on a procession, accompanied by tableaux, dance groups, music bands, decorated elephants, horses and camel followed by torchlight parade. It has lent its name to dishes; Mysore Pak, Mysore Masala Dosa, art; Mysore Painting and sari; Mysore Silk Sari. Mysore is a classic example of architectural and cultural heritage. The total harmony of buildings, sites, lakes, parks and open spaces including backdrop of Chamundi hill adds to the city's aesthetics with different cultures and different styles of architecture. The heritage buildings have four distinct architectural styles viz. Indo-Saracenic, Traditional Hindu Style, Greco-Roman and Gothic (Pearl). Thus, the city exhibits both tangible and non tangible elements of heritage character, and therefore, the Government of Karnataka recognized the city as Heritage city and Government of India has selected the city for Urban Renewal Project under cultural and heritage tag and now the UNESCO also has shown interest in identify the city under Heritage tag.

Mysore city has both natural and built heritage components. The city has retained its studiously built character of a native princely city. The most imposing and majestic building in Mysore is the Ambavilas Palace, which is the focal point of the city. It was built in an Indo-Saracenic style. The city is characterized by buildings, gardens, boulevards, and planned markets all these were the contributions of Maharajas, Dewans, and their talented workmanship. Their architectural and urban design elements like vistas, focal points, landmarks, avenues, plazas etc., make it undoubtedly the most important tradition city in India. Albert – Victor road is beautifully laid down street, has a pathway beautifully laid within the Curzon park which and hugging the palace gate and fort with a moat on northern side of the palace as a landmark, represents the vista with edges. The

townscape of the city viewed from Chamundi hills present a skyline of clock tower, statues, palaces, mansions depicts the beauty of the city.

III. HERITAGE RESOURCES OF MYSORE

The heritage resources of Mysore are classified in two categories namely *tangible* elements viz. built heritage resources of significant buildings, structures, monuments, installations associated with architectural, cultural, social, political, economic; precincts of environmental significance or scenic beauty of natural areas, hillocks, lakes/tanks, gardens, street pattern, land marks etc., and *intangible* elements viz. culture, events, arts and crafts, festivals, cuisine, customs, dresses, etc., and are given in the following table.

Table: 1 Heritage Resources of Mysore

TANGIBLE ELEMENTS	
Elements	Heritage Areas/Buildings
Built Structures	
Architectural Monuments	a) Indo-Sarcenic: Ambavilas Main Palace, City Corporation Building b) Traditional Hindu Style: All Temples , Jaganmohan Palace c) Greco-Roman: The Deputy Commissioner's office, CFTRI Building, Krishnaraja Hospital d) Gothic- St. Philomena's Cathedral and Hardwick Church e) European Classical Style: Government House, Lalith Mahal Palace f) Traditional Bungalows: Agraharas
Heritage Areas /Precincts	a) The Palace Complex b) Royal Mansions of Mysore c) Deveraja Market d) Vani Vilasa Market e) Sayaji Rao Road Procession Street f) Church Precincts g) Town Hall and Clock Tower Precincts h) K.R.Hospital Area i) Agraharas of Mysore j) Landsdowne Market k) Chamarajendra Technical Institute l) Maharani Government Women's College m) University Campus
Natural Areas	a) Kukkarahalli and Karanji Lakes environs b) Chamarajendra Zoo c) Chamundi Hills
INTANGIBLE ELEMENTS	
Elements	Heritage components
Culture	Royal Culture
Arts and Crafts	Sandal Wood Carving,
Festivities	Mysore Dasara
Spiritual	Yoga, Meditation
Costumes	Mysore Peta, Mysore Silk Sari
Painting, Poetry and Music	Vijaya Nagar Style of Painting, Paintings of Ravi Verma Great Poets like Kuvempu
Dance	Bhartha Natyam
Fragrance	Jasmine
Cuisine	Mysore Pak, Masala Dosa, Chitranna,

IV. ARCHITECTURAL BUILDINGS

The buildings of Mysore city have been influenced by various styles of architecture, and some of the important styles are;

- 1) Indo – Sarcenic style
- 2) Traditional Hindu style
- 3) Greco – Roman style
- 4) Gothic style
- 5) European Classical style.
- 6) Traditional Bungalows.

A. Indo- Sarcenic Architecture

The Indo Sarcenic buildings of Mysore city is led by Ambavilas Palace. Mixtures of Hindu and Islamic characteristics of architecture are found in all these buildings. The Islamic architectural influences found in these buildings, which were used Islamic pointed and cusped arch openings found in the verandas, projecting minarets near the entrance portico, big bulbous domes in the centre and in the corners of the building on their roof level.



Fig.1 Ambavilas Palace

The Hindu architectural features are the curvilinear chatris, banana and lotus stem brackets attached to the column capitals, motifs of the Hindu gods and goddesses in studiously created niches. The interiors of the buildings have colonnaded court yards with Hindu style architectural motifs on the column brackets. The doors of the palace are carved with figures of Hindu gods and goddesses.

B. Traditional Hindu Style

Jagan Mohan Palace building is the best example of traditional style of architecture in Mysore city. The visual effect of the edifice is enhanced by an appropriately deep foreground.



Fig.2: Jagan Mohan Palace

The rich and eye catching facade is composed of triple gate with rich decoration, rectangular and arched niches on the facade with graduated end bays punctuated with decorative pilasters. The shikara dominates the facade giving the temple look to the palace. All temples in Mysore city exhibit the traditional Hindu style of architecture. Each temple has a Garbhagruha, sukanasi, Navaranga and Mukhamantapa. The Agrahara houses are

another example of traditional style with simple and functional buildings with common masonry wall.

C. Greco – Roman Style

A Vatican dome rising on a drum in circular and octagonal shape dominates the elevation in these structures. The column styles were designed on Tuscan, Ionic and Corinthian; arched and plastered colonnades from the two wings. Greek deities define the tier and the balustrade parapet bends are an agreeable addition to a rich composition. The Chaluvamba Mansion and Krishnaraja Hospital are the best examples for this style.

Krishnarajendra Hospital: Built in 1876, this stately building is predominantly Greco-Roman architecture. Column styles, both in the central pediment and at either end of the facade, are varied between the grounds – floor and the first floor- fluted Tuscan, Ionic and Corinthian. Arched and plastered colonnades from the two wings. A huge dome resting on an octagonal drum, dominates the elevation.



Fig.3: K.R.Hospital

D. Gothic Style:

Spires or long tapering roof-like elongated pyramids that are commonly found in churches are the typical characteristics of gothic style. The main hall or nave with multiple moulded columns culminates in stately arches. Alter is set against arched screens of stone works which are in harmony with the arched vertical lines and tapering vaults of the structure. Pointed arches are the features and the external structure. St. Philomena's Cathedral and Hardwick church are the best example of Gothic style of architecture.

St.Philomenas Church: The plan of the church is Byzantine, very typical of any church. The main hall or nave is designed to accommodate 800 worshippers. The floor plan of the cathedral is in the form of a cross. The long parts of the cross are the nave which is the congregation hall. The two arms of the cross are the transepts. The fourth part containing the altar and the choir is the crossing.

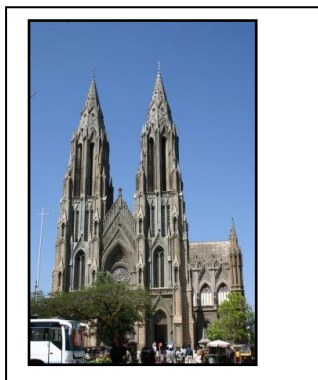


Fig. 4: St. Philomena's Church

E. European Classical Style

These structures have vast garden settings with elegant approach on the front side. They usually consist of a central atrium leading to a banquet hall, with elegant rooms on either side. These structures have an elegant portico. These structures are the royal architectural elements in Mysore.

Lalit Mahal Palace: The building was designed by E.W. Fritchley in 1931 and this was totally aimed at the European visitors coming to Mysore city. The European elements used are regimented pavilion, spherical domes with lanterns placed on colonnaded drums. The building is a two storey composition and it is famous for its twin ionic columns – a projecting porch on the ground floor. On this rests slightly recessed pediment pavilion on the first floor and spherical domes with lanterns, dome which dominates the elevation rises above the circular entrance hall. The interior is highly decorated with stain glass, imported tiles, luxury fittings and Venetian marbles. The interior is a show piece of valuable skills of local craftsman, seen in richly laid decorative motifs on the walls and ceilings, carved wooden shutters and wall panels and myriad details and touches of regal embellishment.



Fig. 5: Lalitha Mahal Palace

F. Residential Architecture

Residential architecture of Mysore city is lead by traditional vernacular architectural buildings with sloped Mangalore tiled houses, colonial bungalows, monkey topped bungalows and a mixture of colonial and Indian decorative style bungalows.

a) Colonial Bungalows : This style of architecture is seen in big bungalows extensively seen in the south east part of the Mysore city. The buildings of the Administrative Training Institute (ATI) campus, Mounted Police building, DGP office are some of the interesting examples of this style of architecture. All these buildings are wooden sloped roof structures and are interesting in terms of their simple planning. The simple variation of roof heights, the use of dormer windows, interesting floral patterns of eve-board and gable end detailing have made the elevations of these buildings look interesting.

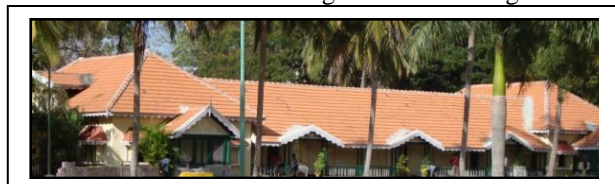


Fig.6 : Administrative Training Institute

b) Monkey Topped Bungalows: Monkey topped bungalows are again a precious part of the Mysore's architectural heritage. The bungalow, as an architectural prototype, has been perhaps the most "endangered species" in the world heritage of architecture. Although, these types of buildings contributed greatly to the architectural image, the most of the privately owned bungalows have deteriorated due to lack of maintenance.

c) Band House: Band house was built in the twenties as a practice hall for the palace band; it now houses the State Reserve Police Mounted Company band. Situated in a garden setting overlooking the Nishat Bagh, the structure is a composition of gables and dormers over the tiled roof and monkey topped lean to verandas. It has a very symmetrical planning which is reflected in the elevation as well.

d) Agraharas: Agraharas which were traditional residential buildings of Mysore, where Brahmins were accommodated. Each of these agraharas was built by the king as a symbol of some important event during his kingship. These are traditional row houses and are predominantly built in Hindu architecture with common walls for a stretch which is then broken at regular intervals. There are many agraharas in the city, viz. Veene Sheshanna Agrahara, Cheluvamba Agrahara, Devamba Agrahara. Srinivasa and Ramanuja Agraharas, which were known for planning and architectural aesthetics.

Ramanuja and Srinivasa Agrahara: Typical residential houses constructed during the first two decades of the century. The plan is in U- shape with landscaped park and around this row houses were built. It also provides facilities for community socializing and play area for children's. Every two room house has a small compound, or veranda and backyard with a common wall construction system.



Fig.7: Traditional Agraharas

V. CULTURAL HERITAGE (INTANGIBLE)

Mysore is known as the "Cultural Capital" of the state and is a fine combination of the historic heritage and contemporary achievements of the city. The Wodeyars were patrons of art and culture and have contributed significantly to the cultural growth of the city. The continuous patronage and support of the kings in every field led to the evolution of a distinct style known as the "Mysore Style" in all the fields like painting, architecture,

music, poetry etc.,. The festivals of Mysore are a fascinating indicator to the cultural unity of the people. Inhabited by people of different faiths and beliefs Mysore becomes a common cultural canopy under which the various social festivals are celebrated by one and all. Dasara festival is a major festival celebrated by the people of Mysore with enough mirth and enthusiasm.

A. Mysore Dasara

Dasara festival has both mythological and historical background and has its origin in the great epic of Mahabharata. The legendary pandava brothers celebrated the festivals to mark of triumph of good over evil. They worshipped hidden weapons which are now being celebrated as "ayudha pooja". The Navaratri is associated with Devi Purnima, celebrated to mark the destruction of evil.



Fig. 8: Dasara Festival

Dasara is the Nadahabba (State festival) of Karnataka state, and Mysore is well known for the festivities that take place during the Dasara period. It is also known as Navaratri (Nine nights) and 10 day festival and it usually falls in the month of October. During this period, various cultural and religious programmes highlighting dance, music and culture of the state of Karnataka are performed. Mysore palace and surrounding areas and buildings are illuminated on all the ten days and prominent cultural programmes are held in Palace and surrounding grounds. The festivities commence with a pooja performed to the goddess Chamundeswari a top the Chamundi hills. One of the main attractions of the festival is Dasara exhibition, which starts during the dasara and continues for around two months. It is held in the grounds opposite to the Mysore palace. The conclusions of the festivities are marked by a colourful Dasara procession popularly known as *Jamboo Savari*. The main attraction of the procession is that the idol of goddess Chamundeshwari is carried in *Golden Howdah* on top of an elephant. Various tableaux created by different state organizations participate in the procession. Musical bands belonging to state police lend music to the procession. The culminating program of the Dasara festivities is the torch-light parade and is also known as Panjina Kavayattu held at night in the Bannimantap grounds on the outskirts of the city.

B. Art, Crafts and Cuisine

Mysore is a land of artists and is known to people for their skills. Mysore art and handicrafts reflects the rich heritage and cultural aura of the city which includes paintings, yoga and silk textiles. Mysore region is rich of natural resources like Sandal wood, silk, the best quality Jasmine flowers which are referred to as Mysore Mallige. Mysore silk is woven into a range of cloths, like Mysore peta, shawls, saris etc. The most famous of them are Mysore silk sari and Mysore silk peta (Turban). Mysore cuisine includes a delicious palate of food with rice as the main ingredient, besides common items like dosa, idli, utthapam, vada sambar and different types of dosa are popular. Traditional lunch of Mysore is a splendid spread that includes a cereal salads like kosambari, pappad, palyas (vegetable salads), chitranna (rice with lime), vangibath and pulivogare. Mysore pak is the most important sweets made of pure ghee are very popular. Mysore is an important spiritual tourism destination.

VI. ISSUES AND APPROACHES

Mysore has extremely rich and varied cultural heritage through its tangible and intangible heritage resources. The heritage resources is threatened by many factors namely uncontrolled developments without any harmony, environmental pressures, and lack of inventories of heritage resources, inadequate heritage legislations and development control, low levels of funding, inadequate expertise, and political will. Besides, built heritage including heritage buildings, monuments and areas are threatened by the decay, obsolescence, deterioration, ignorance. The development control includes zoning regulations, building bye-laws and sub-division regulations are not adequate to prescribe the comprehensive heritage rules and regulations for identifying and managing the heritage areas effectively

The State Archaeological Department has identified few monuments in the city for protection and preservation, but it has no control over the areas beyond protected limits. The planning legislations tends to factor the concept of monuments by neglecting the other types of heritage structures such as built environment, urban design elements, built structures, architecture, imageability and landscapes. For planning and conservation of heritage areas, legislative provisions of the Karnataka Town and Country Planning Act, 1961 is inadequate. The conservation of the heritage areas are to be made as an integral part of Master Plan. The plan will be a statutory document which mandates the Planning Authority (Mysore Urban Development Authority) to undertake conservation measures with detailed planning studies, assessment of heritage areas and involvement of all the stakeholders including local authorities, agencies, NGOs and public.

VII. CONCLUSIONS

Mysore is an historic city ruled by Wodeyars for many centuries and the Wodeyars were patrons of art and culture and have contributed significantly to the cultural

growth of the city. Mysore city is a classic example of architectural and cultural heritage. The prominent styles of architecture are (a) Indo– Sarcenic style (b) Traditional Hindu style (c) Greco – Roman style (d) Gothic style (e) European Classical style and (f) Traditional Bungalows. As a land of the mighty maharajas Mysore has always been an appealing place of grandeur. The city has living heritage in the form of tangible and intangible resources. The total harmony of buildings, sites, lakes, parks and open spaces of Mysore and the back drop of Chamundi hill adds to the city's attraction. The heritage resources are not been addressed properly. In order to address these issues, the conservation of the heritage areas is to be made as an integral part of Master Plan.

REFERENCES

- [1]. Chidambara Swamy and Dr. B. Shankar, Conservation Strategies for Heritage City: Mysore, Vol.3, No.5, International Journal on Recent Trends in Engineering and Technology (IJRTET), ISSN 2158-5563, May 2010.
- [2]. Chidambara Swamy and Dr. B. Shankar, Reprising the Eternal Glory of Udaipur: Issues and Strategies for Heritage Conservation, Vol. 54, World Academy of Science and Engineering, Technology (WASET), June-2009
- [3]. Government of India, Heritage Tool Kit for Preparation of City Development Plan under JNNURM, Ministry of Urban Development, New Delhi, November 2006.
- [4]. Karnataka Town and Country Planning Act. 1961. Department of Town Planning. Govt. of Karnataka, 2006.
- [5]. Report on JNNURM by STUP Consultants Pvt. Ltd. for Department of Tourism, Karnataka on Heritage and Urban renewal of Heritage core under J.N.NURM Scheme detailed
- [6]. Thakur, Nalini (1997), "Rich Past, Dismal Present", Indian Architect and Builder, July.
- [7]. Thapar, B.K. (1989), "Reflections: On the Role of INTACH in India's Conservation Movement", Architecture + Design, Nov-Dec.
- [8]. Urs Nanjaraja (2007), Mysore: Noorinnooru Varshgala Hinde, Abhiruchi Prakashana, Mysore.

BIOGRAPHIES

Dr. Chidambara Swamy received the Bachelor degree in Architecture in 1994 and M.U.R.P degree in Urban and Regional Planning in 1999 from the University of Mysore, Mysore. He is working as the Professor and Head, Department of Architecture, Adhiyamaan College of Engineering-Hosur.. His research interest includes, heritage planning and conservation, city planning.



Dr. B. Shankar received the B.E. degree in Civil Engineering in 1984, M.U.R.P degree in Urban and Regional Planning in 1989 and Ph.D degree in Urban and Regional Planning in 1997 from the University of Mysore, Mysore. He is working as Associate Professor in Urban and Regional Planning at the Institute of Development Studies, University of Mysore, Mysore.. His research interests to include Urban Planning, Urban Poverty, Community Development, Heritage Conservation, and Planning Legislation.

Design a Robust PI Controller for Line of Sight Stabilization System

Amr A. Roshdy¹, Chengzhi Su², Hany F. Mokbel³, Yu Zheng Lin⁴, and Tongyu Wang⁵
^{1,2,3,4,5}(College of Mechanical and Electric Engineering, Changchun University of Science and Technology, Changchun130022, China)

ABSTRACT

Based on the minimization of integral of time-weighted absolute error index (ITAE), a robust proportional-integral (PI) controller is designed to achieve high performance and high stabilization precision for the line of sight (LOS) stabilization system. The system ability to reject outer disturbance, attenuate the measurement noise and its robustness are investigated. The proposed model exhibits a simplicity and applicability for designing a robust control system. Simulation results demonstrate the effectiveness of the designed controller, which offers an excellent performance in the presence of uncertainty and nonlinearity, Improves the outer carrier disturbance rejection, attenuates the measurement noise.

Keywords - integral of time-weighted absolute error index (ITAE), proportional-integral (PI), line of sight (LOS).

1. INTRODUCTION

In recent years, modern control systems are commonly uses the optical sensors such as CCD cameras, optics, laser seekers for target tracking. Due to the disturbance from the carrier, the electro- optical equipment can not work normally and finally lose the target. The line of sight (LOS) stabilized technology is used to isolate the sensor's LOS from carrier disturbance in order to guarantee accurate aiming and tracking for the target at the inertial space [1-4].

Physical systems and external environment is somewhat difficult to model precisely. The external environment may change in an unpredictable manner, and may be subject to significant disturbances. The design of the control systems in the presence of significant uncertainty requires the designer to seek about a robust system. A robust control system exhibits the desired performance despite the presence of significant process uncertainty [5]. The control system is described robust when it has low sensitivity to process change, stable over the range of parameter variations, and the performance continues to meet the specifications in the presence of a set of changes in the system parameters [6].

One of the most popular controllers widely used in the control field is the proportional-integral-derivative (PID) controller [7-9]. Several methods have been proposed for the LOS stabilization control system using PID and other types of controller, however, most of these methods are either concern only with achieving the required performance regardless the effect of process change, uncertainty of the system[10,11], or it is complex and can not be realized easily[12-16].

In this paper, a robust PI controller is applied in order to achieve high control system performance with high robustness in a simple and applicable method based on the minimization of integral of time-weighted absolute error (ITAE) index.

2. ROBUST PI CONTROLLER

2.1. Error signal analysis and system sensitivity

The tracking error $E(s)$ for a closed loop feedback control system shown in Fig. 1 can be defined as:

$$E(s) = R(s) - Y(s) \quad (1)$$

Where $R(s)$ and $Y(s)$ are the system input and output signals, respectively.

For a unity feedback system the output signal $Y(s)$ can be defined as:

$$Y(s) = \frac{G_c(s) G(s)}{1 + G_c(s) G(s)} R(s) + \frac{G(s)}{1 + G_c(s) G(s)} T_d(s) - \frac{G_c(s) G(s)}{1 + G_c(s) G(s)} N(s) \quad (2)$$

Where $G(s)$ is the motor and platform transfer function, $G_c(s)$ is the controller transfer function, $T_d(s)$ and $N(s)$ are the disturbance and measurement noise signals, respectively.

For $L(s) = G_c(s) G(s)$ and using (1) the tracking error can be defined as:

$$E(s) = \frac{1}{1 + L(s)} R(s) - \frac{G(s)}{1 + L(s)} T_d(s) + \frac{L(s)}{1 + L(s)} N(s) \quad (3)$$

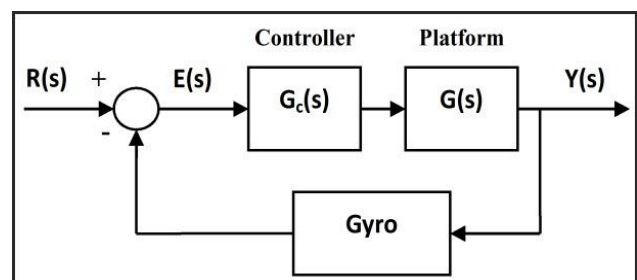


Fig.1. System configuration

System sensitivity is defined as the ratio of the change in the system transfer function to the change of a process transfer function (or parameters) for a small incremental change.

$$S = \frac{\partial T / T}{\partial G / G} = \frac{\partial \ln T}{\partial \ln G} \quad (4)$$

The closed-loop system transfer function T(s) is:

$$T(s) = \frac{G_c(s)G(s)}{1 + G_c(s)G(s)H(s)} \quad (5)$$

For unity feedback system, that is, $H(s) = 1$ and using (4), the sensitivity of the feedback system is:

$$S_G^T = \frac{1}{1 + G_c(s)G(s)} \quad (6)$$

2.2. Disturbance rejection and Measurement noise attenuation

For zero input and zero noise signals, $R(s) = N(s) = 0$, the equation (3) becomes:

$$E(s) = -S(s)G(s)T_d(s) = \frac{G(s)}{1 + L(s)}T_d(s) \quad (7)$$

For good disturbance rejection, the loop gain should be large over the frequencies of interest that associated with the expected disturbance signals.

For zero input and zero disturbance signals, $R(s) = T_d(s) = 0$, the equation (3) becomes:

$$E(s) = C(s)N(s) = \frac{L(s)}{1 + L(s)}N(s) \quad (8)$$

Where $C(s)$ is the complementary sensitivity.

The effect of noise signal on the tracking error can be decreased by increasing the loop gain $L(s)$.

If the controller is designed such that $L(s) \ll 1$, the complementary sensitivity function $C(s)$ will be small and $C(s) \approx L(s)$, then the noise will be attenuated.

In practice, the disturbance signals are often low frequency, while the measurement noise signals are often high frequency. In order to design a robust controller that can reject the disturbance signals and attenuate the measurement noise, the controller should be high gain at low frequencies and low gain at high frequencies.

2.3. Design of Robust PI Controller

The robust PI controller design is done through three steps: The first step is done by selecting the natural frequency ω_n and the damping ratio ζ of the closed loop system which specify the required settling time and percent over shoot, respectively. From Fig. 2 [5] or (9). The damping ratio ζ is decided to specify the percentage of overshoot.

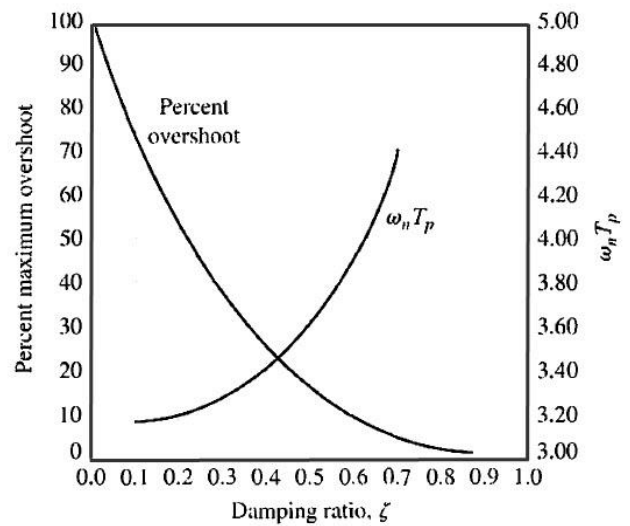


Fig.2. Percent overshoot versus damping ratio.

$$P.O = 100 \exp(-\zeta\pi / \sqrt{1-\zeta^2}) \quad (9)$$

The natural frequency of the closed loop system is calculated using (10) for the required settling time and damping ratio,

$$T_s = 4\tau = \frac{4}{\zeta\omega_n} \quad (10)$$

Where T_s is the settling time, τ is the time constant, ζ is the Damping ratio, and ω_n is the closed loop natural frequency.

Secondly, the two PI coefficients are calculated by using the appropriate optimum equation (Table (1)) and the calculated natural frequency ω_n to obtain $G_c(s)$.

Table 1
The optimum coefficient of $T(s)$ based on the ITAE criterion.

$s + \omega_n$
$s^2 + 1.4\omega_n s + \omega_n^2$
$s^3 + 1.75\omega_n^2 s^2 + 2.15\omega_n^2 s + \omega_n^3$
$s^4 + 2.1\omega_n^3 s^3 + 3.4\omega_n^2 s^2 + 2.7\omega_n^3 s + \omega_n^4$
$s^5 + 2.8\omega_n^4 s^4 + 5.0\omega_n^3 s^3 + 5.5\omega_n^3 s^2 + 3.4\omega_n^4 s + \omega_n^5$
$s^6 + 3.25\omega_n^5 s^5 + 6.60\omega_n^2 s^4 + 8.60\omega_n^3 s^3 + 7.45\omega_n^4 s^2 + 3.95\omega_n^5 s + \omega_n^6$

Finally, a pre-filter $G_p(s)$ is designed to eliminate the zeros in the closed-loop system transfer function and convert it to the general closed loop transfer function in the form:

$$T(s) = \frac{Y(s)}{R(s)} = \frac{b_0}{s^n + b_{n-1} s^{n-1} + \dots + b_1 s + b_0} \quad (11)$$

The coefficients that will minimize the ITAE performance criterion for a step input have been determined for the general closed loop transfer function [17].

3. SIMULATION STUDY

In this model, the plant under consideration consists of a gimbaled payload of 0.05 kg.m² moment of inertia. A rate gyro with scale factor (SF) 500 mV/ %s is used to measure the angular rate of the gimbal in azimuth, the open loop transfer function of motor and gimbal with payload is 50/(0.05s+1).

3.1. Parameter tuning and design of controller and prefilter

Based on these parameters, simulation of the stabilization loop that controlled by robust PI controller is carried out on the azimuth axis. The PI controller parameters (K_p, K_i) are calculated using the optimization algorithm based on the minimization of integral of time-weighted absolute error (ITAE) index. The desired dynamic performance of system imposes that: $T_s=0.02s, P.O < 5%$, and zero steady state error. The optimal PI controller with best ITAE is designed as:

$$G_c = 0.76 + \frac{163.3}{s} \tag{12}$$

The closed loop transfer function without pre-filter is:

$$T(s) = \frac{163260(0.0047s + 1)}{s^2 + 400s + 81640} \tag{13}$$

To eliminate the zeros in the closed-loop system transfer function, improve the over shoot and system performance, a pre-filter $G_p(s)$ should be designed as:

$$G_p = \frac{0.5}{0.0047s + 1} \tag{14}$$

Then the overall system transfer function with pre-filter is:

$$T_o = \frac{81630}{s^2 + 400s + 81630} \tag{15}$$

Fig. 3 shows the system response to a unit step without disturbance and noise. As the figure shows, settling time and percent overshoot satisfy the required performance, and zero steady state error is also satisfied.

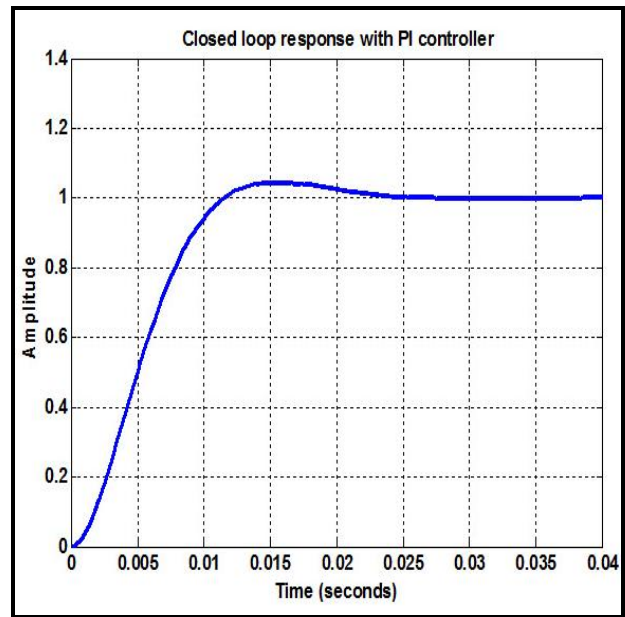


Fig.3. Step response of the PI controlled system without disturbance and noise.

Fig. 4 shows the bode diagram of the closed loop system with the robust PI controller (continuous line) and the output sensitivity (dashed line). As shown in the figure, the output sensitivity is very low at low frequencies. This means that the sensitivity of the system to the process change is very low.

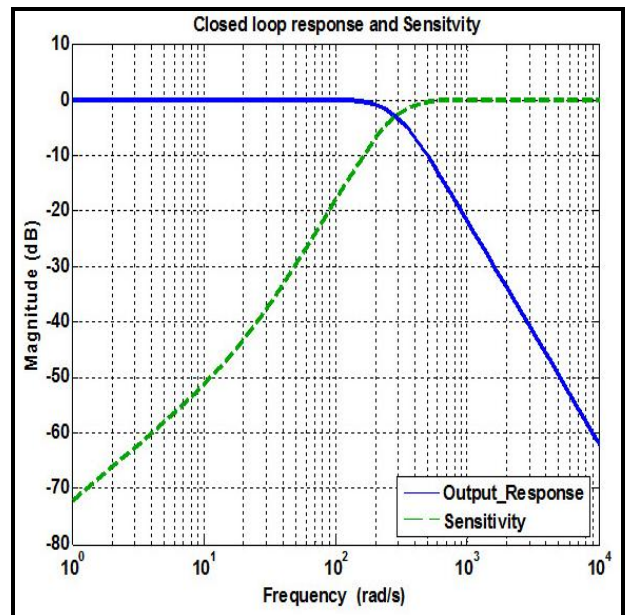


Fig.4. Bode diagram of the robust PI controlled system.

3.2. Performance of disturbance rejection and noise attenuation

Fig. 5 shows the line of sight precision with gyro noise signal shown in Fig. 6 under no outer disturbance. As the figure shows, the stabilization precision of PI controller is less than 0.02 %s, which indicates that this kind of controller can attenuates the nonlinear gyro measurement noise.

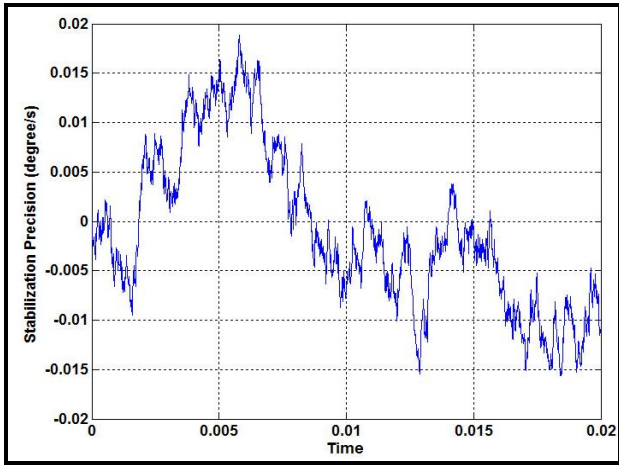


Fig.5. LOS stabilization precision without disturbance.

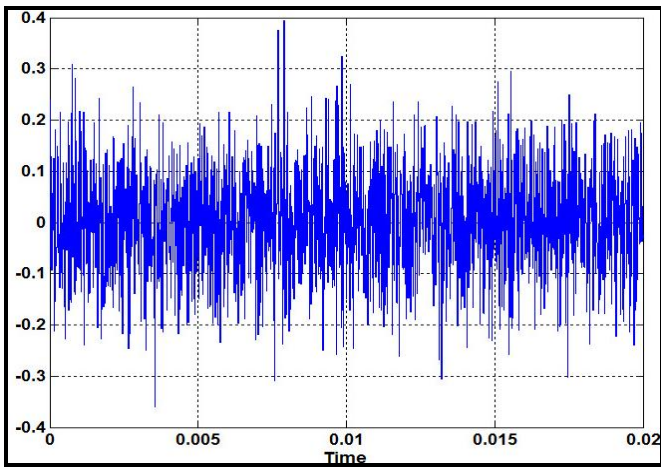


Fig.6. Gyro signal noise.

Fig. 7 shows the line of sight precision with gyro noises under the disturbance of sinusoidal signal with amplitude of 30°/s and frequency 1 Hz. It can be seen that PI controller provides a good stabilization precision.

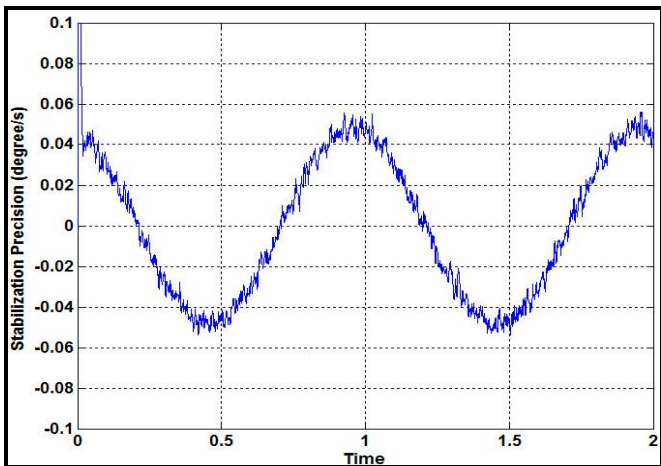


Fig.7. LOS stabilization precision with sinusoidal disturbance.

3.3. Robustness of PI controller

Fig. 8 shows step response of the PI controlled system when the payload changes $\pm 50\%$. Fig. 9 shows step response of the PI controlled system when the motor parameters changes $\pm 50\%$. It can be indicates that the PI controller that designed based on minimization of integral of time-weighted absolute error (ITAE) index has a good robustness.

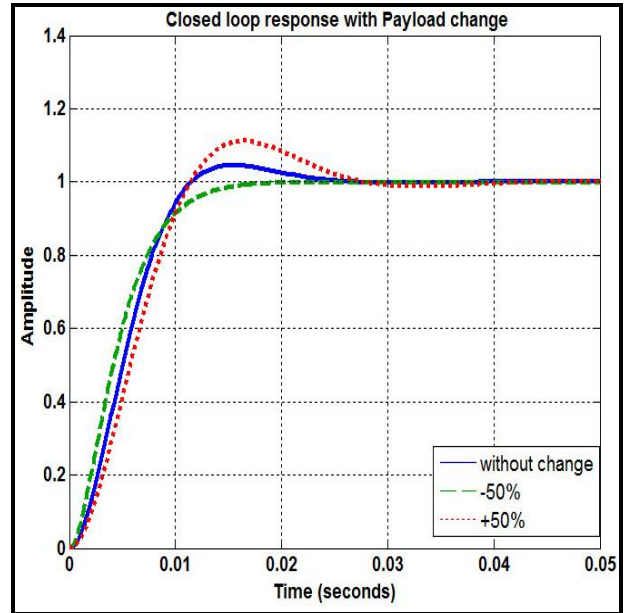


Fig.8. Step response of the PI controlled system when the payload changes $\pm 50\%$.

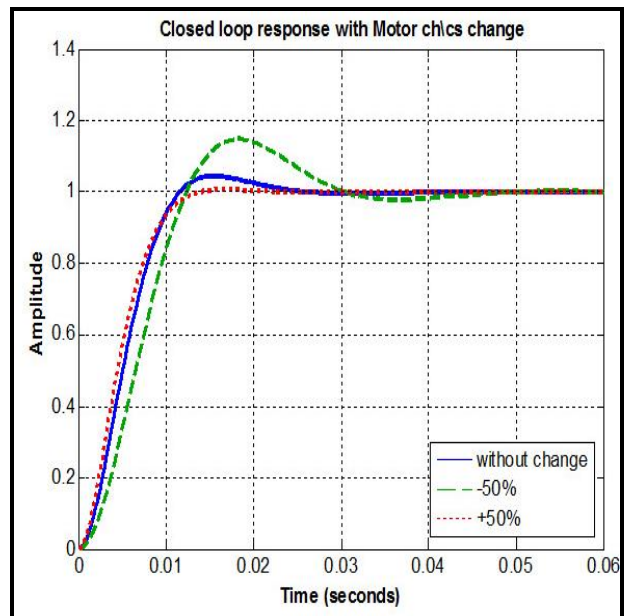


Fig.9. Step response of the PI controlled system when the motor parameters changes $\pm 50\%$.

4. CONCLUSIONS

A design of robust PI controller for the LOS stabilization system that has some nonlinearity and uncertainty is introduced. The optimization based on the minimization of integral of time-weighted absolute error (ITAE) index is used to calculate the PI parameters. The results show that the designed controller specified the required performance, 0.02s settling time, less than 5% overshoot percentage, and zero state error is achieved. The system improves the outer carrier disturbance rejection, and attenuates the measurement noise. The stabilization precision of the control system is found to be about 0.02 %. In addition, the system sensitivity to process change (payload, motor parameters) is low and the controller has a good robustness. The proposed design model is simple, applicable, which achieves high specification and high robustness at the same time.

REFERENCES:

- [1] T.H. Lee, J.H. Nie, and M.W. Lee, A fuzzy controller with decoupling for multivariable nonlinear servo-mechanism with application to real-time control of a passive line of sight stabilization system, *Mechatronics*, 7(1), 1997, 83-104.
- [2] T.H. Lee, K.K. Tan, and M.W. Lee, A variable structure augmented adaptive controller for a gyro-mirror line of sight stabilization platform, *Mechatronics*, 8, 1998, 47-64.
- [3] T. H. Lee, S.S. Ge, and C.P. Wong, Adaptive neural network feedback control of a passive line of sight stabilization system, *Mechatronics*, 8, 1998, 887-903.
- [4] K.C. Tan, T.H. Lee, E.F. Khor, and D.C. Ang, Design and real-time implementation of a multivariable gyro-mirror line-of-sight stabilization platform, *K.C. Tan et al. fuzzy sets and systems*, 128, 2002, 81-93.
- [5] R. C. Dorf, *Modern control systems* (Twelfth ed., Prentice-Hall, 2011).
- [6] G. Zames, Input-Output feedback stability and robustness, *IEEE Control Systems*, 1996, 61-66.
- [7] J.G. Ziegler, and N.B. Nichols, Optimal settings for automatic controllers, *ASME*, 64, 1942, 759-768.
- [8] K.J. Astrom, and T. Haglund, Automatic tuning of PID Controllers, first ed. *Research Triangle Park, NC: Instrum. Soc. Amer*, 1988
- [9] K.J. Astrom, and T. Haglund, PID Controllers: Theory, Design and Tuning, second ed. *Research Triangle Park, NC: Instrum. Soc. Amer*, 1995
- [10] P.J. Kennedy, and R.L. Kennedy, Direct versus indirect line of sight (LOS) stabilization, *IEEE transaction on control systems technology*, 11(1), 2003, 3-15.
- [11] Cheng Jia, Wang Xuanyin, Tong Nanjian, and Li qiang, Research on the stabilization and automatic tracking control in heading using the electric-driven turntable with great load, *Proceeding of ISFP*, 2007, 6-8.
- [12] Huang Yi, Tang Xiaobo, and LV Junfang, Design and simulation of MIMO QFT stabilization controller of an airborne electro-optical tracking and pointing platform, *Asia simulation conf, the 6th Int. Conf. on system simulation and scientific computing, Beijing*, 2005, 24-27.
- [13] Byoung-Uk Nam, Hano-Seong Kim, Ho-Jung Lee, and Dong-Hyun Kim, Optimal speed controller design of the two inertial stabilization systems, *World academy of science, engineering and technology*, 4, . 2008, 155-160.
- [14] Tang Zhiyong, Pei Zhongcai, and Wu Baolin, Research on image stabilizing system based on gyro-stabilized platform with reflector, *Proceeding of SPIE*, 2008, 7128: 71281A.
- [15] Yiming Man, Jianwei Gong, Huiyan chen, Yanhua Jiang, and Yuwen Hu, Design optimization of control parameters for strap down line of sight stable tracking platform based on Taguchi method. *IEEE*, 2009.
- [16] Wei Ji, Bo Xu, and Jinliang Guo, Compound control with hysteresis-band switching for LOS stabilization system, *IEEE*, 2010.
- [17] D. Graham, and R.C. Lathrop, The synthesis of optimum response: criteria and standard forms. *Transaction of the AIEE*, 72(2), 1953, 273-288.

Matlab/Simulink Modeling of Novel Hybrid H-Bridge Multilevel Inverter for PV Application

SRINATH. K

M-Tech Student, Power Electronics and Drives,
Department Of Electrical And Electrical Engineering,
Koneru Lakshmaiah University, Guntur,(A.P),India.

DR. P. LINGA REDDY

Professor,
Department Of Electrical & Electrical Engineering,
Koneru Lakshmaiah University, Guntur,(A.P),India.

Abstract- This paper presents a single-phase multistring Multi-level photovoltaic (PV) inverter topology for grid-connected PV systems with a novel hybrid H- bridge inverter. The proposed novel cascaded Hybrid H-bridge produces higher voltage levels with less number of devices. This will reduce the number of gate drivers and protection circuits requirement, this in turn reduces the cost increase the reliability. Design Procedure for various components of single Hybrid H- bridge cell is given. A cascaded Grid connected PV topology is proposed. Finally a Matlab/Simulink based model is developed and simulation results are presented.

Keywords- PV system, Multilevel Inverter, Cascaded H-Bridge.

I. INTRODUCTION

As the PV system is clean and large enough in the natural quantity available, it has been spotlighted as the future energy sources of promising potentiality, due to the stable supply of the energy and alternative method of responding to the problem of the earth environment followed by the increase of the demand for the electric power supply. Solar-electric-energy demand has grown consistently by 20%–25% per annum over the past 20 years, which is mainly due to the decreasing costs and prices. This decline has been driven by the following: 1) an increasing efficiency of solar cells; 2) manufacturing-technology improvements; and 3) economies of scale [2]. A PV inverter, which is an important element in the PV system, is used to convert dc power from the solar modules into ac power to be fed into the grid. A general overview of different types of PV inverters is given in [3] and [4].

In recent years, multilevel converters have shown some significant advantages over traditional two-level converters, especially for high power and high voltage applications. In addition to their superior output voltage quality. They can also reduce voltage stress across switching devices. Since the output voltages have multiple levels, lower dv/dt is achieved, which greatly alleviates electromagnetic interference problems due to high frequency switching. Over the years most research work has focused on converters with three to five voltage levels, although topologies with very high number of voltage levels were also proposed. In general, the more voltage levels a converter has the less harmonic and better power quality. However, the increase in converter

complexity and number of switching devices is a major concern for multilevel converter. There are several topologies available, being the Neutral Point Clamped [5], Flying Capacitor [6] and Cascaded H-bridge inverter [7] the most studied and used. In recent years many variations and combinations of these topologies have been reported, one of them is the cascaded H-bridge [7-10].

II. HIGH POWER CONVERTERS CLASSIFICATIONS

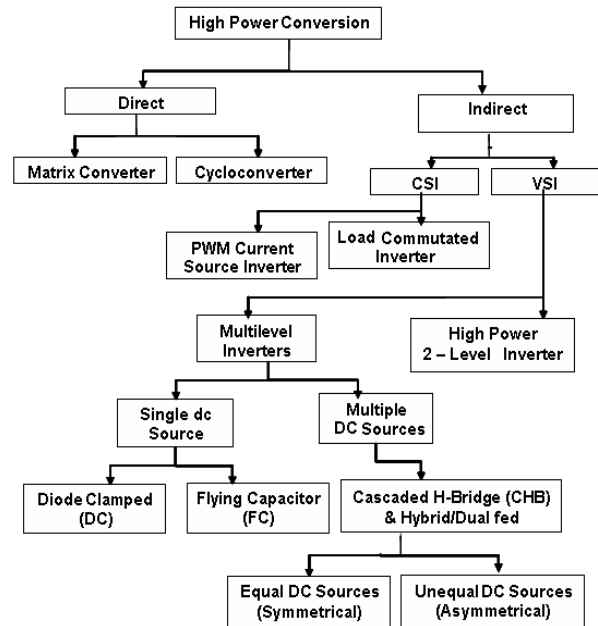


Figure 1 Classification of High power Converters

Fig.1 shows the classification of high power converters. Out of all converters Cascaded bridge configuration is more popular. Cascaded bridge configuration is again classified into 2 types 1) Cascaded Half Bridge 2) Cascaded Full Bridge or Cascaded H-Bridge. In this paper a novel cascaded hybrid H-Bridge topology is proposed for PV application.

A Half H-Bridge

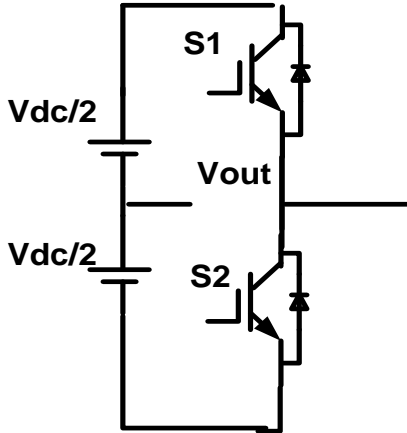


Figure 2 Half Bridge

Fig.2 shows the Half H-Bridge Configuration. By using single Half H-Bridge we can get 2 voltage levels. The switching table is given in Table 1.

Table 1. Switching table for Half Bridge

Switches Turn ON	Voltage Level
S2	$V_{dc}/2$
S1	$-V_{dc}/2$

B Full H-Bridge

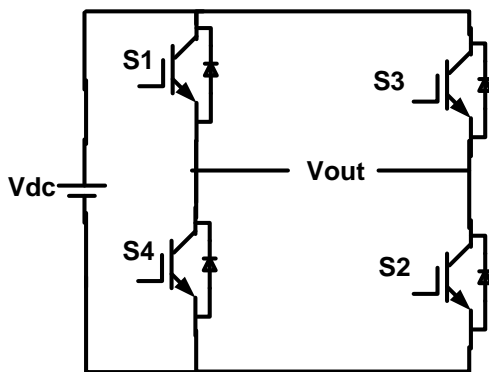


Figure. 3 Full H-Bridge

Fig.3 shows the Full H-Bridge Configuration. By using single H-Bridge we can get 3 voltage levels. The number output voltage levels of cascaded Full H-Bridge are given by $2n+1$ and voltage step of each level is given by V_{dc}/n . Where n is number of H-bridges connected in cascaded. The switching table is given in Table2.

Table 2. Switching table for Full H-Bridge

Switches Turn ON	Voltage Level
S1,S2	V_{dc}
S3,S4	$-V_{dc}$
S4,D2	0

C Hybrid H-Bridge

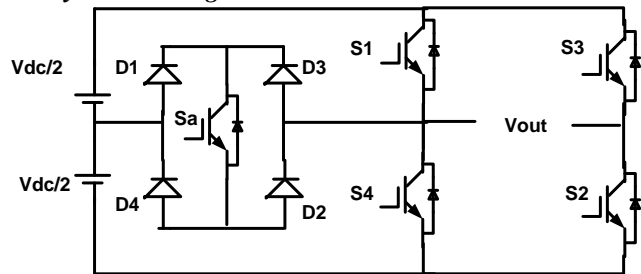


Figure. 4 Hybrid H-Bridges

Fig. 4 shows the Hybrid H-Bridge configuration. By using single Hybrid H-Bridge we can get 5 voltage levels. The 13 number output voltage levels of cascaded Hybrid H-Bridge are given by $4n+1$ and voltage step of each level is given by $V_{dc}/2n$. Where n is number of H-bridges connected in cascaded. The switching table of Hybrid H-Bridge is given in Table 3.

Table 3. Switching table for Hybrid H-Bridge

Switches Turn On	Voltage Level
Sa, S1	$V_{dc}/2$
S1,S2	V_{dc}
S4,D2	0
Sa,S3	$-V_{dc}/2$
S3,S4	$-V_{dc}$

D Cascaded Hybrid H-Bridge

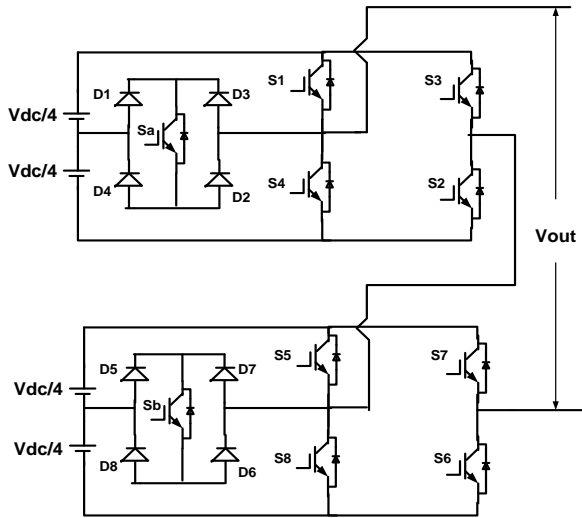


Figure 5. Cascaded Hybrid H-Bridges

Table 4 Switching table for Cascaded Hybrid H-Bridge

Switches Turn On	Voltage Level
Sa,S2,S8,D6	Vdc/4
S1,S2,S8,D6	2Vdc/4
S1,S2,Sb,S6	3Vdc/4
S1,S2,S5,S6	Vdc
S4,D2,S8,D6	0
Sa,S3,S8,D6	-Vdc/4
S3,S4,S8,D6	-2Vdc/4
S3,S4,Sb,S7	-3Vdc/4
S3,S4,S7,S8	-Vdc

The proposed Cascaded Hybrid H-Bridge (CHHB) uses less number of switches to produce more voltage levels. This will reduce Gate Drivers and protection circuit requirement thus it reduce cost and complexity of the circuit. For example for 9 level output the proposed converter uses 10 switches but cascaded H- Bridge converter uses 12 switches. This difference increases as the number of output voltage levels increases.

III. PROPOSED PV SYSTEM

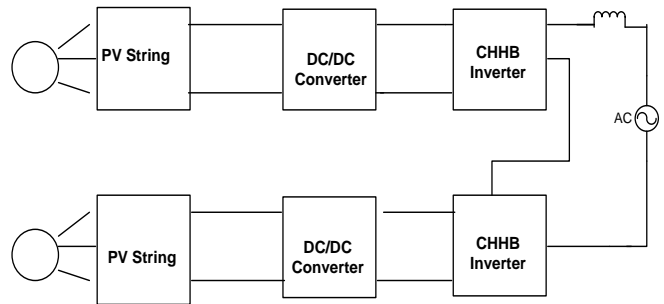


Figure 6. Grid Connected PV System

The general block diagram of PV system is shown in fig.6. The PV string converts solar radiation into DC. Here we are using DC/DC Boost converter to increase the output voltage. The output inverter converts DC into AC and feeding into the grid. The proposed system uses small PV array cascading to produce higher voltage output. This system reduces overall cost and complexity. The Fig.6 shows the proposed PV configuration.

IV. MATLAB/SIMULINK MODELING AND SIMULATION RESULTS

A. Single Hybrid H-Bridge System

Fig. 7 Shows the Matlab/Simulink model of complete PV system. It consists of PV array block, DC/DC converter Block, Hybrid H-Bridge Block.

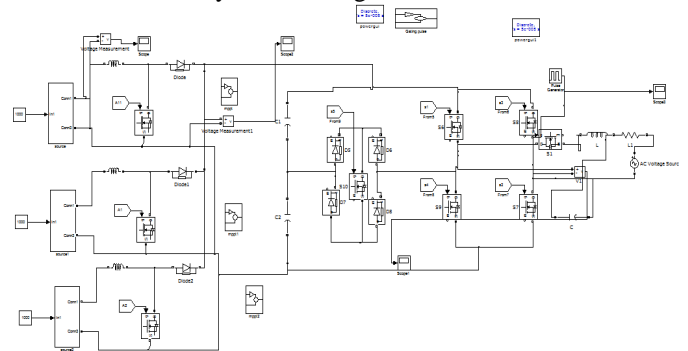


Figure 7 Matlab/Simulink model of Hybrid H-bridge

Fig. 8 shows the inverter input DC voltage and Multilevel AC output voltage. Fig. 9 Shows the five level output of the Hybrid H-Bridge. Fig. 10 shows the grid voltage and current wave forms.

Fig. 11 shows the FFT analyses of grid current. From the figure it is clear that the total THD is 3.2 %.

B. Proposed Cascaded Hybrid H-Bridge System

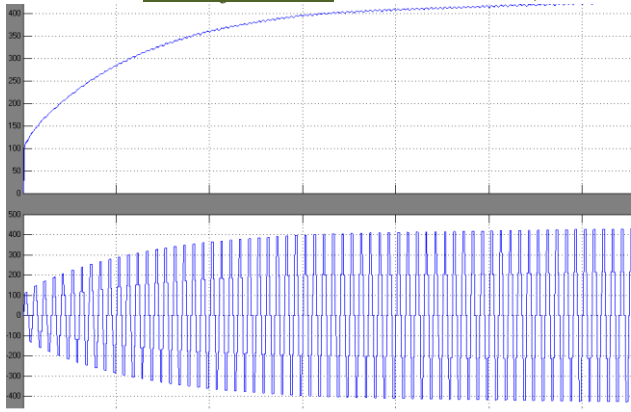


Figure.8 Inverter Input and Output

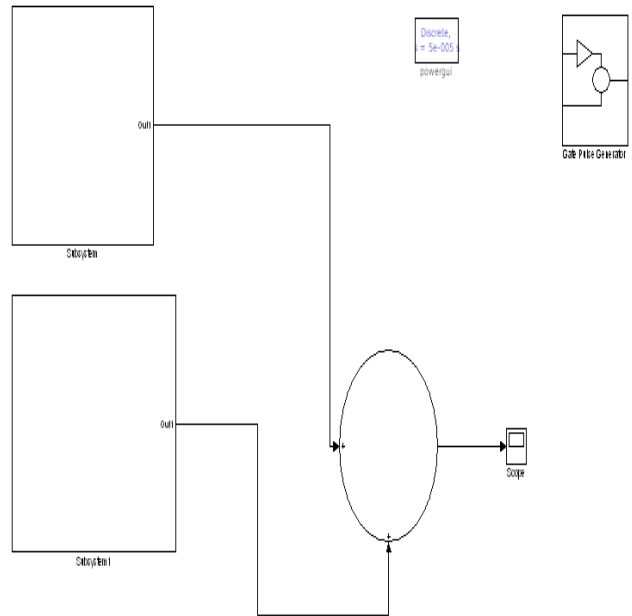


Fig. 12 Cascaded Hybrid H-Bridge

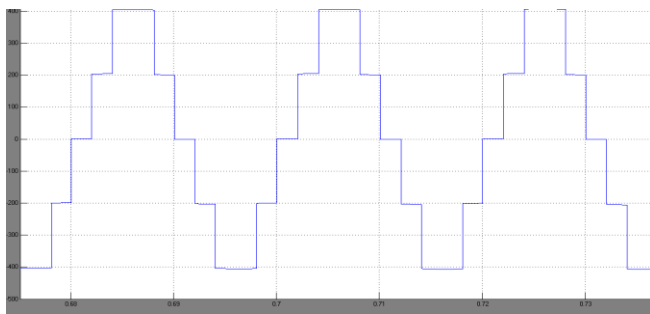


Figure. 9 Five level output of H-bridge

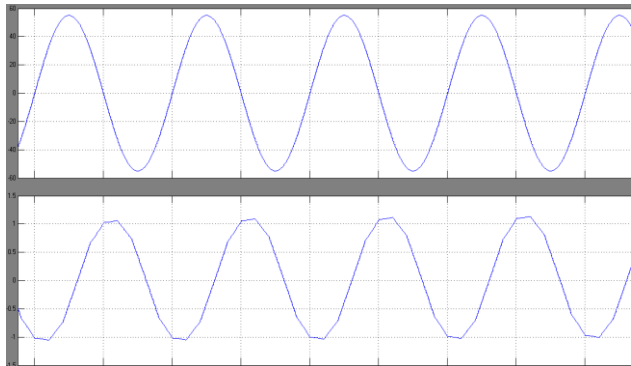


Figure10 Grid voltage and Grid current

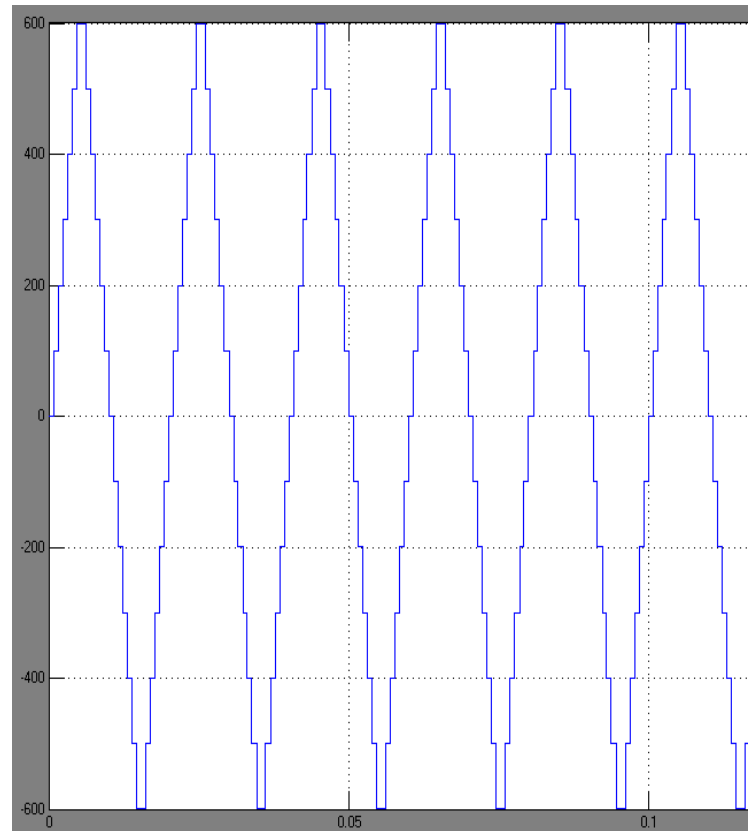


Fig. 13 Eleven level Hybrid H-Bridge

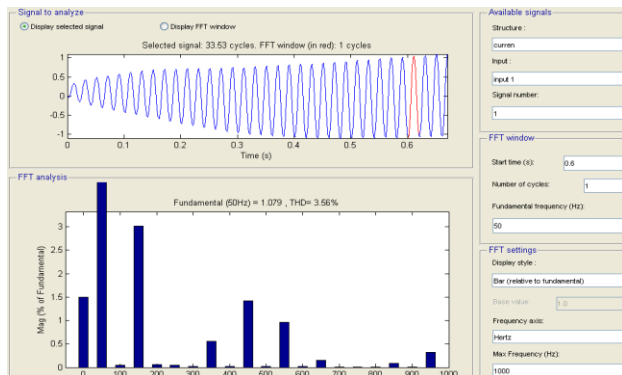


Figure11 FFT of grid current

V. CONCLUSION

This paper presents a single-phase multistring Multi-level photovoltaic (PV) inverter topology for grid-connected PV systems with a novel hybrid H- bridge inverter. The proposed novel cascaded Hybrid H-bridge produces higher voltage levels with less number of devices. This will reduce the number of gate drivers and protection circuits requirement. This in turn reduces the cost & increase the reliability. Design Procedure for various components of single Hybrid H- bridge cell is given. A cascaded Grid connected PV topology is proposed. Finally a Matlab/Simulink based model is developed and simulation results are presented.

VI. REFERENCES

- [1] N. A. Rahim and S. Mekhilef, "Implementation of three-phase grid connected inverter for photovoltaic solar power generation system," in *Proc. IEEE PowerCon*, Oct. 2002, vol. 1, pp. 570–573.
- [2] J. M. Carrasco, L. G. Franquelo, J. T. Bialasiewicz, E. Galvan, R. C. PortilloGuisado, M. A. M. Prats, J. I. Leon, and N. Moreno-Alfonso, "Power-electronic systems for the grid integration of renewable energy sources: A survey," *IEEE Trans. Ind. Electron.*, vol. 53, no. 4, pp. 1002–1016, Aug. 2006.
- [3] S. B. Kjaer, J. K. Pedersen, and F. Blaabjerg, "A review of single-phase grid connected inverters for photovoltaic modules," *IEEE Trans. Ind. Appl.*, vol. 41, no. 5, pp. 1292–1306, Sep./Oct. 2005.
- [4] S. Daher, J. Schmid, and F. L.M. Antunes, "Multilevel inverter topologies for stand-alone PV systems," *IEEE Trans. Ind. Electron.*, vol. 55, no. 7, pp. 2703–2712, Jul. 2008.
- [5] M. Meinhardt and G. Cramer, "Past, present and future of grid-connected photovoltaic- and hybrid-power-systems," in *Proc. IEEE-PES Summer Meeting*, Jul. 2000, vol. 2, pp. 1283–1288.
- [6] S. Kouro, J. Rebolledo, and J. Rodriguez, "Reduced switching-frequency modulation algorithm for high-power multilevel inverters," *IEEE Trans. Ind. Electron.*, vol. 54, no. 5, pp. 2894–2901, Oct. 2007.
- [7] S. J. Park, F. S. Kang, M. H. Lee, and C. U. Kim, "A new single-phase fivelevel PWM inverter employing a deadbeat control scheme," *IEEE Trans. Power Electron.*, vol. 18, no. 18, pp. 831–843, May 2003.
- [8] L. M. Tolbert and T. G. Habetler, "Novel multilevel inverter carrier-based PWM method," *IEEE Trans. Ind. Appl.*, vol. 35, no. 5, pp. 1098–1107, Sep./Oct. 1999.
- [9] Y. Liu, H. Hong, and A. Q. Huang, "Real-time calculation of switching angles minimizing THD for multilevel inverters with step modulation," *IEEE Trans. Ind. Electron.*, vol. 56, no. 2, pp. 285–293, Feb. 2009.
- [10] N. S. Choi, J. G. Cho, and G. H. Cho, "A general circuit topology of multilevel inverter," in *Proc. IEEE 22th Annu. PESC*, Jun. 24–27, 1991, pp. 96–103.
- [9] L.M.Tolber, T.G.Habetler, "Novel Multi level inverter Carrier based PWM Method," *IEEE Ind.Appli.*, vol.35. pp.1098-1107. Sep/Oct 1999.
- [10] Holmes, D. G. and Lipo, T. A., Pulse width modulation for power converters: principles and practice, IEEE.
- [11] T.H.Barton, "Pulse Width Modulation Waveforms – The Bessel Approximatilon", *IEEE-IAS Conference Record*,

A Novel Nine Level Grid-Connected Inverter for Photovoltaic System

THANUJ KUMAR. JALA

M-Tech Scholar, Power electronics & Drives,
Department of Electrical And Electronics Engineering,
KL University, Guntur (A.P), India

G. SRINIVASA RAO

Asst. Prof, Energy Engineering,
Department of Electrical And Electronics Engineering,
KL University, Guntur (A.P), India

Abstract-This paper proposes a single-phase seven-level inverter for grid-connected photovoltaic systems, with a novel pulse width-modulated (PWM) control scheme. Three reference signals that are identical to each other with an offset that is equivalent to the amplitude of the triangular carrier signal were used to generate the PWM signals. The inverter is capable of producing seven levels of output-voltage levels (V_{dc} , $2V_{dc}/3$, $V_{dc}/3$, 0 , $-V_{dc}/3$, $-2V_{dc}/3$, $-V_{dc}$) from the dc supply voltage. In this paper a new nine level inverter with reduced number of switches is proposed and Matlab/Simulink results are presented.

Index Terms—Grid connected, modulation index, multilevel inverter, photovoltaic (PV) system, pulse width-modulated (PWM), total harmonic distortion (THD).

I. INTRODUCTION

The ever-increasing energy consumption, fossil fuels soaring costs and exhaustible nature, and worsening global environment have created a booming interest in renewable energy generation systems, one of which is photovoltaic. Such a system generates electricity by converting the Sun's energy directly into electricity. Photovoltaic-generated energy can be delivered to power system networks through grid-connected inverters. A single-phase grid-connected inverter is usually used for residential or low-power applications of power ranges that are less than 10 kW [1]. Types of single-phase grid-connected inverters have been investigated [2]. A common topology of this inverter is full-bridge three-level.

The three-level inverter can satisfy specifications through its very high switching, but it could also unfortunately increase switching losses, acoustic noise, and level of interference to other equipment. Improving its output waveform reduces its harmonic content and, hence, also the size of the filter used and the level of electromagnetic interference (EMI) generated by the inverter's switching operation [3]. Multilevel inverters are promising; they have nearly sinusoidal output-voltage waveforms, output current with better harmonic profile, less stressing of electronic components owing to decreased voltages, switching losses that are lower than those of conventional two-level inverters, a smaller filter size, and lower EMI, all of which make them cheaper, lighter, and

more compact [3], [4]. Various topologies for multilevel inverters have been proposed over the years. Common ones are diode-clamped [5]– [10], flying capacitor or multi cell [11]–[17], cascaded H-bridge [18]–[24], and modified H-bridge multilevel [25]–[29].

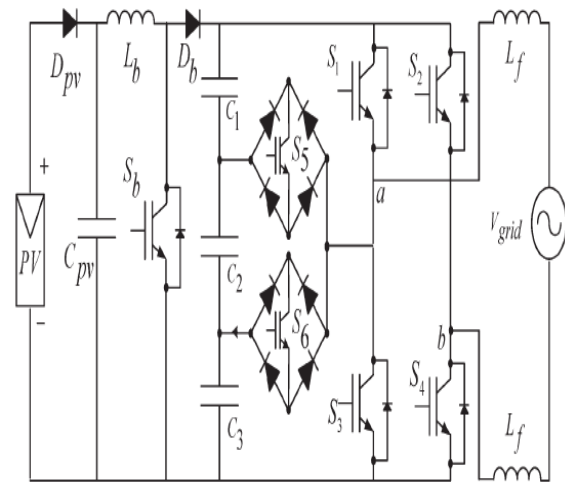


Fig.1. Proposed single-phase seven-level grid-connected inverter for photovoltaic systems.

This paper recounts the development of a novel modified H-bridge single-phase multilevel inverter that has two diode embedded bidirectional switches and a novel pulse width modulated (PWM) technique. The topology was applied to a grid-connected photovoltaic system with considerations for a maximum-power-point tracker (MPPT) and a current-control algorithm.

II. PROPOSED MULTILEVEL INVERTER TOPOLOGY

A Full H-Bridge

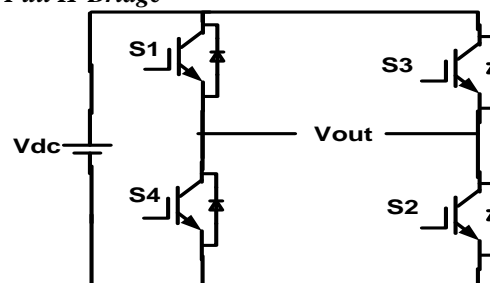


Figure. 2 Full H-Bridge

Fig.2 shows the Full H-Bridge Configuration. By using single H-Bridge we can get 3 voltage levels. The number output voltage levels of cascaded Full H-Bridge are given by $2n+1$ and voltage step of each level is given by V_{dc}/n . Where n is number of H-bridges connected in cascaded. The switching table is given in Table 1.

Table 1. Switching table for Full H-Bridge

Switches Turn ON	Voltage Level
S1,S2	V_{dc}
S3,S4	$-V_{dc}$
S4,S2	0

B Hybrid H-Bridge

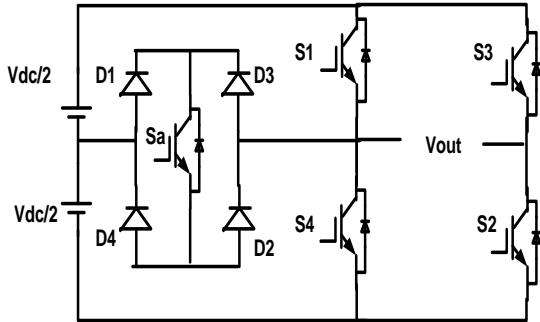


Figure. 3 Hybrid H-Bridge

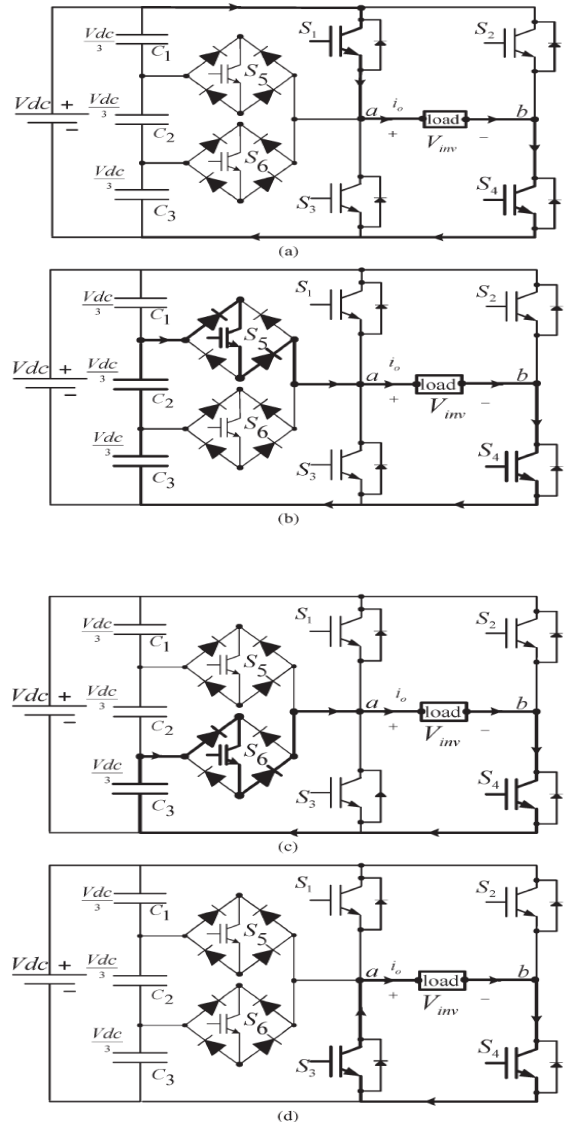
Fig. 3 shows the Hybrid H-Bridge configuration. By using single Hybrid H-Bridge we can get 5 voltage levels. The number output voltage levels of cascaded Hybrid H-Bridge are given by $4n+1$ and voltage step of each level is given by $V_{dc}/2n$. Where n is number of H-bridges connected in cascaded. The switching table of Hybrid H-Bridge is given in Table 2.

Table 2. Switching table for Hybrid H-Bridge

Switches Turn On	Voltage Level
Sa, S1	$V_{dc}/2$
S1,S2	V_{dc}
S4,S2	0
Sa,S3	$-V_{dc}/2$
S3,S4	$-V_{dc}$

The proposed single-phase seven-level inverter was developed from the five-level inverter in [25]–[29]. It

comprises a single-phase conventional H-bridge inverter, two bidirectional switches, and a capacitor voltage divider formed by C_1 , C_2 , and C_3 , as shown in Fig. 1. The modified H-bridge topology is significantly advantageous over other topologies, i.e., less power switch, power diodes, and less capacitor for inverters of the same number of levels. Photo voltaic (PV) arrays were connected to the inverter via a dc–dc boost converter. The power generated by the inverter is to be delivered to the power network, so the utility grid, rather than a load, was used. The dc–dc boost converter was required because the PV arrays had a voltage that was lower than the grid voltage. High dc bus voltages are necessary to ensure that power flows from the PV arrays to the grid. A filtering inductance L_f was used to filter the current injected into the grid. Proper switching of the inverter can produce seven output-voltage levels (V_{dc} , $2V_{dc}/3$, $V_{dc}/3$, 0 , $-V_{dc}$, $-2V_{dc}/3$, $-V_{dc}/3$) from the dc supply voltage. The proposed inverter’s operation can be divided into seven switching states, as shown in Fig. 4(a)–(g).



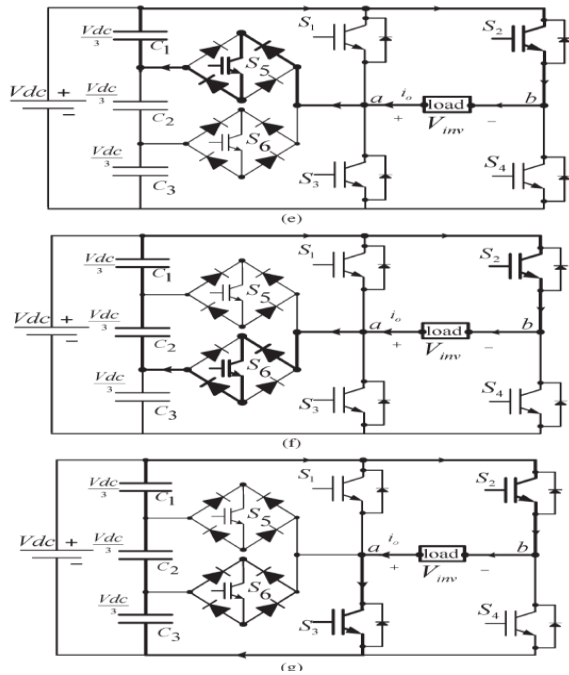


Fig. 4. Switching combination required to generate the output voltage (V_{ab}). (a) $V_{ab} = V_{dc}$. (b) $V_{ab} = 2V_{dc}/3$. (c) $V_{ab} = V_{dc}/3$. (d) $V_{ab} = 0$ (e) $V_{ab} = -V_{dc}/3$. (f) $V_{ab} = -2V_{dc}/3$. (g) $V_{ab} = -V_{dc}$.

OUTPUT VOLTAGE ACCORDING TO THE SWITCHES' ON-OFF CONDITION

v_0	S_1	S_2	S_3	S_4	S_5	S_6
V_{dc}	on	off	off	on	off	off
$2V_{dc}/3$	off	off	off	on	on	off
$V_{dc}/3$	off	off	off	on	off	on
0	off	off	on	on	off	off
0*	on	on	off	off	off	off
$-V_{dc}/3$	off	on	off	off	on	off
$-2V_{dc}/3$	off	on	off	off	off	on
$-V_{dc}$	off	on	on	off	off	off

Table 3. shows the switching combinations that generated the seven output-voltage levels ($0, -V_{dc}, -2V_{dc}/3, -V_{dc}/3, V_{dc}, 2V_{dc}/3, V_{dc}/3$).

III. PWM MODULATION

A novel PWM modulation technique was introduced to generate the PWM switching signals. Three reference signals (V_{ref1} , V_{ref2} , and V_{ref3}) were compared with a carrier signal ($V_{carrier}$). The reference signals had the same frequency and amplitude and were in phase with an offset value that was equivalent to the amplitude of the carrier signal. The reference signals were each compared with the carrier signal. If V_{ref1} had exceeded the peak amplitude of $V_{carrier}$, V_{ref2} was compared with $V_{carrier}$ until it had exceeded the peak amplitude of $V_{carrier}$. Then, onward, V_{ref3} would take charge and would be compared with $V_{carrier}$ until it reached zero. Once V_{ref3} had reached zero, V_{ref2} would be compared until it reached zero. Then, onward, V_{ref1} would be compared with $V_{carrier}$.

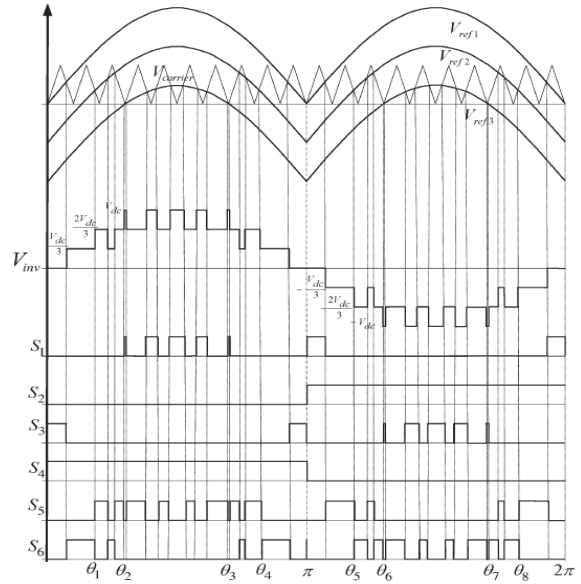


Fig. 5. Switching pattern for the single-phase seven-level inverter.

Fig.5 shows the resulting switching pattern. Switches S_1, S_3, S_5 , and S_6 would be switching at the rate of the carrier signal frequency, whereas S_2 and S_4 would operate at a frequency that was equivalent to the fundamental frequency. For one cycle of the fundamental frequency, the proposed inverter operated through six modes. Fig. 6 shows the per unit output-voltage signal for one cycle. The six modes are described as follows:

- Mode 1 : $0 < \omega t < \theta_1$ and $\theta_4 < \omega t < \pi$
- Mode 2 : $\theta_1 < \omega t < \theta_2$ and $\theta_3 < \omega t < \theta_4$
- Mode 3 : $\theta_2 < \omega t < \theta_3$
- Mode 4 : $\pi < \omega t < \theta_5$ and $\theta_8 < \omega t < 2\pi$
- Mode 5 : $\theta_5 < \omega t < \theta_6$ and $\theta_7 < \omega t < \theta_8$
- Mode 6 : $\theta_6 < \omega t < \theta_7$.

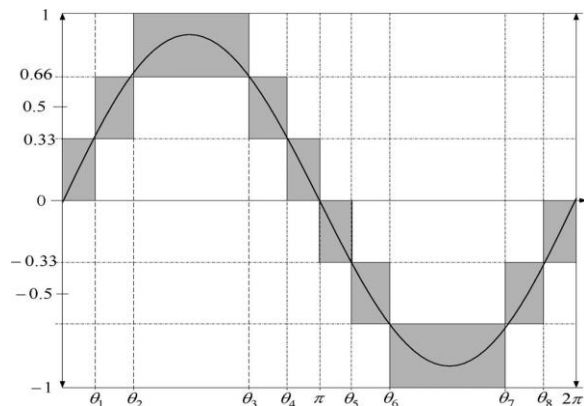


Fig. 6. Seven-level output voltage (V_{ab}) and switching angles.

IV CONTROL SYSTEM

Fig. 7 shows, the control system comprises a MPPT algorithm, a dc-bus voltage controller, reference-current generation, and a current controller. The two main tasks of the control system are maximization of the energy transferred from the PV arrays to the grid, and generation of a sinusoidal current with minimum harmonic distortion, also under the presence of grid voltage harmonics. The proposed inverter utilizes the perturb-and-observe (P&O) algorithm for its wide usage in MPPT owing to its simple structure and requirement of only a few measured parameters. It periodically perturbs (i.e., increment or decrement) the array terminal voltage and compares the PV output power with that of the previous perturbation cycle. If the power was increasing, the perturbation would continue in the same direction in the next cycle; otherwise, the direction would be reversed. This means that the array terminal voltage is perturbed every MPPT cycle; therefore, when the MPP is reached, the P&O algorithm will oscillate around it.

The P&O algorithm was implemented in the dc–dc boost converter. The output of the MPPT is the duty-cycle function. As the dc-link voltage V_{dc} was controlled in the dc–ac sevenlevel PWM inverter, the change of the duty cycle changes the voltage at the output of the PV panels. A PID controller was implemented to keep the output voltage of the dc–dc boost converter (V_{dc}) constant by comparing V_{dc} and $V_{dc\ ref}$ and feeding the error into the PID controller, which subsequently tries to reduce the error. In this way, the V_{dc} can be maintained at a constant value and at more than $\sqrt{2}$ of V_{grid} to inject power into the grid. To deliver energy to the grid, the frequency and phase of the PV inverter must equal those of the grid; therefore, a grid synchronization method is needed. The sine lookup table that generates reference current must be brought into phase with the grid voltage (V_{grid}).

A PI algorithm was used as the feedback current controller for the application. The current injected into the grid, also known as grid current I_{grid} , was sensed and fed back to a comparator that compared it with the reference current $I_{gridref}$. $I_{gridref}$ is the result of the MPPT algorithm. The error from the comparison process of I_{grid} and $I_{gridref}$ was fed into the PI controller. The output of the PI controller, also known as V_{ref} , goes through an anti windup process before being compared with the triangular wave to produce the switching signals for S_1 – S_6 . Eventually, V_{ref} becomes V_{ref1} , V_{ref2} and V_{ref3} can be derived from V_{ref1} by shifting the offset value, which was equivalent to the amplitude of the triangular wave. The mathematical formulation of the PI algorithm and its implementation in the DSP are discussed in detail in [28].

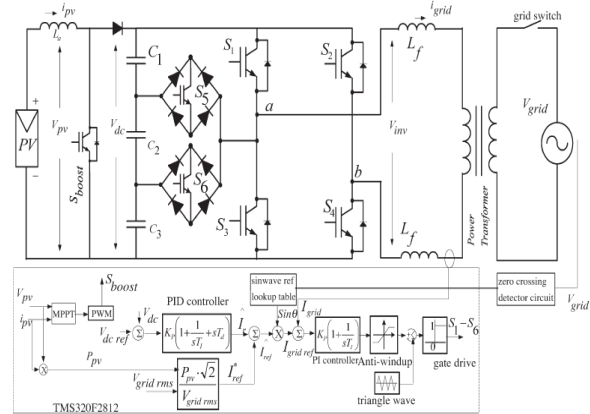


Fig. 7. Seven-level inverter with closed-loop control algorithm.

V. MATLAB/SIMULINK MODEL and SIMULATION RESULTS

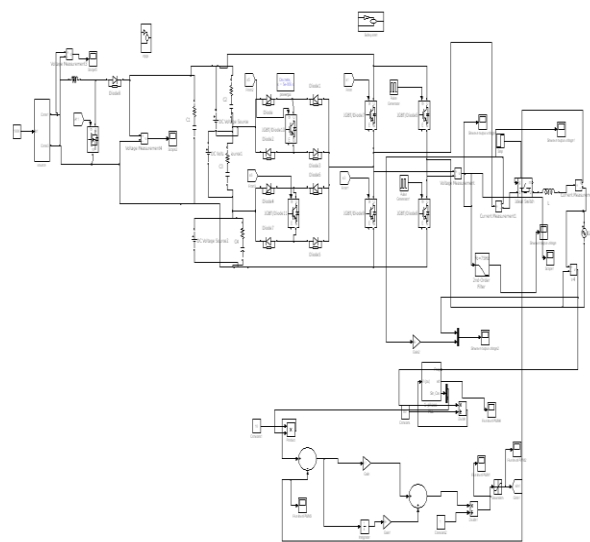


Fig. 8 Matlab/Simulink model of Grid connected PV system

Fig. 8 shows the Matlab/ Simulink model of grid connected photovoltaic system. It consist of a DC to DC conversion stage and Dc to AC multilevel inversion stage.

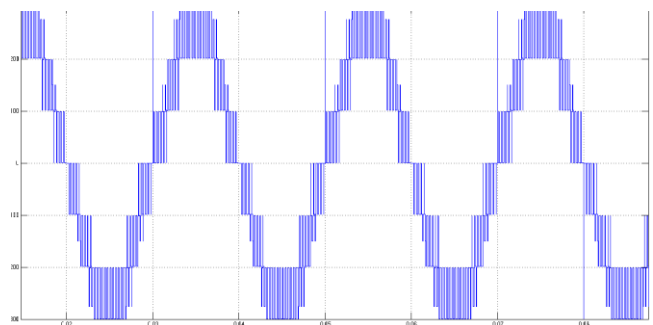


Fig. 9 Seven Level Voltage output

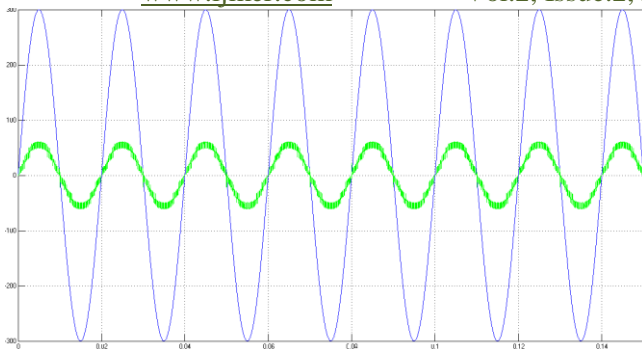


Fig.10 Grid Voltage and Grid Current

Fig. 9 shows the seven level PWM output. Fig. 10 show sthe grid voltage and grid current. From the figure it is clear that grid voltage and current are inphase.

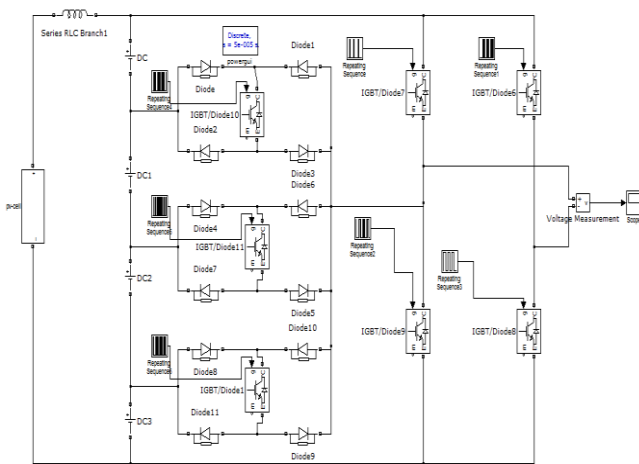


Fig.11 Matlab/Simulink mode of proposed Nine level Inverter

Fig. 11 shows the Matlab/Simulink model of proposed nine level Hybrid H-Bridge inverter.

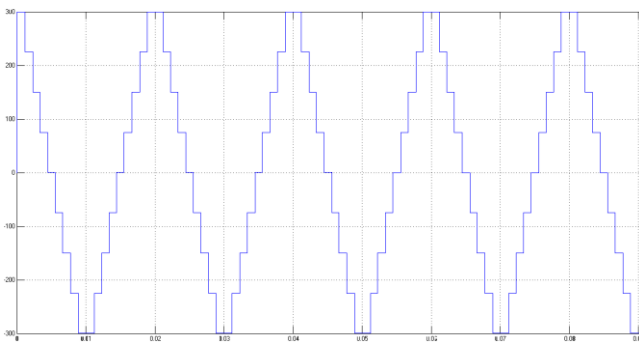


Fig.12 Nine level output of proposed converter

Fig. 12 shows the output of proposed nine level inverter. In proposed converter for nine level seven switches are required. In order to produce the same levels cascaded H-Bridge requires sixteen switches.

Multilevel inverters offer improved output waveforms and lower THD. This paper has presented a novel PWM switching scheme for the proposed multilevel inverter. It utilizes three reference signals and a triangular carrier signal to generate PWM switching signals. The behavior of the proposed multilevel inverter was analyzed in detail. By controlling the modulation index, the desired number of levels of the inverter’s output voltage can be achieved. Finally a nine level hybrid H-bridge inverter is proposed and simulation results are presented.

VI. REFERENCES

- [1] M. Calais and V. G. Agelidis, “Multilevel converters for single-phase grid connected photovoltaic systems—An overview,” in *Proc. IEEE Int. Symp. Ind. Electron.*, 1998, vol. 1, pp. 224–229.
- [2] S. B. Kjaer, J. K. Pedersen, and F. Blaabjerg, “A review of single-phase grid connected inverters for photovoltaic modules,” *IEEE Trans. Ind. Appl.*, vol. 41, no. 5, pp. 1292–1306, Sep/Oct. 2005.
- [3] P. K. Hinga, T. Ohnishi, and T. Suzuki, “A new PWM inverter for photovoltaic power generation system,” in *Conf. Rec. IEEE Power Electron. Spec. Conf.*, 1994, pp. 391–395.
- [4] Y. Cheng, C. Qian, M. L. Crow, S. Pekarek, and S. Atcitty, “A comparison of diode-clamped and cascaded multilevel converters for a STATCOM with energy storage,” *IEEE Trans. Ind. Electron.*, vol. 53, no. 5, pp. 1512– 1521, Oct. 2006.
- [5] M. Saeedifard, R. Iravani, and J. Pou, “A space vector modulation strategy for a back-to-back five-level HVDC converter system,” *IEEE Trans. Ind. Electron.*, vol. 56, no. 2, pp. 452–466, Feb. 2009.
- [6] S. Alepuz, S. Busquets-Monge, J. Bordonau, J. A. M. Velasco, C. A. Silva, J. Pontt, and J. Rodríguez, “Control strategies based on symmetrical components for grid-connected converters under voltage dips,” *IEEE Trans. Ind. Electron.*, vol. 56, no. 6, pp. 2162–2173, Jun. 2009.
- [7] J. Rodríguez, J. S. Lai, and F. Z. Peng, “Multilevel inverters: A survey of topologies, controls, and applications,” *IEEE Trans. Ind. Electron.*, vol. 49, no. 4, pp. 724–738, Aug. 2002.
- [8] J. Rodriguez, S. Bernet, B. Wu, J. O. Pontt, and S. Kouro, “Multilevel voltage-source-converter topologies for industrial medium-voltage drives,” *IEEE Trans. Ind. Electron.*, vol. 54, no. 6, pp. 2930–2945, Dec. 2007.
- [9] M. M. Renge and H. M. Suryawanshi, “Five-level diode clamped inverter to eliminate common mode voltage and reduce dv/dt in medium voltage rating induction motor drives,” *IEEE Trans. Power Electron.*, vol. 23, no. 4, pp. 1598–1160, Jul. 2008.
- [10] E. Ozdemir, S. Ozdemir, and L. M. Tolbert, “Fundamental-frequencymodulated six-level diode-

clamped multilevel inverter for three-phase stand-alone photovoltaic system," *IEEE Trans. Ind. Electron.*, vol. 56, no. 11, pp. 4407–4415, Nov. 2009.

- [11] R. Stala, S. Pirog, M. Baszynski, A. Mondzik, A. Penczek, J. Czekonski, and S. Gasiorek, "Results of investigation of multicell converters with balancing circuit—Part I," *IEEE Trans. Ind. Electron.*, vol. 56, no. 7, pp. 2610–2619, Jul. 2009.
- [12] R. Stala, S. Pirog, M. Baszynski, A. Mondzik, A. Penczek, J. Czekonski, and S. Gasiorek, "Results of investigation of multicell converters with balancing circuit—Part II," *IEEE Trans. Ind. Electron.*, vol. 56, no. 7, pp. 2620–2628, Jul. 2009.
- [13] P. Lezana, R. Aguilera, and D. E. Quevedo, "Model predictive control of an asymmetric flying capacitor converter," *IEEE Trans. Ind. Electron.*, vol. 56, no. 6, pp. 1839–1846, Jun. 2009.
- [14] M. F. Escalante, J.-C. Vannier, and A. Arzandé, "Flying capacitor multilevel inverters and DTC motor drive applications," *IEEE Trans. Ind. Electron.*, vol. 49, no. 4, pp. 809–815, Aug. 2002.
- [15] A. Shukla, A. Ghosh, and A. Joshi, "Static shunt and series compensations of an SMIB system using flying capacitor multilevel inverter," *IEEE Trans. Power Del.*, vol. 20, no. 4, pp. 2613–2622, Oct. 2005.
- [16] J. Huang and K. A. Corzine, "Extended operation of flying capacitor multilevel inverter," *IEEE Trans. Power Electron.*, vol. 21, no. 1, pp. 140–147, Jan. 2006.
- [17] F. Z. Peng, "A generalized multilevel inverter topology with self voltage balancing," *IEEE Trans. Ind. Appl.*, vol. 37, no. 2, pp. 611–617, Mar./Apr. 2001.
- [18] E. Villanueva, P. Correa, J. Rodríguez, and M. Pacas, "Control of a singlephase cascaded H-bridge multilevel inverter for grid-connected photovoltaic systems," *IEEE Trans. Ind. Electron.*, vol. 56, no. 11, pp. 4399–4406, Nov. 2009.
- [19] L. M. Tolbert, F. Z. Peng, T. Cunnyngham, and J. N. Chiasson, "Charge balance control schemes for cascaded multilevel converter in hybrid electric vehicles," *IEEE Trans. Ind. Electron.*, vol. 49, no. 5, pp. 1058–1064, Oct. 2002.
- [20] K. A. Corzine, M. W. Wielebski, F. Z. Peng, and J. Wang, "Control of cascaded multilevel inverters," *IEEE Trans. Power Electron.*, vol. 19, no. 3, pp. 732–738, May 2004.
- [21] J. I. Leon, S. Vazquez, S. Kouro, L. G. Franquelo, J. M. Carrasco, and J. Rodriguez, "Unidimensional modulation technique for cascaded multilevel converters," *IEEE Trans. Ind. Electron.*, vol. 49, no. 5, pp. 1058–1064, Oct. 2002.
- [22] C.-C. Hua, C.-W. Wu, and C.-W. Chuang, "A digital predictive current control with improved sampled inductor current for cascaded inverters," *IEEE Trans. Ind. Electron.*, vol. 56, no. 5, pp. 1718–1726, May 2009.
- [23] S. Vazquez, J. I. Leon, L. G. Franquelo, J. J. Padilla, and J. M. Carrasco, "DC-voltage-ratio control strategy for multilevel cascaded converters fed with a single DC source," *IEEE Trans. Ind. Electron.*, vol. 56, no. 7, pp. 2513–2521, Jul. 2009.
- [24] C. Cecati, F. Ciancetta, and P. Siano, "A multilevel inverter for photovoltaic systems with fuzzy logic control," *IEEE Trans. Ind. Electron.*, vol. 57, no. 12, pp. 4115–4125, Dec. 2010.
- [25] G. Ceglia, V. Guzman, C. Sanchez, F. Ibanez, J. Walter, and M. I. Gimenez, "A new simplified multilevel inverter topology for DC-AC conversion," *IEEE Trans. Power Electron.*, vol. 21, no. 5, pp. 1311–1319, Sep. 2006.
- [26] V. G. Agelidis, D. M. Baker, W. B. Lawrance, and C. V. Nayar, "A multilevel PWM inverter topology for photovoltaic applications," in *Proc. IEEE ISIE, Guimarães, Portugal, 1997*, pp. 589–594.
- [27] S. J. Park, F. S. Kang, M. H. Lee, and C. U. Kim, "A new single-phase five-level PWM inverter employing a deadbeat control scheme," *IEEE Trans. Power Electron.*, vol. 18, no. 3, pp. 831–843, May 2003.
- [28] J. Selvaraj and N. A. Rahim, "Multilevel inverter for grid-connected PV system employing digital PI controller," *IEEE Trans. Ind. Electron.*, vol. 56, no. 1, pp. 149–158, Jan. 2009.
- [29] N. A. Rahim and J. Selvaraj, "Multi-string five-level inverter with novel PWM control scheme for PV application," *IEEE Trans. Ind. Electron.*, vol. 57, no. 6, pp. 2111–2121, Jun. 2010.



J. Thanuj Kumar got his bachelor degree in 2010 from SSIET, NUZVID. Present he is pursuing his masters degree in power electronics & derives in KL UNIVERSITY, VADDESWAREM. He is interested in power electronics & circuit theory.



G. Srinivasa Rao got his bachelor degree in 2007 from Dr. Paul Raju College of Engineering, BADRACHALAM & Masters degree in 2010 From NIT, TIRUCHHI. Present he is Asst. Professor in EEE Department in KL UNIVERSITY. He is interested in energy engineering, power electronics.

Conservation Strategies for Srirangapatna Town: Evaluation of Heritage Buildings

Shankar B¹, Uma S²

¹(Associate Professor in Urban and Regional Planning, Institute of Development Studies University of Mysore, Mysore)

²(Lecturer in Architecture, JSS Polytechnic College, Mysore)

ABSTRACT

There is large number of heritage sites in India and Srirangapatna is one of the prominent heritage sites. It is an island town, situated on Bangalore-Mysore highway, encircled by the river Cauvery. There are many significant heritage areas/precincts and monuments located within the fort, which is one of the principal, elements that add up to the character of Srirangapatna. Over the years, the ever increasing developmental pressures and neglect of monuments/heritage areas and their environs resulted in decay factors, which call for evolving harmonious strategies and conservation measures. The conservation measures, if taken in time, it will save Srirangapatna from gradual but imminent destruction for sustainable development. The paper presents the historical background of heritage areas and monuments of Srirangapatana and their significance. Significance Assessment is carried-out using mapping procedure for delineating the heritage areas. It suggests the conservation measures by reinvigorating the heritage areas within the fort.

Key Words: Significance Assessment, Fort, Heritage Areas, Mapping and Monuments

I. INTRODUCTION

The historic past is visibly being eroded by human and natural forces. There is a vital need of appreciation of rich heritage; for identifying the avenues for preservation, conservation, adaptive reuse and restoration; for the sake of cultural continuity and document them for posterity. Many of India's architectural and cultural heritage sites, which were recognized so far, they constitute a unique civilization legacy, as valuable as the monuments that are legally protected by Archaeological Survey of India (ASI) and State Achieves Department. The Archaeological Survey of India protects monuments that are more than 100 years old and are of national importance. The monuments of state importance are protected by the State Archaeological Department. Hardly, 5000 monuments at the national level and 3500 at the state level are being conserved by national and State governments respectively. But, considering India's vast cultural heritage, these numbers are not significant and their focus is monument-centric. Nowhere else in India, one can find such a profusion of monuments as in Karnataka. No wonder then, that Karnataka has been called the "Cradle of Stone Architecture in India". The magnificent World Heritage Sites at Hampi and

Pattadakal, the exquisite temples at Belur, Halebid and Somnathpur, the cave temples of Badami, Aihole, and the

stately forts and domes of Srirangapatna and Bijapur resurrect Karnataka's historical and cultural affluence.

Forts have always been a prime necessity of all ages. The possessive instinct of mankind has played a vital role in acquiring territories and mustering the riches and this has made the fort an essential requisite for a king to protect and preserve the wealth accumulated. In India the existence of Forts dates back to B.C. 300 and Srirangapatna is renowned for its seemingly impregnable fort, associated with the great ruler Tippu Sultan. Srirangapatna has undergone major changes over the centuries. Being a place of pilgrimage it has seen countless battles, some of which have shaken the foundation of its massive fort wall, that still stand as a testament to the greatness of Srirangapatna's glorious past. Distinguished ruling dynasties like The Gangas, Hoysalas, Vijayanagar Kings, The Wodeyars of Mysore and Hyder Ali & Tippu have left their indelible impression on the cultural legacy of this town. Innumerable monuments are a living testimony of this heritage and they are of national, state and local importance. As a mark of recognition, the state government notified Srirangapatna and other towns viz. Mysore, Bijapur, Bidar, Gulbarga and Kittur as Heritage towns in 2005. Srirangapatna aspires to be an international destination for its cultural, spiritual, natural, historical, architectural, and religious and tourism dynamism. But, it is losing its charm as the places near the fort, monuments, temples, mosques, fort gates etc., have been encroached by commercial establishments, illegal constructions, and not much concern from government agencies/authorities including people at large. The paper presents the significance assessment of heritage areas using mapping procedure and suggests conservation measures and strategies for sustenance of the historical Srirangapatna town.

2.0 BACKGROUND OF SRIRANGAPATNA

Srirangapatna is a Town Municipal Council, having a population of 23,729 as per 2001 census. It is a taluk headquarters in the Mandya District of Karnataka State. The population growth rate of Srirangapatana during the decade 1991-2001 was 8.32 per cent, which is lower than the state's growth rate of 17.5 per cent. But the growth rates during the decades 1971-81, 1981-91 was 28.64 % and 20.77 %. It is an island town built in 894 AD on Bangalore-Mysore highway encircled by the river Cauvery. The name Srirangapatna has been derived from a 1000 year old temple dedicated to Lord Sriranganatha. The town is located at 12.41° N 76.7° E and has an average elevation of 679 metres (2227 feet), on the Deccan Plateau with an area of 8.6sq.kms. The climate is

warm and the temperature ranges between 14°C and 34.5°C. The average annual rainfall is 810 mm maximum and 217mm minimum. The religion has played a major role in the history of Srirangapatna. Both Hindu and Muslim rulers have made major contributions to the town in the form of temples, mosques, tombs, gardens etc. These buildings were not only functioned as religious places but also acted as cultural centres and at sometime supported the economy of the town. The town constituted Hindu religion (74%), followed by Muslims(24%) and the rest are Christians and Sikhs. The town is steeped in history not only with its rich historical, cultural, religious, architectural heritage but also in scientific and technological innovations.

III. SHRIRANGAPATNA FORT

The Fort is one of the principal elements to the character of Srirangapatna. The island of Srirangapatna is surrounded by a great stone fort wall that rises up sharply from the banks of the river Cauvery. The Srirangapatna Fort was constructed on the western end of the island in 1454 AD and is one of the most formidable forts in India. The fort was so formidable that a great military authority who visited it in 1880 A.D., pronounced it as the second strongest in India. The Fort, constructed on the western end of the island, is an irregular pentagon with a perimeter of about 4 k.m. The aerial view of Srirangapatna is as follows.



Fig.1: Aerial View of Srirangapatana Fort Area

Source: Google Earth, 2008

It contains 240 acres of land and in 1897 had about 1500 houses with about 5400 inhabitants. It was originally built by Thimmanna Hebbbar, Chieftain of Nagamangala who got permission from the Vijayanagara emperor Devaraya II to build a mud fort here in 1454 A. D. Later Kanteerava Narasaraja Wodeyar and the succeeding rulers strengthened the fort. To the two walls of fortification, Tippu sultan added a third inner line of fortification. The principal entrance to the fort is the Elephant gate on the south side. This gateway bears an inscription in Persian which mentioned the year of foundation of the fort in 1219 of Tipu Sultan's Mauludi era. The other important gates are Water gate near the Gangadhareswara temple, Jibi or Krishna gate near the Krishna temple and the Bangalore gate in the eastern wall. It is one of the most formidable forts in India.

IV. MONUMENTS

Srirangapatna has innumerable monuments that are of national, state and local importance. The list of the

monuments recognized by Archaeological Survey of India and State Archaeology Department, which are located in the Local Planning Area (LPA) of Srirangapatna is given in the table 1.

Table 1 : List of ASI and State Monuments within LPA

ASI Monuments	State Monuments
Ancient Palace Site and Remains	Krishnamurthy's Bungalow
Colony Baileys Dungeon	Mummadi Krishnaraja Wodeyar Birth place
Daria Daulat Bagh	Srirangapatna Fort
Gumbaz containing tomb of Tipu Sultan	Bateri 2 No
Jumma Masjid	Gun powder stores 8 no
Obelisk Monuments & Fort walls	Hanging Bridge
Spot where Tipu's body was found	Moat around Fort
Sri Kanteerava Statue in Narasimha Temple	Rangamba 2No
Sri Ranganathaswamy Temple	Ruined palace of Mirsadik
Thomas Inman's Dungeon	Tuppada kola

Source: State Archaeological Department, Karnataka

V. SIGNIFICANCE ASSESSMENT OF HERITAGE MONUMENTS

Mapping procedure is a powerful tool to assess the significance of the heritage monuments and its areas. It helps to delineate a "heritage area"/zones, precincts and monuments of importance for prioritizing the action plan. The monuments are to be classified as built or natural or cultural types. Then, the monuments are categorised as historical or architectural or aesthetic or cultural or combination of the four. The monuments are to be graded depending on their significance, type and category. The evaluation criteria are given in the table 2.

Table 2: Evaluation Criteria for Heritage Monuments

	Main Criterion	Sub-criterion	Rank
Built Heritage	Historical	Very Significant	5
		Moderately Significant	3
		Not so Significant	1
	Architectural	Outstanding	5
		Average	3
		Poor	1
	Aesthetic	Significant	5
		Modest	3
		Poor	1
	Cultural	High	5
		Medium	3
		Low	1
Natural Heritage	Historical Value	Very Significant	5
		Moderately Significant	3
		Not so Significant	1
	Landscape	Significant	5
		Modest	3
		Not so Significant	1
Cultural Heritage	Historical	Very Significant	5
		Moderately Significant	3
		Not so Significant	1
	Uniqueness	Outstanding	5
		Average	3
		Poor	1

A. Step by Step Procedure for Mapping

The Primary objective is to identify an area that is of special value and is in need of special planning strategies that take care of potential and prospects of the area in the context of resources compatibility. Each of the resource is characterized by a set of criteria. Each criterion is given rank on a 3-point scale. Each rank is given a binary scoring, that is 1, if present else 0. The summation of ranks gives the value of each resource.

Step 1: To assess the architectural quality of built heritage, the criteria can be –outstanding, moderately significant and poor. If an artifact ‘A’ is assessed as of ‘significant’ value, the rank will be 5, whereas for Historical importance, the same artifact may be described as ‘not so significant’. Hence it will get a minimum value of 1.

Step 2: Each rank is given a binary scoring, that is 1, if present else 0.

The Artifact criteria assessment rank score

	Rank	Score
A Architectural - Very Significant	5	1
- Not so Significant	1	1
Alternatively, if it is historically insignificant Historical- insignificant	0	0

Step 3: The summation of (rank x score) gives the value of each resource.

$$V_k = \sum_{n=1}^j R \times S$$

Where,

- V- total value in each category
- k- resource category
- S Score for each criteria
- R- Rank for each criterion
- n- criteria
- j- total number of criteria in each category

Thus, in the above example value becomes

$$V=(5 \times 1)+1 \times 1=6$$

Step 4: The geographical area is subdivided in to smaller chunks like plots. For simplicity purpose, a network of grids has been adopted. The grid spacing has been taken as 110 meters. The cumulative values are assigned to grids containing the resources.

Step 5: The different potential area maps for built, natural and cultural heritage are prepared.

Step 6: These maps are superimposed to get the final value of the grids. The total value of each grid, V, is then represented by the generalized formulae as follows:

$$V = \sum_{k=1}^p V_k$$

Where,

- k-category of resources
- p-number of categories

Step 7: The values are divided into 3 ranges to get areas of high, moderate and low potential. This helps to identify the core and buffer areas. The high potential areas give the possible location of the core area, the medium and the low potential areas imply the buffer area. The graphical representation thus obtained will guide in delineating the

Heritage site. Physical, natural and administrative boundaries are considered to get the final boundaries of various areas. The methodology has been followed to delineate the core and buffer area. Schematic Diagram showing Mapping of Heritage Resources and its Significance.

V2	V3	V3	V1	V2
V3	V2	V2	V2	V3
V3	V2	V1	V1	V2
V3	V2	V1	V1	V3
V2	V2	V3	V3	V3

V1 : 1 to 3 Low potential

V2 : 4 to 6 Medium potential

V3 : 7 to 9 High potential

B. Heritage Monuments and their Significance

The significance of the Heritage monuments of the Fort area has been evaluated based on the ranking of monuments. Table 3 shows the ranking of heritage monuments. Based on the ranking of monuments, the mapping has been carried out and is shown in Fig. 2

Table 3: Heritage Monuments and the Total Ranking

Sl. No.	Places of interest	Historical	Architecture / Landscape	Aesthetic/ Uniqueness	Cultural	Ranking
1	Ancient Palace Site	5	-	3	-	8
2	Colony Baileys Dungeon	5	5	3	-	13
5	Jumma Masjid	1	5	3	5	14
6	Obelisk & Fort walls	3	3	1	-	7
7	Tipu's body was found	3	-	-	-	3
9	Ranganathaswamy Temple	5	5	5	5	20
10	T. Inman's Dungeon	3	3	3	-	9
11	Krishnamurthy's Bungalow	3	3	3	-	9
12	Mummadi Krishnaraja Wodeyar's Birth place	3	1	1	-	5
13	Srirangapatna Fort	5	5	5	-	15
14	Bateri 2 No	5	3	3	-	11
15	Gun powder stores 8 no	5	3	1	-	9
16	Hanging Bridge	3	1	-	-	4
17	Moat around Fort	5	5	5	-	15
18	Ranagamba 2No	3	3	1	-	7
20	Tuppadakola	3	3	3	-	9

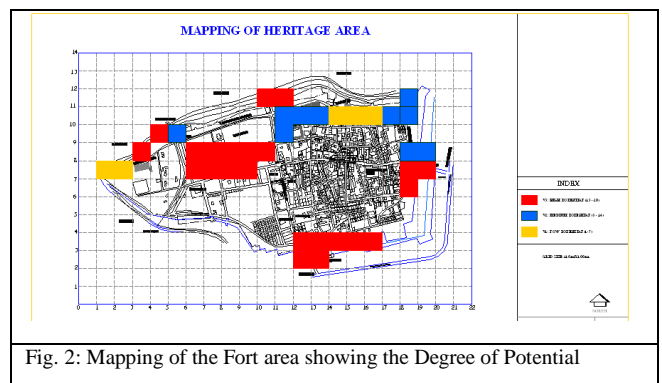


Fig. 2: Mapping of the Fort area showing the Degree of Potential

In the Fig. 2, high potential area (red colour area) requires first phase of conservation and will receive the highest level of conservation and management efforts. Limited development should be encouraged and be in conformity with the area. Medium (Blue colour) and low (yellow) potential areas will be taken up for the conservation in successive phases.

VI. DELINEATION OF HERITAGE AREAS

The Fort Area where the monuments of historic, religious and cultural importance are located is to be declared as “Heritage Area” which needs to be delineated on the following grounds for heritage conservation. Most of the heritage buildings are scattered along the Cauvery River, which shows that water was a major element for development and also forms a natural barrier. The monuments are located towards the Northern part of the Fort. The tourists visit only Sri Ranganathaswamy Temple due to its Historic, Cultural and Religious significance; other monuments are being neglected either by the authorities, tourists or residents. The prominence of other monuments could be recognized by interconnecting them in a Heritage Trail. i.e., “Heritage area” and is marked where all the important monuments are connected. The “Heritage Area”, which was delineated from the mapping procedure, is to be developed and conserved in a holistic approach. The delineated heritage area is shown in Fig. 3.

The area delineated as “Heritage Area” has following shortfalls and are: negligence of monuments by the authorities as well as the residents; temporary commercial establishments near the monuments; absence of organized parking; encroachment of the fort area and the places near the monuments; inaccessibility to the monuments; lack of awareness and knowledge about the importance of the monuments by the authorities as well as the residents; absence of vision to envisage Heritage management as a tool to develop tourism economy and diversified image of the facades around the area.

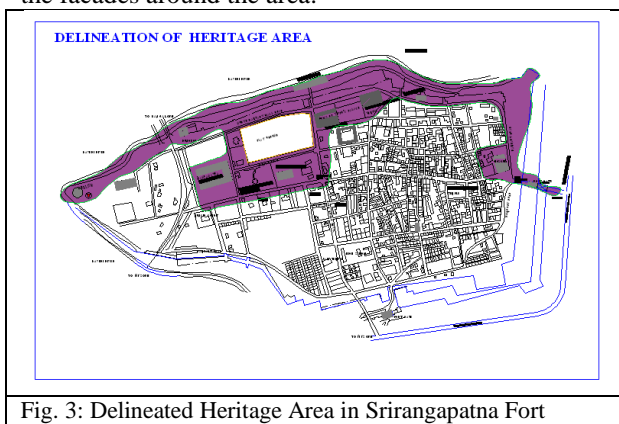


Fig. 3: Delineated Heritage Area in Srirangapatna Fort

VII. CONSERVATION STRATEGIES

The following strategies are suggested for planning and conservation of heritage areas, buildings and precincts in the Town of Srirangapatna:

- i) The monuments and buildings of historical, architectural, archaeological and cultural significance need to be identified and published in the gazetteer.
- ii) The listing of buildings shall be based on the age of the building, its special value of architecture or

cultural reasons or historical periods, its relevance to history, its association with well known character or event, its value as a part a part of group of buildings and the uniqueness of the building or any object or structures fixed to the building or forming part of land and comprised within the cartilage of the building not only within the Fort Area but also within the Local Planning Area.

- iii) The areas under conservation shall be suitably treated for landscape and as far as possible shall be utilised for social and cultural activities
- iv) The Planning Authority has to develop guidelines for development, re-development, additions, alterations, repairs, renovation and reuse of heritage building within the LPA.
- v) Citizens need to be involved and awareness programmes need to be undertaken for effective implementation of heritage plans and programmes.
- vi) Management Action Plan for Heritage Areas including precincts to be worked out in consultation with various stakeholders namely Town Municipal Council of Srirangapatana, ASI, Archaeological and Heritage Commissioners Officers, Town Planning and other agencies including NGOs.
- vii) The Area delineated as Heritage Area (depicted in the map) need to develop special plans for conservation and improvement of controlled areas and alteration or demolition of any building is prohibited in the controlled conservation areas without the consent of the Planning Authority and Municipality as well. The Fort Area should be considered as *Special Area* and needs special treatment to conserve the heritage value for retaining the character. In order to preserve aesthetic environs around these monuments, it is necessary to declare areas surrounding these monuments as *zones of special control* and impose the following regulations around these monuments:
 - Buildings upto a height of 3.5 mts from the ground level is permissible within the distance of 100-300 meters from the premises of the monuments.
 - Building up to inclusive of first floor or upto a height of 7 mts from ground level whichever is less only is permissible in the area beyond 300 mts from the premises of the monuments within the fort area.

viii) Following conservation measures and strategies are required to arrest the damage and decay in the fort heritage area:

- a. The Fort has a perimeter of 3.7 km. and the conservation of the entire fort requires huge amount and time. Hence conservation of the fort can be carried out in phased manner. The fort along the river, towards the Northern side has not been damaged much due to the inaccessibility and the presence of huge trees. As this part of the fort has rampart, first phase of conservation is to be taken up here.
- b. The North Rampart Road is lined with monuments and it provides a beautiful view to the fort, if

- conserved. As the monuments are located on the edge of the town and are not intervened with the developments, the conservations measures can be effectively carried out.
- c. The movement of local traffic is very less on North Rampart Road and this is an added advantage for the tourist movement and there is an ample space is available for parking.
 - d. The fort has two gates namely Southern Gate or Mysore gate and Eastern Gate or Bangalore Gate, which is known only by researchers, academicians, Archaeologists etc.,. These Gates are to be conserved to depict the Historicity.
 - e. The encroachments near the Bangalore Gate are to be cleared and proper alternative arrangements are to be provided.

II. CONCLUSIONS

The history of the town is written in its old buildings and streets. Though a town should have new structures, it is not wise to lose the old buildings, as every building has some history related to it. The conservation cannot be the sole concern of government departments, but it has to be a coordinated effort of local authorities, architects, related professionals, private organizations and millions of individuals. The conservation strategies presented here leads to enhance the historical, architectural, cultural and aesthetic aspects of the town by giving a rebirth to the dyeing monuments. The conservation measures, if taken in time will save Srirangapatna from gradual but imminent destruction.

REFERENCES

- [1]. Ashtosh Joshi. (2007), "Regeneration of Indian Historic Cities", The Journal of The Indian Institute of Architects, Volume 72, Issue 12, pp. 20-22.
- [2]. Deborah Thiagarajan and Pierre Pichard. (1989), "The Listing of Heritage – Pondicherry", Architecture + Design, A Journal for the Indian Architects, Vol. VI, No. 1, pp. 52-54.

- [3]. Dipaneeta Das and Sanghamitra (2007), " Mapping of Heritage Resources and Planning for Sustainable tourism in Temple town of Vishnupur", W.B., ITPI Journal, Institute of Town Planners, India, Vol. 4, No. 3. pp. 16-26.
- [4]. Issar, T. P. (1991), "The Royal City", Mytec Process Pvt. Ltd., Bangalore.
- [5]. Krishna Menon, A. G. (1989), Conservation in India, Architecture + Design, A Journal for the Indian Architects, Vol. VI, No. 1, pp. 22-27.
- [6]. Kulbhushan and Minakshi Jain. (1989), "The Listing of Heritage – Jaiselmer", Architecture + Design, A Journal for the Indian Architects, Vol. VI, No. 1, pp. 49-51.
- [7]. Mysore State Gazetteer (1967), Mandya District, Gazetteer of India.
- [8]. Neetu Kapoor. (2007), " Redevelopment of Heritage Zone", The Journal of The Indian Institute of Architects, Volume 75, Issue 10, pp. 9-10.

BIOGRAPHIES



Dr. B. Shankar received the B.E. degree in Civil Engineering in 1984, M.UR.P 1989 and Ph. D in Urban and Regional Planning from the University of Mysore, Mysore. He is working as Reader in Urban and Regional Planning at the Institute of Development Studies, University of Mysore from July 2007. He has 20 years of experience in the field of urban and regional planning. His current interest includes heritage conservation, planning legislation, governance and management.



S. Uma received the B.Arch in Architecture and M. Tech in Urban and Regional Planning in 2009 from the University of Mysore, Mysore. She is working as Lecture in JSS Polytechnic, Mysore. Her current interest includes heritage conservation and Architectural Buildings.

Fuzzy Approach to Voltage Collapse based Contingency Ranking

Dr. Shobha Shankar

(Department of Electrical and Electronics Engineering,
Vidyavardhaka College of Engineering, Mysore, India)

ABSTRACT

The importance of preventing the voltage collapse is gaining importance due to increase in dependency on the use of electricity. This has compelled the utilities to maintain high system reliability. The evaluation of a power systems ability to withstand dangerous contingencies and to survive to a normal or acceptable operating point is a prerequisite for security analysis. Fast and accurate security assessment, has become a key issue to ensure secure operation of power system. Steady-state security assessment enables the operating personnel to know which system disturbances or contingencies may cause limit violations and force the system to enter into emergency state. Line outages often cause blackouts due to voltage collapse. Voltage Stability Margin of the system on occurrence of specific contingency gives good information about the severity of the contingency of the system. This paper presents fuzzy approach to voltage collapse based contingency ranking. It uses L index as Voltage Collapse Proximity Indicator. This indicator is used as post contingent quantity in addition to bus voltage profiles to evaluate contingency ranking. The proposed approach is tested under simulated condition on IEEE-30 bus system.

Keywords: Composite Index, Fuzzy Set, L index, Voltage Collapse Proximity Indicator, Voltage Stability Margin

I. INTRODUCTION

A power system is said to be operating in secure state, if the system remains in a reliable, normal operating state for every contingency case under consideration. Due to time limitation in real-time situations, those contingency cases which are potentially harmful to the system must be picked out and detailed analysis is carried out only for these cases. This process of ranking the contingencies according to their severities is referred to as contingency ranking. In the past, contingency rankings were carried out using the algorithms based on line loadings and bus voltages [1]-[3]. As the recent power systems are experiencing the threat of voltage instability, the contingencies are required to be ranked incorporating this phenomenon. A method based on curve fitting approach is proposed and is compared with continuation power flow method, multiple load flow method and test function method [4]. A new partitioning technique based on tangent vector to the bifurcation manifold is proposed. A tangent vector clustering technique is used for the identification of the critical area with respect to the collapse point at any loading condition. It is used for the computation of new voltage stability index, which speeds

up the computation of the collapse point [5]. The second order information derived from the Singular Value Decomposition analysis of the load flow Jacobian matrix is used to obtain the contingency ranking [6]. The implementation of both Point of Collapse method and Continuation method for the computation of voltage collapse point (saddle-node bifurcations) and its application to detection and solution of voltage stability problem is demonstrated [7]. Fuzzy set theory is a very powerful tool to model uncertainty and to incorporate human experience and heuristics [8]-[13]. A fuzzy set based reasoning approach for contingency ranking is developed using line flows and bus voltage deviations as post contingency quantities to achieve desired contingency list [14].

Line outage often causes blackouts due to voltage collapse. This signifies that reduction in loadability margin under each line outage condition should be given due attention in the ranking process. Voltage Stability margin of the system on occurrence of specific contingency gives good information about the severity of the contingency of the system. Though, the system pre-contingency operating point may be away from the voltage collapse point, contingency will push the system close to proximity to voltage collapse point. Hence, computation of voltage stability margin at this operating point serves as a good indicator of criticality of contingency. The changes in voltage stability margin are computed using static voltage collapse proximity indicator. This paper uses L index as Voltage Collapse Proximity Indicator to rank line outage contingencies. Fuzzy approach is used to combine the effect of voltage collapse proximity indicator and bus voltages to effectively rank the line outage contingencies. The bus voltage profiles and L index are expressed in fuzzy set notation before they are processed by the fuzzy reasoning rules. The severity indices are also divided into different categories based on extensive off-line analysis. The fuzzy rules are used to evaluate the severity of each post contingent quantity. The severity of a contingency is determined by evaluating composite index, which is the summation of severity index of L index and severity of bus voltage profiles. The Fuzzy inference structure FIS is tested in MATLAB 7 Fuzzy Toolbox. The proposed approach is tested under simulated condition on IEEE-30 bus system.

II. L INDEX

L - Index is widely used Voltage Collapse Proximity Indicator for various studies. Among the various indices for voltage-stability and voltage collapse prediction, the L

index gives fairly consistent results. This is an accurate indicator and is easily computed [15].

A. Mathematical Formulation

Consider a system where n is the total number of buses, with $1, 2, \dots, g$ generator buses, and $g+1, g+2, \dots, g+s$ SVC buses, $g+s+1, \dots, n$, the remaining $(n-g-s)$ buses. For a given system operating condition, using the load-flow results, the voltage-stability L - index is computed as,

$$L_j = \left| \sum_{i=1}^g F_{ji} \frac{V_i}{V_j} \right| \quad (1)$$

Where $j = g + 1, \dots, n$ and all the terms within the sigma on the right hand side are complex quantities. The values of F_{ji} are complex and are obtained from the network Y-bus matrix. For a given operating condition,

$$\begin{bmatrix} I_G \\ I_L \end{bmatrix} = \begin{bmatrix} Y_{GG} & Y_{GL} \\ Y_{LG} & Y_{LL} \end{bmatrix} \begin{bmatrix} V_G \\ V_L \end{bmatrix} \quad (2)$$

Where I_G , I_L , V_G , and V_L represent complex current, voltage vectors at the generator nodes and load nodes. $[Y_{GG}]$, $[Y_{GL}]$, $[Y_{LL}]$ and $[Y_{LG}]$ are corresponding partitioned portions of the network Y-bus matrix.

Rearranging, we obtain

$$\begin{bmatrix} V_L \\ I_G \end{bmatrix} = \begin{bmatrix} Z_{LL} & F_{LG} \\ K_{GL} & Y_{GG} \end{bmatrix} \begin{bmatrix} I_L \\ V_G \end{bmatrix} \quad (3)$$

$$\text{Where, } [F_{LG}] = -[Z_{LL}]^{-1}[Y_{LG}] \quad (4)$$

For stability, the index L_j must not be violated (maximum limit = 1) for any node j . Hence, the global indicator L describing the stability of the complete subsystem is given by $L = \text{maximum of } L_j$, for all j load buses. An L index value away from 1 and close to 0 indicates improved system security. For an unloaded system with generator/load buses voltage at 1.0 p.u. the L indices for load buses are closest to zero, indicating that the system has maximum stability margin. For a given network, as the load/generation increases, the voltage magnitude and angles change near maximum power-transfer condition and the voltage-stability index L_j values for load buses tend to close to unity, indicating that the system is close to voltage collapse. While the different methods give a general picture of the proximity of the system voltage collapse, the L index gives a scalar number to each load bus. The L indices for given load condition are computed for all the load buses. The maximum of the L -indices gives the proximity of the system to voltage collapse.

III. FUZZY APPROACH TO CONTINGENCY RANKING

Fuzzy logic provides an excellent framework to effectively model uncertainty in human reasoning with the use of linguistic variables with membership function. The use of fuzzy logic is increasing in the power systems problems, as it is an intelligent processing. Many promising applications have been reported in the broad fields of system control, optimization, diagnosis, information processing, decision support, system analysis

and planning. In modern power systems, voltage alone cannot be used for assessing voltage security. Due to increased use of compensating devices which raise voltage to normal levels even when adequate reactive support is lacking, voltage becomes a poor indicator of security. The fuzzy approach uses L index as post contingent quantity in addition to bus voltage profiles to evaluate contingency ranking. The bus voltage profiles and L index are expressed in fuzzy set notation before they are processed by the fuzzy reasoning rules. The severity indices are also divided into different categories based on extensive off-line analysis. The fuzzy rules are used to evaluate the severity of each post contingent quantity. The severity of a contingency is determined by evaluating composite index, which is the summation of severity index of L index and severity of bus voltage profiles. The Fuzzy inference structure FIS is tested in MATLAB 7 Fuzzy Toolbox.

A. Bus Voltage Profiles

The post contingent bus voltage profiles are divided into three categories using fuzzy set notations: low voltage (LV), below 0.95 p.u.; normal voltage (NV), 0.95-1.05 p.u.; and over voltage (OV), above 1.05 p.u. The boundaries of these categories are fuzzified based on extensive off-line analysis performed for various load conditions. Trapezoidal membership function is used for describing bus voltage profile shown in Fig. 1.

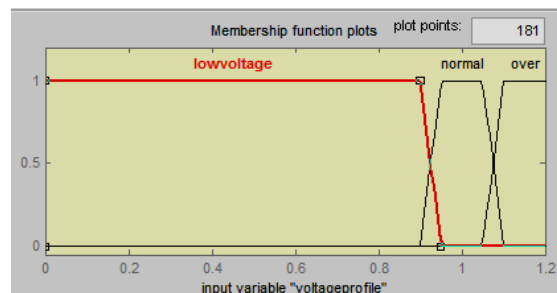


Fig. 1 Membership function for 3 linguistic variables of bus voltage profiles

B. L index

The post contingent L index are divided into five categories using fuzzy set notation; very small (VS), 0-0.18; small (S), 0.24-0.36; medium (M), 0.42-0.56; high (H), 0.62-0.76; very high (VH) 0.82-1.0. Each category represents a severity class of the L index. The boundaries of these categories are fuzzified based on extensive off-line analysis. Fig. 2 shows the membership function of L index.

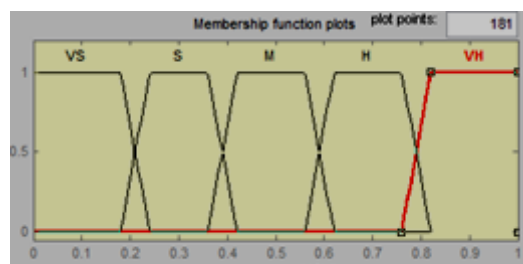


Fig. 2 Membership function for 5 linguistic variables of L index

The fuzzy rules used for evaluation of severity index of bus voltage profiles and L index are given in the following Table 1. Centre of area or gravity method is used for defuzzification.

Table 1: Fuzzy Rules

Post contingent quantity	Severity index
L index: VS S M H VH	VLS LS BS AS MS
Voltage : LV NV OV	MS BS AS

Note: VLS- very less severe; LS- less severe; BS- below severe; AS – above severe; MS – more severe.

C. Severity Index of Post Contingent Quantities

The output membership functions used to evaluate the severity of bus voltage profile are also divided into three categories using fuzzy set notation. As the linguistic variables are imprecise, each linguistic variable covers a range rather than a single severity index. The boundaries of these categories are fuzzified based on extensive off-line analysis. Trapezoidal membership function is used for describing a linguistic variable.

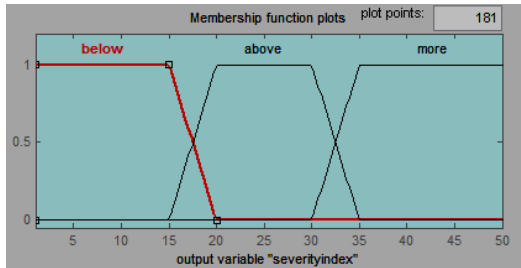


Fig. 3 Membership function for severity index of bus voltage profile

The output membership functions used to evaluate the severity of L index are divided into five categories using fuzzy set notation. Trapezoidal membership function is used for describing a linguistic variable.

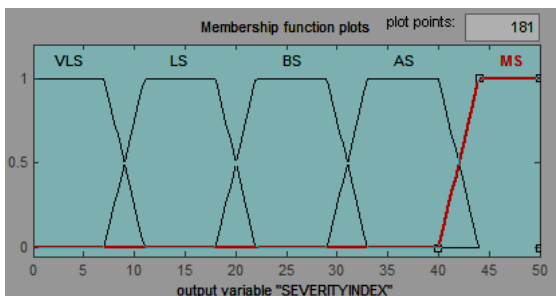


Fig. 4 Membership function for severity index of L index

The overall severity index (composite index) for a particular line outage is given by $CI = SI_L + \sum SI_{VP}$; Where, SI_L is the severity index of L index for a particular line outage and $\sum SI_{VP}$ is the sum of severity index of all bus voltage profiles for a particular line outage. Thus, the overall severity index indicates the actual severity of the system for a contingency.

IV. METHODOLOGY

The major steps involved in this approach for contingency ranking is as follows

- For the given system, considering a line outage at a time, load flow study is performed to determine bus voltage profiles.
- L index is computed using (1) and is used as post contingent quantity.
- Assuming trapezoidal membership function, the bus voltage profiles and L index are represented in fuzzy set notation.
- Severity index of L index and bus voltage profiles are also represented in fuzzy set notation.
- Using Fuzzy-If-Then rules overall severity index for bus voltage profiles and L index is determined. The Fuzzy Inference System is tested in MATLAB 7 Fuzzy Toolbox.
- Composite index is found using the formula $CI = SI_L + \sum SI_{VP}$
- The above procedure is repeated for all the line outages and the contingencies are ranked based on composite index.

V. TEST RESULTS

The proposed approach is tested under simulated condition on IEEE-30 bus system. A.C load flow is carried out to select the heavily loaded lines based on Voltage Collapse Proximity Indicator. The IEEE-30 bus system consists of 6 generators, 2 shunt capacitors and 41 transmission lines. Contingency screening is carried out to identify all the heavily loaded lines. On contingency screening total 13 transmission line outages are considered for ranking. The line outages considered for ranking are listed in Table 2.

Table 2 List of Line Outage Contingencies in IEEE 30 bus system

Contingency no.	Type of contingency	From bus	To bus
1	SLO	1	2
2	SLO	1	3
3	SLO	3	4
4	SLO	2	6
5	SLO	4	6
6	DLO	1	3
		2	4
7	DLO	2	4
		2	5
8	DLO	2	4
		3	4
9	DLO	3	4
		2	5
10	DLO	2	5
		2	6
11	DLO	2	6
		4	6
12	DLO	4	6
		5	7
13	DLO	4	6
		6	7

Simulations were carried out to compute L index and bus voltage profiles for all the contingencies listed in the Table 2. Table 3 and 4 shows the ranking using Fuzzy approach for 100% and 140% load. Fuzzy approach effectively ranks contingencies under different load conditions. Table 5 shows the ranking based on L index and Minimum Singular Value of load flow Jacobian matrix [16] using Fuzzy approach.

Table 3 Contingency Ranking Based on L index using Fuzzy Approach: 100 % load

Line outages	SI _{V(SUM)}	SI _L	CI	Rank
1-2	189.08	31.90	220.98	1
1-3	188.88	14.63	203.51	7
3-4	189.32	11.70	201.02	9
2-6	190.55	6.21	196.76	13
4-6	190.58	9.60	200.18	11
1-3,2-4	184.14	21.10	205.24	5
2-4,2-5	186.45	20.30	206.75	4
2-4,3-4	184.94	20.20	205.14	6
3-4,2-5	185.73	22.40	208.13	3
2-5,2-6	185.06	23.90	208.96	2
2-6,4-6	183.71	19.40	203.11	8
4-6,5-7	191.01	19.90	200.91	10
4-6,6-7	186.45	12.90	199.35	12

Table 4 Contingency Ranking Based on L index using Fuzzy Approach: 140 % load

Line outages	SI _{V(SUM)}	SI _L	CI	Rank
1-2	486.88	44.30	513.18	1
1-3	173.32	32.80	206.12	8
3-4	173.67	30.60	204.27	9
2-6	173.67	21.40	195.07	13
4-6	174.62	23.30	197.92	11
1-3,2-4	463.56	41.30	504.86	5
2-4,2-5	470.65	39.30	509.95	4
2-4,3-4	453.84	41.30	495.14	6
3-4,2-5	485.48	42.20	527.6	2
2-5,2-6	481.77	41.30	523.07	3
2-6,4-6	171.68	41.20	212.88	7
4-6,5-7	174.62	23.40	198.02	10
4-6,6-7	175.19	21.30	196.49	12

Table 5 Comparison of Contingency Ranking using Fuzzy Approach based on L index and MSV

Line outages	100% load		140% load	
	L Index	MSV	L Index	MSV
1-2	1	1	1	1
1-3	7	7	8	7
3-4	9	9	9	9
2-6	13	10	13	13
4-6	11	12	11	12
1-3,2-4	5	5	5	5
2-4,2-5	4	4	4	4
2-4,3-4	6	6	6	6
3-4,2-5	3	2	2	2

2-5,2-6	2	3	3	3
2-6,4-6	8	8	7	8
4-6,5-7	10	11	10	10
4-6,6-7	12	13	12	11

From the above results, it can be observed that the contingency ranking obtained using L index and MSV is in close agreement with each other. The proposed fuzzy based composite index is accurate in ranking the contingencies. The contingencies ranked using this index provides very useful information about the impact of the contingency on the system as a whole and helps in taking necessary control measures to reduce the severity of the contingency avoiding possible voltage collapse. The fuzzy approach is very effective in modelling imprecision and uncertainty in power system. Thus, fuzzy reasoning mimic's experienced human operator judgement. Fuzzy approach for contingency ranking will serve as a powerful tool for power system operator to foresee the possible occurrence of voltage collapse and initiate appropriate action.

VI. CONCLUSIONS

Fuzzy approach is used for combining the effect of L index with bus voltage profiles for ranking the contingencies. Fuzzy approach effectively ranks contingencies under different load conditions. The Fuzzy approach is flexible in incorporating human experience and heuristics. It includes the imprecision of linguistic terms associated with voltages and L index translates them into numerical values, which offers more flexibility, better insight into reality than conventional methods. Through proper tuning of membership functions in fuzzy representation, the approach can mimic experienced operators' performance in conducting contingency ranking.

REFERENCES

- [1]. F. Albuyeh, A. Bose and B.Heath, "Reactive Power Considerations in Automatic Contingency Selection", *IEEE Transactions On Power Apparatus and Systems, Vol. PAS-101, No. 1*, pp. 107- 112, January 1982.
- [2]. S. Vemuri and R. E. Usher, "On-line Automatic Contingency Selection Algorithms", *IEEE Transaction on Power Apparatus and Systems, Vol. PAS-102, pp.346-354*, February 1983.
- [3]. D. G. Taylor and L.J. Maahs, "A reactive contingency analysis algorithm using MW and MVAR distribution factors", *IEEE Transactions on Power Systems, Vol. 6, No. 1*, pp. 349-355, February 1991.
- [4]. G.C. Ejebe, G.D. Irissari, S. Mokhtari, O. Obadina, P. Ristanovic, J. Tong, "Methods for Contingency Screening and Ranking for Voltage Stability Analysis of Power Systems", *IEEE Transactions on Power Systems, Vol. 11, No. 1*, pp. 350-356, February 1996.
- [5]. Antonio C. Z. de Souza, Claudio A. Canizares and Victor H. Quintana, "New Techniques to Speed Up voltage Collapse Computations Using Tangent Vectors", Approved by IEEE Power System

BIOGRAPHY

Shobha Shankar received the B.E. degree in Electrical Engineering in 1994, M.Tech degree in Power Systems in 1997 from the University of Mysore, Mysore. She obtained her Ph.D. degree from Visveswaraya Technological University in 2011. She is working as Professor in the Department of Electrical and Electronics Engineering, Vidyavardhaka College of Engineering, Mysore, India. Her areas of interest are AI applications to Power System Studies, Voltage and Reactive Power Control.

- Engineering committee of the IEEE Power Engineering Society of publication in *IEEE Transactions on Power Systems*, Nov. 1996.
- [6]. Alberto Berizzi, Yong-Gang, Zeny, Paolo Marannino, Alessandro Vaccarini, and Pierangela A. Scrapellini, "A Second Order Method for Contingency Severity Assessment with respect to Voltage Collapse", *IEEE Transaction on Power Systems*, Vol. 15, No.1, pp. 81-87, February 2000.
- [7]. Claudio A. Canizares and Fernando L. Alvarado, "Point of Collapse and Continuation Methods for Large AC/DC Systems", *IEEE Transactions on Power Systems*, Vol.8, No.1, pp.1-8, February 1993.
- [8]. P. Marannino, A. Berizzi, M. Merlo, G. Demartini, "A Rule-based Fuzzy Logic Approach for the Voltage collapse Risk Classification", *IEEE Power Engineering Society Winter Meeting*, Vol. 2, pp. 876-881, 2002.
- [9]. P.R. Bijwe, M. Hanmandlu, V.N.Pande, "Fuzzy power flow solutions with reactive limits and multiple uncertainties", *Electric Power systems Research*, No. 76, pp.145-152, 2005.
- [10]. A. Narendranatha Udupa, D. Thukaram, K. Parthasarathy, "An expert fuzzy control approach to voltage stability enhancement", *Electrical Power and Energy Systems*, No. 21, pp.279-287, 1999.
- [11]. N. Yadaiah, A. Ganga Dinesh Kumar, J.L. Bhattacharya, "Fuzzy based coordinated controller for power system stability and voltage regulation", *Electric Power systems Research*, No. 69, pp.169-177, 2004.
- [12]. Carson W. Taylor, Mani V. Venkatasubramanian, Yonghong Chen, "Wide Area Stability and Voltage Control", *VII Symposium of Specialists in Electric Operational and Expansion Planning*, Brazil 2000.
- [13]. V. Mirinda and J.T. Saraiva, "Fuzzy Modelling of Power System Optimal Load Flow", *IEEE Transactions on Power Systems*, Vol.7, No.2, pp. 843-849, May 1992.
- [14]. Ching-Tzong Su and Chien-Tung Lin, "A New Fuzzy Control Approach to Voltage Profile Enhancement for Power Systems", *IEEE Transactions on Power Systems*, Vol. 11, No. 3, pp. 1654-1659, August 1996.
- [15]. P. Kessel, H. Glavitsch, "Estimating the Voltage Stability of a Power System", *IEEE Transactions on Power Delivery*, Vol. PWRD-1, No.3, July 1986.
- [16]. Tiranuchit and R.J. Thomas, "A Posturing Strategy against Voltage Instabilities in Electric Power Systems", *IEEE Transactions on Power Systems*, Vol. PWRS-3, No.1, February 1988.

Cell Coverage Area and Link Budget Calculations in GSM System

Purnima K. Sharma
Doctoral candidate
UTU, Dehradun (India)

R. K. Singh
Professor
KEC, Dhawarahat (India)

Abstract

The initial establishment of a Wireless system is very expensive and time consuming process. Due to this it is require to develop a mathematical model before establishment of such type of systems. The Calculation of path loss, link budgets etc are in the part of wireless system designing. Radio propagation is profoundly site specific and varies considerably depending on topography, frequency of operation, speed of mobile terminal, interface sources and other dynamic factor. To predict signal coverage and achieve data rates, it is important to characterize radio channel through key parameters and a mathematical model. In This paper we discussed the parameters which are affecting the communication performance and the coverage range of the cell. The coverage starts within the cell, by estimating the affecting parameters on the signal power level in the uplink and downlink at the practical circumstances that means at the mobile station at the cell boundary, or in a high fading region, taking into consideration the factors causing fading and other losses is the signal power.

Keywords: Global system for Mobile Communication (GSM), path loss, link budget, coverage area, Base Transceiver Station (BTS).

I. Introduction

The provision of wireless telephony network in a serving area requires planning and design in the most effective manner. In the design process the service providers generates a set of system requirements concerning the type of the desired system (e.g. Global system for Mobile Communication GSM, Code Division Multiple Access CDMA etc.), The main principle inside cellular network is replacement of a single high power transmitter by many small power transmitters and In this case each low power transmitter covers a small area or small range called a cell. Cellular networks are completely based on the technique of frequency reuse, so that the narrow radio spectrum will get maximum use, as shown in Fig.1. In cellular radio networks, A small area is covered by one base station and other base stations are installed with small overlapping areas. Neighboring cells require using different frequencies to evade interference, but the same frequency can be reused in distant cells. The entire coverage area is splitter into many small hexagonal cells so that to increase the capacity of entire network and a decrease in the reuse of frequency [2].

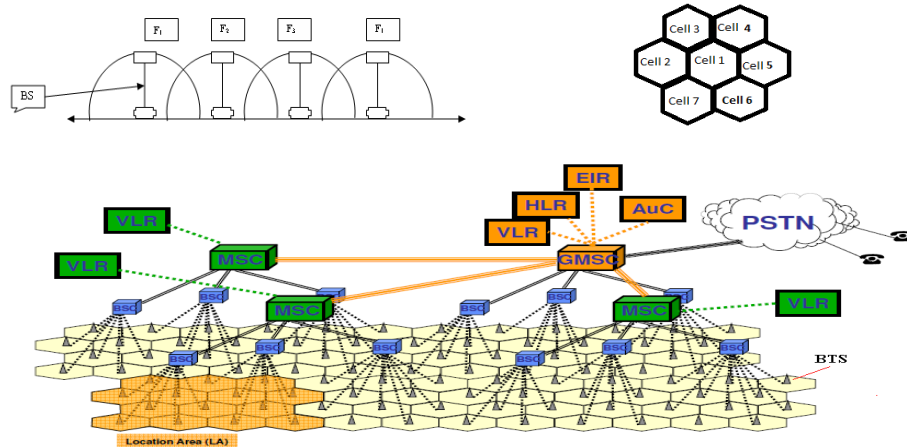


Fig. 1 Concept of cell and frequency reuse^[1]

- SIM Subscriber Identity Module
- MS Mobile Station
- BTS Base Transceiver Station
- BSC Base Station Controller
- MSC Mobile services Switching Center
- VLR Visitor Location Register

- HLR Home Location Register
- VLR Vistor Location Register
- EIR Equipment Identity Register
- AC Authentication Center
- PSTN Public Switched Telecomm Network
- ISDN Integrated Services Digital Network

Propagation models mainly focus to predict the received signal strength within some range from the transmitter, as well as the variation in the received signal strength in a close spatial proximity to a particular location. Propagation models which predict the signal strength for a random transmitter- receiver (T-R) separation distance are very useful in calculating the radio coverage area of a transmitter. On the other hand, propagation models that characterize the rapid fluctuations of the received signal strength over very short travel distances are called small-scale or fading models. Propagation models are also useful for predicting signal attenuation or path loss. Calculated path loss information is useful for controlling system performance or coverage to achieve perfect reception [1-4].

II. Coverage Area

A cellular network is a radio network distributed over land areas called cells, each served by at least one fixed-location transceiver known as a cell site or base station. These cells joined together provide radio coverage over a large geographic area. This radio network enables a large number of portable transceivers (e.g., mobile phones, pagers, etc.) to communicate with each other and with fixed transceivers and telephones anywhere in the network, via base stations, even if some of the transceivers are moving through more than one cell during transmission. The cell and network coverage depend mainly on natural factors such as geographical aspect/propagation conditions, and on human factors such as the landscape (urban, suburban, rural), subscriber behavior etc. The ultimate quality of the coverage in the mobile network is measured in terms of location probability. For that, the radio propagation conditions have to be predicted as accurately as possible for the region. Three main mechanisms that impact the signal propagation are depicted [5]. Those mechanisms are:

- *Reflection*. It occurs when the electromagnetic wave strikes against a smooth surface, whose dimensions are large compared with the signal wavelength.
- *Diffraction*. It occurs when the electromagnetic wave strikes a surface whose dimensions are larger than the signal wavelength, new secondary waves are generated. This phenomenon is often called *shadowing*, because the diffracted field can reach the receiver even when shadowed by an impenetrable obstruction (no line of sight).
- *Scattering*. It happens when a radio wave strikes against a rough surface whose dimensions are equal to or smaller than the signal wavelength.

There are two ways in which radio planners can use propagation models. They can either create their own propagation models for different areas in a cellular network, or they can use the existing standard models, which are generic in nature and are used for a whole area. The advantage of using their own model is that it will be more accurate, but it will also be immensely time-consuming to construct. Usage of the standard models is economical from the time and money perspective, but these models have limited accuracy. The empirical models use existing equations obtained from results of several measurement efforts. Some of the path loss models are as follows [6]:

- a. Simplified Path Loss Model
- b. Stanford University Interim (SUI) Model
- c. Okumura's Model
- d. Hata Model
- e. COST231 Extension to Hata Model
- f. ECC-33 model
- g. Walfisch- Bertoni Model
- h. Longley rice model
- i. Egli Propagation Model
- j. Bullington model
- k. Epstein-Peterson model

The above mentioned all the models are designed by calculating field data in different environments. Path loss determine the cell ranges. For GSM there are three cell ranges:

- Large cells, cell radius is 1 Km and normally it exceeds 3 Km.
- Small cells, cell radius 1 Km - 3 Km.
- Microcells: of radius in the range of 200 m – 300 m. The propagation in the above three cell sizes is determined by diffraction and scattering [1].

Additional loss called indoor loss (penetration loss) which varies greatly depending on type of material, architecture (numbers of windows), floor within building, etc. [9]. The figures 2,3 and 4 shows the path loss variation with cell radius and with the help of calculation of path loss in different areas we can determine the coverage area.

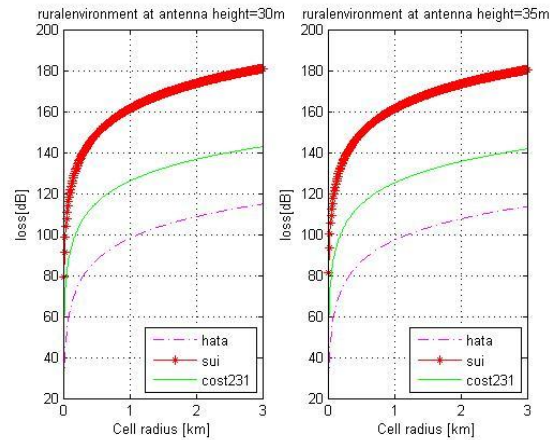


Fig. 2 The variation of path loss with cell radius in rural environment at different antenna height

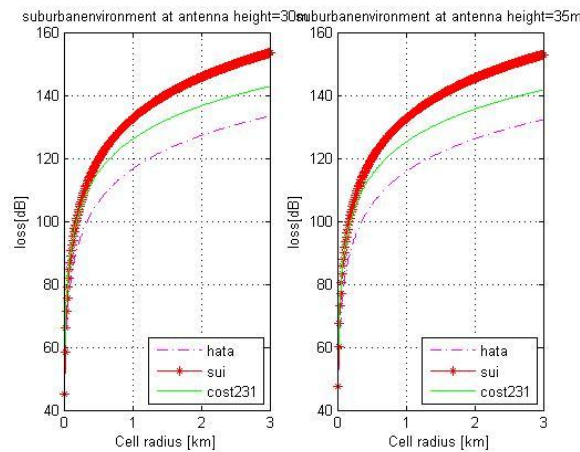


Fig. 3 The variation of path loss with cell radius in suburban environment at different antenna height

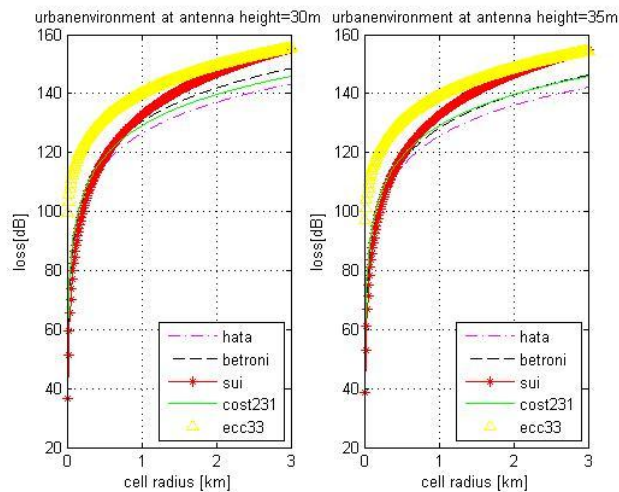


Fig. 4 The variation of path loss with cell radius in urban environment at different antenna height

III. Link Budget and its Calculations

Link budget is calculation of all the gains and losses in a transmission system. The link budget looks at the elements that will determine the signal strength arriving at the receiver. it is necessary to calculate link budget in the complete design of radio communication system. link budget calculations are used for calculating the power levels required for cellular communications systems, and for investigating the base station coverage. These link budget calculations are also used within wireless survey tools.

These wireless survey tools will not only look at the way radio signals propagate, but also the power levels, antennas and receiver sensitivity levels required to provide the required link quality. The link budget includes the following parameter [8-10].

- Transmitter power.
- Antenna gains (both transmitter antenna gain and receiver antenna gain).
- Antenna feeder losses.
- Path loss
- Receiver sensitivity

In order to formulate a link budget equation, it is required to look into all the areas where gains and losses may occur between the transmitter and the receiver. The calculation of the basic link budget is very easy.

$$\text{Received power (dBm)} = \text{Transmitted power (dBm)} + \text{gains (dbm)} - \text{losses (dBm)} \tag{1}$$

In basic calculation of link budget equation it is assumed that the power spreads out equally in all directions from the transmitter source. The indirect meaning is that the antenna used is an isotropic source, radiating equally in all directions. This is good for theoretical calculations, But not for practical calculations. A typical link budget equation for a radio communications system may look like the following:

$$P_{RX} = P_{TX} + G_{TX} + G_{RX} - L_{TX} - L_{FS} - L_{FM} - L_{RX} \tag{2}$$

Where: P_{RX} = received power (dBm)

P_{TX} = transmitter output power (dBm)

G_{TX} = transmitter antenna gain (dBi)

G_{RX} = receiver antenna gain (dBi)

L_{TX} = transmit feeder and associated losses (feeder, connectors, etc.) (dB)

L_{FS} = free space loss or path loss (dB)

L_{FM} = many-sided signal propagation losses (these include fading margin, polarization mismatch, losses associated with medium through which signal is travelling, other losses...) (dB)

L_{RX} = receiver feeder losses (feeder, connectors, etc.) (dB)

The objective of power budget calculation is to balance the uplink and down link. The receive signal sensitivity may be different because the mobile station and the base transceiver station has different Radio frequency architecture. The power of BTS can be adjusted to balance the whole link. The power balance (uplink and down link) decide the cell range. Here we can see two conditions those are

- The down link is greater than the uplink: It results in Range of BTS greater than Range of MS, Call dropped on uplink after initiation of handover, and Coverage area is smaller in reality than the prediction. This condition is most frequent.
- The uplink is greater than the down link: It results in Range of BTS less than Range of MS, and No coverage problem from MS to BTS.

The condition i.e the uplink > down link, is better than uplink < down link.

(A) Illustrative calculations of MS and BTS sensitivities:

It is minimum signal level at the input that leads to the signal to noise at the output, higher than a threshold E_b/N_0 related to the modulator performance [9].

Parameter	Value
Boltzmann's constant (K)	1.38×10^{-23} J/K ⁰
Absolute temperature (T)	300 K ⁰
Equivalent noise bandwidth (B_{eq}).	200 KHz
Intrinsic characteristic of the modulator (E_b/N_0).	8 dBm
Noise figure	8 dBm

$$R_{MS} = 10 \log_{10}(KTB_{eq}) + \frac{E_b}{N_0} + NF \tag{3}$$

Mobile station sensitivity (R_{MS}) = -120+8+ 8= -104dBm

The same as for MS but NF=-2

BTS Sensitivity= -114dBm

(B) Uplink Budget and Cell Range:

(a) Transmitting End:

$$EIRP = P_{Tx} + L_{AF} + G_{ME} \tag{4}$$

Transmitter(Mobile equipment (ME) or MS)	Parameter Value
1. Transmitter power of ME (P_{Tx})	33dBm
2. MS or ME antenna gain (isotropic antenna) (G_{ME})	0
3. Connector loss or Antenna feeder loss (L_{AF})	3
4. Effective isotropic radiated power (EIRP)	33 dBm
5. Mobile station antenna height (h_m)	1.5m

(b) Receiving End:

$$R_s = EIRP - L_p - I_M - F_M - L_C + G_{BTS} \tag{5}$$

Receiver (BTS)	Parameter value
1. Receiver sensitivity (R_s)	-114dBm
2. Body loss (B_L)	3dB
3. BTS receiving antenna gain (G_{BTS})	14dB
4. Interference margin (I_M)	2
5. Fast fade margin (F_M)	5dB
6. Connector loss (L_C)	3dB
7. Base station antenna height (h_b)	30m or 35m

Using equation (4)

$$EIRP=33-0-0=33dB$$

Using equation (5) below:

$$R_s = EIRP - L_p - I_M - F_M - L_C + G_{BTS}$$

$$-114 = 33 - L_p - 2 - 5 - 3 + 14$$

Therefore $L_p = 151dB$

(i) Hata model

Using Hata model pathloss calculation equation

$$L_p = L_{50,urban} (dB) = 69.55 + 26.16 \log_{10}(f_c) - 13.82 \log_{10}(h_{te}) - a(h_{re}) + (44.9 - 6.55 \log_{10}(h_{te})) \log_{10}(d) \tag{6}$$

Where,

$a(h_{re})$ is a correction factor for the mobile antenna height based on the size of the coverage area.

$$a(h_{re}) = 3.2(\log_{10}(11.75h_{re}))^2 - 4.97 \text{ dB} \tag{7}$$

$h_{re}=1.5$; (receiver height in meter), $f_c=900$ MHz and d =Cell radius in kilometer

BTS antenna height(h_{te})=35m

$$L_{50,Urban}(dB) = 125.4949 + 34.7864 \log_{10} d$$

$$151 = 125.4949 + 34.7864 \log_{10} d$$

$$(151 - 125.4949) / 34.7864 = \log_{10} d$$

$$d = 5.41 \text{ km}$$

BTS antenna height=30m

$$L_{50,Urban}(dB) = 126.4201 + 35.2249 \log_{10} d$$

$$151 = 126.4201 + 35.2249 \log_{10} d$$

$$(151 - 126.4201) / 35.2249 = \log_{10} d$$

$$d = 4.9865 \text{ km}$$

(ii) Cost-231 model

The path loss calculation formula is given by

$$PL=46.3+33.9\log_{10}(f) - 13.82\log_{10}(h_{bs}) - ah_m + (44.9 - 6.55\log_{10}(h_{bs}))\log_{10} d + c_m \tag{8}$$

Where $ah_m = 3.20(\log_{10}(11.75h_r))^2 - 4.97$, for $f > 400$ MHz

BTS antenna height (h_{bs})=35m
 PL=125.1107+34.7864log₁₀d+3
 151=125.1107+34.7864log₁₀d+3
 d=4.5499km

BTS antenna height (h_{bs})=30m
 PL=126.0359+35.224log₁₀d+3
 151=129.0359+35.2249og₁₀d
 d=4.2024km

(iii) Walfisch-Bertoni model

The formula to calculate the path loss is

$$LF=89.5-10\log((\rho^*(s)^{0.9})/((H_b-h_m)^2))+21\log(f)-18\log(h_b-H_b)+38\log(d); \tag{10}$$

$$\rho = \sqrt{\left(\frac{s}{2}\right)^2 + (H_b - h_m)^2}; \tag{11}$$

ρ =path distance from the building edge to the mobile , d =distance in km, h_m =receiver height in meter, s =spacing between in meter, H_b =building height in meter, h_b =antenna height in meter, f =freq in MHz.

BTS antenna height(h_b)=35m
 LF=122.4831+38log₁₀d
 (151-122.4831)/38= log₁₀d
d=5.6286 km

BTS antenna height(h_b)=30m
 LF=124.7320+38log₁₀d
 (151-124.7320)/38= log₁₀d
d=4.9121 km

(C) Down Link Budget and cell range

(a) Transmitting End:

$$EIRP = P_{TXB} - L_{cableB} - L_c + G_{TXB} \tag{12}$$

Transmitter(BTS)	Parameter Value
1. Out put power of BTS (P_{TXB})	44.5dBm (general value)
2. Transmitter antenna gain (G_{TXB})	18 dB
3. Cable loss (L_{CableB})	2dB
4. EIRP	
5. Combiner loss (L_c)	2dB

(b) Receiver End:

$$R_s = EIRP - L_p - B_{LM} - I_D - L_s - L_{CC} + G_{MS} \tag{13}$$

Receiver (MS or ME)	Parameter value
1. Mobile station Sensitivity (R_{SM})	-104dBm
2. Body loss (B_{LM})	3dB
3. MS receiving antenna gain (G_{BTS})	18dB
3. Interference margin (I_M)	3dB
4. Fast fade margin (F_M)	5dB
5. Connector loss (L_C)	2dB

$$R_s = EIRP - L_p - B_{LM} - I_M - F_M - L_C + G_{MS} \tag{14}$$

$R_s = -104 = EIRP - 151 - 3 - 3 - 5 - 2 + 18$ therefore $EIRP = 52$

$$52 = P_{\text{TXB}} - 2 - 2 + 18 \quad \text{therefore} \quad P_{\text{TXB}} = 38 \text{ dBm}$$

By analysing the whole calculations we found an imbalance of ($P_{\text{TX}} - P_{\text{TXB}}$)=5dB between uplink and down link. This can be rectified or compensated by increasing the BTS power by 5 dB. Or by adding 4-6 dB to the BTS output power, so that balance is maintained in the down link also [1].

IV. Conclusions

In this paper we calculated path loss by different models in different environments like urban, suburban and rural at two different transmitting antenna heights. The result of this analysis helps the network designers at the initial level of designing a wireless network and to define the coverage area. In this paper we also discussed about link budget analysis to achieve a balance between uplink and down link received signal because MS and BTS have different RF architectures and different sensitivities. Since RF link balance depends on parameters like BTS transmitter power, BTS combiner loss and BTS receiver diversity gain. The link budget analysis decides the cell coverage area.

References:

- [1] Dr. S. A. Mawjoud, "Evaluation of Power Budget and Cell Coverage Range in Cellular GSM System" AI-Rafidain Engineering vol.16 no.1, page no.37-47 in 2008.
- [2] M. R. Karim & M. Sarraf, "W-CDMA and cdma 2000" for 3G Mobile Network", McGraw-Hill Telecom. Professionals pp. 332-334, 2002.
- [3] Armoogum.V, Soyjaudah.K.M.S, Fogarty.T and Mohamudally.N, "Comparative Study of Path Loss using Existing Models for Digital Television Broadcasting for Summer Season in the North of Mauritius", Proceedings of Third Advanced IEEE International Conference on Telecommunication, Mauritius Vol. 4, pp 34- 38, May 2007.
- [4] K.Ayyappan, P. Dananjayan, " PROPAGATION MODEL FOR HIGHWAY IN MOBILE COMMUNICATION SYSTEM", Ubiquitous Computing and Communication Journal, Volume 3 Number 4, page no.61-66.
- [5] Rappaport, T.S., "Wireless Communications", Prentice-Hall, Upper Saddle River, New Jersey, Ch. 3 and 4, 1996.
- [6] Dinesh Sharma, Purnima K. Sharma, Vishal Gupta, R.K.Singh, "A Survey on Path Loss Models used in Wireless Communication System Design" in IJRTE Vol. 3, No. 2 in 2010.
- [7] Asiacecell Handbook, www.asiacecell.com chapter 4, pp. 25.
- [8] Intuitive guide to principles of communications, www.complextoreal.com.
- [9] <http://www.radio-electronics.com/info/propagation/path-loss/rf-signal-loss-tutorial.php>.
- [10] http://www.tranzeo.com/allowed/Tranzeo_Link_Budget_Whitepaper.pdf
- [11] http://ece483.cankaya.edu.tr/uploads/files/Day-02_GSM%20Network%20Architecture.pdf

Authors



Mrs Purnima K Sharma was born on 2nd June 1983 in Eluru, Andhra Pradesh (India). She received her M.Tech. degree in Communication and Signal Processing Engineering from NAGARJUNA UNIVERSITY (A.P.), India. She is an Associate Member of the IETE. She has published several Research papers in national and international journals/conferences. She is presently a research scholar in UTTARAKHAND TECHNICAL UNIVERSITY, Dehradun (INDIA). Her present research interest is in Image Processing and Wireless Communication.



Dr. R.K. Singh Professor, KEC, Dwarahat, Almora, Jointly submitting research and development project in UCOST, Uttarakhand. He is a member of the academic staff of Kumaon Engineering College, Dwarahat, Almora, where he is a professor in the department of Electronics and Communication Engineering. Dr. Singh has given his contribution to the area of Microelectronics, Fiber Optic Communications, and Solid State Devices. He has published several research papers in seminar/conference and journal papers. He is a member of several institutional and educational bodies. Before joining Kumaon Engineering College, Dwarahat, he has worked in Birla Institute of Technology and Sciences (BITS), Pilani, and Central Electronics Engineering Research Institute (CEERI) Pilani. At present he is serving as OSD, in the newly established Technical University of Uttarakhand known as Uttarakhand Technical University, Dehradun.

Electrical Conductivity and Dielectric Properties of Copper Doped Nickel Ferrites Prepared By Double Sintering Method

G. Ravi Kumar^{1*}, K. Vijaya Kumar², Y. C. Venudhar¹

¹Department of Physics, Osmania University, Hyderabad, India;

²Department of Physics, JNTUH College of Engineering, Nachupally (Kondagattu), Karimnagar-Dist., A. P., India.

Abstract

Ni-Cu ferrites of different compositions were prepared by a conventional double sintering ceramic technique. Electrical conductivity of Ni-Cu ferrites of various compositions have been investigated from room temperature to well beyond the Curie temperature. Composition and frequency dependent dielectric properties of mixed Ni-Cu ferrites have been measured at room temperature in the frequency range 1 to 13 MHz using a HP 4192A impedance analyser. Plots of $\log(\sigma T)$ versus $10^3/T$ are linear and have shown a transition near the Curie temperature. The activation energy in the ferromagnetic region is in general less than that in the paramagnetic region. Plots of dielectric constant (ϵ') versus frequency have shown a normal dielectric behavior of spinel ferrites. The frequency dependence of dielectric loss tangent ($\tan \delta$) is found to be abnormal, giving a peak at certain frequency for all mixed Ni-Cu ferrites. An attempt is made to explain the conduction mechanism in Ni-Cu ferrites and a qualitative explanation is given for the composition and frequency dependence of the dielectric constant and dielectric loss tangent.

Key words: Ni-Cu ferrites, Electrical conductivity, Dielectric properties, Activation energy, Curie temperature, Electrical resistivity, Fe^{2+} concentration.

1. Introduction

The copper substituted nickel ferrites find a variety of applications at radio and microwave frequencies [1, 2]. Particularly no information is available on electrical conductivity and dielectric properties of Ni-Cu ferrites prepared by a conventional double sintering ceramic technique in the literature. Moreover, there is a need for a thorough study of electrical and dielectric properties of these ferrites possessing desired application in microwave devices. The dielectric behavior of the Mn-Zn-Gd ferrites as a function of frequency and composition was reported by Ravi Kumar and Ravinder [3]. A strong correlation between conduction mechanism and the dielectric behavior of ferrites has been reported by Iwauchi [4]. The dielectric properties of Mn-Zn-Er ferrites were investigated by Ravinder and Vijaya Kumar [5]. The dielectric behavior of Ni-Zn-Gd ferrites was studied by Ravinder *et al* [6]. With a view of understanding the dielectric phenomena in mixed Ni-Cu ferrites, we have undertaken a systematic study of the electrical conductivity as a function of composition and temperature and the dielectric behavior as a function of frequency and composition.

2. Experimental details

Polycrystalline samples of nickel-copper ferrites having the chemical compositions $\text{Ni}_{1-x}\text{Cu}_x\text{Fe}_2\text{O}_4$, where $x = 0.2, 0.4, 0.6$ and 0.8 were prepared by the conventional double sintering ceramic technique. The samples were pre-sintered for 6 hr in air at 800°C . Final sintering of the specimens was carried out for 6 hr at 1200°C . The electrical conductivity measurements were carried out by two-probe method [7]. The dielectric measurements were made from 1-13 MHz by a HP 4192 A impedance analyser.

3. Results and discussion

Experimental data for the mixed Ni-Cu ferrites are given in Table-1, which includes the compositional formulae of all the ferrites under investigation and the values of electrical conductivity at room temperature. It can be seen from the table that the values of electrical conductivity are decreased with the increase of copper content from 0.2 to 0.8. This observation is in agreement with the result reported by Rezlescu *et al.* [8], who found that the resistivity of Li-Zn ferrites increased with the increase of zinc content. Among all the Ni-Cu ferrites the specimen with the composition $\text{Ni}_{0.2}\text{Cu}_{0.8}\text{Fe}_2\text{O}_4$ exhibits highest value of electrical resistivity ($\rho = 1.21 \times 10^7$ Ohm. cm).

Table-1: Electrical conductivity data of mixed Ni-Cu ferrites at room temperature.

Sl. No.	Ferrite composition	Electrical conductivity(σ) ($\text{Ohm}^{-1}\text{Cm}^{-1}$)	Seebeck coefficient (S) ($\mu\text{v/K}$)
1	$\text{Ni}_{0.8}\text{Cu}_{0.2}\text{Fe}_2\text{O}_4$	2.82×10^{-5}	-424
2	$\text{Ni}_{0.6}\text{Cu}_{0.4}\text{Fe}_2\text{O}_4$	4.68×10^{-6}	-342
3	$\text{Ni}_{0.4}\text{Cu}_{0.6}\text{Fe}_2\text{O}_4$	6.78×10^{-7}	-312
4	$\text{Ni}_{0.2}\text{Cu}_{0.8}\text{Fe}_2\text{O}_4$	8.26×10^{-8}	-278

The values of the Seebeck coefficient of mixed Ni-Cu ferrites at room temperature are calculated from the observed values of thermo emf, and are also included in Table-1 to facilitate the discussion. It can be seen from the table that the sign of the Seebeck coefficient is negative for all the ferrites under investigation which indicates that the predominant conduction mechanism in these ferrites is of n-type semiconductors.

The temperature dependence of electrical conductivity of mixed Ni-Cu ferrites of various compositions has been investigated from room temperature to well beyond the Curie temperature. Plots of $\log(\sigma T)$ versus temperature ($10^3/T$) are shown in Figs. 1-4. It can be seen from the figures that the value of $\log(\sigma T)$ increases linearly with increasing temperature up to a certain temperature $T_c(\text{K})$ at which a change of slope has occurred. The Curie temperatures for the Ni-Cu ferrite specimens under investigation have been determined by using a gravity method [9].

The ferrite specimen is made to attach itself to a bar magnet due to the magnetic attraction and the combination is suspended inside a furnace, where temperature can be varied up to 1000 K. As the temperature of the system is increased, at a particular temperature the specimen loses its spontaneous magnetization and becomes paramagnetic. This temperature is taken as the approximate Curie point of the specimen. The temperature of the specimen is measured by a chromel-alumel thermocouple in the furnace.

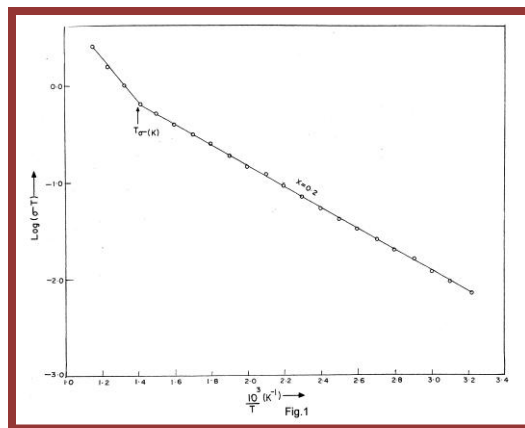


Fig.1: Plot of $\log(\sigma T)$ versus temperature for $\text{Ni}_{0.8}\text{Cu}_{0.2}\text{Fe}_2\text{O}_4$ ferrite.

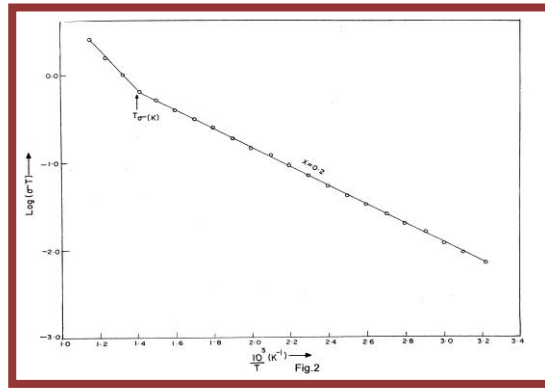


Fig.2: Plot of $\log(\sigma T)$ versus temperature for $\text{Ni}_{0.6}\text{Cu}_{0.4}\text{Fe}_2\text{O}_4$ ferrite.

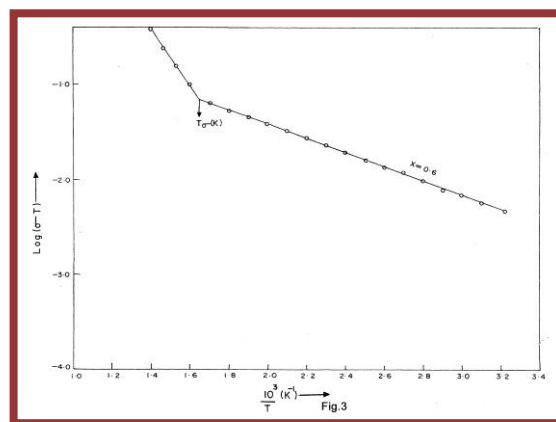


Fig.3: Plot of $\log(\sigma T)$ versus temperature for $\text{Ni}_{0.4}\text{Cu}_{0.6}\text{Fe}_2\text{O}_4$ ferrite.

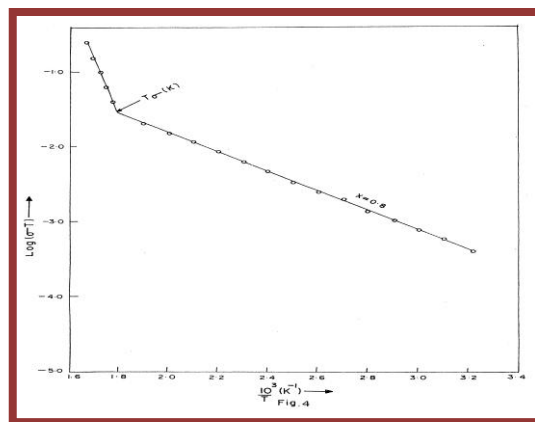


Fig.4: Plot of $\log(\sigma T)$ versus temperature for $\text{Ni}_{0.2}\text{Cu}_{0.8}\text{Fe}_2\text{O}_4$ ferrite.

The transition temperatures $T_{\sigma}(\text{K})$ are given in Table-2 along with the Curie temperatures $T_c(\text{K})$ determined by gravity method. It can be seen from Table-2 that the transition temperature $T_{\sigma}(\text{K})$ corresponds to the magnetic transition since it is nearer to the observed Curie temperature $T_c(\text{K})$ for all the ferrites under investigation.

Table-2: Transition temperatures and activation energies for Ni-Cu ferrites.

Sl. No	Ferrite composition	$T_c(K)$	$T_o(K)$	Activation energy		$\Delta E=E_2-E_1$	Resistivity(ρ) (Ohm.Cm)
				Ferri-magnetic region (E_1) eV	Para-magnetic region (E_2) eV		
1	$Ni_{0.8}Cu_{0.2}Fe_2O_4$	709	710	0.34	0.62	0.28	3.55×10^4
2	$Ni_{0.6}Cu_{0.4}Fe_2O_4$	674	672	0.29	0.58	0.29	2.14×10^5
3	$Ni_{0.4}Cu_{0.6}Fe_2O_4$	609	608	0.26	0.49	0.23	1.48×10^6
4	$Ni_{0.2}Cu_{0.8}Fe_2O_4$	558	559	0.24	0.44	0.20	1.21×10^7

Fig.5 shows the variation of Curie temperature with copper content. It can be noted from the figure that the value of $T_c(K)$ decreases with the increase of copper content. Similar kind of behavior is found in case of Ni-Cu-Zn ferrites prepared by citrate precursor method investigated by Mukesh C. Dimri *et. al* [10]. The decrease of Curie temperature with increase of copper content can be explained on the basis of the number of magnetic ions present in the two sub-lattices and their mutual interactions. As Fe^{3+} ions are gradually replaced by copper ions, the number of magnetic ions begins to decrease at both sides, which also weakens the strength of all exchange interactions of the type $Fe_A^{3+} - O^{2-} - Fe_B^{3+}$. Thus, the thermal energy required to offset the spin alignment decreases, thereby decreasing the Curie temperature. A similar decrease of the $T_c(K)$ with the composition was also observed by several investigators in various ferrite systems [11-13].

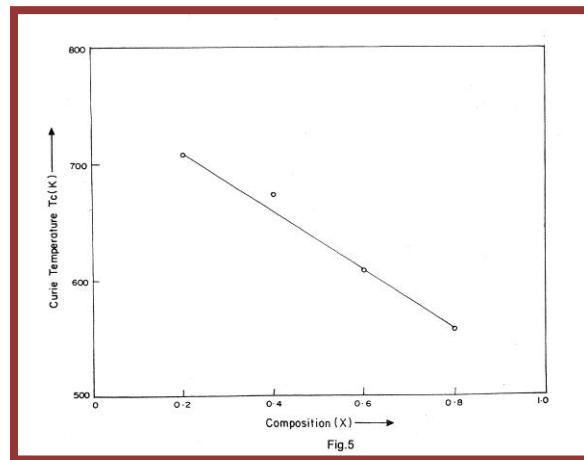


Fig.5: Variation of Curie temperature with copper content.

The existence of the kinks or transitions in the neighborhood of the Curie point has been explained by the theory given by Irkin and Turov [14]. It was shown theoretically that on passing through the Curie point a change must occur in the gradient of the straight line [15] and the magnitude of effect depends on the exchange interaction between the outer and inner electrons which alters at the Curie point. The experimental observation of the transition near the Curie point in the case of mixed Ni-Cu ferrites is thus in conformity with the theory developed by Irkin and Turov [14]. Similar transitions in the neighborhood of the Curie point have also been observed by Lanje and Kulkarni in Ca-La [16] ferrites and Ravinder in the case of Cu-Cd ferrites [17].

The activation energies in the ferrimagnetic region and paramagnetic region are calculated from the slopes of $\log(\sigma T)$ versus $(10^3/T)$ and presented in Table-2. The values of activation energy decrease with increase of copper content. It can be seen from the table that the activation energy in the paramagnetic region is higher than that in the ferrimagnetic region. This result is in agreement with the theory developed by Irkin and Turov [14]. Similar results have been observed in the case of Li-Ti [18] and Li-Mg [19] ferrites. The kink will be larger for cases in which there is a stronger exchange interaction between the outer and inner electrons. The size of this kink can be smaller or larger in various ferrites depending on their structural peculiarities, and also the value of electrical resistance. The earlier experiments have shown that the larger kinks are characteristic of ferrites which have small specific resistance because in these materials the activation energy is comparable with the magnitude of the energy of the spontaneous magnetization which is 'released' as a result of the magnetic transition.

The magnitude of the kink as determined by the difference between the activation energies in ferrimagnetic and paramagnetic regions (ΔE) is given in column-6 of Table-2. The values of resistivity for the Ni-Cu ferrites of different compositions which are under investigation are furnished in the column-7 of Table-2. An inspection of these two columns reveals that ΔE decreases as resistivity increases. Generally, the change of slope is attributed to change in conductivity mechanism. The conduction at lower temperature (< below Curie temperature) is due to hopping of electrons between Fe^{2+} and Fe^{3+} ions, whereas at higher temperature (> above Curie temperature) it is due to polaron hopping [20-23]. The calculated activation energies in the paramagnetic region (E_2) are greater than 0.40 eV which clearly suggest that the conduction is due to polaron hopping.

The room temperature values of the dielectric constant (ϵ'), dielectric loss tangent ($\tan \delta$) and complex dielectric constant (ϵ'') of mixed Ni-Cu ferrites are given in Table-3. The values of electrical conductivity (σ) and Fe^{2+} concentration were also included in the table to facilitate discussion. It can be seen from the table that the ϵ' , $\tan \delta$ and ϵ'' of the mixed Ni-Cu ferrites decrease with the decrease of concentration of Fe^{2+} ions. Among all the ferrites, the specimen with the composition $Ni_{0.8}Cu_{0.2}Fe_2O_4$ exhibits the highest value of dielectric constant, dielectric loss tangent and complex dielectric constant.

Table-3: Composition dependence of room temperature dielectric data for Ni-Cu ferrites at 1 MHz.

S. No	Ferrite composition	ϵ'	Tan δ	ϵ''	σ ($\Omega^{-1}.cm^{-1}$)	Fe^{2+} concentration (%)
1	$Ni_{0.8}Cu_{0.2}Fe_2O_4$	428	0.96	411	2.82×10^{-5}	0.99
2	$Ni_{0.6}Cu_{0.4}Fe_2O_4$	394	0.79	311	4.68×10^{-6}	0.92
3	$Ni_{0.4}Cu_{0.6}Fe_2O_4$	312	0.62	193	6.78×10^{-7}	0.84
4	$Ni_{0.2}Cu_{0.8}Fe_2O_4$	254	0.54	137	8.26×10^{-8}	0.62

The dielectric studies of Ba-Co-Cu ferrites as a function of composition and frequency was investigated by Hongguo *et al* [24]. Ranga Mohan *et al* [25] have investigated the dielectric behavior of Ni-Zn ferrites as a function of temperature and frequency. Iwauchi [4] reported a strong correlation between the conduction mechanism and the dielectric behavior of the ferrites starting with the supposition that the mechanism of the polarization process in ferrites is similar to that of the conduction process. They observed that the electronic exchange between $Fe^{2+} \leftrightarrow Fe^{3+}$ results in local displacement determining the polarization of the ferrites.

A similar explanation is proposed for the composition dependence of the dielectric constants of the ferrites under investigation. It can be observed from the Table-3 that the composition $Ni_{0.8}Cu_{0.2}Fe_2O_4$ has the maximum divalent iron ion concentration among all the mixed Ni-Cu ferrites. Correspondingly the dielectric constant for this specimen has a value of 428 at 1 MHz. This high value can be explained on the basis of the fact that it has maximum number of ferrous ions whose exchange $Fe^{2+} \leftrightarrow Fe^{3+}$ gives rise to maximum dielectric polarization. Table-3 reveals that the variation of the dielectric constant of Ni-Cu ferrites runs parallel to the variation of available ferrous ions on octahedral sites. It is significant to note that $Ni_{0.2}Cu_{0.8}Fe_2O_4$ which has the lowest ferrous ion concentration, possesses the lower dielectric constant. It is also pertinent to mention that the variation of electrical conductivity with composition (Table-3) runs parallel to the variation of ferrous ion concentration. Thus, it

is the number of ferrous ions on the octahedral sites that play a predominant role in the processes of conduction as well as dielectric polarization. This result is in agreement with the assumption made by Rabinkin and Novikova [26].

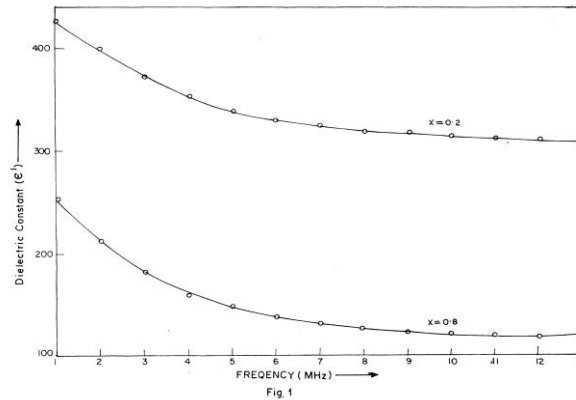


Fig.6: Plot of dielectric constant (ϵ') versus frequency for $\text{Ni}_{1-x}\text{Cu}_x\text{Fe}_2\text{O}_4$ (where $x=0.2$ and 0.8).

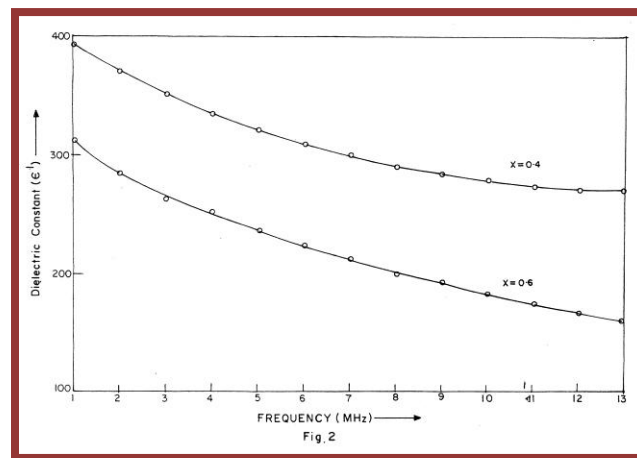


Fig.7: Plot of dielectric constant (ϵ') versus frequency for $\text{Ni}_{1-x}\text{Cu}_x\text{Fe}_2\text{O}_4$ (where $x=0.4$ and 0.6).

The variation of dielectric constant as a function of frequency for mixed Ni-Cu ferrites for different compositions is shown in Figs. 6 and 7. It can be seen from the figures that the value of dielectric constant decreases continuously with increasing frequency. The decrease of dielectric constant with increase of frequency of the applied electric field can also be explained on the basis of Koop's theory, which assumes that the ferrites are made up of well conducting grains separated by a thin layer of poorly conducting grain boundaries [9, 27-29]. The dispersion of dielectric constant is maximum for $\text{Ni}_{0.8}\text{Cu}_{0.2}\text{Fe}_2\text{O}_4$. The decrease of dielectric constant with increase of frequency as observed in the case of mixed Ni-Cu ferrites is a normal dielectric behavior. This normal dielectric behavior was also observed by several investigators [30-33]. The normal dielectric behavior of spinel ferrites was explained by Rezlescu and Rezlescu [34]. Following their work, the dependence of the dispersion of the dielectric constant on composition can be explained. The observation that $\text{Ni}_{0.8}\text{Cu}_{0.2}\text{Fe}_2\text{O}_4$ shows a maximum dielectric dispersion among all the mixed Ni-Cu ferrites may be explained on the basis of the available ferrous ions on octahedral sites. In the case of $\text{Ni}_{0.8}\text{Cu}_{0.2}\text{Fe}_2\text{O}_4$ the ferrous ion content is higher than that in other mixed Ni-Cu ferrites. As a consequence, it is possible for these ions to be polarized to the maximum possible extent. Further, as the frequency of the externally applied electric field increases gradually, and though the same number of ferrous ions is present in the ferrites material, the dielectric constant (ϵ') decreases from 428 at 1 MHz to 330 at 13 MHz. This reduction occurs because beyond a certain frequency of the externally applied electric field the electronic exchange between ferrous and ferric ions i.e. $\text{Fe}^{2+} \leftrightarrow \text{Fe}^{3+}$ can not follow the alternating field. The variation of the dispersion of ϵ' with composition can also be explained on the same lines as above.

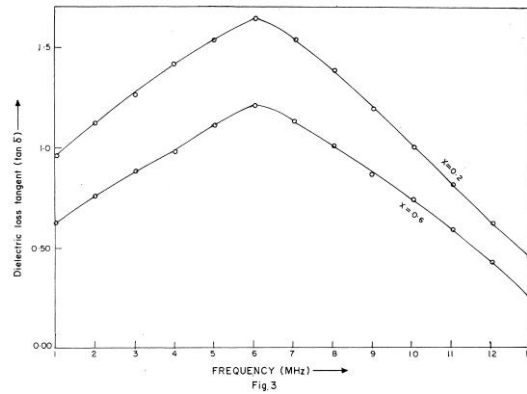


Fig.8: Plot of dielectric loss tangent (tan δ) versus frequency for Ni_{1-x}Cu_xFe₂O₄ (where, x=0.2 and 0.6).

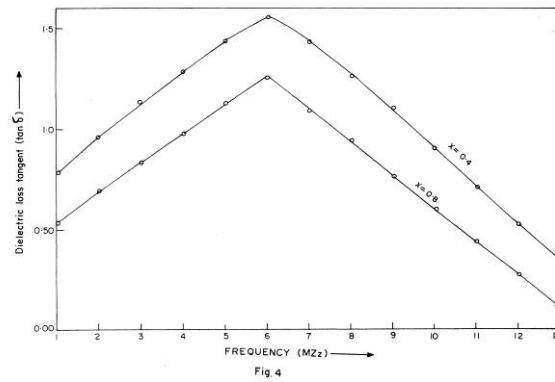


Fig.9: Plot of dielectric loss tangent (tan δ) versus frequency for Ni_{1-x}Cu_xFe₂O₄ (where x=0.4 and 0.8).

The variation of tan δ with frequency for Ni-Cu ferrites is shown in Figs. 8 and 9. It can be seen from the figures that for all Ni-Cu ferrites, tan δ shows a maximum at a frequency of 6 MHz. A qualitative explanation can be given for the occurrence of the maximum in the tan δ versus frequency curves in the case of mixed Ni-Cu ferrites. As pointed out by Iwauchi [4], there is a strong correlation between the conduction mechanism and the dielectric behavior of ferrites. The conduction mechanism in n-type ferrites is considered as due to hopping of electrons between Fe²⁺ and Fe³⁺. As such, when the hopping is nearly equal to that of the externally applied electric field, a maximum of loss tangent may be observed. Thus, it is possible for all Ni-Cu ferrites the hopping frequencies are of the appropriate magnitude to observe a loss maximum at 6 MHz.

Conclusions

Among all the Ni-Cu ferrites the specimen with the composition Ni_{0.2}Cu_{0.8}Fe₂O₄ exhibits highest value of electrical resistivity (ρ=1.21x10⁷ Ohm. cm). The sign of the Seebeck coefficient is negative for all the ferrites under investigation which indicates that the predominant conduction mechanism in these ferrites is of n-type semiconductors. The value of T_c(K) decreases with the increase of copper content. Among all the ferrites, the specimen with the composition Ni_{0.8}Cu_{0.2}Fe₂O₄ exhibits the highest value of dielectric constant, dielectric loss tangent and complex dielectric constant. For all Ni-Cu ferrites, tan δ shows a maximum at a frequency of 6 MHz.

References

- [1]. T. Kohane and B. D. Silerman
J. Phys. Soc. Jpn. 17 (1962) 249.
- [2]. J. J. Green, J. S. Wawgh and B. J. Healy
J. Appl. Phys., 35 (1964) 1006.
- [3]. B. Ravi Kumar and D. Ravinder
Materi. Lett. 53 (2002) 437.
- [4]. K. Iwauchi
Japan. J. Appl. Phys., 10 (1971) 1520.
- [5]. D. Ravinder and K. Vijaya Kumar
Bull. Mater. Sci. 24 (2001) 505.
- [6]. D. Ravinder, K. Vijaya Kumar and P. Balayya
Materi. Lett. 48 (2001) 210.
- [7]. V. R. K. Murthy and J. Sobhanadri
Phys. Stat. Solidi A. 38 (1976) 647.
- [8]. N. Rezlescu, D. Condurach, P. Petairu and E. Luca
J. Am. Ceram. Soc. 57 (1974) 40.
- [9]. D. Ravinder
Ph. D. Thesis, Osmania University, 1988.
- [10]. Mukesh C. Dimri, A. Verma, Subhash C. Kashyap, D. C. Dubea, O. P. Thakur and Chandra Prakash
Materials Science and Engineering B. 133 (2006) 42.
- [11]. D. Ravinder
Materi. Lett. 44 (2000) 130.
- [12]. R. Satyanarayana, S. Ramana Murthy and T. Seshagiri Rao
J. Less. Common. Met. 86 (1982) 115.
- [13]. V. K. Babber, J. S. Chander and S. P. Sud
J. Materi. Sci. Lett. 14 (1995) 763.
- [14]. Y. P. Irkin and E. A. Turov
Sov. Phys. JETP 33 (1957) 673.
- [15]. J. Smith and H. P. J. Wijn
Ferrites, Philips Technical Library, London, 1959, p. 234.
- [16]. N. Y. Lanje and D. K. Kulkarni
J. Magn. Magn. Mater. 234 (2001) 114.
- [17]. D. Ravinder
Materi. Letts. 43 (2000) 129.
- [18]. R. Manjula and V. R. K. Murthy
J. Appl. Phys. 59 (1986) 2929.
- [19]. D. Ravinder, L. Balachander and Y. C. Venudhar
Materi. Letts. 49 (2001) 267.
- [20]. M. I. Kringer
Phys. Status Solidi B 79 (1979) 9.
- [21]. M. K. Klings
J. Phys. C. 8 (1975) 3595.
- [22]. N. F. Mott and R. W. Gurey
Electronic Process in Ionic Crystal, Oxford University Press, Oxford, 1948.
- [23]. A. Verma, O. P. Thakur, C. Prakash, T. C. Goel and R. G. Mendiratta
Materials Science and Engineering B 116 (2005) 1.
- [24]. Hongguo Zhang, Ji Zhou, Yongli Wang, Longtu Li, Zhengxing Yue and Zhilun Gui
Materi. Lett. 55 (2002) 351.
- [25]. G. Ranga Mohan, D. Ravinder, A. V. Ramana Reddy and B. S. Boyanov
Materi. Lett. 40 (1999) 39.
- [26]. L. I. Rabinkin and Z. I. Novikova
Ferrites Minsk, (1960) p.146 (In Russian).

- [27]. M. A. El Hiti
J. Magn. Magn. Mater. 164 (1996) 187.
- [28]. E. Melagiriappa, H. S. Jayanna and B. K. Chougule
Mater. Chem. Phys. 112 (2008) 68.
- [29]. Q. Chen, P. Du, W. Huang, L. Jin, W. Weng and G. Han
Appl. Phys. Lett. 90 (2007) 132907.
- [30]. S. Thakur, S. C. Katyal and M. Singh
Appl. Phys. Lett. 91 (2007) 262501.
- [31]. M. Pal, P. Brahma, D. Chakravorthy and D. C. Agrawal
J. Magn. Magn. Mater. 147 (1995) 208.
- [32]. A.V. Ramana Reddy, G. Ranga Mohan, D. Ravinder and B. S. Boyanov
J. Materi. Sci. 34 (1999) 3169.
- [33]. A. M. Saikh, S. S. Balland and B. K. Chougule
J. Magn. Magn. Mater. 195 (1999) 384.
- [34]. N. Rezlescu and E. Rezlescu
Phy. Status Solidi A, 23 (1974) 575.

A Novel of Bidirectional DC-DC converter drive

N.MAHESH

M-Tech Scholar, Power Electronics and Drives,
Department Of Electrical And Electrical Engineering,
Koneru Lakshmaiah University, Guntur,(A.P), India.

D.SESHI REDDY

Associate professor,
Department Of Electrical And Electrical Engineering,
Koneru Lakshmaiah University, Guntur,(A.P),India.

Abstract: - A Novel of bidirectional DC-DC converter drive is presented in this paper. The circuit configuration of the proposed converter is very simple. The proposed converter employs a coupled inductor with same winding turns in the primary and secondary sides. In step-up mode, the primary and secondary windings of the coupled inductor are operated in parallel charge and series discharge to achieve high step-up voltage gain. In step-down mode, the primary and secondary windings of the coupled inductor are operated in series charge and parallel discharge to achieve high step-down voltage gain. Thus, the proposed converter has higher step-up and step-down voltage gains than the conventional bidirectional DC-DC boost/buck converter. Under same electric specifications for the proposed converter and the conventional bidirectional boost / buck converter, the average value of the switch current in the proposed converter is less than the conventional bidirectional boost / buck converter. The operating principle and steady-state analysis are discussed in detail. Finally, a 70 / 210 V simulation circuit is simulated in MATLAB/Simulink to verify the performance for the automobile dual - battery drive system.

Index Terms: - Bidirectional DC-DC converter drive, coupled inductor.

I. Introduction

Bidirectional DC-DC converters are used to transfer the power between two DC sources in either direction. These converters are widely used in applications, such as hybrid electric vehicle energy systems [1]-[4], uninterrupted power supplies [5], [6], fuel-cell Hybrid power systems [7]-[10], PV hybrid power systems [11], [12] and battery chargers [13]-[15]. Many bidirectional DC-DC converters have been researched. The bidirectional DC-DC fly back converters are more attractive due to simple structure and easy control. However, these converters suffer from high voltage stresses on the power devices due to the leakage-inductor energy of the transformer. In order to recycle the leakage inductor energy and to minimize the voltage stress on the power devices, some literatures present the energy regeneration techniques to clamp the voltage stress on the power devices and to recycle the leakage-inductor energy, some literatures research the isolated bidirectional DC-DC converters, which include the half-bridge types and full-bridge types.

These converters can provide high step-up and step-down voltage gain by adjusting the turn's ratio of the transformer. For non-isolated applications, the non-isolated bidirectional DC-DC converters, which include the conventional boost/buck types, multi-level type, three-level type, sepic/zeta type, switched-capacitor type, and coupled-inductor type, are presented. The multi-level type is a magnetic-less converter, but 12 switches are used in this converter. If higher step-up and step-down voltage gains are required, more switches are needed. This control circuit becomes more complicated. In the three-level type, the voltage stress across the switches on the three-level type is only half of the conventional type. However, the step-up and step-down voltage gains are low. Since the sepic/zeta type is combined of two power stages, the conversion efficiency will be decreased.

The development of bidirectional dc-dc converters has recently become increasingly important for clean-energy vehicle applications because battery-based energy storage systems are required for cold starting and battery recharging [16], [17], [18]. Bidirectional converters transfer power between two dc sources in both directions. However, back-up power from the battery is supplied using a bidirectional converter, which is employed in many uninterrupted power supplies (UPS), the front-end stage for clean-energy sources and dc motor driver circuits. The dc back-up energy system typically consists of numerous low-voltage-type batteries. Although a storage battery series string can provide high voltage, slight mismatches or temperature differences can cause a charge imbalance when the series string is charged as a unit Charge equalization cycles must be employed to correct this imbalance. However, conventional approaches to this process will stress the batteries, shorten their life and are limited to low-capacity power. Batteries arranged in parallel strings can enhance the power redundancy supplied by a battery and alleviate the problems caused by storage battery series strings. However, the output voltage remains low in this parallel connection configuration. A highly efficient bidirectional DC-DC converter with high-voltage diversity is a key component for batteries connected in parallel. Bidirectional DC - DC converters with transformer-based structures are the most common topologies. Soft switching techniques are generally applied to reduce the corresponding switching losses. These mechanisms with isolated transformers have high conduction losses because four to nine power switches are required. Many applications call for high-step-up converters that do not require isolation, such as the front-end converter

with dual inputs. Accordingly, practical implementation is complex and costly. Switched-capacitor dc-dc converters have attracted much attention as an alternative method for providing bidirectional power flow control. However, increased switching loss and current stress are the critical drawbacks. The primary challenge is to design a circuit that has few switching devices and capacitors. Generally, the bidirectional converter in the UPS must generally boost 48–400 V, which is appropriate for eightfold step-up voltage gain. Zhao and Lee developed a family of highly efficient, high-step-up dc-dc converters by adding only one additional diode and a small capacitor [19]. This capacitor can recycle leaked energy and eliminate the reverse-recovery problem. In this approach the magnetic core can be regarded as a fly-back transformer and most energy is stored in the magnetic inductor.

1.1 COUPLED INDUCTOR:

The pair of coupled coils shown in figure has currents, voltages and polarity dots indicated. In order to show $M_{12} = M_{21}$ we begin by letting all currents and voltages are zero, thus establishing zero initial energy storage in the network. We then open –circuit the right-hand terminal pair and increase I_1 from zero to some constant value I_1 at time $t = t_1$. The power entering the network from left at any instant is

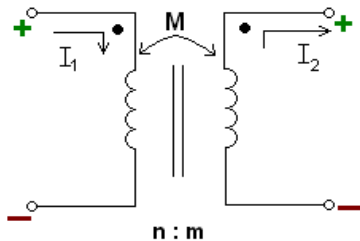


Fig 1 Coupled inductors

$$V_1 i_1 = L_1 \frac{di_1}{dt} i_1 \tag{1}$$

and the power entering from the right is

$$V_2 I_2 = 0 \tag{2}$$

Since $i_2=0$

The energy stored within the network when $i_1 = I_1$ is thus

$$\int_0^{t_1} v_1 i_1 dt = \int_0^{I_1} l i_1 di_1 = \frac{1}{2} L I_1^2 \tag{3}$$

We now hold I_1 constant, $i_1 = I_1$, and let I_2 change from zero at $t=t_1$ to some constant value I_2 at $t=t_2$. The energy delivered from the right-hand source is thus

$$\int_{t_1}^{t_2} v_2 i_2 dt = \int_0^{I_2} l_2 i_2 di_2 = \frac{1}{2} L_2 I_2^2 \tag{4}$$

However, even though the value of I_1 remains constant, the left-hand source also delivers energy to the network during this time interval

$$\int_{t_1}^{t_2} v_1 i_1 dt = \int_{t_1}^{t_2} M I_2 \frac{di_2}{dt} i_1 dt = M I_2 I_1 \int_0^{I_2} di_2 = M I_2 I_1 I_2 \tag{5}$$

The total energy stored in the network when both i_1 and i_2 have reached constant values is

$$W_{total} = \frac{1}{2} L_1 I_1^2 + \frac{1}{2} L_2 I_2^2 + M_{12} I_1 I_2 \tag{6}$$

Now, we may establish the same final currents in this network by allowing the currents to reach final values to the reverse order

$$W_{total} = \frac{1}{2} L_1 I_1^2 + \frac{1}{2} L_2 I_2^2 + M_{21} I_1 I_2 \tag{7}$$

The only difference is the interchange of the mutual inductance M_{21} and M_{12}

$$M_{12} = M_{21} = M \quad \text{and}$$

$$W = \frac{1}{2} L_1 I_1^2 + \frac{1}{2} L_2 I_2^2 + M I_1 I_2 \tag{8}$$

If one current enters a dot-marked terminal while the other leaves a dot marked terminal

$$W = \frac{1}{2} L_1 I_1^2 + \frac{1}{2} L_2 I_2^2 - M I_1 I_2 \tag{9}$$

From equations 8 and 9 we derived final values of the two currents as constant, these “constants” can have any value and the energy expressions correctly represent the energy stored when the instantaneous values i_1 and i_2 are I_1 and I_1 respectively

$$W(t) = \frac{1}{2} L_1 [i_1(t)]^2 + \frac{1}{2} L_2 [i_2(t)]^2 \pm M [i_1(t)] [i_2(t)] \tag{10}$$

1.1.1 The coupling coefficient

The degree to which M approaches its maximum value is described by the coupling coefficient, defined as

$$K = \frac{M}{\sqrt{L_1 L_2}} \tag{11}$$

$$\text{Since } M \leq \sqrt{L_1 L_2} \tag{11}$$

$$0 \leq k \leq 1$$

The larger values of the coefficient of coupling are obtained with coils which are physically closer, which are wound or oriented to provide a larger common magnetic flux, or provided with a common path through a material which serves to concentrate and localize the magnetic flux. Coils having a coefficient of coupling close to unity are said to be tightly coupled.

1.2 DC MACHINE: Back EMF induced in motor armature. When current passed through the armature of dc machines and its field coils excited torque is established and motor rotates the direction of rotation can be reversed by reversing either armature current or polarity of the magnets. Rotation of the armature gives rise to an induced emf which according to Lenz's law, will oppose the flow of current. Hence if

E_a =the numerical value of the induced emf.

V_a =the numerical value of the applied voltage.

The armature currents is given by

$$I_a = (V_a - E_a) / r_m$$

$$V_a = E_a + I_a r_m$$

$$\text{The power input } V_a I_a = E_a I_a + I_a^2 r_m \quad (12)$$

The emf generated by the armature must have a perfectly definite value for particular value of the load current

$$E_a = V_a - I_a r_m \quad (13)$$

The induced emf is also determined from ordinary considerations of flux, number of conductors and speed, and its thus

$$E_a = Z_e \times 2p \phi n \quad (14)$$

From above 13 and 14 equations are equal we get

$$V_a - I_a r_m = Z_e \times 2p \phi n$$

$$n = \frac{V_a - I_a r_m}{Z_e \times 2p \phi} \quad (15)$$

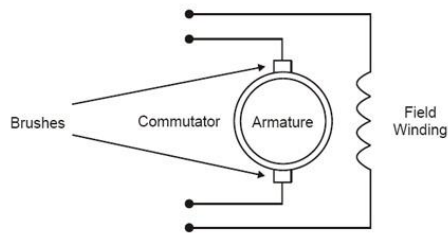


Fig 2 Dc motor basic parts

Hence the speed of dc motor may be controlled by

1. Varying the value of the flux.
2. Varying the value of the voltage applied to the motor armature
3. Varying the value of the effective number of conductors in series.

1.2.1 Field control:- In field control the applied armature voltage v is maintained constant. Then the speed is represented by equation as

$$\omega_m \propto \frac{1}{I_f} \quad (16)$$

1.2.2 Armature control:- In this the field current is maintained constant. Then the speed is derived from the equation as

$$\omega_m = (v - i_a R_a) \quad (17)$$

Hence, varying the applied voltage changes speed. Reversing the applied voltage changes the direction of rotation of the motor

1.2.3 Armature and Field control:- By combination armature and field control for speeds below and above the rated speed, respectively, a wide range of speed control is possible

$$T_e = K \phi_f i_a \quad (18)$$

Can be normalized if it is divided by rated torque

Which is expressed as

$$T_{er} = K \phi_{fr} i_{ar} \quad (19)$$

$$T_{en} = \frac{T_e}{T_{er}} = K \frac{\phi_f i_a}{K \phi_{fr} i_{ar}} = \phi_{fn} i_{an}, p.u. \quad (20)$$

Normalized eliminates machine constants, compacts the performance equation, and enables the visualization of performance characteristics regardless of machine size on same scale. the normalized torque, flux and armature current are

$$T_{en} = \frac{T_e}{T_{er}}, p.u. \quad (21)$$

$$\phi_{fn} = \frac{\phi_f}{\phi_{fr}}, p.u. \quad (22)$$

$$i_{an} = \frac{i_a}{i_{ar}}, p.u. \quad (23)$$

As the armature current is maintained at 1 p.u

$$T_{en} = \phi_{fn}, p.u. \quad (24)$$

Hence normalized electromagnetic torque characteristics coincides with normalized field flux, similarly the air gap power is,

$$p_{an} = e_n i_{an}, p.u \tag{25}$$

Where e_n is the normalized induced emf.

As i_{an} is set to 1 p.u., the normalized air gap power becomes

$$p_{an} = e_n, p.u \tag{26}$$

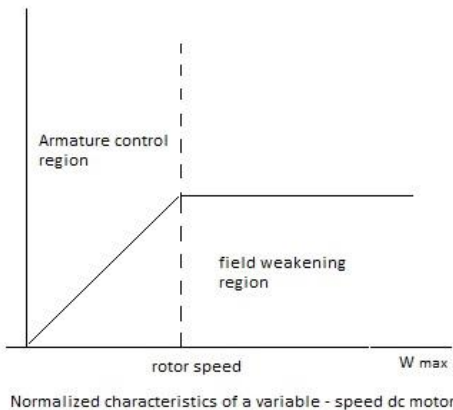


Fig 3 normalized characteristics of variable –speed DC motor

II. STEP-UP MODE

The proposed converter in step-up mode is shown in Fig 5. The pulse width modulation (PWM) technique is used to control the switches S_1 and S_2 simultaneously. The switch S_3 is the Synchronous rectifier.

2.1 CCM Operation

Mode 1: During this time interval, S_1 and S_2 are turned on and S_3 is turned off. The current flow path

is shown in Fig 5(a). The energy of the low-voltage side V_L is transferred to the coupled inductor. Meanwhile, the primary and secondary windings of the coupled inductor are in parallel. The energy stored in the capacitor C_H is discharged to the load. Thus, the voltages across L_1 and L_2 are obtained as

$$u_{L1} = u_{L2} = V_L \tag{27}$$

By substituting above equations we get

$$\frac{di_{L1}(t)}{dt} = \frac{di_{L2}(t)}{dt} = \frac{V_L}{(1+k)L'} \tag{28}$$

Mode-2: During this time interval S_1 and S_2 are turned on and S_3 is turned off. The current flow path is shown in Fig. 5(b). The energy of the low-voltage side V_L is transferred to the coupled inductor. Meanwhile, the primary and secondary windings of the coupled inductor are in parallel. The energy stored in the capacitor C_H is discharged to the load. Thus, the voltages across L_1 and L_2 are obtained as

$$i_{L1} = i_{L2}$$

$$u_{L1} + u_{L2} = V_L - V_H \tag{29}$$

By substituting above equations we get

$$\frac{di_{L1}(t)}{dt} = \frac{di_{L2}(t)}{dt} = \frac{V_L - V_H}{2(1+k)L'} \tag{30}$$

By using the state-space averaging method, the following equation is derived from

$$\frac{DV_L}{(1+k)L} + \frac{(1-D)(V_L - V_H)}{2(1+k)L} = 0 \tag{31}$$

By simplifying we get

$$G_{CCM(step-up)} = \frac{V_H}{V_L} = \frac{1+D}{1-D} \tag{32}$$

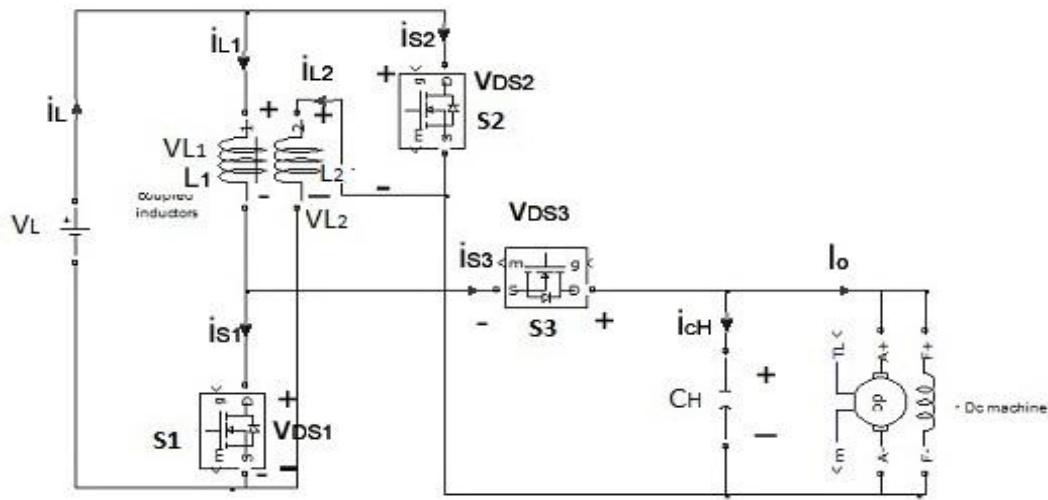


Fig4 step up mode

Fig 5: Some typical waveforms of the proposed converter in step-up mode (a) CCM operation (b) DCM operation (c) Mode 3 for DCM Mode

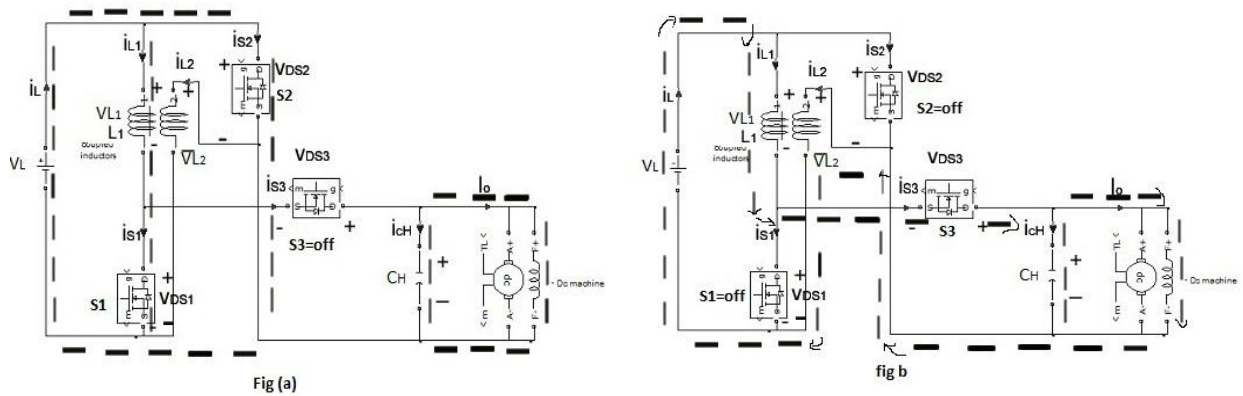


Fig (a)

fig b

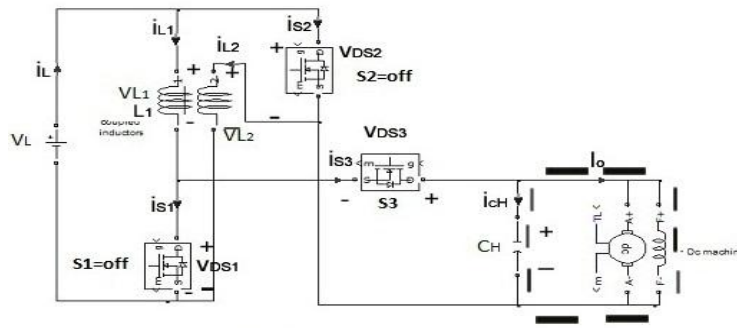


fig (c)

2.2 DCM Operation

Mode 1: During this time interval, S_1 and S_2 are turned on and S_3 is turned off. The current flow path is shown in Fig. 5(a) The operating principle is same as that for the mode 1 of CCM operation

$$I_{L1p} = I_{L2p} = \frac{V_L D T_s}{(1+k)L} \quad (33)$$

Mode 2: During this time interval, S_1 and S_2 are turned off and S_3 is turned on. The current flow path is shown in Fig 5 (b). The low-voltage side V_L and the coupled inductor are in series to transfer their energies to the capacitor C_H and the load. Meanwhile, the primary and secondary windings of the coupled inductor are in series. The currents i_{L1} and i_{L2} through the primary and secondary windings of the coupled inductor are decreased to zero at $t = t_2$. From eqn, another expression of I_{L1p} and I_{L2p} is given by

$$I_{L1p} = I_{L2p} = \frac{(V_H - V_L) D_2 T_s}{2(1+k)L} \quad (34)$$

Mode 3: During this S_1 and S_2 are still turned off and S_3 is still turned on. The current flow path is shown in Fig 5(c). The energy stored in the coupled inductor is zero. Thus, i_{L1} and i_{L2} are equal to zero. The energy stored in the capacitor C_H is discharged to the load. From above equation, is derived as follows

$$D_2 = \frac{2DV_L}{V_H - V_L} \quad (35)$$

From Fig, the average value of the output capacitor current during each switching period is given by

$$I_{cH} = \frac{\frac{1}{2} D_2 T_s I_{L1p} - I_o T_s}{T_s} = \frac{1}{2} D_2 I_{L1p} - I_o \quad (36)$$

By substituting above values we get

$$I_{cH} = \frac{D^2 V_L^2 T_s}{(1+k)L(V_H - V_L)} - \frac{V_H}{R_H} \quad (37)$$

Since I_{cH} is equal to zero under steady state, above equations can be rewritten as follows:

$$\frac{D^2 V_L^2 T_s}{(1+k)L(V_H - V_L)} = \frac{V_H}{R_H} \quad (38)$$

Then, the normalized inductor time constant is defined as

$$T_{LH} \equiv \frac{L}{R_H T_s} = \frac{L f_s}{R_H} \quad (39)$$

where f_s is the switching frequency. Substituting above equations we get, the voltage gain is given by

$$G_{DCM(step-up)} = \frac{V_H}{V_L} = \frac{1}{2} + \sqrt{\frac{1}{4} + \frac{D^2}{(1+k)\tau_{LH}}} \quad (40)$$

2.3 Boundary Operating Condition of CCM and DCM

When the proposed converter in step-up mode is operated in boundary conduction mode (BCM), the voltage gain of CCM operation is equal to the voltage gain of DCM operation. From above equations, the boundary normalized inductor time constant $\tau_{LH,B}$ can be derived as follows

$$\tau_{LH,B} = \frac{D(1-D)^2}{2(1+k)(1+d)} \quad (41)$$

The curve of $\tau_{LH,B}$ is plotted in Fig. If τ_{LH} is larger than $\tau_{LH,B}$, the proposed converter in step-up mode is operated in CCM.

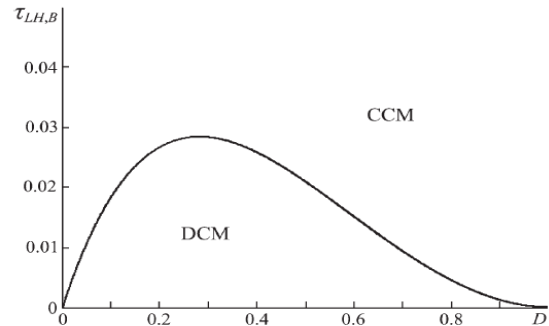


Fig-6 Boundary condition of the proposed converter in step-up mode (assuming $k = 1$)

III. STEP-DOWN MODE

The proposed converter in step-down mode of operation, the PWM technique is used to control the switch S_3 . The switches S_1 and S_2 are the synchronous rectifiers

3.1 CCM Operation

Mode 1: During this time interval, S_3 is turned on and S_1/S_2 are turned off. The current flow path is shown in Fig 8(a). The energy of the high-voltage side V_H is transferred to the coupled inductor, the capacitor C_L , and the load.

$$i_{L1} = i_{L2}$$

$$u_{L1} + u_{L2} = V_H - V_L \quad (42)$$

By substituting we get

$$\frac{di_{L1}(t)}{dt} = \frac{di_{L2}(t)}{dt} = \frac{V_H - V_L}{2(1+k)L} \quad (43)$$

Mode 2: During this S_3 is turned off and S_1/S_2 are turned on. The current flow path is shown in Fig 8(b). The energy stored in the coupled inductor is released to the capacitor CL and the load.

Thus, the voltages across $L1$ and $L2$ are derived as

$$u_{L1} = u_{L2} = -V_L \quad (44)$$

By substituting we get

$$\frac{di_{L1}(t)}{dt} = \frac{di_{L2}(t)}{dt} = -\frac{V_L}{(1+k)L} \quad (45)$$

By using the state space averaging method, the following equation is obtained from

$$\frac{D(V_H - V_L)}{2(1+k)L} - \frac{(1-D)V_L}{(1+k)L} = 0 \quad (46)$$

By simplifying we get

$$G_{CCM(step-down)} = \frac{V_L}{V_H} = \frac{D}{2-D} \quad (47)$$

3.2 DCM Operation:

Mode 1: During this time interval, S_3 is turned on and S_1/S_2 are turned off. The current flow path is shown in Fig 8(a). The operating principle is same as that for the mode 1 of CCM operation. From, the two peak currents through the primary and secondary windings of the coupled inductor are given by

$$I_{L1p} = I_{L2p} = \frac{(V_H - V_L)DT_s}{2(1+k)L} \quad (48)$$

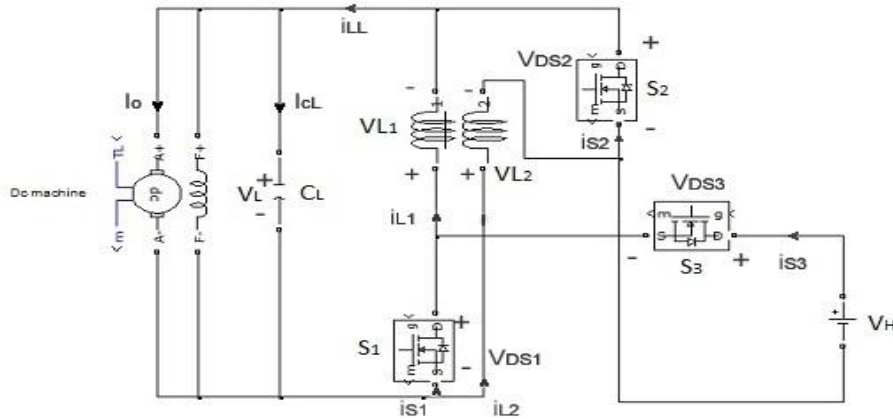
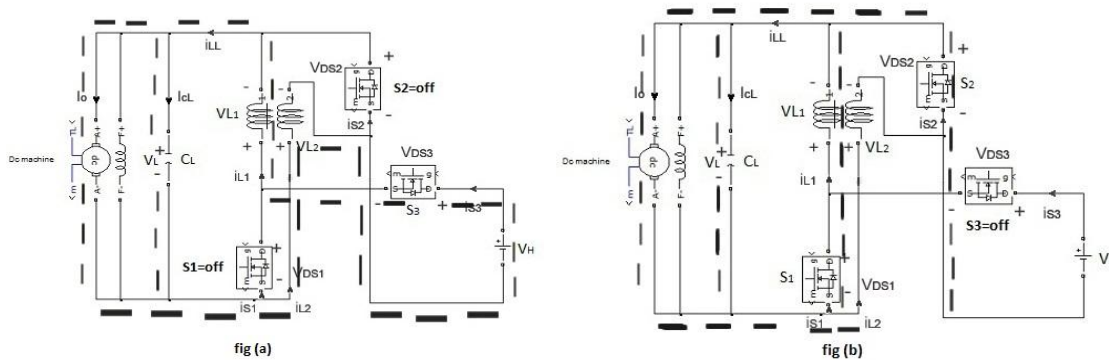
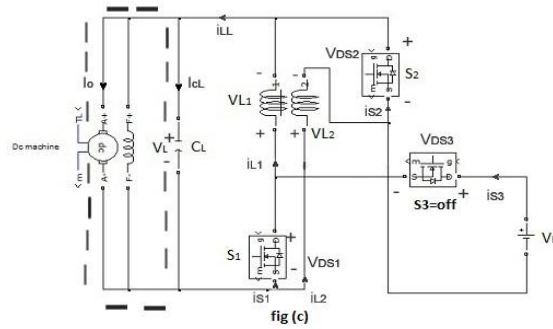


Fig 7 Step-down mode

Fig 8 Current flow path of the proposed converter in step-down mode. (a) Mode 1. (b) Mode 2. (c) Mode 3 for DCM operation





Mode 2: During this S_3 is turned off and S_1/S_2 are turned on. The current flow path is shown in Fig 8(b). The energy stored in the coupled inductor is released to the capacitor C_L and the load. The currents i_{L1} and i_{L2} through the primary and secondary windings of the coupled inductor are decreased to zero at $t = t_2$. From, another expression of I_{L1p} and I_{L2p} is given as

$$I_{L1p} = I_{L2p} = \frac{V_L D_2 T_s}{(1+k)L} \quad (49)$$

Mode 3: During this time interval, S_3 is still turned off and S_1/S_2 are still turned on. The current flow path is shown in Fig 8(c). The energy stored in the coupled inductor is zero. Thus, i_{L1} and i_{L2} are equal to zero. The energy stored in the capacitor C_L is discharged to the load.

$$D_2 = \frac{D(V_H - V_L)}{2V_L} \quad (50)$$

The average value of the output capacitor current during each switching period is given by

$$I_{CL} = \frac{\frac{1}{2}DT_s I_{L1p} + \frac{1}{2}D_2 T_s (2I_{L1p}) - I_o T_s}{T_s} = \frac{1}{2}DI_{L1p} + D_2 I_{L1p} - I_o \quad (51)$$

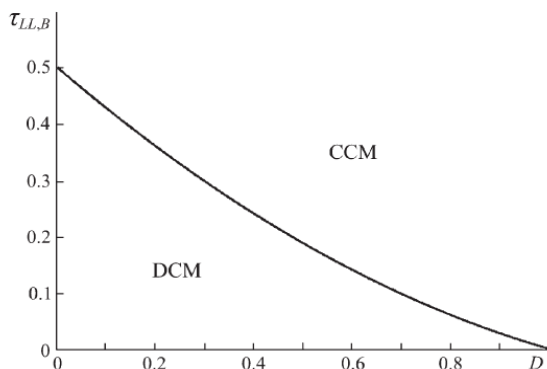


Fig 9 Boundary condition of the proposed converter in step-down mode

By substituting we get

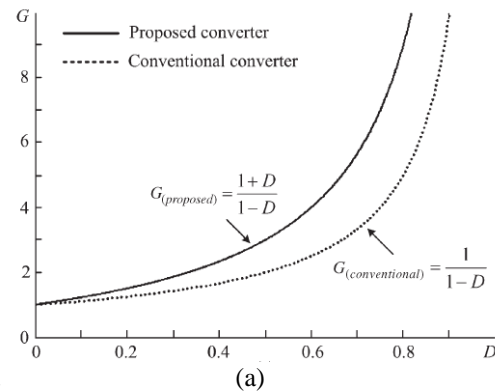
$$\frac{D^2 T_s [(V_H - V_L)V_L + (V_H - V_L)^2]}{4(1+k)LV_L} = \frac{V_L}{R_L} \quad (52)$$

$$G_{DCM(step-down)} = \frac{V_L}{V_H} = \frac{2}{1 + \sqrt{1 + \frac{16(1+k)\tau_{LL}}{D^2}}} \quad (53)$$

3.3 Boundary Operating Condition of CCM and DCM

When the proposed converter in step-down mode is operated in BCM, the voltage gain of CCM operation is equal to the voltage gain of DCM operation, the boundary normalized inductor time constant τ_{LL} , B can be derived as follows

$$\tau_{LL,B} = \frac{(1-D)(2-D)}{2(1+k)} \quad (54)$$



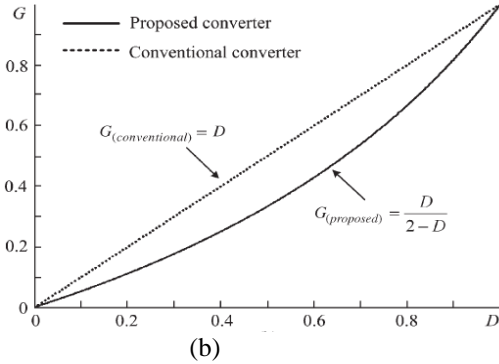


Fig 10 Voltage gain of the proposed converter and conventional bidirectional boost/buck converter in CCM operation in (a) Step-up mode (b) Step-down mode

IV RESULTS

In order to verify the performance of the proposed converter, a 70/210-V simulation circuit is built in the MATLAB / Simulink for the hybrid electric system. The electric specifications and circuit components are selected as $V_L = 70\text{ V}$, $V_H = 210\text{ V}$, $f_s = 50\text{ kHz}$, $P_o = 200\text{ W}$, $C_L = C_H = 330\text{ }\mu\text{F}$, $L_1 = L_2 = 15.5\text{ }\mu\text{H}$ ($rL_1 = rL_2 = 11\text{ m}\Omega$). Also, MOSFET IRF3710 ($V_{DSS} = 100\text{ V}$, $R_{DS(ON)} = 23\text{ m}\Omega$, and $I_D = 57\text{ A}$) is selected for S_1 , S_2 , and S_3 . Some results in step-up and step-down modes are shown in the waveforms of load voltage in Fig 11 and Fig 14 and the DC machine performance characteristics waveforms in Fig 12 and Fig 15, and the input current i_L and the coupled inductor currents i_{L1} and i_{L2} in Fig 13 for step-up mode. It can be seen that i_{L1} is equal to i_{L2} . The current i_L is double of the level of the coupled-inductor current during S_1/S_2 ON-period and equals the coupled-inductor current during S_1/S_2 OFF-period. Fig. 16 shows the waveforms of the current i_{LL} and the coupled-inductor currents i_{L1} and i_{L2} in step-down mode. It can be observed that i_{L1} is equal to i_{L2} . The current i_{LL} equals to the coupled-inductor current during S_3 ON-period and is double of the level of the coupled-inductor current during S_3 OFF-period.

Moreover, the prototype circuit of the conventional bidirectional boost/buck converter is also implemented in the laboratory. The electric specifications and circuit components are selected as $V_L = 14\text{ V}$, $V_H = 42\text{ V}$, $f_s = 50\text{ kHz}$, $P_o = 200\text{ W}$, $L_1 = 28\text{ }\mu\text{H}$ ($rL_1 = 15\text{ m}\Omega$), $C_L = C_H = 330\text{ }\mu\text{F}$. At full-load condition, the measured efficiency of the proposed converter is 92.7% in step-up mode and is 93.7% in step-down mode. Also, the measured efficiency of the proposed converter is around 92.7%–96.2% in step-up mode and is around 93.7%–96.7% in step-down mode

Step-up mode:

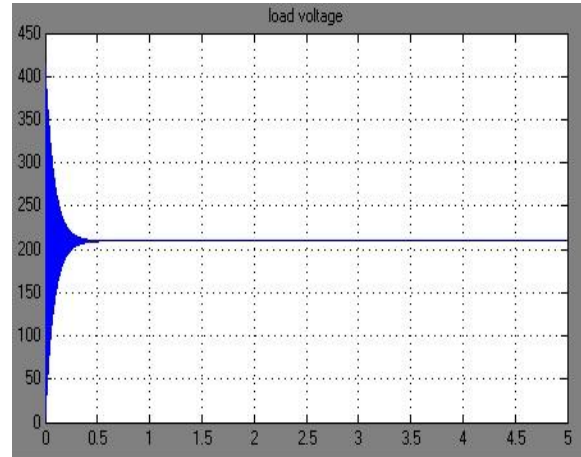


Fig 11 load voltage for step up mode

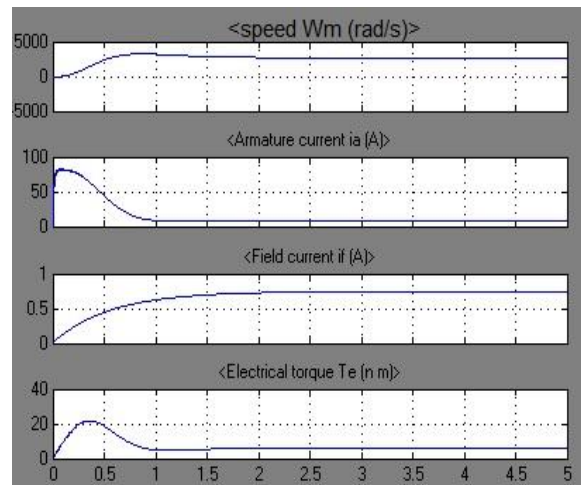


Fig 12 DC machine performance characteristics

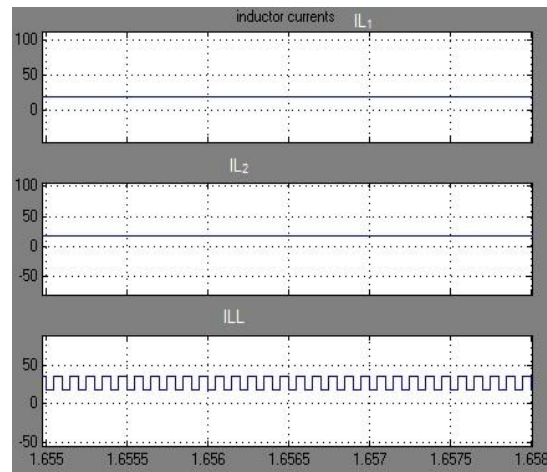


Fig 13 Inductor currents Step-down mode:

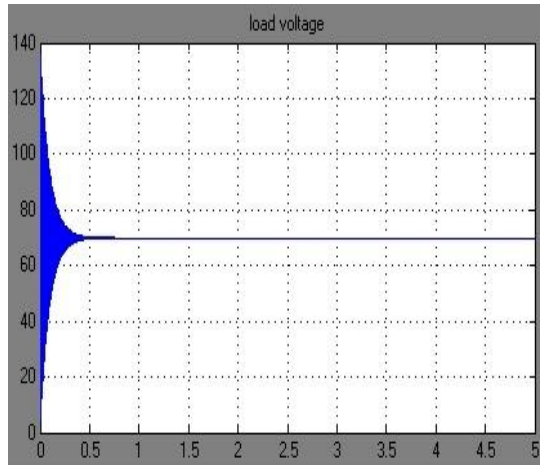


Fig 14 load voltage for step up mode

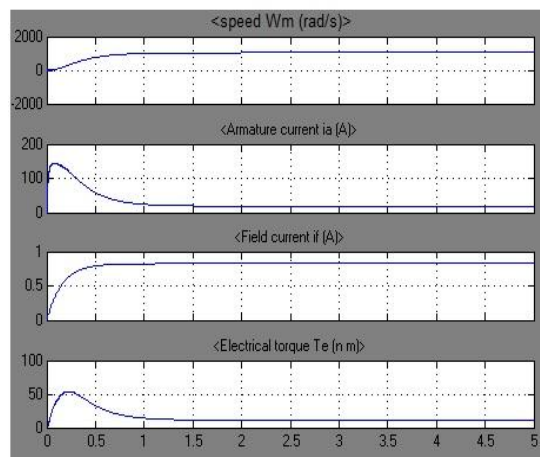


Fig 15 DC machine performance characteristics

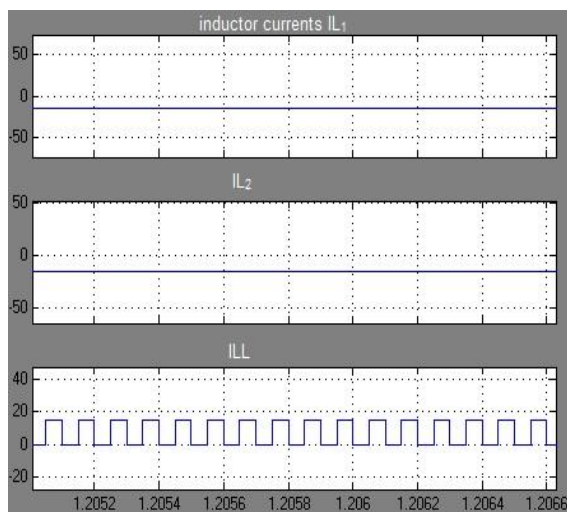


Fig 16 inductor currents

V CONCLUSION

This paper researches a novel bidirectional dc–dc converter drive. The circuit configuration of the proposed converter is very simple. The proposed converter has higher step-up and step-down voltage gains and lower average value of the switch current than the conventional bidirectional boost/buck converter which drives the hybrid vehicle. From the simulation results, it is seen that the waveforms agree with the operating principle and steady-state analysis. At full-load condition, the measured efficiency is 92.7% in stepup mode and is 93.7% in step-down mode. Also, the measured efficiency is around 92.7%–96.2% in step-up mode and is around 93.7%–96.7% in step-down mode, which are higher than the conventional bidirectional boost/buck converter drive.

VI REFERENCES

- [1] M. B. Camara, H. Gualous, F. Gustin, A. Berthon, and B. Dakyo, "DC/DC converter design for supercapacitor and battery power management in hybrid vehicle applications— Polynomial control strategy," *IEEE Trans. Ind. Electron.*, vol. 57, no. 2, pp. 587–597, Feb. 2010.
- [2] T. Bhattacharya, V. S. Giri, K. Mathew, and L. Umanand, "Multiphase bidirectional flyback converter topology for hybrid electric vehicles," *IEEE Trans. Ind. Electron.*, vol. 56, no. 1, pp. 78–84, Jan. 2009.
- [3] Z. Amjadi and S. S. Williamson, "A novel control technique for a switched-capacitor-converter-based hybrid electric vehicle energy storage system," *IEEE Trans. Ind. Electron.*, vol. 57, no. 3, pp. 926–934, Mar. 2010.
- [4] F. Z. Peng, F. Zhang, and Z. Qian, "A magnetic-less dc–dc converter for dual-voltage automotive systems," *IEEE Trans. Ind. Appl.*, vol. 39, no. 2, pp. 511–518, Mar./Apr. 2003.
- [5] A. Nasiri, Z. Nie, S. B. Bekiarov, and A. Emadi, "An on-line UPS system with power factor correction and electric isolation using BIFRED converter," *IEEE Trans. Ind. Electron.*, vol. 55, no. 2, pp. 722–730, Feb. 2008.
- [6] L. Schuch, C. Rech, H. L. Hey, H. A. Grundling, H. Pinheiro, and J. R. Pinheiro, "Analysis and design of a new high-efficiency bidirectional integrated ZVT PWM converter for DC-bus and battery-bank interface," *IEEE Trans. Ind. Appl.*, vol. 42, no. 5, pp. 1321–1332, Sep./Oct. 2006.
- [7] X. Zhu, X. Li, G. Shen, and D. Xu, "Design of the dynamic power compensation for PEMFC distributed power system," *IEEE Trans. Ind. Electron.*, vol. 57, no. 6, pp. 1935–1944, Jun. 2010.

- [8] G. Ma, W. Qu, G. Yu, Y. Liu, N. Liang, and W. Li, "A zero-voltageswitching bidirectional dc-dc converter with state analysis and softswitching-oriented design consideration," IEEE Trans. Ind. Electron., vol. 56, no. 6, pp. 2174-2184, Jun. 2009.
- [9] F. Z. Peng, H. Li, G. J. Su, and J. S. Lawler, "A new ZVS bidirectional dc-dc converter for fuel cell and battery application," IEEE Trans. Power Electron., vol. 19, no. 1, pp. 54-65, Jan. 2004.
- [10] K. Jin, M. Yang, X. Ruan, and M. Xu, "Three-level bidirectional converter for fuel-cell/battery hybrid power system," IEEE Trans. Ind. Electron., vol. 57, no. 6, pp. 1976-1986, Jun. 2010.
- [11] R. Gules, J. D. P. Pacheco, H. L. Hey, and J. Imhoff, "A maximum power point tracking system with parallel connection for PV stand-alone applications," IEEE Trans. Ind. Electron., vol. 55, no. 7, pp. 2674-2683, Jul. 2008.
- [12] Z. Liao and X. Ruan, "A novel power management control strategy for stand-alone photovoltaic power system," in Proc. IEEE IPEMC, 2009, pp. 445-449.
- [13] S. Inoue and H. Akagi, "A bidirectional dc-dc converter for an energy storage system with galvanic isolation," IEEE Trans. Power Electron., vol. 22, no. 6, pp. 2299-2306, Nov. 2007.
- [14] L. R. Chen, N. Y. Chu, C. S. Wang, and R. H. Liang, "Design of a reflexbased bidirectional converter with the energy recovery function," IEEE Trans. Ind. Electron., vol. 55, no. 8, pp. 3022-3029, Aug. 2008.
- [15] S. Y. Lee, G. Pfaelzer, and J. D. Wyk, "Comparison of different designs of a 42-V/14-V dc/dc converter regarding losses and thermal aspects," IEEE Trans. Ind. Appl., vol. 43, no. 2, pp. 520-530, Mar./Apr. 2007.
- [16] Wensong Yu, Hao Qian, Jih-Sheng Lai "Design of High-Efficiency Bidirectional DC-DC Converter and High-Precision Efficiency Measurement" IEEE conf on power electronics pp-685-690 2008 july
- [17] W. C. Liao T. J. Liang H. H. Liang H. K. Liao *L. S. Yang **K.C. Juang J. F. Chen" Study and Implementation of a Novel Bidirectional DC-DC Converter with High Conversion Ratio" IEEE conf on power electronics pp-134-140. jan 2011
- [18] Rou-Yong Duan and Jeng-Dao Lee" Soft Switching Bidirectional DC-DC Converter with Coupled Inductor" IEEE conf on power electronics pp-2797-2802. jan 2011
- [19] R.-Y. Duan, J.-D. Lee" High-efficiency bidirectional DC-DC converter with coupled inductor" Published in IET Power Electronics

Received on 21st December 2010 Revised on 31st March 2011

Author Profile



N. Mahesh received B.Tech from Lakireddy Balireddy College of engineering, India in 2010. Presently he is pursuing M.Tech in KL University. His areas of interests are power electronics, DC Machines and networks theory.



D.Seshi Reddy, received B.E and M.Tech from Andhra University college of engineering and National Institute of Technology Calicut, India in 2002 And 2004, respectively. Presently he is pursuing Ph.D from JNT university, hyderabad. Since 2007, he has been with the department of electrical and electronics engineering, KL University, where he is currently an associate professor. He has published more than ten journals and conferences recent trends in power system. His current research interests include measurement of power quality problems, Flexible AC transmission systems.

Three-Phase Five-Level PWM DC-DC Converter Using H-Bridge

E.Bhasker¹, M.Kiran Kumar²

*(Student, Department of Electrical and Electronics Engineering, KL University, India)

** (Assistant Professor, Department of Electrical and Electronics Engineering, KL University, India)

Abstract- A three-phase dc-dc converter based on the three-phase neutral point clamped (NPC) commutation cell is proposed, which is intended for use in applications where the energy from a medium dc bus voltage needs to be processed. In this paper, all six continuous conduction modes (CCMs) are described, presenting the main waveforms and equations. For the discontinuous conduction modes the main equations are also provided for a complete converter characterization. Finally a H-bridge is proposed to get five levels.

Keywords: - DC-DC converter, neutral point clamped (NPC), three-phase transformer.

I. INTRODUCTION

Recently, there has been increased interest in three phase dc-dc conversion for high-power applications [1]–[10]. The major reason is that three-phase dc-dc converters can achieve lower power component current stresses and also considerably reduce input and output filter requirements, when compared to single-phase topologies [3], [4]. Moreover, three phase high-frequency transformer can handle higher power levels than single-phase ones, although they have the same size. All these characteristics make the use of three-phase dc-dc converters a very attractive solution when high power density and high efficiency are required.

Some solutions use three-phase resonant converters where soft-switching can be achieved, thus increasing the converter efficiency. On the other hand, the number of power components and also the converter volume are increased due to the addition of reactive power elements. Other promising solutions are the non resonant soft-switched three-phase converters. These combine the advantage of a reduced number of power components, due to the use of non resonant converters, with reduced switching losses by means of soft-switching techniques.

A non resonant hard-switched three-phase dc-dc converter was published in [1], and its circuit is shown in Fig. 1(a). It is composed of a three-phase inverter connected to the primary side of a three-phase high-

frequency transformer. The secondary side of the transformer feeds a three-phase rectifier, and the output stage of the converter is composed of an $L-C$ filter and the load. The concept of resonance applied to the three-phase dc-dc converter can be observed in the converter proposed in [5], which is depicted in Fig. 1(b). This converter can operate under zero-voltage-switching (ZVS) or zero-current-switching (ZCS) conditions, with the drawback of using three additional capacitors to achieve the desired resonance.

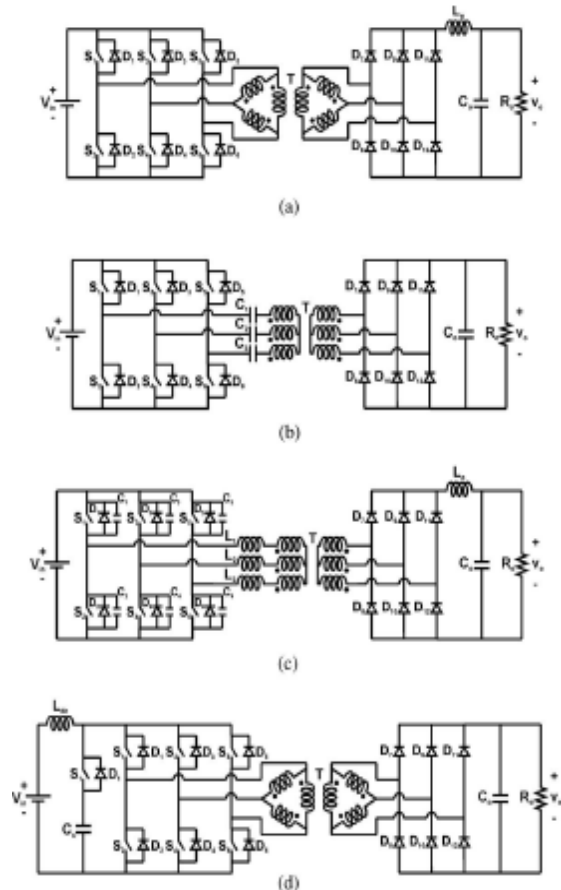


Fig. 1. Previously reported three-phase dc-dc converters: (a) non resonant

Hard-switched [1]; (b) resonant soft-switched [5]; (c) non resonant soft switched [6]; (d) non resonant with active clamp [7]. Non resonant soft-switched three-phase dc-dc converters were also proposed in [6] and [7], and their circuits are shown in Fig. 1(c) and (d), respectively. The converter depicted in Fig. 1(c) can achieve ZVS for all switches and control the output voltage by means of an asymmetrical PWM. Therefore, upper and lower commutation cell switches are subjected to different current stresses.

II. PROPOSED THREE-PHASE DC-DC CONVERTER

The circuit of the proposed three-phase three-level pulse width-modulated (TPTL-PWM) dc-dc converter is shown in Fig. 2. Basically, it is composed of a neutral point clamped (NPC) inverter connected to the primary side of a three-phase high-frequency transformer, the secondary side of which is, in turn, connected to a three-phase rectifier.

Diodes $D1-D12$ are intrinsic to switches $S1-S12$ and $D13-D18$ are clamping diodes. One important characteristic of this converter is that the inductance is placed between the inverter and the rectifier stage. Therefore, the leakage inductance of the transformer T may be used in favor of the converter operation, and inductors L_{in} are added to the circuit whenever the value of the leakage inductance is not sufficiently large. Capacitor C_o comprises the purely capacitive output filter, which is an attractive solution due to the reduced ripple produced in current i_o . Resistor R_o represents the load fed by the converter

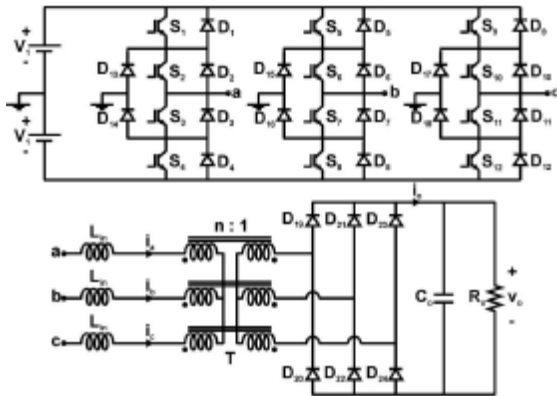


Fig. 2. Proposed three-phase three-level PWM dc-dc converter

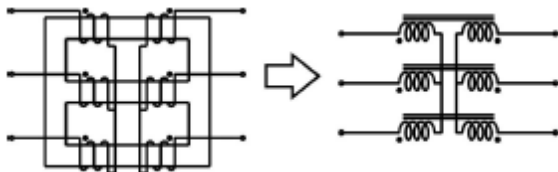


Fig. 3. Three-phase transformer and the equivalent symbol used for its Representation.

III. PRINCIPLE OF OPERATION

Due to publication space limitations, only the continuous conduction modes (CCM) will be described herein. For discontinuous conduction modes (DCM) only the resulting equations will be provided. A given operation mode is classified as discontinuous if there is no current flowing through the inductor L_{in} during at least one operation stage. Otherwise, the mode is considered to be continuous. In this paper, all six CCM operation modes will be described and mathematically analyzed. Each operation mode is composed of 18 operation stages. However, the analysis of three stages is sufficient to generate all linearly independent equations that completely describe a given operation mode, due to PWM and converter symmetry. During the analysis, all components will be treated as ideal.

A. CCM Mode 1

In CCM, whenever the duty cycle is within the interval $0 \leq D < 1/3$, the converter operates in mode 1. Three operation stages for this mode are shown in Fig. 4.

- 1) First stage (t_0, t_1)—Starts when $S3$ is turned off. Since current i_a has a negative value, the diodes $D1$ and $D2$ start conducting. In the bridge rectifier diodes $D20$, $D22$, and $D23$ are conducting. The condition of ZVS turn-on for $S1$ and $S2$ is only achieved if these switches

are turned on during the first stage. When current i_a becomes positive this stage ends.

- 2) Second stage (t_1, t_2)—At the time instant $t = t_1$ the value of current i_a becomes positive, therefore $S1$ and $S2$ assume this current. Moreover, diode $D20$ is blocked and $D19$ starts conducting. This stage ends when switch $S1$ is turned off.
- 3) Third stage (t_2, t_3)—After $S1$ is blocked, diode $D13$ starts conducting in order to maintain current i_a flowing. At the time instant $t = t_3$ switch $S10$ is turned off and the third stage ends.

B. CCM Mode 2

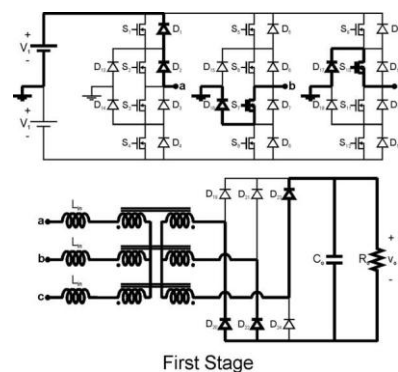
For a duty cycle interval of $1/3 \leq D < 2/3$ there are two possible operation modes in CCM. One of them is described in this subsection. Fig. 5 shows three operation stages for this mode.

- 1) First stage (t_0, t_1)—At the time instant $t = t_0$ switch $S3$ is turned off and diodes $D1$ and $D2$ start conducting. Diodes $D20$, $D22$, and $D23$ are conducting in the bridge rectifier. As soon as switch $S8$ is turned off this stage ends.
- 2) Second stage (t_1, t_2)—Blocking switch $S8$ implies that diode $D16$ starts conducting to guarantee the continuity of current i_b . Both $S1$ and $S2$ must be turned on during the first or the second stage, in order to achieve ZVS turn-on for these switches. At time $t = t_2$ the direction of current i_a is reversed and the second stage ends
- 3) Third stage (t_2, t_3)—Since the i_a value has become positive, this current starts flowing through switches $S1$ and $S2$. In the bridge rectifier, the blocking of diode $D20$ occurs, and $D19$ starts conducting. This stage persists until switch $S10$ is turned off.

C. CCM Mode 3

Mode 3 is the second possibility of converter operation for the duty cycle interval of $1/3 \leq D < 2/3$ in CCM. As provided in the previous modes, three operation stages are shown in Fig. 6.

- 1) First stage (t_0, t_1)—Starts when switch $S3$ is turned off, and therefore diodes $D1$ and $D2$ assume the current i_a . In the bridge rectifier, diodes $D20$, $D22$ and $D23$ are forward biased. It is important to note that ZVS turn-on is only achieved if switches $S1$ and $S2$ are turned on during the first stage. When $t = t_1$ the current i_a becomes positive and the first stage ends.



First Stage

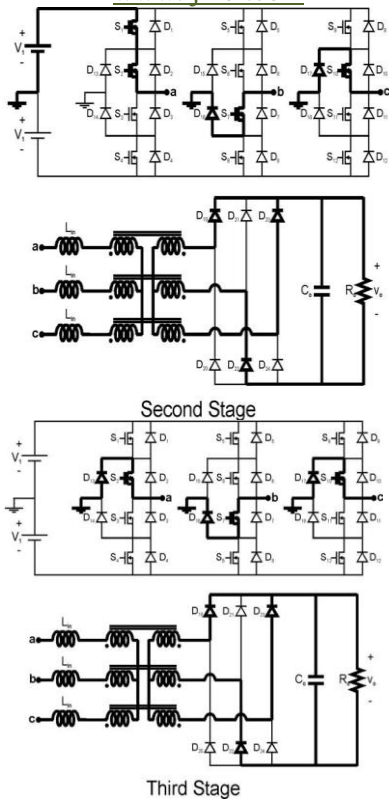


Fig. 4. Three operation stages for mode 1

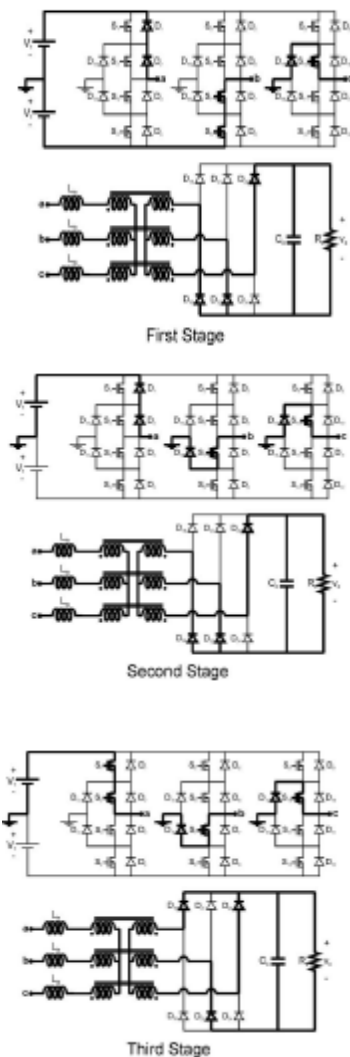


Fig. 5. Three operation stages for mode 2.

- 2) Second stage (t_1, t_2)—At time $t = t_1$ switches S_1 and S_2 start conducting the current i_a . Therefore, the diode D_{20} blocks and D_{19} starts conducting. As soon as switch S_8 is turned off the second stage is finished.
- 3) Third stage (t_2, t_3)—In order to guarantee the continuity of current i_b , diode D_{16} starts conducting when switch S_8 is turned off. The third stage will persist until switch S_{10} is turned off.

C. CCM Mode 4

The three remaining continuous conduction operation modes are observed when the converter operates with duty cycle values within the range of $2/3 \leq D \leq 1$. One of them is called mode 4 and is described in this section. Three operation stages for this mode are depicted in Fig. 7.

- 1) First stage (t_0, t_1)—When switch S_3 is turned off the first stage starts. At this moment, diodes D_1 and D_2 assume the current i_a . The diodes D_{20} , D_{21} , and D_{23} are forward biased in the bridge rectifier. The stage ends when current i_b changes its signal.
- 2) Second stage (t_1, t_2)—The second stage begins when the direction of current i_b is reversed and it starts flowing through switches S_7 and S_8 . Therefore, the blocking of the diode D_{21} occurs and D_{22} starts conducting. This stage finishes when switch S_9 is turned off.
- 3) Third stage (t_2, t_3)—After switch S_9 is blocked, diode D_{17} starts conducting, beginning the third stage. It is important to note that ZVS turn-on condition for S_1 and S_2 is only achieved if these switches are turned on during the first four operation stages. When switch S_{10} is turned off this stage ends.

D. CCM Mode 5

Mode 5 is another possible operation mode when the converter operates with duty cycle within the range of $2/3 \leq D \leq 1$. Fig. 8 shows three operation stages for this mode.

- 1) First stage (t_0, t_1)—Begins when switch S_3 is turned off. Thus, current i_a starts flowing through diodes D_1 and D_2 . In the bridge rectifier, the diodes D_{20} , D_{22} , and D_{23} are in conduction. At the time instant $t = t_1$, switch S_9 is turned off and this stage ends.
- 2) Second stage (t_1, t_2)—With the blocking of S_9 the diode D_{17} starts conducting. The condition of ZVS turn-on for S_1 and S_2 will only occur if these switches are turned on during the first or the second stage. As soon as current i_a becomes positive the second stage is finished.
- 3) Third stage (t_2, t_3)—After the direction of i_a is reversed switches S_1 and S_2 assume this current. Moreover, the diode D_{20} is blocked while D_{19} starts conducting. At the time instant $t = t_3$ switch S_{10} is turned off and this stage ends.

E. CCM Mode 6

The last CCM operation mode to be described is mode 6. As for the last two modes the duty cycle is within the range of $2/3 \leq D \leq 1$. Three operation stages for this mode are shown in Fig. 9.

- 1) First stage (t_0, t_1)—At the time instant $t = t_0$ the switch S_3 is turned off and diodes D_1 and D_2 assume the

current i_a . Diodes D_{20} , D_{22} and D_{23} are conducting in the bridge rectifier. This stage ends when current i_a becomes positive.

- 2) Second stage (t_1 , t_2)—As the direction of current i_a is reversed switches S_1 and S_2 start conducting. Therefore, the blocking of diode D_{20} occurs and D_{19} starts conducting. It is also important to note that S_1 and S_2 must be turned on during the first or the second stage, thus ZVS turn-on is achieved for both switches. The second stage persists until switch S_9 is turned off at the time instant $t = t_2$.
- 3) Third stage (t_2 , t_3)—After the blocking of switch S_9 the diode D_{17} starts conducting to guarantee the continuity of current i_c . When switch S_{10} is turned off this stage finishes.

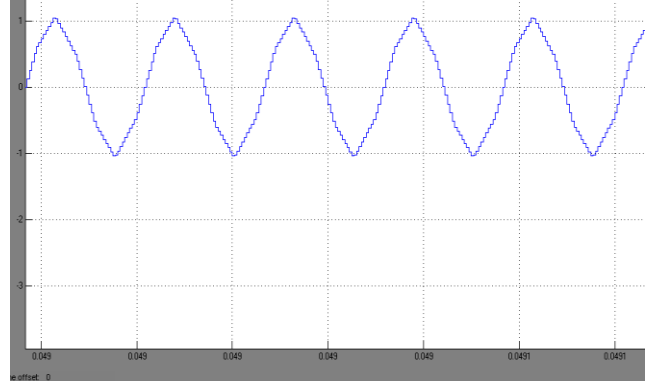


Fig. 7 Inductor Current

Fig.6 shows the diode clamped inverter output voltage. Fig. 7 shows the inductor current and Fig.8 shows the switch voltage.

III MATLAB/SIMULINK MODEL

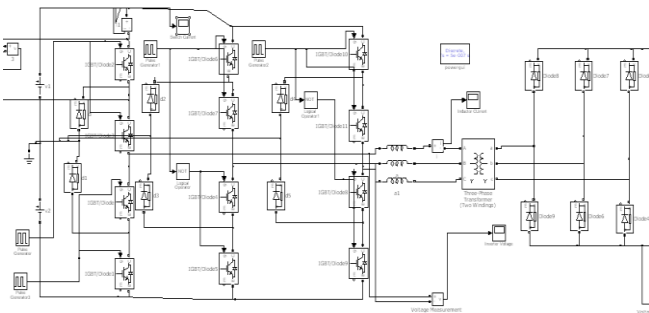


Fig. 5 Matlab/ Simulink Model

Fig. 5 shows the Matlab/Simulink model of three level diode clamped DC to DC converter.

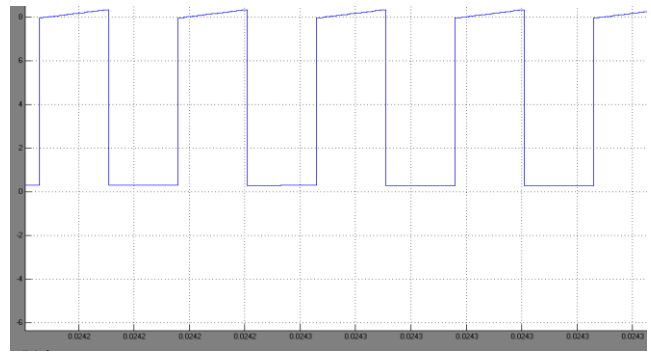


Fig. 8 Voltage across the switch

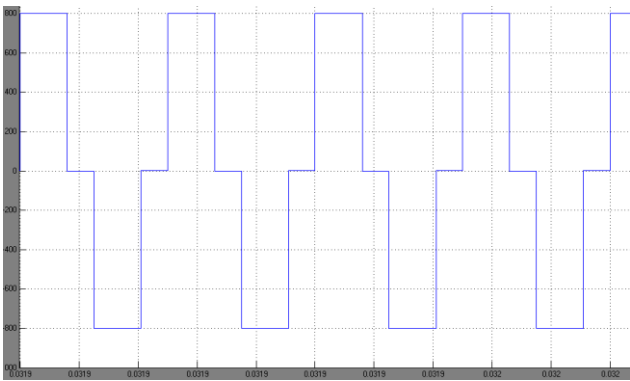


Fig. 6 Diode clamped inverter output voltage

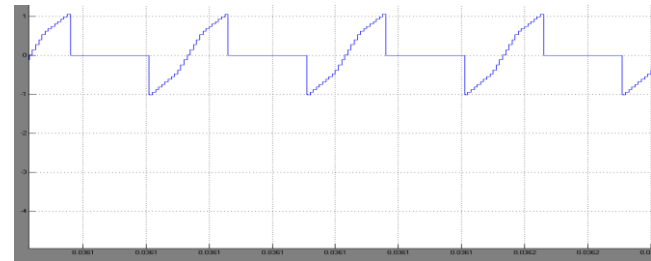


Fig. 9 Switch Current

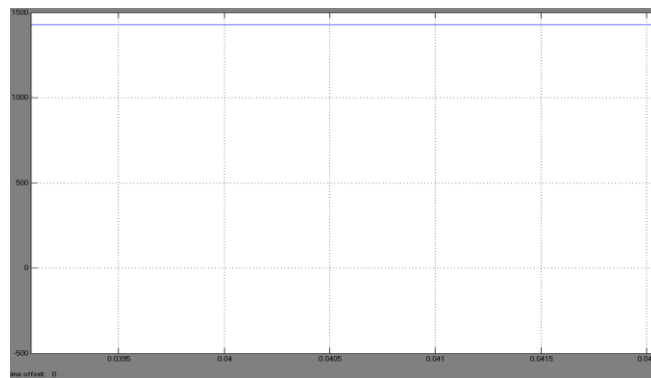


Fig. 10 DC output voltage

Fig. 9 shows the switch current and Fig. 10 shows the DC output voltage.

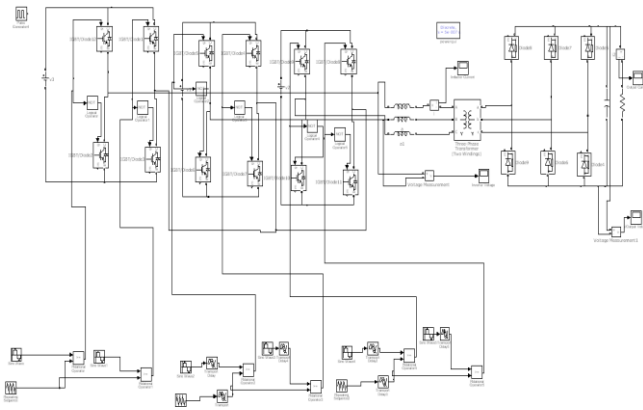


Fig. 11 Three phase H-Bridge DC to DC converter

Fig.11 Shows the Matlab/Simulink model of proposed DC to DC converter. In the proposed converter a H-bridge is used.

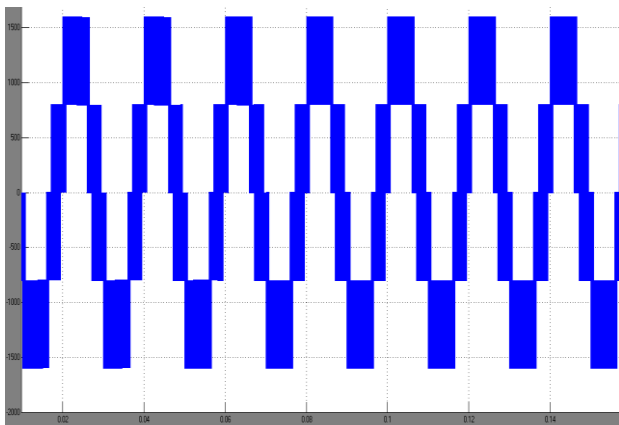


Fig. 12 Five level PWM output

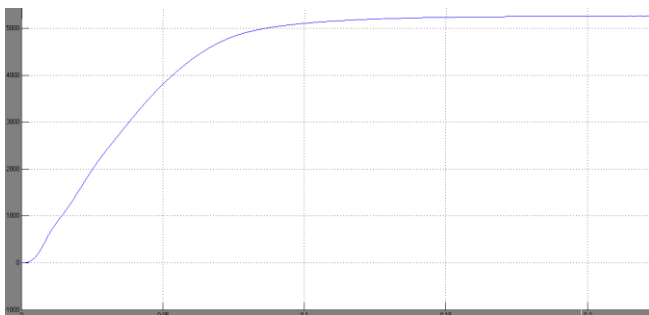


Fig.13 DC output Voltage

Fig.12 shows the Five level PWM output and Fig. 13 shows the corresponding DC output.

IV CONCLUSION

A three-phase three-level PWM dc-dc converter was proposed. Theoretical analysis results for both CCM and DCM operation were presented, allowing a complete static characterization of the proposed converter through its output characteristic graph. In this paper a new five level H-Bridge

DC to DC converter is proposed and simulation results are presented.

V REFERENCES

- [1] R. Prasad, P. D. Ziogas, and S. Manias, "Analysis and design of a three-phase offline DC-DC converter with high frequency isolation," in *Proc. IAS*, 1988, pp. 813-820.
- [2] P. D. Ziogas, A. R. Prasad, and S. Manias, "A three-phase resonant dc/dc converter," in *Proc. IEEE Power Electron. Specialists Conf.*, 1991, pp. 463-473.
- [3] R.W. A. A. De Doncker, D. M. Divan, and M. H. Kheraluwala, "A three-phase soft-switched high-power density dc/dc converter for high-power applications," *IEEE Trans. Ind. Appl.*, vol. 27, no. 1, pp. 63-73, Jan./Feb.1991.
- [4] A. K. S. Bhat and R. L. Zheng, "A three-phase series-parallel resonant converter-analysis, design, simulation, and experimental results," *IEEE Trans. Ind. Appl.*, vol. 32, no. 4, pp. 951-960, Jul./Aug. 1996.
- [5] J. Jacobs, A. Averberg, and R. De Doncker, "A novel three-phase DC/DC converter for high-power applications," in *Proc. IEEE Power Electron. Specialists Conf.*, 2004, pp. 1861-1867.
- [6] D. S. Oliveira and I. Barbi, "A three-phase ZVS PWM DC/DC converter with asymmetrical duty cycle for high power applications," *IEEE Trans. Power Electron.*, vol. 20, no. 2, pp. 370-377, Mar. 2005.
- [7] H. Cha and P. Enjeti, "A novel three-phase high power current-fed DC/DC converter with active clamp for fuel cells," in *Proc. IEEE Power Electron. Specialists Conf.*, 2007, pp. 2485-2489.
- [8] T. Song, H. S. H. Chung, S. Tapuhi, and A. Ioinovici, "A high input voltage three-phase ZVZCS dc-dc converter with $V_{in}/3$ voltage stress on primary switches," in *Proc. IEEE Power Electron. Specialists Conf.*, 2007, pp. 350-356.
- [9] D. V. Ghodke, K. Chatterjee, and B. G. Fernandes, "Three-phase three level, soft switched, phase shifted PWM dc-dc converter for high power applications," *IEEE Trans. Power Electron.*, vol. 23, no. 3, pp. 1214-1227, May 2008.
- [10] C. Liu, A. Johnson, and J. Lai, "A novel three-phase high-power soft switched DC/DC converter for low-voltage fuel cell applications," *IEEE Trans. Ind. Appl.*, vol. 41, no. 6, pp. 1691-1697, Nov./Dec. 2005.

Entropy Change Index as a Measure of Cardio-Thermal Physiological Stress Response

Satish C. Boregowda¹, Rodney Handy^{2*}, Robert E. Choate³, and Carol A. Boregowda⁴

¹Sandia National Laboratories, PO Box 5800, Albuquerque, NM 87185

^{2*}Purdue University, West Lafayette, IN 47907

³Western Kentucky University, Bowling Green, KY 42101

⁴American Council of Exercise Certified Personal Trainer, Albuquerque, NM 87111

ABSTRACT

The present study describes the application of a thermodynamics-based entropy approach to model and measure human cardio-thermo-physiological stress response. Using Maxwell relations, this approach combines three physiological measures (blood pressure, heart rate, and core body temperature) to provide a quantitative measure of cardio-thermal stress response in terms of entropy change. This entropy change expression provides a mathematical link between cardiovascular and thermoregulatory responses based on the principles of thermodynamics. The experimental data was obtained from a NASA Johnson Space Center study involving seven subjects to demonstrate this methodology. The three physiological measures were taken under four conditions (Rest, 40% VO_2 peak, 65% VO_2 peak, and Recovery) in five-minute intervals during the course of the entire eighty-minute physiological test. The entropy change computed from the experimental data was normalized to obtain an entropy change index (ECI). Further, it is statistically established that ECI could be used in addition to individual measures such as blood pressure, heart rate, and core body temperature to assess human stress response and performance.

Keywords – cardio-thermal physiology; entropy change index; stress; thermodynamics.

1. INTRODUCTION

Several studies have made significant efforts to quantify human cardio-thermal physiological stress response. Most of these earlier studies examine physiological strain or stress response using a single or at most two physiological indicators. In an experimental study conducted by Moran et al. [1] combines two physiological responses including core body temperature and heart rate, to develop a *Physiological Strain Index (PSI)*. The limitation of PSI is that it is statistically based and empirical in nature, which limits its application to specific populations and measurement of heat stress. Since the human cardio-thermal physiological system consists of many interconnected physiological processes controlled by a complex nervous system, single physiological indicators provide a very narrow representation of the human response system. It is only by

recognizing the interaction among human subsystems in their response to any stimuli that one could begin the investigation of human physiological responses. In this regard, the studies conducted by Boregowda et al. [2, 3] and Palsson et al. [4] have made an effort to develop an *Entropy Change Index (ECI)* that utilizes three physiological variables such as blood pressure, heart rate, and core body temperature. It is postulated that the entropy change in a living system is nothing but increased physiological disorder. The Maxwell relations are used to quantify abstract entropy change in terms of multiple measurable quantities such as pressure, volume, temperature, and electro-magnetic fields [5, 6]. An analogy between physical and human physiological systems is conceptualized and the properties of a non-living system are mapped to that of a living system. In this regard, the physical fluid-thermal system characterized by pressure (P), volume (V), and temperature (T) are directly mapped to that of a living human cardio-thermal physiological system's blood pressure (BP), heart rate (HR), and core body temperature level (CBT), respectively.

2. MODELING AND FORMULATION

In the scope of the present study, the cardiovascular and thermoregulatory systems which are responsible for the responses such as blood pressure (BP), heart rate (HR), and core body temperature (CBT) are considered in the thermodynamic analysis. In an earlier study [3], the physiological responses were taken under static conditions at only three different time intervals. However, the present study utilizes the NASA experimental data, which contains continuous physiological responses in five-minute intervals for a total of eighty minutes. This study provides an opportunity to examine the variation of entropy change on a moment-to-moment basis and thereby provides a better view of cardio-thermoregulatory response to stress.

The philosophical approach behind the present study is based on the premise established by Harvard Physicist P.W. Bridgman [7], who stated that - "It must be admitted. I think, that laws of thermodynamics have a different feel from most other laws of physics. There is something more palpably verbal about them – they smell more of their human origin..." It is observed that the human cardio-thermo-physiological system is regarded as an open

thermodynamic system that exchanges energy and matter with the surroundings. It has been shown that the increased disorder (or change in entropy) in a cardio-thermo-physiological system in response to any stressor is defined to be mathematically equivalent to the Entropy change index (ECI) and is stated under Postulate I as follows:

Postulate I. The normalized entropy which represents the ratio of the entropy change (ΔS) in a cardio-thermo-physiological system of interest during the resting state and stressor to that of resting state (average entropy change, $(\Delta S)_{Avg. Rest}$ during rest) is expressed as an Entropy change index (ECI).

As shown in Equations (1), if the cardio-thermo-physiological responses, which include blood pressure (BP), heart rate (HR), and core body temperature (CBT) are equivalent to pressure (P), volume (V), and temperature (T) in a fluid-thermal system, then the entropy is written as follows:

$$\text{Physical Entropy} = f \{ \text{Pressure, Volume, and Temperature} \} \quad (1a)$$

$$\text{Physiological Entropy} = f \{ \text{Blood Pressure, Heart Rate, and Core Body Temperature} \} \quad (1b)$$

By applying the Maxwell relations of thermodynamics to model the human cardio-thermo-physiological system, the (ECI) is calculated as follows:

$$(\Delta S) = [(BP - BP_0) \times (HR - HR_0)] / [CBT - CBT_0] \quad (2)$$

$$(\Delta S)_{Avg. Rest} = [(BP_{Avg. Rest} - BP_0) \times (HR_{Avg. Rest} - HR_0)] / [CBT_{Avg. Rest} - CBT_0] \quad (3)$$

$$ECI = (\Delta S) / (\Delta S)_{Avg. Rest} \quad (4)$$

Where, ECI = entropy change index for cardio-thermal physiological system, dimensional units
 BP = blood pressure (systolic or diastolic), mm Hg
 HR = heart rate, beats per minute
 CBT = core body temperature (average of esophageal, rectal, and intestine temperatures), °C
 BP₀ = HR₀ = ST₀ = 0 (Reference States)
 BP_{Avg. Rest} = average blood pressure (systolic or diastolic) during the resting state (20 minutes)
 HR_{Avg. Rest} = average heart rate during the resting state (20 minutes)
 CBT_{Avg. Rest} = average core body temperature during the resting state (20 minutes)

It is restated that normalized entropy change in the form of an entropy change index (ECI) could be postulated as a physiological reflection of a disorder and thus a measure of physiological stress as per Postulate II.

Postulate II: The non-dimensional entropy change, a measure of disorder in a human cardio-thermal physiological system and is equivalent to cardio-thermal physiological stress response.

$$ECI = f \{ BP, HR, \text{ and } CBT \} \equiv \text{Cardio-Thermal Physiological Stress Response} \quad (5)$$

3. METHODS

The data was obtained from a NASA experimental study conducted by Lee et al. [8] involving seven subjects who participated in the investigation. Subjects completed a health screening, which was administered by a qualified physician in the NASA-Johnson Space Center Human Test Subject Facility. Testing procedures were reviewed and approved by the NASA-Johnson Space Center Institutional Review Board. Subjects completed a supine graded exercise test on a cycle ergometer to determine peak oxygen consumption (VO_{2pk}) in this posture. From these data, exercise intensities corresponding to 40% and 65% of supine VO_{2pk} were determined for use during the subsequent submaximal exercise test. During the exercise tests, simultaneous measurements of core body temperatures (esophageal, rectal, and intestinal temperatures), blood pressure, and heart rate were made.

4. RESULTS AND ANALYSIS

Please refer to **Appendix A** for an illustrative example followed by figures and tables in **Appendix B**. The monitoring of entropy change index (ECI) is shown in Figures 1 and 2. Figure 1 depicts the entire time-series systolic blood pressure-based ECI data for all seven subjects. Similarly, the variation diastolic blood pressure-based ECI data is shown in Figure 2. It is clear from these figures that there are individual differences in how subjects respond to different levels of exercise.

A descriptive statistical analysis is conducted on each of the data streams pertaining to all seven subjects. The ECI statistical measures such as mean and standard deviation are computed for each of the subjects under four conditions. These conditions include - resting state, 40% $VO_{2 peak}$, 65% $VO_{2 peak}$, and recovery. The data are shown in Tables 2 and 3 for $(ECI)_{SBP}$ and $(ECI)_{DBP}$, respectively. The data shown in Tables 2 and 3 are shown graphically in Figures 3 and 4. These figures reflect individual variation in mean response to four different exercise conditions. It clearly shows that there is more variation among subjects during the exercise conditions of 40% $VO_{2 peak}$ and 65% $VO_{2 peak}$. The resting state and recovery do not indicate any variation in stress responses. The entropy change index (ECI) provides a holistic measure of human cardio-thermal stress response to varying exercise conditions. Using ECI, the human performance analysts could develop a scale to measure the

level of physiological condition of athletes, astronauts, fire fighters, police, military personnel, and other emergency personnel who perform their tasks in extreme environments.

5. CONCLUSION

The results from this study offer some preliminary indications suggesting that the entropy change index (ECI) could be used as an index to measure the levels of physiological stress response to varying exercise conditions. Data from a NASA experimental study was used to validate the proposed Entropy change index (ECI) as a measure of cardio-thermal physiological stress response. The descriptive statistical results indicate that the ECI holds a promise as a metric to measure and evaluate human physiological stress, performance, and levels of conditioning. The combined measure of ECI provides a systems view of varying levels of physiological conditioning. Thus, the engineering thermodynamics-based ECI is would provide the fields of medicine and health sciences with something which has long been sorely missing - a scientifically sound and useful way of quantifying human cardio-thermal physiological stress response as a single number.

ACKNOWLEDGEMENTS

The authors wish to thank Dr. Alan Pope of NASA Langley Research Center for partially supporting this research project.

REFERENCES

- [1] D. S. Moran, A. Shitzer, and K. B. Pandolf, (1998). A physiological strain index to evaluate heat stress,

American Journal of Physiology – Regulatory, Integrative and Comparative Physiology, 275, 1998, R129-R134.

- [2] S. C. Boregowda, S. N. Tiwari, S. K. Chaturvedi, and D. R. Redondo, Analysis and quantification of mental stress and fatigue using Maxwell relations from thermodynamics,” *Journal of Human Ergology*, 26(1), 1997, 7-16.
- [3] S.C. Boregowda and W. Karwowski, Modeling of human physiological stresses: A thermodynamics-based approach, *Occupational Ergonomics*, 5(4), 2005, 235-248.
- [4] O. S. Palsson, S. C. Boregowda, and B. K. Downing, The relationship between an objective stress index (OSI) and stress-related physical symptoms, *Journal of Applied Psychophysiology and Biofeedback*, 23(2), 1998, 125.
- [5] H. Callen, *Thermodynamics and an introduction to thermostatics* (NY: Wiley, 1985).
- [6] E.P. Gyftopoulos and G. P. Beretta, *Thermodynamics* (Mineola, NY: Dover Publications, 2005).
- [7] P. W. Bridgman, *The nature of thermodynamics* (NY: Harpers and Row Publishers, 1961)
- [8] M. C. S. Lee, W. J. Williams, and S. M. Schnieder, (2000). *Core temperature measurement during submaximal exercise: esophageal, rectal, and intestinal temperature* (Houston, TX: NASA Johnson Space Center Technical Report NASA/TP-2000-210133, 2000).

APPENDIX A: ILLUSTRATIVE EXAMPLE

This section contains a sample calculation of the entropy change index in a stepwise manner. Each one of the physiological measures - BP, HR, and CBT, used in the calculation of entropy change indices, pertain to subject #1. Let us consider subject#1, whose physiological stress response values during the resting state are given in Table 1.

Table 1: Average Values of Physiological Responses during the Resting State

Time (Min)	TES	TREC	TIN	HR	SBP	DBP
0.00	37.08	37.10	37.26	55.00	104.00	65.00
5.00	37.03	37.00	37.21	67.00	102.00	68.00
10.00	37.08	37.00	37.19	55.00	105.00	65.00
15.00	37.03	36.95	37.16	55.00	103.00	65.00
20.00	36.97	36.90	37.10	58.00	100.00	64.00
Average	37.04	36.99	37.18	58.00	102.80	65.40

The average value of the entropy change during the resting state is given by Eq (3) and is rewritten by replacing $BP_{Avg. Rest}$ with the Systolic Blood Pressure ($SBP_{Avg. Rest}$) as follows:

$$(\Delta S)_{Avg. Rest} = [(SBP_{Avg. Rest} - SBP_0) \times (HR_{Avg. Rest} - HR_0)] / [CBT_{Avg. Rest} - CBT_0]$$

Where, $SBP_{Avg. Rest} = 102.80$ mm Hg
 $HR_{Avg. Rest} = 58.00$ bpm

$$CBT_{Avg. Rest} = 36.99 \text{ }^{\circ}\text{C}$$

$$SBP_O = HR_O = CBT_O = 0 \text{ (Reference states)}$$

By substituting the above values of physiological variables in Eq (7), we get,

$$(\Delta S)_{Avg. Rest} = [(102.80 - 0.0) \times (58.00 - 0.00)] / [36.99 - 0.0] = 161.19 \text{ mm Hg.bpm/oC}$$

The change in entropy during the stressor (rest and exercise) using systolic blood pressures is computed by rewriting the Eq. (2) with systolic blood pressure for the entire time series (at five-minute intervals). For the sake of brevity, the calculations are shown at 0th,..., 20th,...40th,...60th,...80th minutes as follows:

$$(\Delta S) = [(SBP-SBPO) \times (HR-HRO)] / [CBT-CBTO]$$

$$(\Delta S)_{SBP, 0,min} = [(104.00 - 0.0) \times (55.00 - 0.00)] / [37.10 - 0.0] = 154.19 \text{ mm Hg.bpm/oC}$$

:

$$(\Delta S)_{SBP, 20,min} = [(100.00 - 0.0) \times (58.00 - 0.00)] / [36.90 - 0.0] = 157.18 \text{ mm Hg.bpm/oC}$$

:

$$(\Delta S)_{SBP, 40,min} = [(134.00 - 0.0) \times (92.00 - 0.00)] / [37.10 - 0.0] = 332.29 \text{ mm Hg.bpm/oC}$$

:

$$(\Delta S)_{SBP, 60,min} = [(165.00 - 0.0) \times (112.00 - 0.00)] / [37.46 - 0.0] = 493.33 \text{ mm Hg.bpm/oC}$$

:

$$(\Delta S)_{SBP, 80,min} = [(118.00 - 0.0) \times (63.00 - 0.00)] / [37.36 - 0.0] = 198.98 \text{ mm Hg.bpm/oC}$$

The systolic blood pressure-based entropy change index (ECI) SBP is calculated accordingly as follows:

$$(ECI)_{SBP, 0 \text{ min}} = (\Delta S)_{SBP, 0 \text{ min}} / (\Delta S)_{Avg. Rest} = 154.19 / 161.19 = 0.96$$

:

$$(ECI)_{SBP, 20 \text{ min}} = (\Delta S)_{SBP, 20 \text{ min}} / (\Delta S)_{Avg. Rest} = 157.18 / 161.19 = 0.98$$

:

$$(ECI)_{SBP, 40 \text{ min}} = (\Delta S)_{SBP, 40 \text{ min}} / (\Delta S)_{Avg. Rest} = 332.29 / 161.19 = 2.06$$

:

$$(ECI)_{SBP, 60 \text{ min}} = (\Delta S)_{SBP, 60 \text{ min}} / (\Delta S)_{Avg. Rest} = 493.33 / 161.19 = 3.06$$

:

$$(ECI)_{SBP, 80 \text{ min}} = (\Delta S)_{SBP, 80 \text{ min}} / (\Delta S)_{Avg. Rest} = 198.98 / 161.19 = 1.23$$

In a similar manner, the rest of the (ECI)_{SBP} are computed for the remaining six subjects. Similarly, the (ECI)_{DBP} values are computed for the all seven subjects and the results are provided in the results and analysis section and corresponding figures and tables are provided in the next Appendix B.

APPENDIX B: FIGURES AND TABLES (Refer to Section 4 on RESULTS AND ANALYSIS)

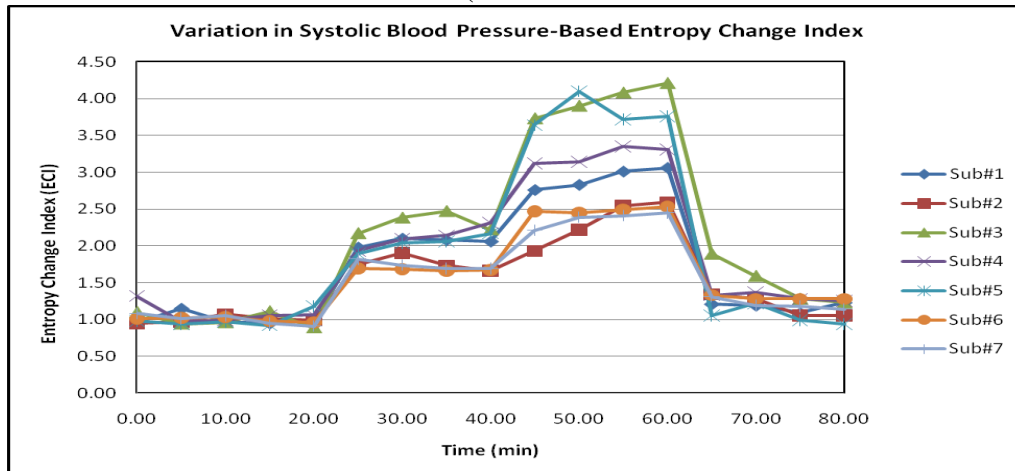


Figure 1. Continuous Monitoring of (ECI)_{SBP}

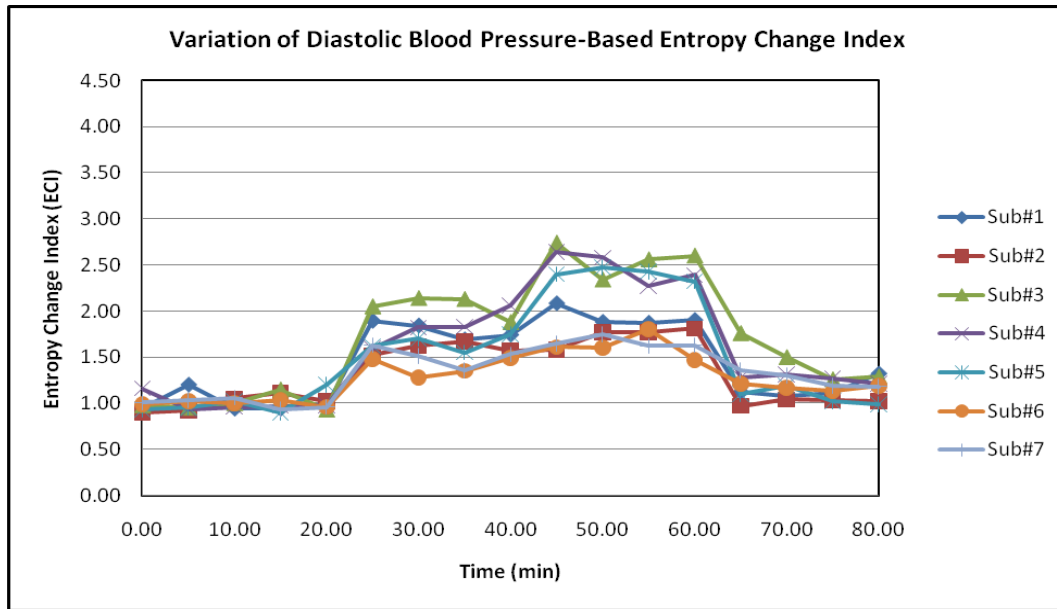


Figure 2. Continuous Monitoring of $(ECI)_{DBP}$

Table 2: Average $(ECI)_{SBP}$ Values under Four Exercise Conditions

Subjects	Resting State		40% VO2 Peak		65% VO2 Peak		Recovery	
	Mean	SD	Mean	SD	Mean	SD	Mean	SD
1	1.00	0.08	2.05	0.05	2.91	0.15	1.18	0.06
2	1.00	0.05	1.76	0.10	2.32	0.31	1.18	0.15
3	1.00	0.10	2.31	0.14	3.98	0.21	1.50	0.31
4	1.08	0.14	2.12	0.16	3.23	0.12	1.30	0.05
5	1.00	0.10	2.04	0.12	3.81	0.20	1.05	0.12
6	1.00	0.03	1.68	0.01	2.48	0.04	1.29	0.02
7	1.00	0.07	1.74	0.06	2.36	0.10	1.20	0.08

Table 3: Average (ECI)_{DBP} values under Four Exercise Conditions

Subjects	Resting State		40% VO2 Peak		65% VO2 Peak		Recovery	
	Mean	SD	Mean	SD	Mean	SD	Mean	SD
1	1.00	0.11	1.79	0.09	1.93	0.10	1.16	0.11
2	1.00	0.09	1.59	0.06	1.73	0.10	1.02	0.03
3	1.00	0.09	2.05	0.12	2.56	0.16	1.45	0.23
4	1.08	0.09	1.83	0.19	2.47	0.17	1.27	0.04
5	1.00	0.12	1.65	0.09	2.40	0.06	1.07	0.09
6	1.00	0.02	1.40	0.10	1.62	0.13	1.17	0.04
7	1.00	0.05	1.51	0.11	1.66	0.06	1.25	0.09

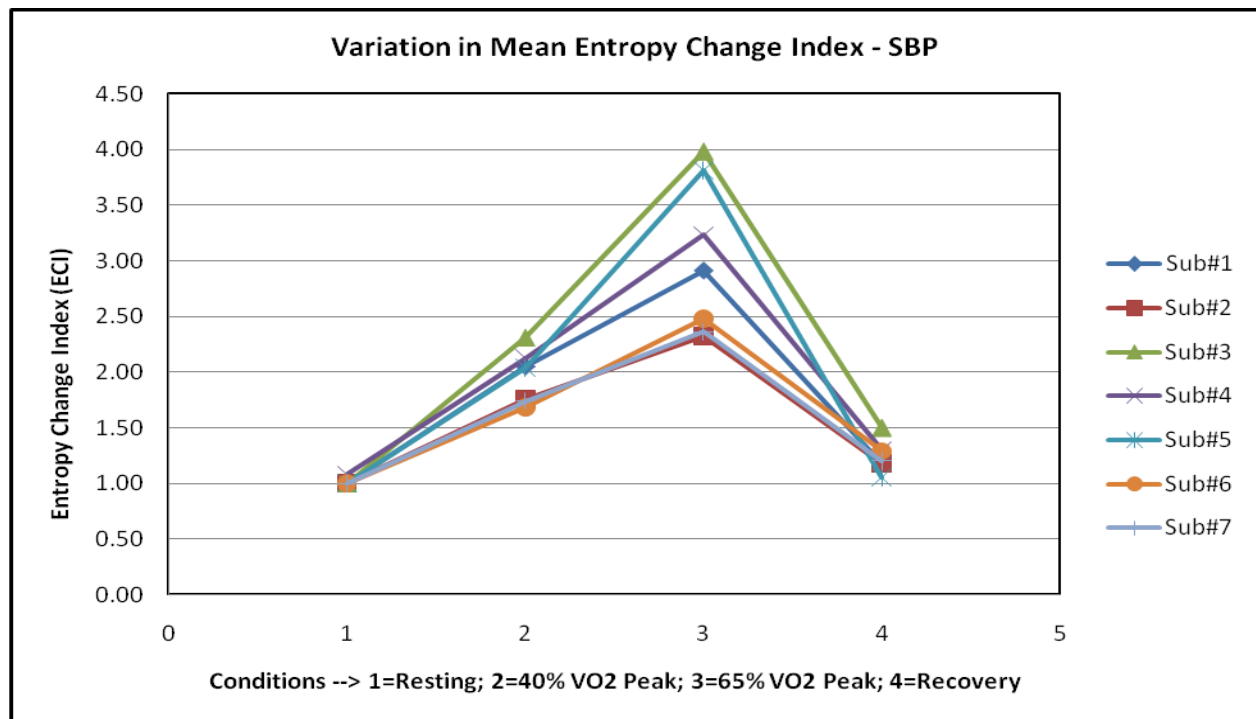


Figure 3. Monitoring of Mean (ECI)_{SBP} – Indicates Individual Variation

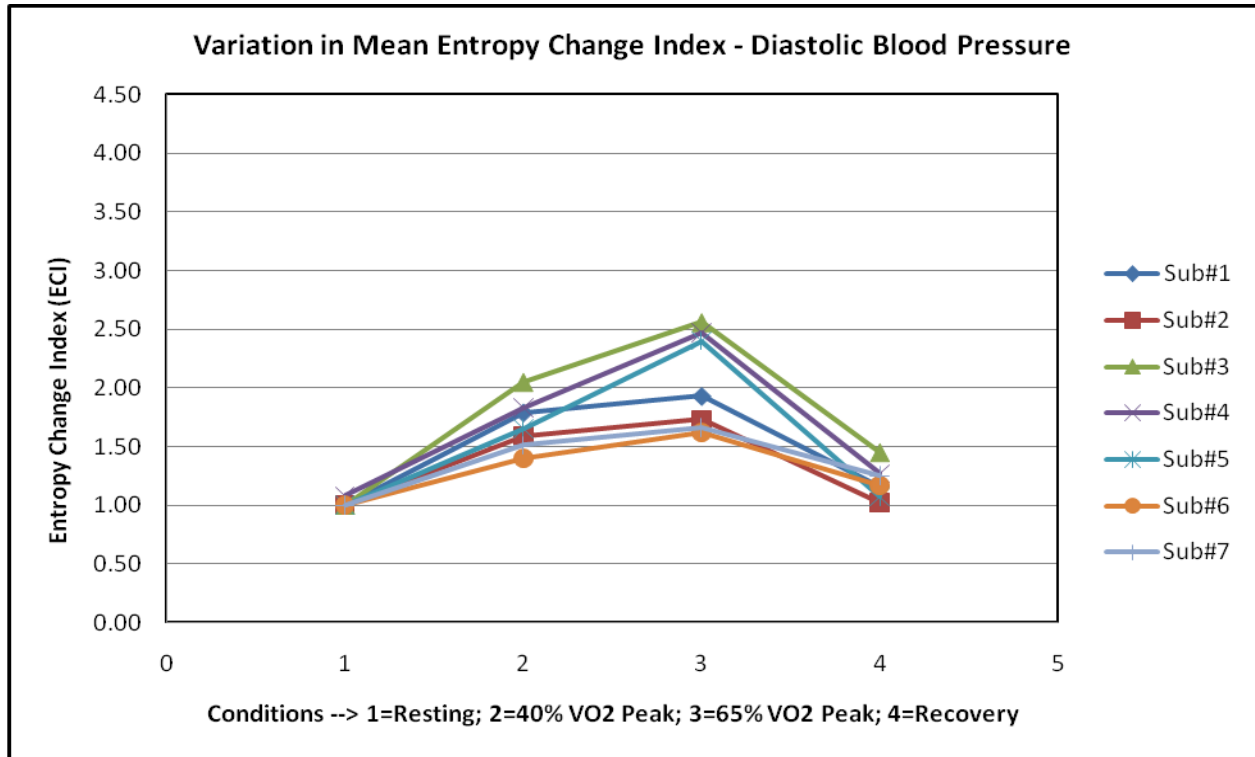


Figure 4. Monitoring of Mean (ECI)_{DBP} – Indicates Individual Variation

Effect of High Speed Drawing on Properties of High Carbon Steel Wires

¹Prakash Gawali, ²Amitesh Paul, ³G.R. Selokar

¹(Mechanical Engg. Deptt. SSSIST Sihore, M.P)

²(Mechanical Engg. Deptt. SSSIST Sihore, M.P)

³(Mechanical Engg. Deptt. SSSIST Sihore, M.P)

Abstract- The use of high speed in the wire drawing process become very common because of increase in customer demands and production rate. In this work the effect of high speed drawing (25m/sec) on mechanical and technological properties of high carbon steel wire has been investigated. Wire rod 5.50mm from steel grade 0.46% carbon and 0.71% carbon were drawn to 1.35mm in 13 draws and two speeds 8m/sec and 25m/sec. After each draw the following properties were determined; tensile strength (T_s), temperature (T), number of twists (N_t), number of bends (N_b). A large drop in the number of has been observed for final wires because of increased draw speed. However, there is also an advantage as the wire surface is much smoother after drawing at high speed than at low speed. The results were practically and statistically estimated.

Keywords- Wire drawing, temperature, tensile strength, speed.

INTRODUCTION

In the wire drawing process, the cross section is reduced by the pulling it through a conical die which is inserted in the die box and the wire is pulled by cylindrical drum which is run by electric motor [1].

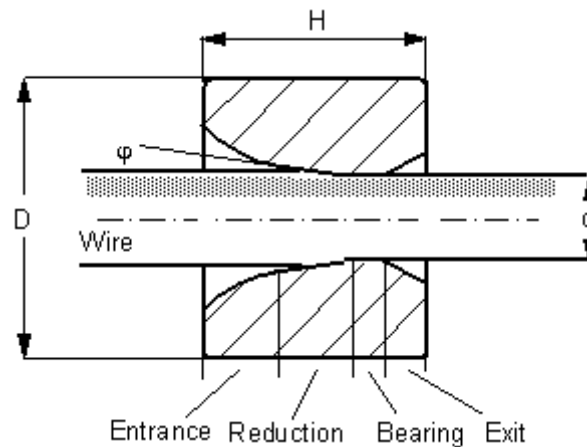


Fig. 1 Area reduction in wire drawing

The major variables in the drawing process are reduction in cross sectional area, die angle, friction along the die work piece interfaces and drawing speed. For successful drawing operation, careful selection of the process parameters should be carried out. The drawing speed depends on wire material as well as reduction in area for high drawing speeds[2], the heat generated does not have sufficient time to dissipate and a substantial rise in the temperature [3, 4] occurs which has detrimental effect on the quality of product.

Wire drawing operations employing high area reduction and improved lubrication and friction conditions not only save energy, but also reduce production cost by avoiding intermediate passes and annealing operations [5].

Heat generation in wire drawing was first addressed by Siebel and Kobitzsch. [6]. An early refinement of this analysis was made by Korst.[7]. The approach is still widely used today in estimating the temperature rise in wire drawing. While the model predicts that the maximum temperature rise in wire varies with the square root of the drawing speed. It has been observed in experiments to vary linearly with the drawing speed[5]. As well as the cube root of the speed [8]. More recently, this temperature rise was observed to be independent of drawing speed.[9]

Intensifications of the drawing process can be achieved by an increase of a single and a total reduction or by an increase of a drawing speed. However, in practical, technical and economical advantages with a faster speed are remarkable higher than during drawing with maximum reductions because a higher drawing speed increases the production yield for a specific drawing machine. There has been a trend in wire manufacturing to using high-speed multi hole drawing systems. This application is very important for further industry development but at the same time it is necessary to know the effect of this type of process of not only for the mechanical properties of the drawn wires, but also the factors such as die wear, lubricant section, die cooling of the dies, drawing drums and others.

Experimental procedure

The material used to the investigation was rise rod about diameter 5.50mm of low carbon steel after TRIP type heat treatment. The chemical composition of used steel in the investigation is presented in table 1.

TABLE 1

The chemical composition of TRIP steel

Mass contents in %								
C	Mn	Si	P	S	Cu	Ni	Mo	Sn
0.46	1.40	0.80	0.01	0.07	0.025	0.01	0.006	0.004
0.71	1.30	0.70	0.015	0.08	0.020	0.01	0.004	0.004

TABLE 2

The volumetric phase contain

Phase contain			
Ferte, %	Bainite, %	Retained austenite +~Martensite ¹ , %	Retained austenit ² %
71.3	15.8	8.5	6.9

After heat treatment and metallographic investigation which confirmed used TRIP type structure, TRIP steel wires drawn in 13 drafts with different drawing speed from diameter 5.5mm to 1.35mm by using classical die with sintered carbides about angle $2\alpha = 12^\circ$. In table 3, the main parameters of drawing process are shown, where: V – drawing speed, A – medium single draft, A_t – total draft in percentage.

TABLE 3

The parameters of drawing process

Variant	Drawing machine	Carbon %	V, m/s	Drafts number	A%	At%
A	BB-8	C – 46	8	13	20	93.98
B	BB-8	C- 46	25	13	20	93.98
A	BB-8	C – 71	8	13	20	93.98
B	BB-8	C – 71	25	13	20	93.98

In order to estimate the influence of drawing speed on mechanical properties of wires with TRIP effect, described relation between tensile strength T_s, Temperature T in °C uniform elongation in total draft function for wires drawn according to variant A (V = 8 m/s), B (V = 25m/s).

For better estimation of the influence of drawing speed on properties TRIP steel wires in the work, modeling of wire drawing process (in Drawing 2D program) has been carried out. It has been estimated: temperatures, non-dilatation strain and internal stresses drawn wires. Used in program model multi passes drawing (with a few following after themselves single draft) allows to dissolve coastal task with the range of theory of temperature and tensile strength by the variation of the carbon and speed

Table 4

Schedule of draws and mean values of mechanical and technological properties of wires of steel C46. Draw speed 25m/s. and 8m/s.

V= 25m/s C 46									
L _P	φ	A _P	A _t	T _s	T	E _l	C _t	N _b	N _t
	(mm)	(%)	(%)	(MPa)	⁰ C	(%)	(%)		
1.	5.50	0.0	-	793	-	8.7	43	14	13
2.	4.91	20	20	872	99	2.6	21	13	14
3.	1.80	20	89.29	1626	239	1.8	53.4	13	28
4.	1.63	20	91.22	1705	250	1.4	52.6	11	30
5.	1.49	20	92.68	1783	261	1.6	51	11	32
6.	1.35	20	93.98	1852	274	1.7	48	10	34
V= 8m/s C 46.									

1.	5.50	0.0	-	793	-	8	44	14	13
2.	4.91	20	20	867	94	3	48	13	15
3.	1.80	20	89.29	1600	235	2	51	13	32
4.	1.63	20	91.22	1650	242	2.1	53	12	34
5.	1.49	20	92.68	1757	250	1.8	50	12	36
6.	1.35	20	93.98	1820	260	1.7	48	11	40

Table 5

Schedule of draws and mean values of mechanical and technological properties of wires of steel C71. Draw speed 25m/s. and 8m/s.

V= 25m/s C 71									
L _P	φ	A _P	A _t	T _s	T	E _l	C ₊	N _b	N _t
	(mm)	(%)	(%)	(MPa)	⁰ C	(%)	(%)		
1.	5.50	0.0	-	1038	-	8	46.8	13	12
2.	4.91	20	20	1117	114	2	19.7	12	13
3.	1.80	20	89.29	1871	253	1.8	53.5	12	26
4.	1.63	20	91.22	1950	254	1.5	51.8	11	28
5.	1.49	20	92.68	2018	264	1.6	51.4	10	30
6.	1.35	20	93.98	2097	276	1.7	47.3	9	32
V= 8m/s C 71.									

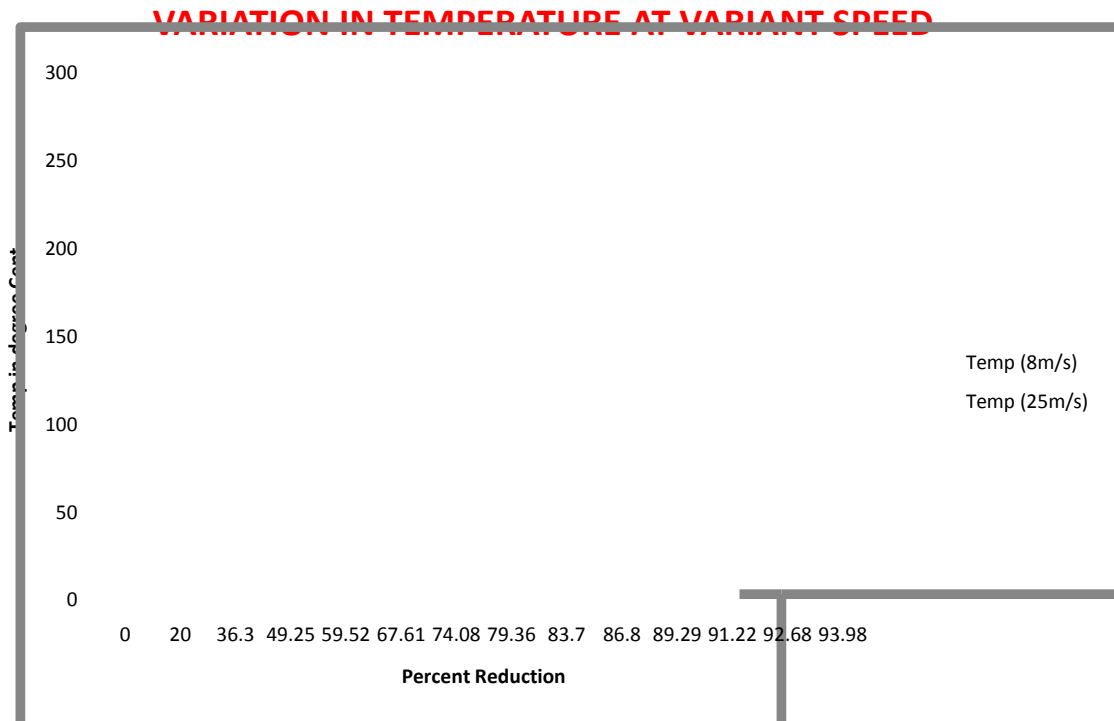
1.	5.50	0.0	-	1038	-	8.7	46.8	13	12
2.	4.91	20	20	1062	108	2.8	50.7	13	14
3.	1.80	20	89.29	1792	221	2.3	53.9	13	30
4.	1.63	20	91.22	1870	238	2.1	53.2	12	32
5.	1.49	20	92.68	1956	242	1.7	50.1	11	34
6.	1.35	20	93.98	1980	256	1.8	48.1	10	36

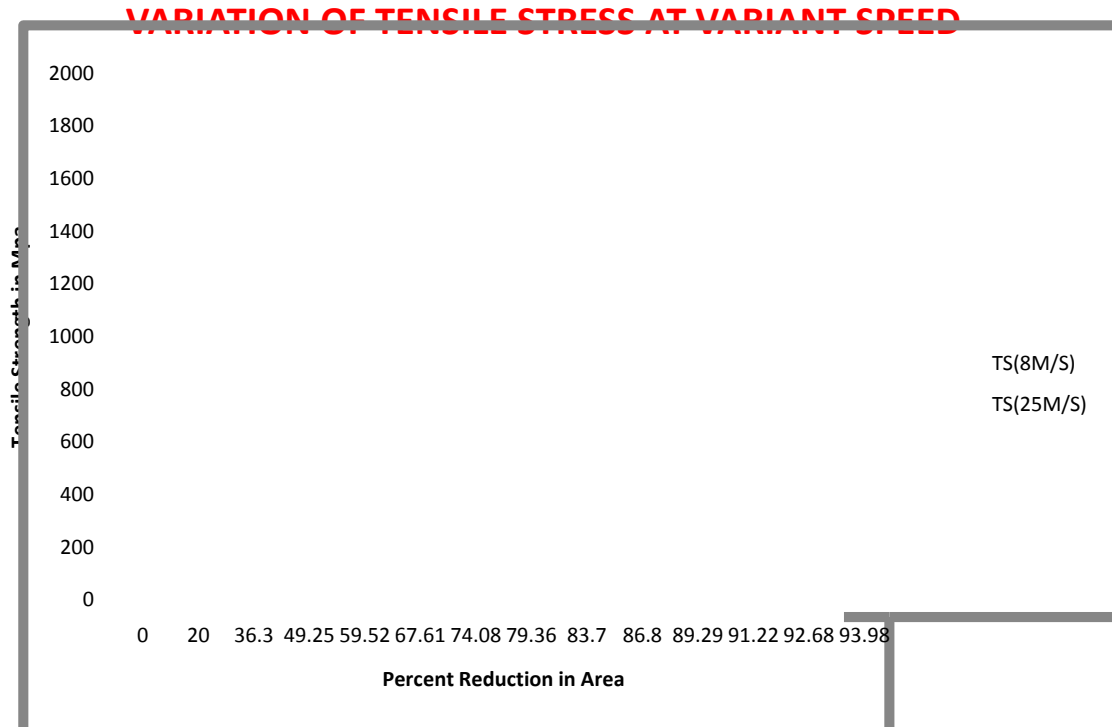
- ϕ = Wire diameter in mm
- A_p = Area reduction per pass in %
- A_t = Total area reduction in %.
- T_s = Tensile strength, MPa.
- T = Temp. rise in $^{\circ}C$ in each pass.
- E_l = Total elongation %.
- C_t = Total contraction%

RESEARCH RESULTS: WIRE PROPERTIES

The wire rod were examined at Tata steel plant for the following properties: tensile strength (T_s) in MPa, total elongation (E_l) in %, contraction (C_t), number of twists N_t , Number of bends N_b . The mean values in the table were calculated for the mechanical properties of the 1.35mm wire drawn from the 5.5mm wire rod (steel C 46) at two draw speeds (8m/s and 25m/s). Table 5 shows the same values for the wire drawn from the 5.5mm wire rod (C-71) at draw speeds (8m/s to 25m/s).

The following parameters were calculated for each draw: average temperature on the cross section of the wire (T), wire surface temperature (T_s). Table 4 shows the value of calculated parameters for all draws with a speed 8m/s for steel C46 at a speed of 25m/s. Table 5 shows the value of A , A_t , T_s , T , N_b , N_t for all draws for steel C71 at a speed of 8m/s and 25m/s in the final. The wire surface was observed with an optical microscope at the magnification of 400x.





On the base of a preliminary analysis of data from tables 1-4 and others, it has been decided that process parameters and mechanical properties of tested wires will be estimated for all initial draws, three final draws and last one. This will be helpful in precisely estimating the effect of the draw speed on the above mentioned features of the process and wires, it can be stated that value of draw stress component in the initial group of draws are independent of a draw speed(for given steel grade). Also that they increase for the final three draws and are highest for the last draw. The calculated values of this draw stress component for test wires made from steel C46 are lower than those made from steel C71. A similar relationship can be seen for the frictional component of draw stress. In general, the contribution of the friction component in a draw stress is smaller than that for a deformation one.

Regarding the effect of draw speed on temperature of a wire surface, Table 4 and 5 shows that it is similar at a slow draw speed, 8m/s, for all three groups of analyzed draws for steel C46. The result, respectively are: draws (1-10) 100 - 140⁰C, draws (11-12) 240 - 250⁰C and for last draw, 255- 260⁰C. Drawing at a speed of 25m/s for this same steel, the comparative surface temperatures are : draws (1-10) 100 - 240⁰C, draw (11-12) 260 - 265⁰C and for last draw 274 - 276⁰C. Drawing wires made from the C71 steel resulted in higher surface temperature than for all analyzed wires made from C46 steel, but also in this case for a draw speed of 8m/s the temperature goes on increasing as the carbon percentage increase for draw (1-10) the temperature rise is 10-15⁰c for draw (11-12) temperature rise is 4-8⁰c for last draw the temperature rise is 4⁰c. For a speed of 25m/sec for the considered group of draw the temperature rise for draw (1-10) is 15⁰c, for draw (11-12) temperature rise is 3-4⁰c, for last draw temperature rise is 2⁰c.

Regarding the effect of drawing speed on number of bends, Table 4 and Table 5 shows that the number of bends for draw (1-10) having same value, for draw (11-12) the number of bend decrease by 1, for last draw the number of bend decreased by 1. But as the carbon percentage increases from C46 to C71 the number of bends decreased by 1.

Regarding the effect of drawing speed on the torsion value, Table 4 and Table 5 shows that for C46 as the speed varies from 8m/sec to 25m/sec the torsion value for draw (1-5) increases by 1, for draws (6-13) increases by 2. And as the carbon increases from C46 to C71 the torsion value for draw (1-5) decreases by 1, for draw (6-13) decreases by 2.

Conclusions

1. The increase of speed from 8m/sec to 25m/sec caused the increase of tensile strength about 5-6%.
2. The increase of speed causes rise in temperature, which is required to reduce to avoid strain hardening and wire breakage.
3. The increase in speed causes to reduce number of bends by 8-10%.and also as the carbon percentage increase the number of bends goes on decreasing.
4. Higher speed decreases the number of twists observed.
5. At higher speed it is observed that the surface of the wire is smoother than at lower speed.
6. At higher speed the number of bends decreases and it again decreases by increases in the carbon percentage.

References

1. http://en.wikipedia.org/wiki/Wire_drawing
2. A.K.Lis, J. Lis, Effect of hot deformation and cooling rate on phase transformations in low carbon bainitic steel, proceeding of 11th international scientific Conference CAM3S'2005 "Contemporary Achievements in Mechanics, Manufacturing and Material Science" Gliwice – Zakopane 2005, (CD-ROM).
3. J.W. Pilaczyk, Z.Muskalski, B Golis, S. Wiewiorowska, M. Sliga, Influence of heat treatment of trip steel wire rod on structure and mechanical properties. Conference Proceedings "Global technologies for Emerging Market's", New Delhi, India 2006, 171-182.
4. M. Suliga, Z. Muskalski, the influence of single draft on mechanical-technological properties of TRIP steel wires, Metallurgist-news Metallurgist (2007) 353-356.
5. J.Adamezyk., A.Grajcar, heat treatment of TRIP- aided bainitic steel, proceeding of the 11th International scientific conference CAM3S'2005' Contemporary Achievements in Mechanics, Manufacturing and Materials Science, Gliwiczakopane2005(CD-ROM).
6. A.K. Lis, B.Gajda, Modeling of the DP and trip microstructure in the CMnAlSi automotive steel, Proceeding of the 11th International scientific conference CAM3S'2005 "Contemporary achievements in mechanics, manufacturing and the material science", Gliwice-Zakopane 2005, (CD-ROM).
7. A. Grajcar, Effect of hot working in the $\gamma + \alpha$ range on a retained austenite fraction in TRIP- aided steel, journal of Achievements in Materials and Manufacturing Engineering 22/2 (2007) 79-82.
8. A. Gajda, A.K. Lis, Thermal processing of CMnAlSi steel at ($\gamma+\alpha$) temperature range, Journal of Achievements in Materials and Manufacturing Engineering 18(2006) 355-358.
9. P.J. Jacaues, A. Petein, P. Harlet, Improvement of mechanical properties through concurrent deformation and transformation: Newsteels for the 21st century, TRIP – International Conference on TRIP aided high strength Ferrous alloys, GRIPS- Proceeding, Ghent (2002) 281-286.

Multiphase Bidirectional Flyback Converter Topology for Induction Motor Drive

CH KRISHNA PRASAD

M-Tech Scholar, Power Electronics,
Department Of Electrical And Electronics Engineering
Koneru Lakshmaiah University, Guntur (A.P), India.

K.P PRASAD RAO

M.Tech. in Power Electronics & power System,
Asst. Professor, Department of EEE
Koneru Lakshmaiah University, Guntur (A.P), India.

Abstract—For hybrid electric vehicles, the batteries and the drive dc link may be at different voltages. The batteries are at low voltage to obtain higher volumetric efficiencies, and the dc link is at higher voltage to have higher efficiency on the motor side. Therefore, a power interface between the batteries and the drive's dc link is essential. This power interface should handle power flow from battery to motor, motor to battery, external genset to battery, and grid to battery. This paper proposes a multi-power-port topology which is capable of handling multiple power sources and still maintains simplicity and features like obtaining high gain, wide load variations, lower output-current ripple, and capability of parallel-battery energy due to the modular structure. The scheme incorporates a transformer winding technique which drastically reduces the leakage inductance of the coupled inductor. Finally the proposed converter is applied to a induction motor drive. Matlab/Simulink software and simulation results are presented.

Index Terms- Bidirectional flyback converter, hybrid electric vehicle, leakage inductance, Induction Motor Drive.

I. INTRODUCTION

Power electronics is an enabling technology for the development of electric or hybrid electric vehicles. For both ac and dc motor drives used in electric and hybrid electric vehicles, the basic requirement for efficient control is that the power electronic circuit should be capable of handling bidirectional power flow, i.e., energy transfer should be possible from battery to motor during motoring mode and motor to battery during regeneration. Now, the need for a bidirectional power converter should be properly examined. A battery can be used as a dc bus if the motor is rated for that voltage level. Thus, bidirectional power flow is not a problem because of the bidirectional power-handling capacity of a standard two-level three-phase inverter and also sinking and sourcing capacity of the battery. However, the traction motor should be rated for higher voltage to achieve higher efficiency for a given power rating. Therefore, the dc bus voltage should be maintained high enough to match the motor voltage rating in series. However, if too many batteries are connected in series, then the volumetric efficiency of the battery comes down. Therefore, there is a need for a bidirectional converter which interfaces the low-voltage battery with a high voltage dc bus and maintains a bidirectional power flow.

Reference [2] shows the use of a bidirectional converter for a permanent-magnet ac motor- driven electric vehicle. Reference [3] shows the use of a cascaded bidirectional buck–boost converter for the use in dc-motor-driven electric vehicle. Both schemes emphasize the importance of bidirectional dc–dc converter for electric vehicle application. The dc–dc converters can be divided into hardswitching converters and soft-switching converters. Because of the low efficiency of hard-switching converters, recently, soft-switching techniques are getting popular. Reference [4] proposes ZVS techniques for different nonisolated dc–dc converters. There is a limit on the voltage gain that can be achieved using a buck–boost or a boost converter. It is not desirable to operate the boost or the buck–boost converter at very high duty ratio because of very high capacitor current ripple. Thus, the solution is to go for isolated topologies for getting the high voltage gain in between the battery and the dc bus.

Reference [6-10] proposes a coupled-inductor winding technique which reduces the leakage inductance to a very less value and without the use of any snubber, and that very less voltage spike be achieved during switching transients. Next, the paralleling of four batteries is done using a four-phase flyback topology, and outputs of all the four phases are connected to the same dc link. To reduce the current ripple through the dc-link capacitor, all the four phases are switched at a fixed 75% duty cycle with 90° (considering one switching period as 360°) phase difference between subsequent phases. This configuration is also suitable for connecting multiple power sources. For battery charging from mains, a front-end converter is used which uses the same dc bus. Thus, the same flyback converter is used for battery charging. For series–parallel hybrid electric vehicles, the output of the synchronous generator can be connected to the same dc bus through a rectifier.

II. FOUR PHASE BIDIRECTION FLYBACK CONVERTER

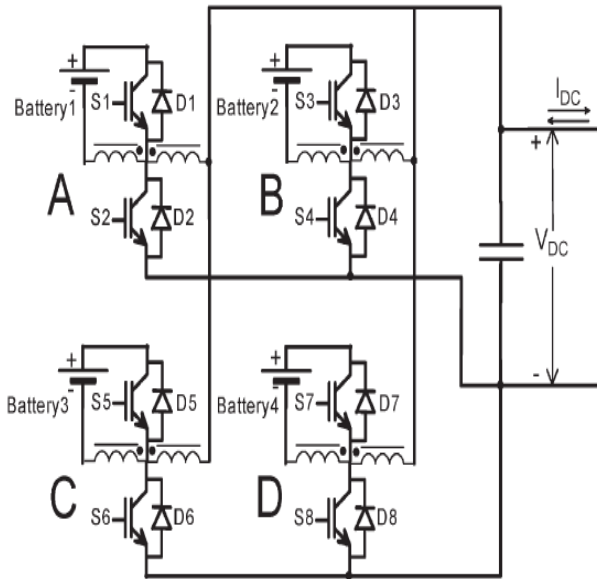


Figure-1 Fly Back Converter

If we consider the first converter, then, during forward power flow, S1 and D2 are active, and during reverse power flow, S2 and D1 are active as well. During forward power flow, active switches S1, S3, S5, and S7 get switching pulses of 75% duty cycle with 90° phase difference between subsequent phases, as shown in Fig. 2(a). During reverse power flow, active switches S2, S4, S6, and S8 get switching pulses of 25% duty cycle which are 90° phase shifted to each other, as shown in Fig. 2(b). Fig. 2(c) and (d) shows the ideal switch voltage and current waveforms assuming continuous conduction mode (CCM) for forward and reverse power flows, respectively.

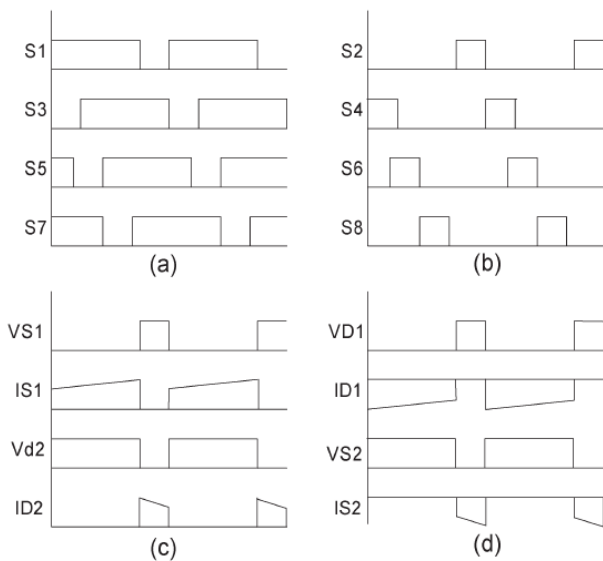


Figure-2 Gating Pulses

CCM is not the only conduction mode for this bidirectional converter. This can also operate in critical conduction mode (CRM) or discontinuous conduction mode (DCM), depending on the load. During forward power flow, if the load is very less, then the converter can go into CRM or DCM, similar to any standard flyback converter. However, for circuit design, only CCM is considered. As no snubber is used, circuit design involves the design of the inductor and the capacitor. The load connected at the output of the converter is a three-phase inverter connected to the motor. Thus, the capacitor voltage ripple is dominated by the dc-link current ripple of the inverter, and capacitor value is decided depending on that ripple.

III. CONTROL SCHEME

Simple hysteresis voltage control is used for dc-link voltage regulation for power management in the proposed MPP scheme. During power flow in the forward direction, i.e., from the battery to the dc bus, the duty cycles of switching voltages of S1, S3, S5, and S7 are fixed at 75%, while switches S2, S4, S6, and S8 are permanently off. During reverse power flow, S1, S3, S5, and S7 are permanently off, and S2, S4, S6, and S8 are switched at 25% duty cycle. Therefore, during forward power flow, the voltage is boosted by a factor of three, and during reverse power flow, the voltage is stepped down by a factor of three. It is to be noted that this voltage boost is only due to duty-cycle operation. The coupled-inductor turns ratio is fixed in such a way that during full-load operation in forward mode, the converter output voltage is the rated dc bus voltage V_{dc} . For an operating condition with lesser load, the series voltage drop in the converter will be less. Thus, the dc-link voltage will get increased from the rated value because of fixed duty cycle of operation. At a voltage $V_{dc} + \nu_1$, the pulses to switches S1, S3, S5, and S7 are stopped. If the load is still drawing current, then it will discharge the capacitor. When the voltage reaches V_{dc} , again, the switching pulses are given to S1, S3, S5, and S7. Therefore, during light-load conditions, the voltage is maintained between V_{dc} and $V_{dc} + \nu_1$. If there is no load, then the voltage will also be maintained in between V_{dc} and $V_{dc} + \nu_1$. However, during regeneration, even if switches S1, S3, S5, and S7 are off, because of reverse power flow, the voltage will increase beyond $V_{dc} + \nu_1$. This is the time when energy should flow back to the battery. Thus, at a voltage $V_{dc} + \nu_1 + \nu_2$, switches S2, S4, S6, and S8 are pulsed, and because of the flyback action, current flows into the battery, and the battery gets charged.

IV. MATLAB/SIMULINK MODEL AND SIMULATION RESULTS

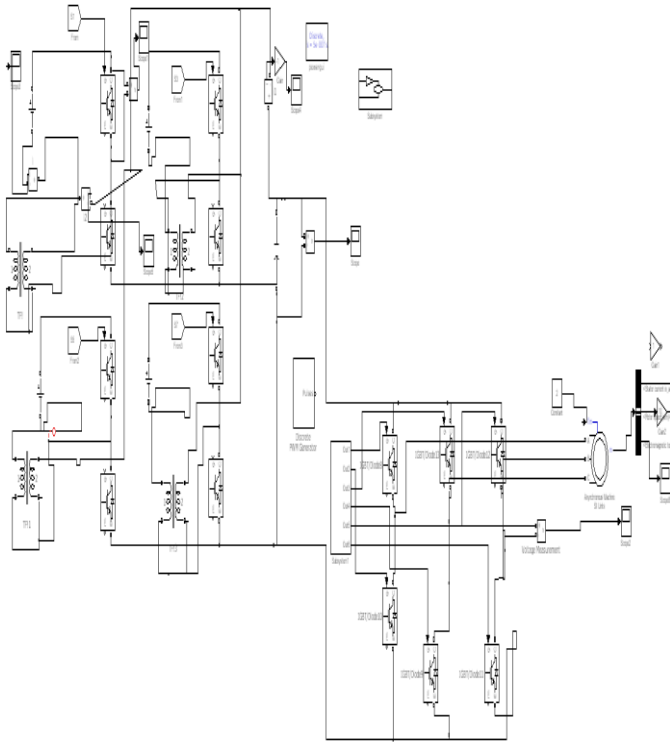


Figure-3 Fly Back Converter with Induction Motor Drive

Fig. 3 shows the Matlab/Simulink model of proposed flyback converter with induction motor drive. Here the motor is supplied with pwm inverter.

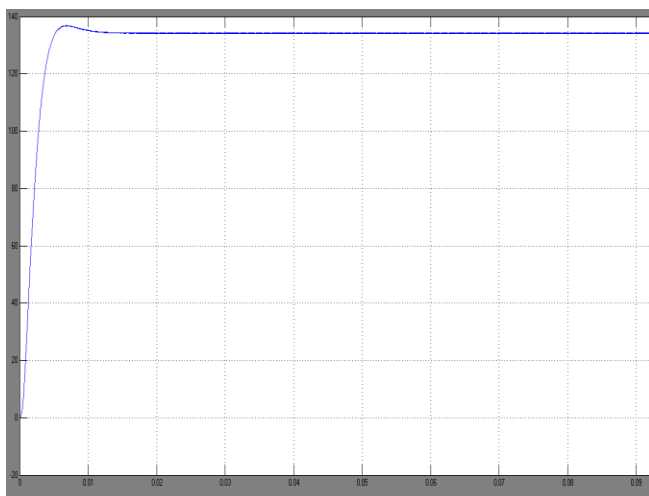


Figure-4 Fly Back Converter DC output voltage

Fig.4 shows the DC output voltage of flyback converter. Here output voltage is 400 v.

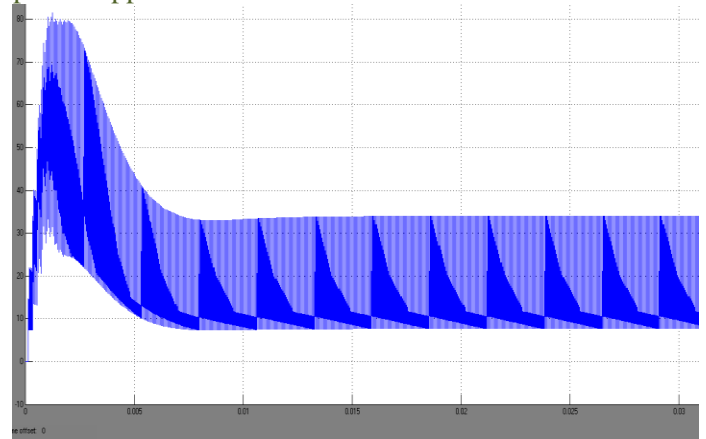


Figure-5 Coupled Inductor current

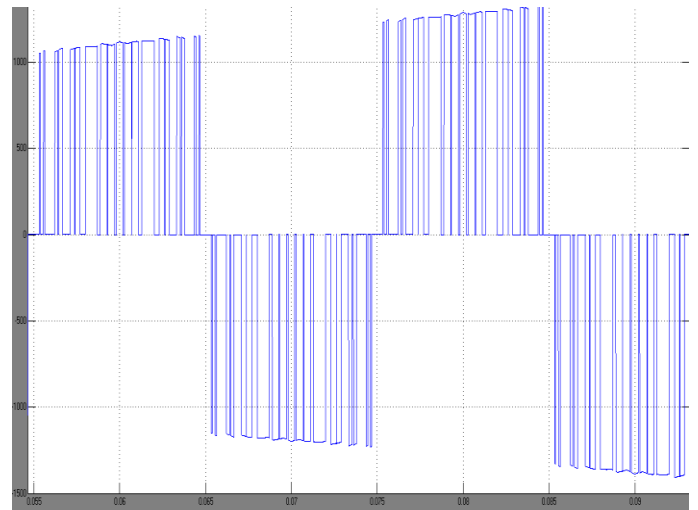


Figure-6 PWM Inverter output

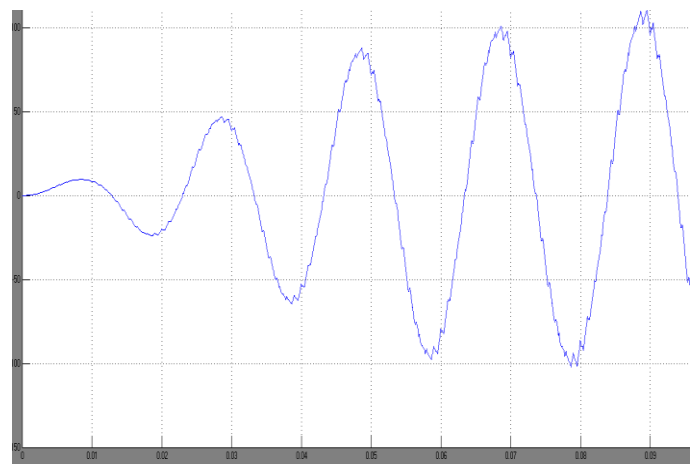


Figure-7 Induction Motor Stator current

Fig 5 shows the coupled inductor current. Fig 6 shows the PWM ac output of the inverter. Fig 7 shows the induction motor stator current.

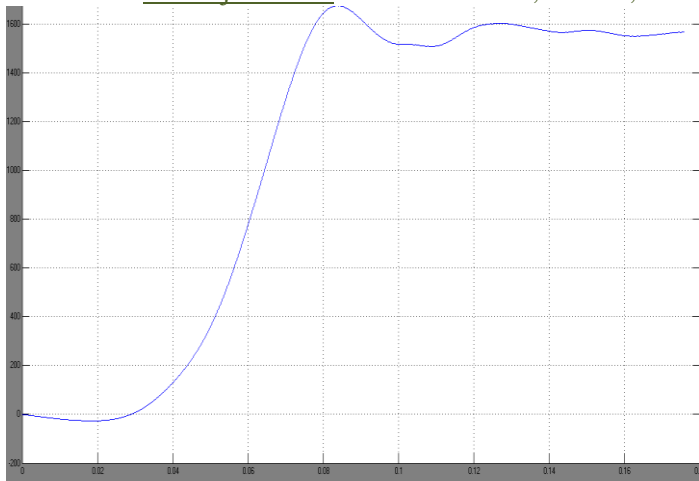


Figure-9 Induction motor speed

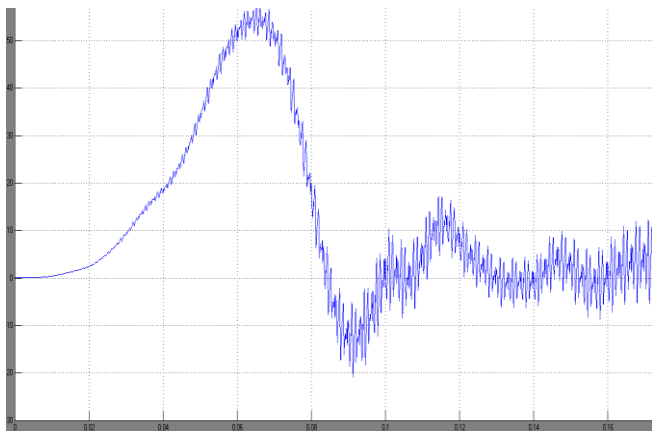


Figure-8 Induction Motor Torque

Fig.9 and 10 shows the induction motor speed and torque performance respectively. Here the motor is reaching a steady state speed of 1500 rpm.

V.CONCLUSION

This paper proposes a four-phase bidirectional flyback dc-dc converter which serves the role of an MPP interface for electric and hybrid electric vehicle applications. The bidirectional nature of the converter allows battery charging during regeneration and also from mains. The multiple phases give the flexibility of paralleling multiple batteries. Simple hysteresis control is used for converter control. Because of the four converters operating with 90° phase shift with fixed 75% duty cycle of operation, the capacitor ripple current is also reduced. The novel transformer design technique drastically reduces the leakage inductance and eliminates the requirement of snubber. Furthermore, it should be noted that the MPP interface could be made between any given battery voltage and dc-link voltage by only tuning the turnsratio of the flyback transformers. A SIMULINK based model is developed and Simulation results are presented.

VI.References

- [1] A. Emadi, Y. J. Lee, and K. Rajashekara, "Power electronics and motor drives in electric, hybrid electric, and plug-in hybrid electric vehicles," *IEEE Trans. Ind. Electron.*, vol. 55, no. 6, pp. 2237–2245, Jun. 2008.
- [2] F. Caricchi, F. Crescimbin, G. Noia, and D. Pirolo, "Experimental study of a bidirectional DC-DC converter for the DC link voltage control and the regenerative braking in PM motor drives devoted to electrical vehicles," in *Proc. IEEE APEC*, Orlando, FL, Feb. 1994, vol. 1, pp. 381–386.
- [3] F. Caricchi, F. Crescimbin, F. G. Capponi, and L. Solero, "Study of bi-directional buck-boost converter topologies for application in electrical vehicle motor drives," in *Proc. IEEE APEC*, Feb. 1998, vol. 1, pp. 287–293.
- [4] C.-M. Wang, "Novel zero-voltage-transition PWM DC-DC converters," *IEEE Trans. Ind. Electron.*, vol. 53, no. 1, pp. 254–262, Feb. 2006.
- [5] B.-R. Lin and F.-Y. Hsieh, "Soft-switching zeta-flyback converter with a buck-boost type of active clamp," *IEEE Trans. Ind. Electron.*, vol. 54, no. 5, pp. 2813–2822, Oct. 2007.
- [6] F. Z. Peng, H. Li, G.-J. Su, and J. S. Lawler, "A new ZVS bidirectional DC-DC converter for fuel cell and battery application," *IEEE Trans. Power Electron.*, vol. 19, no. 1, pp. 54–65, Jan. 2004.
- [7] H. S.-H. Chung, W.-L. Cheung, and K. S. Tang, "A ZCS bidirectional flyback DC/DC converter," *IEEE Trans. Power Electron.*, vol. 19, no. 6, pp. 1426–2434, Nov. 2004.
- [8] O. Garcia, P. Zumel, A. de Castro, and J. A. Cobos, "Automotive DC-DC bidirectional converter made with many interleaved buck stages," *IEEE Trans. Power Electron.*, vol. 21, no. 6, pp. 578–586, May 2006.
- [9] L. Solero, A. Lidozzi, and J. A. Pomilio, "Design of multiple-input power converter for hybrid vehicles," in *Proc. IEEE APEC*, vol. 2, pp. 1145–1151.
- [10] M. Michon, J. L. Duarte, and M. Hendrix, "A three port bi-directional converter for hybrid fuel cell systems," in *Proc. IEEE PESC*, Aachen, Germany, Jun. 2004, pp. 4736–4742.

A STUDY ON SOME OPERATIONS OF FUZZY SOFT SETS

Manoj Borah¹, Tridiv Jyoti Neog², Dusmanta Kumar Sut³

¹Deptt. of Mathematics, Jorhat Institute of Science & Technology, Jorhat, Assam, India

²Deptt. of Mathematics, D.K. High School, Jorhat,

³Deptt. of Mathematics, N.N.Saikia College, Titabor, Assam, India

ABSTRACT

The purpose of this paper is to study some operations and results available in the literature of fuzzy soft sets. Instead of taking the notion of complement of a fuzzy soft set put forward by Maji, throughout our work, we have taken the notion of complement of a fuzzy soft set put forward by Neog and Sut.

Keywords – Fuzzy Set, Soft Set, Fuzzy Soft Set.

1. INTRODUCTION

In many complicated problems arising in the fields of engineering, social science, economics, medical science etc involving uncertainties, classical methods are found to be inadequate in recent times. Molodtsov [2] pointed out that the important existing theories viz. Probability Theory, Fuzzy Set Theory, Intuitionistic Fuzzy Set Theory, Rough Set Theory etc. which can be considered as mathematical tools for dealing with uncertainties, have their own difficulties. He further pointed out that the reason for these difficulties is, possibly, the inadequacy of the parameterization tool of the theory. In 1999 he initiated the novel concept of Soft Set as a new mathematical tool for dealing with uncertainties. Soft Set Theory, initiated by Molodtsov [2], is free of the difficulties present in these theories. In 2011, Neog and Sut [9] put forward a new notion of complement of a soft set and accordingly some important results have been studied in their work.

In recent times, researches have contributed a lot towards fuzzification of Soft Set Theory. Maji et al. [6] introduced the concept of Fuzzy Soft Set and some properties regarding fuzzy soft union, intersection, complement of a fuzzy soft set, De Morgan Law etc. These results were further revised and improved by Ahmad and Kharal [1]. Recently, Neog and Sut [8] have studied the notions of fuzzy soft union, fuzzy soft intersection, complement of a fuzzy soft set and several other properties of fuzzy soft sets along with examples and proofs of certain results.

In this paper, we have studied some operations and results available in the literature of fuzzy soft sets. Instead of taking the notion of complement of a fuzzy soft set put forward by Maji et al. [6], throughout our work, we have taken the notion of complement of a fuzzy soft set put forward by Neog and Sut [7].

2. PRELIMINARIES

In this section, we first recall the basic definitions related to soft sets and fuzzy soft sets which would be used in the sequel.

2.1. Soft Set [2]

A pair (F, E) is called a soft set (over U) if and only if F is a mapping of E into the set of all subsets of the set U .

In other words, the soft set is a parameterized family of subsets of the set U . Every set $F(\varepsilon), \varepsilon \in E$, from this family may be considered as the set of ε -elements of the soft set (F, E) , or as the set of ε -approximate elements of the soft set.

2.2. Soft Null Set [5]

A soft set (F, A) over U is said to be null soft set denoted by $\tilde{\varphi}$ if $\forall \varepsilon \in A, F(\varepsilon) = \varphi$ (Null set)

2.3. Soft Absolute Set [5]

A soft set (F, A) over U is said to be absolute soft set denoted by \tilde{A} if $\forall \varepsilon \in A, F(\varepsilon) = U$.

2.4. Soft Subset [5]

For two soft sets (F, A) and (G, B) over the universe U , we say that (F, A) is a soft subset of (G, B) , if

(i) $A \subseteq B$,

(ii) $\forall \varepsilon \in A, F(\varepsilon)$ and $G(\varepsilon)$ are identical approximations and is written as $(F, A) \subseteq (G, B)$.

Pei and Miao [4] modified this definition of soft subset in the following way –

2.5. Soft Subset Redefined [4]

For two soft sets (F, A) and (G, B) over the universe U , we say that (F, A) is a soft subset of (G, B) , if

(i) $A \subseteq B$,

(ii) $\forall \varepsilon \in A, F(\varepsilon) \subseteq G(\varepsilon)$ and is written as

$(F, A) \subseteq (G, B)$.

(F, A) is said to be soft superset of (G, B) if (G, B) is a soft subset of (F, A) and we write $(F, A) \supseteq (G, B)$.

2.6. Union of Soft Sets [5]

Union of two soft sets (F, A) and (G, B) over a common universe U , is the soft set (H, C) , where $C = A \cup B$ and $\forall \varepsilon \in C$,

$$H(\varepsilon) = \begin{cases} F(\varepsilon), & \text{if } \varepsilon \in A - B \\ G(\varepsilon), & \text{if } \varepsilon \in B - A \\ F(\varepsilon) \cup G(\varepsilon), & \text{if } \varepsilon \in A \cap B \end{cases}$$

and is written as $(F, A) \cup (G, B) = (H, C)$.

2.7. Intersection of Soft Sets [5]

Intersection of two soft sets (F, A) and (G, B) over a common universe U , is the soft set (H, C) , where $C = A \cap B$ and $\forall \varepsilon \in C, H(\varepsilon) = F(\varepsilon) \cap G(\varepsilon)$ (as both are same set) and is written as $(F, A) \tilde{\cap} (G, B) = (H, C)$.

Pei and Miao [4] pointed out that generally $F(\varepsilon)$ or $G(\varepsilon)$ may not be identical. Moreover in order to avoid the degenerate case, Ahmad and Kharal [1] proposed that $A \cap B$ must be non-empty and thus revised the above definition as follows.

2.8. Intersection of Soft Sets Redefined [1]

Let (F, A) and (G, B) be two soft sets over a common universe U with $A \cap B \neq \emptyset$. Then Intersection of two soft sets (F, A) and (G, B) is a soft set (H, C) where $C = A \cap B$ and $\forall \varepsilon \in C, H(\varepsilon) = F(\varepsilon) \cap G(\varepsilon)$.

We write $(F, A) \tilde{\cap} (G, B) = (H, C)$.

2.9. AND Operation of Soft Sets [5]

If (F, A) and (G, B) be two soft sets, then “ (F, A) AND (G, B) ” is a soft set denoted by $(F, A) \wedge (G, B)$ and is defined by $(F, A) \wedge (G, B) = (H, A \times B)$, where

$H(\alpha, \beta) = F(\alpha) \cap G(\beta), \forall \alpha \in A$ and $\forall \beta \in B$, where \cap is the operation intersection of two sets.

2.10. OR Operation of Soft Sets [5]

If (F, A) and (G, B) be two soft sets, then “ (F, A) OR (G, B) ” is a soft set denoted by $(F, A) \vee (G, B)$ and is defined by $(F, A) \vee (G, B) = (K, A \times B)$, where

$K(\alpha, \beta) = F(\alpha) \cup G(\beta), \forall \alpha \in A$ and $\forall \beta \in B$, where \cup is the operation union of two sets.

2.11. Complement of a Soft Set [9]

The complement of a soft set (F, A) is denoted by $(F, A)^c$ and is defined by $(F, A)^c = (F^c, A)$, where $F^c: A \rightarrow P(U)$ is a mapping given by $F^c(\varepsilon) = [F(\varepsilon)]^c$ for all $\varepsilon \in A$.

2.12. Fuzzy Soft Set [6]

A pair (F, A) is called a fuzzy soft set over U where $F: A \rightarrow \tilde{P}(U)$ is a mapping from A into $\tilde{P}(U)$.

2.13. Fuzzy Soft Class [1]

Let U be a universe and E a set of attributes. Then the pair (U, E) denotes the collection of all fuzzy soft sets on U with attributes from E and is called a fuzzy soft class.

2.14. Fuzzy Soft Null Set [6]

A soft set (F, A) over U is said to be null fuzzy soft set denoted by \emptyset if $\forall \varepsilon \in A, F(\varepsilon)$ is the null fuzzy set $\bar{0}$ of U where $\bar{0}(x) = 0 \forall x \in U$.

2.15. Fuzzy Soft Absolute Set [6]

A soft set (F, A) over U is said to be absolute fuzzy soft set denoted by $\tilde{1}$ if $\forall \varepsilon \in A, F(\varepsilon)$ is the absolute fuzzy set $\bar{1}$ of U where $\bar{1}(x) = 1 \forall x \in U$.

2.16. Fuzzy Soft Subset [6]

For two fuzzy soft sets (F, A) and (G, B) in a fuzzy soft class (U, E) , we say that (F, A) is a fuzzy soft subset of (G, B) , if

- (i) $A \subseteq B$
(ii) For all $\varepsilon \in A, F(\varepsilon) \subseteq G(\varepsilon)$ and is written as $(F, A) \subseteq (G, B)$.

2.17. Union of Fuzzy Soft Sets [6]

Union of two fuzzy soft sets (F, A) and (G, B) in a soft class (U, E) is a fuzzy soft set (H, C) where $C = A \cup B$ and $\forall \varepsilon \in C,$

$$H(\varepsilon) = \begin{cases} F(\varepsilon), & \text{if } \varepsilon \in A - B \\ G(\varepsilon), & \text{if } \varepsilon \in B - A \\ F(\varepsilon) \cup G(\varepsilon), & \text{if } \varepsilon \in A \cap B \end{cases}$$

And is written as $(F, A) \tilde{\cup} (G, B) = (H, C)$.

2.18. Intersection of Fuzzy Soft Sets [6]

Intersection of two fuzzy soft sets (F, A) and (G, B) in a soft class (U, E) is a fuzzy soft set (H, C) where $C = A \cap B$ and $\forall \varepsilon \in C, H(\varepsilon) = F(\varepsilon) \cap G(\varepsilon)$ (as both are same fuzzy set) and is written as $(F, A) \tilde{\cap} (G, B) = (H, C)$.

Ahmad and Kharal [1] pointed out that generally $F(\varepsilon)$ or $G(\varepsilon)$ may not be identical. Moreover in order to avoid the degenerate case, he proposed that $A \cap B$ must be non-empty and thus revised the above definition as follows -

2.19. Intersection of Fuzzy Soft Sets Redefined [1]

Let (F, A) and (G, B) be two fuzzy soft sets in a soft class (U, E) with $A \cap B \neq \emptyset$. Then Intersection of two fuzzy soft sets (F, A) and (G, B) in a soft class (U, E) is a fuzzy soft set (H, C) where $C = A \cap B$ and $\forall \varepsilon \in C, H(\varepsilon) = F(\varepsilon) \cap G(\varepsilon)$. We write $(F, A) \tilde{\cap} (G, B) = (H, C)$.

2.20. Complement of a Fuzzy Soft Set [7]

The complement of a fuzzy soft set (F, A) is denoted by $(F, A)^c$ and is defined by $(F, A)^c = (F^c, A)$ where $F^c: A \rightarrow \tilde{P}(U)$ is a mapping given by $F^c(\alpha) = [F(\alpha)]^c, \forall \alpha \in A$.

2.21. AND Operation of Fuzzy Soft Sets [6]

If (F, A) and (G, B) be two fuzzy soft sets, then “ (F, A) AND (G, B) ” is a fuzzy soft set denoted by $(F, A) \wedge (G, B)$ and is defined by $(F, A) \wedge (G, B) = (H, A \times B)$, where

$H(\alpha, \beta) = F(\alpha) \cap G(\beta), \forall \alpha \in A$ and $\forall \beta \in B$, where \cap is the operation intersection of two fuzzy sets.

2.22. OR Operation of Soft Sets [6]

If (F, A) and (G, B) be two fuzzy soft sets, then “ (F, A) OR (G, B) ” is a fuzzy soft set denoted by $(F, A) \vee (G, B)$ and is defined by $(F, A) \vee (G, B) = (K, A \times B)$, where

$K(\alpha, \beta) = F(\alpha) \cup G(\beta), \forall \alpha \in A$ and $\forall \beta \in B$, where \cup is the operation union of two fuzzy sets.

3. A STUDY ON THE OPERATIONS IN FUZZY SOFT SETS

In this section, we shall endeavour to study the basic operations and results available in the literature of fuzzy soft sets. Ahmad and Kharal [1] has pointed out that the null (resp., absolute) fuzzy soft set as defined by Maji et al. [6], is not unique in a fuzzy soft class (U, E) , rather it depends upon $A \subseteq E$. As such whenever we would refer to a fuzzy soft null set or fuzzy soft absolute set, we would refer to the set $A \subseteq E$ of parameters under consideration. In case of soft sets, this has already been pointed out by Ge and Yang in [10] and accordingly they have studied some basic results regarding soft sets. Here, we put forward some results of fuzzy soft sets in our way. We are using the notation (φ, A) to represent the fuzzy soft null set with respect to the set of parameters A and the notation (U, A) to represent the fuzzy soft absolute set with respect to the set of parameters A .

3.1. Proposition

$$1. (\varphi, A)^c = (U, A)$$

Proof. Let $(\varphi, A) = (F, A)$

Then $\forall \varepsilon \in A$,

$$\begin{aligned} F(\varepsilon) &= \{x, \mu_{F(\varepsilon)}(x) : x \in U\} \\ &= \{(x, 0) : x \in U\} \end{aligned}$$

$$(\varphi, A)^c = (F, A)^c = (F^c, A), \text{ where}$$

$$\begin{aligned} \forall \varepsilon \in A, F^c(\varepsilon) &= (F(\varepsilon))^c \\ &= \{x, \mu_{F(\varepsilon)}(x) : x \in U\}^c \\ &= \{x, 1 - \mu_{F(\varepsilon)}(x) : x \in U\} \\ &= \{(x, 1 - 0) : x \in U\} \\ &= \{(x, 1) : x \in U\} \\ &= U \end{aligned}$$

$$\text{Thus } (\varphi, A)^c = (U, A)$$

$$2. (U, A)^c = (\varphi, A)$$

Proof. Let $(U, A) = (F, A)$

Then $\forall \varepsilon \in A$,

$$\begin{aligned} F(\varepsilon) &= \{x, \mu_{F(\varepsilon)}(x) : x \in U\} \\ &= \{(x, 1) : x \in U\} \end{aligned}$$

$$(U, A)^c = (F, A)^c = (F^c, A), \text{ where}$$

$$\forall \varepsilon \in A, F^c(\varepsilon) = (F(\varepsilon))^c$$

$$\begin{aligned} &= \{x, \mu_{F(\varepsilon)}(x) : x \in U\}^c \\ &= \{x, 1 - \mu_{F(\varepsilon)}(x) : x \in U\} \\ &= \{(x, 1 - 1) : x \in U\} \\ &= \{(x, 0) : x \in U\} \\ &= \varphi \end{aligned}$$

$$\text{Thus } (U, A)^c = (\varphi, A)$$

$$3. (F, A) \tilde{\cap} (\varphi, A) = (F, A)$$

Proof. We have

$$\begin{aligned} (F, A) &= \{\varepsilon, (x, \mu_{F(\varepsilon)}(x)) : x \in U\} \quad \forall \varepsilon \in A \\ (\varphi, A) &= \{\varepsilon, (x, 0) : x \in U\} \quad \forall \varepsilon \in A \\ (F, A) \tilde{\cap} (\varphi, A) &= \{\varepsilon, (x, \max(\mu_{F(\varepsilon)}(x), 0)) : x \in U\} \quad \forall \varepsilon \in A \\ &= \{\varepsilon, (x, \mu_{F(\varepsilon)}(x)) : x \in U\} \quad \forall \varepsilon \in A \\ &= (F, A) \end{aligned}$$

$$\text{Thus } (F, A) \tilde{\cap} (\varphi, A) = (F, A)$$

$$4. (F, A) \tilde{\cap} (U, A) = (U, A)$$

Proof. We have

$$\begin{aligned} (F, A) &= \{\varepsilon, (x, \mu_{F(\varepsilon)}(x)) : x \in U\} \quad \forall \varepsilon \in A \\ (U, A) &= \{\varepsilon, (x, 1) : x \in U\} \quad \forall \varepsilon \in A \\ (F, A) \tilde{\cap} (U, A) &= \{\varepsilon, (x, \max(\mu_{F(\varepsilon)}(x), 1)) : x \in U\} \quad \forall \varepsilon \in A \\ &= \{\varepsilon, (x, 1) : x \in U\} \quad \forall \varepsilon \in A \\ &= (U, A) \end{aligned}$$

$$\text{Thus } (F, A) \tilde{\cap} (U, A) = (U, A)$$

$$5. (F, A) \tilde{\cap} (\varphi, A) = (\varphi, A)$$

Proof. We have

$$\begin{aligned} (F, A) &= \{\varepsilon, (x, \mu_{F(\varepsilon)}(x)) : x \in U\} \quad \forall \varepsilon \in A \\ (\varphi, A) &= \{\varepsilon, (x, 0) : x \in U\} \quad \forall \varepsilon \in A \\ (F, A) \tilde{\cap} (\varphi, A) &= \{\varepsilon, (x, \min(\mu_{F(\varepsilon)}(x), 0)) : x \in U\} \quad \forall \varepsilon \in A \\ &= \{\varepsilon, (x, 0) : x \in U\} \quad \forall \varepsilon \in A \\ &= (\varphi, A) \end{aligned}$$

$$\text{Thus } (F, A) \tilde{\cap} (\varphi, A) = (\varphi, A)$$

$$6. (F, A) \tilde{\cap} (U, A) = (F, A)$$

Proof. We have

$$\begin{aligned} (F, A) &= \{\varepsilon, (x, \mu_{F(\varepsilon)}(x)) : x \in U\} \quad \forall \varepsilon \in A \\ (U, A) &= \{\varepsilon, (x, 1) : x \in U\} \quad \forall \varepsilon \in A \end{aligned}$$

$$\begin{aligned} (F, A) \tilde{\cap} (U, A) &= \{ \{ \varepsilon, (x, \min(\mu_{F(\varepsilon)}(x), 1)) \} : x \in U \} \quad \forall \varepsilon \in A \\ &= \{ \{ \varepsilon, (x, \mu_{F(\varepsilon)}(x)) \} : x \in U \} \quad \forall \varepsilon \in A \\ &= (F, A) \end{aligned}$$

Thus $(F, A) \tilde{\cap} (U, A) = (F, A)$

7. $(F, A) \tilde{\cap} (\varphi, B) = (F, A)$ if and only if $B \subseteq A$

Proof.

We have for (F, A)

$$F(\varepsilon) = \{ \{ x, \mu_{F(\varepsilon)}(x) \} : x \in U \} \quad \forall \varepsilon \in A$$

Also, let $(\varphi, B) = (G, B)$, Then

$$G(\varepsilon) = \{ \{ x, 0 \} : x \in U \} \quad \forall \varepsilon \in B$$

Let $(F, A) \tilde{\cap} (\varphi, B) = (F, A) \tilde{\cap} (G, B) = (H, C)$, where

$C = A \cup B$ and $\forall \varepsilon \in C$,

$H(\varepsilon)$

$$\begin{aligned} &= \begin{cases} \{ \{ x, \mu_{F(\varepsilon)}(x) \} : x \in U \}, & \text{if } \varepsilon \in A - B \\ \{ \{ x, \mu_{G(\varepsilon)}(x) \} : x \in U \}, & \text{if } \varepsilon \in B - A \\ \{ \{ x, \max(\mu_{F(\varepsilon)}(x), \mu_{G(\varepsilon)}(x)) \} : x \in U \}, & \text{if } \varepsilon \in A \cap B \end{cases} \\ &= \begin{cases} \{ \{ x, \mu_{F(\varepsilon)}(x) \} : x \in U \}, & \text{if } \varepsilon \in A - B \\ \{ \{ x, 0 \} : x \in U \}, & \text{if } \varepsilon \in B - A \\ \{ \{ x, \max(\mu_{F(\varepsilon)}(x), 0) \} : x \in U \}, & \text{if } \varepsilon \in A \cap B \end{cases} \\ &= \begin{cases} \{ \{ x, \mu_{F(\varepsilon)}(x) \} : x \in U \}, & \text{if } \varepsilon \in A - B \\ \{ \{ x, 0 \} : x \in U \}, & \text{if } \varepsilon \in B - A \\ \{ \{ x, \mu_{F(\varepsilon)}(x) \} : x \in U \}, & \text{if } \varepsilon \in A \cap B \end{cases} \end{aligned}$$

Let $B \subseteq A$

Then

$$\begin{aligned} H(\varepsilon) &= \begin{cases} \{ \{ x, \mu_{F(\varepsilon)}(x) \} : x \in U \}, & \text{if } \varepsilon \in A - B \\ \{ \{ x, \mu_{F(\varepsilon)}(x) \} : x \in U \}, & \text{if } \varepsilon \in A \cap B \end{cases} \\ &= F(\varepsilon) \quad \forall \varepsilon \in A \end{aligned}$$

Conversely, let $(F, A) \tilde{\cap} (\varphi, B) = (F, A)$

Then $A = A \cup B \Rightarrow B \subseteq A$

8. $(F, A) \tilde{\cap} (U, B) = (U, B)$ if and only if $A \subseteq B$

Proof.

We have for (F, A)

$$F(\varepsilon) = \{ \{ x, \mu_{F(\varepsilon)}(x) \} : x \in U \} \quad \forall \varepsilon \in A$$

Also, let $(U, B) = (G, B)$, Then

$$G(\varepsilon) = \{ \{ x, 1 \} : x \in U \} \quad \forall \varepsilon \in B$$

Let $(F, A) \tilde{\cap} (U, B) = (F, A) \tilde{\cap} (G, B) = (H, C)$, where

$C = A \cup B$ and $\forall \varepsilon \in C$,

$H(\varepsilon)$

$$\begin{aligned} &= \begin{cases} \{ \{ x, \mu_{F(\varepsilon)}(x) \} : x \in U \}, & \text{if } \varepsilon \in A - B \\ \{ \{ x, \mu_{G(\varepsilon)}(x) \} : x \in U \}, & \text{if } \varepsilon \in B - A \\ \{ \{ x, \max(\mu_{F(\varepsilon)}(x), \mu_{G(\varepsilon)}(x)) \} : x \in U \}, & \text{if } \varepsilon \in A \cap B \end{cases} \\ &= \begin{cases} \{ \{ x, \mu_{F(\varepsilon)}(x) \} : x \in U \}, & \text{if } \varepsilon \in A - B \\ \{ \{ x, 1 \} : x \in U \}, & \text{if } \varepsilon \in B - A \\ \{ \{ x, \max(\mu_{F(\varepsilon)}(x), 1) \} : x \in U \}, & \text{if } \varepsilon \in A \cap B \end{cases} \\ &= \begin{cases} \{ \{ x, \mu_{F(\varepsilon)}(x) \} : x \in U \}, & \text{if } \varepsilon \in A - B \\ \{ \{ x, 1 \} : x \in U \}, & \text{if } \varepsilon \in B - A \\ \{ \{ x, 1 \} : x \in U \}, & \text{if } \varepsilon \in A \cap B \end{cases} \end{aligned}$$

Let $A \subseteq B$

Then

$$\begin{aligned} H(\varepsilon) &= \begin{cases} \{ \{ x, 1 \} : x \in U \}, & \text{if } \varepsilon \in B - A \\ \{ \{ x, 1 \} : x \in U \}, & \text{if } \varepsilon \in A \cap B \end{cases} \\ &= G(\varepsilon) \quad \forall \varepsilon \in B \end{aligned}$$

Conversely, let $(F, A) \tilde{\cap} (U, B) = (U, B)$

Then $B = A \cup B \Rightarrow A \subseteq B$

9. $(F, A) \tilde{\cap} (\varphi, B) = (\varphi, A \cap B)$

Proof.

We have for (F, A)

$$F(\varepsilon) = \{ \{ x, \mu_{F(\varepsilon)}(x) \} : x \in U \} \quad \forall \varepsilon \in A$$

Also, let $(\varphi, B) = (G, B)$, Then

$$G(\varepsilon) = \{ \{ x, 0 \} : x \in U \} \quad \forall \varepsilon \in B$$

Let $(F, A) \tilde{\cap} (\varphi, B) = (F, A) \tilde{\cap} (G, B) = (H, C)$, where

$C = A \cap B$ and $\forall \varepsilon \in C$,

$$\begin{aligned} H(\varepsilon) &= \{ \{ x, \min(\mu_{F(\varepsilon)}(x), \mu_{G(\varepsilon)}(x)) \} : x \in U \} \\ &= \{ \{ x, \min(\mu_{F(\varepsilon)}(x), 0) \} : x \in U \} \\ &= \{ \{ x, 0 \} : x \in U \} \end{aligned}$$

Thus $(F, A) \tilde{\cap} (\varphi, B) = (\varphi, A \cap B)$

10. $(F, A) \tilde{\cap} (U, B) = (F, A \cap B)$

Proof.

We have for (F, A)

$$F(\varepsilon) = \{ \{ x, \mu_{F(\varepsilon)}(x) \} : x \in U \} \quad \forall \varepsilon \in A$$

Also, let $(U, B) = (G, B)$, Then

$$G(\varepsilon) = \{ \{ x, 1 \} : x \in U \} \quad \forall \varepsilon \in B$$

Let $(F, A) \tilde{\cap} (U, B) = (F, A) \tilde{\cap} (G, B) = (H, C)$, where

$C = A \cap B$ and $\forall \varepsilon \in C$,

$$\begin{aligned} H(\varepsilon) &= \{ \{ x, \min(\mu_{F(\varepsilon)}(x), \mu_{G(\varepsilon)}(x)) \} : x \in U \} \\ &= \{ \{ x, \min(\mu_{F(\varepsilon)}(x), 1) \} : x \in U \} \end{aligned}$$

$$= \{x, \mu_{F(\varepsilon)}(x) : x \in U\}$$

Thus $(F, A) \tilde{\cap} (U, B) = (F, A \cap B)$

It is well known that De Morgan Laws inter-relate union and intersection via complements. Maji et al [6] gave the following proposition-

3.2. Proposition

1. $((F, A) \tilde{\cup} (G, B))^c = (F, A)^c \tilde{\cup} (G, B)^c$
2. $((F, A) \tilde{\cap} (G, B))^c = (F, A)^c \tilde{\cap} (G, B)^c$

Ahmad and Kharal [1] proved by counter examples that these propositions are not valid. However the following inclusions are due to Ahmad and Kharal [1]. They proved these results with the definition of complement initiated by Maji et al. [6]. Below we are giving the proof in our way.

3.3. Proposition

For fuzzy soft sets (F, A) and (G, B) over the same universe U , we have the following -

1. $((F, A) \tilde{\cup} (G, B))^c \subseteq (F, A)^c \tilde{\cup} (G, B)^c$
2. $(F, A)^c \tilde{\cap} (G, B)^c \subseteq ((F, A) \tilde{\cap} (G, B))^c$

Proof.

1. Let $(F, A) \tilde{\cup} (G, B) = (H, C)$, where $C = A \cup B$ and $\forall \varepsilon \in C$,

$$H(\varepsilon) = \begin{cases} F(\varepsilon), & \text{if } \varepsilon \in A-B \\ G(\varepsilon), & \text{if } \varepsilon \in B-A \\ F(\varepsilon) \cup G(\varepsilon), & \text{if } \varepsilon \in A \cap B \end{cases}$$

$$= \begin{cases} \{x, \mu_{F(\varepsilon)}(x)\}, & \text{if } \varepsilon \in A-B \\ \{x, \mu_{G(\varepsilon)}(x)\}, & \text{if } \varepsilon \in B-A \\ \{x, \max(\mu_{F(\varepsilon)}, \mu_{G(\varepsilon)})\}, & \text{if } \varepsilon \in A \cap B \end{cases}$$

Thus

$$((F, A) \tilde{\cup} (G, B))^c = (H, C)^c = (H^c, C), \text{ where } C = A \cup B \text{ and } \forall \varepsilon \in C,$$

$$H^c(\varepsilon) = (H(\varepsilon))^c = \begin{cases} (F(\varepsilon))^c, & \text{if } \varepsilon \in A-B \\ (G(\varepsilon))^c, & \text{if } \varepsilon \in B-A \\ (F(\varepsilon) \cup G(\varepsilon))^c, & \text{if } \varepsilon \in A \cap B \end{cases}$$

$$= \begin{cases} \{x, 1 - \mu_{F(\varepsilon)}(x)\}, & \text{if } \varepsilon \in A-B \\ \{x, 1 - \mu_{G(\varepsilon)}(x)\}, & \text{if } \varepsilon \in B-A \\ \{x, 1 - \max(\mu_{F(\varepsilon)}, \mu_{G(\varepsilon)})\}, & \text{if } \varepsilon \in A \cap B \end{cases}$$

$$= \begin{cases} \{x, 1 - \mu_{F(\varepsilon)}(x)\}, & \text{if } \varepsilon \in A-B \\ \{x, 1 - \mu_{G(\varepsilon)}(x)\}, & \text{if } \varepsilon \in B-A \\ \{x, \min(1 - \mu_{F(\varepsilon)}(x), 1 - \mu_{G(\varepsilon)}(x))\}, & \text{if } \varepsilon \in A \cap B \end{cases}$$

Again,

$$(F, A)^c \tilde{\cup} (G, B)^c = (F^c, A) \tilde{\cup} (G^c, B) = (I, J), \text{ say}$$

Where $J = A \cup B$ and $\forall \varepsilon \in J$,

$$I(\varepsilon) = \begin{cases} F^c(\varepsilon), & \text{if } \varepsilon \in A-B \\ G^c(\varepsilon), & \text{if } \varepsilon \in B-A \\ F^c(\varepsilon) \cup G^c(\varepsilon), & \text{if } \varepsilon \in A \cap B \end{cases}$$

$$= \begin{cases} \{x, \mu_{F^c(\varepsilon)}(x)\}, & \text{if } \varepsilon \in A-B \\ \{x, \mu_{G^c(\varepsilon)}(x)\}, & \text{if } \varepsilon \in B-A \\ \{x, \max(\mu_{F^c(\varepsilon)}(x), \mu_{G^c(\varepsilon)}(x))\}, & \text{if } \varepsilon \in A \cap B \end{cases}$$

$$= \begin{cases} \{x, 1 - \mu_{F(\varepsilon)}(x)\}, & \text{if } \varepsilon \in A-B \\ \{x, 1 - \mu_{G(\varepsilon)}(x)\}, & \text{if } \varepsilon \in B-A \\ \{x, \max(1 - \mu_{F(\varepsilon)}, 1 - \mu_{G(\varepsilon)})\}, & \text{if } \varepsilon \in A \cap B \end{cases}$$

We see that $C = J$ and $\forall \varepsilon \in C, H^c(\varepsilon) \subseteq I(\varepsilon)$

$$\text{Thus } ((F, A) \tilde{\cup} (G, B))^c \subseteq (F, A)^c \tilde{\cup} (G, B)^c$$

2. Let $(F, A) \tilde{\cap} (G, B) = (H, C)$,

Where $C = A \cap B$ and $\forall \varepsilon \in C$,

$$H(\varepsilon) = F(\varepsilon) \cap G(\varepsilon) = \{x, \min(\mu_{F(\varepsilon)}(x), \mu_{G(\varepsilon)}(x))\}$$

$$\text{Thus } ((F, A) \tilde{\cap} (G, B))^c = (H, C)^c = (H^c, C),$$

Where $C = A \cap B$ and $\forall \varepsilon \in C$,

$$H^c(\varepsilon) = (F(\varepsilon) \cap G(\varepsilon))^c = \{x, 1 - \min(\mu_{F(\varepsilon)}(x), \mu_{G(\varepsilon)}(x))\}$$

$$= \{x, \max(1 - \mu_{F(\varepsilon)}(x), 1 - \mu_{G(\varepsilon)}(x))\}$$

$$\text{Again, } (F, A)^c \tilde{\cap} (G, B)^c = (F^c, A) \tilde{\cap} (G^c, B) = (I, J), \text{ say}$$

Where $J = A \cap B$ and $\forall \varepsilon \in J$,

$$I(\varepsilon) = F^c(\varepsilon) \cap G^c(\varepsilon) = \{x, \min(\mu_{F^c(\varepsilon)}(x), \mu_{G^c(\varepsilon)}(x))\}$$

$$= \{x, \min(1 - \mu_{F(\varepsilon)}(x), 1 - \mu_{G(\varepsilon)}(x))\}$$

We see that $C = J$ and $\forall \varepsilon \in C, I(\varepsilon) \subseteq H^c(\varepsilon)$

$$\text{Thus } (F, A)^c \tilde{\cap} (G, B)^c \subseteq ((F, A) \tilde{\cap} (G, B))^c$$

3.4. Proposition (De Morgan Inclusions)

For fuzzy soft sets (F, A) and (G, B) over the same universe U , we have the following -

1. $(F, A)^c \tilde{\cap} (G, B)^c \subseteq ((F, A) \tilde{\cup} (G, B))^c$
2. $((F, A) \tilde{\cap} (G, B))^c \subseteq (F, A)^c \tilde{\cup} (G, B)^c$

Proof

1. Let $(F, A) \tilde{\cup} (G, B) = (H, C)$, where $C = A \cup B$ and $\forall \varepsilon \in C$,

$$H(\varepsilon) = \begin{cases} F(\varepsilon), & \text{if } \varepsilon \in A-B \\ G(\varepsilon), & \text{if } \varepsilon \in B-A \\ F(\varepsilon) \cup G(\varepsilon), & \text{if } \varepsilon \in A \cap B \end{cases}$$

$$= \begin{cases} \{x, \mu_{F(\varepsilon)}(x)\}, & \text{if } \varepsilon \in A-B \\ \{x, \mu_{G(\varepsilon)}(x)\}, & \text{if } \varepsilon \in B-A \\ \{x, \max(\mu_{F(\varepsilon)}, \mu_{G(\varepsilon)})\}, & \text{if } \varepsilon \in A \cap B \end{cases}$$

Thus

$$((F, A) \tilde{\cup} (G, B))^c = (H, C)^c = (H^c, C), \text{ where } C = A \cup B \text{ and } \forall \varepsilon \in C,$$

$$\begin{aligned} H^c(\varepsilon) &= (H(\varepsilon))^c \\ &= \begin{cases} (F(\varepsilon))^c, & \text{if } \varepsilon \in A-B \\ (G(\varepsilon))^c, & \text{if } \varepsilon \in B-A \\ (F(\varepsilon) \cup G(\varepsilon))^c, & \text{if } \varepsilon \in A \cap B \end{cases} \\ &= \begin{cases} \{x, 1 - \mu_{F(\varepsilon)}(x)\}, & \text{if } \varepsilon \in A-B \\ \{x, 1 - \mu_{G(\varepsilon)}(x)\}, & \text{if } \varepsilon \in B-A \\ \{x, 1 - \max(\mu_{F(\varepsilon)}, \mu_{G(\varepsilon)})\}, & \text{if } \varepsilon \in A \cap B \end{cases} \\ &= \begin{cases} \{x, 1 - \mu_{F(\varepsilon)}(x)\}, & \text{if } \varepsilon \in A-B \\ \{x, 1 - \mu_{G(\varepsilon)}(x)\}, & \text{if } \varepsilon \in B-A \\ \{x, \min(1 - \mu_{F(\varepsilon)}(x), 1 - \mu_{G(\varepsilon)}(x))\}, & \text{if } \varepsilon \in A \cap B \end{cases} \end{aligned}$$

Again, $(F, A)^c \tilde{\cap} (G, B)^c = (F^c, A) \tilde{\cap} (G^c, B) = (I, J)$, say
Where $J = A \cap B$ and $\forall \varepsilon \in J$,

$$\begin{aligned} I(\varepsilon) &= F^c(\varepsilon) \cap G^c(\varepsilon) \\ &= \{x, \min(\mu_{F^c(\varepsilon)}(x), \mu_{G^c(\varepsilon)}(x))\} \\ &= \{x, \min(1 - \mu_{F(\varepsilon)}(x), 1 - \mu_{G(\varepsilon)}(x))\} \end{aligned}$$

We see that $J \subseteq C$ and $\forall \varepsilon \in J, I(\varepsilon) = H^c(\varepsilon)$

$$\text{Thus } (F, A)^c \tilde{\cap} (G, B)^c \subseteq ((F, A) \tilde{\cup} (G, B))^c$$

2. Let $(F, A) \tilde{\cap} (G, B) = (H, C)$, Where $C = A \cap B$ and $\forall \varepsilon \in C$,

$$\begin{aligned} H(\varepsilon) &= F(\varepsilon) \cap G(\varepsilon) \\ &= \{x, \min(\mu_{F(\varepsilon)}(x), \mu_{G(\varepsilon)}(x))\} \end{aligned}$$

$$\text{Thus } ((F, A) \tilde{\cap} (G, B))^c = (H, C)^c = (H^c, C),$$

Where $C = A \cap B$ and $\forall \varepsilon \in C$,

$$\begin{aligned} H^c(\varepsilon) &= (F(\varepsilon) \cap G(\varepsilon))^c \\ &= \{x, 1 - \min(\mu_{F(\varepsilon)}(x), \mu_{G(\varepsilon)}(x))\} \\ &= \{x, \max(1 - \mu_{F(\varepsilon)}(x), 1 - \mu_{G(\varepsilon)}(x))\} \end{aligned}$$

Again,

$$(F, A)^c \tilde{\cup} (G, B)^c = (F^c, A) \tilde{\cup} (G^c, B) = (I, J), \text{ say}$$

Where $J = A \cup B$ and $\forall \varepsilon \in J$,

$$I(\varepsilon) = \begin{cases} F^c(\varepsilon), & \text{if } \varepsilon \in A-B \\ G^c(\varepsilon), & \text{if } \varepsilon \in B-A \\ F^c(\varepsilon) \cup G^c(\varepsilon), & \text{if } \varepsilon \in A \cap B \end{cases}$$

$$= \begin{cases} \{x, \mu_{F^c(\varepsilon)}(x)\}, & \text{if } \varepsilon \in A-B \\ \{x, \mu_{G^c(\varepsilon)}(x)\}, & \text{if } \varepsilon \in B-A \\ \{x, \max(\mu_{F^c(\varepsilon)}(x), \mu_{G^c(\varepsilon)}(x))\}, & \text{if } \varepsilon \in A \cap B \end{cases}$$

$$= \begin{cases} \{x, 1 - \mu_{F(\varepsilon)}(x)\}, & \text{if } \varepsilon \in A-B \\ \{x, 1 - \mu_{G(\varepsilon)}(x)\}, & \text{if } \varepsilon \in B-A \\ \{x, \max(1 - \mu_{F(\varepsilon)}, 1 - \mu_{G(\varepsilon)})\}, & \text{if } \varepsilon \in A \cap B \end{cases}$$

We see that $C \subseteq J$ and $\forall \varepsilon \in C, H^c(\varepsilon) = I(\varepsilon)$

$$\text{Thus } ((F, A) \tilde{\cap} (G, B))^c \subseteq (F, A)^c \tilde{\cup} (G, B)^c$$

De Morgan Laws are valid for fuzzy soft sets with the same set of parameter. Thus for fuzzy soft sets, we have the following De Morgan Laws:

3.5. Proposition (De Morgan Laws)

For fuzzy soft sets (F, A) and (G, A) over the same universe U , we have the following -

1. $((F, A) \tilde{\cup} (G, A))^c = (F, A)^c \tilde{\cap} (G, A)^c$
2. $((F, A) \tilde{\cap} (G, A))^c = (F, A)^c \tilde{\cup} (G, A)^c$

Proof.

$$\begin{aligned} \text{1. Let } (F, A) \tilde{\cup} (G, A) &= (H, A), \text{ where } \forall \varepsilon \in A, \\ H(\varepsilon) &= F(\varepsilon) \cup G(\varepsilon) \\ &= \{x, \max(\mu_{F(\varepsilon)}, \mu_{G(\varepsilon)})\} \end{aligned}$$

Thus

$$\begin{aligned} ((F, A) \tilde{\cup} (G, A))^c &= (H, A)^c = (H^c, A), \text{ where } \forall \varepsilon \in A, \\ H^c(\varepsilon) &= (H(\varepsilon))^c \\ &= (F(\varepsilon) \cup G(\varepsilon))^c \\ &= \{x, 1 - \max(\mu_{F(\varepsilon)}, \mu_{G(\varepsilon)})\} \\ &= \{x, \min(1 - \mu_{F(\varepsilon)}(x), 1 - \mu_{G(\varepsilon)}(x))\} \end{aligned}$$

$$\text{Again, } (F, A)^c \tilde{\cap} (G, A)^c = (F^c, A) \tilde{\cap} (G^c, A) = (I, A), \text{ say}$$

Where $\forall \varepsilon \in A$,

$$\begin{aligned} I(\varepsilon) &= F^c(\varepsilon) \cap G^c(\varepsilon) \\ &= \{x, \min(\mu_{F^c(\varepsilon)}(x), \mu_{G^c(\varepsilon)}(x))\} \\ &= \{x, \min(1 - \mu_{F(\varepsilon)}(x), 1 - \mu_{G(\varepsilon)}(x))\} \end{aligned}$$

$$\text{Thus } ((F, A) \tilde{\cup} (G, A))^c = (F, A)^c \tilde{\cap} (G, A)^c$$

2. Let $(F, A) \tilde{\cap} (G, A) = (H, A)$, where $\forall \varepsilon \in A$,

$$\begin{aligned} H(\varepsilon) &= F(\varepsilon) \cap G(\varepsilon) \\ &= \{x, \min(\mu_{F(\varepsilon)}, \mu_{G(\varepsilon)})\} \end{aligned}$$

Thus

$$\begin{aligned} ((F, A) \tilde{\cap} (G, A))^c &= (H, A)^c = (H^c, A), \text{ where } \forall \varepsilon \in A, \\ H^c(\varepsilon) &= (H(\varepsilon))^c \\ &= (F(\varepsilon) \cap G(\varepsilon))^c \\ &= \{x, 1 - \min(\mu_{F(\varepsilon)}, \mu_{G(\varepsilon)})\} \end{aligned}$$

$$= \{x, \max(1 - \mu_{F(\varepsilon)}(x), 1 - \mu_{G(\varepsilon)}(x))\}$$

$$= \{x, \max(\mu_{F(\alpha)}(x), \mu_{G(\beta)}(x))\}$$

Again, $(F, A)^c \tilde{\cup} (G, A)^c = (F^c, A) \tilde{\cap} (G^c, A) = (I, A)$, say

Where $\forall \varepsilon \in A$,

$$I(\varepsilon) = F^c(\varepsilon) \cup G^c(\varepsilon)$$

$$= \{x, \max(\mu_{F^c(\varepsilon)}(x), \mu_{G^c(\varepsilon)}(x))\}$$

$$= \{x, \max(1 - \mu_{F(\varepsilon)}(x), 1 - \mu_{G(\varepsilon)}(x))\}$$

Thus $((F, A) \tilde{\cap} (G, A))^c = (F, A)^c \tilde{\cup} (G, A)^c$

Maji et al [6] proved the following De Morgan Types of results for fuzzy soft sets (F, A) and (G, B) over the same universe U . We can verify that these De Morgan types of results are valid in our way also.

3.6. Proposition

For fuzzy soft sets (F, A) and (G, B) over the same universe U , we have the following -

$$1. ((F, A) \wedge (G, B))^c = (F, A)^c \vee (G, B)^c$$

$$2. ((F, A) \vee (G, B))^c = (F, A)^c \wedge (G, B)^c$$

Proof.

1. Let $(F, A) \wedge (G, B) = (H, A \times B)$,

Where $H(\alpha, \beta) = F(\alpha) \cap G(\beta)$, $\forall \alpha \in A$ and $\forall \beta \in B$,

where \cap is the operation intersection of two fuzzy sets.

Thus

$$H(\alpha, \beta) = F(\alpha) \cap G(\beta)$$

$$= \{x, \min(\mu_{F(\alpha)}(x), \mu_{G(\beta)}(x))\}$$

Thus

$$((F, A) \wedge (G, B))^c = (H, A \times B)^c$$

$$= (H^c, A \times B), \text{ where } \forall (\alpha, \beta) \in A \times B,$$

$$H^c(\alpha, \beta) = (H(\alpha, \beta))^c$$

$$= \{x, 1 - \min(\mu_{F(\alpha)}(x), \mu_{G(\beta)}(x))\}$$

$$= \{x, \max(1 - \mu_{F(\alpha)}(x), 1 - \mu_{G(\beta)}(x))\}$$

Let $(F, A)^c \vee (G, B)^c = (F^c, A) \vee (G^c, B) = (O, A \times B)$,

Where $O(\alpha, \beta) = F^c(\alpha) \cup G^c(\beta)$, $\forall \alpha \in A$ and $\forall \beta \in B$,

where \cup is the operation union of two fuzzy sets.

$$= \{x, \max(\mu_{F^c(\alpha)}(x), \mu_{G^c(\beta)}(x))\}$$

$$= \{x, \max(1 - \mu_{F(\alpha)}(x), 1 - \mu_{G(\beta)}(x))\}$$

It follows that $((F, A) \wedge (G, B))^c = (F, A)^c \vee (G, B)^c$

2. Let $(F, A) \vee (G, B) = (H, A \times B)$,

Where $H(\alpha, \beta) = F(\alpha) \cup G(\beta)$, $\forall \alpha \in A$ and $\forall \beta \in B$,

where \cup is the operation union of two sets.

Thus

$$H(\alpha, \beta) = F(\alpha) \cup G(\beta)$$

Thus

$$((F, A) \vee (G, B))^c = (H, A \times B)^c$$

$$= (H^c, A \times B), \text{ where } \forall (\alpha, \beta) \in A \times B,$$

$$H^c(\alpha, \beta) = (H(\alpha, \beta))^c$$

$$= \{x, 1 - \max(\mu_{F(\alpha)}(x), \mu_{G(\beta)}(x))\}$$

$$= \{x, \min(1 - \mu_{F(\alpha)}(x), 1 - \mu_{G(\beta)}(x))\}$$

Let $(F, A)^c \wedge (G, B)^c = (F^c, A) \wedge (G^c, B) = (O, A \times B)$,

Where $O(\alpha, \beta) = F^c(\alpha) \cap G^c(\beta)$, $\forall \alpha \in A$ and $\forall \beta \in B$,

where \cap is the operation intersection of two fuzzy sets.

$$= \{x, \min(\mu_{F^c(\alpha)}(x), \mu_{G^c(\beta)}(x))\}$$

$$= \{x, \min(1 - \mu_{F(\alpha)}(x), 1 - \mu_{G(\beta)}(x))\}$$

It follows that $((F, A) \vee (G, B))^c = (F, A)^c \wedge (G, B)^c$

4. CONCLUSION

We have made an investigation on existing basic notions and results on fuzzy soft sets. Some new results have been stated in our work. Future work in this regard would be required to study whether the notions put forward in this paper yield a fruitful result

5. REFERENCES

- [1] B. Ahmad and A. Kharal, "On Fuzzy Soft Sets", Advances in Fuzzy Systems, Volume 2009.
- [2] D. A. Molodtsov, "Soft Set Theory - First Result", Computers and Mathematics with Applications, Vol. 37, pp. 19-31, 1999
- [3] D. Chen, E.C.C. Tsang, D.S. Yeung, and X.Wang, "The parameterization reduction of soft sets and its applications," Computers & Mathematics with Applications, vol. 49, no.5-6, pp. 757-763, 2005.
- [4] D. Pei and D. Miao, "From soft sets to information systems," in Proceedings of the IEEE International Conference on Granular Computing, vol. 2, pp. 617-621, 2005.
- [5] P. K. Maji and A.R. Roy, "Soft Set Theory", Computers and Mathematics with Applications 45 (2003) 555 - 562
- [6] P. K. Maji, R. Biswas and A.R. Roy, "Fuzzy Soft Sets", Journal of Fuzzy Mathematics, Vol 9, no.3, pp.-589-602, 2001
- [7] T. J. Neog, D. K. Sut, "On Fuzzy Soft Complement and Related Properties", Accepted for publication in International Journal of Energy, Information and communications (IJEIC).
- [8] T. J. Neog, D. K. Sut, "On Union and Intersection of Fuzzy Soft Sets", Int.J. Comp. Tech. Appl., Vol 2 (5), 1160-1176
- [9] T. J. Neog and D. K. Sut, "A New Approach To The Theory of Soft Sets", International Journal of Computer Applications, Vol 32, No 2, October 2011, pp 1-6
- [10] Xun Ge and Songlin Yang, "Investigations on some operations of soft sets", World Academy of Science, Engineering and Technology, 75, 2011, pp. 1113-1116

Creation of physical characteristics information for Natural Resources Management Using Remote sensing and GIS : A Model study

SS. Asadi¹, B.V.T.Vasantha Rao² and S.K.Sekar³

¹(Research Scholar, Centre for Disaster Mitigation & Management, VIT University, Vellore-632014, Tamilnadu)

²(Assistant professor, Dept. of Civil Engineering, p.v.p.siddhardha Institute of Technology, Kannure, Vijayawada)

³(Director, Centre for Disaster Mitigation & Management, VIT University, Vellore-632014, Tamilnadu)

ABSTRACT

Natural resources are required for agriculture, forestry, rangeland, urbanization and many other developmental activities satisfying human needs. creation of these resources information system with the help of Remote sensing and Geographic Information System (GIS) tools could be helpful in getting the precise and valuable spatial information in understanding the present scenario contemplating with the past data and predicting the future trends. The main objective of the study is to evaluate and map the physical characteristics in the study area and to develop methods for its efficient utilization of natural resources for sustainable management using remote sensing and GIS. The thematic layers are derived from IRS-P6, LISS-IV, MX satellite imagery (Fig.4) and Survey of India (SOI) (Fig.5) topomaps using visual interpretation technique. These maps are converted to digital format and further integrated in ARCGIS software for the generation of final outputs. This study recommends effective soil and water conservation measures to increase the subsurface aquifer capacity and identifies suitable cropping patterns, which help in reduced soil erosion, increased moisture conservation and improved productivity of the soil. The physical characterization of an area is also useful to plan the basic minimum needs of farmers, thereby improving their socio-economic conditions and helps in evolving a broad national policy which can be applied by decision makers for sustainable development of any given area.

Keywords: Physical characterization, Natural resources management, Remote sensing, Geographical Information System, Sustainable development.

1. INTRODUCTION

Natural resources are very much value for supporting agriculture, forestry, mining and human settlement. these are also have social, ecological and cultural uses and values. As with most environmental concepts, natural resources cannot be considered in isolation from other components of the environment. Comprehensive information about the status of the natural resources and their utilization is essential for any area treatment and management (Veerlapati Govardhan 1993). Among others, status of water resources, land evaluation for irrigation, cropping pattern and land use are the important factors that influence soil and water use efficiency, not only for optimizing agricultural production but also for control of the twin problems of soil and water which are usually associated with overuse and mismanagement in a study area (Isobel 1998). Periodic mapping and monitoring of Natural resources and their utilization status is therefore important for formulation of appropriate strategies for planning and implementation of ameliorative and development measures. This can be achieved by conventional ground surveys or by application of modern technology of remote sensing with limited ground studies. The conflicting demand of human activities and the pressure of increasing population have made it essential to plan the use of land in an optimal manner, so as to reap maximum benefits for the millions of human beings (Arakeri 1984). The constant pressure of growing population, increased demand for food, fodder and fuel wood combined with intensive industrial activity have led to large-scale environment degradation and ecological imbalance. Hence in order to use natural resources optimally, it is necessary to have first hand information about the existing land and then assess the location in the study area. Remote sensing, because of its advantage like synoptic view, repetitive coverage and multi spectral and multi sensor data availability, have been universally accepted as a powerful technology for resources survey mapping and regular monitoring (Prithvish Nag 1992). Remote sensing data with rapid in-time availability, high resolution and low cost product is an important tool for planning activities and can be used to study the physical characteristics of terrain depicting various Natural resources (Agarwal and Garg). These maps as a reliable input can be put to a Geographic Information System (GIS) to describe natural resources both renewable and non-renewable as well as cultural and human resource (Anji Reddy 2003)

2. OBJECTIVES

- To create the physical characteristics information of the study area for effective management and future development.
- To create spatial digital database consisting of land use/land cover, drainage, physiography, soil and slope maps using IRS P6 satellite data, SOI toposheets and ground data on ARCGIS platform
- To generate attribute data base consisting of statistical details of each of the above thematic layers
- To suggest suitable conservation and land use management practices

3. DESCRIPTION OF STUDY AREA

The study area is part of Prakasam District of Andhra Pradesh in India. Prakasam is an administrative district in the state of Andhra Pradesh with the district headquarters located at Ongole. There are a total of 56 mandals in this district occupying an area of 17,626 km² with a population of 3,054,941 (as of 2001 census). Some of the main towns in Prakasam district are Markapur, Chirala, Addanki, Kandukur, Giddalur, Podili, Dornala, Cumbum, Kanigiri and Chimakurthi. Prakasam district occupies an area of 17626 SqKm² with various agricultural, mining and quarrying, manufacturing and other household industries. However, the study area Vetapalem mandal of prakasam district is located at Longitude of 80^o .15' 29'' to 80^o .24' 30'' and Latitude of 15^o 42'53'' to 15^o 49' 53''. Vetapalem mandal has five Revenue villages and belong to Chirala constituency. (KothaPeta, NayaniPalli, PandillaPalle, PullariPalem and Vetapalem).

3.1 Village's spatial extent:

KOTHAPETA:	Longitude	:	80 ^o .20' 18'' to 80 ^o . 24' 30''
	Latitude	:	15 ^o 45'51'' to 15 ^o 49' 53''.
NAYANIPALLI:	Longitude	:	80 ^o .18' 12'' to 80 ^o . 21' 57''
	Latitude	:	15 ^o 44'20'' to 15 ^o 48' 1.53''.
PANDILLAPALLE:	Longitude	:	80 ^o .15' 29'' to 80 ^o . 17' 35''
	Latitude	:	15 ^o 44'20'' to 15 ^o 46' 53''
PULLARIPALEM:	Longitude	:	80 ^o .16' 51'' to 80 ^o . 20' 7.42''
	Latitude	:	15 ^o . 42'53'' to 15 ^o . 46'9.93''
VETAPALEM:	Longitude	:	80 ^o .16' 39'' to 80 ^o . 19' 51''
	Latitude	:	15 ^o . 45' 37'' to 15 ^o . 48'40''

The area of vetapalem mandal is 95.24 sq.kms .it has a total population of 67990 as per 2001 census, of which 28063 comprises rural and 39927 urban population. The mandal decadal growth rate is 7.40 in between 1991-2001

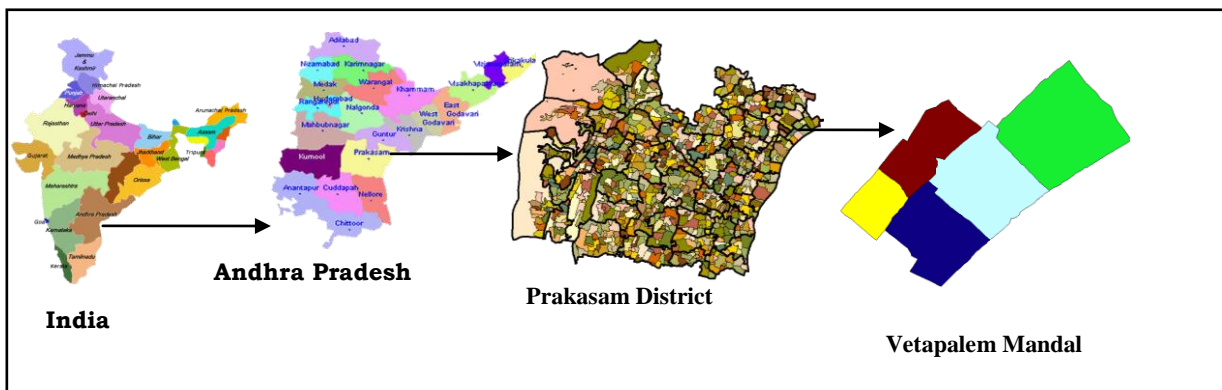


Fig.1: Location map of the study area

s.no	village name	village area in ha.	village area in sq.kms.
1	Pandillapalli	873	8.73
2	Pullaripalem	1348	13.48
3	Kothapeta	3031	30.31
4	Nayanipalli	2188	21.88
5	Vetapalem	2084	20.84

Tab.1: Village wise area in ha & Sq.Km.

4. METHODOLOGY

4.1 Data Collection

Different data products required for the study include SOI toposheets bearing the number 66A06NW,66A06SE,66A06SW on 1:25,000 scale, data of IRS-P6, LISS-IV, MX satellite imagery obtained from National Remote Sensing Agency (NRSA) and collateral data collected from related Government organizations and demographic data.

4.2 Data Input and Conversion

IRS-P6 satellite imageries collected from NRSA are geo-referenced using the ground control points with SOI toposheets as a reference output in ERDAS Image processing software. The study area is then delineated and subsetted from the data based on the latitude and longitude values and a final hard copy output is prepared for further interpretation.

4.3 Database Creation and Analysis

Creating a GIS spatial database is a complex operation, which involves data capture, verification and structuring processes. Raw geographical data are available in many different analogue and digital forms such as toposheets, aerial photographs, satellite imageries and tables. Out of all these sources, the source of toposheet is of much concern to natural resource scientist and an environmentalist (John R.Jensen 2003). In the present study, different thematic layers viz., base, drainage, slope, physiography, land use/ land cover and geomorphology are generated from toposheet and satellite data using visual interpretation technique.

The paper-based maps are converted to digital mode using scanning and automated digitization process. These maps are prepared to a certain scale and show the attributes of entities by different symbols or coloring. The location of entities on the earth's surface is then specified by means of an agreed co-ordinate system. It is mandatory that all spatial data in a GIS are located with respect to a frame of reference. For most GIS, the common frame of reference co-ordinate system is that of plane, Orthogonal Cartesian co-ordinates oriented conventionally North-South and East-West. This entire process is called geo-referencing. The same procedure is also applied on remote sensing data before it is used to prepare thematic maps from satellite data. This digitized data is then exported to ARC/INFO and further processed in ArcView GIS software to create digital database for subsequent data analysis.

5. RESULTS AND DISCUSSION

5.1 Base map

A topographic map is a representation of the shape, size, position and relation of the physical features of an area. The base map is prepared using SOI toposheet on 1:25,000 scale and updated with the help of satellite imagery. It consists of various features like the road network, settlements, water bodies Ramperu River, canals, The South central railway line passes through the study area and vegetation etc. delineated from the toposheet. The map thus drawn is scanned and digitized to get a digital output. The information content of this map is used as a baseline data to finalize the physical features of other thematic maps. Since the topo sheets are very old all the features like roads, railways, settlements etc are updated with the help of rectified and scaled satellite imageries of the area. The major settlements in the present study area are etc

5.2 Transport map

In the study area all the settlements are connected either by Metalled road or Un-Metalled road. Railway network (south central railway) passes through vetapalem village. The **image** shows the transport network map (Fig.7) of the Vetapalem Mandal.

5.3 Drainage Map

The drainage map (Fig.6) prepared from the toposheet forms the base map for the preparation of thematic maps related to surface and groundwater. All the rivers, tributaries and small stream channels shown on the toposheet are extracted to prepare the drainage map. Care is taken that the boundaries of rivers/ water bodies appearing on land use /land cover map or base map are perfectly matched with those on the toposheet. All the drainage lines are examined very closely and final drainage map is prepared. The study area is a first, second order streams and Ramperu River, canals are present. The present study area dendrite and prellal drainage are present. The flowing of water is tamed through construction of number of tanks and channels.

5.4 Watershed Map

Watersheds are hydrological units that are considered to be efficient and appropriate for assessment of available resources and subsequent planning and implementation of various development programmes. The watershed map (Fig.11) is prepared in accordance with the National Watershed Atlas and River Basin Atlas of India, 1985. According to this, India is divided into 6 regions (River Basin Atlas of India, 1985). The present study area comes under Region-4 and part of basin C, catchment 4, sub-catchment D, The study area is covered (4C4D1, 4C4D2) watersheds partially. In the 4C4D1 watershed Three sub watersheds is coming that is 4C4D1c,4C4D1d,4c4D1g, In the 4C4D2 One sub watershed is coming that is 4C4D2a.

5.5 Slope map

Slope has been categorized into different classes following a guidelines of all India Soil and Land Use Survey (ALS & LUS). To prepare the slope map on 1:25,000 scale survey of India topo sheets with 10m contour intervals have been used.

Slope classes 1, and 2 are observed in the study area . Most of the study area is covered by nearly level slope class (86% of the study area). Small part of the study area comes under very gently sloping (14%) .

5.6 Physiography

The purpose of Physiography layer is to understand disposition and distribution of barriers of winds. The Physiography is prepared using the contours derived from Survey of India topo sheets. Their physiography categories are demarcated in the map as Plains, Undulating land and Hills. The high slope areas not only pose physical constrains for developmental activities but also act as barriers for dispersion of air polluting emissions. The plains occupy the total study area, which indicates nearly level, gently sloping and very gently sloping terrain.

5.7 Land Use/Land Cover

The LU/LC map (Fig.8) of the study area is prepared from satellite imagery using visual interpretation technique. This technique consists of a set of image elements, which help in the recognition or interpretation of various land use /land cover features systematically on the enhanced satellite imagery during the classification of features (Lillesand and Kiefer 1994). The land use/ Land cover classification system used in this study is the system, which is pioneered by United States Geological Survey (USGS) and is modified by National Remote Sensing Agency (NRSA) according to Indian conditions. A preliminary image classification key is prepared for the fused pictorial data and is used during interpretation process. The base map is overlaid on the satellite imagery. Then the features of LU/LC classes are extracted and transferred from the satellite pictorial data. The doubtful areas (due to similar spectral response and spectral signature) identified during the preliminary image classification are listed out before ground verification. The doubtful areas are physically verified by field observation, based on which, corrections and modifications of misclassified land use/land cover details are carried out for preparation of final maps so as to extract the entropy or information content in accordance with the above thematic maps.

Land use / land cover map showing the spatial distribution of various categories and their aerial extent is vital for the present study. The spatial distributions of various land uses are interpreted based on IRS-P6, LISS-IV, MX satellite data. The land use/land cover categories such as built-up land, agriculture, forest, water body and wastelands have been identified and mapped for the study area Major part of the study area is covered Single crope(18%),Wetkands(1%),Cashew Plantationa(6%), Casuarina plantations(3%),Doublecrop (20%),Dried fishponds(2%),Fish ponds(2%),Grass lands(5%),Land with Scrub(3%),Land without Scrub(9%),Plantations(8%),Reserved forest(6%),Residential Area(9%),River Drain(3%),Salt pans(1%),Raod(1%) has been observed on the study area.

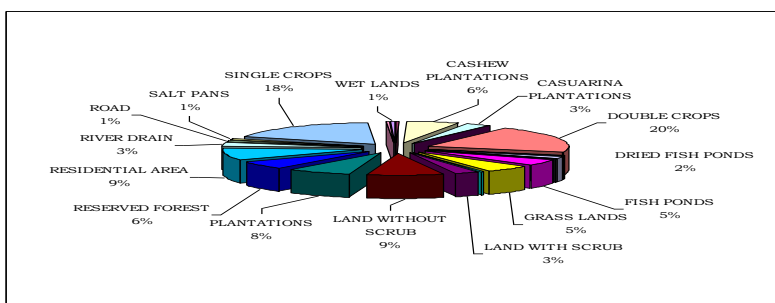


Fig.2: Pie Chart showing percentage distribution of Land use/ Land cover in the study area

5.7.1 Crops Cultivated in the study area:

Food Crops	:	Paddy
Food grains	:	Ground nuts, Cashewnuts.
Cereals	:	Rice
Milletts	:	Jowar, Bajra, Maize and Ragi
Pulses	:	Redgram and Green gram
Condiments and Spices	:	Onions, Chillies and Tamarind
Non-food crops	:	Cotton, Tobacco, Casuarina
Oil seeds	:	Groundnut, Sunflower

5.8 Geomorphology

Information on landforms is an important input for land management, soil mapping and identification of potential zones of groundwater occurrence. The aspects of morphography, morphogenesis, morphochronology and morphometry are vital inputs in preparation of geomorphologic maps (Fig.9). The geomorphological processes, which result from manifold effects of geological and climatological changes, leave their distinctive imprint upon landforms and each geomorphological process develops its own particular assemblage of landforms. Different landforms are identified through interpretation of satellite imagery together with ground truth data to enable the evaluation of groundwater potential of the study area The geomorphological classes observed in the study area are Alluvial plain, Coastal plain with deep weathering (CPD), Coastal plain with moderate weathering (CPM), Coastal plain with Shallow weathering (CPS), Tanks, Settlements, River.

Map Unit	Geomorphic Unit Description	Hydro Geology & Structure	Description	Ground Water Prospects
CPD CPM CPS Alluvial plain	Coastal plain shallow, moderate, deep weathering	Unconsolidated to semi consolidated Sand, Silt & Clay.	Gently sloping plain along the coast formed by marine action with Coastal Plain Moderate to Deep, Salt Flat, Mud flat and Beach.	Fresh water occurs as a thin layer over brackish water in the beach ridges and elevated tracts occupied by wind blown sand.

Tab.2: Description of Geomorphic Units

5.9 Structures

Structural features found in the study area are lineaments i.e., conformed lineament and inferred lineaments. The conformed lineaments are observed in the central portion of the study area towards west to east and major conformed lineaments are observed in SW corner of the study area. The inferred lineament is observed in NW, SW and SE corner of the study area.

5.10 Soil

The soil map (Fig.10) depicting different soil classes identified from the satellite imagery and their aerial extents are obtained through GIS analysis. Soil Sample strips were randomly selected for further field verification. Field visits were made to study soil profile characteristics and to correlate the interpretation units with the soils of the study area. Intensive profile examinations were carried out in the sample strips. Soil samples were collected from representative profiles for analysis in the laboratory. Random observations were however also made outside the sample strips in order to account for variation in soil therein. The soil profile data along with their taxonomic classification were incorporated into image interpretation units. Based on observations in the field, soil boundaries drawn during preliminary visual interpretation were modified and a legend showing soil series and associations was prepared. Subsequently the soil scape boundaries were transferred onto base maps prepared from Survey of India toposheet at 1:25,000 scale. In the study area Alluvial loamy soils(227), Clayey soils with crusting low (231), medium(232) Available Water Capacity (AWC), Red coastal clayey soils (241), Black cracking clay (246), Coastal clay soils(233) are observed.

6. CONCLUSION AND RECOMMENDATION

By studying the existing scenario of study area through the spatial analysis of agriculture activities, socio-economic and their impacts on the land and water resources using Remote Sensing and GIS tools, following conclusions are drawn.

1. Through the analysis of physical characteristics attribute data, gives the information of affected by erosion. In future this may lead to consequential problems to the major water bodies. This could be best controlled by construction of gully control bunds and extensive reforestation / afforestation or through agricultural soil conservation and management practices.
2. As irrigation water requirement varies with different crops, cropping pattern in the study area is to be changed for optimum utilization of this resource. Crops like pulses, vegetables should be cultivated, which may result lower requirement of water, fertilizer and also pesticide load.
3. The three key activities that are essential for the management of Resources.
 - Irrigation management
 - Catchment management
 - Drainage basin monitoring and management

To address these three activities planners need physical characteristic information on comprehensive lines. Hence, the present work, concentrated on the development of physical characteristics for study area.

4. This study has been concluded to above stated findings. But this study will be useful as input base line data for models like LWAT (Land and Water Assessment Tool) that give more precise and detailed long term predictions on Natural resources.

7. REFERENCES

1. Agarwal, C.S. and Garg, P.K. Text book of Remote Sensing in Natural Resources Management.
2. Anji Reddy, M. 2003. Remote Sensing and Geographic information Systems. 2nd Edition. B.S. Publications, India.
3. Arakeri, H.R. and Roy Donahue, 1984. Principles of soil Conservation and Water Management. Oxford and IBH Publishing CO. Ltd.
4. Cracknell, A.P. and Hayes, L.W.B. 1996. Introduction to Remote Sensing. Chapman and Hall Publications, New York.
5. Handbook of Statistics, Rangareddy district 2001. Chief Planning Officer, Director of Census Operation, Andhra Pradesh.

6. Isobel W. Heathcote, 1998. Integrated Watershed management – Principles and practice. John Wiley and Sons Inc, New York.
7. John R.Jensen, 2003. Remote Sensing of the Environment- An Earth Resource Perspective. Pearson Education Publication.
8. Lillesand, T.M. and Kiefer, R.W. 1994. Remote Sensing and image Interpretation. Wiley Publication, New York.
9. Prithvish Nag, 1992. Thematic Cartography and Remote Sensing. Concept Publishing Company, New Delhi, India.
10. Seshagiri Rao, K.V. 2003. Watersheds - Comprehensive Development. B.S. Publications, Hyderabad, India.
11. Veerlapati Govardhan, 1993. Remote Sensing and Water Management in Command Areas. International Book Distributing Company (Publishing Division), Lucknow, India

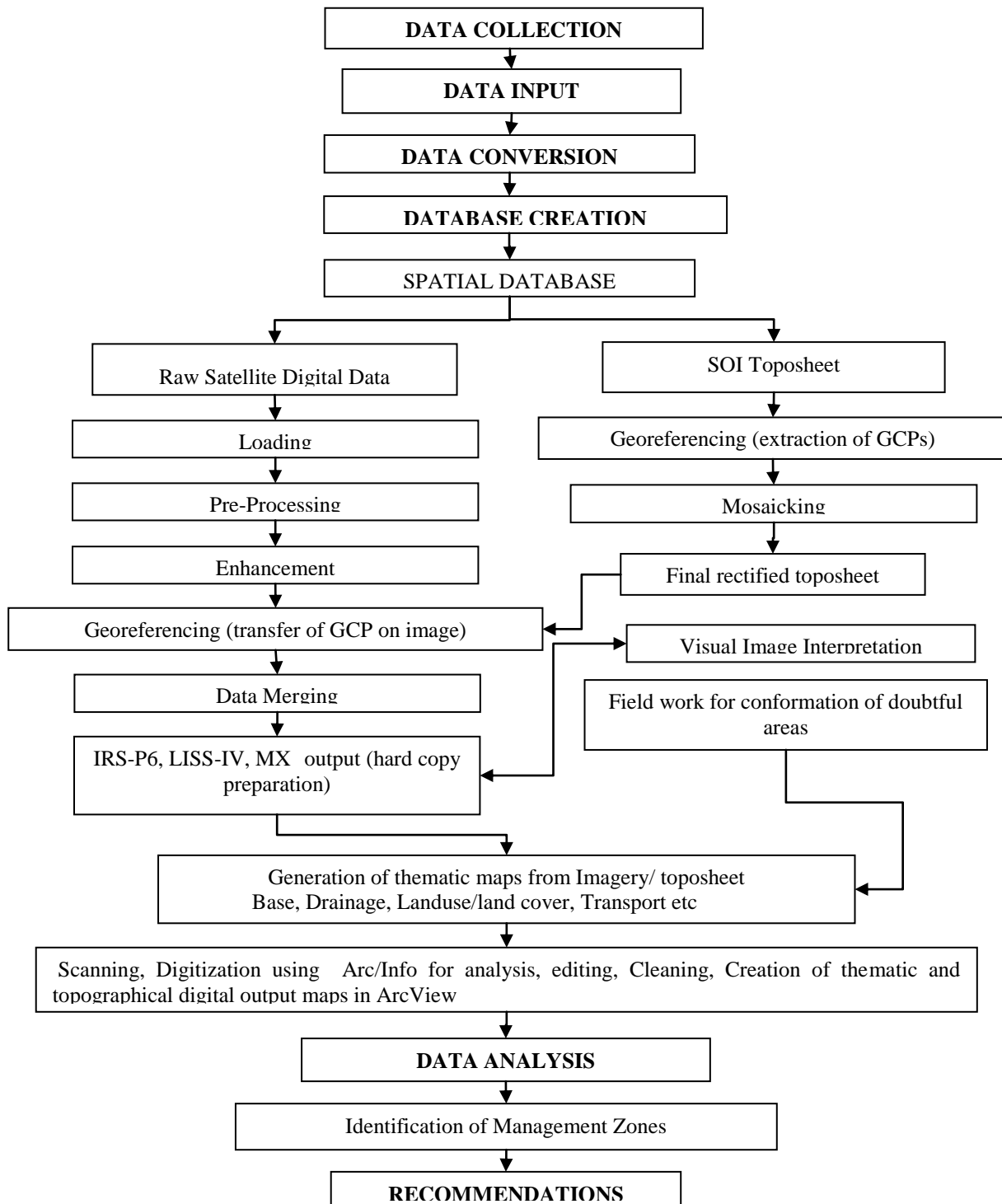


Figure 3: Flow chart showing the methodology adopted for the present study

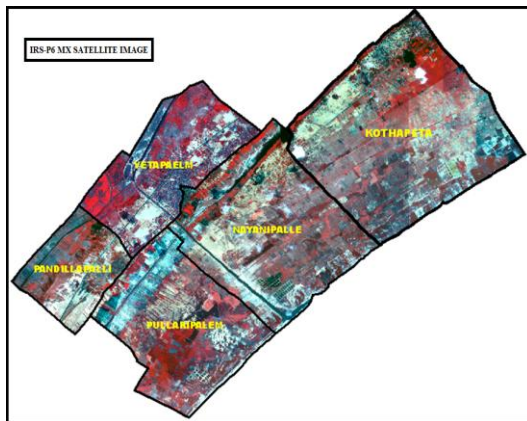


Fig.4:Satellite Image

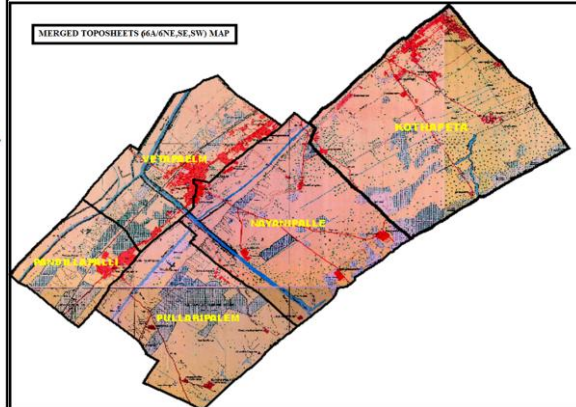


Fig.5:Merged Toposheet

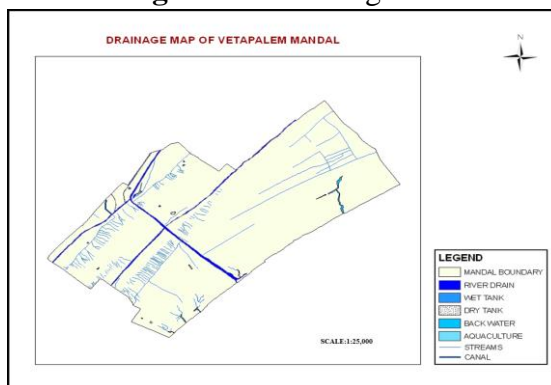


Fig.6:Drainage Map

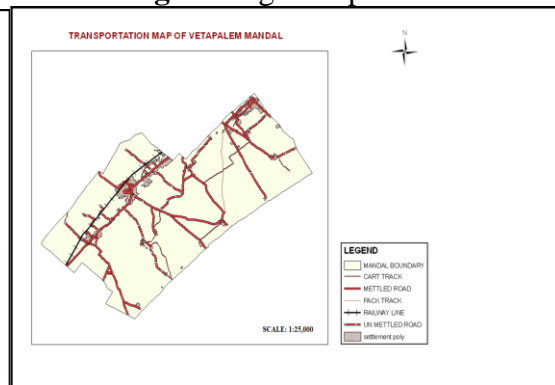


Fig.7: Transport network Map

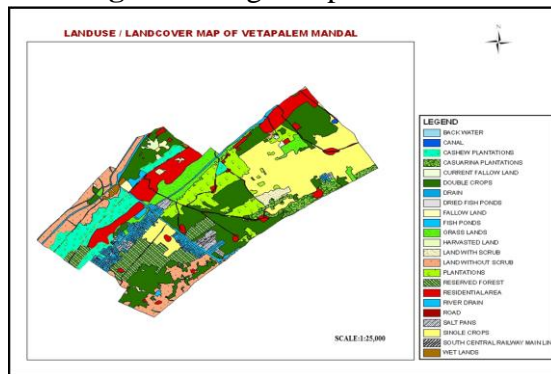


Fig.8:Landuse/Landcover Map

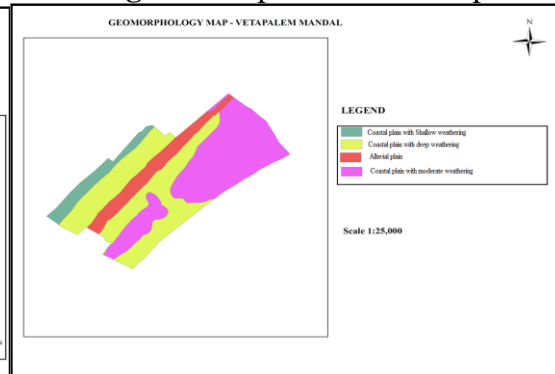


Fig.9:Geomorphology Map

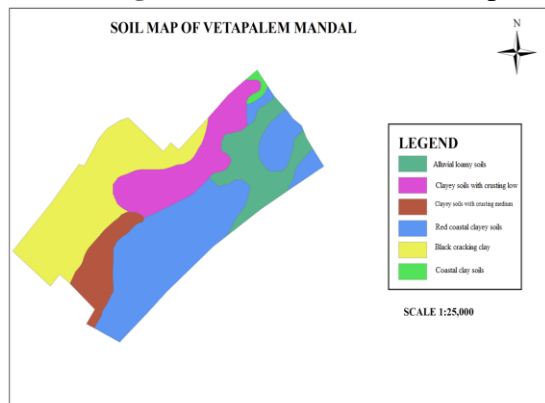


Fig.10:Soil Map

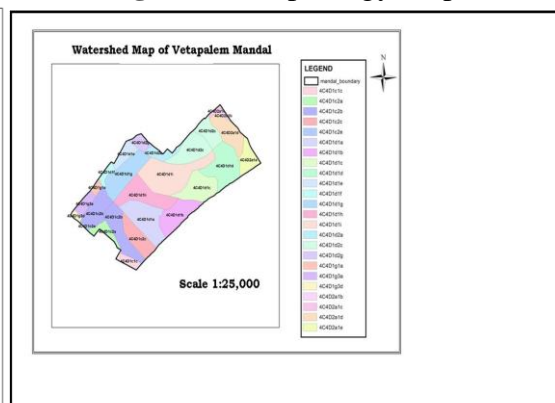


Fig.11:Watershed Map

Analysis and Design of a Quasi-TEM Slotted Tube Resonator for UHF-MRI

Kamila Aliane¹, Nadia Benabdallah², Nasreddine Benahmed¹,
Rachid Bouhmidj¹ and Fethi Tarik Bendimerad¹

¹Department of Telecommunications, University Abou Bekr Belkaid-Tlemcen,

²Department of Physics, Preparatory School of Sciences and Technology (EPST-Tlemcen),
Tlemcen, Algeria

ABSTRACT

Using the finite element method (FEM) and method of moments (MoM) in two dimensions, the electromagnetic (EM) analysis and design of a quasi-TEM slotted tube resonator (STR) are presented. The modeling of this resonator consists in analyzing the even- and odd-mode characteristic impedances (Z_{0e} , Z_{0o}), effective dielectric constants (ϵ_{effe} , ϵ_{effo}), the primary inductive and capacitive matrices ($[L]$, $[C]$) and simulates the frequency response of S_{11} at the RF port of the designed inhomogeneous MRI probe using transmission line method (TLM). As an application, we present the design results of a UHF-MRI probe loaded with a human head model of average relative dielectric constant of 64 and using the optimum configuration of the TEM STR. The probe with high Q operates at 340 MHz (proton imaging at 8 T) and has -130.6 dB minimum reflections. The UHF-MRI probe using quasi-TEM STR is easy to construct, inexpensive, and simple to operate. Furthermore, the coil presented here may be constructed to work at different resonances frequencies.

Keywords - Biological load, EM-parameters, high Q, frequency response, FEM, MoM and TLM calculations, human head model, Quasi-TEM slotted tube resonator, S-parameters, UHF-MRI probe.

I. INTRODUCTION

Magnetic resonance imaging (MRI) is widely used to obtain clear images inside human body, especially high water content tissues such as muscle, brain etc. The fundamental principle of MRI is to receive nuclear magnetic resonance signals induced by radiating electromagnetic (EM) wave pulse to human body which is placed inside the high intensity static magnetic field. MRI is a method that has been developed by Lauterbur [1], Mansfield and Grannell [2] and is based on the knowledge of nuclear magnetic resonance (NMR) technique. The 2003 Nobel Prize in physiology or medicine was awarded to these scientists responsible for the development of nuclear magnetic resonance as an imaging technique. MRI has since become a standard clinical method.

The MRI system is composed of various elements including radio frequency (RF) coil, which plays an essential role in imaging. Several types of RF coils, such as saddle coil [3], transverse electromagnetic birdcage coil resonator (TEM

BCR) [4-5], TEM slotted elliptical tube resonator (TEM SER) [6-9] and TEM slotted tube resonator (TEM STR) [10-11] have been developed to use for different usages. Among these RF coils, the TEM STR has gradually come to be employed since it can produce the uniform magnetic field and can suppress the electric field.

This article is a continuation of our previous paper that appeared in Physics in Medicine and Biology magazine [12]. In support of the analysis and design of a high-Q quasi-TEM resonator for UHF-MRI applications based on loaded slotted tube resonator, we developed effective approaches based on the use of the finite element method (FEM) and the method of moments (MoM).

For this type of quasi-TEM resonator, there are no numerical or experimental results in the scientific literature. For this reason we were obliged, for the same geometrical and physical parameters of our quasi-TEM resonator, to make simulations by using our two numerical approaches (FEM and MoM).

The aim of this work is to determine, for the optimum configuration of the quasi-TEM STR, the even- and odd-mode characteristic impedances (Z_{0e} , Z_{0o}), effective dielectric constants (ϵ_{effe} , ϵ_{effo}), the primary inductive and capacitive matrices ($[L]$, $[C]$) and simulates the frequency response of S_{11} at the RF port of the designed loaded UHF-MRI probe using transmission line method (TLM) [13].

To demonstrate our numerical methods, the design results of a quasi-TEM MRI probe with high Q and -130.6 dB minimum reflection loaded with a human head model of average relative dielectric constant of $\epsilon_r=64$ [14] for proton imaging at 8 T (340 MHz) will be presented.

II. QUASI-TEM SLOTTED TUBE RESONATOR

The quasi-TEM slotted-tube resonator is schematically shown in Fig. 1-a. This coil is assumed to be lossless and consists of two conductive sheets, containing the biological load of dielectric constant ϵ_r , t thick carrying opposite currents on each side of an inner cylinder of radius r_c . The conductive sheets are connected at the ends with capacitors to the cylindrical outer shield of radius r_b (Fig. 2).

The cross section of the quasi-TEM STR is presented in Fig. 1-b. The angle θ is called the "window angle". The quasi-TEM STR structure generally performs as well as inhomogeneous cylindrical birdcage coils, with the advantages of being easier to construct and operate.

In reference [12], we have shown that for $r_b=2.4r_c$ and $t=0.2r_c$, the optimum field homogeneity for an unloaded

slotted tube resonator (i.e. TEM STR) is obtained for a window angle of 60°. Unfortunately changes introduced by human biological loads with high dielectric constants in the quasi-TEM resonator are not negligible, because of the non homogeneity of the structure. For this reason we adapted our previous numerical tools based on FEM and MoM approaches used in [12] to analyze slotted tube resonator loaded with biological elements.

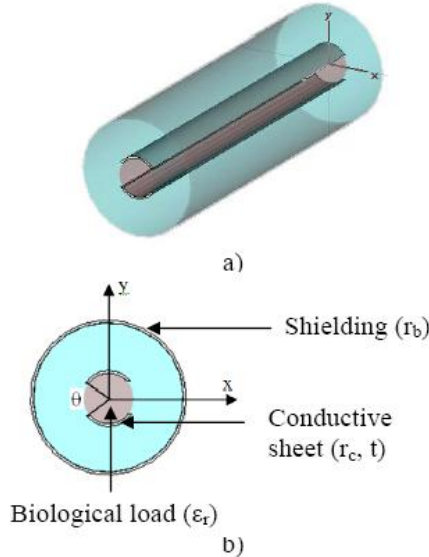


Fig. 1. (a) Quasi-TEM slotted tube resonator and (b) Cross section of the quasi-TEM STR.

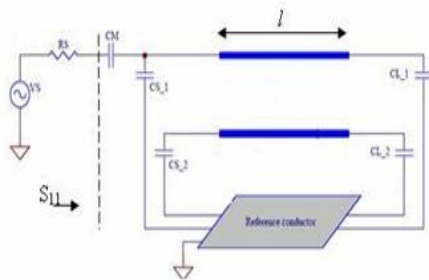


Fig. 2. Schematic circuit of the UHF-MRI probe using quasi-TEM STR resonator.

III. EM-PARAMETERS OF THE QUASI-TEM STR

The electromagnetic properties of the quasi-TEM slotted-tube resonator can be described in terms of its primary parameters [L], [C] and its secondary parameters: the even- and odd-mode characteristic impedances (Z_{0e} , Z_{0o}), effective dielectric constants (ϵ_{effe} , ϵ_{effo}), and the loaded quality factor Q.

where:

$$[L] = \begin{bmatrix} L_{11} & L_{12} \\ L_{21} & L_{22} \end{bmatrix} \quad [C] = \begin{bmatrix} C_{11} & C_{12} \\ C_{21} & C_{22} \end{bmatrix}$$

The inductance matrix [L] contains the self-inductances of the sheets on the diagonal, and the mutual inductances between sheets in the off-diagonal terms.

Matrix [C] accounts for the capacitive effects between the two conductive sheets, characterizing the electric field energy storage in the quasi-TEM STR.

The coefficients for these matrices are obtained by solving a two-dimensional static field problem using FEM [15-16] and MoM methods [17].

For the FEM approach and under FreeFEM environment [18], the solution is obtained by solving the Laplace's equation (Fig. 3-a):

$$\text{div} [\epsilon_r \nabla_i V(x, y)] = 0 \quad (1)$$

subject to:

$V = 1$ volt on the i^{th} conductor's surface.

$V = 0$ on all others conductors.

This solution represents the distribution of the potential V at the different mesh nodes of the structure (Fig. 3-b).

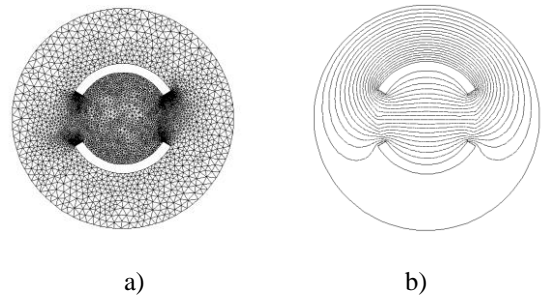


Fig. 3. FEM meshes on (a) and potential distribution on (b).

When the potential V is known, we calculate the i^{th} row of the [C] matrix from the electric charge on each conductor.

$$C_{ij} = \frac{1}{V_0} \oint_{l_j} q_s dl \quad (2)$$

Where $V_0=1$ volt, $q_s = \epsilon_0 \epsilon_r E_N$, l_j represents the contour around the j^{th} conductor and E_N is the normal component of the electric field.

In the high-frequency limit, i.e. the skin depth is sufficiently small such that current flow occurs only on the surface of the conductors, the inductance matrix [L] can be obtained from the matrix [C₀] [12]. The inductance matrix in terms of [C₀] calculated for ($\epsilon_r = 1$) is:

$$[L] = \mu_0 \epsilon_0 [C_0]^{-1} \quad (3)$$

For the MoM approach, the numerical calculations of the EM-parameters of the studied resonator were carried out with LINPAR for windows (Matrix Parameters for Multiconductor Transmission Lines), a 2D software for numerical evaluation of the quasi static matrices for multiconductor transmission lines embedded in piecewise-homogeneous dielectrics [17]. The technique used in the program is based on an electrostatic analysis. In this analysis the dielectrics are replaced by bound charges in a vacuum, and the conducting bodies are replaced by free charges. A set of integral equations is derived for the charge distribution from the boundary conditions for the electrostatic potential and the normal component of the electric field. The method of moments is applied to these equations, with a piecewise-constant (pulse) approximation for the total charge density and the Galerkin technique. LINPAR for windows can analyse arbitrary planar transmission lines and can also analyse any other structure defined by the user.

For our slotted tube-line quasi-TEM resonator, we were obliged to supply the cross section of the structure and all relevant dielectrics characteristics including the segmentation by using our programs in FORTRAN (Figure 4).

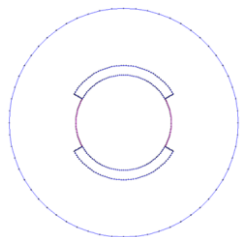


Fig. 4. Segmentation of the charged surfaces of the slotted tube-line quasi-TEM resonator.

When the EM-parameters are determined, it is possible to estimate the resonance spectrum (S_{11}) of the resonator shown in Fig. 2 using our programs based on the transmission line method (TLM).

The MRI probe developed for this article consists of the STR resonator with length l , matching capacitor C_M , and terminating capacitors C_{Si} and C_{Li} ($i=1, 2$).

The loaded quality factor (Q) of the quasi-TEM resonator can be estimated from the reflection-parameter (S_{11}) sweep with frequency [12]:

$$Q = \frac{f_r}{f_u - f_l} \quad (4)$$

where

f_r =the resonance frequency of the circuit,

f_u =3-dB frequency above the resonance frequency, and

f_l =the 3-dB frequency below the resonance frequency.

IV. RESULTS

We applied our modified and coherent FEM and MoM-based numerical tools to the analysis and design of an MRI resonator using quasi-TEM STR. The FEM and MoM approaches make it possible to simulate the performance of a design and decide if a given set of constraints makes it possible to realize the UHF-probe.

To design a loaded MRI probe operating at 8 Tesla (i.e 340 MHz) and using the optimum configuration of the TEM STR (for $\theta=60^\circ$), we analyzed the structure shown in figure 2 with the following set of features:

an inner cylinder radius (r_c) of 36.83mm;

a sheet thickness (t) of (0.2 r_c); and

biological loads of dielectric constants ϵ_r listed in table 1 [19].

Table I: Load properties at 340 MHz.

Load type	ϵ_r [19]
Fat	5,14
Bone-Cortical	13,91
Bone-Cancellous	21,84
Nerve	36,80
White-Matter	41,85
Skin	43,07
Cartilage	44,82
Mixed-GM-WM	49,45
Dura	52,23
Mucosa	52,69
Cerebellum	54,40
Cornea	55,40
Gray-Matter	57,05
Blood	57,50
Tongue	59,64
Muscle	65,57
Vitreous-Humor	68,30
CSF	69,08

Our FEM and MoM approaches were employed as shown in figures 3 and 4 to determine the EM-parameters of the quasi-TEM resonator. As discussed above, the integration of the normal flux over the conductor contours determines the per-unit-length parameter matrices. For instance, table 2 lists the elements of the [L] and [C] matrices for $\epsilon_r=65.57$. This table shows clearly the good coherence between the results obtained by our two numerical approaches for inhomogeneous slotted tube-line.

Table II: Primary EM-parameters of inhomogeneous STR loaded with a biological element of a dielectric constant of 65.57

	$C_{11}=C_{22}$ (pF/m)	$C_{12}=C_{21}$ (pF/m)	$L_{11}=L_{22}$ (nH/m)	$L_{12}=L_{21}$ (nH/m)
FEM	778.9	-723.7	233.0	62.04
MoM	781.1	-743.0	234.4	66.04

In table 3, we present the influence of the dielectric constants ϵ_r at 340 MHz of the biological load on the EM-parameters of the slotted tube-line quasi-TEM resonator. This table with the results obtained for the elements of the matrix [L] listed into table 2 and which does not vary with the biological properties, are essential for the design of inhomogeneous MRI probes operating at 8 T.

First, we designed a MRI probe using unloaded slotted tube-line TEM resonator with the following features: a resonator length, l (with respect to the wavelength in free space λ_0), of 22 cm ($l=0.25 \lambda_0$); a matching capacitor, C_M , with value of 28.63 pF, and source and load terminating capacitors, C_S and C_L , respectively, both with value of 1.38 pF.

For the same length (i.e. $l=22$ cm) of the unloaded MRI probe, we introduced a given biological load with a

dielectric constant (ϵ_r) of table 1 into the MRI resonator and we tuned the matching capacitor C_M , and the terminating capacitors C_{Si} and C_{Li} until resonance. At 340 MHz, the obtained values of these capacitors are given in table 4 for each biological load.

From this table, it appears clearly that the value of the matching capacitor varies between 20 and 30 pF, whereas the value of the source and load terminating capacitors varies between 1 and 2 pF for MRI experiences using the optimum configuration of quasi-TEM STR.

Finally, the simulated frequency responses of S_{11} at the RF port for the designed MRI probe using both an unloaded TEM resonator and a quasi-TEM STR with dielectric constant ϵ_r of 65.57 (for example) are shown in figure 5 using both our programs (TLM) and MATPAR software [20]. Table 5 lists the values of the S_{11} -parameter for MRI probes designed to operate at 340 MHz with and without the biological load.

From figure 5, it appears that the results obtained from our programs using TLM are in very good agreement with those obtained using MATPAR software. Furthermore the biological load introduced into the STR improves the value of the reverse transmission, S_{11} at 340 MHz. Using Eq. 4, Q was estimated to be very superior to 500.

Table IV: Values of the matching (C_M), source (C_S) and load (C_L) terminating capacitors at resonance for MRI experiences using STR.

Load type	C_M (pF)	$C_{Si} = C_{Li}$ (pF)
Air	28.63	1.38
Fat	20.0	1.00
Bone-Cortical	30.0	2.00
Bone-Cancellous	27.5	1.80
Nerve	20.7	1.10
White-Matter	20.0	1.00
Skin	20.0	1.00
Cartilage	30.0	1.00
Mixed-GM-WM	30.0	2.00
Dura	30.0	2.00
Mucosa	30.0	2.00
Cerebellum	30.0	2.00
Cornea	30.0	2.00
Gray-Matter	29.6	2.00
Blood	29.5	1.99
Tongue	29.24	1.91
Muscle	29.86	1.71
Vitreous-Humor	28.1	1.67
CSF	28.82	1.67

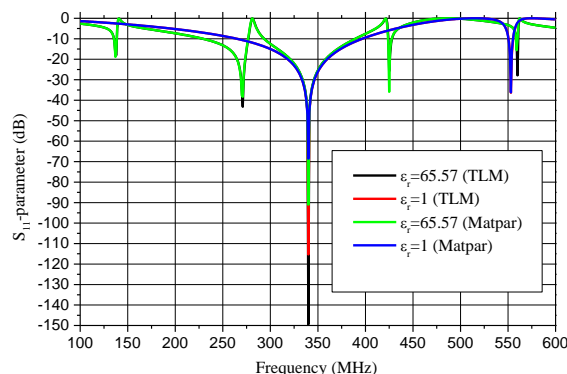


Fig. 5. Reverse transmission, S_{11} , at the RF port of the designed high Q MRI probe using STR.

Table V: S_{11} -parameter obtained using TLM and MATPAR software.

	S_{11} from TLM (dB)	S_{11} from MATPAR (dB)
TEM STR	-115,30	-68,55
Quasi-TEM STR	-149,42	-91,02

All the numerical results shown into this paper were obtained while considering only one biological element which filled completely the quasi-TEM STR volume for the following geometrical parameters:

- a given inner cylinder radius (r_c);
- a sheet thickness (t) of $(0.2 r_c)$;
- a window angle (θ) of 60° ; and
- a resonator length, l (with respect to the wavelength in free space λ_0), of 22 cm ($l=0.25\lambda_0$).

In practice for UHF-MRI proton imaging at 8 T these results remain always valid when the quasi-TEM STR is filled by inhomogeneous biological load (like human head).

In reference [14], 18 tissue types, in addition to air, were identified in the images given in figure 6 in order to obtain a detailed human head structure. These included: blood, bone-cancellous, bone-cortical, cartilage, cerebellum, cornea, cerebro spinal fluid (CSF), dura, fat, gray-matter (GM), mucosa, muscle, nerve, skin, tongue, vitreous-humor, white-matter (WM), and mixed-GM-WM.

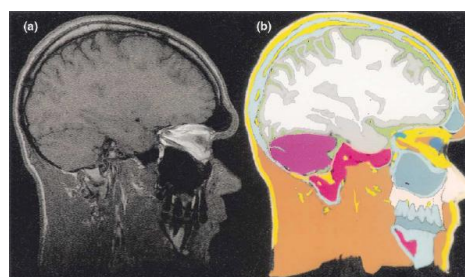


Fig. 6. (a) An MRI image (b) its equivalent anatomically detailed human head model used in [14].

If we consider that the average relative dielectric constant of the human head is 64 [14], then the wavelength inside the head is approximately 11 cm. As a result, the EM-parameters of the quasi-TEM STR loaded with the human head model obtained from our MoM analyses include even- and odd-mode characteristic impedances (Z_{0e} , Z_{0o}) of 88.76 Ω and 10.64 Ω , effective dielectric constants (ϵ_{effe} , ϵ_{effo}) of 1.03 and 22.53 and primary inductive and capacitive matrices ($[L]$, $[C]$) as follows:

$$[L] = \begin{bmatrix} 234.4 & 66.04 \\ 66.04 & 234.4 \end{bmatrix} \left(\frac{nH}{m} \right);$$

$$[C] = \begin{bmatrix} 763.4 & -725.2 \\ -725.2 & 763.4 \end{bmatrix} \left(\frac{pF}{m} \right).$$

Figure 7 presents the simulated frequency responses of S_{11} at the RF port of the UHF-MRI probe using quasi-TEM STR loaded with the human head model. For matching capacitor C_M of 29.8 pF and terminating capacitors C_{Si} and C_{Li} both of 1.75 pF, the probe operates at 340 MHz (proton imaging at 8 T) and has -130.6 dB minimum reflections.

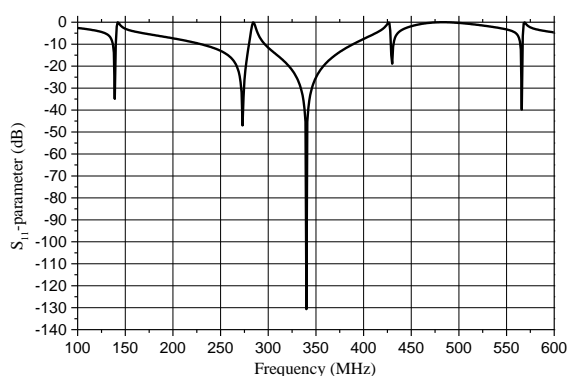


Fig. 7. Reverse transmission, S_{11} , at the RF port of the UHF-MRI probe using quasi-TEM STR loaded with the human head model.

V. CONCLUSION

This article presents the analysis and the design of UHF-MRI probe with high Q, operating at 8 T (i.e. 340 MHz) and using the optimum configuration of the slotted tube-line quasi-TEM resonator.

A finite element method and a method of moments programs have been adapted and employed to accurately characterize the even- and odd-mode characteristic impedances (Z_{0e} , Z_{0o}), effective dielectric constants (ϵ_{effe} , ϵ_{effo}), the primary inductive and capacitive matrices ($[L]$, $[C]$) of the loaded MRI resonator.

These EM parameters of the slotted tube-line can be also used for the design of other microwave components like couplers.

When the EM-parameters have been determined, it is possible to simulate the frequency response of S_{11} at the RF port of the designed quasi-TEM resonator loaded with any biological element.

The quasi-TEM UHF-MRI probe with high Q, operating at

340 MHz and using STR loaded with a human head model of average relative dielectric constant of 64, has -130.6 dB minimum reflections and is easy to construct, inexpensive, and simple to operate.

In addition, the quasi-TEM STR presented here may be constructed to work at different resonances frequencies.

REFERENCES

- [1] PC Lauterbur, Image formation by induced local interactions: examples employing nuclear magnetic resonance, *Nature*, 242, 1973, 190-191.
- [2] P. Mansfield, PK. Grannell, NMR diffraction in solids?, *J. Phys.* 1973, C 6: L422-L426.
- [3] C. E. Garrido Salmon, E. L. G'ea Vidoto, M. J. Martins and A. Tann'us, Optimization of Saddle Coils for Magnetic Resonance Imaging, *Brazilian Journal of Physics*, 36(1A), 2006, 4-8.
- [4] G. Bogdanov and R. Ludwig, A Coupled Microstrip Line Transverse Electromagnetic Resonator Model For High-Field, *Magn. Reson. Med.*, 47, 2002, vol. 47, pp. 579-593.
- [5] R. Ludwi, G. Bodgdanov, J. King, A. Allard, and C.F. Ferris, A dual RF resonator system for high-field functional magnetic resonance imaging of small animals, *Journal of Neuroscience Methods*, 132, 2004, 125-135.
- [6] S. Crozier, LK. Forbes, WU. Roffmann, K. Luescher and DM. Doddrell, A methodology for current density calculations in high-frequency RF resonators, *Concepts Magnetic Resonance*, 9, 1997, 195-210.
- [7] MC. Leifer, Theory of the quadrature elliptic birdcage coil, *Journal of Magnetic Resonance Medicine*, 38, 1997, 726-732.
- [8] S. Bobrof and MJ. McCarth, Variations on the slotted-tube resonator: Rectangular and elliptical coils, *Journal of Magnetic Resonance Imaging*, 17, 1999, 783-789.
- [9] N. Benabdallah, N. Benahmed and B. Benyoucef, Analyzing a resonator for MRI applications, *Microwaves and RF*, 46(11), 2007, 92-98.
- [10] D. W. Alderman and D. M. Grant, An efficient decoupler coil design which reduces heating in conductive samples in superconducting spectrometers, *J. Magn. Reson.*, 34, 1979, 425-433.
- [11] S. Li, Q.X. Yang, M.B. Smith, RF coil optimization: Evaluation of B1 field homogeneity using field histograms and finite element calculations, *Mag. Reson. Imaging*, 1994, vol. 12, pp. 1079-1087.
- [12] N. Benabdallah, N. Benahmed, B. Benyoucef, R. Bouhmidi and M' Khelif, EM analysis of the slotted-tube resonator with circular cross section for MRI applications, *Journal of Physics in Medicine and Biology*, 52, 2007, 4943-4952.
- [13] R. P. Clayton, *Analysis of Multiconductor Transmission Lines* (New York: John Wiley, 2008).
- [14] T.S. Ibrahim, R. Lee, B. A. Baertlein, A. M. Abduljalil, H. Zhu and P. L. Robitaille, Effect of RF coil excitation on field inhomogeneity at ultra high fields: A field optimized TEM resonator, *Mag. Res. Imag.*, 19, 2001, 1339-1347.
- [15] R. Bouhmidi, N. Benabdallah, N. Benahmed and M'. Khelif, Design coupled microstrip resonators for MRI, *Microwaves and RF*, 46(3), 2007, 59-66.

- [16] N. Ben Ahmed, M. Feham, and M. Khelif, Analysis and design of a coupled coaxial line TEM resonator for magnetic resonance imaging, *Journal of Physics in Medicine and Biology*, 51, 2006, 2093-2099.
- [17] A.R. Djordjevic, D.Darco, M.C. Goran, T.K. Sarkan, *Circuit Analysis Models for Multiconductors Transmission Lines* (Artech House, 1997).
- [18] www.Freefem.org
- [19] C. Gabriel, *Compilation of dielectric properties of body tissues at RF and microwave frequencies* (AL/OE-TR-1996-0037, 1996).
- [20] A.R. Djordjevic, M. Bazdar, G. Vitosevic, T. Sarkar, and R. F. Harrington, *Scattering parameters of microwave networks with multiconductor transmission lines* (Artech House, Norwood, MA, 1990).

Table III: EM-parameters of the quasi-TEM STR at 340 MHz.

Load type	ϵ_r	ϵ_{eff0}	ϵ_{eff0}	$Z_{0e}(\Omega)$	$Z_{0o}(\Omega)$	$C_{11}=C_{22}$ (pF/m)	$C_{12}=C_{21}$ (pF/m)
Air	1	1	1	90.11	50.47	51.51	-14.54
Fat	5,14	1.02	2.42	89.21	32.44	98.9	-61.13
Bone-Cortical	13,91	1.026	5.42	88.92	21.68	198.1	-160.1
Bone-Cancellous	21,84	1.028	8.13	88.85	17.71	287.6	-249.5
Nerve	36,80	1.029	13.24	88.80	13.87	456.4	-418.3
White-Matter	41,85	1.029	14.96	88.79	13.05	513.4	-475.3
Skin	43,07	1.029	15.38	88.78	12.87	527.2	-489.1
Cartilage	44,82	1.03	15.98	88.78	12.63	546.9	-508.8
Mixed-GM-WM	49,45	1.03	17.56	88.78	12.05	599.2	-561.1
Dura	52,23	1.03	18.51	88.77	11.73	630.6	-592.4
Mucosa	52,69	1.03	18.67	88.77	11.68	635.8	-597.6
Cerebellum	54,40	1.03	19.25	88.77	11.51	655.1	-616.9
Cornea	55,40	1.03	19.59	88.77	11.41	666.3	-628.2
Gray-Matter	57,05	1.03	20.15	88.77	11.24	685.0	-646.8
Blood	57,50	1.03	20.31	88.77	11.20	690.0	-651.9
Tongue	59,64	1.03	21.04	88.76	11.01	714.2	-676.0
Muscle	65,57	1.03	23.06	88.76	10.51	781.1	-743.0
Vitreous-Humor	68,30	1.03	24.0	88.76	10.31	811.9	-773.8
CSF	69,08	1.03	24.26	88.76	10.25	820.7	-782.6

Design Optimization of the Inner Gimbal for Dual Axis Inertially Stabilized Platform Using Finite Element Modal Analysis

Hany F. Mokbel*, Lv Qiong Ying, Amr A. Roshdy, Cao Guo Hua

College of Mechanical and Electric Engineering,
Changchun University of Science and Technology, Changchun, Jilin, China

ABSTRACT

For the purpose of stabilizing the Line Of Sight (LOS) of Electro-Optical (EO) surveillance and tracking system, a Dual Axis Inertially Stabilized Platform (ISP) is required to isolate the LOS from the carrier disturbances and also for the tracking of the moving target. In this work an Elevation over Azimuth ISP has been designed on the Pro/E software and the first five modes of the Natural Frequency were determined by the ANSYS software. For improving the dynamic performance of the overall system, the design was optimized based on the Finite Element Method (FEM) Modal Analysis. Firstly, the weight of the payload carrying frame was decreased by 35% and the 1st torsional mode of vibration was increased by 22% of the original design. Secondly, the overall dynamic performance of the inner gimbal was optimized and the dynamic performance increased by 75%. Reading in the results declares that the FEM Modal Analysis is an effective tool to optimize the system's dynamic performance to assure the optimal working conditions far from the resonating failure.

Keywords- Design Optimization, Inertially Stabilized Platform (ISP), Modal Analysis.

1. Introduction

The process of aiming, tracking and targeting on a moving target simply requires recognizing the target within the field of view, capture this target, following it, and finally giving the order to fire on the target [1]. This actually requires an optical sensor to obtain the field of view, a signal processing to recognize the target, a control system for the target tracking loop, an Inertially Stabilized Platform (ISP) to achieve continuous and stable Line Of Sight (LOS) between the optical sensor and the target, and finally the weapon system to fire on the target. The orthogonal dual axis stabilized platform is the minimum required set of ISPs to achieve the efficient stabilization [2]. The design process of the ISP is a case sensitive, which means that according to the specified function and requirements of the system, the design should be tailored.

In Electro-Optical Tracking system, the carrier vibration in the Yaw (Azimuth), Pitch (Elevation) and Roll directions induces the LOS sensor to rock and causes the image blurred and affects the pick-up of the target's distance, leads to failing of the tracking performance [3,4]. Therefore, the LOS stabilization technology must be used to isolate the LOS from carrier disturbance in order to

guarantee accurate aiming and tracking of the target at the Inertial Space.

In our work we are seeking to design a dual-axis ISP that is used to stabilize the LOS of surveillance CCD Camera and a Laser Distance Meter carried on a ground vehicle moves on different terrains. The design is following the classical concept of the Elevation over Azimuth rotation. A rotary stage with $\pm 360^\circ$ continuous travel, Direct-drive, slotless and brushless servomotor is used for the Azimuth scanning. A massive structure is used to carry the Elevation gimbals. Another frameless, brushless servomotor is used to rotate the inner gimbal in the Elevation direction. The stall torque and peak torque are 0.2 and 0.82 N.m respectively. The rotation limit for the Elevation direction is -20° : $+90^\circ$. An optical encoder is used with the Azimuth rotary stage while the Elevation servo motor includes the Hall Effect sensors for the positioning feedback. The rotation speed for both directions is 90/s. MEMS gyros are used in both orthogonal directions for angular velocity measurements. Preloaded high performance axial ball bearing is used for supporting the gimbals. The Elevation gimbal consists of the Electro-Optical payload, the payload carrying frame and the front and back hoods that surrounding the inner gimbal and facing the environment. The servo robust PI controller was performed with the C++ and simulated on The MATLAB software. The Original design was done on the Pro/E software as a 3D solid model as shown in Fig. 1, 2. The overall dimensions are 278 x 200 x 256 mm (L x W x H), and an overall mass of 10.2 Kg.

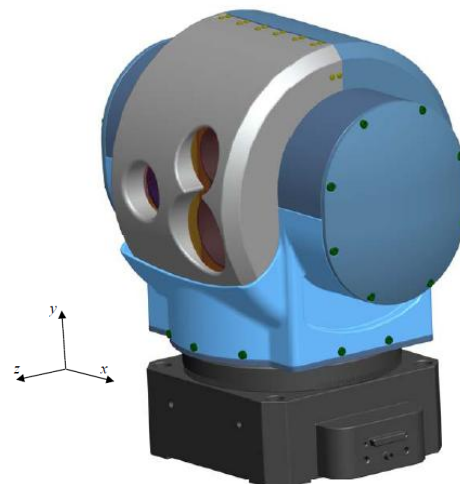


Fig. 1: Dual Axis Inertially Stabilized Platform (ISP).

In the actual working conditions, the *ISP* is subjected to five major loads [5], namely; (1) The gravity load due to the weight of its components, which is a combined loading of bending and torsion, (2) The fatigue load due to the cyclic rotation and loading, (3) Stress due to temperature changing, (4) Air resistance loading, and (5) Shock loads due to terrain's obstacles.

The design had been structurally tested for the static and fatigue loading and found to be conservative, the thermal stresses due to the change in temperature from -20° to $+45^{\circ}$ were found to be within the allowable limits for stress and deflection. The limitation of the design due to the vibration's Natural Frequencies of its components is still the main point under consideration in this work. So, the research is going to optimize the design to have the highest Natural Frequency and minimum weight within the allowable stiffness and strength.

Every mechanical structure exhibits natural modes of vibration (*dynamic response*) [6]. A structural mode can be thought of as a shape and a frequency at which the structural shape resonates. The shape and frequency of a mode are primarily a function of the structure's stiffness, damping and mass distribution. Determining the first few natural modes of vibration for a structure is of great importance to assure that the applied loads or the working conditions frequencies will never meet these Natural Frequencies to avoid resonance and failure. The *ISP* consists of many components working simultaneously. Of them the inner gimbal is the critical one. So, optimizing its dynamic performance will optimize and improve the overall system's dynamic performance.

2. Modal analysis using FEM

Finite Element Method (FEM) is the most frequently used method for computational modal analysis [7]. It is common to use the *FEM* to perform this Modal Analysis because, like other calculations using the *FEM*, the object being analyzed can have arbitrary shape and the results of the calculations are acceptable [8]. The types of equations which arise from modal analysis are those seen in Eigen-systems. The physical interpretation of the Eigen-values and Eigen-vectors those come from solving the system are representing the frequencies and the corresponding mode shapes.

The modal representation of a mechanical structure can be determined analytically if a lumped mass-spring system is concerned [9]. In the general case of a continuous structure, a numerical approximation by means of a *FEM* is made, dividing the structure into a finite number of physical coordinates. The equations of motion describing this approximated system in the time and Laplace domains are given by:

$$[M]\{\ddot{x}(t)\} + [C]\{\dot{x}(t)\} + [K]\{x(t)\} = \{f(t)\} \quad (1)$$

$$s^2[M] + s[C] + [K]\{X(s)\} = \{F(s)\} \quad (2)$$

Where, $[M]$, $[C]$, & $[K]$ represents; mass, damping and stiffness matrices respectively. The solution of these equations leads to an Eigen-value problem that is solved in terms of the modal parameters. The limitations of the

FEM approach lie in the increasing model size required to properly describe complex structures with appropriate detail. This leads to higher model construction and calculation times, but even more important, there remain inherent modeling accuracy limitations, related to the modeling of structural junctions, non-homogeneous elements, complex materials etc [10]. Modal analysis has become a major technology in the quest for determining, improving and optimizing dynamic characteristics of structures.

3. The *ISP*'s FEM Modal Analysis Models

The limited portion of the *ISP*'s design appears clearly to be the inner gimbal that rotates in the Elevation direction (*about x-axis in Fig.1*) and then rotates with its supporting frame in the Azimuth direction (*about y-axis in Fig.1*). So, its Natural Frequency is the most important parameter in controlling the Natural Frequency of the system. The design of the inner gimbal was made to be symmetric about the axis of rotation, small counter weights were used to achieve this symmetry. The inner gimbal consists of the payload carrying frame, the Electro-optics payload, and the front and back hoods. They form about 16%, 64% and 20% of the inner gimbal mass respectively. The *FEM* Modal Analysis Optimization will be carried on three steps; (1) Optimizing the payload carrying frame, (2) The payload carrying frame with the Electro-Optical payload, and (3) The whole inner gimbal with the front and back hoods. Again, the purpose of the design optimization process is to reduce the mass and increase the values of the natural frequencies for the first few modes of vibration (*dynamic performance*). The 3D solid models of these three cases are shown in *Fig.2*.

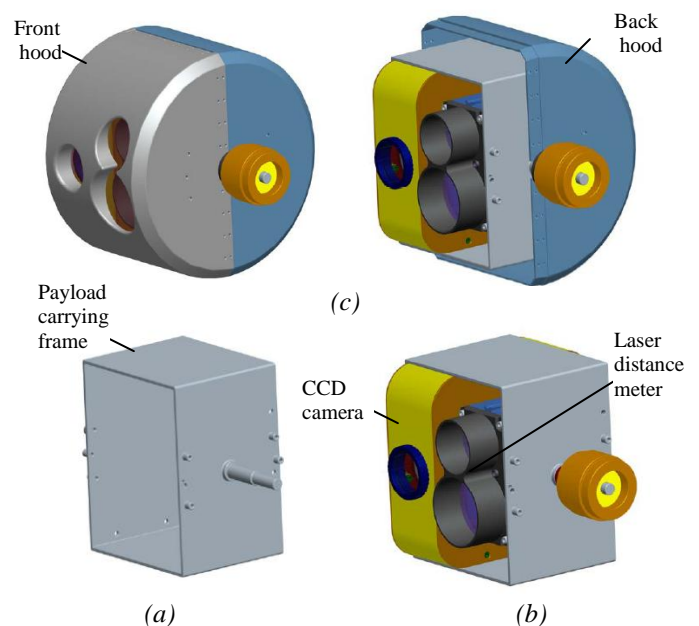


Fig. 2: (a) the payload carrying frame, (b) the payload carrying frame with the Electro-Optical payload, and (c) The whole inner gimbal with the front and back hoods.

The 3D Models of the three Cases were transformed in IGES format and imported into the ANSYS 12.1 software to be analyzed for the first five vibration modes (natural frequencies). In ANSYS this is called Modal Analysis. Many simplifications had to be made to the 3D model to be read by the ANSYS. Of course these simplifications are not of great importance in the analysis but they must be done to declare the model from the very fine details that couldn't be digitized by a non specialized 3D modeling software or may take a lot of time and effort from the solver and restricts the solution ability.

3.1 The payload carrying frame FEM Modal Analysis

In the ANSYS software , the element type was chosen to be solid 45 (Brick 8 node), the material properties for the payload carrying frame was the properties of the common Aluminum alloys with density $2.79355e-9$ tonne/mm³, Modulus of elasticity 73084.4 MPa and Poisson's ratio of 0.33. The solid model was consisted of 237 key-points, 96 lines, 92 areas and 1 volume. The finite element model, Fig. 3.a, was consisting of 10268 nodes and 51873 elements. A free mesh with tetrahedral shapes was applied. The Analysis type was set to modal analysis with the Block Lanczos extraction method, and normalizing the mode shapes to the mass matrix. The boundary conditions were applied to the left and right supporting area on which the bearings are mounted. The problem was solved for the first 5 modes of the natural frequencies (Fig. 3 and Table 1).

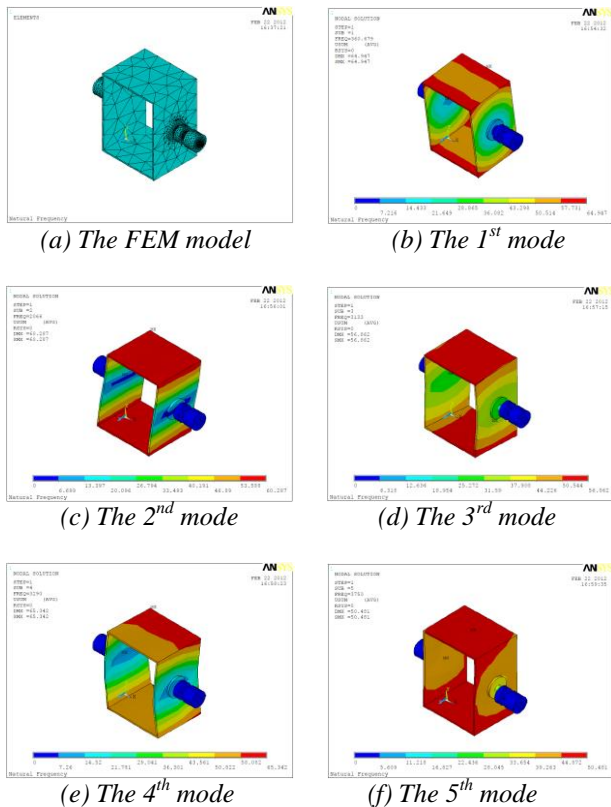


Fig. 3: The FEM model and the first 5 modes of the Natural Frequency for the original payload frame.

The results of the Modal Analysis shows good dynamic performance for the payload carrying frame, where the 1st torsional mode about the axis of rotation appears at

360.68 Hz followed by a large amplitude with the 1st longitudinal bending in x direction at 2066 Hz. This dynamic performance still can be improved by decreasing the mass of the payload frame by digging 4 rectangular holes (95x35x3 mm), 2 in the upper and 2 in the lower side, and another 4 rectangular ones (60x30x3 mm), 2 in the right and 2 in the left side. This lightning the frame about 35% of its original mass, from 0.490 Kg to 0.318 Kg. The modified model's FEM Modal Analysis results are shown in Fig. 4 and Table 1.

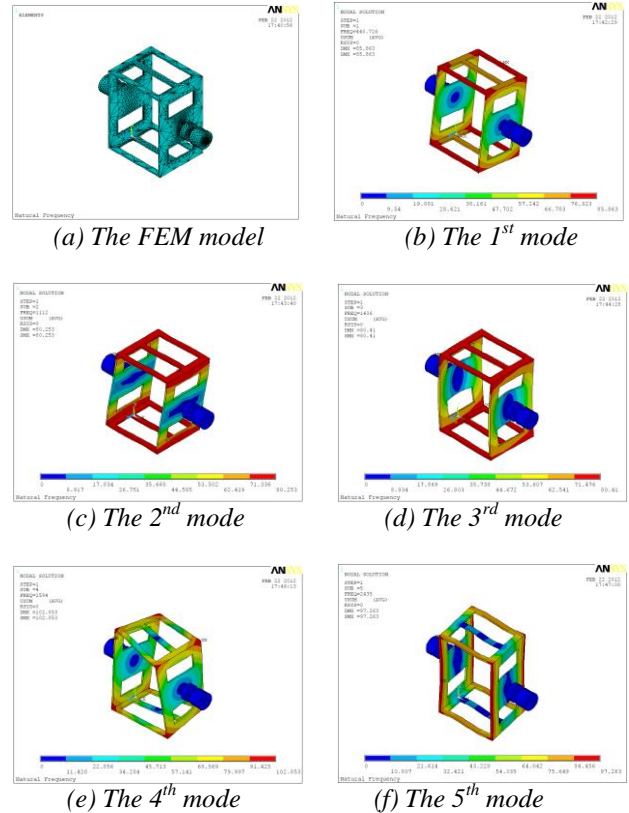


Fig. 4: The FEM model and the first 5 modes of the Natural Frequency for the modified payload frame.

Table 1: Comparison of the original and Modified first five modes of vibration for the payload carrying frame

Mode Number	Natural Frequency				Change %
	Original		Modified		
1	360.68	1 st Torsion mode about x axis	440.73	1 st Torsion mode about x axis	+22.2
2	2066	1 st longitudinal bending in ±x direction	1112.1	1 st longitudinal bending in ±x direction	-46.17
3	3133.2	2 nd Torsion mode about x axis	1406	2 nd longitudinal bending in x direction	-55.13
4	3289.9	Combined longitudinal and lateral bending in x and -z directions	1593.9	Combined lateral bending and rotation in ±y directions	-51.55
5	3750	1 st Vertical bending in y direction	2435.4	3 rd longitudinal bending in ±x direction	-35.06

It is clearly shown that; decreasing the mass by 35% and softening the structure by digging the 8 rectangular holes has obviously changed the modes of vibration's shape and amplitude. As expected, the mass lightning has improved the dynamic performance by increasing the 1st rotational vibration mode to 440.73 Hz

(22.2% higher than the original design). On the other hand, the next 4 modes have dramatically decreased by about 35% to 55% as shown in Table 1. But these results are still very satisfactory for the design.

3.2 The payload carrying frame with the Electro-Optical payload FEM Modal Analysis

In this section the dynamic performance of the payload carrying frame with the Electro-Optical payload will be analyzed. The analysis will be created using the same condition as the discussed above for the payload frame Modal Analysis. The 3D solid model is shown in Fig. 1.b, and the FEM Modal Analysis results for the first 5 natural frequencies are shown in Fig. 5 and Table 2 respectively. Herein, the overall mass of the structure has increased from 0.318 Kg for only the payload carrying frame to 2.29 Kg for both the frame and the payload. Moreover, the overall structure's stiffness is increased due to the tightening of the carrying frame on the payload.

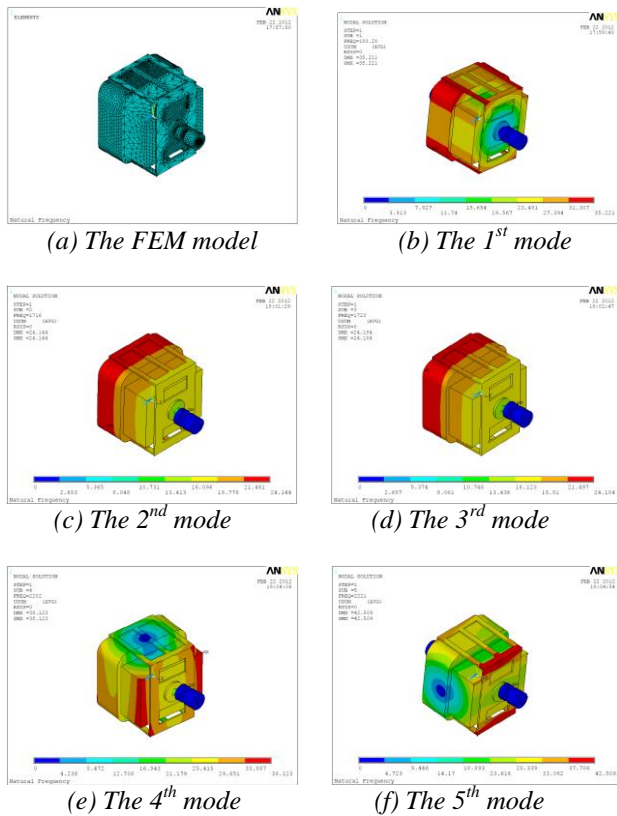


Fig. 5: The FEM model and the first 5 modes of the Natural Frequency for the payload and the payload frame.

Of course, the results are completely different from those shown in the previous section due to the great change in the overall structural stiffness, damping and mass distribution. The amplitude of the 1st torsional mode of vibration about the rotation axis (x-axis) has dropped to 180.29 Hz, while the next four natural frequencies have also dropped, but still having high amplitudes. So, to improve the dynamic performance for this structure, we are going to stiffen it against twisting about the x-axis, by increasing the shaft shoulder diameter in the region connecting the rotating driving shaft with the payload carrying frame body from 12 mm to 16.2 mm for a length

of 9 mm. Although this amendment is not necessary from the point of view of the static and fatigue failure analysis, but it's so beneficial from the point of view of the dynamic performance. The results of the modified structure Modal Analysis are shown in Fig. 6 and Table 2 for the first 5 modes of Natural Frequencies.

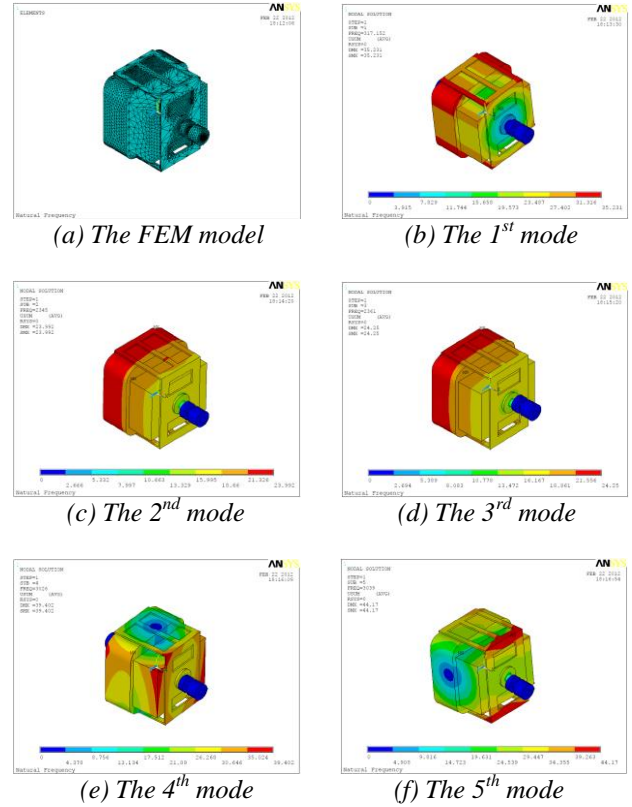


Fig. 6: The FEM model and the first 5 modes of the Natural Frequency for the modified design.

Table 2: The original and modified first five modes of vibration for the payload and the payload frame

Mode number	Natural Frequency			Description
	Original	Modified	Change %	
1	180.29	317.15	75.9	1 st Torsion mode about x axis
2	1716.3	2345	36.63	Combined vertical bending in y direction and longitudinal bending in x direction
3	1722.5	2360.8	37.06	Combined lateral bending in z and y directions
4	2201.6	3025.8	37.44	lateral Bending in ±Z direction
5	2220.5	3039	36.86	vertical bending in ± y direction

After applying the modifications to the structure, the 1st torsional mode of vibration about the rotation axis has been improved to 317.15 Hz, increased about 75.9%, and the following 4 modes of vibration have kept their shapes, but with an increasing in the Natural Frequency of about 37% of the original value. The purpose for optimizing the design to keep its Natural Frequency as high as possible

is to withstand the drop in it when augmented working components are added to the system. As mentioned before, the Natural Frequency of the system is a function of the overall structural stiffness, damping and mass distribution. So, in a working dual axis *ISP*, the two orthogonal rotating gimbals mechanisms are expected to gain a reduced structure's stiffness especially with the all rotating fine structures mounted on it. This will be declared when adding the front and rear hoods to the inner Elevation gimbal structure in the next section.

3.3 The whole inner gimbal with the front and back hoods FEM Modal Analysis

To check the convenience of the design optimization process for the inner gimbal, a final analysis for the whole inner gimbal with the front and back hoods has been made. The 3D solid model is shown in Fig. 2.c. As a result for increasing the 3D solid model size and details, the FEM model size has increased too. Despite the many assumptions and details' simplifications that have been carried out to the design to be handled with the FEM ANSYS software, the size of the FEM model is still too large. It was consisting of 66925 nodes and 242411 elements. The free mesh option couldn't mesh the model because of the fine details, so, the mesh tool with the smart size option was used to refine the mesh. The dynamic behavior of the model is shown in Fig.7 and Table 3. Where, the first 5 Natural Frequency's modes are demonstrated and compared with those without the front and back hoods.

Table 3: The first five modes of Natural Frequency for the whole inner gimbal

Mode number	Natural Frequency	Change %	Description
1	205.29	-0.35.27	Torsion about x axis for the inner components
2	327.01	-80.95	longitudinal bending in - x direction for the front and back hoods
3	545.39	-68.34	Front and back hoods contoured deformation
4	1261.4	-42.71	Optical sights aperture deformation
5	1753.9	-21.01	longitudinal bending in x direction for the inner components

Adding the front and rear hoods has increased the mass with 0.652 Kg to achieve a system's new mass of 2.942 Kg with an increase of about 28.47%. Also, the cylindrical shape of the front and back hoods with the shell structure and Electro-Optical sighting devices' apertures have decrease the assembly's overall stiffness. Leading to new mode shapes depending on the accumulated subassemblies. An expected decrease in the 1st torsional mode shape has happened with consequential decreasing in the amplitude of the following few orders of the natural frequencies. The new obtained Natural Frequency of the 1st order mode of vibration is 205.29 Hz, with a drop of 35.27% from the previously obtained one without adding the front and back hoods. From the conservative design point of view, keeping the 1st Natural Frequency of the inner gimbal higher than 150 Hz is fairly enough to assure the convenient dynamic performance of the inner gimbal subassembly under the probability of some imperfections in the manufacturing process. Hence, the design optimization process of the *ISP*'s inner gimbal using the FEM Modal Analysis has achieved successfully a desired dynamic performance.

4. Conclusion

The system's overall Natural Frequency is depending on the Natural Frequencies of its individual components and subassemblies. The shape and frequency of a natural vibration's mode are a function of the structural stiffness, damping and mass distribution. Due to the accumulation effect of the Natural Frequencies of the different *ISP*'s component, the overall Natural Frequency was decreased from that of the individual ones. To withstand this reduction, the Natural Frequency of the individual components was optimized using FEM Modal Analysis. The payload carrying frame mass decreased by 35%, and its Natural Frequency increased from 360.68 Hz to 440.73 Hz. For the subsystem of the payload and the carrying frame, the 1st Natural Frequency increased from 180.29 Hz to 317.15 Hz. This led to a Natural Frequency of 205.29 Hz for the overall inner gimbal assembly, which is above the desired value of 150 Hz that assures the convenient dynamic performance of the inner gimbal. The FEM Modal Analysis of the *ISP*'s Inner Gimbal has proved to be an effective method for optimizing the design to achieve the least mass and appropriate dynamic performance.

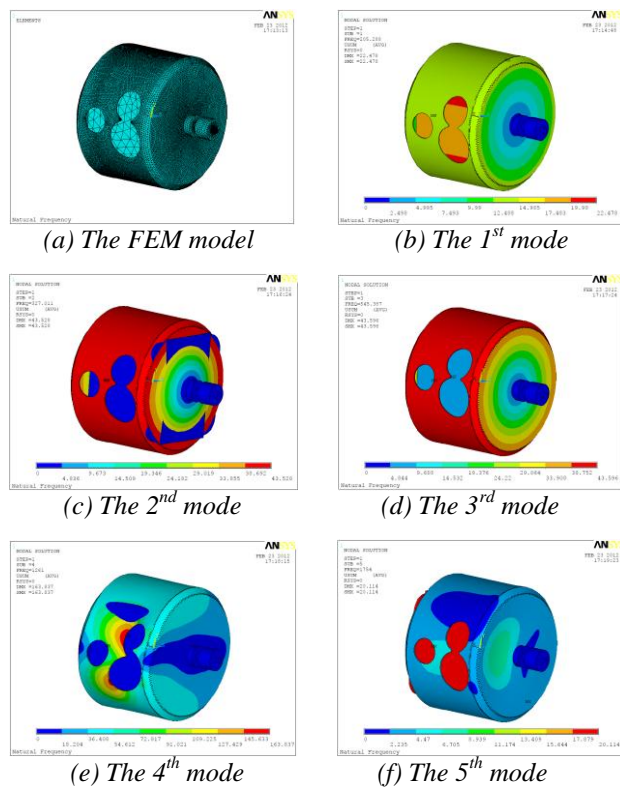


Fig. 7: The FEM model and the first 5 modes of the Natural Frequency for the whole inner gimbal.

References

- [1] M. K. Masten, Inertially Stabilized Platforms for Optical Imaging Systems, Tracking Dynamic Targets With Mobile Sensors, *IEEE Control Systems Magazine*, Vol. 28, 2008, pp. 47 –64.
- [2] J.M. Hilkert, Inertially Stabilized Platform Technology, Concepts And Principles, *IEEE Control Systems Magazine*, Vol. 28, 2008, pp. 26 – 46.
- [3] P. J. Kennedy, and R. L. Kennedy, Direct Versus Indirect Line of Sight (LOS) Stabilization: *Proc. IEEE Transactions on Control Systems Technology*, vol. 11, no. 1, 2003, pp. 3-15.
- [4] Y. Man, J. Gong, H. Chen, Y. Hu, and Y. Jiang, Design and Research of Intelligent Vehicle Strapdown Line-of-Sight Stabilization Platform System: *Proc. IEEE Intelligent Vehicles Symposium*, 2009, pp. 1251-1254.
- [5] Q. Zou, H. L. Ma, Y. H. Hu, and J. W. Ding, The lightweight design of the inner framework of the opto-electronic stabilization platform based on finite element analysis: *IEEE 18Th International Conference on Industrial Engineering and Engineering Management (IE&EM)*, Vol. 1, 2011, pp. 521 –525.
- [6] David V. Hutton, *Fundamentals of Finite Elements Analysis* (McGraw-Hill, NY 10020, 2006).
- [7] Z. Bai, Y. Zhao, W. Ma, and H. Tian, Modal analysis for small satellite system with finite element method: *Proc. 2nd International Symposium on Systems and Control in Aerospace and Astronautics (ISSCAA)*, 2008, pp.1-5.
- [8] H. V. d. Auweraer, Structural Dynamics Modeling using Modal Analysis, Applications, Trends and Challenges: *Proc. of the 18th IEEE Instrumentation and Measurement Technology Conference*, Vol. 3, 2001, pp. 1502 –1509.
- [9] Z. X. yang, Y. Ruixia, et al, Structure Optimal Design of Roll Gimbal for an Aerial Three-Axis ISP Based on FEM Modal Analysis: *3rd International Conference on Measuring Technology and Mechatronics Automation*, Vol. 3, 2011, pp. 373 – 376.
- [10] Z. Zhu, et al, Integrated ADAMS+MATLAB Environment for Design of an Autonomous Single Wheel Robot: *IEEE 35th Annual Conference of Industrial Electronics*, 2009, pp.2253-2258.

An Open Innovation Business Model Based on Collective Intelligence

Prof. A. Maithili¹

Dr. R. Vasantha Kumari²

Mr. S. Rajamanickam³

*(Director, Master of Computer Applications, Pope John Paul II College of Education, Puducherry) India

** (Principal, KWC, Puducherry) India

*** (Research Scholar, Pope John Paul II College of Education, Puducherry) India

ABSTRACT:

It is proposed to have a study on a business model based on Collective Intelligence. Collective intelligence is defined as the ability of a group to solve more problems than its individual members. The idea brings that a group of people can solve problems efficiently and offer greater insight and a better answer than any one individual could provide. The present paper focuses on an open innovative business model based on collective intelligence as well as various forms and roles of collective intelligence in the business applications. A special work is carried out towards the implementation of collective intelligence at different levels of society. Technical concepts like Dialogic, Co-evolutionary, Flow-based, Statistical and Human-machine CI are applied for open innovative business model.

Keywords - Collective Intelligence – Artificial Intelligence – CI Layers – CI Forms – Innovation Business Model – ABCD - CCI.

1. INTRODUCTION:

Collective Intelligence refers to harnessing the power of a large number of people to solve a difficult problem as a group. The idea is that a group of people can solve problems efficiently and offer greater insight and a better answer than any one individual could provide. Collective Intelligence can also be a valuable marketing tool. Collective intelligence is the capacity of human communities to evolve towards higher order complexity and harmony, through such innovation mechanisms as variation-feedback-selection, differentiation-integration-transformation, and competition.

Collective intelligence is about making our application more valuable by tapping into wise crowds. More formally, collective intelligence (CI). Collective intelligence is an active field of research that predates the web. Scientists from the fields of sociology, mass behavior, and computer science have made important contributions to this field. When a group of individuals collaborate or compete with each other, intelligence or behavior that otherwise didn't exist suddenly emerges; this is commonly known as collective intelligence. The actions or influence of a few individuals slowly spread across the community until the actions become the norm for the community.

Collective intelligence is powering a new breed of applications that invite users to interact, contribute content, connect with other users, and personalize the site experience. Users influence other users. This influence spreads outward from their immediate circle of influence until it reaches a critical number, after which it becomes the norm.

Useful user-generated content and opinions spread virally with minimal marketing. Intelligence provided by users can be divided into three main categories. First is direct information/intelligence provided by the user. Reviews, recommendations, ratings, voting, tags, bookmarks, user interaction, and user-generated content are all examples of techniques to gather this intelligence. Reviews, recommendations, ratings, voting, tags, bookmarks, user interaction, and user-generated content are all examples of techniques to gather this intelligence. Second is indirect information provided by the user either on or off the application, which is typically in unstructured text.

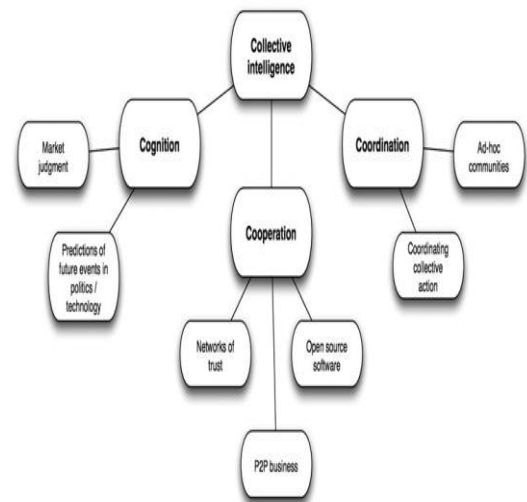


Fig.1 Collective Intelligence

Blog entries, contributions to online communities, and wikis are all sources of intelligence for the application. Third is a higher level of intelligence that's derived using data mining techniques. Recommendation engines, use of predictive analysis for personalization, profile building, market segmentation, and web and text mining are all examples of discovering and applying this higher level of intelligence.

II. COMPUTER SCIENCE AND ARTIFICIAL INTELLIGENCE:

Artificial Intelligence (AI) is the area of computer science focusing on creating machines that can engage on behaviors that humans consider intelligent. The ability to create intelligent machines has intrigued humans since ancient times and today with the advent of the computer and 50 years of research into AI programming techniques, the dream of smart machines is becoming a reality. Researchers are creating systems which can mimic human thought, understand speech, beat the best human chess player, and countless other feats never before possible.

III. APPLICATIONS OF ARTIFICIAL INTELLIGENCE:

1. Deduction, reasoning and problem solving: Early AI researchers developed algorithms that imitated the step-by-step reasoning that humans use when they solve puzzles or make logical deductions. By the late 1980s and '90s, AI research had also developed highly successful methods for dealing with uncertain or incomplete information, employing concepts from probability and economics.

For difficult problems, most of these algorithms can require enormous computational resources most experience a "combinatorial explosion": the amount of memory or computer time required becomes astronomical when the problem goes beyond a certain size. The search for more efficient problem-solving algorithms is a high priority for AI research.

2. Knowledge representation: Knowledge representations are central to AI research. Many of the problems machines are expected to solve will require extensive knowledge about the world. Among the things that AI needs to represent are objects, properties, categories and relations between objects; situations, events, states and time causes and effects; knowledge about knowledge (what we know about what other people know) and many other, less well researched domains. A representation of "what exists" is an ontology (borrowing a word from traditional philosophy), of which the most general are called upon ontologies.

3. Learning: Machine Learning has been central to AI research from the beginning. In 1956, at the original Dartmouth AI summer conference, Ray Solomonoff wrote a report on unsupervised probabilistic machine learning: "An Inductive Inference Machine". Unsupervised learning is the ability to find patterns in a stream of input. Supervised learning includes both classification and numerical regression. Classification is used to determine what category something belongs in, after seeing a number of examples of things from several categories. Regression is the attempt to produce a function that describes the relationship between inputs and outputs and predicts how the outputs should change as the inputs change. In reinforcement the agent is rewarded for good responses and punished for bad ones. These can be analyzed in terms

of decision theory, using concepts like utility. The mathematical analysis of machine learning algorithms and their performance is a branch of theoretical known as computational learning theory.

4. Natural language processing: The natural learning processing gives machines the ability to read and understand the languages that humans speak. A sufficiently powerful natural language processing system would enable natural language user interfaces and the acquisition of knowledge directly from human-written sources, such as Internet texts. Some straightforward applications of natural language processing include information retrieval (or text mining) and machine translation.

5. Motion and manipulation: The field of robotics is closely related to AI. Intelligence is required for robots to be able to handle such tasks as object manipulation and navigation, with sub-problems of localization (knowing where you are), mapping (learning what is around you) and motion planning (figuring out how to get there).

VI. CONSCIOUSNESS AND COLLECTIVE INTELLIGENCE:

If we think of consciousness as the ability to be aware of the external environment and our presence within it, one of the potential advantages of Collective Intelligence would be an increased awareness of more elements of our environment and a wider range of potential options for how to interact with it.

The real power of CI in relationship to consciousness goes deeper. One of the areas that most scientists and thinkers struggle with in the field of consciousness is explaining how it is created. At this point the best we can figure is that it is an emergent phenomenon that arises from the interaction of the comparatively simple elements that underlie it. In the case of a human brain it is the collective interaction of neurons. In the case of a bee hive it is the collective interactions of all the hive's members. The key to how CI enhances consciousness, resides in the mystery of the synapse.

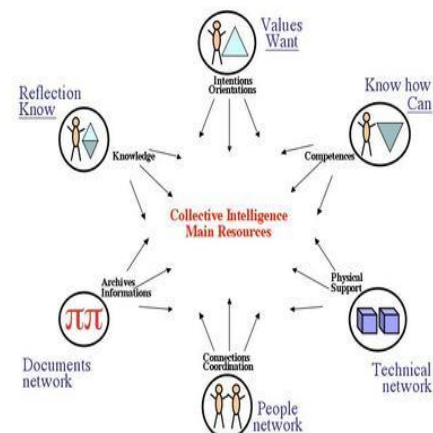


Fig.2 Collective Intelligence Resources.

V. BENEFITS OF COLLECTIVE INTELLIGENCE:

1. Higher retention rates: The more users interact with the application, the stickier it gets for them, and the higher the probability that they'll become repeat visitors.
2. Greater opportunities to market to the user: The greater the number of interactions, the greater the number of pages visited by the user, which increases the opportunities to market to or communicate with the user.
3. Higher probability of a user completing a transaction and finding information of interest: The more contextually relevant information that a user finds, the better the chances that he'll have the information he needs to complete the transaction or find content of interest. This leads to higher click-through and conversion rates for your advertisements.
4. Boosting search engine rankings, the more users participate and contribute content, the more content is available in your application and indexed by search engines. This could boost your search engine ranking and make it easier for others to find your application.

V. FORMS OF COLLECTIVE INTELLIGENCE:

There are many forms, manifestation of CI, and correspondingly, many tribes of its practitioners.

1. Dialogic CI: A diverse group of participants suspend their old mental models and engage in dialogue that values the emergent whole higher than its parts. Variations of this approach include Bohmian dialogue, generative conversation and enlightened communications.

2. Co-evolutionary CI: This form of CI builds on the power of such evolutionary mechanisms generating intelligence over time as trial and error, differentiation and integration, competition and collaboration, etc. Its examples include: ecosystems, sciences, and cultures.

3. Flow-based CI: A group of people become so absorbed in a shared activity that they experience being completely at one with it and one another. Ensembles, high-performance sport teams, astronauts, and others in that state of communion, report on both an enhanced state of autonomy, and collective intelligence.

4. Statistical CI: Individuals thinking and acting separately in large crowds can reach successful conclusion about their collective cognitive, coordination or predictive challenges. Examples include the intelligence of markets and cases popularized in the Wisdom of Crowds.

5. Human-machine CI: This form of CI leverages the synergy of the human mind and its electronic extensions, drawing on the best capacities of both. The "collective"

includes symbiotic networks of humans and computers working together and developing compound capabilities. It can also support all other forms of CI.

VI. LAYERS OF COLLECTIVE INTELLIGENCE:

The five layers that constitute the collective Intelligence will be described in the following subsections.

1. Personal Intelligence: The Personal Intelligence layer deals with enabling users to both upload and access multimedia information submitted to the intelligent services using a range of devices, from mobile phones to PDA's and personal computers. Once multimedia content is submitted to the intelligent services, a series of processing and analysis procedures take place in order to exploit, share and reuse the extracted knowledge. Users and context modeling paradigms will be employed to enable personalized access to the content and knowledge available from the proposed applications. Applications and services based on collective intelligence would be expected to have reached their peak of usage by 2015.



Fig.3 Personal Intelligence

2. Media Intelligence: The first and main step towards efficient "Media Intelligence" deals with automated analysis and semantics extraction from raw visual, textual or audio content and associated metadata. Analysis focuses on each modality in isolation and without taking into account any contextual information or the social environment. However, it does take into account prior knowledge, either implicit, in the form of supervised learning from training data, or explicit, in the form of knowledge driven approaches.

Extracting knowledge from raw data forms a huge research problem on its own so work in this field is expected to advance current existing state-of-the-art techniques for each modality, while a significant effort will be devoted on

- Adapting to the individual domains of interest and intelligence methodologies,
- Handling heterogeneity of unstructured user-contributed resources and
- Supporting interoperability with contextual information.

Three main processes are proposed, text analysis, visual information analysis and speech analysis.

In text analysis process, textual information is of fundamental importance in every scenario where humans are involved. They are used to pass information explicitly to other people. Textual information is pervasive and – with the coming into existence of the Web - its availability is increasing. Intelligent techniques are required to enable automatic Information Extraction (IE) from text and make this information available for further processing.

Visual information, that is, still images and especially video, tend to impose huge requirements on current repositories or social networks in terms of storage or transmission due to the size of the data involved, yet its contribution to the knowledge and intelligence of related applications remains insignificant. Research in disciplines like image processing, pattern recognition and computer vision has been ongoing for decades but satisfactory performance can usually only be achieved in constrained domains, scales and environments.

Speech is a natural, pervasive and efficient means for communication among people. Therefore, it is the privileged modality in many situations where safety and convenience issues require hands- and eyes-free interaction with computers or ask for a direct access to information (no menu navigation, no typing). Its ubiquitous and easy-to-use character makes also speech the primary communication channel in emergency scenarios.

3. Mass Intelligence: Masses of users contribute their knowledge to communities in the Web 2.0. They organize and share media such as images on Flickr, videos on YouTube, bookmarks on Delicious, personal opinions, and others. Within such systems, the users can provide feedback by valuating the content provided and conduct assessments. This can be done, e.g., by participating in discussions and answering questions in a community portal.

Thus, Mass Intelligence combines the information from mass user feedback in order to extract patterns and trends that cannot be extracted by single content items. Facts and trends will be recognized and modeled by interpreting user feedback on a large scale. The key research challenge of Mass Intelligence is the questions whether this mass of users can give new insights that would not be possible by considering the individual.

4. Social Intelligence: Social intelligence results from the monitoring, analysis, recognition, and understanding of the needs and capabilities of individuals and communities from their information usage and communication interaction patterns. Social intelligence delivers social information which may be used to improve other processes.

At its simplest, social intelligence can be seen as a social markup process on actors and communication acts which provides social information as part of the pragmatic dimension of communication. For instance, consider the recognition of “hubs” in emergency situations such as during a hurricane. Providing these well-connected individuals with critical information will reach a broad set of people rapidly with minimal communication requirements, because the hubs are the individuals that spread messages most effectively. Or, consider the identification of authorities. In media intelligence or mass intelligence, content of these users should receive more emphasis and attention.

Watzlawick's communication model serves as the base for deriving the social intelligence layer. Social intelligence consists of three interconnected layers, namely the content layer of communication messages, the meta-layer of communication messages, and the structural information layer derived from social interaction which represents the state of the communication process in a community.

Analysis at the meta-communication layer needs a strong link to mediainelligence: For example, digital audio streams coming to a emergency callcenter may be analyzed for emotions. Recognizing emotions may help in evaluating the urgency of the situation. In another setting, pictures about holiday resorts may be classified according to their emotional appeal. The exact wording of messages contains hints on the social background of the sender, so does the pronunciation of speech.

5. Organizational Intelligence: In contrast to Personal Intelligence, the Organizational Intelligence deals with the sharing of knowledge between the individual members of an organization. As a consequence, the role of Organizational Intelligence is to bring the right piece of knowledge at the right time to the right person of the organization in order to support decision making. This knowledge is not necessarily produced by individuals, but rather by the interaction with Personal, Media, Mass, and Social Intelligence. The persons addressed with Organizational Intelligence can be either within the organization or member of an external organization. Traits of professional organizations such as enterprises and governmental agencies are strong and often legally enforceable rules and boundaries. The associations of persons to the organization or parts of the organization are typically clearly defined such as a person being member of the R&D department, human resources, etc. In addition, also the role is typically known like head of group or silver command in emergency response. In contrast, non-professional organizations are only loosely coupled. The association of persons to the non-professional organization can be fuzzy such as being member of a neighborhood community or a group of friends. In addition, the roles may not be clearly defined in non-professional organizations. For example, for a group of friends that is planning and spending a weekend trip to a foreign city it is typically not

clear or even defined who takes the organizer, leader etc., role in the group.

The goal of Organizational Intelligence is to best support the professional as well non-professional organizations in carrying out its tasks and achieving its goals. To this end, we need to know the actors involved in the organization and how they are organized. We aim at modeling and managing the information flows and decision processes within the organizations. Here, we need to understand the decisions that are to be made, processes to be carried out, and which tasks are to accomplish to reach the goals.



Fig.4 Layers of Collective Intelligence.

VII. COLLECTIVE INTELLIGENCE AT DIFFERENT LEVELS OF SOCIETY:

Given the central importance of collective intelligence, let us take a closer look at this phenomenon. The following examples show how collective intelligence might be applied at a variety of levels: in groups, organizations and communities.

1. Groups: An individual IQ test compares individuals' problem-solving skills with the problem-solving capabilities of others their age. In a similar manner, we could demonstrate the existence of group intelligence by comparing how well various groups solve problems.

In a classic experiment, group intelligence was measured by presenting small groups of executives with a hypothetical wilderness survival problem. All-female teams arrived at better solutions (as judged by wilderness experts) than all-male teams. The women's collective problem-

solving capabilities were enhanced by their collaborative style, while the men's efforts to assert their own solutions led them to get in each other's way. Significantly, the resulting difference in collective intelligence did not occur because the individual women were smarter than the individual men, but rather because of a difference in gender-related group dynamics.

2. Organizations: Can whole organization exhibit intelligence? In November 1997, 750 forest service employees used a technique called Open Space Technology to create, in just three days, a shared vision of change, including action plans. The vision that this group generated covered all facets of forest service activity, and the employees were genuinely excited about implementing the action plans they themselves had developed. This one-time exercise had a lasting effect upon the larger system.

Several organizations and networks, such as the Society for Organizational Learning, research and promote the capacity for organizational intelligence by helping corporations build a culture of ongoing, high-quality dialogue that examines the whole-system dynamics in and around the organization. Just as group intelligence depends on things such as group process, organizational intelligence depends on organizational factors. These factors range from an organizational culture that promotes dialogue to organizational memory systems (files, records, databases, minutes, etc.). They include systems that collect and utilize feedback (learning inputs) from inside and outside the organization, as well as efforts to understand the feedback dynamics (cycles and interdependencies) that govern the organization as a living system. When such things are in place, an organization can create, accumulate and use understandings and solutions which become part of the organization itself knowledge that outlasts the tenure of individual employees and executives. In other words, the organization is learning, exercising its intelligence and applying it in life the same way an individual does.

3. Communities: What would community intelligence look like? Perhaps we see a budding example of it in Chattanooga, Tennessee, which in the early 1980s was reeling from local recession, deteriorating schools, and rising racial tensions. Several dozen citizens formed Chattanooga Venture, an on-going, cross-class, multi-racial organization that involved hundreds of people in an inclusive effort to set and achieve community goals. Of 34 specific city-wide goals set in 1984, 29 were completed by 1992, at which point Chattanooga Venture again convened hundreds of citizens to create new community goals. Among the goals realized through this process was the creation of Chattanooga's Neighborhood Network, which organized and linked up dozens of neighborhood associations to help people co-create a shared future right where they lived, enhancing their community intelligence even further. Chattanooga Venture provides a glimpse of the sort of ongoing collective intelligence we could build to solve problems, to learn together, and to generate a better life right at home.

There are many other inspiring examples of the effort to develop community intelligence. Many of these have been carried out using the approach of Asset Based Community Development (ABCD). This community organizing approach does not directly address a community's problems or treat citizens as clients in need of services from government and nonprofit agencies. Rather, it sees citizens as assets and as co-creators of their community.

ABCD organizers help citizens discover map and mobilize the assets that are hidden away in all the people who live in their community, as well as in the community's informal associations and formal institutions. Those resources, brought out of their isolation and into creative synergy with each other, are then used to realize the community's visions.

VIII. AN OPEN INNOVATION BUSINESS MODEL BASED ON COLLECTIVE INTELLIGENCE:



Fig.5 Collective Intelligence Business Model.

Open innovation and crowd sourcing can utilize the same business model, in that they both apply the collective intelligence system for innovation and problem solving.

The primary consideration pertains to the organization in which the business model is being implemented. When going outside the organization for input from others, it is necessary for managers of companies to make sure the internal organization understands the goals to collect knowledge of the crowd community. It is also just as important to attend to the internal knowledge, and include internal staff in the effort.

Understanding the internal organization and identification of where there are gaps is critical when deploying an open innovation business model.

The second tenet addresses the market segmentation; which customer groups are being targeted and the makeup of each group. Value is determined through the customers' lens; therefore it is important to know which customer to target. The customer that is being targeted is the base for the community that will participate in the collective intelligence system. The market segment defines competitive scope and addresses the strategic question of where does the product compete?. Market segmentation focuses on the division of the markets customer base to create a competitive advantage. Understanding the market segmentation is critical to both the business model, and ultimately competitive advantage. By focusing on the specific customer base, the organizational teams will have a better understanding of the buyer needs and their purchasing behaviors and the differences between the segments. Noting the differences between segments also helps to define the value chain for a competitive advantage. For example, the affluence of the community may require special services that cost more, but also provide greater value for that segment versus another. Market segments also have variables such as product variety, buyer type, channel, and geographic locations. Each variable impacts the breakdown of segments by creating the differentiating factors of the segment.

The third tenet requires that managers understand which parts of the value chain best support the delivery of the offering, and to reach differentiation in the open innovation business model over other business models. The value network connects the internal components of the value chain with the external components and is at the core of the business model. Connecting the components requires support from marketing, sales, support, and finance. Most importantly it requires an understanding of the customer and their needs. All of these factors lead to the development of a competitive advantage. Technology is connected to this principle, that understanding the role of technology in competitive advantage is the value chain. A firm, as a collection of activities, is a collection of technologies. This concept does not ignore the importance of process, but rather it focuses on the importance of technology as the supporting element in the value chain. Technology supports every aspect of the value chain from primary activities to support activities. Knowing where technology supports these activities in the value chain is important, as the CI system requires technology to connect with the community and harvest the information it produces bridging the internal and external knowledge.

The fourth tenet is revenue generation where the primary focus is on the cost structure and the margins associated to a product or service. Managers should ask questions such as how much will a customer pay?; How much will the product or service cost to create?; and How is value created and delivered?. There are several things to consider when looking at cost structure and margins, including (a) price, (b) costs, and (c) margins, which drive

the value proposition. Understanding the cost structure is important in the open innovation business model as it also drives sustainability.

The final tenet in the open innovation business model is competitive strategy. Competitive strategy focuses on creating differentiating factors in the value chain in ways that make them difficult for competitors to replicate. This requires internal focus on key processes and the use of resources to support and sustain the business model.

IX. ROLE OF COLLECTIVE INTELLIGENCE IN AN ORGANIZATION:

The goal of this study is to provide executive leadership and their teams with information about how to use collective intelligence, specifically crowd sourcing and open innovation, to support innovation as a way to create a competitive advantage. The final outcome of the study is presented in the form of a set of five recommendations for how these two types of external knowledge should be implemented to support innovation.

Role 1: Focus on creating an innovative organizational culture, in which experimentation and failure are supported and encouraged.

Role 2: Create a collective intelligence (CI) system by answering the four primary questions: Who is performing the task? Why are they doing it? What is being accomplished? How is it being done?

Role 3: Focus on the utilization of an open innovation business model by developing a plan for and defining the primary tenets of the model, to include (a) value proposition, (b) market segmentation, (c) value chain, (d) revenue generation, and (e) competitive strategy.

Role 4: Map out the four types of innovation: 1) Neutral, 2) Positive, 3) Negative, and 4) Open. An organization should operate in all 4 quadrants, but for market leadership open innovation is the most critical.

Role 5: Understand how the CI system can be deployed into the value chain where internal and external knowledge is leveraged. Define how the CI system will integrate with the current value chain and which parts exist to support the system and which elements need to be developed.

X. ADVANCEMENT OF COLLECTIVE INTELLIGENCE:

While people have talked about collective intelligence for decades, new communication technologies especially the Internet now allow huge numbers of people all over the planet to work together in new ways. The recent successes of systems like Google and Wikipedia suggest that the time is now ripe for many more such systems, and the goal of the MIT Center for Collective

Intelligence (CCI) is to understand how to take advantage of these possibilities.

XI. CCI RESEARCH PROJECTS:

1. Climate CoLab: Using new collaboration tools, to harness the collective intelligence of large numbers of people to address the problem of global climate change.

2. Collective Prediction: To combine human and machine intelligence in flexible new ways to make accurate predictions about future events such as product sales, political events, and outcomes of medical treatments.

3. Deliberatorium: This is exploring how to integrate ideas from argumentation theory and social computing to help large numbers of people enumerate the issues, ideas, and tradeoffs for complex problems with much greater signal-to-noise and much more systematic organization than existing (e.g. forum, wiki, or idea-sharing) technologies.

4. Nonlinear Negotiation: This project is investigating ways to help large numbers of individuals come to agreements about complex problems with many interdependent issues.

5. Enabling Knowledge Management: This project explores how emerging media technologies, including social computing and virtual reality can enable new more powerful modes of knowledge management.

CONCLUSIONS & FURTHER ENHANCEMENT:

1. Collective intelligence is defined as the ability of a group to solve more problems than its individual members.
2. The idea brings that a group of people can solve problems efficiently and offer greater insight and a better answer than any one individual could provide.
3. The applications of Collective Intelligence enhance an innovative business model for an enterprise.
4. Role of Collective Intelligence in an enterprise brings effectiveness.
5. Further work will be carried out towards the Collective Prediction and Nonlinear Negotiation.

REFERENCES:

Journal Papers:

- [1] Collective Intelligence for Competitive Advantage: Crowd sourcing (February 2010) Sean Lane, University of Oregon.
- [2] Collective Intelligence and its Implementation on the Web: Algorithms to develop a collective mental map (January 2011) Francis Heylinghen, University of Brussels.
- [3] The Collective Stance in Modeling Expertise in Individuals and Organizations (December 2009) Gaines B. R, International Journal of Expert Systems

- [4] Selection of Organization at the Social Level: Obstacles and Facilitators of Meta System transactions (July 2005) Heylighen F. & Campbell D.T, The Journal of General Evolution.
- [5] Symbiotic Intelligence: Self-organizing knowledge on distributed networks driven by human interaction (November 2009) Johnson N., Rasmussen S., Smith S., Int. Conference on Artificial Life, MIT Press, Boston.

Books:

- [6] Levy (2010), Collective Intelligence: Mankind's Emerging World in Cyberspace Plenum, New York.
- [7] Linstone H. and Turoff M. (2011), The Delphi Method: techniques and applications, Reading MA: Addison – Wesley.
- [8] Smith J.B. (2009), Collective Intelligence in Computer – Based Collaboration Erlbaum, New York.
- [9] T. O'Really (2008), Design Patterns and Business Models for the Next Generation of Software.
- [10] G.T.Schreiber and H. Akkermans (2006), Knowledge Engineering and Management, MIT Press, Cambridge, MA, USA.
- [11] Olivier Zara (2008), Managing Collective Intelligence: Towards a New Corporate Governance, FYP Edition, France.

Thesis:

- [12] Wen Dong (2011) Thesis Defense: Modeling the structure of Collective Intelligence, MIT Press, Cambridge, USA.
- [13] Ekpe, Basse (2011) Theories of Collective Intelligence and Decision-Making: Towards a viable United Nations Intelligence System, University of Huddersfield.

eHealth model for Himachal Pradesh

Arvind Rehalia , Dr SVAV Prasad

Abstract: This paper presents a electronic health set for HP. This can be a good option for providing medical facilities in rural area of the HP.As internet plays a main role in the infrastructure of India. Internet can be used to enhance medical facilities in the rural India. This paper proposes a complete model for HP using internet. This model can be call as ehealth model for HP.
Key words: PBI,EPR

1. Himachal Pradesh

Himachal is a state in the north of India having area of 55673 km square. Having total population of 6856509. Having Census Villages 20690 and Inhabited Villages 17495

Rural Population 6167805 and urban population 6,88,704. There are twelve district of HP. They are Kangra, Hamirpur, Mandi, Bilaspur, Una, Chamba, Lahul and Spiti, Sirmaur, Kinnaur, Kullu, Solan and Shimla. There are two Medical colleges in HP: RPMC Tanda, Kangra and IGMC Shimla

2. Medical facilities in HP

Average rural Population covered	Type of Health centre
2952	One sub center
13615	One Primary Health Centre
83739	One Community Health Centre

3. Working model

There will be two groups group-1 and group-11. These groups are divided on the basis of distance from the medical college to the concerned district. Group -1 is connected with the medical college kangra and the group -11 is connected to IGMC shimla as it is these district are near to shimla.

Group –I (Medical college kangra)

Kangra,Chamba,Hamirpur,Mandi,Una and Kullu

Group-II(IGMC Shimla)

Shimla,Sirmour,Kinnuaur,Bilaspur,Laul and spiti, and Solan

Block diagram of the system

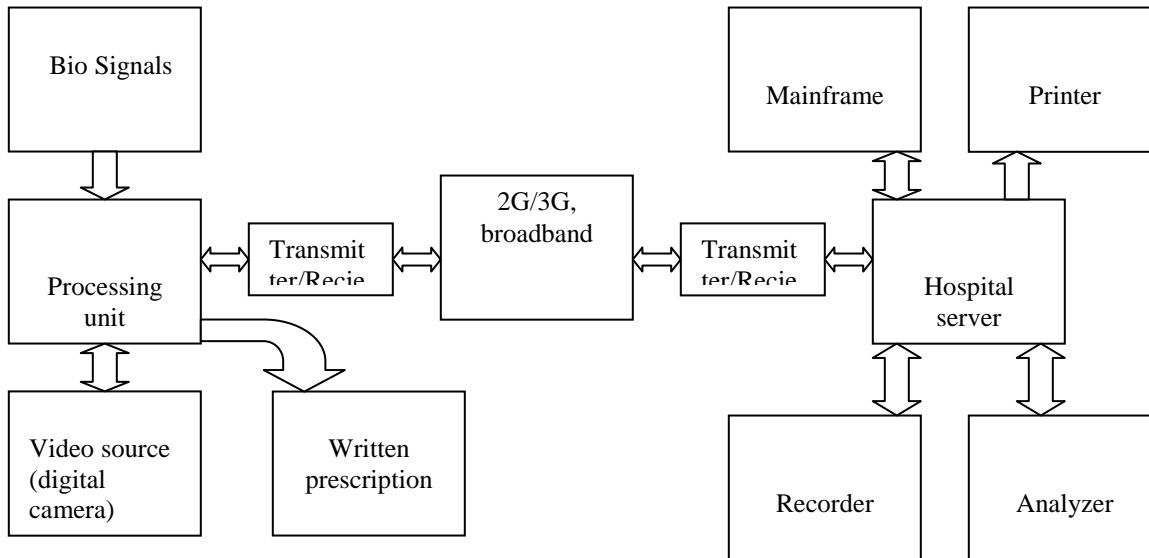


Fig .1

Bio signals

Biosignals are the signals received from the portable biomedical instruments. As we can have ECG,EEG, BP and temperature measurement. We can have this measurements on the computer using various interface.

Video source

In case of 3G we can transmit video signal also which can help the doctor in proper diagnosis. In other case we can send the clip of the patient using MMS.

Printer

Printer is used on both sides at the remote end and the hospital end for the printing purposes.

Analyzer

Analyzer here is general physician who has to diagnose anemia and give the prescription according the patient conditions.

Main frame

Mainframes are mainly a powerful computers used by corporate and governmental organizations for big applications, bulk data processing. here it is used for the storage of data i.e electronic health records.

EPR

An electronic health record (EHR) which is sometimes also called as

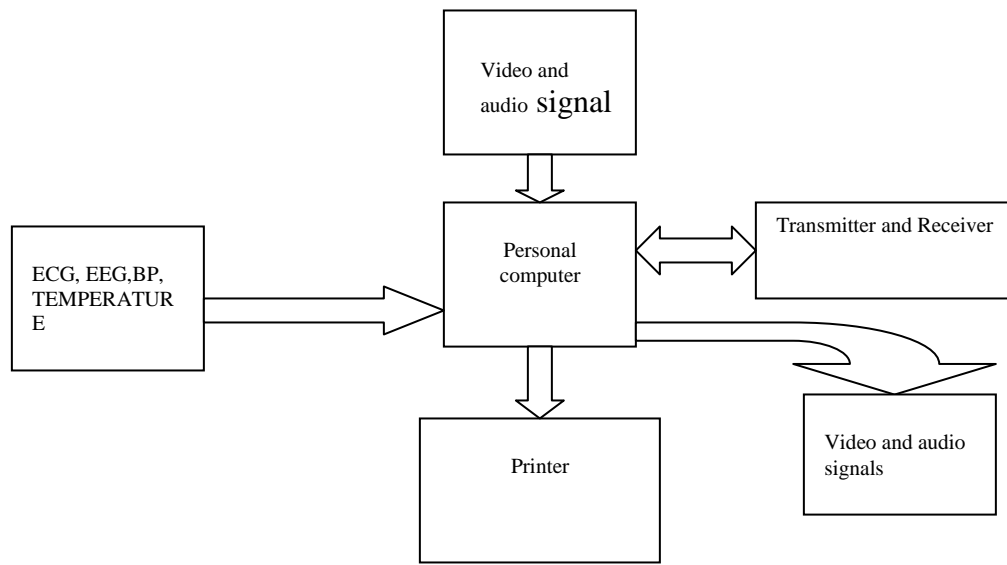


Fig.2

electronic patient record (EPR) is a concept which can be defined as an organised and systematic collection of patient’s health information electronically. It is a record in digital format and is capable of being shared across different health care units with the help of network connected information systems. These records generally include a whole range of data including their basic details or demographics of patient, their medical history, medication status, allergies, laboratory test results, radiology images, vital signs or symptoms of the disease. These records will be available to the doctors on there PCs. EPR will be available in the hospital server room.

Realibility

Realibility is the main requirement of the system. There is lot of error in the measurement system. There is error due human interference We will make the data more reliable. We will make the system more secure so that no body can easily access or disturb the data. The data will remain secure. There will be locks for the security of the whole system. For checking the realibility model is required. Model will be developed according the equipment / instruments used in the whole system.

Security of data

Security of data is the demand of time. Our data should be very much secured .various layers and types of information security control are appropriate to databases, including Access control , Auditing , Authentication , Encryption ,Integrity controls, Backups, Application security. But in this system access control, backups and application security will be used.

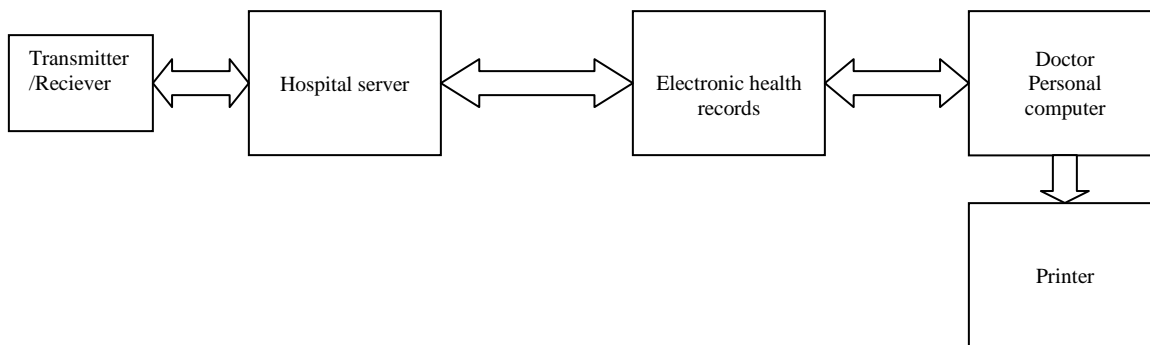


Fig.3

Village end

In village a room and a technical operator will be required. That room is installed with computer. That computer will be interfaced with ECG,EEG, BP machine, printer, webcam, speakers. That computer will be provided internet facilities through landline phone. For making this system more robust we will be having manually operated portable biomedical instruments in this

room. For internet we will having wireless internet connection (dongle) in case of broadband landline system failure. In case of failure in the interface of instruments with computer operator can mail the values of patient reading using manual PBI.

Hospital end

In the hospital a operator will be available in every department. That operator and doctor will receive the mail of the patient operator will upgrade database and the doctor will reply the mail to the operator and the patient. Operator will again upgrade the database. This database will be available on the doctors PC. Doctor can refer the database. The administrator / operator can only make changes in the database.

4 Communication link

Communication modes in the state are

Broadband:

Broadband is available with BSNL in HP. various plans of broadband are available in HP The term broadband refers to a telecommunications signal or device of greater bandwidth, in some sense, than another standard or usual signal or device and the broader the band, the greater the capacity for traffic.

2G

2G (or 2-G) is short for second-generation wireless telephone technology. Three primary benefits of 2G networks over their predecessors were that phone conversations were digitally encrypted; 2G systems were significantly more efficient on the spectrum allowing for far greater mobile phone penetration levels; and 2G introduced data services for mobile, starting with SMS text messages. 2G has been superseded by newer technologies such as 2.5G, 2.75G, 3G, and 4G; however, 2G networks are still used in many parts of the world.

3G

Third generation mobile is also available in various cities of HP. We can use 3G dongle for having internet facilities at village end. 3G or 3rd generation mobile telecommunications is a generation of standards for mobile phones and mobile telecommunication services fulfilling the International Mobile Telecommunications-2000 (IMT-2000). Its services include wide-area wireless voice telephone, mobile Internet access, video calls and mobile TV. To meet the IMT-2000 standards, a system is required to provide peak data rates of at least 200 kbit/s (about 0.2 Mbit/s). However, many services advertised as 3G provide higher speed than the minimum technical requirements for a 3G service. Recent 3G releases, often denoted 3.5G and 3.75G, also provide mobile broadband access of several Mbit/s to smartphones and mobile modems in laptop computers.

5 whole processes

Patient:

Patient has to go to the hospital. He has to fill the form in the hospital. That form is given to the receptionist. Receptionist will give a slip to the patient on which following information will be given.

Registration: Name :Raj Kumar

Mail id: raj.kumar@ehphealth.com

Password: raju

Patient id: 13572

Doctor Id: ca.01tanda@ehphealth.com

operator :op.02tanda@ehphealth.com

The doctor id will vary according to the disease which the patient is suffering from. ehphealth will be the server address hospital have to own.

After his checkup patient does not need to come back to hospital for repeated checkups.

He has to go to his village center. He has to show his slip to the operator. Then village operator will mail the current condition of the patient to the doctor and the concerned departmental operator through the patients mail id. Doctor will study his mail and will reply his suggestion to both patient and the departmental operator through mail. Departmental operator will add all these suggestions to the data base. Village operator can send patients ECG,EEG ,BP, Temperature etc record to doctor if required by doctor.

Departments

There are various type of doctors there id will be given as

General physician

Gp.01tanda@ehphealth.com

Gp.02tanda@ehphealth.com

Gp.03tanda@ehphealth.com

Oprator

op.01tanda@ehphealth

Cardiology

ca.01tanda@ehphealth.com

ca.02tanda@ehphealth.com

ca.03tanda@ehphealth.com

operator

op.02tanda@ehphealth.com

Surgery

Su.01tanda@ehphealth.com

Su.02tanda@ehphealth.com

Su.03tanda@ehphealth.com

Operator

op.03tanda@ehphealth.com

Village

Every center will get one one mail id. The id will be given below and the password will be available with the operator sitting in the village or center

Kangra.takoli@ehphealth.com

kangra.rehan@ehphealth.com

kangra.jassur@ehphealth.com

6 Shannon Law

Normally large bandwidth is required for transmission so that a large amount of data can be transmitted with high speed.. This helps reducing the cost of data transmission. Shannon's law gives the relation between bandwidth B Hz and signal to noise ratio (S/N) is given below by equation

$$C = B \log_2 (1+S/N)\text{bps}$$

Where S is the average signal power in watts and N is the random noise power in watts.

7 Managing system

There will be a centre at the population of 200 person. Every 10 centers will be headed by one person among these ten. One center among 10 centers will be opened in night. That will remain the same. Equipment will be checked every month. Maintaince staff can be called if required.Patient has to pay the nominal fee as per government norms for various tests.

8 Merits

- This system will help us to provide medical facility in every village of the state.
- This system will provide job to opportunity to local people
- This system will help in checking the number of patients of particular disease.
- Patient does not need to visit doctor again and again.

9 Demerits

- Used only for pre and post operative treatments
- If data is wrong then prescription will be wrong
- Some technical knowledge is required to the patient

10 Future scope

This system can be used to make world free from diseases. It can be used to remove epidemics from the society. This concept can be used for developing for improving health sector. This concept can be further converted into virtual hospitals.

References

1. Wikipedia.com.
2. Jim Black, Fernando Koch, Liz Sonenberg, Rens Scheepers, Ahsan Khandoker, Edgar Charry, Brian Walker, Nay Lin Soe (2009) Mobile Solutions for Front-Line Health Workers
3. United Nations Foundation. (2009). MHealth for Development. [Online]. Available: <http://www.unfoundation.org/globalissues/technology/mhealth-report.html>
4. Pindter Medina J, Gonzalez Villarruel, Tovar Corona B 2009 "Proposal of M-HEALTH," J E," Technology de Monterrey, Campus Estado de Mexico. 2009
5. 802.11-wikipedia, <http://en.wikipedia.org/wiki/802.11>.
6. C. Otto, Milenkovic, A., Sanders, C., Jovanov, E., "System architecture of a wireless body area sensor network for ubiquitous health monitoring," Journal of Mobile Multimedia, vol. 1, pp. 307-326, 2006.
7. F. Halsall, Data Communications, Computer Networks and Open Systems, 4th ed: Addison-Wesley, 1996.
8. J. Gutierrez, Callaway, E., Barrett, R., Low-Rate Wireless Personal Area Networks: IEEE Press, 2004.
9. W. Stallings, Wireless Communications and Networks, 2nd ed: Pearson/Prentice Hall, 2005
10. S. Cheekiralla, and Engels, D., "A Functional Taxonomy of Wireless Sensor Network Devices.," in Second IEEE/CreateNet Workshop on Broadband Advanced Sensor Networks. Boston, USA, 2005.

Selection of Effective Control Technique in Analysis of Pulsed Power Loads

D. Rajalakshmi¹, L. Jeniferamla²,

¹(Department of Electrical Electronics Engineering)

²(Department of Electrical and Electronics Engineering)

ABSTRACT

This paper considers the effect of Pulsed Power Loads (PPLs) on micro-grid power systems, such as those on warships, pulsed weapons and recovery systems. A design metric to describe the disturbance of PPLs on power systems is presented. A control strategy utilizes the design metric to reduce the impact of PPL. This strategy is based on identifying the optimal charging profile. Using simulation, it is shown the proposed strategy is highly effective in reducing the adverse impact of pulsed-power loads by reducing the impulse response of capacitor current. This paper outlines an approach to analyze the effects of such loads upon the electric power grid using the proposed technique trapezoidal based control (TBC) and a charging profile is developed for the existing analysis technique limit based control (LBC). Both the control techniques are compared to find the effective approach in reducing the impact of pulsed power loads.

Keywords: Marine vehicles, military aircraft, power quality, energy storage, pulsed power systems.

I. INTRODUCTION

Pulsed Power Loads (PPLs) are of significant interest in navy applications such as future warship development. It is often the case in such loads that the energy storage element is charged over a finite interval of time, and then rapidly discharged [1]. The charging of the energy storage device is an intermittent load which disturbs the power system. Examples of this class of system include high power radars, electromagnetic launch and recovery systems, and pulsed weapons such as rail guns [2], [3]. The power requirements of the charge cycle on such loads can extend into tens of megawatt range with a charge interval on the order of seconds to minutes [4]. The discharge duration is normally much shorter, and is often essentially instantaneous compared to the charge interval wherein energy is accumulated from the power system. These pulses can cause significant disturbance to the rest of the power system [2], [5]. The goal of this work is to minimize the system impact of these Pulsed Power Loads (PPLs) by designing the capacitor current. This work begins with the development of a metric to describe the disturbance caused by a PPL [1]. This metric is then solved to obtain an optimal power trajectory. A state feedback based approach to achieving this desired trajectory is then set forth. The PPL in this system uses capacitor energy storage and is designed to emulate a rail gun application. Through simulation studies, the performance of two types of control strategies such as limit based control (LBC) and trapezoidal based control (TBC) is compared to obtain an effective approach. It is shown that the performance of the proposed control (TBC) is significantly superior to the existing control (LBC) in terms of reducing the impulse response of capacitor current. One method to reduce the impact of pulsed loads is through the introduction of supplementary energy storage devices, such as flywheels [2],[5]. While effective, such an approach clearly adds mass and expense to the system.

Another method to reduce the disruption caused by PPLs is through load coordination. In such an approach, the base load is shed in order to accommodate the pulsed load, so that the total system load remains constant. Such an approach is considered in [5], [7], and [8]. As an alternative to LBC, auxiliary energy storage, and coordination strategies, a trapezoidal-based control (TBC) was set forth. This control was based on using a trapezoidal load profile. The parameters governing the shape of the trapezoid were selected so as to minimize the disruption caused by the pulsed load. However, this work assumed *a priori* that the trapezoidal power profile was the optimal shape. Here using simulation it is proved that the proposed scheme is effective in reducing the impact of PPL by eliminating the impulse response. And a charging profile is developed for the existing control to identify the optimal trajectory.

II. CIRCUIT DESCRIPTION

The circuit topology of the PPL is depicted in Fig. 1. The circuit includes an input filter and a buck converter. The input filter is designed to reduce the high frequency current ripple associated with the buck converter from entering the power distribution system. The buck converter regulates the current i_l so as to charge the energy storage capacitor C_{es} according to the desired profile.

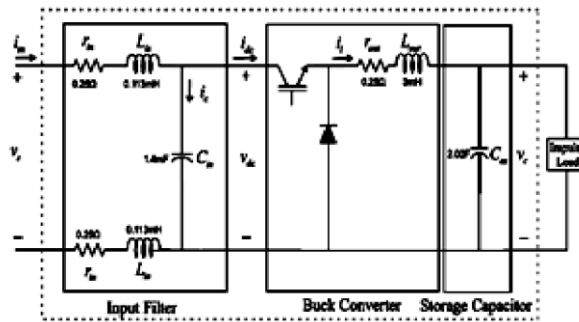


Fig.1.circuit diagram

The pulsed load is that part of the PPL which discharges the capacitor. The storage capacitor used here plays an important role in PPL.the aim is to charge and discharge the capacitor as soon as possible subjected to current and power limits. This paper is entirely concerned with the generation of capacitor current and thereby reducing the impulse response obtained during charging and discharging of capacitor. In the circuit, the energy storage capacitor is emulated so that the energy storage does not need to be physically achieved, and to make it easier to achieve the appearance of a rapid discharge.

III. DESIGN METRIC AND NORMALIZATIONS

The first step in minimizing the system impact of the PPL is to define a metric to describe the disturbance caused by the PPL. A natural choice for such a metric would be related to the bus voltage during and after the PPL charge cycle. However, the problem with such an approach is that the evaluation of the metric becomes not only a function of the PPL, but also of the system, and thereby every component and control parameter therein. Thus, in this work, an alternate metric is proposed, one which only involves the PPL.The disturbance of a PPL on a system is related to its time power profile. This profile is denoted as $P_p(t)$ and is referred to as the power trajectory herein. The power trajectory must satisfy several constraints. First, the power trajectory must be such that the desired energy is obtained. Thus

$$\int_0^{T_p} P_p(t)dt = \Delta E_p^* \quad (1)$$

where ΔE_p^* is the incremental additional energy to be stored in the energy storage element during the charge cycle and T_p is the period of the charge cycle. Note that prior to the charge cycle, the amount of energy stored is not necessarily zero. This initial energy storage is denoted E_{po} .Second, it is desirable that the power trajectory is a continuous function of time. Thus it is required that

$$Pp(t) \in C_0 \quad (2)$$

where C_0 is the set of continuous functions. This facilitates implementation in the presence of parasitics, and also limits the bandwidth of the PPL disturbance on the system. By definition, a pulsed load is an intermittent transient load. Requirement (2) is thus coupled with the requirement that

$$Pp(0) = Pp(Tp) = 0 \quad (3)$$

Finally, it is desired that the system disturbance caused by the trajectory is minimized. In order to quantify this last point, observe that if the PPL were not pulsed, i.e. were a constant, then there would be no disturbance at all. Hence, one philosophy for a disturbance metric is to define the metric in terms of the time rate of change of the power trajectory. To this end, the disturbance metric

$$dp = \sqrt{\frac{1}{T_p} \int_0^{T_p} \left(\frac{dPp(t)}{dt} \right)^2 dt} \quad (4)$$

is proposed. In (4) dP_p/dt , is the time rate of change of power into the PPL. Before proceeding to explore the solution to this problem, it is convenient to normalize quantities of interest so that the results are readily scaled. To this end, the base energy will

$$E_p^\wedge = \frac{(E_p - E_{po})}{\Delta E_p^*} \quad (5)$$

Next, time is normalized to the charge cycle period T_p . Thus, normalized time is defined

$$t^{\wedge} = \frac{t}{T_p} \tag{6}$$

Finally, the base power is defined as

$$P_{p,b} = \frac{E_p^*}{T_p} \tag{7}$$

whereupon normalized power may be expressed

$$P_p^{\wedge}(t) = \frac{P_p(t)}{P_{p,b}} \tag{8}$$

In terms of normalized quantities, (1)-(4) become

$$\int_0^1 P_p^{\wedge}(t^{\wedge}) dt^{\wedge} = 1 \tag{9}$$

$$P_p^{\wedge}(t^{\wedge}) \in C_o \tag{10}$$

$$P_p^{\wedge}(0) = P_p^{\wedge}(1) = 0 \tag{11}$$

$$dp^{\wedge} = \frac{d_p T_p}{P_{p,b}} = \sqrt{\int_0^1 \left(\frac{dP_p^{\wedge}(t)}{dt^{\wedge}} \right)^2 dt^{\wedge}} \tag{12}$$

respectively. The metric function and constraints can be solved to find the optimal power trajectory. The next section of this paper will show this by applying the metric to a desired power profile.

IV. OPTIMAL TRAPEZOIDAL TRAJECTORY

In this section, the metric defined in the previous section will be used to find the optimal power trajectory subject to a trapezoidal power profile. This case is of interest because of its straightforward implementation. The trapezoidal power trajectory is depicted in Fig.2 where t_r^{\wedge} is the normalized rise time, t_f^{\wedge} is the normalized fall time, and P_{pk}^{\wedge} is the normalized peak power.

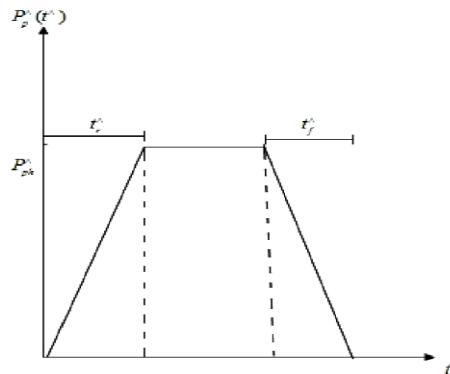


Fig.2.trapezoidal power trajectory

Finding the optimal trajectory involves finding the parameters of the trapezoid which minimize the performance metric. As a prologue to this optimization, it is convenient to define the objective

$$g_p^{\wedge} = d_p^{\wedge 2} \tag{13}$$

Therefore, (12) becomes

$$g_p^{\wedge} = \int_0^1 \left(\frac{dP_p^{\wedge}(t^{\wedge})}{dt} \right)^2 dt \tag{14}$$

Minimization of \hat{g}_p is exactly equivalent to minimization of \hat{d}_p but results in a simpler development. Mathematically, the trapezoidal trajectory may be expressed

$$P_p^\wedge(t^\wedge) = \begin{cases} \frac{P_{pk}^\wedge}{t_r^\wedge} t^\wedge & (t^\wedge \leq t_r^\wedge) \\ P_{pk}^\wedge & (t_r^\wedge < t^\wedge \leq 1 - t_f^\wedge) \\ -\frac{P_{pk}^\wedge}{t_f^\wedge} t^\wedge + \frac{P_{pk}^\wedge}{t_f^\wedge} (1 - t_f^\wedge) & (1 - t_f^\wedge < t^\wedge \leq 1) \end{cases} \quad (15)$$

Substitution of (15) into (9) yields the constraint

$$P_{pk}^\wedge \left(1 - \frac{t_r^\wedge}{2} - \frac{t_f^\wedge}{2} \right) = 1 \quad (16)$$

The time derivative of the trapezoidal profile is given by

$$\frac{dP_p^\wedge}{dt^\wedge} = \begin{cases} \frac{P_{pk}^\wedge}{t_r^\wedge} & (t^\wedge \leq t_r^\wedge) \\ 0 & (t_r^\wedge < t^\wedge \leq 1 - t_f^\wedge) \\ -\frac{P_{pk}^\wedge}{t_f^\wedge} & (1 - t_f^\wedge < t^\wedge \leq 1) \end{cases} \quad (17)$$

Substitution of (17) into (14) yields

$$\hat{g}_p = P_{pk}^{\wedge 2} \left(\frac{1}{t_r^\wedge} - \frac{1}{t_f^\wedge} \right) \quad (18)$$

and combining the constraint (16) and (18) manipulating yields

$$\hat{g}_p = \frac{1}{\left(1 - \frac{t_s^\wedge}{2}\right)^2} \frac{4t_s^\wedge}{(t_s^{\wedge 2} - t_\Delta^{\wedge 2})} \quad (19)$$

where

$$t_s^\wedge = t_r^\wedge + t_f^\wedge \quad (20)$$

Equations (15) can be viewed as a parametric relationship between P_p^\wedge and E_p^\wedge . Eliminating from the parametric relationship yields

$$P_p^\wedge = f_p(E_p^\wedge) = \begin{cases} \frac{3}{2} \sqrt{4E_p^\wedge} \dots \dots \dots (E_p^\wedge \leq \frac{1}{4}) \\ \frac{3}{2} \dots \dots \dots (\frac{1}{4} < E_p^\wedge \leq \frac{3}{4}) \\ \frac{3}{2} \sqrt{-4(E_p^\wedge - 1)} \dots \frac{3}{4} < E_p^\wedge \leq 1 \end{cases} \quad (21)$$

Suggested values for E_{LT}^\wedge and E_{HT}^\wedge range from 0.001-0.05 and 0.95-0.999, respectively. At this point, a new control method derived from the metric to minimize system impact of the PPL has been presented.

V. CONTROL DESCRIPTION

The control description of pulsed power loads can be described by charge discharge control and capacitor current command synthesizer. The charge discharge layer formulates charge and discharge commands and the current synthesizer utilize the desired charge profile and generate the capacitor current accordingly.

5.1. Charge discharge control

The charge/discharge control is presented in [6] shows a modified control used herein. The difference between the control in [6] and this control is the addition of the one-shot or control variable. The inputs to the control are a command to enable the charging of the capacitor, a command to discharge, the filtered voltage across the energy storage capacitor, the desired capacitor voltage for firing, and the current measured voltage of the energy storage capacitor. The outputs of this control are the actual charging status, (high to charge) and the actual discharge status, (high to discharge). Provided that a discharge sequence is not underway and that the capacitor voltage is below the voltage sufficient for firing, setting high will cause the charge status to go high, whereupon the capacitor will be charged. The oneshot flag is high if a single shot is desired and low if it is desired to repeatedly go through the firing sequence as rapidly as possible. If is reset after a charge period, the PPL will repeat the charge and discharge sequence. If the energy storage capacitor voltage is above the threshold when the oneshot flag is enabled, and if is high, a discharge sequence is enabled. During the discharge sequence, the net effect of the control is that the charge status will be disabled for a period of time defined by and the discharge status will be enabled for the last seconds of this cycle. This provides a short period of time when both the charge and discharge cycles are disabled.

5.2. Capacitor current synthesizer

This layer of the control formulates the capacitor current command. The proposed control scheme trapezoidal based control is set forth. Therefore the two control schemes will be considered and compared. The first control scheme charges the capacitor as rapidly as possible subject to current and power limits without including a storage time, the waveform is parabolic. The second control scheme generates the capacitor current which makes use of storage time. The shape of the waveform is trapezoidal. This scheme was suggested in [9]. The second control scheme is the one proposed herein.

5.2.1 Current and Power Limit Based Current Command Synthesizer (LBC)

The current and power limit based current command synthesizer control, is shown in Fig. 3.

The basic philosophy of the control is to charge the capacitor as rapidly as possible subject to a peak capacitor current limit $i_{c,max}$ and a peak power limit $P_{c,max}$. Inputs to this control are the target final capacitor voltage, v_{c1}^* , the measured capacitor voltage, v_c , and the charge status, e_c . As can be seen, the measured capacitor voltage is first filtered by a low pass filter with time constant τ_{inf} and then subtracted from the command. The voltage error is then multiplied by a proportional gain K_{sf} and limited to a dynamic limit $i_{c,limit}$.

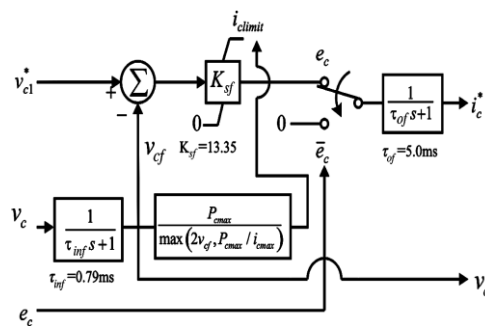


Fig.3.LBC current command synthesizer

Note that K_{sf} is selected to be large enough that the limit is almost always in effect until the point where V_{cf} becomes very close to v_{c1}^* ; after this point the capacitor voltage approaches the target voltage asymptotically. For this reason the target voltage v_{c1}^* is set slightly higher than the minimum voltage to fire, v_{c2}^* . The output of above control is capacitor current, i_c which is derived and then plotted using simulation. The simulation results are shown in fig.4.a,4.b,4.c the parameters such as capacitor current, i_c , load voltage, v_L , input current, i_c , are plotted. The simulation parameters for limit based control are listed in table I

TABLE 1
LBC SIMULATION PARAMETERS

V_{c1}^*	410 V	Target capacitor firing voltage
V_{c2}^*	405 V	Minimum capacitor firing voltage
$P_{c,max}$	13.52 kW	Capacitor power limit
$i_{c,max}$	40.52 A	Capacitor current limit

LBC transient study results (simulation)

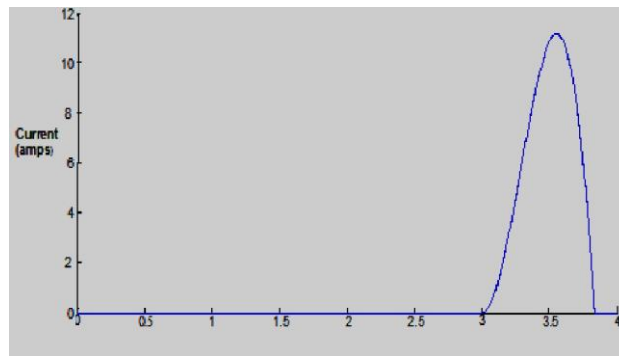


Fig.4.a.capacitor current, i_c .

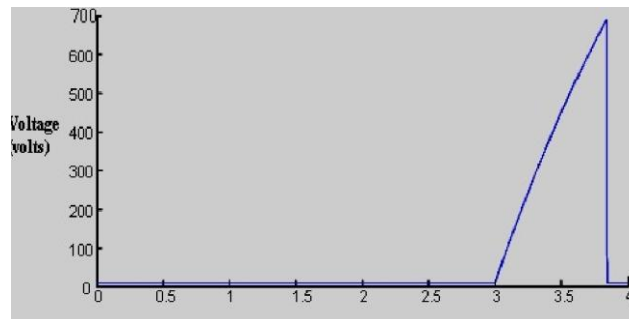


Fig.4.b.load voltage, V_L

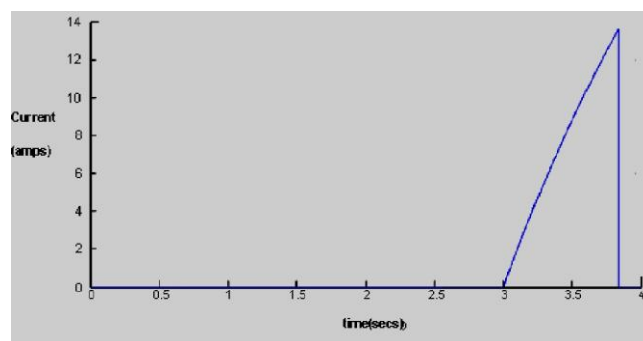


Fig.4.c.GTO current

5.2.2 Trapezoidal Capacitor Current Command Synthesizer (TBC)

The trapezoidal capacitor current command synthesizer control, or trapezoid based control (TBC), is based on (21). Note that this synthesizer results is a trapezoidal power profile; the capacitor current is a trapezoidal waveform. Like the LBC current command synthesizer, the output of this control is i_c^* . The control is shown in Fig. 5.

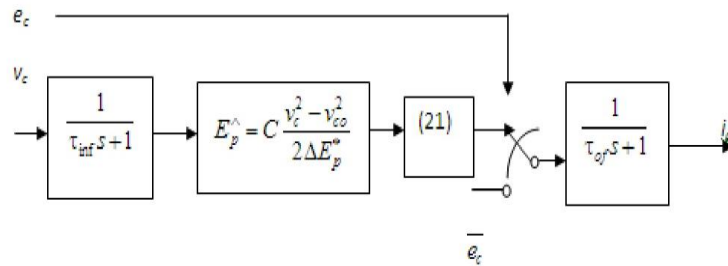


Fig.5.TBC current command synthesizer

The inputs to the control are the measured capacitor voltage v_c and the charge status, e_c . As can be seen, the measured capacitor voltage is filtered and fed into the normalized energy block, equation (5). This normalized energy is then fed into the current command synthesis block determines the preliminary current command. The output of the synthesizer is the capacitor current command, which is the output of the command synthesis block switched by the status of e_c . The control parameters for the TBC are listed in Table II. The control parameters are used in estimation of capacitor current, i_c , mathematically. It is proved that the mathematical calculation is almost equal to the simulation result. it is found that the mathematically calculated value of, i_c is 11.2A.and from simulation results it can be seen that the capacitor current value is 11A.

TABLE II
TBC SIMULATION PARAMETERS

Parameter	Value	Description
T_{inf}	0.79 ms	Time constant of input filter
T_{oj}	5.0 ms	Time constant of output filter
K_c	13.35	Current forward gain

TBC transient study results (simulation)

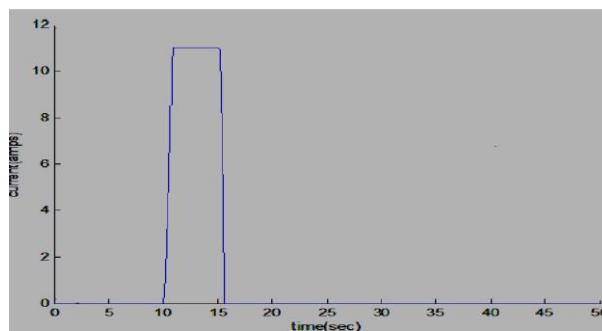


Fig.6.capacitor current

VI. SIMULATION RESULTS

In this section, simulation results for the two control methods are presented. A comparison of the disturbance to the system caused by both controls is presented. First the simulation result for limit based control with the capacitor current of 11A is generated as per the metric described above and the corresponding load voltage of 700V is obtained. Second, a simulation result for the trapezoidal control with a capacitor current of 11A is obtained. These results illustrate that the effect of pulsed power loads is reduced using trapezoidal based control. The impulse response of LBC is eliminated using TBC.

6.1. LBC Study

In this study, the system is initially in steady-state. At $t=3s$, a charging cycle is initiated. The goal is to charge the capacitor from 0 to 162 kJ in 3.8 s. Fig.6.a and 6.b depicts the results for the LBC. Variables depicted include the PPL capacitor current, i_c , the PPL load voltage, V_L , the dc current into the PPL, and the current in the GTO. These variables are all defined in Fig. 4.a, 4.b, 4.c.

As can be seen, the capacitor voltage ramps up nearly linearly in time, although there is a slight inflection at 3.5s, which corresponds to the control switching from the capacitor current limit to the power limit. The bus voltage is seen to gradually droop during the course of the charge cycle; however at the end of the charge cycle the bus voltage rises sharply and a pronounced peak occurs. The input current can be seen to rise nearly linearly until the control enters constant power mode, at which point the input current becomes constant. The peak value of input current is 14 A the current goes down as the power limit takes effect. The results of LBC are purely based on capacitor current derivation. It can be seen that the waveform is parabolic. The storage time is not included, the capacitor is charged in 0.5s and then rapidly discharged in 0.5s, and the load responds when the capacitor charges and discharges. Thus an optimal trajectory is formulated for the existing control.

6.2. TBC Study

Fig.6 depicts the performance of the TBC control. In this case, the capacitor current i_c is a trapezoidal waveform which eliminates the impulse response of the load. The aim of this control is to charge and discharge the capacitor as rapidly as possible with a short storage time. Thus the capacitor is charged in 0.5s and discharged in 0.5s with a storage time of 4s depending upon the application. The sudden dip in load voltage and current is avoided in this case. Due to the above result the sudden drop of voltage and current does not occur. The storage time is introduced in this strategy so that the load is not disturbed during the discharge of current. Thus this method is proved to be superior in eliminating the impulse response and thus it reduces the impact of pulsed power loads. It can be seen that, the capacitor current rises upto 11A as in LBC. The most significant difference between the two strategies in terms of waveform are the capacitor current, i_c . This result shows an advantage of the TBC over the LBC in its ability to function in large scenarios.

VII. CONCLUSION

A metric for describing the impact of PPLs on micro-grid power systems has been presented. This metric has been solved for an optimal power trajectory subject to a trapezoidal power profile in proposed scheme. The existing scheme is solved for a parabolic charging profile. The trapezoidal trajectory has been utilized in an application setting to validate its improvement to the power system. Thus the charging and discharging of an energy storage element will not disturb the power system. The results show that the developed power trajectory of trapezoidal control reduces the impact on the pulsed power loads by eliminating the impulse response as compared to the limit based control.

REFERENCES

- [1] J. Crider and S. D. Sudhoff, "Reducing impact of pulse power loads on microgrid power systems," *IEEE Trans. Smart Grid*, vol.1, no.3, dec 2010.
- [2] S. Kulkarni and S. Santoso, "Impact of pulse loads on electric ship power system: With and without flywheel energy storage systems," in *Proc. IEEE Electric Ship Technol. Symp. (ESTS 2009)*, pp. 568–573.
- [3] J. J. A. van der Burgt, P. van Gelder, and E. van Dijk, "Pulsed power requirements for future naval ships," in *Dig. Tech. Papers 12th IEEE Int. Pulsed Power Conf. 1999*, vol. 2, pp. 1357–1360.
- [4] H. Smolleck, S. J. Ranade, N. R. Prasad, and R. O. Velasco, "Effects of pulsed-power loads upon an electric power grid," *IEEE Trans. Power Del.*, vol. 6, no. 4, pp. 1305–1314, 1991.
- [5] L. N. Domaschk, A. Ouroua, R. Hebner, O. E. Bowlin, and W. B. Colson, "Coordination of large pulsed loads on future electric ships," presented at the 13th Electromagn. Launch Technol. Symp., Potsdam, Germany, May 2006.
- [6] M. Steurer, M. Andrus, J. Langston, L. Qi, S. Suryanarayanan, S. Woodruff, and P. F. Ribeiro, "Investigating the impact of pulsed power charging demands on shipboard power quality," in *Proc. IEEE Electric Ship Technol. Symp. (ESTS 2007)*, pp. 315–321.
- [7] B. Cassimere, C. Rodrijuez Valdez, S. Sudhoff, S. Pekarek, B. Kuhn D. Delisle, and E. Zivi, "System impact of pulsed power loads on a laboratory scale integrated fight through power (IFTP) system," presented at the Electric Ship Technol. Symp., Philadelphia, PA, July 25–27, 2005.
- [8] S. D. Sudhoff, B. T. Kuhn, E. Zivi, D. E. Delisle, and D. Clayton, "Impact of pulsed power loads on naval power and propulsion systems," presented at the 13th Int. Ship Control Syst. Symp., Orlando, FL, Apr. 7–9, 2003, Paper 236.

- [9] M. Bash, R. R. Chan, J. Crider, C. Harianto, J. Lian, J. Neely, S. Pekarek, S. D. Sudhoff, and N. Vaks, "Medium voltage DC testbed for ship power system research," presented at the IEEE Electric Ship Technol. Symp., Baltimore, MD, Apr. 20–22, 2009.
- [10] J. Crider and S. D. Sudhoff, "Reducing power system impact of pulsed power loads," presented at the Electric Machinery Technol. Symp., Philadelphia, PA, May 19–20, 2010
- [11] R. Hebner, "An electromagnetic gun power supply as a component of an electric ship power system," presented at the ASNE High Powered Weapons Syst. Elect. Ships Annapolis, MD, 2004. H. A. Toliyat, S. Talebi, P. McMullen, H. Co, and A. Filatov, "Advanced
- [12] High-speed flywheel energy storage systems for pulsed power applications," in *Proc. IEEE Elect. Ship Technol. Symp.*, 2005, pp. 379–386.
- [13] F. Paulo, B. K. Ribiero, M. L. Johnson, A. A. Crow, and L. Yilu, "Energy storage systems for advanced power applications," *Proceedings of the IEEE*, vol. 89, no. 12, pp. 1744-1756, Dec. 2001.
- [14] J. E. Van Ness, "Response of Large Power Systems to Cyclic Load Variations," *IEEE Trans. PAS*, Vol. PAS-85, pp. 723-727, July 1966.
- [15] K. R. Rao and L. Jenkins, "Studies on Power Systems that are Subjected to Cyclic Loads," *IEEE Trans. PAS*, Vol. 3, No. 1 (Feb.1988), pp. 31-37.
- [16] Electromagnetic Transients Program Rule Book, Electric Power Research Institute, Palo Alto, CA, 1986.

ACKNOWLEDGEMENT

D. Rajalakshmi received her bachelor's degree from Shanmuga college of Engineering, Tanjore, Tamilnadu, India in Electrical and Electronics Engineering during 2000. She received her Master's degree from Alagappa College of Engineering and Technology, Karaikudi, India during 2006. She is currently working as Assistant Professor at the department of Electrical and Electronics Engineering in Kumaraguru College of Technology, Coimbatore, India.

L. Jeniferamla received her bachelor's degree from Maharaja Institute of Technology, Coimbatore, Tamilnadu, India in Electrical and Electronics Engineering during 2010. She is currently doing her master's degree in Power Electronics and Drives at Kumaraguru College of Technology. Her interests include power electronics and electrical machines.

Control Scheme for a UPQC With Integration of Series-and Shunt-Active Filters

N.Ravi Varma¹, K.Neelima²

*(Student, Department of Electrical and Electronics Engineering, KL University, India)

** (Assistant Professor, Department of Electrical and Electronics Engineering, KL University, India)

ABSTRACT

This paper deals with UPQC with integration of series-and shunt – active filters. The UPQC is one of the major custom power solutions capable of mitigating the effect supply voltage sags at the point of common coupling (PCC) or load. A UPQC employs a control method in which the series compensator injects a voltage that leads the supply current by 90° . So that the series compensator at steady state consume no active power. However, the UPQC has some disadvantages. First, there is limitation in rating when using upqc for series compensation.

Second, there is a phase difference between the input and output voltage in proportion to the severity of voltage sags. As a result, it cannot offer effective compensation for voltage drops. This paper discusses the control strategy of the UPQC with a focus on the flow of instantaneous active and reactive power inside the UPQC. The validity of proposed control scheme has been investigated by simulation using matlab/simulink.

Keywords - voltage sag, reactive power, UPQC, power injection, voltage Capacity

I. INTRODUCTION

With significant development of power electronics technology, the proliferation of nonlinear loads such as static power converters has deteriorated power quality in power transmission/distribution systems. Notably, voltage harmonics resulting from current harmonics produced by the nonlinear loads have become a serious problem in many countries to cause power quality decrease. The harmonic currents flowing through the source impedance of the utility supply can cause voltage distortion at the point of common coupling (PCC). This results in a malfunction of control, protection and system monitoring devices.

Loads that operate with a poor power factor show ineffective use of the volt-ampere rating of utility equipments.

To solve these problems, passive power filters have been widely used for a long time[1].although they are simple in structure they can cause unwanted resonance and amplify harmonic currents.

To overcome the disadvantage of passive power filter, research in active power filters has been carried out actively [2]-[5]. Active power filters can be classified as series or parallel according to their system configuration. The combination of series and parallel active power filter is called the unified power-quality compensator (UPQC). The UPQC employs a quadrature injection method which controls voltage sags and offers economical compensation.

The required energy for compensation can be reduced if the reactive power is used when injecting a voltage that has an phase difference with the source current. Therefore, this paper proposed the status of active series and shunt filter to the UPQC for power conditioning in industrial plants and distribution systems, and simulation results are carried out by using matlab/simulink. Moreover, in following sections theoretical analysis and control method are described.

II. UPQC

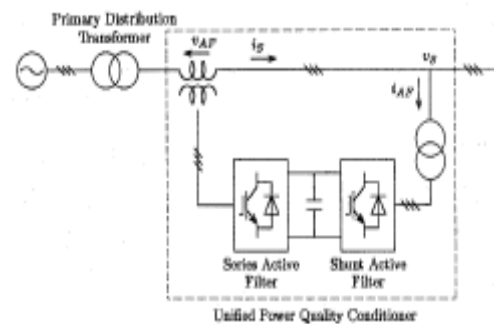


Fig.1. Integration of UPQC with series active and shunt active filter.

Fig. 1 shows the integration of a series active filter and a shunt active filter is referred to as “the unified power quality conditioner”,and is due to its similarity in power circuit configuration to the “upfc”, proposed by Gyugyi[6].

Fig.2. shows a simple configuration of the UPQC. The series compensator controls voltage sag by injecting V_{inj}

which leads the source current by 90° . The parallel compensator performs power factor correction through reactive power compensation, harmonic elimination, and DC link charging

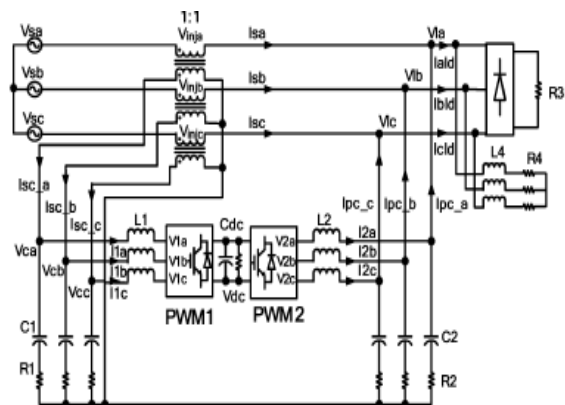


Fig.2. Configuration of the UPQC

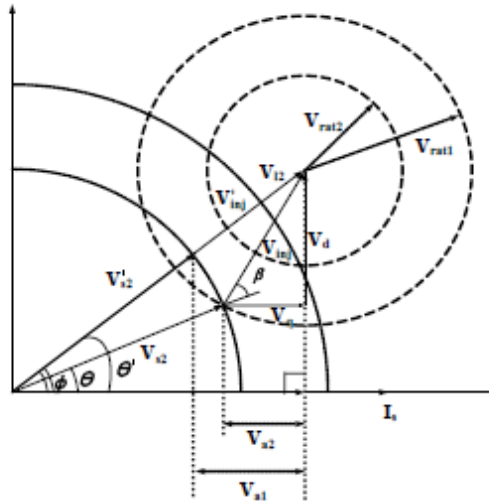


Fig.3. Voltage compensation of reactive power without parallel compensator

Fig.3. shows the energy saving of voltage compensation using reactive power without a parallel compensator. Each of the abbreviations refers to the following:

- V_s : Source voltage phasor
- V_{inj} : Injected voltage
- V_l : Load side voltage phasor
- V_{rat} : Voltage injection limit of series compensator
- I_s : Load current phasor
- V_{a1} : Active power component of in-phase injection voltage V_{inj}
- V_{a2} : Active power component of V_{inj} , injected by a phase advance of β with respect to V_s
- β : Phase advance angle of V_{inj} , with respect to V_s
- θ : Phase angle difference between V_s and V_l without a parallel compensator
- ϕ : Load power factor

The phasor diagram shows that voltage compensation is possible, when β increases, the needed active power decreases with minimum power. Active power $V_{a1}I_s$ is required when V_{inj} is injected in phase with load voltage V_{l2} . If a voltage that leads the source voltage by β is injected, only $V_{a2}I_s$ which is smaller than $V_{a1}I_s$ is consumed. V_{s2} and V_{s2}' are source voltages according to the two cases. However, there is a phase difference between the input and output voltages, a transient state will occur when the source voltage decreases or returns to a normal value. The magnitude of the injected voltage must be larger than that used for in-phase injection.

Therefore, considering the limits of series compensator as shown in Fig.3, voltage compensation is possible V_{inj} which leads the source voltage by β with minimum energy consumption. In this case the problem of a phase difference between input and output voltage will be overcome because β is calculated, and the time to reach a calculated value can be controlled.

In Fig. 3 when β increases, θ decreases and the injected active power decreases. β Depends on the level of voltage sag and the limits of the series compensator, but the power factor θ can be controlled by a parallel compensator. Therefore, if the parallel compensator controls the power factor, the effective power can be reduced.

III. PHASOR DIAGRAM

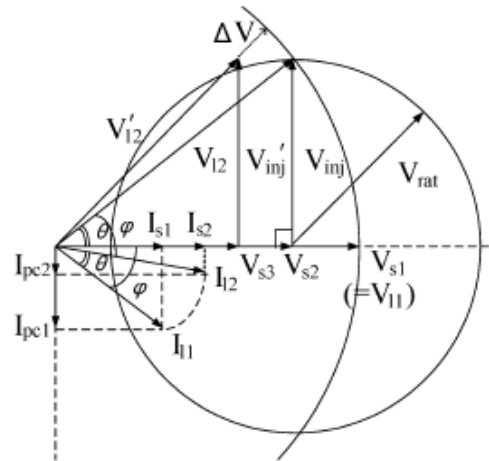


Fig.4. Phasor diagram of UPQC

Fig.4. is a phasor diagram showing the UPQC performance. When the source voltage is the rated voltage V_{s1} , load voltage V_{l1} equals to V_{s1} the load current I_{l1} flows with power factor θ with respect to the output voltage V_{l1} . This current is supplied by the parallel compensator current I_{c1} and source current I_{s1} .

When voltage sag occurs, V_{s1} becomes V_{s2} and V_{inj} injected from the series compensator compensates output voltage which has the same amplitude as V_{s1} . At this moment V_{l1} , the load voltage before the voltage sag, has a phase difference of θ with V_{l2} , the load voltage after compensation. The load current I_{l2} is also supplied by the parallel compensator current I_{c2} , and source current I_{s2} . Voltage compensation is possible with minimum energy.

IV. VA REQUIREMENT OF UPQC

From the phasor diagram of Fig. 4, it can be found that for each phase of fundamental power frequency [7].

$$V_{l1} = V_{l2} = V_{s1} = \text{constant.} \quad (1)$$

If load current are assumed $I_l = I_{l1} = I_{l2} = \text{constant}$, with fundamental power factor equal to $\cos \phi$, active power demand in the load remains the same

$$V_{s1} I_{s1} = V_{l1} I_{l1} \cos \phi = \text{constant} \quad (2)$$

In the case of sag, when $V_{s2} < V_{s1}$, if x denotes the rate of sag ($0 \leq x \leq 1$), then

$$V_{s2} = (1-x)V_{s1} \quad (3)$$

Now, to maintain constant active power

$$V_{s1} I_{s1} = V_{s2} I_{s2} \quad (4)$$

$$I_{s2} = \frac{I_l \cos \phi}{1-x} \quad (5)$$

As the injected voltage is produced in the quadrature with the supply, the resulting load voltage V_{l2} makes the angle θ with the supply V_{s2} .

$$V_{inj} = \sqrt{V_{s1}^2 - V_{s2}^2} \quad (6)$$

$$\frac{V_{inj}}{V_{s2}} = \tan \theta, V_{inj} = V_{s2} \tan \theta, V_{inj} = (1-x)V_{s1} \tan \theta \quad (7)$$

The series VA rating is given by

$$V_{inj} I_{s2} = V_{s1} I_l \cos \phi \tan \theta \quad (8)$$

The parallel compensator current rating is

$$I_{pc} = \frac{\sqrt{((1-x)^2 + \cos^2 \phi - 2 \cos \phi \cos(\phi - \theta))(1-x)}}{(1-x)} I_{l2} \quad (9)$$

The parallel VA rating is given by

$$V_{l2} I_{pc} = \frac{\sqrt{((1-x)^2 + \cos^2 \phi - 2 \cos \phi \cos(\phi - \theta))(1-x)}}{(1-x)} V_{l2} I_{l2} \quad (10)$$

V. PROPOSED METHOD

Compensation with active power and minimum power injection

As shown in Fig.4, when compensation of voltage sag is not possible using only reactive power, when voltage sag occurs, V_{s1} , becomes V_{s2} , and V_{inj} injected from the series compensator voltage rating V_{rat} and voltage sag V_{s2} determine whether the active power will be used or not. Sags of all ranges can be compensated for using only reactive power. In this case, $\beta = 90^\circ$, injected voltage from the series compensator V_{inj} is

$$V_{inj} = \sqrt{V_{l2}^2 - V_{s2}^2} \quad (11)$$

If $V_{rat} < \sqrt{V_{l2}^2 - V_{s2}^2}$, the level of voltage sags V_{s2} must be consider.

$$V_{inj} = V_{rat} \quad (12)$$

$$\beta = \pi - \cos^{-1}((V_{s2}^2 + V_{inj}^2 - V_l^2) / 2V_{s2}V_{inj}) \quad (13)$$

$$V_{inj} = \sqrt{V_{l2}^2 + V_{s2}^2 - 2V_{l2}V_{s2} \cos \theta} \quad (14)$$

The active and reactive power of the series compensator is as follows:

$$P = V_{inj} I_{s2} \cos \beta \quad (15)$$

$$Q = V_{inj} I_{s2} \sin \beta \quad (16)$$

The series compensator is able to compensate with minimum active power and maximum reactive power [7],[8].

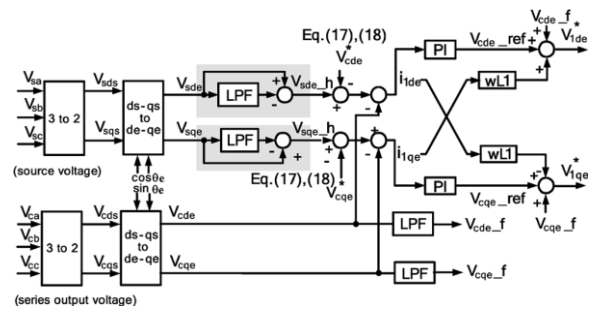


Fig.5. Synchronous reference frame controller for a series active compensator.

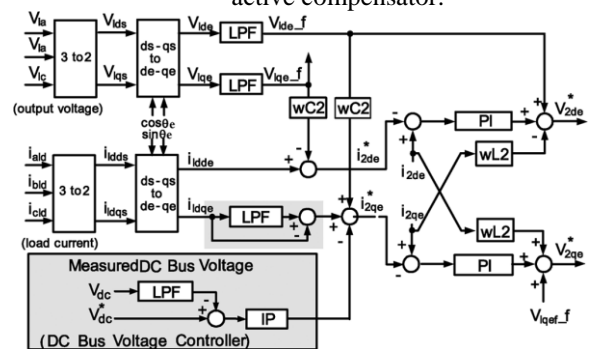


Fig.6. Synchronous reference frame controller for a parallel active compensator.

Fig.5 and 6 show the control block diagram of the series compensator and parallel compensator in synchronous reference frame. Series compensator is the implemented voltage control scheme that receives three phase input and output voltage and supplies reference [6][7].

Three phase input voltage is transformed to a stationary reference frame, and to the synchronous reference frame, which is through HPF (1-LPF). Harmonics are separated, and a reference for harmonics compensation is provided. Through PI control of reference of compensation of input voltage harmonics and EQ (17,(18)) controlling portion of reactive and active power and feedback of output voltage, reference of series compensator is provided.

$$V_c^* d^e = V_{rat} \sin \beta \tag{17}$$

$$V_c^* q^e = V_{rat} \cos \beta \tag{18}$$

$$V_{inj}^2 = (V_c^* d^e)^2 + (V_c^* q^e)^2 \tag{19}$$

$$\beta = \arctan(V_c^* d^e / V_c^* q^e) \tag{20}$$

Cut-off frequency of source voltage and output voltage of serial converter are 5Hz, and 100Hz, respectively. PI gains are 1, 150. Parallel compensators are implemented using a current control scheme that receives load voltage, current and supply reference The load current is transformed to the stationary reference frame, the synchronous reference frame, which is through the HPF (1-LPF). Harmonics are separated, and a reference for harmonics compensation is provided.

Cut-off frequency of load voltage and current are 100Hz, and 100Hz, respectively. PI gains are 1.23, 150. Additionally, through the feed-forward term of $\omega L2$ and $\omega C2$, decoupling between d axis and q axis is possible. The IP controller for DC voltage control is used.

Fig. 7 shows the flow chart of series compensator control

VI. SIMULATION RESULTS

The proposed algorithms were studied by simulation tools ACSL (Advanced Continuous Simulation Language).

System parameters are shown in Table. 1. and Fig 8 shows the simulink model of system implementation

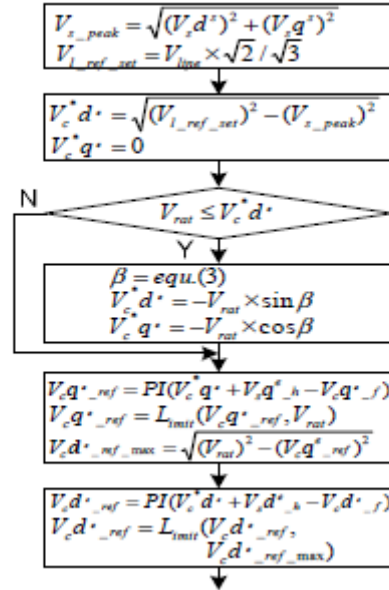


Fig.7. Flow chart of series compensator control

Table.1. SYSTEM PARAMETERS

Parameters	Value
Source Voltage (V_{sa}, V_{sb}, V_{sc})	220[V],60[HZ]
Line Impedance (L_s)	0[μ H]
DC-link Capacitor (C_{dc})	6800[μ F]
DC-link Voltage (V_{dc})	400[V]
L_1	0.35[mH]
L_2	1.3[Mh]
R_3	25[Ω]
R_4, R_5	10[Ω],5mH
C_1, R_1	50[μ F],1[Ω]
C_2, R_2	50[μ F],1[Ω]

Figure .8 shows the simulation diagram of the implemented system.

From Fig10 to Fig 11. Show the simulation results of the UPQC In the simulation, is the input voltage, is the input current, is the output voltage, and is the active power and reactive power of the series compensator.

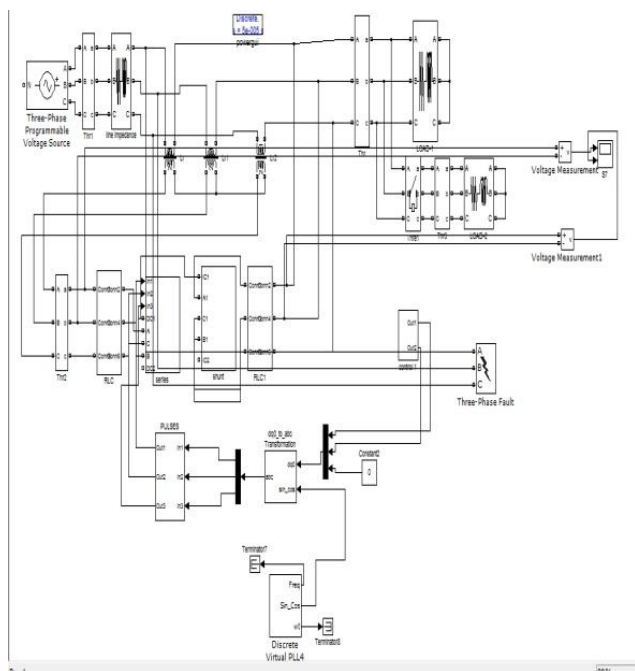


Fig.8. Diagram of test system with UPQC

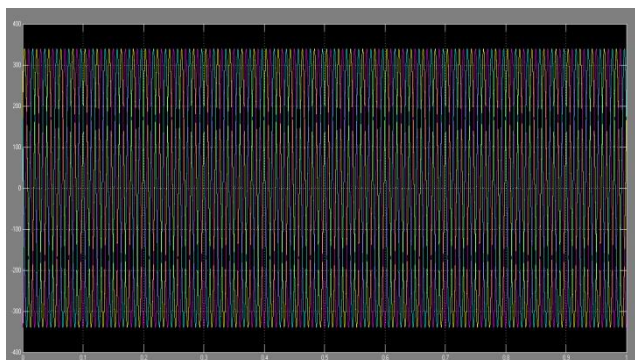


Fig.9. Output load voltage fully compensated

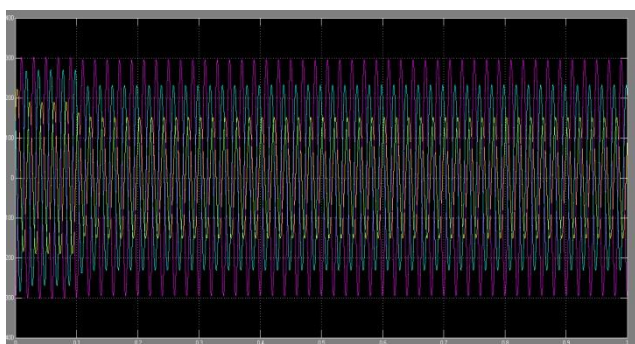


Fig.10. Source Voltage with fault

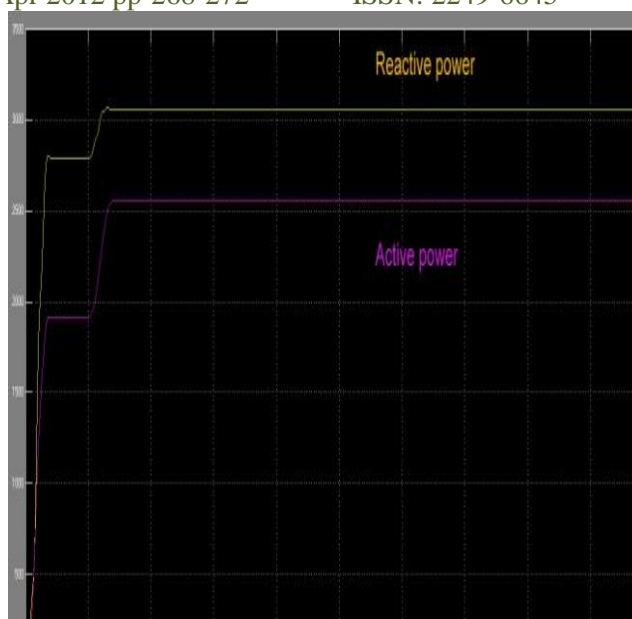


Fig.11.Reactive and Active power

Despite voltage sags, the output voltage is controlled to have constant magnitude. This is because the injected voltage from the series compensator is adequate to maintain the output voltage, and the transient state of the output voltage exists because of the phase difference of the input and output voltage.

VII. CONCLUSION

This paper discussed the control methods for a UPQC. The conventional UPQC-Q cannot compensate for the voltage sag effectively with limitations on the rating of the series compensator and a phase difference between the input and the output voltage. When there are limitations on the rating and a phase difference, the proposed control scheme can compensate for the voltage sag effectively and economically by using minimum active power. The control algorithm and mathematical models were proposed, and then simulation is done. Further we can replace RL load with ac induction motor and simulation can be done.

REFERENCES

- [1] H. Akagi, "New trends in active filters for power conditioning," IEEE Trans. Ind. Appl., vol. 32, no. 6, pp. 1312-1322, Nov./Dec. 1996.
- [2] J. Allmeling, "Control structure for harmonic compensation in active filters," IEEE Trans. Power Electron., vol. 19, no. 2, pp. 508-515, mar. 2004.
- [3] B. Singh, K. Al-Haddad, and A. Chandra, "A review of active filters for power quality improvement," IEEE Trans. Ind. Electron., vol. 46, no. 5, pp. 960-971, oct. 1999.
- [4] H. Fujita and H. Akagi, "The unified power quality conditioner: The integration of series- and shunt-active filters," IEEE Trans. Power Electron., vol. 13, no. 2, pp. 315-322, mar. 1998.
- [5] Li, B.H., Choi, S.S., Vilathgamuwa, D.M., "A New Control Strategy for Energy-Saving Dynamic Voltage Restoration," Power Engineering Society Summer Meeting, 2000. IEEE, Volume 2, 16-20 Jul. 2000, 1103-1108.
- [6] B. Han, B. Bae, S. Beak, and G. Jang, "New configuration of UPQC for medium-voltage application," IEEE Trans. Power Del., vol. 21, no. 3, pp. 1438-1444, Jul. 2006.
- [7] Woo Cheol Lee, Dong Myung Lee, "New Control Scheme for a Unified Power Compensator-Q With Minimum Active Power Injection," IEEE Trans on power delivery. Vol. 25, no. 2, April. 2010.

Enhancement of Vehicular Ad-Hoc Networks Using Vehicle Platoon Aware Data Access

P.AGITH

FINAL ME-COMM SYSTEMS SRI SHAKTHI INSTITUTE OF ENGG AND TECHNOLOGY,
L&T BYPASS, COIMBATORE.

ABSTRACT:

Vanets(Vehicular Ad hoc Networks) is used for communicating data between vehicles and with roadside infrastructures. Due to high mobility of vehicles the topology changes dynamically which degrades the performance of data access in VANETs. To overcome this problem, we use Vehicle Platoon Aware Data Access solution in Vehicular Ad - Hoc Networks. Here vehicles use a part of their buffer to replicate data for other vehicles in the same platoon to share data with them. If a vehicle leaves a platoon, it prefetches the interested data in advance and transfers it to other vehicles so that they can still access the data. To improve the data access performance in VANETs, a vehicle platooning protocol is configured to recognize platoon formation and to predict platoon splits. Next a data management part is configured to lead platoon members to replicate and prefetch the most interested data so that both data availability and data access performance can be achieved. Simulation results display that vehicle platoon aware data access can efficiently improve the data access performance in vehicular Ad - Hoc networks.

INTRODUCTION:

Innovations in low- cost wireless connectivity together with peer - to - peer co - operative systems is transforming next generation vehicular ad hoc networks. Inside the moving vehicles both drivers and passengers are able to get and share their interested data such as news, video clips, music [1]. But due to high vehicle mobility, the topology of VANETs dynamically changes which results frequent disconnections. Thus,data access performance in vehicular ad hoc networks is lower compared to other conventional wired networks.

To improve the data access performance and to reduce the effect of intermittent connectivity, data replication has been widely used nowadays[2]. With data replication we can increase the data availability and reduce the query delay if there is enough memory space available in the vehicles. To connect vehicles with road side infrastructure easily and quickly and to get the data, the data must strategically placed. Also the contact time of the vehicles may not be long enough to transmit all the data items. For data replication nodes need to transmit data from other nodes and which will result in huge bandwidth and power cost for big volume of data. With these issues we do not expect that nodes in VANET such as vehicles or in - vehicle mobile devices and sensors would be able to replicate all the data items in the network. Thus, we need to design a new fast and convenient data access solutions for VANET.

Our solution is based on vehicle platoon [3] in VANETs, where vehicles form a group while in motion. Vehicles can contribute part of their buffer to replicate and share data for other vehicles, if they move as a relatively stable platoon. Cooperative replication can reduce data redundancy in the same platoon by which more data can be stored in the same platoon reducing the data access delay and improving the data availability. However some vehicles may depart from the platoon and the data replicated by the vehicle will not be available for other nodes in the same platoon. To rectify this problem, the departing vehicle should prefetch its most interested data and transfer it to other platoon members. For this vehicles should be able to detect the split process in advance so that they can prefetch and transfer the data.

Here we use Vehicle Platoon Aware Data Access solution in Vehicular Ad - Hoc Networks. Vehicles use a part of their buffer to replicate data for other vehicles in the same platoon to share data with them. If a vehicle leaves a platoon, it prefetches the interested data in advance and transfers it to other vehicles so that they can still access the data. To improve the data access performance in VANETs, a vehicle platooning protocol is configured to recognize platoon formation and to predict platoon splits. Next a data management part is configured to lead platoon members to replicate and prefetch the most interested data so that both data availability and data access performance can be achieved. We use cost effective data replication algorithms to find the best vehicle to replicate each data in a platoon. We also use data prefetch and transfer heuristics when a split is detected. Simulation results display that vehicle platoon aware data access can efficiently improve the data access performance in vehicular Ad - Hoc networks.

PRELIMINARIES

A. Data Access In VANET

For vehicles to access data vehicle-to-vehicle approach, which is more flexible and cost effective in VANETs, particularly in rural or highway areas, which lack roadside infrastructure support. The vehicle-to-vehicle approach has been widely used in the literature [1], [5]–[6], [8] and will be used in this paper.

B. Platoon-Based Mobility Model

In VANETs, vehicles usually move as a platoon. Although there have been a few group mobility models such as the reference point group mobility (RPGM) [9] and its

variations [7], they may not be directly applied to VANETs. We assume that each vehicle platoon has a group motion vector (GM) that defines the movement of the entire platoon. The group motion vector follows the road layouts. All vehicles in the same platoon share the same group motion vector and have different random motion vectors (RM) due to their mobility deviation. The movement of each vehicle in each time slot is decided by the group motion vector and its own random motion vector. Supposing that the velocity of each vehicle follows a normal distribution $N(\mu, \delta^2)$, where μ is the average velocity and δ is the variance, because vehicles in the same platoon have the same average moving velocity and deviation, they share the same normal distribution parameter μ and δ .

When a vehicle meets a platoon, it may join the platoon or stay alone. If the vehicle joins the platoon, it will follow the mobility pattern of the platoon with the corresponding velocity $N(\mu, \delta^2)$; otherwise, it keeps its own mobility pattern. Vehicles may leave the platoon when they 1) choose different routes at the road intersections or highway exits or 2) simply accelerate or decelerate

C. System Model

There are m vehicles in the network, which are denoted as V_i ($i = 1 \dots m$), and each vehicle can store several data items in its buffer. There are n data items, which are denoted as D_j ($j = 1 \dots n$), and each data item D_j has a size S_j . Each vehicle requests its interested data from time to time. The request frequency of vehicle V_i to data D_j is represented by f_{ij} . Note that the global access frequency of data D_j , i.e., $\sum_{i=1}^m f_{ij}$, represents the popularity of the data. Fiore and Härrö [10] showed that vehicles in the same platoon are relatively well connected. They are able to communicate with each other, either directly or through a small number of vehicle relays. Therefore, we assume that each platoon member knows the data replication arrangement within the platoon. Thus, after receiving a data request, the vehicle can easily locate the nearest platoon member that has the data. Each platoon has a "platoon leader," which can be selected based on different criteria and easily identified with the vehicles' periodic beacons [31], [32]. The main responsibility of the platoon leader is to maintain the data replication cycle (DRC) of the platoon and initiate the data-replicating process. At the beginning of each DRC, the "platoon leader" calculates the best replication arrangement based on some data replication algorithm and informs other platoon members to replicate data according to it. We assume that all vehicles are equipped with communication devices and Global Positioning Systems (GPSs). With the availability of a GPS system, it is practical for the vehicle to locate its position with certain accuracy so that vehicles can estimate not only their distance but the relative positions to each other as well.

PLATOONING PROTOCOL

A. Protocol Overview

The first component of V-PADA is the vehicle-platooning protocol, which is used to quickly identify the

platoon and predict the split process. At any given time, each vehicle stays at one of the following states: 1) Initial; 2) Join; 3) Quasi-Split; and 4) Split. When a vehicle enters the network, it is at the Initial state. Later, when it meets other vehicles in the same direction, it may join them as a platoon member. After one vehicle is detected to join the platoon, it enters the Join state and sends out a platoon-join message to all platoon members to announce that a new member has joined the platoon. The message contains the information of vehicle ID, its interest list, data list, and buffer size. As the platoon leader receives this message, it will use the information to determine the best data replication arrangement for the next replication cycle. When one vehicle detects mobility anomaly it switches its state to Quasi-Split, where the anomaly will be further analyzed. If the anomaly comes from the change of road layout (e.g., the platoon is passing a curving road), the anomaly is resolved, and the vehicle returns to the Join state. Otherwise, if the vehicle is detected to split from the platoon, it enters the Split state. It sends out a platoon-split message to inform other platoon members that it is going to leave the platoon. At the same time, it starts to prefetch its interested data and transfer its buffered data to nearby platoon members. It is possible that messages may be lost for some reasons such as channel interference or collisions. Both join and split actions can always be detected by neighboring vehicles through its beacons. Furthermore, existing reliable and efficient broadcasting techniques [4] can be used to provide reliable message delivery.

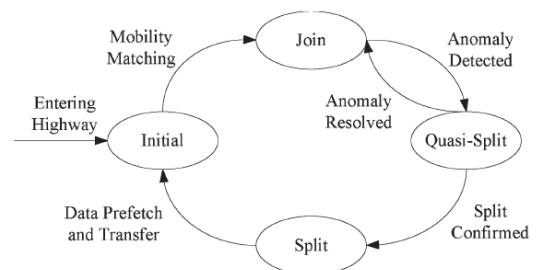


Fig.1. State transition diagram of vehicles in V-PADA

B. Stochastic Time Series Analysis for Platoon Identification

In V-PADA, each vehicle maintains a Cartesian coordinate system, where the moving direction is the X-axis. Each vehicle (called monitoring vehicle) chooses the nearby vehicle as its reference vehicle. The coordinate of the reference vehicle is represented by its shortest distances to the X-axis and the Y-axis, which are denoted by Δy and Δx , respectively. The monitoring vehicle and its reference vehicle periodically exchange their movement profile through beacon messages, by which the monitoring vehicle can get a series of relative coordinates of the reference vehicle in terms of Δx and Δy . Then, by analyzing the Δx and Δy series, the monitoring vehicle can estimate the relative motion deviation between two vehicles and determine whether they are in the same platoon or not. If the motion deviation is consistently small, the monitoring vehicle can determine that it may have already joined the platoon. During monitoring, the time interval between any two successive observations of Δx (or

Δy) is equal to the same beacon cycle; thus, the whole monitoring process can be regarded as a discrete and same-spaced process $\{X_t\}$ (and $\{Y_t\}$ for the Δy series). Therefore, in V-PADA, we can use the stochastic time series analysis on the observed position series to provide precise and automatic platoon identification.

C. Split Prediction

After joining a platoon, the monitoring vehicle keeps monitoring its reference vehicle and its own mobility pattern, so that it can quickly detect the split and have more time to prefetch and transfer data.

1) Anomaly Detection: The most intuitive approach in detecting mobility anomaly is only based on the distance between the monitoring vehicle and its reference vehicle. A mobility anomaly is detected when the distance becomes larger than a predefined threshold. However, it is difficult to find the appropriate threshold. If the threshold is large while the monitoring vehicle and the reference vehicle are close to each other, the anomaly may not be detected, even after a relative large position change. If the distance threshold is small, it may result in high false positives, even if the monitoring vehicle only moves a little bit.

To address the weaknesses of the a fore mentioned approaches, we propose to use the 2-D relative position change between the monitoring vehicle and its reference vehicle to detect mobility anomaly. In this approach, we still use the Cartesian coordination system to determine the relative position of the reference vehicle in terms of Δx and Δy and use time series analysis on the relative position change to detect mobility anomaly. The standard position deviation and the detection confidence interval, the detection boundary can be represented by a rectangle. If the diagonal of the rectangle is $2d$, any mobility anomaly that results in a relative position deviation of distance d can be detected. This approach can precisely determine the relative motion between the two vehicles and thus can be used to quickly detect any abnormal position change.

2) Two-Step Split Prediction: In the position-change-based approach, a large position change may come from the following reasons: 1) The vehicle is splitting from the platoon, or 2) the vehicle still stays with the platoon but the platoon changes its moving direction due to road layout such as a curve. Although the vehicle is in the same platoon as its reference vehicle, the observed relative position changes much in two successive observations due to the road curve, resulting in a false alarm of a vehicle split. To mitigate the false alarm issue and quickly detect the split, we design a two-step split prediction method based on the following idea. If a vehicle moves on a straight road, its moving direction is usually stable; otherwise, if it is passing a curve road, its moving direction may continuously change. Furthermore, if a vehicle splits from the platoon, its distance to the reference vehicle increases as they move further apart; if the vehicle is still within the platoon, its distance from the reference vehicle may not change too much, even if they are moving on a curve road. By first analyzing the moving direction (the first step)

and then comparing their relative distance deviation (the second step), we can differentiate different splitting scenarios and reduce the false alarm rate due to road curvature

3) Reference Vehicle Selection: We have three rules for selecting the reference vehicle in a platoon. They are given as Rule I: A vehicle always chooses the vehicle in front of it (if any) as its reference vehicle. Rule I guarantees that the reference vehicle will pass the exit before the monitoring vehicle

Rule II: Each vehicle prefers the vehicle that is close to it as its reference vehicle. Rule II considers the communication reliability between the vehicle and its reference

Rule III: Multiple reference vehicles can improve the detection accuracy. By using multiple reference vehicles at the same time, a more accurate split prediction can be achieved.

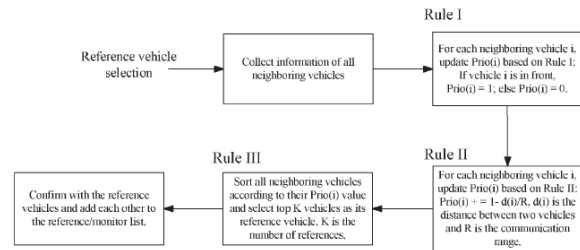


Fig.2. Reference vehicle selection

In V-PADA, each vehicle selects its reference vehicles based on these three rules when it joins the platoon. When a reference vehicle is detected to split from the platoon, it will also apply these rules to find a new reference for its monitoring vehicle.

PLATOON-BASED DATA MANAGEMENT

In V-PADA, we exploit the platooning behavior to optimize the data access. First, we analyze the intraplatoon data replication problem and propose a cost-effective but centralized data replication algorithm called best-location data replication to help vehicles cooperatively access their interested data inside the platoon. The main purpose of the best-location replication algorithm is to optimally place data replicas at their best locations inside the platoon so that the vehicles in the same platoon can hold more interested data to avoid the long delay and low availability of accessing data not in the platoon. Second, we extend the best-location algorithm to a more scalable distributed algorithm called neighboring data replication, where each vehicle cooperatively replicates data with their directly connected neighboring nodes. Finally, we provide heuristics for vehicles to prefetch and transfer data before vehicle splits so that vehicles can still access their interested data after split.

A. Intraplatoon Data Replication

In V-PADA, data replication is periodically executed based on a predefined DRC that is maintained by the platoon leader. At the beginning of each DRC, the platoon leader calculates the best intraplatoon replication for each data item according to the data replication algorithm and then notifies all platoon members, with which each vehicle can buffer the most appropriate data replicas. In the following, we first formulate the intraplatoon data replication problem and then propose a new cost-effective replication algorithm that can remove data redundancy and reduce the data access cost.

1. Best-Location Data Replication Algorithm: The basic idea behind the best-location data replication algorithm is to find the best location (vehicle) to place each data replica so that the overall data redundancy and data access cost within the platoon are minimized

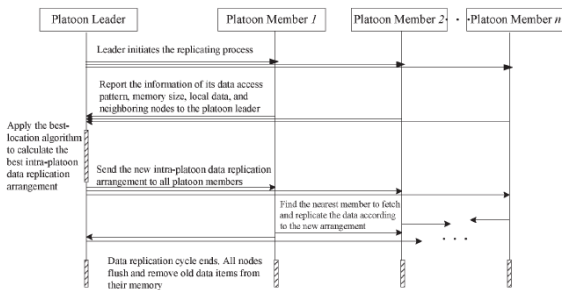


Fig.3. Implementation of the best location data replication

2. Neighboring Data Replication Algorithm: The best location data replication algorithm can find the best vehicle to allocate each data item inside the vehicle platoon. However, this algorithm requires all platoon members to report their own information to the platoon leader. After the platoon leader collects all information, it calculates the best allocation of all data replications and notifies all platoon members. Obviously, this algorithm is centralized and may have large message overhead. To make the replication algorithm more scalable to large platoons, we propose a distributed data replication algorithm called neighboring data replication. In the neighboring replication algorithm, each vehicle only contacts with its directly connected neighbors, instead of all platoon members, and tries to find the best neighboring vehicle to replicate each data item and eliminate the data redundancy.

The neighboring data replication algorithm eliminates the replica duplication among neighboring vehicles. Furthermore, it only requires the node to contact its neighboring vehicles to make the replication decision, which saves more communication overhead, compared with the best-location algorithm.

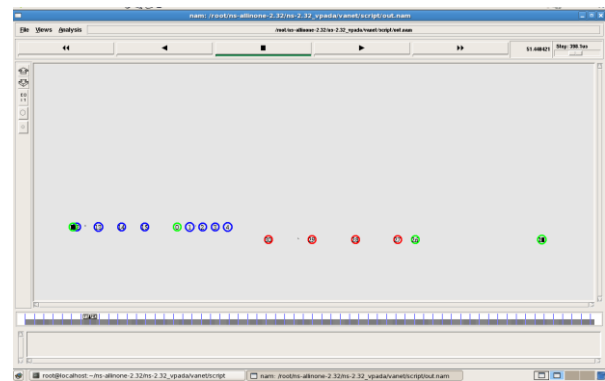
B. Data Prefetch and Transfer on Splitting

By cooperative replication, the two proposed data replication algorithms can eliminate intraplatoon data redundancy and then reduce the data access cost. However, the advantage of cooperative replication will be affected by

platoon splitting. From the splitting vehicle point of view, it may not be able to access the most interested data placed at other platoon members after it is disconnected from the platoon. From the vehicle platoon point of view, if there are some primary data copies buffered at the splitting vehicle, the splitting may also significantly affect the intraplatoon data access. Moreover, if the primary data copy is the only data copy in the platoon, other platoon members will not be able to access the data after splitting. To address this problem, the splitting vehicle should prefetch its most interested data and transfer its buffered primary data copies to other platoon members. More specifically, after a vehicle is confirmed as “split,” it begins to immediately prefetch its interested data based on its own data access probability.

Because all vehicles know the arrangement of data replications within the platoon, the splitting vehicle can easily locate the nearest nodes that have the data and prefetch it. To ensure that the split will not affect the data access of other platoon members, the splitting vehicle should transfer as many primary data copies as possible to its nearest neighbor that buffers duplicate copies of other data and replaces them with its primary data copies. With data prefetch and transfer, the splitting vehicle can still locally access its interested data, and the negative effects on other platoon members can be minimized.

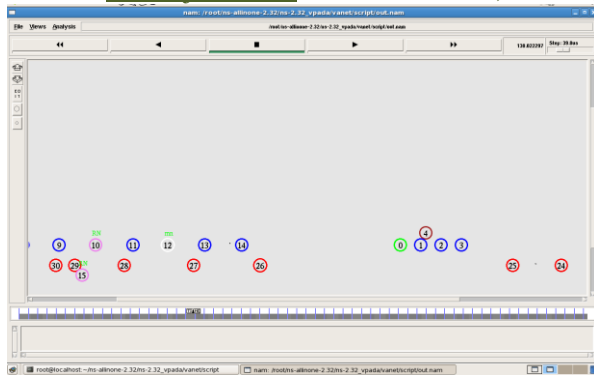
RESULTS:



(a)



(b)



(c)

Fig.4. Vehicular Ad-Hoc Networks Using V-PADA

We implement V-PADA in the Ns-2 simulator. In the simulation 30 vehicles move on the highway following the speed limits. The vehicles are divided in two and move in opposite direction as in a bidirectional road. There are seven platoons in the simulation setup and the vehicles enter the highway and move through these platoons. The top row where the nodes move from left to right of the screen is indicated as blue color. The bottom lane where the vehicles move from right to left is indicated as red. In the simulation two nodes deviate from the lanes to simulate anomaly. Node 15 moves from lane 1 to join lane 2 and node 4 leaves the lane 1 and rejoins the same lane afterwards. V-PADA monitor the movement of nodes and switches the nodes between reference nodes and mobile nodes which is also indicated. The messages transferred between the nodes like beacon messages and data are got in a separate trace file from which the results can be depicted.

CONCLUSION:

We have proposed V-PADA, which is a novel vehicle-platoon-aware data access solution for VANETs. V-PADA makes use of the “vehicle platoon” mobility pattern to collaboratively replicate data and optimize data access among vehicles. V-PADA consists of two components. Simulation results have shown that V-PADA outperforms other data access solutions in VANETs. The proposed solution in this paper is not limited to VANETs and can be extended to other mobile ad hoc networks. In the future, we will look into solutions for mobility anomaly detection in more complicated road structures and solutions for cooperative data access with the support of roadside infrastructures. Furthermore we can get the information available from neighboring platoons to decrease the query delay .

REFERENCES:

- [1] Y. Zhang, J. Zhao, and G. Cao, “Roadcast: A popularity aware content sharing scheme in VANETs,” in Proc. IEEE ICDCS, 2009, pp. 223–230.
- [2] Y. Huang, P. Sistla, and O. Wolfson, “Data replication for mobile computers,” in Proc. ACM SIGMOD, 1994, pp. 13–24.

- [3] D. Gerlough and M. Huber, “Traffic flow theory—A monograph,” Transp. Res. Board, Washington, DC, Special Rep. 165, 1975.
- [4] J. Zhao, Y. Zhang, and G. Cao, “Data pouring and buffering on the road: a new data dissemination paradigm for vehicular ad hoc networks,” IEEE Trans. Veh. Technol., vol. 56, no. 6, pp. 3266–3277, Nov. 2007.
- [5] J. Zhao and G. Cao, “Vadd: Vehicle-assisted data delivery in vehicular ad hoc networks,” IEEE Trans. Veh. Technol., vol. 57, no. 3, pp. 1910–1922, May 2008.
- [6] A. Skordylis and N. Trigoni, “Delay-bounded routing in vehicular ad-hoc networks,” in Proc. ACM MobiHoc, 2008, pp. 341–350.
- [7] K. Wang and B. Li, “Efficient and guaranteed service coverage in partitionable mobile ad-hoc networks,” in Proc. IEEE INFOCOM, 2002, pp. 1089–1098.
- [8] D. Jiang, Q. Chen, and L. Delgrossi, “Optimal data rate selection for vehicle safety communications,” in Proc. ACM VANET, 2008, pp. 30–38.
- [9] X. Hong, M. Gerla, G. Pei, and C. Chiang, “A group mobility model for ad hoc wireless networks,” in Proc. ACM MSWiM, 1999, pp. 53–60.
- [10] M. Fiore and J. Härrri, “The networking shape of vehicular mobility,” in Proc. ACM MobiHoc, 2008, pp. 261–272.

Author



P. AGITH FINAL ME-COMM SYSTEMS
SRI SHAKTHI INSTITUTE OF ENGG AND
TECHNOLOGY, L&T BYPASS, COIMBATORE.

Control of a Three-Phase Cascaded H-Bridge Multilevel Inverter for Stand-alone PV System

M RAGHU VAMSI GOUTHAM¹, VENU GOPALA RAO M²

*(Student, Department of Electrical and Electronics Engineering, KL University, India)

** (Professor & Hod, Department of Electrical and Electronics Engineering, KL University, India)

Abstract- This paper presents a three-phase cascaded H-bridge converter for a stand-alone photovoltaic (PV) application. The multilevel topology consists of several H-bridge cells connected in series, each one connected to a string of PV modules. The adopted control scheme permits the independent control of each dc-link voltage, enabling, in this way, the tracking of the maximum power point for each string of PV panels. Additionally, low ripple sinusoidal-current waveforms are generated with almost unity power factor. The topology offers other advantages such as the operation at lower switching frequency or lower current ripple compared to standard two-level topologies. Simulation and experimental results are presented for different operating conditions.

Index Terms—Multilevel inverters, photovoltaic (PV) power systems, power conversion.

INTRODUCTION

Stand-alone Three-phase photovoltaic (PV) systems are nowadays recognized for their contribution to clean power generation. A primary goal of these systems is to increase the energy injected to the grid by keeping track of the maximum power point (MPP) of the panel, by reducing the switching frequency, and by providing high reliability. In addition, the cost of the power converter is also becoming a decisive factor, as the price of the PV panels is being decreased [1]. This has given rise to a big diversity of innovative converter configurations for interfacing the PV modules with the grid. Currently, the state-of-the-art technology is the two-level multi string converter. This converter consists of several PV strings that are connected with dc–dc converters to a common dc–ac converter [2], [3]. This topology features several advantages such as the independent tracking of the MPP of each string to the existing plant. This converter topology can reach peak efficiencies up to 96% [4]. In the last years, multilevel converter topologies have been also considered in PV applications [5]. These converter topologies can generate high-quality voltage waveforms with power semiconductor switches operating at a frequency near the fundamental [6]. Although, in low-power applications, the switching frequency of the power switches is not restricted, a low switching frequency can increase the efficiency of the converter [7]. Additionally, multilevel converters feature several dc links, making possible the independent voltage control and the tracking of the MPP in each string. This

characteristic can increase the efficiency of the PV system in case of mismatch in the strings, due to unequal solar radiation, aging of the PV panels, and different type of the cells or accumulation of dust in the surface of the panels [8]. and the possibility to scale the system by plugging more strings

Among the available multilevel converter topologies, the cascaded multilevel converter constitutes a promising alternative, providing a modular design that can be extended to allow a transformerless connection to the grid [9], [10]. Additionally, this topology features power semiconductors with a lower rating than the standard two-level configurations, allowing cost savings [5]. Last but not the least, multilevel topologies feature several freedom degrees that make possible the operation of the converter even under faulty conditions, increasing, in this way, the reliability of this system. In spite of all these characteristics, the cascaded multilevel topology has also disadvantages, as the strings of PV panels are not grounded and extra measures have to be taken in order to avoid currents due to stray capacitances between the panel and the earth [9].

In order to properly operate a cascaded converter with n cells, the independent control of the dc-link voltages and the control of the grid current i_s (Fig. 1) are necessary. This task must be accomplished by using the n available actuation signals corresponding to the modulation units of each cell. Several methods have been proposed to the control of this configuration. In [12]–[14], the reference signals for the modulation units of each cell are multiplied by a factor that depends on the voltage in each dc link and the power that the corresponding string of PV panels is delivering. Unfortunately, no experimental results are given. Other approaches operate only under equal dc-link voltages [15], which is not adequate for the tracking of the MPP in each string. In [16] control methods based on passivity controllers have been presented. The experimental results show that independent control of the dc-link voltages is possible.

However, the equations for the controller are not explicitly described, and high-performance control platforms are required for real-time implementation of the proposed control schemes

In this paper, a simple scheme based on the algorithm presented in [16] is applied for the control of a PV cascaded converter system. The control scheme is enhanced with MPP tracking (MPPT) algorithms that independently adjust

the reference of the dc-link voltages in order to maximize the generated energy

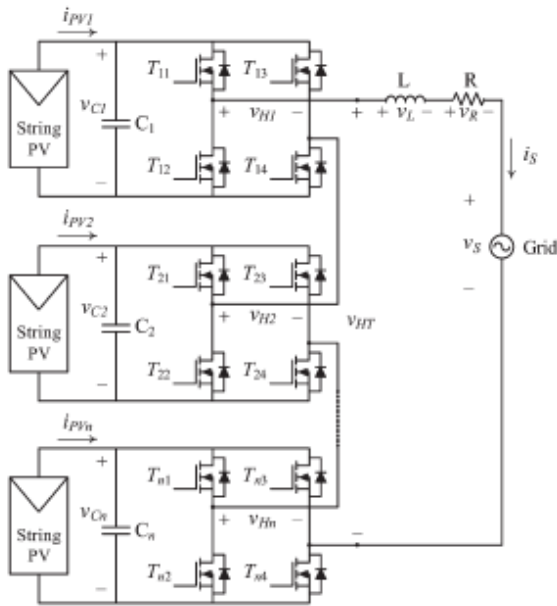


Fig. 1. Topology for grid connection.

In addition, the quality of the grid currents is improved by using, for the measurement of the dc voltages, a digital 100-Hz band reject filter

This paper is organized as follows. First, the converter topology is presented in Section II. Then, the control principle is explained in Section III. The model necessary for the design of the controllers is described in Section IV. The last section shows the simulation and experimental results that validate the proper operation of the converter. The results demonstrate that this topology can inject to the grid sinusoidal input currents with unity power factor, even under conditions of unequal solar radiation of the string of PV cells.

$$\frac{di_s}{dt} = \frac{1}{L} \left(\sum_{j=1}^n (S_j v_{Cj}) - R i_s - v_s \right) \quad (2)$$

$$\frac{dv_{Cj}}{dt} = \frac{1}{C_j} (i_{pvj} - S_j i_s), \quad (3)$$

III. CONTROL SCHEME

The control strategy is based in the classical scheme for the control of a single H-bridge converter connected to the grid. In [12]–[16], this idea has been extended for the case of n cells connected in series for the control of an active rectifier. From these different control schemes, only [16] seems to be suited for this application because they are able to operate with different dc-link voltages. In this paper, the control scheme proposed in [16] is used for this application by adding MPPT controllers in the voltage reference.

The scheme in Fig. 2 includes $n + 1$ control loops: n of them are used to adjust the capacitor voltage in each dc link, and the other one is necessary for the generation of a sinusoidal input current with unity power factor. As shown in Fig. 2, the sum of the dc-link voltages V_{C1} to V_{Cn} is controlled through

a PI that determines the amplitude of the input current \hat{i}_s . By multiplying the output of this controller with a normalized sinusoidal signal in phase with the voltage grid, a suitable reference for the current loop is obtained

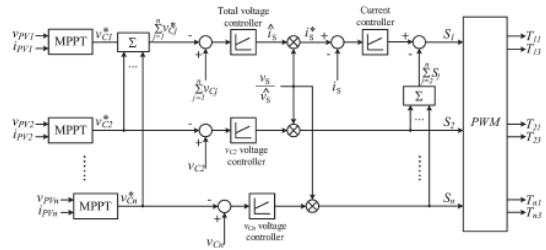


Fig. 2. Proposed control scheme.

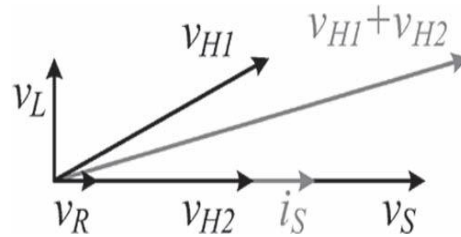


Fig. 3. Phasor diagram.

IV. SYSTEM MODELING AND CONTROLLER DESIGN

In this section, the tuning procedure for the three control loops in Fig. 4 is described. The design of the filter for the mitigation of the 100-Hz harmonic component in the input current i_s is also addressed.

A. Current Loop

Since the dynamic of the current loop is much faster than the dynamic of the voltage loop, the design for the controller will mainly consider this dynamic and the delay time of the converter and the modulator. The plant is given by

$$G_i(s) = \frac{I_s(s)}{V_{HT}(s)} = \frac{I_s(s)}{V_{HT}(s) + V_{H2}(s)} = \frac{1}{L_s + R} \quad (4)$$

The simplified control scheme of the current control loop is shown in Fig. 4(a). The design of the current controller assumes that grid voltage v_s is a slowly variant disturbance for the current loop. For this reason, it will not be considered.

measurements and MPPT blocks are intentionally avoided because it is necessary to assure the proper tracking of the optimum power point.

The digital filters work according to the principle shown in Fig. 5. The original signal $V(t)$ is delayed by a half cycle and then added to the original waveform to obtain the dc component of the signal. A block diagram of the complete control scheme, including the two 100-Hz filters, is shown in Fig. 6.

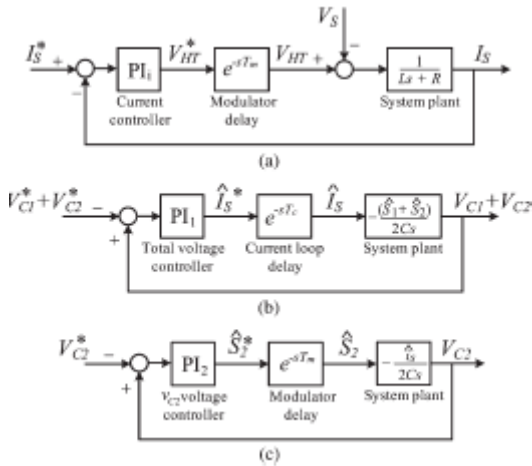


Fig. 4. (a) Current loop. (b) Total voltage loop. (c) Second cell voltage loop

B. Voltage Loop

Two PI controllers are necessary for the independent control of each dc-link voltage. In order to design the controllers, suitable transfer functions are obtained by the linearization of (3) with $j = 1, 2$ around the nominal operating point. In this case, it will be considered that the system operates at a nominal radiation of 1 kW/m² and at 25 °C. As a first step, the transfer function of the loop that considers the total dc-link voltage will be calculated. The derivation of this expression is documented reproduced here for the sake of completeness. Adding these two equations yields

$$S_1 i_s + S_2 i_s = i_{PV1} + i_{PV2} - C_1 \frac{dv_{C1}}{dt} - C_2 \frac{dv_{C2}}{dt} \tag{5}$$

By considering only the dc component of the term $S_1 i_s + S_2 i_s$ the last equation is equivalent to

$$\frac{\hat{S}_1 \hat{i}_s + \hat{S}_2 \hat{i}_s}{2} = i_{PV1} + i_{PV2} - C_1 \frac{dv_{C1}}{dt} - C_2 \frac{dv_{C2}}{dt} \tag{6}$$

where \hat{x} indicates the maximum value of x .

C. Mitigation of the 100-Hz Harmonic Component in the Input Currents

Using this control configuration, a harmonic component of the triple of the fundamental frequency appears in the input current i_s . In order to mitigate this harmonic component in the current, a band reject filter centered in 100 Hz has been placed between the voltage measurements v_{C1} and v_{C2} and the inputs of voltage controllers, as shown in Fig. 6. In this way, the 150-Hz harmonic component is eliminated from the current references. Note that filters between PV voltage

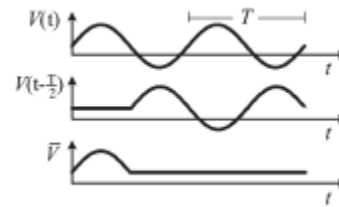


Fig. 5. Filter principle.

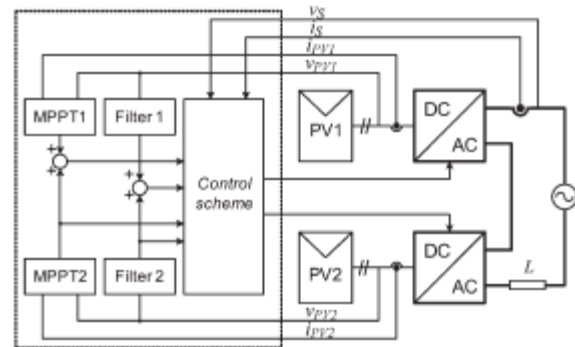


Fig. 6. Proposed control scheme with MPPT and band reject filters.

V. MATLAB/SIMULINK MODEL

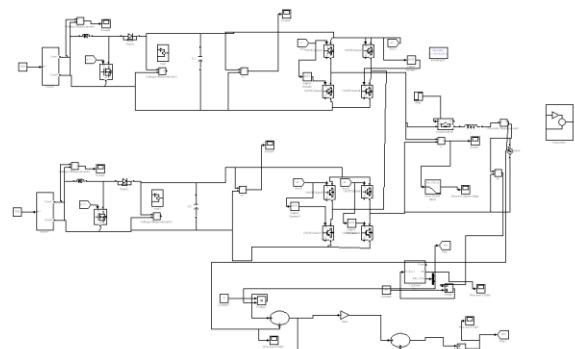


Fig.7 Matlab/Simulink Model

Fig.7 shows the Matlab /Simulink model of grid connected PV system. It consists of a PV string, DC to DC converter and inverter.

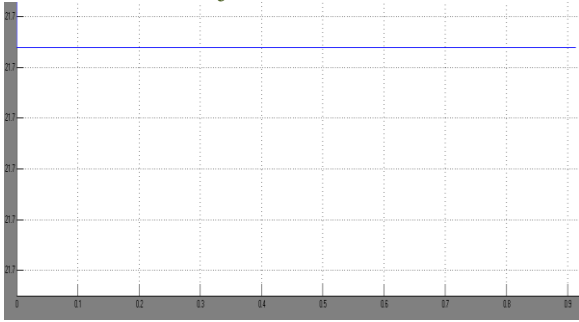


Fig.8 PV cell output

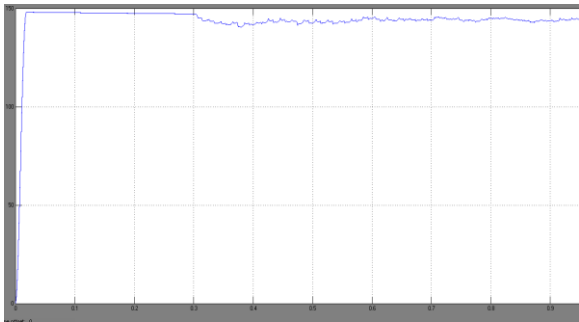


Fig.9 Inverter input voltage

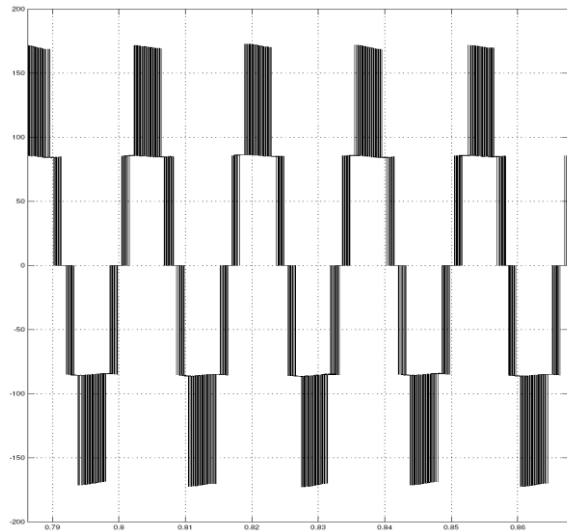


Fig.10 Five level output voltage

Fig.8 shows the PV cell output and Fig.9 shows the inverter input voltage. Fig. 10 shows Five level PWM out put voltage.

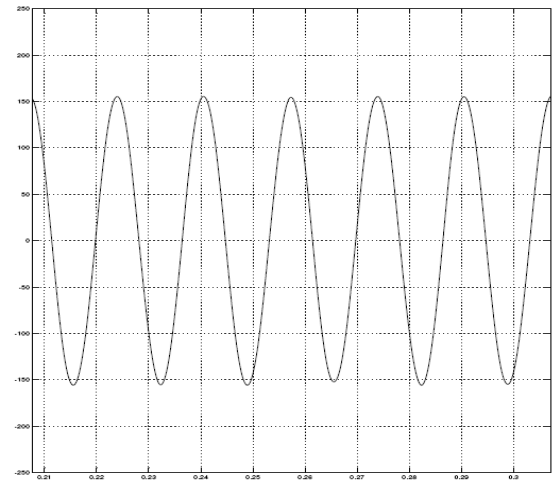


Fig.11 Filtered output voltage

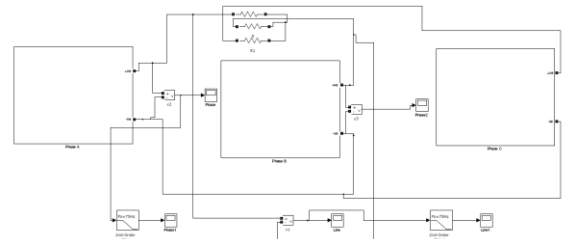


Fig.12 Three Phase Blocks

Fig.12 shows the Three phase standalone PV system with cascaded multilevel inverters. Fig. 13 shows the corresponding five level phase voltage.

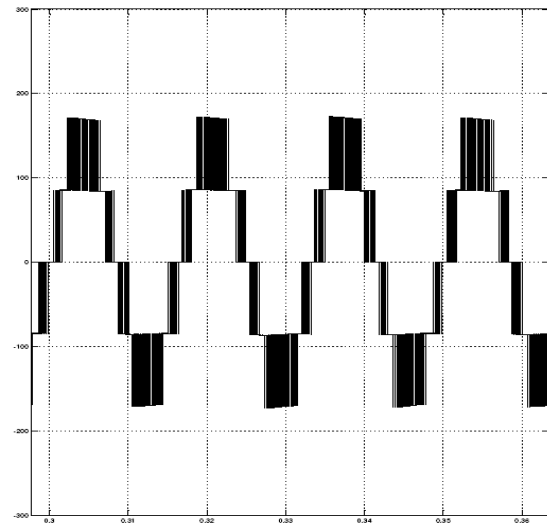


Fig.13 Output voltage

VI. CONCLUSION

In this paper, a cascaded H-bridge multilevel converter has been proposed as a feasible multistring topology for PV applications. The converter features several advantages such as the generation of high-quality currents, the capacity to operate at a lower switching frequency than a two-level converter, and the modularity

that can reduce the cost of the solution. The converter is first controlled using a scheme proposed for multilevel active rectifiers and improved by adding MPPT algorithms. A three phase cascaded H-Bridge for standalone system is proposed. A Matlab/Simulink based model is developed and simulation results are presented.

VII. REFERENCES

- [1] Elena Villanueva and Pablo Correa, "Control of a single-Phase cascaded H-bridge Multi level Inverter for grid-connected photovoltaic Systems", *IEEE TRANSACTIONS ON INDUSTRIAL ELECTRONICS, VOL. 56, NO. 11, NOVEMBER 2009*
- [2] S. Kjaer, J. Pedersen, and F. Blaabjerg, "A review of single-phase gridconnected inverters for photovoltaic modules," *IEEE Trans. Ind. Appl.*, vol. 41, no. 5, pp. 1292–1306, Sep./Oct. 2005.
- [3] M. Meinhardt and G. Cramer, "Multi-string converter: The next step in evolution of string converter technology," in *Proc. 9th Eur. Conf. Power Electron. Appl.*, 2001. [CD-ROM].
- [4] S. Khajehoddin, A. Bakhshai, and P. Jain, "A novel topology and control strategy for maximum power point trackers and multi-string gridconnected PV inverters," in *Proc. 23rd Annu. IEEE APEC*, Feb. 2008, pp. 173–178.
- [5] Sunny Boy 5000tl Multi-String Operating Instructions, SMA, Niestetal, Germany, Oct. 2008. [Online]. Available: www.sma.de
- [6] S. Daher, J. Schmid, and F. Antunes, "Multilevel inverter topologies for stand-alone PV systems," *IEEE Trans. Ind. Electron.*, vol. 55, no. 7, pp. 2703–2712, Jul. 2008.
- [7] J. Rodriguez, J.-S. Lai, and F. Z. Peng, "Multilevel inverters: A survey of topologies, controls, and applications," *IEEE Trans. Ind. Electron.*, vol. 49, no. 4, pp. 724–738, Aug. 2002.
- [8] E. Ozdemir, S. Ozdemir, L. Tolbert, and B. Ozpineci, "Fundamental frequency modulated multilevel inverter for three-phase stand-alone photovoltaic application," in *Proc. 23rd Annu. IEEE APEC*, Feb. 2008, pp. 148–153.
- [9] S. Busquets-Monge, J. Rocabert, P. Rodriguez, S. Alepuz, and J. Bordonau, "Multilevel diode-clamped converter for photovoltaic generators with independent voltage control of each solar array," *IEEE Trans. Ind. Electron.*, vol. 55, no. 7, pp. 2713–2723, Jul. 2008.
- [10] M. Calais and V. Agelidis, "Multilevel converters for single-phase grid connected photovoltaic systems—An overview," in *Proc. IEEE ISIE*, Jul. 1998, vol. 1, pp. 224
- [11] H. Ertl, J. Kolar, and F. Zach, "A novel multicell DC–AC converter for applications in renewable energy systems," *IEEE Trans. Ind. Electron.*, vol. 49, no. 5, pp. 1048–1057, Oct. 2002.
- [12] P. Correa, M. Pacas, and J. Rodriguez, "Predictive torque control for inverter-fed induction machines," *IEEE Trans. Ind. Electron.*, vol. 54, no. 2, pp. 1073–1079, Apr. 2007.
- [13] O. Alonso, P. Sanchis, E. Gubia, and L. Marroyo, "Cascaded H-bridge multilevel converter for grid connected photovoltaic generators with independent maximum power point tracking of each solar array," in *Proc. 34th Annu. IEEE PESC*, Jun. 2003, vol. 2, pp. 731–735.
- [14] J. Negroni, F. Guinjoan, C. Meza, D. Biel, and P. Sanchis, "Energysampled data modeling of a cascade H-bridge multilevel converter for grid-connected PV systems," in *Proc. 10th IEEE Int. Power Electron. Congr.*, Oct. 2006, pp. 1–6.
- [15] S. Khajehoddin, A. Bakhshai, and P. Jain, "The application of the cascaded multilevel converters in grid connected photovoltaic systems," in *Proc. IEEE EPC*, Montreal, QC, Canada, Oct. 2007, pp. 296–301.
- [16] B.-R. Lin and H.-H. Lu, "New multilevel rectifier based on series connection of H-bridge cell," *Proc. Inst. Elect. Eng.—Electr. Power Appl.*, vol. 147, no. 4, pp. 304–312, Jul. 2000.

Performance Analysis of MIMO Systems using Orthogonal Space Time Coding over Rayleigh Fading Channel

P. Satyanarayana¹, M. Ajay Babu², Dr. Habibullah Khan³, M. Mallikarjun⁴

^{1,2}(Assoc. Professors, Dept of ECE, KL University)

³(Professor, Head of ECE Dept, KL University)

⁴(M.Tech student, Dept of ECE, KL University, Guntur, Andhra Pradesh, India.

Abstract: Emerging demands for high data rate services and high spectral efficiency are the key driving forces for the continued technology evolution in wireless communications. MIMO technology has attracted attention in wireless communications, because it offers significant increases in data throughput and link range without additional bandwidth or transmit power. It achieves this by higher spectral efficiency (more bits per second per hertz of bandwidth) and link reliability or diversity (reduced fading). Orthogonal space-time block codes (STBC's) have received considerable attention in recent open-loop multiple-input-multiple-output (MIMO) wireless communication because they allow low decoding complexity and guarantee full diversity. This paper presents a detailed study of space-time block coding (STBC) schemes including orthogonal STBC for 3x4 antennas and high-coding rate STBC. Finally, STBC 3x4 techniques is implemented in MATLAB and analyzed the performance according to their bit-error rates using BPSK, QPSK.

Keywords: Diversity, Multiple Input and Multiple Output (MIMO), Orthogonal space-time coding (OSTBC), Channel State information (CSI), Pair-wise Error Probability.

I. INTRODUCTION

MIMO wireless systems have captured the attention of international standard organizations. The use of MIMO has been proposed multiple times for use in the high-speed packet data mode of third generation cellular systems (3G) as well as the fourth generation cellular systems (4G). MIMO has also influenced wireless local area networks (WLANs) as the IEEE 802.11n standard exploits the use of MIMO systems to acquire high throughputs. MIMO systems employing space-time coding strategies to support greatly enhanced performance. Space-Time coding [5], [4], uses the advantage of transmitter diversity, is an effective technique to improve the performance of wireless communication systems. In space-time coding, different signals are simultaneously transmitted from different transmit antennas. The signal which is received is the superposition of the different transmitted signals, and the detection process needs estimates of the channel parameters [3]. All these designs were based on the assumption that channel state information is perfectly known at the receiver, but unknown at the transmitter.

The work presented in this paper is motivated by the observation that for the special case of STBC 3x4 (3 transmitter and 4 receiver) and high code-rate STBC, it is possible to obtain exact closed-form expression for the pair-wise error probability. An exact PEP expression would serve as an attractive alternative to previously derived bounds for evaluating performance [6]. Our expressions are derived from the PDF of the phase of the received signal. Simulated PEP results of STBC 3x4 using BPSK and QPSK are presented.

II. System model: MIMO

When a transmitter and a receiver, with an appropriate channel coding and decoding scheme, are equipped with multiple antennas, the presence of multipath fading can be improved over a Rayleigh fading channel.

Space-time-coded MIMO systems with N_T transmit antennas and N_R receive antennas is showed in the figure. In the space-time coded MIMO systems, bit stream is mapped into symbol stream $\{x_i\}_{i=1}^N$. As depicted in Figure a symbol stream of size N is space-time-encoded into $\{x_i\}_{i=1}^N$, $t=1, 2, 3, \dots, T$, where i is the antenna index and t is the symbol time index. Note that the number of symbols in a space-time codeword is $N_T \cdot T$ (i.e., $N = N_T \times T$). In other words $\{x_i\}_{i=1}^N$, $t=1, 2, 3, \dots, T$, forms a space-time codeword. As N symbols are transmitted by a codeword over T symbol times, the symbol rate of the space-time-coded system example shown in the figure is given as

$$R = \frac{N}{T} (\text{Symbols / Channel use}) \quad (1)$$

At the receiver side, the symbol stream $\{\tilde{x}_i\}_{i=1}^N$ is estimated by using the receive signals $\{y_j^{(t)}\}_{j=1}^{N_R}$, $t=1, 2, \dots, T$. Let h_{ij}^t denotes the Rayleigh-distributed channel gain from the i^{th} transmit antenna to the j^{th} receive antenna over the t^{th} symbol period ($i=1; 2; \dots; N_T$), ($j=1; 2; \dots; N_R$), and $t=1; 2; \dots; T$). If we assume that the channel gains do not change during T symbol periods, the symbol time index $\{h_{ij}^t\}$ can be omitted. Furthermore, as long as the transmit antennas and receive antennas are spaced sufficiently apart, $N_R \times N_T$ fading gains can be assumed to be statistically independent [3]

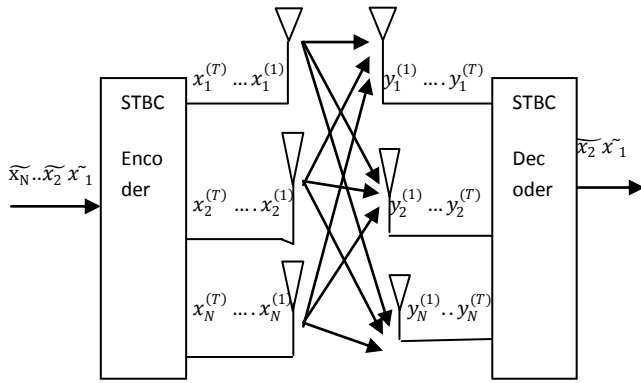


Figure.1 Block diagram of Space-time coded MIMO systems

. If x_i^t is the transmitted signal from the i^{th} transmit antenna during t^{th} symbol period, the received signal at the j^{th} receive antenna during t^{th} symbol period is

$$y_j^{(t)} = \sqrt{\frac{E_x}{N_0 N_T}} [h_{j1}^{(t)} h_{j2}^{(t)} \dots h_{j3}^{(t)}] \begin{bmatrix} x_1^{(t)} \\ x_2^{(t)} \\ \vdots \\ x_{N_T}^{(t)} \end{bmatrix} + Z_j^{(t)} \quad (2)$$

Where Z_j^t is the noise process at the j^{th} receive antenna during t^{th} symbol period, which is modeled as the ZMCSCG noise of unit variance, and E_x is the average energy of each transmitted signal. Meanwhile, the total transmitted power is constrained as

$$\sum_{i=1}^{N_T} E \{ |x_i^{(t)}|^2 \} = N_T, \quad t=1,2,\dots,T \quad (3)$$

Variance is assumed to be 0.5 for real and imaginary parts of h_{ij} .

Considering the relationship in Equation (2) for N_R receive antennas, while assuming quasi-static channel gains (i.e. $h_{ji}^t = h_{ji}$, $t = 1, 2, \dots, T$), the system equation is given as

$$\begin{bmatrix} y_1^{(1)} & y_1^{(2)} & \dots & y_1^{(T)} \\ \vdots & \vdots & & \vdots \\ y_{N_R}^{(1)} & y_{N_R}^{(2)} & \dots & y_{N_R}^{(T)} \end{bmatrix} = \sqrt{\frac{E_x}{N_0 N_T}} \begin{bmatrix} h_{11} & h_{12} & \dots & h_{1N_T} \\ \vdots & \vdots & & \vdots \\ h_{N_R1} & h_{N_R2} & \dots & h_{N_R N_T} \end{bmatrix} \begin{bmatrix} x_1^{(1)} & x_1^{(2)} & \dots & x_1^{(T)} \\ \vdots & \vdots & & \vdots \\ x_{N_T}^{(1)} & x_{N_T}^{(2)} & \dots & x_{N_T}^{(T)} \end{bmatrix} + \begin{bmatrix} Z_1^{(1)} & Z_1^{(2)} & \dots & Z_1^{(T)} \\ \vdots & \vdots & & \vdots \\ Z_{N_R}^{(1)} & Z_{N_R}^{(2)} & \dots & Z_{N_R}^{(T)} \end{bmatrix} \quad (4)$$

III. Orthogonal Space Time Block Codes

In higher order STBC in-order to facilitate computationally-efficient ML detection at the receiver, the following property is required:

$$XX^H = c(|x_i^1|^2 + |x_i^2|^2 + \dots + |x_i^T|^2) I_{N_T} = c \|x_i\|^2 I_{N_T} \quad (5)$$

Consider transmitting antennas $N_T=3$ transmitting complex space time block codes in 8 time slots with coding rate of 1/2, while satisfying a full rank condition

$$X_{3,complex}^{low\ rate} = \begin{bmatrix} x_1 & -x_2 & -x_3 & -x_4 & x_1^* & -x_2^* & -x_3^* & -x_4^* \\ x_2 & x_1 & x_4 & -x_3 & x_2^* & x_1^* & x_4^* & -x_3^* \\ x_3 & -x_4 & x_1 & x_2 & x_3^* & -x_4^* & x_1^* & x_2^* \end{bmatrix} \quad (6)$$

Space-time block codes can be used for various numbers of receive antennas. However, only a single receive antenna is assumed. We express the received signals from a single receive antenna as

$$[y_1 y_2 y_3 y_4 y_5 y_6 y_7 y_8] = \sqrt{\frac{E_x}{3N_0}} [h_1 h_2 h_3] \begin{bmatrix} x_1 & -x_2 & -x_3 & -x_4 & x_1^* & -x_2^* & -x_3^* & -x_4^* \\ x_2 & x_1 & x_4 & -x_3 & x_2^* & x_1^* & x_4^* & -x_3^* \\ x_3 & -x_4 & x_1 & x_2 & x_3^* & -x_4^* & x_1^* & x_2^* \end{bmatrix} + [Z_1 Z_2 Z_3 Z_4 Z_5 Z_6 Z_7 Z_8] \quad (7)$$

The above input-output relation can be also expressed as

$$\begin{bmatrix} y_1 \\ y_2 \\ y_3 \\ y_4 \\ y_5 \\ y_6 \\ y_7 \\ y_8 \end{bmatrix} = \sqrt{\frac{E_x}{3N_0}} \begin{bmatrix} h_1 & h_2 & h_3 & 0 \\ h_2 & -h_1 & 0 & -h_3 \\ h_3 & 0 & -h_1 & h_2 \\ 0 & h_3 & -h_2 & -h_1 \\ h_1^* & h_2^* & h_3 & 0 \\ h_2^* & -h_1^* & 0 & -h_3^* \\ h_3^* & 0 & -h_1^* & h_2^* \\ 0 & h_3 & -h_2^* & h_1^* \end{bmatrix} \begin{bmatrix} x_1 \\ x_2 \\ x_3 \end{bmatrix} + \begin{bmatrix} Z_1 \\ Z_2 \\ Z_3 \\ Z_4 \\ Z_5 \\ Z_6 \\ Z_7 \\ Z_8 \end{bmatrix} \quad (8)$$

Again, using the orthogonality of the above effective channel matrix, the received signal is modified as

$$y_{eff} = H_{eff}^H y_{eff} = 2 \sqrt{\frac{E_x}{3N_0}} \sum_{j=1}^3 |h_j|^2 I_4 X_{eff} + Z_{eff} \quad (9)$$

Using the above result, the ML signal detection is performed as

$$x_{i,ML} = Q \left(\frac{y_{eff,i}}{2 \sqrt{\frac{E_x}{3N_0}} \sum_{j=1}^3 |h_j|^2} \right) \quad i = 1, 2, 3, 4 \quad (10)$$

If a decoding complexity at the receiver is compromised, however, higher coding rates can be achieved by the following codes:

$$X_{3,complex}^{high\ rate} = \begin{bmatrix} x_1 & -x_2^* & \frac{x_3^*}{\sqrt{2}} & \frac{x_3^*}{\sqrt{2}} \\ x_2 & x_1^* & \frac{x_3^*}{\sqrt{2}} & \frac{-x_3^*}{\sqrt{2}} \\ \frac{x_3}{\sqrt{2}} & \frac{x_3}{\sqrt{2}} & \frac{(-x_1-x_1^*+x_2-x_2^*)}{2} & \frac{(x_2+x_2^*+x_1-x_1^*)}{2} \end{bmatrix} \quad (11)$$

Coding rate is $R = 3/4$

Decoding of higher coding rates can be achieved by the following equations

$$[y_1 y_2 y_3 y_4] = \sqrt{\frac{E_x}{3N_0}} [h_1 h_2 h_3] \begin{bmatrix} x_1 & -x_2^* & \frac{x_3^*}{\sqrt{2}} & \frac{x_3^*}{\sqrt{2}} \\ x_2 & x_1^* & \frac{x_3^*}{\sqrt{2}} & \frac{-x_3^*}{\sqrt{2}} \\ \frac{x_3}{\sqrt{2}} & \frac{x_3}{\sqrt{2}} & \frac{(-x_1-x_1^*+x_2-x_2^*)}{2} & \frac{(x_2+x_2^*+x_1-x_1^*)}{2} \end{bmatrix} \mathbf{0} + [Z_1 Z_2 Z_3 Z_4] \quad (12)$$

Using the equation (12), the ML signal detection is performed as

$$x_{i,ML} = Q \left(\frac{y_{eff,i}}{2 \sqrt{\frac{E_x}{3N_0} \sum_1^3 |h_j|^2}} \right) \quad i = 1,2,3,4 \quad (13)$$

Effective channel construction for $X_{3,complex}^{high\ rate}$ is rather more complex than the previous coding.

IV. Pair-wise error Probability

Pair-wise error probability is defined as probability of transmitting C^1 and detecting it as C^2 , when there is no other code-words. It is represented as

$$P(C^1 \rightarrow C^2)$$

Conditional probability is written as, refer to [6].

$$P(C^1 \rightarrow C^2/H) = Q \left(\sqrt{\frac{\gamma}{2} Tr[H^H(C^2 - C^1)^H \cdot (C^2 - C^1)H]} \right) \quad (14)$$

According to the Orthogonality conditional PEP is written as

$$P(C^1 \rightarrow C^2/H) = Q \left(\sqrt{\frac{\gamma}{2} k \sum_{k=1}^k |S_k^2 - S_k^1|^2 Tr[H^H \cdot H]} \right) = Q \left(\sqrt{\frac{\gamma}{2} k \sum_{k=1}^k |S_k^2 - S_k^1|^2 \sum_{n=1}^N \sum_{m=1}^M |\alpha_{n,m}|^2} \right) \quad (15)$$

Euclidian distance between T_x and detected symbol is given by

$$d_E = \sqrt{\sum_{k=1}^k |S_k^2 - S_k^1|^2} \quad P(C^1 \rightarrow C^2/H) = Q \left(\sqrt{\frac{\gamma}{2} k d_E^2 \sum_{n=1}^N \sum_{m=1}^M |\alpha_{n,m}|^2} \right) \quad (16)$$

To calculate PEP, one needs to integrate above equation weighted by density of path gains

$$P(C^1 \rightarrow C^2/H) = \frac{1}{\pi} \int_0^{\frac{\pi}{2}} \exp \left(\frac{-k\gamma d_E^2 \sum_{n=1}^N \sum_{m=1}^M |\alpha_{n,m}|^2}{4 \sin^2 \phi} \right) d\phi = \frac{1}{\pi} \int_0^{\frac{\pi}{2}} \prod_{m=1}^M \prod_{n=1}^N \exp \left(\frac{-k\gamma d_E^2 |\alpha_{n,m}|^2}{4 \sin^2 \phi} \right) d\phi \quad (17)$$

Let the path gains are independent from each other. The integral over the distribution of the path gains is same as product of MN equal integrals

$$i.e. \prod_{m=1}^M \prod_{n=1}^N = \int_0^{\infty}$$

$$P(C^1 \rightarrow C^2/H) = \frac{1}{\pi} \int_0^{\frac{\pi}{2}} \left[\int_0^{\infty} \exp \left(\frac{-k\gamma d_E^2 x}{4 \sin^2 \phi} \right) \delta_{\chi}(x) dx \right]^{MN} d\phi$$

Where $f_{\chi}(x) = e^{-x}, x > 0$ is the pdf of $|\alpha_{n,m}|^2$. Moment Generating Function of exponential distribution for $\mu < 1$ is given by

$$M_{\chi}(\mu) = E[e^{\mu x}] = \int_0^{\infty} e^{\mu x} f_{\chi}(x) dx = \int_0^{\infty} e^{\mu x} e^{-x} dx = \frac{1}{1-\mu} \quad (18)$$

$$\text{Since } \mu = \frac{-k\gamma d_E^2 x}{4 \sin^2 \phi}$$

$$P(C^1 \rightarrow C^2) = \frac{1}{\pi} \int_0^{\frac{\pi}{2}} \frac{1}{1 + \frac{k\gamma d_E^2}{4 \sin^2 \phi}} = \frac{1}{\pi} \int_0^{\frac{\pi}{2}} \left[\frac{\sin^2 \phi}{\sin^2 \phi + k \frac{\gamma}{4} d_E^2} \right]^{MN} d\phi \quad (19)$$

The generalized expression of PEP for STBC is given by

$$P(C^1 \rightarrow C^2) = \frac{1}{2} \left\{ 1 - \sqrt{\frac{a}{1+a}} \sum_{i=0}^{MN-1} \binom{2i}{i} \left[\frac{1}{4(1+a)} \right]^i \right\}$$

$$\text{Where } a = k \frac{\gamma}{4} d_E^2 \quad (20)$$

N=Number of Transmitters
M=Number of receivers

V. Simulation Results

In this work, MATLAB is used to test the BER performance of the Rayleigh fading channel model for STBC with transmitters ($N_T = 3$) and receivers ($N_R = 4$) for different code rates. Results are shown below. From the results it is observed that in the case of BPSK the BER decrease as SNR increases rather than in the case of QPSK.

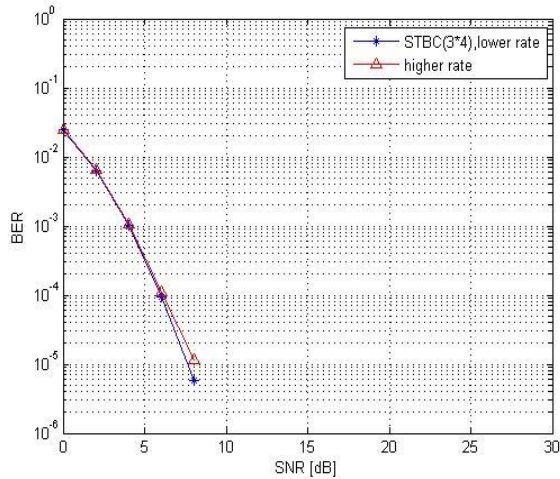


Figure 2. BER versus SNR of STBC using BPSK

By using the complex space time block code shown in the equation (6) with low code rate and equation (11) with high code rate, it is also observed that nearly same probability of error can be achieved.

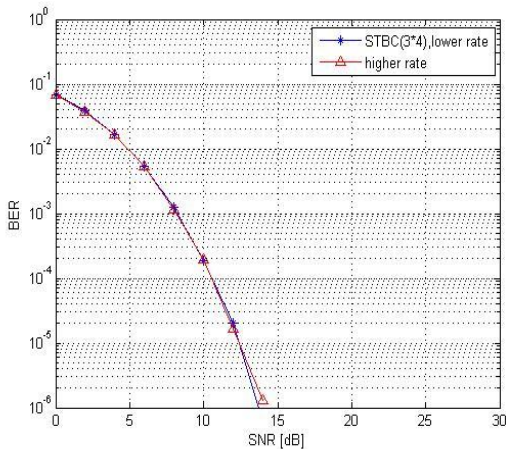


Figure 3. BER versus SNR of STBC using QPSK

VI. Conclusion

This paper provides need and advantages of MIMO systems. A basic introduction to Space-Time Coding was provided by presenting STBC system model. We then discussed block codes schemes for the cases of 3 transmit antennas and 4 receive antennas. High data rate code Scheme also discussed. The encoding and decoding

algorithm for each were presented. Generalized pair-wise error probability (PEP) for the STBC was presented. Finally from the simulation results we conclude that data rate can be increased by using high rate code in STBC. It is also seen that same BER can be achieved in STBC by using high rate codes as that of using low rate codes if decoding complexity is compromised at the receiver.

REFERENCES

- [1] H. Sampath, S. Talwar, J. Tellado, V. Erceg, and A. Paulraj, "A fourth-generation MIMO-OFDM broadband wireless system: design, performance, and field trial results," *IEEE Communications Magazine*, vol. 40, no. 9, pp. 143–149, 2002.
- [2] A. Molisch, *Wireless Communications*. Wiley-IEEE Press, 2005
- [3] V. Tarokh, H. Jafarkhani, and A. Calderbank, "Space-time block coding for wireless communications: performance results," *IEEE Journal on selected areas in communications*, vol. 17, no. 3, pp. 451–460, 1999
- [4] G. Tsoulos, *MIMO system technology for wireless communications*. CRC Press, 2006.
- [5] B. Vucetic and J. Yuan, *Space-Time Coding*, England, Wiley, 2003.
- [6] V. Tarokh, H. Jafarkhani, and A.R. Calderbank, "Space-time block codes from orthogonal designs", *IEEE Transactions on Information Theory*, Vol. 45, No. 5, pp. 1456-1467, July 1999.
- [7] G. G. Raleigh and J. M. Cioffi, "Spatio-Temporal Coding for Wireless communication", *IEEE Transaction on Communication*, Vol. 46, No. 3, pp. 357-366, March 1998.
- [8] M.K. Simon, "Evaluation of average bit error probability for space-time coding based on a simpler exact evaluation of pair-wise error probability," *International Journal on Communications and Networks*, vol. 3, no. 3, pp. 257–264, Sept. 2001.
- [9] M. Uysal and C. N. Georghiades, "Error performance analysis of spacetime codes over Rayleigh fading channels," *J. Commun. Networks*, vol. 2, no. 4, pp. 351–355, Dec. 2000.

Author Profile



Mr. P. Satyanarayana was born on 20th May, 1977 in A.P, India. He received the B.Tech degree from Nagarjuna University in 2000, A.P and M.Tech degree from JNTU Kakinada in 2004. He is working as Associate Professor in ECE dept at K L University. His interested fields include wireless communication, VLSI, DSP and Embedded Systems. His research area is Wireless Communication.



Mr. M. Mallikarjun was born on dec 9th 1988 in A.P, India. He received the B.Tech degree in Electronics & communications engineering from Sri Venkateswara University in 2010. Presently he is pursuing M.Tech Communication and Radar Systems in KL University.



Mr. M. Ajay Babu was born On 25th May, 1963 in A.P, India. He received the B.Tech degree from Nagarjuna University in 1985, A.P and M.Tech degree from JNTU Kakinada in 2000. He is working as Associate Professor in ECE dept at K L University. His interested fields include antennas and wireless communication.



Dr. Habibullah Khan born in India, 1962. He obtained his B.E. from V R Siddhartha Engineering College, Vijayawada during 1980-84. M.E from C.I.T, Coimbatore during 1985-87 and PhD from Andhra University in the area of antennas in the year 2007. He is having more than 20 years of teaching experience and having more than 20 international, national journals/conference papers in his credit. Dr. Habibullah Khan presently working as Head of the ECE department at K.L. University. He is Member Board of Studies in ECE and EIE of Acharya Nagarjuna University, Guntur. He is a fellow of I.E.T.E, Member IE, SEMCE and other bodies like ISTE. His research interested areas includes Antenna system designing, microwave engineering, Electro magnetics and RF system designing.

Broadly Tunable Chromium Doped Zinc Selenide Laser in the Mid-Infrared Region

Burhan Davarcioglu¹, M. Bahadir Baysal²

^{1,2}(Department of Physics, Aksaray University, Aksaray, Turkey)

ABSTRACT

Cr²⁺:ZnSe is one of the most studied and effective laser materials which meet all the previous mentioned requirements. The new active materials as well as new methods of other wavelengths generation are desired. One of the new materials investigated thoroughly in the past is ZnSe crystal doped with chromium ion. Recently, Cr²⁺ doped chalcogenide lasers have emerged as an attractive source of tunable laser radiation in the 2-3 μm region. In contrast to many other transition metal doped solids, Cr²⁺ ions in II-VI materials can exhibit significantly higher quantum yields at room temperature. Thermal diffusion doping is the widely used postgrowth technique for the preparation of Cr²⁺:ZnSe samples. Further optimization of the materials preparation are needed to obtained laser quality samples for future mid-infrared laser performance testing. The important advantage of Cr²⁺:ZnSe is the availability of the technologically developed and low cost polycrystalline material which makes the idea of the practical tunable diode pumped Cr²⁺:ZnSe laser feasible. Solid state tunable mid-infrared laser radiation sources operating at room temperature are required for many applications in spectroscopy, including chemical monitoring, ranging, remote sensing, medical diagnosis, medical treatment, and also for coherent pumping of solid state lasers as well as nonlinear optical materials.

Keywords – Cr²⁺:ZnSe laser, Transition metal doped II-VI, Tunable mid-infrared, Solid state, Room temperature, Transition metal ion doped

I. INTRODUCTION

Recently, transition metal ions (Cr²⁺, Co²⁺, Ni²⁺, Fe²⁺, etc...) doped zinc and cadmium chalcogenides (ZnSe, ZnTe, CdSe, CdTe, etc...) have been evaluated as an innovative class of laser media. Divalent transition metal doped II-VI chalcogenide laser materials have recently attracted much attention due to their interesting features; room temperature operation between 2 and 5 μm, broad tunability, possibility of direct diode pumping and continuous wave (cw) operation [1]. Cr²⁺ doped broadband II-VI chalcogenide lasers, which were first suggested and later studied, represent nowadays the only room temperature, diode pump able, and simple alternative to the existing mid-infrared laser sources, based either on cryogenic crystalline lasers or on cascaded quantum well materials, or use of nonlinear frequency down conversion approaches [2].

The development of the diode pumped Cr²⁺:ZnSe laser, better understanding of the earlier phenomena is important, since it allows optimization of the preparation techniques of the concentrated Cr²⁺:ZnSe crystals used in the diode

pumped systems with respect to their spectroscopic and laser quality [1]. The spectroscopic properties of transition metal doped II-VI compounds have been investigated for more than four decades now; technologically, these dopants were regarded as undesired impurities that acted as luminescence “killers” in visible emitting phosphors. Scientifically, highly resolved absorption spectra (usually obtained at low temperature) provided data for tests of crystal field theories. The need for a compact (diode pumped), efficient, room temperature operated broadly tunable mid-infrared solid state laser has proven a strong driving force for the investigation of transition metal doped chalcogenides as a new class of laser media [3, 4].

Chromium doped chalcogenides, and particularly Cr²⁺:ZnSe have demonstrated to be extremely attractive for room temperature laser operation. Up to now, room temperature pulsed lasing has been demonstrated for Cr²⁺:ZnSe [4, 5]. An all solid state Cr²⁺:ZnSe pulsed laser using strained layer InGaAsP/InP laser diodes for direct laser diode pumping has also been demonstrated. More recently, the first cw room temperature operation of a broadly tunable Cr²⁺:ZnSe laser has also been achieved, with a tuning range from 2138 to 2760 nm, the broadest wavelength tuning yet demonstrated from any room temperature cw laser [3].

The mid-infrared wavelength range, which is also often called a “molecular fingerprint” region, and in particular, the range between 2 and 5 μm is characterized by the presence of the strong fundamental and overtone vibrational absorption lines of atmospheric constituents, vapours and other gases. The crystalline solid state lasers which operate room temperature and have the largest relative bandwidth of the central wavelength of the laser can provide very high power levels retaining the good beam quality and narrow spectral linewidth at the wide tuning range. In combination with near infrared diode lasers as pump sources these lasers can offer stability, efficiency and compactness as well as the broad spectral coverage and tuning ranges, which are generally inaccessible for semiconductor lasers [6]. Cr²⁺ ions are incorporated in a tetrahedral coordination in II-VI semiconductor hosts, which is in contrast to the octahedral coordination of transition metal doped oxide and fluoride crystals. The tetrahedral coordination of transition metal ions in II-VI semiconductors directly effects the crystal field energy level splitting, electron-phonon interactions, emission quantum yields, and provides radiative emission further into the mid-infrared spectral region. Polycrystalline ZnSe and CdTe windows have proven to be promising candidates as host materials for Cr²⁺ ions. In addition, ternary Cd based II-VI materials are also being considered as novel Cr²⁺ laser hosts [7]. A typical feature of transition

metal impurities in semiconductors in general, and of chromium in II-VI compounds in particular is the existence of several possible charge states of a given transition metal ion in a given host. Thus, although the neutral charge state of chromium in II-VI semiconductors is Cr^{2+} , both Cr^{1+} ($3d^5$) and Cr^{2+} ($3d^3$) may exist.

Presently available coherent mid-infrared sources include lead salt diode lasers, which produce milliwatt powers and require cryogenic techniques, some rare earth ion lasers, whose tenability is limited, and nonlinear optical devices like Raman shifters, frequency mixers, and optical parametric oscillator. The latter class offers the widest tunability but may require injection seeding with one or shorter wavelength lasers to obtain good wavelength stability, linewidth, and output mode quality. In spite of rapidly occurring improvements in materials properties and phase matching techniques, the nonlinear optical schemes remain too complex for many applications [4].

Besides basic research applications, such tunable lasers are of particular importance for environmental monitoring, military countermeasures, medical applications and remote sensing [3]. Availability, since recently, of the room temperature diode pumped broadband tunable solid state lasers as simple and compact alternative to semiconductor lasers and nonlinear optical frequency conversion devices in this wavelength region is a significant step forward in remote sensing and trace gas detection, as well as in other medical applications [6]. Currently available tunable sources in this spectral range often suffer from drawbacks such as cryogenic operation (the lead salt diode lasers), complexity (the broadly tunable optical parametric oscillators) or narrow tuning range.

High sensitivity spectroscopic detection is of special importance for trace gas sensing applications that have an increasing impact in numerous areas including fundamental spectroscopy, atmospheric chemistry, industrial process, and medical diagnostics. The infrared spectral region has the considerable advantage of being the location of relatively strong absorption molecular bands. The tunable lasers used in these techniques do not allow simultaneous coverage of broad spectral ranges. The broadband detection is required when there is a need to selectively detect several molecular gas species simultaneously by means of high sensitivity absorption spectroscopy [8].

For analyzing the broadband laser emission spectrum, Fourier transform spectrometers appear as the most efficient instruments. They need only one single detector. Furthermore, time resolved Fourier transform interferometers are available, which permit temporal sampling of the laser transient spectral dynamics observed in the repetitive pulsed operation mode. These results in the measurement of numerous spectra observed at different generation times under the same experimental sample conditions. This allows precise determination of equivalent absorbing paths by verifying the consistency of the time evolution of different spectral lines, making possible accurate line intensity measurement by intracavity laser absorption spectroscopy [9].

Since the first demonstrations in 1995 at Lawrence Livermore National Laboratory the laser related research largely focused around $\text{Cr}^{2+}:\text{ZnSe}$, $\text{Cr}^{2+}:\text{ZnS}$ and $\text{Cr}^{2+}:\text{CdSe}$ lasers. Namely, zinc chalcogenides doped with Cr^{2+} , Co^{2+} , Ni^{2+} , and Fe^{2+} , and demonstrated efficient, room temperature lasing action near $2.5 \mu\text{m}$ by using $\text{Cr}^{2+}:\text{ZnSe}$ and $\text{Cr}^{2+}:\text{ZnS}$ [4, 5]. Transition metal doped chalcogenide lasers are of high interest because of their versatility, broad room temperature wavelength tenability, demonstrated high optical efficiencies, potential to be scaled to high powers via direct diode pumping and relative novelty. To date, cw gain switched and mode locked laser operation has been demonstrated. Material advantages can include broad absorption and emission bands, high fluorescence quantum efficiencies at room temperature, moderate gain cross sections, and minimal susceptibility to loss mechanisms, such as excited state absorption or up conversion [10].

Additionally, cw $\text{Cr}^{2+}:\text{ZnSe}$ laser has been shown to operate with greater than 50% optical to optical efficiency at room temperature and to be continuously tunable from 2.138 to $2.760 \mu\text{m}$. Direct quasi cw diode pumping of a pulsed $\text{Cr}^{2+}:\text{ZnSe}$ laser has also been demonstrated and describe cw mode locked operation of a $\text{Cr}^{2+}:\text{ZnSe}$ laser [11]. However, in this case the gain element is made of a new $\text{Cr}^{2+}:\text{ZnSe}$ laser material: hot pressed $\text{Cr}^{2+}:\text{ZnSe}$ ceramic gain media. It is noteworthy that the technology of hot pressed $\text{Cr}^{2+}:\text{ZnSe}$ ceramic is in the very early stage of development [12].

The used ceramic samples were fabricated with relatively low Cr concentration for spectroscopic characterization and optimization of the technological processes. For this reason in our current laser experiments with the $\text{Cr}^{2+}:\text{ZnSe}$ ceramic media we used the available ceramic gain element with significantly lower Cr doping level as compared to the $\text{Cr}^{2+}:\text{ZnSe}$ polycrystalline samples. This leads to much higher cw lasing threshold and much lower output power as compared to the polycrystalline $\text{Cr}^{2+}:\text{ZnSe}$. In this work, we describe broadly tunable chromium doped zinc selenide laser in the mid-infrared region.

II. TRANSITION METAL BASED SOLID STATE LASERS

Historically, the first tunable cw solid state lasers were those based on the divalent 3d transition metal ions. It should be noted that the existing transition metal ions, lasing on the 3d-3d transitions in the mid-infrared can be divided into two major groups: those ions, which occupy octahedral sites (Co^{2+} and Ni^{2+} in halides), and those, which can be found in tetrahedral positions (Cr^{2+} , Co^{2+} , Ni^{2+} , and Fe^{2+} in chalcogenides). The electric dipole transitions of the ions in octahedral sites (possessing inversion symmetry) are parity forbidden and have therefore generally low oscillator strength and long lifetime. The Cr^{2+} ions reside in II-VI hosts in tetrahedral sites. These sites do not possess inversion symmetry and are characterized by the high oscillator strength (high cross section) and short lifetime of typically a few microseconds [5]. The other distinguishing feature of the Cr^{2+} ions in tetrahedral sites is the relatively low crystal field splitting, placing optical transitions into infrared.

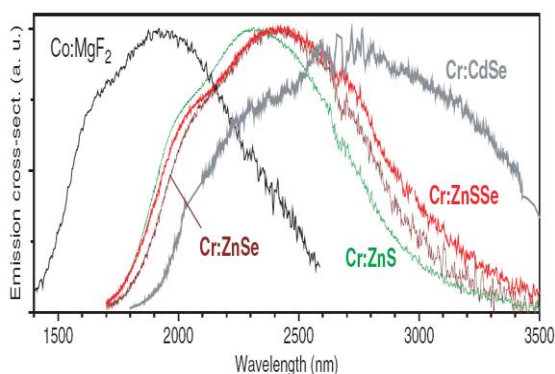


Figure 1. Gain curves of the existing ultra broadband mid-infrared lasers at room temperature [6]

The transition metal ions doped II-VI semiconductor compounds are promising materials for laser operation in the mid-infrared spectrum especially for the possibility of wavelength tuning in a broad range. Broadband transition metal ion doped solid state lasers are being frequently used as a constituent driving part of the optical parametric devices. At the same time they represent an attractive and simple alternative to these somewhat more complex and costly devices in the mid-infrared. In the recent years along with the Ti:sapphire based lasers systems, parametrically converting radiation to the mid-infrared, a lot of attention of researchers was devoted towards the alternative compact and cost effective cw and ultrashort pulsed sources based on Cr^{2+} doped crystals of the II-VI family. In the last decade a number of such sources have been developed in the “molecular fingerprint” range ~ 2 and $3.5 \mu\text{m}$ (Fig. 1).

At longer wavelengths ($2 \mu\text{m}$) the multiphonon relaxation processes set the fundamental limit for obtaining cw room temperature laser operation from vibronic transitions. Because of this the majority of the known vibronically broadened laser transitions in the mid-infrared are quenched at room temperature. At room temperature the latter is close to unity in $\text{Cr}^{2+}:\text{ZnSe}$ and is comparably high in other chalcogenide materials. This provides $\text{Cr}^{2+}:\text{ZnSe}$ the highest gain among vibronic lasers and enables efficient room temperature operation. It is not surprise that in the following years $\text{Cr}^{2+}:\text{ZnSe}$ draw a lot attention as a room temperature broadly tunable cw laser operating around $2.5 \mu\text{m}$ [2, 13, 14]. Since all the higher lying states are singlets or triplets, the excited state absorption transitions from the upper state are spin forbidden. Altogether this ensures that $\text{Cr}^{2+}:\text{ZnSe}$ has the highest gain among all vibronic solid state lasers and enables efficient broadband room temperature operation. One of the crystals of this family, $\text{Cr}^{2+}:\text{ZnSe}$, exhibited efficient room temperature diode pumped cw and mode locked operation also in the ceramic form. These lasers are nowadays probably the simplest and the most cost effective light sources in this wavelength region [11, 15, 16].

II.1. THE MATERIAL AND SPECTROSCOPIC PROPERTIES

The material and spectroscopic properties of the most important crystalline hosts for Cr^{2+} ion are summarized in Table 1 and Table 2 respectively. Among the listed crystals especially $\text{Cr}^{2+}:\text{ZnSe}$, $\text{Cr}^{2+}:\text{ZnS}$ and $\text{Cr}^{2+}:\text{CdSe}$ distinguished by their remarkable characteristics.

Table 1. Material properties of Cr^{2+} doped laser crystals [6]

	ZnSe	ZnS	CdSe
Crystal structure	cubic	Mixed-polytype	Cubic, uniaxial
Lattice constant (\AA)	5.67	5.4	6.05
Transparency range (μm)	0.5-20	0.4-14	0.8-18
Hardness	120	160	70
Refractive index	2.45	2.27	2.47
Thermal conductivity ($\text{W/m}^\circ\text{C}$)	18	17	4
Thermal expansion ($10^{-6}/^\circ\text{C}$)	7.3	6.4	4.9
dn/dT ($10^{-6}/^\circ\text{C}$)	70	46	98
Bandgap (eV)	2.8	3.8	1.7

The materials can be produced by a variety of methods, including several direct growth techniques and diffusion doping. The principal material disadvantages include a high dn/dT (the change in refractive index with temperature) and, for some applications, a short energy storage time. The high dn/dT is an issue because it can lead to strong thermal lensing, which complicates high power laser designs. $\text{Cr}^{2+}:\text{CdSe}$ has a somewhat larger lattice constant than $\text{Cr}^{2+}:\text{ZnSe}$ and $\text{Cr}^{2+}:\text{ZnS}$ (Table 1). The Cr^{2+} emission is therefore shifted by 100-200 nm towards the infrared and spreads out to over $3.5 \mu\text{m}$. If not rather inferior to $\text{Cr}^{2+}:\text{ZnSe}$ thermo optical properties, this laser crystal would be a perfect candidate for cw lasing beyond $3 \mu\text{m}$. Similarly to $\text{Cr}^{2+}:\text{ZnSe}$ and due to the same reason, the lifetime of $6 \mu\text{s}$ in $\text{Cr}^{2+}:\text{CdSe}$ does not change between 60 and 300 K. The peak absorption and emission cross section were measured to be $3 \times 10^{-18} \text{ cm}^2$ and $2 \times 10^{-18} \text{ cm}^2$ respectively [17].

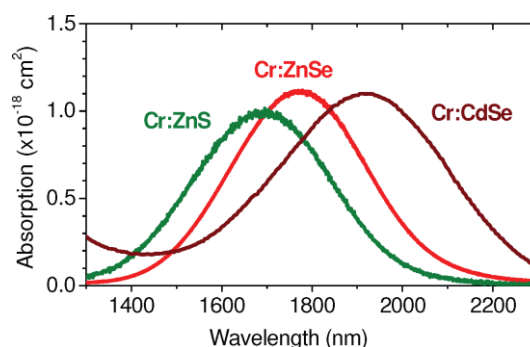


Figure 2. Absorption spectra of $\text{Cr}^{2+}:\text{ZnSe}$, $\text{Cr}^{2+}:\text{ZnS}$ and $\text{Cr}^{2+}:\text{CdSe}$ [6]

Table 2. Spectroscopic and laser characteristic of Cr^{2+} doped laser materials [6]

	ZnSe	ZnS	CdSe
Peak emission	130	140	200
Cross section σ_{emission}	90	75	-
Peak absorption	110	100	300
Cross section $\sigma_{\text{absorption}}$	87	52	-
Saturation intensity (kW/cm^2)	11	14	8
Luminescence bandwidth (nm)	900	800	550
Relative bandwidth	0.41	0.34	0.25
Optical quantum efficiency	1	0.73	1
Slope efficiency (%)	53	71	48
Cw output power (W)	1.8	0.7	-
Output energy (mJ-average pow.)	0.43	0.1	0.8
Mode locked output power (mW)	120	140	-
Pulse duration (fs)	80	1×10^{-3}	-
Diode pumping	yes	yes	no

The spectroscopic properties of Cr^{2+} (d^4) ion in II-VI compounds have been extensively studied since back in the sixties [18-20] and later in the seventies-eighties [21-25]. The absorption and emission spectra of Cr^{2+} ion in $\text{Cr}^{2+}:\text{ZnSe}$, $\text{Cr}^{2+}:\text{ZnS}$ and $\text{Cr}^{2+}:\text{CdSe}$ are depicted in Fig.1 and Fig. 2 respectively. A broad absorption band centered around $\sim 1.8 \mu\text{m}$ in $\text{Cr}^{2+}:\text{ZnSe}$, around $\sim 1.7 \mu\text{m}$ in $\text{Cr}^{2+}:\text{ZnS}$ and around $\sim 1.9 \mu\text{m}$ in Cd compounds allows pumping by Tm doped lasers, which are available as pulsed and cw sources of over 100 W average power and recently also as fiber lasers with even higher power [6]. It should be here that these media are characterized by high transition cross section, all being the results of inversion symmetry at the Cr^{2+} site (Table 2). Another important point is the additional broadening of the fluorescence spectrum due to the large Jahn-Teller splitting of the ground state, reaching 340 cm^{-1} and 300 cm^{-1} in $\text{Cr}^{2+}:\text{ZnSe}$ and $\text{Cr}^{2+}:\text{ZnS}$ respectively [20]. Among other II-VI compounds ZnS is distinguished by the largest energy gap of 3.8 eV, the smallest lattice constant and the correspondingly blue shifted fluorescence peaking around $2.1 \mu\text{m}$ (the corresponding emission cross section peaking around $2.3 \mu\text{m}$). As in case of $\text{Cr}^{2+}:\text{ZnSe}$ the measurements yielded decreased radiative lifetime of $5 \mu\text{s}$ and correspondingly corrected absorption and emission cross sections of $\sim 1 \times 10^{-18} \text{ cm}^2$ and $1.4 \times 10^{-18} \text{ cm}^2$ respectively. $\text{Cr}^{2+}:\text{ZnS}$, otherwise very similar to $\text{Cr}^{2+}:\text{ZnSe}$ is characterized by a more rapid onset of the thermally activated nonradiative decay with temperature (Fig. 3). Relatively to the 77 K lifetime the room temperature lifetime drops by $\sim 24\%$. The difference between $\text{Cr}^{2+}:\text{ZnSe}$ and $\text{Cr}^{2+}:\text{ZnS}$ may be explained by a higher maximum phonon frequency in this crystal (compare $\sim 250 \text{ cm}^{-1}$ in ZnSe and $\sim 350 \text{ cm}^{-1}$ in ZnS) [26, 27]. On the positive side there are the lowest dn/dT and the best hardness and the highest damage threshold among the Cr^{2+} doped media. All this makes $\text{Cr}^{2+}:\text{ZnS}$ especially attractive for high power applications.

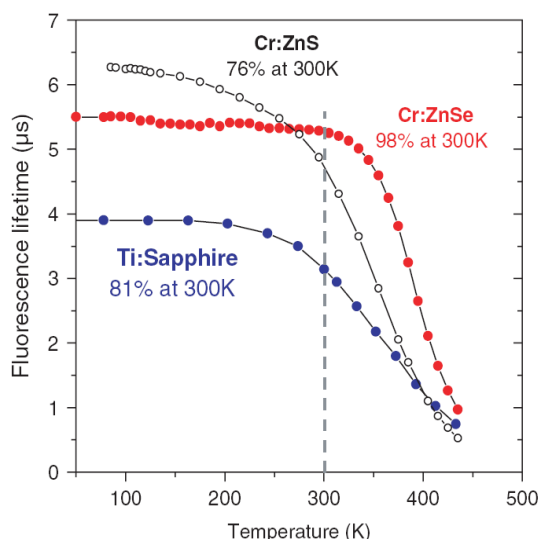


Figure 3. Temperature dependence of the active ion lifetime in $\text{Cr}^{2+}:\text{ZnSe}$, $\text{Cr}^{2+}:\text{ZnS}$ and Ti:sapphire [6]

II.2. $\text{Cr}^{2+}:\text{ZnSe}$ LASER COMPONENTS

Active material, $\text{Cr}^{2+}:\text{ZnSe}$ crystal grown by the special Bridgman method was prepared in the form of 6 mm thick block. The concentration of Cr^{2+} active ions in ZnSe matrix

was $\sim 1.0 \times 10^{19} \text{ cm}^{-3}$. The measured single pass absorption of $\text{Cr}^{2+}:\text{ZnSe}$ crystal in rectangular position was $\sim 36\%$ and $\sim 33\%$ for the wavelength $1.66 \mu\text{m}$ and $1.97 \mu\text{m}$, respectively. The setup for testing laser properties $\text{Cr}^{2+}:\text{ZnSe}$ crystal is shown in Fig. 4. Here, the test crystal is a thin, uncoated slab with parallel faces near the center of a confocal cavity. Test crystals were placed at the center of a confocal resonator whose dielectric coated mirrors had 20 cm radii of curvature. Coatings were centered at $\sim 2350 \text{ nm}$ and covered the 2200-2520 nm range. So far, most of the laser testing has been done with crystals grown by the Bridgman technique. Inspection with a microscope shows that these samples are not homogeneous, but have inclusions and/or voids which are tentatively attributed to selenium rich or metal rich precipitates [28]. With no tuning elements in the laser cavity, both the $\text{Cr}^{2+}:\text{ZnSe}$ and $\text{Cr}^{2+}:\text{ZnS}$ lasers operated at the emission peak of $\sim 2350 \text{ nm}$ with a bandwidth $\sim 40 \text{ nm}$. In that wavelength region, the mirror reflectivities were fairly constant, and ground state absorption from Cr^{2+} appears to be nonexistent.

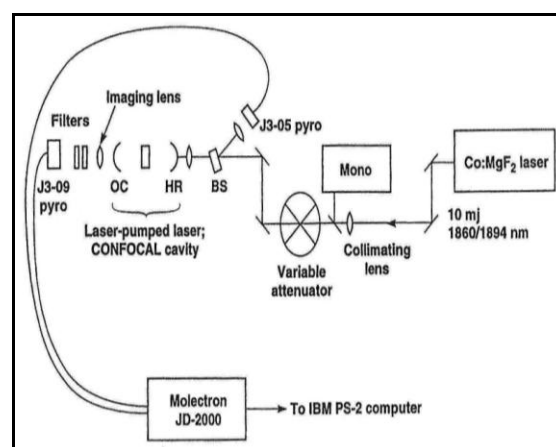


Figure 4. Experimental setup for testing Cr^{2+} laser [4]

We review the fluorescence properties of the $\text{Cr}^{2+}:\text{ZnSe}$ medium. In particular, we present data that show how the lifetime and the fluorescence efficiency vary with the active ion concentration. An empirical fit is also obtained for the concentration dependence of the lifetime. We further discuss the models used for the determination of the absorption cross section from cw and pulsed absorption saturation measurements. Since lifetime data are needed in the cw analysis of saturation.

$\text{Cr}^{2+}:\text{ZnSe}$ is attractive for room temperature cw laser applications because of a near unity fluorescence quantum efficiency at 300 K, a high gain cross section ($\sigma_{\text{emission}} \sim 9 \times 10^{-19} \text{ cm}^2$), and extremely wide vibronically broadened absorption and emission bands. Additionally, the Cr^{2+} ion in the ZnSe host effectively has a two term electronic structure (transitions to higher lying levels are spin forbidden and, presumably, very weak) that precludes losses that are due to excited state absorption or upconversion but allows four level laser action [13]. All of them report Cr^{2+} lifetime in various chalcogenides to be a few microseconds and not quenched up to $\sim 300 \text{ K}$. The extensive lifetime measurements were carried out in the last years for mainly polycrystalline as well as for single crystalline $\text{Cr}^{2+}:\text{ZnSe}$

crystals [29]. The latter study report only negligible increase of the lifetime from 5.4 μ s at 77 K to 5.6 μ s at 300 K.

To summarize, the advantages of Cr^{2+} doped chalcogenide materials include:

- Broad absorption bands (relaxed pump wavelength constraints)
- Broad emission bands (enables very broad laser tuning)
- Large emission cross sections (for instance, $\sigma_{\text{emission}} \sim 8 \times 10^{19} \text{ cm}^2$ in ZnSe)
- Minimal problems of excited state absorption (no spin allowed excited state transitions from the upper laser level)
- High fluorescence quantum efficiencies at 300 K (enables efficient room temperature laser operation)
- High thermal conductivities (18 $\text{Wm}^{-1} \text{K}^{-1}$ for ZnSe, 17-27 $\text{Wm}^{-1} \text{K}^{-1}$ ZnS, and 6-7 $\text{Wm}^{-1} \text{K}^{-1}$ for CdSe)
- Ability to produce material by several techniques (modified Bridgman growth technique and by diffusion doping)
- Readily available host material (polycrystalline material can be diffusion doped) [10].

III. EXPERIMENTAL PROCEDURE

The fundamental reason for the lack of tunable solid state mid-infrared lasers is the paucity of known materials luminescent in that region; the usual explanation for the long wavelength cutoff in the luminescence is the rapid onset of radiation less decay associated with multiphonon emission. As the electronic transition energy gap declines with increasing emission wavelength, the multiphonon emission rate overtakes and ultimately overwhelms the radiative transition rate, quenching the luminescence. Naturally, when solid state host dopant systems are considered, the long wavelength emission properties depend crucially on the choices of host and dopant [4]. Recently we undertook a spectroscopic study to search for potential laser materials for the 2-5 μ m range. Here, in finding a new class of tunable mid-infrared lasers Cr^{2+} ions in II-VI hosts (ZnSe). This class of lasers shows potential for high slope efficiency at room temperature, use of long wavelength laser diodes as pump sources, and coverage of most of the 2-3 μ m range.

The low phonon frequencies of heavy ion host materials give rise to infrared transparency, such that low loss windows, lenses, etc., for high power 10.6 μ m operation are conveniently fabricated from ZnSe and other II-VI compounds. As the energy gap law tell us, the multiphonon emission rate for a given is reduced as the phonon frequency is lowered. So, the tendency for luminescence quenching is reduced on this account as well [4].

To our knowledge, based on the scientific literature, the potential for laser action went unrecognized in spite of spectroscopic research spanning three decades. Our recent spectroscopic characterization focused on properties relevant to laser performance: absorption and emission cross sections, emission lifetimes, emission quantum yields, and the likelihood of significant excited state absorption. Most of the measurements were made at room temperature (Fig. 5), without regard to spectroscopic fine structure or detailed spectral assignments [5]. In this experiment tunability

between 2.1 μ m and 2.85 μ m was achieved at up to 10 W output power. Based on the analysis of the mechanical, thermal, spectroscopic, and laser properties of Cr^{2+} :ZnSe, the output powers over 10 W in cw regime and several Watts in the mode locked or amplifier regime can be anticipated. A representative room temperature optical absorption spectrum for Cr^{2+} doped ZnSe is shown in Fig. 5. The Cr^{2+} concentration in this particular sample was determined to be $5 \times 10^{18} \text{ cm}^{-3}$. For reference, the fundamental (band to band) absorption of an undoped ZnSe sample at $\sim 440 \text{ nm}$ is also shown (see dotted line).

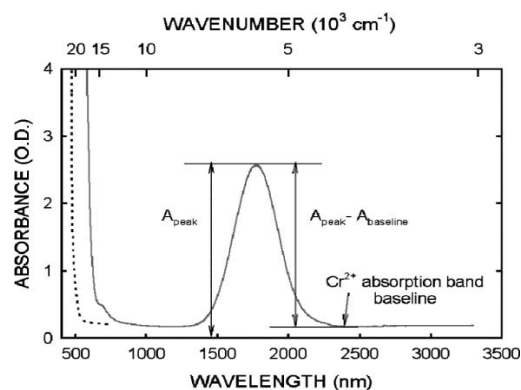


Figure 5. Room temperature absorption spectrum of a Cr^{2+} doped ZnSe sample [3]

The following achievements so far have been demonstrated with Cr^{2+} doped ZnSe laser: cw TEM₀₀ output power over 1.7 W, as well as over 1100 nm tunability and narrow linewidth operation (A laser schematic is shown in Fig. 6).

Crystals were longitudinally pumped and placed in a three mirror resonator. Laser crystals were 2-3 mm thick and oriented at Brewster's angle. A key feature of this design is the use of a gold mirror to double pass the pump light through the laser crystal while maintaining good pump and cavity mode overlap. This enabled the laser to produce higher output power and use more of the pump beam than a single pass device, without sacrificing efficiency. Laser line widths were on the order of 35-50 nm, similar to the pulsed lasers described previously.

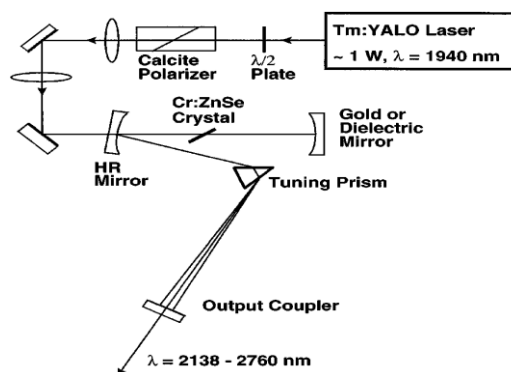


Figure 6. Schematic of the optical system and laser cavity used for most of the Cr^{2+} :ZnSe laser experiments [13]

Diode pumping has been realized in a quasi cw regime in transversal pumped scheme, and recently, the cw operation of the diode end pumped Cr^{2+} :ZnSe laser has been reported

[1]. They present the diode pumped room temperature cw $\text{Cr}^{2+}:\text{ZnSe}$ laser, which is tunable over 350 nm. The laser delivered around 2.5 mm up to 70 mW of polarized radiation in a single transverse mode.

$\text{Cr}^{2+}:\text{ZnSe}$ is one of the most studied and effective active laser materials which meet all the previous mentioned requirements. So far the $\text{Cr}^{2+}:\text{ZnSe}$ crystal samples were produced mainly by the diffusion doping technique. In their study they have investigated $\text{Cr}^{2+}:\text{ZnSe}$ bulk crystal samples grown by the special Bridgman method. The Cr^{2+} ion concentration was $1 \times 10^{19} \text{ cm}^{-3}$. $\text{Cr}^{2+}:\text{ZnSe}$ crystal bulks with a diameter up to 50 mm and a length up to 100 mm were produced. From the bulk the $\text{Cr}^{2+}:\text{ZnSe}$ dispersive prism was polished. This $\text{Cr}^{2+}:\text{ZnSe}$ dispersive prism was utilized as a laser active material and simultaneously as a wavelength tuning element inside the laser resonator [30].

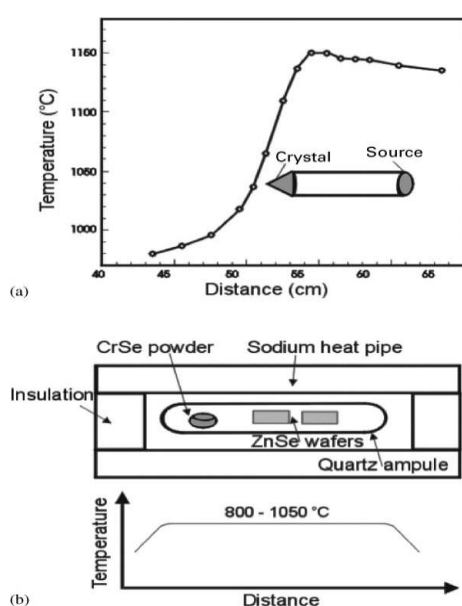


Figure 7. Experimental setup for the preparation of $\text{Cr}^{2+}:\text{ZnSe}$ samples by (a) physical vapor transport, (b) solid state diffusion doping [3]

In general, dopant concentration levels of the order of 10^{18} - 10^{19} cm^{-3} are usually needed to provide device required characteristics. Compared with melt grown and post growth diffusion doped ZnSe crystals, physical vapor transport grown chromium doped ZnSe possesses the highest optical quality and lowest loss [4]. Concentrations in excess of $10^{19} \text{ Cr}^{2+} \text{ ions/cm}^3$ comparable to the previously reported values for melt grown Cr^{2+} doping ZnSe material, have been obtained by diffusion doping and physical vapor transport growth. The setup for both the physical vapor transport growth and diffusion doping methods are shown in Fig. 7.

However, the reported luminescence lifetimes varied considerably from sample to sample. A specific goal of the present study was to perform a systematic study that will comparatively evaluate the luminescent properties of ZnSe samples doped with chromium during growth by physical vapor transport with samples doped post growth by thermal diffusion.

We report the experimental observation of the significant change of the upper laser level population under low power visible excitation, which is explained by the enhanced charge transfer process. For laser experiments, three laser crystals were available, two of them grown by physical vapor transport and one by chemical vapor transport methods. The crystals were diffusion doped with Cr^{2+} ions reaching concentration between $5 \times 10^{18} \text{ cm}^{-3}$ and $2 \times 10^{19} \text{ cm}^{-3}$. The crystal thickness varied between 1.5mm and 3 mm, providing over 80% absorption at the pump wavelength of 1600 nm.

III.1. SPECTROSCOPIC MEASUREMENTS

Transmission and absorption measurements were performed using Bruker Equinox 55 Fourier transform FTIR spectrophotometer (Department of Physics, METU, Ankara-Turkey). A selective group of Cr^{2+} doped ZnSe and CdTe windows possessing different absorption coefficients and Cr^{2+} concentration were further evaluated for mid-infrared laser applications.

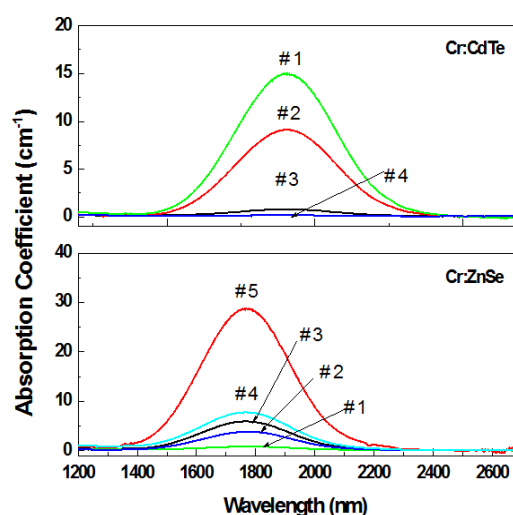


Figure 8. Absorption spectra of $\text{Cr}^{2+}:\text{ZnSe}$ and $\text{Cr}^{2+}:\text{CdTe}$ polycrystalline window materials [31]

In addition, the absorption and emission properties of a series of Cr^{2+} doped single crystals including CdTe. The $\text{Cr}^{2+}:\text{ZnSe}$ and $\text{Cr}^{2+}:\text{CdTe}$ series was evaluated for possible compositional effects, which may alter the spectroscopic properties of Cr^{2+} ions. The mid-infrared emission measurements were performed using a Tm fiber laser operating at 1907 nm. The emission was detected with an InSb detector and dispersed by a 0.3 m spectrometer with a 150 g/mm grating blazed at 2000 nm. A series of samples with different Cr^{2+} concentrations was prepared for $\text{Cr}^{2+}:\text{ZnSe}$ and $\text{Cr}^{2+}:\text{CdTe}$ windows. The background corrected absorption spectra of $\text{Cr}^{2+}:\text{ZnSe}$ and $\text{Cr}^{2+}:\text{CdTe}$ windows are shown in Fig. 8.

The successful incorporation of Cr^{2+} ions into the II-VI materials (windows) is evidenced by the strong absorption bands centered at $\sim 1750 \text{ nm}$ for $\text{Cr}^{2+}:\text{ZnSe}$ and at $\sim 1900 \text{ nm}$ for $\text{Cr}^{2+}:\text{CdTe}$ [10, 31]. All samples exhibited the characteristic absorption and emission features of tetrahedral coordinated ions. The mid-infrared emission properties of these materials are promising for solid state laser development in the 2-3 μm spectral region.

III.2. NANOCRYSTALLINE Cr²⁺:ZnSe LASER

The Cr²⁺ doped laser materials are characterized by high gain and an intrinsically low lasing threshold, as well as by such remarkable spectroscopic features as the absence of excited state absorption and high quantum yield. The active media can be obtained by diffusion doping of metallic chromium into the ceramic ZnSe. Along with several other techniques of producing ceramic ZnSe, the latter is often obtained by hot pressing the micro and nanocrystalline ZnSe powder. Cr²⁺:ZnSe lasers can be operated in pulsed mode by using a second pulsed pump laser whose wavelength overlaps with the absorption band. The peak powers obtainable from pulsed pump sources are typically high and lasing can thus be achieved at lower average pump powers than those needed for cw pumping.

An important feature, distinguishing the Cr²⁺ doped materials from all the other solid state lasers combines the properties of semiconductors with that of the traditionally used in solid state lasers dielectric materials. Cr²⁺ doped materials possess the excellent laser properties along with the interesting physics as well as optical and nonlinear properties, distinguishing them from the traditionally used dielectric laser media. This opens up an exciting white field of research and new opportunities for the use of these materials in laser and nonlinear optical applications, as well as for direct electrical pumping.

Because of the semiconductor nature of II-VI compounds the charge transfer processes play an important role in these materials. The most important features of these materials, which distinguish them from other oxide and fluoride laser crystals:

1. Noncentrosymmetric tetrahedral sites for Cr²⁺ ions. This leads to the partially allowed electric dipole transitions and large absorption and emission cross sections (10^{18} cm²).
2. Covalent rather than ionic type of bonding leads to the fact that intraionic laser processes are not purely intracentral in these materials, which results in high probability of charge transfer processes and explains multiple valency of transition metal ions, especially in highly concentrated samples ($\sim 10^{19}$ cm⁻³), as required for diode pumping.
3. Semiconductor nature of the crystals implies that charge transfer processes generate free carriers leading to photorefractive phenomena, it also leads to the high second and third order nonlinearity of the host crystal.

As it has been recently shown, the charge transfer processes in some cases may affect the laser performance of Cr²⁺:ZnSe and Cr²⁺:ZnS lasers with the active ions in tetrahedral sites [1, 32]. In both these lasers we observed a novel effect of sensitization (modulation) of the induced radiation around 2.5 μ m with only a few milliwatt of the visible and near infrared radiation (470-770 nm). The reported phenomenon is of the photorefractive nature and involves charge transfer to chromium ions, similar to the mechanism of photorefractive, which takes place in other transition metal doped chalcogenides.

Summarizing, the described effect of sensitization of induced radiation can be used for both, electrical pumping of Cr²⁺ laser, and for opto-optical switching. Indeed, the "zero to one" switching was realized in Cr²⁺:ZnSe laser by switching on and off the probe beam, whereas the laser changed its condition from the state with no lasing to the state with laser operation. This was a proof of principle demonstration of using a diode pumped solid state laser as an alternative type of switching device. Maybe one of the most exciting developments in Cr²⁺ doped lasers recently was the demonstration of the first Cr²⁺:ZnSe random nanolaser, based on nanometer (down to 200 nm) sized Cr²⁺:ZnSe powder emitting around 2.4 μ m.

High quality transparent ceramic laser gain media have a number of potential advantages over conventional solid state gain elements: absence of internal stress typical for single crystals; negligible scattering losses common for polycrystalline media such as ZnSe; flexibility in the spatial distribution of the gain centers, which allows for efficient compensation of thermal lensing effects (which are very problematic for conventional Cr²⁺:ZnSe media). Therefore, fabrication of high quality Cr²⁺:ZnSe ceramic gain media is of a great interest for development of advanced mid-infrared laser systems.

IV. CONCLUSION

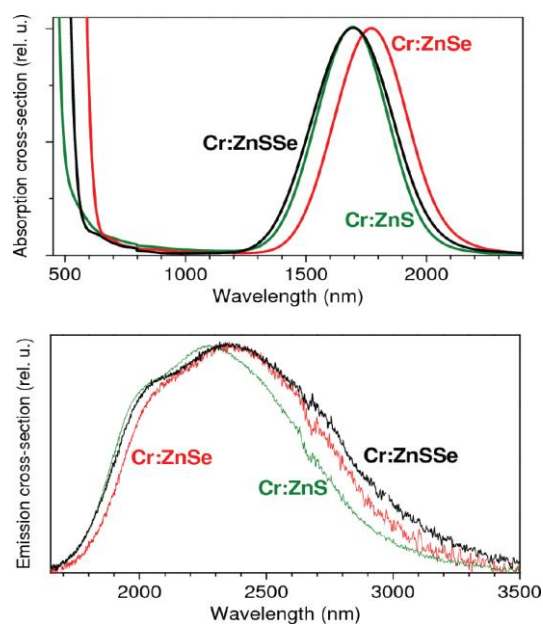
We have provided a comprehensive review of the work on the development of Cr²⁺:ZnSe lasers. A detailed account of the preparation methods and spectroscopic characterization techniques was presented. Diffusion doping was described in detail and various methods for the determination of the diffusion coefficient were discussed. Pulsed, cw, and mode locked operations of the Cr²⁺:ZnSe lasers were also reviewed.

Summarizing, Cr²⁺ doped lasers have come of age and already entered several real world applications, such as gas analysis, ultra sensitive spectroscopy, and quantum optics. As an extension of previous work, we present the results of a systematic study which investigates the synthesis of Cr²⁺:ZnSe and Fe²⁺:ZnSe samples by thermal diffusion. In particular, we have measured how the diffusion parameters such as temperature and time influence the chromium and iron concentrations inside the host and determined the diffusion coefficient for both Cr²⁺:ZnSe and Fe²⁺:ZnSe. In the case of Cr²⁺:ZnSe, we have further characterized the spatial transverse uniformity of the diffusion doped samples.

The results of the absorption and room temperature luminescence measurements are given in Fig. 9 and summarized in Table 3. As seen in Fig. 1, the high quality absorption due to predominantly Cr²⁺ ions could be obtained in this crystal with peak absorption coefficient of 9.5 cm⁻¹ the maximum around 1.69 μ m. The room temperature lifetime was measured to be 3.7 μ s, which is close to the corresponding value measured in concentrated Cr²⁺:ZnSe and Cr²⁺:ZnS, as are the corresponding values for absorption and emission cross sections. However, emission bandwidth is noticeably broader than in Cr²⁺:ZnSe or Cr²⁺:ZnS and is peaked at the same wavelength as in Cr²⁺:ZnSe (Fig. 9).

Table 3. Main spectroscopic data of Cr²⁺ doped laser materials [6]

	ZnSe	ZnS	ZnSSe
Absorption peak (nm)	1770	1695	1696
Absorption width (nm)	355	350	400
Gain peak (nm)	2400	2315	2410
Gain bandwidth (nm)	850	800	930
Lifetime at 300 K (μs)	4.8	4.3	3.7

Figure 9. Comparison of the absorption (upper graph) and fluorescence (lower graph) spectra of Cr²⁺:ZnSe, Cr²⁺:ZnS, and Cr²⁺:ZnSSe [6]

The most impressive results have been obtained so far using the Cr²⁺:ZnSe crystals. The Cr²⁺:ZnS crystal was less studied as a laser material due to the lack of good optical quality single crystals. Having similar spectroscopic properties to Cr²⁺:ZnSe, Cr²⁺:ZnS is known to have a larger band gap, better hardness, a higher thermal shock parameter (5.3 W/m^{1/2} and 7.1 W/m^{1/2} in Cr²⁺:ZnSe and Cr²⁺:ZnS, respectively [33]), and the lower dn/dT than in Cr²⁺:ZnSe (Table 1). At the same time, the temperature quenching of the Cr²⁺:ZnS lifetime starts at lower temperatures, than in Cr²⁺:ZnSe (Fig. 3), which might be a serious disadvantage, especially in cw applications. With proper cooling, however, the power handling capability of this material should be on par or better than that of Cr²⁺:ZnSe, making Cr²⁺:ZnS attractive for high power applications.

It is noteworthy that as a result of numerous experiments with Cr²⁺:ZnSe gain media we found that there are no significant advantages of using single crystalline over the polycrystalline ZnSe host material. However, from practical point of view, the technology for polycrystalline active elements is much cheaper, and high quality undoped polycrystalline ZnSe material is widely available in various sizes for further thermal diffusion Cr²⁺ doping. For these reasons, all the experiments with high power Cr²⁺:ZnSe lasers, where relatively long gain elements are required,

were conducted with the polycrystalline Cr²⁺:ZnSe gain media. There are several reasons why the Cr²⁺:ZnS a laser system performs much better than the Cr²⁺:ZnSe laser in our arrangement. First of all, the emission wavelength of the pump diode is ~1685 nm, which is practically at the maximum of absorption curve of Cr²⁺:ZnS gain media. Secondly, the Cr²⁺:ZnS gain element has about 1.70 times higher Cr²⁺ concentration that the Cr²⁺:ZnSe gain element used in the experiments. As a result of these two factors more pump power is absorbed by the Cr²⁺:ZnS gain crystal than by the Cr²⁺:ZnSe gain element and we observe higher overall efficiency on the incident pump for the Cr²⁺:ZnS laser system. Undoubtedly, more careful design of the Cr²⁺:ZnSe gain element will allow one to obtain similar output characteristics as for the Cr²⁺:ZnS diode pumped laser.

Nowadays, femtosecond pulses in this wavelength range are being produced by multi stage parametric frequency converters based on Ti:sapphire laser, which are rather bulk and inefficient in comparison to the directly diode pumped Cr²⁺:chalcogenide lasers, emitting in this wavelength region. In the last few years picosecond mode locking, both active and passive, has been achieved in Cr²⁺:ZnSe and Cr²⁺:ZnS laser [11]. The first works used an acousto optic modulator to mode lock the laser with the shortest pulses being 4 ps at up to 400mW output power. Later, the first semiconductor saturable absorber mode locked Cr²⁺:ZnSe laser generating 11 ps pulses at 2.5 μm at 400mW output power was demonstrated [11]. The pulse duration was presumed to be limited by some intrinsic limitation like an etalon. For some time the reported pulse durations were in the picosecond range. To overcome a picosecond barrier in Cr²⁺ lasers became therefore a highly desirable, but also a very challenging task. Recently we could finally identify the physical cause of this picosecond barrier, which was due to the water absorption lines in the resonator around 2.5 μm. Finally we should note that Cr²⁺:ZnSe is capable of power scaling and producing up to 1 μJ pulses directly from the oscillator. Looking into the future one can envisage broadband tunable and high power Cr²⁺:ZnSe based nanocrystalline doped fiber lasers, operating in the very interesting for remote sensing and trace gas sensing applications wavelength region around 2.5 μm. Development of such a laser, which would be complementary to the existing Tm fiber laser at 1.9 μm, will be a leap forward in the fiber laser technology. Therefore, medical applications as ophthalmology, tissue cutting and welding, neurosurgery, dermatology and bioimaging would benefit from broadband and rapidly tunable coherent sources in this wavelength region.

ACKNOWLEDGEMENTS

We would especially like to thank Dr. Te-yuan CHUNG (Department of Optics and Photonics, National Central University, Taiwan-China), for his constant encouragement and help stimulating discussions of this research. We are grateful to Professor Dr. K. Jyrki KAUPPINEN (Physics Department, Laboratory of Optics and Spectroscopy, University of Turku, Turku-Finland) for the opportunity to perform this work and his valuable comments on the manuscript.

REFERENCES

- [1] E. Sorokin and I.T. Sorokina, Tunable diode-pumped continuous-wave Cr^{2+} :ZnSe laser, *Applied Physics Letters*, 80(18), 2002, 3289-3291.
- [2] I.T. Sorokina, E. Sorokin, A.D. Lieto, M. Tonelli, R.H. Page and K.I. Schaffers, Efficient broadly tunable continuous-wave Cr^{2+} :ZnSe laser, *Journal of the Optical Society of America B*, 18(7), 2001, 926-930.
- [3] A. Burger, K. Chattopadhyay, J.O. Ndap, X. Ma, S.H. Morgan, C.I. Rablau, C.H. Su, S. Feth, R.H. Page, K.I. Schaffers and S.A. Payne, Preparation conditions of chromium doped ZnSe and their infrared luminescence properties, *Journal of Crystal Growth*, 225(2-4), 2001, 249-256.
- [4] R.H. Page, K.I. Schaffers, L.D. DeLoach, G.D. Wilke, F.D. Patel, J.B. Tassano, S.A. Payne, W.F. Krupke, K.-T. Chen and A. Burger, Cr^{2+} -doped zinc chalcogenides as efficient, widely tunable mid-infrared lasers, *IEEE Journal of Quantum Electronics*, 33(4), 1997, 609-619.
- [5] L.D. DeLoach, R.H. Page, G.D. Wilke, S.A. Payne and W.F. Krupke, Transition metal-doped zinc chalcogenides: spectroscopy and laser demonstration of a new class of gain media, *IEEE Journal of Quantum Electronics*, 32(6), 1996, 885-895.
- [6] I.T. Sorokina, Broadband mid-infrared solid-state lasers, *Topics in Applied Physics*, 79, 2003, 255-350.
- [7] U. Hömmerich, J.T. Seo, A. Bluiett, M. Turner, D. Temple, S.B. Trivedi, H. Zang, S.W. Kutcher, C.C. Wang, R.J. Chen and B. Schumm, Mid-infrared laser development based on transition metal doped cadmium manganese telluride, *Journal of Luminescence*, 87-89, 2000, 1145-2000.
- [8] N. Picque, F. Gueye and G. Guelachvili, Time-resolved Fourier transform intracavity spectroscopy with a Cr^{2+} :ZnSe laser, *Optics Letters*, 30(24), 2005, 3410-3412.
- [9] V.M. Baev, T. Latz and P.E. Toschek, Laser intracavity absorption spectroscopy, *Applied Physics B: Lasers and Optics*, 69(3), 1999, 171-202.
- [10] T.J. Carrig, Transition-metal-doped chalcogenide lasers, *Journal of Electronic Materials*, 31(7), 2002, 759-769.
- [11] T.J. Carrig, G.J. Wagner, A. Sennaroglu, J.Y. Jeong and C.R. Pollock, Mode-locked Cr^{2+} :ZnSe laser, *Optics Letters*, 25(3), 2000, 168-170.
- [12] S. Mirov, V. Fedorov, I. Moskalev and D. Martyshkin, Recent progress in transition metal doped II-VI mid-IR lasers, *Journal of Specification Topics in Quantum Electronics*, 13(3), 2007, 810-827.
- [13] G.J. Wagner, T.J. Carrig, R.H. Page, K.I. Schaffers, J.O. Ndap, X. Ma and A. Burger, Continuous-wave broadly tunable Cr^{2+} :ZnSe laser, *Optics Letters*, 24(1), 1999, 19-21.
- [14] A. Sennaroglu, A.O. Konza and C.R. Pollock, Continuous-wave power performance of a 2.47 μm Cr^{2+} :ZnSe laser: experiment and modelling, *IEEE Journal of Quantum Electronics*, 36(10), 2000, 1199-1205.
- [15] E. Sorokin, S. Naumov and I.T. Sorokina, Ultrabroadband infrared solid-state lasers, *IEEE Journal of Selected Topics in Quantum Electronics*, 11(3), 2005, 690-712.
- [16] E. Sorokin, I.T. Sorokina, A.D. Lieto, M. Tonelli and P. Minguzzi, Mode-locked ceramic Cr^{2+} :ZnSe laser, *OSA Trends in Optics and Photonics*, 83, (Advanced Solid-State Lasers), 2003, Optical Society of America, Washington, pp. 227-230.
- [17] K.L. Schepler, S. Kueck and L. Shiozawa, Cr^{2+} emission spectroscopy in CdSe, *Journal of Luminescence*, 72-74, 1997, 116-117.
- [18] J.T. Vallin, G.A. Slack, S. Roberts and A.E. Hughes, Near and far infrared absorption in Cr doped ZnSe, *Solid State Communications*, 7(17), 1969, 1211-1214.
- [19] J.T. Vallin, G.A. Slack, S. Roberts and A.E. Hughes, Infrared absorption in some II-VI compounds doped with Cr, *Physical Review B*, 2(11), 1970, 4313-4333.
- [20] M. Kaminska, J.M. Baranovski, S.M. Uba and J.T. Vallin, Absorption and luminescence of Cr^{2+} (d^4) in II-VI compounds, *Journal of Physics C: Solid State Physics*, 12(11), 1970, 2197-2214.
- [21] G. Grebe and H.J. Schulz, Luminescence of Cr^{2+} centers and related optical interactions involving crystal field levels of chromium ions in ZnS, *Zeitschrift für Naturforschung A*, 29(12), 1974, 1803-1809.
- [22] G. Grebe, G. Roussos and H.J. Schulz, Infrared luminescence of ZnSe:Cr crystals, *Journal of Luminescence*, 12-13, 1976, 701-705.
- [23] R. Renz and H.J. Schulz, Temperature dependence of the lifetime of excited states for 3d transition element centers in II-VI crystals, *Journal of Luminescence*, 24-25(1), 1981, 221-224705.
- [24] G. Goetz and H.J. Schulz, Decay of internal luminescence transitions of 3d-impurities in II-VI compounds-recent experiments and refined interpretations, *Journal of Luminescence*, 40-41, 1988, 415-416.
- [25] H. Pradella and U.W. Pohl, Luminescence of the Cr^+ center in ZnSe, *Physica Status Solidi B*, 141(2), 1987, K143-K146.
- [26] A.K. Arora, E.K. Suh, U. Debska and A.K. Ramdas, Raman-scattering study of the high-pressure phase transition in $\text{Zn}_{1-x}\text{Mn}_x\text{Se}$, *Physical Review B*, 37(6), 1988, 2927-2932.
- [27] O. Brafman and S.S. Mitra, Raman effect in wurtzite and zinc-blende-type ZnS single crystals, *Physical Review*, 171(3), 1968, 931-934.
- [28] K.T. Chen, M.A. George, Y. Zhang, A. Burger, C.H. Su, Y.G. Sha, D.C. Gillies and S.L. Lehoczky, Selenium precipitation in ZnSe crystals grown by physical vapor transport, *Journal of Crystal Growth*, 147(3-4), 1995, 292-296.
- [29] U. Demirbas, A. Sennaroglu and M. Somer, Synthesis and characterization of diffusion-doped Cr^{2+} :ZnSe and Fe^{2+} :ZnSe, *Optical Materials*, 28(3), 2006, 231-240.
- [30] P. Koranda, M.E. Doroshenko, H. Jelinkova, J. Sulc, M. Nemeč, T.T. Basiev, V.K. Komar and M.B. Kosmyna, Broadly tunable Cr:ZnSe laser, 2007 and the International Quantum Electronics Conference. CLEOE-IQEC 2007, European Conference on, 17-22 June 2007.
- [31] I.T. Sorokina, Cr^{2+} -doped II-VI materials for lasers and nonlinear optics, *Optical Materials*, 26(4), 2004, 395-412.
- [32] I.T. Sorokina, E. Sorokin, S. Mirov, V. Federov, V. Badikov, V. Panyutin and K. Schaffers, Broadly tunable compact continuous-wave Cr^{2+} :ZnS laser, *Optics Letters*, 27(2), 2002, 140-142.
- [33] R.H. Page, L.D. DeLoach, G.D. Wilke, S.A. Payne, R.J. Beach and W.F. Krupke, Cr^{2+} -doped II-VI crystals: new widely tunable, room-temperature mid-IR lasers, *Lasers and Electro-Optics Society Annual Meeting (8th Annual Meeting Conference Proceedings)*, 1, 1995, 449-450.

Thermodynamic Assessment of Multiple Physiological Stress Responses Using Maxwell Relations

Satish C. Boregowda¹, Robert E. Choate², Rodney Handy³, and Olafur S. Palsson⁴

¹Sandia National Laboratories, PO Box 5800, Albuquerque, NM 87185

²Western Kentucky University, Bowling Green, KY 42101

³Purdue University, West Lafayette, IN 47907

⁴University of North Carolina School of Medicine, Chapel Hill, NC 27599

ABSTRACT

The present study introduces a macroscopic thermodynamic methodology to quantify entropy change in a human physiological system using Maxwell relations. This approach combines three physiological measures (mean arterial pressure, heart rate, and finger skin temperature) to provide a measure of entropy change (ΔS). The experimental data was collected from a study that included eighty-two subjects (49 males and 33 females). The three physiological measures were taken under three conditions (relaxation, stressor task, and recovery) during the physiological test profile. The entropy change (ΔS) is computed using Maxwell relations in terms of measurable mean arterial pressure, heart rate, and skin temperature. The average values of the physiological responses ($n=49$ males and $n=33$ females) are used in the modified Maxwell relations to compute the entropy change from relaxed state to stressor and recovery states for male and female subjects respectively. The results demonstrate that stressor task and recovery do have an impact on human physiology, which is indicated in entropy change values. The entropy change characterizes the human body from a thermodynamics viewpoint and could be valuable for the study of human physiology.

Keywords - entropy change; human physiology; Maxwell relations; stress; thermodynamics.

1. INTRODUCTION

Numerous studies have been conducted by researchers to apply thermodynamics to model and investigate human physiology. Earlier work done one by Schrodinger [1] establishes the fact that the human life processes are indeed thermodynamic in nature and hence thermodynamic laws can be used to model human physiology. Nicolis and Prigogine [2] have applied the second law of thermodynamics to model open living systems and thereby derived an expression for entropy generation. The earlier studies by Iberall et al. [3-5] have demonstrated the utility of thermodynamics to model integrated dynamics of human physiology. Harold Morowitz [6] has indicated that the knowledge of the biological state without an energetically significant measurement would lead to a violation of the

second law of thermodynamics. It has been hypothesized by Bridgman [7] that the laws of thermodynamics are intrinsically positioned to model the physiological behavior of living systems. The most recently discovered thermodynamics-based Constructal Theory, developed by Adrian Bejan [8, 9] has been used to model pulsating transport phenomena in biological systems Magin et al. [10]. Recently, in studies conducted by Silva et al. [11, 12], entropy generation and human aging are examined using nutritional and physical activity data. Ichiro Aoki [13, 14] has measured entropy flow and production in basal and exercising conditions. Most of these past studies have made significant efforts to apply laws of thermodynamics to study living systems, but none of them have utilized Maxwell relations to combine multiple human physiological responses to measure entropy change. In this regard, the studies conducted by Boregowda et al. [15-17] and Palsson et al. [18] have presented the development and preliminary verification of a physiological entropy change. The purpose of this study is to model human physiological system on a macroscopic as a simple system using Maxwell relations.

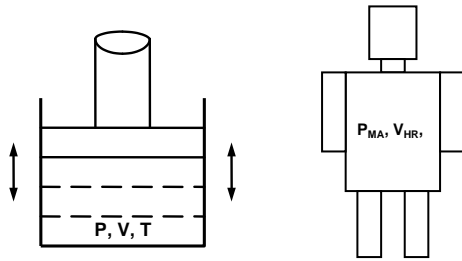
2. MODELING AND FORMULATION

The modeling is based on the idea that Maxwell relations can be used to calculate entropy change in terms of measurable physical quantities such as pressure, volume, and temperature [19, 20]. An analogy between physical and human physiological systems is conceptualized and the properties of a non-living system are mapped to that of a living system as shown in Table 1 and Figure 1. The physical system characterized by pressure (P), volume (V), and temperature (T) are mapped to that of a human system - mean arterial pressure (P_{MA}), heart rate (V_{HR}), and skin temperature (T_s), respectively.

2.1 Assumptions

(a) Human physiological stress response system is considered as a simple system from a macroscopic perspective for the purpose of this study. This makes it possible to apply Maxwell relations to examine human physiology from a thermodynamics perspective.

(b) Mean arterial pressure, Heart rate, and Skin temperature are equivalent to Pressure, Volume, and Temperature, respectively as shown in Fig. 1.



Entropy (S) = f (P, V, T) Entropy (S) = f (P_{MA}, V_{HR}, T_S)

Figure 1. Similarity analysis of simple mechanical and human physiological systems

(c) The heart rate is an indirect measure of stroke volume of blood in the heart region and is thus used in the place of stroke volume. Please note that heart rate (in beats per minute) is equal to cardiac output (mL/min) divided by stroke volume (mL/beat).

(d) The ratio of partial changes in two physiological variables is accompanied by constancy in the third variable as this is the basis of Maxwell relations. For example, when there is a partial change in heart rate with respect to partial change in entropy, the mean arterial pressure remains constant.

Table 1: Comparing Two Simple Systems: Mechanical and Human

Physical Variables (Simple Mechanical System)	Physiological Variables (Simple Human System)
Pressure (P)	Mean Arterial Pressure (P _{MA})
Volume (V)	Heart Rate (V _{HR})
Temperature (T)	Skin Temperature (T _S)
Entropy (S)	Physiological Entropy (S _P)

2.2 Derivation of Physiological Entropy Change

Let us begin with mathematics by considering a variable z that is a continuous function of x and y (Callen, 1985).

$$z = f(x,y) \tag{1}$$

It is convenient to write the above equation in the following form:

$$dz = M dx + N dy$$

Where $M = (\partial z / \partial x)_y$; $N = (\partial z / \partial y)_x$

If in Eq. (1), x, y, and z are all point functions (i.e., quantities that depend only on the state and are independent of the path), the differentials are exact differentials. Therefore, in order for Eq. (1) to be an exact differential equation, the following condition must be satisfied:

$$(\partial M / \partial y)_x = (\partial N / \partial x)_y \tag{2}$$

Eq. (2) is called the Exactness Condition.

Maxwell relations are derived from the property relations of thermodynamic potentials by invoking the exactness condition. For a simple human physiological system, there are four thermodynamic potentials:

- Internal Energy: $dU_P = T_S dS_P - P_{MA} dV_{HR}$
- Enthalpy: $dH_P = T_S dS_P + V_{HR} dP_{MA}$
- Helmoltz Function: $dA_P = -P_{MA} dV_{HR} - S_P dT_S$
- Gibbs Function: $dG_P = V_{HR} dP_{MA} - S_P dT_S$

The following Maxwell relations are obtained by invoking the exactness condition on the above four property relations:

$$(\partial T_S / \partial V_{HR})_{S_P} = -(\partial P_{MA} / \partial S_P)_{V_{HR}} \tag{3a}$$

$$(\partial T_S / \partial P_{MA})_{S_P} = (\partial V_{HR} / \partial S_P)_{P_{MA}} \tag{3b}$$

$$(\partial P_{MA} / \partial T_S)_{V_{HR}} = (\partial S_P / \partial V_{HR})_{P_{MA}} \tag{3c}$$

$$(\partial V_{HR} / \partial T_S)_P = -(\partial S_P / \partial P_{MA})_{T_S} \tag{3d}$$

The above-mentioned partial derivatives are approximated to form a modified set of Maxwell relations that are used in the present experimental study to compute the physiological entropy change:

$$(\Delta T_S / \Delta V_{HR})_{S_P} = -(\Delta P_{MA} / \Delta S_P)_{V_{HR}} \tag{4a}$$

$$(\Delta T_S / \Delta P_{MA})_{S_P} = (\Delta V_{HR} / \Delta S_P)_{P_{MA}} \tag{4b}$$

$$\Delta P_{MA} / \Delta T_S)_{V_{HR}} = (\Delta S_P / \Delta V_{HR})_{P_{MA}} \tag{4c}$$

$$(\Delta V_{HR} / \Delta T_S)_{P_{MA}} = -(\Delta S_P / \Delta P_{MA})_{T_S} \tag{4d}$$

Any of the above relations, (4a)-(4d), could be used to quantify ΔS_P , the human physiological entropy change.

Using the mechanical to human system mapping provided in the Table 1, let us consider the expression $z = f(x,y)$ with $z =$ physiological enthalpy (H); $x =$ physiological entropy (S_p); and $y =$ mean arterial pressure (P_{MA}); $M =$ skin temperature (T_s); and $N =$ heart rate (V_{HR}). Using the enthalpy-based thermodynamic potential and invoking the exactness condition, we have, for the simple human physiological system shown on the right-hand side of Figure 1, the following absolute entropy change:

$$\Delta SP_p = \left| (\Delta P_{MA} \times \Delta V_{HR}) / \Delta T_s \right| \quad (5)$$

Where, $\Delta P_{MA} =$ Change in mean arterial pressure from relaxed to stressor and recovery states

$\Delta V_{HR} =$ Change in heart rate from relaxed to stressor and recovery states

$\Delta T_s =$ Change in skin temperature from relaxed to stressor and recovery states

$\Delta S_p =$ Change in physiological entropy change from relaxed to stressor and recovery states

The Equation (5) is based on the logic and examples demonstrated in Ref. [20]. If one were to consider either Internal energy or Gibbs function to define human physiological function, then one would get a negative sign preceding the entropy change (ΔS_p). This negative sign is ignored in this study because it is the magnitude of entropy departure that determines the change in the physiological state. This deviation may be positive or negative depending on the imposed external stressor and the internal physiological condition. As demonstrated in Aoki [13, 14], the physiological entropy change (ΔS_p) is given by $\Delta S_p = S_{pflow} + S_{p_{gen}}$. Especially, physiological entropy generation, $S_{p_{gen}}$, is a kind of global measure which specifies how violent motions and reactions are occurring in nature. Hence, the entropy generation in the human physiological system shows the extent of activeness within the body as a whole; so the entropy generation is a significant quantity which characterizes the human body from thermodynamic and holistic (i.e., considering a human body as a whole) viewpoints. It has been demonstrated by Aoki [13, 14] that for human physiological system under basal or light exercise conditions, the $S_{p_{gen}}$ is always positive that satisfies the second law of thermodynamics. On the other hand, S_{pflow} , arising due to heat and mass transfer between the body and its environment, can be positive or negative. This would result in ΔS_p acquiring either a positive or negative sign depending on the nature of activity and environmental conditions. Further, the net flow entropy being negative implies that human body absorbs "negative entropy" from its surroundings as Schrodinger [1] asserted. This is just the physical basis for ordered structures and functions in the human body to be maintained.

With this physical understanding, we consider only the absolute value of the entropy change for the purpose of this study. The human physiological entropy change could be considered as a composite measure of change in the whole physiological state in response to any external stimuli or stressor. However, if a single physiological indicator such as mean arterial pressure alone can provide that information, then why do we need this entropy change as a composite measure of physiological response? The answer is: The physiological concepts such as stimulus response (SR) specificity, organ response (OR) specificity, individual response specificity, and autonomic balance make the human physiological response a complex phenomena [21]. Furthermore, the human physiological system comprises of many interconnected physiological processes controlled by a complex nervous system. The single physiological indicators, in this regard, provide a very narrow representation of the human physiological stress response system. It is only by recognizing the interaction among human subsystems in their response to any stressor stimuli that one could build better model of human stress physiology. This study makes an effort to reduce the physiological complexity in terms of a composite entropy change.

3. METHODS

The data in the study was collected on eighty-two senior medical students and family medicine resident physicians (49 males and 33 females), who completed a standard physiological stress profile procedure routinely used for clinical assessment in the Primary Care Medicine Department at Eastern Virginia Medical School. The participants were all healthy (without any major health problems). The physiological data was collected by a ProComp+ biofeedback system connected to a Dell 166 MHz PC computer running a MultiTrace biofeedback software for data processing and analysis, as well as a stand-alone Dinamap 1846 Vital Signs Monitor (Critikon Inc., Tampa, FL). The Stress Profile (Stroops test) is a 20-minute standard testing sequence, during which mean arterial pressure, heart rate, and skin temperature from the palmar surface of the left hand little finger is collected continually during the three following conditions for each subject. The stress profile consists of following phases:

State 1 (Relaxation Period): Relaxing in semi-reclining position with eyes open for three minutes followed by relaxing with eyes closed for three minutes (Total time = 6 minutes).

State 2 (Stressor Period): Solving a series of forty six-second long cognitive tasks presented on a computer screen – Stroops type color-naming tasks and arithmetic problems, which are alternated. The sequence of tasks is the same for all subjects (Total time = 8 minutes).

State 3 (Recovery Period): Relaxing again with eyes open for three minutes followed by relaxing with the eyes closed for three minutes (Total time = 6 minutes). With the Dinamap Vital Signs Monitor and using a mechanically inflated pressure cuff around the subject's right arm, the blood pressure and heart rate are recorded. Using the finger-cuff, the finger skin temperature was measured.

The three physiological recordings were made after State 1 (relaxation period), State 2 (stressor period), and State 3 (recovery period), correspondingly. As one of the goals of the study was to examine the influence of stressors on physiology, the finger skin temperature was a better choice than the core body temperature.

4. RESULTS AND ANALYSIS

The data analysis is performed to demonstrate the utility of Maxwell relations to measure physiological entropy change (ΔS_P) in terms of measurable mean arterial pressure (PMA), heart rate (VHR), and skin temperature (TS). Each one of these physiological measures used in the calculation of entropy change. For the purpose of illustration, let us consider the sample (n=49) of male subjects. The male average physiological measures during relaxation (State 1) are calculated as follows:

$$\begin{aligned}(P_{MA})_{\text{Relaxation}} &= 85.43 \text{ mm Hg} \\ (V_{HR})_{\text{Relaxation}} &= 58.49 \text{ bpm} \\ (T_S)_{\text{Relaxation}} &= 302.09 \text{ K}\end{aligned}$$

Let us consider the male average values during the Stressor Task (State 2). They are as follows:

$$\begin{aligned}(P_{MA})_{\text{Stress}} &= 90.08 \text{ mm Hg} \\ (V_{HR})_{\text{Stress}} &= 62.59 \text{ bpm} \\ (T_S)_{\text{Stress}} &= 300.72 \text{ K}\end{aligned}$$

The physiological entropy change at Stressor Task (State 2) is given by:

$$(\Delta S_P)_2 = \left| \frac{[(P_{MA})_{\text{Stress}} - (P_{MA})_{\text{Relaxation}}] \times [(V_{HR})_{\text{Stress}} - (V_{HR})_{\text{Relaxation}}]}{[(T_S)_{\text{Stress}} - (T_S)_{\text{Relaxation}}]} \right|$$

$$(\Delta S_P)_2 = \left| \frac{[(90.08-85.43) \times (62.59-58.49)]}{[300.72-302.09]} \right| = 13.92 \text{ mm Hg.bpm/K}$$

Let us consider the male average values during the Recovery (State 3). They are as follows:

$$\begin{aligned}(P_{MA})_{\text{Recovery}} &= 86.39 \text{ mm Hg} \\ (V_{HR})_{\text{Recovery}} &= 60.96 \text{ bpm} \\ (T_S)_{\text{Recovery}} &= 301.28 \text{ K}\end{aligned}$$

The physiological entropy change at Recovery (State 3) is given by:

$$(\Delta S_P)_3 = \left| \frac{[(P_{MA})_{\text{Recovery}} - (P_{MA})_{\text{Relaxation}}] \times [(V_{HR})_{\text{Recovery}} - (V_{HR})_{\text{Relaxation}}]}{[(T_S)_{\text{Recovery}} - (T_S)_{\text{Relaxation}}]} \right|$$

$$(\Delta S_P)_3 = \left| \frac{[(86.39-85.43) \times (60.96-58.49)]}{[301.28-302.09]} \right| = 4.23 \text{ mm Hg.bpm/K}$$

The physiological measures at states 1, 2, and 3 are summarized in Tables 2 and 3 and graphically demonstrated in Figures 2-5. The State 1 corresponds to relaxation and is used a reference state to compute change in entropy at state 2 (stressor) and state 3 (recovery), respectively. One can observe in Figures 2-4, the differences in individual physiological stress responses between male and female subjects. The mean arterial pressure and skin temperature responses are higher for males while the heart rate responses are lower in females. It is important to note that mean arterial pressure and heart rate increase from relaxation state to stressor while skin temperature decreases from relaxation to stressor state. There is an inverse relationship between hydrodynamic-related variables, mean arterial pressure and heart rate, and thermally-based skin temperature. It is noted that humans experience cold hands during a stressful situation. Further, once after the stressor is over and during the recovery state, the mean arterial pressure and heart rate decrease to a lower value, but to a value slightly higher than that of relaxed state. The skin temperature on the other hand, increases but to a value lower than that of relaxed state. The individual physiological responses provide limited information about the physiological impact of stressors. However, when they are combined in the form of a physiological entropy change, one can look at the integrated physiological stress response as demonstrated in Figure 5. The relaxation state is taken as the reference, and the entropy change from this reference state to stressor and recovery states are computed. It is clear from Figure 5 that physiological entropy change in female subjects is greater than that of males at both states 2 and 3.

Table 2: Average Male Physiological Stress Responses

Physiological Measures	State 1 (Relaxation)	State 2 (Stress)	State 3 (Recovery)
P_{MA} , mm Hg	85.43	90.08	86.39
V_{HR} , bpm	58.49	62.59	60.96
T_S , K	302.09	300.72	301.28
ΔS_P , mm Hg.bpm/ K	-	13.92	4.23

Table 3: Average Female Physiological Stress Responses

Physiological Measures	State 1 (Relaxation)	State 2 (Stress)	State 3 (Recovery)
P_{MA} , mm Hg	76.73	81.48	77.97
V_{HR} , bpm	62.30	65.09	64.55
T_s , K	300.80	300.31	300.52
ΔS_p , mm Hg.bpm/ K	-	27.05	9.03

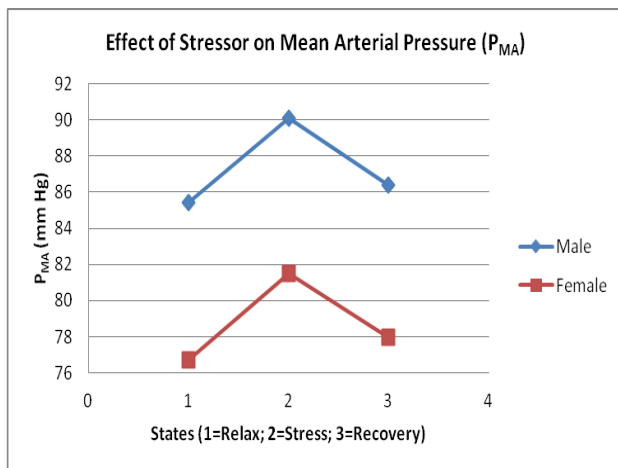


Figure 2. Changes in average mean arterial pressure for male and female Subjects

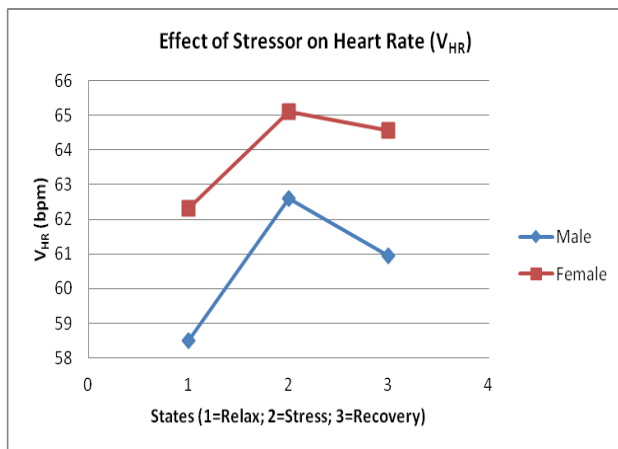


Figure 3. Average changes in heart rate for male and female subjects

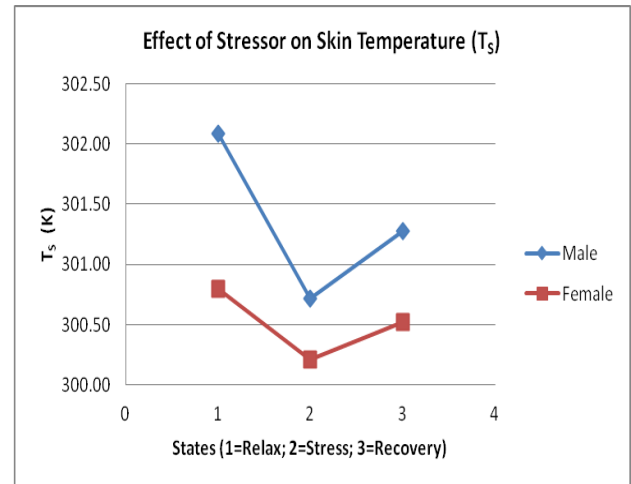


Figure 4. Changes in skin temperature for male and female subjects

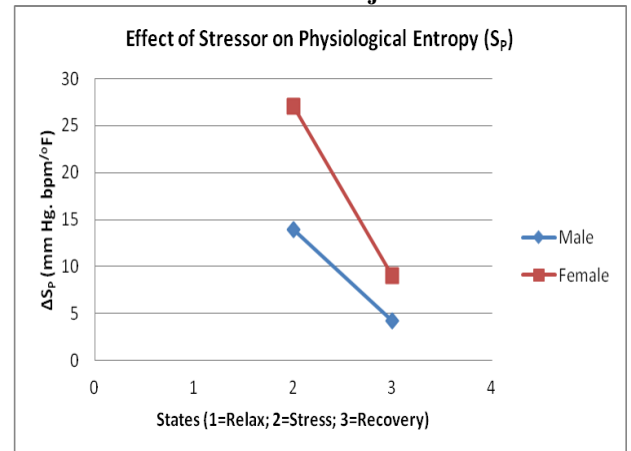


Figure 5. Changes in physiological entropy for male and female subjects

5. CONCLUSION

An analytical model to quantify entropy change in human physiology is developed. The study is based on the premise that Maxwell relations could be used to compute entropy change in terms of measurable physical variables. The pressure, volume, and temperature are equated to mean arterial pressure, heart rate, and skin temperature. Using this analogy, physiological entropy change is computed in both male and female subjects. The experimental study involved 49 male and 33 female subjects and it was conducted in a medical school. The physiological variables were measured at three states, relaxed, stressor task, and recovery. The physiological measures taken during relaxation were taken as the reference. The physiological changes in mean arterial pressure, heart rate, and skin temperature from the reference (state 1) to stressor (state 2) and recovery (state 3) were combined using Maxwell relations to compute entropy changes. The results indicate difference in individual physiological stress responses

between male and female subjects. When these physiological responses are combined in the form of an entropy change, it provides a systems view of human physiological stress response. This integrated physiological entropy change might be of value to medical researchers who are interested in examining whole human physiological stress responses. It is, however, beyond the scope of this study to make any physiological or medical interpretation of entropy change in human systems. The main purpose of this study was to demonstrate the utility of Maxwell relations in human physiology.

ACKNOWLEDGEMENTS

The authors wish to thank Dr. Alan Pope of NASA Langley Research Center for sponsoring this joint research project at Old Dominion University and Eastern Virginia Medical School.

References

- [1] E. Schroedinger, *What is life?* (Cambridge, UK: Cambridge University Press, 1992).
- [2] G. Nicolis and I. Prigogine, *Self-Organization in non-equilibrium systems: From dissipative structures to order through fluctuations* (NY: Wiley, 1977).
- [3] A. S. Iberall, H. Soodak, and F. Hassler, A field and circuit thermodynamics for integrative physiology. I. Introduction to the general notions, *Am. J. Physiology*, 233(1), 1977, 171-180.
- [4] A. S. Iberall, H. Soodak, and F. Hassler, A field and circuit thermodynamics for integrative physiology. II. Power and communicational spectroscopy in biology, *Am. J. Physiology*, 234(1), 1978, 3-19.
- [5] A. S. Iberall, A field and circuit thermodynamics for integrative physiology. III. Keeping the books-a general experimental method, *Am. J. Physiology*, 234(3), 1978, 85-97.
- [6] H. J. Morowitz, *Entropy for Biologists - an Introduction to Thermodynamics* (NY: Academic Press, 1970)
- [7] P. W. Bridgman, *The nature of thermodynamics* (NY: Harpers and Row Publishers, 1961)
- [8] A. Bejan, *Shape and structure from engineering to nature* (NY: Wiley, 2000).
- [9] A. Bejan and S. Lorente, Constructal theory of generation of configuration in nature and engineering, *Journal of Applied Physics*, Article ID 041301, 2006, 10 pages.
- [10] R. L. Magin, S. C. Boregowda, and C. Deodhar, C., Modeling of pulsating peripheral bio-heat transfer using fractional calculus and constructal theory, *International Journal of Design, Nature, and Ecodynamics*, 1(1), 2007, 18-33
- [11] C. A. Silva and K. Annamalai, Entropy generation and human aging: lifespan entropy and effect of physical activity level, *Entropy*, 10(2), 2008, 100–123.
- [12] C. A. Silva and K. Annamalai, Entropy generation and human aging: Lifespan entropy and effect of diet composition and caloric restriction diets, *Journal of Thermodynamics*, Article ID 186723, 2009, 10 pages.
- [13] I. Aoki, Entropy flow and entropy production in the human body in basal conditions, *Journal of Theoretical Biology*, 141(1), 1989, 11–21.
- [14] I. Aoki, Effects of exercise and chills on entropy production in human body, *Journal of Theoretical Biology*, 145(3), 1990, 421–428.
- [15] S. C. Boregowda, S. N. Tiwari, S. K. Chaturvedi, and D. R. Redondo, Analysis and quantification of mental stress and fatigue using Maxwell relations from thermodynamics, *Journal of Human Ergology*, 26(1), 1997, 7-16.
- [16] S. C. Boregowda, O. S. Palsson, S. N. Tiwari, and D. S. Bartolome-Rull, Thermodynamic approach to quantify human stress levels using an objective stress index (OSI), *Journal of Applied Psychophysiology and Biofeedback*, 23(2), 1998, 110.
- [17] S.C. Boregowda and W. Karwowski, Modeling of human physiological stresses: A thermodynamics-based approach, *Occupational Ergonomics*, 5(4), 2005, 235-248.
- [18] O. S. Palsson, S. C. Boregowda, and B. K. Downing, The relationship between an objective stress index (OSI) and stress-related physical symptoms, *Journal of Applied Psychophysiology and Biofeedback*, 23(2), 1998, 125.
- [19] H. Callen, *Thermodynamics and an introduction to thermostatics* (NY: Wiley, 1985).
- [20] E.P. Gyftopoulos and G. P. Beretta, *Thermodynamics* (Mineola, NY: Dover Publications, 2005).
- [21] J. L. Andreassi, *Psychophysiology: Human behavior and physiological stress response* (NJ: Lawrence Erlbaum Associates, 2006).

A NEW CIRCUIT TOPOLOGY FOR OPEN CIRCUIT AND SHORT CIRCUIT FAULT TOLERANT DC-DC CONVERTER

P. KRISHNA CHAND¹, P.SIVA SANKAR²

*(Student, Department of Electrical and Electronics Engineering, KL University) India

** (Assistant Professor, Department of Electrical and Electronics Engineering, KL University) India

ABSTRACT

This paper describes a new design for a fault tolerant H-bridge dc-dc converter. Open circuit and short circuit fault tolerance is achieved using multilevel converter topology in combination with pulse width modulation control strategy allowing a large set of converter switching states to produce bidirectional power flows at any required output voltage. If two switches fail at particular instant then also fault tolerant can be achieved. Fault tolerant ability of proposed converter to recover the required output voltage is verified by computer simulation using MATLAB/SIMULINK with 1kw resistive load.

Keywords- DC-DC power conversion, fault tolerant, multilevel system.

I. INTRODUCTION

DC-DC converters are commonly used in wide variety of applications, including a number of critical applications in which very high levels of reliability are required because the loss of converter operation can have serious consequences. For example, control of car is lost when the supply voltage for a brake-by-wire system has collapsed due to converter failure. Another critical application is the use of dc-dc converter in low-power refrigeration application developed for use in an ambulance to maintain saline temperature within a specific range for immediate injection into a patient [1]. In such an application, the loss of control of the converter voltage can lead to a temperature difference of several degrees and serious medical complications.

In order to achieve highly reliable dc-dc conversion systems, N+M redundancy concepts have been proposed in the past [2], [3]. This is costly option in which one or more additional dc-dc converters are connected in parallel to achieve the required levels of redundancy in case of failure of the main converter. More recently, it has been shown that multilevel dc-ac converter topologies can be operated as fault tolerant circuits [4]-[6]. Multilevel dc-dc converters with multiple dc sources and no magnetic storage components have been proposed recently to achieve variable dc output voltage operation [7]. Initial investigations of the multilevel concept as applied to dc-dc converters for fault tolerant applications have also been presented [8]-[10]. Khan et al., for example, described a

pseudo fault tolerant modular multilevel dc-dc converter [9], which could continue to operate in the event of a short circuit fault in any of the series connected modules the circuit however, could not operate successfully if one of its power devices had experienced an open circuit fault, as recognized by the authors.

Ceglia et al. [11] developed a circuit in that circuit, as proposed by Ceglia et al., suffers from a number of potential problems and drawbacks when operated as a dc-dc converters including high operational losses and long term reliability problems, as some of the switches are required to conduct permanently. In this paper, a new pulse width modulation (PWM) control strategy is developed and applied to modified circuit topology, in which the original converter is extended by the addition of an extra switching leg and bidirectional selector switches, to overcome these problems. If fault occur in an extra switching leg and also in the converter switches we can add one more leg to overcome these problems. In this paper the proposed convert has two auxiliary legs and selector cells so it can be called as HBALSC (H-bridge with auxiliary leg and selector cells).

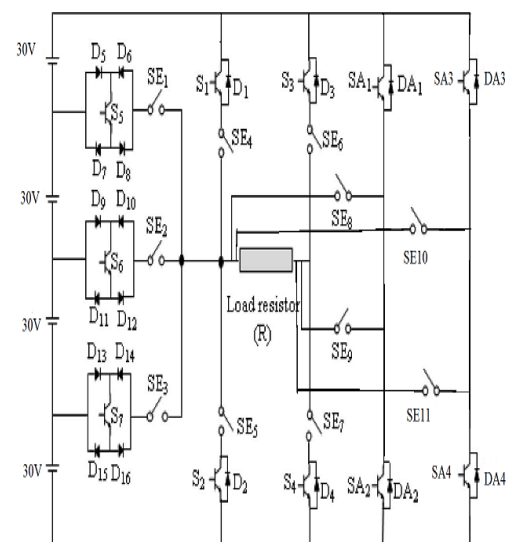


Fig.1.power circuit of the multilevel dc-dc converter

Fig. I shows the proposed H-bridge with two auxiliary leg and selector cells fault tolerant multi level dc-dc converter. The main H-bridge power circuit i.e., power devices S1-S4 and diodes D1-D4 is extended by four auxiliary switches (SA1/DA1, SA2/DA2, SA3/DA3 and SA4/DA4), three selector cells (power devices S5-S7, diodes D5-D16 and bidirectional switches SE1-SE3) and six additional bidirectional switches SE4-SE9 to form the multi level topology. Fault tolerant operation is achieved by using different switching states and controlling the PWM duty cycles of the individual switches to produce the required average output voltage with the minimum number of switches and power diodes.

The paper examines different fault scenarios to demonstrate the full fault tolerant capacity of the proposed converter. Different combinations of switching states and duty cycles are evaluated. The variety of switching combinations and PWM duty cycles provide fault tolerant operation.

II. PROPOSED CONVERTER

The operation of the H-bridge, dc-dc converter with resistive load under normal operating conditions is described in this section.

TABLE I

SWITCHING STATES FOR EACH VOLTAGE LEVEL:

Voltage levels	Current paths
30v	D13, S7, D16, SE3, SE7, S4.
60v	D9, S6, D12, SE2, SE7, S4.
90v	D5,S5,D8,SE1,SE7,S4
120v	S1, SE4, SE7, S4.
0v	SE5, S2, SE7, S4.
-30v	S3, SE6, SE1, D6, S5, D7.
-60v	S3, SE6, SE2, D10, S6, D11.
-90v	S3, SE6, SE3, D14, S7, D15.
-120v	S3, SE6, SE5, S2.

The proposed converter allows bidirectional power flow and depending on the switching states used, can produce nine different output voltage levels (-120, -90, -60, -30, 0, 30, 60, 90, 120V) when operating without PWM control, as shown in Table I. The application of PWM control allows operation at any required average voltage between -120V and +120V. It should be noted here, that the circuit cannot achieve the redundancy needed for fault tolerant operation by varying the switching states alone, each voltage level can be generated by only one switching combination as shown in Table I. The current path for the conduction state corresponding to an output voltage of 30V is shown in Fig. 2 as an example.

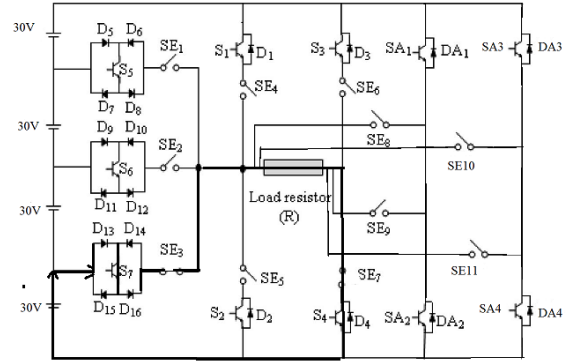


Fig.2. current path for conduction state corresponding to 30v output voltage.

In the following analysis, only forward power flow switch combinations will be considered i.e., no negative voltage switching states will be considered.

Fig.3 shows four output voltage levels V_{Ln} with PWM control at a fixed duty cycle D and a constant switching frequency. Assuming each voltage level is applied for an equal time $T/4$, the average output voltage V_o can be calculated from

$$V_o = \frac{D}{M} \sum_{N=1}^M V_{Ln} \tag{1}$$

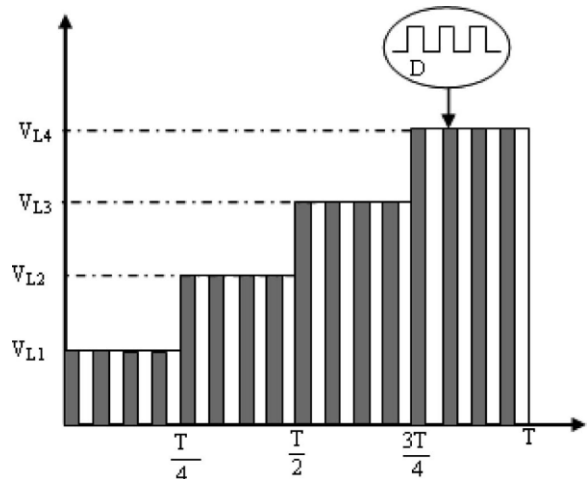


Fig. 3. Output voltage levels.

Where D is the duty cycle, m is the number of voltage levels and V_{Ln} is the output voltage associated with level n .

Equation (1) shows that the different switching states can produce a large number of possible output voltages when combined with all the possible values of converter duty cycles D . For example, Table II shows five possible switching states combinations with different values of D to generate a 60V average output voltage.

TABLE II
 POSSIBLE SWITCH COMBINATIONS TO GENERATE
 60V AVERAGE OUTPUT

State number	Output voltage level			PWM duty cycle D	Average output voltage
	30v	90v	120v		
1	Yes	Yes	Yes	0.75	60v
2	Yes	-	Yes	0.80	60v
3	-	Yes	Yes	0.57	60v
4	-	Yes	-	0.67	60v
5	-	-	yes	0.50	60v

Similarly Table III shows five possible switching states combinations with different values of D to generate a 45V average output voltage.

TABLE III
 POSSIBLE SWITCH COMBINATIONS TO GENERATE
 45V AVERAGE OUTPUT

State number	Output voltage level			PWM duty cycle D	Average output voltage
	30v	90v	120v		
1	Yes	Yes	Yes	0.5625	45v
2	Yes	-	Yes	0.6	45v
3	-	Yes	Yes	0.42	45v
4	-	Yes	-	0.5	45v
5	-	-	yes	0.375	45v

The operation of the proposed converter was investigated using MATLAB/SIMULINK.

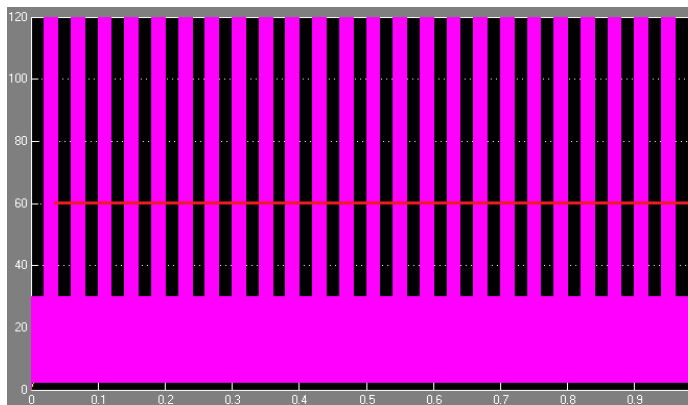


Fig.4. Measured output voltage waveform for $V_o=60V$ PWM duty cycle $D=0.8$ with the voltage levels of 30V and 120V respectively.

Here there are two output voltage levels but the average output voltage is 60v only.

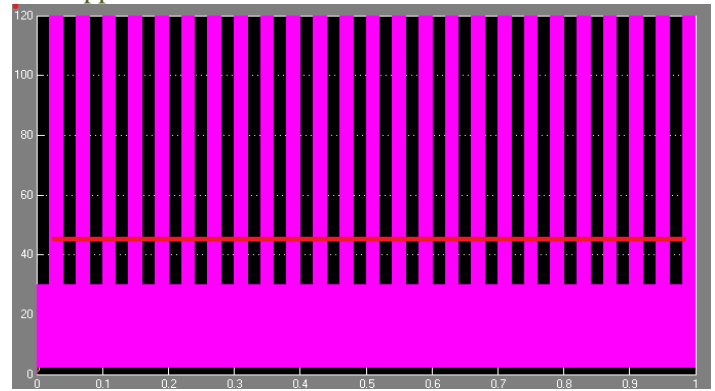


Fig.5. Measured output voltage waveform for $V_o=45V$ PWM duty cycle $D=0.6$ with the voltage levels of 30V and 120V respectively.

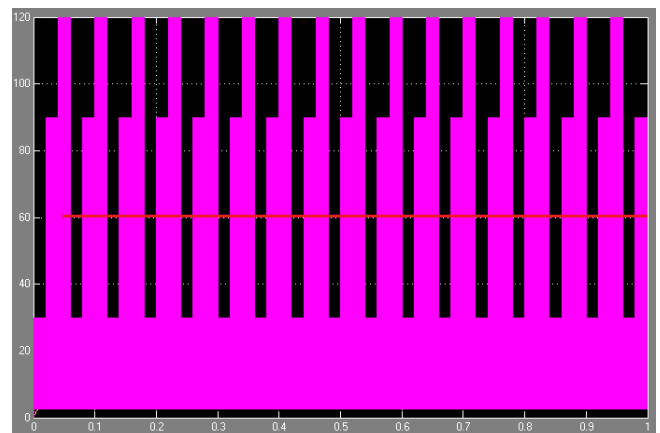


Fig.6. Measured output voltage waveform for $V_o=60V$; PWM duty cycle $D=0.75$ with the voltage levels of 30V, 90V and 120V respectively.

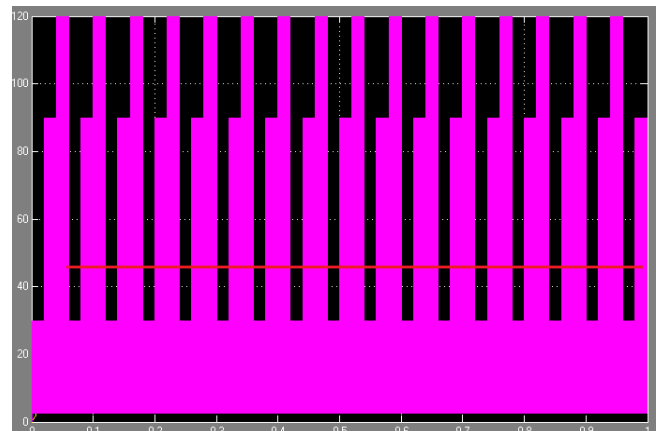


Fig.7. Measured output voltage waveform for $V_o=45V$; PWM duty cycle $D=0.5625$ with the voltage levels of 30V, 90V and 120V respectively.

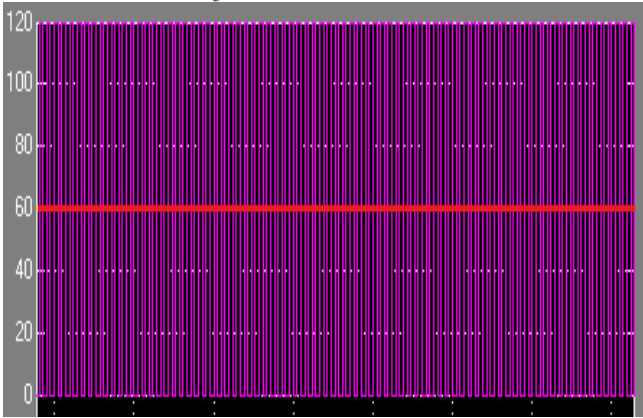


Fig.8. Measured output voltage waveform for $V_o=60V$; PWM duty cycle $D=0.5$ with the voltage levels of 120V respectively.

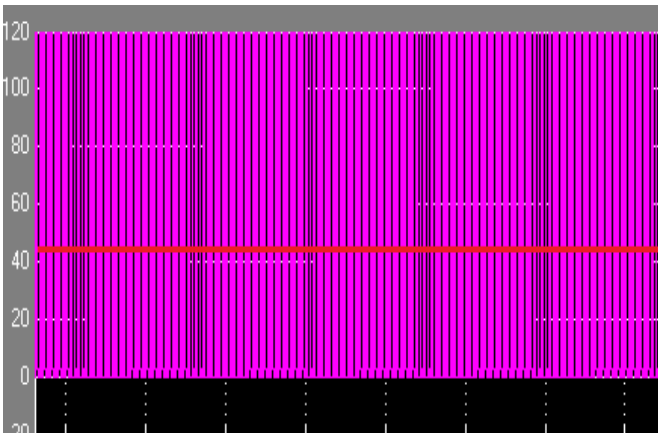


Fig.9. Measured output voltage waveform for $V_o=45V$; PWM duty cycle $D=0.375$ with the voltage levels of 120V respectively.

In Fig 4-9 y-axis represents the voltage divisions and x-axis represents time divisions

Figs. 4, 6, 8 show measured output voltages for three different device switching combinations (states 2, 1 and 5 in table II) to get 60V as average output voltage. Similarly Figs 5, 7, 9 show measured output voltages for three different device switching combinations (states 2, 1, 5 in table III) to get 45V as average output voltage. It is apparent from the figures that PWM control allows alternative switching options for the required output voltage level. Converter operation with the same switch combinations was also simulated using PSpice showing good agreement with measurement.

III. FAULT TOLERANT INVESTIGATION

Fault that can occur in the switches may be open circuit or short circuit fault. In this section both open and short circuit faults are discussed and the fault tolerant behavior of the converter is evaluated using the 60V operating states discussed in section II as an example. Here only one fault can occur at a time or two faults can occur the

proposed converter must demonstrate the ability to detect a short circuit or open circuit component fault and must change the switching states appropriately to recover the required average output voltage. Here voltage and current sensors are used in order to sense the faults.

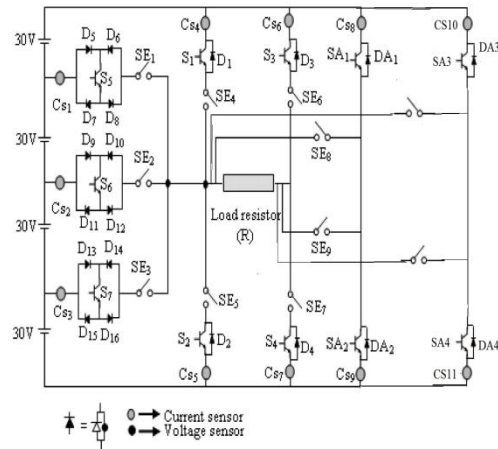


Fig.10. fault tolerant multi level H-bridge dc-dc converter.

Total number of sensors is low when compared with alternative circuit topologies [8]. However, the number sensors can be reduced even further by monitoring the output voltage using a neural network technique [12] or by using a smart IGBT gate drive with self-diagnosis and fault protection [13], the complete fault tolerant of the converter is shown in Fig

IV. OPEN CIRCUIT FAULTS

If an open circuit fault occurs in any of the main switches S1-S4 or D1-D4, the extended additional leg1 must be activated. If the open circuit fault occurs in both main switches and also additional leg1 then activate additional leg2. The switching sequence following an open circuit fault in S1 is discussed here in detail as an example.

Under normal operating conditions, S1 is switched ON and the controller receives a current measurement from C_{S4} . If the controller does not receive this signal while S1 is still switched ON, the controller will flag this as an open circuit fault in S1. The controller now identifies a new switching state that needs to be activated, in this case switches SA1 and SE8, in order to provide the required voltage. Fig 10 shows how SA1 and SE8 are switched on to maintain normal operation at the same output voltage when an open circuit fault occurs in S1. After the fault, the current passing through S1 falls to zero, but load current continues to flow through SA1 and SE8.

- 1: output voltage
- 2: cs4 current signal
- 3: gate signal of SA1
- 4: gate signal of S1

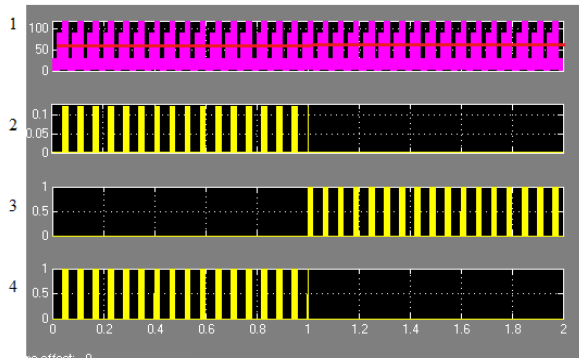


Fig.10. Output voltage waveform before and after an open circuit fault in main switch S1.

Under this conditions i.e., switch S1 is open circuited, load current flowing through SA1 and SE8 controller receives a current measurement from C_{s8} if the open circuit fault occurs in SA1 then controller will identifies a new switching state that needs to be activated now switches SA3 and SE10 will be activated after the fault current passing through SA1 falls to zero and load current continues to flow through SA3 and SE10 as shown in the Fig.11

- 1: output voltage
- 2: CS8 current signal
- 3: gate signal of SA3
- 4: gate signal of SA1

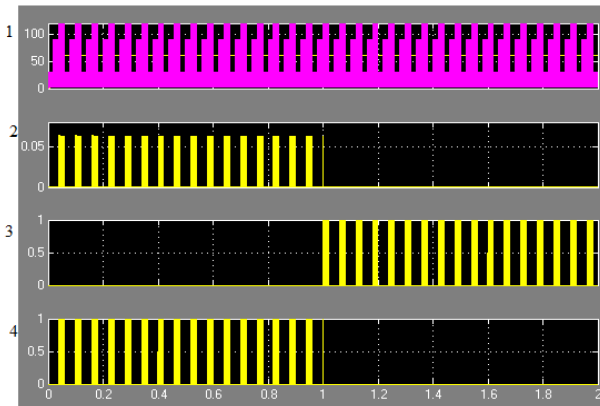


Fig.11. Output voltage waveform before and after an open circuit fault in main switch S1 and auxiliary switch SA1.

If the open circuit fault occurs in any of the selector switching cells (devices S5-S7, diodes D5-D16 and bidirectional switches SE1-SE3), the converter will no longer be able to produce the required average output voltage using the existing switch state combination. For example, under normal operating conditions, the converter produces output voltage levels of 30, 90, 120 with duty cycle off $D=0.75$ to generate $V_o = 60V$. If an open circuit fault were to occur in switch S5 (say), the converter is no longer able to produce a voltage level of 90V leading to the loss of the required 60V output voltage. On detecting the

fault, the sequence of switching states need to change to operate the convert at 120V and a duty cycle of $D=0.5$.

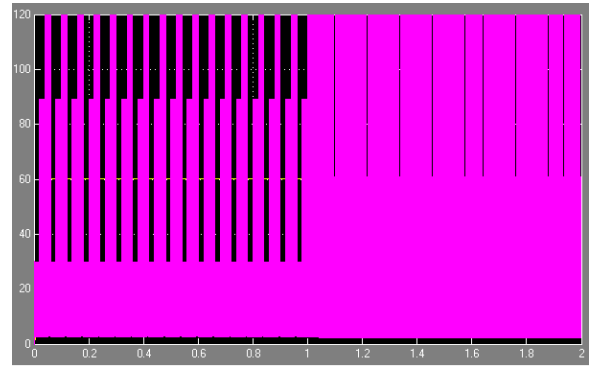


Fig.12. Output voltage waveform when open circuit fault occurs in switch S5

Fig.12. shows measured output voltage waveform when open circuit fault occurs in S5; similar results are obtained when simulating the operation of the circuit under the same fault conditions.

V. SHORT CIRCUIT FAULT

Diode short circuit faults are detected using the voltage sensors circuits shown in Fig13 short circuit faults in the power devices are detected via the gate drive circuits. On detection, short circuit faults are isolated by deactivating the corresponding selector switch. The control of the system is more complex when compared with open circuit faults responses due to the large number of voltage sensors and switches needed to detect and isolate each fault. The switching sequence following a short circuit fault in S1 is discussed here as an example.

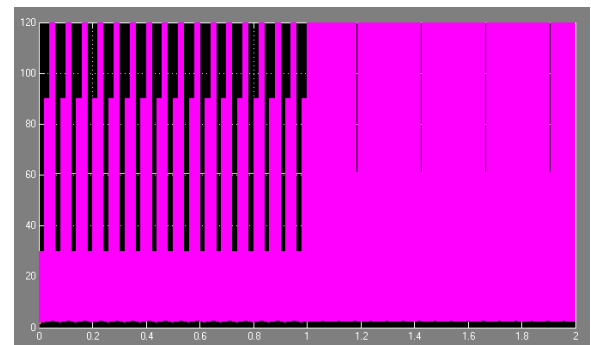


Fig.13. Output voltage waveform when short circuit fault occurs in selector switch S5

If the short circuit fault occurs in switch S1. On detecting the fault, SE4 is switched OFF and SE8 and SA1 switched on to initiate the new conduction state. Fig.13 show output voltage waveform generating 60V average output voltage and voltage after the fault is zero along switch S5.

VI. CONCLUSION

Fault tolerant multilevel H-bridge dc-dc converter topology has been presented in this paper. Different switching states are combined with PWM control to produce and maintain a constant average output voltage despite the occurrence of

FAULT TOLERANT INVESTIGATIONS IN THE DIODES

Switches	ACTIONS	
	Open circuit faults	Short circuit faults
D1	Not involved in forward power flow operation	Deactivate SE4 and activate SA1 and SE8
D2	Not involved in forward power flow operation	Keep SE5 open
D3	Not involved in forward power flow operation	Keep SE6 open
D4	Not involved in forward power flow operation	Deactivate SE7 and activate SA2 and SE9
DA1	Not involved in forward power flow operation	Deactivate SE8 and activate S1 and SE4
DA2	Not involved in forward power flow operation	Deactivate SE9 and activate S4 and SE7
D5	Change to different switching states Combinations and D	Deactivate SE1 and change to different switching states combinations and D
D6	Not involved in forward power flow operation	
D7	Not involved in forward power flow operation	
D8	Change to different switching states Combinations and D	
D9	Change to different switching states Combinations and D	Deactivate SE2 and change to different switching states combinations and D
D10	Not involved in forward power flow operation	
D11	Not involved in forward power flow operation	
D12	Change to different switching states Combinations and D	Deactivate SE3
D13	Change to different switching states Combinations and D	
D14	Not involved in forward	

converter open circuit and short circuit fault. This converter also works even though fault occur in auxiliary leg

APPENDIX

TABLE VI

	power flow operation	and change to different switching states combinations and D
D15	Not involved in forward power flow operation	
D16	Change to different switching states Combinations and D	

Table VII

FAULT TOLERANT INVESTIGATION IN POWER DEVICES

Switches	Actions	
	Open circuit faults	Short circuit faults
S1	Activate SA1 and SE8	Deactivate SE4 and activate SA1 and SE8
S2	Not involved in forward power flow operation	keep SE5 always open
S3	Not involved in forward power flow operation	Keep SE6 always open
S4	Activate SA2 and SE9	Deactivate SE7 and activate SA2 and SE9
SA1	Activate S1 and SE4	Deactivate SE8 and activate S1 and SE4
SA2	Activate S4 and SE7	Deactivate SE9 and activate S4 and SE7
S5	Change to different Switching states combinations and D	Deactivate SE1 and Change to different Switching states combinations and D
S6	Change to different Switching states combinations and D	Deactivate SE2 and Change to different Switching states combinations and D
S7	Change to different Switching states combinations and D	Deactivate SE3 and Change to different Switching states combinations and D

Table VIII
 FAULT TOLERANT INVESTIGATION IN THE POWER
 DEVICES IF TWO SWITCHES FAILS

switches	Open circuit fault	Short circuit fault
S1, SA1	Activate SA3 and SE10	Deactivate SE4 and activate SA3 and SE10
S4, SA2	Activate SA4, SE 11	Deactivate SE47 and activate SA4 and SE11
S3	Not involved in forward power flow operation	Keep SE6 always open
S2	Not involved in forward power flow operation	keep SE5 always open

clamped dc/dc converter featuring fault tolerant capability," *IEEE Trans. Power Electron.*, vol. 24, no. 1, pp. 14–24, Jan. 2009.

- [10] V. Choudhary, E. Ledezma, R. Ayyanar, and R.M. Button, "Fault tolerant circuit topology and control method for input-series and output-parallel modular DC-DC converters," *IEEE Trans. Power Electron.*, vol. 23, no. 1, pp. 402–411, Jan. 2008.
- [11] G. Ceglia, V. Guzman, C. Sanchez, F. Ibanez, J. Walter, and M. I. Gimenez, "A new simplified multilevel inverter topology for DC-AC conversion," *IEEE Trans. Power Electron.*, vol. 21, no. 5, pp. 1311–1319, Sep. 2006.
- [12] S. Khomfoi and L. M. Tolbert, "Fault diagnostic system for a multilevel inverter using a neural network," *IEEE Trans. Power Electron.*, vol. 22, no. 3, pp. 1062–1069, May 2007.
- [13] C. Lihua, F. Z. Peng, and C. Dong, "A smart gate drive with self-diagnosis for power MOSFETs and IGBTs," in *Proc. 23rd Annu. IEEE Appl. Power Electron. Conf. Expo. (APEC 2008)*, pp. 1602–1607.

REFERENCE

- [1] M. R. Holman and S. J. Rowland, "Design and development of a new cryosurgical instrument utilizing the Peltier thermoelectric effect," *J. Med. Eng. Technol.*, vol. 21, no. 3–4, pp. 106–110, 1997.
- [2] P. A. Kullstam, "Availability, MTBF and MTTR For repairable M out of N system," *IEEE Trans. Rel.*, vol. R-30, no. 4, pp. 393–394, Oct. 1981.
- [3] R. V. White and F. M. Miles, "Principles of fault tolerance," in *Proc. IEEE Appl. Power Electron. Conf. Expo.—APEC*, San Jose, Costa Rica, 1996, pp. 18–25.
- [4] A. Chen, L. Hu, L. Chen, Y. Deng, and X. He, "A multilevel converter topology with fault-tolerant ability," *IEEE Trans. Power Electron.*, vol. 20, no. 2, pp. 405–415, Mar. 2005.
- [5] X. Kou, K. A. Corzine, and Y. L. Familiant, "A unique fault-tolerant design for flying capacitor multilevel inverter," *IEEE Trans. Power Electron.*, vol. 19, no. 4, pp. 979–987, Jul. 2004.
- [6] B. Francois and J. P. Hautier, "Design of a fault tolerant control system for a N.P. C. multilevel inverter," in *Proc. IEEE Int. Symp. Ind. Electron.*, L'Aquila, Italy, 2002, vol. 4, pp. 1075–1080.
- [7] S. Miaosen, P. F. Zheng, and L. M. Tolbert, "Multilevel DC-DC power conversion system with multiple DC sources," *IEEE Trans. Power Electron.*, vol. 23, no. 1, pp. 420–426, Jan. 2008.
- [8] K. Ambusaidi, V. Pickert, and B. Zahawi, "Computer aided analysis of fault tolerant multilevel DC-DC converters," in *Proc. IEEE Conf. Power Electron., Drives Energy Syst. Ind. Growth*, New Delhi, India, 2006, pp. 1–6.
- [9] F. H. Khan and L. M. Tolbert, "Multiple load-source integration in a multilevel modular capacitor

Impact of GCIs Performance on Power Quality of Smart Grid using Fuzzy Logic

Prof.M.Nirmala,G.Karthikeyan

Dept. of Electrical and Electronics Engineering, Kumaraguru College of Technology
Coimbatore-641 049, India

ABSTRACT

The operating performance of the Grid Connected Inverters (GCIs) in windmill is highly important related to stable and safety operation of a “Smart Grid” (SG). These inverters control features not only cover the renewable energy conversion and active power feeding into the utility grid but also they cover the grid voltage stabilization, supporting with reactive power of the grid in case of voltage dips. The GCIs support to meet the power quality standards by means of their fast acting of control abilities. Decentralized suppliers must contribute to the control of the grid by delivering active and reactive power. This paper gives an overview on the necessary features of GCIs, the importance of GCI on power quality and introduces some simulation results using fuzzy logic controller to avoid the over current problem during voltage dip under short circuit fault condition.

Keywords- Smart Grid, Power Quality, Grid Connected Inverter, Windmill, Fuzzy logic controller.

I. INTRODUCTION

As we know very well the common power quality problems occurs generally in grids are below:

- Magnitude of the supply voltage
- Voltage fluctuations
- Voltage dips and short supply interruptions
- Voltage and current distortion

The SGs’ standardization is recently running in Technical Committees of IEC, IEEE and EN.

The power quality problems should be notable not only in Centralized Generation systems but also in Smart Grid systems as well.

The main reason for the changes in RMS voltage value in a power network is the load variations. It is common that the utility network voltage level is strongly influenced by local power flows. The reactive power flows are highly important in this case. Since they have very strong influence on the voltage stability. The voltage fluctuations are caused mainly by industrial high power consumption as arc furnaces, cold and hot iron mills, etc.

Voltage dips are short time reductions of the voltage level which is normally longer than 10 ms and typically caused by short circuits at the distribution network or at large industrial consumer side and last as long as the protection acting time.

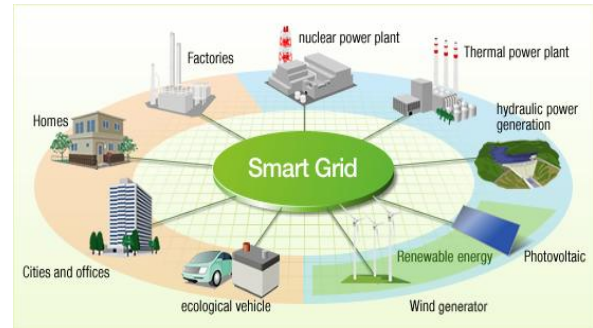


Fig 1. Typical Smart Grid arrangement

The distorted (not fully sinusoidal) current and voltage have been occurred in normal operating condition. The utility networks are used by various power electronics devices (old type among them). The conventional thyristor and diode converters produce mostly integer multiples of the fundamental harmonics [1]. The total harmonic distortion THD calculation is typically required up to 50th order harmonics. The relevant standards define the limit of the maximum current and voltage THD value.

The voltage dip due to short circuit in the distribution network and the slight over current is shown and discussed in [2]. The rise of reactive power to compensate the active power because of the effect of capacitor voltage also discussed.

Classical PI controllers can be used for current control in Grid Connected Inverters. A reasonable performance can be obtained with a constant gain PI controller, designed for certain operating point. However, when the working point changes due to the variations in system parameters, transient response cannot be quick enough and inverter current quality cannot reach the required level. That’s why the Fuzzy logic controller is implemented here.

Here our main objective is to avoid voltage dip, over current effect and also to improve the response time by using fuzzy logic controller.

II. PERFORMANCE REQUIREMENTS OF GCI

The Grid connected inverter can be adapted to the above mentioned operating conditions and also it contribute to maintain the grid power quality too [3]. GCIs shall provide voltage control in grid and keeping the defined slope in the actual Grid Code or Site Specific Connection Agreement (SSCA).

As an example the German Grid Codes have been amongst the most important driving documents

regulating the connection of large wind farms to the conventional (not DG) grid [4].

The most recent Grid Codes require the wind farm among other things to contribute the

- Reactive power exchange and voltage control
- Fault-ride through support in the case of balanced faults
- Defined behaviour in case of unbalanced faults
- Post Fault Active Power Recovery

2.1.Reactive power exchange and voltage control:

The Grid Codes specify the power factor at nominal active wind park power output over a defined connection voltage range.

Some grid codes needs of the implementation of voltage control functionality as it is well known for other generators [4]. The reactive power generation that may be leading or lagging and active filtering capability is highly depend on the inverter limits and the converted actual active power.

Reactive power has to be provided depending on the system voltage following a droop characteristic. Thereby, the provided reactive power is a linear function of the system voltage. Parameters such as target voltage and droop slope have to be altered remotely by the overriding controller.

The nature of faults with various fault currents and voltage dips has occurred not only in a centralized generation system but also in a Smartgrid (where is a distributed generation (DG) concept) and there are cases when have to “ride through” or switch off the grid connected inverter. The fault ride through (FRT) capability of GCIs improves the reliability of the Smart grid operation. This is the main advantage of the GCI.

During a dip the GCI shall provide reactive current as high as possible to boost the local voltage. Fig 2 introduce this requirement. A typical requirement is that after the recovery of grid voltage to 90%, the GCIs shall restore the injected active power at least 90% of their pre-fault values. The restoration time of the injected active power shall be less than 1 second if the fault time is longer than 140 msec (unless plant input power has reduced).

The local voltage could contain fluctuations and specific harmonics generated by consumers [3] (e.g. old type of thyristor converters). Some local active power fluctuation has occurred due to load rejections somewhere on the network.

GCIs can provide an active power filtering functions (with limited power range).

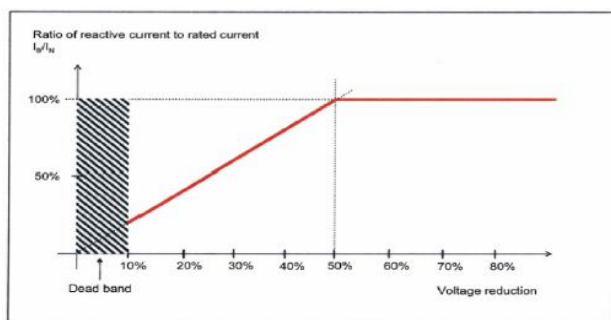


Fig 2. Reactive current requirement during faults

In a SG where is a distributed power generation, Grid connected inverter contribute in connection with the frequency control by means of modification of the output power moreover it can be equipped with power system stabilizer(PSS) to increase the system damping. During a power as well as frequency oscillation on the grid the PSS should provide an artificial damping effect to help suppression of the grid oscillation.

III.STRUCTURE OF GCIS

The grid connected windmill system with back to back voltage source inverter is shown in fig 3. The grid connected inverter output generally connected with an LCL third level harmonic filter [6] plus an EMC filter [7] while the machine side converter output contains only a du/dt filter circuit. The grid side inverter output contains a step up transformer which is used to connect to the medium voltage network.

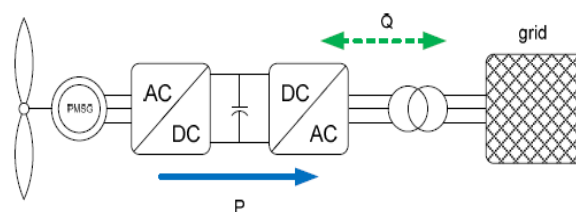


Fig 3. Grid connected windmill system

The grid side converter which is of the type of two or multilevel IGBT inverters make possible to control the reactive power according to the actual demand of the Active power. The inverters apply modulation frequency (3-5 kHz) providing a good dynamic behaviour and it makes the possibility to eliminate some current harmonics with low order numbers [8], [9] coming from the medium voltage side of the grid. This is the main advantage of the grid connected inverter.

IV.STRUCTURE OF CONTROLLER

The generator side converter controller algorithm is based on the rotor flux oriented reference frame for calculations. The active power is controlled by the I_q current component and the reactive power is by the I_d current component. It is shown in fig 4.

The torque controller feedback signal is calculated from the (i_q x ψ_{pm}) [2]. In case of high speed and stator voltage range the field weakening controller sets the I_d component.

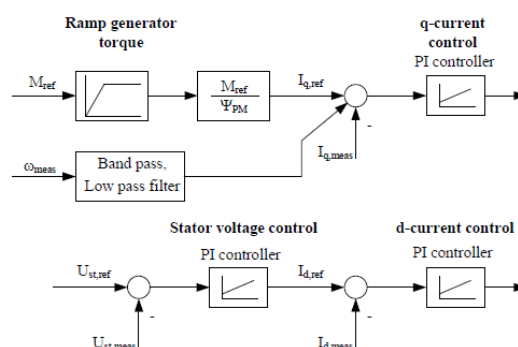


Fig 4. Generator side controllers

The controller algorithm of grid side controllers is carried out in grid voltage-oriented d-q reference frame.

The fuzzy controller which is responsible for both d-current and q-current component which is shown in fig.5.

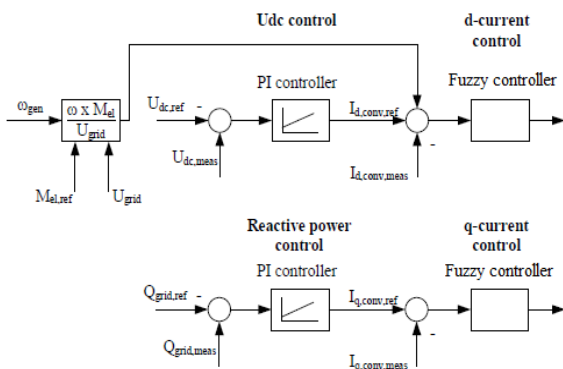


Fig 5. Grid side controller using Fuzzy logic.

V. FUZZY LOGIC CONTROLLER

As we know the Fuzzy logic controller (FLC) is used to improve the response time, here it is implemented in grid side controller. Here the fuzzy controller is used instead of the PI controller which is used in [2], for the purpose to reduce the over current effect during the voltage dip period and also to improve the response time. For the d- current control, the measured value and reference value of d component current is compared and the error value is given as one of the input to the fuzzy controller.

Similarly, for q-current control the measured, reference value of q component current is compared and the error value is given as one of the input. The change in error value is another input for fuzzy controller in both cases d and q, and it is given by introducing the delay circuit to the error value.

In FLC the error and the change of error are scaled and quantised. During the tuning of the controller, the values of scaling factor are obtained by trial and error. The scaling factor for the error is denoted as SFe and for the change of error is denoted as SFce. And then the fuzzified values are kept within a certain range.

In Fuzzy logic controller, there are three membership functions are used as positive, negative and zero. It is shown with respective rules in table below. The operating points of each membership function is selected in order to get the effective output with better response time for all output parameters. Similarly for both inputs, the limits of three membership functions are selected to obtain better outputs. The simulations mainly focused on to verify the converter operation when voltage dips [10], [11] have occurred by short circuit at the high voltage grid. The main target was to avoid over current what would trip the system and to feed the required reactive current into the grid. There was also very important to keep a stable intermediate DC voltage level avoiding over-voltage and to provide smooth operation conditions in the smart grid.

TABLE 1

FUZZY-RULE-BASED MATRIX

Change in Error	NS	Z	PS
Error			
NS	NS	NS	Z
Z	NS	Z	PS
PS	Z	PS	PS

VI.SIMULATION DIAGRAM

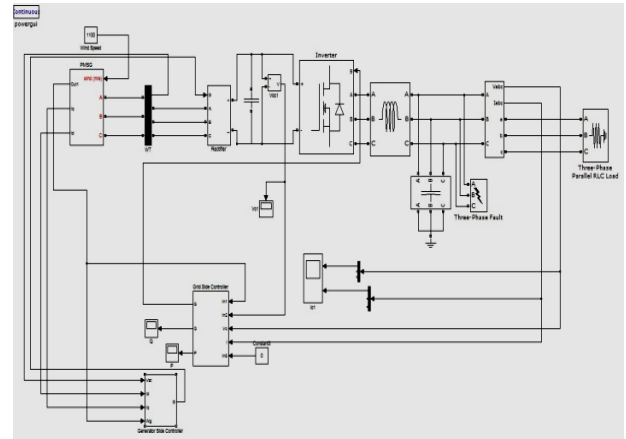


Fig 6.MATLAB model for GCI influence on power quality improvement using Fuzzy controller.

VII. SIMULATION RESULTS

The simulated system was a windmill equipped with the full converter (back to back). The simulations made in MATLAB/Simulink. The power circuit blocks were made from the SimPowerSystem toolbox blocks and control system blocks were made using basic Simulink blocks. And the main advantage of using SimPowerSystems is that the power system is similar to the schematic diagrams made in Pspice. The windmill consists of full converter which is of 4.8kW.

The important data of the system is:

Table-2
Data of the system

Parameter	Values
Nominal Power	4.8 kW
Nominal DC link voltage	200 V
Wind speed	1100 rpm
PMSG pole pairs	2
PMSG no load voltage	300 V

The simulation was performed during the period of 100ms and 50% voltage dip at the grid voltage. Fig 7.a shows the grid voltage at the frequency of 60Hz and grid current verses time during voltage dip.

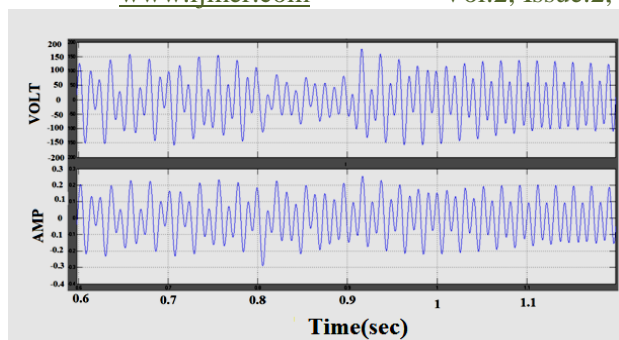


Fig 7.a Grid Voltage and Current with voltage dip from 0.8 to 0.9 time period

Fig 7.b shows the Active power drop during the period of voltage dip and correspondingly fig 7.c shows the reactive power rise to compensate the active power drop. The intermediate DC voltage can be followed on the fig 7.d

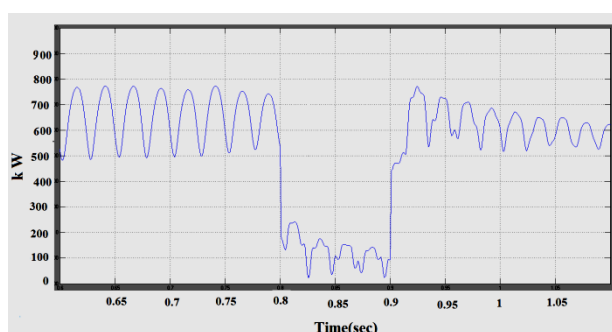


Fig 7.b Active Power

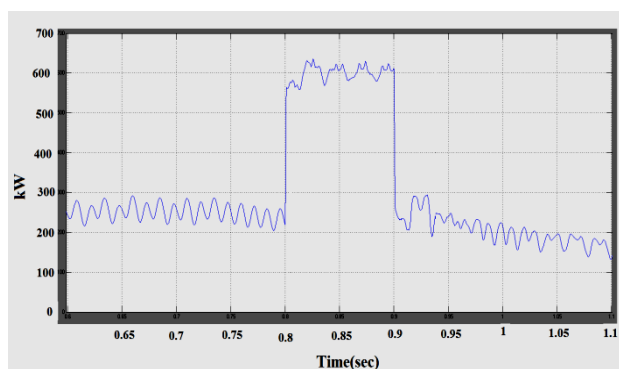


Fig 7.c Reactive Power

The capacitor voltage rise boost up the reactive power to compensate the active power. The magnitude of capacitor voltage and reactive power shows the statement above. During the period of voltage dip on the grid voltage the fed power of the generator increases the intermediate DC voltage level on the capacitor bank and it stabilizes the voltage without any overshooting.

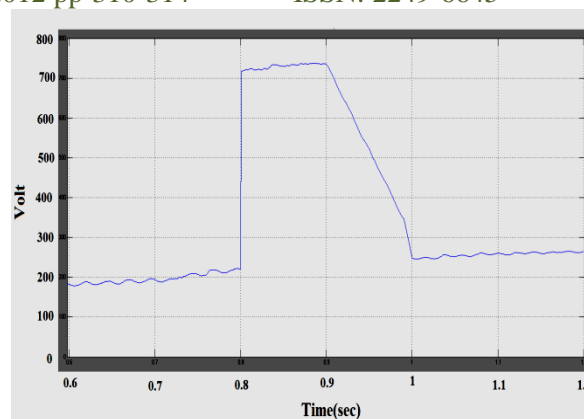


Fig 7.d Capacitor Voltage

VIII.CONCLUSION

This paper has focussed on the performance of the grid connected inverter and the effect of Smart grid operating conditions. The simulations includes the voltage dip due to short circuit on the distribution network and the results highly concentrated on the Over current elimination, grid voltage stabilization and reactive power exchange by GCIs performance using fuzzy logic is shown above.

The presented simulation results is all about the safety and smooth operation of the consumers on the smart grid due to the partly decentralized voltage control in whiles the GCI operation parameters have not exceeded the adjusted limits. The presented simulation results have been obtained by using MATLAB Sim power System tools.

ACKNOWLEDGEMENTS

The authors wish to thank the family members who have provided full support.

REFERENCES

- [1] T. H. Ortmeier, K. R. Chakravarthi, and A. A. Mahmoud: The Effects of Power System Harmonics on Power System Equipment and Loads, Power Apparatus and Systems, IEEE Transactions on Vol PAS-104 pp.
- [2] Erno paal, Zoltan, "Grid Connected Inverters Influence on power quality of smart grid", IEEE transactions 14th International Power Electronics and motion control conference, EPC-PEMC 2010.
- [3] Power Electronics and Control for Renewable Energy Systems tutorial EPE 2009 2555-2563, 1985.
- [4] Grid Code Requirements Concerning Connection and Operation of Wind Turbines in Germany IEEE 2005
- [5] Voltage characteristics of electricity supplied by public distribution networks: BS EN50160, 2007.
- [6] M. Liserre, F. Blaabjerg, and R. Teodorescu: Grid Impedance Estimation via Excitation of LCL – Filter Resonance, Industry Applications, IEEE Transactions on Vol 43 pp. 1401-1407, 2007.

- [7] Electromagnetic compatibility (EMC). Limits for harmonic current emissions BS EN61000-3-2, 2006.
- [8] M. Armstrong, D. J. Atkinson, C. M. Johnson, and T. D. Abeyasekera: Low order harmonic cancellation in a grid connected multiple inverter system via current control parameter randomization, Power Electronics, IEEE Transactions on Vol 20 pp. 885-892, 2005. EPE 2009
- [9] V. Staudt, S. Menzer, Andreas Steimel : On-line Active Filter Experiment Combining Theory, Simulation and Measurement EPE 2009
- [10] Chong H., Li R., Bumby J.: Unbalanced-grid-fault ride-through control for a wind turbine inverter, IEEE Transactions on Industrial Applications, vol.44, no. 3, pp. 845-856, May/June. 2008.
- [11] Teninge, Alexander: New Design Control Dedicated To Low Voltage Ride Through of Wind Plant EPE 2009.
- [12] Whei-Min Lin, Chih-Ming Hong, Ming-Rong Lee, Cong-Hui Huang and Chung-Chi Huang."Fuzzy Sliding Mode-Based Control for PMSG Maximum Wind Energy Capture with Compensated Pitch Angle".
- [13] Chian-Song Chiu, Teng-Shung Chiang, and Ya-Ting Lee, "Maximum Power control of Wind Energy Conversion Systems via a T-S Fuzzy Model-based Approach", IEEE transactions.
- [14] Liyong Yang, Zhigang Chen, Peie Yuan, Zhenguo Chang, "A Novel Fuzzy Logic and Anti-windup PI Controller for a Rectifier with Direct Driven Permanent Magnet Synchronous Generator", IEEE transaction 2009.
- [15] Sudeendra kumar K., Leslin Verghese, K. K. Mahapatra,"Fuzzy Logic based Integrated Control of Anti-lock Brake System and Collision Avoidance System using CAN for Electric Vehicles" IEEE transaction, 2009.

AUTHOR'S BIOGRAPHY

M.NIRMALA received her B.E degree in Electrical and Electronics Engineering from Bharathiyar University, India in 2001 and M.E degree in Power Electronics and Drives from Anna University Chennai, India in 2006. She is currently working as Senior Grade Assistant Professor in Kumaraguru College Of Technology, Coimbatore, India. Her main research is in Power Quality of Smart Grid and her areas of interest is Applications of Smart grid, Load Side Management in distribution, FACTS devices and their control.



G.KARTHIKEYAN was born in Salem, India in 1989. He received the B.E (Electrical and Electronics Engineering) degree in Maharaja Engineering College, Coimbatore, India in 2010. Now he is doing M.E (Power Electronics and Drives) in Kumaraguru College of Technology, Coimbatore, India. His areas of interest are Power Electronics and Drives, Power Quality and

Peristaltic Transport of Incompressible Non-Newtonian Second Order Fluid through A Flexible Cylindrical Channel

Dr. G.Kathyayani

Assistant Professor, Department of Applied Mathematics, Yogi Vemana University,
Kadapa

ABSTRACT:-

In this Chapter we discuss, peristaltic transport of Incompressible Non-Newtonian second order fluid through a flexible cylindrical channel, making use of long wavelength approximation. The perturbation analysis is carried out to obtain the velocity field, the streamlines, and shear stress. The computational analysis has been carried out for drawing streamlines, velocity profiles, and the stress which are plotted for different sets of governing parameters.

KEY WORDS: - Non –Newtonian Second order fluid.

1. INTRODUCTION:-

Peristalsis is well known to physiologists to be one of the major mechanisms for fluid transport in many biological system. In particular peristaltic mechanism may be involved in urine transport from kidney to bladder through the ureter, movement of chime in the gastrointestinal tract, transport of spermatozoa in the ducts, Efferentes of the mole reproductive tracts and in the cervical canal, movement of ovum in the fall opian tubes, transport of lymph in the lymphatic vessel is and in the vasomotion of small blood vessels. In addition, peristaltic pumping occurs in many practical applications involving biomechanical systems.

The study of the mechanism of peristalsis, in both mechanical and physiological situations, has become the object of scientific research. Since the first investigation of Latham (2), Several theoretical and experimental attempts have been made to understand peristaltic action in different situations. All such investigations seem to differ in various details. Taking muscle action in the tube wall, into in a book by Liron (3). The roller pump is an engineering example working on the principle of peristalsis with the tube being compressed by rotating rollers or by a series of mechanical fingers. All the important literature upto 1978 on peristaltic transport has been documented by Rath (4). Later, Srivastava and Srivastava (5) have presented an exhaustive list of theoretical contributions to this field, classifying them according to the geometry under consideration and the parameters describing the flow. Tackabatako et.al. (6) have studied numerically the influence of finite wave length and Reynolds number on the efficiency of peristaltic pumping.

In a more recent paper, Srivastava investigated the problem of peristaltic transport of blood by assuming a single layered casson fluid, which ignores the presence of peripheral layer.

2.FORMULATION AND SOLUTION OF THE PROBLEM:-

Consider the peristaltic transport of an incompressible second order fluid through a co-axial cylinders with inner wall being rigid and outer wall flexible. The unsteady axisymmetric flow is generated by imposing peristaltic wave on the flexible outer cylinder.

Following ‘Coleman & Noll (1) the constitutive equation for an impressible second order fluid is

$$\tau_{ij} = - P_{ij} + 2 \mu_1 d_{ij} + 2 \mu_2 e_{ij} + 4 \mu_3 d_i^\alpha d_{\alpha j} \quad (1.1)$$

where $d_{ij} = \frac{1}{2} (V_{i,j} + V_{j,i})$

$$e_{ij} = \frac{1}{2} (a_{i,j} + a_{j,i} + 2 V_{,j}^m V_{m,j}) \quad (1.2)$$

τ_{ij} is the stress – tensor of the second order fluid.

P_{ij} is the stress tensor in its hydrostatic state.

V_i and a_i indicate components of fluid velocity and acceleration and J indicates their derivatives in J^{th} direction.

μ_1 , μ_2 and μ_3 are the co-efficients of viscosity, elastico – viscosity and cross-viscosity respectively and ρ is the density of the fluid.

The governing equation of linear momentum in the tensor form is

$$\rho \left(\frac{\partial v_i}{\partial t} + V_j V_{i,j} \right) = \tau_{ij,j} \quad (1.3)$$

The equation of continuity is $\nabla_{i,i} = 0$

(1.4)

Choosing cylindrical frame reference (r,θ, z) the equation of motion of the axisymmetry flow of an incompressible second order fluid are

$$\rho \left(\frac{\partial u}{\partial t} + u \frac{\partial u}{\partial r} + w \frac{\partial u}{\partial z} \right) = \frac{\partial}{\partial r} \tau_{rr} + \frac{1}{r} (\tau_{rr} - \tau_{\theta\theta}) \tag{1.5}$$

$$\rho \left(\frac{\partial w}{\partial t} + u \frac{\partial w}{\partial r} + w \frac{\partial w}{\partial z} \right) = \frac{\partial}{\partial r} \tau_{rz} + \frac{1}{r} \tau_{rz} \tag{1.6}$$

The equation of continuity is

$$\frac{\partial}{\partial r} (ru) + \frac{\partial}{\partial z} (rw) = 0 \tag{1.7}$$

where $\tau_{rr} = -P + 2\mu_1 \frac{\partial u}{\partial r} + 2\mu_2 \left[u \frac{\partial^2 u}{\partial r^2} + \frac{\partial u}{\partial z} \frac{\partial w}{\partial r} + w \frac{\partial^2 u}{\partial r \partial z} + 2 \left(\frac{\partial u}{\partial z} \right)^2 + \left(\frac{\partial w}{\partial r} \right)^2 \right]$

$$+ \mu_3 \left[4 \left(\frac{\partial u}{\partial r} \right)^2 + \left(\frac{\partial w}{\partial r} \right)^2 + \left(\frac{\partial u}{\partial z} \right)^2 \right] \tag{1.8}$$

$$\tau_{zz} = -P + 2\mu_1 \frac{\partial w}{\partial z} + 2\mu_2 \left[u \frac{\partial^2 w}{\partial z \partial r} + \frac{\partial u}{\partial z} \frac{\partial w}{\partial r} + \left(\frac{\partial w}{\partial z} \right)^2 + w \frac{\partial^2 w}{\partial z^2} + \left(\frac{\partial u}{\partial z} \right)^2 + \left(\frac{\partial w}{\partial z} \right)^2 \right]$$

$$+ \mu_3 \left[4 \left(\frac{\partial w}{\partial z} \right)^2 + \left(\frac{\partial w}{\partial r} + \frac{\partial u}{\partial z} \right)^2 \right] \tag{1.9}$$

$$\tau_{rz} = \mu_1 \left[\frac{\partial w}{\partial r} + \frac{\partial u}{\partial z} \right] + \mu_2 \left[\frac{\partial u}{\partial r} \frac{\partial w}{\partial r} + u \frac{\partial^2 w}{\partial r^2} + \frac{\partial w}{\partial r} \frac{\partial w}{\partial z} + w \frac{\partial^2 w}{\partial r \partial z} + \frac{\partial u}{\partial z} \frac{\partial u}{\partial r} \right]$$

$$+ u \frac{\partial^2 u}{\partial z \partial r} + \frac{\partial w}{\partial z} \frac{\partial u}{\partial z} + w \frac{\partial^2 u}{\partial z^2} \Big] + \mu_3 \left[2 \left(\frac{\partial w}{\partial r} + \frac{\partial u}{\partial z} \right) \left(\frac{\partial w}{\partial z} + \frac{\partial u}{\partial r} \right) \right] \tag{1.10}$$

$$\tau_{\theta\theta} = -P + 2\mu_1 \frac{u}{r} + 2\mu_2 \left[\frac{u}{r} \frac{\partial u}{\partial r} + \frac{u^2}{r^2} \right] + 4\mu_3 \frac{u^2}{r^2} \tag{1.11}$$

$$\tau_{r\theta} = \tau_{\theta z} = 0 \tag{1.12}$$

The inner rigid pipe is of radius ‘a’ and a wave of contraction and expansion is imposed on the outer flexible pipe r = b. The fluid motion is due to the peristaltic action of this wave.

$$r = b + \delta \sin 2 \pi \left(\frac{z + ct}{\lambda} \right)$$

imposed on the outer cylinder.

- where
- c is the wave speed
 - λ is the wave length
 - δ is amplitude of the wave
 - b is the mean radius of the outer pipe

The flow becomes steady with reference to the wave frame moving along with the wave and some speed ‘c’.

The relevant boundary conditions are

$$\left. \begin{aligned} w = 0 & \quad \text{on} & r = r_1 \\ w = 0 & \quad \text{on} & r = r_2 + b (=f) \\ u = 0 & \quad \text{on} & r = r_1 \end{aligned} \right\} \tag{1.13}$$

$$2\pi \int_{r_1}^f wrdr = q$$

Introduce the following non-dimensional variables as

$$z^* = \frac{z + ct}{\lambda}; r^* = \frac{r}{\lambda}, \epsilon = \frac{b}{\lambda} (\epsilon \ll 1);$$

$$(w^*, u^*) = \left(\frac{w}{c}, \frac{U}{c \epsilon} \right); p^* = \frac{P}{\rho c^2}; t^* = \frac{ct}{\lambda}; \chi = \frac{\delta}{b}$$

$$\phi = \frac{a}{b}; q^* = \frac{\bar{q}}{\pi a^2 c}; Q^* = \frac{\bar{Q}}{\pi a^2 c}; \theta^* = \frac{\bar{\theta}}{\pi a^2 c}$$

and
$$q^* = \theta^* \left(2\phi - \frac{\phi^2}{2} \right)$$

and making use of the long wavelength approximation ($\epsilon \ll 1$),

The expression for the stream function is

$$\psi = \psi_0 + \epsilon \psi_1 + \dots$$

$$\Rightarrow \psi = C_1 + C_2 r + C_3 r \log r + C_4 r^3 + \epsilon [C_5 + C_6 r^2 + C_7 r^2 \log r + C_8 r^4 + R \{ -\frac{1}{3} l_1 r - \frac{1}{8} l_2 r^2 (\log r)^2 - \frac{1}{3} l_3 r^3 + \frac{1}{16} l_4 r^4 \log r + \frac{1}{140} l_5 r^5 - \frac{1}{32} l_6 r^6 + \frac{1}{3} l_7 (3 r \log r + 4r) - \frac{1}{16} l_8 r^2 \log r + \frac{1}{9} l_9 r^3 (3 \log r - 4) + \frac{1}{32} l_{10} r^2 (4 (\log r)^2 + 21) \} - \frac{R}{S_1} \{ -\frac{1}{16} \log r - 3 l_{12} r - \frac{1}{8} l_{13} r^2 (\log r)^2 + \frac{9}{8} l_{14} r^4 \log r - \frac{1}{64} l_{15} (2 (\log r)^2 + 5 \log r) + \frac{1}{45} l_{16} r^1 + \frac{3}{8} l_{17} r^2 \log r + l_{18} (\frac{(\log r)^3}{3} + \frac{5}{4} (\log r)^2 + \frac{17}{8} \log r) - \frac{1}{45} l_{19} r^1 (45 \log r + 84) - 2 \frac{R}{S_2} \{ -\frac{1}{16} l_{20} \log r - 3 l_{21} r - \frac{1}{8} l_{22} r^2 (\log r)^2 + \frac{27}{8} l_{23} r^4 \log r - \frac{1}{45} l_{24} r^1 - \frac{5}{32} l_{25} (2 (\log r)^2 + 5 \log r) + \frac{1}{16} l_{26} r^2 \log r - \frac{1}{135} l_{27} r^1 (45 \log r + 84) \}] \tag{1.14}$$

$$u = -\frac{1}{r} \frac{\partial \psi}{\partial z} = -\frac{1}{r} [C_{1z} + C_{2z} r + C_2 (2 \pi \lambda \cos 2 \pi z) + C_{3z} r \log r + C_3 (2 \pi \chi \cos 2 \pi z) \log r + C_3 (2 \pi \chi \cos 2 \pi z) + C_{4z} r^3 + 3 C_4 r^2 (2 \pi \chi \cos 2 \pi z)] \tag{1.15}$$

$$w = \frac{1}{r} \frac{\partial \psi}{\partial r} = \frac{C_2}{r} + C_3 \left(\frac{\log r}{r} + \frac{1}{r} \right) + 3 C_4 r + \epsilon [2 C_6 + 2 C_7 \log r + C_7 + 4 C_8 r^2 + R \{ -\frac{1}{3} l_1 \frac{1}{r} - \frac{1}{4} l_2 ((\log r)^2 + \log r) - l_3 r + \frac{1}{4} l_4 r^2 \log r + \frac{1}{16} l_4 r^2 + \frac{1}{28} l_5 r^3 - \frac{3}{16} l_6 r^4 + \frac{1}{3} l_7 (3 \frac{1}{r} \log r + \frac{7}{r}) - \frac{1}{16} l_8 (2 \log r + 1) + l_9 (r \log r - r) + \frac{1}{32} l_{10} (8 (\log r)^2 + 8 \log r + 42) \} - \frac{R}{S_1} \{ -\frac{1}{16} l_{11} \frac{1}{r^2} - 3 l_{12} \frac{1}{r} - \frac{1}{4} l_{13} ((\log r)^2 + \log r) + \frac{9}{8} l_{14} (4 r^2 \log r + r^2) - \frac{1}{64} l_{15} (\frac{4}{r^2} \log r + \frac{5}{r^2}) - \frac{1}{45} l_{16} \frac{1}{r^3} + \frac{3}{8} l_{17} (2 \log r + 1) + l_{18} (\frac{(\log r)^2}{r^2} + \frac{5}{2 r^2} \log r + \frac{17}{8 r^2}) + l_{19} (\frac{1}{r^3} \log r + \frac{39}{45 r^3}) \} - 2 \frac{R}{S_2} \{ l - \frac{1}{16} l_{20} \frac{1}{r^2} - 3 l_{21} \frac{1}{r} - \dots \}]$$

$$\frac{1}{8} l_{22} ((\log r)^2 + \log r) + \frac{27}{8} l_{23} (4 r^2 \log r + r^2) - \frac{1}{45} l_{24} \frac{1}{r^3} - \frac{5}{32} l_{25} (4 \frac{\log r}{r^2} + \frac{5}{r^2}) + \frac{1}{16} l_{26} (2 \log r + 1) + \frac{1}{3} l_{27} (\frac{\log r}{r^3} + \frac{39}{45r^3}) \} \} \} \quad (1.16)$$

3. STRESS ON THE WALL:-

The stress on the flexible wall of the pipe in the non-dimensional form is

$$(\tau)_{r=s} = \frac{\left(\frac{1}{2} \left(\frac{\partial w}{\partial r} + \frac{\partial u}{\partial z} \right) (1 - s_z^2) + \left(\frac{\partial u}{\partial r} - \frac{\partial w}{\partial z} \right) s_z \right)}{(1 + s_z^2)}$$

Substituting w and u; and then τ has been evaluated for different values of the governing parameters for the first order approximation. The stresses on the boundaries are evaluated and tabulated in tables 1-3. We observe that the stress τ increases (& decreases) with an increase in S₁ (& S₂) for fixed values of other parameters while an increase in R increases the stress for variation in all other parameters.

Table - 1
Stress (□) on the flexible boundary with S₁ Variation

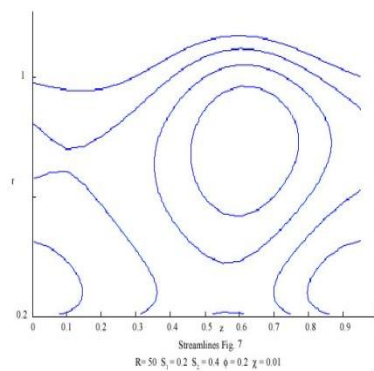
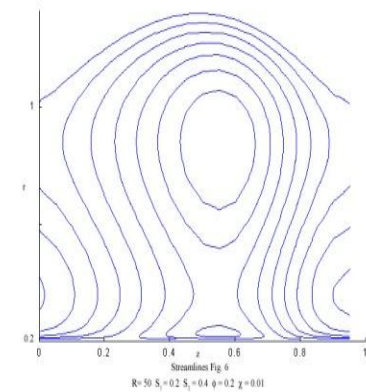
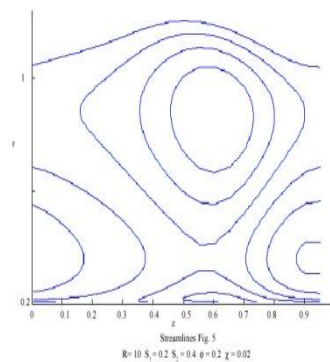
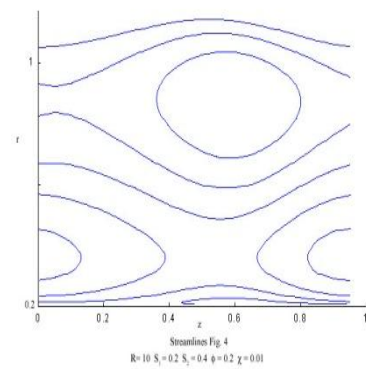
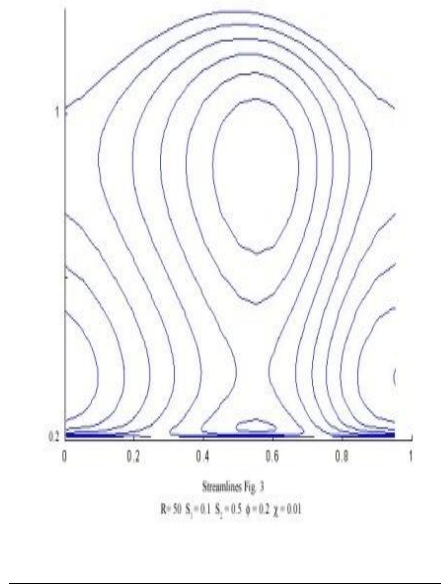
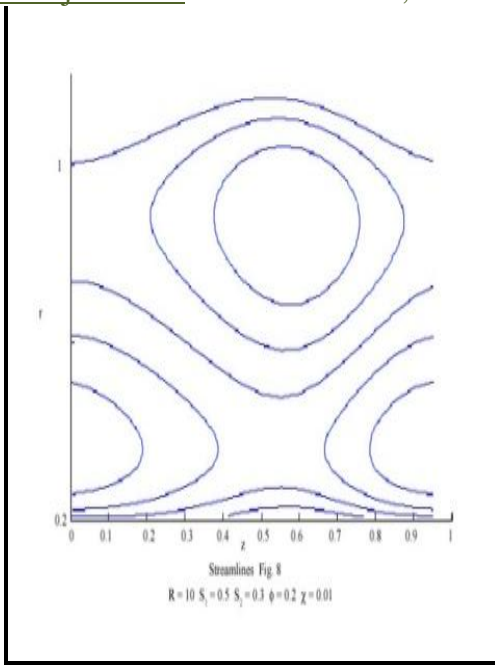
	I	II	III	IV	V	VI	VII	VIII	IX	X
S ₁ =0.1	21.6156	11.8361	8.57624	6.94633	6.94633	11.0482	5.8447	4.11019	3.24293	2.72258
S ₁ =0.2	20.1432	10.3637	7.10384	5.47392	5.47392	10.2745	5.07092	3.3364	2.46915	1.94879
S ₁ =0.3	19.6524	9.87286	6.61303	4.98312	4.98312	10.0165	4.81299	3.07848	2.21122	1.69086
S ₁ =0.4	19.407	8.62746	6.36763	4.73772	4.73772	9.88757	4.68403	2.94951	2.08225	1.5619
S ₁ =0.5	19.2597	9.48022	6.22039	4.59048	4.59048	9.81019	4.60665	2.87213	2.00488	1.48452

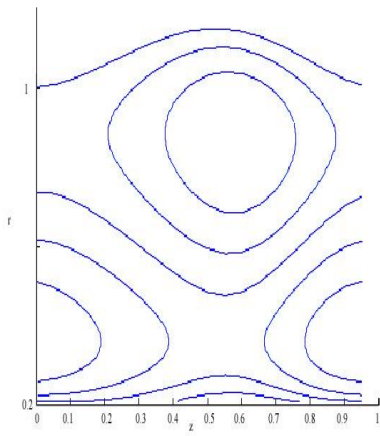
	I	II	III	IV	V	VI	VII	VIII	IX	X
□	0.02	0.02	0.02	0.02	0.02	0.01	0.01	0.01	0.01	0.01
R	20	20	20	20	20	20	20	20	20	20
Z	1/8	1/8	1/8	1/8	1/8	1/8	1/8	1/8	1/8	1/8
S	1.01414	1.01414	1.01414	1.01414	1.01414	1.00701	1.00701	1.00701	1.00701	1.00701
S ₂	0.1	0.2	0.3	0.4	0.5	0.1	0.2	0.3	0.4	0.5
□	0.1	0.1	0.1	0.1	0.1	0.1	0.1	0.1	0.1	0.1

4. DISCUSSION:-

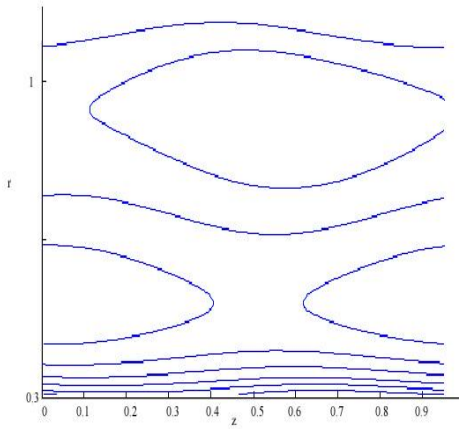
The streamlines are plotted for different variations in the governing parameters in a unit distance along axial direction. We observe from streamline pattern for all variations in R, S₁, S₂ & χ clearly exhibit the flow separation in the vicinity of the inner cylinder. An increase in R the trapping of the fluid with formation of bolus (closed stream lines) may be observed from (Fig 1). A further increase in R, (Fig 2) give rise to an interesting pattern with fluid near by bolus circulating around the bolus and the flow on either sides being separated by this trapped fluid. When S₁ is increased this formation of bolus is weakened with only one bolus appearing near the flexible cylinder(Fig 3). However the trapping once again flowing when the amplitude of the boundary wave is increased (Fig 4).When R is sufficiently large irrespective of the values of S₁ & S₂ or similar interesting pattern of bell shaped streamlines are observed (Fig 5).

Fixing R and S₁, S₂ greater than 0.3 whether S₁ ≥ S₂, the streamline pattern shows two bolus formation. But S₁ < S₂ these two bolus are not separated from the lower region near the rigid cylinder while for S₁ > S₂ this trapped fluid is separated from the lower region (Figs 6 & 7). This phenomenon of appearance of single bolus may also be observed even for higher and almost equal values of S₁ & S₂ (Figs 8 & 9). An increase in S₁, retards w in the lower region and enhances near the outer cylinder (Figs 10&11). For a fixed S₁ the behaviour of w with increase in S₂ is similar to that of variation in S₁ (Fig 12&13), although the retardation near the flexible cylinder is comparably faster. The magnitude of w at lower values of S₂ (≤ 0.5) is higher compared to its values at S₂ (> 0.5). Fixing S₁ and S₂ and other parameters an increase in R enhances w in the lower region and retards the same in the upper region adjacent to the flexible boundary (Figs 14&15).

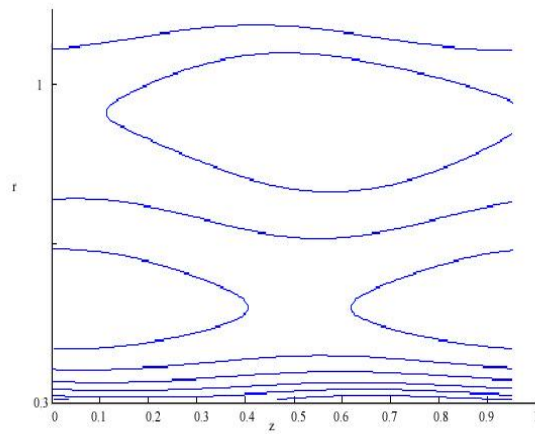




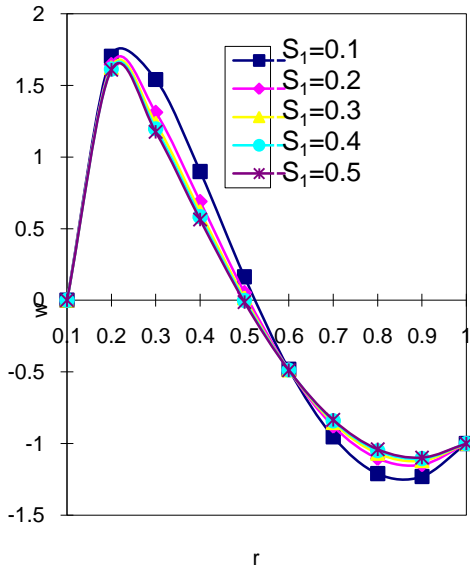
Streamlines Fig. 8
 $R=10 S_1=0.5 S_2=0.3 \phi=0.2 \chi=0.01$



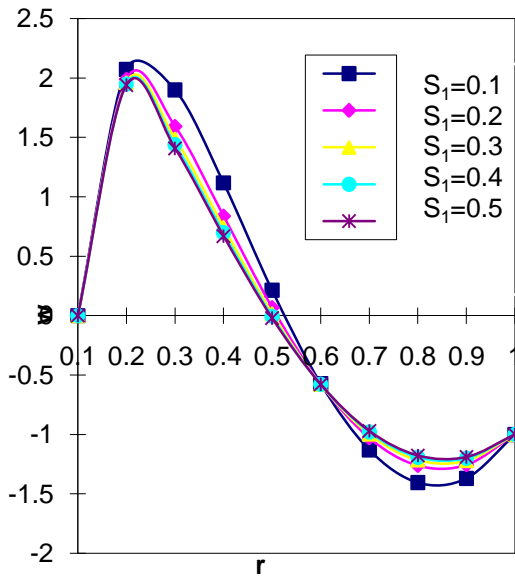
Streamlines Fig. 12
 $R=20 S_1=0.5 S_2=0.5 \phi=0.3 \chi=0.01$



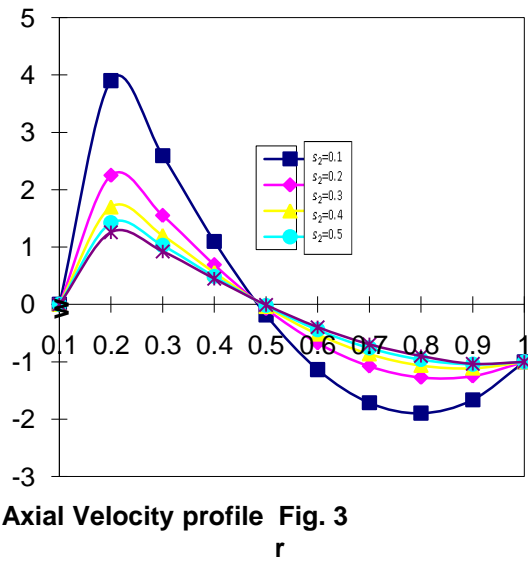
Streamlines Fig. 12
 $R=20 S_1=0.5 S_2=0.5 \phi=0.3 \chi=0.01$



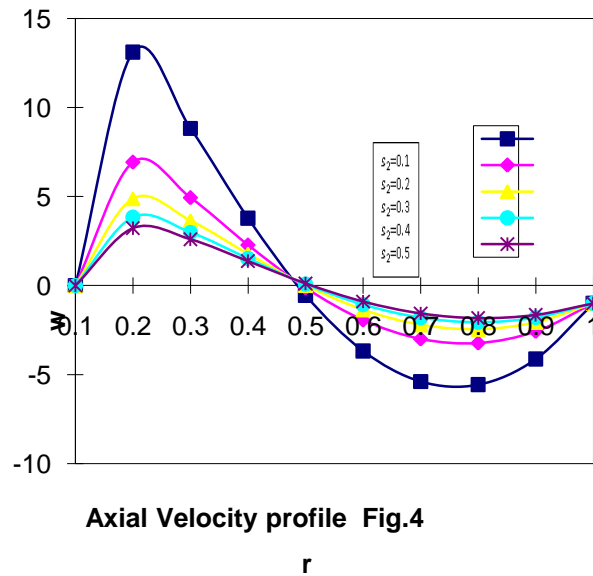
Axial Velocity profile Fig. 1
 $\chi=0.01, S_2=0.5, Q=1 \quad R=10, Z=0, \phi=0.1$



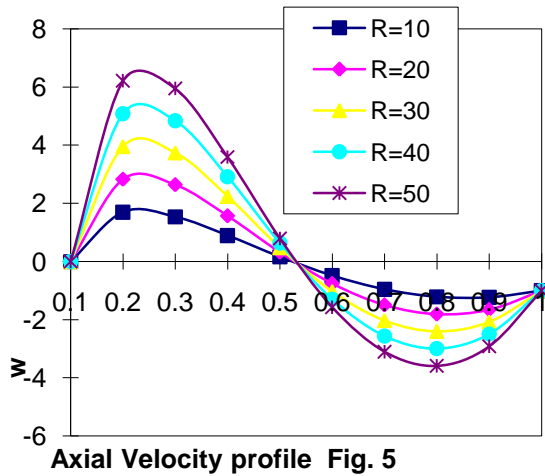
Axial Velocity profile Fig. 2
 $\chi=0.01, S_2=0.5, Q=1 \quad R=20, Z=1/8, \phi=0.1$



Axial Velocity profile Fig. 3
 $\chi=0.01, S_1=0.5 \quad R=10, Z=1/8, \phi=0.1$



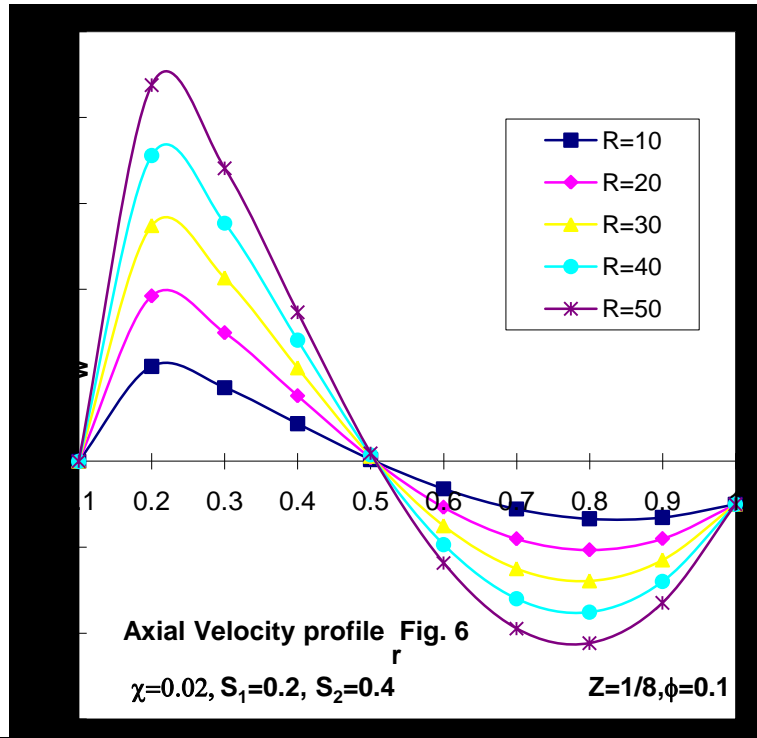
Axial Velocity profile Fig.4
 $\chi=0.02, O=1, S_1=0 \quad R=20, Z=1/8, \phi=0.1, E=0.01$



$\chi=0.01, S_1=0.1, S_2=0.5$

$z = 0, \phi=0.1$

r



$\chi=0.02, S_1=0.2, S_2=0.4$

$Z=1/8, \phi=0.1$

r

5. REFERENCES:-

1. Coleman B.D. and Noll W.: J. Appl. Phys., V. 30, p. 1508, (1959).
2. Latham, T.W.: M.S. Thesis, MIT, Cambridge, Mass, (1966).
3. Liron, N.: Horizons in Bio-Chemistry and Biophysics, V 5, pp. 161 -182. Addison – Wesley, Reading, M.A. (1978).
4. Rath, H.J. :Peristaltische stromungen, Springer – Verlag, Berlin, Heidelberg, New York (1980).
5. Srivastava, L.M.; and Srivastava, V.P.: J. Bio mechanics V. 17, p.821, 1984.
6. Takabatake, S.; Ayukawa, K; and Mori.: J. Fluid Mech, V. 193, p.267, (1988).

Performance Analysis and Enhancement of Routing Protocol in Manet

Jaya Jacob*, V.Seethalakshmi**

*II MECS, Sri Shakthi Institute of Engineering and Technology, Coimbatore, India

**Associate Professor-ECE, Sri Shakthi Institute of Engineering and Technology, Coimbatore, India

ABSTRACT

MANET (Mobile Adhoc Network) is a self organizing and self configuring network without the need of any centralized base station. In MANETs, the nodes are mobile and battery operated. As the nodes have limited battery resources and multi hop routes are used over a changing network environment due to node mobility, it requires energy efficient routing protocols to limit the power consumption, prolong the battery life and to improve the robustness of the system. This paper evaluates the performance of various adhoc routing protocols such as DSDV, AODV, DSR, TORA and AOMDV in terms of energy efficiency and it also proposes a new routing algorithm that modifies AOMDV and it provides better performance compared to all the above protocols. Simulation is done using NS-2(version NS-2.34).

Key Terms— AODV, AOMDV, DSR, DSDV, TORA, MANET, Energy efficient routing

I. INTRODUCTION

MANET is a wireless infrastructure less network having mobile nodes. Communication between these nodes can be achieved using multi hop wireless links. Each node will act as a router and forward data packets to other nodes. Mobile adhoc networks are operating without any centralized base station. It uses multi hop relaying. Since the nodes are independent to move in any direction, there may be frequent link breakage. The advantage of MANET is its instant deployment.

Various protocols have been developed for adhoc networks such as TORA(Temporally Ordered Routing Algorithm), DSDV (Destination-Sequenced Distance Vector), DSR (Dynamic Source Routing),AODV(Ad-Hoc On Demand Routing), AOMDV (Ad hoc On-demand Multipath Distance Vector Routing). These protocols offer varying degrees of efficiency. This paper aims to find out an energy efficient routing protocol. It also aims to limit power consumption of mobile nodes in the network in order to prolong the network life time. The main objective of this paper is to analyze AOMDV protocol for ways it could be improved. This can be done by measuring energy with respect to network size and taking into consideration the remaining battery power. It also proposes further research into more efficient protocols or variants of existing protocols such as AOMDV. This paper also proposes a new routing algorithm based on node residual energy and it is applied on AOMDV so that the new algorithm provides better

performance than DSDV, DSR, AODV, TORA and AOMDV.

II. ROUTING PROTOCOLS IN MANET

Routing Protocol is used to find valid routes between communicating nodes. They do not use any access points to connect to other nodes .It must be able to handle high mobility of the nodes. Routing protocols can be mainly classified into 3 categories

- Centralized versus Distributed
- Static versus Adaptive
- Reactive versus Proactive

In centralized algorithms, all route choices are made by a central node, while in distributed algorithms, the computation of routes is shared among the network nodes. In static algorithms, the route used by source destination pairs is fixed regardless of traffic condition. It can only change in response to a node or link failure. This type of algorithm cannot achieve high throughput under a broad variety of traffic input patterns. In adaptive routing, the routes used to route between source-destination pairs may change in response to congestion.

2.1 Proactive (Table-Driven) Routing Protocols

In this family of protocols, nodes maintain one or more routing tables about nodes in the network. These routing protocols update the routing table information either periodically or in response to change in the network topology. The advantage of these protocols is that a source node does not need route-discovery procedures to find a route to a destination node. On the other hand the drawback of these protocols is that maintaining a consistent and up-to-date routing table requires substantial messaging overhead, which consumes bandwidth and power, and decreases throughput, especially in the case of a large number of high node mobility. There are various types of Table Driven Protocols: Destination Sequenced Distance Vector routing (DSDV), Wireless routing protocol (WRP), Fish eye State Routing protocol (FSR), Optimized Link State Routing protocol (OLSR), Cluster Gateway Switch Routing protocol (CGSR), Topology Dissemination Based on Reverse Path Forwarding (TBRPF).

2.2 Reactive (On-Demand) Routing Protocols

For protocols in this category there is an initialization of a route discovery mechanism by the source node to find the route to the destination node when the source node has data packets to send. When a route is

found, the route maintenance is initiated to maintain this route until it is no longer required or the destination is not reachable. The advantage of these protocols is that overhead messaging is reduced. One of the drawbacks of these protocols is the delay in discovering a new route. The different types of reactive routing protocols are: Dynamic Source Routing (DSR), Ad-hoc On-Demand Distance Vector routing (AODV), Adhoc On-demand Multipath Distance Vector Routing Algorithm (AOMDV) and Temporally Ordered Routing Algorithm (TORA).

III. OVERVIEW OF SELECTED ROUTING PROTOCOLS

3.1 TORA: The Temporally Ordered Routing Algorithm (TORA) is a highly adaptive, efficient and scalable distributed routing algorithm based on the concept of link reversal. TORA is proposed for highly dynamic, mobile, multi hop wireless networks. It is a source initiated routing protocol. It finds multiple routes from a source node to a destination node. The main feature of TORA is that the control messages are localized to a very small set of nodes near the occurrence of a topological change. To achieve this, the nodes maintain routing information about adjacent nodes. The protocol has three basic functions: Route creation, Route maintenance and Route erasure. TORA can suffer from unbounded worst-case convergence time for very stressful scenarios. TORA has a unique feature of maintaining multiple routes to the destination so that topological changes do not require any reaction at all. The protocol reacts only when all routes to the destination are lost. In the event of network partitions the protocol is able to detect the partition and erase all invalid routes.

3.2 DSDV: Destination Sequence Distance Vector (DSDV) is a proactive routing protocol and is based on the distance vector algorithm. In proactive or table-driven routing protocols, each node continuously maintains up-to-date routes to every other node in the network. Routing information is periodically transmitted throughout the network in order to maintain routing table consistency. The routing table is updated at each node by finding the change in routing information about all the available destinations with the number of nodes to that particular destination. Also, to provide loop freedom DSDV uses sequence numbers, which is provided, by the destination node. In case, if a route has already existed before traffic arrives, transmission occurs without delay. However, for highly dynamic network topology, the proactive schemes require a significant amount of resources to keep routing information up-to-date and reliable.

In case of failure of a route to the next node, the node immediately updates the sequence number and broadcasts the information to its neighbors. When a node receives routing information then it checks in its routing table. If it does not find such entry into the routing table then updates the routing table with routing information it has found. In case, if the node finds that it has already entry into its routing table then it compares the sequence number of the received information with the routing table entry and updates the information.

3.3 DSR: Dynamic Source Routing DSR is a reactive protocol. This protocol is one of the example of an on-demand routing protocol that is based on the concept of source routing. It is designed for use in multi hop ad hoc networks of mobile nodes. It allows the network to be completely self-organizing and self-configuring and does not need any existing network infrastructure or administration. DSR uses no periodic routing messages like AODV, thereby reduces network bandwidth overhead, conserves battery power and avoids large routing updates. However, it needs support from the MAC layer to identify link failure. The DSR routing protocol discovers routes and maintains information regarding the routes from one node to other by using two main mechanisms: (i) Route discovery – Finds the route between a source and destination and (ii) Route maintenance –In case of route failure, it invokes another route to the destination. DSR has a unique advantage by virtue of source routing. As the route is part of the packet itself, routing loops, either short – lived or long – lived, cannot be formed as they can be immediately detected and eliminated. This property of DSR opens up the protocol to a variety of useful optimizations. If the destination alone can respond to route requests and the source node is always the initiator of the route request, the initial route may be the shortest. This routing protocol apply the concept of source routing, which means that the source determines the complete path from the source node to the destination node, that the packets have to traverse, and hence ensures routing to be trivially loop-free in the network. The packet in DSR carries all information pertaining to route in its preamble (header) thus permitting the intermediate nodes to cache the routing information in their route tables for their future use.

3.4 AODV: The Ad-hoc On-Demand Distance Vector (AODV) routing protocol builds on the DSDV algorithm, it is an on demand routing algorithm, but in contrast to DSR it is not a source based routing scheme rather every hop of a route maintains the next hop information by its own. Operation of the protocol here is also divided in two functions, route discovery and route maintenance. At first all the nodes send Hello message on its interface and receive Hello messages from its neighbors. This process repeats periodically to determine neighbor connectivity. When a route is needed to some destination, the protocol starts route discovery. The source sends Route Request Message to its neighbors. If a neighbor has no information on the destination, it will send message to all of its neighbors and so on. Once request reaches a node that has information about the destination (either the destination itself or some node that has a valid route to the destination), that node sends Route Reply Message to the Route Request Message initiator. In the intermediate nodes (the nodes that forward Route Request Message), information about source and destination from Route Request Message is saved. Address of the neighbor that the Route Request Message came from is also saved. In this way, by the time Route Request Message reaches a node that has information to answer Route Request Message; a path has been recorded in the intermediate nodes. This path identifies the route that Route Request

Message took and is called reverse path. Since each node forwards Route Request Message to all of its neighbors, more than one copy of the original Route Request Message can arrive at a node. When a Route Request Message is created at the initiator, it is assigned a unique id. When a node receives Route Request Message, it will check this id and the address of the initiator and discard the message if it had already processed that request.

3.5 AOMDV: Ad-hoc On-demand Multi path Distance Vector Routing protocol is an extension to the AODV protocol for computing multiple loop-free and link disjoint paths. The routing entries for each destination contain a list of the next-hops along with the corresponding hop counts. All the next hops have the same sequence number. This helps in keeping track of a route. For each destination, a node maintains the advertised hop count, which is defined as the maximum hop count for all the paths, which is used for sending route advertisements of the destination. Each duplicate route advertisement received by a node defines an alternate path to the destination. Loop freedom is assured for a node by accepting alternate paths to destination if it has a less hop count than the advertised hop count for that destination. Because the maximum hop count is used, the advertised hop count therefore does not change for the same sequence number. When a route advertisement is received for a destination with a greater sequence number, the next-hop list and the advertised hop count are reinitialized.

3.6 MODIFIED AOMDV (ENERGY_ AOMDV):

The concept behind the modified protocol is to find the nodal residual energy of each route in the process of selecting path, select the path with minimum nodal residual energy and sort all the routes based on the descending order of nodal residual energy. Once a new route with greater nodal residual energy is emerging, it is again selected to forward rest of the data packets. It can improve the individual node's battery power utilization and hence prolong the entire network's lifetime.

The steps involved are:

1. Find the nodal residual energy of each route in the route discovery process.
2. Find the path with minimum nodal residual energy.
3. Sort out all the routes based on the descending value of nodal residual energy
4. Select the route with maximal nodal residual energy to forward the data packets.

IV. PROBLEM DEFINITION

The main limitation of adhoc system is the availability of power. Power consumption is governed by no. of processes and overheads required to maintain connectivity in addition to running onboard electronics. Early "death" of some mobile nodes due to energy depletion may cause several problems such as network partition and communication interruption. Therefore it is required to limit the power consumption of mobile nodes,

prolong the battery life and to maintain the robustness of the system.

V. METHODOLOGY

In the existing system, different routing protocols in MANETs are compared by many researchers. They compared EE-OLSR with OLSR. Some implemented overhead reduction and efficient energy management for DSR in MANET. Some compared the performance of DSR and DSDV based on the node termination rate as well as the overall throughput of the network. Some researchers compared AODV and DSR in terms of pause time and no. of nodes. These works provide detailed performance analysis on adhoc routing protocols but energy performance was not addressed. It does not reflect the topological change.

In the proposed system, various routing protocols such as AODV, DSR, DSDV, TORA and AOMDV are compared with respect to more metrics and a new routing algorithm based on energy constraint node cache that modifies AOMDV so that it consumes minimum energy compared to AOMDV. Protocol performances are tested in higher mobility situations. This work tries to optimize delay, bandwidth and overhead and reflects much better the topological change. Routing protocols are analyzed in terms of energy efficiency.

VI. RESULTS AND DISCUSSION

The Simulation is carried out in NS2 under LINUX platform. The aim of these simulations is to analyze the AOMDV protocol by comparing it with other protocols (AODV, DSR, TORA and DSDV) for its efficiency in terms of energy consumption, delay, packet delivery ratio, packet lost and throughput. A new protocol is designed based on AOMDV so that the new protocol had better performance than AOMDV in all the above parameters. The following table shows that the important parameters chosen for the NS2 simulation:

Table 6.1 Simulation Parameters

Simulation Time	100s
Topology Size	1000m x 1500m
Number Of Nodes	50
MAC Type	MAC 802.11
Radio Propagation Model	Two Ray Model
Radio Propagation Range	250m
Pause Time	0s
Max Speed	4m/sec-24m/sec
Initial Energy	100J
Transmit Power	0.4W
Receive Power	0.3W
Traffic Type	CBR
CBR Rate	512 bytes x 6 per second
Number of Connections	50

6.1 Simulation parameters

1. Packet delivery ratio

It is the ratio of the data packets delivered to the destinations to those generated by the sources.

2. Energy consumption

This is the ratio of the average energy consumed in each node to total energy.

3. End to end delay

This is the ratio of the interval between the first and second packet to total packet delivery.

4. Throughput

The throughput metric measures how well the network can constantly provide data to the sink. Throughput is the number of packet arriving at the sink per ms.

5. Number of Packets dropped:

This is the number of data packets that are not successfully sent to the destination during the transmission. In this study the time versus number of packets dropped have been calculated.

B. Simulation Results

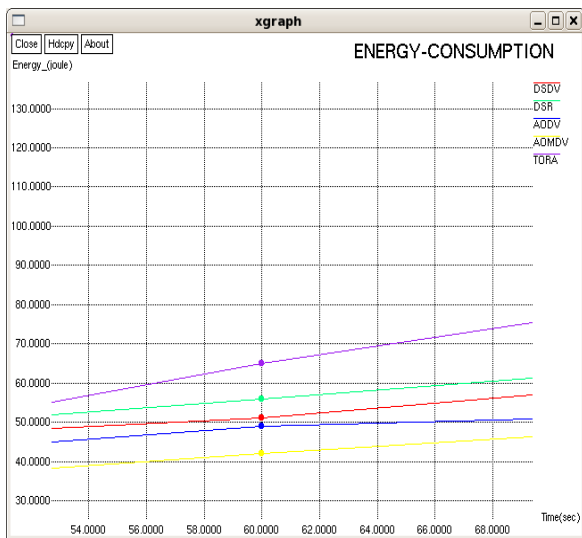


Fig 6.1 Comparison of Energy consumption versus time for DSDV, DSR, TORA, AODV and AOMDV using 50 nodes

Figure 6.1 shows the Comparison of Energy consumption versus time for DSDV, DSR, TORA, AODV and AOMDV using 50 nodes. It shows that the energy consumption of networks using AOMDV is minimum compared to TORA, AODV, DSR and DSDV. TORA is consuming maximum energy. AODV is consuming lesser energy than TORA, DSR and DSDV.

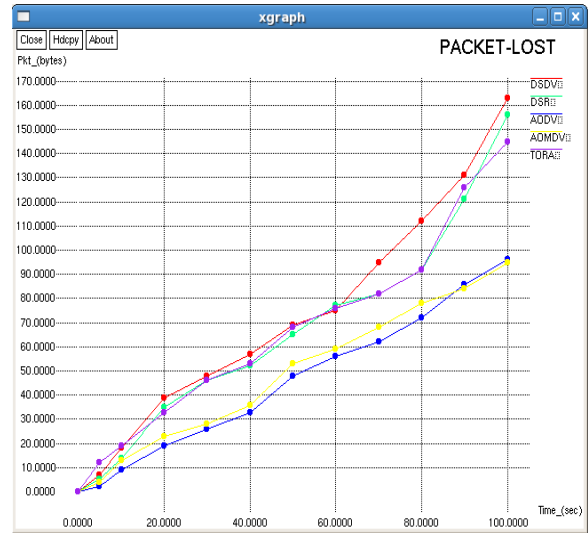


Fig 6.2 Comparison of Packet lost versus time for DSDV, DSR, TORA, AODV and AOMDV using 50 nodes

Figure 6.2 shows the comparison of Packet lost versus time for DSDV, DSR, TORA, AODV and AOMDV using 50 nodes. Packet loss is minimum using AODV compared to DSR and DSDV. It shows that the packet lost is minimum for AODV and AOMDV compared to the other 3 protocols.

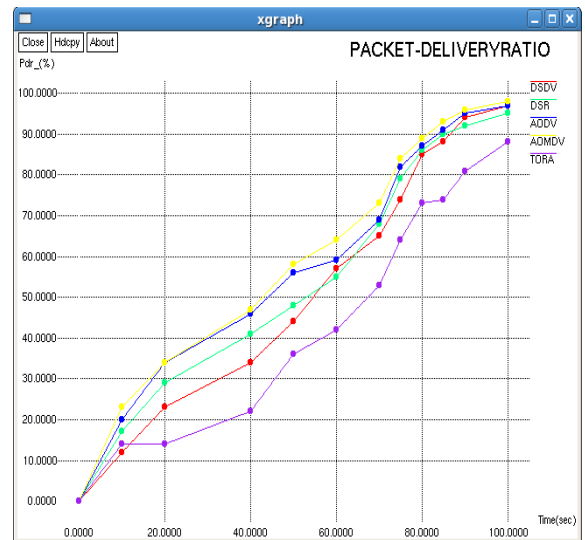


Fig 6.3 Comparison of Packet delivery ratio versus time for DSDV, DSR, TORA, AODV and AOMDV using 50 nodes

Figure 5.4 shows the comparison of Packet delivery ratio versus time for DSDV, DSR, TORA, AODV and AOMDV using 50 nodes. It shows that the packet delivery ratio of networks using AOMDV is better compared to AODV, TORA, DSR and DSDV. TORA has poor packet delivery ratio than all the other protocols.



Fig 6.4 Comparison of End to end delay versus time for DSDV, DSR, TORA, AODV and AOMDV using 50 nodes

Figure 6.4 shows the comparison of end to end delay versus time for DSDV, DSR, TORA, AODV and AOMDV using 50 nodes. It shows that the end to end delay is minimum using AOMDV compared to AODV, TORA, DSR and DSDV. TORA is having the highest end to end delay compared to all the other protocols.

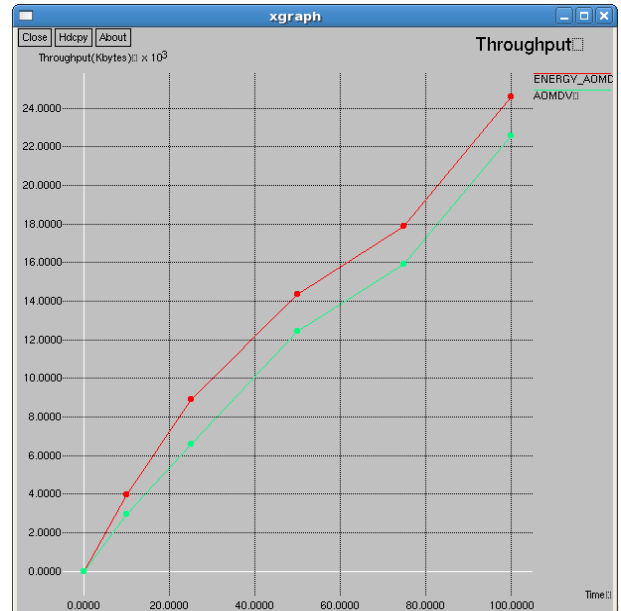


Fig 6.6 Comparison of throughput for AOMDV and ENERGY_AOMDV using 60 nodes

Figure 6.6 shows the comparison of throughput for AOMDV and ENERGY_AOMDV using 60 nodes. It shows that the throughput is maximum for ENERGY_AOMDV compared to AOMDV.

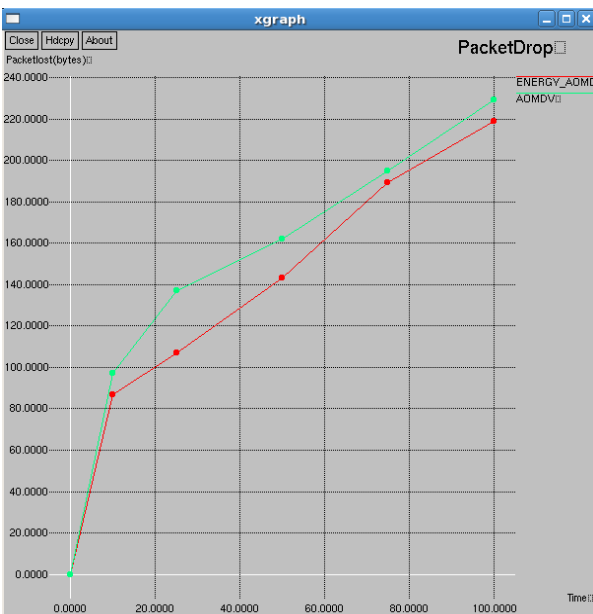


Fig 6.5 Comparison of packet lost for AOMDV and ENERGY_AOMDV using 60 nodes

Figure 6.5 shows the comparison of packet lost for AOMDV and ENERGY_AOMDV using 60 nodes. It shows that the packet lost is minimum for ENERGY_AOMDV compared to AOMDV.

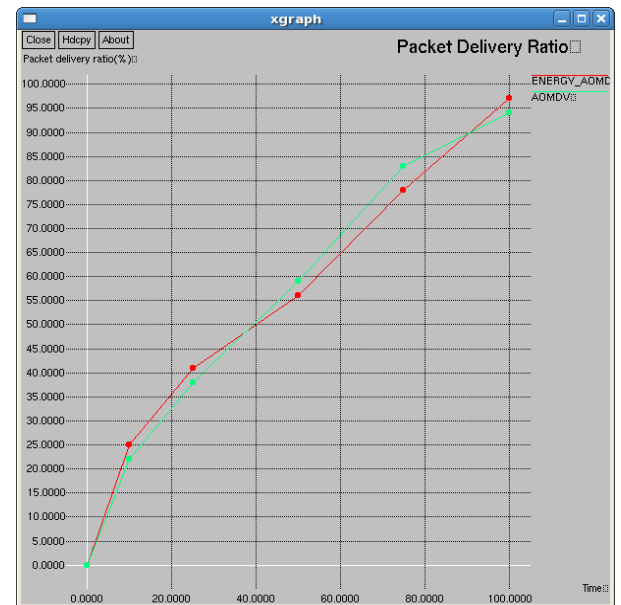


Fig 6.7 Comparison of packet delivery ratio for AOMDV and ENERGY_AOMDV using 60 nodes

Figure 6.7 shows the comparison of packet delivery ratio for AOMDV and ENERGY_AOMDV using 60 nodes. It shows that the packet delivery ratio is better for ENERGY_AOMDV compared to AOMDV.

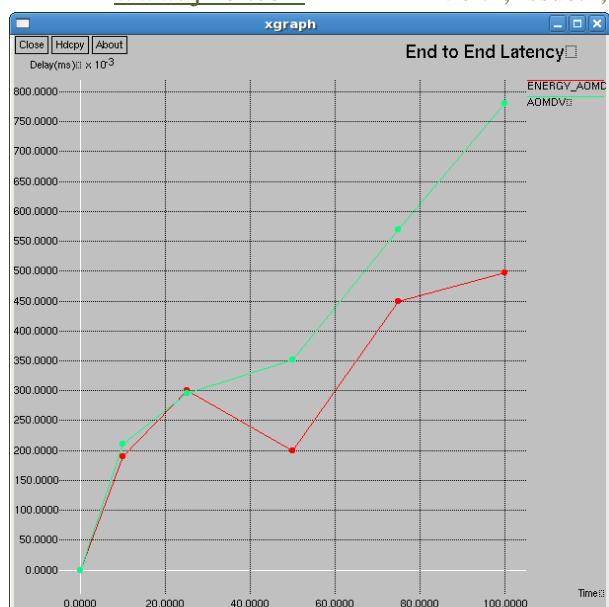


Fig 6.8 Comparison of end to end delay for AOMDV and ENERGY_AOMDV using 60 nodes

Figure 6.8 shows the comparison of packet lost for AOMDV and ENERGY_AOMDV using 60 nodes. It shows that the end to end delay is minimum for ENERGY_AOMDV compared to AOMDV.



Fig 6.9 Comparison of energy consumption for AOMDV and ENERGY_AOMDV using 60 nodes

Figure 6.9 shows the comparison of packet lost for AOMDV and ENERGY_AOMDV using 60 nodes. The green colored line indicates AOMDV and the red colored line indicates ENERGY_AOMDV. It shows that the energy consumption is minimum for ENERGY_AOMDV compared to AOMDV.

MANETs. Emphasis is on protocols that could be suitable for the implementation of scalable system in high node density environments such as in manufacturing or product distribution industries.

VII. CONCLUSION

In this paper we have evaluated the performance of different routing protocols such as, AOMDV, AODV, DSDV, TORA and DSR in MANET in different network environments. AOMDV is analyzed as the best protocol compared to AODV, TORA, DSR and DSDV. Then the result will be compared with performance of modified AOMDV. Results will be obtained as modified AOMDV providing better performance compared to AOMDV, AODV, TORA, DSR and DSDV protocols.

VIII. FUTUREWORK

This paper proposes further research into more efficient protocols or variants of existing protocols and network topologies that can improve the performance of

REFERENCES

- [1] V. Kanakaris*, D. Ndzi and D. Azzi., Ad-hoc Networks Energy Consumption: A review of the Adhoc Routing Protocols, Journal of Engineering Science and Technology Review 3 (1) (July 2010)
- [2] Yumei Liu, Lili Guo, Huizhu Ma, Tao Jiang, Energy Efficient on-demand Multipath Routing Protocol for Multi-hop Ad Hoc Networks
- [3] S. Giannoulis, C. Antonopoulos, E. Topalis, S. Koubias, ZRP versus DSR and TORA: A comprehensive survey on ZRP performance, IEEE Transactions on Industrial Informatics Vol. 3, No. 1, pp. 63-72 (Feb. 2007)
- [4] D. Maltz, Y. Hu, The Dynamic Source Routing Protocol for Mobile Adhoc Networks, Internet Draft, Available: <http://www.ietf.org/internetdrafts/draft-ietf-manet-dsr-10.txt>, July 2004
- [5] C. Perkins and E. Royer, Ad Hoc On-demand Distance Vector (AODV) Routing, Internet Draft, MANET working group, draft-ietf-manetaodv-05.txt, March 2000
- [6] A. H. Abd Rahman, Z. A. Zukarnain, Performance Comparison of AODV, DSDV and I-DSDV Routing Protocols in Mobile Ad Hoc Networks, European Journal of Scientific Research Vol. 31, No. 4, pp. 556-576 (June 2009)
- [7] L. Junhai, X. Liu, Y. Danxia, Research on multicast routing protocols for mobile ad-hoc networks, Science Direct Vol. 52 Issue 5, pp. 988-997(April 2008).

Energy-Aware SCC Mac Protocol Design For Wireless Sensor Networks

Manoj Kumar.K*, Ilango Sambasivam.S#

*PG Student, #Professor,

Sri Shakthi Institute of Engineering and Technology,
Coimbatore, Tamil Nadu, India

ABSTRACT

Wireless Sensor Networks (WSN) is mainly characterized by dense deployment of sensor nodes which collectively transmit information about sensed events to the sink. Energy efficiency is a major concern in the design of Wireless Sensor Networks. Due to the spatial correlation between sensor nodes subject to observed events, it may not be necessary for every sensor node to transmit its data. Hence the spatial correlation can be exploited on the Medium Access Control (MAC) layer. The spatial correlation-based collaborative MAC (SCC-MAC) protocol which aims to reduce the energy consumption of the network by exploiting spatial correlation in WSN. Here the number of nodes sending information about an event is decreased by spatial correlation properties.

The performance of SCC-MAC, SMAC and IEEE802.11a based on Energy Consumption, Packet Delivery Rate and Goodput using Network Simulator (ns-2 v2.29) is analyzed in this project. Sensor-Medium Access Control (SMAC) is a contention-based protocol designed specifically for WSN. In which nodes take turns to sleep and wake-up to listen for a while. In IEEE 802.11, each node keeps listening to all transmissions from its neighbors in order to perform effective virtual carrier sensing. The results show according to Energy Consumption, SCC-MAC is better than SMAC and IEEE802.11a the number of nodes sending information about an event is decreased so less energy is consumed here. Also by considering Packet Delivery Rate, SCC-MAC is better than SMAC and IEEE802.11a because due to less number of packets transmitted to sink collision is reduced here.

1. INTRODUCTION

Wireless Sensor Networks (WSN) is event based systems that rely on the collective effort of several micro sensor nodes observing a physical phenomenon. Typical WSN applications require spatially dense sensor deployment in order to achieve satisfactory coverage. As a result, several sensor nodes record information about a single event in a sensor field. Due to the high density in the network topology, the sensor records may be spatially correlated subject to an event. The degree of spatial correlation increases with the decreasing inter node separation. Wireless sensor nodes can be powered by batteries, or some form of ambient energy (e.g. temperature differences). Since batteries have only a limited capacity,

and ambient energy is limited itself, energy consumption is central in the design of wireless sensor hardware and software.

1.1 RELATED WORK

The information theoretical aspects of the correlation are explored in depth in [8]. More recently, the relation between distortion, spatio-temporal bandwidth and power for large sensor networks is investigated. However, no correlation (spatial or temporal) between sensor observations is considered in [9]. Moreover, none of the above solutions develop communication network protocols.

1.1.1 Spatial correlation

Typical WSN applications require spatially dense sensor deployment in order to achieve satisfactory coverage. As a result, multiple sensors record information about a single event in the sensor field. Due to high density in the network topology, spatially proximal sensors observations are highly correlated with the degree of correlation increasing with decreasing inter node separation.

1.1.2 Temporal correlation

The nature of the energy-radiating physical phenomenon constitutes the temporal correlation between each consecutive observation of a sensor node. The degree of correlation between consecutive sensor measurements may vary according to the temporal variation characteristics of the phenomenon.

2. MAC PROTOCOL DESIGN

2.1 CLASSIFICATIONS

The MAC protocol is classified into two different types: Contention-Free and Contention-Based.

2.1.1 Contention-free MAC

It is based on reservation and scheduling. Each node announces a time slot that it wants to use the coordinator of the network. This coordinator schedules requests and allocates each node its respective time slot. In this way, a node can access the channel without colliding with others because it is the only node which can transmit during its time slot. Bluetooth, TRAMA and LEACH are examples of this type of MAC. This technique guarantees low energy consumption because each node in the network

works only during its time slot therefore no collisions. The major disadvantage of this technique is that it is not well adaptable to topology changes and is therefore non-scalable. This MAC protocols for WSN are designed to support low energy consumption. Hence, they do not take the multi-hop latency into account.

2.1.2 Contention-based MAC

It is a protocol where every node accesses the channel in competition. Before transmitting a message, a node listens to the channel to see whether there is already a transmission in the medium. If the channel is busy, it waits for a random time and retries to check out the channel later. If the channel is free, it transmits the message. The most well-known example of this technique is the IEEE 802.11 for wireless LAN network. However, in a sensor network, the devices are small and very sensitive to energy consumption. Therefore, the MAC technique of IEEE 802.11 is not suitable for sensor networks.

S-MAC is considered to be the first MAC protocol proposal for sensor networks which tries to reduce energy consumption. In S-MAC, nodes are periodically set in listen and sleep mode, where the listen time is approximately 10% of the sleep time. In sleep mode, sensors switch off the radio to save energy. Hence, they can save up to 90% of energy compared to the normal protocols where nodes always stay active. Sensors synchronize their communication during the listen period. If a node does not have any messages to send, it switches its radio off during the sleep mode. On the contrary, it switches its radio on to transmit or receive messages. During listen time, sensors access the channel using the carrier sense multiple access with collision avoidance method (CSMA/CA).

2.2 MAC PROTOCOL DESIGN CHALLENGES

2.2.1 Major Sources of Energy consumption

➤ Collision: The first one is the collision. When a transmitted packet is corrupted due to interference, it has to be discarded and the follow on retransmissions increase energy consumption. Collision increases latency also.

➤ Overhearing: The second is overhearing, meaning that a node picks up packets that are destined to other nodes.

➤ Packet Overhead: The third source is control packet overhead. Sending and receiving control packets consumes energy too and less useful data packets can be transmitted.

➤ Idle listening: The last major source of inefficiency is idle listening i.e., listening to receive possible traffic that is not sent. This is especially true in many sensor network applications. If nothing is sensed, the sensor node will be in idle state for most of the time. The main goal of any MAC protocol for sensor network is to

minimize the energy waste due to idle listening, overhearing and collision.

2.2.2 MAC Performance Matrices

➤ Energy Consumption per bit: The energy efficiency of the sensor nodes can be defined as the total energy consumed / total bits transmitted.

➤ Average Delivery Ratio: The average packet delivery ratio is number of packets received to the number of packets sent averaged over all the nodes.

➤ Network Throughput: The network throughput is defined as the total number of packets delivered at the sink node per time unit. This is also called as Goodput.

3. PROPOSED SPATIAL CORRELATION-BASED COLLABORATIVE MEDIUM ACCESS CONTROL (SCC-MAC)

As the nodes exhibit spatial correlation not all the nodes are required to transmit the sensed information to the base station. A SCC-MAC protocol is proposed for spatially correlated wireless sensor network. This protocol based on the correlation selects which of the sensor node has to transmit data to the sink. This node is called the representative node. Iterative Node Selection Algorithm (INS) is executed for each simulation so that representative nodes can easily be identified. Fig: 1 shows block diagram of SCC-MAC protocol. After execution of INS algorithm the representative node executes E-MAC when it has to transmit the data or it executes N-MAC algorithm when it receives a packet which has to be forwarded to the base station.

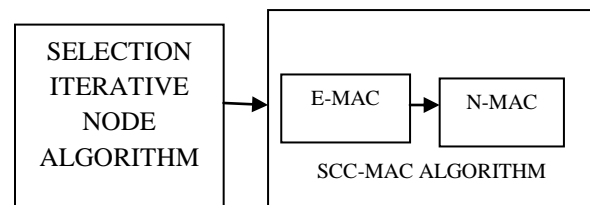


Fig: 1 BLOCKS DIAGRAM FOR PROPOSED SCC-MAC PROTOCOL

3.1 THE ITERATIVE NODE SELECTION (INS) ALGORITHM

The Iterative Node Selection (INS) algorithm is used to find the number and location of the representative nodes in WSN. INS tries to find the ideal locations of representative sensor nodes such that the required distortion can be maintained at the sink. Based on the INS Algorithm results, the SCC-MAC protocol is performed distributive by each sensor node to achieve the required performance. The INS algorithm requires only the statistical properties of the node distribution as input and provides a correlation radius value for distributed operation as output. In order to exploit the spatial correlation between sensor nodes and to improve

the performance of the WSN, our MAC protocol tries to create the correlation regions distributive. Note that the INS algorithm determines the representative nodes that would achieve the minimum distortion given the number of representative nodes. However, since this centralized information is not suitable for distributed control, only the correlation radius, r_{corr} , is informed to the individual nodes, so that they try to form the correlation regions in a distributed manner and choose the representative nodes, accordingly. Since the INS algorithm resides at the sink and requires no location information, no additional energy consumption is introduced at the sensor nodes which perform only the SCC-MAC protocol.

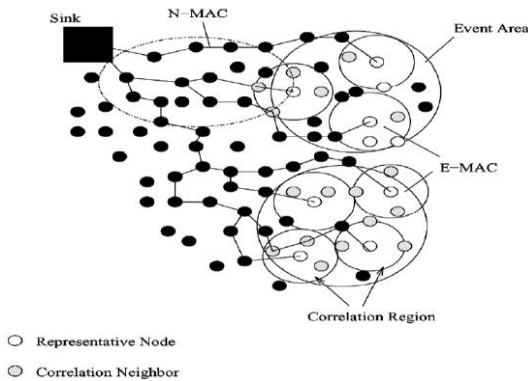


Fig: 2 E-MAC and N-MAC.

3.2 PROPOSED SCC-MAC PROTOCOL DESIGN

The spatial SCC-MAC protocol aims to collaboratively regulate sensor node transmissions. The distortion constraint can be achieved even though the number of nodes sending information about an event is decreased. In order to achieve these goals, the INS algorithm, which resides at the sink, determines the correlation radius, for a distortion constraint. This information is then broadcast to each sensor node during the network setup. The SCC-MAC protocol, which is implemented at each sensor node, then performs MAC distributive. SCC-MAC exploits spatial correlation in the MAC layer by using the correlation radius, to suppress the redundant information from being injected into the WSN. When a specific source node, transmits its event record to the sink, all of its correlation neighbors have redundant information with respect to the distortion constraint. This redundant information, if sent, increases the overall latency and contention within the correlation region, as well as wasting scarce WSN energy resources. Hence, the medium access is performed for two reasons:

- **Source Function:** Source nodes with event information perform medium access in order to transmit their packets to the sink.
- **Router Function:** Sensor nodes perform medium access in order to forward the packets received

from other nodes to the next destination in the multi-hop path to the sink.

SCC-MAC protocol contains two components corresponding to the source and router functionalities.

- **Event MAC (E-MAC)** filters out the correlated records
- **Network MAC (N-MAC)** ensures prioritization of route-thru packets.

3.2.1 Packet Structure

The RA of the RTS frame is the address of the STA on the wireless medium that is the intended immediate recipient of the next Data or Management frame. The TA is the address of the STA transmitting the RTS frame. The Duration value is the time, in microseconds, required to transmit the next Data or Management frame, plus one CTS frame, plus one ACK frame, plus three SIFS intervals.

RTS Packet Structure CTS Packets Structure

FRAME CONTROL	DURATION	RA	TA	FH	FCS
---------------	----------	----	----	----	-----

FRAME CONTROL	DURATION	RA	FH	FCS
---------------	----------	----	----	-----

DATA Packet Structure

MAC HEADER	FH	FRAME BODY	FCS
------------	----	------------	-----

Fig.3 Structures for RTS, CTS and DATA packets

When a sensor node records an event, it sets the FH field of the RTS and DATA packets related to the transmission of the sensor record. All nodes overhearing the RTS with FH field set, determine that the transmission is related to source functionality and perform E-MAC. Once a node receives the DATA packet, it clears the FH field, indicating that the packet is a route-thru packet. The node, then, simply forwards the packet to the next hop. Nodes accessing the medium for router functionality do not set the FH field in their RTS packets and perform N-MAC.

3.3.2 Event MAC (E-MAC)

All sensor nodes contend for the medium for the first time so that the representative nodes are selected by the help of the spatial-reuse property of the wireless channel. This initial phase is called as the first contention phase and is explained as follows.

- **First Contention Phase (FCP):** In the first contention phase, all nodes with event information contend for the medium for the first time using

RTS/CTS/DATA/ACK structure. Access the channel while others have to backoff.

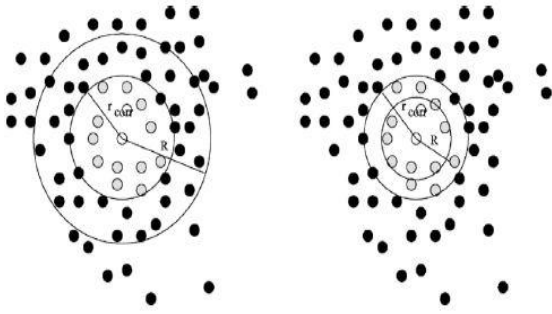


Fig. 4 Two cases for E-MAC. The figure shows two cases for correlation region, r , and transmission region, R .

The protocol procedure for the correlation neighbors depends on the relation between the transmission range, R , of the sensor nodes and the correlation radius, r_{corr} . Hence, all the correlation neighbors of the node can hear the transmission of node n_i . As a result, the redundancy due to correlation can be totally removed by the already ongoing transmission from the representative node. However, in the case when $r_{corr} > R$, some of the correlation neighbors of node cannot hear the transmission of node. Hence, the redundancy cannot be filtered out completely with respect to the total distortion constraint.

3.3.3 Network MAC (N-MAC)

When a packet is routed to the sink, it may traverse through nodes corresponding to other concurrent events. However, since the correlation has already been filtered out using E-MAC, the route-thru packet must be given priority over the packets generated by another concurrent event. This is the reason why we need a Network MAC (N-MAC) component. When an intermediate node receives a DATA packet, it performs N-MAC to further forward that packet to the next hop. The route-thru packet is given precedence in two phases. When a correlation neighbor receives an RTS regarding a route-thru packet during the random listening period of the SSS, it switches from SSS to receive state and receives the packet. During the transmission, the representative node defers its transmission and the route-thru packet is received by the correlation neighbor.

6. RESULT AND CONCLUSION

6.1 RESULT

Proposed SCC-MAC protocol is implemented in NS2 simulator and it is compared with already existing MAC S-MAC and IEEE 802.11 protocol. The following parameters were considered for simulation

Table 6.1 Parameters to be considered

Channel	Wireless channel
Propagation	Two Ray propagation
MAC protocol	SMAC, IEEE802.11 & SCC-MAC
Queue	Priority queue
Queue length	150
Antenna	Omni antenna
Area	1000*1000
Number of nodes	10,20,30,40 and 50
Initial Energy	1000 joules
Routing protocol	AODV
Simulation time	20 seconds

The simulation results for sensor topology of 10 nodes and 50 nodes randomly deployed in a sensor field is presented. The sensor nodes are modeled according to the wireless node module and energy model. The transmission range of each node is 100 m. Each simulation is performed for 20 s.

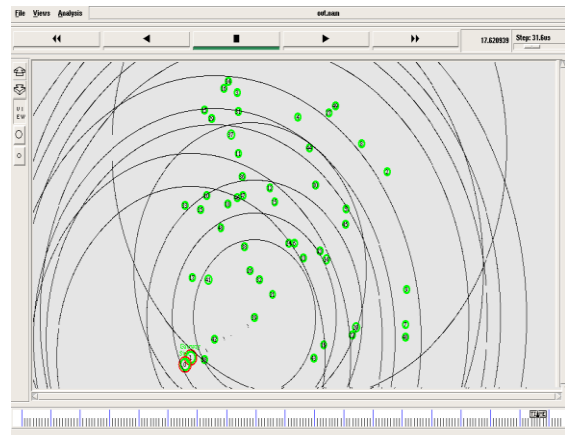


Figure.5 50 nodes transmitting data to sink node

Figure.5 shows there are 50 sensor nodes transmitting their packets to sink node, before packet transmission acknowledgement signals are transmitted.

6.1.1 Average Energy Consumption

Average energy of a node is computed. From Fig.6, In IEEE 802.11, each node keeps listening all transmissions from its neighbors in order to perform effective virtual carrier sensing, which is a significant waste of energy. In S-MAC nodes go into periodic sleep mode during which it switches the radio off and sets a timer to awake later. The energy consumption is reduced in SCC-

MAC number of nodes sending the information is reduced due to correlation of the data.

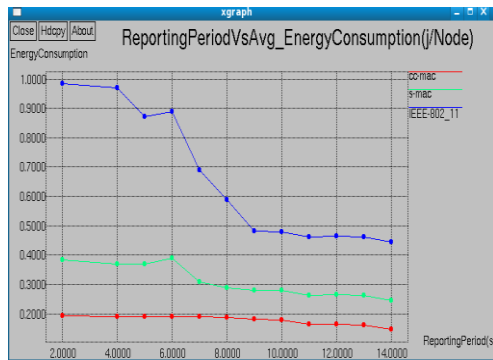


Figure 6 Average Energy consumption

6.1.3 Packet Drop Rate

This metric shows the performance of the MAC protocol in terms of medium access overhead introduced in terms of wasted number of packets. Packet drop ratio is inversely proportional to packet delivery.

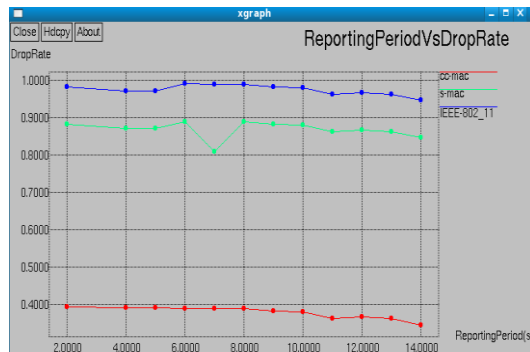


Figure.7 Packet Drop Rate

From Fig.7 SMAC nodes go into periodic sleep mode during which it switches the radio off and sets a timer to awake later so that it leads to drop some of the packets during its sleep mode but in SCC-MAC the nodes are always in active so it never drops the packets

6.2 CONCLUSION

Exploiting spatial correlation at the MAC layer is a powerful means of reducing the energy consumption in WSN under collective performance limits. This can be achieved by collaboratively regulating medium access so that redundant transmissions from correlation neighbors are suppressed. By allowing only a subset of sensor nodes to transmit their data to the sink, the proposed MAC protocol not only conserves energy, but also minimizes unnecessary channel access contention and thereby improves the packet drop rate without compromising the event detection latency.

REFERENCE

- [1] "An Adaptable Energy-Efficient Medium Access Control Protocol for Wireless Sensor Networks", Justin T. Kautz, Barry E. Mullins, Rusty O. Baldwin, Scott R. Graham, 2007
- [2] "Energy Efficient Cluster header Selection Algorithm in WSN", Inbo Sim, KoungJin Choi, KoungJin Kwon and Jaiyong Lee, 2008
- [3] "On the Adaptivity of today's Energy-Efficient MAC Protocols under varying Traffic Conditions", Philipp Hurni, Torsten Braun, 2009
- [4] "Energy Efficient and Delay Optimized TDMA Scheduling for Clustered Wireless Sensor Networks", Liqi Shi and Abraham O. Fapojuwo, 2009
- [5] "Energy Efficient Cross-Layer MAC Protocol for Wireless Sensor Networks", Bouabdellah KECHAR, Ahmed LOUZANI, Larbi SEKHRI, Mohamed Faycal KHELFI, 2008
- [6] "Energy Efficient Token Based MAC Protocol for Wireless Sensor Networks", Soumya Ray, Subhasis Dash, Nachiketa Tarasia, Anuja Ajay, Amulya Ratan Swain, 2011
- [7] "Wireless Sensor Networks: Delay Guarantee and Energy Efficient MAC Protocols", Marwan Ihsan Shukur, Lee Sheng Chyan, Vooi Voon Yap, 2009
- [8] "M. Gastpar and M. Vetterli, "Source-channel communication in sensor networks," *Proc. 2nd Int. Workshop on Information Processing in Sensor Networks (IPSN'03)*, vol. 219, pp. 162-177, 2003.
- [9] M. C. Vuran, Ö. B. Akan, and I. F. Akyildiz, "Spatio-temporal correlation: theory and applications for wireless sensor networks," *Comput. Netw. J. (Elsevier)*, vol. 45, no. 3, pp. 245-259, Jun. 2004
- [10] Mehmet C. Vuran, Member and Ian F. Akyildiz, Fellow, "Spatial Correlation-Based Collaborative Medium Access Control in Wireless Sensor Networks", 2004
- [11] K. A. Arisha, M. A. Youssef, and M. Y. Younis, "Energy-aware TDMA-based MAC for sensor networks," *Comput. Netw. J. (Elsevier)*, vol. 43, no. 5, pp. 539-694, Dec. 2003.
- [12] S. Bandyopadhyay and E. J. Coyle, "Spatio-temporal sampling rates and energy efficiency in wireless sensor networks," in *Proc. IEEE INFOCOM*, Mar. 2004, vol. 3, pp. 1728-1739.
- [13] "Power, spatio-temporal bandwidth, and distortion in large sensor networks," *IEEE J. Sel. Areas Commun.*, vol. 23, no. 4, pp. 745-754, Apr. 2005.
- [14] W. Ye, J. Heidemann, and D. Estrin, "Medium access control with coordinated adaptive sleeping for wireless sensor networks," *IEEE/ACM Trans. Netw.*, vol. 12, no. 3, pp. 493-506, Jun. 2004.

Morphology Based Number Plate Localization for Vehicular Surveillance System

Thota Sridevi¹, Chilukuri Sindhu², Pendyala Naga Praveen Kumar²,
Perupogu.Sagar²

¹Associate professor, Department of ECE, K.L.University, Guntur, A.P, India

²Project Students, Department of ECE, K L University, Guntur, A.P, India

ABSTRACT

Number Plate Recognition systems are used to track and monitor the moving vehicles by automatically extracting the number plates. The objective of this system is to recognize vehicles based on license plate information. The images of passing vehicles are taken at surveillance system and those images will be processed. Proposed method uses simple morphological open and close operations using different structuring elements and Global Thresholding for plate localization. Connected component labeling is used for plate recognition from all other candidates. We have proposed a method to locate number plate using efficient algorithm for plate feature extraction, Labeling & searching plate region. By overcoming the difficulties in existing methods, proposed method results in high detection rate.

Keywords: - Morphological operations, Labeling Global Thresholding, Number plate localization.

I. INTRODUCTION

The license plate recognition of vehicle is an important part of the **Intelligence Traffic Control System**. Number Plate recognition system have wide range of applications like traffic surveillance, tracing of stolen cars, identification of dangerous drivers and Automatic Electronic Toll Collection system [2][3] [4]. The objective is to extract and recognize License plate information from car images without any human intervention. One of its main advantages is the ability to capture information in the plates, at high traffic flow and speeds, and when it is difficult to manually record [1].The Number Plate recognition

System has mainly three components. They are image Acquisition system, image processing system and display unit. In this paper we have proposed a method for Plate Localization. Plate localization requires two major tasks. The first one is to separate Number Plate area from Non-Number Plate area and second one is plate adjustment.

The most commonly used method for license plate Recognition is the combination of **edge detection and mathematical morphology** [5] [6]. In this method detection rate is affected by the quality of the image.

Color based image processing methods are not suitable for cases where the background has the same color of the plate or in countries where multiple colors are used (e.g. China). In Texture based feature extraction methods like **SVM and Gabor Transformation**, the computation complexity will limit its usability [2]. Many plate localization algorithms have been developed using the above mentioned methods. However, these algorithms are either having low detection rate or high computation complexity.

We are proposing an efficient algorithm based on the mathematical morphology which produces high detection rate than existing methods. This paper presents a method based on the open and close morphological operations with different structuring elements for number plate localization. This method utilizes open and close morphological operation and Global Thresholding to enhance plate region and eliminate non-plate region. Finally the plate region is obtained based on Connected Component Labeling and geometrical relationship of numbers on plate.

II. SYSTEM OVERVIEW:

License plate is a pattern with high variations of contrast. This feature is useful to locate the plate and is robust to the changes of lighting conditions and orientation of image taken. The open and close morphological operations are used to extract the contrast features within the plate. This is a relatively stable method when subjected to different image alterations or conditions [2] [6].

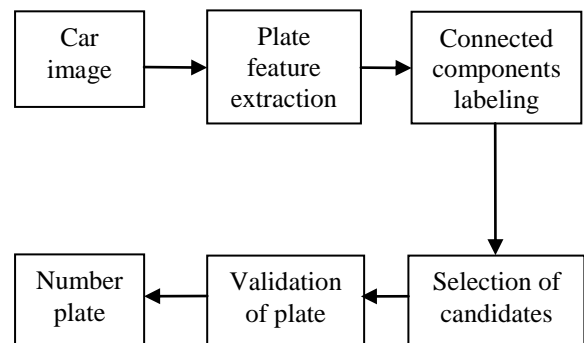


Fig. 1: Block Diagram of System

The license plate localization consists of three major stages:

- Morphological operations for extracting plate features
- Labeling the connected components
- Selection of candidate regions
- Validation of plate region.

Fig. 1 shows the block diagram of the Plate Localization. Each stage is explained further in the next sub unit.

III. PLATE LOCALIZATION:

The Car image is passed through two open & one close morphological operations and Global Thresholding in order to maximize the elimination of non-plate regions.

3.1. Plate Feature Extraction:

Fig. 2 illustrates the plate feature extraction stage. The original RGB image is given to system and it will be converted into gray scale image which is passed to first Opening operation. Morphological Opening is erosion followed by a dilation used to eliminate small and narrow parts of an image [2] [7]. Rectangular structuring element (SE) is used for opening operation and this step is used to smooth the background illumination.

SE is a matrix containing 1's and the centre of the matrix is called 'Origin'. The size of SE is based on the resolution of the original image, plate region and it should be related to size of character. We have taken SE size as 4×30 . This opening operation can effectively erase plate region and keep non-plate region from grayscale image. Background of image will be obtained in this step. The next step is to subtract the background image from the grayscale image of car and the result is Highlighted Plate region. Fig. 3 shows the Highlighted Plate region.

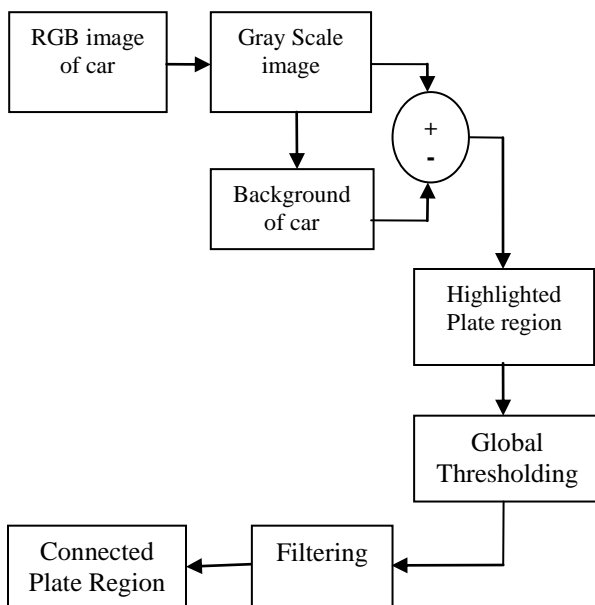


Fig. 2: Block Diagram Plate Feature Extraction



Fig. 3: Highlighted Plate Region

The output of this stage is converted to binary using Global Thresholding. This operation will further eliminate non-plate regions. The algorithm for Global Thresholding is given below [8]

1. An initial threshold (T) is chosen (any random value).
2. The image is segmented into object and background pixels, creating two sets:
 - a) $G_1 = \{f(i,j) > T\}$ (object pixels)
 - b) $G_2 = \{f(i,j) < T\}$ (background pixels)
3. The average of each set is computed.
 - a. $m_1 = \text{average of } G_1$
 - b. $m_2 = \text{average of } G_2$
4. A new threshold is created that is the average of m_1 and m_2

$$T' = (m_1 + m_2) / 2$$
5. Repeat the steps two to four using new threshold value, until the new threshold equal to previous one.



Fig. 4: Binary image

Still some unnecessary information would remain in the binary image. To eliminate the rest of non-plate regions other two Morphological operations are used. The first one is another opening operation which is performed to filter the small and narrow elements.

Here 'diamond' shaped Structuring Element is used for removing such small elements. The SE used is a 'diamond' shaped matrix that has a radius $R=2$, where inside the 'diamond' all 1's will be present and outside of it all 0's will be present. When this diamond shaped structure is used during the opening operation only diamond-shaped

regions containing 1's will remain and other elements will be removed. If radius is greater than 2, plate region may get damaged. This operation is very useful to erase net shaped and narrow lines that are surrounding the plate area [2] [4]. Fig. 6 shows the resulting image.



Fig. 6: Filtered image

The above operation can efficiently erase most of the unwanted elements but some pixels in the plate region can also be eliminated. Therefore closing operation is used to completely fill the plate region thereby to connect the pixels. The morphological close operation is a dilation followed by erosion, which is normally used for fusing small holes and filling narrow aperture [2]. In this step, a 4×12 'rectangle' shaped SE is used for the closing operation. The result obtained after performing the close operation is shown in Fig. 7. The size of the SE depends on the size of the plate region and resolution of image.



Fig. 7: Connected Plate Region

From Fig. 7 we can observe that, the plate region is a group of connected pixels which can be easily extracted using some known geometrical conditions like Width/Length ratio and their ranges.

3.2 Labeling the Connected Components:

In binary images analysis objects are usually extracted by means of the connected components labeling operation, which is assigning a unique label to each maximal connected region of foreground pixels. The classical sequential labeling algorithm relies on two subsequent scans of the image. In the first scan, a temporary label is assigned to each foreground pixel based on the values of its neighbors already visited by the scan. When a foreground pixel with two foreground neighbors carrying

different labels is found, the labels associated with the pixels in the neighborhood are registered as being equivalent. After completion of the first scan equivalences are processed to determine equivalence classes. Then, a second scan is run over the image so as to replace each temporary label by the identifier of its corresponding equivalence class.

Here we have used a **Two-scan labeling algorithm** unlike the classical approach, where equivalences are processed during the first pass in order to determine the correct state of equivalence classes at each time of the scan. This is obtained by **merging** classes as soon as a new equivalence is found, the data structure used to support the merging being a simple 1D array. This approach allows the check for a conflict to be carried out on class identifiers rather than on labels.

TWO- SCAN Labeling Algorithm:

1. First scan is started and check for pixel value,
If $l(i, j) = 0$, go to next pixel.
2. Else If $l(i, j) = 1$ then check following
 - a. If $l(i-1, j) = l(i, j-1) = 0$ then assign new label.
 - b. If $l(i-1, j) = 0$ or $l(i, j-1) = 0$ then assign label related to non zero pixel.
 - c. If both are equal then assign any value.
 - d. If labels of two neighbors are not equal, mark as equivalence and go for merging
3. Repeat step 1 and step 2 for all pixels
4. In second scan label values are changed according to their corresponding class identifier

3.3 Selection of Potential Candidates:

Labeled image is taken as input to this stage. Two geometrical conditions are used to select potential candidates from all the labeled elements. Assume the extracted plate region is of size $W \times L$. The first criterion is the ratio r between the width and length of plate and it must matches with ratio specified. The second criterion is the ranges of W and L ; they must be within given range. For this, the given ranges of W and L must be large enough to cover most of the possible sizes of the plate region. These two steps in selection of potential candidates can effectively reduce the number of candidate regions. However, there may arise some Candidates that are other than the actual plate. These fake candidates need to be eliminated using validation criteria.

```

For each Label
{
[r c] = Region with Label K
pwidth=max(c)-min(c);
pheight=max(r)-min(r) ;
If width and height satisfies selection criteria
{
% validation

```

```

Compute complementary binary of selected
Candidate
Label the connected components in selected
Candidate
For each Label
{
  [ro co] = Region with Label K1
  cwidth =max (co)-min (co);
  cheight =max (ro)-min (ro);
  If W/H of k1th label is within given range
  Increment ccnum by one
}
If ((ccnum<=15) && (ccnum>=2))
  Display the region having kth label
}
}

```

Fig. 8: Selection and Validation Procedure

3.4 Validation of Selected Candidates:

The validation criterion is based on counting the number of connected component from each potential candidate. For this purpose the complemented binary image of potential candidate is taken. After this connected components present in the complementary binary image will be Labeled. The connected components that meet the geometrical conditions of the character on the plate (i.e width/length ratio of the character) will be taken into consideration. In general, in an original plate region this connected components count must be in between 2 to 15 and for fake regions this count is less than 2 or greater than 15. Therefore, using this process all the non number plate regions can be filtered out. So at this stage actual plate region can be obtained.

Once the plate region coordinates obtained, the final number plate can be extracted from the original binary image.

IV. RESULTS:



G463FJK



AP 16 BW 5434



AP 16 BU 4070

V. CONCLUSION & FUTURE SCOPE

In this paper, we have presented an efficient algorithm based on Morphological operations and Geometrical relationship for Number Plate Localization. This method has low computation complexity and also detection rate is improved than existing methods. This work can be extended to detect all kinds of vehicles and this can be applied to design a real time system for Tracking vehicles, tracing stolen cars and Automatic Gate Control System.

ACKNOWLEDGEMENT

The authors like to express their gratitude towards the management & department of ECE, K L University for their support and encouragement during this work.

REFERENCES:

- [1] P. V. Suryanarayana, Suman K. Mitra, Asim Banerjee and Anil K. Roy, "A Morphology Based Approach for Car License Plate Extraction", *IEEE Indicon 2005 Conference*, Chennai, India, 11-13 Dec. 2005
- [2] Xiaojun Zhai, Faycal Benssali and Soodamani Ramalingam, "License Plate Localization based on Morphological Operations", *2010 11th Int. Conf. Control, Automation, Robotics and Vision*, Singapore, 7-10th December 2010
- [3] C. N. E. Anagnostopoulos, I.E. Anagnostopoulos, V. Loumos et al. "A license plate-recognition algorithm for intelligent transportation system applications," *IEEE Trans. Intel. Transp. Syst.*, pp. 377-391, 2006.
- [4] F. Lian, Y. Fan, Y. Zhang, "Study of technology in electronic toll collection [J]," *Computer Engineering and Application*, Vol. 43(5), pp. 204-207, 2007.
- [5] M. Vargas, S. L. Toral, F. Barrero, F. Cortés, "A license plate extraction algorithm based on edge statistics and region growing," *International Conference on Image Analysis and Processing (ICIAP)*, pp. 317-326, 2009.
- [6] J. Hsieh, S. Yu, and Y. Chen, "Morphology-based license plate detection from complex scenes," *Proceedings of the 16th International Conference on Pattern Recognition (ICPR'02) Volume 3*, pp. 1051-1055, 2002.
- [7] The Math Works, Inc. *Image Processing Toolbox 6 User Guide*. 2009.
- [8] R.C.Gonzalez, R.E. Woods, *Digital Image Processing*, Addison-Wesley, 2002.

Quality improvement of image using adaptive bilateral filter and neural networks

T.Ravi¹, Ch.Mounika², Ch. Rajesh Babu³, T.Prasanth⁴
(Department of Electronics and Communication Engineering, KL University, India)

ABSTRACT

In this paper we present a adaptive bilateral Filter (ABF) with neural networks for enhancing sharpness and suppressing noise. Increasing the slope at edges ABF sharpens the image and doesn't contain the halo. Undershoot and overshoot are not produced. Significantly sharper images are restored using ABF when compared with bilateral filter, un sharp mask(USM). It is better than other filters in noise removal also. The back propagation neural network we apply makes more efficient in sharpening the image.

Keywords– back propagation neural network, bilateral filter, image restoration, sharpness enhancement

I. INTRODUCTION

The problem here is to develop a filter that removes noise and also sharpens the edges simultaneously. So we have to design a filter first of all which uses a better method for sharpening without halo and secondly it should be able to remove noise effectively.

We can employ conventional filters for noise removal, which work efficiently in smooth regions but blurring of the image takes place especially at the edges. A lot of effort is put in designing a noise removal by preserving the edges. These efforts were resulted in "SUSAN" filter and "bilateral filter". Bilateral filter adopts low pass Gaussian filter for both domain and range filter. The domain low pass Gaussian filter gives higher weight to pixels that are spatially close to center pixel. The range low pass Gaussian filter gives higher weight to pixels that are similar to center pixel in gray value. By combining domain filter and range filter we can produce bilateral filter which will reduce noise and enhances the sharpness. Gaussian filter that is oriented along the edge will do the averaging along the edges and reduce in gradient direction. For this reason bilateral filter can smooth the noise and preserve the edge details.

In terms of image sharpening un sharp mask (USM) has certain disadvantages: First It sharpens the image by adding halo(undershoot and overshoot). Second it amplifies the noise information present in the image instead of suppressing the noise and reduce the quality of image. To reduce the first problem we have several slope restoration algorithms. Those algorithms modify the edge information normally or horizontally or vertically i.e in 1D only. The ABF will restore the edge slope, without need to locate edge normal's. So ABF with neural networks is efficient to implement. This will produce clean, crisp edges. To reduce the noise levels in an image

we use Gaussian low pass filter which will remove the noise.

II. GAUSSIAN FILTER

The impulse response of a Gaussian filter is Gaussian function. Gaussian filter is designed to give no overshoot or undershoot to input image while minimizing the rise and fall time. The output of Gaussian filter is the convolution of input signal with a Gaussian function.

$$G = \exp(-(X^2+Y^2)/(2*\sigma^2))$$

where X is the distance from the origin in the horizontal axis, Y is the distance from the origin in the vertical axis, and σ is the standard deviation of the Gaussian distribution. In case of 2D, the above formula gives a surface whose outputs are concentric circles with a Gaussian distribution from the center point. The original pixel's value assigns heaviest weight to center pixel (having the highest Gaussian value) and smaller weights to neighboring pixels as their distance from the original pixel increases. The main advantage of Gaussian function is it will be non-zero at every point on the image, it means that the entire image should be included in the calculation of each pixel.

III. ADAPTIVE BILATERAL FILTER

The impulse response of ABF is

$$f[m, n] = \sum_k \sum_l h[m, n; k, l] g[k, l]$$

$f[m, n]$ is restored image, $h[m, n; k, l]$ is the response at $[m, n]$ to an impulse at $[k, l]$, and $g[m, n]$ is the degraded image.

$$h[m, n; m_0, n_0] = I(\Omega_{m_0, n_0}) r_{m_0, n_0}^{-1} e^{-\left(\frac{(m-m_0)^2 + (n-n_0)^2}{2\sigma_d^2}\right)} \cdot e^{-\frac{1}{2} \left(\frac{g[m, n] - g[m_0, n_0] - \zeta[m_0, n_0]}{\sigma_r[m_0, n_0]}\right)^2} \quad (2)$$

where $[m_0, n_0]$ is the center pixel of the window, $\Omega_{m_0, n_0} = \{[m, n] : [m, n] \in [m_0 - N, m_0 + N] \times [n_0 - N, n_0 + N]\}$, $I(\cdot)$ denotes the indicator function, and m_0, n_0 normalizes the volume under the filter to unity.

The main two modifications in ABF compared to bilateral filter is

1. The offset ζ is introduced in range filter
2. Both offset ζ and σ_r are locally adaptive.

If ζ is equal to zero and by making σ_r constant we get bilateral filter.

For domain filter the value of $\sigma_d = 1.0$ will make the filter adaptive.

By varying the values of ζ and σ_r we get a powerful filter which will produce both smoothing and sharpening to the

given noisy image. It sharpens the image by increasing the slope of the edges. To understand the ABF working completely we should know the role of ζ and σ .

The range filter can be assumed as one dimensional filter which will process the histogram of image. For conventional bilateral filter, the range filter is located on the histogram at the gray value of the current pixel and removes the pixel values which are farther away from the center pixel value.

By adding the offset ζ to the range filter, we can shift the range filter on the histogram. As before, let Ω_{m_0, n_0} denote the set of pixels in the $(2N + 1) \times (2N + 1)$ window of pixels centered at $[m_0, n_0]$. Let MIN, MAX, and MEAN denote the operations of taking the minimum, maximum, and average

value of the data in Ω_{m_0, n_0} , respectively.

Let $\Delta_{m_0, n_0} = g[m_0, n_0] - \text{MEAN}(\Omega_{m_0, n_0})$.

We can define the ABF in terms of Gaussian filter as

1.No offset (conventional bilateral filter):

$$\zeta[m_0, n_0] = 0,$$

2.Shifting towards the MEAN: $\zeta[m_0, n_0] = -\Delta_{m_0, n_0}$

3.Shifting away from the MEAN, to the MIN/MAX:

$$\zeta[m_0, n_0] =$$

$$\begin{aligned} & \text{MAX}(\Omega_{m_0, n_0}) - g[m_0, n_0], \text{ if } \Delta_{m_0, n_0} > 0, \\ & \text{MIN}(\Omega_{m_0, n_0}) - g[m_0, n_0], \text{ if } \Delta_{m_0, n_0} < 0, \\ & 0, \text{ if } \Delta_{m_0, n_0} = 0. \end{aligned} \quad - (3)$$

By shifting the range filter towards $\text{MEAN}(\Omega_{m_0, n_0})$ will blur the image. By Shifting the range filter away from $\text{MEAN}(\Omega_{m_0, n_0})$ will sharpen the image. In the case of operation No. 3, the range filter is shifted to the MAX or the MIN depending on Δ_{m_0, n_0} . The reason behind these observations is the transformation of the histogram of the input image by the range filter. The conventional bilateral filter without offset does not significantly alter the histogram or edge slope. Shifting the range filter to $\text{MEAN}(\Omega_{m_0, n_0})$ at each pixel will redistribute the pixels towards the center of the histogram. On the other hand, if we shift the range filter further away from the $\text{MEAN}(\Omega_{m_0, n_0})$, pixels will be compressed and the slope will be increased. We need to point out here that shifting the range filter based on Δ_{m_0, n_0} is very sensitive to noise.

The parameter σ of the range filter controls the width of the range filter. If σ is large compared to the range of the data in the window, the range filter will assign similar weights to every pixel in the range. Therefore, it does not have much effect on the overall bilateral filter. On the other hand, a small σ will make the range filter dominate the bilateral filter. By making ζ and σ adaptive and jointly optimizing both parameters, we transform the bilateral filter into a much more powerful and versatile filter. To smooth a pixel, we can shift the range filter towards $\text{MEAN}(\Omega_{m_0, n_0})$, and/or use a large σ which enables the spatial Gaussian filter to take charge in bilateral filtering. To sharpen a pixel, we can shift the range filter away from $\text{MEAN}(\Omega_{m_0, n_0})$ towards $\text{MAX}(\Omega_{m_0, n_0})$ or $\text{MIN}(\Omega_{m_0, n_0})$, depending on whether it is above or below the midpoint of the edge slope. At the same time, we reduce σ accordingly. With a small σ , the range

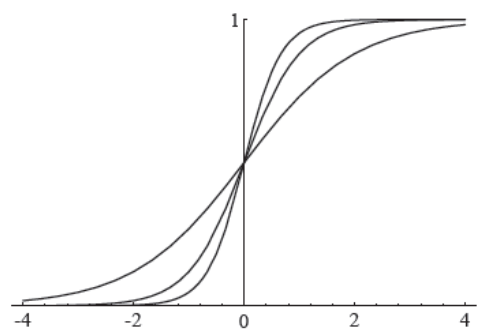
filter dominates the bilateral filter and effectively pulls up or pushes down the pixels on the edge slope.

IV.BACK PROPAGATION ALGORITHM

The main advantage of multilayered networks is they are capable of computing a wide range of functions than networks with a single layer networks. The number of iterations increases as the no. of parameters increases. But advantage of Back propagation algorithm is it will reduce the no. of iterations to be computed. Back propagation algorithm will minimize the error by using gradient descent. So in this method we calculate gradient of each step. The activation function used here is sigmoid.

$$s_c(x) = \frac{1}{1 + e^{-cx}}.$$

Here c is a constant. By varying the value of c we can get different curves



above curves are for values $c=1, c=2, c=3$.

The sigmoid values vary from 0 to 1 strictly. The output expression is given by

$$\frac{1}{1 + e^{\sum w_i x_i - \theta}}$$

Where W_i = weights $i=1, 2, 3, \dots, n$

X_i = Inputs

$-\theta$ = bias

The algorithm in back propagation is divided into four steps

1. Feed forward computation
2. Back propagation to output layer
3. Back propagation to hidden layer
4. Weight updates

The iterations are stopped when the error function value became small. Back propagation is the Most common method of obtaining the many weights in the network. In this we use supervised training

This algorithm depends on minimizing the error of the network using the derivatives of the error function whose properties are

► Simple

► Slow

► Prone to local minima issues

In back propagation we use mean square error

$$E = (\text{target} - \text{output})^2$$

Where E is the error.

Partial derivatives of the error with respect to the weights: Output Neurons:

$$\text{let: } \delta_j = f'(\text{net}_j) (\text{target}_j - \text{output}_j)$$

$$\frac{\partial E}{\partial w_{ji}} = -\text{output}_i \delta_j$$

j = output neuron

i = neuron in last hidden

Hidden Neurons:

$$\text{let: } \delta_j = f'(net_j) \sum (\delta_k w_{kj})$$

$$\partial E / \partial w_{ji} = -output_i \delta_j$$

j = hidden neuron

i = neuron in previous layer

k = neuron in next layer

Here the calculation of derivatives move backwards so it is called back propagation. In the direction of derivatives we have maximum increase in error. Where as the maximum decrease in error results in back ward direction. The maximum decrease in error function is given as

$$w_{new} = w_{old} - \alpha \partial E / \partial w_{old}$$

where α is the learning rate.

The learning rate α plays an important role in the convergence. If learning rate is too small then it converge extreme slowly. If it is too large it may not converge.

Momentum

It try to converge the network. The main advantage is it applies smoothed averaging to change in weights.

$$\Delta_{new} = \beta \Delta_{old} - \alpha \partial E / \partial w_{old}$$

$$w_{new} = w_{old} + \Delta_{new}$$

β is the momentum coefficient

It acts as a low-pass filter and reduce the rapid fluctuations

V. RESULTS



Fig: Original image



Fig: After applying Adaptive Bilateral Filter



Fig: After applying Back Propagation network.

Laser Ignition in Internal Combustion Engines

Pankaj Hatwar¹, Durgesh Verma²

*(Lecturer, Department of Mechanical Engineering, Nagpur Institute of Technology/Nagpur University, India

** (Lecturer, Department of Mechanical Engineering, Nagpur Institute of Technology/Nagpur University, India

ABSTRACT

Nowadays, internal combustion engines play a dominant role in transportation and energy production. Ignition of a combustible material is usually defined as an initiation of a self sustained reaction which propagates through the combustible material even after removing the ignition source. Conventional ignition systems, like spark plugs or heating wires are well suited but suffer from disadvantages Electrode erosion, influence the gas flow as well as restricted positioning possibilities are the main motives in search of alternatives to conventional ignition systems. A laser based ignition source, i.e. replacing the spark plug by the focused beam of a pulsed laser, has been envisaged for some time. Also, it was tried to control auto ignition by a laser light source.

In this paper, a laser ignition source has the potential of improving engine combustion with respect to conventional spark plugs.

Keywords: Laser ignition, spray-guided combustion, homogeneous combustion, high pressure, hydrogen, biogas, gasoline.

1. INTRODUCTION

Combustion processes of various kinds are widely used in industrial as well as in everyday life, like combustion engines. In most cases, a well defined ignition location together with a well defined ignition time of combustion processes is of great importance. Ignition of a combustible material is usually defined as an initiation of a self sustained reaction which propagates through the combustible material even after removing the ignition source.

Conventional ignition systems, like spark plugs or heating wires are well suited but suffer from disadvantages. Electrode erosion, influences an the gas flow as well as restricted positioning possibilities are the main motives in search of alternatives to conventional ignition systems. Additionally, violent combustion processes can even destroy the ignition system and thus inhibit repeated ignitions.

On the other hand, it is well known that short and intensive laser pulses are able to produce an "optical breakdown" in air. Necessary intensities are in the range between $10^{10} \dots 10^{11} \text{W/cm}^2$. At such intensities, gas molecules are dissociated and ionized within the vicinity of the focal spot of a laser beam and a hot plasma is generated. This plasma is heated by the incoming laser beam and a strong shock wave occurs. The expanding hot plasma can be used for the ignition of a combustible material. Other laser ignition methods, like thermal ignition of a combustible due to heating of a target or resonant absorption which generates radicals are not able to fulfill the requirements on a well defined ignition

location or time and will not be discussed further. In the past, this optical breakdown has been used for ignition of gas mixtures many times. 1, 2, 4-7 In most cases, only slow combustion processes have been investigated. This article will present some basics of laser ignition together with results achieved by operating a laser ignition system on an internal combustion engine for a long period of time. Basics of fast combustion processes will be discussed briefly.

2. IGNITION OF COMBUSTIBLES

2.1. Spark plug ignition

Conventional ignition of a combustible requires that a high voltage is applied to the electrodes of the spark plug. The field strength reaches values of approximately $3 \cdot 10^5 \text{V/mm}^3$. Electrons are accelerated by the field and hit other atoms or molecules, thus ionizing additional atoms and an avalanche-like reproduction of ionized atoms occurs and the compressed fuel/air-mixture is ignited. For ignition of an inflammable gas mixture, the overall energy balance has to be positive within a small volume near the ignition location. Energy delivered by the spark together with the exothermal heat of reaction have to exceed energy losses caused by heat conduction and radiation losses together with the required activation energy of the molecules. Other ignition systems, like heating wires are not as fast as required or are destroyed after one ignition sequence. Additionally, several problems occur with conventional ignition which is caused by the fact that the ignition location cannot be chosen optimally.

2.2. Laser ignition

As mentioned earlier, only laser ignition by optical breakdown fulfils the requirements on a well defined ignition location and time. A powerful short pulse laser beam is focused by a lens into a combustion chamber and near the focal spot a hot and bright plasma is generated, see fig. 1.

2.2.1. Mechanisms of laser ignition

A high voltage is applied onto the electrodes of a spark plug. The field strength reaches values in the range of approximately $3 \cdot 10^4 \text{V/cm}$ between the electrodes of a conventional spark plug.^{2, 8}

In the case of a laser ignition system the laser beam is responsible for ignition of the combustible. Since the intensity of an electromagnetic wave is proportional to the square of the electric field strength $I^2 = \epsilon_0 / \mu_0 E^2$, (ϵ_0 = dielectric coefficient, μ_0 . . . permeability of free space) one can estimate that the intensity should be in the order of $2 \cdot 10^6 \text{W/cm}^2$, which is several orders of magnitude

lower as indicated by experiments on laser ignition. One reason is that in most cases there are not enough electrons within the irradiated volume to start an avalanche electron multiplication, thus generating hot plasma. Only at very high laser intensities a "multi photon" process where several photons hit the atom at nearly the same time⁹ frees the first few electrons. Following the generation of initial electrons, a cascade ionization process generates the hot plasma finally.¹⁰

Such multi photon ionization processes can only happen at very high irradiation levels (in the order of $10^{10} - 10^{11} \text{W/cm}^2$)^{2,3} where the number of photons is extremely high. For example, nitrogen has an ionization energy of approximately 14.5 eV, whereas one photon emitted by a Nd:YAG laser has an energy of 1.1 eV, thus more than 13 photons are required for ionization of nitrogen.



(a) 1064 nm



(b) 532 nm

Figure 1. Optical breakdown in air generated by a Nd:YAG laser

If electron diffusion out of the irradiated volume is neglected, the number of electrons increase exponentially during the laser pulse with the duration t $N = N_0 e^{t/\tau} = N_0 2^k$,(1) where τ is the characteristic time constant of the cascade process and k is the number of generations of electrons at the end of the laser pulse. Finally, the number of electrons exceeds the breakdown threshold and a bright and hot plasma is generated. Multiplication time constant is usually quite short (approx. 1 ns).¹⁰ Reaction velocities of combustion processes are several orders of magnitude slower. As a result, laser ignition fulfils the requirements on a well defined ignition time since there is almost no time delay

between the laser pulse and the development of hot plasma.

The required pulse energy of a laser system for ignition can be estimated by the following calculation roughly.

It is well known that the diameter d of a focused laser beam depends on the wavelength, the diameter of the unfocused beam and the focusing optics.

$$d = 2 \cdot w_f = 2 \cdot M^2 \frac{2}{\pi} \lambda F/D$$

where M^2 is the beam quality, F is the focal length of the optical element and D is the diameter of the laser beam with the wavelength λ . A reasonable radius w_f is in the range of approximately 100 μm and within a spherical volume $V = 4\pi w_f^3 / 3$ the number of molecules depend on the pressure and temperature according to the ideal gas law: $N = pV/kT$,(3) with the pressure p , temperature T and Boltzmann's constant $k = 1.38 \cdot 10^{-23} \text{J/K}$.

Since not all molecules within the irradiated volume will be dissociated and ionized, one can assume that approximately 10^{13} electrons will be present at the end of the laser pulse. Dissociation and ionization requires a certain amount of energy which has to be delivered by the laser beam. First the dissociation energy W_d is required and finally $2N$ atoms are ionized (ionization energy W_i). Using known values¹² for $W_d = 9.79 \text{ eV}$ and $W_i = 14.53 \text{ eV}$ for nitrogen, the energy for dissociating and ionizing all particles inside the volume can be calculated as

$$W = N \cdot (W_d + 2W_i) \dots (4)$$

For a spot radius of about 100 μm the estimation gives required pulse energy for ionization in the order of approximately 0.1 mJ.

3. COMBUSTION

After a successful ignition event the flame propagates through the combustible. Usually, one can distinguish between different types of combustion processes.² Slow combustion processes (deflagrations): Reaction velocity is mainly determined by heat conductivity. Propagation velocity is less than the speed of sound. Fast combustion processes (detonations): Reaction velocity is determined by a strong shock front moving at supersonic velocity. Propagation velocity is greater than the speed of sound.

Slow combustion processes are easier to control and are not as violent as fast combustion processes. Pressure and temperature gradients inside deflagrations are always smaller and stress on components is lower, too. In the case of very high heat of reaction the relation between the temperatures which can be achieved during a deflagration and a detonation approach a threshold value greater one:

$$T_{\text{detonation}}/T_{\text{deflagration}} = 2\gamma^2/\gamma + 1, (5)$$

where $\gamma = c_p/c_v$. . . describes the adiabatic coefficient of the combustible. Pressures and expansion velocities within a detonation can reach several 100 MPa and several 1000 m/s, whereas in deflagrations pressures and expansion velocities are much lower. It is obvious that slow combustion processes are far more important than violent detonations but it is a matter of fact that some needs on a reliable ignition system for detonations exist.

4. EXPERIMENTAL

4.1. Ignition of slow combustion processes

A laser ignition system has been used for ignition of an internal combustion engine. Since results have already been published,1, 15–18 only a brief overview is given here. Technical data of the research engine and the laser used for the experiments are summarized in table 1, the experimental setup is shown in fig. 2.

Table 1. Technical data of the research engine and the Nd:YAG laser used for the experiments.

Research engine		Q-switched Nd:YAG laser	
Number of cylinders	1	Pump source	Flash lamp
Number of valves	1	Wavelength	1064 or 532 nm
Injector	Multi-hole	Maximum pulse energy	160 mJ
Stroke	85 mm	Pulse duration	6 ns
Bore	88 mm	Power Consumption	1 kW
Displacement volume	517 cm ³	Beam diameter	6 mm
Compression ratio	11.6	Type	Quantel Brilliant

Pressure within the combustion chamber has been recorded as well as fuel consumption and exhaust gases. The laser was triggered at well defined positions of the crankshaft, just as with conventional ignition systems. Pulse energies, ignition location and fuel/air ratios have been varied during the experiments. The engine has been operated at each setting for several hours, repeatedly. All laser ignition experiments have been accompanied by conventional spark plug ignition as reference measurements

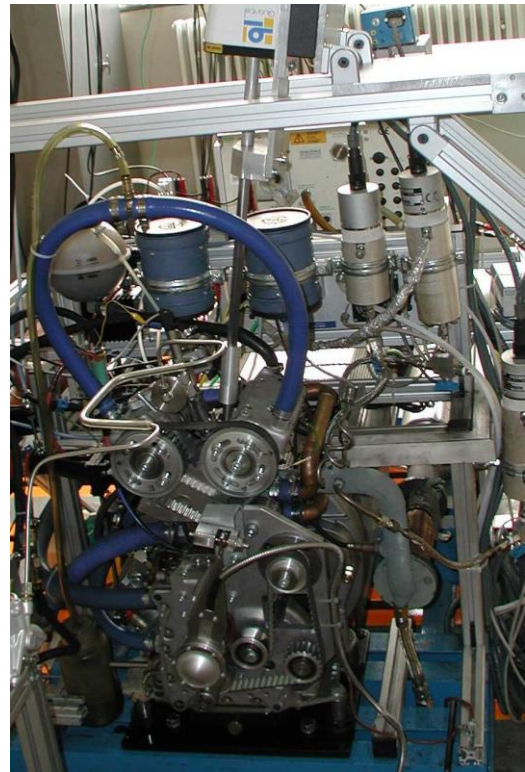
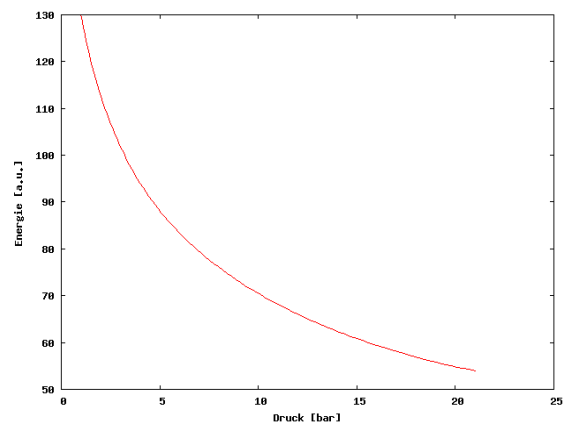
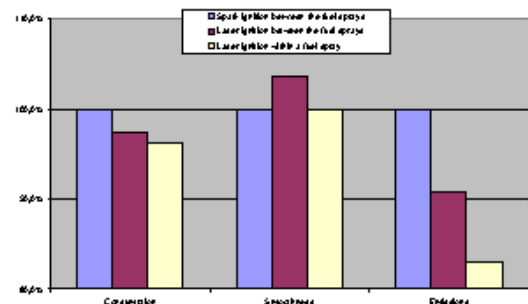


Figure 2. Research engine with the q-switched Nd:YAG laser system (top)



(a)

Pressure dependence on the required pulse energy for successful ignition.



(b)

Comparison between conventional spark plug ignition and laser ignition

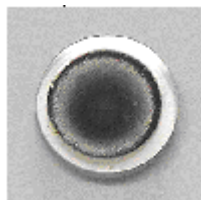
Figure 3. Experimental results on laser ignition of a direct injected combustion engine

5. RESULTS

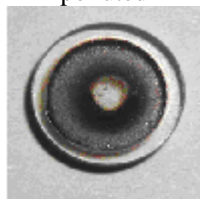
Measurements on the dependence of the pressure on the required pulse energy for ignition are summarized in fig. 3(a). Results indicate that the required pulse energy for successful ignition decreases with increasing pressure.

Results on consumption measurements are summarized in fig. 3(b). Compared to conventional spark plug ignition, laser ignition reduces the fuel consumption by several per cents. Exhaust emissions are reduced by nearly 20%. Additionally, a frequency-doubled Nd:YAG laser has been used to examine possible influences of the wavelength on the laser ignition process. No influences on the required pulse energy for successful ignition could be found.

Best results in terms of fuel consumption as well as exhaust gases have been achieved by laser ignition within the fuel spray. As already mentioned, it is not possible to use conventional spark plugs within the fuel spray.



(a) After 20 h operation with spark plug ignition, heavily polluted



(b) Immediately after 100 laser pulses. Beam area is cleaned by the laser beam

Figure 4. Beam entrance window

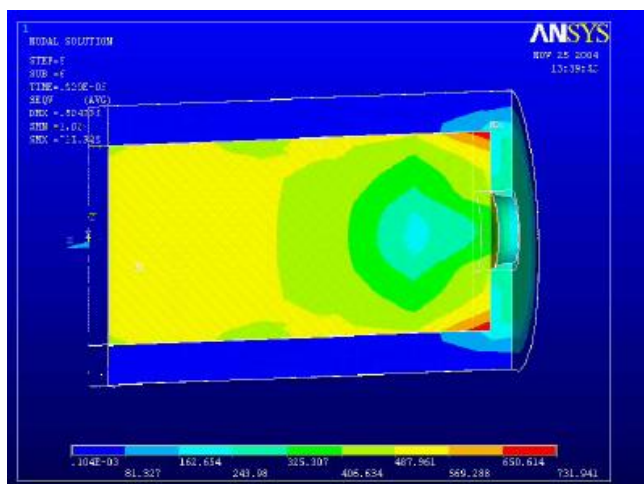


Figure 5. Equivalent vonMises stress on a beam entrance window. Maximum pressure is 500 MPa, pressure rise within 1 μ s since they will be destroyed very rapidly. Laser ignition doesn't suffer from that restriction. Additionally, even with a heavily polluted beam entrance

windows the direct injection engine could be operated successfully see fig. 4.

6. SIMULATIONS

6.1. Ignition of fast combustion processes

As already mentioned, fast combustion processes (i.e. detonations) show a more violent behavior, i.e. pressures and temperatures rise very quickly. In most cases, conventional ignition systems - like heating wires - are destroyed by the acting forces during the explosion. Nevertheless, there is a need on a reliable and repeatable ignition source which is not destroyed by the rapid combustion process. One possibility would be laser ignition but it is clear that one of the most critical points is the beam entrance window into the explosion chamber. Since pressures and temperatures can reach very high values in very short periods of time during a detonation stress on a beam entrance window is very high, too. FEM-simulations should help to clarify the question if a window can withstand the pressures during such violent combustion processes, see fig. 5. Results of the simulations indicate that a carefully designed beam entrance window will be able to withstand even pressures and temperatures caused by fast combustion processes. Nevertheless, only real-world experiments can prove the validity of the FEM-simulation.

7. SUMMARY

Laser induced ignition of slow combustion processes has been examined. The feasibility of a laser-induced ignition system on a direct injected gasoline engine has been proven in long-term experiments. Main advantages are the almost free choice of the ignition location within the combustion chamber, even inside the fuel spray.

Significant reductions in fuel consumption as well as reductions of exhaust gases show the potential of the laser ignition process. Results indicate that pollution of the beam entrance window is not critical as expected; even heavily polluted windows have had no influence on the ignition characteristics of the engine. Measurements show that the required pulse energy for successful ignition decreases with increasing pressure.

Fast combustion processes (detonations) show a much more violent character than slow deflagrations. FEM simulations indicate that a well designed beam entrance window can probably withstand pressures and temperatures during a detonation. Additional work is necessary to prove the results of the simulations by experiments.

REFERENCES

1. G. Liedl, D. Schu"ocker, B. Geringer, J. Graf, D. Klawatsch, H. Lenz, W. Piock, M. Jetzinger, and P. Kapus, "Laser induced ignition of gasoline direct injection engines," in Proc. SPIE, 5777, pp. 955-960, 2004. Invited paper.
2. P. D. Ronney, "Laser versus conventional ignition of flames," Optical Engineering 33 (2), pp. 510-521, 1994.

3. M.-C. Gower, "Krf laser-induced breakdown of gases," *Optics Communications* 36(1), pp. 43–5, 1981.
4. J. Syage, E. Fournier, R. Rianda, and R. Cohn, "Dynamics of flame propagation using laser induced spark initiation: Ignition energy measurements," *Journal of Applied Physics* 64 (3), pp. 1499–1507, 1988.
5. M. Lavid, A. Poulos, and S. Gulati, "Infrared multiphoton ignition and combustion enhancement of natural gas," in *SPIE Proc.: Laser Applications in Combustion and Combustion Diagnostics*, 1862, pp. 33–44, 1993.
6. J. Ma, D. Alexander, and D. Poulain, "Laser spark ignition and combustion characteristics of methane-air mixtures," *Combustion and Flame* 112 (4), pp. 492–506, 1998.
7. R. Hill, "Ignition-delay times in laser initiated combustion," *Applied Optics*. 20 (13), pp. 2239–2242, 1981.
8. Bergmann and Schaefer, *Lehrbuch der Experimentalphysik: Elektrizität und Magnetismus*, vol. 2, Walter de Gruyter Berlin, 1981.
9. T. Huges, *Plasma and laser light*, Adam Hilger, Bristol, 1975.
10. C. DeMichelis, "Laser induced gas breakdown: A bibliographical review," *IEEE Journal of Quantum Electronics* 5(4), pp. 188–202, 1969.
11. W. Koechner, *Solid-State Laser Engineering*, vol. 1, Springer, 1999.
12. D. R. Lidde, ed., *CRC Handbook of Chemistry and Physics*, CRC Press, 2000.
13. L. D. Landau and E. Lifschitz, *Hydrodynamik*, vol. 6 of *Lehrbuch der theoretischen Physik*, Harri Deutsch, *Lehrbuch der theoretischen Physik* ed., 1991.
14. G. Ben-Dor, O. Igra, and T. Elperin, eds., *Handbook of Shock Waves: Theoretical, Experimental and Numerical Techniques*, vol. 1, Academic Press, 2001.
15. B. Geringer, J. Graf, D. Klawatsch, H. P. Lenz, G. Liedl, D. Schu"ocker, W. F. Piock, M. Jetzinger, and P. Kapus, "Laserinduzierte Z"undung an einem Otto-DI-Brennverfahren der zweiten Generation," in *Fortschritt- Berichte VDI 24. Internationales Wiener Motorensymposium*, 15.-16. Mai 2003, 2 12(539), pp. 87–109, VDI Verlag D"usseldorf, 2003.
16. B. Geringer, J. Graf, D. Klawatsch, H. Lenz, G. Liedl, D. Schu"ocker, W. Piock, M. Jetzinger, and P. Kapus, "Laserz"undung - ein neuer Weg f"ur den Ottomotor?," *MTZ - Motortechnische Zeitschrift* 3, pp. 214–219, 2004.
17. B. Geringer, J. Graf, D. Klawatsch, H. Lenz, G. Liedl, D. Schu"ocker, W. Piock, M. Jetzinger, and P. Kapus, "Laserinduzierte Z"undung an einem Otto-DI-Brennverfahren der zweiten Generation," in *24. Internationales Wiener Motorensymposium*, H.-P. Lenz, ed., pp. 87 – 109, VDI Verlag GmbH, D"usseldorf, 15.- 16. Mai 2003.
18. M. Jetzinger, *Unkonventionelle Z"undsysteme und Laserz"undung bei Ottomotoren*. PhD thesis, TU Wien, 2002.
19. R. Bielak, "Fe-simulations of detonations." *priv.Comm.*, 2005.

Performance and Analysis of Hybrid Multilevel Inverter fed Induction Motor Drive

CHEKKA G K AYYAPPA KUMAR¹, V. ANJANI BABU¹, K.R.N.V.SUBBA RAO¹,
MD. HYDAR ALI¹, K.SURYA SURESH², MD. MAZAR HUSSAIN³

¹Student, Department of EEE, Sri Vasavi Institute of Engineering and Technology, Nandamuru, AP, INDIA

²Faculty, Department of EEE, Sri Vasavi Institute of Engineering and Technology, Nandamuru, AP, INDIA

³H.O.D, Department of EEE, Sri Vasavi Institute of Engineering and Technology, Nandamuru, AP, INDIA

ABSTRACT

This paper presents the Five level inverter with single DC source which is used to generate a five level output with two bridges and six switches and performance of three phase induction motor is analyzed when connected to PV array For this two identical dc sources of 50V each for two bridges in five levels using Multi level inverter and five level output is obtained by using a single DC source of 100V with six switches. A virtual DC source (charged capacitor acts as virtual DC source) is used for getting the output. The same technique is implemented for three-phase circuit i.e. by using single DC source. An asynchronous motor (three-phase) is connected as load and its performance characteristics are analyzed. And further the DC source is replaced by a renewable resource such as solar panels, fuel cell etc. and DC voltage is obtained. Performance characteristics of three-phase asynchronous motor are analyzed with PV array connected. The method can be easily extended to an m-level inverter. The cascaded inverter is subjected to other modulation scheme. Simulations have been carried out in MATLAB-Simulink to study the performance of the proposed prototype.

KEYWORDS: Cascaded H Bridge inverter, Induction motor, PV array, THD, Virtual DC source.

I. INTRODUCTION

A multilevel inverter not only achieves high power ratings, but also enables the use of renewable energy sources. Renewable energy sources such as photovoltaic, wind and fuel cells, which can be easily interfaced to a multilevel inverter system for high power applications The topologies of multilevel inverters are classified in to three types the Flying capacitor inverter, the Diode clamped inverter and the Cascaded bridge inverter.

The proposed prototype use of r multilevel inverter has five level associated with a six number of power switches [1-3] with the use of single dc source In normal five level inverter use of this two identical dc sources of with two bridges in five levels using Multi level inverter and five level output is obtained in proposed circuit by using a single DC source. The same technique is implemented for three-phase circuit i.e. by using single DC source. An asynchronous motor (three-phase) is connected as load and its performance characteristics are analyzed. And

further the DC source is replaced by a renewable resource such as solar panels, fuel cell etc. and DC voltage is obtained. Performance characteristics of three-phase asynchronous motor are analyzed with PV array connected. To develop the model of hybrid multilevel inverter, a simulation is done based on MATLAB/SIMULINK platform

II. PV ARRAY

Photons of light with energy higher than the band-gap energy of PV material can make electrons in the material break free from atoms that hold them and create hole-electron pairs. These electrons however, will soon fall back into holes causing charge carriers to disappear. If a nearby electric field is provided, those in the conduction band can be continuously swept away from holes toward a metallic contact where they will emerge as an electric current. The electric field within the semiconductor itself at the junction between two regions of crystals of different type, called a p-n junction. [4]

The PV cell has electrical contacts on its top and bottom to capture the electrons. When the PV cell delivers power to the load, the electrons flow out of the n-side into the connecting wire, through the load, and back to the p-side where they recombine with holes [4]. Note that conventional current flows in the opposite direction from electrons.

2.1 MATHEMATICAL MODEL OF THE PV ARRAY

2.1.1. SIMPLIFIED EQUIVALENT CIRCUIT:

A solar cell basically is a p-n semiconductor junction. When exposed to light, a current proportional to solar irradiance is generated. The circuit model of PV cell is illustrated in Fig.1. Standard simulation tools utilize the approximate diode equivalent circuit shown in Fig. 4 in order to simulate all electric circuits that contain diodes. The model is based on two-segment piecewise linear approximation. The circuit consists of R_{on} in series with voltage source V_{on} .

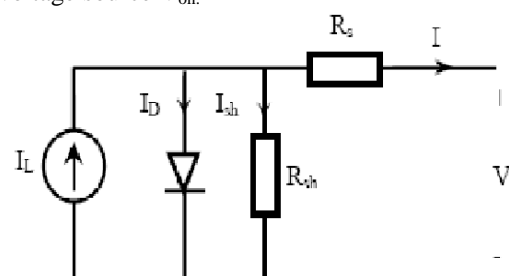


Fig. 1: Circuit model of PV solar cell

2.2. THEORETICAL MATHEMATICAL MODEL:

The equation [1] & [2] that are used to solve the mathematical model of the solar cell based on simple equivalent circuit shown in Fig. 1, are given below;

$$I_D = I_0 \left[e^{\frac{q(V+I R_s)}{K T}} - 1 \right] \dots\dots\dots (1)$$

$$I = I_L - I_0 \left[e^{\frac{q(V+I R_s)}{K T}} - 1 \right] - \frac{V+I R_s}{R_{sh}} \dots\dots\dots (2)$$

Where:

- I is the cell current in (A).
- q is the charge of electron = 1.6x10⁻¹⁹ (coul).
- K is the Boltzmann constant (j/K).
- T is the cell temperature (K).
- I_L is the light generated current (A).
- I₀ is the diode saturation current.
- R_s, R_{sh} are cell series and shunt resistance (ohms).
- V is the cell output voltage (V).

2.3. PV CHARACTERISTICS:

2.3.1 CURRENT VS VOLTAGE CHARACTERISTICS:

Equation (1) was used in computer simulation to obtain the output characteristics of a solar cell, as shown in the figure4. This curve clearly shows that the output characteristics of a solar cell are non linear and are crucially influenced by solar radiation, temperature and load condition

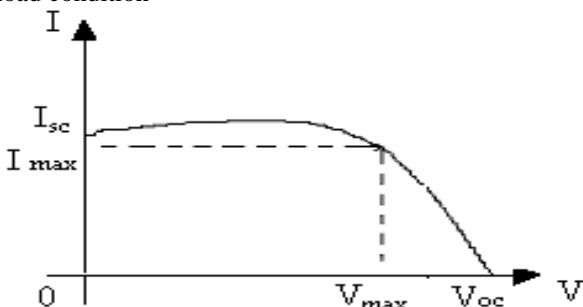


Fig. 2: Output Characteristics Of Solar Cell

2.3.2 POWER VS VOLTAGE CHARACTERISTICS:

Figure 3 shows the typical Power versus Voltage curve of the PV array. In this figure, P is the power extracted from PV array and V is the voltage across the terminals of the PV array [7].

The characteristics have different slopes at various points. When maximum power is extracted from PV array the system is operating at MPP where slope is zero. The PV curve varies according to the current insolation and temperature. When insolation increases, the power available from PV array increases whereas when temperature increases, the power available from PV Array decreases.

2.3.3 VARIATION IN AVAILABLE ENERGY DUE TO SUN'S INCIDENT ANGLE:

PV cell output with respect to sun's angle of incidence is approximated by a cosines function at sun angles from 0° to 50°. Beyond the incident angle of 50° the available solar energy falls off rapidly as shown in the figure 4. Therefore it is convenient and sufficient within the normal operating range to model the fluctuations in photocurrent (I_{ph}) versus incident angle is given by Eq(3). [8].

$$I_{ph} = I_{max} \cos \theta \dots\dots\dots (3)$$

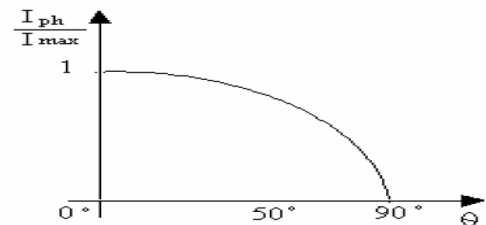


Fig 3: Power Vs Voltage

The graph shown in fig.4 is used to find the maximum power extracted from the sun when the PV arrays are inclined a different angles. From the figure we observe that Max power is obtained when the slope of the PV array is equal to zero.

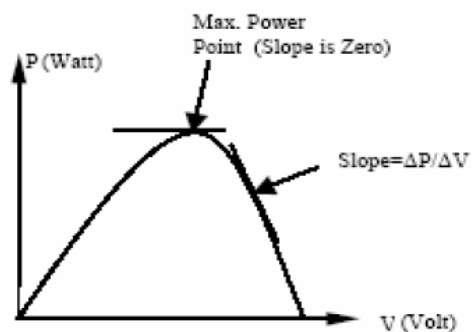


Fig. 4: Variation In Available Energy Due Sun's Incident Angle Variation.

III .CASCADED MULTILEVEL INVERTER

In this paper the use of one half bridge and one full bridge to get five level output wave as output.

3.1 VIRTUAL DC SOURCES

Virtual DC sources are nothing but charged capacitors. These charged capacitors are used to get the required output voltage with changing in levels. The main advantage of using the virtual dc source is to minimize the voltage sources (PV arrays) which results in decreasing of installation cost.

3.2 MULTI-LEVEL INVERTER

Three different major multilevel converter structures have been applied in industrial applications cascaded H-bridges converter with separate dc sources, diode clamped, and flying capacitors. Before continuing discussion in this topic, it should be noted that the term multilevel converter is utilized to refer to a power electronic circuit that could operate in an inverter or rectifier mode. The cascaded h bridge multilevel inverter focused on this paper.

3.3.1 Cascaded H-Bridges: A single-phase structure of an m-level cascaded inverter is illustrated in Figure 10. Each separate dc source (SDCS) is connected to a single-phase full-bridge, or H-bridge, inverter. Each inverter level can generate three different voltage outputs, $+V_{dc}$, 0, and $-V_{dc}$ by connecting the dc source to the ac output by different combinations of the four switches, $S_1, S_2, S_3,$ and S_4 . To obtain $+V_{dc}$, switches S_1 and S_4 are turned on, whereas $-V_{dc}$ can be obtained by turning on switches S_2 and S_3 . By turning on S_1 and S_2 or S_3 and S_4 , the output voltage is 0. The ac outputs of each of the different full-bridge inverter levels are connected in series such that the synthesized voltage waveform is the sum of the inverter outputs. The number of output phase voltage levels m in a cascade inverter is defined by $m = 2s+1r$. The phase voltage v_{an}

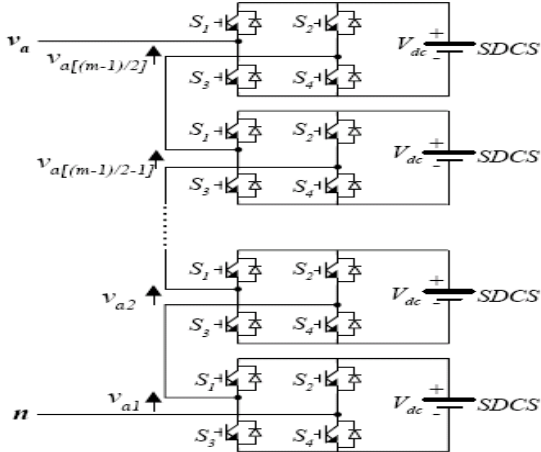
$$= v_{a1} + v_{a2} + v_{a3} + \dots + v_{an}$$


Fig.5. Single-phase structure of a m level multilevel cascaded H bridge inverter.

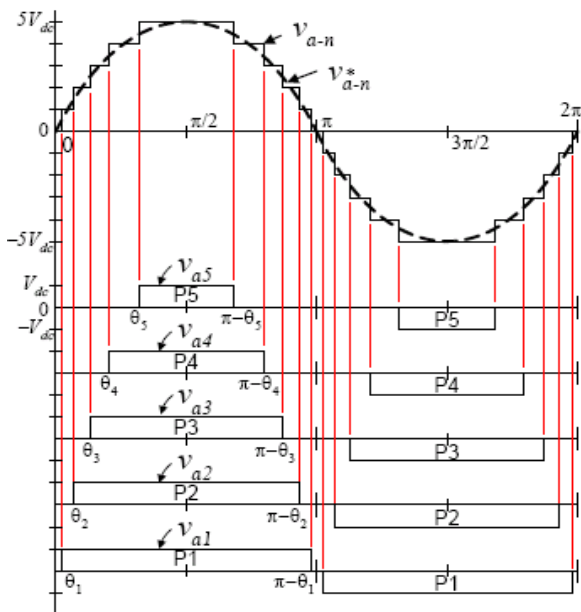


Fig.6 Output phase voltage waveform of an 11-level cascade inverter with 5 separate dc sources

Multi level inverters divide the main DC supply voltage into several smaller DC sources which are used to synthesize an AC voltage into a stair case, or stepped, approximation of the desired sinusoidal waveform. A waveform generated with five DC sources each one with one volt magnitude approximates the desired sinusoid, as shown in figure 11. The five DC sources (five steps) produced peak to peak voltage of 10V using eleven discrete levels

3.4 MLI WITH SINGLE DC SOURCE:

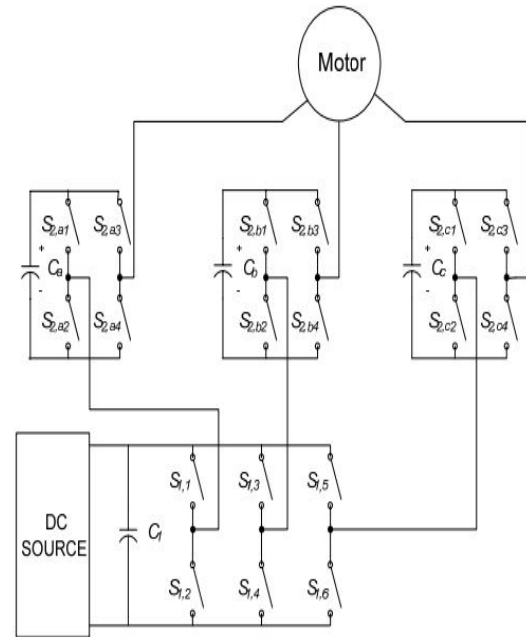


Fig.7. Topology of the hybrid multilevel inverter.

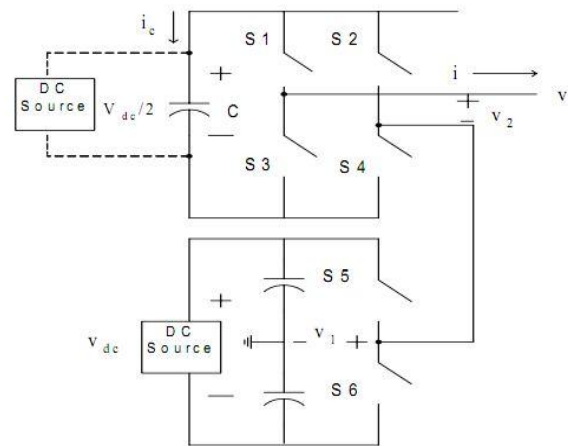


Fig.8. Simplified single-phase topology of the hybrid multilevel inverter.

Fig. 7 shows the topology of the proposed hybrid shows the topology of the proposed hybrid multilevel inverter. A simplified single-phase topology is shown in Fig.8. The bottom is one leg of a standard 3-leg inverter with a dc power source. The top is an H-bridge in series with each standard inverter leg. The H-bridge can use a separate dc power source or a capacitor as the dc power source [5][6].

The output voltage v_1 of this leg (with respect to the ground) is either $+V_{dc}/2$ (S_5 closed) or $-V_{dc}/2$ (S_6 closed). This leg is connected in series with a full H-bridge which in turn is supplied by a capacitor voltage. If the capacitor is kept charged to $V_{dc}/2$, then the output voltage of the H-bridge can take on the values $+V_{dc}/2$ (S_1, S_4 closed), 0 (S_1, S_2 closed or S_3, S_4 closed), or $-V_{dc}/2$ (S_2, S_3 closed). An example output waveform that this topology can achieve is shown in the top of Fig. 14. When the output voltage $v = v_1 + v_2$ is required to be zero, one can either set $v_1 = +V_{dc}/2$ and $v_2 = -V_{dc}/2$ or $v_1 = -V_{dc}/2$ and $v_2 = +V_{dc}/2$. It is this flexibility in choosing how to make that output voltage zero that is exploited to regulate the capacitor voltage

Consequently, the amount of capacitor voltage the scheme can regulate depends on the phase angle difference of output voltage and current.

IV. INDUCTION MOTOR:

In recent years the control of high-performance induction motor drives for general industry applications and production automation has received widespread research interests. Induction machine modeling has continuously attracted the attention of researchers not only because such machines are made and used in largest numbers but also due to their varied modes of operation both under steady and dynamic states. Traditionally, DC motors were the work horses for the Adjustable Speed Drives (ASDs) due to their excellent speed and torque response. But, they have the inherent disadvantage of commutator and mechanical brushes, which undergo wear and tear with the passage of time. In most cases, AC motors are preferred to DC motors, in particular, an induction motor due to its low cost, low maintenance, lower weight, higher efficiency, improved ruggedness and reliability. All these features make the use of induction motors a mandatory in many areas of industrial applications. The advancement in Power electronics and semiconductor technology has triggered the development of high power and high speed semiconductor devices in order to achieve a smooth, continuous and low total harmonics distortion (THD).

Three phase induction motors are commonly used in many industries and they have three phase stator and rotor windings. The stator windings are supplied with balanced three phase ac voltages, which produce induced voltages in the rotor windings due to transformer action. It is possible to arrange the distribution of stator windings so that there is an effect of multiple poles, producing several cycles of magneto motive force (mmf) around the air gap. This field establishes a spatially distributed sinusoidal flux density in the air gap.

In this paper three phase induction motor as a load. The equivalent circuit for one phase of the rotor is shown in figure. 10(a).

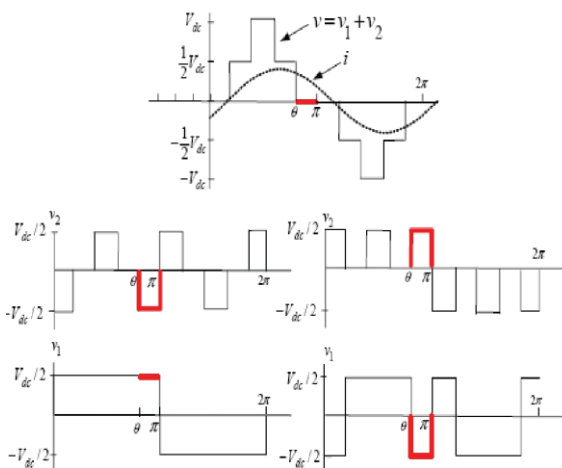


Fig.9. Capacitor voltage regulation process.

When only a dc power source is used in the inverter, that is, the H-bridge uses a capacitor as the dc power source, the capacitor's voltage regulation control details are illustrated in Fig.9. During $\theta_1 \leq \theta \leq \pi$, the output voltage in Fig.9 is zero and the current $i > 0$. If S_1, S_4 are closed (so that $v_2 = +V_{dc}/2$) along with S_6 closed (so that $v_1 = -V_{dc}/2$), then the capacitor is discharging ($i_c = -i < 0$ see Fig. 14) and $v = v_1 + v_2 = 0$. On the other hand, if S_2, S_3 are closed (so that $v_2 = -V_{dc}/2$) and S_5 is also closed (so that $v_1 = +V_{dc}/2$), then the capacitor is charging ($i_c = i > 0$ see Fig. 14) and $v = v_1 + v_2 = 0$. The case $i < 0$ is accomplished by simply reversing the switch positions of the $i > 0$ case for charge and discharge of the capacitor. Consequently, the method consists of monitoring the output current and the capacitor voltage so that during periods of zero voltage output, either the switches S_1, S_4 , and S_6 are closed or the switches S_2, S_3, S_5 are closed depending on whether it is necessary to charge or discharge the capacitor.

As Fig.9 illustrates, this method of regulating the capacitor voltage depends on the voltage and current not being in phase. That means one needs positive (or negative) current when the voltage is passing through zero in order to charge or discharge the capacitor.

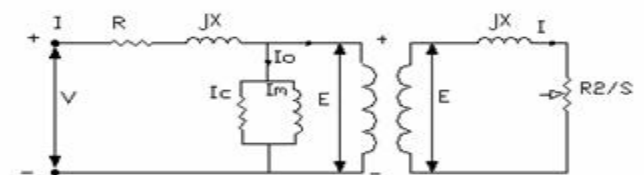


Fig. 10 (a). Steady state Equivalent circuit of an induction motor

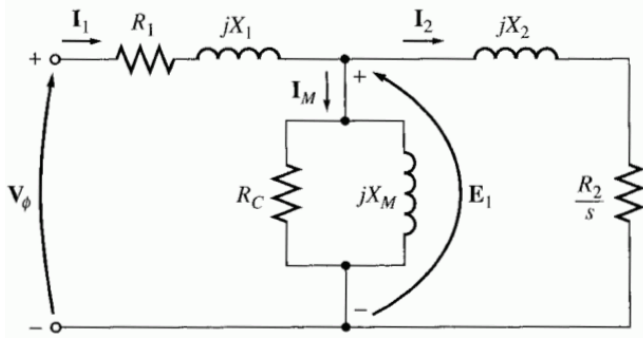


Fig.10 (b). Equivalent circuit refer to stator

The rotor current is

$$I_r = \frac{sE_r}{R_r + jX_r} \dots\dots\dots (4)$$

$$= \frac{E_r}{\frac{R_r}{s} + jX} \dots\dots\dots (5)$$

The complete circuit model with all parameters referred to the stator is in figure. Where R_s and X_s are the per phase resistance and leakage reactance of the stator winding. X_m represents the magnetizing reactance. R_r and X_r are the rotor resistance and reactance referred to the stator. I_r is the rotor current referred to the stator. There will be stator core loss, when the supply is connected and the rotor core loss depends on the slip.

V. PROPOSED CIRCUIT:

The proposed prototype consists of three phase five level inverter interfaced with a PV module is as shown in the fig.11. This paper deals with an asymmetrical inverter so that the use of virtual DC with that the method of using a single source the required five level output is achieved. The combination of multi level inverter with a single DC source and PV arrays will reduce the initial cost of the circuit and also maintenance cost of the circuit.

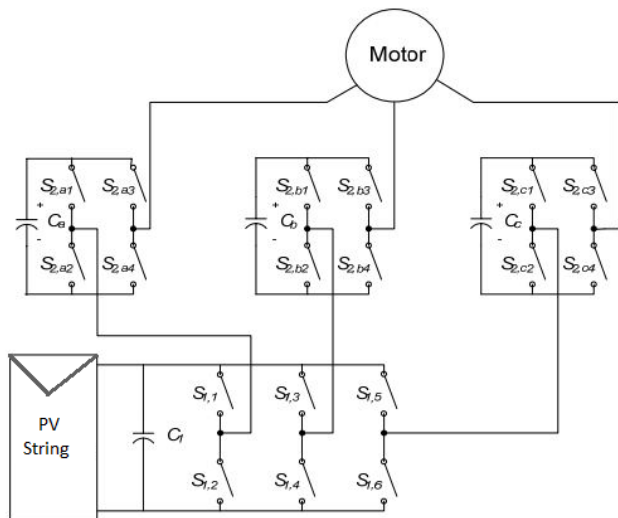


Fig.11 proposed circuit with PV array

An asynchronous motor is connected to the circuit as load. And the performance characteristics are obtained for the connected motor.

VI. SIMULATION RESULTS

A single phase five level inverter with single DC source simulated and as shown in fig.12. and corresponding five level output with the use of a single DC source shown in fig.13. Similarly three phase five level inverter simulated as shown in figure.14. and corresponding the three phase line to ground voltages separately shown in fig.15. The proposed PV module is shown in the figure 16. It is worth mentioning that the output voltage of the PV string arrays should be chosen based on the grid nominal voltage and the minimum desired operating power of each cell. If the power generated by all strings is equal, the output voltage of all cells will be equal. A PV Array contains six series-connected 100-V 1000-Wp PV panels. Simulations have been carried out in MATLAB-Simulink.

A three phase asynchronous motor is connected to the proposed circuit shown in fig 17. The circuit is simulated to show the performance characteristics of motor. Fig.18 Shows the stator currents, all the values are variable in nature up to 0.8 sec and then rated stator current are become stable in nature. The rotor currents of an asynchronous motor had shown in fig.19 the frequency of stator currents generally much higher than to the rotor currents. The speed of rotor is nearly 152.2rad/sec as per the results of speed-time curve, shown in fig.20. The torque of motor was calculated by using the equations [7] & [8] and the calculated torque will be equal to the obtained torque during simulation as shown in fig.21

$$S = \frac{N_s - N}{N_s} \dots\dots\dots (7)$$

$$T = \frac{V_2^2 * SR_2}{\sqrt{R_2^2 + (SX_2)^2}} \dots\dots\dots (8)$$

The THD of inverter output voltage and Harmonic spectrum of the simulation system is as shown in the fig. 22 which shows the results are well within the specified limits of IEEE standards. The experimental and simulated results are show satisfactory results in term of total harmonic distortion and output voltage and current waveform shapes. To verify the validity of the proposed Hybrid Five level inverter fed induction motor drive. The results of both output voltage and FFT analysis are verified by simulating the main circuit using MATLAB.

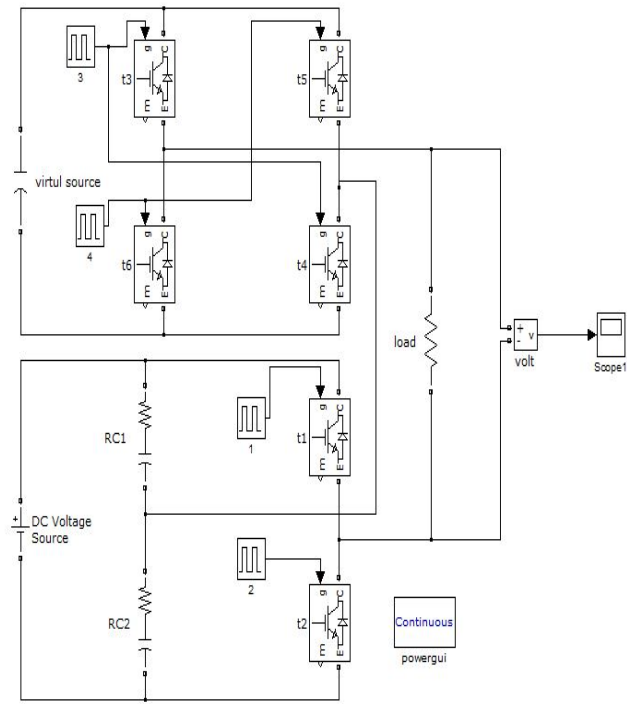


Fig.12 single phase five level inverter with a single DC source

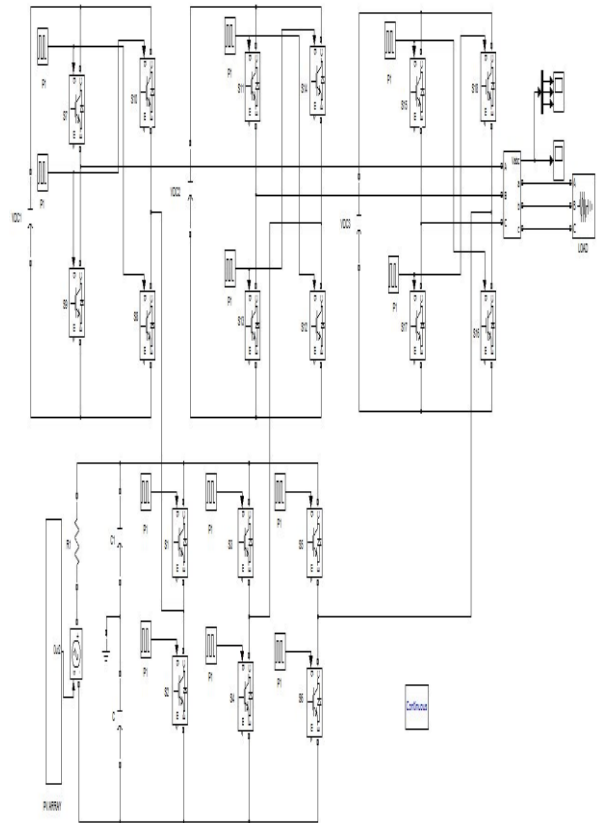


Fig. 17: Schematic of proposed of three phase Five level Inverter

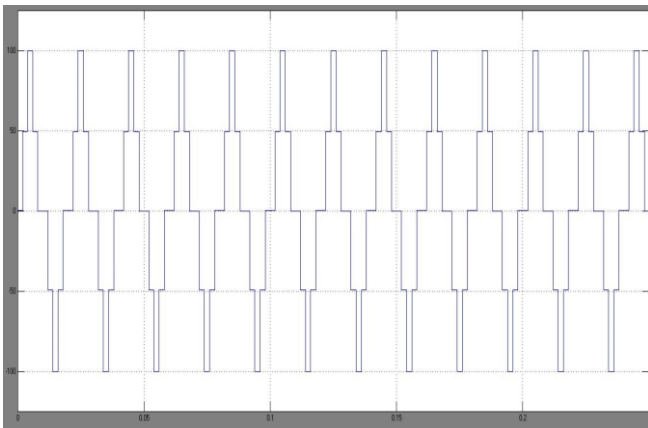


Fig.13 Five Level Inverter output Voltage with a single DC source.

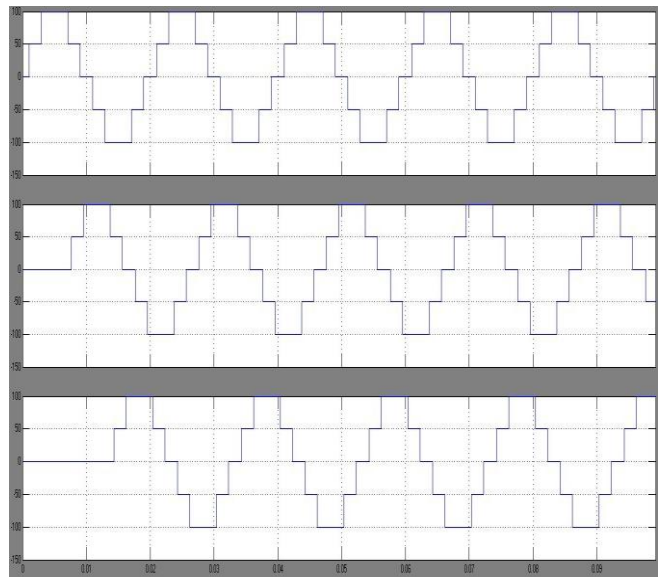


Fig.15. Three phase Line to ground voltage

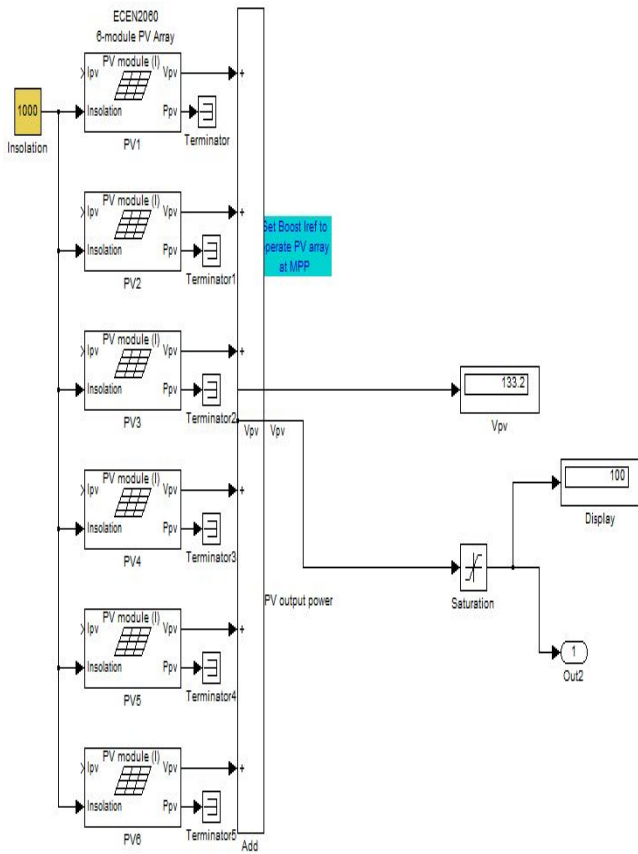


Fig.16: PV array module

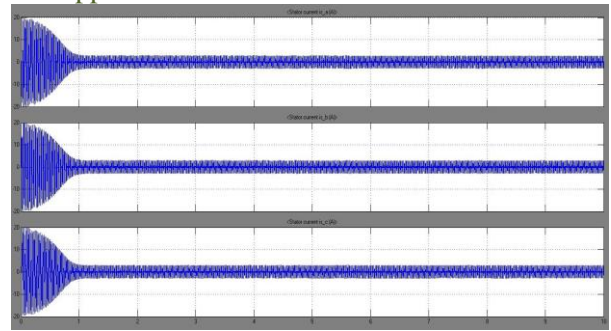


Fig.18 stator currents of asynchronous motor

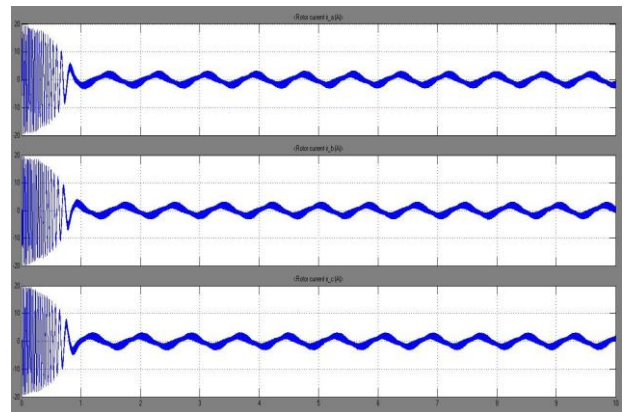


Fig.19 rotor currents of asynchronous motor

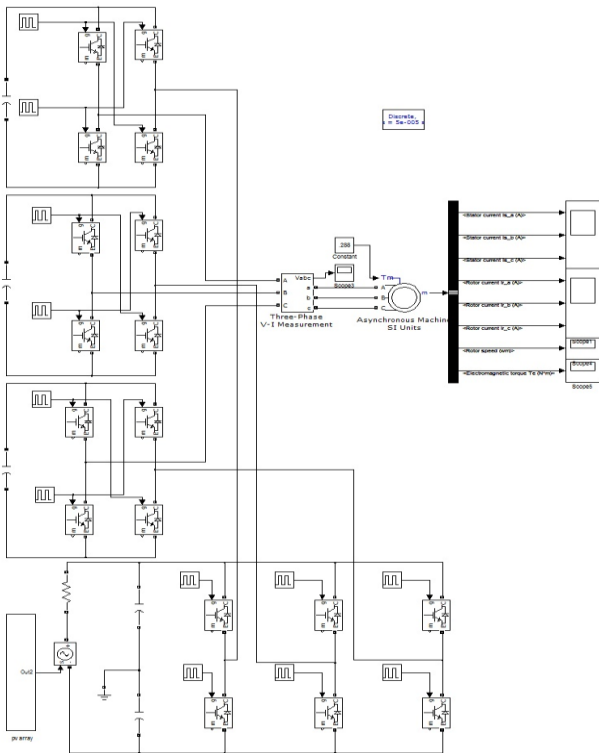


Fig.17 .Schematic of proposed Prototype

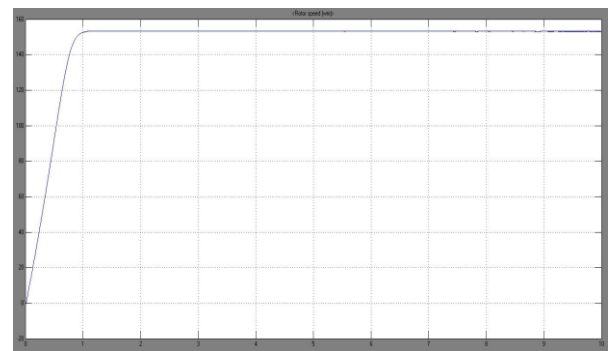


Fig.20 speed- time curve

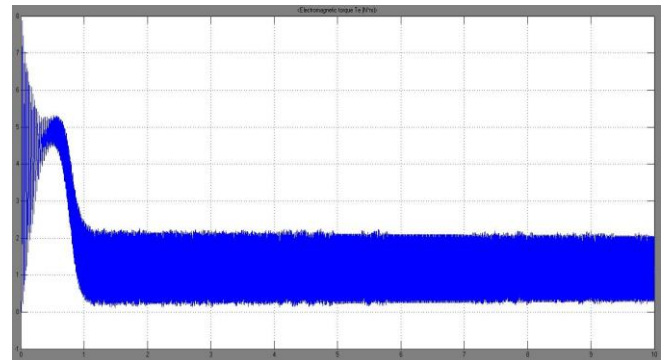


Fig.21 torque with respect to time

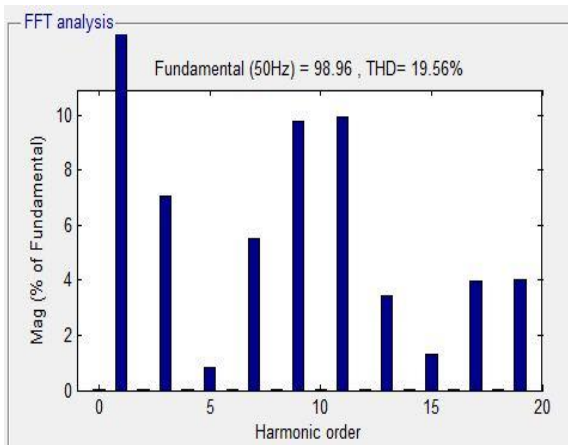


Fig. 22. FFT analysis

VII. CONCLUSION

This paper presented an Three phase five-level cascade H-bridge Inverter, which uses single DC source and PV system as DC source and connected to three phase induction motor is used as load to observe the performance characteristics of the motor. The proposed Multilevel Inverter fed Induction Motor FFT Analysis THD value is 19.56 voltage of 98.2 V. The method can be easily extended to an m-level inverter. The cascaded inverter is subjected to other modulation scheme. Simulations have been carried out in MATLAB–Simulink to study the performance of the proposed prototype

VIII REFERENCES

- [1] L. M. Tolbert, F. Z. Peng, T. G. Habetler, "Multilevel converters for large electric drives," *IEEE Transactions on Industry Applications*, vol.35, no. 1, Jan. /Feb. 1999, pp. 36-44.
- [2] J. S. Lai and F. Z. Peng, "Multilevel converters – A new breed of power converters," *IEEE Transactions on Industry Applications*, vol. 32, no.3, May. /June 1996, pp. 509-517.
- [3] J. Rodriguez, J. Lai, and F. Peng, "Multilevel inverters: a survey of topologies, controls and applications," *IEEE Transactions on Industry Applications*, vol. 49, no. 4, Aug. 2002, pp. 724-738.
- [4] Masters, Gilbert M. Renewable and Efficient Electric Power Systems John Wiley & Sons Ltd, 2004.
- [5] D. Zhong B. Ozpineci, L. M. Tolbert, J. N. Chiasson, "Inductor less DC-AC cascaded H-Bridge multilevel boost inverter for electric/hybrid electric vehicle applications," *IEEE Industry Applications Conference*, Sept. 2007, pp. 603-608.
- [6] J. Liao, K. Corzine, M. Ferdowsi, "A new control method for single-DC-source cascaded H-Bridge multilevel converters using phase-shift modulation," *IEEE Applied Power Electronics Conference and Exposition*, Feb. 2008, pp.886-890.
- [7] K.A Corzine, and Y.L Familiant, "A New Cascaded Multi-level H-Bridge Drive", *IEEE Trans. Power.Electron.*, vol.17, no.1, pp.125-131. Jan 2002.
- [8] Philip T.Krein, Robert S.Balog and Xin Geng, "High-Frequency Link Inverter for fuel cells Based on Multiple Carrier PWM", *IEEE Transactions on Power Electronics*, Vol 19, NO.5, Sep 2004.

An Analysis of Morphological Operation Using Arbitrary Structuring Element

A.P. Ilayaraja, M. P. Gopinath

School of computing science and Engineering, VIT University, India.

ABSTRACT

Mathematical morphology with spatially variant structuring elements outperforms translation-invariant structuring elements in various applications. However, supporting a variable structuring element shape imposes an overwhelming computational complexity, dramatically increasing with the size of the structuring element. Dilation and erosion are often used in combination to implement image processing operations. The image content and the number of gray levels used does not influence the computing time required. The operator for each size and shape of the structuring element must be done separately, but here the filtering with multiple structuring elements is done in one operation and this reduces the computational requirements very much. The method finds applications in the areas like granulometrices, dilation-erosion scale spaces, and template matching using the hit-or-miss to transform. In this paper we are proposing about the computational performance advantage over existing methods where structuring elements are used that cannot be easily decomposed into linear structuring elements.

Keywords - Dilations, Erosions, Granulometrices, Hit-Or-Miss Transforms, Mathematical Morphology, Structuring Elements.

I. INTRODUCTION

Mathematical Morphological have a most fundamental morphological operators [9] like dilation and erosion with structuring elements (S.E.). It has become common tools for both image filtering and analysis of binary and gray-scale images since the development of efficient algorithms [2]. It is based on the algebra of nonlinear operators operating on objects shape and in many respects to take place the liner algebra system of convolution. Morphological operations simplify images, and quantify and preserve the main shape characteristics of objects. Morphological operations are applied to image pre-processing, enhancing the object structure, segmenting objects from the background, quantitative description of objects. Algorithms are fixed to liner structuring element and shapes like rectangles that can be decomposed [4] in to a series of linear structuring elements. All methods based on decomposition of 2-D S.E.s [3] into linear S.E.s share the same limitation: many shapes they cannot be decomposed at all or either cannot be decomposed efficiently.

One of the very interesting and effective algorithms for the speed calculation on established computers of the basic morphological operation for 2-D images is presented in [5]. Still, that algorithm cannot be extended directly to 3-D images, because chain coding has not an equivalent in three

dimensions. In the binary case, efficient algorithms for some 2-D shapes like circles do exist, but these cannot efficiently be extended to the gray-scale case, for which polygonal approximations of circles usually are used instead. Because larger circles this estimation is given to be either too coarse or too computationally intensive, since the number or liner S.E.s required is proportional to the diameter of the circle. Van Droogenbroeck and Talbot [1] proposed an efficient algorithm for computing morphological operation with arbitrary 2-D shapes using a histogram, which makes the computing time of their algorithm dependent on the number of gray levels used. Efficient implementations for particularized hardware have also been analysed extensively, such as the decomposition of arbitrary shapes into 3×3 blocks [6]. The important for those case where S.E. cannot be decomposed, where the algorithms that efficiently perform morphological operations with arbitrary S.E.s. but also where ever a generic algorithm is desired such as image processing libraries, which often have number of specialized routines for specific cases, and a direct implementation for arbitrary S.E. moreover, for many application the benefits of using the faster specialized algorithm available alternatively of using one a bit slightly less efficient generic algorithm does not outbalance the coast involved in adapting the methods used. S.E. shape decompositions require some design and programming efforts that can be avoided if a generic algorithm is used [7]. To calculate for one pixel p of the image the complete histogram based on the intensity of the pixels around p matching the element of the S.E. After erosion the value of p is the minimum intensity in the histogram which has a value >0 . For all succeeding pixels of the image, the histogram is efficiently update and the position of its minimum intensity changes only if i) a new minimum value is shifted into the histogram, which can be kept track when the histogram is updated, or ii) when the current minimum is shifted out of the histogram, in which case the algorithm searches for the first following intensity which is now represented in the histogram. This paper [8], present a new technique for performing morphological operators with any 2-D structuring element that always outperforms existing algorithms for arbitrary structuring elements, and which has two advantages: i) it is independent of both image content and the number of gray levels used, and ii) application of a single operator using many different S.E.s can be computed somewhat more efficiently, which may be useful for granulometries [9, 2] and erosion dilation scale spaces [10]. Compared to Van Droogenbroeck and Talbot's method, it has the further advantage that it also works on floating point data.

II. ALGORITHM

Discussion here to discrete 2-D gray scale images f and erosion with 2-D flat S.E.s A . Be noted that our method can be easily modified for 3-D images and other morphological operation. All images f have their origin top-left and that images are processed in scan-line order.

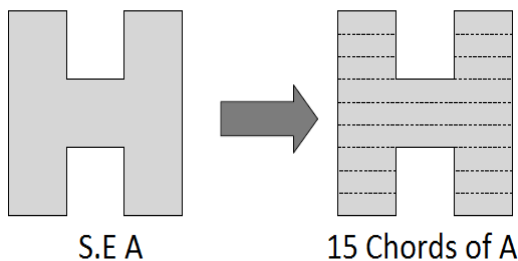


Fig. 1. decomposition of S.E. A into chords

Like the previous method, our approach to enhance the computational efficiency of erosion is by reducing the number the repeated comparisons performed by the implementation of its definition.

$$(f \ominus A) = \min_{z \in A} f(p + z) \quad (1)$$

Our algorithm disintegrates an arbitrary S.E. into a series of chords, i.e., runs of highlight pixels of maximum level as demonstrated in fig. for letter H. each chord is represented by a triplet containing.(i) its y -offset with respect to the origin of the S.E.,(ii) its minimal x -position, and (iii) its length l . For each S.E. the number chords the minimum and maximum y -offsets y_{min} and y_{max} , and minimum and maximum and minimum and maximum x -values x_{min} and x_{max} ,and the maximum chord length l_{max} occurring in A . Obviously, for each shifted S.E. we can compute the minimum value within the each chord, and compute for all chords with minimum of all chord-minimum, and also we compared minimum of all pixels within the shifted S.E. Other way to do this when a image processing in row y , is by creating an auxiliary 2-D array $W_v(i, x)$ for each image row v between $y - y_{min}$ and $y - y_{max}$. Each array start at index i runs from 0 to l_{max} , inclusive, and x from x_{min} to $X + x_{max} - 1$, including , with X the X dimension of image f . Each value $W_v(i, x)$ is defined asy

$$W_v(i, x) = \min_{u \in [x, x+i]} f(u, v) \quad (2)$$

In each array cab be computed in l_{max} comparisons per pixel.now compute the minimum over in $N_c - 1$ further comparisons per pixel. We compute for each value of x is $(f \ominus A)(x, y) = \min_{j \in \{0, 1, \dots, N_c - 1\}} \min_{y+y_j} (l, x + x_{min,j})$ (3)

In which $y_j, x_{min,j}$ and l_j denote the y -offset, length l of chord j and minimum x position. This version has a computational complexity per pixel of $O(l_{max} + N_c)$.

```

/* Copy image data into Wv(0, :)*
for (x = 0; x < X; x++)
Wv(0, x) = f(x, v);
/* Pad copied data on either side of copied row */
for (x = xmin; x < 0; x++)
Wv(0, x) = f(0, v);

```

```

for (x = X; x < X + xmax - 1; x++)
Wv(0, x) = f(X - 1, v);
/* Compute minima of runs of length 2n, starting at each x
*/
for (i = 1; i <= log2(lmax - 1); i++)
for (x = xmin; x < X + xmax - 1 - 2i - 1; x++)
Wv(i, x) = min(Wv(i-1, x), Wv(i-1, x+2i-1))

```

Fig. 2. Pseudo code for computing W_v in time proportional to $\log(l_{max})$

We can reduce both complexities using the following observation. We can compute the minimum of any chord length l_j from the minima of two run length of $2^n j$ with $n_j = \lceil \log_2(l_j - 1) \rceil$. If we modify our chord description to contain n , and two x values $x_{1,j} = x_{min,j}$ and $x_2 = x_{min,j} + l_j - 2^{n_j}$, we can compute the minimum of each chord by just one additional comparison per chord.

We only need to store $\lceil \log_2(l_{max} - 1) \rceil$ minimum values per pixel, which can be computed in $\lceil \log_2(l_{max} - 1) \rceil - 1$ comparisons per pixel, as shown in figure 2. Our computation for the erosion now becomes

$$(f \ominus A)(x, y) = \min_{j \in \{0, 1, \dots, N_c - 1\}} (\min(W_{y+y_j}(n_j, x + x_{1,j}), (W_{y+y_j}(n_j, x + x_{2,j}))) \quad (4)$$

In which $x_{1,j}$ and $x_{2,j}$ are the x_1 and x_2 values of chord j . This means we can compute any erosion for any structuring element in time and memory complexity $O(N_c + \log l_{max})$ per pixel. Figure 3 shows the pseudo code for computing the erosion on a single line. The algorithm mention above regarding image content is independent in its time complexity, unlike the method of Van Droogenbroek and Talbot [1]. Both their method and our method extend readily to 3-D. In our case we need to augment the S.E. with az_{min} and z_{max} , each chord with a z -offset, and the arrays W_v , need to be replaced by $W_{v,z}$.

```

/* Compute the minima for the first chord */
for (x = 0; x < X; x++)
g(x, y) = min(Wy+y0(n0, x + x1,0),
Wy+y0(n0, x + x2,0));
/* Compute for all other chords */
for (j = 1; j <= Nc; j++)
for (x = 0; x < X; x++)
g(x, y) = min(g(x, y), Wy+y0(n0, x + x1,j),
Wy+y0(n0, x + x2,j));

```

Fig.3. Pseudo code for performing the erosion on one image line, in which the output image line is given by $g(x, y)$.

This shows that one comparison per pixel for the first chord of the S.E. is needed, and two per pixel for each next one.

II. ARCHITECTURE DIAGRAM

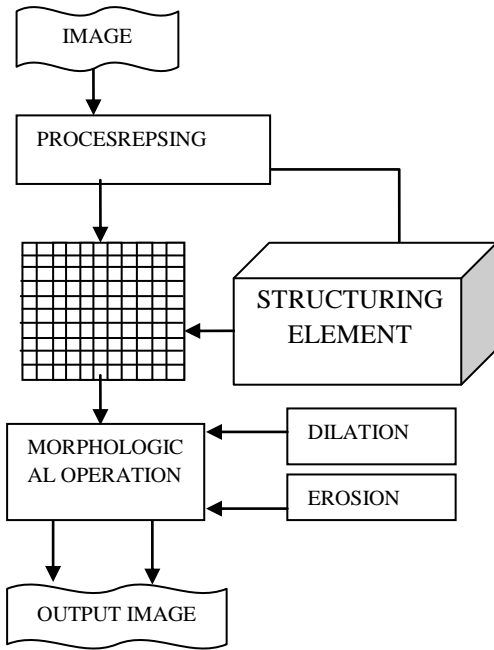


Fig. 4. Architecture diagram

V. EXPERIMENTS

In our method we can optimise the computation time with direct implementation, here we only consider foreground pixels of the S.E. and the algorithm of Van Droogenbroeck and Talbot's [1] method using circular, H-shaped, checkerboard, rectangular, and octagon structuring elements to applied on two bit 2160 x 1440 gray scale images. For the comparison of the computation time of the native program and the program developed, we consider the foreground pixels of the image, with the usage of Van Droogenbroeck and Talbot's using the circular, check board, octagon, rectangular and H-shaped structuring elements are applied to two bit 2160 x 1440 gray scale. In this process the noise distribution in the original and the generated image are uniform. Further in order to measure the affect of gray scale numbers on the computation time of the process the original image is converted to the 16 bit version and then varying the gray scale value of the image. The Fig. 5&6 shows the computation time for the system configuration of 2.26 GHZ Intel core i3 processor based on PC, with 3 GB of RAM. A thin letter of H S.E and the circular S.E of increasing width were taken as the shapes of S.E. As discussed previously, the computation time required for the operators shape and size of the image with our method is much more reduced compared to all the other methods taken individually.

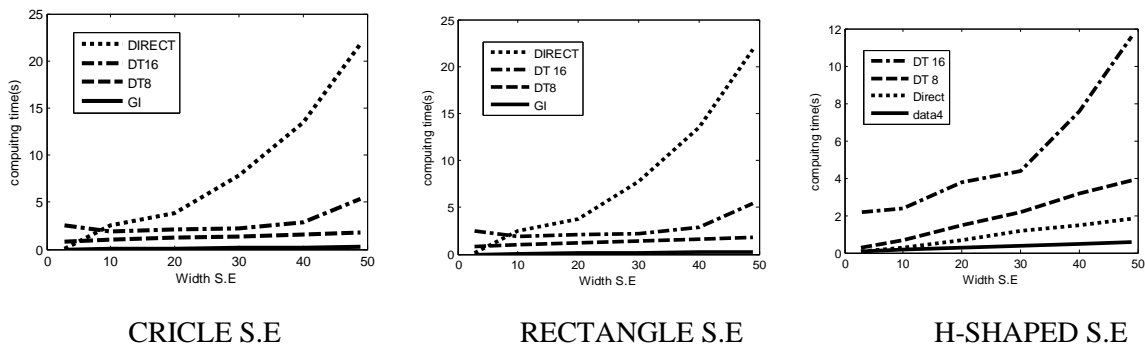


Fig. 5 required computing time for erosions with strutting element circle(left) ,rectangular(middle), H-shaped(left) using naive method, the Van Droogenbroeck- Talbot(DT8 and DT16),and our proposed (GI) algorithm on a natural image.

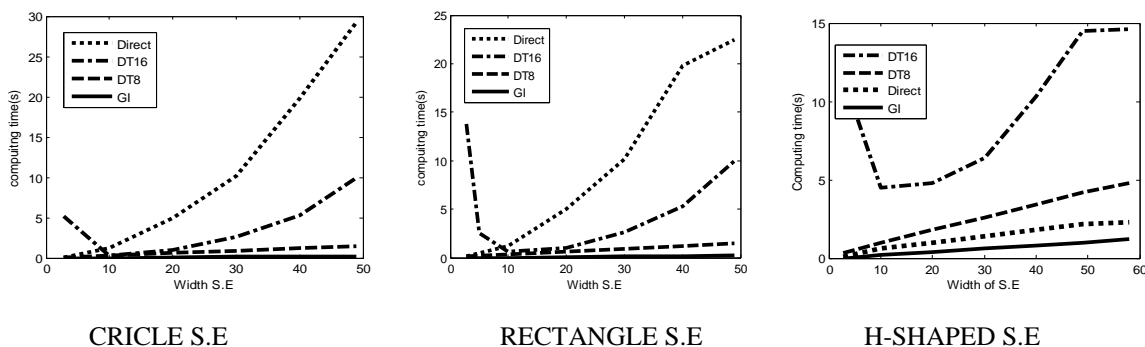


Fig.6 required computing time for erosions with strutting element circle(left) ,rectangular(middle), H-shaped(left) using naive method, the Van Droogenbroeck- Talbot(DT8 and DT16),and our proposed (GI) algorithm on a noise image.

To estimate the speed gain of this method called “New multi erode”, the process was compared with the computation time of the existing method referred to as “DT many erode” and our method. From the fig it is very much evident that the method proposed has more execution speed compared to

the existing method. For the 8-bit original image, the computation times are as follows: single erosion with a circle of diameter 49 – 2.03 sec for DT method, the computation time for the same diameter in the native method is 1.15 sec and for our method is 0.99s. A the

computation time for our methods is not dependent on the number of gray levels in the image, 16 bit and 8 bit images gives almost the same computation time. Even on the floating data only 30% speed had to be compromised. The existing method is not so dense when a very small S.Es are used with a 16-bit image, The fig refers to the same and give the reason for the long computing time for the smallest circular S.E. when the low perimeter area ratio such as circular and square are considered our method and the existing DT method gives the highest speed gain compared to the native method. The fig also shows the computation time for the thin letter shaped S.E instead of circle. The computation time for the single erosion using the letter H of width 49 on the 8-bit natural image are 3.96s, 5.51s and 2.31 for the DT method, native method and our method respectively. While the DT method needed 10.90s, for the 16-bit image. Finally our method offers a small improvement of 10 % over the existing methods called as “many-erode” version, as expected. It should be noted that the equal sized S.E with different shapes gives a reduction in the computation time instead of using the increasingly sized S.Es. the algorithm shows no change in the computing time between different images with the same size. The main difference in the computation time for the image is due to the difference in the scales being used due the difference in the computing time for the Van Droogenbroeck and Talbot algorithm [1].

V. CONCLUSION

An advanced method was proposed with arbitrary 2-D flat structuring elements to compute morphological operations. The method which was proposed is independent of the number of grey levels in the image called computational complexity. This method has good computational performance compared to other existing methods, when S.E.s are used that cannot be easily decomposed into linear structuring elements. A single operator like the computation of the granulometries and dilation or erosion scale spaces are used on multiple S.E.s, better improvement is achieved. Afterwards the results are compared and computed once were stored in an auxiliary array, and reused for filtering of all succeeding S.E.s i.e; existing DT method arbitrary S.E.s can be used. Our advanced method performs very well compared to the existing method; mainly the applications which have the images with higher bit depth as common like medical imaging are used. Other than this improvement our advanced method can handle floating point images easily which is not possible in the DT method.

REFERENCES

- [1] Marc Van Droogenbroeck and Hugues Talbot, “Fast computation of morphological operations with arbitrary structuring elements,” *Pattern Recogn. Lett.*, vol. 17, pp.1451–1460, 1996.
- [2] S. Batman and E. R. Dougherty, “Size distributions for multivariate morphological granulometries: Texture classification and statistical properties,” *Opt. Eng.*, vol. 36, no. 5, pp. 1518–1529, May 1997.
- [3] M. van Herk, “A fast algorithm for local minimum and maximum filters on rectangular and octagonal

- kernels,” *Pattern Recogn. Lett.*, vol. 13, pp. 517–521, 1992.
- [4] M. Van Droogenbroeck and M.J. Buckley, “Morphological erosions and openings: Fast algorithms based on anchors”, *Journal of Mathematical Imaging and Vision*, vol. 22, pp. 121–142, 2005.
- [5] L. Vincent, “Morphological transformations of binary images with arbitrary structuring elements,” *Image Process.*, vol. 22, pp. 3–23, Jan. 1991.
- [6] H. Park and R. T. Chin, “Decomposition of arbitrarily shaped morphological structuring elements,” *IEEE Trans. Pattern Anal. Mach. Intell.*, vol. 17, no. 1, pp. 2–15, Jan. 1995.
- [7] Erik R. Urbach, Associate Member and Michael H. F. Wilkinson, “Efficient 2-D Gray scale Morphological Transformations with Arbitrary Flat Structuring Elements,” *IEEE Trans* vol. 17, no. 1, january 2008.
- [8] E. R. Urbach and M. H. Wilkinson, “Efficient 2-d grayscale dilations and erosions with arbitrary flat structuring elements,” *Proc. Int. Conf. Image Processing*, 2006, pp. 1573–1576.
- [9] J. Serra, “*Image Analysis and Mathematical Morphology*,” vol. 1, Academic Press, New York, 2 edition, 1982.
- [10] P. T. Jackway and M. Deriche, “Scale-space properties of the multiscale morphological dilation-erosion,” *IEEE Transactions on Pattern Analysis and Machine Intelligence*, vol. 18, pp. 38–51, 1996.

Author Profile



Ilayaraja AP, M.Tech degree in Computer Science and Engineering from VIT university Vellore 2012, B.E degree in Computer Science and Engineering from Saraswati velu college of engineering sholingur, India in 2010



Gopinath MP, working as Assistant professor in School of Computing Science and Engineering at VIT University, Vellore, India.

Power-Management Strategies for a Grid-Connected PV-FC Hybrid System By Using Fuzzy Logic Controller

P.PRADEEP KUMAR

M-Tech Scholar, Power systems,
Department of Electrical and Electronics Engineering,
K L University, Guntur (A.P), India.

B.KIRAN BABU

Assistant Professor,
Department of Electrical & Electronics Engineering,
K L University, Guntur (A.P), India.

ABSTRACT

This paper presents a method of maximum power point tracking, MPPT using adaptive fuzzy logic control for grid connected photovoltaic system. The system composed of photovoltaic module, boost converter and the fuzzy logic controller. The maximum power point tracking control is based on adaptive fuzzy logic to control ON/OFF time of MOSFET switch of boost converter. The complete simulation results using Simulink software for the whole system containing the PV array, boost converter, and fuzzy controller were presented. The control strategy for the boost converter and the whole system is carried out by using field programmable gate array (FPGA). The FPGA used is a Spartan 3E from Xilinx. The code of the control system is shown in VHDL language.

Index Terms- Maximum power point tracking, fuzzy logic controller ,photovoltaic array,Pemfc(proton exchange membrane fuel cell) model

Introduction

Renewable energy is currently widely used. One of these resources is solar energy. The photovoltaic (PV) array normally uses a maximum power point tracking (MPPT) technique to continuously deliver the highest power to the load when there are variations in irradiation and temperature. The disadvantage of PV energy is that the PV output power depends on weather conditions and cell temperature, making it an uncontrollable source. Furthermore, it is not available during the night. In order to overcome these inherent drawbacks, alternative sources, such as PEMFC, should be installed in the hybrid system. By changing the FC output power, the hybrid source output becomes controllable. However, PEMFC, in its turn, works only at a high efficiency within a specific power range [1], [2]. The hybrid system can either be connected to the main grid or work autonomously with respect to the grid-connected mode or islanded mode, respectively. In the grid-connected mode, the hybrid source is connected to the main grid at the point of common coupling (PCC) to deliver power to the load. When load demand changes, the power supplied by the main grid and hybrid system must be properly changed. The power delivered from the main grid and PV array as well as PEMFC must be coordinated to meet load demand. Generally the hybrid source has two control modes: 1) unit-power control (UPC) mode and feeder-flow control (FFC) mode. In the UPC mode, variations of load demand are compensated by the main grid because the hybrid source output is regulated to reference power. Therefore, the reference value of the hybrid source output must be determined. In the FFC mode, the feeder flow is regulated to a constant, the extra load demand is picked up by the hybrid source, and hence, the feeder reference power must be known. Here Fuzzy logic or fuzzy set theory is a new method of controlling the MPPT is implemented in obtaining the peak power point. It has the advantage of being robust, fast in response. Fuzzy controller operates in two basic modes coarse and fine modes. The proposed fuzzy operating strategy is to coordinate the two control modes and determine the reference values of the fuzzy control so that all constraints are satisfied. This operating strategy will minimize the number of operating mode changes, improve performance of the system operation, and enhance system stability.

2. SYSTEM DESCRIPTION

A. Structure of Grid-Connected Hybrid Power System The system consists of a PV-FC hybrid source with the main grid connecting to loads at the PCC as shown in Fig. 1.

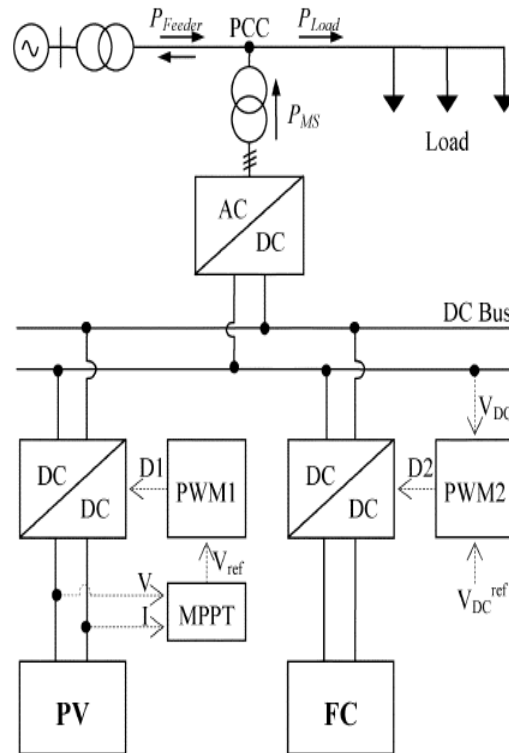


Fig. 1. Grid-connected PV-FC hybrid system.

The photovoltaic [3], [4] and the PEMFC [5], [6] are modelled as nonlinear voltage sources. These sources are connected to dc–dc converters which are coupled at the dc side of a dc/ac inverter.

The dc/dc connected to the PV array works as an MPPT controller. Many MPPT algorithms have been proposed in the literature, such as incremental conductance (INC), constant voltage (CV), and perturbation and observation (P&O). The P&O method has been widely used because of its simple feedback structure and fewer measured parameters [7]. The P&O algorithm with power feedback control [8]–[10] is shown in Fig. 2. As PV voltage and current are determined, the power is calculated. At the maximum power point, the derivative dp/dv is equal to zero. The maximum power point can be achieved by changing the reference voltage by the amount of Δv_{ref} .

B. PV Array Model

The mathematical model [3], [4] can be expressed as

$$I = I_{ph} - I_{sat} \{ \exp[q / AKT(V + I R_S)] - 1 \} \dots \dots \dots (1)$$

Equation (1) shows that the output characteristic of a solar cell is nonlinear and vitally affected by solar radiation, temperature, and load condition. Photocurrent I_{ph} is directly proportional to solar radiation G_a

$$I_{ph}(G_a) = I_{sc} G_a / G_{as} \dots \dots \dots (2)$$

The short-circuit current of solar cell I_{sc} depends linearly on cell temperature $I_{sc}(T) = I_{scs}[1 + \Delta I_{sc}(T - T_s)]$
 $\dots \dots \dots (3)$

Thus, I_{ph} depends on solar irradiance and cell temperature

$$I_{ph}(G_a, T) = I_{scs} G_a / G_{as} I_{scs}[1 + \Delta I_{sc}(T - T_s)] \dots \dots \dots (4)$$

I_{sat} depends on solar irradiation and cell temperature and can be mathematically expressed as follows

$$I_{sat}(G_a, T) = I_{ph}(G_a, T) / e(V_{oc}(T) / V_t(T)) - 1 \dots \dots \dots (5)$$

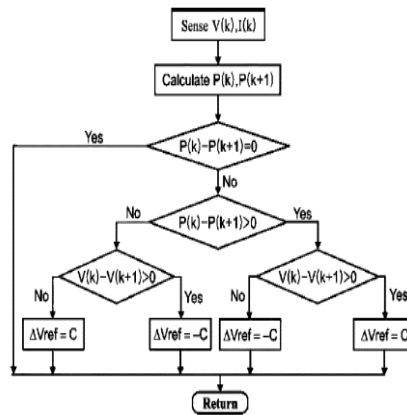


Fig. 2. P&O MPPT algorithm.

C. PEMFC Model

The PEMFC steady-state feature of a PEMFC source is assessed by means of a polarization curve, which shows the nonlinear relationship between the voltage and current density. The

PEMFC output voltage is as follows [5]:

$$V_{out} = E_{Nerst} - V_{act} - V_{ohm} - V_{conc} \dots\dots\dots (6)$$

Where E_{Nerst} is the “thermodynamic potential” of Nerst, which represents the reversible (or open-circuit) voltage of the fuel cell. Activation voltage drop V_{act} is given tafel equation as

$$V_{act} = T[a + b \ln(I)] \dots\dots\dots (7)$$

where are the constant terms in the Tafel equation (in volts per Kelvin). The overall ohmic voltage drop V_{ohm} can be expressed as

$$V_{ohm} = IR_{ohm} \dots\dots\dots (8)$$

The ohmic resistance

R_{ohm} of PEMFC consists of the resistance of the polymer membrane and electrodes, and the resistances of the electrodes .The concentration voltage drop V_{conc} can be expressed as

$$V_{conc} = -(RT / ZF) \ln(1 - I / I_{limit}) \dots\dots\dots (9)$$

3. 1. Fuzzy Controller

Fuzzy logic or fuzzy set theory is a new method of controlling the MPPT in obtaining the peak power point. It has the advantage of being robust, fast in response . Fuzzy controller operates in two basic modes coarse and fine modes. Input variables of fuzzy controller are dp_{ph} / dI_{ph} (where P_{ph} is PV array output power and I_{ph} is PV array output current) and Change of it. These variables are expressed in terms of linguistic variables or labels such as PB (positive big), PS (positive small), ZE (zero), NS (negative small), NB (positive big) using basic fuzzy subset. There are three stages in this control algorithm, namely fuzzification, inference method and defuzzification. An error function (E) and a change of error (ΔE) are created during fuzzification. These variables are then compared to a set of pre-designed values during inference method, in order to determine the appropriate response. Defuzzification is for converting the fuzzy subset of control form inference back to values. The E and ΔE function is compared to the graph a & b to obtain a variable NB or ZE, then this parameter will be used to locate the respective the output function (dD) from the fuzzy rule table.

ΔE \ E	NB	NS	ZE	PS	PB
NB	ZE	ZE	NB	NB	NB
NS	ZE	ZE	NS	NS	NS
ZE	NS	ZE	ZE	ZE	PS
PS	PS	PS	PS	ZE	ZE
PB	PB	PB	PB	ZE	ZE

Table 1. Fuzzy rule Table

This is the table of prefixed scales, which indicates the “location” of the peak power point A perturb and observe method is employed in the project due to the easy manipulation of the module and more importantly, low power loss through the process.

The IncCond method only offers little improvement over the P&O method underslowly changing atmospheric conditions. Different modules and schemes have been used to implement peak power point tracking using a microcontroller. One of those techniques which are often used is one that based on the dP/dV method . Other methods include heavy mathematical calculation and modeling . Due to the lack of resource on the PIC microcontroller and the complexity in programming, mathematical modeling method is not recommended. On the other hand, dP/dV method offers simpler design and quicker response as well as a stable solution. Therefore it is used in this work. It also offers several other useful features such as good steady state and transient response, flexibility in the control algorithm.

3.2 Logic Controller

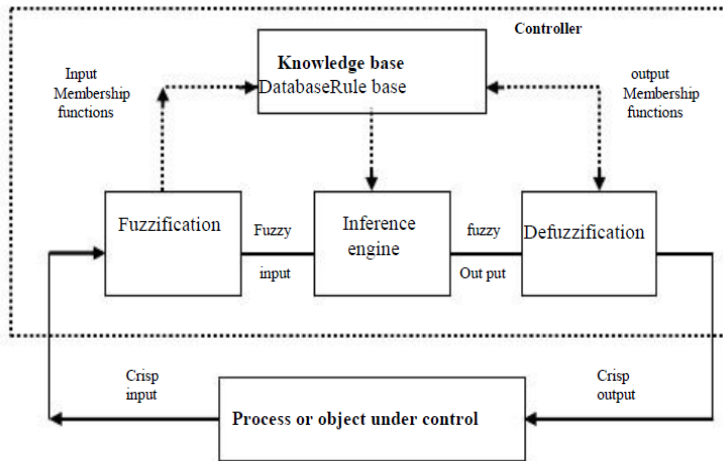


Figure.16 The fuzzy logic controller (a basic structure)

3.2.1 Fuzzy Knowledge Base Controller

The fuzzy knowledge base controller is basic part of fuzzy logic control which is composed of 3 parts: fuzzification, inference engine and defuzzification as we shown in the figure.16 and we will described below.

1) Fuzzification

Membership function’s value are assigned to the linguistic variables, using seven fuzzy subsets : NB (Negative Big), NM(Negative Medium), NS (Negative small), ZE (Zero), PS (Positive small), PM (Positive Medium), and PB (Positive Big). The partition of fuzzy subsets and the shape of membership function which can adapt shape up to appropriate system are shown in Fig.16. The value of error (e) and change of error (de) are normalized by input scaling factor β_e and β_{de} . In this system input scaling has designed between -1 to 1.

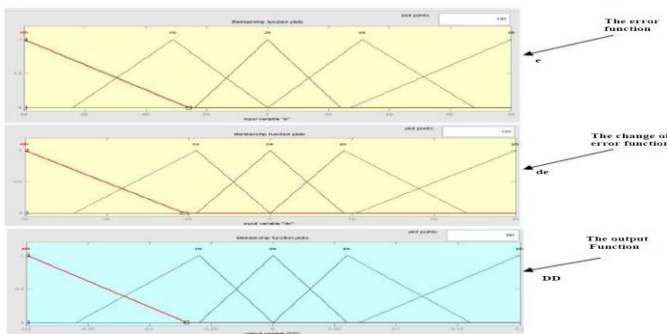


Figure.17 Fuzzy logic membership function after tuning.

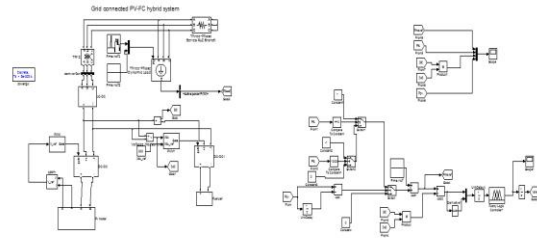
2) Inference Method

The composition operation by which a control output can be generated. Several composition methods such as MAX-MIN and MAX-DOT have been proposed in the literature. The commonly used method is MAX-MIN (AND connection) as we used in our search . The output membership function of each rule is given by the MIN (minimum)

operator, MAX(maximum) operator. Table 2 shows the rule table for fuzzy logic controller.

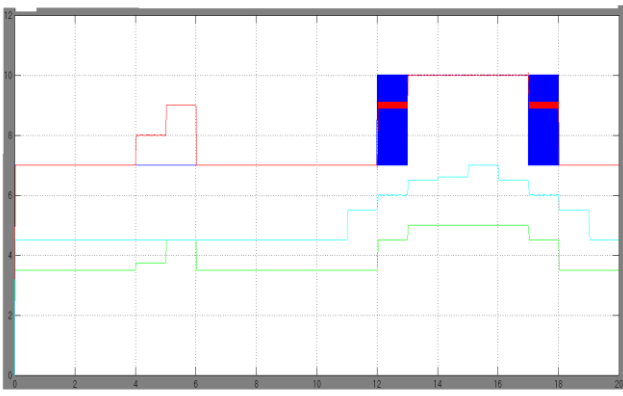
(3) Defuzzification: As the plant usually required a nonfuzzy value of control, a defuzzification stage is needed. Defuzzification for this system is the height method. The height method is both very simple and very fast method.

Matlab based simulink model

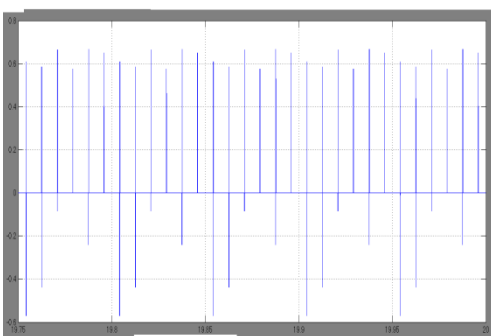


Simulation Results Without hysteresis

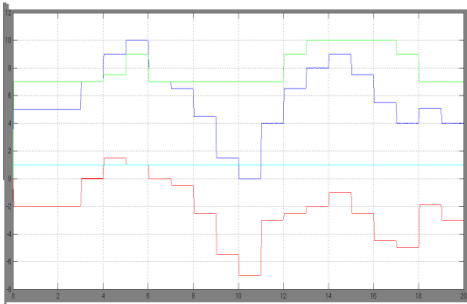
1.a).Operation Strategy of the Whole System



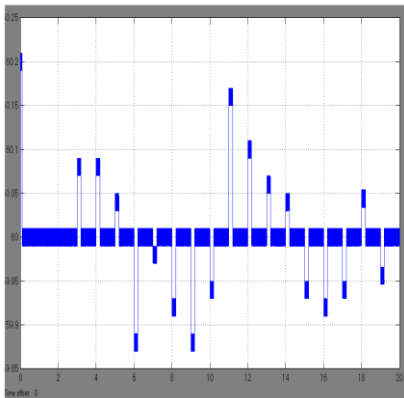
b. Changing of the operating modes



2. a. Operating Strategy of the whole system

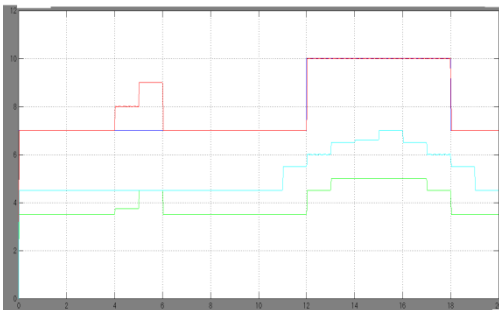


b. Change of operating modes:



3. Improving operating performance by using hysteresis

a. The operating strategy of the hybrid source

**Conclusion:**

The method of maximum power point tracking, MPPT using adaptive control for grid connected photovoltaic system is presented for better performance of the whole system. The maximum power point tracking control is based on adaptive fuzzy logic to control ON/OFF time of MOSFET switch of boost converter. The complete simulation results are shown by using Simulink software for the whole system containing the PV array, boost converter, and fuzzy controller are also shown above.

References:

- [1] T. Bocklisch, W. Schufft, and S. Bocklisch, "Predictive and optimizing energy management of photovoltaic fuel cell hybrid systems with shorttime energy storage," in Proc. 4th Eur. Conf. PV-Hybrid and Mini-grid 2008, pp.8-15.
- [2] J. Larminie and A. Dicks, Fuel Cell Systems Explained. New York: Wiley, 2003.
- [3] W. Xiao, W. Dunford, and A. Capel, "A novel modeling method for cells," in Proc. IEEE 35th Annu. Power Electronics Specialists Conf.,
- [4] D. Sera, R. Teodorescu and P. Rodriguez, "PV panel model based on datasheet values," in Proc. IEEE Int. Symp. Industrial Electronics, Jun. 4-7, 2007, pp. 2392-2396.
- [5] C. Wang, M. H. Nehrir, and S. R. Shaw, "Dynamic models and model validation for PEM fuel cells using electrical circuits," IEEE Trans. Energy Convers, vol. 20, no. 2, pp. 442-451, Jun. 2005.

- [8] C. Hua and C. Shen, "Comparative study of peak power tracking techniques for solar storage system," in Proc. 13th Annu. Applied Power Electronics Conf. Expo., Feb. 1998, vol. 2, pp. 679–685.
- [9] A. Hajizadeh and M. A. Golkar, "Power flow control of grid-connected fuel cell distributed generation systems," J. Elect. Eng. Technol., vol. 3, no. 2, pp. 143–151, 2008.
- [10] C. Hua and J. R. Lin, "DSP-based controller application in battery validation for PEM fuel cells using electrical circuits," IEEE Trans.
- [11] Energy Convers., vol. 20, no. 2, pp. 442–451, Jun. 2005.
- [12] C. Hua and C. Shen, "Comparative study of peak power tracking techniques for solar storage system," in Proc. 13th Annu. Applied Power Electronics Conf. Expo., Feb. 1998, vol. 2, pp. 679–685.
- [13] A. Hajizadeh and M. A. Golkar, "Power flow control of grid-connected fuel cell distributed generation systems," J. Elect. Eng. Technol., vol. 3, no. 2, pp. 143–151, 2008.
- [14] C. Hua and J. R. Lin, "DSP-based controller application in battery storage of photovoltaic system," in Proc. 22nd IEEE Int. Conf. Industrial Electronics, Control, and Instrumentation, Aug. 5–10, 1996, vol. 3, pp. 1750–1810.
- [15] C. Hua, J. Lin, and C. Shen, "Implementation of a DSP-controlled photovoltaic system with peak power tracking," IEEE Trans. Ind. Electron., vol. 45, no. 1, pp. 99–107, Feb. 1998.
- [16] E. Koutroulism and K. Kaalitzakis, "Development of a microcontroller- based, photovoltaic maximum power point tracking control system," IEEE Trans. Power Electron., vol. 16, no. 1, pp. 46–54, Jan. 2001.
- [17] N. Mohan, T. M. Undeland, and W. P. Robbins, Power Electronics, Converters, Applications and Design, 2nd ed. New York: Wiley,

ENERGY FROM THE EXISTING RESOURCES

***J.BANUCHANDAR, *S.DEEPA, *N.TAMILARASI,
#J.PARKAVI**

*Electronics and Communication Engineering,
P.SR Engineering College, sivakasi
#Electrical and Electronics Engineering,
Mepeco Schlenk Engineering college, sivakasi

ABSTRACT:

In the upcoming years the electrical energy will be the main source for world's growth. We all know that the consumption of electrical energy is increasing whereas the resources are depleting. Terrestrial renewable systems (hydroelectric, geothermal, ocean thermal, waves, and tides) cannot dependably provide adequate power. However expanding nuclear fission power would require breeder reactors, but there is intense political resistance to that idea because of concerns about proliferation, nuclear contamination of the environment, and cost So we have to switch over to renewable energy resources. Over the 21-st century, a global stand-alone system for renewable power would cost thousands of trillions of dollars to build and maintain. Energy costs could consume most of the world's wealth. We need a power system that is independent of earth's biosphere and provides an abundant energy at low cost. In this paper we are discussing how our natural satellite MOON can help us in such case. We have explored the space enough to build space laboratories. It is also possible to build a power station in moon as we have adequate knowledge on robotics. Moreover, we have construction materials in moon which reduces the erection cost as well as the transportation cost. Moon gets more sunlight than earth and it has abundant quantity of Helium-3 resources which is not present on earth. Here we are describing the power production methods from Solar and Helium-3 resources in moon. Also we are describing the power transmission from moon to earth via Microwaves.

INTRODUCTION:

Prosperity for everyone on Earth by 2050 will require a sustainable source of electricity equivalent to 3 to 5 times the commercial power currently produced. Because of the low average incomes in developing countries like India, however, this energy must be provided at one-tenth the present total cost per kilowatt-hour

Currently, commercial energy production on Earth raises concerns about pollution, safety, reliability of supply, and cost. These concerns grow as the world's nations begin to expand existing systems to power a more prosperous world. Such growth could exhaust coal, oil, and natural gas reserves in less than a century, while the production and burning of these fossil fuels pollute the biosphere. The new system we are going to adopt should be eco-friendly, economic and should satisfy the future energy requirements. . Lunar power stations constructed on the moon from common lunar materials could provide the clean, safe, low-cost commercial electric energy needed on Earth.

In this paper we are going to discuss two methods of getting energy from moon.

- Lunar Solar Power Station
- Lunar Helium-3 Power Station
- Micro wave Power Transmission

LUNAR SOLAR POWER GENERATION:

Although energy coming directly to Earth from the sun is renewable, weather makes the supply variable. Very advanced technologies, such as 30% efficient solar cells coupled with superconducting power transmission and storage, imply solar arrays that would occupy more space on earth rather than in moon. The 10 billion people living on Earth in 2050 will require 20 Terawatts (TW) of power. The Moon receives 13,000 TW of power from the sun. It is evident that harnessing just 1% of the solar power and directing it toward Earth could replace fossil fuel power plants on Earth.

LUNAR SOLAR COLLECTORS:

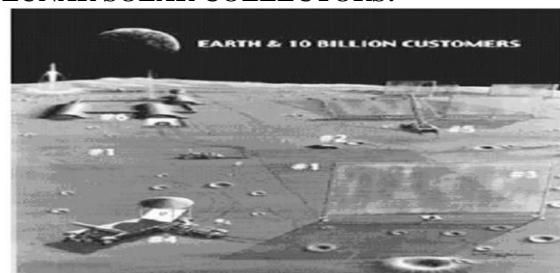


Figure 1. In this lunar power base, sunlight hits the solar converter, which transmits power via underground wires to a microwave generator, which in turn illuminates a microwave reflector. All such reflectors, when viewed from Earth, overlap to form a "lens" that can direct a narrow power beam toward Earth.

- 1).Solar converter.
- 2).Microwave generator.
- 3).Microwave reflector.
- 4).Mobile factory.
- 5).Assembly units.
- 6). Habitat / Manufacturing units

The LSP System uses 10 to 20 pairs of bases—one of each pair on the eastern edge and the other on the western edge of the moon, as seen from Earth—to collect on the order of 1% of the solar power reaching the lunar surface.

The moon receives sunlight continuously except during a full lunar eclipse, which occurs approximately once a year and lasts for less than three hours. Each lunar power base consists of tens of thousands of power plots distributed in an elliptical area to form fully segmented, phased-array radar that is solar-powered. Each demonstration power plot consists of four major subsystems. Solar cells collect sunlight and buried electrical wires (not shown) carry the solar energy as electric power to microwave generators. Basically Solar cells usually operate more efficiently under concentrated light. The manufactures are developing concentrators which further increase the cost to improve the solar cell efficiency. In our case there is no need of any concentrators as the moon can receive the sunlight without any obstacles and hence the cost gets reduced.

LUNAR HELIUM-3 POWER GENERATION:

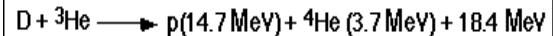
HELIUM-3:

Helium-3 (He-3) is a light, non-radioactive isotope of helium with two protons and one neutron. Helium-3 is magnificent and an environmentally friendly fuel, an effective energy source. But unfortunately it is not found on Earth, while the Moon has vast resources of it. The helium-3 will be extracted by the lunar bulldozers. The amounts of helium-3 needed as a replacement for conventional fuels should not be underestimated. Scientists estimate there are about 1 million tons of helium 3 on the moon, enough to power the world for thousands of years. Helium-3 has the potential to be the fuel for a new generation of clean nuclear fusion power plants. Unfortunately, helium-3 is also exceptionally rare on the Earth. There is, however, thought to be an abundant supply of helium-3 on the surface of the Moon. NASA, some Russian corporations, China and India have therefore announced plans or

intentions to establish bases on the Moon over the next couple of decades in order to mine helium-3.

Given that one Space Shuttle cargo bay of helium-3 could power the United States for a year, a new helium-3 Space Race and related infrastructure development may become one of the most significant aspirations and accomplishments in human history. Mining lunar helium-3 may also become a large part of our "solution" to the oil shortage, broader fossil fuel depletion, and climate change.

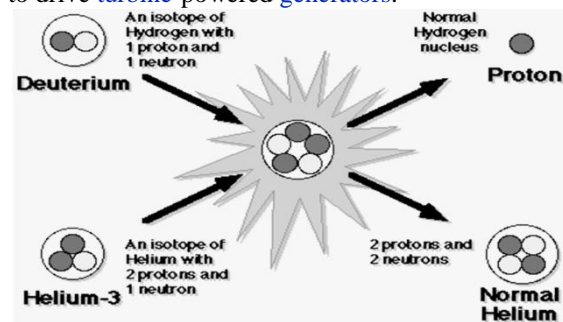
ENERGY PRODUCTION:



The total amount of energy produced in the ${}^3\text{He} + {}^2_1\text{H}$ reaction is 18.4 MeV, which corresponds to some 493 megawatt-hours (4.93e8 Wh) per three grams (one mole) of ${}^3\text{He}$. A second-generation approach to controlled fusion power involves combining helium-3 (${}^3_2\text{He}$) and deuterium (${}^2_1\text{H}$). This reaction produces a helium-4 ion (${}^4_2\text{He}$) and a high-energy proton positively charged hydrogen ion (${}^1_1\text{p}$) and (alpha particle). There is no radiation threat of helium-3 fusion as the life time of radioactive proton is very less than that of fission.

CONVERSION TO ELECTRICAL ENERGY:

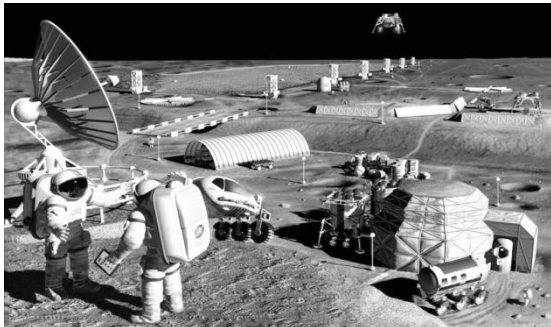
The most important potential advantage of this fusion reaction for power production as well as other applications lies in its compatibility with the use of electrostatic fields to control fuel ions and the fusion protons. Protons, as positively charged particles, can be converted directly into electricity, through use of solid-state conversion materials as well as other techniques. Potential conversion efficiencies of 70 percent may be possible, as there is no need to convert proton energy to heat in order to drive turbine-powered generators.



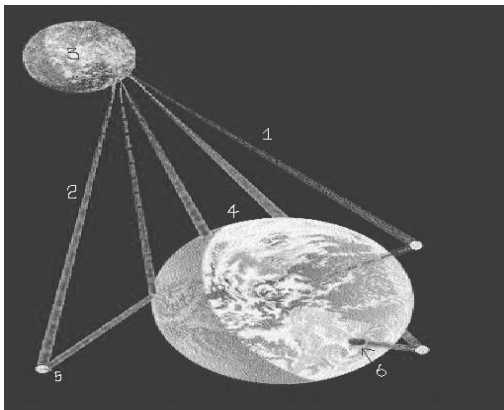
CONSTRUCTION:

One of the most significant steps towards self-sufficiency and independence from the Earth will be the use of lunar materials for construction. At least seven major potential lunar construction materials have been identified. These include concrete, sulfur concrete, cast basalt, sintered basalt, fiber glass, cast glass, metals. All of these materials may be used to construct a future

lunar base. The basalt materials can be formed out of lunar regolith (soil) by a simple process of heating and cooling, and are the most likely to be used to build the first bases.



With the gravity level of the moon being 1/6th that of Earth, lunar structures can carry a load that is six times that of those on Earth. This allows for structures that are thicker and can provide better micrometeorite, radiation and thermal shielding for the crew. Researchers designed solar-powered robotic equipment that would scoop up the top layer of lunar soil and place it into a robotic unit. The soil would be heated, thus separating the helium-3 from other lunar material. The spent material then would be dropped off the back of the moving robotic miner. Because the Moon has one-sixth the Earth's gravity, relatively little energy would be required to lift the material.



ADVANTAGES:

There are so many advantages in installing power plants on moon. They are
Unlike Earth, the surface of the moon is compatible with the construction of extremely large areas of thin solar collectors and their dependable operation over many decades.
No oxygen, water, atmospheric chemicals, or life is present to attack and degrade thin solar collectors.
No wind, rain, ice, fog, sleet, hail, driven dust, or volcanic ash will coat and mechanically degrade them.
Moonquakes and meteor impacts produce only tens of nanometers of ground motion. Micro meteors erode thin solar collectors less than 1 mm every 1 million years. Rectenna are projected to cost approximately \$0.004/kWe•h, which is less than

one-tenth of the current cost of most commercial electric energy

The production of lunar base requires the components which can be get from the moon itself. Bulk soil and separated soil fractions can be melted by concentrated sunlight and formed into thin glass sheets and fibers or sintered into rods, tubes, bricks, and more complex components. Silicon, aluminum, and iron can be chemically extracted from lunar soil for fabrication of solar cells. This reduces erection cost.

Helium-3 would offer lower capital and **operating costs** than their competitors due to less technical complexity, higher conversion efficiency, smaller size, the absence of radioactive fuel, no air or water **pollution**.

CONCLUSION:

The Lunar Power System is a reasonable alternative to supply earth's needs for commercial energy without the undesirable characteristics of current options. The system can be built on the moon from lunar materials and operated on the moon and on Earth using existing technologies. More-advanced production and operating technologies will significantly reduce up-front and production costs. The energy beamed to Earth is clean, safe, and reliable.

ACKNOWLEDGMENT

We would like to express our sincere thank to our beloved principal, staff members and special thanks to our friends Kaliraj and Balasubramanian.

The materials available with the listed reference books have a significant impact on this paper. We gratefully thank to the authors and publications of these reference books.

REFERENCE

1. Mark Z. Jacobson and Mark A. Delucchi (30 December 2010). "Providing all global energy with wind, water, and solar power, Part I: Technologies, energy resources, quantities and areas of infrastructure, and materials". *Energy Policy*. Elsevier Ltd.
2. **Renewable energy costs drop in '09** *Reuters*, November 23, 2009.
3. **Solar Power 50% Cheaper By Year End - Analysis** *Reuters*, November 24, 2009.
4. Henning Gloystein (Nov 23, 2011). "Renewable energy becoming cost competitive, IEA says". *Reuters*.
5. "GWEC, Global Wind Report Annual Market Update". Gwec.net. Retrieved 2011-11-21.
6. David Beattie (18 March 2011). "Wind Power: China Picks Up Pace". *Renewable Energy World*.

EYE FOR THE VISUALLY IMPAIRED

***J.BANUCHANDAR, *S.DEEPA, *N.TAMILARASI, #J.PARKAVI**

*Electronics and Communication Engineering,
P.SR Engineering College, sivakasi

#Electrical and Electronics Engineering,
Mepco Schlenk Engineering college, sivakasi

Abstract

The Robotic sonar stick is a novel device designed to help blind or visually impaired users navigate safely and quickly among obstacles and other hazards. During operation, the user pushes the lightweight Robotic sonar stick forward. When the Robotic sonar stick's ultrasonic sensors detect an obstacle, the embedded computer determines a suitable direction of motion that steers the Robotic sonar stick and the user around it. The steering action results in a very noticeable force felt in the handle, which easily guides the user without any conscious effort on his/her part .

I. INTRODUCTION

Many of the visually challenged persons use the white cane – the most successful and widely used travel aid for the blind. This purely mechanical device is used to detect obstacles on the ground, uneven surfaces, holes, steps, and other hazards. The inexpensive white cane is so lightweight and small that it can be folded and slipped into a pocket. The main problem with this device is that users must be trained in its use for more than 100 hours – a substantial “hidden” cost. In addition, the white cane requires the user to actively scan the small area ahead of him/her. The white cane is also not suited for detecting potentially dangerous obstacles at head level. Guide dogs are very capable guides for the blind, but they require extensive training. Fully trained guide dogs cost between \$12,000 and \$20,000, and they are only useful for about five years. Furthermore, many blind and visually impaired people are elderly and find it difficult to care appropriately for another living being.

During the past three decades, several researchers have introduced devices that use sensor technology to improve the blind users' mobility in terms of safety and speed. Examples of these devices, collectively called Electronic Travel Aids (ETAs), are the C-5 Laser Cane, the Mowat Sensor, the Nottingham Obstacle Detector, and the Sonicguide.

These ETAs, however, have not found wide use among their targeted users, likely because the utility of this group of systems is limited. In particular, conventional ETAs suffer from the following three fundamental shortcomings:

- 1) The user must actively scan the environment to detect obstacles (no scanning is needed with the Sonic guide, but it does not detect obstacles at floor level). This procedure is time-consuming and requires the user's constant activity and conscious effort.
- 2) The user must perform additional measurements when an obstacle is detected in order to determine the dimensions and shape of the object. The user must then plan a path around the obstacle. Again, a time-consuming, conscious effort that reduces the walking speed.
- 3) Another problem with all ETAs based on acoustic feedback is their interference (called masking) with sound cues from the environment, reducing the blind person's ability to hear these essential cues .

II. THE ROBOTIC SONAR STICK CONCEPT

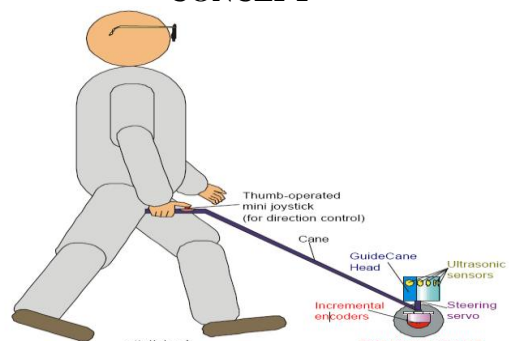


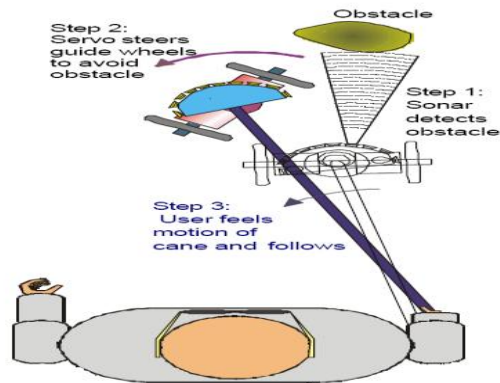
Figure 1: Functional components of the GuideCane.

Figure 1 shows a schematic view of the Robotic sonar stick and its functional components. Much like the widely used white cane, the user holds the Robotic sonar stick in front of himself/herself while walking.

The Robotic sonar stick is considerably heavier than the white cane, but it rolls on passive wheels that support its weight during regular operation. Both wheels are equipped with encoders to determine the relative motion. A servomotor,

controlled by the built-in computer, can steer the wheels left and right relative to the cane. To detect obstacles, the Robotic sonar stick is equipped with ten ultrasonic sensors. A mini joystick located at the handle allows the user to specify a desired direction of motion.

Functional Description



During operation, the user pushes the Robotic sonar stick forward. While traveling, the ultrasonic sensors detect obstacles in a 120° wide sector ahead of the user (see Step 1 in Figure 2). Based on the sonar and encoder data, the embedded computer instantaneously determines an appropriate direction of travel. If an obstacle blocks the desired travel direction, then the obstacle avoidance algorithm prescribes an alternative direction that clears the obstacle and then resumes in the original direction (see Step 2 in Figure 2). Once the wheels begin to steer sideways to avoid the obstacle, the user feels the resulting horizontal rotation of the cane (see Step 3 in Figure 2). In a fully intuitive response, requiring virtually no training time, the user changes his/her orientation to align him/her with the cane at the “nominal” angle. In practice, the user’s walking trajectory follows the trajectory of the Robotic sonar stick similar to the way a trailer follows a truck. Because of the handle’s short length, the user’s trajectory is very close to the Robotic sonar stick’s trajectory. Once the obstacle is cleared, the wheels steer back to the original direction of travel. The new line of travel will be offset from the original line of travel. Depending on the circumstances, the user may wish to continue walking along this new line of travel, or the system can be programmed to return to the original line of travel. This latter option is made possible by the Robotic sonar stick’s dead-reckoning capability.

The user can prescribe a desired direction of motion with the thumb-operated mini joystick. This directional command is discretized into eight directions and is understood to be relative to the Robotic sonar stick’s current direction of motion. For example, if the user presses the button to the left, then the computer adds 90° to the current

direction of motion and, as soon as the new desired motion of travel is free of obstacles, steers the wheels to the left until the 90° left turn is completed. It is important to note that the user can usually indicate a new direction well before the change of direction should occur. In the case of a corridor, if the user presses the button to the left, then the Robotic sonar stick will continue down the corridor until it reaches an intersection or an open door where it can turn to the left. The ability to indicate a desired direction of motion in advance significantly enhances the Robotic sonar stick’s ease-of-use.

The detection of stairs is a particular problem for most ETAs. The Robotic sonar stick offers separate solutions for down steps and up-steps. Down-steps are detected in a fail-safe manner: when a down-step is encountered, the wheels of the Robotic sonar stick drop off the edge until the shock-absorbing bottom hits the step – without a doubt a signal that the user can not miss. Because the user walks about 60 cm behind the Robotic sonar stick, he/she has enough time to stop. Up steps can be detected by additional front-facing sonars as described in; however, this method has not yet been implemented in the Robotic sonar stick. Because the Robotic sonar stick is compact and lightweight, it can easily be lifted up whenever the user needs to cope with stairs

Conventional ETAs are designed to notify the user of obstacles, usually requiring the user to perform additional scanning once the obstacle is detected. The user must evaluate all of the obstacle information, which comprises of the size and proximity of each obstacle, and then decide on a suitable travel direction. In sighted people, such relatively high bandwidth information is processed almost reflexively, usually without the need for conscious decisions. Nature had millions of years of evolution to perfect this skill. However, the evaluation of obstacle information presented by acoustic or tactile signals is a new skill that must be acquired over hundreds of hours of learning. Even then, exercising such a skill requires a great deal of conscious effort, and thus processing time. The required effort further increases with the number of detected obstacles. The Robotic sonar stick is fundamentally different from other devices in that it first analyzes the environment and then computes the momentary optimal direction of travel. The resulting guidance signal is a single piece of information – a direction – which substantially .consequence, it is far easier and safer to follow the low-bandwidth guidance signal of the Robotic sonar stick than to follow the high-bandwidth information of other existing systems. However, reducing the high-bandwidth obstacle information to a momentary optimal direction of travel requires

the implementation of a reliable obstacle avoidance system.

Information Transfer

This advantage can be credited to another unique feature of the Robotic sonar stick: information transfer through direct physical force (also called “haptic display” in the scientific literature). This process is completely intuitive so that everybody can use the system right away without learning how to interpret artificially defined acoustic or tactile signals, as with conventional ETAs. Yielding to external forces is a reflexive process that does not require a conscious effort. Moreover, many blind persons are accustomed to being guided by sighted people in a similar fashion.

III. THE ROBOTIC SONAR STICK SYSTEM

The Robotic sonar stick is a fully embedded system, implementing all components on-board. The main constraints in the mechatronic design of the Robotic sonar stick are size and weight. The mechanical hardware must be as compact and as lightweight as possible so that the user can easily lift the Robotic sonar stick, e.g., for coping with stairs and access to public transportation. For the same reason, the electronic components should require minimal power in order to minimize the weight of the batteries. In addition, both the mechanical and electronic hardware must be designed to facilitate the software’s task, allowing real-time performance with limited on-board processing power.

A. Mechanical Hardware

The Robotic sonar stick consists of three main modules: housing, wheelbase, and handle. The housing, made of acrylic, contains and protects most of the electronic components. The current prototype is equipped with ten Polaroid ultrasonic sensors that are located around the housing. Eight of the sonars are located in the front in a semi-circular fashion with and reduces the information bandwidth. As a Robotic sonar stick with a total angular spacing of 120°. The other two sonars face sideway and are useful for following walls and for going through narrow openings, such as doorways. The sonars are close to the ground so that the Robotic sonar stick can also detect obstacles that protrude only slightly above the ground. One disadvantage of this location is that the sonars sometimes detect minor irregularities in the ground, which erroneously trigger an avoidance maneuver). By placing the sonars at a small upward-looking angle, we hope to eliminate this potential problem with the next prototype.

The housing and wheelbase are about 43 cm (17") wide, 25 cm (10") high, and 23 cm (9") deep. The current Robotic sonar stick prototype weighs about 4 kg (9 lbs). However, we expect that a commercial version can be built that weighs only 2.5 – 3 kg (5.7 – 6.8 lbs).

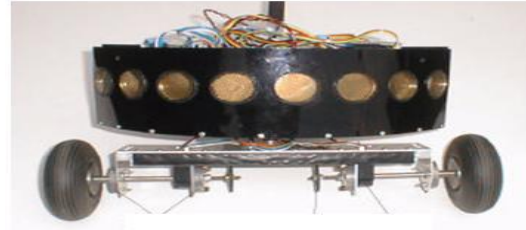


Fig 3: **Our Practical Implementation**

As shown in Figure 3, the wheelbase uses ball bearings to support two unpowered wheels. To perform odometry, both wheels are equipped with lightweight quadrature encoders. Using full quadrature decoding, the resolution of the encoders is 2,000 pulses per revolution, resulting in more than 5 pulses for a wheel advancement of 1 mm. The Robotic sonar stick’s odometry equations are the same as for a differential drive mobile robot. However, because the wheels are unpowered, there is considerably less risk of wheel slippage.

The wheelbase is attached to the housing with a pivot angular spacing of 15°, covering the area ahead of the push-rod couples the wheelbase to the servo, which is fixed to the housing bottom. Because the servo shaft is rigidly linked to the wheelbase, the built-in computer can access the potentiometer inside the servomotor to determine the relative angle between the wheelbase and the housing. This information is important for correctly updating the local map based on the sonar and the odometry data.

The handle serves as the main physical interface between the user and the Robotic sonar stick. It consists of an extruded aluminum bar with a square-shaped profile. A square shape is better than a circular shape as it allows the user to determine the handle’s orientation through tactile contact. The handle is attached to the housing with a hinge, whose angle can be adjusted to accommodate users of different heights.

B. Electronic Hardware

The electronic system architecture of the Robotic sonar stick is shown in Figure 4. The main brain of the Robotic sonar stick is an embedded PC/104 computer, equipped with a 486 microprocessor clocked at 33 MHz. The PC/104 stack consists of four layers. Three of the modules are commercially available, including the motherboard, the VGA utility module, and a miniature 125-MB hard disk. The fourth module, which we custom-built, serves as the main interface between the PC and the sensors (encoders, sonars,

and potentiometer) and actuators (main servo and brakes). The main interface executes many time-critical tasks, such as firing the sonars at specific times, constantly checking the sonars for echoes, generating PWM signals for the servos, and decoding the encoder data. The main interface also acts as an asynchronous buffer for the sonar data. Although the Robotic sonar stick currently uses only ten sonars, the main interface provides hardware and software support for up to 16 sonars.

The main interface is connected to the PC's bi-directional parallel port. The interface preprocesses most of the sensor data before the data is read by the PC. In addition, all communications are buffered. The preprocessing and buffering not only minimize the communications between the PC and the interface, screw and can be rotated by a small servomotor. A PC to control the sensors and actuators. Because the main interface completes all the low-level tasks, almost all of the PC's computational power can be dedicated to medium and high-level tasks. The interface consists mainly of three MC68HC11E2 microcontrollers, two quadrature decoders, a FIFO buffer, and a decoder.

The embedded PC/104 computer provides a convenient development environment. For stationary development, the system is connected to a regular keyboard and a CRT monitor. For mobile tests, the PC is connected to a smaller keyboard and a color LCD screen that is attached to the handle below the developer's hand. The entire system is powered by rechargeable NiMH batteries, allowing mobile testing for several hours. The Robotic sonar stick is thus fully autonomous in terms of power and computational resources.

While the current prototype consists of four PC/104-sized modules, only two of them are required for the final version. While the VGA module is very useful for visual verification and debugging, it is no longer needed after development. In addition, the hard-disk module can be eliminated in the final product, because the final software can be stored in an EPROM on the motherboard. This solid-state solution also eliminates potential problems with the moving parts of the hard-disk, which is sensitive to shocks and vibrations.

The Robotic sonar stick is a semi-autonomous system, providing full autonomy for *local* navigation (Obstacle avoidance), but relying on the skills of the user for *global* navigation (path planning and localization). Combining the skills of a mobile robot with the existing skills of a visually impaired user makes this particular application feasible at the

current stage of mobile robotics research. While reliable global navigation systems might be available in the future, they are not essential for the Robotic sonar stick. Although visually impaired people have difficulties performing fast local navigation without a travel aid, they are in most cases perfectly capable of performing but also minimize the computational burden on the desired direction of travel. To achieve safe travel at fast walking speed through cluttered and unknown environments, the Robotic sonar stick employs several mobile robot obstacle avoidance technologies that were developed earlier at the University of Michigan's Mobile Robotics Lab, as explained next. The ultrasonic sensors are controlled by the *Error Eliminating Rapid*

Ultrasonic Firing (EERUF) method. EERUF allows sonars to fire at rates that are 5-10 times faster than conventional methods. Each of the 10 sonars is fired at a rate of 10 Hz, so that the Robotic sonar stick receives 100 sonar readings per second. However, fast firing with multiple sonars can result in crosstalk, a phenomenon in which one sensor receives the echo from another sensor.

By employing alternating delays before firing each sensor, EERUF is able to detect and reject crosstalk. The faster firing rate improves the reliability of the Robotic sonar stick's obstacle avoidance performance and is necessary for allowing safe travel at fast walking speed. Based on the sensor data, the Robotic sonar stick uses *histogrammic in-motion mapping* (HIMM) to build a local map of its immediate surroundings. The map is represented by a two-dimensional array, called *histogram grid*, which is based on the concept of *certainty grids* pioneered by Moravec and Elfes. HIMM produces high certainty values for cells that correspond to obstacles and keeps low certainty values for cells that were increased because of misreading or moving objects. In the current implementation, the dimensions of the local map are 18 m 18 m with a cell size of 10 cm 10 cm. The map requires less than 32 kilobytes of memory. A discrete scrolling algorithm is implemented so that the finite dimensions of the local map do not limit the Robotic sonar stick's workspace. Based on the information contained in the local map, the local obstacle avoidance algorithm determines an appropriate instantaneous direction of motion. Using the information in the local map instead of solely the current sonar readings, a better obstacle avoidance performance is achieved than with a purely reactive system. The task of the obstacle avoidance algorithm global navigation. The main task of the Robotic sonar stick is to steer around obstacles and to proceed toward the direction of travel. This direction is then used to send the appropriate steering signal to the Robotic sonar

stick's servomotor. Originally, the *vector field histogram* (VFH) obstacle avoidance method was implemented in the Robotic sonar stick. During the Robotic sonar stick development, the original VFH method was successively improved, resulting in the VFH+ and VFH* algorithms. The improved algorithms are more robust by taking into account the width and the trajectory of the Robotic sonar stick, and less likely to direct the Robotic sonar stick into local dead-ends.

IV. FUTURE IMPROVEMENTS

Sonars – The next version of the Robotic sonar stick prototype will be equipped with 13 sonars located in the front in a semi-circular fashion, covering 195° ahead of the Robotic sonar stick. Three additional sonars will be placed on top of the housing to detect overhanging obstacles.

Brakes – Both wheels can be equipped with brakes that can be activated by the onboard computer, for several purposes. In densely cluttered environments, the user can be slowed down if his/her speed is too fast. Or, when the user walks into a dead-end where no avoidance maneuver is possible, e.g., a closed door at the end of a corridor, the system can immediately signal this condition by fully applying the brakes. Brakes can be implemented using off-the-shelf, servo-actuated disk brakes used in model race cars. These brakes are powerful and their dimensions are suitable for the Robotic sonar stick.

Speech output – Speech output could be a very helpful feature if used appropriately. It would allow the Robotic sonar stick to not only guide the user to a desired location, but also to provide additional information about the environment. One useful function could be the instant presentation of location and orientation data. Another useful function would be to warn a user if he/she gets too close to an obstacle, and even telling him/her on which side the obstacle is. Speech output could also be used instead of the brakes to ask the user to slow down or stop.

V. CONCLUSION

The Robotic sonar stick offers innovative solutions for the three fundamental shortcomings of conventional is to determine a suitable direction of motion, i.e., one that is free of obstacles but close to the user's desired ETAs:

1. Because of the sensor array comprising of multiple sonars, the user no longer needs to actively scan the area ahead of him/her. Although not yet implemented in the experimental prototype described in this paper, upward-facing sonars should be relatively easy to implement to detect overhanging obstacles.

2. When the user approaches an obstacle, the Robotic sonar stick does not communicate everything it

Knows about the obstacle to the user. Instead, it analyzes the situation, determines an appropriate direction to avoid the obstacle, steers the wheels in that direction, and thus guides the user around the obstacle without requiring any conscious effort on his/her part. This is possible because a coarse representation of the obstacle's contour is formed in the Robotic sonar stick's local map.

3. The Robotic sonar stick does not use acoustic feedback, so that there is no masking of audio cues on which many blind persons rely heavily.

As a consequence of these advantages, the Robotic sonar stick is intuitive and easy to use. In addition, because the Robotic sonar stick takes care of the local navigation task, it allows the user to fully concentrate on the global navigation task.

ACKNOWLEDGMENT

We would like to express our sincere thank to our beloved principal, staff members and special thanks to our friends Balasubramanian and Kaliraj.

The materials available with the listed reference books have a significant impact on this paper. We gratefully thank to the authors and publications of these reference books.

V. REFERENCES

- [1] J. M. Benjamin, N. A. Ali, and A. F. Schepis, "A Laser Cane for the Blind," *Proc. San Diego Biomedical Symp.* vol. 12, pp. 53-57, 1973.
- [2] D. Bissitt and A. D. Heyes, "An Application of Biofeedback in the Rehabilitation of the Blind," *Applied Ergonomics*, vol. 11, no. 1, pp. 31-33, 1980.
- [3] B. B. Blasch, R. G. Long, and N. Griffin-Shirley, "National Evaluation of Electronic Travel Aids for Blind and Visually Impaired Individuals: Implications for Design," *RESNA 12th Annual Conf.*, New Orleans, Louisiana, pp. 133-134, 1989.
- [4] J. Borenstein and Y. Koren, "Histogramic In-Motion Mapping for Mobile Robot Obstacle Avoidance," *IEEE J. Robot. Automat.*, vol. 7, no. 4
- [5] J. Borenstein and Y. Koren, "The Vector Field Histogram – Fast Obstacle-Avoidance for Mobile Robots," *IEEE J. Robot. Automat.* vol. 7, no. 3. pp. 278-288, June 1991

WIRELESS MODE OF TRANSMISSION

***J.BANUCHANDAR, *S.DEEPA, *N.TAMILARASI, #J.PARKAVI**

*Electronics and Communication Engineering,
P.SR Engineering College, sivakasi

#Electrical and Electronics Engineering,
Mepco Schlenk Engineering college, sivakasi

Abstract –In the present paper the various technologies available so far for wireless transmission of electricity and the need for a Wireless System of Energy Transmission is being discussed to find its possibility in actual practices, their advantages, disadvantages and economical consideration. This paper is mainly concentrated on : i) The most popular concept known as Tesla Theory, ii) The microwave power transmission(MPT) called Solar power satellite, and iii) The highly efficient fiber lasers for wireless power transmission. Many concepts, research papers, patents are available on wireless transmission of electricity but the commercial technologies are yet to be materialized. The paper also discusses the possible ways to get useful and practical results out of all research carried out so far elsewhere. Microwave oven magnetron with electronics to control the output power. The output microwave power ranges from 50 W to 200 W at 2.45GHz. A coaxial cable connects the output of the microwave source to a coax-to-waveguide adapter. This adapter is connected to a waveguide ferrite circulator which protects the microwave source from reflected power. The circulator is connected to a tuning waveguide section to match the waveguide impedance to the antenna input impedance. The slotted waveguide antenna consists of 8 waveguide sections with 8 slots on each section. These 64 slots radiate the power uniformly through free space to the rectenna. The slotted waveguide antenna is ideal for power transmission because of its high aperture efficiency

Key words – Wireless transmission, Tesla theory, Microwave power transmission, Fiber lasers, Collaborative research.

I. INTRODUCTION

In our present electricity generation system we waste more than half of its resources. Especially the transmission and distribution losses are the main concern of the present power technology. Much of this power is wasted during transmission from power plant generators to the consumer.

The resistance of the wire used in the electrical grid distribution system causes a loss of 26-30% of the energy generated. This loss implies that our present system of electrical distribution is only 70-74% efficient. We have to think of alternate state - of - art technology to transmit and distribute the electricity. Now- a- days global scenario has been changed a lot and there are tremendous development in every field. If we don't keep pace with the development of new power technology we have to face a decreasing trend in the development of power sector. The transmission of power without wires may be one noble alternative for electricity transmission.

II. THE TECHNOLOGIES AVAILABLE

In this remarkable discovery of the "True Wireless" and the principles upon which transmission and reception, even in the present day systems, are based, Dr. Nikola Tesla shows us that he is indeed the "Father of the Wireless." The most well known and famous Wardencllyffe Tower (Tesla Tower) was designed and constructed mainly for wireless transmission of electrical power, rather than telegraphy. The most popular concept known is Tesla Theory in which it was firmly believed that Wardencllyffe (Fig.1) would permit wireless transmission and reception across large distances with negligible losses. In spite of this he had made numerous experiments of high quality to validate his claim of possibility of wireless transmission of electricity (Fig.2). But this was an unfortunate Recognize his splendid work otherwise today we may transmit electricity wirelessly and will convert our mother earth a wonderful adobe full of electricity. Fig.1.The 187-foot Wardencllyffe Tower (Tesla Tower) in 1903. This was to be the first broadcasting system in the world. Tesla wanted to transmit electricity from this Tower to the whole globe without wires using the Ionosphere. The source of the transmitted electricity was to be the Niagara Falls power plant. The modern ideas are dominated by microwave power transmission (MPT, Figure 3) called Solar power satellite to be built in high earth orbit to collect sunlight and convert that energy into microwaves, then beamed to a very large antenna

on earth, the microwaves would be converted into conventional electrical power. Fig.2. The basis for Tesla's system for the wireless transmission of electrical power.



Fig 1

William C. Brown, the leading authority on wireless power transmission technology, has loaned this demonstration unit to the Texas Space Grant Consortium to show how power can be transferred through free space by microwaves.

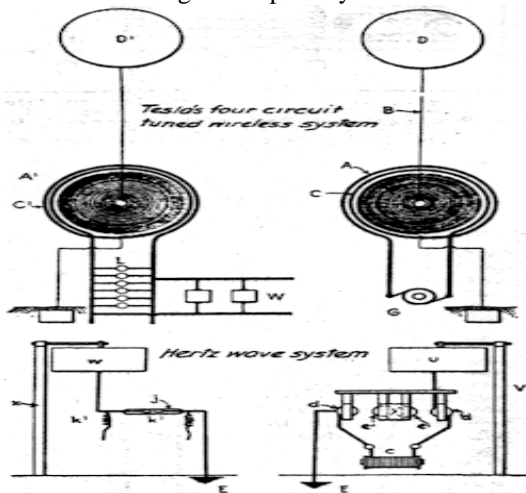


Fig 2

A block diagram of the demonstration components is shown below.

The primary components include a microwave source, a transmitting antenna, and a receiving rectenna. The microwave source consists of a magnetron (not explicitly labeled but implied by the context) and high power handling capability. A rectifying antenna called a rectenna receives the transmitted power and converts the microwave power to direct current (DC) power. This demonstration rectenna consists of 6 rows of dipole antennas where 8 dipoles belong to each row. Each row is connected to a rectifying circuit which consists of low pass filters and a rectifier. The rectifier is a GaAs Schottky barrier diode that is impedance matched to the dipoles by a low pass filter. The 6 rectifying diodes are connected to light bulbs for indicating that the power is received. The light bulbs also dissipated the received power. This rectenna has a 25% collection and conversion

efficiency, but rectennas have been tested with greater than 90% efficiency at 2.45 GHz. The transmission of power without wires is not a theory or a mere possibility, it is now a reality. The electrical energy can be economically transmitted without wires to any terrestrial distance, many researchers have established in numerous observations, experiments and measurements, qualitative and quantitative. These have demonstrated that it is practicable to distribute power from a central plant in unlimited amounts, with a loss not exceeding a small fraction of one per cent, in the transmission, even to the greatest distance, twelve thousand miles - to the opposite end of the globe. This seemingly impossible feat can now be readily performed by electrical researchers familiar with the design and construction of my "high-potential magnifying transmitter," There were three popular theories present in the literature of the late 1800's and early 1900's.

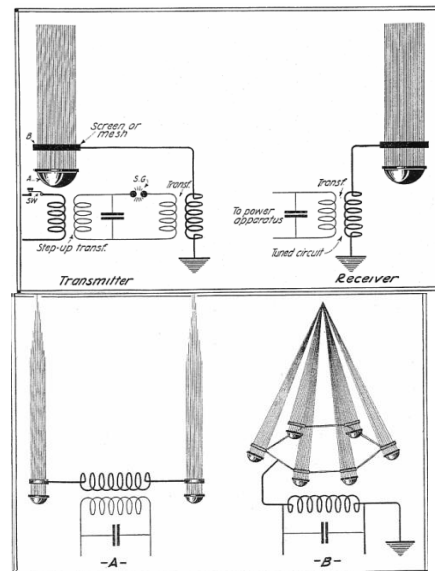


Fig.4. Diagram showing the transmitting & receiving circuit for the transmission & reception of electric power by wireless .Fig.5. Two optical forms of wireless antennae formed of search light beam- ionized atmospheric streams.

III. MERITS, DEMERITS & ECONOMICS OF WIRELESS TECHNOLOGIES

3.1. Merits

An electrical distribution system, based on this method would eliminate the need for an inefficient, costly, and capital intensive grid of cables, towers, and substations. The system would reduce the cost of electrical energy used by the consumer and rid the landscape of wires, cables, and transmission towers. There are areas of the world where the need for electrical power exists, yet there is no method for delivering power. Africa is in need of power to run pumps to tap into the

vast resources of water under the Sahara Desert. Rural areas, such as those in China, require the electrical power necessary to bring them into the 20th century and to equal standing with western nations. The wireless transmission will solve many of these problems. The electrical energy can be economically transmitted without wires to any terrestrial distance, so there will be no transmission and distribution loss.

More efficient energy distribution systems and sources are needed by both developed and under developed nations. In regards to the new systems, the market for wireless power transmission is enormous. It has the potential to become a multi-billion dollar per year market.

The increasing demand for electrical energy in industrial Nations is well documented. If we include the demand of third world nations, pushed by their increasing rate of growth, we could expect an even faster rise in the demand for electrical power in the near future. These systems can only meet these requirements with 90–94 % efficient transmission.

High Transmission Integrity and Low Loss: - To transmit wireless power to any distance without limit. It makes no difference what the distance is. The efficiency of the transmission can be as high as 96 or 97 per cent, and there are practically no losses.

3.2. Demerits

Biological Impact: - One common criticism of the Tesla wireless power system is regarding its possible biological effects. Calculating the circulating reactive power, it was found that the frequency is very small and such a frequency is very biologically compatible [3, 8].

3.3. Economic Impact

The concept looks to be costly initially. The investment cost of Tesla Tower was \$150,000 (1905). In terms of economic theory, many countries will benefit from this service. Only private, dispersed receiving stations will be needed. Just like television and radio, a single resonant energy receiver is required, which may eventually be built into appliances, so no power cord will be necessary! Monthly electric utility bills from old-fashioned, fossil-fuelled, loss prone electrified wire-grid delivery services will be optional, much like “cable TV” of today. In the 21st century, “Direct TV” is the rage, which is an exact parallel of Tesla’s “Direct Electricity.”

V. CONCLUSION

The transmission of power without wires is not a theory or a mere possibility, it is now a reality. The electrical energy can be economically transmitted without wires to any terrestrial distance. Many researchers have established in

numerous observations, experiments and measurements, qualitative and quantitative. Dr.N.Tesla is the pioneer of this invention. Wireless transmission of electricity have tremendous merits like high transmission integrity and Low Loss (90 – 97 % efficient) and can be transmitted to anywhere in the globe and eliminate the need for an inefficient, costly, and capital intensive grid of cables, towers, and substations. The system would reduce the cost of electrical energy used by the consumer and get rid of the landscape of wires, cables, and transmission towers. It has negligible demerits like reactive power which was found insignificant and biologically compatible. It has a tremendous economic impact to human society. Many countries will benefit from this service. Monthly electric utility bills from old-fashioned, fossil-fuelled, loss prone electrified wire-grid delivery services will be optional, much like “cable TV” of today.

Enhanced Autonomous Reconfiguration of Link Failures in Grid Based Wireless Mesh Networks

Gokul Prasad. C*, Vinodh Kumar. B**

*II M.E (CS), ** Assistant Professor (Sr).

Sri Shakthi Institute of Engineering and Technology, Coimbatore, Tamilnadu, India

Abstract:

Link failures is one of major issue in the networking area. So that wireless information communication is the most promising and complicated field. As wireless mesh networks are concerned these provides larger coverages and high data rate information transfer. Even though they provide lot of benefits to the users and several high range applications they still suffer from the occurrences of the link failure. These link failures will occur due to some interferences, different obstacles etc.. By this link failure the information transfer can be lost so the quality of communication cannot be achieved and also the performance of this Wireless Mesh Networks can low. So in order to recover from the link failures Autonomous Reconfiguration System is commonly used. This algorithm provides Autonomous reconfiguration to the links by employing group formation technique. Even though this algorithm provides the recovery for the link failure it provides limitations such as higher delay, low throughput etc. In order to over come the limitations of Autonomous Reconfiguration System (ARS) algorithm, a modified version of Enhanced Autonomous Reconfiguration (E-ARS) have been developed. This algorithm provides a different approach. So that the delay are made low, throughput are made higher and also several other parameters are also analyzed comparing to the ARS. These overall process are shown and simulated using the software called Network Simulator -2 (NS-2).

Key words: Wireless mesh networks, link failure, Enhanced Autonomous Reconfiguration System.

I. INTRODUCTION

Wireless mesh networks are boon to the wireless architecture[1]-[2]. It supports larger applications and it provides several benefits to users such as, no cabling cost, automatic connection to all nodes, network flexibility, ease of installation and it also discovers new routes automatically. These wireless mesh networks are not stand alone it is compatible and interoperable with other wireless networks. It provides greater range of data transfer rates. Wireless mesh networks are preferable compared to the adhoc networks for the easy of network maintenance, robustness etc. These wireless mesh networks consists of two types of devices: mesh routers and mesh clients. The mesh routers contains minimal mobility and this constitutes to form an backbone for the mesh clients. Mesh clients can be worked as router, but the hardware and the software platform may differ and it is much more simpler than the

mesh routers. So that the protocols used for communication can be used at lesser amount. So the chance of packet loss and link failure are more. Information transmission are generally started from the source node to their specified destination. These transmission strategies will be mostly similar while considering several kinds of networks. But the difference in the transmission of information in several networks will mostly vary in terms of different data rates, some networks employ low data rate transfer where as others provide high data rate transfer. The information transmitted should not eaves drop before reaching the specified destination but these are not met in several kinds of networks. Though these wireless mesh networks provide many advantages there may also some disadvantages, multimedia related traffics based on real time delivery are not supported. Because these will be supported only by employing basic schemes which supports those traffic scenarios. If the routing capability are added then there will be energy constraints in the devices, due to this there will be shorter operating life time. Security related schemes are not developed entirely where multi hopping communication took place. Finally, wireless mesh networks does not provide centralized trusted architecture too, to distribute the public keys [3]. If these architecture are provided means there will be some improvement tasks may be there in terms of security. Here in the wireless mesh network, mesh clients should contain power efficient protocols. Mesh routers in the wireless mesh networks perform dedicated routing and configurations.

In this paper, the link failure occurring at the wireless mesh networks have been considered. Generally link failure is one of the major issue which took place in the networking arena. So, different kinds of approaches or algorithms are used to recover this problems. The main task which is carried out in this paper is to recover from link failure is based on the group formation of nodes from the failure occurred node. These group formation based approach will tend to some problems high delay, lesser throughput etc. In order to overcome the limitations of the ARS another approach is used which is called as Enhanced Autonomous Reconfiguration Algorithm (E-ARS) have been used. According to wireless mesh networks the coverage can be increased so that the in formations capacity are higher. In these cases if link failures occurred during transmission means efficient algorithms are used. In this paper E-ARS results are compared with Autonomous Reconfiguration System (ARS) [4] algorithm results these link failures.

II. EXISTING TECHNIQUES

By employing this resource allocation algorithm algorithm optimal reconfiguration plan has been generated but these requires global configuration changes which is an difficult one while considering the frequent link failures[5]-[7]. There is some drawback in above mentioned algorithm so in order to recover from these drawbacks greedy channel assignment algorithm [8] is used. In this algorithm network changes requirement is reduced to some extent by employing the changes in the settings only to the failure links. This algorithm also provides some drawbacks, it cannot provide higher improvements in the network. The higher improvement can only be achieved while considering the neighbouring nodes additional to the failure links. Finally the fault tolerant routing protocols is used. These protocols use local rerouting [9] or multipath routing [10] so that the failure links are avoided by path diversity. In the multipath routing scheme the ticket based probing is employed. These ticket based probing provides a ticket which is used to search one path. . These tickets are given by the source node. It is based on the state informations only. Suppose if there is tighter requirements in connection , then more number of tickets will be given. Then the probing , it is also considered as routing messages. These routing messages are being transmitted from the source node to the destination in order to find the least cost path . These routing messages should atleast carry one ticket regularly. This ticket based probing provides some advantages, routing overhead is controlled based on number of tickets, there is no need for any node to contain topology related informations, and also it uses stationary links when there is any requirement so by using these stationary links the path will be more stable. This approach is not best suited to achieve better improvements. So an algorithm called as Autonomous Reconfiguration System (ARS) is used. By employing this algorithm the failures links are recovered. In this algorithm, first it checks all the links. It is based on the link measurement technique. Then if the link failure is detected then the group formation will be made from the failure occurred node which are at distances less than 250 ms. Then the energy is calculated for the group formed nodes, for 4 nodes excluding failure occurred node. Then based on highest energy the links are recovered. The highest energy node is elected as leader, it send request message to failure node and it will generate reconfiguration plan and it sends to the leader node. Then in reconfiguration period the changes to node are made so the links are changed. There are different types of overheads occurred by this ARS algorithm such as high drop, low throughput etc.

III. PROPOSED SYSTEM

In the above mentioned Autonomous Reconfigurable System (ARS) algorithm the link failure are recovered but this also produces drawbacks such as, high drop, low throughput etc. In order to recover from these drawbacks, a enhanced form of algorithm called as Enhanced Autonomous Reconfigurable System (E-ARS) was used. The several operation performed in this EARS are,

- Link Monitoring
- Link Failure detection
- Checking energy
- Reconfiguration period

A. Link Monitoring:

Monitoring is an important phenomenon when we consider the link failure. Generally monitoring is the basic operation involved in many link recovery algorithms . Monitoring period is used to monitor the links from which the information is started to the end of that period. In mesh networks it is easier to choose the alternate path when the link failure occurs. Here, since the mesh networks are used there is some general criteria should be met , there should be connectivity between all nodes in the mesh network. These connectivity can be ensured by transmitting test messages to all the nodes from source node. The source node is selected and the information transmitted to destination. Finally the monitoring period is used to detect the link failure and to measure the quality of the links by using hybrid link measurement technique.

B. Link Failure Detection:

After this link monitoring, the failure links are detected. Due to this link failure the packet dropping occurs. These packet loss occurred not only for link failure even they occur if the traffic exhibits some congestion, due to some miscablings etc. then to recover from this failure here no group formation based approach is used because these produces drawbacks such as high drop, low throughput etc..

C. Checking Energy :

Energy is considered to be the important phenomenon.. Generally required energy will be more, when the distances became large and also if the high resources are used .In this paper, the energy is calculated for the neighbouring nodes from the link failure occurred node. Then the node with highest energy is elected as an leader. It will send the request to the failure occurred node and then that node will generate the reconfiguration plan, send to the leader node. Finally the link failures are recovered and transmission continues through the leader node to the destination.

D. Reconfiguration period:

In this period some modifications to links are included. If a failure occurs to a link then there will be loss of information. By using reconfiguration plan send to the leader node the changes to node are made. So that the changes are made to the links. The most important task carried out in this period is the changes must be made to link. In this proposed algorithm , the group formation is removed and also traffic has increased. Because by removing these group formation the overheads such as high drop, low throughput will be overcome. Here the link recovery is based on the highest energy which is at the path in near by distance .Generally if the link failure occurred means the alternative path will be provided from the source node and also the failure information will be send to all the nodes where as in this E- ARS, the failure link information will be send to only the near by nodes based on near by path the information will be transferred. The selecting best path is based on distance . These are the operations involved in the planning period. Then finally, the information transfer took place via the near by nodes to the destination these transmission will be done at the reconfiguration period. So by employing this proposed

algorithm E- ARS , less drop, high throughput etc..can be produced.

IV. RESULTS AND DISCUSSION

Here, ns -2 [11] is used for this simulation environment. In this paper, to perform simulation 25 number of nodes are created and they are placed in the 5x5 grid based formation. These 25 nodes are separated at the distance of about 180 ms to the other nodes. Then routing protocol used here is Destination Sequence Distant Vector (DSDV). Here User Datagram Protocols (UDP) is used. Since the mesh networks is used, the connectivity should be ensured by transmitting test messages from each node to all other nodes. Then the routing path is set. These are set by assigning the traffic, CBR . Here by considering the 25 nodes the number of traffic is made as 6 to reach the destination. Then the information transmission starts from the source node to the destination node. While transmitting the link failures are occurred. Due to this link failure the packet dropping took place. This graph shows that the packet dropping occurred by the Autonomous Reconfigurable System (ARS) is about 21. These packet dropping can be reduced by employing the Enhanced Autonomous Reconfigurable System (EARS) algorithm. Here the packet dropping occurred is 7. It can be shown from the figure 1,

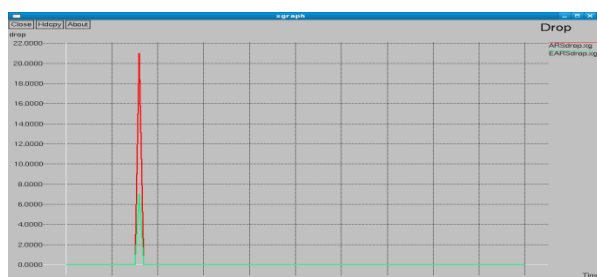


Figure 1: Packet Drop

Then the second parameter which is considered is the energy. These energy are described in terms of joules .Generally the energy consumption will be more when the resources are high. It may vary from node to node. This energy is considered mainly for the ARS algorithm because, based on the highest energy node only the failure recovery can be achieved. Where as in the EARS algorithm the failure recovery will be based on the shortest path from the failure occurred node. But in the both algorithm the energy has been considered, ARS consumes lesser energy when compared to EARS. The main reason for high energy consumption in case of EARS is due to the increased CBR traffic. This can be shown by this energy graph, Since the traffic is set for 12 m sec ,the graph shows higher energy consumption for EARS ,when compared to the ARS. These energy graph is plotted between time vs energy(joules).It can be shown from the figure 2,



Figure 2: Energy Consumed

Then the third parameter which is considered is the packet delivery ratio. The packet delivery ratio are generally described by, ratio of received packets by the send packets. At the starting the packet delivery ratio tend to increase while considering both the algorithms. Since the packet delivery ratios are plotted for each 5 intervals, the ARS produce lesser packet delivery ratio at 10 ms its about 0.76. this is because of the group formation technique employed where as in case of the EARS it produces higher packet delivery ratio at 10 ms its about 0.91. Since the group formation is eliminated in the EARS, it provides higher packet delivery ratio. Then finally after the 20 ms the packet delivery ratio will be same for the both algorithms. Packet delivery ratio is plotted time vs packets. It is shown from the figure .3,

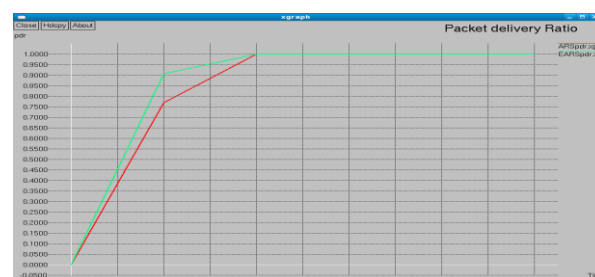


Figure 3 : Packet delivery ratio

The last parameter which is considered is the throughput. The throughput is defined as the average rate of successful message delivery through the communication link. It is generally expressed in terms of kb/s (kilo bits/sec) .But these can also be expressed in terms of data packets per time slot. While considering the throughput for the ARS algorithm , it tends to increase from 7 ms. Since it is the starting time for transmission. Then it will be constant from 8 ms to 9.5 ms because at that time there is no transmission will be occurred. Because during this time only the packet dropping and group formation are employed. Then from 9.6 ms the throughput will tends to increase and finally they are kept constant levels from 10.5ms to end of simulation time , 50ms. Its value is about 119. Then while considering throughput for EARS, it also tends to increase from 7ms. Here also the transmission started from this time only. Then it will be constant from 8 to 8.6 ms then based on the shortest path only link are recovered instead of group formation. So that the time will be reduced and finally the throughput will be high for EARS .finally its value is about 127. It can be shown through from this figure 4,



Figure 4 : Throughput

CONCLUSION

In this paper, the link failure recovery is considered as the main objective. It is done by using Autonomous Reconfigurable System algorithm. Though this algorithm provides link recovery, some kinds of limitations such as high drop, low throughput etc.. are produced. These are due to the group formation technique which is employed from the failure occurred node. In order to overcome from this limitations, a new enhanced algorithm called as Enhanced Autonomous Reconfiguration algorithm is used. These provides low drop, high throughput etc.. Only the energy consumption is more compared to Autonomous Reconfigurable System (ARS) algorithm. This is because the traffic is increased compared to the Autonomous Reconfigurable System algorithm.

REFERENCES

- [1] I. Akyildiz, X. Wang, and W. Wang, "Wireless mesh networks: A survey," *Comput. Netw.*, vol. 47, no. 4, pp. 445–487, Mar. 2005.
- [2] "Data communication and Networking" by Behrouz A. Forouzan.
- [3] "Wireless communications practices and principles" by T.S Rappaport.
- [4] Kyu-Han Kim, *Member, IEEE*, and Kang G. Shin, *Fellow, IEEE, ACM*, "Self-Reconfigurable Wireless Mesh Networks" *IEEE/ACM TRANSACTIONS ON NETWORKING*, VOL. 19, NO. 2, APRIL 2011.
- [5] M. Alicherry, R. Bhatia, and L. Li, "Joint channel assignment and routing for throughput optimization in multi-radio wireless mesh networks," in *Proc. ACM MobiCom*, Cologne, Germany, Aug. 2005, pp. 58–72.
- [6] M. Kodialam and T. Nandagopal, "Characterizing the capacity region in multi-radio multi-channel wireless mesh networks," in *Proc. ACM MobiCom*, Cologne, Germany, Aug. 2005, pp. 73–87.
- [7] A. Brzezinski, G. Zussman, and E. Modiano, "Enabling distributed throughput maximization in wireless mesh networks: A partitioning approach," in *Proc. ACM MobiCom*, Los Angeles, CA, Sep. 2006, pp. 26–37.
- [8] A. Raniwala and T. Chiueh, "Architecture and algorithms for an IEEE 802.11-based multi-channel wireless mesh network," in *Proc. IEEE INFOCOM*, Miami, FL, Mar. 2005, vol. 3, pp. 2223–2234.
- [9] S. Nelakuditi, S. Lee, Y. Yu, J. Wang, Z. Zhong, G. Lu, and Z. Zhang, "Blacklist-aided forwarding in static multihop wireless networks," in *Proc. IEEE SECON*, Santa Clara, CA, Sep. 2005, pp. 252–262.

- [10] S. Chen and K. Nahrstedt, "Distributed quality-of-service routing in ad hoc networks," *IEEE J. Sel. Areas Commun.*, vol. 17, no. 8, pp. 1488–1505, Aug. 1999.
- [11] "The network simulator - ns -2" [Online]. Available: <http://www.isi.edu/nsnam/ns>

CLOUD COMPUTING AN OVERVIEW

Pradip Patil¹, Gurudatt Kulkarni², Amruta Dongare³

1,2Lecturer in Marathwada Mitra Mandal's Polytechnic, 3Student DYP Pune (BE)

Abstract: - The emergence of cloud computing provides many opportunities for academia, the information technology (IT) industry and the global economy as an information technology revolution. Cloud computing is an increasingly popular paradigm for accessing computing resources. In practice, cloud service providers tend to offer services that can be grouped into three categories: software as a service, platform as a service, and infrastructure as a service. Cloud computing, with the revolutionary promise of computing as a utility, has the potential to transform how IT services are delivered and managed. Yet, despite its great promise, even the most seasoned professionals know little about cloud computing or how to define it.

Keyword: - PaaS, SaaS, Cloud, Public Cloud

1.0 INTRODUCTION:-

Cloud computing is Web-based processing, in which distributed assets, programs, and information are supplied to computers and other devices (such as smart phones) on demand through the Internet. Cloud computing is a natural development of the prevailing adoption of virtualization, Service-oriented structures and utility computing. [1] Details are abstracted from buyers, who no longer have required for know-how in, or command over, the expertise infrastructure in the cloud that carries them. The period cloud is utilized as a metaphor for the Internet, founded on the cloud drawing utilized to comprise the phone network in the past, and subsequent to depict the Internet in computer mesh design drawings as an abstraction of the inherent infrastructure it represents.

2.0 HISTORY OF CLOUD COMPUTING [1]

The concept of cloud computing was invented in 2002 by Amazon, a leading e-business, which had invested in a fleet of huge machines, sized to handle the heavy load of orders made on their site at the time of Christmas, but Instead, the unused balance of the year. Under-sizing their fleet would have caused downtime of their website at peaks, thereby jeopardizing their business during the holidays (a big part of their turnover) (Grossman 2009). Their idea has been to open these unused resources to businesses to hire them on demand. Since then, Amazon has invested heavily in this area and continues to expand its fleet and services. Recently, other players in the IT world such as Google and Microsoft, in turn, offer similar services. These cloud services based on the data center hardware (digital stations) huge (only these large companies can afford), and in software on virtualization techniques offer enterprise customers of IT resources. It varies the size over time (no

need to purchase and maintain on-site large servers) a few minutes to start up a new server in the Cloud. Instead of several months in situ it can absorb large load peaks (the suppliers offer CPU and high-performance network) the availability of which is guaranteed by contract (eg, less than 5 minutes of downtime per year, if not refund) (Armsbrust, 2009).

3.0 CLOUD COMPUTING MODELS:-[3]

Cloud Providers offer services that can be grouped into three categories.

3.1. Software as a Service (SaaS): In this model, a complete application is offered to the customer, as a service on demand. A single instance of the service runs on the cloud & multiple end users are serviced. On the customers side, there is no need for upfront investment in servers or software licenses, while for the provider, the costs are lowered, since only a single application needs to be hosted & maintained. Today SaaS is offered by companies such as Google, Salesforce, Microsoft, Zoho, etc.

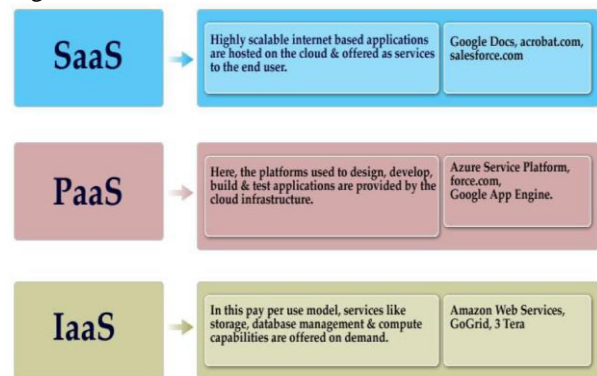


Figure 3.1 Cloud Computing Models

3.2. Platform as a Service (PaaS): Here, a layer of software, or development environment is encapsulated & offered as a service, upon which other higher levels of service can be built. The customer has the freedom to build his own applications, which run on the provider's infrastructure. To meet manageability and scalability requirements of the applications, PaaS providers offer a predefined combination of OS and application servers, such as LAMP platform (Linux, Apache, MySQL and PHP), restricted J2EE, Ruby etc. Google's App Engine, Force.com, etc are some of the popular PaaS examples. [2]

3.3. Infrastructure as a Service (IaaS): IaaS provides basic storage and computing capabilities as standardized services over the network. Servers, storage systems,

networking equipment, data centre space etc. are pooled and made available to handle workloads. The customer would typically deploy his own software on the infrastructure. Some common examples are Amazon, GoGrid, 3 Tera, etc.

of the Internet. The appellation 'public' does not consistently indicate free, even admitting it can be chargeless or adequately be use with less cost. This also doesn't mean that the cloud users' personal info and data is exposed to the public. This model provides an expandable, rate efficient means to set up cloud services.[6]

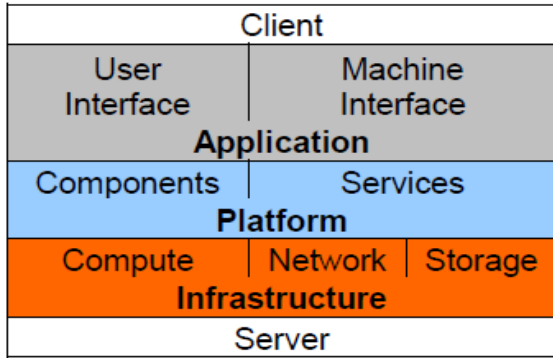


Figure 3.2 Cloud Computing Stack[5]

4.0 FOUR DEPLOYMENT MODELS:- [4,6]

- **Private Cloud:** - The cloud infrastructure is operated solely for an organization. It may be managed by the organization or a third party and may exist on premise or off premise. The information and development are control within the group with no the limitations of the system bandwidth, safety measures exposures and legal necessities. Additionally, private cloud services propose the user have power over of the cloud infrastructure, humanizing protection and resiliency.
- **Community Cloud:-** The cloud infrastructure is shared by several organizations and supports a specific community that has shared concerns (e.g., mission, security requirements, policy, and compliance considerations). It may be managed by the organizations or a third party and may exist on premise or off premise.

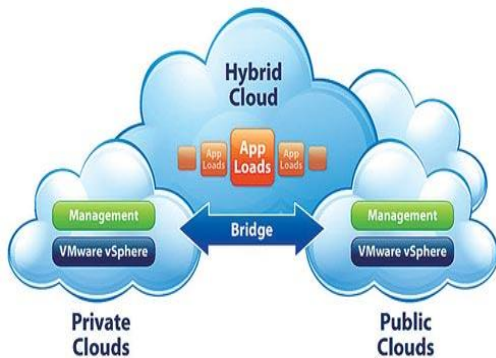


Figure 4.0 Deployment Models

- **Hybrid Cloud:-** The cloud infrastructure is a composition of two or more clouds (private, community, or public) that remain unique entities but are bound together by standardized or proprietary technology that enables data and application portability (e.g., cloud bursting for load-balancing between clouds).

5.0 CHARACTERISTICS:-[3]

Cloud computing has a variety of characteristics, with the main ones being:

- **Shared Infrastructure** — Uses a virtualized software model, enabling the sharing of physical services, storage, and networking capabilities. The cloud infrastructure, regardless of deployment model, seeks to make the most of the available infrastructure across a number of users.
- **Dynamic Provisioning** — Allows for the provision of services based on current demand requirements. This is done automatically using software automation, enabling the expansion and contraction of service capability, as needed. This dynamic scaling needs to be done while maintaining high levels of reliability and security.
- **Network Access** — Needs to be accessed across the internet from a broad range of devices such as PCs, laptops, and mobile devices, using standards-based APIs (for example, ones based on HTTP). Deployments of services in the cloud include everything from using business applications to the latest application on the newest smart phones.
- **Managed Metering** — Uses metering for managing and optimizing the service and to provide reporting and billing information. In this way, consumers are billed for services according to how much they have actually used during the billing period. In short, cloud computing allows for the sharing and scalable deployment of services, as needed, from almost any location, and for which the customer can be billed based on actual usage.

6.0 BENEFITS OF CLOUD COMPUTING:-

As cloud computing begins to take hold, several major benefits have become evident:

- **Public Cloud:** - The cloud infrastructure is made available to the general public or a large industry group and is owned by an organization selling cloud services. In plain words, public cloud casework or services are described as being accessible to cloud users from a third party account provider by means
- **Costs:-** The cloud promises to reduce the cost of acquiring, delivering, and maintaining computing power, a benefit of particular importance in times of fiscal uncertainty. By enabling agencies to purchase only the computing services needed, instead of investing in complex and expensive IT infrastructures,

agencies can drive down the costs of developing, testing, and maintaining new and existing systems.

- **Access:**- The cloud promises universal access to high-powered computing and storage resources for anyone with a network access device. By providing such capabilities, cloud computing helps to facilitate telework initiatives, as well as bolster an agency's continuity of operations (COOP) demands.
- **Scalability and Capacity:** - The cloud is an always-on computing resource that enables users to tailor consumption to their specific needs. Infinitely scalable, cloud computing allows IT infrastructures to be expanded efficiently and expediently without the necessity of making major capital investments. Capacity can be added as resources are needed and completed in a very short period of time.
- **Resource Maximization:** - Cloud computing eases the burden on IT resources already stretched thin, particularly important for agencies facing shortages of qualified IT professionals.
- **Collaboration:** - The cloud presents an environment where users can develop software-based services that enhances collaboration and fosters greater information sharing, not only within the agency, but also among other government and private entities.
- **Customization:** - Cloud computing offers a platform of tremendous potential for creating and amending applications to address a diversity of tasks and challenges. Its inherent agility means that specific processes can be easily altered to meet shifting agency needs, since those processes are typically changeable by making a configuration change, and not by driving redevelopment from the back-end systems (Heyward and Rayport, 2009)

7.0 CLOUD COMPUTING CHALLENGES [6]

The following are some of the notable challenges associated with cloud computing, and although some of these may cause a slowdown when delivering more services in the cloud, most also can provide opportunities, if resolved with due care and attention in the planning stages.

- **Security and Privacy** —Two of the more “hot button” issues surrounding cloud computing relate to storing and securing data, and monitoring the use of the cloud by the service providers. These issues are generally attributed to slowing the deployment of cloud services. These challenges can be addressed, for example, by storing the information internal to the organization, but allowing it to be used in the cloud.
- **Lack of Standards** — Clouds have documented interfaces; however, no standards are associated with these, and thus it is unlikely that most clouds will be interoperable. The Open Grid Forum is developing an Open Cloud Computing Interface to resolve this issue and the Open Cloud Consortium is working on cloud computing standards and practices.

- **Continuously Evolving** — User requirements are continuously evolving, as are the requirements for interfaces, networking, and storage. This means that a “cloud,” especially a public one, does not remain static and is also continuously evolving.
- **Compliance Concerns** — The Sarbanes-Oxley Act (SOX) in the US and Data Protection directives in the EU are just two among many compliance issues affecting cloud computing, based on the type of data and application for which the cloud is being used. The EU has a legislative backing for data protection across all member states, but in the US data protection is different and can vary from state to state. As with security and privacy mentioned previously, these typically result in Hybrid cloud deployment with one cloud storing the data internal to the organization.

CONCLUSION:-

Cloud computing users avoid capital expenditure (CapEx) on hardware, software, and services when they pay a provider only for what they use. Consumption is usually billed on a utility (resources consumed, like electricity) or subscription (time-based, like a newspaper) basis with little or no upfront cost. Other benefits of this approach are low barriers to entry, shared infrastructure and costs, low management overhead, and immediate access to a broad range of applications. In general, users can terminate the contract at any time (thereby avoiding return on investment risk and uncertainty), and the services are often covered by service level agreements (SLAs) with financial penalties. Cloud computing offers real alternatives to IT departments for improved flexibility and lower cost. Markets are developing for the delivery of software applications, platforms, and infrastructure as a service to IT departments over the “cloud”

REFERENCES:-

1. “Cloud Computing As an Emerging Paradigm” , Smitha Nayak and Ammar Yassir, IJCSNS International Journal of Computer Science and Network Security, VOL.12 No.1, January 2012
2. “A Short Introduction to Cloud Platforms an Enterprise-Oriented View”, David Chappell August 2008, Sponsored by Microsoft Corporation.
3. “Cloud Computing Building a Framework for Successful Transition”, Prem Jadhvani Senior Solutions Architect, GTSI.
4. “Introduction to Cloud Computing”, Dialogic Corporation
5. “Cloud Computing: A Study of Infrastructure as a Service (IaaS)”, Sushil Bhardwaj, Leena Jain, Sandeep Jain, International Journal of Engineering and Information Technology
6. <http://cloudcomputingtechnologybasics.blogspot.in/2011/08/cloud-computing-deployment-models.html>

Communications for Energy Conservation

Vineela Malae, Dr.M.V.Bhaskar Reddy

Abstract: The carbon foot prints are produced due to ecological and/or environmental impact of green house gases. Consumption of higher energy is one of the factors to increase the intensity of carbon. To get rid the problem i.e., the consumption of the higher electricity, the upcoming smart intelligent grid technology can be gainfully utilized to reduce the consumption of electric energy which ultimately reduces the carbon-foot prints.

In this paper, I express my sight and different views of the others, how and what extent of the smart-grid technologies could reduce the carbon-footprints.

Keywords: Smart grid, carbon foot prints, emissions, electricity, smart grid potential

1. Introduction

The intensity of carbon footprint is increasing day by day, which is one of the factors to causes the environmental pollution. Here we are considering and studying one of the factors for causing to increase the carbon foot print, i.e. conservation of electrical energy. It must have to decrease the use of electrical energy and also avoid to wasting of it. Here the identified problems are 1) How to reduce the carbon foot print 2) How to conserve the electrical energy-these two are interdependent and 3) How to get a good quality of power? The present grid technology and the related distribution system, a significant percentage of generated power is lost before it reaches the point of consumption. Here the problem is how to minimize the lost of energy during transmission and distribution. An updated technology is needed to solve this problem.

The interesting thing in these studies, are some of the identified problems are inter-reliant. If we reduce the use of electrical energy it leads to decrease the carbon foot print which is one of the aspects to protect the environment. Next the attention task is conservation of electrical energy. The difficult part of this is how to decrease the use of electrical energy and also to work for effective fruitful communication. Calendar days are not increasing but the customers and consumption are increasing day by day .The author intention is to decrease the total consumption of energy without depending the number of users and simultaneously to get a good quality of power. Here the mission is which technology is needed for this operation for the conservation of energy with cost effective and how to develop the quality of contact throughout the world.

The hard tasks are to conserve the energy and also to use of renewable energy. One of the main problems with the renewable energy is difficult to plan it is because whether the wind may blow or not and the sun may shine or not. For conservation of electrical energy to install smart grid Technology this will help to minimize the wastage of current. The US government (Jan, 2009) said

that they are planning to install 40 million smart meters and to set up 3000 miles transmission lines [1].

It is basically turning the electrical grid into a new network which uses microprocessors and software to work competently and to connect generation of renewable energy. It means that the smart grids make use of wireless sensor networks, software and calculating the how much energy is utilized by the consumer, accordingly, the customer should adjust their habits to minimize the consumption. In the end we want smart grid technology to cut down the consumption of the electrical energy to fight against global warming.

Mainly, the power generation resources are fossil fuels. The power produced, are not fully utilized and loss of power is heavily occurred and they are not taken proper precautions to overcome the problem. Further, they are not developed the grids at suitable distances. Moreover, transmission lines are very, very longer distances which causes the heavy loss of energy through transmission and they are not developed about the generation of power from the renewable sources. Initially we have not divided the source of energy types like 1) energy from wind 2) energy from solar system 3) energy from tides 4) energy from fossil fuels.etc. Along with the existing energy we have to make compulsory to use some percentage of renewable energy by making a law throughout the world to make the balanced distributed types of power.

The governments all over the world have been forced to think about the climate changes with introducing of proper motivational programs on smart grid Technology .Moreover, reducing the use of energy (fossil fuel energy) it also trim down the use of fossil fuels which protects not only the atmosphere but also the earth crust.

A smart grid technology is an understanding concept to know about the micro consumption of power it ensures reinforcing the global competitiveness and entirely to accommodates clean energy and probably reduce the carbon foot print. The efficiency, safety and reliability of the electricity transmission and distribution system can be improved by transforming the current electricity grids into an interactive (customers/operators) service network or the smart grid [3].

Advanced Metering Infrastructure (AMI) provides consumers with the ability to use electricity more efficiently and provides utilities with the ability to monitor and repair their network in real time. The AMI gained some grip in the industry suggesting the accuracy and process improvement of meter reading and its control and suggesting for managing power quality and asset management. [3]

The coming electric grids will be integrated by using the available alternate forms of energy resources. It means that, the design of the grids may need to change to install smart grids. To carry this work and to make the design, it is not a single discipline and it needs a multidiscipline and also it requires from the help of concern governments. The interdisciplinary research approach

needed in many fields those are 1). Advance systems engineering courses such as intelligent systems and Adaptive Controls, and controlling the design of the new tools. 2) Attract the producers of the electricity by giving some subsidies from the government part. 3). Ecological sciences [4].

At present the Denmark people realized and using the renewable energy at the rate of 40 percent of its electricity from wind turbines of various sizes distributed throughout this nation's grid. Denmark offers some interesting lessons about how to handle huge amounts of distributed generation, an input trend likely as the grid becomes more refined [2].

2. Related Events

2.1. The carbon footprint - outlook

Alternative energy (or) renewable energy sources is not destroyed and it is alternative to traditional sources. Fossil fuels/ or nuclear power must be consumed (gas or coal in energy grids, oil for transportation and uranium in nuclear energy) to produce energy. The vehicle to grid (V2G) concept means of storing energy and releasing it back into the electric grid on demand [5]. Climate change is a global problem. All countries in the world work together to install both the energies alternative energy and low emission energy. The following table shows the total world energy consumption and generation [5].

Table. 1 Type of resources

Type of resource	The world energy consumption in %	The world energy generation in %
Combustible Renewable and Waste Energy	10.6	-
Hydro	2.2	16.1
Nuclear	6.5	15.7
Gas	20.9	19.6
Oil	34.3	6.7
Coal	25.1	39.8
Other	0.4	2.1

2.2. The concept of carbon emission reduction (smart grid) technology

One of the greatest threats in front of our society is global warming. It is a collective responsibility of all the nations to reduce the carbon foot print. The research teams and the industries of the concern field to help to overcome this challenging problem, is to save the universe from pollution of the carbon footprints. The societies have to focus on carbon emissions not for the increasing the generation of electricity. Electrical energy is more expensive is some sort of price on carbon. Governments also think to introduce variable tariff depends what kind of energy is utilized by the customer. The price of electricity generated by the fossil fuels is expensive it is because of the carbon foot print. The alternative method is to install the smart grid technology in the conventional grids to reduce the consumption of energy.

The electric industry is to build unbiased, convert from centralized to non-centralized and much

interact with the consumers. The smart grid technology undertake to modify the whole business model and also it reduces the consumption of energy ultimately it decreases the carbon foot print. The smart grids symbolize for a vision of up grading the digital distribution system and extensive distance transmission grids by using robust two-way communications, advanced and superior sensors and distributed computers to improve the efficiency, reliability and safety of power delivery and use [6].

This sort of technology helps to reduce the energy consumption and load balancing via distributed generation and it mainly helps to reduce the carbon foot print.

The central concept of smart grid is to include screening, analyze, control and communication competence, to the national electricity delivery grid system, to make best use to reduce the energy utilization and causes the reduction of carbon foot print. Furthermore, it is found to take new technologies like plug-in hybrid electric vehicles, different kinds of distributed transmission, cosmological energy, smart metering, lighting management systems, distribution computerization, etc [6].

Smart Grid is increasingly seen as a means to facilitate climate friendly renewable energy sources (renewable) and to enable efficient use of electricity. For example, modern electrical networks can link wind and solar power with electric cars. A consequence of Smart Grid is a drastic increase in use of electronics in the power system [7]. This makes the satisfactory function of electrical and electronic equipment vital for realization of a robust Smart Grid.

2.3. The smart 2 grid technology (putting 'smart' into smart grid)

The European Government's are planning strategically to make compulsory the carbon emission reduction targets. The UK itself alone is planning to reduce, 34% of carbon footprint by the year 2020 and up to 80% by the year 2050. The function of the smart meters is to transmit and receive the detailed data of the energy use. This sort of two-way strategic exchange of message, the consumers can play a far more active role in the supply chain by taking higher control over their own energy consumption and also the carbon emissions and to know power price.

Smart meters can only make available or supply for the function of their intelligent, provided, if it is supported by a flawless communication structure which provides bidirectional transmission of consumption and control data in real time. This can be done exactly by the broadband power line (BPL). This technology is already widely put in operation in one of the major European countries, Germany. The BPL technology is based on just like internet protocol based communication platform. Here, each ray of power becomes broadband based data interface and the power grids change into the intelligent systems. The BPL can works straight away with any measuring device (meter) from any hawkers.

In terms of savings point of view, it is a merit and involves low cost. Remote metering will give a detailed picture of power consumption. Supplier can introduce marginal price tariffs at non-peak hours. It avoids, to

reduce, the consumption during the peak hours by the consumers. Significantly, BPL is not a stationary technology it means that additional smart grid applications can be executed in a phase wise manner. In future the power grid net works also used to balance the load management via automatic and help to regulate the load by the user such as domestic devices etc [8].

Distributed net work operators (DNOs) in UK are owned by a small number such as Scottish power, EDF etc. They are the licensed one distribute electricity in their ear marked region. DNOs are in a major position to take advantage of on the benefits of BPL. UK is taking an important step in the direction of reducing the UK's carbon footprint through a joint venture of DNOs and BPL by supporting the combination of different kinds of renewable energies [8].

2.4. The pacific northwest national laboratory (PNNL) –outlook

As for the report of PNNL (Pacific Northwest National Laboratory) from the department of energy's by installing of smart grids in the conventional grids decreases the carbon emission up to 12% by the year 2030. This report illustrates a direct link between the smart grid and carbon foot print. The intelligent grid reduces the consumption of energy and emissions of carbon by using directly a new technology and indirectly by using renewable energy. It is estimated that 442million metric tons the carbon emissions is prevented to allow in the atmosphere in every year by upgrading the conventional grids by using the smart grid technology. In the view of the Pratt, PNNL research scientist, the main aim is to make the grid into smart is to prune the carbon emissions, conservation of energy and to accommodate more renewable [9].

Direct mechanism reduce electricity consumption and carbon emissions and where as the indirect mechanism reduces the cost of deploying and operating efficiency and renewable. By combining the effects of both the mechanisms it leads to reduce the carbon foot prints by a very substantial percentage of 12 or more than it.

2.5. An over view of association of british bookmakers (ABB) UK

The United Kingdom's (UKs) conventional power grid is based on large centralized energy stations, it has executed very well in releasing secure and reliable energy over the years. Meanwhile the UK Government decided to implement to use the energy from renewable resources by 15% of the total energy required to UK by 2020, Nevertheless, the existing grids to be modified as per the new technology. For example, energy will be produced from offshore wind farms in the North Sea or the North of Scotland or from community based district heating schemes. At present it needs the intelligent grids which can receive the energy from all the sources of the different types of energy which supplies the power with less carbon foot print [10].

In view of the ABB philosophy of smart grid which includes four types of elements. 1) HVDC light, 2) FACTS, 3) WAMS and 4) Distribution net work management [10].

HVDC light is a patented one to ABB for a high voltage direct current technology which stands for the voltage source converters (VSCs) and it is confirmed that it is an environmentally free from the carbon footprints, a way to design the flow of energy transmission and distribution system for the system of underground cable or net work interconnection or submarine link.

Flexible AC Transmission Systems (FACTS) can help to improve the capacity of existing transmission networks and also it can enhance the security, capacity and flexibility of power transmission systems [10]. The consumers of the energy will get more current with a minimal impact of the environment.

WAMS Wide area of monitoring system technology is to monitor the grid power flow and to develop to know how it behaves in all the situations to be dynamic control. Phasor measurement units (PMU's) is an electronic device installed throughout the energy grid to provide highly accurate time stamping, the data supplied by each PMU is corresponding to the equivalent time stand[10].

The advantages of WAMS: The grid workers contain the ability to securely1) optimize the design capacity of their transmission property 2) optimize the savings of the either decrease or remove the revenue losses from the outages of transmission system.3) allow more rapid and co ordinate recovery after outages.

The above three elements of the intelligent grid focus mainly on the transmission network ,different types of renewable energy resources and energy storage devices like large batteries, flywheels, compressed air etc and so on to help to maintain the delivery of supply with security[10].

DISTRIBUTION NET WORK MANAGEMENT:

There is a pressure on the government to adopt feed-in-tariff schemes which it promotes the small scale renewable energy production. Consider an example a cultivator of a form house using a connection with 11kv If he install a small collection of three 6kW wind turbines of distributed energy storage or a mixed energy (Different kinds of renewable energy- single wind turbines, wind farms, solar PV on houses, waste to energy and biomass etc)[10].

ABB stands assist to expand guidelines and suggest skill solutions based on its wealthy global experience in the power efficiency region. The agreement made by the two parties ABB and MIIT (Ministry of Industry and Information Technology) to work closely and to arrange different programs like energy efficiency seminars, technology trainings, to visit onsite to rectify the problems and consultancy, etc, to help small and medium sized enterprises (SMEs) gain logical information and technological knowledge to apply energy conservation and reduction of emission.

Mr. Koch said ABB is a pioneer in the power competence technology field in the UN Climate Change meeting in Copenhagen, stands in an only one of its brand position to contribute to this by serving industries which put away more than 70% of the total energy in China. ABB

Power can be transferred from one grid to another needed one without building a new power grid by using a HVDC Technology. This approach reduces the

power loss through transfer and it indirectly helps to reduce the carbon footprints.[14]

3. The potential of smart grid

A group of authors elucidated different mechanisms by which the smart grid technological system could reduce carbon footprints. The report provides additional information to the research in each smart grid area.

Direct mechanisms are mainly for the benefiting from the conservation effect of consumers being more aware about their own energy use, which include incorporating smart grid-enabled diagnostics in residential and commercial buildings; adding more plug-in hybrid electric vehicles to the market; and benefiting from the conservation effect of consumers being more aware about their own energy use. Indirect mechanisms are for cost effect, successful operations and renewable.

According to Pratt, the combined effect of both the mechanisms, it could reduce the electric grid's carbon foot print at a marginal rate of 12% or more, and also he added renewable portfolios, goals of 20% to 30% set for the electricity sector by the time frame of two decades in many states as a part of national carbon policy [11].

4. Mechanisms considered

Pratt et al led a team analyzed different mechanisms, by which the smart grid technique could reduce carbon emissions. They also proposed suggestions for future extensions for the findings to fulfill the goals for decreasing the carbon intensity in coming two decades. For this, research and development work for the smart grid funding being given by the department of energy (DOE) [12].

The smart grid-Direct and Indirect impacts: The smart grid impacts can be divided into direct and indirect mechanisms. The main function of the direct reduction is the smart grid itself generate to savings in energy and/or emissions consumed or by reducing generation requirements. Whereas indirect reductions are related to smart grid functions are producing cost savings. It concludes that both the mechanisms are involved the rate of reduction in the energy and carbon footprints up to 12% by direct mechanisms and up to the 6% by indirect by coming two decades [13].

5. Conclusions

The carbon footprint is not an individual problem but it is a global one. For the optimal reduction of the carbon footprint, the alternate and advanced newer cutting edge technology like a broadband power line (BPL) which have to connect geographically throughout the world to decrease the emission of carbon. The public awareness and counseling is an important thing for the conservation of the energy which reduces the carbon footprint. To know the proper utilization of the energy, it is on the shoulders of everyone to avoid the wastage of power. In addition, the government policies, also has to be amended. Further, each government makes it to compulsion to use all kinds of energy resources and make it to proportional ratio of each kind of energy. The entire nation encouraged to develop a multi distributed power

grid system in the different zones, towns or individual homes make into green areas to produce surplus energy which may use for further developmental activity of the society.

A global call given on Saturday, March 27 at 8.30pm Earth hour 2010 to save the earth by switch off the power for an hour. Really it is fantastic public awareness program and it is a sign of commitment against the global warming. Make all the cities to smart cities, towns to smart towns, villages to smart villages, homes to smart homes and finally it should be a smart nation, ultimately it will become a smart world.

10. References

- [1] FAQ: Smart Grid, earth2tech, <http://earth2tech.com/2009/01/26/faq-smart-grid/>, Jan 26, 2009, Katie Fehrenbacher.
- [2] Peter Asmus, Reinventing Electric Utilities: Competition, Citizen Action and Clean Power (Island Press, 1997). This article is adapted from a piece appearing in the May issue of The Electricity Journal, May Island Press, 1997
- [3] Transformation of energy systems: The control room of the future. Adrian Clark, Christopher J. Pavlovski, Jeff Fry
- [4] Smart Grid Design for Efficient and Flexible Power Networks Operation and Control, from IEEE Xplore, James A Momoh.
- [5] Global Warming, Alternative Energy renewable, <http://www.global-greenhouse-warming.com/alternative-energy.html>
- [6] Xu Wei , Zhou Yu-hui , Zhu Jie-lin, Energy-efficient Distribution in Smart Grid, March 02,2010 at utilizati 03:33:34 EST from IEEE Xplore.
- [7] Magnus Olofsson, Director-General Swedish National Electrical Safety Board, Kristinehamn, Sweden, Electrical power quality and utilization, 10th International conference, electrical power quality and utilization, Sept 15-17, 2009, Lodz, Poland.
- [8] Intelligent utility, @ where the smart grid meets business and reality, <http://www.intelligentutility.com/article/10/03/puttin-g-smart-smart-grid>
- [9] Pacific Northwest National Laboratory, the Smart Grid: An Estimation of the Energy and CO2 Benefits, Pamela Harrington, December 2009.
- [10] Peter Jones, Head of Technology for ABB Power UK, outlines the key elements that comprise ABB's approach to smart grids.
- [11] Smart grid conference, October 4- 6, 2010 - Los Angeles Convention Center, CA, Pratt.
- [12] The Smart Grid: an Introduction", prepared for the U.S. Department of Energy by Litos Strategic Communication
- [13] Smart grid could reduce emissions by 12 percent, January 28, 2010; Anne Haas, PNNL, (509) 375-3732/[PNNL report evaluates smart grids' impact on carbon emissions].
- [14] www.abb.com

GSM Based LAN Monitoring and Controlling

**Prof. Mamata Bhamare, Tejashree Malshikare, Renuka Salunke,
Priyanka Waghmare**

Department of computer engineering, MIT pune-411038, India

ABSTRACT

The project aims to develop various network utilities which are required to effectively monitor a LAN network. It aims to develop an integrated software solution that allows a network administrator to remotely monitor his LAN by his cell. In a concern, computers are grouped together to form a network to manage and control activities of network while in office is an easy task, but while you are outstation/away from office to monitor and controlling of network instead of depending on third party information you can always have your cell phone serve the purpose login anytime to application and see who is busy with what in the office. This project is to provide the maximum details about the network to the administrator on their mobile phone, when administrator when administrator is away from office/goes out station.

Keywords - LAN, GSM,SMS, J2SE, WWW, MODEM

I. INTRODUCTION

Today the world is rapidly changing the statement "We are in the world" to "world is in our hand". The main aim our project is to control and monitor the network from our wireless handheld device i.e. cell phone from anywhere irrespective of distance. say you have a LAN setup at your setup at your office. Sitting at home you want to learn the LAN status. You can do so by storing this project in your cell phone and executing the same. In the era of project mobile devices, wireless devices are widely used and it has penetrated every part of our life, but remote monitoring of network through mobile device is still a mirage, this project is an effort to make this mirage a reality, and this is where the genesis of this of this project lies. Consider a LAN setup with the server machine connected to GSM service provider via a GSM modem. The interaction between the clients and the wireless media happens through this server. A small text file residing any of the client or server machine can be opened in your cell phone.

II. FEATURES CONTROLLED BY SYSTEM

1.1 NET VIEW :

Get in your cell phone, the list of entire client's in LAN. Keep pinged every time to check the latest status of the PC's.

1.2 PROCESS VIEW:

Get the list of all processes running in the remote machine.

1.3 ACTIVATE PROCESS:

Activate different processes in either the server machine or any of the client's.

1.4 KILL PROCESS:

Kill the desired processes in either the server or clients.

1.4 READ:

You can read the drives, folders, files of any of the client machines/ the server machine from cell.

1.5 OPEN FILE:

A small text file residing in any of the client or the server machine can be opened in your cell phone.

1.6 BROADCAST MESSAGES:

Broadcast messages to clients, server from cell.

1.7 NEW FILE:

Create a new document in the cell phone and save the same in either the server and client machine.

1.8 SHUT DOWN:

Shut down the client machine from mobile.

III. ARCHITECTURE OF PRAPOSED SYSTEM

Administrator sends his request through through SMS using his phone via GSM modem to the server. Server then recognizes the client machine which administrator is supposed to monitor and extract data from locally cached data buffer where latest 15 sec data of every machine is updated or stored and sends this info to the administrator as response.

Administrator is provided with a GUI based application in J2ME to send command message instantly without the need to retype message every time. Server sends command to the clients like start process, shutdown process, kill process, create, delete, send task list, compile code.

Through the GSM service provider the communication is done with the GSM modem which communicates with the server and the server communicates with the client. All clients are controlled and monitored by administrator via a series of SMS.

The administrator controls the LAN through his mobile even he is at the remote place. The clients cannot send back or communicate to the administrator the communication is unidirectional it is not two way.

The mobile used can be any mobile having GSM facility in it. Also the administrator can check the network load on the LAN by typing only a command. In this also serial USB interface and set of commands is used for administrator to communicate to clients.

The efforts that have been made regarding developing a LAN monitoring system are increasing everyday. But a lot of them are still in their initial stages. One of the softwares that are available in the market is ActiveXperts SMS

Messaging Server but it has quite different application from our project. Active SMS messaging server is windows based software package that enables you to send, receive and process SMS and email messages.

User can use his/her mobile phone to query a database in his computer via SMS.

LAN monitoring using GSM technology can be used in offices, malls as well as college or university level.

clients connected to server all clients have name given to it. Below we see the block diagram of GSM based LAN monitoring.

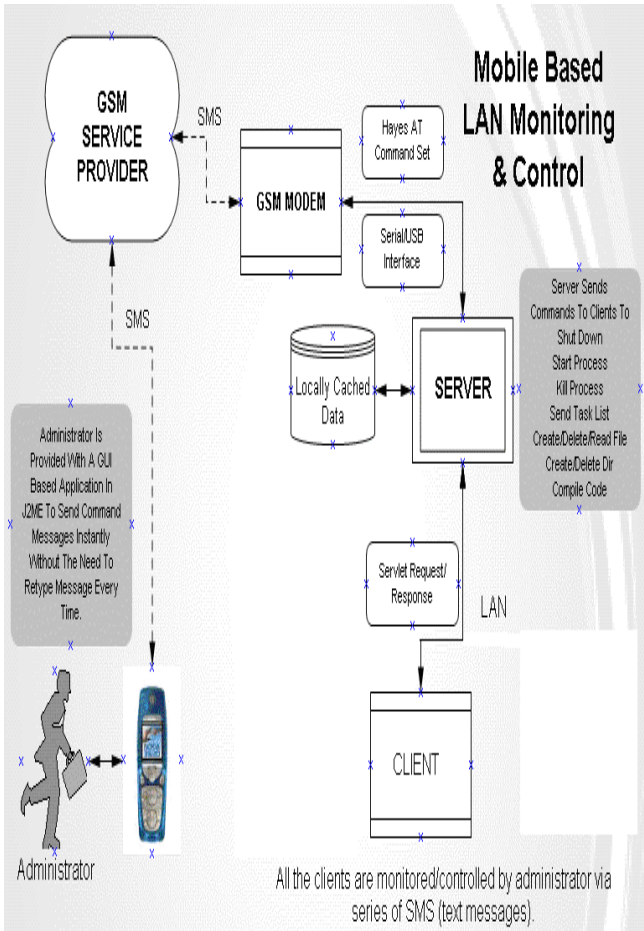


Fig.1 Architecture of mobile(GSM) Based LAN monitoring and control.

IV. BLOCK DIAGRAM OF PROPOSED SYSTEM

From the block diagram of proposed system we see that from mobile SMS is send to server through GSM modem. In SMS there is mobile number of the user, client name and operations to be perform on the client. That SMS is send to server then server recognise the client from all clients.

By using SMS parser we recognise the SMS fully, by process builder class we perform that process on that client.

Then after completion of that requested operation n the client, client send the response to the server. Then server send response to the administrator through GSM modem again SMS parsing is used to send SMS to administrator that specify that operations on the client is performed.

There is no any database maintained there is only one temporary database or we can say file. Through database we get the data we needed. There is many

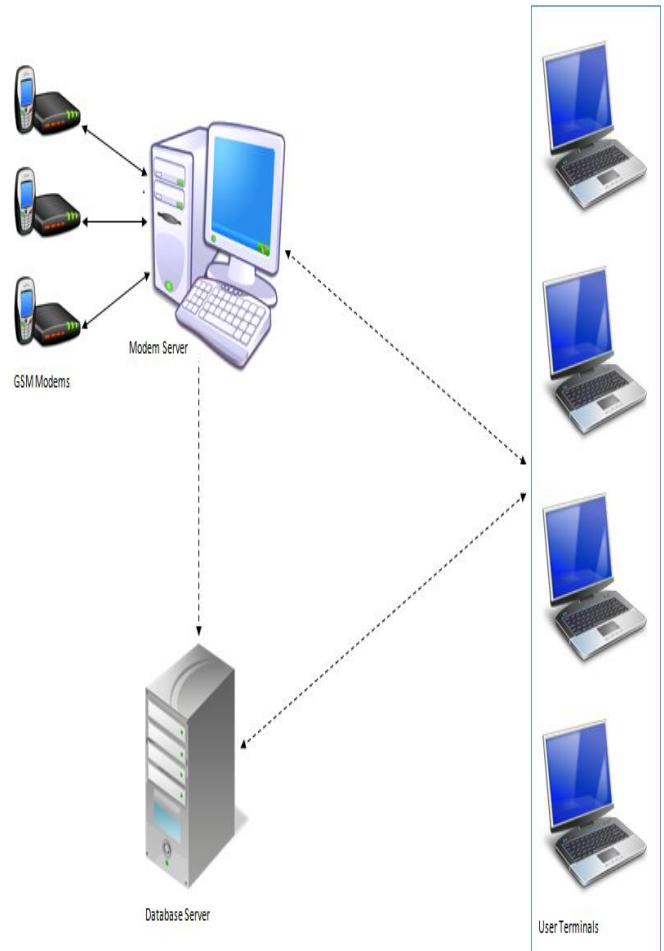


Fig 2. Block diagram of proposed system

V. TECHNOLOGY USED IN PROPOSED SYSTEM

In GSM Based LAN monitoring system we use technology like

1. SERVLET:

By using servlet in these system we communicate with client and server.

2. NET BEANS:

For better programming we use net beans for designing this system.

3. PROCESS BUILDER:

This class is used in this system which is very important to create operating system processes.

4. ABSTRACT WINDOW TOOLKIT:

This is java's toolkit used for windowing ,graphics and user interface creation for this system.

5. J2EE:

It is collection of java programming API's used for java platform programs. It is used to program this system.

VI. APPLICATIONS OF PROPOSED SYSTEM

1. LAN monitoring at the university/college level can be used for monitoring, logging and retention of network packets that traverse university networks. The goal of this project is to maintain confidentiality, integrity and availability of the university network infrastructure and information assets.
2. LAN monitoring at the office level can be used to monitor the office LAN by the administrator at any time if at a particular point he/she cannot be present there. He/she does not have to depend on any third party information regarding the LAN and can instead check the LAN status himself using his mobile.
3. LAN monitoring at the malls is used to monitor all information of malls by administrator at any time if at particular time he/she cannot be present there.

- [8] Ren Fengyuan, Huang Haining, Lin Chuang, Wireless sensor network, *Journal of Software*, Vol. 14, No. 7, March, 2003.

BOOKS:

- [9] Hegering ,Heinz-Gerd, Sebastian Abeck, Bernhard Neumair , *Integrated Management of Networked Systems:concepts, architecture, Operational Application Networking* (Morgan Kaufmann, 1999).

VII. CONCLUSION

This paper explains the basics of GSM based LAN monitoring.SMS remains the most efficient communication system for pushing the content on to the mobile devices. The software developed is a server based software application that provides ability to send and receive SMS messages through GSM network and communicates through standard TCP/IP protocol.

ACKNOWLEDGMENT

We are thankful to the department of computer engineering, MIT , for their kind support.

REFERENCES**JOURNAL PAPERS:**

- [1] B. Woodward, R. S. H. Istepanian, and C. I. Richards, Design of a telemedicine system using a mobile telephone, *IEEE Trans. on Information Technology in Biomedicine*, vol.5, no. 1, pp. 13–15, March. 2001.
- [2] Jinwook C., Sooyoung Y., Heekyong P., and Jonghoon C, MobileMed: A PDA-based mobile clinical information system, *IEEE Trans. on Information Technology in Biomedicine*, vol. 10, no.3, July 2006.
- [3] Md.Asdaque Hussain and Kyung Sup Kwak, Positioning in Wireless Body Area Network using GSM, *IEEE trans. on International Journal of Digital Content Technology and its Applications Vol 3, Number 3*, September 2009.
- [4] Peersman, G., Cvetkovic, S., The Global System for mobile Communications Short Message Service, *IEEE Personal Communications*, , June 2000
- [5] Collese, S., Di Tria, P., Morena, G. Short Message service based applications in the GSM network, *5th IEEE International Symposium on Personal, Indoor and Mobile Radio Communications*, 1994.
- [6] Coskun and H. Ardam, A Remote Controller for Home and Office Appliances by Telephone, *IEEE Trans. Consumer Electron.* , vol. 44, no. 4, November 1998.
- [7] Daldal Nihat, GSM Based Security and Control System, M.Sc. Term Project, *Gazi University, Ankara*, 2003.

Road Marking Detection for Vision Based Driver Assistance System

Thota Sridevi¹, Shaik Rahamthulla², Joneboyina Pradeep²,
Gurram Chandra Roshini²

¹Associate professor, Department of ECE, K.L.University, Guntur, A.P, India

²Project Students, Department of ECE, K L University, Guntur, A.P, India

ABSTRACT

Vision Based Driver Assistance Systems are in-vehicle systems that are designed to increase road safety by helping drivers to become better aware of the road. These systems will provide a better view of road on display to guide the drivers by enhancing the visibility of road in adverse weather conditions, to avoid collisions. The goal of each Driver Assistance System is to make driving easier and safer. We are designing a system, which will give us information about Road markings. Our Motto is to develop an efficient algorithm for Road marking detection, tracking and warning for Vision based Driver Assistance systems in real time. The Algorithm consists of five steps, video grabbing, pre-processing, edge detection, Hough transform and post processing. We are implementing this algorithm to overcome the disadvantages of existing methods.

Keywords – Driver assistance system, Edge detection, Hough transform, road markings

I. INTRODUCTION

Driver Assistance Systems are in-vehicle systems that are designed to increase road safety by helping drivers to become better aware of the road [1]. Vision based systems will provide a better view of road on display to guide the drivers. Few examples of Driver Assistance systems are GPS maps, Advanced Front-lighting System (AFS), 3D In-Dash Visualization, Collision Avoidance systems. Every system is designed with a specific application. Similarly, in this paper we are developing a road marking detection and tracking algorithm for assisting the driver using driver assistance systems. Road markings on the surface of the road are used for the control, warning, guidance or information of road users and to guide advanced driver assistance systems. Already existed methods [2] for road marking detection are, **positive negative gradients algorithm** is able to detect vertical and curved markings. But only one line is processed at a time. Horizontal markings in an image are not detected and spatial continuity of lane markings is not exploited in this extractor. **Steerable filters** are used to achieve spatial continuity by using Gaussian filters. These filters are optimal for one marking width and they are unable to tackle large width range. **Top-hat filter**, which uses convolution at many scales and can handle large width range. Like positive

negative gradient extractor this is also dedicated to vertical lane markings. **Global thresholding** is used to extract markings by global gray level thresholding. But it will not work due to variations in lighting conditions within an image. **Local threshold** [3] extraction is used to avoid lighting variations and in this extraction thresholding is done by comparing each pixel with a fixed threshold level. **Symmetrical local threshold** uses threshold level and left, right intensity averages for extraction. In this the processing is done line by line similar to Top-hat filter and positive negative gradient extractors.

To overcome the disadvantages of above specified methods, we are designing an algorithm with five steps, video grabbing, pre processing, Edge detection, Hough transform, post processing. These steps will be explained in preceding sections.

II. BLOCK DIAGRAM

Block diagram of the proposed model consists of '3' units

- Video grabbing (Image acquisition)
 - video acquisition
 - Converting video to frames
- Image processing unit
 - Pre processing
 - Edge detection
 - Hough transform
 - Post processing
- Output or Display unit

III. PROPOSED ROAD MARKING ALGORITHM

3.1 Algorithm

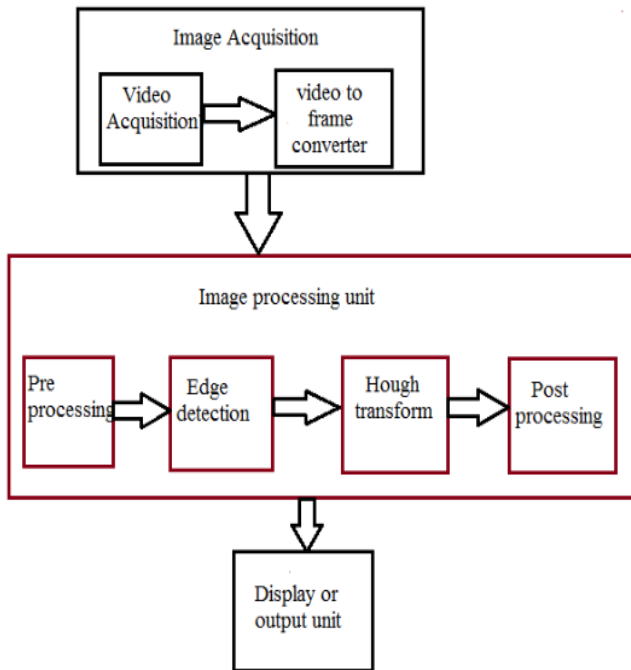


Fig: 2.1 Block diagram for Road marking detection

2.1 Image Acquisition

In this paper, we are considering Highway road video with less traffic as test video. This video is converted to frames for further processing. This converting process is known as Video Grabbing.

2.2 Image processing unit

Each frame is preprocessed if its quality is poor. Generally applied preprocessing techniques are Smoothing techniques. Frames may contain the unnecessary information like trees, sky etc. This information is cropped from the image in preprocessing. After pre-processing Canny Edge detection is employed to the image which will give the fine details of image. Hough transform is applied to the resultant image to detect the road markings as lines. If any extra lines were occurred they will be removed in post processing.

2.3 Output or Display unit

Generally used display units for driver assistance systems are visual Monitors, Warning Alarms or Combination of both. In this paper, we are displaying results on visual monitors.

```

    Video is converted to frames
    For each frame
    {
        Find the edges in the image by canny method.
        For all pixels in edge detected image
            If the pixel is an edge
                For all angles [0 180]
                    Calculate the Rho value
                    Increment the position (Rho, theta) in
                    Hough matrix
                Locate the highest values in Hough matrix
                Draw lines for located values
            }
    }
    Convert output frames (images) to video.
  
```

for edge detection are Gradients or Second order derivatives. Mostly used operators like Robert, Sobel and Prewitt are derived from gradients [4]. In this paper we are using sobel operator in canny edge detection.

3.2.1 Canny edge detection

Canny detection algorithm consists of five steps

- Gaussian Smoothing
- Gradient Analysis
- Non-maximum Suppression
- Hysteresis Thresholding
- Edge Linking

Step1: First step involves smoothing the image [4] by convolving with the Gaussian filter. Smoothing is to reduce the noise within an image

Gaussian smoothing function is given by

$$G(x,y) = \frac{1}{2\pi\sigma^2} e^{-\frac{x^2+y^2}{2\sigma^2}} \dots\dots\dots (1)$$

Where σ is standard deviation

2-D convolution operation is

$$I'(x,y) = \sum_{k=-N}^N \sum_{l=-N}^N g(k,l)I(x-k,y-l) \dots\dots\dots (2)$$

Where m= slope and c = y-intercept

Where g (k, l) = Convolution Kernel
 I(x, y) = Original image

The larger the width of Gaussian mask, the lower is the detector's sensitivity to noise.

Step2: This step is to find edge strength by taking the gradient of the image using Sobel operator. The sobel operator uses a pair of 3x3 convolution masks [5], one estimating gradient in X-direction and one in Y-direction

+1	+2	+1
0	0	0
-1	-2	-1

Gy

-1	0	+1
-2	0	+2
-1	0	+1

Gx

Magnitude of edge strength is given by [4]:
 $|G| = \sqrt{Gx^2 + Gy^2}$ (3)

Angle of orientation of the edge is given by:
 $\theta = \tan^{-1}(Gy/Gx)$ (4)

Step3: Once the edge direction is known, the next step is to relate the edge direction to one of the nearest four possible directions (0, 45, 90,135 degrees) [6]. Along the edge direction it finds the local maxima and suppresses the remaining pixels. This step is to maintain the single pixel thin edges and to minimize false edges.

Step4: In this step we will keep two thresholds high, low to detect strong and weak edges. Two thresholds are used to allow the little intensity variations near threshold level [4]. Strong edges are considered as true edges and weak edges may or may not be true.

Step5: Any pixel that is connected to the strong edge and that have a value greater than low threshold are also selected as edge pixel [6].

Performance of canny algorithm depends on the adjustable parameters σ and the threshold values.

3.3 Hough transform

Hough transform is a technique used to find shapes like lines, circles, ellipses, etc that are mathematically expressed in a binary digital image. In our project, we considered only straight lines [7]. Edge detected binary image is given as input to the Hough transform.

General equation for a straight line is

$y=m*x+c$ (5)

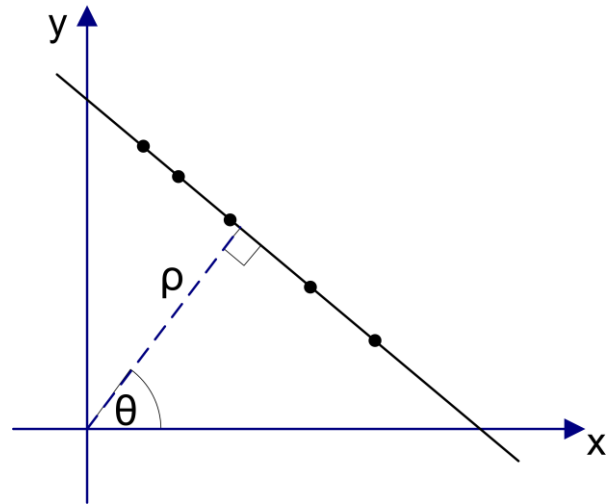


Fig 3.1: Rho 'ρ' and theta 'θ' representation of a straight line.

But in representation of (m, c) parameter space a disadvantage is that, both m and c goes towards infinity when the line becomes more and more vertical. So we are going for another expression of line with some parameters that have limited boundaries [5]. If 'ρ' is the distance from the origin to the line along a vector perpendicular to the line and the angle 'θ' is the angle between the x-axis and the 'ρ' vector.

The line equation is written as:

$\rho = x*\cos(\theta) + y*\sin(\theta)$ (6)

Boundaries of (ρ, θ) are $\rho \in [-D,D]$ where D is the diagonal of the image and $\theta \in [0, 180]$ in degrees. Using the above equation each pixel in spatial co-ordinates is represented with a unique parameter set (ρ,θ) in the Hough space. The result of the Hough transform is stored in a matrix called as Accumulator. Matrix dimensions are 'ρ' values and 'θ' values along two dimensions. The element with the highest value tells what line is most represented in the input image.

IV. RESULTS



Fig 4.1: input image

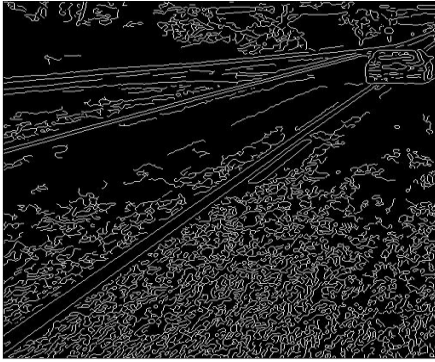


Fig 4.2: Edge detected image



Fig4.3: Image after indicating road markings

V. CONCLUSION & FUTURE SCOPE

In this paper, we have presented an efficient algorithm with edge detection and Hough transform for road marking detection. We concentrated mainly on straight lines and the results produced gave the solution for the problems occurred with the other filters and existed methods. This application is specifically for highways or less traffic areas where this system is exactly required.

This work can be extended to all types of road shapes. And this can be extended to tracking also and this can be applied to design a real time system for driver assistance.

ACKNOWLEDGEMENTS

The authors like to express their thanks to the management and department of ECE, K L University for their support and encouragement during this work.

REFERENCES

- [1] Prof. Ferit Küçükay, Janine Berghol, "Driver Assistant Systems"
- [2] Thomas Veit, Jean-Philippe Tarel, Philippe Nicolle and Pierre Charbonnier, P (2008), "Evaluation of Road Marking Feature Extraction" published in *IEEE transactions on image processing*, vol. 15, no. 3, 2006
- [3] Alberto Broggi, "A Massively Parallel Approach to Real-Time Vision-Based Road Markings Detection" Published in *IEEE*.
- [4] John Canny, P (1986), "A Computational Approach to Edge Detection" published in *IEEE*.
- [5] R. C. Gonzalez and R. E. Woods, *Digital image processing* (2nd edition, Prentice-Hall, 2002)
- [6] Ehsan Nadernejad, Sara Sharifzadeh, P (2008), "Edge Detection Techniques Evaluations and Comparisons"
- [7] Bryan S. Morse, Brigham Young University, "Segmentation (Edge Based, Hough Transform)"
- [8] N. Aggarwal and W. C. Karl, "Line detection in images through regularized Hough transform," presented at the *Conf. Information Science Systems*, 1999.
- [9] Hong Shan Neoh, Asher Hazanchukp, P (2005), "Adaptive Edge Detection for Real-Time Video Processing using FPGAs" published in *ALTERA*
- [10] Sergei Azernikov, P (2008), "sweeping solids and manifolds"
- [11] Thomas B. Moeslund. *Image and video processing*. August 2008

A NOVEL APPROACH OF IMPEDANCE SOURCE CASCADED MULTILEVEL INVERTER

Prof. V. Kandasamy¹, R.C. Manojchakkaravarthi²

1. Associate Professor, Department of Electrical and Electronics Engineering, Kumaraguru College Of Technology, Coimbatore.
2. PG Scholar, Kumaraguru College Of Technology, Coimbatore.

ABSTRACT: This paper deals with simulation of impedance source cascaded multilevel inverter. Impedance network in the cascaded multilevel inverter circuit will perform buck/boost operation. The use of Z-source inverter in industrial applications greatly increases its reliability by highly immune to EMI noises, improves power factor and reduces harmonic current and common-mode voltage. This impedance network reduces one stage(buck-boost) of power conversion system. Using impedance source multilevel inverter there is no problem of shoot through. This paper illustrate effective utilization of non – conventional resource(wind) which is used as source of one of the H bridge in cascaded multilevel inverter.

KEYWORDS: Z-source inverter ,Electromagnetic Interference(EMI) and cascaded multilevel inverter.

I.INTRODUCTION

In a traditional voltage-source inverter, the two switches of the same-phase leg can never be gated on at the same time because doing so would cause a short circuit (shoot through) to occur, which would destroy the inverter. In addition, the maximum output voltage obtainable can never exceed the dc bus voltage. Each converter generates a square wave voltage waveform with different duty ratios, which together form the output voltage waveform. These limitations can be overcome by the new Z-source inverter [1],[2]. In addition, the reliability of the inverter is greatly improved because the shoot through caused by electromagnetic interference (EMI) noise can no longer destroy the circuit. Thus, it provides a low-cost and reliable. Multilevel inverters synthesizing a large number of levels have a lot of merits such as improved output waveform, a smaller filter size, a lower EMI (Electro Magnetic Interference), and other advantages. The principle advantage of using multilevel inverters is the low harmonic distortion obtained due to the multiple voltage levels at the output and reduced stresses on the switching devices used. Due to their ability to synthesize waveforms with a better harmonic spectrum and attain higher voltages, multi-level inverters are receiving increasing attention in the past few years. The benefits are especially clear for medium-voltage drives in industrial applications [5],[6] and are being considered for future Naval ship propulsion systems. The multilevel inverter was introduced as a solution to increase the converter operating voltage above the voltage limits of classical semiconductors. Multilevel voltage source inverter (VSI) has been recognized as an important alternative to the normal two levels VSI, especially in high power application

[4]. Using multilevel technique, the output voltage amplitude is increased, switching devices stress is reduced and the overall harmonics profile is improved. Several multilevel topologies are reported [1, 2, 3], and the most popular topology is Cascaded Multilevel Inverter (CMI). It offers several advantages compared to other topologies such as simple circuit layout, less components counts, modular in structure and avoid unbalance capacitor voltage problem. However as the number of output level increases, this topology becomes highly cumbersome because the number of power devices is increases.

II.IMPEDANCE NETWORK

The circuit diagram of impedance network is shown in the Fig. 1. It consists of a pair of capacitors and inductors respectively. The value of capacitors and inductors can be chosen based on the output voltage requirement. A diode is connected in the impedance network as shown Fig. 1 to block the reverse flow of current. A voltage type impedance source inverter can assume all active and null switching states of VSI. Unlike conventional VSI, a impedance source fed inverter has a unique feature of allowing both power switches of a phase leg to be turned ON simultaneously (shoot-through state) without damaging the inverter.

The impedance network changes the circuit configuration from that of a voltage source to an impedance source (i.e. Z-source). It allows the VSI to be operated in a new state called the shoot-through state in which the two switching devices in the same leg are simultaneously switched-on to effect short-circuit of the dc link [3]. During this state, energy is transferred from the capacitors to inductors, thereby giving rise to the voltage boost capability of the impedance source fed inverter.

The impact of the phase leg shoot-through on the inverter performance can be analyzed by considering the circuit diagram shown in Fig. 1.

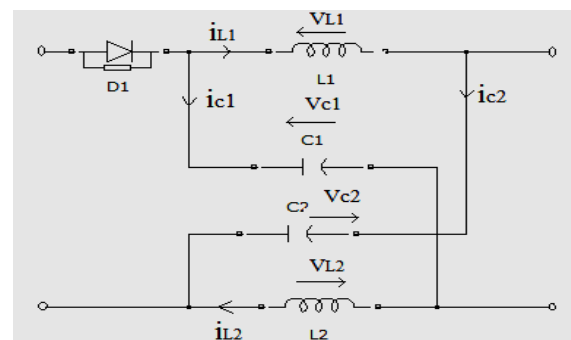


Fig. 1 Impedance network

When the impedance network is in non – shoot – through state unlike normal voltage source inverter it can assume a third distinct state for inductive voltage boosting by turning ON two switches from any phase-leg simultaneously to create a short-circuit across the inverter dc-link ($v_i = 0V$). Doing so will not damage any semiconductor devices because the energy supplied by the dc source and shunt capacitors is prevented from surging instantaneously by the Z- source inductors. Therefore (assuming $L_1 = L_2 = L$ and $C_1 = C_2 = C$):

$$v_{L1} = v_{L2} = v_L = v_{C1} = v_{C2} = v_C \dots\dots\dots (1)$$

$$v_L = v_{dc} - v_C \dots\dots\dots (2)$$

$$v_i = 2v_C - v_{dc} \dots\dots\dots (3)$$

III.IMPEDANCE SOURCE SEVEN LEVEL CASCADED MULTILEVEL INVERTER

Simulated configuration of impedance source seven level cascaded multilevel inverter is shown in Fig.2. It consists of twelve IGBT/Diode switches. Each H bridge consists of four switches respectively.

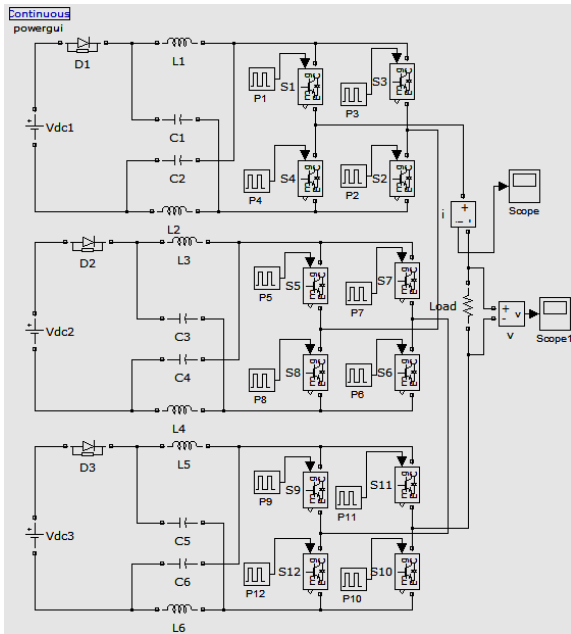


Fig. 2 Simulation diagram of impedance source Cascaded multilevel inverter

Source for each H bridge is fed from impedance network. This voltage will be less or greater than input dc voltage. Nature of the load is pure resistive. Based on the values of inductor pairs and capacitor pairs in a impedance network magnitude of Vdc is chosen. Since each H bridge in an inverter circuit can provide three voltage levels(zero, positive dc voltage and negative dc voltage). So switching state is defined for H bridge in an inverter circuit as shown in below table.

Table 1: switching states

SHi	SLi	SRi	Vgi	idci
-1	0	1	-v _{dc}	-i _s
0	0	0	0	0
0	1	1	0	0
1	1	0	v _{dc}	i _s

From above table, it can be seen that the general relationships for ith H bridge are

$$V_{gi} = (S_{Li} - S_{Ri}) V_{dci} \dots\dots\dots (4)$$

$$id_{ci} = (S_{Li} - S_{Ri}) i_s \dots\dots\dots (5)$$

Where,

SLi = Left arm switch in ith H bridge

SRi = Right arm switch in ith H bridge

SHi = Switching states for ith H bridge

Vgi = inverter output voltage for ith H bridge

Idci = Inverter dc current for ith H bridge

i_s = Source current

IV.WIND MODEL

Three phase permanent magnet synchronous generator is used in this proposed paper because of its advantages such as they do not require an additional DC supply for the excitation circuit, it avoids the use of slip rings, hence it is simpler and maintenance free and condensers are not required for maintaining the power factor in synchronous generators, as it is required in induction generator.

This permanent magnet synchronous generator output voltage is rectified using uncontrolled rectifier block and the ripples in the output is reduced by implementing the LC filter in a circuit. This filtered output is then connected as dc source of one of the H bridge in a impedance source cascaded multilevel inverter. This output voltage from permanent magnet synchronous generator is controlled by varying the preset model of synchronous generator and the wind speed.

In this paper wind model is implemented for first H bridge of impedance source seven level cascaded multilevel inverter as shown in Fig 3.

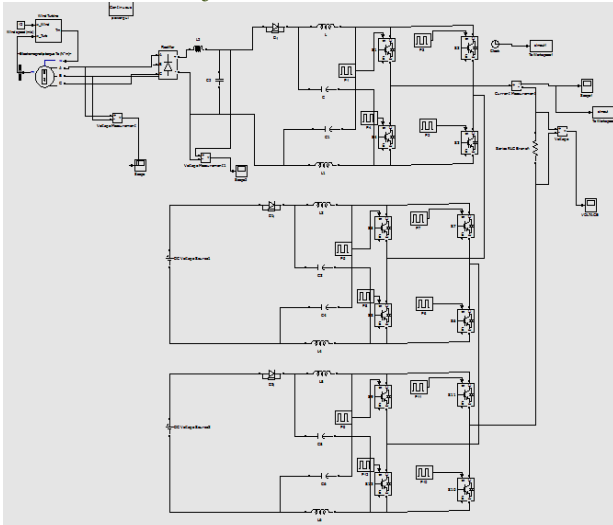


Fig. 3 Simulation diagram of impedance source Cascaded multilevel inverter with wind model

The output dc voltage from wind model is fed to the impedance network of first H bridge of impedance source cascaded multilevel inverter. This dc voltage from the rectifier block of wind model can be buck or boosted as based on requirement of the circuit.

Implemented wind model in impedance source cascaded multilevel inverter is shown in Fig.4

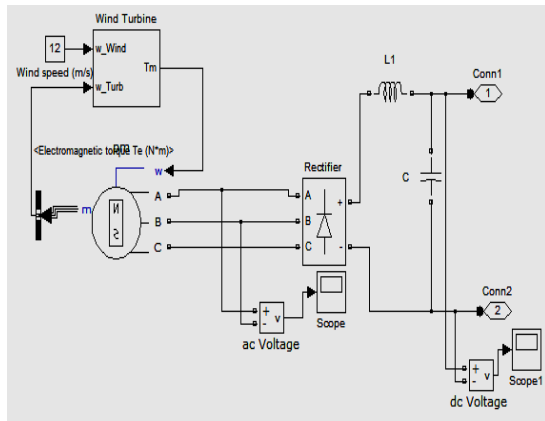


Fig.4. Simulation diagram of Wind model

V. RESULTS AND DISCUSSIONS

Experimental output voltage waveform for impedance source seven level cascaded multilevel inverter is shown in Fig. 5. Input dc voltage for second and third H bridge is given as 70V and for first H bridge 100V dc voltage will be supplied from the wind model. This 70V is boosted to 100V with the help of impedance network. This can be observed in below output voltage waveform.

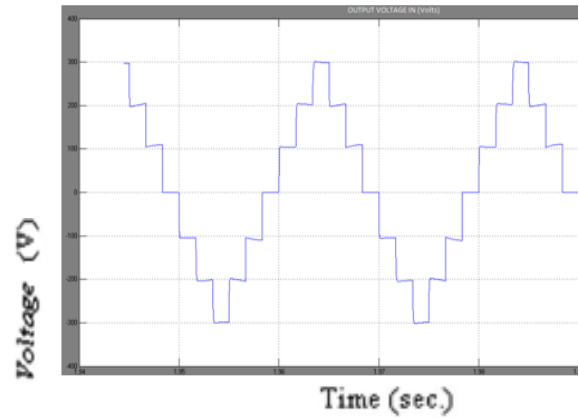


Fig. 5 Experimental output voltage waveform

Experimental output current waveform for impedance source seven level cascaded multilevel inverter is shown in Fig. 6. Load used for this simulation is resistive load of 50Ω. So the output current will be 6A. This can be observed in below output current waveform.

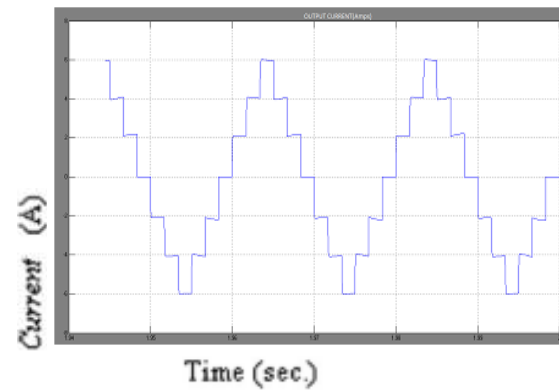


Fig. 6 Experimental output current waveform

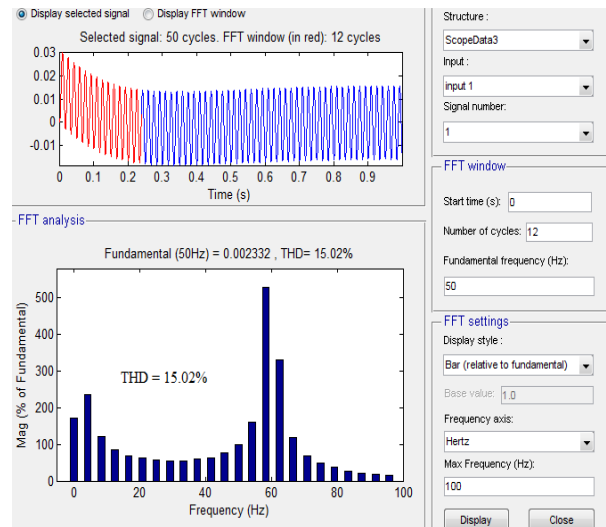


Fig. 7 Measured THD

For the above experimental output waveform THD of 15.02% is obtained which is shown in above Fig. 7.

VII.CONCLUSION

From the simulation output of impedance source cascaded multilevel inverter the ripple contents and the harmonics in the output voltage of the inverter is reduced. Impedance source cascaded multilevel inverter topology have ability to produce any desired output ac voltage, even greater than the line voltage, regardless of the input voltage, thus reducing motor ratings and provide ride-through during voltage sags without any additional energy storage elements and impedance network in each bridge can do both buck and boost operation based on the values of inductors and capacitors in the network. The presented simulation results have been obtained by using MATLAB sim power system tool.

VII.REFERENCES

- [1] S. Rajakaruna and Y.R.L. Jayawickarma, "Designing Impedance Network of Z-Source Inverters," in Proceedings IPEC'05, Volume2, pages 962-967, 2005.
- [2] Fang Zheng Peng, "Z-Source Inverter for Motor Drives," in *Proceedings IEEE Power Electronics Specialists Conference*, pp. 249-254, Germany, 2004.
- [3] F. Z. Peng, "Z-source inverter," *IEEE Trans. Ind. Appl.*, vol. 39, no. 2, pp. 504 – 510, Mar./Apr. 2003.
- [4] B. K. Bose, *Power Electronics and Variable Frequency Drives*. UpperSaddle River, NJ: Prentice- Hall, 2002.
- [5] P.W. Hammond, "Medium voltage pwm drive and method," U.S. Patent 5 625 545, April 1997.
- [6] M. D. Manjrekar, P. K. Steimer, and T. A. Lipo, "Hybrid multilevel power conversion system: a competitive solution for high power applications," *IEEE Trans. Ind. Applicat.*, vol. 36, pp. 834–841, May/June 2000.

AUTHORS BIOGRAPHY



V.KANDASAMY received the B.E degree in Electrical and Electronics Engineering from Bharathiyar University, Coimbatore, India in 1998, the M.E degree in VLSI Design from SASTRA University, Thanjavur, India in 2003, pursuing Phd degree in Electrical Engineering from Anna University, Tamilnadu, India. He is currently as Associate Professor at Kumaraguru College of Technology, Coimbatore, India. His current research Wind Energy Power Converters, IPGA based Design, Embedded based system development.



R. C. MANOJ

CHAKKARAVARTHI was born in Sathyamangalam, India in 1987. He received the B.E (Electrical and Electronics Engineering) degree in Bannari Amman Institute Of Technology, Coimbatore, India in 2010. Now he is doing M.E (Power Electronics and Drives) in Kumaraguru College of Technology, Coimbatore, India. His areas of interest are Power Electronics and Drives, Power Quality and Renewable Energy.

A Novel Voltage and Frequency Control Scheme for a Wind Turbine Driven Isolated Asynchronous Generator

¹K. Premalatha, ²S. Vasantha rathna, ³R.K.Isvarya

^{1,3}Department of EEE, Kumaraguru College of Technology, Coimbatore.

²Coimbatore Institute of Technology, Coimbatore.

Abstract

This paper deals with the control of voltage and frequency of a wind turbine driven isolated asynchronous generator. The controller consists of an IGBT (Insulated Gate Bipolar Junction Transistor) based 3-leg voltage source converter and a battery at its DC link. The controller is having bidirectional flow capability of active and reactive powers by which it controls the system voltage and frequency with varying wind speed and load conditions. Inverted sine carrier pulse width modulation switching strategy is used in VSC to enhance the fundamental output voltage and to minimize the switching losses. The proposed system is simulated in MATLAB using Simulink and PSB (Power System Block-set) toolboxes.

Keywords: Isolated asynchronous generator, wind energy conservation system, voltage and frequency controller, Inverted sine carrier PWM.

1. Introduction

There has been an exponential increase in the energy demand during the last few decades, which has accelerated the depletion of the world fossil fuels. Environmental concerns and international policies are supporting new interests and developments of small scale renewable power generation [1, 2]. As a renewable energy source the wind power is one of the prominent energy sources and various types of electrical generators such as synchronous generator, asynchronous generators in squirrel cage and slip ring rotor construction [3-6], reluctance generators [7] have been reported in standalone applications. It is reported in the literature that in small scale wind power generation, a capacitor excited squirrel cage asynchronous generator (CEAG) which is also known as isolated asynchronous generator (IAG) is a most suitable candidate where the grid connection is not accessible because of its low cost, robustness, less maintenance and high power density (W/kg) [3, 4]. However the magnitude and frequency of the generated voltage depends upon the wind speed, the amount of excitation and the load.

In this paper, a voltage and frequency (VF) control scheme for an isolated capacitor excited asynchronous generator driven by wind turbine with Inverted sine carrier PWM technique in VSC is proposed to enhance the fundamental output voltage [8].

2. Principle of operation

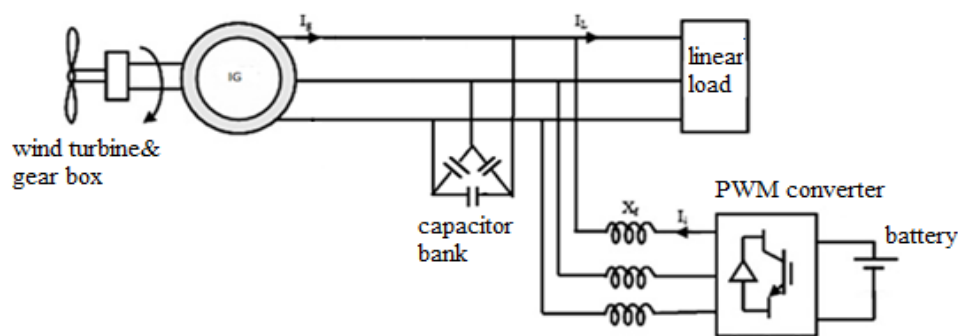


Fig 1 Schematic diagram of wind turbine driven isolated asynchronous generator feeding linear load

Fig. 1 shows a schematic diagram of wind turbine-driven asynchronous generator along with VSC. The delta connected capacitor bank is used to generate the rated voltage at no load while additional demand of the reactive power is met by the controller. The proposed controller is having bidirectional flow capability of active and reactive powers and it controls the voltage by controlling the reactive power while the frequency is controlled by the active power control.

The basic principle of operation is that at high wind speed the generated power is also high and accordingly for frequency regulation the total generated power should be consumed otherwise difference of mechanical and electrical power is stored in the revolving components of the generator and by which the speed of the generator and in turn it increases the output frequency. Therefore this additional generated power is used to charge the battery to avoid the frequency variation as

stated above. During deficiency of the generated power, when there is an insufficient wind power to meet the consumer demand an additional required active power is supplied by the battery to the consumer loads. In this manner, the battery energy storage system based voltage and frequency controller also provides load leveling and frequency regulation.

3. Modeling of the proposed system

A. Modeling of the wind turbine

The mechanical system consists of a wind turbine and the gear ratio is selected such that the IAG generates the rated voltage at rated frequency and a rated wind speed of 12m/s to extract the maximum power from the wind turbine. The aerodynamic power generated by the wind turbine can be expressed as

$$P = 0.5\rho AC_p v_w^3 \tag{1}$$

where ρ is the specific density of air,

A is the swept area of the blades,

v_w is the wind speed and

C_p is the performance co-efficient.

Turbine characteristics is given by

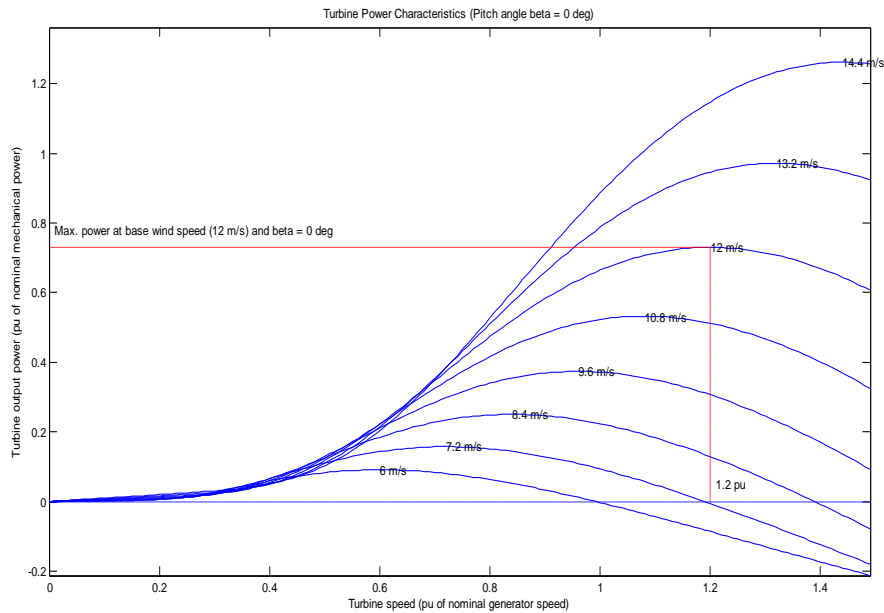


Fig 2 Turbine characteristics

B. Modeling of Asynchronous generator

The electrical system consists of an asynchronous generator with the excitation capacitor. The Asynchronous generator model is established using rotating (d, q) field reference. Stator and rotor voltage equations are given by

$$V_{sd} = R_s i_{sd} + \frac{d}{dt} \lambda_{sd} - \omega_d \lambda_{sq} \tag{2}$$

$$V_{sq} = R_s i_{sq} + \frac{d}{dt} \lambda_{sq} - \omega_d \lambda_{sd} \tag{3}$$

$$V_{rd} = R_r i_{rd} + \frac{d}{dt} \lambda_{rd} - \omega_{dA} \lambda_{rq} \tag{4}$$

$$V_{rq} = R_r i_{rq} + \frac{d}{dt} \lambda_{rq} - \omega_{dA} \lambda_{rd} \tag{5}$$

Where $V_{sd}, V_{sq}, V_{rd}, V_{rq}$ are the direct and quadrature axes stator and rotor voltage.

R_s, R_r are the stator and rotor resistance,

$i_{sd}, i_{sq}, i_{rd}, i_{rq}$ are the direct and quadrature axes stator and rotor current,

$\lambda_{sd}, \lambda_{sq}, \lambda_{rd}, \lambda_{rq}$ are the flux linkages and

ω_d is the angular velocity.

Electromagnetic torque is expressed as

$$T = P/2 L_m (i_{sq} i_{rd} - i_{sd} i_{rq}) \tag{6}$$

where L_m is the mutual inductance.

C. Modeling of controller

Voltage-source converter (VSC) is connected to a battery of 1500VAh at its dc link and provides a switched voltage waveform.

Line to line voltage is given by

$$v_{ab} = v_{an} - v_{bn} \quad (7)$$

$$v_{bc} = v_{bn} - v_{cn} \quad (8)$$

$$v_{ca} = v_{cn} - v_{an} \quad (9)$$

Phase voltage is given by

$$\begin{bmatrix} v_{an} \\ v_{bn} \\ v_{cn} \end{bmatrix} = v_{dc} \begin{bmatrix} 2/3 & -1/3 & -1/3 \\ -1/3 & 2/3 & -1/3 \\ -1/3 & -1/3 & 2/3 \end{bmatrix} \begin{bmatrix} a \\ b \\ c \end{bmatrix} \quad (10)$$

Where a, b, c are switching variable vector

4. Control strategy

The control strategy of the proposed voltage and frequency controller is based on the generation of reference source currents. Three-phase reference source currents are having two components such as active and reactive components. One is in phase or active power component while other one is in quadrature or reactive power component for regulating the frequency and voltage respectively.

A. In Phase Component of Reference Source Currents

For generating the active power component of reference source current, the output of the frequency Proportional-Integral (PI) controller is compared with the rated generator current (I_G) and the difference in these two currents is considered as amplitude of in-phase component of reference current. The multiplication of amplitude of in-phase component of reference current with in-phase unit amplitude templates (u_a, u_b and u_c) yields the in-phase component of reference source currents. These templates (u_a, u_b and u_c) are three-phase sinusoidal functions, which are derived by dividing the AC voltages v_a, v_b and v_c by their amplitude V_t .

The rated current of the generator is calculated as

$$I_G = \sqrt{2} (P_{rated}) / (\sqrt{3} V_{rated}) \quad (11)$$

Where P_{rated} and V_{rated} are rated power and rated line voltage of the asynchronous generator.

The instantaneous line voltage at the asynchronous generator terminals (v_a, v_b and v_c) amplitude is computed as

$$V_t = \{(2/3)(v_a^2 + v_b^2 + v_c^2)\}^{1/2} \quad (12)$$

The unity amplitude templates are having instantaneous value in phase with instantaneous voltage (v_a, v_b and v_c) which are derived as

$$u_a = v_a / V_t; u_b = v_b / V_t; u_c = v_c / V_t \quad (13)$$

B. Quadrature Component of Reference Source Currents

To generate the quadrature component of reference source current, another set of sinusoidal quadrature quantity amplitude unity template (z_a, z_b and z_c) is obtained from in-phase unit templates (u_a, u_b and u_c). The multiplication of these components with output of AC voltage PI controller gives the quadrature or reactive power component of reference source current.

z_a, z_b and z_c are another set of unit templates having a phase shift of 90° leading with the corresponding unit templates u_a, u_b and u_c which are computed as follows

$$\begin{bmatrix} z_a \\ z_b \\ z_c \end{bmatrix} = \begin{bmatrix} 0 & -1/\sqrt{3} & 1/\sqrt{3} \\ \sqrt{3}/2 & \sqrt{3}/2 & -\sqrt{3}/2 \\ -\sqrt{3}/2 & \sqrt{3}/2 & -\sqrt{3}/2 \end{bmatrix} \begin{bmatrix} u_a \\ u_b \\ u_c \end{bmatrix} \quad (14)$$

C. Reference Source Currents

Total reference source currents are the sum of in-phase component and quadrature components of the reference source currents as

$$i_{sa}^* = i_{sad}^* + i_{saq}^* \quad (15)$$

$$i_{sb}^* = i_{sbd}^* + i_{sbq}^* \quad (16)$$

$$i_{sc}^* = i_{scd}^* + i_{scq}^* \quad (17)$$

D. PWM Current Controller

Reference source currents (i_{sa}^*, i_{sb}^* and i_{sc}^*) are compared with sensed source currents (i_{sa}, i_{sb} and i_{sc}). The current errors are computed as

$$i_{saerr} = i_{sa}^* - i_{sa} \quad (18)$$

$$i_{sberr} = i_{sb}^* - i_{sb} \quad (19)$$

$$i_{scerr} = i_{sc}^* - i_{sc} \quad (20)$$

These current errors are amplified and the amplified signals are compared with fixed frequency (5 KHz) inverted sine carrier wave to generate gating signals for IGBTs of VSC of the controller.

E. Inverted sine carrier PWM

The control scheme uses an inverted sine (high frequency) carrier that helps to maximize the output voltage for a given modulation index.

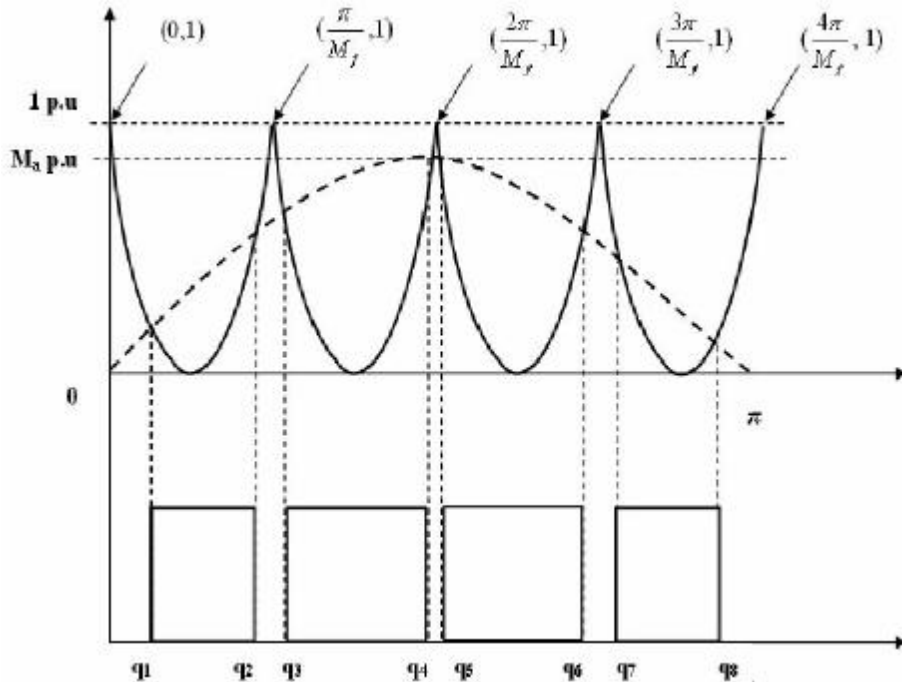


Fig 3 Inverted sine carrier PWM pulse pattern

For the ISCPWM pulse pattern, the switching angles may be computed as the same way as SPWM scheme. The equations of inverted sine wave are given by (21) and (22) for its odd and even cycles respectively. The switching angles for ISCPWM scheme can be obtained from (23) and (24).

$$y = 1 - \sin[M_f x - \frac{\pi}{2}(i - 1)] \tag{21}$$

$$y = 1 - \sin[M_f x - \frac{\pi}{2}(i - 2)] \tag{22}$$

$$M_a \sin q_i + \sin [M_f q_i - \frac{\pi}{2}(i - 1)] = 1 \quad \text{for } i=1,3,5,\dots \tag{23}$$

$$M_a \sin q_i + \sin [M_f q_i - \frac{\pi}{2}(i - 2)] = 1 \quad \text{for } i=2,4,6,\dots \tag{24}$$

Where M_a - Modulation index

M_f - Frequency ratio

q_i - Intersection between the inverted sine waveform

5. Simulation Results

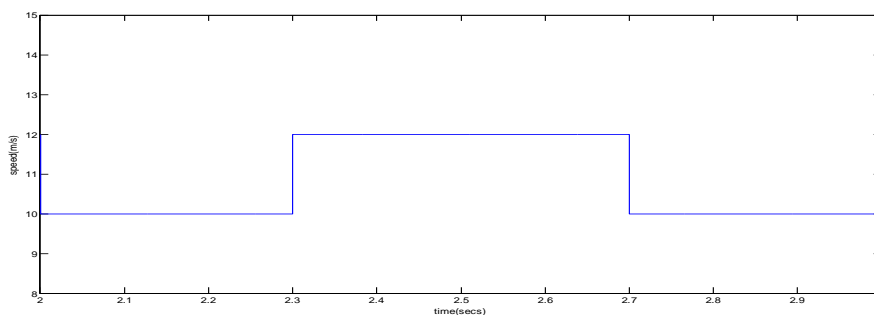
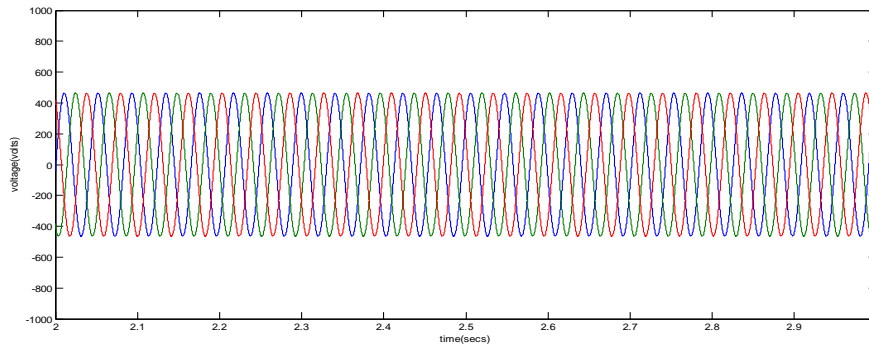
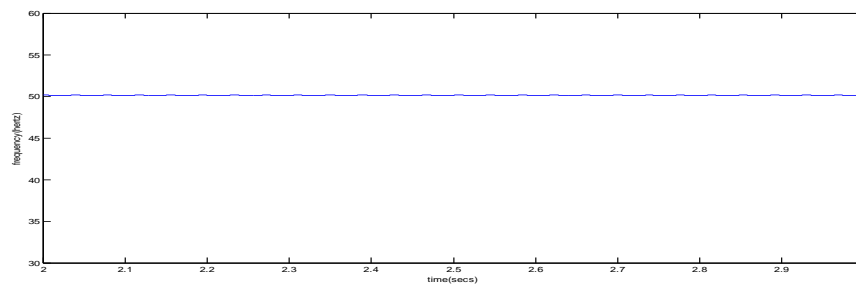


Fig4 Wind speed variation

**Fig 5 Load voltage waveform****Fig 6 Frequency waveform**

A 7.5KW, 415V, 50Hz asynchronous machine is used as an IAG. Fig. 4, 5 and 6 show the performance of the controller for varying wind speeds at constant consumer load. At 2 s, the wind speed is 10m/s and the consumer load (5kW) is applied at the generator terminals. It is observed that due to insufficient power generation at low wind speed an additional load power is supplied by the battery to regulate the frequency. At 2.3 s as the wind speed is increased from 10m/s to 12m/s, output power of the generator is increased so that at particular load now the power supplied by the battery is reduced because now the load demand is met by the generator itself. At 2.7s, the wind speed is again reduced and the additional power is supplied by battery.

6. Conclusion

The performance of the proposed Inverted sine carrier PWM based VSC for isolated asynchronous generator driven by wind turbine is demonstrated. The proposed controller has been found suitable with simple control strategy to regulate the voltage and frequency under varying wind speeds. Also it presents a novel PWM scheme (ISC PWM) for controlling the output of an inverter with improved fundamental component values and to reduce the switching losses of the converter.

References:

- [1] Bhim Singh and Gaurav Kumar Kasal, "Analysis and Design of Voltage and Frequency Controllers in a Constant Power Applications", in Proc of IEEE International Conf on Power Electronics Drives and Energy Systems (PEDES'06), New Delhi, India, Dec 12-15, 2006.
- [2] Siegfried Heier, "Grid Integration of Wind Energy Conversion Systems", IEEE Trans. on Energy Conversion, Vol. 19, No. 1, March 2004, pp.136-143.
- [3] T.F. Chan and L.L. Lai, "A novel excitation scheme for a stand-alone three-phase induction generator supplying single-phase loads", IEEE Trans. on Energy Conversion, Vol. 19, No. 1, March 2004, pp.136-143
- [4] T.F. Chan, and L.L. Lai, "Single-phase operation of a three phase induction generator using a novel current-injection method", IEEE Trans. on Energy Conversion, Vol. 20, No.2, June 2005, pp. 308-315.
- [5] M Ermis, H. B Ertan, M Demirekler, "Various induction generator schemes for wind electricity- generation", Electric Power Systems Research, Vol. 23, No.1, Jan1992, pp 71-83.
- [6] T.F. Chan, K.A. Nigim, L.L. Lai, "Voltage and frequency control of self-excited slip-ring induction generators", IEEE Trans. on Energy Conv, Vol. 19 1No.1, Mar 2004, pp 81-87.
- [7] Y.S. Wang, L Wang, "Minimum Loading resistance and its effects on performance of an isolated self-excited reluctance generator", IEE Proc.Gen. Trans. and Dist. Vol. 148, No.3, May 2001, pp 251-256.
- [8] R.Nandha kumar and Jeevananthan, " Inverted sine carrier pulse width modulation for fundamental fortification in DC-AC converters".

Author Biography

K. Premalatha received B.E. in Electrical and Electronics Engineering from Madras University, Tamilnadu, India, in 1997, M. Tech. in Power Electronics and Drives from SASTRA University, Tamilnadu, India, in 2002 and pursuing Ph.D. in Electrical Engineering at Anna university, Coimbatore, Tamilnadu, India. Currently she is Asso. Professor in Electrical & Electronics Engineering at Kumaraguru College of Technology, Tamilnadu, India. She is Life Member in Systems Society of India and ISTE. Her research interest includes Power Quality, Power Electronics and Wind Energy Conversation systems.

S. Vasantharathna received B.E. in Electrical Engineering from Bharathiar University, Tamilnadu, India, 1989, M. E. in Power Systems from Bharathiar University, Tamilnadu India, 1994 and Ph.D. in Electrical Engineering from Bharathiar University University, Tamilnadu, India, 2006. Currently she is Asso. Professor in Electrical & Electronics Engineering at Coimbatore Institute of Technology, Tamilnadu, India. She is Member of IEEE, and Life Member of ISTE. Her research interest includes Operating systems, Power and Energy Systems and Signal Processing.

R. K. ISVARYA received bachelor degree from Sona College Of Technology, Salem in Electrical and Electronics Engineering in 2010. She is currently doing her master degree in Power Electronics and Drives at Kumaraguru College Of Technology, Coimbatore.

Improvement of Crankshaft Assembly Supply Chain Using Lean Techniques-A Case Study

G.Saranya¹, Mr. S.B. Nithyananth²

*Second year M.E Industrial Engineering, Kumaraguru College of Technology, Coimbatore, India

** Assistant professor, Department of mechanical engineering, Kumaraguru College of Technology, Coimbatore, India

ABSTRACT

In today's competitive business world, companies require small lead times, low costs and high customer service levels to survive. Because of this, companies have become more customers focused. Manufacturing industries face continuous pressure to reduce the price to remain in the market. The objective of this paper is to identify areas of wastes and how these can be reduced or eliminated using lean Techniques from the crankshaft assembly supply chain of a leading Two Wheeler Manufactures in south India. It is useful to map the dynamics of the supply chain focusing on how the demand information is passed from the final customer, back to the material suppliers and manufactures inside the company. So in this paper attempt has been made to find work in process, lead time, Inventory carrying costs and reduction of value in terms of Rupees from the current process to the proposed process.

Keywords-Lean, Supply Chain, Waste Reduction, Value Stream Mapping

1. Introduction

Success in modern manufacturing industry directly correlates to how a company handles global competition. Cost effective solutions and practices are essential to stay competitive in the market. Many manufacturing facilities have experienced the drastic changes and are in a process of undergoing physical and cultural transformation to adopt the concept of lean thinking. Lean has been originally created and defined as the process of eliminating waste (Womack et al. 1990) Toyota along with the support a system to reduce or eliminate waste and non-value added activities from the various processes (Ohno, 1988; Shingo and Dillon, 1988). The conceptual framework for categorizing all of the tools and practices of lean production in five basic areas:

- **Value:** Define value from the standpoint of the customer. However, in reality, the final customer is the only one who can specify the value of a specific product or service by paying a price for it.
- **Value stream:** View your product delivery system as a continuous flow of processes that add value to the product.
- **Flow:** The product should constantly be moving through the value stream towards the customer at the pace of demand.
- **Pull:** Product should be pulled through the value stream at the customer's demand rather than being pushed on to the customer.

- **Perfection:** The never-ending pursuit of eliminating waste in the system such that the products can flow seamlessly through the value stream at the rate of demand.

2. Literature Review

Consumers today are frequently requesting a greater range of products which in turn puts a greater demand on the processing plants and supply chains. The supply chain has been defined by Stevens (1989) as "a system whose constituent parts include material suppliers, production facilities, distribution services and customers linked together via feed forward flow of materials and feedback of information".

A supply chain is dynamic and involves the constant flow of information, product and funds between different stages. A typical supply chain may involve a variety of stages such as:

- Customers
- Retailers
- Wholesalers/Distributors
- Manufacturers
- Component/Raw material suppliers

The appropriate design of the supply chain will depend on both the customer's needs and the roles of the stages involved.

This paper will show how inventory reductions can be made throughout the supply chain in the industry by using Value Stream Mapping to analyse the processes involved in manufacturing and to identify key areas of wastage and possible solutions to overcome these.

Value Stream Mapping (VSM) was chosen as a tool to gather information on the crankshaft assembly supply chain because it has been used successfully by many organisations to plan and identify internal improvements [1]. Furthermore when used appropriately it can help the process industry eliminate waste, maintain better inventory control, improve product quality, and obtain better overall financial and operational control [2].

Jones and Womack (2000) define Value Stream Mapping as 'The simple process of directly observing the flows of information and materials as they now occur summarising them visually and then envisioning a future state with much better performance'.

Value Stream Mapping has been used in previous work by Jones and Womack (1996) & Rother and Shook (1999). These studies focussed on lean manufacturing and how

waste can be reduced/eliminated from the value stream. Further studies carried out by Abdulmalek, Rajgopal (2005); Seth, Gupta (2005) & Hines et al (1998) also adopted the 'lean' approach to manufacturing and identified the opportunities for lean techniques and product improvements in the manufacturing sectors. More recently value stream maps have been used to understand the flow of material and information in office activities.

The ultimate goal of VSM is to identify all types of waste in the value stream and to take steps to try and eliminate these (Rother and Shook, 1999). Waste can be any part of a process that takes time and resources but adds no value to the product and can even include something as small as taking extra footsteps to bring a product to another part of the factory.

Hines et al (1999) discovered that for the vast majority of the time whilst products are within the defined supply chain no value is being added [3].

Value Stream Mapping aids in the development of a "current state map" which shows a visual representation of how the company is currently operating; it records process information and information flow which can be used to identify key wastes, problems and opportunities [4]. Once the current state map has been analysed the future state map can then be produced to show how the company could operate more effectively.

Taylor (2005) stated "Value Stream Maps are a very effective method for summarising, presenting and communicating the key features of a process within an organisation".

The aims of this research were to:

- Understand the 'current state' of the crankshaft supply chain.
- Identify key areas of waste, problems and opportunities across the supply chain.
- Develop a 'future state vision' of each of the supply chains.
- Develop an 'action plan' to achieve the future state.

3. Methodology

This section describes the methodological approaches adopted for this research. This includes the value stream mapping of the crankshaft assembly supply chain and semi structured interviews with key respondents to further enhance the information captured from the shop floor [4]. The Value stream mapping for the case study was carried out based on the methods used by Jones and Womack (1996) and Rother and Shook (1999). These methods were used because value stream mapping tools were first popularised by these authors. Value stream mapping was carried out whilst walking around the factory floor and talking to key individuals in each area [5].

The data collection started in the suppliers department through each of the individual processes identifying the linkages between the states of production and establishing the flow of information and material resources. Data such as process cycle times (CT) and number of workers were also recorded to add to the current state map so an overview of how the company currently operates could be viewed. In

order to convert the data obtained into a current state map icons were drawn representing each of the process steps and flow of materials [6].

Logistics, supplier and production control icons were added including the truck icons to show deliveries from suppliers and deliveries to the logistics warehouse [7]. Electronic information flow icons were added to show information sent to and from customers and suppliers and a timeline was placed alongside the current state map to show the approximate process times [8]. Upon completion of the mapping exercise an interview guide was designed in order to gain more detailed information about each of the companies with regards to their suppliers, customers and processes, for example:

- Customer demand
- Ordering Frequency
- Shipping frequency

The questions were open ended and were designed to allow a greater understanding of the company and the way in which each of the processes played a part in the manufacturing of the product. The questions were asked to those representatives whom the site managers had identified as being the most knowledgeable in those particular areas [9].

These interviews allowed a rapport to develop between the researcher and the interviewee therefore allowing the researcher to probe and divulge on the respondent's answers. This information was vital in understanding what the company does and how they achieve this. The data from value stream mapping and the semi structured interviews was used to construct the current state map of the company. This map shows the processes and information flows of how manufacturing currently operates throughout the factory [10]. It is important to note that only the main product line (identified by the site managers) in the factory was mapped since Value Stream Mapping is a very time consuming process.

4. Application of VSM in a manufacturing industry: a case study

A case study conducted at a two wheeler manufacturing company is presented and some of the observations may be useful to the practicing engineers in implementing VSM in small, medium and large enterprises. Much of the earlier work have attempted complementary lean manufacturing tools in large scale industries and have recorded their experiments. Hence, there is a need to implement such a lean tool in small and medium size industries.

1.1 Selection of Critical Product Family

The first step is the selection of the critical part family. After the thorough study of all part families, one part family was rather preferred over all the product families. The crankshaft assembly is one of the main assemblies in an engine. It consists of several parts namely the flywheel, connecting rod, LH and RH shaft, key, plug, washer, crankpin etc.

1.2 Documentation of Supplier and customer Information

Interaction with the manager revealed information regarding its suppliers and customer’s requirement. It was understood, the company has a wide range of customers. The details about the raw materials, its vendors, location and the component costs were also collected.

1.3 Current State Map

Fig. 1 below shows the current state map. The crankshaft assembly consists of ten components that are sourced by different suppliers from various parts of the country. These parts are initially processed at the machine shop. Then the process of crankshaft assembly, engine and vehicle assembly takes place. This current state map includes lead time, work in progress (WIP), transportation time etc. It indicates different processes and the links between them. It illustrates information flows as well as

material flows. As per the current state the production control department provides daily and monthly schedule electronically to the assembly stations and its suppliers respectively. The box below the suppliers indicates the lead time, inventory and finished goods (in days) at each supplier stage. A large amount of inventory is carried at each stage increasing the net value of the chain. Inventories of about 300 sets were carried after each assembly stage. The assembled vehicles are transported daily to the customers. The company produces 300 numbers of crankshaft assemblies daily.

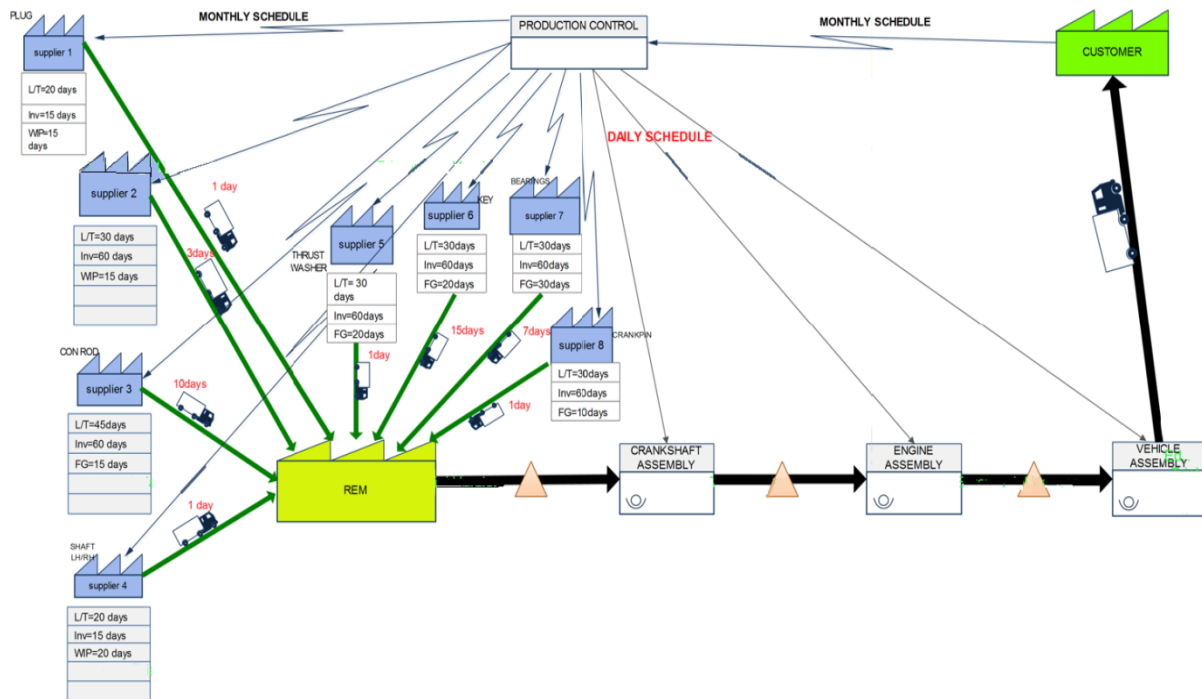


Figure 1 Current State Map

D. Future State Map

Workings on the gap areas identified by the VSM of the current state of crankshaft assembly supply chain, some modifications are proposed as indicated in Fig. 2. By analysing the current state map the lead time and the amount of inventory are the problems identified. Lean production was about creating value for the customers with minimum amount of waste and a high degree of quality.

The positive points of reducing inventory are as follows:

- Reducing tied up capital
- Smoothing production flow
- Lowering space rental costs
- Shortening throughput time

Reducing inventory also reduces other areas of wastes.

The possible solutions for reducing these wastes are listed below:

- Bringing the parts to arrive directly at the assembly station the lead time can be reduced.
- Inclusion of Supermarkets before the assembly of crankshaft and after the vehicle assembly eliminates the inventory.
- Implementing pull system can reduce the unnecessary inventory and the cost incurred in carrying those inventory.

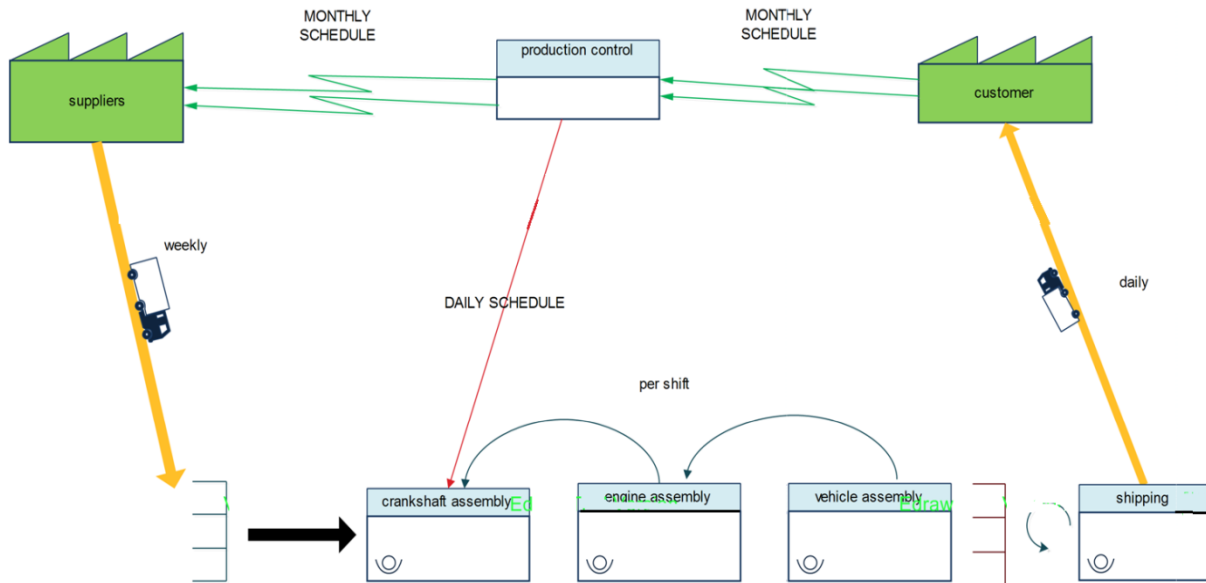


Figure 2 Future State Map

5. Conclusion

This study shows how VSM supports the lean supply chain and identifies potential opportunities for continuous improvement to eliminate waste. Culture change is a long term philosophy is highlighted as the foundational for Toyota and other companies to sustain success. This paper not only shows the value of VSM as a supply chain tool for implementing lean production; but also provides industrial insight for those hesitant companies to effectively implement lean supply chain [9]. We also discuss how a complex supply chain problem can be systematically analyzed and improved effectively by value stream mapping. Future research may consider the use of the proposed VSM system for other non-manufacturing industries.

REFERENCES

- [1] Abuthakeer, S.S., Mohanram, P.V. and Mohan Kumar, G. (2010), Activity Based Costing Value Stream Mapping, *International Journal of Lean Thinking*, Vol. 1, No. 2, pp. 51-64.
- [2] Ajit Kumar Sahoo, Singh, N.K. and Ravi Shankar et al., (2008), Lean philosophy: implementation in a forging company, *Int J Adv Manuf Technol*, Vol. 38, No.4.
- [3] Alvair Silveira Torres Jr., and Ana Maria Gati (2009), Environmental Value Stream Mapping (EVSM) as Sustainability Management Tool, *PICMET Proceedings*, Vol. 12, No.3.pp. 1689-1698.
- [4] Ayşegül Özkavukcu and M.Bülent Durmuşoğlu (2008), Production Smoothing Decisions with Seasonal Variation through Value Stream, *IEEE*, Vol. 7, No. 1, pp. 130-135.
- [5] Barroso, A.P., Machado, V.H., and Cruz Machad, V. (2009), Identifying Vulnerabilities in the Supply Chain, *Proceedings of the IEEE IEEM*, Vol. 40.
- [6] Bhim Singh, Suresh K. Garg and Surrender K. Sharma (2011), Value stream mapping: literature review and implications for Indian industry, *Int J Adv Manuf Technol*, Vol. 53, No.15.
- [7] Carrie Steinlicht and Andrew Neary et al., (2010), Program Development Work in Progress: Value Stream Mapping the Educational Process Outcomes, *40th ASEE/IEEE Frontiers in Education Conference*, Vol.91.
- [8] Chitturi, R.M., Glew, D.J., and Paulls, A. (2009), Value stream mapping in a job shop, *IEEE*, Vol.63.
- [9] Cruz Machado, V., and José Tavares (2007), Modelling Organizations Based on Value Streams, *Proceedings of IEEE IEEM*, Vol.3, No. 7, pp. 362-366.
- [10] Fawaz A. Abdulmalek and Jayant Rajgopal (2007), Analyzing the benefits of lean manufacturing and value stream mapping via simulation: A process sector case study, *Int. J. Production Economics*, Vol. 107, No. 18.

Review of Various Reaction Parameters and Other Factors Affecting on Production of Chicken Fat Based Biodiesel

Jagadale S. S., Jugulkar L. M.

Department of Automobile Engineering, RIT Sakharale 415414, Sangli, Maharashtra, India

Abstract:

This paper represents review of various reaction parameters and other factors which affects the production of chicken fat biodiesel. These are following reaction parameters which affect the production of chicken fat based biodiesel are temperature, molar ratio, reaction time, catalyst concentrations, physical properties and composition, Purity of Reactants, Mixing Intensity, type of catalyst used and other factors affects which are Free Fatty Acid (FFA) and Moisture level Contains in feedstock.

Key words: Biodiesel, chicken fat, alternative fuel, reaction parameters, catalyst.

1.1 Effect of temperature:

To study the effect of temperature on biodiesel yield, the molar ratio of methanol to oil was fixed as 6:1 and the catalyst concentration as 1%. The reaction time is also fixed for 60 minute. The result obtained was displayed in figure 1. A maximum yield of biodiesel was reached at 50°C. An increased temperature up to 70 °C resulted in lower yield. Using similar catalyst but different feedstock's [2]. Obtained opposite results in which an increase temperature up to 70°C led to maximum yield of biodiesel. Further increase in temperature lowered the biodiesel yield due to the evaporation of methanol. This result was also observed by other researchers.

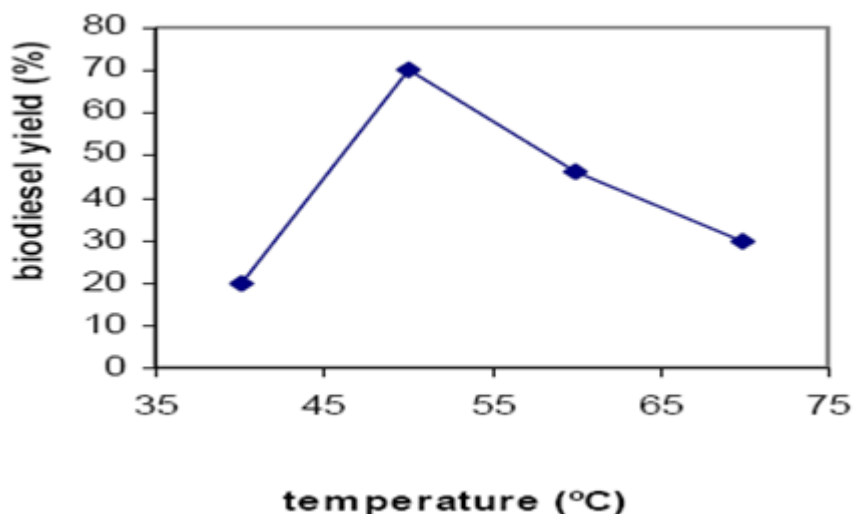


Fig.1 Effect of temperature on the biodiesel production.
Reaction condition: molar ratio of methanol to oil 6:1,
Catalyst concentration 1%, Reaction time 60 minute

Other researchers [3] also studied the transesterification of refined oil using methanol with the molar ratio of alcohol to oil (6:1) and NaOH (1% w/w of oil) in three different temperatures. After 0.1 h, ester yields were 94, 87 and 64% for 60°, 45° and 32°C, respectively. After 1 h of reaction, the ester formation was identical for 60° and 45°C and was slightly lower for 32°C. The maximum yield of esters were obtained in the temperatures ranging from 60–80°C at a molar ratio of 6:1 and further increase in the temperature decreases the conversion.[2]

1.2 Effect of molar ratio:

The effect of molar ratio methanol to oil was shown in figure 2. The temperature, reaction time and catalyst concentration was fixed as 50°C, 60 minute and 1% respectively. As the molar ratio of methanol to oil increased from 3:1 to 6:1, the production yield also increased. Further increase resulted in lower yield. The optimum molar ratio of methanol to oil was determined as 6:1 for maximum yield (75.4%) of biodiesel fuel from chicken fat using CaO catalysts. Therefore, we concluded that to elevate the

biodiesel yield and excess methanol feed was effective to a certain extent. The molar ratio of alcohol to triglyceride is the most important variable affecting the biodiesel yield. The stoichiometric ratio for the transesterification requires three moles of alcohol and one mole of triglyceride to yield three moles of biodiesel and one mole of glycerol. However, transesterification is an equilibrium reaction in which a large excess of alcohol is required to drive the reaction to the forward direction. However, the high molar ratio of alcohol to vegetable oil interferes with the separation of glycerin because of the increase in solubility. When glycerin remains in solution, it helps to drive the equilibrium back to the left, lowering the yield of esters [4].

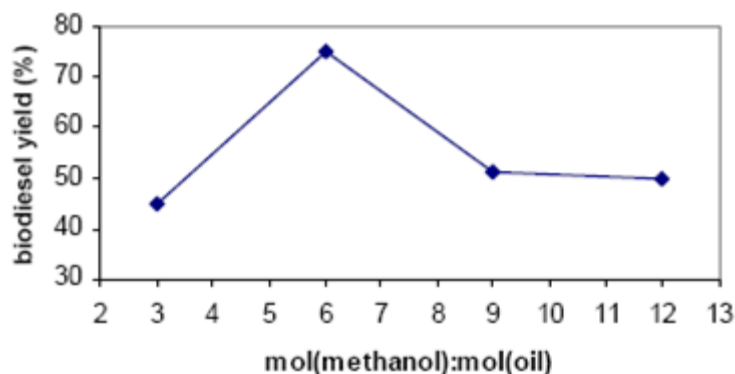


Fig.2.Effect of methanol to oil molar ratios on the biodiesel production.
Reaction condition: temperature of 50°C, catalyst concentration 1%,
Reaction time: 60minute.

1.3 Effect of catalyst concentrations:

A catalyst functions to accelerate the reaction rates. For transesterification reaction, an increasing amount of heterogeneous catalyst caused the slurry (mixture of catalyst to reactant) too viscous giving rise to a problem of mixing and a demand of higher power consumption for adequate stirring. On the other hand, when the catalyst loading amount was not enough, maximum production yield could not be reached. To avoid this kind of problem, an optimum amount of catalyst concentration had to be investigated. The effect of catalyst concentration on the biodiesel yields was shown in figure 3.

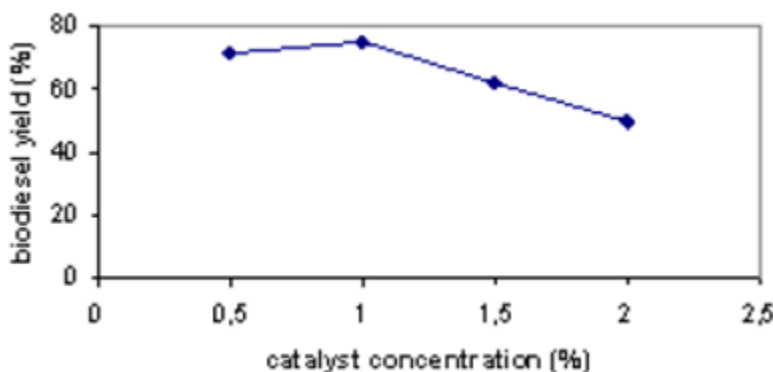


Fig.3.Effect of catalyst concentration on the biodiesel Production.
Reaction condition: temperature of 50°C, molar ratio of methanol to
Oil ratio 6:1, reaction time of 90minute.

Other variables such as reaction time, temperature and molar ratio of methanol to oil were kept constant. The maximum biodiesel yield was obtained with 1% catalyst concentration. The figure indicated that the biodiesel yield decreased with different catalyst concentration. Methanolysis of soybean oil with potassium hydroxide catalyst 1% (w/w of oil) also gave the best yields and viscosities of the esters. Alkaline metal oxides are the most active catalysts for methanolysis since they give very high yield (98%) in shorter reaction times (30 min), even if they are applied at low molar concentrations (0.5 mol%). [6][10][11] The acid catalysts also give very high yield of alkyl esters at high temperatures (around 100°C) but the reactions are slow and take around 3 h to reach the same conversion., acid catalysts generally require 0.5–1 mol% catalyst concentration to achieve around 99% conversion.[1].

1.4. Effect of Reaction time:

The figure 4 presented the biodiesel yield versus reaction time. It showed that there was a great jump from 30 minute to 60 minute which indicated that the reaction was very rapid in the beginning. The Biodiesel yields then increased slowly and remained nearly constant thereafter.[7] transesterified peanut, cottonseed, sunflower and soybean oil with methanol-oil molar ratio of 6:1 and 0.5% (w/w of oil) sodium methoxide catalyst at 60°C. Around 80% yield was observed after 1 min for soybean and sunflower oils. After 1 h, the conversion was almost the same for all the four oils (93–98%). studied the effect of reaction time on transesterification of beef tallow with methanol and the reaction was found to be very slow during the first minute due to mixing and dispersion of methanol into beef tallow. For the first 5 min, the reaction proceeded very fast. The production of beef tallow methyl esters reached the maximum value at about 15 min.

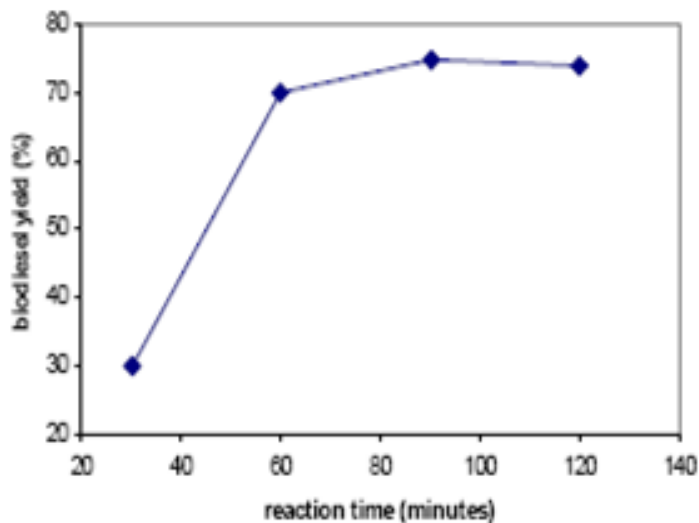


Fig.4. Effect of reaction time on the biodiesel production.

Reaction condition: temperature of 50°C,

Molar ratio of methanol to oil 6:1, catalyst concentration 1%

1.5. Effect of Physical Properties and composition:

The fatty acid composition of as-synthesized biodiesel was determined by GC analysis and the results were shown in table 1. The oleic acid is the dominant component of biodiesel synthesized from chicken fat, followed by palmitic acid. The other fatty acid contents are lower than 10 % by wt.

Table 1. Composition of as-Synthesized Fatty Acid Methyl Esters (FAME).

Sr. No.	Fatty Acid Methyl Ester	Percentage (% By Wt.)
1	Miristic	0.59
2	Stearic	0.89
3	Linoleic	7.33
4	Palmitic	24.04
5	Oleic	60.98
6	Palmitoleic	4.42

The characteristic as-synthesized biodiesel was determined for six important properties of biodiesel fuel and compared with Indonesian national standard for biodiesel. The results are displayed in table 2 which clearly show within limit of Indonesian standard for biodiesel

TABLE II. THE CHARACTERISTICS OF AS-SYNTHESIZED BIODIESEL

Sr. No.	Characteristic	Unit	Biodiesel	Standard Range
1	Density	Kg/m ³	879	850 to 890
2	Kinematic Viscosity	Mm ² /s	4.1	2.3 to 6.0
3	Water Content	% vol.	178	Min. 100
4	Cetane Number	-	73.73	Min. 51
5	Iodine number	gr Iod/100 gr	29.36	Max. 115
6	Acid Number	Mg KOH/gr	0.58	Max. 0.8

1.6 Effect of Mixing Intensity:

To achieve perfect contact between the reagent and oil during transesterification, they were mixed together. It has been observed that during the transesterification reaction, the reactants initially form a two phase liquid system. The mixing effect has been found to play a significant role in the slow rate of reaction. As phase separation ceases, mixing on the kinetics of the transesterification process forms the basis for process scale up and design. The mixture is stirred

At about 650 to 700 rpm for one hour. It was found that phase separation occurs after 3-4 minutes stirring but maximum ester yield was reached after 30 minutes of stirring. [4][5]

1.7 Effect of Purity of Reactants:

Impurity in oil affects the conversion level considerably. It is reported that about 65-84% conversion into esters using crude vegetable oils have been obtained as compared to 94-97%

Yields refined oil under the same reaction conditions. The free fatty acids in the crude oils have been found to interface with the catalyst. This problem can be solved if the reaction is carried out under high temperature and pressure conditions. [4][5].

1.8 Effect of Catalyst Type:

Considerable research has been done on biodiesel made from virgin vegetable oils (e.g., peanut oil, palm oil, soybean oil, sunflower oil) using homogeneous alkali catalysts. The majority of biodiesel today is produced by alkali-catalyzed (e.g., NaOH, KOH) transesterification with methanol, with results in a relatively short reaction time. However the vegetable oil and alcohol must be substantially anhydrous and have low free fatty acid content, because the presence of water or free fatty acid or both promotes soap formation. Soap formed lowers the yield of esters and renders the downstream separation of the products difficult, requiring additional processing. Another drawback arises from the use of homogeneous base catalyst is difficulty in purification of byproduct glycerol and the need of wastewater treatment. To alleviate these problems, use of a solid base catalyst was proposed. Solid base catalysts have many advantages, such as mild reaction condition, easy separation, and high activity and less contaminant. In this investigation, waste chicken fats as feedstock for biodiesel production have relatively high amount of free fatty acids and water content results in the production of soap in the presence of alkali catalyst. Thus, additional steps to remove any water and either the free fatty acids or soap from reaction mixture are required. The use of solid base catalyst for the production of biodiesel from fats produced from waste chicken skins and determined suitable condition. Heterogeneous catalyst is best suited due to its cheap price, minor toxicity, high availability and high basic strength [1].

1.9 Effect of Free Fatty Acid (FFA) Contains:

The problem with processing waste chicken fat oils is that they usually contain large amounts of free fatty acids that cannot be converted to biodiesel using an alkaline catalyst due to formation of fatty acid salts (soap). The soaps can prevent separation of

the biodiesel from the glycerin fraction. An alternative method is to use acid catalysts, which are able to esterify free fatty acids investigated the relationship between FFA level and triglyceride transesterification during acid catalyzed biodiesel production. To prepare esters with a high yield using alkaline catalysis, it is necessary for the feedstock to have a low FFA value. The FFA value is a measure of the number of acidic functional groups in a sample and is measured in terms of the quantity of potassium hydroxide required to neutralize the sample. [11]

1.10 Effect of Moisture level:

The moisture levels of the collected waste chicken fats vary widely, being as high as 18%. Therefore, it is not possible to convert these oils to biodiesel by using a single process. One drawback of biodiesel is that there is an inverse relationship between biodiesel's oxidative stability and its cold flow properties. Saturated compounds are less prone to oxidation than unsaturated compounds but they raise the cloud point of the fuel. The reaction of FFAs with alcohol produces ester, but also water that inhibits the of the transesterification glycerides. This is due to the effect of the water produced when the FFAs react with the alcohol to form esters. The coincidence of the lines indicates that water formation is the primary mechanism limiting the completion of the acid catalyzed esterification reaction with FFAs. [11]

Conclusion

To get the maximum production of chicken fat base biodiesel reaction parameters are as follows, at 50°C gets maximum production keeping other parameters constant. The optimum molar ratio of methanol to oil was determined as 6:1 for maximum yield (75.4%) of biodiesel fuel from chicken fat using heterogeneous catalysts. The maximum biodiesel production was obtained with 1% catalyst concentration. It showed that there was a great jump from 30 minute to 60 minute which indicated that the reaction was very rapid in the beginning, the biodiesel yields then increased slowly and remained nearly constant thereafter. The mixing effect has been found to play a significant role in the slow rate of reaction, It was found that phase separation occurs after 3-4 minutes stirring but maximum ester yield was reached after 30 minutes of stirring. Heterogeneous catalyst is best suited due to its cheap price, minor toxicity, high availability and high basic strength. Due to the high level of FFA in the waste chicken fats, transesterification cannot be applied directly. It is necessary to reduce the FFA level of the oil by using an acid catalyst process. With traditional alkali catalyzed processes, free fatty acids escape conversion into esters by reacting with the catalyst to form soaps with acid catalyzed processes. The moisture levels of the collected waste chicken fats vary widely, being as high as 18%, therefore, it is not possible to convert these oils to biodiesel by using a single process.

References

1. Amir Awaluddin, Saryono, Adhy Prayitno and Tearful Amri, "Transesterification of Waste Chicken Fats for Synthesizing Biodiesel by CaO as Heterogeneous Base Catalyst", International Conference on Energy and Sustainable Development: Issues and Strategies, (2010), Pp.1-5.
2. Awaluddin A., "Production of Biodiesel from a Used Frying Oil and Crude Palm Oil Using Heterogeneous Catalyst CaO", In Proceedings of the Fifth Riau University and UKM Malaysia, Indonesia, August 2008 Pp. 272-280.
3. Meher L.C., Sagar D.V., Naik S.N., "Technical Aspects of Biodiesel Production by Transesterification-a Review", Renewable and Sustainable Energy Reviews, 10 (3) Pp. 248-268.
4. B.K. Barnwal, M.P.Sharma, "Prospect of Biodiesel Production from vegetable oil in India", Renewable and sustainable energy reviews (2004) Pp. 238-246.
5. Anjana Srivastava, Ram Prasad, "Triglycerides -Based Diesel fuels", Renewable and sustainable energy reviews (2002).Pp.111-133.
6. Feuge R.O., Gros A.T. Modification of vegetable oils Alkali Catalyzed In transesterification of peanut oil with ethanol", J Am Oil Chem. Soc 1949, 26(3) Pp.97-10.
7. Freeman B., Pryde E.H., Mounts T.L. 1984 Variable affecting the yields of Fatty esters from transesterified vegetable oils J. Am Oil Chem. Soc 61:1638-1643.
8. Jitputti J., Kitiyanan B., Rangsunvigit P.,Bunyakiat K., Attanatho L., Jenvanitpanjaku P. Transesterification of Crude Palm Kernel Oil and Crude Coconut by different Solid Catalysts. 2006 Chem. Eng J 116:61-66.
9. Krishnangura K., Simamaharnnop K., "Continuous transmethylation of Palm oil in an organic solvent." J Am Oil Chern. Soc. 1992, 69(2):166-169.
10. Formo M.W., 1954 , "Ester reactions of fatty materials", J Am Oil Chern Soc 31:548-559.
11. Mustafa Canakci, "The potential of restaurant waste lipids as biodiesel feedstocks" Department of Mechanical Education, Kocaeli University, 41380 Umuttepe-Izmit, Turkey, 2005, Pp.168-176.

Fuzzy logic controller of a series active power filter for Power Quality improvement

Uma Mahesh.J*, Musthak Ahmed Shaik**

*Student, Department of Electrical Engineering, KL University, India

** Assistant professor, Department of Electrical Engineering, KL University, India

ABSTRACT

Here a control algorithm for a series active power filter is proposed. It is constituted by series active filter and shunt passive filter. The control strategy is based on instantaneous reactive power theory. So that the voltage wave form injected by active power filter is able to compensate the reactive power and the load current harmonics. The control algorithm was designed by using fuzzy logic controller for a better performance. Simulations have been carried out on the MATLAB-Simulink platform with different loads and variations in source impedance.

Keywords – Active power filter, Harmonics, Instantaneous reactive power theory, Power quality, fuzzy logic controller

I. INTRODUCTION

Now a days Harmonic current is the major problem in electrical power system due to the increase of non-linear loads. Harmonic current drawn from a supply by waveform at the point of common coupling (PCC) due to the source impedance.

One traditional solution to mitigating the harmonics problems in the use of passive filters. In fact, this is a quite traditional solution to preventing load harmonic currents from flowing into the source or other loads. For the design of passive filter, it is necessary to know the source impedance, which is not constant and depends directly on system configuration.

This means that the filtering characteristics of the passive filter is strongly influenced by system impedance. In addition, there are several problems may occur.

1. The series and/or parallel resonance occurs between the source impedance and the shunt filter impedance.
2. The compensation characteristics heavily depend on the system impedance because the source impedance has to be greater than the shunt filter impedance in order to eliminate source current harmonics.
3. They are not suitable for variable loads

To avoid the above –mentioned problems regarding the applications of passive filters, it would be interesting to combine the shunt passive filter with series active filter.

An active power filter, APF, typically consists of a three phase pulsewidth modulation (PWM) voltage source inverter. Which is connected in series to the ac source. It is possible to improve the compensation characteristics of the shunt filters. This topology is as shown in fig.1, where v_c is the

voltage that the inverter should generate to achieve the objective of the proposed control algorithm.

There are several different techniques have been applied to obtain a control signal for the active filter.

In this paper, a control strategy based on instantaneous reactive power theory is proposed, it is applied by considering a balanced and resistive load as ideal load. Thus, the strategy obtains the reference voltage is obtained to achieving ideal behavior for the set of hybrid filter-load. When the source voltages are sinusoidal and balanced the power factor is unity, in other words, the load reactive power is compensated and the source current harmonics are eliminated. By this means, it is possible to improve the passive filter compensation characteristics with our depending on the system impedance, since the set load-filter would present resistive behavior. It also avoids the danger that the passive filter behaves as a harmonic drain of closed loads, and like wise, the risk of possible series and/or parallel resonances with the rest of the system. In addition, the compensation is also possible with variable loads, not affecting the possible the passive filter detuning.

Recently, fuzzy logic controller has generated a great deal of Interest in various applications and has been introduced in the power electronics field.

The advantages of fuzzy logic controllers over the conventional PI controller are that they do not need an accurate mathematical model; they can work with imprecise inputs, can handle nonlinearity, and may be more robust than the conventional PI controller.

The control algorithm was designed by using fuzzy logic controller for a better performance. Simulations have been carried out on the MATLAB-Simulink platform with different loads and variations in source impedance.

II. SERIES ACTIVE POWER FILTER

It is well known that series active power filters compensate current system distortion caused by non-linear loads by imposing a high impedance path to the current harmonics which forces the high frequency currents to flow through the LC passive filter connected in parallel to the load. The high impedance imposed by the series active power filter is created by generating a voltage of the same frequency that the current harmonic component that needs to be eliminated. Voltage unbalance is corrected by compensating the

fundamental frequency negative and zero sequence voltage components of the system.

In a three-phase system, The vector transformations from the phase reference system a-b-c to $\alpha - \beta - 0$ coordinates can be obtained, thus

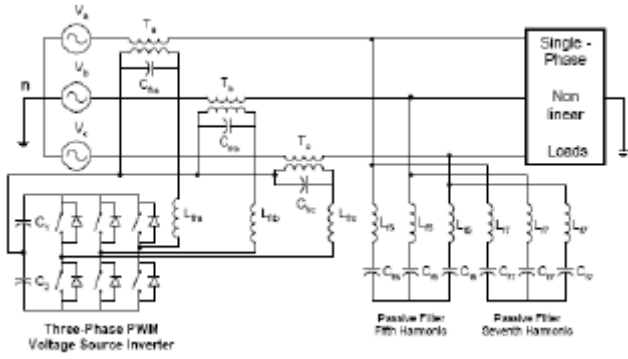


Fig.1.The proposed series active power filter topology with shunt passive filter.

$$\begin{bmatrix} v_0 \\ v_\alpha \\ v_\beta \end{bmatrix} = \sqrt{2/3} \begin{bmatrix} 1/\sqrt{2} & 1/\sqrt{2} & 1/\sqrt{2} \\ 1 & -1/2 & -1/2 \\ 0 & \sqrt{3}/2 & -\sqrt{3}/2 \end{bmatrix} \begin{bmatrix} v_a \\ v_b \\ v_c \end{bmatrix} \quad (2)$$

$$\begin{bmatrix} i_0 \\ i_\alpha \\ i_\beta \end{bmatrix} = \sqrt{2/3} \begin{bmatrix} 1/\sqrt{2} & 1/\sqrt{2} & 1/\sqrt{2} \\ 1 & -1/2 & -1/2 \\ 0 & \sqrt{3}/2 & -\sqrt{3}/2 \end{bmatrix} \begin{bmatrix} i_a \\ i_b \\ i_c \end{bmatrix} \quad (3)$$

III. COMPENSATION STRATEGY

Electric companies try to generate electrical power as sinusoidal and balanced voltages so it has been obtained as a reference condition in the supply. Due to this fact, the compensation target is based on an ideal reference load which must be resistive, balanced and linear. It means that the source currents are collinear to the supply voltages and the system will have unity power factor. Therefore, at the point of common coupling (PCC), the following expression will be satisfied:

$$v = R_e i \quad (1)$$

Here, R_e is the equivalent resistance, v is the voltage vector on the connection point, and i is the supply current vector.

Fig. 2 shows the configuration active filter connected in series with passive filter connected in shunt with the load.

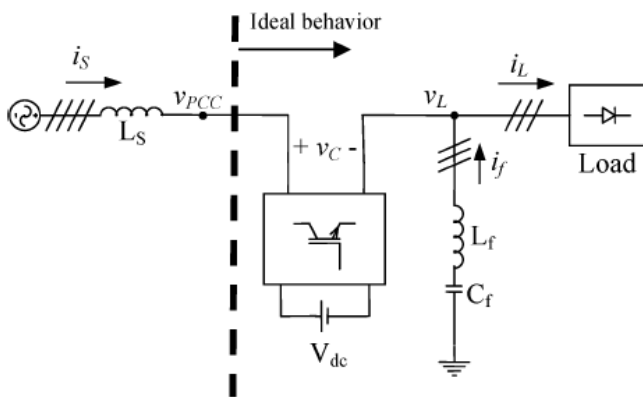


Fig.2. System with compensation equipment.

In low voltage distribution systems, there is usually the presence of single-phase loads. That produces severe unbalance voltages and currents in the system. For this reason, even if the voltage source is balanced, the PCC voltage cannot be balanced due to the presence of unbalanced three-phase loads and/or single-phase loads. A compensating system will have to avoid the propagation of the voltage imbalance from the PCC to other consumers.

The instantaneous real power and imaginary power is defined by the equations as

$$p = v_\alpha i_\alpha + v_\beta i_\beta \quad (4)$$

$$q = v_\alpha i_\beta - v_\beta i_\alpha \quad (5)$$

The voltage vector can be calculated as

$$v_L = \frac{p}{i_{\alpha\beta}^2} i_{\alpha\beta} + \frac{q}{i_{\alpha\beta}^2} i_{\alpha\beta} \perp \quad (6)$$

The average power supplied by the source will be

$$P_s = I_1^2 R_e \quad (7)$$

I_1^2 is the square rms value of the fundamental harmonics of the source current vector. The compensator instantaneous power is difference between the total real instantaneous power required by the load (p_L) and the instantaneous power supplied by the source (p_s), i.e.,

$$p_c = p_l - p_s \quad (8)$$

When the average values are calculated in this equation and taking into account that the active power exchanged by the compensator has to be null, Eq(8) can be rewritten as follows:

$$0 = \frac{1}{T} \int p_l dt - I_1^2 R_e \quad (9)$$

Therefore, the equivalent resistance can be calculated by

$$R_e = \frac{\frac{1}{T} \int p_l dt}{I_1^2} = \frac{P_L}{I_1^2} \quad (10)$$

Where P_L is the load average power.

The aim is that the compensation equipment and load have ideal behaviour from the PCC. The upstream voltage of the active filter can be calculated as follows:

$$v_{pcc} = \frac{P_L}{I_1^2} i \tag{11}$$

where i is the source current vector. Thus, the reference signal for the output voltage of the active filter is as follows:

$$v_c^* = v_{pcc} - v_L = \frac{P_L}{I_1^2} i - v_L \tag{12}$$

That is, when the active filter generates this compensation voltage, the set load and compensation equipment will behave as a resistor with a R_e value.

Finally, if currents are unbalanced and nonsinusoidal, a balanced resistive load is considered as ideal reference load. Therefore, the equivalent resistance must be defined by the equation

$$R_e = \frac{P_L}{I_1^{+2}} \tag{13}$$

Here, I_1^{+2} is the square rms value of the positive sequence fundamental component. In this case, (12) is modified, where I_1 is replaced by I_1^+ , now eq(12) becomes

$$v_c^* = \frac{P_L}{I_1^{+2}} i - v_L \tag{14}$$

IV. FUZZY LOGIC CONTROLLER

The fuzzy control algorithm is implemented to control the load phase voltage based on processing of the voltage error $e(t)$ and its variation $\Delta e(t)$ in order to improve the dynamic of SAF.

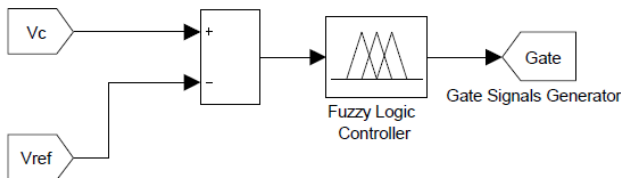


Fig.3. Fuzzy controller structure block diagram

The main advantages of fuzzy control are its linguistic description, independence of mathematical model, robustness, and its universal approximation. A fuzzy logic controller is consisting of four stages: fuzzification, knowledge base, inference mechanism and defuzzification. The knowledge base is composed of a data base and rule base and is designed to obtain good dynamic response under uncertainty in process parameters and external disturbances. The data base consisting of input and output membership functions, provides information for the appropriate fuzzification operations, the inference mechanism and defuzzification. The inference mechanism uses a collection of linguistic rules to convert the input conditions into a fuzzified output. Finally, defuzzification is used to convert the fuzzy outputs into control signals. In designing of a fuzzy control system, the formulation of its rule set plays a key role in improvement of the system performance.

V. SIMULATION RESULTS

The system shown in Fig. 1 has been simulated in the Matlab- Simulink platform to verify the proposed control. Each power device has been modeled using the SimPowerSystem toolbox library. The power circuit is a three-phase system supplied by a sinusoidal balanced three-phase 100-V source with a source inductance of 5.8 mH and a source resistance of 3.6 ohm. The inverter consists of an Insulated Gate Bipolar Transistor (IGBT) bridge. On the dc side, two 100-V dc sources are connected. An LC filter has been included to eliminate the high frequency components at the output of the inverter. The passive filter is constituted by two LC branches tuned to the fifth and seventh harmonics. Each element value as shown in below table.

source	Ls=5.8mH;Rs=3.6ohm
Passive filter	L5=13.5mH;C5=30 μF L7=7.5mH;C7=30 μF
Ripple filter	Lr=13.5mH;Cr=50 μF

A. Nonlinear Balanced load:

In this case, the nonlinear load consists of an uncontrolled three-phase rectifier with an inductance of 55 mH and a 25 resistor connected in series on the dc side.

Given below Fig.4 shows the simulink diagram of a series active power filter. The source current of a phase 'a' current wave form with and without filters as shown in below Fig.5.&6..

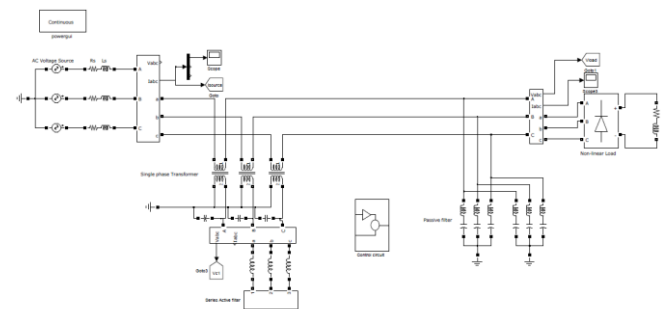


Fig.4. Simulink model diagram of a series active filter when it's connected to balanced load.

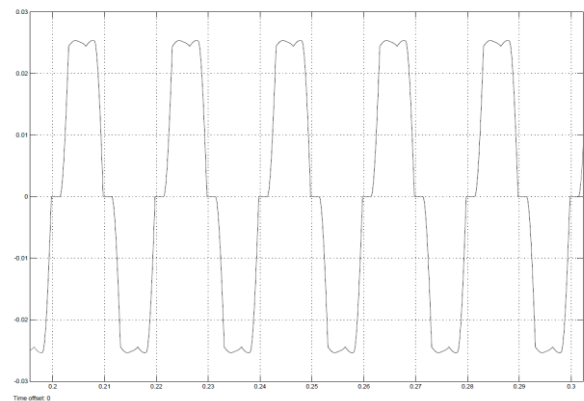


Fig.5. source current of the phase 'a' without filter

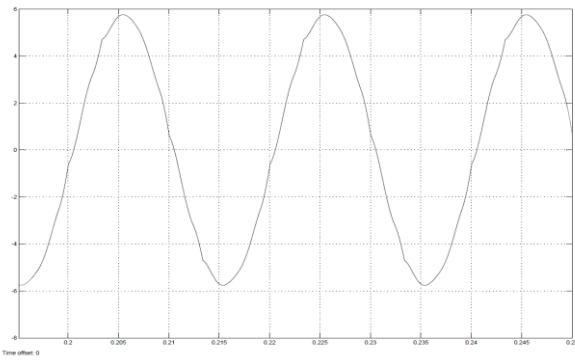


Fig.6.Source current when active filter connected.

B. Nonlinear unbalanced load:

In this case, the three-phase load is built with three singlephase uncontrolled rectifiers with capacitors and resistors connected in parallel at the dc side.

The simulink model of a series active filter which is connected to unbalanced load as shown in Fig.7 and the source current with and with out filters as shown in Fig.8&9.

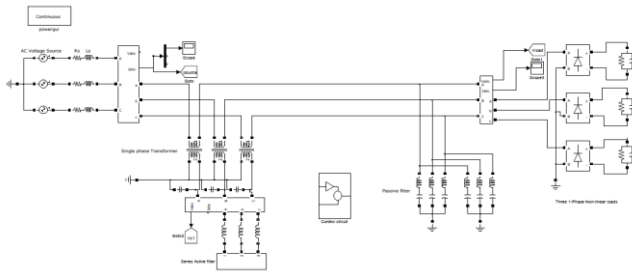


Fig.7. Simulink model diagram of a series active filter when it's connected to unbalanced load.

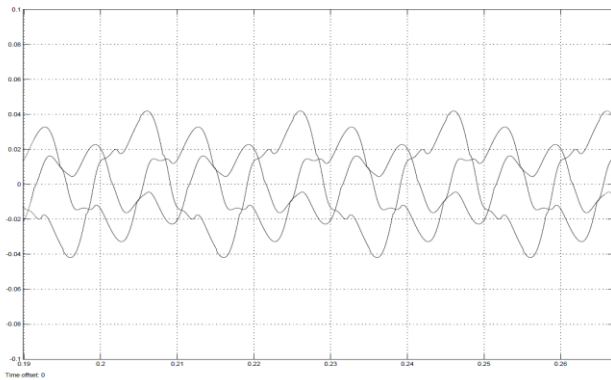


Fig.8.source current wave form without filter

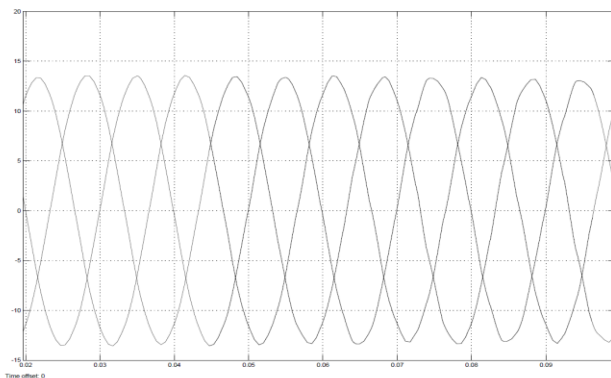


Fig.9.Source current when active filter connected.

VI. CONCLUSION

A novel control strategy based on the dual formulation of compensation system principles is proposed. It is applied by considering a balanced and resistive load as ideal load. Thus, the determined reference voltage is obtained to attain the objective of achieving ideal behavior for the set hybrid filter load. With this strategy is possible to improve the passive filter compensation characteristics without depending on the system impedance, since the set load filter would present resistive behavior. It also avoids the danger that the passive filter behaves as a harmonic drain of close loads, and likewise, the risk of possible series and/or parallel resonances with the rest of the system. In addition, the compensation is also possible with variable loads, not affecting the possible passive filter detuning.

REFERENCES

1. J. C. Das, "Passive filters-potentialities and limitations," *IEEE Trans. Ind. Appl.*, vol. 40, no. 1, pp. 232–241, Jan. 2004.
2. H. Akagi, "Active harmonic filters," *Proc. IEEE*, vol. 93, no.12,pp.2128–2141,Dec.2005.
3. H. Yang and S. Ren, "A practical series-shunt hybrid active power filter based on fundamental magnetic potential self-balance," *IEEE Trans. Power Del.*, vol. 23, no.4pp2089–2096,Oct.2008.
4. F. Z. Peng, H. Akagi, and A. Nabae, "A novel harmonic power filter," in *Proc.IEEE/PESC*,Apr.1988,pp.1151–1159.
5. F. Z. Peng, H. Akagi, and A. Nabae, "A new approach to harmonic compensation in power systems-a combined system of shunt passive and series active filters," *IEEE Trans. Ind. Appl.*, vol. 26, no. 6, pp. 983–990, Nov./Dec. 1990.
6. H. Zhong, P. Chen, Z. Lu, Z. Qian, and H. Ma, "Three-phase fourwire series hybrid active power filter with fundamental current bypass channel," in *Proc. Industrial Electronics Society (IECON)*, Nov. 2004, vol. 1, pp. 536–539.
7. F. Z. Peng and J. S. Lai, "Generalized instantaneous reactive power theory for three phase power system," *IEEE Trans Instrum. Meas.*, vol. 45, no. 1, pp. 293–297, 1996.
8. R. S. Herrera and P. Salmerón, "Instantaneous reactive power theory:A comparative evaluation of different formulations," *IEEE Trans. Power Del.*, vol. 22, no. 1, pp. 595–604, Jan. 2007.
9. A. Hamadi, K. El-Haddad, S. Rahmani and H. Kankan, Comparison of fuzzy logic and Proportional Integral Controller of Voltage Source Active Filter Compensating Current Harmonics and Power Factor, IEEE International Conference on Industrial Technology (ICIT), 2004. pp. 645-650.
10. S. Saad, L. Zellouma, Fuzzy logic controller for three-level shunt active filter compensating harmonics and reactive power, Elsevier, Electric Power Systems Research79(2009)1337–1341.

A novel traveling wave solution for the generalized combined KdV and mKdV equation using the generalized $\left(\frac{G'}{G}\right)$ -expansion method

Y. S. Hamed^{1,2} and T. A. Nofal^{1,3}

¹Department of Mathematics, Faculty of Science, Taif university, Taif , El-Haweiah, P.O.Box 888, Zip Code 21974, Kingdom of Saudi Arabia (KSA).

²Department of Engineering Mathematics, Faculty of Electronic Engineering, Menouf 32952, Menofia University, Egypt.

³Department of Mathematics, Faculty of Science, El Minia University, El Minia, Egypt.

ABSTRACT

In this paper, the generalized $\left(\frac{G'}{G}\right)$ -expansion

method is used for construct an innovative explicit traveling wave solutions involving parameters of the generalized combined KdV and mKdV equation $u_t + a(t)u_x + b(t)uu_x + c(t)u^2u_x + e(t)u_{xxx} = 0$, for any arbitrary functions $a(t), b(t), c(t)$ and $e(t)$.

The properties of this method is that gives an explicit solutions other than the other methods and also gives especial solutions.

Keywords - Combined KdV and mKdV equation,

Generalized $\left(\frac{G'}{G}\right)$ - expansion method, Traveling wave solutions.

I. INTRODUCTION

Phenomena in physics and other fields are often described by nonlinear evolution equations (NLEEs). When we want to understand the physical mechanism of phenomena in nature, described by nonlinear evolution equations, exact solutions for the nonlinear evolution equations have to be explored. For example, the wave phenomena observed in fluid dynamics [1,2], plasma and elastic media [3,4] and optical fibers [5,6], etc. In the past several decades, many effective methods for obtaining exact solutions of NLEEs have been proposed, such as Hirota's bilinear method [7], Backlund transformation [8], Painlevé expansion [9], sine-cosine method [10], homogeneous balance method [11], homotopy perturbation method [12--14], variational iteration method [15--18], asymptotic methods [19], non-perturbative methods [20], Adomian decomposition method [21], tanh-function method [22- 26], algebraic method [27-30], Jacobi elliptic function expansion method [31- 33], F-expansion method [34--36] and auxiliary equation method [37- 40]. Recently, Wang et al. [41] introduced a new direct

method called the $\left(\frac{G'}{G}\right)$ -expansion method to look for

travelling wave solutions of NLEEs. Nofal et al. [45] used

the improved $\left(\frac{G'}{G}\right)$ - expansion method for construct

explicit the traveling wave solution involving parameters of the fifth- order KdV equation. Hamed et al. [46] introduced

the improved $\left(\frac{G'}{G}\right)$ - expansion method for construct

explicit the traveling wave solutions involving parameters of the $(3+1)$ -dimensional Potential equation. Elagan et

al. [47] used the generalized $\left(\frac{G'}{G}\right)$ - expansion method for

construct an innovative explicit traveling wave solutions involving parameters of the Fitz Hugh-Nagumo equation.

Hamed et al. [48] used the generalized $\left(\frac{G'}{G}\right)$ -expansion

method for construct an innovative explicit traveling wave solution involving parameter of the generalized combined KdV and mKdV equation.

Consider the generalized combined KdV and mKdV equation

$$u_t + a(t)u_x + b(t)uu_x + c(t)u^2u_x + e(t)u_{xxx} = 0, \tag{1.1}$$

where $a(t), b(t), c(t)$ and $e(t)$ are functions of t .

Eq. (1.1) where $a(t) = 0$ and $b(t), c(t), e(t)$ are constants has been widely used in many physical fields such as plasma physics, fluid physics, solid-state physics

and quantum field theory. When $a(t) = c(t) = 0$, and $b(t), e(t)$ are constants Eq. (1.1) becomes KdV equation. When $a(t) = b(t) = 0$, and $c(t), e(t)$ are constants Eq. (1.1) is mKdV equation. KdV equation and mKdV equation had been studied by many authors. Recently, Zhang [42] obtained some exact solutions of Eq. (1.1) where $a(t) = 0$, and $b(t), c(t), e(t)$ are constants by tanh function method and the direct method. Recently Eq. (1.1) has solved by Zhenya [43] using a generalized approach based on Riccati equation when and $a(t), b(t), c(t), e(t)$ are all constants. In this paper

we try to solve Eq.(1.1) using generalized $\left(\frac{G'}{G}\right)$ -expansion method when $a(t), b(t), c(t)$ and $e(t)$ are functions of t . The $\left(\frac{G'}{G}\right)$ -expansion method is based on the assumptions that the travelling wave solutions can be expressed by a polynomial in $\left(\frac{G'}{G}\right)$, and that $G = G(\xi)$ satisfies a second order linear ordinary differential equation (LODE):

$G'' + \lambda G' + \mu G = 0$, where

$$G' = \frac{dG(\xi)}{d\xi}, G'' = \frac{d^2G(\xi)}{d\xi^2}, \xi = x - Vt, V \text{ is a}$$

constant. The degree of the polynomial can be determined by considering the homogeneous balance between the highest order derivative and nonlinear terms appearing in the given NLEE. The coefficients of the polynomial can be obtained by solving a set of algebraic equations resulted

from the process of using the method. By using the $\left(\frac{G'}{G}\right)$ -

expansion method, Wang et al. [41] successfully obtained more travelling wave solutions of four NLEEs. Very

recently, Zhang et al. [44] proposed a generalized $\left(\frac{G'}{G}\right)$ -

expansion method to improve the work made in [41]. The main purpose of this paper is to use generalized

$\left(\frac{G'}{G}\right)$ -expansion method to solve the generalized

FitzHugh-Nagumo equation. The performance of this method is reliable, simple and gives many new solutions, its

also standard and computerizable method which enable us to solve complicated nonlinear evolution equations in mathematical physics. The paper is organized as follows.

In Section 2, we describe briefly the generalized $\left(\frac{G'}{G}\right)$ -

expansion method, where $G = G(\xi)$ satisfies the second order linear ordinary differential equation

$$G'' + \lambda G' + \mu G = 0, \xi = p(t)x + q(t).$$

In Section 3, we apply this method to the generalized Mkdv equation. In section 4, some conclusions are given.

II. DESCRIPTION THE GENERALIZED $\left(\frac{G'}{G}\right)$ -

EXPANSION METHOD

Suppose that we have the following nonlinear partial differential equation

$$P(u, u_t, u_x, u_{tt}, u_{xt}, u_{xx}, \dots) = 0, \quad (2.1)$$

we suppose its solution can be expressed by a polynomial

$\left(\frac{G'}{G}\right)$ as follows:

$$u(\xi) = \sum_{i=1}^n \alpha_i(t) \left(\frac{G'}{G}\right)^i + \alpha_0(t), \alpha_j(t) \neq 0, \quad (2.2)$$

where $\alpha_0(t)$ and $\alpha_j(t)$ are functions of t ($j = 1, 2, \dots, n$) and $\xi = \xi(x, t)$ is a function of x, t to be determine later, $G = G(\xi)$ satisfies the second order linear ordinary differential equation

$$G''(\xi) + \lambda G'(\xi) + \mu G(\xi) = 0, \quad (2.3)$$

To determine u explicitly we take the following four steps.

Step 1. Determine the integer n by balancing the highest order nonlinear terms and the highest order partial derivative of u in Eq. (2.1).

Step 2. Substitute Eq.(2.2) along with Eq. (2.3) into Eq.

(2.1) and collect all terms with the same order of $\left(\frac{G'}{G}\right)$

together, the left hand

side of Eq. (2.1) is converted into a polynomial in $\left(\frac{G'}{G}\right)$.

Then set each coefficient of this polynomial to zero to derive a set of over-determined partial differential equations for $\alpha_0(t)$, $\alpha_i(t)$ and ξ .

Step 3. Solve the system of all equations obtained in step 2 for $\alpha_0(t)$, $\alpha_i(t)$ and ξ by use of Maple.

Step 4. Use the results obtained in above steps to derive a series of fundamental solutions of Eq. (2.3) depending

on $\left(\frac{G'}{G}\right)$, since the solutions of this equation have been

well known for us, then we can obtain exact solutions of Eq. (2.1).

III. THE GENERALIZED COMBINED KDV AND MKDV EQUATION

In this section, we apply the generalized $\left(\frac{G'}{G}\right)$ -expansion

method to solve the generalized FitzHugh-Nagumo equation, construct the traveling wave solutions for it as follows:

Let us first consider the generalized KdV equation

$$u_t + a(t)u_x + b(t)uu_x + c(t)u^2u_x + e(t)u_{xxx} = 0, \tag{3.1}$$

where $a(t), b(t), c(t)$ and $e(t)$ are functions of t . There is no any method gvae the exact solution of the above equation before. In order to look for the traveling wave solutions of Eq. (3.1) we suppose that

$$u(x, t) = u(\xi), \xi = p(t)x + q(t) \tag{3.2}$$

Suppose that the solution of Eq. (3.1) can be expressed by a

polynomial in $\left(\frac{G'}{G}\right)$ as follows

$$u(\xi) = \sum_{i=1}^n \alpha_i(t) \left(\frac{G'(\xi)}{G(\xi)}\right)^i + \alpha_0(t) \tag{3.3}$$

considering the homogeneous balance between u_{xxx} and u^2u_x in Eq. (3.1) we required that $n+3=2n+n+1$, then $n=1$. So we try to find a solution of the form

$$u(t, x) = \alpha_0(t) + \alpha_1(t) \frac{G'(\xi)}{G(\xi)}, \tag{3.4}$$

where G satisfies

$$G' + \lambda G' + \mu G = 0.$$

It is easy to see that $p(t)$ must be a constant function assuming that $\alpha_1(t)$ is not zero on any interval of positive length. Substituting Eq.(3.4) into Eq.(3.1) along with Eq.(2.3) and comparing the coefficients of

$\left(\frac{G'}{G}\right)^k, k=0,1,2,3,4$ we obtain the following equations

$$\alpha'_0 = \alpha_1 \mu (q' + ap + b\alpha_0 p + c\alpha_0^2 p + ep^3(2\mu + \lambda^2)) \tag{3.5}$$

$$\alpha'_1 = \alpha_1 (q'\lambda + ap\lambda + b\alpha_0 p\lambda + b\alpha_1 p\mu + c\alpha_0^2 p\lambda + 2c\alpha_0 \alpha_1 p\mu + ep^3\lambda(8\mu + \lambda^2)) \tag{3.6}$$

$$-\alpha_1 q' = \alpha_1 p (a + b\alpha_0 + b\alpha_1 \lambda + c\alpha_0^2 + 2c\alpha_0 \alpha_1 \lambda + c\alpha_1^2 \mu + ep^2(8\mu + 7\lambda^2)) \tag{3.7}$$

$$-\alpha_1 p (b\alpha_1 + 2c\alpha_0 \alpha_1 + c\alpha_1^2 \lambda + 12ep^2 \lambda) = 0 \tag{3.8}$$

$$-\alpha_1 p (c\alpha_1^2 + 6ep^2) = 0. \tag{3.9}$$

We solve Eq.(3.9) for α_1 , Eq.(3.8) for α_0 and Eq.(3.7) for q' . We obtain (choosing one solution of Eq.(3.9)

$$\alpha_1 = p \sqrt{\frac{-6e}{c}} \tag{3.10}$$

$$\alpha_0 = -\frac{b}{2c} + \frac{1}{2} p \lambda \sqrt{\frac{-6e}{c}} \tag{3.11}$$

$$q' = \frac{p}{4c}(-4ac + b^2 + 2cep^2\lambda^2 - 8ep^2\mu c) \quad (3.12)$$

$$u(t, x) = -\frac{1}{2} + \sqrt{6} \tanh\left(x - \frac{1}{3}t^3 - \frac{7}{8}t^2\right), \quad (3.18)$$

Now we substitute Eq.(3.9), Eq.(3.10), Eq.(3.11) into Eq.(3.6) and obtain $\alpha_1' = 0$ implies that

$$e(t) = rc(t) \quad (3.13)$$

Where r is constant.

we substitute Eq.(3.9), Eq.(3.10), Eq.(3.11) into Eq.(3.5) and obtain $\alpha_0' = 0$ implies that

$$b(t) = sc(t) \quad (3.14)$$

Where S is constant.

Therefore, the solution of the Eq.(3.5), Eq.(3.6), Eq.(3.7), Eq.(3.8) and Eq.(3.9) is as follows. We must assume Eq.(3.13) and Eq.(3.14) otherwise there is no solution. Then $q(t)$ is obtained from Eq.(3.12) by

$$q'(t) = \frac{p}{4}(-4a(t) + s^2c(t) + 2rp^2\lambda^2c(t) - 8rp^2\mu c(t)) \quad (3.15)$$

Moreover, α_0 and α_1 are constant functions

$$\alpha_0(t) = \frac{1}{2}(-s + \sqrt{-6rp\lambda}) \quad (3.16)$$

and

$$\alpha_1(t) = \sqrt{-6rp}. \quad (3.17)$$

As an example, take

$$p = 1, r = -1, s = 1, \lambda = 0, \mu = -1$$

and

$$c(t) = t, \quad a(t) = t^2, \quad G(\xi) = \cosh \xi.$$

Then

$$\alpha_0 = -\frac{1}{2}, \quad \alpha_1 = \sqrt{6}, \quad q(t) = -\frac{1}{3}t^3 - \frac{7}{8}t^2.$$

We obtain that

with

$$\xi = x - \frac{1}{3}t^3 - \frac{7}{8}t^2$$

is a solution of equation Eq.(3.1). One can check with the computer that u given by Eq.(3.18) is really a solution of Eq.(3.1).

IV. CONCLUSION

This study shows that the generalized $\left(\frac{G'}{G}\right)$ -expansion

method is quite efficient and practically will suited for use in finding exact solutions for the problem considered here. New and more general exact solutions for any arbitrary functions $a(t), b(t), c(t)$ and $e(t)$ are obtained, there is no any method before, gave any exact solution for this equation. Also we construct an innovative explicit traveling wave solutions involving parameters of the generalized combined KdV and mKdV equation.

ACKNOWLEDGEMENTS

The authors thank the reviewers for their valuable comments.

REFERENCES

- [1] A.K. Ray, J.K. Bhattacharjee, Standing and travelling waves in the shallow-water circular hydraulic jump, *Phys Lett A* 371 (2007) 241--248.
- [2] I.E. Inan, D. Kaya, Exact solutions of some nonlinear partial differential equations, *Physica A* 381 (2007) 104--115.
- [3] V.A. Osipov, An exact solution for a fractional disclination vortex, *Phys Lett A* 193 (1994) 97--101.
- [4] P.M. Jordan, A. A. Puri, note on traveling wave solutions for a class of nonlinear viscoelastic media, *Phys Lett A* 335 (2005) 150--156.
- [5] Z. Y. Yan, Generalized method and its application in the higher-order nonlinear Schrodinger equation in nonlinear optical fibres, *Chaos Solitons Fract* 16 (2003) 759--766.
- [6] K. Nakkeeran, Optical solitons in erbium doped fibers with higher order effects, *Phys Lett A* 275 (2000) 415--418.
- [7] R. Hirota, Exact solution of the Korteweg-de Vries equation for multiple collisions of solitons, *Phys. Rev. Lett.* 27 (1971) 1192--1194.
- [8] M.R. Miurs, Backlund Transformation, Springer, Berlin, 1978.

- [9] J. Weiss, M. Tabor, G. Carnevale, The Painlevé property for partial differential equations, *J. Math. Phys.* 24 (1983) 522--526.
- [10] C.T. Yan, A simple transformation for nonlinear waves, *Phys. Lett. A* 224 (1996) 77--84.
- [11] M.L. Wang, Exact solution for a compound KdV--Burgers equations, *Phys. Lett. A* 213 (1996) 279--287.
- [12] M. El-Shahed, Application of He's homotopy perturbation method to Volterra's integro-differential equation, *Int. J. Nonlinear Sci. Numer. Simul.* 6 (2005) 163--168.
- [13] J.H. He, Homotopy perturbation method for bifurcation of nonlinear problems, *Int. J. Nonlinear Sci. Numer. Simul.* 6 (2005) 207--208.
- [14] J.H. He, Application of homotopy perturbation method to nonlinear wave equations, *Chaos Solitons Fractals* 26 (2005) 695--700.
- [15] J.H. He, Variational iteration method -- a kind of nonlinear analytical technique: some examples, *Int. J. Nonlinear Mech.* 34 (1999) 699--708.
- [16] J.H. He, Variational iteration method for autonomous ordinary differential systems, *Appl. Math. Comput.* 114 (2000) 115--123.
- [17] L. Xu, J.H. He, A.M. Wazwaz, Variational iteration method -- reality, potential, and challenges, *J. Comput. Appl. Math.* 207 (2007) 1--2.
- [18] E. Yusufoglu, Variational iteration method for construction of some compact and noncompact structures of Klein--Gordon equations, *Int. J. Nonlinear Sci. Numer. Simul.* 8 (2007) 153--158.
- [19] J.H. He, Some asymptotic methods for strongly nonlinear equations, *Int. J. Mod. Phys. B* 20 (2006) 1141--1199.
- [20] J.H. He, Non-Perturbative Methods for Strongly Nonlinear Problems, Dissertation, de-Verlag im Internet GmbH, Berlin, 2006.
- [21] T.A. Abassy, M.A. El-Tawil, H.K. Saleh, The solution of KdV and mKdV equations using Adomian Pade approximation, *Int. J. Nonlinear Sci. Numer. Simul.* 5 (2004) 327--340.
- [22] W. Malfliet, Solitary wave solutions of nonlinear wave equations, *Am. J. Phys.* 60 (1992) 650--654.
- [23] E.G. Fan, Extended tanh-function method and its applications to nonlinear equations, *Phys. Lett. A* 227 (2000) 212--218.
- [24] Z.S. Lü, H.Q. Zhang, On a new modified extended tanh-function method, *Commun. Theor. Phys.* 39 (2003) 405--408.
- [25] S. Zhang, T.C. Xia, Symbolic computation and new families of exact non-travelling wave solutions of (3 + 1)-dimensional Kadomstev—Petviashvili equation, *Appl. Math. Comput.* 181 (2006) 319--331.
- [26] S. Zhang, Symbolic computation and new families of exact non-travelling wave solutions of (2 + 1)-dimensional Konopelchenko--Dubrovsky equations, *Chaos Solitons Fractals* 31 (2007) 951--959.
- [27] E.G. Fan, Travelling wave solutions in terms of special functions for nonlinear coupled evolution systems, *Phys. Lett. A* 300 (2002) 243--249.
- [28] E. Yomba, The modified extended Fan sub-equation method and its application to the (2 + 1)-dimensional Broer--Kaup--Kupershmidt equation, *Chaos Solitons Fractals* 27 (2006) 187--196.
- [29] S. Zhang, T.C. Xia, A further improved extended Fan sub-equation method and its application to the (3 + 1)-dimensional Kadomstev—Petviashvili equation, *Phys. Lett. A* 356 (2006) 119--123.
- [30] S. Zhang, T.C. Xia, Further improved extended Fan sub-equation method and new exact solutions of the (2 + 1)-dimensional Broer--Kaup—Kupershmidt equations, *Appl. Math. Comput.* 182 (2006) 1651--1660.
- [31] S.K. Liu, Z.T. Fu, S.D. Liu, Q. Zhao, Jacobi elliptic function expansion method and periodic wave solutions of nonlinear wave equations, *Phys. Lett. A* 289 (2001) 69--74.
- [32] Z.T. Fu, S.K. Liu, S.D. Liu, Q. Zhao, Jacobi elliptic function expansion method and periodic wave solutions of nonlinear wave equations, *Phys. Lett. A* 290 (2001) 72--76.
- [33] E.J. Parkes, B.R. Duffy, P.C. Abbott, The Jacobi elliptic-function method for finding periodic-wave solutions to nonlinear evolution equations, *Phys. Lett. A* 295 (2002) 280--286.
- [34] Y.B. Zhou, M.L. Wang, Y.M. Wang, Periodic wave solutions to a coupled KdV equations with variable coefficients, *Phys. Lett. A* 308 (2003) 31--36.
- [35] D.S. Wang, H.Q. Zhang, Further improved F-expansion method and new exact solutions of Konopelchenko--Dubrovsky equation, *Chaos Solitons Fractals* 25 (2005) 601--610.
- [36] S. Zhang, T.C. Xia, A generalized F-expansion method and new exact solutions of Konopelchenko--Dubrovsky equations, *Appl. Math. Comput.* 183 (2006) 1190--1200.
- [37] Sirendaoreji, J. Sun, Auxiliary equation method for solving nonlinear partial differential equations, *Phys. Lett. A* 309 (2003) 387--396.
- [38] S. Zhang, T.C. Xia, A generalized auxiliary equation method and its application to (2 + 1)-dimensional asymmetric Nizhnik--Novikov—Vesselov equations, *J. Phys. A: Math. Theor.* 40 (2007) 227--248.
- [39] S. Zhang, T.C. Xia, A generalized new auxiliary equation method and its applications to nonlinear partial differential equations, *Phys. Lett. A* 363 (2007) 356--360.
- [40] S. Zhang, A generalized auxiliary equation method and its application to the (2 + 1)-dimensional KdV equations, *Appl. Math. Comput.* 188 (2007) 1--6.
- [41] M.L. Wang, X.Z. Li, J.L. Zhang, The $\left(\frac{G'}{G}\right)$ -expansion method and travelling wave solutions of nonlinear evolution equations in mathematical physics, *Phys. Lett. A* 372 (2008) 417--423.
- [42] J.F., Zhang, New solitary wave solutions of the combined KdV and mKdV equation, *Internat. J. Theoret. Phys.* , 1998,37(5) : 1541--1546.
- [43] Y. Zhenya, and Z. Hongqing, explicit exact solutions for the generalized combined KdV and mKdV equation, *Appl. Math. J. Chinese Univ. Ser. B*, 16(2), (2000), 156--160.

- [44] S. Zhang, J.L. Tong, W. Wang, A generalized $\left(\frac{G'}{G}\right)$ -expansion method for the mKdV equation with variable coefficients, *Phys. Lett. A* 372 (2008) 2254--2257.
- [45] T. A. Nofel, M. Sayed, Y. S. Hamed and S. K. Elagan, The Improved $\left(\frac{G'}{G}\right)$ -Expansion Method For Solving The Fifth-Order KdV Equation, *Annals of Fuzzy Mathematics and Informatics*, 3(1), (2012), 9--17.
- [46] Y. S. Hamed, M. Sayed, S. K. Elagan and E. R. El-Zahar, The Improved $\left(\frac{G'}{G}\right)$ -Expansion Method for Solving (3+1)- Dimensional Potential- YTSF Equation, *Journal of Modern Methods in Numerical Mathematics*, 2(1-2), (2011), 32--38.
- [47] S. K. Elagan, M. Sayed and Y. S. Hamed, An innovative solutions for the generalized FitzHugh-Nagumo equation by using the generalized $\left(\frac{G'}{G}\right)$ -expansion method, *Applied Mathematics*, 2, (2011), 470--474.
- [48] Y. S. Hamed, M. Sayed and S. K. Elagan, A new exact solution for the generalized combined KdV and mKdV equation using the generalized $\left(\frac{G'}{G}\right)$ -expansion method, *International Journal of Applied Mathematics and Computation*, 3(3), (2011), 200--205.

Straw Bale in construction of building and its future in India

***Pragyan Bhattarai, *Dharma Raj Dhakal,* Keshab Neupane,
K. Shyam Chamberlin

*(Students, Department of civil Engineering, K.L.University,Andra Pradesh,India)

** (Faculty,Department of Civil Engineering, K.L.University, Andra Pradesh, India)

ABSTRACT

The advancement in the field of technology have influence environment in utmost extend so everyone is worried about the environment and its tremendous impact in our life. It is obvious that people want to live in eco-friendly houses making it as a part of environment and their life. Thought it is a challenging job, we can still use our resources and manpower for the creation of innovative eco-friendly houses. Straw house can be one of the best alternative for the country like india where agriculture is still the main source of income and production of straw is tremendous. But, those straws are either burned or ploughed back to soil leading to the production of harmful gas as carbon forming black cloud which seriously cause chronic chest diseases and also burning fills the air with gaseous and particulate pollutants, and soils generally can't absorb all the materials as quickly as needed so ploughed back to soil is also not a effective implementation. Straw bale construction can be one of the best alternatives as it is renewable resources having tremendous features as cost effective with high health value, Aesthetics value, thermal performance, Fire resistance, light weight and eco-friendly in nature. We also can go with the various techniques of construction as load bearing straw bale construction or non load bearing construction as per the circumstances. Straw bale construction can be one of the best alternative for all kind of people for constructing a economic building with a sustainable material.

Keywords –Straw bale construction, renewable resource, Eco-friendly houses, high health and aesthetic value, sustainable material.

I. INTRODUCTION

Straw is a natural fiber which we get as a byproduct from the agriculture. It is the plant structure between the root crown and the grain head which is composed of cellulose, hemi cellulose, lignens and silica. It is being produced by the process of photosynthesis, a natural and non polluting process by solar energy. We can get this from wheat, rice, oats, hops, barley. Among this rice straw is the toughest one due to high silica content. It is an annually renewable agricultural residue which is being produce in ample amount in most of the countries. It is also considered as the waste product and is being wasted by burning or any other way which is having impact on the environment directly or indirectly. It is being produced by the collaboration of environment so use of this in construction would be obviously a environmental friendly and would have a lots of merits for our quality life. Burning of the straw lead to black cloud which cause serious chronic cheast diseases and

carbon evolved from it would affect the quality of environment. Straw which is produced has become one of the headache for the farmers as it won't decay easily. The world largest straw producing countries like China, India and other agricultural country have not been able to utilize it for productive work up till now. In india it is used for paper factory for production of papers and some other purposes but this is not enough for proper utilization and still these country are wasting in ample amount. The use of straw for the construction has been commenced long back. Straw bales were first used by the settlers of the sand hills region of Nebraska. In 1890's Nebraska commenced this straw bale for building buildings, churches, schools, officials and grocery stores. In those times they focus in stability of bale wall system , structural stability, plastering and moisture control. So, straw bale construction has been a boom for the economic environmental building alternative.

Straw bale is simply a compressed bundle of straw which is arranged in square, rectangular or round shape attached with wire or twins. Straw is the dry steams of cereal grains left after the seed heads have been removed (Austin city code Volume-II, section 3603). Bale density varies according to the type of grains, moisture level and degree of compaction provided by the baler¹. The dimension of straw bale can vary as per circumstance but the standard size can be 900mm x 450mm x 350mm / 584mm x 1168mm x 400mm.Straw bales are light which means a straw bale wall weights 65% less than an equivalent brick wall and 62% less than concrete block wall.

Size of bale(in mm)	900 x 450 x 350/ 584 x 1168 x 400
Modulus of Elasticity	1379 KPa
Compressive Stresses	More than 482.7 KPa

Compressive test on unplastered walls 2438mm high gave yield stresses of 27.6-34.5KPa(straw bale construction by Bruce King ,P.E).

II. ANALYSIS

Straw bale have omnipotent scope in India. As, India is one of the largest country enlisted in production of straw bale. Since, still large population is solely depended upon the agriculture so potential of straw bale construction in India is exclusively high. As, 46% of total land(32,87,590 sq.km) of India is agricultural land so out of total population (1,17,09,38,000) 58.4% is solely depended upon agriculture

as per 2010 study. Among them 41.6% of total population lies below poverty level(2005 world bank estimation) which means these people are not able to meet quality shelter and being in a good house is a dream for them. It is clear that building construction in today’s context is very expensive and it can’t be accessible to them so quality of life stander for them is very low but it is basic human right to get access for good shelter and this can be possible through straw bale construction. As straw is considered as a waste material and it is locally available in ample quantity so use in construction is environmental friendly. According to the 1995 report from Department of Energy(DOE) House of straw adds that the construction cost of a structural straw bale wall is about one fourth that of comparably insulated conventional wall.

III. ENVIRONMENTAL PERFORMANCE

The study of straw bales shows that it is highly eco friendly in its production, placement, function and operation and maintenance to reconstruction. It depicts that it is produced in environment and it requires low energy for procurement for comfort, creativity and aesthetics. The environmental issue encompasses the following features.

<p>1. Fire Resistance</p>	<p>It has good resistance against fire since straw bale are tightly packed making it too dense (i.e lack in oxygen) which do not support the combustion (American Society For Testing and Material). The test conducted at the Richmond Field Station in 1997 by student of California Berkeley reflect that timber resist fire for 8 minute, un-rendered straw bale resist fire for 30 min and rendered straw bale resist for 2 hours.</p>
<p>2. Thermal insulation</p>	<p>Straw bales has thick straw wall, which creates the insulating gap between external and internal part of wall, helps to resist the flow of heat at higher level and it aid to save energy. Rice straw is class A insulating material</p>

<p>3. Sound Insulation</p>	<p>Straw is fibrous material and it resists the sound waves controlling noise pollution which also helps to save energy.</p>
<p>4. Structural capacity</p>	<p>The structural performance of straw bale construction is high. Load bearing straw bale method can withstand up till three storied whereas frame helps to improve the stability more than load bearing straw bale method.</p>
<p>5. Durability and moisture resistance</p>	<p>Though straw is the biological product and is biodegradable, It is highly durable in absent of excess moisture (>15%) and the air. Till the straw bale is well protected and is allowed to become waterlogged ,it can last many years with moderate maintenance and Reasonably expected to have lifetime of 100 years or more.(5.8 straw bale, Paul Downton)</p>
<p>6. Resistance against termites and pests</p>	<p>Clean and dry straw have less nutrition so it is unable to support paste population for long in itself. Also wall build with tightly pressed straw bale provide fewer space to paste to live.</p>
<p>7. Toxicity and moisture resistance</p>	<p>Being a naturally available material straw bale is nontoxic in nature and produces no harmful chemicals due to its inert nature. The straw bale is also having</p>

	good breathability allowing air to slowly permeate the structure without moisture penetration.
8. Availability	Straw is agricultural by product and locally available .so it is easily accessible for any one. Transportation is not require which also helps in controlling the fuel consumption .

Table1. Features of straw

In this way straw is having lots of benefits which helps a lot for the quality of life and it also aid in fulfilling the green concept to some extent due to its tremendous features. There might be several problem that we might encounter but tactful and astute plan can lead for the best straw house. Water penetration is also major problem, straw left in a moist generally above 20% moisture content and 10 degree temperature will support for the growth of molds which leads to decay of straw. Long term creep deflection of the bale wall can be the major problem so to avoid this pre-compression of the wall is highly admired. Load bearing straw bale building in high snow or earthquake prone areas can tentatively be designed by using cement stucco skins.

With this observation we can conclude that straw is one of the promising materials for the green construction because of its performance in collaboration with the environment.

IV. COST EFFICIENCY

Straw is easily, cheaply available material and require limited transportation and do not require any transformation and can be easily handled. It does not require much skilled man power for procurement and construction. As it is agricultural product so it acts as renewable resource which helps to reduce the use of non renewable resource and reduce the cost whose relation is depicts in figure 1.

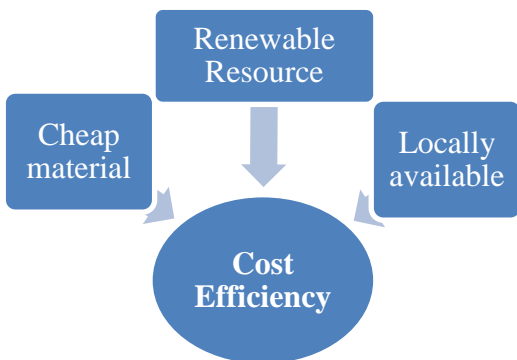


Fig.1 Relation of cost efficiency with various components.

V. CONSTRUCTION

Various methods are used for the construction. The main aim is to achieve good compression of bales to minimize settlement and movement to fulfill the structural and well being requirements. Well compressed bales of water content less than 15% is preferable.

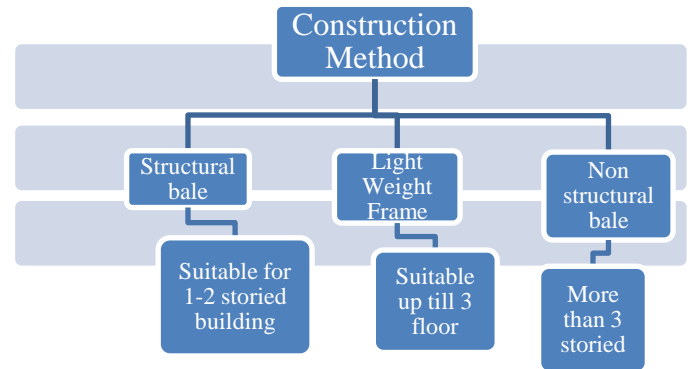


Chart1. Construction method of straw house

Construction of straw house can be done in various ways which is described below

Structural Bale House-

It is also known as Nebraska style and is considered as the first technique of construction. The entire load is being beared by the straw in this case so it is also known as load bearing method. It can be used for simple and one to two storied building. In this case door should not exceed 50% of wall surface. In this process roof of the building is constructed at last.

Light Weight Frame-

It is also known as timber framework method in which firstly timber framework is prepared and in those frame only straw is installed. This method would be suitable for up till 3 floors. In this timber would be an additional material or any other framework material. In this frame should be provided for doors and windows. In this roof should be constructed at first only.

Non Structural Bale –

It is also known as in fill method. In this building with post and beams are made with timber or steel. In this weight is supported by the frame. Wood, Steel or concrete framework and the bales are simply infill insulator blocks between the posts. It gives great stability and cost is also high in compare to others. In this also roof should be constructing at first. In this way, as per the accessibility we can select any one way of construction which encompass ancient till modern way of construction. If our budget is low than selection of Nebraska style of construction is more preferable than others.

Bale walls, when covered with plaster, drywall, or stucco are considered to have the equivalent fire resisting rating as a wood frame construction with same wall finishing system (Austin straw bale code, 3605.1 general). From the Austin straw bale code 3605.2 for all the method of construction the nominal minimum bale wall thickness must be 14 inches.

VI. OBSERVATIONS

Fig.2 clarify that straw bale house is sound resistance in compare to others types of houses. Sound can transmit more in open space where as straw wall resist sound more in compare to brick wall.

Fig3. Shows that energy consumed in straw house is far less than that of others. As it acts as sound and heat insulation and have other tremendous advantages so energy consumed in this type of building is reduced in maximum extend than that of others.

Table 2. Reflects that straw house is very cheap in construction and we can save a lot from straw bale construction making it affordable to all for constructing quality house for quality lifestyle.

Table3. Explains for the last 10 years a increasing number of load bearing straw bale buildings have been built in the UK. Walls formed from stacked bales of straw are used as load bearing walls in low rise, specially for one storied building. The average bulk density was 125 kg/m³ (average moisture content at testing was 13.5%), varying between 118 and 137 kg/m³. The bale density that was recommended varies between 100 and 110 kg/m³. The maximum loads for unplastered straw bale walls has been found at between 4.2 and 19.2 kN/m, with respect to bale type, orientation (laid flat or on edge) and the use of internal reinforcing bars. Displacements reported at a maximum load of unplastered walls similarly vary between 72 and 198 mm. The maximum reported loads for plastered bale walls, of comparable construction, vary between 21 and 66 kN/m.



Fig 4. Static load test

A maximum permissible service load of approximately 19 kN/m² (9.6 kN) is often used in straw bale wall design. The maximum applied load of the lime rendered wall was over four times greater. However, the maximum load of one unplastered wall was only 13% higher, though the standard bale wall achieved a maximum loading nearly three times higher. Hence, under sustained loading unplastered straw

bale walls demonstrated viscoelastic behavior. The walls creep with time under load following an initial instantaneous deformation, immediately recovering some deformation on load removal, followed by further time dependent recovery but exhibiting a final permanent deformation. Pre-compression improved initial stiffness of the straw bale wall. Maximum vertical load capacity and initial stiffness was improved by the inclusion of hazel spikes. Maximum vertical load capacity and initial stiffness was impaired by the use of half bales.

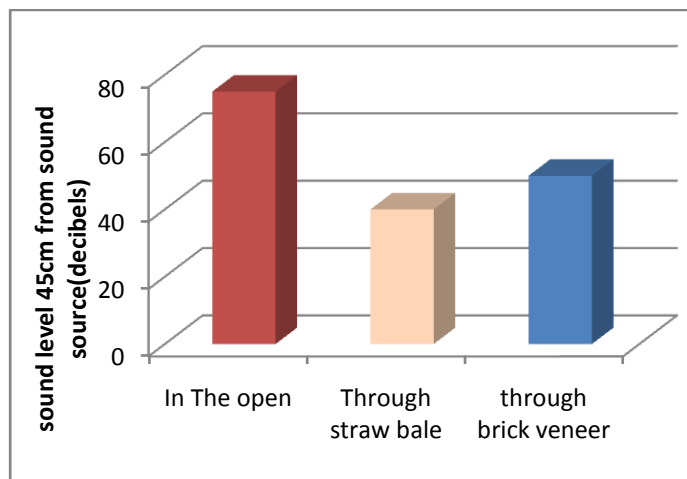


Fig 2- Sound transmission through straw bale and brick veneer walls compared with sound level in the open

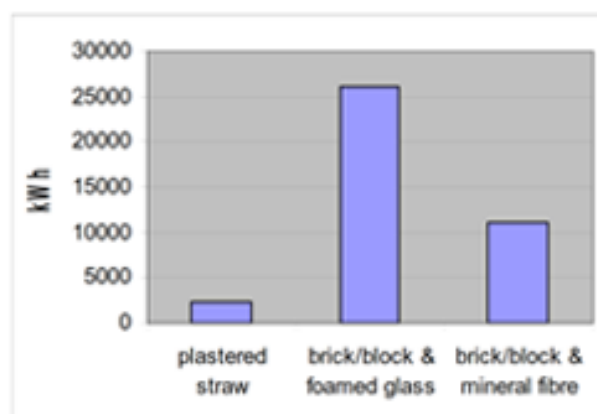


Fig 3.energy consumed by plastered straw

Building	Construction Cost	Energy	Total	Saving
Straw Bale	\$40000	\$60000	\$100000	\$102000
Conventional	\$82000	\$120000	\$202000	-----

Table2. Comparison of cost for construction between straw bale and conventional as per working group report.

Wall	Initial wall stiffness (kN/mm)	Maximum applied load (kN)	Settlement at maximum load (mm)
Standard construction	0.11	27.6	220
Pre-compressed wall	0.22	19.2	120
Half-bales	0.087	10.9	140
No hazel spikes	0.077	11.7	165
Lime rendered wall	5.62	41.1	55

Table3. Static load test

VII. CONCLUSION

In this emerging world where the rising need of housing is increasing day by day due to tremendous growing of rural and urban population has been a pressuring issue. Without compromising affordability, quality and maintaining the component of earth system has been a challenging task where Straw Bale can be one of the promising building material that meet the overall housing need and energy efficient goal of most of the developing countries like India, Nepal, Bhutan etc where agriculture act as the backbone of development. India being one of the largest countries for production of straw but most of those is considered as waste and limited are only used for productive type but if we can utilize them for construction in the form of straw bale then staying in good house won't be limited to dream for people. It aids to maintain the quality of living stander of people because straw house fulfills serviceability and helps to maintain the environmental quality. Straw is getting lots of preference in many countries because it is cost effective with high health value, Aesthetics value, thermal performance, Fire resistance, light weight and eco-friendly in nature. It also has good response against earthquake so it can be constructed in earthquake prone areas as well. So, profound research and awareness regarding straw bale construction should be enhanced in developing countries land agriculture countries like India for effective implementation of straw bale house.

REFERENCES

- [1] Mark C. Tatum, MSEE, PE "Straw Bale Construction and Building Codes ", Auburn University ,Auburn, Alabama
- [2] Bou-Ali, Ghailene, "Straw Bales and Straw-Bale Wall Systems", University of Arizona, Tucson, 1993.
- [3] Garas G., Allam M. and El Dessuky R. STRAW BALE CONSTRUCTION AS AN ECONOMIC ENVIRONMENTAL, ARPN Journal of Engineering and Applied Sciences, VOL. 4, NO. 9, NOVEMBER 2009 ,ISSN 1819-6608
- [4] Steen, Athena Swentzell; Steen, Bill & Bainbridge, David "The straw bale house" Chelsea "Green Publishing Co. (ISBN 0-930031-71-7) U.S.A. 1994.
- [5] Watts, K., Wilkie, K., Thompson, K., and Corson, J. "Thermal and Mechanical Properties of Straw Bales As They Relate to a Straw House" Canadian Society of Agricultural Engineering Paper No 95-209, Ottawa, Ontario, 1995.
- [6] Mohamed Salah Gharib Elsayed "Straw Bale is Future House Building Material" ,Architect -Egypt

- [7] Stephens, Don, and Budinger & Associates, Inc. laboratory test July 13, Spokane, Washington 2000.
- [8] Robert Bakker, Edwin Keijsers, and Hans van der Beek "Alternative Concepts and Technologies for Beneficial Utilisation of Rice Straw" Wageningen UR Food & Biobased Research ,Number Food & Biobased Research number 1176 ,ISBN-number 978-90-8585-755-6,December 31st, 2009
- [9] Bruce King, PE, "Load-Bearing Straw Bale Construction", Ecological Building Network, 2003.
- [10] Bruce King1, "Agricultural ByProducts in Construction", Ecological Building Network, 2010.
- [11] U.S. Department of Energy,Energy efficiency and Renewable Energy, " Straw House", April, 1995
- [12] Robert Hilton," Straw Bale Construction: Is Straw Bale Construction suitable for Self-Builders in Britain?", 'M.Arch dissertation, Welsh School of Architecture, 2007.
- [13] John Straube "Moisture Properties of Plaster and Stucco for Strawbale Buildings" Peter Walker, "Compression load testing straw bale walls", Dept. Architecture & Civil Engineering University of Bath, Bath , May 2004.

Computer Aided Engineering and Machine Drawing: a modern method

Rajashekar Patil¹ and Dr. S. Mohan Kumar²

¹Assistant Professor and ²Principal

Department of Mechanical Engineering, Shri Dharmasthala Manjunatheswara College of Engineering & Technology, Dharwad, India.

ABSTRACT

The rapid change in teaching of engineering drawing using computer aided design (CAD) technology makes a tremendous change on the staff/students in teaching/understanding engineering drawing in technical institutions. Mastering CAD technology has become order of the day for staff/students especially in technical institutions. CAD course have become a compulsory subject in many technical university and institution. This paper is a research on the teaching of Computer Aided Engineering Drawing (CAED) and Computer Aided Machine Drawing (CAMD) courses. The problems are discussed on the present and future development of course content and teaching methods of these subjects. There are several solutions are evolved in designing the content, difficulty of the course and also improving the teaching methodology.

Keywords - Computer Aided Design, Computer Aided Engineering Drawing, Computer Aided Machine Drawing, content, teaching methods

1. INTRODUCTION

Objectives of drawing are (1) Accuracy: The drawings are not useful to the maximum extent if they are not accurate. (2) Speed "Conversion of Time into Money" in industry. There is no place for the slow technician, or engineer. Speed is not attained in a hurry; it should be with intelligent and continuous work. It comes with practice. (3) Legibility: Drawing is a means of communication to others, and that it should be clear and legible to serve its purpose. Care should be taken especially in dimensioning and lettering.

The introduction of the one of the best ways to communicate one's ideas is through some form of picture or drawing. This is especially true for the engineer. The purpose of course content is to give you the basics of engineering sketching and drawing. The Computer Aided Engineering Drawing and Computer Aided Machine Drawing is developing with a faster rate in many universities, computer have become an important tool in present day to draft, design and developmental process. Variety of CAD software's are available for drawing two dimensional (2D), three dimensional (3D) modeling and also for various views of an object to suit the CAED and CAMD courses as well as to meet the industrial standards. These CAD software and hardware can finish the task starting from 2D, 3D, smart dimensioning, converting 2D to 3D or 3D to 2D of front view, top view, side view, bottom view, rare view and isometric wire frame model with and without hidden edges of 3D objects, 3D rapid rendering, even physical properties of 3D objects or even section of 3D objects (solids). Every engineering students/engineering faculty/engineer has to

create drawing as per their or others requirement in the society. The creation will start with an idea in a brain and drawing on a paper or computer aided engineering drawing using CAD software. Therefore CAED course is very important in the present day technology for all disciplines of engineering. Hence, it is proved that drawing is the language of engineers. The teaching of CAED and CAMD courses will get an excellent development and achieved many creative results. However, these are small problems in content and teaching methods for these courses. This paper will try to explore these problems and excel with better solutions. Also it is very important for technical university/institutions to recruit the teaching faculty for CAED and CAMD courses [1].

2. PRESENT AND FUTURE DEVELOPMENT OF CAED AND CAMD COURSES FOR TEACHING

In early 1950's the study of CAD has began but the technology developed in mid 1990's. at that time, the computers, software and hardware were very expensive and options for CAED and CAMD were very less with limited funds. The technical universities/institutions set up these courses only for few disciplines that to for higher semesters. After computers become popular and economical the technical universities/institutions started to provide these courses and improving them. CAD software also provided attention to education sector to improve the standard quality of 2D drawings and 3D modeling of machine parts which in turn can directly manufacture using rapid prototyping machine [2].

At present, mechanical and industrial production engineering department in many universities/institution has CAED and CAMD course to meet the need of training the student as per course. The CAED and CAMD courses are been allotted into two different year/semester CAED based on 2D drawings using CAD software and CAMD is based on 3D modeling, assembling and simulation using CAD software. In first year/semester for all discipline of engineering 2D is taught and in higher semester or second year 3D is taught. Presently Teaching method of CAED and CAMD uses, chalk & talk, physical wooden models, power point presentations, audio and video interleave, macro media flash and 3D studio max software are used as teaching aid for better understanding for students.

CAED courses have become compulsory course with professional training subject. For example, there are two compulsory courses CAED in I/II semester for all discipline of engineering and CAMD in III/IV semester for certain discipline of engineering. These subjects have made very good teaching results. The students studying these subjects

can easily understand, practice and complete a course with better knowledge, this knowledge can be used for designing a new product and create their vacancies to jobs for themselves.

To promote these courses, the technical universities/institutions started separate labs and dedicated software with trained teaching and supporting staff to increase the creditability of the courses. The other disciplines of engineering like, electrical, bio-technology, civil etc wherever 2D drawings and 3D modeling is required started using this method to increase its efficiency of the courses.

In future CAED and CAMD courses gain lot of importance because every customer needs his product to be designed and developed in a unique way and further it should be tracked with designing, analysis, developing and manufacturing and to be maintained through out the life of the product in a systematic and technical way, also customer wants to see his product in every stage of life of product and customer wants to suggest on improvement of the product.

3 CURRENT PROBLEMS IN CAED AND CAMD COURSE TEACHING

3.1 Course difficulty: The number of hours for CAED and CAMD curriculum mentioned is not sufficient. Teachers should be well prepared with teaching aids like power point presentation, flash movie, audio video interleave, etc., with time constraints. Students cannot complete the syllabus well within the time. The reason for this is initially student need basic as well as advanced knowledge of course. Secondly, teachers with CAED and CAMD experience in technical university and institution are very few. So it is difficult to increase the standard of the courses. Thirdly CAD software has also complex or sometimes no solution for some of the operation like knurling. Fourthly every year new versions of CAD software are released with new technology and new commands with different tool bars and menu bars and also in between the software patches will be released, these patches are updates of software which has to be downloaded and updated or sometimes macro's has to be written. With all these problems a course become slightly difficult compare to other courses.

3.2 Content: CAD is widely used in technical universities/institutions. In this paper it is starting from 2D drawing in the I/II semester, then to 3D modeling in III/IV semester and finally converting 3D to 2D. Setting CAED and CAMD content becomes a problem because of CAD software gives solution. Selection of CAD software required to teach, number of hours required, marks/grades allocation for each individual chapters in the course. Usually in all technical universities/institution the number of teaching hours will be same for all courses and also same number of marks/grades for all courses. Number of problems will arise here while setting the content of these CAED and CAMD course because of which more number of hours is added in course. Some technical universities/institutions misunderstand the present day requirement with respect to industry. Hence, the content should be clear with concepts and strong theoretical background and also fit the industrial standards. If it is not so, content will be failing to meet the requirements of industries. Some deemed

universities/institutions are failing to keep pace with technological developments and also lack of knowledge in implementing these courses. Students also need lot of time to meet the needs and requirements of industries.

3.3 Scheme of evaluation and scheme of examination: For each chapter and for each problem sketching (free hand drawing) and also drafting on computer to get CAD solutions using software is made so that students can understand and practice in a better way. Credits/marks are sub-divided as per practical class and on number of problems solved in a time frame. Then 40% of weightage is given to sketching and 60% for computer solutions. Separate question paper is prepared by the universities/institutions for each students i.e., each individual student has to get different question paper. These setting of question paper individual is a tedious and evaluating them is also tedious unless it is online. Finally, manual evaluation is done for cross checking and quality of evaluation.

3.4 CAED and CAMD teaching methods: Traditional teaching methods uses chalk and talk which is not sufficient for a better understanding. Teachers can also use power point presentation, audio video interleave, flash movie etc for modern methods of teaching. Some colleges are using both the traditional methods and modern methods. Teaching methods also based on knowledge of teachers and facility available at the source. Initially the concepts, theoretical knowledge, procedure and solution to the problems are taught in a conventional class room and then these are experienced in practical at CAD laboratory. This theoretical and practical takes a lot of time, hence it cannot produce good learning effects.

4 SOLUTIONS

4.1 Dynamic Curriculum: Since every year new versions of CAD software are released with new technology and new commands with different tool bars and menu bars and also patches will be released and also other full featured software will continue to emerge. It is very easy to establish a dynamic curriculum. In a limited number of hours and credits, the most important technology can be selected and every year/semester new curriculum can be made. Further more with the help of tutorials the student can learn simple operations themselves and also online solutions creates collaborative learning in this way students can create a CAED and CAMD domain to accomplish a complete knowledge system. Initially proper software should be selected because in the present day world many CAD software are emerging. There are many software available which gives the same output. Software which have more options and functions used by many organizations will be the best choice. Secondly, the syllabus as per the semester without extending the more number of hours required to complete the syllabus. Thirdly update the content and credits regularly. Finally these CAED and CAMD course are to be used to finish later product design in future.

4.2 On line question paper and evaluation: To avoid malpractices universities/institutions can use online question paper through internet with timer so that once student start answering the question the timer will start and when completed and submitted the answers the timer stops. Here even it will be helpful to note what time is taken to solve the

problems by the students. Since every question of engineering drawing will have definite solutions with options and with the same solutions and optional solutions a custom made or web based software can be developed where in the super impose of solutions on students question solved problems wherein based on the differences or similarity the credits/marks can be allotted and finally the results are displayed on the web portals.

4.3 Enhancing the teaching methodology: Teachers will use chalk and talk method, power point presentation, audio video interleave, flash movie, etc simultaneously they can also use the same CAD software for teaching. Wherein teachers can create solids like cube, prisms, pyramids, cylinder, cone etc very easily with simple commands and can also show front view, top view, side view and other views necessary as per content. Different color can also be added for every surface to give clear picture of an object. Not only views even these solids can cut at different angles and show the full sectional views, half sectional views, broken view, etc., for example cone can easily be sectioned at different angles where one can teach complete conic section (circle, ellipse, parabola and hyperbola). CAD software acts as an excellent tool for teaching in classroom and also in practical laboratory. Another example in assembly of screw jack modeling of all parts and assembling in CAD software virtually and further in assembly some parts can be made ground and some parts moving to give motion. The simulation is done to see working of the screw jack, exploded view of screw jack is analyzed and physical properties of screw jack are obtained. Even load to screw jack is applied for analysis, results are verified. Finally, the file is saved in audio video interleave with voice and these files will be an excellent teaching aids.

4.4 Preparing the students to establish an excellent learning concept: Students to establish good learning concept, step 1. the concept should be understood. Step 2 student should understand the difference between engineering drawing and computer aided engineering drawing wherein the concept remains same, only the tools are changed i.e, instead of using the mini-drafter, pencil and various types of pencils, eraser and other accessories student will be using CAD

software. Step 3 the student should know the importance between sketch capacity and skills using the CAD software. Step 4 There should be through interaction between the students and the faculty, one of the problem found that student often completely depend upon computer to solve the problem. Students spend maximum time in learning and understanding the software, here faculty should pay attention to clarify that the software is a merely tool for computer aided engineering drawing. In addition, students should know CAED and CAMD is not only for 2D drawings and 3D modeling , student should understand about the complete development process under the aspect of computer aided engineering. That is conceiving an idea in a brain, concept and visualization about any new product to be development should be new learning concept. A case study is taught with case method and also real time problems can be taken and solved for better understanding so that students think independently instead of always following textbook step by step.

5. CONCLUSION

Computer Aided Engineering Drawing and Computer Aided Machine Drawing is a course communicates a precise description of a part with all details and better visualizations. Students improve in efficiency of designing the machine parts. The solutions provided in this paper are guiding teaching community with improved teaching methods and strengthening with proper resources. Hoping a good learning concepts are created for students. CAED and CAMD courses will be starting point for product life cycle management in academia and industry and also students will be industry ready for production.

REFERENCES

- [1] C. N. Reffold, Teaching and Learning Computer-Aided Engineering Drawing, *International Journal of Engng Ed.* , Vol. 14, (4), 1998, 276-281.
- [2] Shouqian Sun, Qi Huang, Lingyun Sun and Chai Chunlei, Research on Computer-Aided Industrial Design Technologies for Product innovation, *the Journal of designing in china*, 1(1), 2005, 78-79.

TABLE
 Comparison between Engineering Drawing and Computer Aided Engineering Drawing

Particulars	Engineering Drawing	Computer Aided Engineering Drawing
Tools	Drawing board, Mini-drafter, Pencil, Eraser, Compass, Dividers, Set Squares, etc.,	Computer & CAD software
Point & Line Thickness	Depends upon types of pencil	Can be fixed (ex: projection line thickness as 0.05mm)
Storing Space	Drawing sheets needs lot of space	Since drawing are in digital form and smaller files than bitmapped images needs very less space
Preservation	Possible but difficult	Very easy because of digital file
Transfer	Possible but difficult	Very easy through out the Globe via internet
Precise	Depends upon the skill of individual	Very less skill is required because of software
3D detailed drawing	It has to be drawn	Can be acquired by a single command
Scalability	It has to be drawn	Can be acquired by a single command
Efficient	Less efficient because use of many tools	Since software is very efficient
Conversion from 3D to 2D	Not possible	Possible
Animation	Not possible	Possible
Editing	Not Possible	Possible and even online via internet
Analysis & Testing without actual produce	Not Possible	Possible using analysis software
Virtual Manufacturing	Not Possible	Possible using software
Prototyping	Not Possible	Possible using Prototyping machines

Enhancement of Power Quality using active power filter in a Medium-Voltage Distribution Network switching loads

M. CHANDRA SEKHAR¹, B. KIRAN BABU²

*(Student, Department of Electrical and Electronics Engineering, KL University, India)

** (Assistant Professor, Department of Electrical and Electronics Engineering, KL University, India)

Abstract--- This paper Discuss about the problem occurring in the medium voltage distribution network such problems reactive power, harmonics and unbalanced load current compensation of Medium voltage Distribution systems. It proposes a simple and inexpensive solution to enhance power quality when a particular connection to the high voltage transmission network. It presents the design of a active power filter and BLDC motor connected to MV level of power distribution system it main task is to regulate 132 kV voltage level. Reconfiguration of the power delivery network imposes new constraints in a distribution substation so that the reactive compensation should be increased. The topology of a shunt hybrid active filter is analyzed. The possibility of different levels of reactive power compensation is implemented. The proposal shows very good performance for different load demands. This scheme is simulated using MATLAB/SIMULINK for Brushless DC (BLDC) motor loads. Results are presented to verify the effectiveness of the control of sinusoidal by using active power filter (APF).

Index Terms— Active power filter, harmonic distortion, power quality, reactive power, BLDC, THD, passive filter, pcc.

INTRODUCTION

The increase of non linear loads and equipments are the major problems for the purpose of harmonics as well as unbalance loads such as power supplies voltage distortion and current harmonics problem for utilities at distribution systems [1],[3]. Then, power electronics appears as an essential interface to improve power quality [2]. The usage of point of common coupling loads to the unbalanced and distorted currents and three phase distorted voltages. Active power filter uses power electronic switching to generate harmonic currents that cancel the harmonic currents from a non linear load.

The use of traditional compensation with capacitor banks and passive filters produce harmonic propagation, i.e., harmonic voltage amplification due to the resonance between line inductances and shunt capacitors. Therefore, different active solutions have been continuously analyzed in recent years [4]–[6]. A lot of research on different topologies has been done. To improve

power quality [5]. The correct placement of the active filters in a distribution system has been investigated [7]. A lot of care is taken on different control strategies to obtain the desired objectives [8]–[13].

Voltage distortions in different points of the network, together with the working conditions of the capacitor banks, were verified by means of harmonic flow [14]. Therefore, a hybrid solution is proposed here to solve the particular problem of enhancing the 132-kV level in a radial connection of the medium-voltage (MV) network. Among all the compensation alternatives, the hybrid topologies appear very attractive in the distribution networks where some passive compensation is already installed. In particular, the hybrid shunt active filter formed with the connection of a low-rate active filter in series with one or several passive filters is gaining attention [4], [9]–[10].

Different filter using to improve power quality [5]. The main use of compensation with capacitor bank and active power filter the main advantage of Active power filter in a distribution systems [7] which includes methods like Instantaneous reactive power theory, modified p-q theory, synchronous reference frame theory, instantaneous $id-iq$ theory. The implementation of a new control algorithm for a three phase shunt active filter to regulate load terminal voltage, eliminate harmonics, correct supply power-factor, and balance the nonlinear unbalanced loads. A three-phase insulated gate bipolar transistor (IGBT) based current controlled voltage source inverter (CC-VSI) with a dc bus capacitor is used as an active filter (AF).

II. SYSTEM SPECIFICATIONS

The 132 Kv network distribution systems is connected to the 500kv high voltage transmission system two points work on the radial network connected to only one point demand at different substations [14].the loads at different substations at commercial and residential . So it is difficult to identify harmonics sources in case of industrial plants. The system can represented by an ideal voltage source of 132kv connected to two transformers. 132 KV/34.5/13.8 kV and 15/10/15 MVA. There are no load at 34.5kv level both transformers are connected in parallel to 13.8 KV .where capacitor bank are placed the short circuit power at 13.8 KV is nearly 150MVA .based on power flow and harmonics studies on network [14].power demand 20.9 MVA with $\cos\phi=0.78$ harmonics peak currents are

$I_5=50.3A, I_7=35.1A, I_{11}=15.1A,$ and $I_{13}=11.4A,$
 resulting in a total harmonics distortion of $THD_1=5\%$

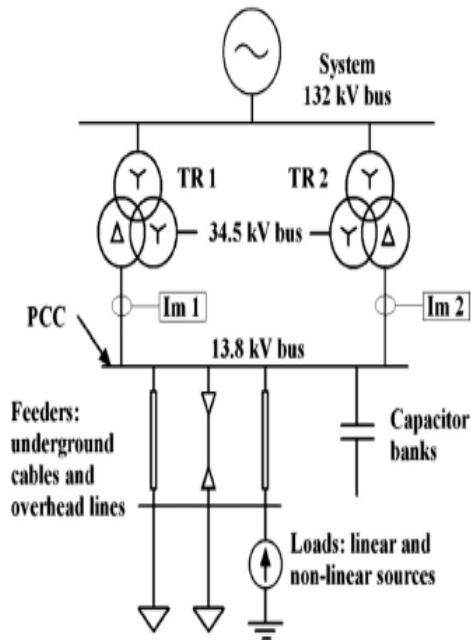


Fig .1. One line diagram of network model

Fig.1. one line diagram of network model for DS a three phase model of the network is constructed on MATLAB/SIMULINK non linear loads take discontinuous current and thus it inject harmonics .reactive power compensation can increase the steady state transmissible power and the voltage profile along the line since reactive power is used for voltage control in distribution system

III. HYBRID ACTIVE FILTER COMPENSATION

The hybrid active power filter consists of passive filter connected in series with a controlled voltage sources the active power filter is used to compensate harmonics while reactive currents are damped by the passive filter the structures of the proposed SHAPF fig 3 (a) Three phase pulse width modulation (PWM) voltage source converter (VSI) connected in series with one or more passive filter there are connected to grid systems without need of transformers .the passive filters consists of simple LC filters near certain harmonics frequencies .

Basically active power filter acts a controlled voltage source the system line currents to become sinusoidal

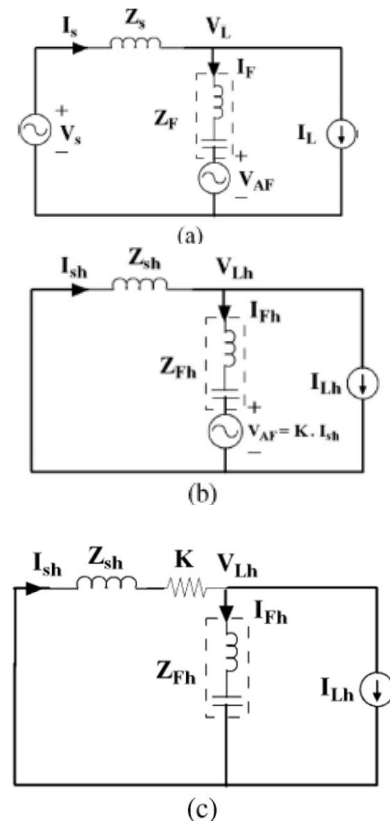


Fig.2. single -phase equivalent circuits of the system with hybrid active power filter connected (a) total equivalent circuit (b) Equivalent circuit for harmonics component (c) Resistive equivalence of the harmonics filter

DESIGN OF HYBRID ACTIVE FILTER

The control systems has two main parts while generating the voltage references of PWM VSI 1) Eliminate the harmonics from the line currents 2)control the dc voltage of the VSI therefore the analysis and design of the SHAPF may be sub divided into the passive filter PWM VSI and the control block. Hybrid Active Power Filter (HAPF) topologies have been developed to solve the problems of harmonic currents and reactive power effectively.

A. PASSIVE FILTER

The passive filter has three main functions reactive compensation absorption of harmonics currents produced by the load and coupling of the inverter to grid .because load is variable of different levels of reactive compensation .

B. COMPARISION OF PASSIVE FILTER AND ACTIVE FILTER

	Passive filter	Active filter
Harmonic control by order	Very difficult	Possible via parameters
Harmonic current control	Requires filter for each frequency	Simultaneously monitors many frequencies
Dimension	Large	Small
Weight	High	Low
Influences of a frequency variation	Reduced effectiveness	No effect

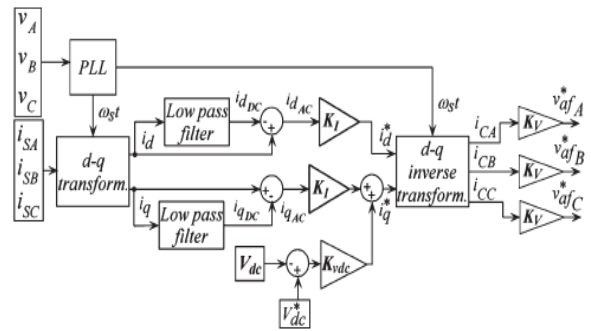


Fig.3 (b). Control block diagram of the SHAPF

C.PWM VSI

The PWM VSI is a two level three phase VSI with IGBT [2],[12]-[15] using sinusoidal modulation

The inverter is connected to the 13.8 Kv bus or point of common coupling (pcc) through the passive filter since the LC filter presents high impedances at the ripple produced by the inverter output voltage where as the inductor of each passive filter function like coupling inductors to connect the converter to the network the passive filter at lowest frequency is connected in order to better filter harmonics generated by the PWM .

When higher harmonics are required for the SHAPF the voltage level in the dc side the voltage rating for the power IGBT and the switching frequency required to follow the references currents are higher the hysteresis current control based hybrid shunt active filter to improve the Quality of Power in distribution line by minimizing the harmonics .

D. control system voltage generator

The control system measures at the secondary windings of the transformer (Im1 and Im2 in fig 1). Then supply current (iSA, iSB, iSC)

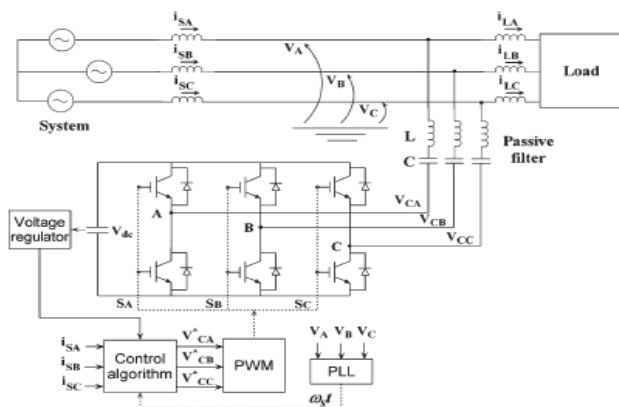


Fig. 3 (a), structure of the proposed SHAPF

A. Active power filter control method

In an active power filter, a controller determines the harmonics that are to be eliminated. The output of this controller is the reference of a three-phase current controlled inverter. The principle of a shunt active filter. The nonlinear load is connected to the power system and is supplied by the non sinusoidal current .The active power filter is connected in parallel to the mains, on the point of common coupling PCC, and supplies the current harmonics needed to maintain the source current sinusoidal. Traditionally active power filter shunt active filters were proposed as a means of removing

B. Application of BLDC MOTOR (brush less dc motor)

Blcdc motor more advantage it has high power density has compared to other motors fast response and high power and size also small .where three phase source is connected to rectifier and inverter connected with the help of BLDC motor

Brushless DC motors will be more complex than normal DC motor Brushless DC motors (BLDC motors , BL motors) also called electronically commutated motors (ECMs, EC motors) are synchronous electric motors powered by direct-current (DC) electricity and achieving electronic commutation systems, instead of mechanical commutators and brushes . Brushless DC motors have got a higher power density than AC along with brush DC motors. A brushless DC motor (BLDC) is a synchronous electric motor electronically controlled commutation method. A Brushless DC Motors are employed in a number of applications in several industries.

The brushless dc motor is much better than the ac synchronous motor. The brushless DC motor is usually run at exact rates of speed from 100 revolutions per minute as much as 3000 rpm.

The primary advantages of brushless D.C. motors are:

- Low Maintenance
- No Brush Sparking

- High Operating Speeds
- High Efficiency
- Compact Size
- Fast Response

A three phase source supply is coming \rectifier source side connected to a shunt active power filter without no need of non sinusoidal harmonics so we need harmonics eliminates so we need to connected active power filter .

For drive applications but also in distribution systems the advantages of IGBT compared to thyristors are mainly the ability of turning off current actively .this leads to reduced filter size because of increased switching frequency and reactive power is no longer needed for the communication process.

Using reactive power compensation can increase the steady state transmissible power and the voltage profile along the line .since reactive power is used for voltage control in distribution systems.

MATLAB/SIMULINK MODEL FOR BLDC MOTOR

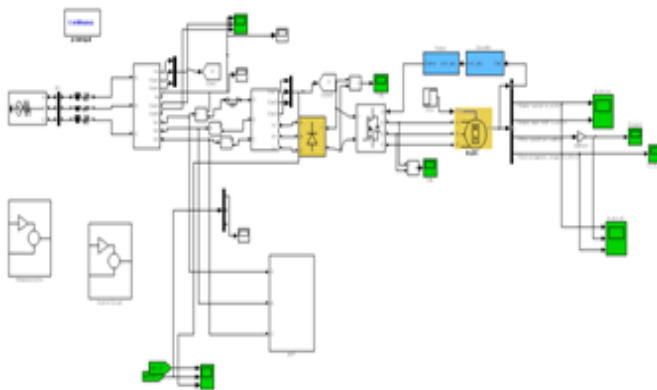


Fig 8(b) shows the Matlab /Simulink model of control block of bldc motor

SIMULATION RESULTS:

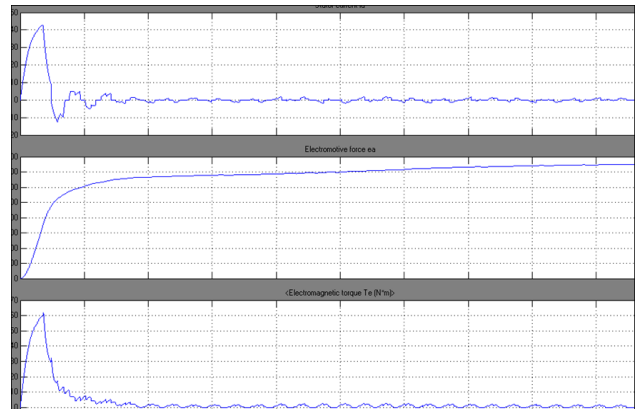


Fig 9(a) stator current, electromotive force, electromagnetic torque

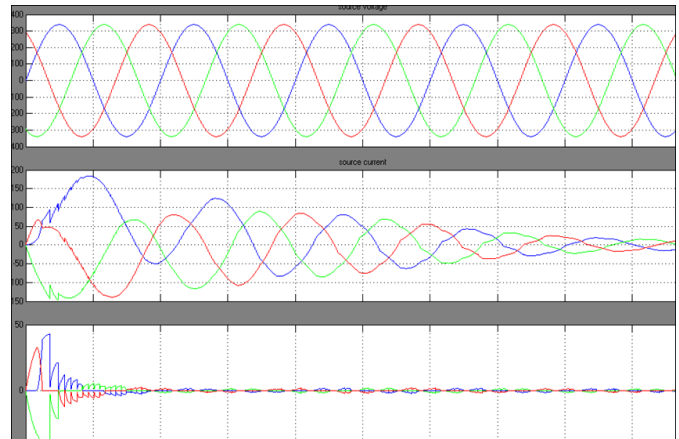


Fig 9(c) .source voltage and source current

IV. MATLAB SIMULATION

The unbalanced was realized by disconnecting phase-a from the diode bridge. The BLDC motor load is applied to the Bldc motor more advantage it has more high power density has compared to other motors fast response and high power and size also small

V. RESULTS AND DISCUSSION

The simulation of the Active power filter system is carried out with different types of loads i.e., a linear R-L load, a nonlinear load i.e., a diode bridge converter load and BLDC motor load. The load compensation is demonstrated for these types of loads using APFILTER system for as well as set. The following observations are made on the basis of obtained simulation results under different system conditions. Electronic devices. The current drawn by these modern devices is non-sinusoidal and therefore contains harmonics

B. ACTIVE POWER FILTER Operation under Non-Linear Load

Fig. 5 shows the performance of the ACTIVE POWER FILTER with under nonlinear loading conditions. The load compensation in terms of harmonic mitigation is also being provided by during this condition. Phase-a load is reconnected again to the diode bridge and the load is reduced to its initial value. BLDC MOTOR

C. ACTIVE POWER FILTER Operation under BLDC motor Load

In the above discussion we have connected source as active power filter set and loads like (linear ,nonlinear as well as BLDC loads) to be connected to v_{ccp} to maintain constant voltage by using BLDC motor to compensate unbalance loads and harmonics and reactive power compensation purpose

By generating maximum amount of reactive power and by sending active power it will be possible from source end to load end loads.

VI. CONCLUSION

IT has sinusoidal voltages at PCC and currents with compensated and equivalent linear balanced unity power factor loads.

In this paper, a to enhance power quality in a medium voltage distribution network has been proposed as a feasible active power filter topology for BLDC MOTOR applications. And torque speed characteristics. The active power filter feature several advantages such as the harmonics elimination power quality in a medium voltage distribution network A Matlab/Simulink based model is developed and simulation results are presented.

REFERENCES:

- [1] E. Acha, V. G. Agelidis, O. Anaya-Lara, and T. J. E. Miller, *Power Electronic Control in Electrical Systems*, ser. Newnes Power Engineering. Oxford, U.K.: Newnes, 2002.
- [2] F. Blaabjerg, R. Teodorescu, M. Liserre, and A. V. Timbus, "Overview of control and grid synchronization for distributed power generation systems," *IEEE Trans. Ind. Electron.*, vol. 53, no. 5, pp. 1398–1409, Oct. 2006.
- [3] J. Arrillaga and N. R. Watson, *Power System Harmonics*, 2nd ed. New York: Wiley, 2003.
- [4] H. Akagi, E. Watanabe, and M. Aredes, *Instantaneous power theory and applications to power conditioning*, ser. Power Engineering. Piscataway, NJ: IEEE Press, 2007.
- [5] B. Singh, K. Al-Haddad, and A. Chandra, "A review of active filters for power quality improvement," *IEEE Trans. Ind. Electron.*, vol. 46, no. 5, pp. 960–971, Oct. 1999.
- [6] B. R. Lin and C. H. Huang, "Implementation of a three-phase capacitor clamped active power filter

- under unbalanced condition," *IEEE Trans. Ind. Electron.* vol. 53, no. 5, pp. 1621–1630, Oct. 2006.
- [7] L. Moran, J. Mahomar, and J. R. Dixon, "Careful connection, selecting the best point of connection of shunt active power filters in multibus power distribution systems," *IEEE Ind. Appl. Mag.*, vol. 10, no. 2, pp. 43–50, Mar./Apr. 2004
- [8] D. O. Abdeslam, P. Wira, J. Merckle, D. Flieller, and Y. Chapuis, "A unified artificial neural network architecture for active power filters," *IEEE Trans. Ind. Electron.*, vol. 54, no. 1, pp. 61–76, Feb. 2007
- [9] R. Inzunza and H. Akagi, "A 6.6-kV transformer less shunt hybrid active filter for installation on a power distribution system," *IEEE Trans. Power Electron.*, vol. 20, no. 4, pp. 893–900, Jul. 2005
- [10] A. Luo, Z. Shuai, W. Zhu, R. Fan, and C. Tu, "Development of hybrid active power filter based on the adaptive fuzzy dividing frequency-control method," *IEEE Trans. Power Del.*, vol. 24, no. 1, pp. 424–432, Jan. 2009
- [11] *Recommended Practices and Requirements for Harmonic Control in Electrical Power Systems*, 1993. IEEE Std. 519-1992.
- [12] M. Cichowlas, M. Malinowski, M. P. Kazmierkowski, D. L. Sobczuk, P. Rodriguez, and J. Pou, "Active filtering function of three-phase PWM boost rectifier under different line voltage conditions," *IEEE Trans. Ind. Electron.*, vol. 52, no. 2, pp. 410–419, Apr. 2005.
- [15] K. M. Cho, W. S. Oh, Y. T. Kim, and H. J. Kim, "A new switching strategy for pulse width modulation (PWM) power converters," *IEEE Trans. Ind. Electron.*, vol. 54, no. 1, pp. 330–337, Feb. 2007.

Handwritten Amazigh Character Recognition System Based on Continuous HMMs and Directional Features

M. Amrouch, Y. Es-saady, A. Rachidi, M. El Yassa, D. Mammass

IRF-SIC Laboratory, University Ibn Zohr, Agadir, Morocco

ABSTRACT

This paper proposes a global approach to the recognition of handwritten Amazigh characters. The method used is based on continuous Hidden Markov Models and directional features. The input provided to our system is a vector of features extracted directly from an image of Amazigh characters using sliding windows technique based on hough transform. The obtained vector is translated into a sequence of observations that is used for the learning phase. This task involves several of processing steps, typically, pre-processing, normalization, skeletonization and features extraction. Finally the class of the input characters is determined by the Viterbi classifier. The experimental result indicates the promising prospect of this approach.

Key words- Handwritten Amazigh characters, Hidden Markov Models, Directional features.

I. INTRODUCTION

The off-line recognition of handwritten characters is one of the hottest subjects in pattern recognition. This field has a number of applications such as reading addresses on envelopes, amounts on bank checks, and so on. These various applications need a particular and small lexicon from specific domains. Several approaches have been used so far for Latin and Arabic script recognition, some of them are based on Hidden Markov Model [1][2][3][4][5][6]. Furthermore the Amazigh (Tifinagh) characters recognition remains less explored. Indeed, research done up to now is very limited, but there are few attempts. In the literature devoted to Amazigh, we find approaches based on statistical, geometrical and syntactical approaches [7][8][9][10][11]. For more details on the survey of this language refer to [12].

The Figure 1 represents the repertoire of Tifinagh which is recognized and used in Morocco with their correspondents in Latin characters. The number of the alphabetical phonetic entities is 33, but Unicode codes only 31 letters plus a modifier letter to form the two phonetic units: ⵍ^w (g^w) and ⵎ^w (k^w).



Fig 1. Tifinagh characters adopted by the Royal Institute of Amazigh culture with their correspondents in Latin characters

The automatic treatment of this script compared with other types of writing (Arabic and Japanese) appears simple. Indeed, the Amazigh alphabet is never cursive, which facilitates the operation of segmentation. The Amazigh script is written from left to right; it uses conventional punctuation marks accepted in Latin alphabet. Regarding the figures, it uses the Arabic Western numerals. The majority of graphic models of the characters are composed by segments. Moreover, all the segments are vertical, horizontal, or diagonal.

The use of HMMs discrete to these handwritten characters is limited to our previous contribution [10]. This method is based on a discriminating model which associates one or more model by class. We obtained a recognition rate 90,4% on a handwritten character database [13]. The recognition errors are assigned, in the one hand, to the methods used for the estimation of the probabilities of the observation symbols, and secondly, to the topology models. The introduction of continuous HMMs (CHMMs) and the use of other model architectures can reduce the error rate of our system.

In order to improve the performance of our system, we suggest to address the problem of Amazigh handwritten characters recognition by Continuous Hidden Markov Models with various topologies per model.

The remaining parts of this paper develop as follows. Section (2) briefly introduces the conventional hidden Markov models whereas section. Section (3) presents an overview of our system. As to section (4), it sheds light on the pre-processing techniques and methods. Section (5) presents the process of extracting vector features and generation of the sequences of observations from an image of Tifinagh letter. Section (6) is focused on the learning and classification steps. In addition, section (7) is concerned with the numerical results. The paper finally

concludes with an analysis of the results and a description of future work.

discriminating models and we decide for the class of the character.

II. THE BASIC CONCEPTS OF HMM

An HMM is a doubly stochastic process with an underlined stochastic process (Markov chain) that is not observable (it is hidden), but can only be observed through another set of stochastic processes that produce the se-quence of observed symbols. The elements of the first order HMM are formally defined as follows :

N : the number of states;

T : the number of observations or possible symbols;

q_t : the state of the system at the time t ;

M : size of the observed sequence;

$A = \left\{ a_{ij} = p\left(s_j / s_i\right) \right\}; \sum_{j=1}^N a_{ij} = 1$: is the matrix of the

probability of transitions;

$\Pi = \left\{ \pi_i = p\left(s_i\right) \right\}; \sum_{i=1}^N \pi_i = 1$: is the vector of the initial

probabilities;

$B = \left\{ b_i\left(o_k\right) = p\left(o_k / s_i\right) \right\}; \sum_{k=1}^T b_i\left(o_k\right) = 1$: are the

probabilities of the observation symbols with $b_i(o_k)$ are practically estimated by an M mixture of multivariate Gaussian distributions:

$$b_j\left(o_t\right) = \sum_{k=1}^M c_{jk} \square\left(o_t, \mu_{jk}, \sigma_{jk}\right) \quad 1 \leq j \leq M, \sum_{k=1}^M c_{jk} = 1$$

$$\square\left(o_t, \mu_{jk}, \sigma_{jk}\right) = \frac{1}{2\pi \sqrt{|\sigma_{jk}|}} \exp\left(-1/2\left(o_t - \mu_{jk}\right) \sigma_{jk}^{-1} \left(o_t - \mu_{jk}\right)^T\right)$$

\square : denotes a normal Gaussian distribution;

c_{jk} : The weight of the k^{th} mixture component;

μ_{jk} : Mean vector associated;

σ_{jk} : Covariance matrix associated.

The parameters of an HMM can be denoted by $\lambda = (N, M, A, B, \Pi)$. There are three basic algorithms that establish the use of HMM, for-ward-back algorithm, Viterbi algorithm and Baum-Welch algorithm [14].

III. THE WHOLE RECOGNITION SYSTEM

Figure 3 illustrates the block diagram of the proposed system. The system is divided into steps. All of them are performed prior to training and testing process, and includes: image acquisition, pre-processing and features extraction. The objective is to acquire the character image, pre-process it and then decompose it into vertical bands. Each bands image is transferred into a sub-sequence of features.

Those directional features are extracted from vertical windows along the line image using the Hough transformation. Then the sequences of observations are generated. In the training step, we involve the Hidden Markov Model of each character, with a Baum-Welch process, by the various sequences of observations. The classification is done by the search for the characters

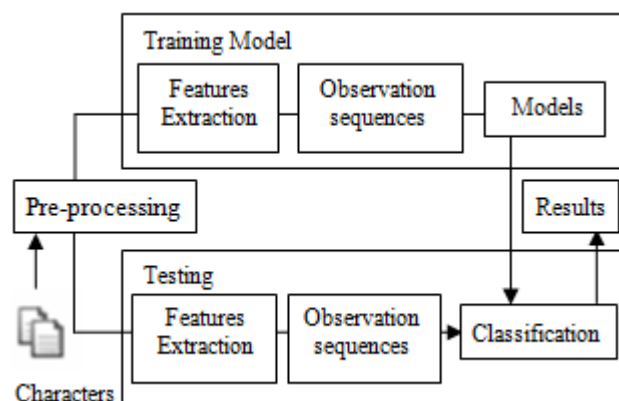


Fig 2. System overview

IV. PREPROCESSING

The variability in the Tifinagh handwritten characters to be recognized becomes more prominent. This situation complicates the recognition process. To adapt the characteristics of the Amazigh handwritten characters to our recognition system, eliminate noise in the image and simplify subsequent treatments, a number of pre-processing operations are applied. As the binarization, smoothing, normalization, skeletonization.

The binarization enhances the useful information from the background of the image; the choice of threshold is important. As a result, we use Otsu's algorithm [15] which chooses the threshold to minimize the interclass variance of the black and white pixels.



Fig 3. Results of binarization Otsu algorithm to the character « R » (a) input letter; (b): binarization (level=0.8196)

The operation of smoothing is applied to remove noise introduced by the image acquisition systems.



Fig 4. Results of smoothing algorithm to the character « R »; (a) input letter; (b): after smoothing

The normalization task is necessary to bring the same size to the characters 96x96. These characters can have different sizes that will influence the parameters stability caused by the variability of styles or by the expansion /

reduction operations of image size; these operations are performed by the size normalization algorithm [16].

The skeletonization or Thinning is an important pre-processing step for many image analysis operations. The main objectives of thinning in image processing and pattern recognition are to reduce data storage while at the same time retaining its topological properties, to reduce transmission time and to facilitate the extraction of morphological features from digital patterns. Thinning reduces the amount of data to be stored by transforming a binary image into a skeleton, or line drawing. The thinning algorithm used herein for testing is the Rutovitz algorithm [17]. This algorithm is selected for its preservation of connectivity and topology of the characters. Figure 5 shows a sample input character image and the results of skeleton algorithm.



Fig 5. Results of skeleton Rutovitz algorithm to the characters «Θ», «†», «⚡», «⊗» (a) input letter; (b): skeleton

V. EXTRACTION OF PRIMITIVES

In order to build the directional feature vector sequence, the image is divided into vertical and horizontal windows or frames. The sliding window is shifted along the word image from left to right. According to the size of the images' characters (96 × 96 pixels), we obtained, in total, 16 horizontal and 16 vertical bands and the intersections of these bands form 256 cells; each one has 6x6 pixels (see figure 6). For each area, we calculate the presence rates of the six orientations and we determine the dominant direction based on the Hough Transform. This algorithm gives a set of discriminating characteristics using the character pixels representation that facilitates recognition [18]. The steps of the Hough algorithm are summarized below:

Initialization of the Hough Transform accumulator
 For each black pixel of the image (x_i, y_i)
 $0 \leq x_i \leq n$ et $0 \leq y_i \leq m$, with n is width the image and m its height.
 $0 \leq \theta < 180^\circ$
 $\rho_k = x_i \cos \theta_k + y_i \sin \theta_k$
 To increment the cell of the table of accumulator corresponding to the couple (ρ_k, θ_k) .

In the experimentation, the displacement $\Delta\theta$ is equal to 30, consequently the Hough accumulator will contain information on of the six orientations (0°, 30°, 60°, 90°, 120° et 150°). Finally, we memorize these dominant directions which will be used for the generation of observations.

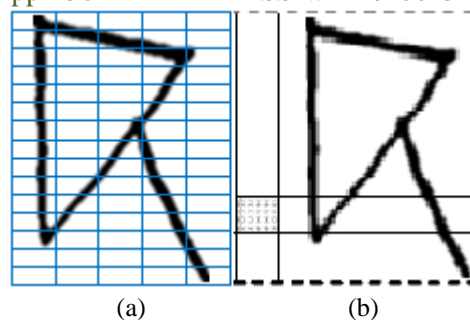


Fig 6. Dividing the image into windows and cells

VI. GENERATION OF THE OBSERVATIONS SEQUENCES

For the generation of the sequence of observations' task, we select the minimum of the primitives representing the dominant directions. In each area, we consider the rate of the dominant direction. Thereafter, we represent, by a symbol in the sequence of observations, a set of adjacent areas that have same rates considered from the left to the right. The symbols which can be emitted are 6 corresponding to the 6 basic orientations (cf figure 7).

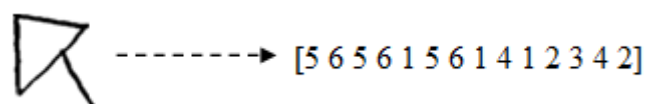


Fig 7. Sequence of the character k (κ)

VII. HIDDEN MARKOV MODELS RECOGNIZER

When considering the alphabet such as those involved in the recognition of Tifinagh characters, it is possible to build a different model for each character. Therefore, our handwriting modelling is carried out at the character as whole. This approach is called discriminating hidden Markov model. In this strategy, for each class of the problem (each letter of the alphabet) a model is constructed. Then for recognizing an input letter, the score for matching the character to each model is computed. The class related to the model that has the maximum score gives the result of recognition. In the literature, various models and architectures were proposed for the use of the hidden Markov models in the handwritten recognition [19][20]. In our work, we opted for a left-right topology where the number of states is strictly lower than the number of horizontal bands of the character (see figure 8). Thus, the bands of the extremities supply no observation. Indeed, the number of states per hidden Markov models is equal to all models.

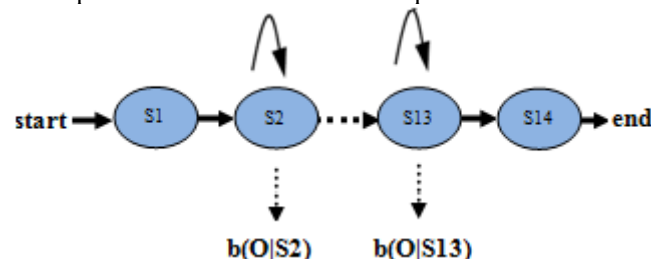


Fig 8. Left to right HMM topology for character models

6.1 Learning

The images of characters are translated into sequences of observations, which must be deduced from the model

that generated them. Once the topology of the model is chosen, each letter has its own model. Therefore, the learning allows to estimate the probabilities of the inputs, the transitions and the emissions which model the characters. To do this, we use the standard procedure of Baum-Welch [20][21]. This iterative procedure is used to train the HMM characters to adjust their parameters.

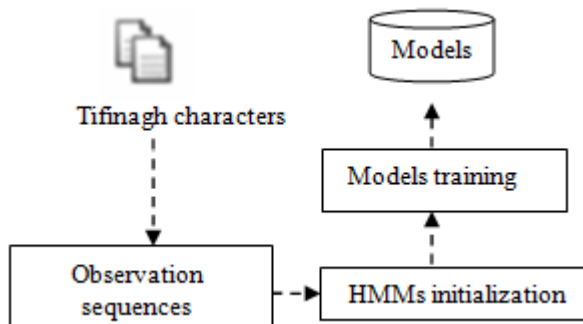


Fig 9. Learning overview

The algorithm will re-estimate the Hidden Markov Model of each character until the probability of generating the sequence of observations is maximal. The best Hidden Markov Model found is recorded to form a database of learning (cf Figure 9).

6.2 Classification

In the learning step, we obtain so many hidden Markov models as the number of characters. The recognition is made at first by the search of the discriminating model among every selected hidden Markov models of each character. We calculate, by the Viterbi algorithm [21], the probability of the observations sequences of the character to be recognized that the models can generate. Afterward, we have a set of models where every model is associated with a score. The elected model is the one possessing the biggest score (see figure 10).

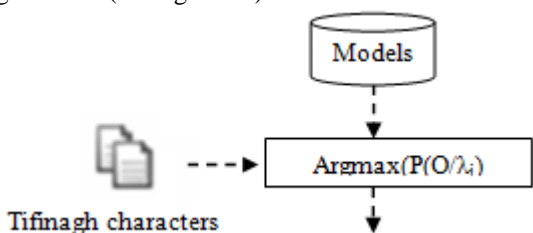


Fig 10. Classification overview

VIII. EXPERIMENTAL RESULTS

A series of experiments have been performed to evaluate the effectiveness of the proposed approach. These experiments were performed on database of isolated Amazigh handwritten characters (AMHCD) [13]. This database contains 780 variations for each character led to an overall of 24180 isolated Amazigh handwritten characters (780 × 31). Some Amazigh handwriting samples are given in Table 2.

In our experiment, 16120 character images (i.e. 2/3 the AMHCD) from the portion of AMHCD were used to train the HMMs models. The other character images (i.e. 1/3 the AMHCD) were used to test identification performance. Some results according to the number of states and the number of mixtures are listed in Table 1,

Figure 11 and Figure 12. Note that the number of states in our modeling represents a series of vertical bands.

This experimental results illustrate that this proposed approach for the handwritten character Tifnagh is more promising than our previous approach which is based on HMM discrete[10] and which gives a rate of 90, 4% of good recognition.

TABLE 1
Recognition rate on database AMHCD

Number of states	6	8	10	12	14
Number of mixtures	1-2	1-2	1-2	1-2	1-2
Recognition rate	96, 21%	96, 56%	96, 88%	97, 3 8%	97, 89%

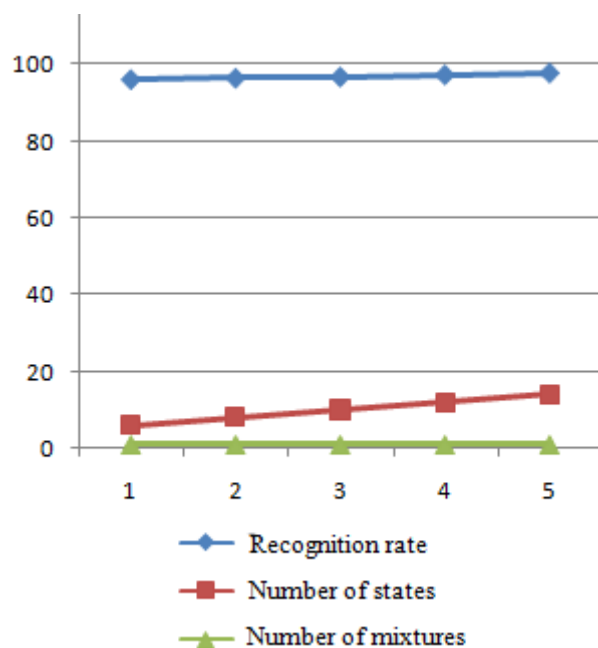


Fig 11. The progressing recognition rate according to the number of states with one mixture

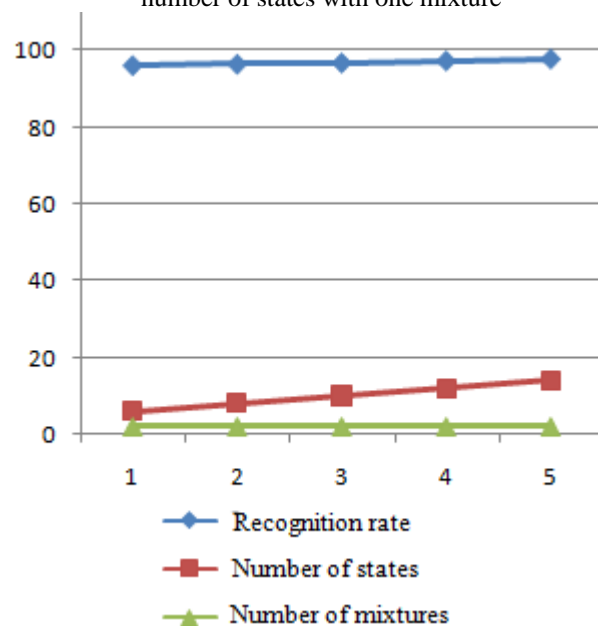


Fig 12. The progressing recognition rate according to the number of states with 2 mixtures

TABLE 2. Handwritten Tifinagh characters

Printed Amazigh characters	Writer 1	Writer 2	Writer 3	Writer 4	Printed Amazigh characters	Writer 1	Writer 2	Writer 3	Writer 4
ⵓ					ⵓ				
ⵙ					ⵙ				
ⵔ					ⵔ				
ⵖ					ⵖ				
ⵗ					ⵗ				
ⵘ					ⵘ				
ⵙ					ⵙ				
ⵛ					ⵛ				
ⵜ					ⵜ				
ⵝ					ⵝ				
ⵞ					ⵞ				
ⵟ					ⵟ				
ⵠ					ⵠ				
ⵡ					ⵡ				
ⵢ					ⵢ				
ⵣ					ⵣ				
ⵤ					ⵤ				
ⵥ					ⵥ				
ⵦ					ⵦ				
ⵧ					ⵧ				
⵨					⵨				
⵩					⵩				
⵪					⵪				
⵫					⵫				
⵬					⵬				
⵭					⵭				
⵮					⵮				
ⵯ					ⵯ				
⵰					⵰				
⵱					⵱				
⵲					⵲				
⵳					⵳				
⵴					⵴				
⵵					⵵				
⵶					⵶				
⵷					⵷				
⵸					⵸				
⵹					⵹				
⵺					⵺				
⵻					⵻				
⵼					⵼				
⵽					⵽				
⵾					⵾				
⵿					⵿				
ⶀ					ⶀ				
ⶁ					ⶁ				
ⶂ					ⶂ				
ⶃ					ⶃ				
ⶄ					ⶄ				
ⶅ					ⶅ				
ⶆ					ⶆ				
ⶇ					ⶇ				
ⶈ					ⶈ				
ⶉ					ⶉ				
ⶊ					ⶊ				
ⶋ					ⶋ				
ⶌ					ⶌ				
ⶍ					ⶍ				
ⶎ					ⶎ				
ⶏ					ⶏ				
ⶐ					ⶐ				
ⶑ					ⶑ				
ⶒ					ⶒ				
ⶓ					ⶓ				
ⶔ					ⶔ				
ⶕ					ⶕ				
ⶖ					ⶖ				
⶗					⶗				
⶘					⶘				
⶙					⶙				
⶚					⶚				
⶛									

doctorat, Université René Descartes, Paris 5 décembre 2004.

- [6] R. Al haji, C. Mokbel, L.Likformansulem: Combination of HMM-Based Classifiers for the Recognition of Arabic Handwritten Words, *Proceedings of the International Conference on Document Analysis and Recognition, ICDAR*, vol. 2, pp. 959- 963, 2007.
- [7] A. Djematen, B. Taconet, A. Zahour: A Geometrical Method for Printing and Handwritten Berber Character Recognition. *Fourth International Conference Document Analysis and Recognition, ICDAR'97*, P.564, 1997.
- [8] Y. Es Saady, A. Rachidi, M. El Yassa, D. Mammass : Printed Amazigh Character Recognition by a Syntactic Approach using Finite Automata, *ICGST-GVIP Journal, Vol 10, Issue 2, June 2010*.
- [9] R. El Ayachi, K. Moro, M. Fakir, B. Bouikhalene, "On the Recognition of Tifinaghe Scripts", *Journal of Theoretical and Applied Information Technology*, vol.20 (2), pp.61-66, 2010.
- [10] M. Amrouch, M. Elyassa, A. Rachidi, D. Mammass: "Handwritten Amazigh Character Recognition Based on Hidden Markov Models", *ICGST-GVIP Journal, vol.10, Issue 5, pp.11-18, 2010*.
- [11] Y. Es Saady, A. Rachidi, M. El Yassa, D. Mammass, Amazigh Handwritten Character Recognition based on Horizontal and Vertical Centerline of Character, *International Journal of Advanced Science and Technology*, vol.33, pp.33-50, August, 2011.
- [12] Y. Es Saady, *Contribution au développement d'approches de reconnaissance automatique de caractères imprimés et manuscrits, de textes et de documents amazighes* , PhD thesis, Université Ibnou zohr- Agadir, 2012.
- [13] Y. Es Saady, Ali Rachidi, Mostafa El Yassa and Driss Mammass, AMHCD: A Database for Amazigh Handwritten Character Recognition Research. *International Journal of Computer Applications* 27(4):44-, New York, USA August 2011.
- [14] Lawrence R. Rabiner, A Tutorial on Hidden Markov Models and Selected Applications in Speech Recognition, *Proceedings of the IEEE, Vol. 77, No. 2, 1989*.
- [15] N. Otsu, A threshold selection method from gray-scale histogram, *IEEE Trans. Systems, Man, and Cybernetics*, 8:62–66, 1978.
- [16] S.N. Srihari & E.J. Keubert: Integration of handwritten address interpretation technology into the United States postal service remote computer reader system. *ICDAR*, pp. 892–896, 1997.
- [17] D. Rutovitz: Pattern recognition. *Journal of Royal Statistical Society*, 129:504–530, 1966.
- [18] H. Maitre : Un panorama de la transformation de Hough, *Traitement de signal vol2, 1985*.
- [19] X. Dupré: *Contributions à la reconnaissance de l'écriture cursive à l'aide de modèles de Markov cachés*, Thèse de doctorat, Université René Descartes - Paris V, 2004.
- [20] E. poisson: *Architecture et Apprentissage d'un système hybride de Neuro-Markovien pour la reconnaissance de l'écriture Manuscrite en-ligne*, Thèse de doctorat, université de Nantes, 2005.
- [21] E. Augustin: *Reconnaissance de mots manuscrits par systèmes hybrides Réseaux de Neurones et Modèles de Markov Cachés*, thèse, Paris, 2001.

Conservation of Heritage Areas in the City of Panaji: A Case Study of Fontainhas Area

Shaikh Ali Ahmed¹, Dr. B. Shankar²

¹Planning Assistant, North Goa Planning and Development Authority, Panaji

²Associate Professor, Institute of Development Studies, University of Mysore, Mysore

ABSTRACT

Panaji is the capital city of the state of Goa, and the city has been declared as a Heritage City under the JNNURM for urban renewal scheme. The city is spotted as one of the most attractive tourist destinations in India. Panaji is known for its Indo-Portuguese cultural heritage having a number of heritage structures, buildings, monuments and sites of significant importance. The Outline Development Plan 2011 has identified as many as 40 buildings, houses, sites and monuments in the City. It has many heritage structures, monuments and areas, which needs to be addressed for conservation. These heritage structures and areas have come under tremendous threat of new developments due to improper approach by the agencies involved in conserving including the people at large. The paper focuses on Fontainhas heritage areas by addressing the issues that are faced by the heritage area and proposes planning measures for regulating the heritage conservation areas for harmonious development in the City of Panaji.

Key Words: Heritage Areas, Significance Assessment, Conservation, Strategies

I. INTRODUCTION

Panaji was a small fishing village with lots of coconut trees, creeks and fields. For centuries, it remained so and was a neglected ward of Taleigao village with the only massive structure, Palace of Adil Shah by the Mandovi River. In 1632 the 3.2km causeway linking Panjim with Ribandar village known as the "Pointe de Linhares" was built. It was the longest bridge at that time when it was constructed. During this time, against the backdrop of the decline of Old Goa, the idea of Panjim becoming the Capital of Goa slowly gained momentum. The then Viceroy, shifted his residence from Panelim (near Old Goa) to Panjim in the newly re-modelled Adil Shah Fort, since known as "Idalcao's Palace". He began the process of slowly reclaiming land, initiated public projects, drainage systems and was also responsible for many of its government buildings and set the stage for Panjim to evolve into a magnificent city. By a royal decree on March 22, 1843, its status was elevated to a "City" and became the capital of Goa and was called "Nova Goa".

There are two old sections of the city existing today, one called "Fontainhas" and the other "San Tome". The hillock overlooking the city is called "Altinho".

II. HERITAGE AREAS OF PANAJI

Panaji is the capital city of the state of Goa, and housing beautiful residential, Institutional buildings having rich architectural heritage. The certain areas in the city of Panaji have been designated as conservation/ preservation areas. These areas can be easily identified due to the existence of monuments and structures having rich architectural heritage. The Outline Development Plan 2011 of Panaji has declared five areas as "Conservation Zone", and marked as "F" in the plan are: (1) Campal, (2) Mandovi river fronts (3) Fontainhas & Portais, (4) Altinho and (5) Fonduvem, Ribandar. The area comprises of 62.00 hectares' and works out to be 15 percent of the settlement area approximately of the settlement area approximately of Panaji Municipal limit excluding the unbuildable slope.

III. HISORICAL BACKGROUND OF FONTAINHAS

Fontainhas was once a palm grove with huts surrounding it in 1818. When the capital shifted from Old Goa to the new city, space was at a premium. Saline lands and mangroves were filled up and paddy fields created to accommodate the population that sought refuge here. The new area was given a new name. It was called Palmar Ponte in a sort of continuity with the name Ponte de Linhares, the bridge that brought them over into the new city. Many rivulets ran down the hill slope of Altinho to join the Ourem Creek on one side and subsequently the river Mandovi. The area was inhabited by "oil sellers, sailors, fishermen and tailors". One of the oldest houses in the precinct, Panjim Poussada (Gallery Gitanjali) was once the Ghanekar family mansion, ghan being the Konkani word for an oil press and ghanekars being the traditional name for the profession of oil pressers. Oil pressing was an important profession in traditional India. Oil meant for illumination and is a very important factor in the days before electricity.

Its mediterranean appearance, narrow streets and over hanging balconies, this old district or "Latin Quarter" lying along the banks of the Ancient Ourem creek has a different atmosphere from the main city. The entire area is set out at the base of hillside (Altinho) and the natural springs on the hillside, gave the name Fontainhas to the area. The areas of Fontainhas and Portais were the first areas to be inhabited here on account of the creek and the presence of fresh water springs.

A. Characteristics of Fontainhas Area

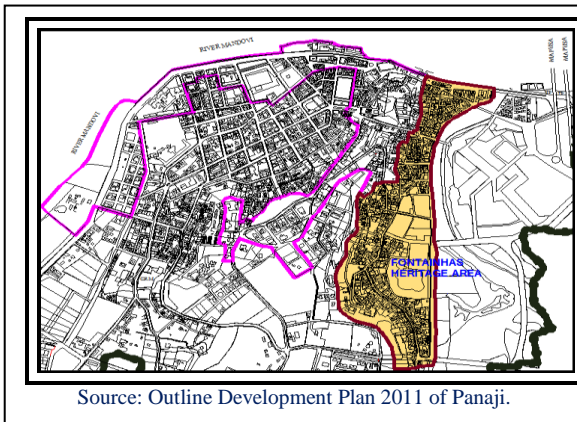
Fontainhas area is having organic growth with informal layouts streets and stepped accesses. The area is having high density and mixed land uses. Interactive built-up

open spaces responding to human scale, lot of distinctive Architectural styles, the buildings together form a cohesive group. In the absence of tree cover, buildings overlooking narrow streets, lanes provide shaded walkways and create an interesting play of light and shadow.

The basic material used in the construction of the houses in the ward of Fontainhas was *taipa* (wetted mud), reinforced with bamboo netting and coconut husk or coir. The walls were plastered with a mixture of lime and cane jaggery (gur). Many houses have retained the original plaster which is almost 200 years old.

IV. FONTAINHAS HERITAGE AREA

The area consists of medieval Panaji in contact with the grid iron pattern for the rest of Panaji. The land use pattern is predominantly mixed commercial and residential.



Source: Outline Development Plan 2011 of Panaji.

The narrow roads and buildings with similar architectural character make a distinct homogenous group creating a human and warm scale demands a compassionate approach. The Fontainhas Heritage area being the first areas to be inhabited here on account of the creek and the presence of fresh water springs after the construction of "Ponte de Linhares". The area is having as many as heritage structures which require identification. The City Corporation of Panaji and Goa Heritage Action Group have published a book "Walking in and around Panaji" depicting the building details in Fontainhas. The Goa Land Development and Building Construction Regulation 2010 have declared 40 sites, monuments, houses and buildings in the City of Panaji. The City has a number of unidentified Heritage monuments and buildings of importance specially Fontainhas area which requires identification. Some of the Heritage Resources of Fontainhas areas are identified as follows:

1. Maruti Temple, Houses of
2. Veira Velho,
3. Mario Ribeiro Santana
4. Lima Fernandes,
5. Christopher Nazareth,
6. Diogo Fonseca,
7. Mr. Rodrigues,
8. Ivo Fernandes,
9. Old Mint House,
10. Residence of Superintendent of Post offices,
11. Hotel Republica,
12. Fontainhas Spring (Fonte Fenix),
13. St. Sebastian Chapel,
14. Sao Tome Chapel,
15. Chapel of Portais,
16. House of Mr. Fernandes.



Fig. 1. View of the Maruti Temple



Fig. 2. View of the Hotel Republica



Fig. 3. View of the Heritage resources in Fontainhas having Indo-Portuguese Architecture



Fig. 4. View of the Portais Chapel



Fig. 6. Cars seen parked in front of the St. Sebastian Chapel.



Fig. 7. Cars seen parked in front of the House of Mario Ribeiro de Santana, Listed Heritage Structure.



Fig. 8. Heritage Houses in dilapidated condition due to non maintenance.

V. PROBLEMS OF FONTAINHAS AREA

The problems faced by the Fontainhas area are depicted in the map below:

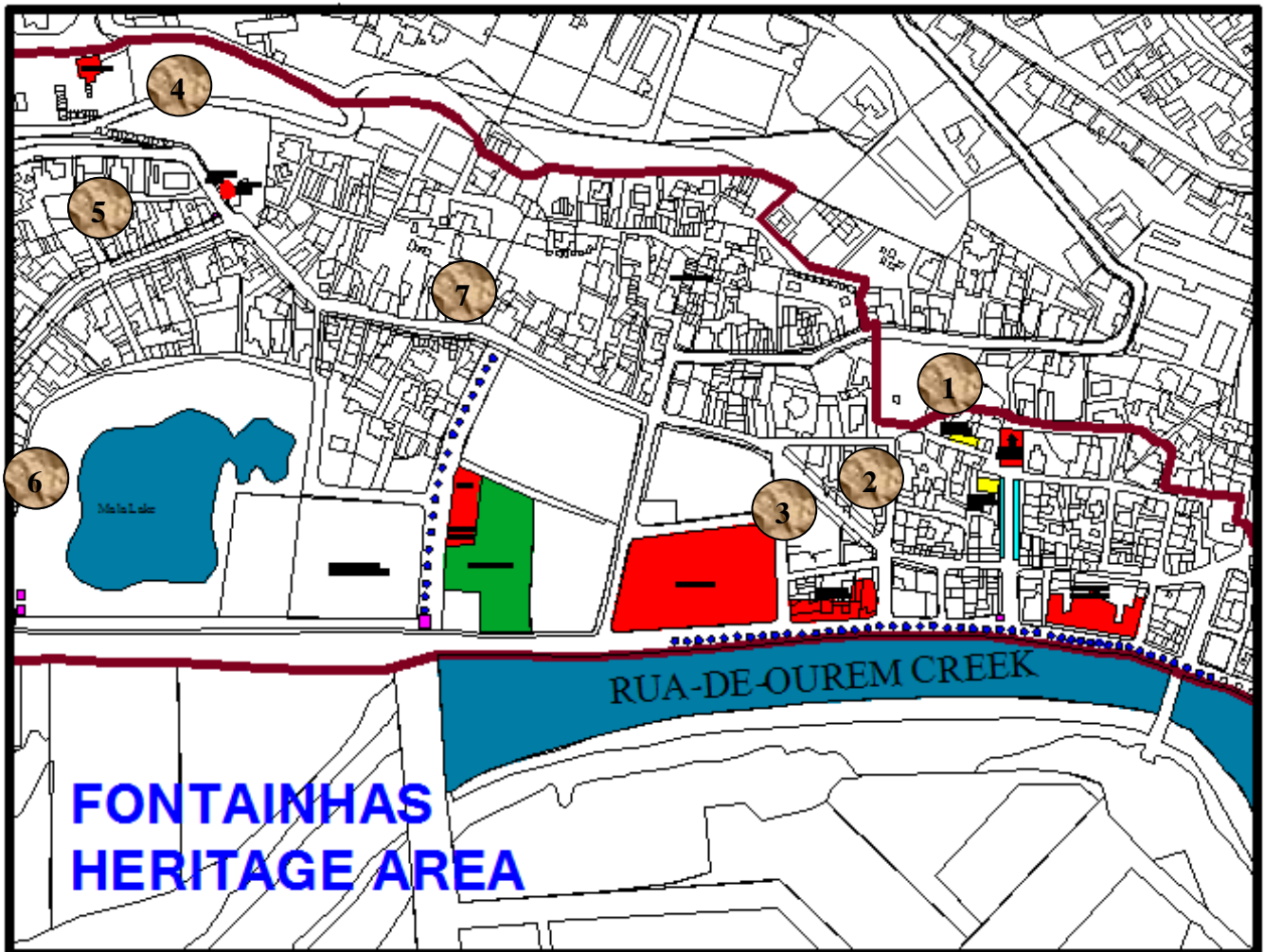


Fig. 5. Problems in Certain Parts of Fontainhas Areas

VI. REGULATIONS CONTROLLING THE DEVELOPMENT IN THE AREA

The Goa (Regulation of Land Development and Building Construction) Act, and The Goa Land Development and Building Construction Regulation, 2010 regulates the development in the Fontainhas Heritage area and covers under Zone (F) “Conservation Zone” in the regulations.

The Outline Development Plan 2011 of Panaji has earmarked this area as Conservation Zone and has designated the residential zone as (F-S), Commercial zone as (F-C) and Institutional zone as (F-P).

Table 1: Regulations applicable to Conservation areas

Area of plot	Max. permissible coverage	Max. permissible FAR	Max. height in metres	Remarks
COMMERCIAL ZONE (F-C)				
Plot below 300 sq.mts.	70%	200	12.00 (G+3)	An additional floor could be allowed in special cases in stepped formation not exceeding a total of 15.00 mts.
Plot below 301 to 1000 sq.mts.	60%	180	12.00 (G+3)	
Plot above 1001 sq.mts.	60%	180	12.00 (G+3)	
RESIDENTIAL ZONE (F-S)				
Plot below 300 sq.mts.	70%	140	7.60 (G+1)	An additional floor could be allowed in special cases in stepped formation not exceeding a total of 9.00 mts.
Plot below 301 to 1000 sq.mts.	60%	120	7.60 (G+1)	
INSTITUTIONAL ZONE (F-P)				
Plot below 500 sq.mts.	60%	120	7.60(G+2)	
Plot above 501 sq.mts.	50%	100	7.60(G+2)	
<i>Note:</i> In case of existing 100% coverage, additional FAR totalling to max of 200 FAR could be considered and granted by the conservation committee on case to case basis in commercial conservation zone in Panaji.				

Source: The Goa Land Development and Building Construction Regulation 2010

VII. PLANNING ISSUES OF FONTAINHAS AREA

The Fontainhas Heritage area consists of medieval Panaji having narrow lanes, stepped accesses, on the base of hill of Altinho, having partly sloping and partly flat land. The area consists of many old buildings and predominantly of mixed land use and provides scope for expansion of new buildings and re-development which should be done with respect to the Architecture and space character of the area and demands a compassionate approach.

- [1]. Traffic gets congested during the peak hours of the day due to seven schools which conflicts the office and school timings.
- [2]. The area being organic in nature with narrow streets, lanes, stepped accesses and dead ends there is no alternate provision of road for diversion of traffic.
- [3]. Age old Heritage resources have developed cracks in the walls due to non maintenance.
- [4]. Buildings of sizeable height of 15.00 metres on the stretch of land abutting the Rua de Ourem Creek road have hidden the visibility of Heritage structures in the area.
- [5]. No Incentives to the owners of the Heritage houses for maintenance and repairs.
- [6]. Buildings of fine Architecture and aesthetic importance have been sacrificed for modern architecture in the name of new development.
- [7]. Allowing more Coverage and FAR in the heritage precincts will develop the area more congested and the very character of the area will be lost. No parking facility is in the area even for the residents.

X. REFERENCES

VIII. PLANNING STRATEGIES

The Fontainhas Heritage area consists of number of heritage resources which are of high value and importance needs identification and proper management. The heritage resources of significant value if not identified in time then, there is a very fear of getting demolished for the new development and the very purpose of protecting the heritage and transferring to the future generation in the context of Sustainable Development will be lost. The conservation planning strategy to include the following:

- (1) Heritage resources that are of importance and high significance in the Heritage Fontainhas areas should be identified and listed so that these resources are well protected having regard to harmony when new development are allowed.
- (2) The new development in the area should confirm to the aesthetics and characteristics of the surrounding area in terms of elevation, height, bulk, roof pattern, colour scheme and materials used.
- (3) The narrow roads in Fontainhas Heritage area should be made pedestrian so that the people can take a free walk in the area admiring the Historical place.
- (4) Provision of intra non-polluting electric vehicle transport service within the area for residents only.
- (5) An area of 1000 sq.mts should be acquired for the purpose of development of multi-storeyed parking for the residents only, where each owner of the house will contribute his equal share for life time parking in the construction of multi-storeyed parking.
- (6) No parking zone should be made in this area except for residents.
- (7) Incentives in the form of rebate in taxation should be given to the owners of the Heritage houses for maintenance of Heritage properties from spoliation and disfiguration.
- (8) Effective and well thought Heritage Conservation regulations should be developed for regulating harmonious development in the area.
- (9) The present regulation has remained ineffective in controlling haphazard development in the Conservation area.

IX. CONCLUSION

The Fontainhas area continues to be a focal point for Heritage tourists and travellers with a taste of past glories. There are still clusters of quaint old houses in particular on one street in Portais and around St. Sebastian Chapel, which should be maintained. Progress is inevitable and in generally a desired process but should be sustainable. The changes seen in the areas of heritage over the years are due to ineffective legislation and development control. The conservation Regulations has remained ineffective in controlling the heritage areas from disorganized developments.

A sound policy towards the conservation is required and managed successfully. There is also a strong need to revise the present conservation regulations for regulating the heritage areas towards harmonious and sustainable development.

BIOGRAPHIES

- [1] Joshi C., et al, *World Heritage Series- Old Goa*, Archaeological Survey of India, Goa.
- [2] Government of Goa, Regional Plan Goa, 2001 and 2021, Town & Country Planning Department, Goa.
- [3] Government of Goa, The Ancient Monuments and Archaeological Sites and Remains Act, No. 24 of 1958, Government of India.
- [4] Government of Goa, The Goa Ancient Monuments and Archaeological Sites and Remains Act, 1978 and Rules, 1980.
- [5] Government of Goa, The Goa Town and Country Planning Act and Rules, Government of Goa, Planning and Development Authority (Development Plan), Regulations, 1989, Panjim Planning and Development Authority, Panjim.
- [6] Report of the Tourism Master Plan: GOA- 2011 final report prepared by Consulting Engg. Services (I) Ltd. For Government of Goa, Department of Tourism.
- [7] Government of Goa, The Goa (Regulation of Land Development and Building) Act, 2008 and The Goa Land Development and Building Construction Regulation 2010, second edition November 2011.
- [8] Government of Goa, Panaji, a search for identity, Oct. 1997 published by North Goa Planning and Development Authority.
- [9] The Panaji City Corporation, *Walking In and Around Panaji-Goa*, Goa Heritage Action Group, January 2005.
- [10] Vasco Pinho, Snapshots of Indo-Portuguese History – I, November 2009, Panaji.



Shaikh Ali Ahmed received M.Tech in Urban and Regional Planning from the University of Mysore, Mysore. Presently, he is working as Planning Assistant in North Goa Planning Authority, Panaji. He is Associate Member of the Institute of Town Planners, India, He is presently pursuing his Ph.D in Urban and Regional Planning at the Institute of Development Studies, University of Mysore. His research interests to include heritage conservation, heritage legislation.

Y



Dr. B. Shankar received the B.E. degree in Civil Engineering in 1984, M.U.R.P degree in Urban and Regional Planning in 1989 and Ph.D degree in Urban and Regional Planning in 1997 from the University of Mysore, Mysore. He is working as Associate Professor in Urban and Regional Planning at the Institute of Development Studies, University of Mysore, Mysore. He was a Senior Faculty Member in the Administrative Training Institute and State Institute of Urban Development, Mysore, Government of Karnataka. He co-ordinated capacity building and training Programmes of Urban Poverty Alleviation Programmes of Karnataka State. His research interests to include Urban Planning, Urban Poverty, Community Development, Heritage Conservation, and Planning Legislation.

Space Vector Modulated Voltage Source Converter for Stand Alone Wind Energy Conversion System

¹K. Premalatha, ²T. Brindha

^{1,2}Department of EEE, Kumaraguru College of Technology, Coimbatore

Abstract

This paper proposes a voltage and frequency controller for a wind turbine-driven independent asynchronous generator. The proposed controller consists of IGBT (Insulated Gate Bipolar Transistor) based three phase voltage source converter along with battery energy storage system at its DC bus and it inherently adapts to the changes in the rotor speed while maintaining a near constant voltage and frequency at the load terminals. The controller is having bidirectional flow capability of active and reactive powers by which it controls the system voltage and frequency with varying wind speed and load conditions. Among various modulation strategies, Space vector pulse width modulation technique is used in the controller, because it increases the fundamental output voltage. Also they allow reducing commutation losses and the harmonic content of the output voltage, and to obtain higher amplitude modulation indexes. The proposed space vector modulated voltage source converter is modeled and simulated in MATLAB using Simulink and PSB (Power System Block-set) toolboxes.

Keywords: Independent Asynchronous Generator, Wind Energy Conversion System, Battery Energy Storage System, Space Vector Pulse Width Modulation.

1. Introduction

Differential heating of the earth's surface by the sun causes the movement of large air masses on the surface of the earth, i.e., the wind. Wind energy is the one of the most abundantly available forms of renewable energy and has emerged as a viable alternative to conventional non-renewable energy sources. It has proved to be the most promising renewable energy source because of its environment friendliness, sufficient availability, and good conversion efficiency. Electricity derived from wind power provides an alternative to conventional generation that would be used to achieve substantial reduction of fossil fuel use and industrial effluents like carbon dioxide. The wind generation system is the most competitive of all the environmentally clean and safe renewable energy sources. However in wind turbines, variations in speed of the wind and load changes are common phenomena. These variations affect the magnitude of generated voltage and frequency, which in turn influence the magnitude of the machine impedance [10].

Current utilization of renewable energy systems in the form of wind, small hydro and bio-gas have led to the massive use of grid connected and independent asynchronous generator. In grid connected systems the reactive power for setting up magnetic field in machine is drawn from the grid itself. In standalone systems, no external ac power supply is available for setting up the magnetic field in the machine.

Besides being commonly used as drives in the industry, three phase asynchronous generators have earned much attention because of the qualities such as ruggedness, fault tolerance and constructional simplicity and constitute the biggest sector in the present wind power industry [1]. Also induction machine is less prone to sudden torque disturbances as compared with a synchronous machine.

It should be noted that one of the key issues in standalone system is reliability and simplicity in control structure. The space vector pulse width modulation (SVPWM) technique is one of the most popular techniques gained interest recently (Trzynadlowski, 1994). SVPWM technique has been increasingly used in the last decade because it allows reducing commutation loss and the harmonic current of output voltage and results in higher magnitude of fundamental output voltage. It provides voltage utilization of $2/\sqrt{3}$ times of sine PWM and obtains higher amplitude modulation indexes if compared with the conventional sinusoidal PWM technique.

In this paper, a voltage and frequency control schemes is proposed for an independent asynchronous generator with capacitor excitation system. The proposed control scheme presented in this paper optimized cost of the system by requiring reduced number of current sensors and provides a fast response. The proposed voltage and frequency controller is realized using IGBT (Insulated Gate Bipolar Transistor) based voltage source converter (VSC) whose gating signals are provided by SVPWM technique and the performance of the controller is investigated in different wind speed condition for linear load in MATLAB using simulink and PSB toolboxes.

2. Principle of operation

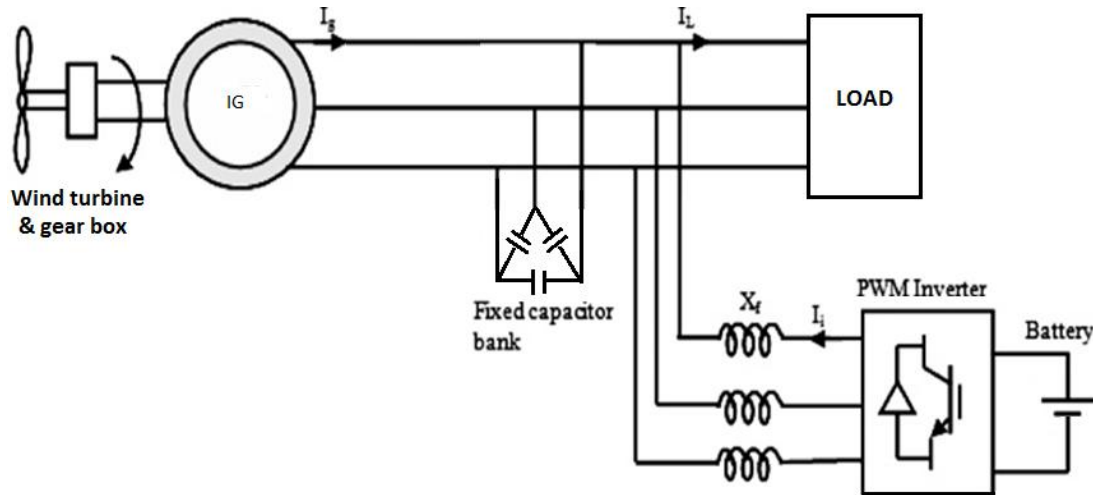


Fig.1 Schematic diagram of wind turbine driven asynchronous generator

Fig.1 shows a schematic diagram of wind turbine-driven asynchronous generator along with a proposed controller. A squirrel cage induction generator whose excitation is provided from two sources, viz., one fixed capacitor bank and parallel connected three phase voltage source converter with DC bus supported by battery energy storage system. The proposed controller is having bidirectional flow capability of active and reactive powers and thus it controls the frequency and voltage respectively. The basic principle of this operation is that, when there is high wind speed, the generated power is also high and accordingly for frequency regulation, the total generated power should be consumed otherwise difference of electrical power and mechanical power is stored in the revolving components of the generator and in turn it increases the output frequency. Therefore this additional generated power is used to charge the battery to avoid the variation in frequency. Also when there is low speed, there will be deficiency of the generated power. An additional required power is supplied by the battery energy storage system to the non-linear load.

3. PWM voltage source inverter

The PWM VSI used here is a three phase VSI with six switches. Each switch (S1, S2, S3, S4, S5 & S6) in the inverter branch is composed of semiconductor devices connected with antiparallel diode. The semiconductor device is a controllable device and diode is for protection..

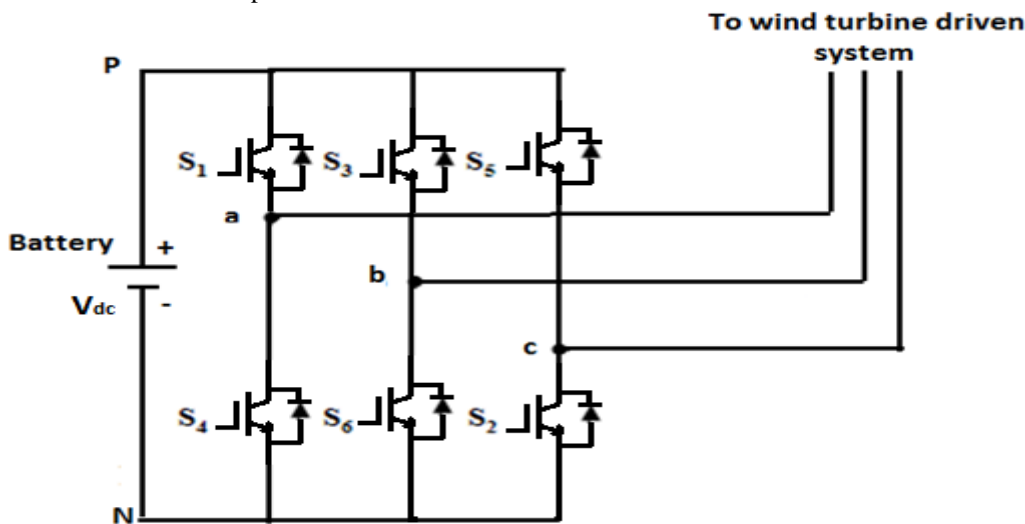


Fig.2 Three phase voltage source pwm inverter

Phase voltage vectors $[V_{an}, V_{bn}, V_{cn}]$ represented as

$$\begin{bmatrix} V_{an} \\ V_{bn} \\ V_{cn} \end{bmatrix} = \frac{1}{3} V_{dc} \begin{bmatrix} 2 & -1 & -1 \\ -1 & 2 & -1 \\ -1 & -1 & 2 \end{bmatrix} \begin{bmatrix} a \\ b \\ c \end{bmatrix} \tag{1}$$

Line-line voltage vector [V_{ab} , V_{bc} , V_{ca}] can be calculated as

$$\begin{bmatrix} V_{ab} \\ V_{bc} \\ V_{ca} \end{bmatrix} = V_{dc} \begin{bmatrix} 1 & -1 & 0 \\ 0 & 1 & -1 \\ -1 & 0 & 1 \end{bmatrix} \begin{bmatrix} a \\ b \\ c \end{bmatrix} \tag{2}$$

4. Space Vector PWM Technique

The concept of voltage space vector is in analogy with the concept of flux space vector as used in three-phase ac machine. The magnitude of the resultant flux due to all phase winding is, however, fixed at 1.5 times the peak magnitude due to individual phase winding. Hence, the resultant voltage space vector will be rotating uniformly at the synchronous speed and will have magnitude equal to 1.5times the peak magnitude of the phase voltage.

Knowing that the inverter cannot produce ideal sinusoidal voltage waveform, a good pwm inverter aims to remove low frequency harmonic components from the output voltage at the cost of increasing high frequency distortion. The high frequency ripple in the output voltage can easily be filtered by a small external filter or by the load inductance itself. In terms of voltage space vectors, the above trade-off between low and high frequency ripples means that the resultant voltage vector will have two components (i) a slowly moving voltage vector of constant magnitude and constant speed superimposed with (ii) a high frequency ripple component whose direction and magnitude changes abruptly.

Table. 1 switching vectors, phase voltages and output line-line voltages

Voltage vector	switching vector			phase voltage			line – line voltage		
	A	b	C	V_{an}	V_{bn}	V_{cn}	V_{ab}	V_{bc}	V_{ca}
V0	0	0	0	0	0	0	0	0	0
V1	1	0	0	2/3	-1/3	-1/3	1	0	-1
V2	1	1	0	1/3	1/3	-2/3	0	1	-1
V3	0	1	0	-1/3	2/3	-1/3	-1	1	0
V4	0	1	1	-2/3	1/3	1/3	-1	0	1
V5	0	0	1	-1/3	-1/3	2/3	0	-1	1
V6	1	0	1	1/3	-2/3	1/3	1	-1	0
V7	1	1	1	0	0	0	0	0	0

The space vector PWM technique aims to realize this slowly rotating voltage space vector from the state vectors. In voltage source converter, six power transistors (S1 to S6) that shape the output voltage will have eight possible switching combinations. Out of these eight combinations, two combinations wherein all the upper switches or all the lower switches are simultaneously ON result in zero output voltage (V0, V7). These two combinations are referred as null states. The remaining six switching combinations, wherein either two of the upper switches and one of the lower switch conduct or vice versa, are active states results in voltage (V1 to V6). This PWM technique approximates the reference voltage by a combination of these switching patterns (V0 to V7) and should be rotating with fixed magnitude and speed in the voltage plane.

To implement the space vector PWM, the voltage equations in the *abc* reference frame can be transformed into the stationary *dq* reference frame that consists of the horizontal (d) and vertical (q) axes as depicted in Fig.3

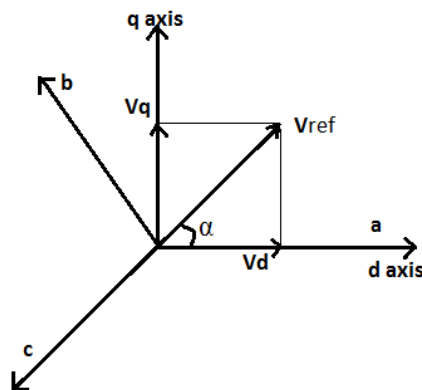


Fig.3 voltage space vector and its component in (d,q)

$$\therefore \begin{bmatrix} V_d \\ V_q \end{bmatrix} = \frac{2}{3} \begin{bmatrix} 1 & -\frac{1}{2} & -\frac{1}{2} \\ 0 & \frac{\sqrt{3}}{2} & -\frac{\sqrt{3}}{2} \end{bmatrix} \begin{bmatrix} V_{an} \\ V_{bn} \\ V_{cn} \end{bmatrix} \quad (3)$$

$$|\bar{V}_{ref}| = \sqrt{V_d^2 + V_q^2} \quad (4)$$

$$\alpha = \tan^{-1}\left(\frac{V_q}{V_d}\right) = \omega_s t = 2\pi f_s t \quad (5)$$

Where f_s is fundamental frequency

This transformation is equivalent to an orthogonal projection of $[a, b, c]^T$ onto the two-dimensional d-q plane. Six non zero vectors (V_1 to V_6) shape the axes of a hexagonal as depicted in fig. 4, and feed power to the load. The angle between any two adjacent non zero vectors is 60 degrees. Meanwhile, two zero vectors (V_0 and V_7) are at the origin and apply zero voltage to the load. The objective of space vector PWM technique is to approximate the reference voltage V_{ref} using the eight switching patterns.

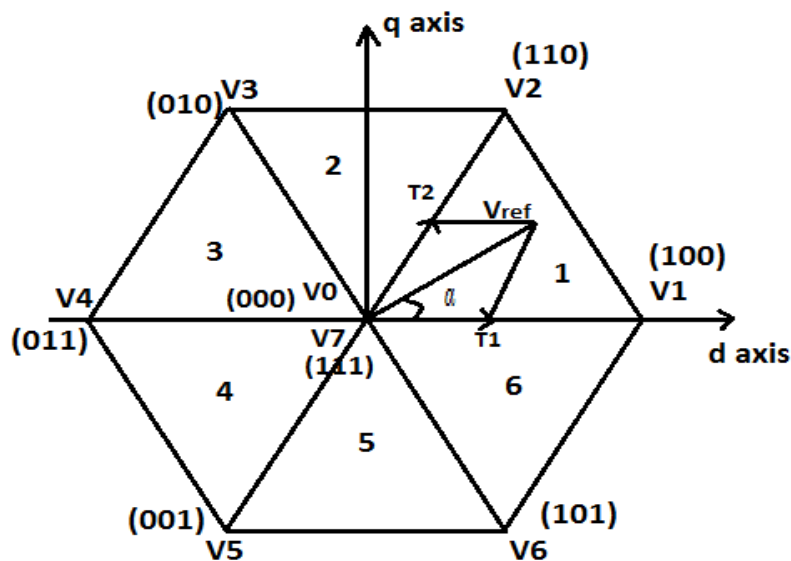


Fig.3 Basic switching vectors and sectors

For voltage space vector V_{ref} , the inverter may be continuously switched at high frequency between V_1 and V_2 active states. The resultant vector V_{ref} so realized will occupy the mean angular position of V_1 and V_2 and the magnitude of the resultant vector can be found to 0.866 times the magnitude of V_1 and V_2 (being vector sum of $0.5V_1$ and $0.5V_2$). Further, the magnitude of the resultant voltage vector can be controlled by injecting suitable duration of null state. Hence switching time duration (T_1 , T_2 and T_0) at sector 1 can be calculated as

$$T_1 = T_z \cdot a \cdot \frac{\sin(\pi/3 - \alpha)}{\sin(\pi/3)} \text{ and}$$

$$T_2 = T_z \cdot a \cdot \frac{\sin(\alpha)}{\sin(\pi/3)}$$

$$\therefore T_0 = T_z - (T_1 + T_2), \quad \left(\text{where, } T_z = \frac{1}{f_s} \text{ and } a = \frac{|\bar{V}_{ref}|}{\frac{2}{3}V_{dc}} \right) <$$

The switching time for each transistor (S1 to S6) can be estimated by space vector PWM switching patterns at each sector. Based on the pattern, the switching time at each sector is summarized in table 2.

Table. 2 Switching time calculation at each sector

SECTOR	Upper Switches (S1, S3, S5)	Lower Switches (S4, S6, S2)
1	$S1 = T1 + T2 + T0/2$ $S3 = T2 + T0/2$ $S5 = T0/2$	$S4 = T0/2$ $S6 = T1 + T0/2$ $S2 = T1 + T2 + T0/2$
2	$S1 = T1 + T0/2$ $S3 = T1 + T2 + T0/2$ $S5 = T0/2$	$S4 = T2 + T0/2$ $S6 = T0/2$ $S2 = T1 + T2 + T0/2$
3	$S1 = T0/2$ $S3 = T1 + T2 + T0/2$ $S5 = T2 + T0/2$	$S4 = T1 + T2 + T0/2$ $S6 = T0/2$ $S2 = T1 + T0/2$
4	$S1 = T0/2$ $S3 = T1 + T0/2$ $S5 = T1 + T2 + T0/2$	$S4 = T1 + T2 + T0/2$ $S6 = T2 + T0/2$ $S2 = T0/2$
5	$S1 = T2 + T0/2$ $S3 = T0/2$ $S5 = T1 + T2 + T0/2$	$S4 = T1 + T0/2$ $S6 = T1 + T2 + T0/2$ $S2 = T0/2$
6	$S1 = T1 + T2 + T0/2$ $S3 = T0/2$ $S5 = T1 + T0/2$	$S4 = T0/2$ $S6 = T1 + T2 + T0/2$ $S2 = T2 + T0/2$

5. Results and discussions:

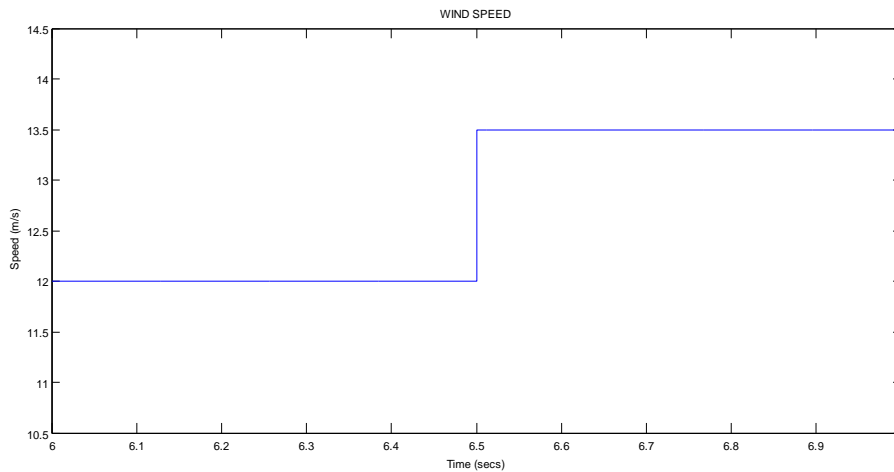


Fig. 4 Wind speed variation

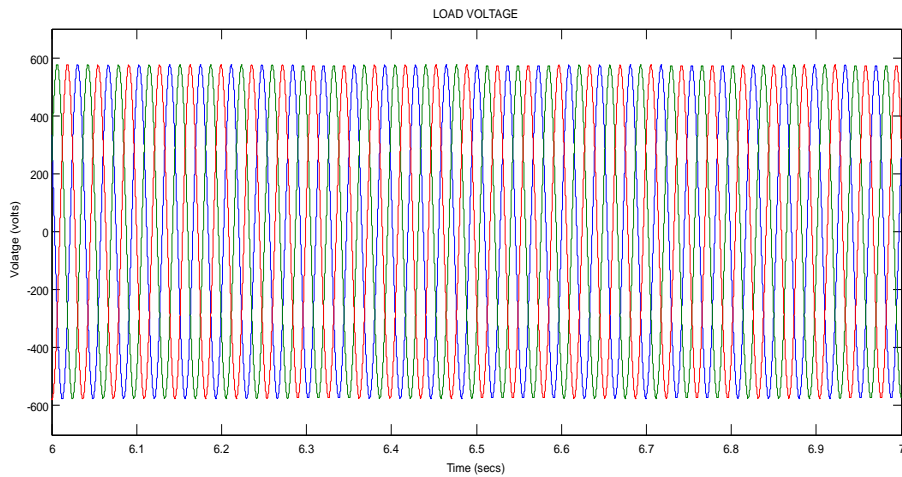


Fig. 5 Load Voltage

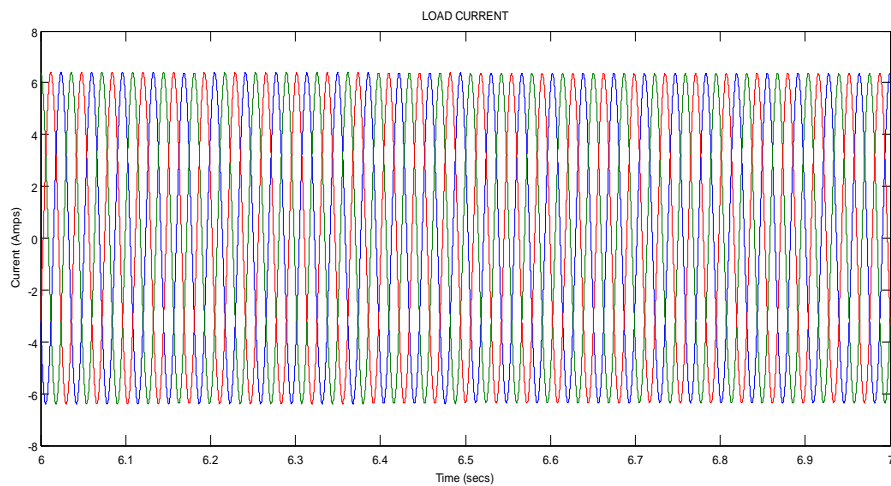


Fig.6 Load Current

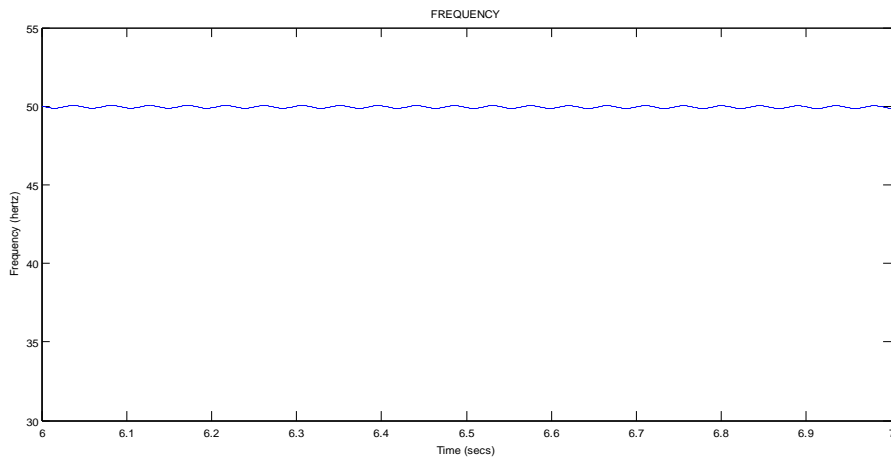


Fig. 7 Frequency

The performance of the proposed controller for a stand alone wind energy conversion system under varying wind speeds are shown in Figs 4-7. At 6 secs, the wind speed is 12m/s, it is observed that due to insufficient power generation at low wind speed an additional power is supplied by the battery to regulate the frequency. At 6.5 secs, the wind speed is increased from 12m/s to 13.5m/s, an output power is increased so that at particular load now the power supplied by the battery energy storage system is reduced because now demand is met by the generator itself and having the availability of enough wind power.

5. Conclusion:

A standalone wind energy conversion system based on asynchronous generator has been modeled and simulated in the MATLAB using the Simulink and PSB tool boxes. The proposed controller with space vector PWM technique is used to regulate the voltage and frequency under varying wind speeds. The space vector PWM technique reduces the commutation loss and increases the magnitude of fundamental output voltage. The performance of the system has been demonstrated under different wind speed variation (dynamic conditions). It has been observed that the controller results in satisfactory operation under different dynamic conditions along with voltage and frequency control. Moreover, the controller has a capability of harmonic elimination and load balancing.

References:

- [1] S.N.Bhadra, D.kastha and S.Banerjee, Wind Electical Systems, Oxford University Press, 2005.
- [2] Hegde, R.K.: 'A wind driven self excited induction generator with terminal voltage controller and protection circuits'. IEEE Int. Conf. on Power Conversion, April 1993, pp. 484 – 489.
- [3] Murthy, S.S., Bhim, S.: 'Capacitive var controllers for induction generators for autonomous power generation'. IEEE Int. Conf. on Power Electronics, Drives and Energy Systems for Industrial Growth, January 1996, vol. 2, pp. 679 – 686.
- [4] Mustafa, A.A.-S., Eui-Cheol, N., Thomas, A.L.: 'Controlled shunt capacitor self-excited induction generator'. IEEE Int. Conf. on Industry Applications, October 1998, vol. 2, pp. 1486 - 1490 .
- [5] Eduardo, S., Gustavo, B.: 'Voltage-frequency control of a self excited induction generator', IEEE Trans. Energy Convers., 1999, 14, (3), pp. 394 – 401.
- [6] Naidu, M., Walters, J.: 'A 4-kW 42-V induction-machine-based automotive power generation system with a diode bridge rectifier and a PWM inverter', IEEE Trans. Ind. Appl., 2003, 39, (5), pp. 1287 – 1293.
- [7] Seyoum, D., Rahman, M.F., Grantham, C.: 'Inverter supplied voltage control system for an isolated induction generator driven by a wind turbine'. IEEE Int. Conf. on Industry Applications, October 2003, vol. 1, pp. 568 – 575.
- [8] Ahmed, T., Katsumi, N., Mutsuo, N.: 'Advanced control of PWM converter with variable-speed induction generator', IET Electr. Power Appl., 2007, 1, (2), pp. 239 – 247.
- [9] Wu, J.-C.: 'AC/DC power conversion interface for self-excited induction generator', IET Renew. Power Gener., 2009, 3, (2), pp. 144 - 151
- [10] R.S Bhatia., D.K Jain., B. Singh and S.P. Jain, "Battery energy storage system for power conditioning of renewable energy sources", in Proc. of IEEE Conference on Power Electronics and Drive Systems, Dec. 2005, pp.501-506.
- [11] B. Singh and G.K Kasal. "Voltage and frequency controller for a small scale wind power generation", in Asian Power Electronics Journal, Vol. 2, No. 1, Apr 2008, pp. 37-44.

Authors Biography

K. Premalatha received B.E. in Electrical and Electronics Engineering from Madras University, Tamilnadu, India, in 1997, M. Tech. in Power Electronics and Drives from SASTRA University, Tamilnadu, India, in 2002 and pursuing Ph.D. in Electrical Engineering at Anna university, Coimbatore, Tamilnadu, India. Currently she is Asso. Professor in Electrical & Electronics Engineering at Kumaraguru College of Technology, Tamilnadu, India. She is Life Member in Systems Society of India and ISTE. Her research interest includes Power Quality, Power Electronics and Wind Energy Conversation systems.

T. BRINDHA received bachelor degree from Sona College Of Technology, Salem in Electrical and Electronics Engineering in 2010. She is currently doing her master degree in Power Electronics and Drives at Kumaraguru College Of Technology, Coimbatore.

Self-Excitation and Voltage Control of an Induction Generator in an Independent Wind Energy Conversion System

¹K. Premalatha, ²S.Sudha

^{1,2}Department of EEE, Kumaraguru College of Technology, Coimbatore.

Abstract

This paper proposes an excitation system and voltage control for a Squirrel Cage Induction Generator in an independent wind energy conversion system. Energy is considered to be very promising alternative for power generation because of its tremendous environment, social, and economic benefits. Of all wind power technologies, the variable speed systems employing the Squirrel Cage Induction Generator are the cheapest and simplest. A voltage source converter directly interfaces the Squirrel Cage Induction Generator through dc load network and also be the DC link of an inverter. The Squirrel Cage Induction Generator which is excited using voltage source converter connected to a single capacitor and battery on the DC side. In this paper, Space vector pulse width modulation technique is used because of their easier digital realization, efficient use of supply voltage and better dc bus utilization. A controller is specifically designed that keeps the DC bus voltage at a constant value under wind speed and electrical load variations. The proposed system with its controller is modeled and simulated using MATLAB/SIMULINK software.

Keywords: Squirrel Cage Induction Generator (SCIG), Space Vector Pulse Width Modulation (SVPWM), Voltage Source Converter (VSC), Wind Energy Conversion System (WECS).

1. Introduction

The development and utilization of wind energy to satisfy the electrical demand has received considerable attention in recent years, owing to the concerns regarding the dwindling energy resources and enhanced public awareness of the potential impact of the conventional energy systems on the environment. Improvements in wind generation technologies will continue to encourage the use of wind energy in both grid connected and stand-alone systems. Owing to the random nature of the wind, the wind generators behave quite differently from the power system planners and engineers to carefully consider the reliability issues [1] associated with the wind energy sources.

Squirrel-cage induction machines (SCIM) still have an edge over these approaches in terms of cost and ruggedness [2-3]. These advantages are significant and far outweigh the somewhat inferior power density and efficiency of the SCIM, especially for remote WECS installations connected to an isolated power grid. In isolated systems [4], no external ac power supply is available for setting up the magnetic field in the machine and in this mode it is called self-excited induction generator (SEIG). In these schemes, excitation power is supplied by a battery which is connected at the IG terminals. The performance of the machine is strongly influenced by the value of the terminal capacitor. It has been suggested that the terminal voltage of such machines can be controlled by the excitation capacitor. A switched capacitor approach allows the terminal voltage to be controlled in steps, whereas with a voltage source converter (VSC) connected to the SCIG terminals, smooth voltage control is possible [5]. SCIG control schemes using VSC with battery support have been discussed in [6]. The system is further simplified by optimizing the battery bank. A battery is connected across the dc bus and by switching on the power converter, initial excitation is provided. As the terminal voltage starts building up its charge the dc bus capacitors and both voltages increase in tandem. After the dc bus voltage increases beyond battery voltage, the battery is disconnected. However, the use of ac capacitor banks makes the systems costlier and less reliable, which detract from the inherent robustness of the SCIM.

In this paper, induction motor fed by voltage source converter (VSC) with a space vector modulation (SVM) is proposed [7]. Space vector PWM (SVPWM) technique is one of the most popular techniques gained interest recently (Trzynadlowski, 1994). This technique results in higher magnitude of fundamental output voltage, increases the overall system efficiency, minimizes the THD as well as switching loss, it is feasible to implement compared to sinusoidal PWM.

2. System Description

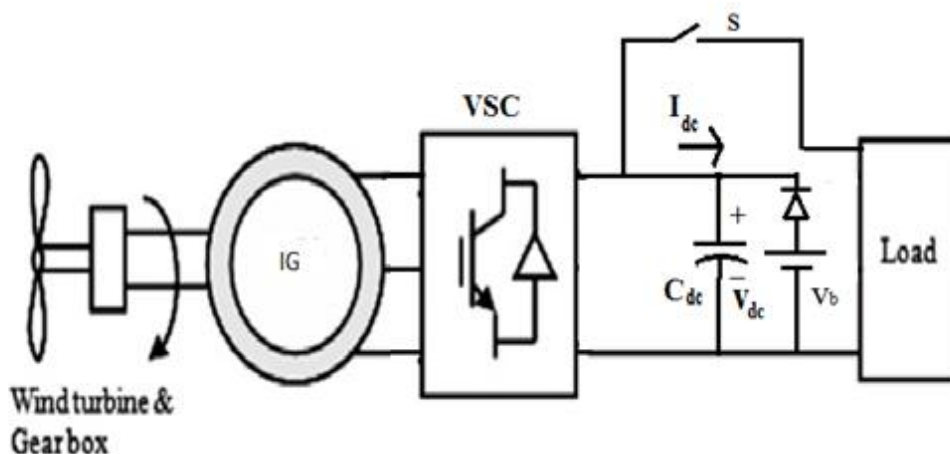


Fig.1 schematic representation of the system

The overall system configuration is shown in Fig. 1. Induction generator is driven by the wind turbine and that is connected to the DC load by means of the Voltage Source Converter (VSC). The proposed system starts its excitation process from an external battery V_b . The external battery V_b helps to charge the capacitor and also start the build up of flux in core. When the generated voltage rises to value higher than V_b then the diode blocks the flow of current to the battery and then the diode is replaced by a switch.

Initial voltage in the dc bus is supplied to the terminal voltages of unexcited machine in turn there is voltage buildup because of the residual magnetism of the magnetic core, and therefore rectified by the anti-parallel diodes of the VSC. Voltage build-up is achieved by controlling the machine slip speed. The rotor flux is maintained at its rated value to ensure increased terminal voltage, hence higher output power, at higher turbine speed. The proposed scheme is verified through simulation on MATLAB-SIMULINK platform. All simulation results are validated using a 2.2KW SCIG coupled with wind turbine. DC voltage and speed are sensed and fed back for control which is based on the space vector modulation technique.

3. System modeling

The main components of the proposed system are shown in Fig.1. The components are IG, WT, and VSC those modeling are explained below.

3.1 Mathematical model of induction machine

The dynamic model [8] of induction machine using rotating d-q reference frame, whose stator and rotor voltage equation is given by

$$V_{sd} = R_s i_{sd} + \frac{d}{dt} \lambda_{sd} - \omega_d \lambda_{sq} \quad (1)$$

$$V_{sq} = R_s i_{sq} + \frac{d}{dt} \lambda_{sq} - \omega_d \lambda_{sd} \quad (2)$$

$$V_{rd} = R_r i_{rd} + \frac{d}{dt} \lambda_{rd} - \omega_{dA} \lambda_{rq} \quad (3)$$

$$V_{rq} = R_r i_{rq} + \frac{d}{dt} \lambda_{rq} - \omega_{dA} \lambda_{rd} \quad (4)$$

Where V_{sd} , V_{sq} , V_{rd} , V_{rq} are the direct and quadrature axes stator and rotor voltage.

R_s , R_r are the stator and rotor resistance

i_{sd} , i_{sq} , i_{rd} , i_{rq} are the direct and quadrature axes stator and rotor current

λ_{sd} , λ_{sq} , λ_{rd} , λ_{rq} are flux linkages

ω_d is the angular velocity.

Electromagnetic torque is expressed as

$$T = \frac{P}{2} L_m (i_{sq} i_{rd} - i_{sd} i_{rq}) \quad (5)$$

Where L_m is the mutual inductance .

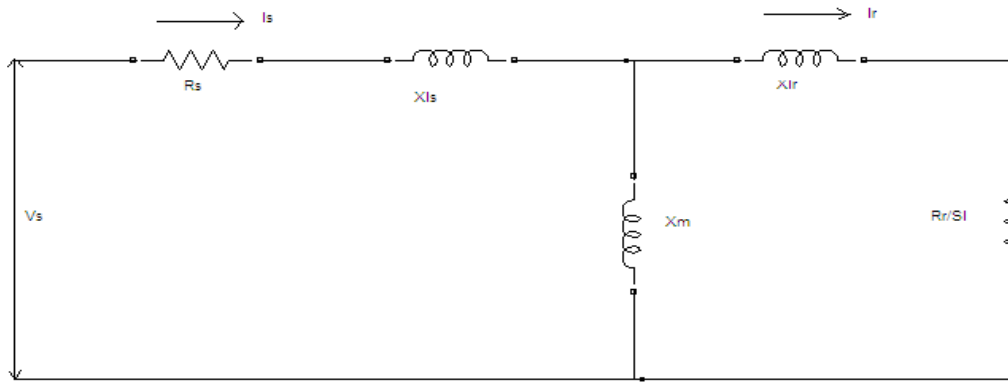


Fig.2 Per phase steady-state circuit of induction machine

3.2. Modeling of Wind Turbine (WT)

Wind turbines are used to generate electricity from the kinetic power of the wind. Historically they were more frequently used as a mechanical device to turn machinery. The output power of wind turbine is given by

$$P_m = C_p(\lambda, \beta) \frac{\rho A}{2} V_{wind}^3 \quad (6)$$

- Where, P_m - mechanical output power of wind turbine,
- C_p - performance coefficient of wind turbine (0.48-0.5),
- ρ - Air density (kg/m^3),
- A - Area of the blades (m^2),
- V_{wind} - wind speed (m/s),
- λ - Tip speed ratio (V_{tip}/V_{wind}),
- β - Blade pitch angle (deg).

The Power - Speed characteristics for wind turbine which are illustrated in Fig.4.

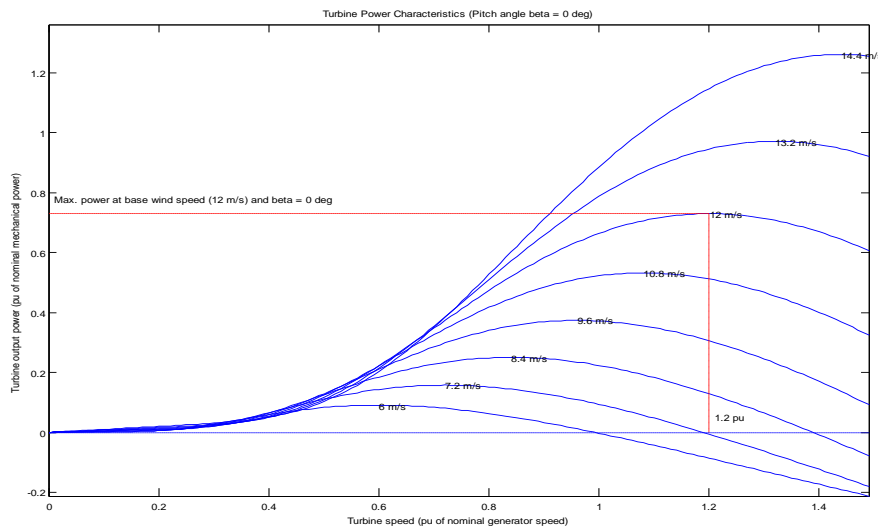


Fig.3 Power-Speed characteristics of WT

3.3. Modeling of VSC

Voltage-source converter (VSC) is connected to a single capacitor and battery on the DC side. The VSC is switched by SVM technique and the line to line voltages are given by

$$v_{ab} = v_{an} - v_{bn} \quad (7)$$

$$v_{bc} = v_{bn} - v_{cn} \quad (8)$$

$$v_{ca} = v_{cn} - v_{an} \quad (9)$$

Phase voltage is given by

$$\begin{bmatrix} v_{an} \\ v_{bn} \\ v_{cn} \end{bmatrix} = v_{dc} \begin{bmatrix} 2/3 & -1/3 & -1/3 \\ -1/3 & 2/3 & -1/3 \\ -1/3 & -1/3 & 2/3 \end{bmatrix} \begin{bmatrix} a \\ b \\ c \end{bmatrix} \quad (10)$$

Where a, b, c are switching variable vector

4. Control Scheme based on SVM

SVM treats the sinusoidal voltage as a constant amplitude vector rotating at constant frequency. This PWM technique approximates the reference voltage V_{ref} by a combination of the eight switching patterns (V_0 to V_7). The proposed control scheme based on SVM which are shown in fig. 5. The speed and load errors are directly sent through PI controllers. Controllers generate voltage reference V_d and V_q in the stator flux frames. SVM is calculated from V_d and V_q and then drives the inverter. To implement the space vector PWM, the voltage equations in the abc reference frame can be transformed into the stationary dq reference frame that consists of the horizontal (d) and vertical (q) axes as depicted in Fig.4

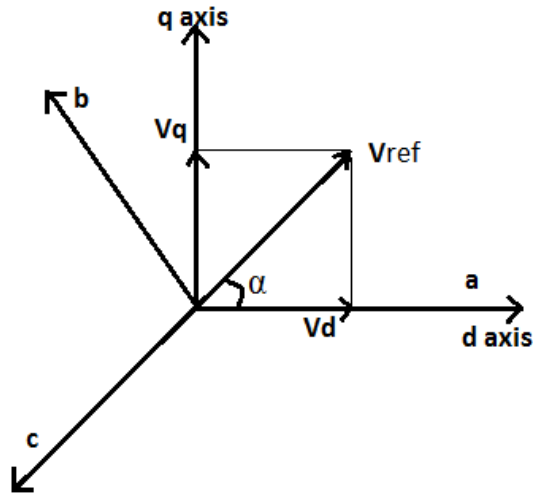


Fig. 4 The relationship of abc reference frame and stationary dq reference frame.

According to the relationship among abc and dq axes, we can get the following equation.

$$\begin{bmatrix} V_d \\ V_q \end{bmatrix} = \frac{2}{3} \begin{bmatrix} 1 & -\frac{1}{2} & -\frac{1}{2} \\ 0 & \frac{\sqrt{3}}{2} & -\frac{\sqrt{3}}{2} \end{bmatrix} \begin{bmatrix} V_{an} \\ V_{bn} \\ V_{cn} \end{bmatrix} \quad (11)$$

$$V_{ref} = \sqrt{V_d^2 + V_q^2} \quad (12)$$

$$\theta_s = \tan^{-1} \left(\frac{V_q}{V_d} \right) = \omega t = 2\pi f t \quad (13)$$

Where f = fundamental frequency

The objective of space vector PWM technique is to approximate the reference voltage vector

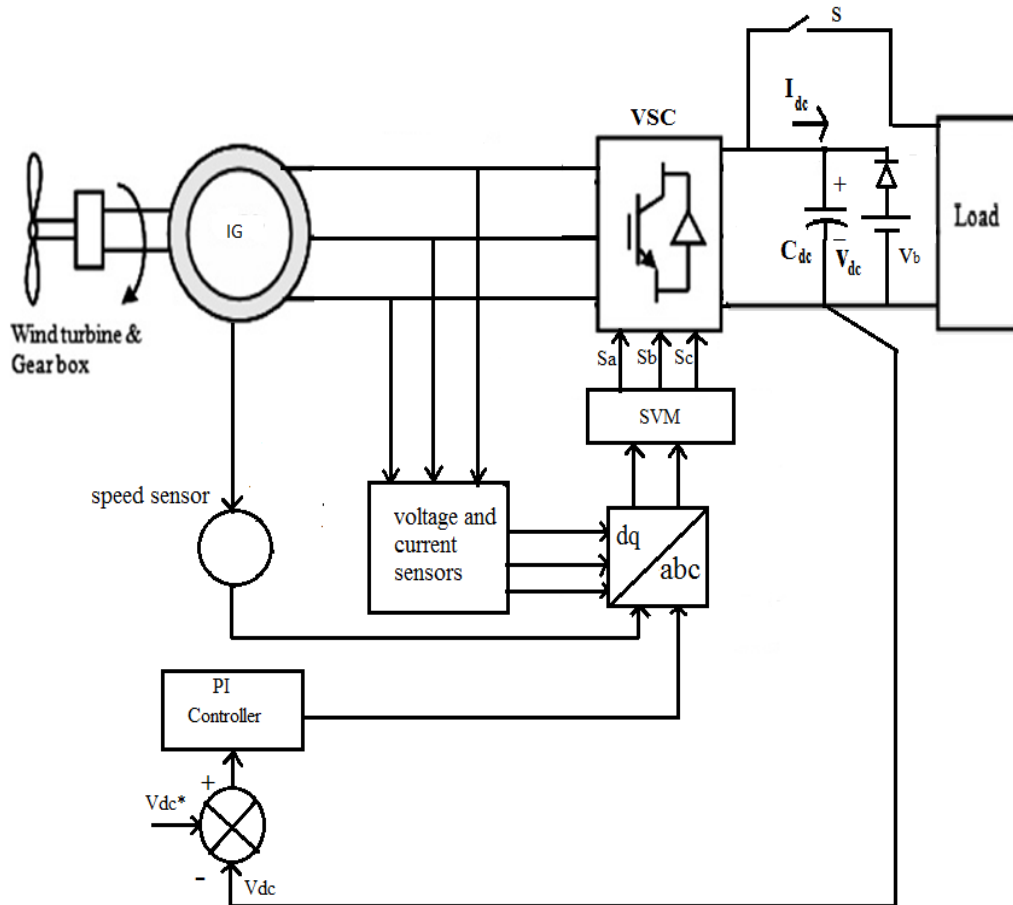


Fig. 5 Control Scheme

Vref using the eight switching patterns. One simple method of approximation is to generate the average output of the inverter in a small period, T to be the same as that of Vref in the same period. The Fig.6 shows the basic switching vector and sector which are shown below.

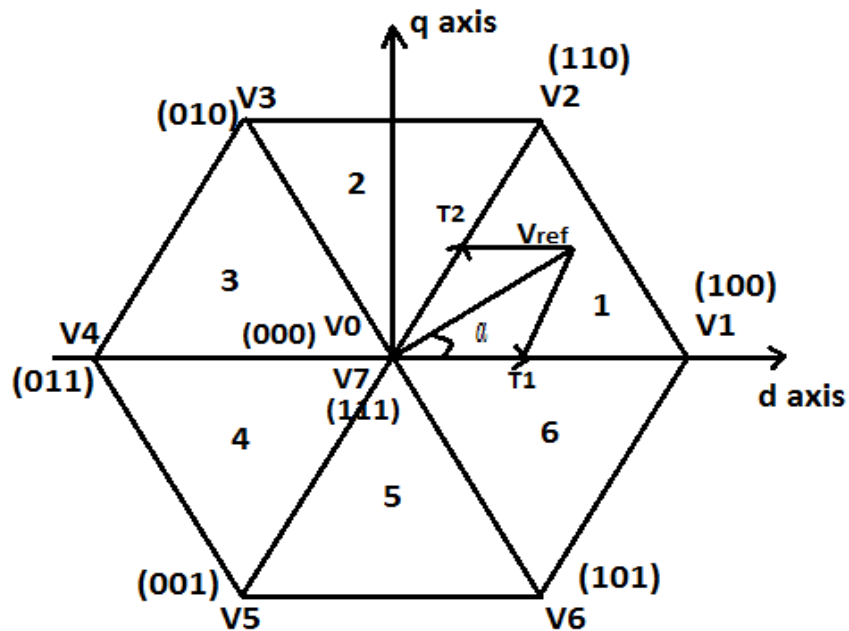


Fig. 6 Basic switching vector and sector

The vectors (V_1 to V_6) divide the plane into six sectors (each sector: 60 degrees). For each sector, the switching time duration (T_1, T_2, T_0) are calculated by

$$T_1 = \frac{\sqrt{3} T_z |\bar{v}_{ref}|}{V_{dc}} \left(\sin \frac{n\pi}{3} \cos \theta_s - \cos \frac{n\pi}{3} \sin \theta_s \right) \quad (14)$$

$$(15) \\ T_0 = T_z - T_1 - T_2$$

$$T_2 = \frac{\sqrt{3} T_z |\bar{v}_{ref}|}{V_{dc}} \left(-\sin \frac{(n-1)\pi}{3} \cos \theta_s - \cos \frac{(n-1)\pi}{3} \sin \theta_s \right)$$

$$(16)$$

The switching time at each sector is summarized in table 1.

SECTOR	UPPER SWITCHES (S1, S3, S5)	LOWER SWITCHES (S4, S6, S2)
1	S1 = $T_1 + T_2 + T_0/2$ S3 = $T_2 + T_0/2$ S5 = $T_0/2$	S4 = $T_0/2$ S6 = $T_1 + T_0/2$ S2 = $T_1 + T_2 + T_0/2$
2	S1 = $T_1 + T_0/2$ S3 = $T_1 + T_2 + T_0/2$ S5 = $T_0/2$	S4 = $T_2 + T_0/2$ S6 = $T_0/2$ S2 = $T_1 + T_2 + T_0/2$
3	S1 = $T_0/2$ S3 = $T_1 + T_2 + T_0/2$ S5 = $T_2 + T_0/2$	S4 = $T_1 + T_2 + T_0/2$ S6 = $T_0/2$ S2 = $T_1 + T_0/2$
4	S1 = $T_0/2$ S3 = $T_1 + T_0/2$ S5 = $T_1 + T_2 + T_0/2$	S4 = $T_1 + T_2 + T_0/2$ S6 = $T_2 + T_0/2$ S2 = $T_0/2$
5	S1 = $T_2 + T_0/2$ S3 = $T_0/2$ S5 = $T_1 + T_2 + T_0/2$	S4 = $T_1 + T_0/2$ S6 = $T_1 + T_2 + T_0/2$ S2 = $T_0/2$
6	S1 = $T_1 + T_2 + T_0/2$ S3 = $T_0/2$ S5 = $T_1 + T_0/2$	S4 = $T_0/2$ S6 = $T_1 + T_2 + T_0/2$ S2 = $T_2 + T_0/2$

From the table.1, the switching times of each transistor are calculated which helps to control the VSC.

5. Simulation Results

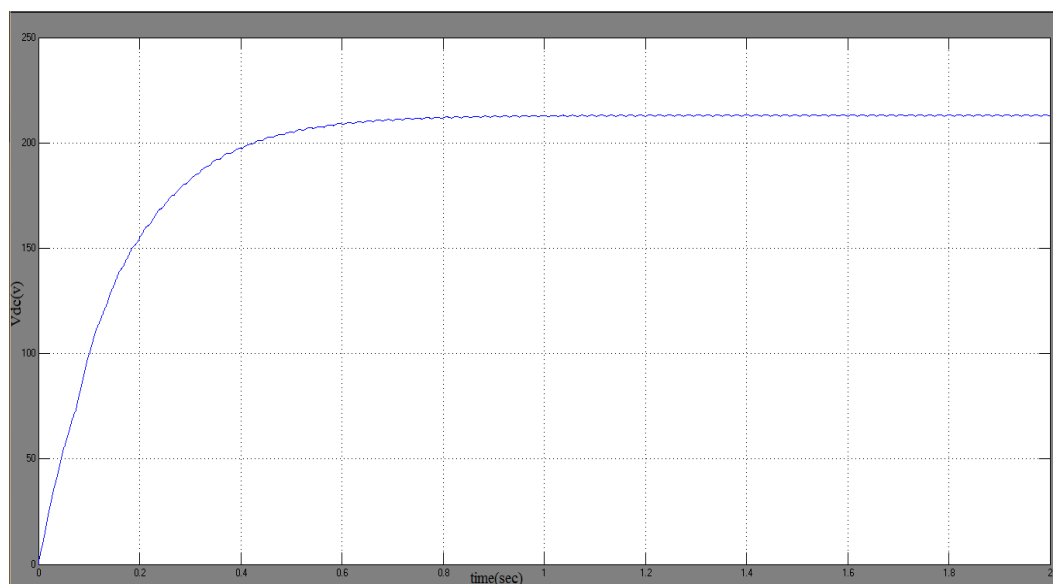


Fig.7 DC Bus voltage

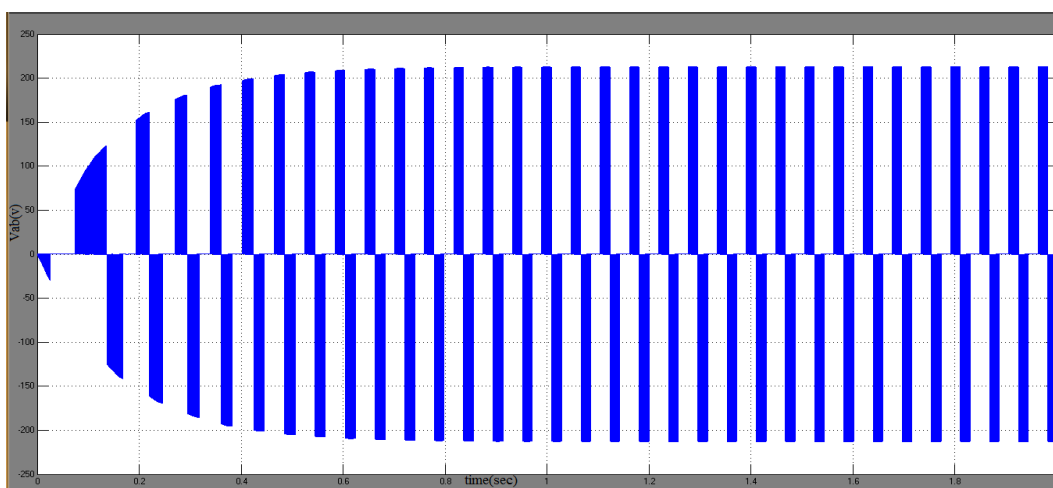


Fig. 8 Line to Line voltage of Induction Generator

The DC bus voltage build up process for variable wind speed and load for a capacitance value of $1500\mu\text{F}$ is shown in the fig.7. When the capacitance is large it takes longer time to reach its steady state value. If the capacitance is too small, there will not be enough exciting current and as a result there will not be voltage build up. For variable rotor speed the voltage build up process starts with the low frequency and then rises until it reaches its steady state value. For low valve battery, the voltage is maintained at 220v.

The Fig. 7 shows the DC Bus voltage and Fig.8 shows the line to line voltage of induction generator. It is observed that the value of the DC bus voltage is maintained at constant value even if the rotor speed changes at 1.5 sec. This is achieved by the SVM controller.

6. Conclusion

This proposed system has an effective method of power generation in WECS using SCIG. A novel scheme for dc bus voltage build up is presented which requires no capacitor bank at IG terminals. This ensures good dynamic control of dc bus voltage with very small changes in speed and load. A scheme of enhancement of power extraction by maintaining constant voltage has been proposed, thereby resulting in better utilization of IG and WT. The proposed method provides the achievement of better utilization and reliable solution for large wind form installations.

References:

- [1] R. Billinton and G. Bai, "Generating capacity adequacy associated with wind energy," *IEEE Trans. Energy Convers.*, vol. 19, no. 3, pp. 641-646, Sep. 2004.
- [2] L. Chen and Y. Y. Hsu, "Controller design for an induction generator driven by a variable-speed wind turbine," *IEEE Trans. Energy Convers.*, vol. 21, no. 3, pp. 625-630, Sep. 2006.
- [3] L. A. C. Lopes and R. G. Almeida, "wind driven self-excited induction generator with voltage and frequency regulated by a reduced-rating voltage source inverter," *IEEE Trans. Energy Convers.*, vol. 21, no. 2, pp. 297-304, Jun. 2006.
- [4] I. Alan, T. A. Lipo, "Control of a polyphase induction generator-induction motor power conversion system completely isolated from the utility," *IEEE Trans. Ind. Appl.*, 1994, 30, (3), pp. 636-647
- [5] S.N. Bhadra, K.V. Ratnam, A. Manjunath, "Study of voltage build up in a self-excited, variable speed induction generator/static inverter system with DC side capacitor," *Proc. IEEE PEDES'96*, New Delhi, India, January 1996, vol. 2, pp. 964-970
- [6] D. Seyoum, M. F. Rahman C. Grantham, "Terminal voltage control of a wind turbine driven isolated induction generator using stator oriented field control," *Proc. IEEE APEC'03, Miami Beach, FL, USA*, February 2003, vol. 2, pp. 846-852
- [7] D. Casadei, G. Serra, A. Tani, and L. Zarri, "Matrix converter modulation strategies: A new general approach based on space-vector representation of the switch state," *IEEE Trans. Ind. Electron.*, vol. 49, no. 2, pp. 370-381, Apr. 2002
- [8] P. C. Krause, O. Wasynczuk, S. D. Sudhoff, "Analysis of electric machinery and drive systems" (John Wiley & Sons, 2002, 2nd edn.)

Author Biography

K. Premalatha received B.E. in Electrical and Electronics Engineering from Madras University, Tamilnadu, India, in 1997, M. Tech. in Power Electronics and Drives from SASTRA University, Tamilnadu, India, in 2002 and pursuing Ph.D. in Electrical Engineering at Anna university, Coimbatore, Tamilnadu, India. Currently she is Asso. Professor in Electrical & Electronics Engineering at Kumaraguru College of Technology, Tamilnadu, India. She is Life Member in Systems Society of India and ISTE. Her research interest includes Power Quality, Power Electronics and Wind Energy Conversion systems.

S. SUDHA received bachelor degree from KSR College Of Engineering, Thiruchengode in Electrical and Electronics Engineering in 2009. She is currently doing her master degree in Power Electronics and Drives at Kumaraguru College Of Technology, Coimbatore.

GB-hash: Hash Functions Using Groebner Basis

Dhananjay Dey¹, Prasanna Raghaw Mishra¹, Indranath Sengupta²

¹SAG, DRDO, Metcalfe House, Delhi - 110 054, INDIA.

²Department of Mathematics, Jadavpur University, Kolkata, WB - 700 032, INDIA.

Abstract

In this paper we present an improved version of HF-hash [DMS] viz., GB-hash: Hash Functions Using Groebner Basis. In case of HF-hash, the compression function consists of 32 polynomials with 64 variables, which were taken from the first 32 polynomials of hidden field equations challenge-1 by forcing last 16 variables as 0. In GB-hash we have designed the compression function in such way that these 32 polynomials with 64 variables form a minimal Groebner basis of the ideal generated by them with respect to graded lexicographical (grlex) ordering as well as with respect to graded reverse lexicographical (grevlex) ordering. In this paper we will prove that GB-hash is more secure than HF-hash as well as it is little bit faster than HF-hash.

Keywords: Dedicated hash functions, differential attack, Groebner basis, preimage attack.

1 Introduction

After recent cryptanalytic attack on MD5 [WY] and SHA-1 [WYY], the security of their successor, SHA-2 family [NIST], against all kinds of cryptanalytic attacks has become an important issue. Although many attacks [GH], [MPRR], [MPRR1], [NB], [IMPR], [SS] on the reduced round of SHA-256 are published between 2003 to 2008, but no result gives any practical threat to the security of SHA-256 till now. In the mean time NIST announced SHA-3 competition in 2007 and the final SHA-3 candidate will be declared by the second quarter of this year. All hash functions submitted for the SHA-3 competition [NIST1] are divided on the following broad category: *balanced Feistel network, unbalanced Feistel network, wide pipe design, key schedule, MDS matrix, output transformation, S-box and feedback register*. But it is still an important issue to analyse the hash function based on the design principle of MD4 family.

We have already designed a cryptographic hash function viz. HF-hash [DMS] in which we have designed the compression function consisting of 32 polynomials with 64 variables which were taken from the first 32 polynomials of hidden field equations challenge-1 by forcing last 16 variables as 0. The leading monomials of 32 polynomials with respect to graded lexicographical ordering used in HF-hash are the following:

$$x_1x_2, x_1x_3, x_1x_2, x_1x_3, x_1x_3, x_1x_2, x_1x_2, x_1x_2, x_1x_2, x_1x_2, x_1x_3, x_1x_6, x_1x_2, x_1x_2, x_1x_2, x_1x_2, x_1x_2, x_1x_4, x_1x_2, \\ x_1x_2, x_1x_3, x_1x_3, x_1x_5, x_1x_2, x_1x_7, x_1x_2, x_1x_2, x_1x_2, x_1x_2, x_1x_3, x_1x_2, x_1x_2, x_1x_2, x_1x_3.$$

Therefore, there are only six different leading monomials viz. $x_1x_2, x_1x_3, x_1x_4, x_1x_5, x_1x_6$ & x_1x_7 .

To improve the design of the compression function of HF-hash function, we have designed a new hash function viz. GB-hash. The leading monomials of the compression function of 32 polynomials with respect to *grlex* ordering as well as with respect to *grevlex* ordering used in GB-hash are given below:

$$x_1x_2, x_3x_4, x_5x_6, x_7x_8, x_9x_{10}, x_{11}x_{12}, x_{13}x_{14}, x_{15}x_{16}, x_{17}x_{18}, x_{19}x_{20}, x_{21}x_{22}, x_{23}x_{24}, x_{25}x_{26}, x_{27}x_{28}, x_{29}x_{30}, \\ x_{31}x_{32}, x_{33}x_{34}, x_{35}x_{36}, x_{37}x_{38}, x_{39}x_{40}, x_{41}x_{42}, x_{43}x_{44}, x_{45}x_{46}, x_{47}x_{48}, x_{49}x_{50}, x_{51}x_{52}, x_{53}x_{54}, x_{55}x_{56}, x_{57}x_{58}, \\ x_{59}x_{60}, x_{61}x_{62}, x_{63}x_{63}.$$

These 32 polynomials form a minimal Groebner basis for the ideal they generate with respect to *grlex* ordering as well as with respect to *grevlex* ordering. But if any one wants to solve the system of equations formed by these polynomials, (s)he cannot reduce the number of polynomials < 8 with respect to any monomial ordering with the assumption that they form a Groebner basis. So the number of equations cannot be reduced to less than 8.

In this paper we prove that GB-hash is more secure than HF-hash with respect to the preimage resistance as well as the collision search attack in the subsequent sections.

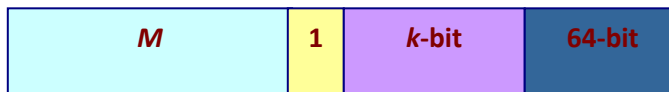
2 GB-hash

GB-hash function can take arbitrary length ($< 2^{64}$) of input and gives 256 bits output. We have designed GB-hash by changing the compression function. The compression function is designed by taking a set of 32 polynomials with 64 variables over $GF(2)$ which form a minimal Groebner basis of an ideal they generate with respect to *grlex* or *grevlex* ordering; where as the compression function of HF-hash consists of 32 polynomials with 64 variables which were taken from the first 32 polynomials of hidden field equations challenge-1 by forcing last 16 variables as 0. For computation of GB-hash, we have taken the padding and parsing procedure, initial value and the 64 constants are the same as HF-hash. For completeness of the algorithm, the computation of hash value of a message M of length l bits is given below:

Padding: First we append 1 to the end of the message M . Let k be the number of zeros added for padding. The 64-bit representation of l is appended to the end of k zeros. The padded message M is shown in the following figure. Now k will be the smallest positive integer satisfying the following condition:

$$l + 1 + k + 64 \equiv 0 \pmod{448}$$

$$\text{i.e., } k + l \equiv 383 \pmod{448}$$



Padded Message

Parsing: Let l' be the length of the padded message. Divide the padded message into $n (= l' / 448)$ 448-bit block i.e. fourteen 32-bit words. Let $M^{(i)}$ denote the i^{th} block of the padded message, where $1 \leq i \leq n$ and each word of i^{th} block is denoted by $M_j^{(i)}$ for $1 \leq j \leq 14$.

Initial Value: Take the first 256 bits initial value i.e., eight 32-bit words from the expansion of the fractional part of π and hexadecimal representation of these eight words are given below:

$$h_0^{(0)} = 243F6A88, h_1^{(0)} = 85A308D3, h_2^{(0)} = 13198A2E, h_3^{(0)} = 03707344,$$

$$h_4^{(0)} = A4093822, h_5^{(0)} = 299F31D0, h_6^{(0)} = 082EFA98, h_7^{(0)} = EC4E6C89.$$

Hash Computation: For each 448-bit block $M^{(1)}, M^{(2)}, \dots, M^{(n)}$, the following four steps are executed for all the values of i from 1 to n .

1. Initialization

$$H_j = h_j^{(i-1)} \text{ for } 0 \leq j \leq 7.$$

2. Expansion

- i. $W_0 \leftarrow H_0$
- ii. $W_j \leftarrow M_j^{(i)}, \text{ for } 1 \leq j \leq 14$
- iii. $W_{15} \leftarrow H_7$

- iv. $W_j \leftarrow \text{rotl}_3(W_{j-16} \oplus W_{j-14} \oplus W_{j-8} \oplus W_{j-1})$, for $16 \leq j \leq 63$, where rotl_k denotes the left rotation by k .

This is the expansion of the message blocks without padding. In the last block we apply padding rule. If $(l+1) > 384$ bits, then we have two extra blocks in the padded message. Otherwise we have one extra block in the padded message. In both the cases, we apply the following expansion rule for the last block so that the length of the message appears in the end of the padded message.

- i. $W_0 \leftarrow H_0$
- ii. $W_1 \leftarrow H_7$
- iii. $W_j \leftarrow M_j^{(i)}$, for $2 \leq j \leq 15$
- iv. $W_j \leftarrow \text{rotl}_3(W_{j-16} \oplus W_{j-14} \oplus W_{j-8} \oplus W_{j-1})$, for $16 \leq j \leq 63$

3. Iteration for $j = 0$ to 63

- i. $T_1 \leftarrow H_1 + H_2 + p(H_3 \| H_0) + K_j$ ¹
- ii. $T_2 \leftarrow H_4 + H_5 + p(H_7 \| H_6) + W_j$
- iii. $H_7 \leftarrow H_6$
- iv. $H_6 \leftarrow H_5$
- v. $H_5 \leftarrow H_4$
- vi. $H_4 \leftarrow \text{rotl}_5(H_3 + T_2)$
- vii. $H_3 \leftarrow H_2$
- viii. $H_2 \leftarrow H_1$
- ix. $H_1 \leftarrow H_0$
- x. $H_0 \leftarrow T_1 + T_2$, where T_1 and T_2 are two temporary variables and $p : Z_{2^{64}} \rightarrow Z_{2^{32}}$ be a function defined by

$$p(x) = 2^{31} \cdot p_1(x_1, \dots, x_{64}) + 2^{30} \cdot p_2(x_1, \dots, x_{64}) + \dots + 1 \cdot p_{32}(x_1, \dots, x_{64}).$$

Since any element $x \in Z_{2^{64}}$ can be represented by $x_1 x_2 \dots x_{64}$, where $x_1 x_2 \dots x_{64}$ denotes the bits of x in decreasing order of their significance. The list of polynomials $p_i(x_1, \dots, x_{64})$ for $1 \leq i \leq 32$ is given in <https://docs.google.com/file/d/0ByA1ZE-dqRLQaDFvRWZGZHVUNFNpSlotWjdTVk8tZw/edit>

The 64 constants K_j are taken from the fractional part of e and are given below:

¹ The operation $\|$ denotes the concatenation and $+$ denotes the addition $\text{mod } 2^{32}$.

$K_0 = AC211BEC$	$K_1 = 5FEFE110$	$K_2 = 112276F8$	$K_3 = 8AE122A4$
$K_4 = 18B3488B$	$K_5 = 00921A36$	$K_6 = 40C045F8$	$K_7 = C8C0A3DA$
$K_8 = C4ABF676$	$K_9 = 6A68C750$	$K_{10} = A37AFE0F$	$K_{11} = 732806F3$
$K_{12} = 25722CB7$	$K_{13} = 3FF43825$	$K_{14} = ACDF96D7$	$K_{15} = 9B53BCD3$
$K_{16} = E34950DE$	$K_{17} = D9780CCB$	$K_{18} = 8B5F9BB7$	$K_{19} = 3D1182ED$
$K_{20} = 1921B44A$	$K_{21} = 7003F30D$	$K_{22} = 42657E31$	$K_{23} = 231E7B55$
$K_{24} = 91E3A28E$	$K_{25} = 95CD4AB0$	$K_{26} = 0A0AC2E3$	$K_{27} = FCDEBE5E$
$K_{28} = FCF1E321$	$K_{29} = 1D136560$	$K_{30} = 2974BF63$	$K_{31} = 70963992$
$K_{32} = 4F5B5107$	$K_{33} = 0072C0C1$	$K_{34} = C99F3C1D$	$K_{35} = C56598D9$
$K_{36} = 77A1D027$	$K_{37} = 36675FB6$	$K_{38} = A40C34E8$	$K_{39} = 46764EAD$
$K_{40} = F8823861$	$K_{41} = 19F66E64$	$K_{42} = 87E10299$	$K_{43} = 4311C8C2$
$K_{44} = 07C102B9$	$K_{45} = 9F4EC8CE$	$K_{46} = 29D81EBA$	$K_{47} = 992744F9$
$K_{48} = 4CDA6790$	$K_{49} = 13DA5357$	$K_{50} = BA6D7772$	$K_{51} = 80673F08$
$K_{52} = B049EE4C$	$K_{53} = 839F8647$	$K_{54} = 736F658B$	$K_{55} = EBE90F9B$
$K_{56} = FA6DC4D1$	$K_{57} = E951630E$	$K_{58} = AFC453E4$	$K_{59} = 159B7483$
$K_{60} = 45EABF9D$	$K_{61} = 4292A60E$	$K_{62} = 17AA0ABD$	$K_{63} = 94E81C30$

4. Intermediate Hash Value

The i^{th} intermediate hash value

$$h^{(i)} = h_0^{(i)} \parallel h_1^{(i)} \parallel h_2^{(i)} \parallel h_3^{(i)} \parallel h_4^{(i)} \parallel h_5^{(i)} \parallel h_6^{(i)} \parallel h_7^{(i)},$$

where $h_j^{(i)} = H_j$ for $0 \leq j \leq 7$. This $h^{(i)}$ will be the initial value for the message block $M^{(i+1)}$.

The final hash value of the message M will be

$$h_0^{(n)} \parallel h_1^{(n)} \parallel h_2^{(n)} \parallel h_3^{(n)} \parallel h_4^{(n)} \parallel h_5^{(n)} \parallel h_6^{(n)} \parallel h_7^{(n)},$$

where $h_i^{(n)} = H_i$ for $0 \leq i \leq 7$.

Process of Implementation: In order to compute GB-hash(M), first the padding rule is applied and then the padded message is divided into 448-bit blocks. Now each 448-bit block is divided into fourteen 32-bit words and each 32-bit word is read in little endian format. For example, suppose we have to read an ASCII file with data 'abcd', it will be read as $0x64636261$.

Test Value of GB-hash

Test values of the three inputs are given below:

GB-hash(a)	=	<i>f1887394 23fab8a8 0512448e 43d6755e da90c8d0 c38c38d0 db7ab991 4645e099</i>
GB-hash(ab)	=	<i>b302d927 033fd17e 1e2ff903 839e4b35 1feb55e2 fadd9f8b dca0adbf 1c719df9</i>
GB-hash(abc)	=	<i>59d647e2 765243b3 49d01559 8392ba30 476c5c65 dfacc415 a7a9de8c 794e8bb9</i>

3. Analysis of GB-hash

In this section we present the complete analysis of GB-hash which includes properties, efficiency as well as the security analysis of this function.

3.1 Properties of GB-hash

This subsection describes the properties of GB-hash required for cryptographic applications.

- i. **Easy to compute:** For any given value x it is easy to compute GB-hash(x) and the efficiency of this hash function is given in section 3.2.
- ii. **One-wayness:** Suppose one knows the GB-hash(x) for an input x . Now to find the value of x , (s)he has to solve the system of polynomial equations consisting of 32 polynomials with 64 variables given in the site for each round operation. Since this system of equations is underdefined, the XL [CKPS] method or any variant of XL [YC] cannot be applied to solve this system.

We will prove that this system of equations cannot be solve in polynomial time using the method described for solving underdefined system of equation in [KPG].

Proposition 3.1. Let G denote the set of polynomials $\{p_1, p_2, \dots, p_{32}\}$, where p_i 's are defined above and G generates an ideal I . Then

- (i) G is a Groebner basis for I with respect to the monomial order grlex as well as with respect to grevlex.
- (ii) If G' is a non-empty subset of G and if G' is a Groebner basis for I with respect to some monomial order, then $\#G' \geq 8$.

Proof 3.1.

- (i) The leading term (lt) of p_1, p_2, \dots, p_{32} in G with respect to the monomial order grlex as well as with respect to grevlex are $x_1x_2, x_3x_4, x_5x_6, x_7x_8, x_9x_{10}, x_{11}x_{12}, x_{13}x_{14}, x_{15}x_{16}, x_{17}x_{18}, x_{19}x_{20}, x_{21}x_{22}, x_{23}x_{24}, x_{25}x_{26}, x_{27}x_{28}, x_{29}x_{30}, x_{31}x_{32}, x_{33}x_{34}, x_{35}x_{36}, x_{37}x_{38}, x_{39}x_{40}, x_{41}x_{42}, x_{43}x_{44}, x_{45}x_{46}, x_{47}x_{48}, x_{49}x_{50}, x_{51}x_{52}, x_{53}x_{54}, x_{55}x_{56}, x_{57}x_{58}, x_{59}x_{60}, x_{61}x_{62}, x_{63}x_{64}$ respectively.

Since $lt(p_i) \times lt(p_j) = lcm(lt(p_i), lt(p_j))$ i.e. $lt(p_i)$ and $lt(p_j)$ are relatively prime then S -polynomial $S(p_i, p_j)$ reduces to zero for $i \neq j$ & $i, j \in \{1, 2, \dots, 32\}$.

This shows that the set of polynomials $\{p_1, p_2, \dots, p_{32}\}$ forms a Groebner basis with respect to grlex or grevlex ordering. Furthermore, no leading monomial of p_i divides the leading monomials of p_j for $i \neq j$. Thus $\{p_1, p_2, \dots, p_{32}\}$ forms a minimal Groebner basis with respect to grlex or grevlex ordering.

- (ii) Let $G_1 = \{p_1, p_2, \dots, p_8\}, G_2 = \{p_9, p_{10}, \dots, p_{16}\}, G_3 = \{p_{17}, p_{18}, \dots, p_{24}\}$ & $G_4 = \{p_{25}, p_{26}, \dots, p_{32}\}$ and $V_1 = \{x_1, x_2, \dots, x_{16}\}, V_2 = \{x_{17}, x_{18}, \dots, x_{32}\}, V_3 = \{x_{33}, x_{34}, \dots, x_{48}\}$ & $V_4 = \{x_{49}, x_{50}, \dots, x_{64}\}$. Therefore, $G = G_1 \cup G_2 \cup G_3 \cup G_4$ and $G_i \cap G_j = \emptyset$ for $i \neq j$. We have chosen the sets G_i 's in such a way that the linear terms of G_i consist of the variables from the set V_i for $1 \leq i \leq 4$. And the non-linear terms of the form $x_j x_k$ are chosen in such a way that $x_j \in V_i$ and $x_k \in \{x_{j+1}, x_{j+2}, \dots, x_{64}\}$ for $1 \leq j \leq 16$ if $i = 1$, for $17 \leq j \leq 32$ if $i = 2$, for $33 \leq j \leq 48$ if $i = 3$ and for $49 \leq j \leq 63$ if $i = 4$.

The sets G_i are selected in a manner that no monomial will appear more than 7 times. Now suppose that the monomial $x_a x_b$ appears 7 times in some G_i . Then if we consider the variable order $x_a > x_b > \dots$, there exists 7 polynomials whose leading terms will be $x_a x_b$. If we compute Groebner basis of these 7 polynomials, there will be only one polynomial in the Groebner basis. Since each G_i contains 8 polynomials, so one has to take at least 2 elements from each G_i to form a Groebner basis with respect to any monomial order.

Thus if G' is a non-empty subset of G and if G' is a Groebner basis for the ideal I with respect to some monomial order, then $\#G'$ is at least 8.

Since the set of polynomials used in designing the compression function of GB-hash can not be reduced to a set consisting of < 8 polynomials such that they form a Groebner basis with respect to any monomial ordering, so by [KPG], we can say that the system of polynomials equations taken from the compression function of GB-hash cannot be solved in polynomial time.

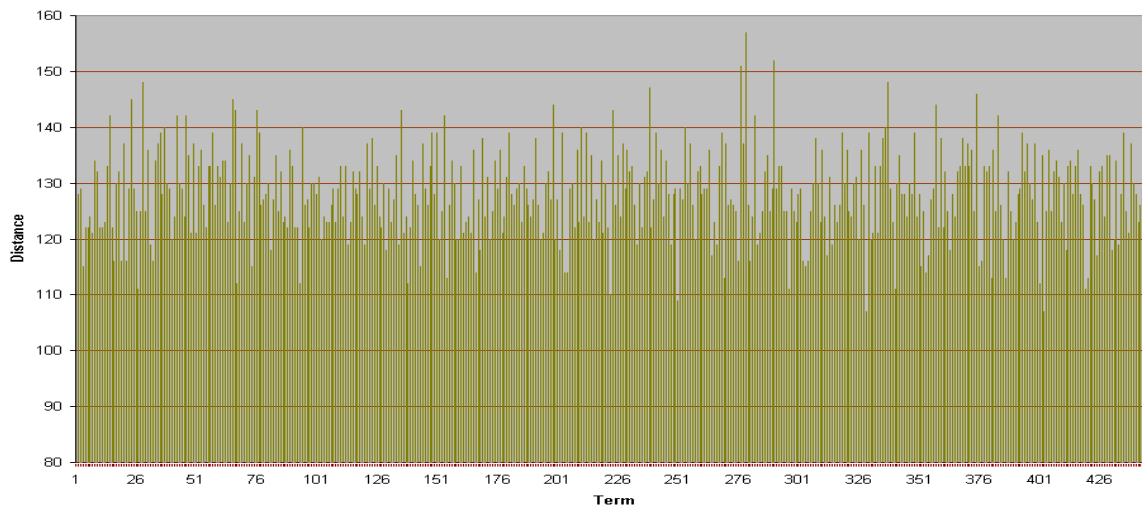
Now, in order to solve this system of equations using the ²Algorithm A given by Courtois et. al. in [CGMT], at least 2^{27} operations are required to solve for one round of GB-hash. Since GB-hash has 64 rounds one has to compute $2^{27 \times 64}$ operations to get back the value of x , for a given GB-hash(x). This is far beyond the today's computation power.

Thus, for any given GB-hash(x), it is difficult to find the input x .

- iii. **Randomness:** We have taken an input file M consisting of 448 bits and computed GB-hash(M). By changing the i^{th} bit of M , the files M_i have been generated, for $1 \leq i \leq 448$. We then computed GB-hash(M_i) of all the 448 files M_i , computed the Hamming distances d_i between GBhash(M) and GB-hash(M_i), for $1 \leq i \leq 448$ and finally computed the distances between corresponding eight 32-bit words of the hash values. The following table shows the maximum, the minimum, the mode and the mean of the above distances.

Changes	W_1	W_2	W_3	W_4	W_5	W_6	W_7	W_8	GB-hash	HF-hash
Max	24	23	25	24	24	23	24	24	157	149
Min	8	7	8	7	6	7	8	8	107	103
Mode	16	16	15	15	15	16	15	16	129	132
Mean	16	16	16	16	16	16	16	16	128	128

Ideally d_i should be 128 for $1 \leq i \leq 448$. But we have found that d_i 's were lying between 107 and 157 for the above files. The following table and the figure show the distribution of the 448 files with respect to their distances.



² which is the best algorithm for solving our system of equations among Algorithms A, B & C

Range of Distance	No. of Files	Percentage GB-hash	Percentage HF-hash
128 ± 5	241	53.79	47.99
128 ± 10	366	81.70	80.80
128 ± 15	425	94.87	93.97
128 ± 20	444	98.88	98.88

iv. **The Bit-Variance Test:** The bit variance test consists of measuring the impact of changing input message bits on the digest bits. More specifically, given an input message, all the small changes as well as the large changes of this input message bits occur and the bits in the corresponding digest are evaluated for each such change. Afterwards, for each digest bit the probabilities of taking on the values of 1 and 0 are measured considering all the digests produced by applying input message bit changes. If $P_i(1) = P_i(0) = 1/2$ for all digest bits $i = 1, 2, \dots, n$, where n is the digest length, then, the one-way hash function under consideration has attained maximum performance in terms of the bit variance test [KZ]. Therefore, the bit variance test actually measures the uniformity of each bit of the digest. Since it is computationally difficult to consider all input message bit changes, we have evaluated the results for only up to 449 files and found the following results:

Number of digests = 449
 Mean frequency of 1s (expected) = 224.50
 Mean frequency of 1s (calculated) = 223.72

The above analysis shows that GB-hash exhibits a reasonably good avalanche effect. Thus it can be used for cryptographic applications.

3.2 Efficiency of GB-hash

The following table gives a comparative study in the efficiency of GB-hash and HF-hash in HP Pentium - D with 3 GHz processor and 512 MB RAM.

File Size (in MB)	GB-hash (in Sec)	HF-hash (in Sec)
1.4	18.76	20.02
4.84	65.45	67.72
7.48	105.28	109.73
12.94	174.87	181.01

The efficiency of GB-hash can be improved by choosing the reduced Groebner basis instead of a minimal Groebner basis.

3.3 Security Analysis

In this paper we have applied a new method for expanding a 512-bit message block into 2048-bit block. For this purpose we have to change the padding rule and the procedure of parsing a padded message. In case of MD-5, SHA-1 & SHA-256, the padded message is divided into 512-bit blocks whereas in case of GB-hash, the padded message is divided into 448-bit blocks. Then two 32-bit words are added to construct a 512-bit block as the input for each iteration, where these two words depend on the previous internal hash updates or chaining variables. So, in each iteration, the 512-bit blocks are not independent from the previous message blocks as in the case of MD-5, SHA-1 or SHA-256. Message expansion algorithm of GB-hash is dependent on

the first and last word of the previous hash. Now if small change is occurred in the inputs, the intermediate hash values will be different. Thus we will get the differences in first and last words of intermediate hash values. These differences along with the rotation in the message expansion formula make impossible to find corrective pattern described in [CJ]. Thus, differential attack by Chabaud and Joux is not applicable to our hash function because one does not have any control over two 32-bit words coming from the previous internal hash updates.

Moreover, a 1-bit difference in any one of 14 initial 32-bit words propagates itself to at least 162 bits of the expanded message since we have taken the 64 round operations. Less than 70 bit difference in expanded message and input message is obtained by changing 1-bit input when 32 or 48 round operations are performed. That is why we have taken 64 round operations for GB-hash function. This makes it impossible to find corrective patterns used by Chabaud and Joux in [CJ], due to the reason that differences propagate to other positions.

The idea of Wang et. al. for finding collision in SHA-0 [WYY1] and SHA-1 [WYY] is to find out the disturbance vectors with low Hamming weight first and then to construct a differential path. To construct a valid differential path, it is important to control the difference propagation in each chaining variable. After identifying the wanted and unwanted differences one can apply the Boolean functions (mainly IF) and the carry effect to cancel out these differences. In particular, when an input difference is 1, the output difference can be 1, -1 or 0. Hence, the function can preserve, flip or absorb an input difference. This gives a good flexibility to construct a differential path. The key of these attacks was the Boolean functions used in compression function which in combination with carry effect facilitate the differential attack.

We have replaced the Boolean functions with 32 polynomials having 64 variables, which form a Groebner basis for the ideal they generate. Now if we change 1 bit in the inputs of GB-hash, the outputs will be the same after one round of operation of the compression function. Because, this input difference will not effect since in our case $W_0 = H_0$. But this input difference will appear in W_1 . Thus, the output differences will be found after two rounds of computing compression function. We have computed the difference propagation of chaining variables for several files having 1 bit input difference and the result is given in the following table.

Round	HF-hash		GB-hash	
	Minimum	Maximum	Minimum	Maximum
2	35	53	34	54
3	63	134	63	132
4	88	144	89	143
5	104	145	99	147

This shows that it is impossible to control the difference propagation of chaining variable after round two as in the case of GB-hash. Therefore, these attacks also are not applicable to GB-hash hash function. Although the cross dependence equation described by Sanadhya and Sarkar in [SS] can be formed in case of GB-hash, the procedure of message expansion as well as the compression function of GB-hash being different from SHA-2 family, this procedure for finding collision cannot be applied in our hash function. Thus, this hash function is also collision resistance against the method described by Sanadhya and Sarkar.

Thus the compression function of GB-hash is collision-resistant against existing attacks. Since IV of GB-hash is fixed and the padding procedure of GB-hash includes the length of the message, therefore by Merkle-Damgard theorem [Dam] [Mer] we can say that GB-hash is collision-resistant against existing attacks.

4 Conclusion

In this paper a dedicated hash function GB-hash has been presented. A system of multivariate polynomials which form a minimal Groebner basis with respect to grlex or grevlex ordering is applied for designing the compression function of our proposed hash function. Analysis of this hash function viz. randomness as well as security proof are also described here. GB-hash differs from the MD family and the SHA family mainly in the procedure of message expansion and the compression function. The advantages of our proposed hash function over the most commonly used hash functions, are that the differential attack applied by Chabaud and Joux in SHA-0 as well as collision search for SHA-1 by Wang et. al. and collision search method applied by Sarkar et. al. for SHA-2 family are not applicable. Further work is going on regarding the improvement of the efficiency as well as the security of GB-hash.

References

- [CGMT] N. Courtois, L. Goubin, W. Meier & J. Tacier, “*Solving Under-defined Systems of Multivariate Quadratic Equation*”, PKC 002, LNCS 2274, pages 211 - 227, Springer-Verlag, 2002.
- [CJ] F. Chabaud & A. Joux, “*Differential Collisions in SHA-0*”, Advances in Cryptology - CRYPTO 098, LNCS 1462, pages 56 - 71, Springer-Verlag, 1998.
- [CKPS] N. Courtois, A. Klimov, J. Patarin & A. Shamir, “*Efficient Algorithms for Solving Over-defined Systems of Multivariate Polynomial Equations*”, EUROCRYPT 2000, LNCS 1807, pages 392 - 407, Springer-Verlag, 2000.
- [Dam] I. B. Damgard, “*A Design Principle for Hash Functions*”, in Advances in Cryptology Crypto 089 pages 416 - 427, Springer-Verlag, 1990.
- [DMS] D. Dey, P. R. Mishra & I. Sengupta, “*HF-hash: Hash Functions Using Restricted HFE Challenge-1*”, in International Journal of Advanced Science and Technology, Vol. 37, pp 129-140, 2011. Available online at <http://www.sersc.org/journals/IJAST/Vol37/11.pdf>
- [GH] H. Gilbert & H. Handschuh, “*Security Analysis of SHA-256 and Sisters*”, Selected Areas in Cryptography, 10th Annual International Workshop, SAC 2003, Revised Papers, LNCS 3006, Springer, 2003.
- [IMPR] S. Indesteege, F. Mendel, B. Preneel & C. Rechberger, “*Collisions and other Non-Random Properties for Step-Reduced SHA-256*”, Cryptology eprint Archive. Available online at <http://eprint.iacr.org/2008/131.pdf>
- [KPG] A. Kipnis, J. Patarin & L. Goubin, “*Unbalanced Oil and Vinegar Signature Schemes*”, Advances in Cryptology EUROCRYPT99, LNCS, 1592, pages 206 - 222 Springer Verlag, 1999.
- [KZ] D.Karras & V. Zorkadis, “*A Novel Suite of Tests for Evaluating One-Way Hash Functions for Electronic Commerce Applications*”, IEEE, 2000.
- [Mer] R. C. Merkle, “*One-way hash functions and DES*”, in Advances in Cryptology Crypto 089, pages 428 - 446, Springer-Verlag, 1990.
- [MPRR] F. Mendel, N. Pramstaller, C. Rechberger & V. Rijmen, “*Analysis of Step-Reduced SHA-256*”, Fast Software Encryption, FSE 2006, LNCS 4047, pages 126 - 143, Springer, 2006.
- [MPRR1] F. Mendel, N. Pramstaller, C. Rechberger & V. Rijmen, “*Analysis of Step-Reduced SHA-256*”, Cryptology eprint Archive. Available online at <http://eprint.iacr.org/2008/130.pdf>
- [NB] I. Nikolic & A. Biryukov, “*Collisions for Step-Reduced SHA-256*”, Fast Software Encryption, FSE 2008, pages 1 - 16. Springer, 2008.
- [NIST] National Institute of Technology, Secure Hash Standard, “*FIPS Publication-180-2*”, 2002. Available online at <http://www.itl.nist.gov/pspubs/>.
- [NIST1] National Institute of Standards and Technology, “*Cryptographic Hash Project*”. Available online at <http://csrc.nist.gov/groups/ST/hash/index.html>
- [SS] S. Sanadhya & P. Sarkar, “*Non-Linear Reduced Round Attacks Against SHA-2 Hash Family*”, Information Security and Privacy -ACISP 2008, LNCS, Springer, 2008.
- [SS1] S. Sanadhya & P. Sarkar, “*Attacking Step Reduced SHA-2 Family in a Unified Framework*”, Available online at <http://eprint.iacr.org/2008/271.pdf>
- [WY] X. Wang & H. Yu, “*How to Break MD5 and Other Hash Functions*”, Advances in Cryptology - EUROCRYPT 2005, LNCS 3494, pages 19 - 35, Springer, 2005.
- [WYY] X. Wang, Y. Yin & H. Yu, “*Finding Collisions in the Full SHA-1*”, in Advances in Cryptology CRYPTO 005, LNCS 3621, pages 17 - 36, Springer, 2005.
- [WYY1] X. Wang, H. Yu & Y. Yin, “*Efficient Collision Search Attacks on SHA-0*”, in Advances in Cryptology CRYPTO 005, LNCS 3621, pages 1 - 16, Springer, 2005.
- [YC] P. Yang & J. Chen, “*All in the XL Family: Theory and Practice*”, Preprint.

TENSILE PROPERTIES OF NATURAL FIBER-REINFORCED EPOXY-HYBRID COMPOSITES

Girisha.C¹, Sanjeevamurthy², Gunti Rangasrinivas³

¹Girisha.C, Mechanical Engineering, Sri Siddhartha Institute of Technology, Tumkur.

²Dr.Sanjeevamurthy, Mechanical Engineering, Sri Siddhartha Institute of Technology, Tumkur.

³Gunti Rangasrinivas, Mechanical Engineering, Sri Siddhartha Institute of Technology, Tumkur.

ABSTRACT

A study has been carried out to investigate the tensile properties of composites made by reinforcing sisal, coconut spathe and ridge gourd as the new natural fibers into epoxy resin matrix. The natural fibers extracted by retting and manual processes were subjected to alkali treatment. The composites fabricated consist of reinforcement in the hybrid combination like sisal-coconut spathe, sisal-ridge gourd and coconut spathe-ridge gourd with the weight fraction of fibers varying from 5% to 30%. It has been observed that the tensile properties increase with the increase in the weight fraction of fibers to certain extent and then decreases. The hybridization of the reinforcement in the composite shows greater tensile strength when compared to individual type of natural fibers reinforced. For all the composites tested the tensile strength of the composite increased for approximately 25% of weight fraction of the fibers and further for the increase in the weight fraction of fiber the strength decreased, also it is found that for the hybrid combination of ridge guard and sisal fibers there is 65% increase in the tensile strength.

Key Words: *Sisal, Ridge gourd, Coconut spathe, Epoxy, Hybrid composite, Tensile Strength.*

1. INTRODUCTION

Natural fibers, as reinforcement, have recently attracted the attention of researchers because of their advantages over other established materials. They are environmentally friendly, fully biodegradable, abundantly available, renewable, cheap and have low density. Plant fibers are light compared to glass, carbon and aramid fibers. The biodegradability of plant fibers can contribute to a healthy ecosystem while their low cost and high performance fulfills the economic interest of industry. When natural fiber-reinforced plastics are subjected, at the end of their life cycle, to combustion process or landfill, the released amount of CO₂ of the fibers is neutral with respect to the assimilated amount during their growth.

Polymeric materials reinforced with synthetic fibers such as glass, carbon and aramid provide advantages of high stiffness and strength to weight ratio as compared to conventional construction materials, i.e. wood, concrete and steel. In spite of these advantages, the widespread use of synthetic fiber-reinforced polymer composite has a tendency to decline because of their high-initial costs and also production of synthetic composites requires a large quantum of energy and quality of

environment suffered because of the pollution generated during the production and recycling of these synthetic materials.

In recent time plant fibers have been receiving considerable attention as substitutes for synthetic fiber reinforcements. Unlike the traditional synthetic fibers like glass and carbon these lignocellulosic fibers are able to impart certain benefits to the composites such as low density, high stiffness, low cost, renewability, biodegradability and high degree of flexibility during processing. Cellulosic fibers like sisal, coconut (coir) and bamboo in their natural form as well as several waste cellulosic products such as shell flour, wood flour and pulp have been used as reinforcing agents of different thermosetting and thermoplastic composites [1–4]. Yan Li, et al [1] reported the chemical composition, properties of sisal fibers and their composites by incorporating the fiber in different matrices before and after treatment by different methods, along with this they present a summary of recent developments of sisal fiber and its composites. The properties of sisal fiber interface between sisal fiber and matrix, properties of sisal fiber-reinforced composites and their hybrid composites. K. Murali Mohan Rao, et al [2] aims at introducing new natural fibers used as fillers in a polymeric matrix enabling production of economical and lightweight composites for load carrying structures. An investigation of the extraction procedures of vakka (*Roystonea regia*), date and bamboo fibers has been undertaken. The cross-sectional shape, the density and tensile properties of these fibers, along with established fibers like sisal, banana, coconut and palm are determined experimentally under similar conditions and compared. The fibers introduced in the present study could be used as an effective reinforcement for making composites, which have an added advantage of being lightweight. S.M. Sapuan, et al [4] have studied the tensile and flexural strengths of coconut spathe and coconut spathe-fiber reinforced epoxy composites and evaluated the possibility of using it as a new material in engineering applications. Samples were fabricated by the hand lay up process (30:70 fiber and matrix ratio by weight). Tensile strength for the coconut spathe-fiber-reinforced composite laminates ranged from 7.9 to 11.6 MPa and flexural strength ranged from 25.6 to 67.2 MPa, implying that the tensile strength of coconut

spathe-fiber is inferior to other natural fibers such as cotton, coconut coir and banana fibers and also found that fiber treatment will improve the interfacial bonding between fiber and matrix leading to better mechanical properties of the spathe-fiber-reinforced composite laminates. Mohd zuhri mohamed yusoff, et al [6] studied the mechanical properties of short random oil palm fiber reinforced epoxy (OPF/epoxy) composites. Empty fruit bunch (EFB) was selected as the fiber and epoxy as the matrix. Composite plate with four different volume fractions of oil palm fiber was fabricated, (5 vol%, 10 vol%, 15 vol% and 20 vol%). The fabrication was made by hand-lay up techniques. The tensile and flexural properties showed a decreasing trend as the fiber loading was increased. The highest tensile properties were obtained for the composite with fiber loading of 5 vol% and there were no significant effect for addition of more than 5 vol% to the flexural properties.

2. MATERIALS AND METHOD

2.1 Selection of Matrix material: Matrix material selected is Epoxy resin CY-230 and HY-951 as binder for the resin. The tensile strength of Epoxy resin CY-230 is 38 MPa.

2.2 Extraction of natural fibers:

The natural fibers such as Sisal (in the form of fibers), Ridge gourd (in the form of natural woven mat), and Coconut leaf sheath (in the form of natural woven mat) were extracted by the process of retting and decorticating.



2.3 Surface treatment:

Alkali treatment of cellulosic fibers, also called mercerization, is the usual method to produce high quality fibers. Alkali treatment improves the fiber-matrix adhesion due to the removal of natural and artificial impurities. Moreover, alkali treatment leads to fibrillation which causes the breaking down of the composite fiber bundle into smaller fibers. In other words, alkali treatment reduces fiber diameter and thereby increases the aspect ratio. Therefore, the development of a rough surface topography and enhancement in aspect ratio offer better fiber-matrix interface adhesion and an increase in mechanical properties. Alkali treatment increases surface roughness resulting in better mechanical interlocking and the amount of cellulose exposed on the fiber surface. This increases the number of possible reaction sites and allows better fiber wetting.

Surface Treatment of the natural fibers was performed by rinsing the fibers in 10% NaOH solution for 24 hours and followed by washing with water. NaOH treatment removed wax and fatty substances and changed surface topography of the fibers [12]

2.4 Preparation of the Specimen:

2.4.1 Mould: A mould made up of GI (gauge 25) sheet of dimension 170X15X3 mm is prepared. Casting of the composite materials is done in this mould by hand lay up process. Later specimens are cut from the prepared casting according to the ASTM (D 638 M) Standard.

2.4.2 Weight fraction of the fiber: The weight of the matrix was calculated by multiplying density of the matrix and the volume (volume in the mould). Corresponding to the weight of the matrix the specified weight percentage of fibers is taken. For hybrid combination the corresponding weight of fiber obtained is shared by two fibers.

2.4.3 Specimen: Mixing the Epoxy resin CY-230 and the hardener HY-951 with a ratio of 10:1. This solution is used as Matrix and the different types of natural fibers are used as reinforcements; the types of composites manufactured are Sisal- Epoxy CY-230, Ridge Guard- Epoxy CY-230, Coconut leaf sheath- Epoxy CY-230 and various hybrid combinations of natural fibers such as Sisal-Coconut leaf sheath- Epoxy CY-230, Sisal -Ridge gourd- Epoxy CY-230, Ridge gourd- Coconut leaf sheath- Epoxy CY-230. The natural fibers are used in varying weight percentages of 5%, 10%, 15%, 20%, 25% and 30%.

2.5 Testing of composite Material:

Tensile test specimens were made according to the ASTM (D 638 M) to measure the tensile properties. The samples were 160 mm long, 12.5mm wide and 3mm thick. The size of the test specimen is eight and average tensile strength has been taken. GI sheet tabs were glued to the ends of the specimen with epoxy

resin so as to prevent the compression of the sample at the grip. The samples were tested at a cross speed of 0.5 mm/min and the corresponding strain occurred was measured using an extensometer.

3. RESULTS AND DISCUSSION

The variation of the mean tensile strength versus fiber percentage is represented in Fig no: 1 to Fig no: 3. Fig: 4 represent the variation of tensile strength of the composites with individual reinforcements namely Sisal fibers, Coconut leaf sheath and Ridge gourd and also the hybrid combinations. The graphs have been plotted taking weight fraction of fiber along the X-axis and Tensile strength (MPa) along the Y-axis.

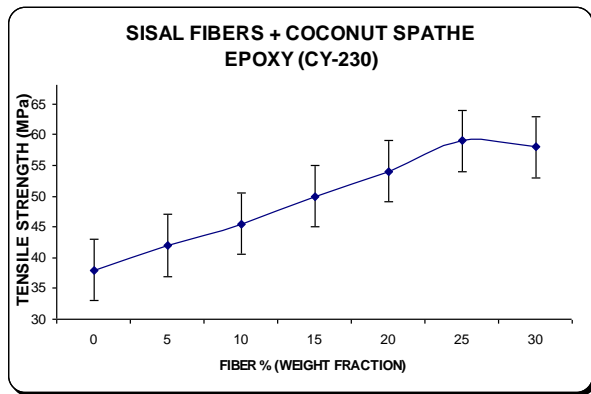


Fig: 1 Tensile Strength of Epoxy-Sisal-Coconut spathe-Hybrid-Composite.

Fig: 1; the combination of fibers used is Sisal and Coconut Spathe. In these composites there is a considerable increase of tensile strength as the percentage of fiber increases to a maximum of 25% and then the strength decreases. The maximum Tensile strength of 59 MPa is obtained for 25% fiber reinforcement, there by 54 % increase in the tensile strength compared with pure Epoxy.

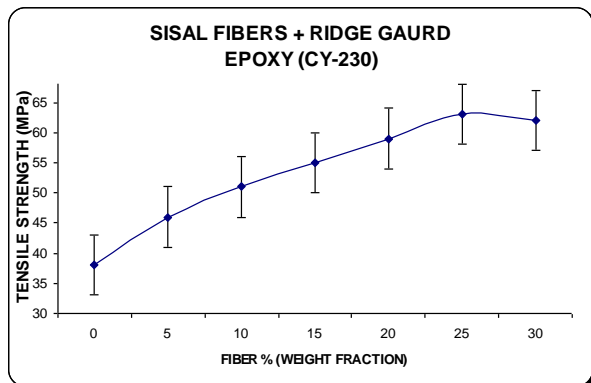


Fig: 2 Tensile Strength of Epoxy-Sisal-Ridge Gourd-Hybrid-Composite.

Fig: 2; the combination of fibers used is Sisal and Ridge Gourd. In these composites there is a considerable increase of tensile strength as the percentage of fiber increases to a maximum % of 25 and then the strength decreases. The maximum Tensile

strength of 63 MPa is obtained for 25% fiber reinforcement, which is the highest tensile strength obtained for the hybrid combination. There is an overall increase of 65% in the tensile strength when compared to pure Epoxy-CY-230 which is used in this work. The increase of tensile strength is due to the increased area of bonding at the interfacial region of the matrix and the reinforcement.

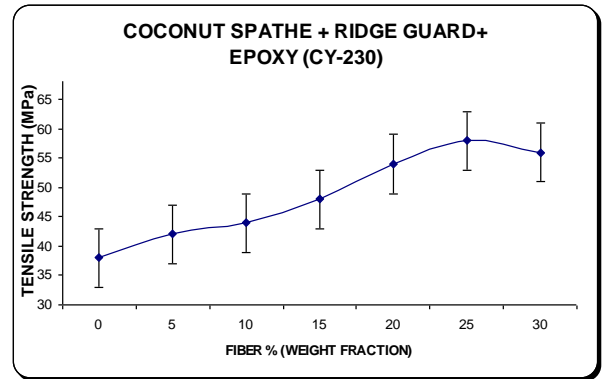


Fig: 3 Tensile Strength of Epoxy-Coconut Spathe-Ridge Gourd-Hybrid-Composite.

Fig: 3; the combination of fibers used is Ridge gourd and Coconut Spathe. In these composites there is a considerable increase of tensile strength as the percentage of fiber increases to a maximum of 25% and then the strength decreases. The maximum Tensile strength of 58 MPa is obtained for 25% fiber reinforcement. This combination gives the lowest tensile strength among the hybrid combinations.

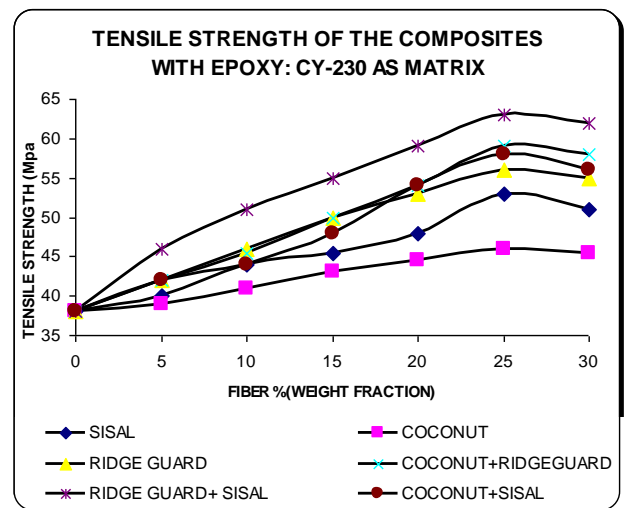


Fig: 4 Tensile strengths of the composites with EPOXY-CY-230 as Matrix.

Fig: 4; shows the variation of tensile strength of all the combination of fibers used. The individual reinforcements like Sisal, Ridge gourd and Coconut spathe have a maximum tensile strength of 53 MPa, 46

MPa and 56 MPa respectively. The variation of tensile strength with respect to the percentage of fiber shows that beyond 25% of fiber the tensile strength decreases. The reason is as the percentage of fiber increases the interaction between the fibers inside the composite increases i.e. there will be higher fiber to fiber contact which leads to poor interfacial bonding between the fiber and the matrix. Due to this poor interfacial bonding effective load transfer will not take place and leads to failure quickly.

4. CONCLUSIONS

Sisal fibers, Coconut leaf sheath and Ridge gourd are effective reinforcement of polymers thus creating a range of technological applications beyond its traditional uses such as ropes, carpets, mats etc.

The incorporation of natural fibers such as Sisal (in the form of fibers), Ridge gourd (in the form of natural woven mat), and Coconut leaf sheath (in the form of natural woven mat) in to the Epoxy matrix shows the moderate improvement in the tensile properties of the composites.

The hybridization of these natural fibers has provided considerable improvement of tensile strength when compared to individual reinforcement; this is mainly due to transfer of loads and shearing of loads among the fibers.

For all the composites tested the tensile strength of the composite increased for approximately 25% of weight fraction of the fibers. The values decrease further for the increase in the weight fraction.

The tensile strength increased by 65% (maximum) for the hybrid combination of Sisal and Ridge guard as reinforcements.

Due to the low density of the natural fibers used compared to the synthetic fibers (Glass fibers, carbon fibers, etc...), the composites can be regarded as a useful light weight Engineering Material.

epoxy composites', *Materials and Design Volume 27, (2006)*, 689–693.

- 6] Mohd zuhri mohamed yusoff, Mohd sapuan salit, Napsiah ismail & Riza wirawan 'Mechanical Properties of Short Random Oil Palm Fiber Reinforced Epoxy Composites', *Sains Malaysiana 39(1) (2010)*: 87–92.
- 7] P. Threepopnatkul, N. Kaerkitcha, N. Athipongarporn . Effect of surface treatment on performance of pineapple leaf fiber–polycarbonate composites', *Composites: Part B, Volume- 40 (2009)* 628–632.
- 8] P.J. Herrera-Franco, A. Valadez-Gonzalez, 'A study of the mechanical properties of short natural-fiber reinforced composites' *Composites: Part B, Volume-36 (2005)*, 597–608.
- 9] Kasama Jarukumjorn , Nitinat Suppakarn, 'Effect of glass fiber hybridization on properties of sisal fiber–polypropylene Composites', *Composites: Part B, vol-40 (2009)*, 623–627.
- 10] A. Valadez-Gonzalez, J.M. Cervantes-Uc, R. Olayo, P.J. Herrera-Franco, 'Effect of fiber surface treatment on the fiber–matrix bond strength of natural fiber reinforced composites', *Composites: Part B , vol 30 (1999)* 309–320.
- 11] Shao-Yun Fu & Bernd Lauke, 'Effects of fiber length and fiber orientation distributions on the tensile strength of short-fiber-reinforced polymers', *Composites Science and Technology, vol-56 (1996)* 1179-1190.
- 12] A.V. Ratna Prasad, G.Nagrasrinivasulu , K. Mohana Rao, 'Mechanical Properties of banana empty fruit bunch fiber reinforced polyester Composites', *Indian Journal of Fiber and Textile research, vol-34 , June 2009*, pp 162-167.

REFERENCES

Journal Papers:

- 1] Yan Li, Yiu-Wing Mai, Lin Ye, 'Sisal fiber and its composites: a review of recent developments'. *Composites Science and Technology, volume 60, (2000)*, 2037-2055.
- 2] K. Murali Mohan Rao, K. Mohana Rao 'Extraction and tensile properties of natural fibers: Vakka, date and bamboo'. *Composite Structures volume 77,(2007)*, 288–295.
- 3] K. Murali Mohan Rao, K. Mohana Rao, A.V. Ratna Prasad, 'Fabrication and testing of natural fibre composites: Vakka, sisal, bamboo and banana'. *Journal of Materials and Design, volume 31, (2010)*, 508–513.
- 4] S.M. Sapuan, M.N.M. Zan, E.S. Zainudin and Prithvi Raj Arora. 'Tensile and flexural strengths of coconut spathe-fibre reinforced epoxy composites', *Journal of Tropical Agriculture 43 (1-2)*: 63-65, 2005.
- 5] S.M. Sapuan , A. Leenie , M. Harimi , Y.K. Beng , 'Mechanical properties of woven banana fiber reinforced

An Enhancement Method for the Compensation of Voltage Sag/Swell and Harmonics by Dynamic Voltage Restorer

U. Vidhu krishnan¹, M. Ramasamy²

¹PG Student, Department of Electrical and Electronics Engineering, K.S.R College of Engineering, Tiruchengode, Namakkal-637 215, Tamilnadu, India.

²Assistant Professor, Department of Electrical and Electronics Engineering, K.S.R College of Engineering, Tiruchengode, Namakkal-637 215, Tamilnadu, India.

Abstract - Now a days, the problem of voltage sags and Swells create a severe impact on sensitive loads in industries . Due to which load shedding and over voltages might occur. Several custom power devices can be used to overcome this problem. Of these power devices Dynamic Voltage Restorer (DVR) is one of the most reliable and efficient custom power devices used in power distribution network. This paper describes DVR principles and voltage compensation methods for balanced / unbalanced voltage sags and swells in a distribution system. Several methods can be included in the DVR system to overcome the voltage sag and swell. Here we use dqo algorithm. There are two important parts in the DVR one is to detect the voltage disturbance and the other is to compensate it as fast as possible. Simulation results were presented to illustrate and understand the performances of DVR under voltage sags/swells conditions. The results obtained by simulation using MATLAB confirmed the effectiveness of this device in compensating voltage sags and swells with very fast response (relative to voltage sag/swell time).

Key words: Dynamic voltage restorer, voltage sag/swell, power factor improvement, total harmonic reduction.

I. INTRODUCTION

IN present days, modern industrial devices are mostly based on electronic devices such as programmable logic controllers and electronic drives. The electronic devices are very sensitive to disturbances and become less tolerant to power quality problems such as voltage sags, swells and harmonics. Voltage dips are considered to be one of the most severe disturbances to the industrial equipments.

Voltage support at a load can be achieved by reactive power injection at the load point of common coupling. The common method for this is to install mechanically switched shunt capacitors in the primary terminal of the distribution transformer. The mechanical switching maybe on a schedule, via signals from a Supervisory Control and Data Acquisition (SCADA) system, with some timing schedule, or with no switching at all. The disadvantage is that, high speed transients cannot be compensated. Some sags are not corrected within the limited time frame of mechanical switching devices. Transformer taps may be used, but tap changing under load is costly.

Another power electronic solution to the voltage regulation is the use of a Dynamic Voltage Restorer (DVR). DVRs are a class of custom power devices for providing reliable distribution power quality. They employ a series of voltage boost technology using solid state switches for compensating voltage sags/swells. The DVR applications

are mainly for sensitive loads that may be drastically affected by fluctuations in system voltage.

A Sources And Effects Of Power Quality Problems

Power distribution systems, ideally, should provide their customers with an uninterrupted flow of energy at smooth sinusoidal voltage at the contracted magnitude level and frequency however, in practice, power systems, especially the distribution systems, have numerous nonlinear loads, which significantly affect the quality of power supplies. As a result of the nonlinear loads, the purity of the waveform of supplies is lost. This ends up producing many power quality problems.

While power disturbances occur on all electrical systems, the sensitivity of today's sophisticated electronic devices makes them more susceptible to the quality of power supply. For some sensitive devices, a momentary disturbance can cause scrambled data, interrupted communications, a frozen mouse, system crashes and equipment failure etc. A power voltage spike can damage valuable components. Power Quality problems encompass a wide range of disturbances such as voltage sags/swells, flicker, harmonics distortion, impulse transient, and interruptions.

- Voltage sag
Voltage sags can occur at any instant of time, with amplitudes ranging from 10 – 90% and a duration lasting for half a cycle to one minute.
- Voltage swell
Voltage swell is defined as an increase in rms voltage or current at the power frequency for durations from 0.5 cycles to 1 min.
- Harmonics
The fundamental frequency of the AC electric power distribution system is 50 Hz. A harmonic frequency is any sinusoidal frequency, which is a multiple of the fundamental frequency. Harmonic frequencies can be even or odd multiples of the sinusoidal fundamental frequency.

II DYNAMIC VOLTAGE RESTORER

Among the power quality problems (sags, swells, harmonics...) voltage sags are the most severe disturbances. In order to overcome these problems the concept of custom power devices is introduced recently. One of those devices is the Dynamic Voltage Restorer (DVR), which is the most efficient and effective modern custom power device used in

power distribution networks. DVR is a recently proposed series connected solid state device that injects voltage into the system in order to regulate the load side voltage. It is normally installed in a distribution system between the supply and the critical load feeder at the Point of Common Coupling (PCC). Other than voltage sags and swells compensation, DVR can also added other features like: line voltage harmonics compensation, reduction of transients in voltage and fault current limitations.

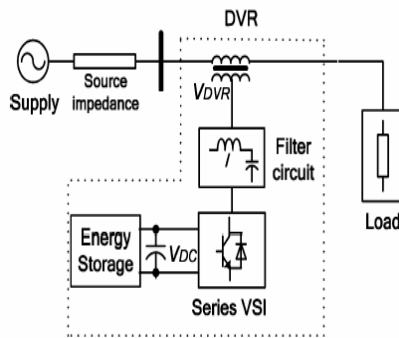


figure 1. Circuit diagram of DVR

III SYSTEM CONFIGURATION

The DVR is a custom power device that is connected in series with the distribution system as shown in figure 1. The main components of the DVR consists of an injection transformer, harmonic filter, series VSI (VSC) an energy storage and control system (as shown in Figure-1).

The basic function of the DVR is to inject a dynamically controlled voltage V_{DVR} generated by a forced commutated converter in series to the bus voltage by means of a booster transformer. The momentary amplitudes of the three injected phase voltages are controlled such as to eliminate any detrimental effects of a bus fault to the load voltage V_L . This means that any differential voltages caused by transient disturbances in the ac feeder will be compensated by an equivalent voltage generated by the converter and injected on the medium voltage level through the booster transformer.

The DVR works independently of the type of fault or any event that happens in the system, provided that the whole system remains connected to the supply grid, i.e. the line breaker does not trip. For most practical cases, a more economical design can be achieved by only compensating the positive and negative sequence components of the voltage disturbance seen at the input of the DVR. This option is Reasonable because for a typical distribution bus configuration, the zero sequence part of a disturbance will not pass through the step down transformer because of infinite impedance for this component.

The DVR has two modes of operation which are: standby mode and boost mode. In standby mode ($V_{DVR} = 0$), the booster transformer's low voltage winding is shorted through the converter.

IV. PROPOSED METHOD

A Main circuit

Once a voltage disturbance occurs, with the aid of dqo transformation based control scheme, the inverter output can be steered in phase with the incoming ac source while the load is maintained constant. As for the filtering scheme of the proposed method, output of inverter is installed with capacitors and inductors.

B Control methods

The basic functions of a controller in a DVR are the detection of voltage sag/swell events in the system; computation of the correcting voltage, generation of trigger pulses to the sinusoidal PWM based DC-AC inverter, correction of any anomalies in the series voltage injection and termination of the trigger pulses when the event has passed. The controller may also be used to shift the DC-AC inverter into rectifier mode to charge the capacitors in the DC energy link in the absence of voltage sags/swells. The dqo method gives the sag depth and phase shift information with start and end times. The quantities are expressed as the instantaneous space vectors. Firstly convert the voltage from a-b-c reference frame to d-q-o reference. For simplicity zero phase sequence components is ignored.

Figure-2 illustrates a flow chart of the feed forward dqo transformation for voltage sags/swells detection. The detection is carried out in each of the three phases.

The control is based on the comparison of a voltage reference and the measured terminal voltage (V_a, V_b, V_c). The voltage sags is detected when the supply

$$\begin{bmatrix} V_d \\ V_q \\ V_o \end{bmatrix} = \begin{bmatrix} \cos(\theta) & \cos\left(\theta - \frac{2\pi}{3}\right) & 1 \\ -\sin(\theta) & -\sin\left(\theta - \frac{2\pi}{3}\right) & 1 \\ \frac{1}{2} & \frac{1}{2} & \frac{1}{2} \end{bmatrix} \begin{bmatrix} V_a \\ V_b \\ V_c \end{bmatrix}$$

The above equation defines the transformation from three phase system a, b, c to dqo stationary frame. In this transformation, phase A is aligned to the d-axis that is in drops below 90% of the reference value whereas voltage swells is detected when supply voltage increases up to 25% of the reference value.

The error signal is used as a modulation signal that allows generating a commutation pattern for the power switches (IGBT's) constituting the voltage source converter. The commutation pattern is generated by means of the Sinusoidal Pulse Width Modulation technique (SPWM); voltages are controlled through the modulation. The block diagram of the Phase Locked Loop (PLL) is illustrated in Figure-2. The PLL circuit is used to generate a unit sinusoidal wave in phase with mains voltage.

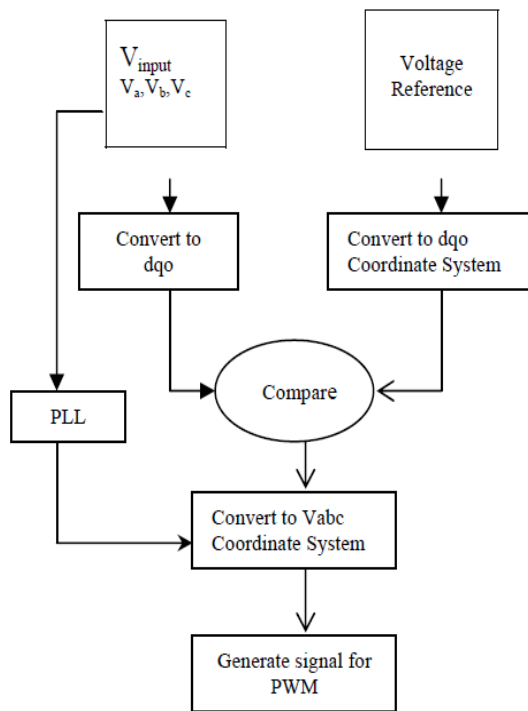


Figure.2 Flow chart of feed forward control technique For DVR based on dqo transformation

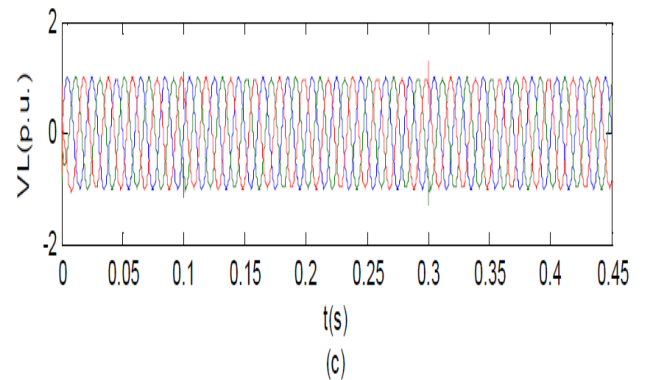
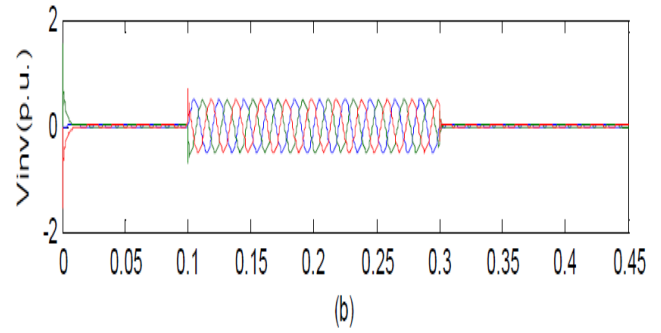
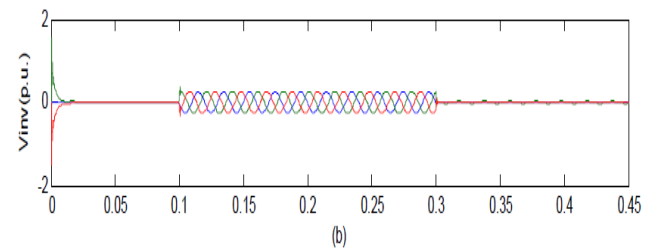
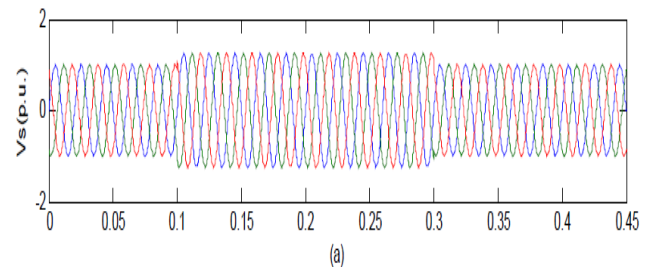
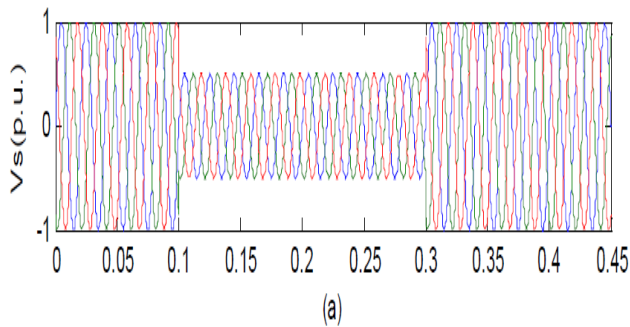


Figure-3. Three-Phase voltage sag(a)-Supply voltage,(b)voltage injected by the DVR,(c)-Load voltage

V. SIMULATION RESULTS AND DISCUSSIONS

A Voltage sags

The first simulation of three phase voltage sag is simulated and a 50% three-phase voltage sag occurring at the utility grid is shown in Figure-3 (a). In Figure-3 (a) also shows a 50% voltage sag initiated at 0.1s and it is kept until 0.3s, with total voltage sag duration of 0.2s. Figures-3(b) and (c) show the voltage injected by the DVR and the corresponding load voltage with compensation. As a result of DVR, the load voltage is kept at 1 pu.



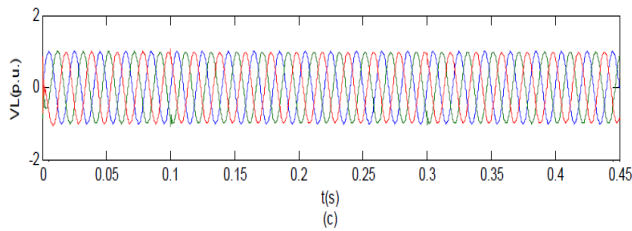


Figure-4. Three phase voltage swell (a) supply voltage, (b) voltage injection by DVR, (c) voltage at load

B Voltage Swells

The second simulation shows the DVR performance during a voltage swell condition. The simulation started with the supply voltage swell is generated as shown in Figure-4 (a). The amplitude of supply voltage is increased about 25% from its nominal voltage. Figures-4(b) and (c) show the injected and the load voltage respectively. As can be seen from the results, the load voltage is kept at the nominal value with the help of the DVR. Similar to the case of voltage sag, the DVR reacts quickly to inject the appropriate voltage component (negative voltage magnitude) to correct the supply voltage.

C Total Harmonic Distortion Without DVR

The third simulation shows the Total Harmonic Distortion (THD) when DVR is not connected in the transmission line. THD is more than 50% when DVR is not connected which would affect the performance and efficiency of the system. Thus the power factor will be decreased. The waveform will be obtained as in fig.5.

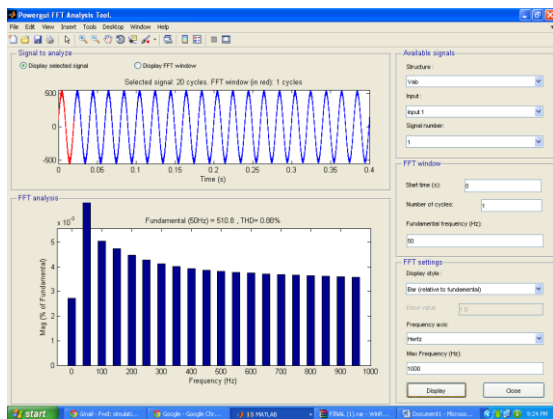


Fig 5 THD without DVR

D Total Harmonic Distortion With DVR

The fourth simulation shows the Total Harmonic Distortion (THD) when DVR is connected in the transmission system. The waveform will be obtained as in fig.6. Here the efficiency and the power factor can be increased when compared to the system without DVR

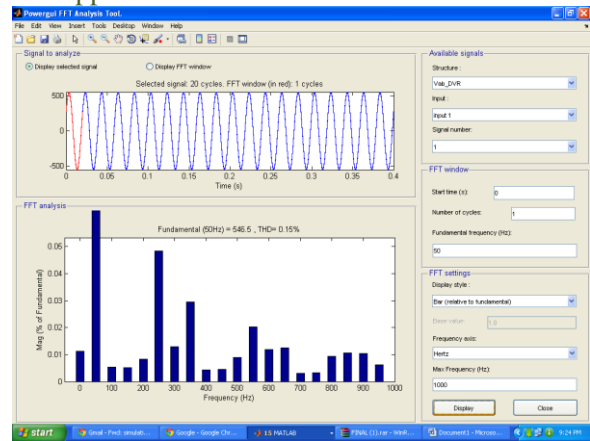


Fig 6 THD with DVR

VI. CONCLUSIONS

The modeling and simulation of a DVR using MATLAB has been presented. A control system based on dqo technique which is a scaled error of the between source side of the DVR and its reference for sags/swell correction has been presented. The simulation shows that the DVR performance is satisfactory in mitigating voltage sags/swells.

The main advantage of this DVR is low cost and its control is simple. It can mitigate long duration voltage sags/swells efficiently. Future work will include a comparison with a laboratory experiments in order to compare simulation and experimental results.

VII REFERENCES

- [1] Rosli Omar and Nasrudin Abd Rahim , "Mitigation of Voltage Sags/Swells using Dynamic Voltage Restorer (DVR)," ARPN Journal of Engineering and Applied sciences, Vol.4, no.4, June 2009
- [2] D.Mahinda Vilathgamuwa, H.M. Wijekoon, and S.S. Choi, "A Novel Technique to Compensate Voltage Sags in Multiline Distribution system," IEEE Trans on Industrial Electronics, vol.53, PP.160 oct 2006.
- [3] N.G. Hingorani, "Introducing Custom Power" IEEE spectrum, Vol.32 PP.41-48, June 2008.
- [4] Francisco Jurado, Manuel Valverde, "Voltage Correction By Dynamic Voltage Restorer Based on Fuzzy Logic Controller," IEEE Trans may 2003.
- [5] Margo P.M. Hery P.M. Ashar, T. Hiyama, "Balanced voltage sag correction using DVR based on Fully polar controller", ICICIC 2007 Conference Proceedings, Kumamoto Japan.
- [6] C. Meyer, R. W. De Doncker, Y. W. Li, and F. Blaabjerg, "Optimized control strategy for a medium-voltage DVR—Theoretical investigations and experimental results", IEEE Trans. Power Electron., vol. 23, no. 6, pp. 2746–2754, Nov. 2008.
- [7] A. Ramasamy, K. I. Rengan, V. K. Ramachandaramurthy "Dynamic Voltage Restorer for Voltage Sag Compensation", International Conference on Power Electronics and Drive Systems (PEDS) 2005, Volume 2, 28-01, Nov. 2005, pp. 1289-1294.
- [8] Bhaskar, M.A.; Dash, S.S.; Subramani, C.; Kumar, M.J.; Gireesh, P.R.; Kumar, M.V.; , "Voltage Quality Improvement Using DVR," Recent Trends in Information, Telecommunication and Computing (ITC), 2010 International Conference on , vol., no., pp. 378-380, 12-13 March 2010
- [9] R. Naidoo and P. Pillay, "A new method of voltage sag and swell detection," IEEE Trans. Power Del., vol. 22, no. 2, pp. 1056–1063, Apr. 2007.
- [10] A. Sannino, J. Svensson, "Static Series Compensator for Voltage Sag Mitigation Supplying Non-linear Loads", in Conf. Rec IEEE/PES, New York, U.S.A., pp. 1147-1152, 2002.

Shielded Micro machined Micro strip Lines Form Ultra-Wideband Band pass Filters

Nasreddine Benahmed¹, Nadia Benabdallah², Kamila Aliane¹,
Fethi Tarik Bendimerad¹

¹Department of Telecommunications, University Abou Bekr Belkaid-Tlemcen, P. O. Box 119, (13000)
Tlemcen, Algeria

²Department of Physics, Preparatory School of Sciences and Technology (EPST-Tlemcen),
Tlemcen, Algeria

ABSTRACT

Using the method of moments (MoM) the analysis and the design of a compact ultra wideband (UWB) bandpass filter using shielded micromachined microstrip lines are presented. The design of the UWB filter is based on the use of impedance steps and coupled-line sections. The center frequency around 6.85 GHz was selected, the bandwidth is between 4-10 GHz, the insertion-loss amounts to around 0.02 dB and the return loss is found higher than 20 dB in a large frequency range (4.8-9 GHz). For the selected center frequency and on a substrate with a dielectric constant of 11.7, the micromachined microstrip filter is only $0.1 \times 0.5 \times 17.45$ mm in size.

Keywords - Analysis and design, compact filter, micromachined microstrip filter, MoM method, ultra wideband bandpass filter.

I. INTRODUCTION

Today's microwave and millimeter-wave markets are driving three important requirements: low cost, performance and small size. Silicon micromachining has been applied to microwave and millimeter-wave circuits in many ways since its introduction in the late 1980s. Micromachining, or sculpting crystal Si can be made using either orientation dependent (anisotropic) or orientation-independent (isotropic) etchants. Silicon micromachined, dielectric membrane supported structures, such as antennas, transmission lines and filters have shown improved performance and have extended the operating range of planar circuits to W-band frequencies and beyond [1-3]. In addition, silicon micromachined-based packaging provides a high isolation self-package without the need for external carriers or external hermetic shielding. This method of circuit integration provides a comprehensive technique to integrate a very large degree of functionality with extremely high density and at a relatively low cost.

The vertically layered structure of the micromachined circuit presents an excellent opportunity for three-dimensional integration, resulting in the potential for substantial reductions in size. Micromachined circuits are an ideal way to integrate MEMS devices and provide components with performance and size advantages from 1 GHz to terahertz regime. However, they demonstrate their greatest promise at K-band and above. Micromachining is truly an excellent integration technology with the

opportunity for an order of magnitude or more reduction in the size, weight and cost of planar circuits, which can have a major impact on radar and communications applications in the military, commercial and space arenas.

Micromachining techniques can be applied to any semiconductor substrate, but the use of Si substrate layers as the foundation of the micromachined structure has major advantages in cost and the direct integration of SiGe and CMOS circuits. High resistivity Si also has mechanical, thermal and electrical properties that compare well with the best ceramics, and as a result has been successfully demonstrated as the substrate of choice in three-dimensional integrated circuit [4]. Cost comparisons have been made for simple circuit applications and show one- and two-orders of magnitude cost reductions over the same circuit packaged in ceramic. Circuit integration based on micromachined fabrication technology promises to be the key to achieving the very demanding cost, size, weight and simplicity goals required for the next advances in communications and radar systems commercial, space and military applications.

Since the Federal Communications Commission (FCC) released the unlicensed use of ultra-wideband (UWB: 3.1 to 10.6 GHz) wireless systems in February 2002 [5], many researchers have started exploring various UWB components, devices, and systems [6], [7]. As one of the key circuit blocks in the whole system, the UWB bandpass filter (BPF) has been studied through the use of the matured filter theory [8] and other techniques [9], [10]. On the basis of impedance steps and coupled-line sections as inverter circuits, several works were interested in the design of planar broadband filters (using microstrip, striplines and CPW [11]) with low loss, compact size, high suppression of spurious responses, and improved stopband performances [11], [12].

In this article, we are interested in the study of an ultra wideband (UWB) bandpass filter using shielded micromachined microstrip lines with Si substrate. The proposed filter has a compact size and can be easily designed and fabricated.

II. SHIELDED MICROMACHINED MICROSTRIP LINES AND NUMERICAL RESOLUTION

The cross-sections of a shielded micromachined microstrip line and coupler are respectively shown in figure 1-a and 1-b. The structures are assumed to be lossless with a microstrip (w) wide and (t) thick and with a dielectric

material (Si) having a relative dielectric constant of $\epsilon_{r2}=11.7$. For the coupler the separation distance between the symmetrical strips is designed by (s).

Electrically, the isolated line of figure 1-a, is described in terms of its inductance and capacitance per unit length (L and C) and in term of its characteristic impedance Z_0 [13]. On the other hand, the electrical properties of the lossless and symmetrical coupler presented in figure 1-b can be described in terms of its primary parameters [L] and [C], and its secondary parameters k, Z_{0e} and Z_{0o} [13-15].

$$\text{Where: } [L] = \begin{bmatrix} L_{11} & L_{12} \\ L_{21} & L_{22} \end{bmatrix}; [C] = \begin{bmatrix} C_{11} & C_{12} \\ C_{21} & C_{22} \end{bmatrix}$$

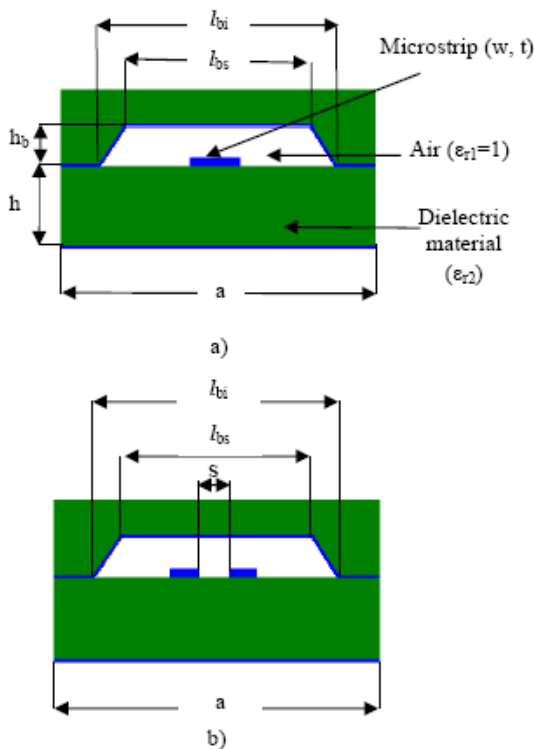


Fig. 1. Cross-sectional views of shielded micromachined microstrip (a) line and (b) coupler (MMC).

The inductance matrix [L] contains the self-inductances on the diagonal ($L_{11}=L_{22}$ are the proper inductances) and the mutual inductances ($L_{12} = L_{21}$) between the two coupled lines.

Matrix [C] accounts for the capacitive effects between the two coupled lines, characterizing the electric field energy storage in the coupler. ($C_{11}=C_{22}$) are the proper capacitances and ($C_{12}=C_{21}$) is the coupling capacitance

$$k = \frac{L_{12}}{L_{11}} = \frac{C_{12}}{C_{11}}; \text{ is the coupling coefficient and } (Z_{0e}, Z_{0o}) \text{ are}$$

respectively the even and the odd mode characteristic impedances of the coupler.

The numerical calculations of these electromagnetic parameters were carried out with LINPAR for windows (Matrix Parameters for Multiconductor Transmission Lines), a 2D Method of Moments (MoM) software for numerical evaluation of the quasi static matrices for multiconductor transmission lines embedded in piecewise-homogeneous

dielectrics [16]. The technique used in the program is based on an electrostatic analysis. In this analysis the dielectrics are replaced by bound charges in a vacuum, and the conducting bodies are replaced by free charges. A set of integral equations is derived for the charge distribution from the boundary conditions for the electrostatic potential and the normal component of the electric field. The method of moments is applied to these equations, with a piecewise-constant (pulse) approximation for the total charge density and the Galerkin technique. LINPAR for windows can analyze arbitrary planar transmission lines and can also analyze any other structure defined by the user.

For our study, we were obliged to supply the cross section of the structures and all relevant dielectrics characteristics including the segmentation by using our programs in FORTRAN.

When the electromagnetic parameters are determined, it is possible to estimate the resulting scattering parameters of the UWB BPF constituted by portions of shielded micromachined microstrip lines using an adapted numerical model [17].

III. ANALYSES AND DESIGN OF UWB FILTER USING MICROMACHINED MICROSTRIP LINES

Figure 2 shows the circuit of the proposed UWB BPF. An isolated micromachined microstrip line in the middle and a coupled line with micromachined coupled microstrips at the two ends [18]. To achieve the specified UWB passband, the three sections of this filter are arranged with the lengths of about one quarter-, one half-, and one quarter-wavelength, i.e., $\lambda/4$, $\lambda/2$ and $\lambda/4$, as marked in figure 2.



Fig. 2. The layout of the proposed UWB BPF using portions of shielded micromachined microstrip.

We applied the MoM-based numerical tool to the analysis and design of the UWB BPF using portions of shielded micromachined microstrip lines. The MoM approach makes it possible to simulate the performance of a design and decides if a given set of constraints makes it possible to realize the filter.

In order to assure for the shielded micromachined microstrip coupler a coupling coefficient of approximately 5 dB, we have varied the distance (s) between the coupled microstrips with the following features: $h_b= h$, $l_{bs}=4h$, $l_{bi}=7h$, $a=10h$, $w=0.17h$ and $t=0.02h$.

The segmentation of the charged surfaces of the coupler using LINPAR is shown in figure 3.



Fig. 3. Segmentation of the charged surfaces used to analyse the cross section of the coupler.

A coupling coefficient of approximately 6 dB was obtained for a separation distance $s=0.1h$, yielding a characteristic impedance of around $\sqrt{Z_{0e} Z_{0o}} = 70 \Omega$ and primary parameters of:

$$[L] = \begin{bmatrix} 625.8 & 327.4 \\ 327.4 & 625.8 \end{bmatrix} \left(\frac{nH}{m} \right);$$

$$[C] = \begin{bmatrix} 138.4 & -68.28 \\ -68.28 & 138.4 \end{bmatrix} \left(\frac{pF}{m} \right)$$

For the middle line of the UWB BPF represented in figure 2, the value of the ratio (w/h) was varied as needed to change the characteristic impedance (Z_0).

Figure 4 shows the segmentation of the charged surfaces used to analyse the cross section of the middle line of the UWB BPF using shielded micromachined microstrip line. A low impedance of 19Ω was chosen for the middle line of the UWB filter.

All of the dimensions and the electromagnetic parameters, obtained for the middle line are provided in table 1.

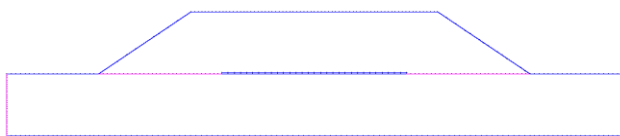


Fig. 4. The segmentation of the charged surfaces used to analyse the cross section of the middle line of the UWB BPF.

Table I: Design parameters for the middle line of the UWB BPF.

Middle line of the UWB BPF	
w/h	3
ϵ_r	11.7
$Z_0 (\Omega)$	19.3
L (nH/m)	158.2
C (pF/m)	436.3

To verify the predicted electrical performance of the circuit presented in figure 2, the proposed UWB BPF using portions of shielded micromachined microstrip lines is simulated using MATPAR software [17]. The designed UWB filter occupies the overall length of 17.45 mm that is about one guided-wavelength at 6.85 GHz. Figure 5 provides plots of the resulting scattering parameters of the designed UWB BPF in the frequency range (2-12) GHz.

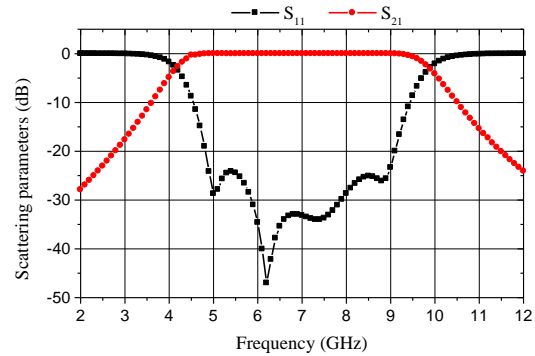


Fig. 5. Simulated responses of the designed UWB bandpass filter

It can be seen that the simulated responses of the UWB BPF with compact size obtained by using portions of shielded micromachined microstrip lines, are in very reasonable agreement with those using classical planar structures. The bandwidth is between 4-10 GHz, the insertion-loss amounts to around 0.02 dB and the return loss is found higher than 20 dB in a large frequency range (4.8-9 GHz).

IV. CONCLUSION

In summary, a compact UWB filter using shielded micromachined microstrip lines is presented, analyzed and designed. The designed filter is only $0.1 \times 0.5 \times 17.45$ mm in size and can be easily designed and fabricated.

The bandwidth is between 4-10 GHz, the insertion-loss amounts to around 0.02 dB and the return loss is found higher than 20 dB in a large frequency range (4.8-9 GHz).

To reach these results, it was necessary to determine the electromagnetic parameters of each portion of the proposed filter ([L], [C], ...). In the frequency range (2-12) GHz, the resolution of the problem is based on the quasi-static assumption and was made by the method of moment.

References

- [1] T.M. Weller, L.P. Katehi and G.M. Rebeiz, High performance microshield line components, *IEEE Transaction on Microwave Theory and Techniques*, 43(3), 1995, 534-543.
- [2] R.F. Drayton, T.M. Weller and L.P. Katehi, Development of miniaturized circuits for high frequency applications using micromachining techniques, *International Journal of Microcircuits and Electronic Packaging*, 18(3), 1995, 217-223.
- [3] Katehi, *Si Micromachining in high frequency applications*, CRC Press, Boca Raton, 1995.
- [4] R. M. Henderson and L.P. Katehi, Silicon-based micromachined packages for high frequency applications, *IEEE Transaction on Microwave Theory and Techniques*, 47(8), 1999, 1600-1607.
- [5] *Revision of Part 15 of the Commission's Rules Regarding Ultra-Wideband Transmission Systems*, FCC ET-Docket 98-153, Feb. 14, 2002.
- [6] G. R. Aiello and G. D. Rogerson, Ultra-wideband wireless systems, *IEEE Microw. Mag.*, 4(2), 2003, 36-47.
- [7] Z. Irahauten, H. Nikoogar, and G. J. M. Janssen, An overview of ultra wide band indoor channel measurements and modeling, *IEEE Microw. Wireless Compon. Lett.*, 14(8), 2004, 386-388.
- [8] G. Matthaei, L. Young, and E. M. T. Jones, *Microwave Filters, Impedance-Matching Networks, and Coupling Structures* (Norwood, MA: Artech House, 1980).
- [9] A. Saito, H. Harada, and A. Nishikata, Development of bandpass filter for ultra wideband (UWB) communication, in *Proc. IEEE Conf. Ultra Wideband Syst. Tech.*, 2003, 76-80.
- [10] L. Zhu, S. Sun, and W. Menzel, Ultra-wideband (UWB) bandpass filters using multiple-mode resonator, *IEEE Microw. Wireless Compon. Lett.*, 15(11), 2005, 796-798.
- [11] J. Gao, L. Zhu, W. Menzel and F. Bögelsack, Short-Circuited CPW Multiple-Mode Resonator for Ultra-Wideband (UWB) Bandpass Filter, *IEEE Microw. Wireless Compon. Lett.*, 16(3), 2006, 104-106.
- [12] M. Meeloon, S. Chaimool and P. Akkaraekthalin, Broadband bandpass filters using slotted resonators fed by interdigital coupled lines for improved upper stopband performances, *Int J Electron Commun (AEU)*, 2008.
- [13] N. Benahmed, N. Benabdallah, F.T. Bendimerad, B. Benyoucef and S. Seghier, Accurate closed-form formulas for the electromagnetic parameters of micromachined shielded membrane microstrip line, in *Proc. IEEE Conf. 8th International Multi-Conference on Systems, Signals & Devices*, 2011.
- [14] N. Benabdallah, N. Ben Ahmed, S. Seghier and R. Bouhmidi, Sliced coaxial cables form compact couplers, *Microwaves and RF*, 46(7), 2007, 90-94.
- [15] N. Benahmed and S. Seghier, Rigorous analytical expressions for the electromagnetic parameters of rectangular coaxial couplers with circular and square inner conductors, *Microwave Journal*, 49(8), 2006, 164-174.
- [16] A.R. Djordjevic, D. Darco, M.C. Goran, T.K. Sarkar, *Circuit Analysis Models for Multiconductors Transmission Lines* (Artech House, 1997).
- [17] A.R. Djordjevic, M. Bazdar, G. Vitosevic, T. Sarkar, and R. F. Harrington, *Scattering parameters of microwave networks with multiconductor transmission lines* (Artech House, Norwood, MA, 1990).
- [18] W. Menzel, L. Zhu, K. Wu and F. Bogelsack, On the design of novel compact broadband planar filters, *IEEE Trans Microwave Theory Tech*, 51(2), 2003, 364-370.

Characterization of Multi-band Rectangular-Triangular Slotted Antenna

¹V. Anitha, ²S. Sri Jaya Lakshmi, ³Habibulla Khan, ⁴I. Sreedevi,
⁴P. Ramakrishna, ⁴J. Lavanya

¹Student, M Tech (C & R), Department of ECE, K L University

²Women Scientist, Department of ECE, K L University

³Professor, Department of ECE, K L University

⁴Students, B Tech, Department of ECE, K L University

ABSTRACT

A multi-band microstrip patch antenna is developed and presented in this paper. The radiating elements in this antenna are composed of rectangular and triangular slots. These slots are engraved in the rectangular and triangular patch, joined together in one structure, and by single probe feed. The rectangular and triangular slots make the antenna to operate at multiband with relatively high gain. Therefore, this antenna can be used for wireless communication applications like WLAN, WiMax and radar system applications.

Key Words: Microstrip antennas, WiMax, WLAN.

1. INTRODUCTION

The design of an efficient wideband small size antenna for recent wireless applications is a major challenge. The microstrip patch antenna have found extensive applications in wireless communication systems owing to their advantages such as low profile, conformability, low fabrication cost and ease of integration with feed network. Microstrip patch antennas comes with drawback of narrow bandwidth, but wireless communication applications require broad bandwidth and relative high gain in order to achieve that we need to increase the substrate thickness, use of low dielectric substrates and various impedance matching feeding techniques and slotting techniques.

The concept of inserting slot array following a chebyshev distribution has proven to give remarkable functionality to an antenna [1]. It causes it to radiate significantly at different ranges of frequencies by using only one single feed point. But, it operates at less number of bands. A rectangle added to an equilateral triangle patch which is fed by a probe has a dual-band operation. With the rapid development of the wireless communication, the tri-band even multi-band antennas are needed to meet the requirement. Stacked microstrip antenna can achieve multi-band circular polarization (CP) radiation more easily than conventional antennas. Generally the stacked microstrip antennas can easily achieve dual-band operation [2]. But the limitations of the stacked microstrip antenna are the size, fabrication complexity, and cost.

In this paper, a single-feed multi-band microstrip patch antenna for wireless communication applications is presented. The multi-band is achieved by the patch,

which represents a combination of a rectangular and an isosceles-triangular patch. The part of the patch formed by the isosceles triangle has the same area as the part formed by the rectangle. The rectangular slots are inserted into the rectangular part, and the triangular slots are inserted into the isosceles-triangular part of the patch. The whole system is fed by a coaxial probe into the substrate, with an input impedance of 50 Ω .

2. ANTENNA DESIGN

The basic structure of the proposed antenna, shown in Figure 1, consists of 3 layers. The lower layer constitutes of ground plane covered by the substrate having a width of 6 cm and a length of 15 cm. The middle layer is the substrate which has a dielectric constant $\epsilon_r = 2.2$ and a height of 0.32 cm. The upper layer, which is the patch, consists of a rectangle with a length of 4 cm and a width of 3 cm, joined with an isosceles triangle having the same area as the rectangular patch and a base of 3 cm and a height of 8 cm.

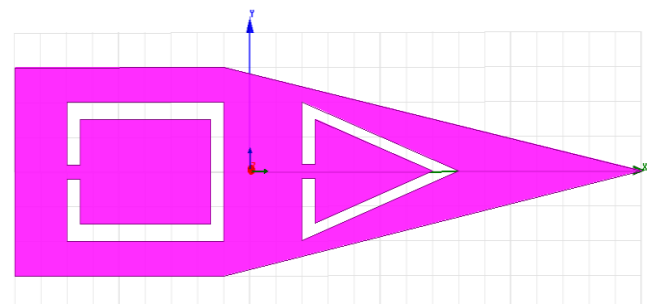


Fig 1: Proposed Patch Structure

Inside the rectangular patch, two rectangular slots were inserted, one with a length of 3 cm and a width of 2 cm and the other with a length of 2.5 cm and a width of 1.5 cm. Also, inside the triangular patch, two triangular slots were inserted, one with a base of 2 cm and a height of 3 cm and the other with a base of 2.5 cm and a height of 2.25 cm. Stubs were used in order to join the rectangular and triangular slots with a length of 0.25 cm and a width of 0.2 cm. Placing of slots into the structure increases the beamwidth and increase resonances.

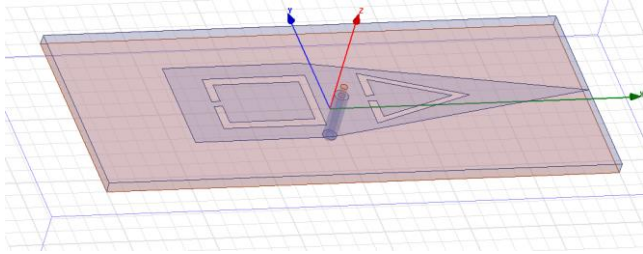


Fig 2: Antenna model

A parametric study and an optimization were done, in order to find the best feeding point of the structure. Several points were tested in order to get an overview of the defined functioning of the antenna, and to monitor the effect of both the rectangular and triangular slots. Figure 2 shows the proposed antenna on Rogers RT/ Duroid 5880 (tm). At first, the feeding point is chosen near the edge of the rectangle on its right-hand side. Results showed the operation of the antenna at less number of bands and also with low gain since the feeding point is bit far from the radiating elements, in order to obtain optimum operation of the antenna. When the feeding point is closer to the radiating elements, the functioning of the antenna is more effective with relatively high gain.

3. RESULTS

A. Return Losses

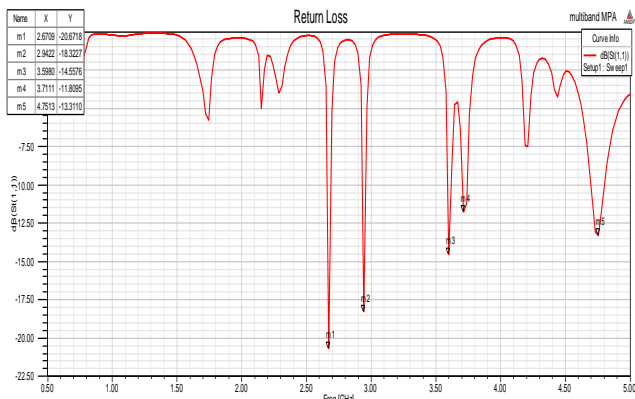


Fig 3: Return loss

From Figure 3, the return losses of the proposed antenna at 2.67 GHz, 2.94 GHz, 3.59 GHz, 3.71 GHz and 4.75 GHz are -20.67 dB, -18.32 dB, -14.55 dB, -11.80 dB and -13.31 dB respectively.

B. Gain

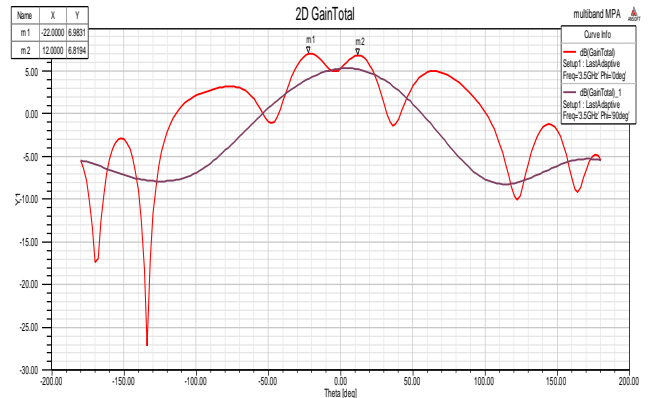


Fig 4: 2D- Gain Total

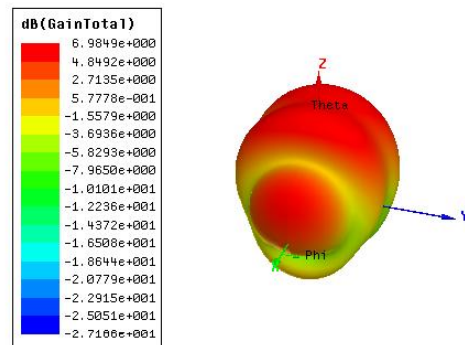


Fig 5: 3D- Gain Total

Figure 4 and Figure 5 shows the gain of the antenna in 2D and 3D patterns. The gain of the proposed antenna is 6.9831 dB.

C. Radiation Patterns

The far electric fields of the rectangular patch are as follows

$$E_{\theta} = \frac{K e^{-j k_0 r}}{r} \cos(k_0 h \sqrt{\epsilon_r} \cos \theta) \frac{\sin(\frac{\pi W}{\lambda_0} \sin \theta \sin \varphi) \cos(\frac{\pi L}{\lambda_0} \sin \theta \cos \varphi) \cos \varphi}{\sin \theta \sin \varphi}$$

$$E_{\varphi} = \frac{-K e^{-j k_0 r}}{r} \cos(k_0 h \sqrt{\epsilon_r} \cos \theta) \frac{\sin(\frac{\pi W}{\lambda_0} \sin \theta \sin \varphi) \cos(\frac{\pi L}{\lambda_0} \sin \theta \cos \varphi) \cos \theta}{\sin \theta \sin \varphi}$$

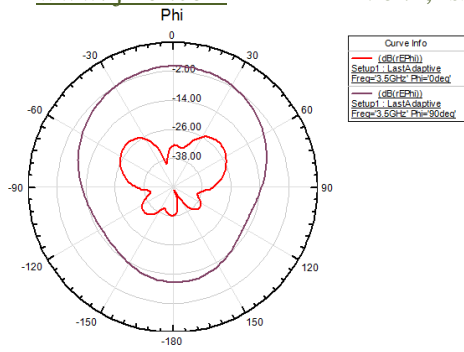


Fig 6: Gain along Phi

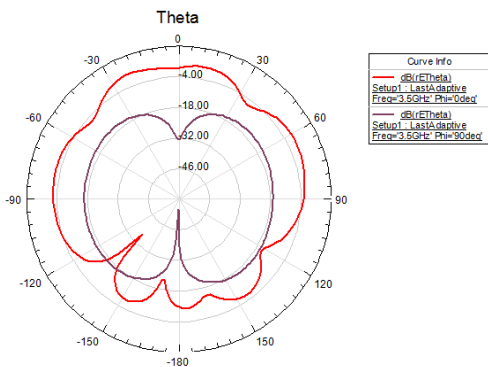


Fig 7: Gain along Theta

The radiation pattern for the proposed antenna for Phi and Theta at 0 deg and 90 deg is shown in the Figure 6 and Figure 7.

D. Field Distributions

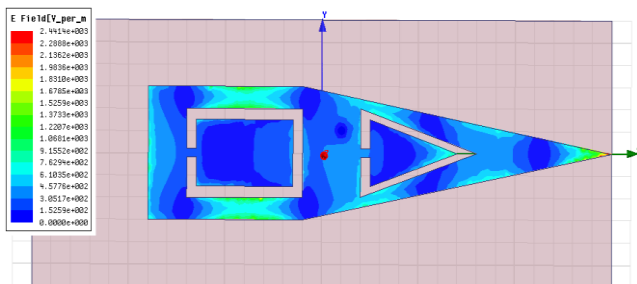


Fig 8: E-field Distributions

The effect produced by an electric charge that exerts a force on charged objects is the E-field and its distribution in the patch is as shown in the Figure 8.

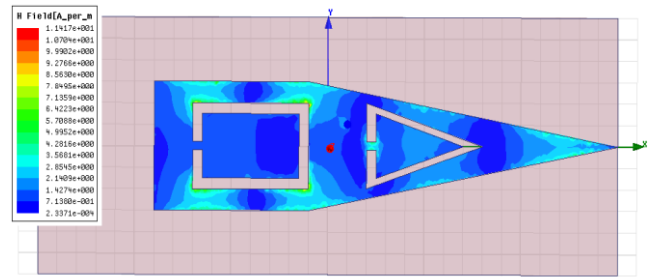


Fig 9: H-field Distributions

The measured intensity of a magnetic field in the patch is shown in Figure 9.

E. Current Distribution

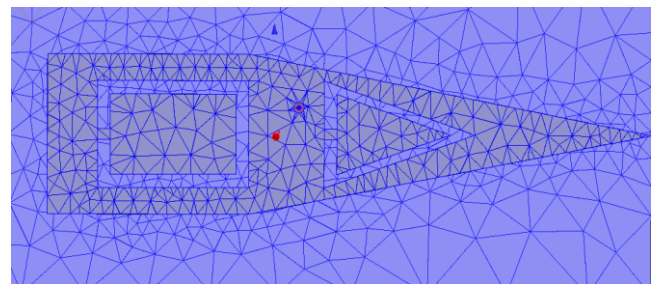


Fig 10: Mesh Plot

Figure 10 shows the current distribution on the patch and from the figure it is clear that current distribution is more on the patch when compared to the substrate.

4. CONCLUSION

From the analysis of multi-band rectangular-triangular slotted patch antenna on Rogers RT/ Duroid 5880 (tm) substrate exhibits broadband resonance with relatively high gain. Thus, this model is well suitable for various S-band applications like wireless CCTV and wireless video links, WLAN applications (2.8 GHz), WLAN, WiMax, wireless WiMax, 802.11a applications (3.5 GHz) and also suitable for radar system applications (4.75 GHz). The antenna is successfully designed and optimized. The results show that the antenna not only has multi-band characteristic but also have good radiation patterns.

5. ACKNOWLEDGMENT

The authors would like to thank the management of KL University, Vijayawada for excellent encouragement during the tenure of work.

6. REFERENCES

- [1] J Costantine, K Y. Kabalan, Ali El-Hajj, and Mohammad Rammal, "A New Multi-band Microstrip Antenna Design for Wireless Communications", *IEEE Transactions on Antennas and Propagation Magazine*, Vol. 49, No. 6, Dec 2007.
- [2] Wen Liao, Qing-Xin Chu and Shu Du, "Tri-band Circularly Polarized Stacked Microstrip Antenna for GPS and CNSS Applications", *IEEE Transactions*, 2010.
- [3] W. S. Chen and F. M. Hsieh, "A Broadband Design for a Printed Isosceles Triangular Slot Antenna for Wireless Communications", *Microwave Journal*, 48, 7, July 2005, pp. 98-112.
- [4] C. A. Balanis, *Antenna Theory Analysis and Design, Second Edition*, New York, Wiley, 1997.
- [5] J. Constantine, *New Multi Band Design for a Microstrip Patch Antenna* Masters thesis, American University of Beirut, October 2006.
- [6] Kin-Lu Wong, *Compact and Broadband Microstrip Antennas*, A Wiley-Interscience Publication, 2002.
- [7] Jawad K. Ali, "A New Compact Size Microstrip Patch Antenna with Irregular Slots for Handheld GPS Application", *Eng. & Technology*, Vol. 26, No. 10, 2008.
- [8] Neenansha Jain, Anubhuti Khare, Rajesh Nema, "E-Shape Microstrip Patch Antenna on Different Thickness for pervasive Wireless Communication", *International Journal of Advanced Computer Science and Applications*, Vol. 2, No. 4, 2011.
- [9] Nishamol M. S., Aanandan C. K., Mohanan P. and Vasudevan K., "Dual Frequency Reconfigurable Microstrip Antenna using Varactor Diodes", *IEEE Transactions*, 2011.
- [10] Salman Haider, "Microstrip Patch Antennas for Broadband Indoor Wireless Systems", 2003.
- [11] T. Sittironnarit and M. Ali, "Analysis and Design of a Dual-Band Folded Microstrip Patch Antenna for Handheld Device Application", *IEEE Southeast Conference Proceedings*, 2002, pp. 255-258.
- [12] P. A. Ambresh, P. M. Hadalgl, "Experimental Results of Compact Dual Frequency Microstrip Slot Antenna", *IJECT* Vol. 2, Issue 3, Sept. 2011.
- [13] David M. Pozar and Sean M. Duffy, "A Dual-Band Circularly Polarized Aperture-Coupled Stacked Microstrip Antenna for Global Positioning Satellite", *IEEE Transactions on Antennas and Propagation*, Vol. 45, No. 11, November 1997.
- [14] Raj Kumar, Nivedita Mishra, "On the Design of Square-Cut Circular Multiband Antenna for Wireless Communication", *2nd International Conference and workshop on Emerging Trends in Technology (ICWET)2011 Proceedings published by International Journal of Computer Applications (IJCA)*.
- [15] S. Hebib, H. Aubert, O. Pascal, N. Fonseca, L. Ries and J. M. Lopez, "Pyramidal multi-band antennas for GPS/Galileo/MicroSat Application", *IEEE* 2007.
- [16] Vinod K. Singh, Zakir Ali, "Dual Band U-Shaped Microstrip Antenna for Wireless Communication", Vol. 2(6), ISSN, 2010.

Resolution of Navier-Stokes equations using mixed finite element method and the (D+N) boundary condition

Jaouad El-Mekkaoui¹, Abdeslam Elakkad², and Ahmed Elkhalfi¹

¹(Laboratoire Génie Mécanique - Faculté des Sciences et Techniques B.P. 2202 - Route d'Imouzzer - Fès Maroc)

²(Discipline: Mathématiques, Centre de Formation des Instituteurs Sefrou, B.P: 243 Sefrou Maroc)

ABSTRACT

In this paper we introduced the Navier-Stokes equations with a boundary (D+N) condition. We have shown the existence and uniqueness of the solution of the weak formulation obtained. We used the discretization by mixed finite element method. In order to evaluate the performance of the method, the numerical results are compared with some previously published works or with others coming from commercial code like Adina system.

Keywords- Navier-Stokes Equations, Finite Element Method, Adina system.

I. INTRODUCTION

The mixed finite element method, based on the velocity-pressure formulation, is being increasingly used for the numerical solution of the Navier-Stokes equations. In this paper we will discuss the mixed finite element method for the nonlinear Navier-Stokes problem with a boundary condition noted (D+N). Under suitable existence and uniqueness conditions of the weak formulation of this problem.

The plan of the paper is as follows. Section II presents the model problem used in this paper. The discretization by mixed finite elements is described in section III. Numerical experiments carried out within the framework of this publication and their comparisons with other results are shown in Section IV.

II. INCOMPRESSIBLE NAVIER-STOKES EQUATIONS

We consider the steady-state Navier-stokes equations for the flow;

$$-\nu \nabla^2 \vec{u} + \vec{u} \cdot \nabla \vec{u} + \nabla p = \vec{f} \text{ in } \Omega \quad (1)$$

$$\nabla \cdot \vec{u} = 0 \text{ in } \Omega \quad (2)$$

Where $\nu > 0$ a given constant is called the kinematic viscosity, \vec{u} is the fluid velocity, p is the pressure field. ∇ is the gradient, $\nabla \cdot$ is the divergence and ∇^2 is the Laplacien operator, $\vec{f} \in [L^2(\Omega)]^2$.

The boundary value problem that is considered is the system (1)-(2) posed on two or three-dimensional domain Ω , with boundary conditions on $\partial\Omega$ noted (D+N) and given by

$$(D+N) : b_0 \vec{u} + \nu \frac{\partial \vec{u}}{\partial n} - \vec{n} p = \vec{t} \text{ and } \vec{u} \cdot \vec{n} = l \text{ in } \partial\Omega, \quad (3)$$

Ω is a bounded and connected domain of \mathbb{R}^2 with a Lipschitz continuous boundary $\partial\Omega$ where \vec{n} denote the outward pointing normal to the boundary, $\vec{t} \in [L^2(\partial\Omega)]^2$ and b_0 is a function defined on $\partial\Omega$ verify: There are two strictly positive constants α_0 and β_0 such that:

$$\alpha_0 \leq b_0(x) \leq \beta_0 \text{ for all } x \in \partial\Omega \quad (4)$$

The presence of the nonlinear convection term $\vec{u} \cdot \nabla \vec{u}$ means that boundary value problems associated with the Navier-stokes equations can have more than one solution.

We define the spaces:

$$h^1(\Omega) = \left\{ u : \Omega \rightarrow \mathbb{R} / u; \frac{\partial u}{\partial x}; \frac{\partial u}{\partial y} \in L^2(\Omega) \right\} \quad (5)$$

$$H^1(\Omega) = [h^1(\Omega)]^2 \quad (6)$$

$$L_0^2(\Omega) = \left\{ q \in L^2(\Omega) / \int_{\Omega} q d\Omega = 0 \right\} \quad (7)$$

$$H_{n,l}^1(\Omega) = \left\{ \vec{v} \in H^1(\Omega) / \vec{v} \cdot \vec{n} = l \text{ in } \partial\Omega \right\} \quad (8)$$

$$V_{n,l}(\Omega) = \left\{ \vec{v} \in H_{n,l}^1(\Omega) / \nabla \cdot \vec{v} = 0 \text{ in } \Omega \right\} \quad (9)$$

$$\tilde{V}_{n,l}(\Omega) = \left\{ \vec{v} \in [D(\Omega)]^2; \vec{v} \cdot \vec{n} = l \text{ in } \partial\Omega \text{ and } \nabla \cdot \vec{v} = 0 \text{ in } \Omega \right\} \quad (10)$$

The standard weak formulation of the Navier-Stokes flow problem (1) – (2)-(3) is the following

find $(\vec{u}, p) \in H_{n,l}^1(\Omega) \times L_0^2(\Omega)$ such that

$$\left\{ \begin{aligned} & \nu \int_{\Omega} \nabla \bar{u} : \nabla \bar{v} d\Omega + \int_{\partial\Omega} b_0 \bar{u} \cdot \bar{v} d\gamma + \int_{\Omega} (\bar{u} \cdot \nabla \bar{u}) \bar{v} d\Omega - \int_{\Omega} p \nabla \cdot \bar{v} d\Omega = \int_{\Omega} \bar{f} \cdot \bar{v} d\Omega + \int_{\Omega} \bar{f} \cdot \bar{v} d\Omega \\ & - \int_{\Omega} q \nabla \bar{u} d\Omega = 0 \end{aligned} \right. \quad (11)$$

for all $(\bar{v}, q) \in H_{n,l}^1(\Omega) \times L_0^2(\Omega)$.

Let the bilinear forms

$$a : H_{n,l}^1(\Omega) \times H_{n,l}^1(\Omega) \rightarrow IR, \quad b : H_{n,l}^1(\Omega) \times L_0^2(\Omega) \rightarrow IR,$$

and the trilinear

$$\text{forms } a : H_{n,l}^1 \times H_{n,l}^1 \times H_{n,l}^1 \rightarrow IR \text{ and}$$

$$a_1 : H_{n,l}^1 \times H_{n,l}^1 \times H_{n,l}^1 \rightarrow IR$$

$$a(\bar{u}, \bar{v}) = \nu \int_{\Omega} \nabla \bar{u} : \nabla \bar{v} d\Omega + \int_{\partial\Omega} b_0 \bar{u} \cdot \bar{v} d\gamma \quad (12)$$

$$b(\bar{u}, q) = - \int_{\Omega} q \nabla \bar{u} d\Omega \quad (13)$$

$$d(q, \Psi) = \int_{\Omega} q \cdot \Psi d\Omega \quad (14)$$

$$c(\bar{z}, \bar{u}, \bar{v}) = \int_{\Omega} (\bar{z} \cdot \nabla \bar{u}) \cdot \bar{v} d\Omega \quad (15)$$

Given the functional $L : L_0^2(\Omega) \rightarrow IR$

$$L(\bar{v}) = \int_{\partial\Omega} \bar{f} \cdot \bar{v} d\Omega + \int_{\Omega} \bar{f} \cdot \bar{v} d\Omega \quad (16)$$

The underlying weak formulation (11) may be restated as

find $(\bar{u}, p) \in H_{n,l}^1(\Omega) \times L_0^2(\Omega)$ such that

$$\begin{cases} a(\bar{u}, \bar{v}) + c(\bar{u}, \bar{u}, \bar{v}) + b(\bar{v}, q) = L(\bar{v}) \\ b(\bar{u}, q) = 0 \end{cases} \quad (17)$$

for all $(\bar{v}, q) \in H_{n,l}^1(\Omega) \times L_0^2(\Omega)$.

In the sequel we can assume that $l = 0$ and $\bar{f} = \bar{0}$ and we will study the existence and uniqueness of the solution of the problem (17), for that we need the following results.

Lemma 2.1.

1) There is two strictly positive constants c_1 and c_2 such that

$$c_1 \|\bar{v}\|_{1,\Omega} \leq \|\bar{v}\|_{J,\Omega} \leq c_2 \|\bar{v}\|_{1,\Omega} \text{ for all } \bar{v} \in H_{n,0}^1(\Omega) \quad (18)$$

With

$$\begin{aligned} \|\bar{v}\|_{J,\Omega} &= \left(\|\bar{v}\|_{1,\Omega}^2 + \|\bar{v}\|_{0,\Omega}^2 \right)^{\frac{1}{2}} \\ &= \left(\int_{\Omega} \nabla \bar{v} : \nabla \bar{v} d\Omega + \int_{\partial\Omega} \bar{v} \cdot \bar{v} d\gamma \right)^{\frac{1}{2}} \end{aligned} \quad (19)$$

$$\begin{aligned} \|\bar{v}\|_{1,\Omega} &= \left(\|\bar{v}\|_{1,\Omega}^2 + \|\bar{v}\|_{0,\Omega}^2 \right)^{\frac{1}{2}} \\ &= \left(\int_{\Omega} \nabla \bar{v} : \nabla \bar{v} d\Omega + \int_{\Omega} \bar{v} \cdot \bar{v} d\gamma \right)^{\frac{1}{2}} \end{aligned} \quad (20)$$

2) $(H_{n,0}^1(\Omega), \|\cdot\|_{J,\Omega})$ is a real Hilbert space

3) There exists $M > 0$ such that

$$a(\bar{u}, \bar{v}) \leq M \|\bar{u}\|_{J,\Omega} \|\bar{v}\|_{J,\Omega} \quad (21)$$

for all $(\bar{u}, \bar{v}) \in H_{n,0}^1(\Omega) \times H_{n,0}^1(\Omega)$

$$4) b(\bar{v}, q) \leq \sqrt{2} \|q\|_{0,\Omega} \|\bar{v}\|_{J,\Omega} \quad (22)$$

for all $(\bar{v}, q) \in H_{n,0}^1(\Omega) \times L_0^2(\Omega)$

5) There exists $m > 0$ such that:

$$c(\bar{z}, \bar{u}, \bar{v}) \leq m \|\bar{z}\|_{J,\Omega} \|\bar{u}\|_{J,\Omega} \|\bar{v}\|_{J,\Omega} \quad (23)$$

for all $\bar{z}, \bar{u}, \bar{v} \in H_{n,0}^1(\Omega)$

$$6) c(\bar{z}, \bar{u}, \bar{v}) = -c(\bar{z}, \bar{v}, \bar{u}) \text{ for all } \bar{z}, \bar{u}, \bar{v} \in V_{n,0}(\Omega) \quad (24)$$

$$7) c(\bar{z}, \bar{u}, \bar{u}) = 0 \text{ for all } \bar{z}, \bar{u}, \bar{u} \in V_{n,0}(\Omega) \quad (25)$$

$$8) a_1(\bar{w}, \bar{v}, \bar{v}) \geq \alpha \|\bar{v}\|_{J,\Omega}^2 \text{ and } a(\bar{v}, \bar{v}) \geq \alpha \|\bar{v}\|_{J,\Omega}^2 \quad (26)$$

for all $\bar{w}, \bar{v}, \bar{v} \in V_{n,0}(\Omega)$

9) $\bar{u}_m \rightarrow \bar{u}$ weakly in $V_{n,0}(\Omega)$ (as $m \rightarrow \infty$) implies that

$$\lim_{m \rightarrow \infty} a_1(\bar{u}_m, \bar{u}_m, \bar{v}) = a_1(\bar{u}, \bar{u}, \bar{v}) \text{ for } \bar{v} \in V_{n,0}(\Omega) \quad (27)$$

Proof. For 1, 2, 3 and 4 see [9].

5) Let $\bar{z}, \bar{u}, \bar{v} \in H_{n,0}^1(\Omega)$, we have

$$|c(\bar{z}, \bar{u}, \bar{v})| \leq \beta' \|\bar{z}\|_{1,\Omega} \|\bar{u}\|_{1,\Omega} \|\bar{v}\|_{1,\Omega},$$

(see lemma 2.1, chapter IV in [6]). (18), (19) and (20) implies

$$|c(\bar{z}, \bar{u}, \bar{v})| \leq \frac{\beta'}{c_1} \|\bar{z}\|_{J,\Omega} \|\bar{u}\|_{J,\Omega} \|\bar{v}\|_{J,\Omega},$$

6) Let $(\bar{z}, \bar{u}, \bar{v}) \in (V_{n,0}(\Omega))^3$, we have

$$\begin{aligned} c(\bar{z}, \bar{u}, \bar{v}) + c(\bar{z}, \bar{v}, \bar{u}) &= \int_{\Omega} \bar{z} \cdot (\nabla \bar{u} \cdot \bar{v} + \nabla \bar{v} \cdot \bar{u}) d\Omega \\ &= \int_{\Omega} \bar{z} \cdot \nabla(\bar{u} \cdot \bar{v}) d\Omega \end{aligned}$$

By Green formula we have

$$c(\bar{z}, \bar{u}, \bar{v}) + c(\bar{z}, \bar{v}, \bar{u}) = \int_{\partial\Omega} (\bar{z} \cdot \bar{n})(\bar{u} \cdot \bar{v}) d\gamma - \int_{\Omega} \text{div } \bar{z}(\bar{u} \cdot \bar{v}) d\Omega$$

Since $\bar{z} \in V_{n,0}(\Omega)$, then $\bar{z} \cdot \bar{n} = 0$ and $\text{div } \bar{z} = \bar{0}$ therefore

$$c(\bar{z}, \bar{u}, \bar{v}) = -c(\bar{z}, \bar{v}, \bar{u})$$

7) It is easy from 6.

8) Let $\bar{w} \in V_{n,0}(\Omega)$, using (24) and (4) then gives then gives

$$\begin{aligned}
 a_1(\bar{w}, \bar{v}, \bar{v}) &= a(\bar{v}, \bar{v}) + c(\bar{w}, \bar{v}, \bar{v}) \\
 &= a(\bar{v}, \bar{v}) \\
 &= \nu \int_{\Omega} \nabla \bar{v} : \nabla \bar{v} d\Omega + \int_{\partial\Omega} b_0 \bar{v} \cdot \bar{v} d\gamma \\
 &\leq \nu \int_{\Omega} \nabla \bar{v} : \nabla \bar{v} d\Omega + \alpha_0 \int_{\partial\Omega} \bar{v} \cdot \bar{v} d\gamma \\
 &\leq \alpha \left(\int_{\Omega} \nabla \bar{v} : \nabla \bar{v} d\Omega + \alpha_0 \int_{\partial\Omega} \bar{v} \cdot \bar{v} d\gamma \right) \\
 &= \alpha \|\bar{v}\|_{J,\Omega}^2
 \end{aligned}$$

with $\alpha = \max(\alpha_0, \nu)$.

9) The same proof of V.Girault and P.A. Raviart in [6] page 115.

Theorem 2.2. b satisfies the inf-sup condition:

There exists a constant $\beta > 0$ such that

$$\sup_{\bar{v} \in H_{n,0}^1(\Omega)} \frac{\int_{\Omega} q \nabla \cdot \bar{v} d\Omega}{\|\bar{v}\|_{J,\Omega}} \geq \beta \|q\|_{0,\Omega} \text{ for all } q \in L_{0,\Omega}^2(\Omega) \quad (28)$$

Proof. Let $q \in L_{0,\Omega}^2(\Omega)$, We have

$$\begin{aligned}
 \sup_{\bar{v} \in H_0^1(\Omega)} \frac{\int_{\Omega} q \nabla \cdot \bar{v} d\Omega}{\|\bar{v}\|_{1,\Omega}} &\geq \beta \|q\|_{0,\Omega} \text{ [6], since} \\
 H_0^1(\Omega) &= \left\{ \bar{v} \in H^1(\Omega) / \bar{v} = \bar{0} \text{ in } \partial\Omega \right\} \subset H_{n,0}^1(\Omega) \\
 \text{and } \|\bar{v}\|_{J,\Omega} &= \|\bar{v}\|_{1,\Omega} \text{ if } \bar{v} \in H_0^1(\Omega), \text{ then}
 \end{aligned}$$

$$\begin{aligned}
 \sup_{\bar{v} \in H_{n,0}^1(\Omega)} \frac{\int_{\Omega} q \nabla \cdot \bar{v} d\Omega}{\|\bar{v}\|_{J,\Omega}} &\geq \sup_{\bar{v} \in H_0^1(\Omega)} \frac{\int_{\Omega} q \nabla \cdot \bar{v} d\Omega}{\|\bar{v}\|_{J,\Omega}} \\
 &= \sup_{\bar{v} \in H_0^1(\Omega)} \frac{\int_{\Omega} q \nabla \cdot \bar{v} d\Omega}{\|\bar{v}\|_{1,\Omega}} \\
 &\geq \beta \|q\|_{0,\Omega}
 \end{aligned}$$

We define the “big” symmetric bilinear form

$$B((\bar{u}, p); (\bar{v}, q)) = a(\bar{u}, \bar{v}) + b(\bar{v}, p) + b(\bar{u}, q) \quad (29)$$

According the theorems 1.2 and 1.4, chapter IV in [6], (26) and (27) ensure the existence at least one

pair $(\bar{u}, p) \in H_{n,l}^1(\Omega) \times L_0^2(\Omega)$ satisfies (17).

We define

$$N = \sup_{\bar{z}, \bar{u}, \bar{v} \in H_{n,0}^1(\Omega)} \frac{|c(\bar{z}, \bar{u}, \bar{v})|}{\|\bar{z}\|_{J,\Omega} \|\bar{u}\|_{J,\Omega} \|\bar{v}\|_{J,\Omega}} \quad (30)$$

$$\|\bar{f}\|_* = \sup_{\bar{v} \in H_{n,0}^1(\Omega)} \frac{\int_{\Omega} \bar{f} \cdot \bar{v} d\Omega}{\|\bar{v}\|_{J,\Omega}} \quad (31)$$

Then a well-know (sufficient) condition for uniqueness is that forcing function is small in the sense that

$$\|\bar{f}\|_* \leq \frac{\nu}{N}$$

(it suffices to apply theorems 1.3 and 1.4 chapter IV in [6]).

Theorem 2.3.

Assume that v and $\bar{f} \in (L^2(\Omega))^2 \leq \frac{\nu^2}{N}$ satisfy the

following condition

$$\left| \int_{\Omega} \bar{f} \cdot \bar{v} d\Omega \right| \leq \delta \frac{\nu^2}{N} \|\bar{v}\|_{J,\Omega} \text{ for all } \bar{v} \in H_{n,0}^1(\Omega) \quad (32)$$

For some fixed number $\delta \in [0,1]$ then there exists a unique solution $(\bar{u}, p) \in H_{n,l}^1(\Omega) \times L_0^2(\Omega)$ of (17) and it holds

$$\|\bar{u}\| \leq \delta \frac{\nu}{N} \quad (33)$$

Proof. The some proof of theorem 2.4 chapter IV in [6].

Lemma 2.4. There are two strictly positive constants s_1 and s_2 such that:

$$s_1 \|\bar{v}\|_{J,\Omega}^2 \leq a(\bar{v}, \bar{v}) \leq s_2 \|\bar{v}\|_{J,\Omega}^2 \quad (34)$$

for all $\bar{v} \in H_{n,0}^1(\Omega)$

Proof. Using (4) and (12) gives,

$$\begin{aligned}
 a(\bar{v}, \bar{v}) &= \nu \int_{\Omega} \nabla \bar{v} : \nabla \bar{v} d\Omega + \int_{\partial\Omega} b_0 \bar{v} \cdot \bar{v} d\gamma \\
 \nu \int_{\Omega} \nabla \bar{v} : \nabla \bar{v} d\Omega + \alpha_0 \int_{\partial\Omega} \bar{v} \cdot \bar{v} d\gamma &\leq a(\bar{v}, \bar{v}) \\
 \text{and } a(\bar{v}, \bar{v}) &\leq \nu \int_{\Omega} \nabla \bar{v} : \nabla \bar{v} d\Omega + \beta_0 \int_{\partial\Omega} \bar{v} \cdot \bar{v} d\gamma \quad (35)
 \end{aligned}$$

We take $s_1 = \text{Min}(\nu, \alpha_0)$ and $s_2 = \text{Max}(\nu, \beta_0)$ we obtain (34).

III. MIXED FINITE ELEMENT APPROXIMATION

Our goal here is to consider the stationary Navier-Stokes equations with boundary condition (D+N) in a two-dimensional domain and to approximate then by mixed finite element method.

Mixed finite element discretization of the weak formulation of Navier-stokes equations gives rise to nonlinear system of algebraic equations.

Two classical iterative procedures for solving this system are Newton iteration and Picard iteration.

Let $T_h; h > 0$, be a family of triangulations of Ω . For any $T \in T_h$, ω_T , is of triangles sharing at least one edge with element T, $\tilde{\omega}_T$ is the set of triangles sharing at least one vertex with T. Also, for an element edge E, ω_E denotes the union of triangles sharing E, while $\tilde{\omega}_T$ is the set of triangles sharing at least one vertex whit E. Next, ∂T is the set of the tree edges of T we denote by $\varepsilon(T)$ and N_T the set of its edges and vertices, respectively.

We let $\varepsilon_h = \bigcup_{T \in T_h} \varepsilon(T)$ denotes the set of all edges split into interior and boundary edges.

$$\varepsilon_h = \varepsilon_{h,\Omega} \cup \varepsilon_{h,\partial\Omega}$$

$$\text{Where, } \varepsilon_{h,\Omega} = \{E \in \varepsilon_h : E \subset \Omega\}$$

$$\varepsilon_{h,\partial\Omega} = \{E \in \varepsilon_h : E \subset \partial\Omega\}$$

We denote by h_T the diameter of a simplex, by h_E the diameter of a face E of T, and we set $h = \max_{T \in T_h} \{h_T\}$.

A discrete weak formulation is defined using finite dimensional spaces $X_{n,0}^h \subset H_{n,0}^1(\Omega)$ and

$$M_0^h \subset L_0^2(\Omega).$$

The discrete version of (11) is:

find $(\bar{u}_h, p_h) \in X_{n,0}^1(\Omega) \times M_0^h(\Omega)$ such that

$$\begin{cases} a(\bar{u}_h, \bar{v}_h) + c(\bar{u}_h, \bar{u}_h, \bar{v}_h) + b(\bar{v}_h, q_h) = L(\bar{v}_h) \\ b(\bar{u}_h, q_h) = 0 \end{cases} \quad (36)$$

for all $(\bar{v}_h, q_h) \in X_{n,0}^1(\Omega) \times M_0^h(\Omega)$ such that

We define the appropriate bases for the finite element spaces, leading to non linear system of algebraic equations. Linearization of this system using Newton iteration gives the finite dimensional system:

find $(\delta\bar{u}_h, \delta p_h) \in X_{n,0}^1(\Omega) \times M_0^h(\Omega)$ such that

$$\begin{cases} c(\delta\bar{u}_h, \bar{u}_h, \bar{v}_h) + c(\bar{u}_h, \delta\bar{u}_h, \bar{v}_h) + v \int_{\Omega} \nabla \delta\bar{u}_h : \nabla \bar{v}_h d\Omega + \int_{\partial\Omega} b_0 \delta\bar{u}_h \cdot \bar{v}_h d\gamma - \int_{\Omega} \delta p_h \nabla \cdot \bar{v}_h d\Omega = R_k(\bar{v}_h) \\ - \int_{\Omega} q_h \nabla \cdot \delta\bar{u}_h d\Omega = r_k(q_h) \end{cases} \quad (37)$$

for all $(\bar{v}_h, q_h) \in X_{n,0}^1(\Omega) \times M_0^h(\Omega)$.

Here, $R_k(\bar{v}_h)$ and $r_k(q_h)$ are the non linear residuals associated with the discrete formulations (36). To define the corresponding linear algebra problem, we use a set of vector-valued basis functions.

$$\{\bar{\varphi}_j\}_{j=1 \dots n_u}, \text{ so that}$$

$$\bar{u}_h = \sum_{j=1}^{n_u} u_j \bar{\varphi}_j; \quad \delta\bar{u}_h = \sum_{j=1}^{n_u} \Delta u_j \bar{\varphi}_j \quad (38)$$

We introduce a set of pressure basis functions $\{\Psi_k\}_{k=1 \dots n_p}$

$$\text{and set } p_h = \sum_{k=1}^{n_p} p_k \Psi_k; \quad \delta p_h = \sum_{k=1}^{n_p} \Delta p_k \Psi_k \quad (39)$$

Where n_u and n_p are the numbers of velocity and pressure basis functions, respectively.

We find that the discrete formulation (38) can be expressed as a system of linear equations

$$\begin{pmatrix} A + N + W & B^T \\ B & 0 \end{pmatrix} \begin{pmatrix} \Delta u \\ \Delta p \end{pmatrix} = \begin{pmatrix} f \\ 0 \end{pmatrix} \quad (40)$$

The system is referred to as the discrete Newton problem. The matrix A is the vector Laplacian matrix and B is the divergence matrix

$$A = [a_{i,j}];$$

$$a_{i,j} = v \int_{\Omega} \nabla \varphi_i : \nabla \varphi_j d\Omega + \int_{\partial\Omega} b_0 \varphi_i \cdot \varphi_j d\gamma \quad (41)$$

$$B = [b_{k,j}]; \quad b_{k,j} = - \int_{\Omega} \Psi_k : \nabla \varphi_j d\Omega \quad (42)$$

for $i, j = 1, \dots, n_u$ and $k = 1, \dots, n_p$.

The vector-convection matrix N and the Newton derivative matrix W are given by

$$N = [n_{i,j}]; \quad n_{i,j} = \int_{\Omega} (\bar{u}_h \cdot \nabla \bar{\varphi}_j) \bar{\varphi}_i d\Omega \quad (43)$$

$$W = [w_{i,j}]; \quad w_{i,j} = \int_{\Omega} (\bar{\varphi}_j \cdot \nabla \bar{u}_h) \bar{\varphi}_i d\Omega \quad (44)$$

For i and $j = 1, \dots, n_u$. The Newton derivative matrix is symmetric.

The right-hand side vectors in (41) are

$$f = [f_i]; \quad f_i = \int_{\Omega} \bar{f} \bar{\varphi}_i d\Omega \quad (45)$$

for $j = 1, \dots, n_u$.

For Picard iteration, we give the discrete problem

$$\begin{pmatrix} A + N & B^T \\ B & 0 \end{pmatrix} \begin{pmatrix} \Delta u \\ \Delta p \end{pmatrix} = \begin{pmatrix} f \\ 0 \end{pmatrix} \quad (46)$$

IV. NUMERICAL SIMULATION

In this section some numerical results of calculations with mixed finite element Method and ADINA System will be presented. Using our solver, we run the Backward-facing step problem (17) with a number of different model parameters.

Example. Backward-facing step problem.

This example represents flow in a rectangular duct with a sudden expansion. A Poiseuille flow profile is imposed on the inflow boundary $\Gamma_1 = (x = -1, 0 \leq y \leq 1)$, and a no-flow (zero velocity) condition is imposed on the walls. The (D+N) condition (47) is applied at the outflow boundary $\Gamma_5 = (x = 5, -1 \leq y \leq 1)$, and automatically sets the mean outflow pressure to zero.

$$\begin{cases} p - \nu \frac{\partial u_x}{\partial x} = 10^{-14} u_x \\ -\frac{\partial u_y}{\partial x} = 10^{-14} u_y \end{cases} \quad (47)$$

With these data, see that the (D+N) condition is satisfied, just take $b_0 = 10^{-14}$ on $\Gamma_5 = (x = 5, -1 \leq y \leq 1)$;

$$b_0 = 10^{28} \text{ on } \Gamma_2 \cup \Gamma_3 \cup \Gamma_4; \quad \vec{t} = (10^{28}; 0) \text{ on } \Gamma_1;$$

$$\vec{t} = (0; 0) \text{ on the other four boundary}$$

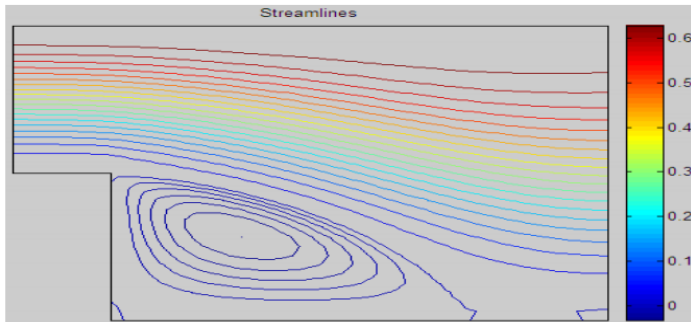


Fig.1. Equally distributed streamline plot associated with a 32×96 square grid, $P_1 - P_2$ approximation and $Re=200$.

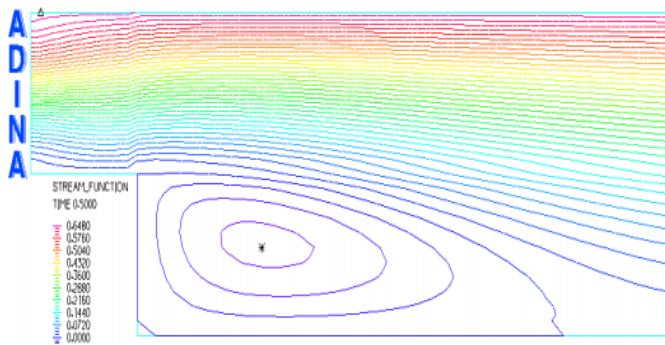


Fig.2. The solution computed with ADINA System. The show the Streamlines associated with a 32×96 square grid.

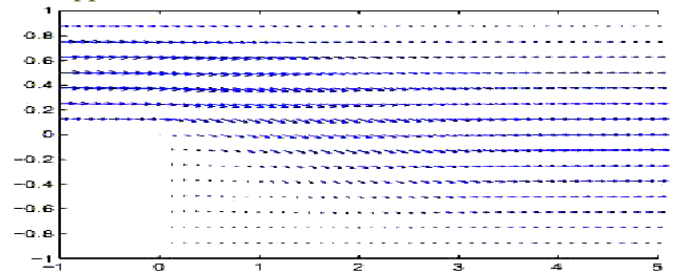


Fig.3. Velocity vectors solution by MFE associated with a 32×96 square grid and $Re=200$.

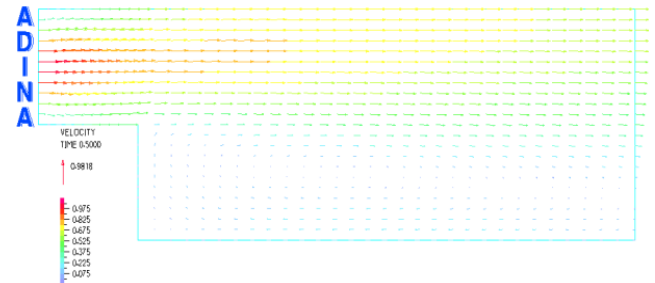


Fig.4. Velocity vectors solution by ADINA system associated with a 32×96 square grid and $Re=200$.

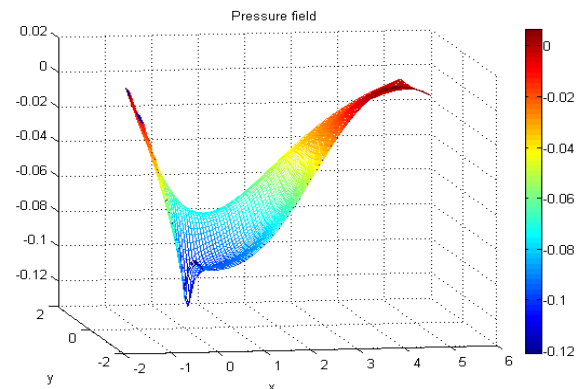


Fig.5. Pressure plot for the flow with a 32×96 square grid.

The two solutions are therefore essentially identical. This is very good indication that our solver is implemented correctly.

V. CONCLUSION

In this work, we were interested in the numerical solution of the partial differential equations by simulating the flow of an incompressible fluid. We applied the mixed finite element method to the resolution of the Navier-Stokes equations with boundary condition noted (D+N). Numerical results, either resulting from the literature, or resulting from calculation with commercial software like Adina system.

ACKNOWLEDGEMENTS

The authors would like to appreciate the referees for giving us the several corrections.

REFERENCES

- [1] Alexandre Ern, Aide-mémoire Eléments Finis, Dunod, Paris, 2005.
- [2] P.A. Raviart, J. Thomas, Introduction l'analyse numérique des équations aux dérivées partielles, Masson, Paris, 1983.
- [3] E. Creuse, G. Kunert, S. Nicaise, A posteriori error estimation for the Stokes problem: Anisotropic and isotropic discretizations, Mathematical Models and Methods in Applied Sciences, 14, 2004, 1297-1341.
- [4] P. Clement, Approximation by finite element functions using local regularization, RAIRO. Analyse, Numérique, 2, 1975, 77-84.
- [5] T. J. Oden, W.Wu, and M. Ainsworth, An a posteriori error estimate for finite element approximations of the Navier-Stokes equations, Computer Methods in Applied Mechanics and Engineering, 111, 1994, 185-202.
- [6] V. Girault and P.A. Raviart, Finite Element Approximation of the Navier-Stokes Equations, Springer-Verlag, Berlin Heidelberg New York, 1981.
- [7] H. Elman, D. Silvester, A. Wathen, Finite Elements and Fast Iterative Solvers: with Applications in Incompressible Fluid Dynamics, Oxford University Press, Oxford, 2005.
- [8] R. Verfurth, A Review of A Posteriori Error Estimation and Adaptive Mesh-Refinement Techniques, Wiley-Teubner, Chichester, 1996.
- [9] J. El-Mekkaoui, A. Elakkad and A. Elkhalfi, A finite element approximation of the Stokes equations with the boundary condition of type (D+N), International Journal of Modern Engineering Research, Vol.2, Issue.1, Jan-Feb 2012, 464-472.
- [10] M. Ainsworth, J. Oden, A posteriori error estimates for Stokes' and Oseen's equations, SIAM Journal of Numerical Analytic, 34, 1997, 228-245.
- [11] R. E. Bank, B.Welfert, A posteriori error estimates for the Stokes problem, SIAM Journal of Numerical Analytic, 28, 1991, 591-623.
- [12] C. Carstensen, S.A. Funken. A posteriori error control in low-order finite element discretizations of incompressible stationary flow problems. Mathematics of Computation, 70, 2001, 1353-1381.
- [13] D. Kay, D. Silvester, A posteriori error estimation for stabilized mixed approximations of the Stokes equations, SIAM Journal on Scientific Computing, 21, 1999, 1321-1336.
- [14] R. Verfurth, A posteriori error estimators for the Stokes equations, Journal of Numerical Mathematics, 55, 1989, 309-325.
- [15] H. Elman, D. Silvester, A. Wathen, Finite Elements and Fast Iterative Solvers: with Applications in Incompressible Fluid Dynamics, Oxford University Press, Oxford, 2005.
- [16] V. John. Residual a posteriori error estimates for two-level finite element methods for the Navier-Stokes equations, Applied Numerical Mathematics, 37, 2001, 503-518.
- [17] D.H. Wu, I.G. Currie. Analysis of a posteriori error indicator in viscous flows. International Journal of Numerical Methods for Heat and Fluid Flow, 12, 2001, 306-327.

Unified Power Quality Conditioner for Enhancement of Power Quality and Hybrid Power Generation Injection to Grid

C.K.Sundarabalan¹, P.Sathishbabu²

*(Student, Department of Electrical and Electronics Engineering, Anna University of Technology Madurai, India

** (Assistant Professor, Department of Electrical and Electronics Engineering, Anna University of Tech. Madurai, India

ABSTRACT

Power quality problems have become more complex at all level of power system. The power electronic based power conditioning devices can be the effective solution to improve the quality of power supplied to the distributed system. UPQC is custom power device, designed to compensate both source current and load voltage imperfections. In this paper the design of combined operation of unified power quality conditioner and a hybrid power generation is proposed. The proposed system is composed of series and shunt inverters, PV array and WECS connected to DC link which is able to compensate the voltage sag, swell, harmonics and voltage interruption. The proposed system is able to inject the active power to grid in addition to its ability in improvement of power quality in distribution system. The performance of the proposed UPQC system is validated through simulations using MATLAB/SIMULINK.

Keywords – Power quality (PQ), Photovoltaic Array (PV), Series Active Filter (SEF), Shunt Active Filter (SAF), Unified Power Quality conditioner (UPQC), Wind Energy Conversion System (WECS).

I. INTRODUCTION

The integration of renewable energy into existing power system presents technical challenges and that requires consideration of voltage regulation, stability, power quality problems [14]. The power quality is an essential customer focused measure and it's greatly affected by the operation of a distribution and transmission network. Nowadays, generation of electricity from renewable sources has improved very much. Since most renewable energy sources are intermittent in nature, it is a challenging task to integrate a significant portion of renewable energy resources into the power grid infrastructure. Traditional electricity grid was designed to transmit and distribute electricity generated by large conventional power plants. The electricity flow mainly takes place in one direction from the centralized plants to consumers. In contrast to large power plants, renewable energy plants have less capacity, and are installed in a more distributed manner at different locations. The integration of distributed renewable energy generators has great impacts on the operation of the grid and calls for new grid infrastructure. UPQC was widely studied by many researchers as an eventual method to improve power quality in distribution system.

The quality of the electrical power is affected by many factors like harmonic contamination, due to non-linear loads, such as large converters, rectifiers, voltage and current flickering due to arc in arc furnaces, sag and swell

due to the switching of the loads etc. One of the many solutions is the use of a combined system of shunt and series active filters like unified power quality conditioner a new member of the custom power family. This device combines a shunt active filter together with a series active filter in a back to back configuration, to simultaneously compensate the supply voltage and the load current or to mitigate any type of voltage and current fluctuations and power factor correction in a power distribution network. UPQC is able to compensate current harmonics reactive power, voltage distortions and control load flow but cannot compensate voltage interruption because of not having sources. The interest in renewable energy has been increasing rapidly because renewable energy might play an important role in the future power system. A small distributed generation (DG) should be interconnected with the power system in order to maintain the frequency and voltage. Several studies proposed on the interconnection system for distributed generation with the power system through the inverter because the inverter gives versatile functions in proving the ability of distributed generation. The attention to distributed generating sources is increasing day by day. The reason is their important roll they will likely play in the future of power systems. Recently, several studies are accomplished in the field of connecting DG to grid using power electronic converters [9]. Here grid interface shunt inverters are considered more where the reason is low sensitiveness of DG to grid parameters and DG power transferring facility using this approach. Although DG needs more controls to reduce the problems like grid power quality and reliability. PV and WECS distributed generation sources which provides a part of human required energy now a day and will provide in the future. The greatest share of this kind of energy in the future will be its usage in interconnected system.

II. PROPOSED SYSTEM

The quality of the power leads to a direct economic impact on utilities, their customers, and suppliers. Custom power devices including power electronic interface can be the effective solution for increasing power quality problems because they can provide fast response and flexible compensation. In this paper UPQC and hybrid power generation combined system has been presented as shown in Fig. 1. The advantage of proposed combined system is voltage interruption compensation and active power injection to grid in addition to the mentioned abilities. Also this proposed system has higher efficiency and functioning ability in compare with other common PVs and WECS also cause reduction in system total cost. In this strategy both load voltage and source current sensing is required for

compensate current harmonics and source voltage interruption simultaneously.

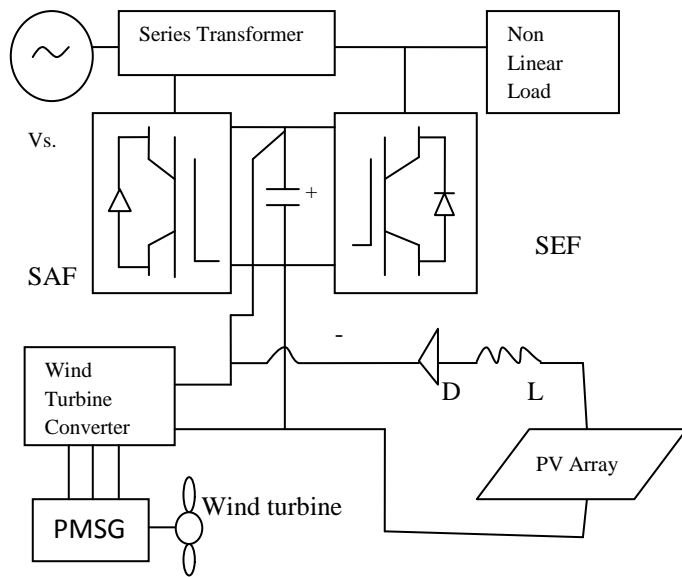


Fig. 1: configuration of proposed system

Normally, UPQC has two voltage source inverters in three phase four wire or three phase three wire configuration. One inverter is called series inverter is connected through transformers between the source and the common connection point. The other inverter called shunt inverter is connected in parallel with the common connection point through transformers. The series inverter operates as voltage source, while the shunt inverter operates as a current source.

UPQC has compensation capabilities for the harmonic current, reactive power compensation, the voltage disturbances, and the power flow control. But UPQC has no capability in compensating the voltage interruption because there is no energy storage. This paper proposes a new configuration of UPQC that has DG connected to the dc link through the rectifier. The UPQC can compensate the voltage interruption in the source, while the DG supplies power to the source and load or load only. There are two operating modes in the proposed system. One is called the interconnected mode, in which the DG provides power to the source and the load. The other is called islanding mode, in which the distributed generation provides power to the load within its power rating.

III. HYBRID SYSTEM MODELING

The Stand-alone hybrid generation systems are usually used to supply isolated areas or locations interconnected to a weak grid. They combine several generation modules, typically assimilating different renewable energy sources. The application of these hybrid topologies reduces the probability of energy supply shortage and, with the incorporation of energy storage; it allows to eliminate the background diesel generator (which is commonly required in generation systems based on a single renewable energy source). In this context, many electrical generation hybrid system frequently combine solar and wind energy sources (taking advantage of their complementary nature) with a

lead-acid battery bank (to overcome periods of scarce generation). The topology of the hybrid system under consideration in this paper is depicted in Fig. 2. The wind generation module is constituted by a windmill, permanent-magnet synchronous generator (PMSG), a rectifier, and a dc/dc converter to interface the generator with the dc bus. The converter commands the voltage on the PMSG terminals, indirectly controlling the operation point of the wind turbine and, consequently, its power generation. The solar module comprises several PV panels connected to the dc bus via a dc/dc converter. Similar to the wind subsystem, the converter controls the operation point of the PV panels. The dc bus collects the energy generated by both modules and delivers it to the load if necessary.

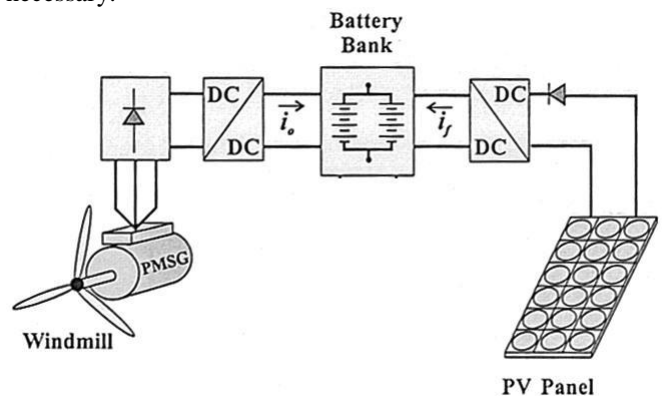


Fig. 2: Hybrid Generation system

The wind turbine of the stand-alone hybrid system already presented in Fig. 2 [11], drives a multi-polar PMSG whose terminal voltage equations can be described by the following matrix expression

$$V_{abc} = R_{sabc} i_{abc} + S \Phi_{m abc} \quad (1)$$

Where R_s is the stator phase winding resistance matrix, Φ_m is the matrix of flux linked by the stator windings, and S is the Laplace operator. Expressing this model in a rotor reference frame, (1) can be written as

$$V_q = -R_s i_q - L_q S i_q - \omega_e L_q i_d + \omega_e \Phi_m \quad (2)$$

$$V_d = -R_s i_d - L_d S i_d - \omega_e L_d i_q \quad (3)$$

and the electromagnetic torque is given by

$$T_e = \frac{3P (\Phi_m i_q + (L_d - L_q) i_d i_q)}{4} \quad (4)$$

Where L_q and L_d are the stator inductances in the d-q axes, $\omega_e = P \omega_m / 2$ is the electrical angular speed, and the number of poles. As it is shown in Fig. 2, the PMSG is linked to the dc bus through a diode bridge rectifier and a dc/dc converter. This configuration presents to the PMSG terminals a pure active power load whose value can be modified through the duty cycle (δ) of the converter. All controls of the hybrid distributed generation are conducted by the inverter control, not only in normal state but also in case of occurring of disturbances such as sags or swells; the wind generator performs only a role of maintaining the dc-

link voltage in constant set point. Moreover, when any even happen in the distribution system, the PMSG supplies power required from the local load through the shunt inverter.

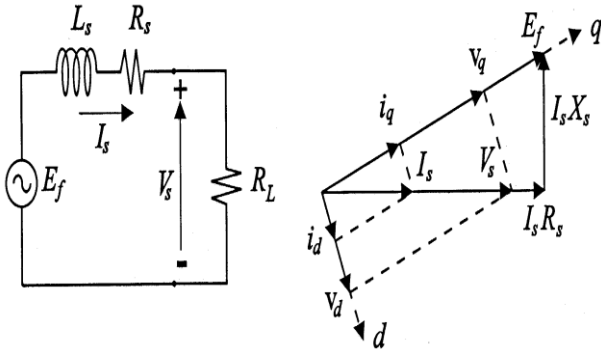


Fig. 3: Phase circuit and phasor diagram of the PMSG.

Fig. 3 shows a simple per phase equivalent circuit of the PMSG working under this condition and its corresponding phasor diagram. V_s and I_s are the line voltage and current in the PMSG terminals, respectively, E_f corresponds to the emf in the stator windings and X_s is the synchronous reactance. From this last figure, using simple mathematical relationships, (2) and (3) can be expressed in terms of the terminal PMSG voltage, as

$$\frac{V_s i_q}{\sqrt{i_q^2 + i_d^2}} = -R_s i_q - L_q S i_q - \omega_e L_q i_d + \omega_e \Phi_m \quad (5)$$

$$\frac{V_s i_d}{\sqrt{i_q^2 + i_d^2}} = -R_s i_d - L_d S i_d - \omega_e L_d i_q \quad (6)$$

Then, assuming a full bridge topology for the dc/dc converter, the relationship between the voltage on the dc bus terminals (V_b) and V_s can be described by the following expression:

$$V_s = \frac{\pi V_b U_x}{3\sqrt{3}} \quad (7)$$

where U_x is a simple function of the dc/dc converter duty cycle δ , given for this configuration by $U_x = Ktr/\delta$, with Ktr the winding ratio of the transformer included in the dc/dc converter. Thus, replacing (7) in (6) and operating, the latter can be rewritten as

$$i_q = -\frac{R_s}{L} i_q - \omega_e i_d + \frac{\omega_e \Phi_m}{L} - \frac{\pi V_b i_q U_x}{3L \sqrt{3(i_q^2 + i_d^2)}} \quad (8)$$

$$i_d = -\frac{R_s}{L} i_d - \omega_e i_q - \frac{\pi V_b i_d U_x}{3L \sqrt{3(i_q^2 + i_d^2)}} \quad (9)$$

Assuming an ideal static conversion, the current injected by the wind subsystem in the dc bus can be readily determined equating the input and output power of the dc/dc converter. As it was previously said, this paper deals with the regulation of the output power of the system by focusing in the control of the wind subsystem. The control design of the photovoltaic subsystem is not under consideration here, so its operation is represented by a variable but measurable current i_f injected in the dc bus. Similarly, assuming an ideal

voltage inverter, the load demand can be referred to the dc side as a measurable output current i_L . Therefore, the current across the battery bank can be written as

$$i_o = \frac{\pi \sqrt{i_q^2 + i_d^2} U_x}{2\sqrt{3}} \quad (10)$$

$$i_b = \frac{\pi \sqrt{i_q^2 + i_d^2} U_x}{2\sqrt{3}} + i_f - i_L \quad (11)$$

where i_f and i_L are measurable currents, and thus, assumed to be known currents. To complete the dynamic model of the system, it is necessary to outline the mechanical dynamic equation of the wind subsystem. Neglecting the friction term, this equation is given by (12)

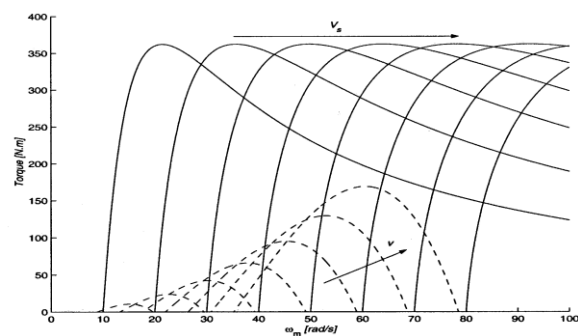


Fig. 4: Turbine and PMSG torque-shaft speed.

$$\dot{\omega}_e = \frac{P(T_t - T_e)}{2J} \quad (12)$$

where J is the inertia of the rotating system and T_t is the turbine torque. Thus, replacing (4) in (12) and considering that in radial flux PMSGs it holds $L_d=L_q=L_s=L$, (12) can be rewritten as

$$\dot{\omega}_e = \frac{P \left(T_t - \frac{3\Phi_m i_q}{4} \right)}{2J} \quad (13)$$

Therefore, considering (8), (11), and (13), and modeling the battery bank as a voltage source E_b connected in series with a resistance R_b and a capacitance C_b , a complete nonlinear dynamical model of the hybrid system may be written as

$$i_q = -\frac{R_s}{L} i_q - \omega_e i_d + \frac{\omega_e \Phi_m}{L} - \frac{\pi V_b i_q U_x}{3L \sqrt{3(i_q^2 + i_d^2)}} \quad (14)$$

$$i_d = -\frac{R_s}{L} i_d - \omega_e i_q - \frac{\pi V_b i_d U_x}{3L \sqrt{3(i_q^2 + i_d^2)}} \quad (15)$$

$$\dot{\omega}_e = \frac{P}{2J} \left(T_t - \frac{3P}{22} \Phi_m i_q \right) \quad (16)$$

$$\dot{V}_c = \frac{1}{C_b} \left(\frac{\pi}{2\sqrt{3}} \sqrt{i_q^2 + i_d^2} U_x + i_f - i_L \right) \quad (17)$$

where V_c is the voltage in the capacitor C_b , and the voltage on the dc bus terminals is given by (18)

$$V_b = E_b + V_c + \left(\frac{\pi}{2\sqrt{3}} \sqrt{i_q^2 + i_d^2} U_x + i_f - i_L \right) R_b \quad (18)$$

Fig. 4 shows in the torque shaft speed plane, the turbine torque (Tt) developed by a horizontal shaft turbine parameterized in terms of the wind speed (dashed line) and the generator torque (Te) curves parameterized in function of Vs in solid line. It is interesting to note that for a given constant voltage in the PMSG terminals, there exists a minimum shaft speed below which the wind subsystem cannot generate.

$$\omega_{elim} = \frac{V_s}{\phi_m} = \frac{\pi V_b U_x}{3\sqrt{3}\phi_m} \quad (19)$$

This lower limit arises naturally from the analysis of the phasor diagram depicted in Fig. 3, since it cannot be built for speeds that induce Ef smaller than Vs. Its expression is obtained in through the steady state analysis of a similar topology, and can be written for the electrical angular speed as given in above equation.

IV. CONTROL STRATEGY FOR UPQC

The control strategy is basically the way to generate reference signals for both shunt and series APF of UPQC. The compensation effectiveness of the UPQC depends on its ability to follow with a minimum error and time delay to calculate the reference signals to compensate the distortions, unbalanced voltages or currents or any other undesirable condition. In the following section an approach based on Unit Vector Templates Generation is explained to extract the reference voltage and current signals for series and shunt active power filters respectively. As for the shunt active filter of the UPQC it is represented by (Vdc/2)U2 with Ish as the first order low-pass interfacing filter and rsh as the losses of the shunt VSI. (Vdc/2)U2 represents the switched voltage across the shunt VSI output of the UPQC. The injection current of the shunt active filter is denoted by Iinj both U1 and U2 take the value of either -1 or 1 depending on the switching signal of the hysteresis control. The instantaneous current of the nonlinear load iL is expanded into 3 terms.

$$U_a = \sin(\omega t)$$

$$U_b = \sin(\omega t - 120) \quad (20)$$

$$U_c = \sin(\omega t + 120)$$

The first term iLp is the load Reference currents and voltages are generated using Phase Locked Loop (PLL).The control strategy is based on the extraction of Unit Vector Templates from the distorted input supply. These templates will be then equivalent to pure sinusoidal signal with unity (p.u.) amplitude [8]. Multiplying the peak amplitude of fundamental input voltage with unit vector templates of equation (20) gives the reference load voltage signals.

$$V_{abc}^* = V_m \cdot U_{abc} \quad (21)$$

The error generated is then taken to a hysteresis controller to generate the required gate signals for series APF. The unit

vector template can be applied for shunt APF to compensate the harmonic current generated by non-linear load. The extractions of three phase voltage reference signals are based on unit vector template generation. A phase Locked Loop (PLL) is used to extract the pure sinusoidal signal at fundamental frequency. The PLL gives signal in terms of sine and cosine functions. Here only sine terms are considered. As we know the supply voltage peak amplitude in advance, we can generate the unity supply voltage signals. To get the unity terminal voltage vector the terminal voltage are sensed and multiplied by a inverse of peak amplitude of fundamental terminal voltage. These unity voltage vectors are then taken into PLL. Thus the output of PLL is equal to the unity terminal voltage at fundamental frequency only. With proper phase angle shifting the unit vector templates for three phase are generated. We also know the desired load voltage level at load voltage, VL, with unit vector templates, gives the reference load voltage signals for series APF. The overall reference signal generation for series APF is shown in Fig. 5.

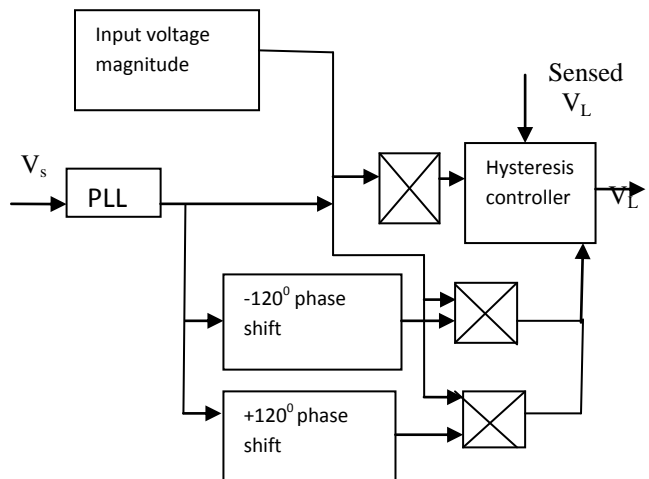


Fig. 5: Reference voltage signal generation for series APF

The shunt APF is used to compensate for current harmonics as well as to maintain the dc link voltage at constant level. To achieve the above mentioned task the dc link voltage is sensed and compared with the reference dc link voltage. A PI controller then processes the error. The output signal from PI controller is multiplied with unit vector templates of equation (1) giving reference source current signals. The source current must be equal to this reference signal. In order to follow this reference current signal, the 3-phase source currents are sensed and compared with reference current signals. The error generated is then processed by a hysteresis current controller with suitable band, generating gating signals for shunt APF. The UPQC uses two back-to-back connected three phase voltage source inverters sharing a common dc bus. The hysteresis controller is used here to control the switching of the both voltage source inverters. UPQC consists of series compensator and shunt compensator. The shunt compensator is controlled by a PWM current control algorithm, while the series converter is controlled by a PWM voltage control algorithm. The effectiveness of an active power filter depends basically on the design characteristics of the current controller, the method implemented to generate the reference current signal

template and gating signal generation used. The control scheme of shunt active filter must calculate the current reference waveform for each phase of the inverter, maintain the dc voltage as constant and generate the inverter gating signals.

4.1 REFERENCE CURRENT SIGNAL GENERATION

The unit vector templates can also be applied for shunt APF to compensate current harmonics currents generated by non-linear load. The shunt APF is used for compensate current harmonics as well as to maintain the dc link voltage at constant level. To achieve the aforementioned task the dc link voltage is sensed and compared with the reference dc link voltage. The error is then processed by a PI controller. The output of the PI controller then will be the peak amplitude of fundamental input current which must be drawn from the supply in order to maintain dc link voltage at constant level and to supply losses associated with UPQC. This peak amplitude is then multiplied with unit vector templates giving reference current signals for shunt APF as shown in Fig. 5. For static shunt compensator the instantaneous current of the nonlinear load i_L is expanded into 3 terms. The first term i_{Lp} is the load functions sent from PLL (Phase Locked Loop) in accordance with equation. (22)

$$I_{Ldq0} = T_{abc}^{dq0} i_{Labc} \tag{22}$$

By this transform, the fundamental positive sequence components are transformed into dc quantities in d and q axes, which can easily be extracted by low-pass, filter (LPF). The switching loss can cause the dc link capacitor voltage to decrease. Other disturbances such as unbalances and sudden variations of loads can also cause this voltage to fluctuate. In order to avoid this, a PI controller is used the input of the PI controller is the error between the actual capacitor voltage and the desired value, its output then added to the reference current component in the d-axis to form a new. All harmonic components are transformed into ac quantities with a fundamental frequency shift.

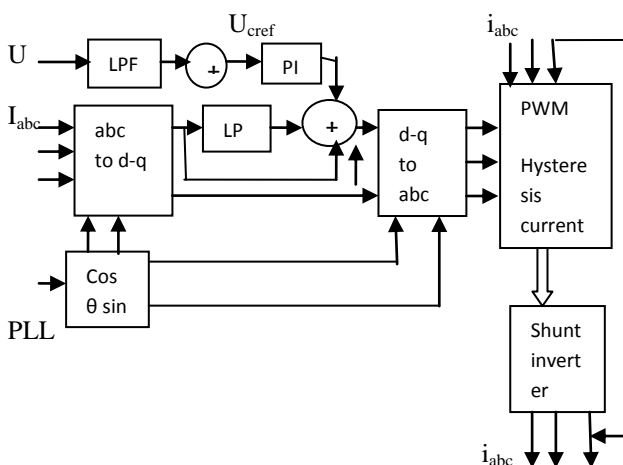


Fig. 6: Control of shunt converter for UPQC

$$I_{Lq} = \tilde{i}_{Lq} + \bar{\bar{i}}_{Lq} \tag{23}$$

$$\text{Since } i_L = i_j + i_c \tag{24}$$

In static series compensator the system side voltage may contain negative-zero-sequence as well as harmonics components which need to be eliminated by the series compensator. The control of the series compensator is shown in Figure.5. The system voltages are detected then transformed into synchronous dq-0 reference frame using equation (6).

$$U_{sdq0} = T_{abc}^{dq0} U_{sabc} = U_{sLi} + U_{sLn} + U_{sLo} + U_{sh} \tag{25}$$

4.2 GATING SIGNAL GENERATION

After extracting the reference voltage and current signals for series and shunt APF, the next step is to force the inverters to follow these reference signals. This can be done by switching the inverter IGBTs in a proper manner. To have the required gating signals, the modulation technique is used. Here the hysteresis band control technique based on PWM strategy is considered for both APF.

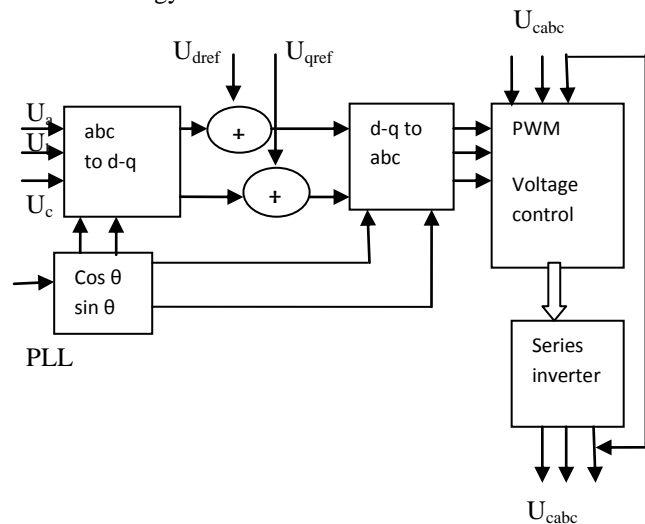


Fig. 7: Control of series converter for UPQC

The generated current reference signal s and the voltage signals for shunt and series APF are compared with actual sensed source current and the actual sensed load voltage respectively. The Hysteresis controller gives the switching instant whenever the error exceeds the hysteresis band.

V. SIMULATION RESULT

This study analyses the feasibility of protecting sensitive loads from power quality problems (voltage sags, flicker, harmonic current compensation, etc.) with compensation being performed at the distribution voltage. To verify the operating performance of the proposed unified power quality conditioner with hybrid power generation in a three phase electrical system, a phase locked loop extraction circuit with hysteresis controlled UPQC is simulated using MATLAB software. Fig. 8 show that the simulation diagram for unified power quality conditioner with hybrid (Photovoltaic's and Wind energy conversion system) power generation. The harmonic current injected by the non linear load appears at the source side giving the distorted source current waveform. Fig. 9 shows the waveform of distorted

supply voltage before compensation. It consists of fundamental frequency as well as the harmonic content due to the non-linear load.

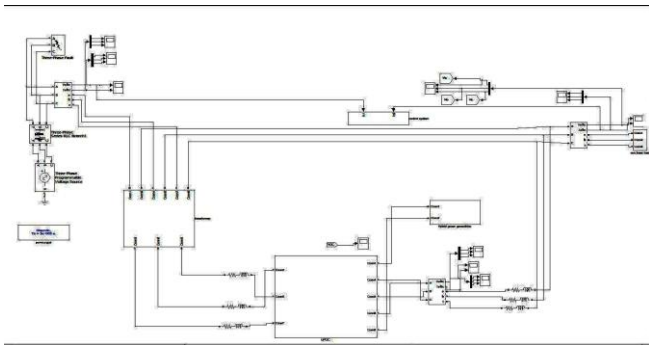


Fig. 8: Simulation diagram for UPQC with hybrid power

distortion. The hybrid power generation system proposed in this paper has the functions of improving power quality, blocking reverse power, and ensuring the continuity of electricity supply.

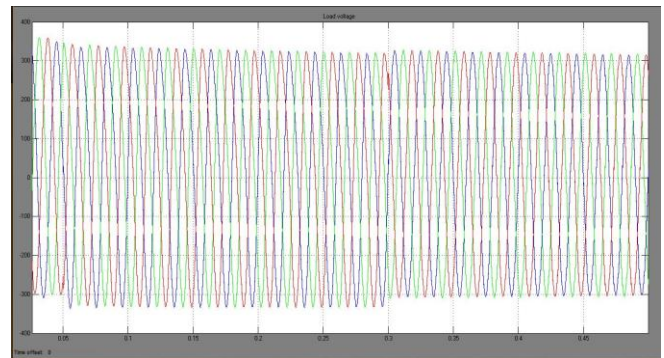


Fig. 11: Compensated load voltage

Fig. 11 shows the waveform of Load voltage after compensation. The waveform is more sinusoidal when compared with Fig. 8 and Fig. 9.

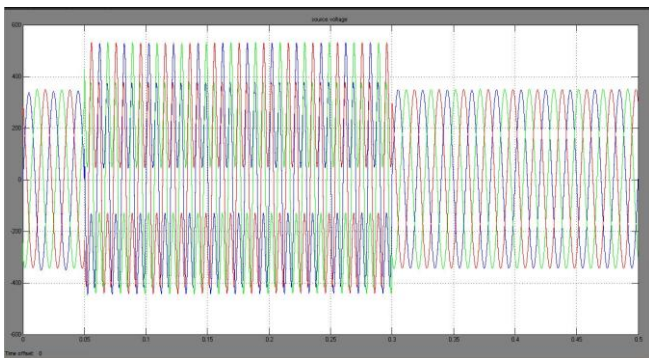


Fig. 9: Distorted source voltage

Fig. 10 shows the waveform of supply voltage interruption before compensation.

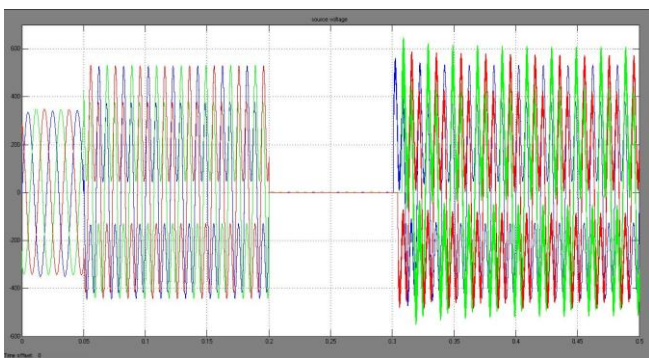


Fig. 10: Source voltage interruption

The main advantage of proposed method is to compensate deep voltage interruption. The interruption voltage present in the supply voltage is eliminated by interconnecting hybrid power generation into unified power quality conditioner through capacitor. The purpose of using this combined system is to reduce the harmonics effectively. The power factor also improved by using the combined system. The proposed model for the UPQC is to compensate input voltage harmonics and current harmonics caused by non linear load. The load current in both case is found to be content of all odd harmonic providing a total harmonic

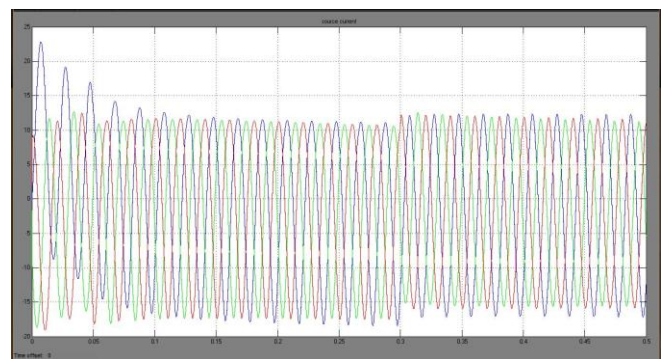


Fig. 12: Distorted source current

Fig. 12 shows the waveform of distorted source current before compensation. It consists of fundamental current as well as the harmonic current due to the non-linear load

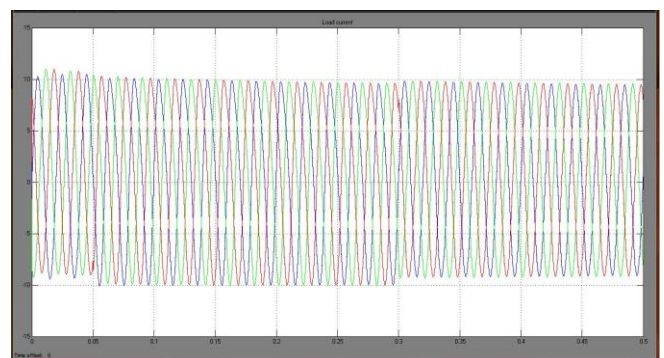


Fig. 13: Compensated load current

The Fast Fourier Transform (FFT) analysis of supply current after compensation the Total Harmonic Distortion of the supply current is reduced to 0.16% from 23.44%. Fig. 13 shows the waveform of Load voltage after compensation. PI controller used to eliminate error between the filter current

and the harmonic current. The purpose of controller is tuned to reduce the particular harmonics. The harmonic current present in the supply current is eliminated by using the shunt compensation device. The distortion present in the supply current is reduced when compared Fig. 12.

VI. CONCLUSION

In this paper, the results of analyzing combined operation of UPQC and hybrid power generation is explained. The proposed system is composed of series and shunt inverters, PV array and wind energy conversion system which can compensate the voltage sag, swell, interruption, and reactive power and harmonics in both islanding and interconnected modes. The advantage of proposed system is reducing the expense of hybrid power generation connection to grid because of applying UPQC shunt inverter and also is the ability of compensating the voltage interruption using UPQC because of connecting distributed generation to DC link. The proposed system can improve the power quality at the point of installation on power distribution system or industrial power systems.

REFERENCES

- [1] H. Akagi, H. Fuzita, A new power line conditional for harmonic compensation in power system, *IEEE Trans. Power Del.*, vol.10, no.3, pp.1570-1575, Jul.1995.
- [2] M.F. Farias, P.E. Battaiotto, Investigation of UPQC for sag compensation in wind farms to weak grid connection, *IEEE Conf.*, .2010.
- [3] N.G. Jayanthi, M. Basu, Rating requirement of UPQC to integrate the fixed speed induction generator type wind generation to the grid, *IET Renew.Power Gener.*, vol. 3, iss. 2, pp.133-143, May 2008.
- [4] M. Davari, H. Yazdanpanahi, Modeling the combination of UPQC and Photovoltaic array with multi input single output dc-dc converter, *IEEE Conf.*, 2008.
- [5] H. Toodeji, S.H. Fathi, Power management and performance improvement in integrated system of variable speed wind Turbine and UPQC, *IEEE Conf.*,2009.
- [6] G. Kinhal, P. Agarwal, Performance investigation of neural network based UPQC, *IEEE Trans. Power Del.*, vol.26, no.1, jan.2011.
- [7] Z. Cheni, E. Spooner, Grid power quality with variable speed wind turbines *IEEE Trans. Energy conversion*, vol.16, no.2, June 2001.
- [8] R.V.D. Ramarao, S.S. Dash, Power quality enhancement by UPQC using ANN and hysteresis control, *Int. jour. Computer app.*, vol.6, no.1, pp.975-8887, Sep.2010.
- [9] B. Han, B. Bae, Combined operation of UPQC with Distributed Generation, *IEEE Trans. Power Del.*, vol.21, no.1, Jan.2006.
- [10] I. Axente, M. Basu, A survey of distribution power quality, *IET Power Elect.*, vol.3, pp.542-551, 2010.
- [11] F. Valenciaga, F. Puleston, Power control of solar/wind generation system without wind measurement a passivity sliding mode approach, *IEEE Trans. Energy Con.*, vol.18, no.4, Dec.2003.
- [12] H. J. Boolean Understanding power quality problems IEEE New york press 2000.
- [13] B. Borowy, Z. Salamech, Methodology for optimally sizing the combination of battery bank and PV array in a wind/PV hybrid system, *IEEE Trans. Energy Con.*, vol.1, pp.367-375, June 1996.
- [14] A. Gosh, G. Ledwich, Power quality enhancement using custom power device, *Kluwer academic publisher*, pp.460, Jul.2002.
- [15] V. Khadkikar, A. Chandra, A novel concept of simultaneous voltage sag/swell and load reactive power compensation utilizing service inverter for UPQC, *IEEE Trans. Power Del.*, vol.26, no.9, Sep.2011.

Heat Transfer Analysis for Bare Tube Immersed In Gas-Solid Fluidized Bed of Large Particles Using Artificial Neural Network

Mahesh P. Joshi¹, Aparna V. Kulkarni²

¹(Lecturer in Marathwada Mitra Mandal's Polytechnic)

²(Lecturer in Sidhant College of Engg.)

Abstract - This paper presents heat transfer analysis of bare tube arrangement in gas-solid (air-solid) fluidized bed of large particles such as mustard(1.1mm), raagi (1.4mm) & bajara(2.1mm) also predictions are done by using Artificial Neural Network (ANN) based on the experimental data. Within the range of experimental conditions influence of bed particle diameter (D_p), fluidizing velocity (U) were studied, which are significant parameters affecting heat transfer. It is observed that the average heat transfer coefficient increases with the increase in fluidizing velocity. Here, feed-forward architecture and trained by back-propagation technique of Artificial Neural Network (ANN) is adopted to predict heat transfer analysis found from experimental results. The network predictions are found to be in very good agreement with the experimental observed values of bare tube heat transfer coefficient (h_b) and Nusselt number of bare tube (Nu_b).

Keywords: Fluidized bed; Heat transfer coefficient; Nusselt number.

I Introduction

Fluidized bed provide nearly isothermal environment with high rate of heat transfer to submerged objects due to thorough mixing, turbulent motion and large contact area between the gas and particles. The information available on bare tube in fluidized beds of large particles is relatively very limited. Also the information on heat transfer studies particularly in fluidized bed by artificial neural network is very limited.[1]

MATLAB is a high-level technical computing language and interactive environment for algorithm development, data visualization, data analysis, and numerical computation. An ANN is also called a simulated neural networks or commonly just neural networks is an interconnected group of artificial neurons and that uses a mathematical or computational model for information processing based on a connectionist approach to computation. A typical ANN consists of three layers, an input layer which takes the input variables from the problem under consideration, a hidden layer made up of artificial neurons that transform the inputs, and an output layer that stores the results. The most commonly used method for prediction in engineering is multi layer perceptrons (MLP).[7]

II Experimental set-up

The experimental facility consists of a square fluidizing column designed with provisions to install bare tube in the bed and other associated subsystems. The facility is suitably instrumented for measurement of bed pressure profile, bed temperature, surface temperature of the heat transfer tube, electrical energy supplied to heat transfer tube and air flow rate. Figure 1.1 shows the schematic of the experimental facility whose various subsystems are described in the following sections.

Air supply to the fluidized bed is from a centrifugal blower having a capacity of 850 m³/hr, which is driven by 0.746 electric motor. The blower sucks air from atmosphere and discharges from its spiral casing outlet into the delivery pipe, where a butterfly valve is provided for control of the air flow rate. The diffuser (tapering section) is provided to minimize the acceleration effects and to improve the quality of fluidization. The plenum chamber is made up of 1.5 mm thick mild steel plate and is fixed to a flange at its top end to accommodate the distributor plate.

In the present investigation, a nozzle type distributor is designed and fabricated, made of 4mm thick mild steel plate, having 24 nozzles arranged in a square array. Each nozzle with 4 holes of 3mm diameter giving an open area 1.5%. The test section consists of a square column in side 0.15 x 0.10 meters and height of 0.4 meter. One pair of opposite walls of the column is made out of 3mm thick fibre glass sheets, to facilitate visual observation, while the other two walls are made of 3mm thick mica sheets. In one of the sheets, two openings at the height of 2cm and 30cm above the distributor plate is provided to measure the bed pressure drop. On the same sheet openings are provided to accommodate thermocouples to measure the bed temperature along the bed height.

The heat transfer bare tube of length 110mm and 27.5mm outer diameter is made of brass. A 25.4mm diameter and 12.5mm diameter cartridge heater of length equal to 110mm is inserted inside the bare tube, supplies electrical heat input which is measured and controlled with a wattmeter. The ends of the heat transfer tube are fitted with nylon plugs of outside diameter 25.4mm and a thickness of 3mm to both ends to reduce axial heat loss. The bare tube heat transfer coefficient was computed from the measured heat input and the temperature of the heater tube surface by using the following relations:

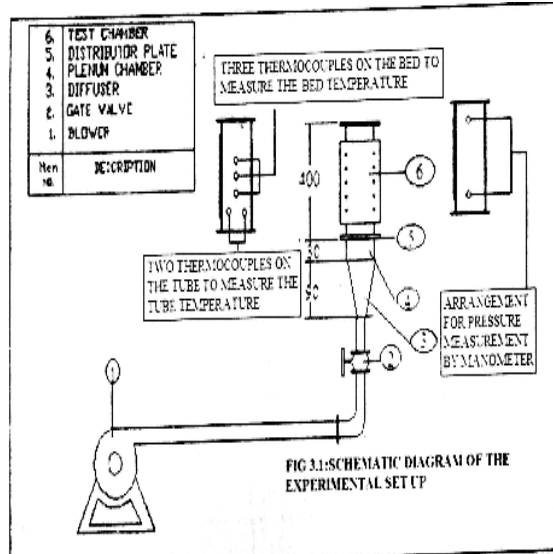
$$hb = Q_b / A_b (T_w - T_b), \quad W/m^2K$$

Where,

- Q_b = measured bare tube heat input, in watts
- A_b = surface area of bare tube, m²
- T_w = heat transfer tube surface temperature,
- T_b = temperature, K [1]

- PARTICLE : BAJARA
- STATIC BED HEIGHT : 80mm
- PARTICLE SIZE : 2.3 mm
- DIAMETER OF TUBE : 27.5 mm

Table-2.2



Sr. No.	Approach Velocity (m/s)	Heater Temperature Tw (°C)		Tw Avg. (°C)	Bed Temperature Tb (°C)			Tb Avg. (°C)	Heat Transfer Coefficient Hb (W/m ² K)
		T1	T2		Tb1	Tb2	Tb3		
1	17.3	155	150	152.5	37	43	36	38.67	48.254
2	18.2	145	140	142.5	36	42	35	37.67	52.40
3	19.0	111	106	108.5	35	40	34	36.33	76.109
4	19.4	105	103	104	34	39	33	35.33	79.988
5	19.8	95	93	94	35	38	33	35	93.098
6	20.6	92	88	90	33	37	32	34	98.086

III Results

2.0 SINGLE BARE TUBE

- PARTICLE : MUSTARD
- STATIC BED HEIGHT : 80mm
- PARTICLE SIZE : 1.1 mm
- DIAMETER OF TUBE : 27.5 mm

- PARTICLE : RAAGI
- STATIC BED HEIGHT : 80mm
- PARTICLE SIZE : 1.3mm
- DIAMETER OF TUBE : 27.5 mm

Table 2.1

Sr. No.	Approach Velocity (m/s)	Heater Temperature Tw (°C)		Tw Avg. (°C)	Bed Temperature Tb (°C)			Tb Avg. (°C)	Heat Transfer Coefficient Hb (W/m ² K)
		T1	T2		Tb1	Tb2	Tb3		
1.	15.8	149	145	147.0	32	37	36	35.0	49.04
2.	16.3	131	128	129.5	32	36	34	34.0	57.52
3.	16.8	111	110	110.5	32	35	34	33.67	71.49
4.	17.3	99	98	98.5	31	34	33	32.67	80.15
5.	17.7	87	86	86.5	31	33	32	32.0	100.78
6.	18.2	84	82	83.0	31	33	32	32.0	107.70

Table -2.3

Sr. No	Approach Velocity (m/s)	Heater Temperature Tw (°C)		Tw Avg. (°C)	Bed Temperature Tb (°C)			Tb Avg. (°C)	Heat Transfer Coefficient Hb (W/m ² K)
		T1	T2		Tb1	Tb2	Tb3		
1	17.3	147	143	145	36	47	37	40	52.31
2	18.2	113	111	112	35	46	36	39	75.24
3	19.0	102	101	101.5	34	45	36	38.33	86.95
4	19.4	94	90	92	33	44	35	37.33	100.47
5	19.8	85	82	83.5	33	42	34	36.33	116.44
6	20.6	82	78	80	32	41	33	35.33	122.96

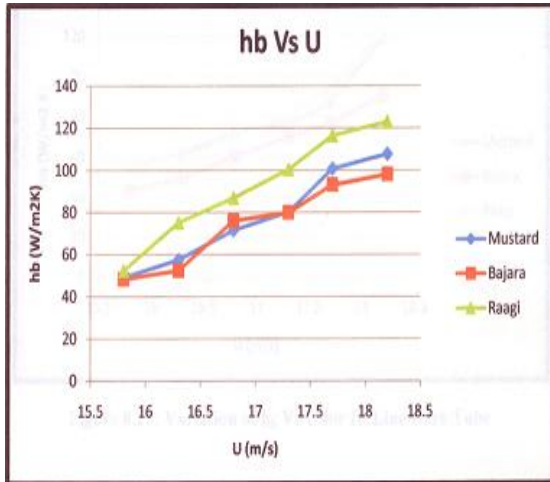


Figure 2.4: Variation of h_b Vs U for Single Tube

3.0 Single bare Tube- Comparison of experimental and predicted values in training large particles, for Heat Transfer Coefficient & Nusselt Number

Table 3.1

h(exp)	h(ann)	% error
49.04	49.0372	0.0057
57.52	57.5241	0.0071
71.49	71.4981	0.0113
80.15	80.1667	0.0208
48.25	48.2621	0.0252
52.4	52.4098	0.0187
76.1	76.1002	0.0002
79.98	79.9806	0.0007
52.31	52.3064	0.0069
75.24	75.2426	0.0034
86.95	86.9559	0.0068
100.47	100.492	0.0218

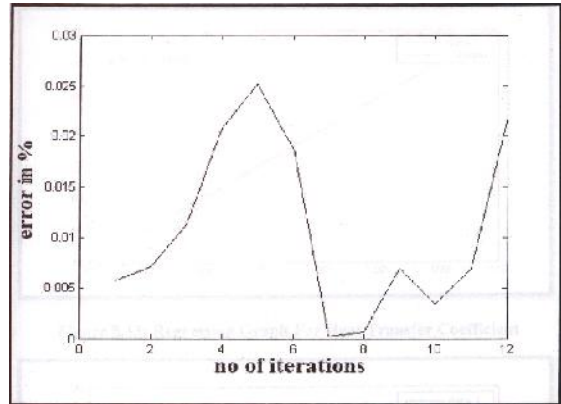


Figure 3.1: Error Graph for Heat Transfer Coefficient

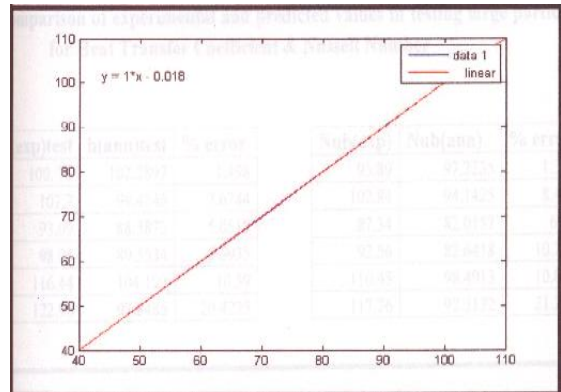


Figure 3.2: Regression Graph For Heat Transfer Coefficient

Table 3.2

Nub(exp)	Nub(ann)	% error
42.97	42.9673	0.0064
51.62	51.6227	0.0053
65.97	65.9747	0.0072
74.97	74.9808	0.0144
41.8	41.7803	0.0471
46.02	46.0129	0.0155
70.11	70.1095	0.0007
74.13	74.1304	0.0005
45.66	45.6567	0.0073
68.64	68.6417	0.0024
80.53	80.5324	0.003
94.23	94.2446	0.0155

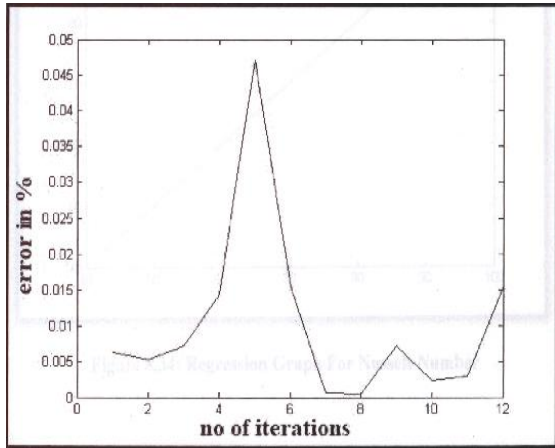


Figure 3.3: Error Graph for Nusselt Number

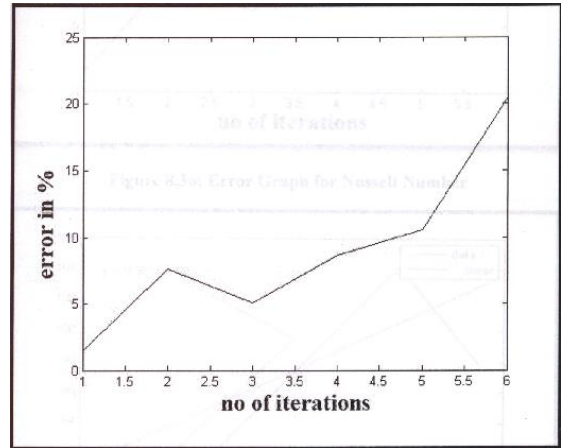


Figure 4.1: Error Graph for Heat Transfer Coefficient

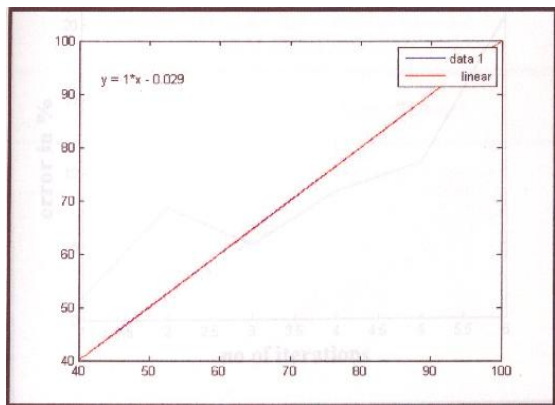


Figure 3.4: Regression Graph For Nusselt Number

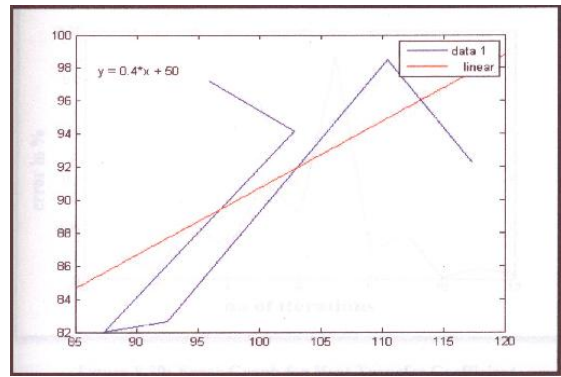


Figure 4.2: Linear Fitting for Heat Transfer Coefficient

4.0 Single bare Tube- Comparison of experimental and predicted values in testing large particles, for Heat Transfer Coefficient & Nusselt Number

Table 4.1

h(exp)test	h(ann)test	% error
100.78	102.2897	1.498
107.7	99.4346	7.6744
93.09	88.3872	5.0519
98.08	89.5534	8.6935
116.44	104.109	10.59
122.96	97.8485	20.4225

Table 4.2

Nub(exp)	Nub(ann)	% error
95.89	97.2235	1.3907
102.84	94.1425	8.4573
87.34	82.0157	6.096
92.56	82.6418	10.7154
110.45	98.4913	10.8272
117.26	92.3132	21.2748

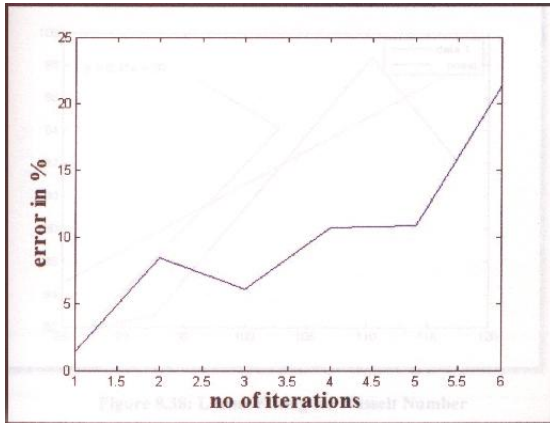


Figure 4.3: Error Graph for Nusselt Number

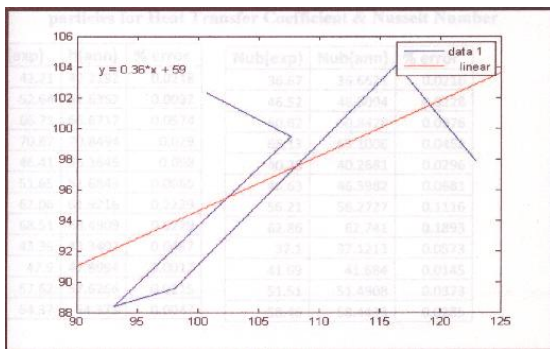


Figure 4.4: Linear Fitting for Nusselt Number

5.0 Single bare Tube- Comparison of experimental and correlated values in large particles, for Heat Transfer Coefficient & Nusselt Number

Table 5.1

h(exp)	h(corr)	% error
49.04	42.04	14.27
57.52	51.34	10.74
71.49	62.45	12.64
80.15	75.46	5.85
100.78	87.44	13.23
107.7	98.15	8.86
48.25	42.11	12.72
52.4	51.24	2.21
76.1	61.15	19.64
79.98	73.12	8.85
93.098	84.04	9.72
98.086	99.59	1.53
52.31	53.7	2.65
75.24	65.67	12.71
86.95	79.812	8.21
100.47	96.433	4.018
116.44	111.75	4.02
122.96	133.75	8.77

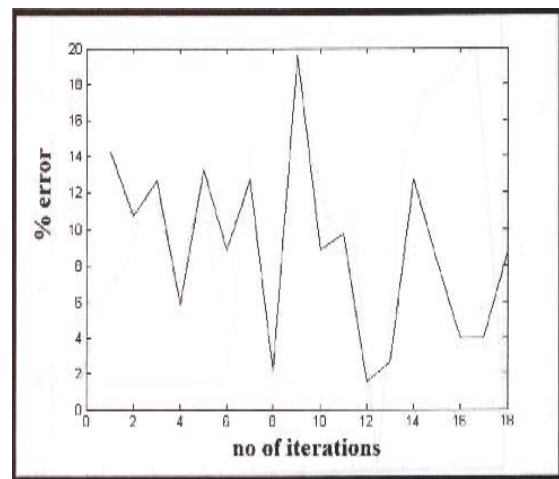


Figure 5.1: Error Graph for Single Tube For Heat Transfer Coefficient

Table 5.2

Nub(exp)	Nub (corr)	% error
42.97	38.81	9.69
51.62	47.44	8.1
65.97	57.65	12.61
74.97	69.66	7.08
95.89	80.72	15.82
102.84	96.61	6.05
41.8	38.416	8.11
46.02	46.7434	0.88
70.11	55.78	20.44
74.13	66.696	10.038
87.3488	76.66	12.236
92.5657	90.84	1.864
45.66	49.73	8.9
68.64	60.8112	11.41
80.53	73.901	8.23
94.23	89.2928	5.24
110.455	103.4834	6.311
117.263	123.8518	5.33

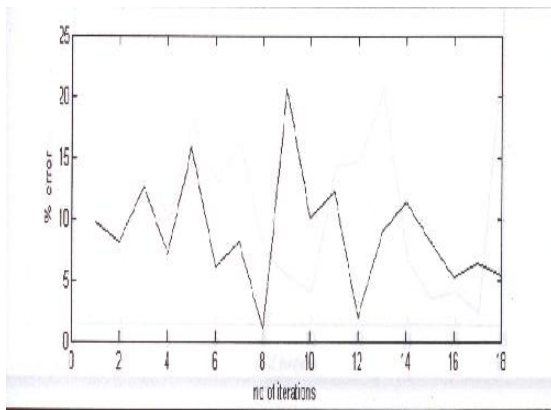


Figure 5.2: Error Graph For Single Tube For Nusselt Number

Conclusion

Heat transfer studies were conducted to obtain heat transfer parameters experimentally for single bare tube immersed in gas solid fluidized bed with air being used as the fluidizing medium at atmospheric condition in the initial stage. Also in the present study 70% of data is used for training and remaining 30% is used for testing. Performance evaluation of the network was done by

regression analysis and most of the result obtained; match very well with experimental data in training and testing. Based on the experimental data & analytical works the following conclusions were drawn:

- Keeping in view the complexity of the bubbling bed, dynamics for modeling & the need to have predictive equation for thermal design of tube bundles immersed in the gas solid fluidized bed it is advantageous to have experimentally based directly usable correlations incorporating physically meaningful & easily measurable process variable. This is true for large particles ($D_p > 1mm$) for which the data is scarce.
- It is observed that the average heat transfer coefficient increases with the increase in the fluidizing velocity.
- It is also observed that the curves are more flatter as the particle size increases. This behavior may be due to gradual change over from unsteady conduction mechanism of heat transfer for particle size greater than 1 mm diameter.
- A new direct correlations for Nusselt number using only easily measurable variables are presented as:

SINGLE BARE TUBE -

MUSTARD :

$$Nub = (1.511 * 10^{-7}) * [(U-Umf)/Umf]^{(1.3746)} * [(Pg * u * Dt)/\mu g]^{(5.0740)} * [Ar]^{(-3.9709)} * [Pr]^{0.3}$$

BAJARA :

$$Nub = (7.24 * 10^{-3}) * [(U-Umf)/Umf]^{(-13.7641)} * [(pg * u * Dt)/\mu g]^{(19.8925)} * [Ar]^{(-8.96139)} * [Pr]^{0.3}$$

RAAGI:

$$Nub = (9.128 * 10^{-3}) * [(U-Umf)/Umf]^{(4.4270)} * [(pg * u * D,)/\mu g]^{(2.0200)} * [Ar]^{(-3.8075)} * [Pr]^{0.3}$$

References

- [1] Mickley, H.S. and Fairbanks, D.F., (1955), "Mechanism of heat transfer to fluidized beds", AIChE J., 1, 374-382
- [2] Subbarao D., Basu, P., (1986), "A model for heat transfer in fluidized beds", Int. J. Heat Mass Transfer, 29, 487-489
- [3] Rhodes. M.J - "Fluidization of particles by fluids" (Wiley, chichester, England -1998)
- [4] Wagialla K.M, Elnashaie S.S and Fakeeha A.H - "Review on heat transfer in gas-solid fluidized beds" Chemical engineering, Eng.Sci(2), pp 331-346.
- [5] Takuya tsuji, Takuya Miyauchi, Satoshi Oh - "Simultaneous measurement of particle motion and temperature in two-dimensional fluidized bed with heat transfer" Kona Powder and Particle Journal No. 28(2010)
- [6] Maan S. Al-Dabbagh - "Experimental study of heat transfer between the shallow fluidized bed and a tube bundle immersed in it" Heat transfer Journal, Jan-2006, pp 24-33.
- [7] Kamble L.V, Dr. Sane N.K, Dr. Ravindranath G, - "Artificial neural network in heat transfer analysis" RDME-2011, pp 14-25.

Mitigation of Faults in the Distribution System by Distributed Static Compensator (DSTATCOM)

P. RAMESH¹, C. SURYA CHANDRA REDDY², D. PRASAD³, D. PRAMEELA⁴, A. ANUSHA⁵

¹Research Scholar, Department of E.EE, S V U College of Engineering, S V University, Tirupati, A.P., India.

² IV B.Tech Student, Department of E.E.E., Sree Vidyanikethan Engineering College, Tirupati, A.P., India.

³ IV B.Tech Student, Department of E.E.E., Sree Vidyanikethan Engineering College, Tirupati, A.P., India.

⁴ IV B.Tech Student, Department of E.E.E., Sree Vidyanikethan Engineering College, Tirupati, A.P., India.

⁵ IV B.Tech Student, Department of E.E.E., Sree Vidyanikethan Engineering College, Tirupati, A.P., India.

Abstract:

This paper proposes a flexible D-STATCOM (Distribution Static Compensator) and its new controller system, that be able to mitigate all types of faults (LG, DLG, LL, 3-PHASE and 3-PHASE TO GROUND), and improve the distribution system performance. This paper validates the performance of D-STATCOM system to mitigate the power quality problems such as voltage flickers, voltage sags/swells harmonics and improve the distribution system performance under all types of system related disturbances and system unbalanced faults (LG, LL, DLG), balanced faults (3-phase fault and 3-phase to ground fault). 12-pulse D-STATCOM configuration with IGBT is designed and the graphic models of the D-STATCOM is developed using the MATLAB/SIMULINK.

Keywords: Distribution System, D-STATCOM, Voltage Sags, Faults.

I.INTRODUCTION

The modern power distribution network is constantly being faced with an ever-growing load demand. Distribution networks experience distinct change from a low to high load level every day. Electric load growth and higher regional power transfers in a largely interconnected network becoming more complex and less secure power system operation. Power generation and transmission facilities are unable to meet these new demands. Many loads at various distribution ends like domestic utilities, computers, process industries, adjustable speed drives, printers, and microprocessor based equipment etc. have become intolerant to voltage fluctuations, harmonic content and interruptions. Electrical power losses in distribution systems correspond to about 70% of total losses in electric power systems. One of the most severe problems faced by distribution networks operators is voltage drop along distribution feeders, which is caused by real and reactive power flow. Voltage control is a difficult task because voltages are strongly influenced by random load fluctuations. Voltage profile can be improved and power losses can be considerably reduced by installing

Custom Power Devices or Controllers at suitable location. These controllers which are also named Distribution Flexible AC Transmission System (D-FACTS) [1] are a new generation of power electronics-based equipment aimed at enhancing the reliability and quality of power flows in low-voltage distribution networks. Custom power is formally defined as the employment of power electronic or static controllers in distribution systems rated up to 38 kV for the purpose of supplying a level of reliability or PQ that is needed by electric power customers who are sensitive to power variations. Custom power devices or controllers [2] include static switches, inverters, converters, injection transformers, master-control modules and energy-storage modules that have the ability to perform current-interruption and voltage-regulation functions within a distribution system.

The STATCOM is applied in distribution system is called D-STATCOM (Distribution STACOM) and its configuration is the same, or with small modifications, oriented to a possible future amplification of its possibilities in the distribution network at low and medium voltage implementing the function so that we can describe as flicker damping, harmonic, filtering and short interruption compensation. D-STATCOM exhibits high speed control of reactive power to provide voltage stabilization, flicker suppression, and other types of system control. The D-STATCOM utilizes a design consisting of a GTO- or IGBT-based voltage sourced converter connected to the power system via a multi-stage converter transformer. This paper proposes a flexible D-STATCOM system designed to mitigate the voltage sags caused by LG, LL, DLG, 3-Phase and 3-Phase to ground faults. And improve the power quality of the distribution system. Reactive power compensation is an important issue in the control of distribution systems. The main reason for reactive power compensation in a system is the voltage regulation increased system stability, better utilization of machines connected to the system, reducing losses associated with the system and to prevent voltage collapse as well as voltage sag. Reactive current increases the

distribution system losses, reduces the system power factor, shrink the active power capability and can cause large-amplitude variations in the load-side voltage [3,4]. Various methods have been applied to mitigate voltage sags. The conventional methods use capacitor banks, new parallel feeders, and uninterruptible power supplies (UPS). The D-STATCOM has emerged as a promising device to provide not only for voltage sag mitigation but also for a host of other power quality solutions such as voltage stabilization, flicker suppression, power factor correction [5]. By a similar argument, the D-STATCOM is also suitable for reducing the impact of voltage transients. The D-STATCOM configuration consists of a typical 12-pulse inverter arrangement, a dc energy storage device; a coupling transformer connected in shunt with ac system, and associated control circuits. The configurations that are more sophisticated use multi pulse and/or multilevel configurations. The VSC converts the dc voltage across the storage device into a set of three-phase ac output voltages. These voltages are in phase and coupled with the ac system of network through the reactance of the coupling transformer [6].

A control method based on RMS voltage measurement has been presented in [7] and [8] where they have been presented a PWM-based control scheme that requires RMS voltage measurements and no reactive power measurements are required. In addition, in this given method, Clark and Park transformations are not required. However, they have been investigated voltage sag/swell mitigation due to just load variation while no balanced and unbalanced faults have been investigated. In this paper, a new control method for mitigating the load voltage sags caused by all types of fault is proposed. In [9] and [10], a Lookup Table is used to detect the proportional gain of PI controller, which is based only on Trial and Error. While in this paper, the proportional gain of the PI controller is fixed at a same value, for all types of faults, by tuning the transformer reactance in a suitable amount. Then the robustness and reliability of the proposed method is more than the mentioned methods. In this method, the dc side topology of the D-STATCOM is modified for mitigating voltage distortions and the effects of system faults on the sensitive loads are investigated and the control of voltage sags are analysed and simulated.

II. THE PROPOSED D-STATCOM STRUCTURE

The basic electronic block of the D-STATCOM is the voltage source inverter that converts an input dc voltage into a three-phase output voltage at fundamental frequency.

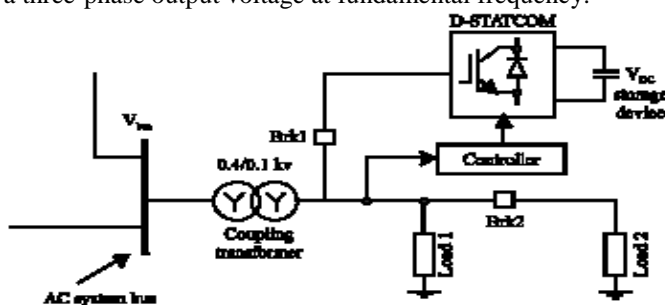


Fig.1 Block diagram of D-STATCOM

These voltages are in phase and coupled with the ac system through the reactance of the coupling transformer. Suitable adjustment of the phase and magnitude of the D-STATCOM output voltages allow effective control of active and reactive power exchanges between the D-STATCOM and the ac system. Fig. 2 shows a typical 12-pulse inverter arrangement utilizing two transformers with their primaries connected in series. The first transformer is in Y-Y connection and the second transformer is in Y-Δ connection. Each inverter operates as a 6-pulse inverter, with the Y-Δ inverter being delayed by 30 degrees with respect to the Y-Y inverter. The IGBTs of the proposed 12-pulse FD-STATCOM are connected anti parallel with diodes for commutation purposes and charging of the DC capacitor [11]. This is to give a 30 degrees phase shift between the pulses and to reduce harmonics generated from the FD-STATCOM.

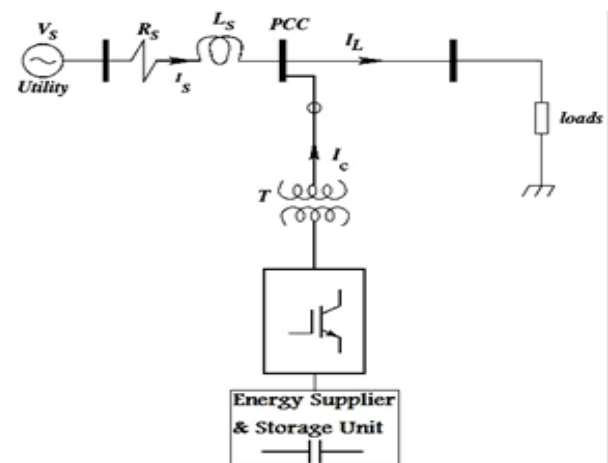


Fig 2: D-STATCOM structure

The coupling transformer injects the three phase voltages to the distributed line which is equal to the line voltage and phase angle.

III. CONTROL STRATEGY

The block diagram of the control scheme designed for the FD-STATCOM is shown in Fig. 3. It is based only on measurements of the voltage V_{RMS} at the load point.

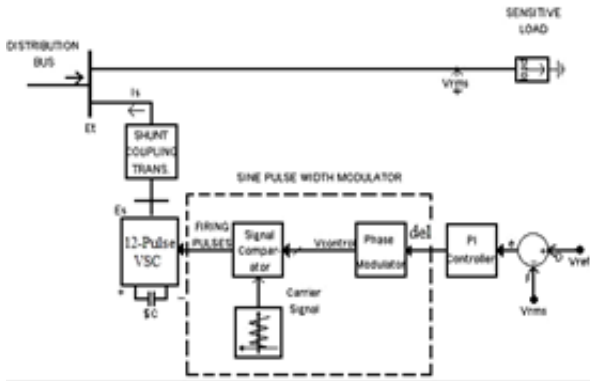


Fig.3. Control scheme designed for the

D-STATCOM

The voltage error signal is obtained by comparing the measured V_{RMS} voltage with a reference voltage, V_{RMSref} . A PI controller processes the difference between these two signals in order to obtain the phase angle δ that is required to drive the error to zero. The angle δ is used in the PWM generator as the phase angle of the sinusoidal control signal. The switching frequency used in the sinusoidal PWM generator is 1450 Hz and the modulation index is 1 [12]. The modulating angle δ is applied to the PWM generators in phase A. The angles of phases B and C are shifted 120 and 240 degrees, respectively.

IV. PROPOSED CONTROL METHOD

In this paper, in order to mitigate voltage sags caused by LG, LL, DLG, 3-Phase and 3-Phase to ground faults and improve the power quality improvement of the distribution system. Considering this fact that all types of fault may occur in distribution system, controller system must be able to mitigate any types of voltage sags. The control of a D-STATCOM is developed to mitigate such problems and enhance power quality and improve distribution system reliability. D-STATCOM is connected to the Y-Y and Y- Δ transformers for creating the 30 degrees phase shift. Harmonics mitigation will takes place by creating the 30 degrees phase shift.

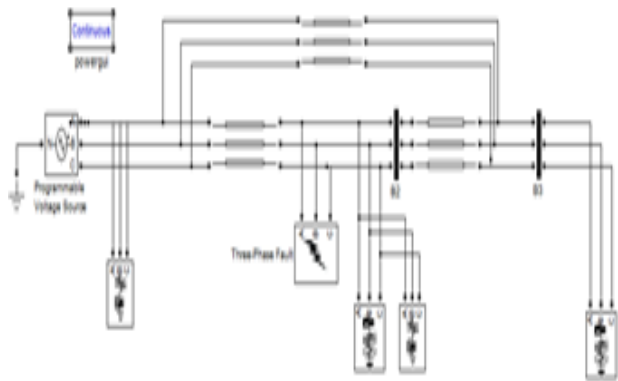


Fig 4: SIMULINK diagram WITHOUT D-STATCOM

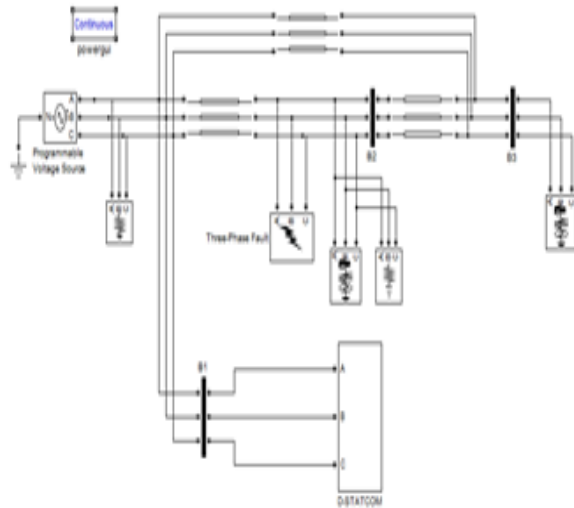


Fig 5: SIMULINK diagram WITH D-STATCOM

parameters	Values
Source 1	25kv
Source2	25KV
Source3	25KV
Load 1	300KW
Load2	200KW
Length BW B1 to B2	25Kkm
Length BW B2 to B3	20Kkm

Table 1: Specifications of test system

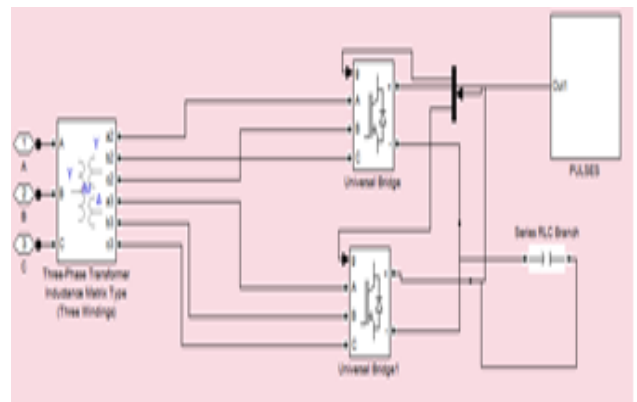


Fig 6: Simulink model for D-STATCOM

V.SIMULATION RESULTS

Fig .4 and Fig.5 are the test system implemented in MATLAB/SIMULINK to carryout simulations for the D-STATCOM. The test system is a distribution system having a voltage of 25 KV and different loads are connected to that voltage. The fault occurred in the test system between 0.1 to

0.15 seconds. The simulations are carried out for both cases where the D-STATCOM is connected to or disconnected from the system. The simulations of the D-STATCOM in fault condition are done using LG, LL, DLG, 3-phase and 3-phase to ground faults.

In this paper, the D-STATCOM uses the proposed control method to mitigate the load voltage sags due to all types of faults; the simulations are done for all types of faults introduced in the 25 KV distribution systems as follows.

A.SIMULATION RESULTS LINE TO GROUND FAULT

Fig 7 shows the voltage and current at the bus2, and fault is injected in the system between 0.1 and 0.15, whenever voltage value is less than the reference value, on that time the D-STATCOM injects voltage into the system and making the voltage profile be unity.

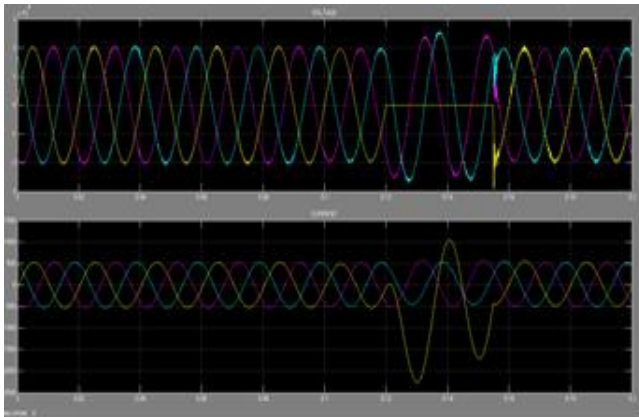


Fig 7: voltage and current at bus2 without D-STATCOM

Fig 8 shows the voltage and current at the bus2 with D-STATCOM, the voltage is continuous and current is also continuous without any deviation.

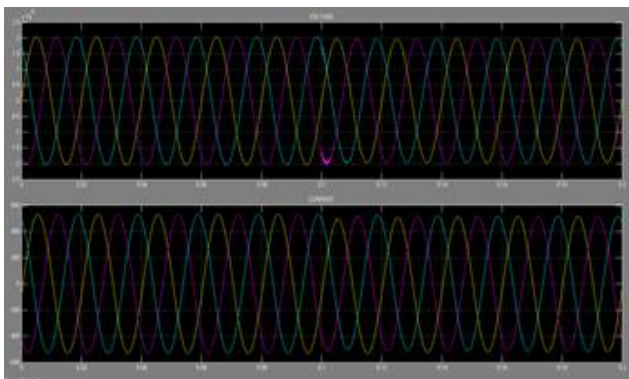


Fig 8: voltage and current at bus2 with DSTATCOM

B.SIMULATION RESULTS DOUBLE LINE FAULT

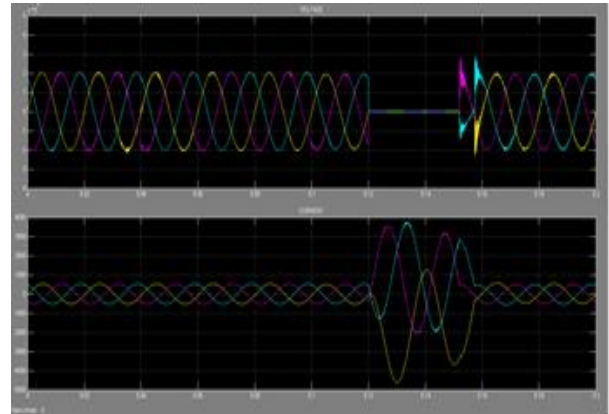


Fig 9: voltage and current at bus2 without D-STATCOM

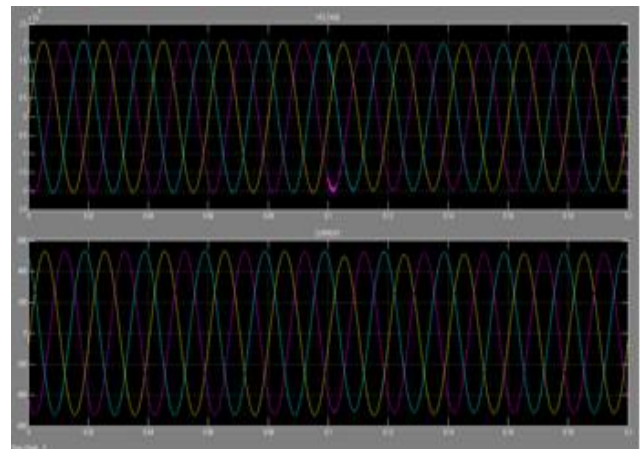


Fig 10: voltage and current at bus2 with D-STATCOM

C.SIMULATION RESULTS FOR DOUBLE LINE TO GROUND FAULT

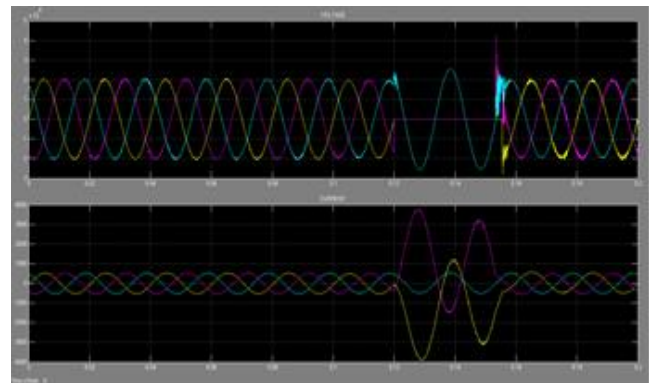


Fig 11: voltage and current at bus2 without D-STATCOM

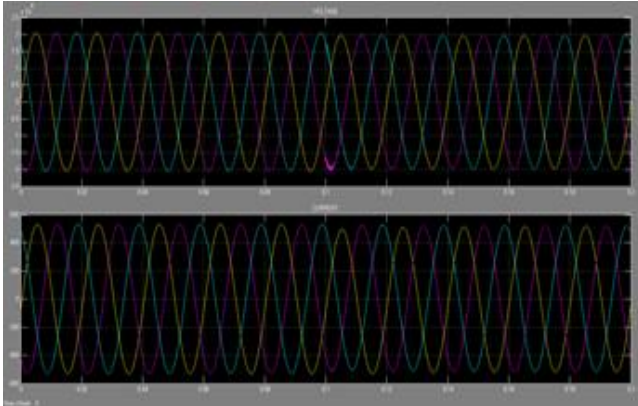


Fig 12: voltage and current at bus2 with D-STATCOM

D.SIMULATION RESULTS FOR 3-PHASE FAULT

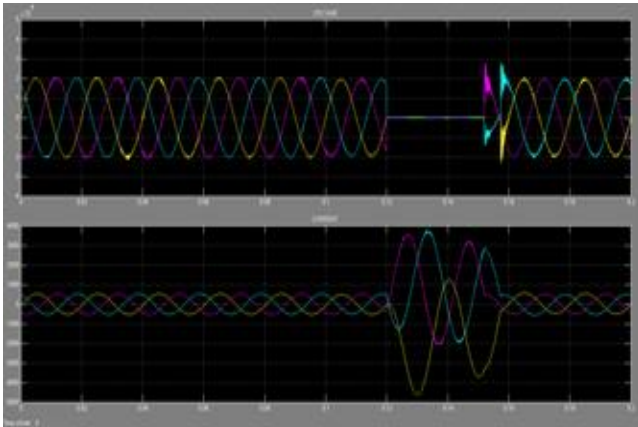


Fig 13: voltage and current at bus2 without D-STATCOM

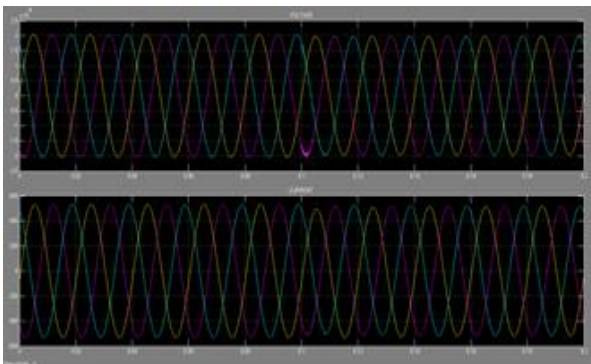


Fig 14: voltage and current at bus2 with D-STATCOM

E.SIMULATION RESULTS FOR 3-PHASE TO GROUND FAULT

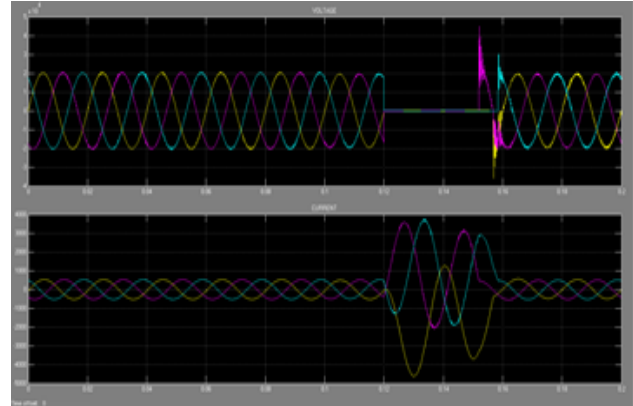


Fig 15: voltage and current at bus2 without D-STATCOM

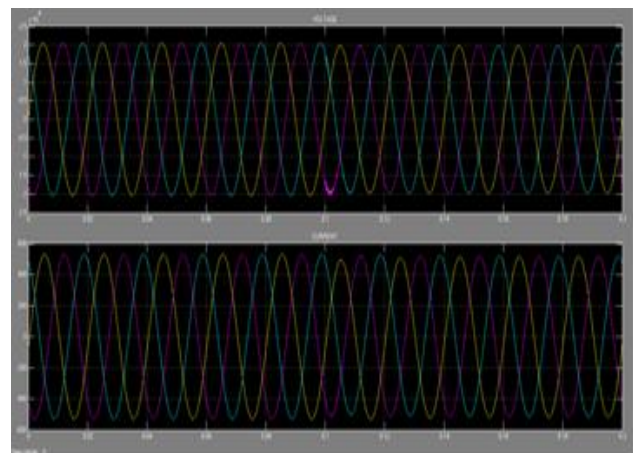


Fig 16: voltage and current at bus2 with D-STATCOM

VI. CONCLUSIONS

In this paper, the D-STATCOM and its control system proposed that could mitigate the voltage sags (such as LG, LL, DLG, 3-Phase and 3-Phase to Ground faults) and improved the power quality of the distribution system such as voltage flickers and power factor correction. The D-STATCOM is connected to the Y-Y and Y- Δ , the harmonics generated by a power electronic component is mitigated by providing the 30 degrees phase shift. The operation of the D-STATCOM and its control system are developed in MATLAB/SIMULINK for mitigating the voltage sags and improving the power quality of the distribution system.

VI. REFERENCES

- [1]. N. Hingorani, "FACTS—Flexible ac transmission systems," in Proc. IEE 5th Int.Conf. AC DC Transmission, London, U.K., 1991, Conf. Pub.345, pp. 1–7.
- [2]. S. Nilsson, "Special application considerations for Custom Power systems," in Proc.IEEE Power Eng. Soc., Winter Meeting 1999, vol. 2, 1999, pp. 1127–1130.
- [3]. C. J. Gajanayake, D. M. Vilathgamuwa, P. C. Loh, F. Blaabjerg, and R. Teodorescu, "A z- source inverter based flexible DG system with P+resonance and repetitive controllers for power quality improvement of a weak grid," in Proc. IEEE Power Electronics Specialists Conference, 2007, pp. 2457-2463.
- [4]. M. I. Marei, E. F. El-Saadany, and M. M. A. Salama, "Flexible distributed generation: (FDG)," in Proc. IEEE Power Engineering Soc. Summer Meeting, 2002, vol. 1, pp. 49- 53.
- [5]. G. F. Reed, M. Takeda, and I. Iyoda, "Improved power quality solutions using advanced solid-state switching and static compensation technologies," in Proc. IEEE Power Engineering Society Winter Meeting, 1999, vol.2, pp. 1132-1137.
- [6]. L. S. Patil and Ms. A. G. Thosar, "Application of D-STATCOM to mitigate voltage sag due to DOL starting of three phase induction motor," in Proc. IEEE International Conference on Control, Automation, Communication and Energy Conservation, 2009, pp. 1-4.
- [7]. O. Anaya-Lara and E. Acha, "Modelling and analysis of custom power systems by PSCAD/EMTDC," IEEE Trans. Power Del., vol. 17, no. 1, pp. 266- 272, Jan. 2002.
- [8]. H. Hatami, F. Shahnia, A. Pashaei, and S.H. Hosseini, "Investigation on D-STATCOM and DVR operation for voltage control in distribution networks with a new control strategy," in Proc. IEEE Power Tech., 2007, pp. 2207-2212.
- [9]. E. Babaei, A. Nazarloo, and S. H. Hosseini, "Application of flexible control methods for D-STATCOM in mitigating voltage sags and swells," in Proc. IEEE International Power and Energy Conference (IPEC), Singapore, 2010, pp. 590-595.
- [10]. S. H. Hosseini, A. Nazarloo, and E. Babaei, "Application of DSTATCOM to improve distribution system performance with balanced and unbalanced fault conditions," in Proc. IEEE Electrical Power and Energy Conference (EPEC), Canada, 2010.
- [11]. N. Mariun, H. Masdi, S. M. Bashi, A. Mohamed, and S. Yusuf, "Design of a prototype D STATCOM using DSP controller for voltage sag mitigation," in Proc. IEEE International Power and Energy Conference, 2004.
- [12]. E. Acha, V.G. Agelidis, O. Anaya-Lara, and T.J.E. Miller, "Power electronic control in electrical systems," Newness Power Engineering Series, 2002, pp. 330-336.

BIOGRAPHIES



P.Ramesh was born in Andhra Pradesh, India, 1982. He received the B.E degree in Electrical and Electronics Engineering from University of Madras, India, in 2003, and the M.Tech. degree in Power electronics and drives from Bharath University, Chennai, India, 2005. From 2005 to 2010 he worked as a faculty in the field of Electrical and Electronics Engineering. Since August, 2010, he has been working toward the Ph.D. degree in the field of Flexible AC Transmission Systems, Sri Venkateswara University College of Engineering, Sri Venkateswara University, India.

ISO-Failure in Web Browsing Using Markov Chain Model and Curve Fitting Analysis

Diwakar Shukla¹, Kapil Verma² and Sharad Gangele³

^[1](Department of Mathematics and Statistics, Sagar University, Sagar M. P. 470003) India.

Associate Member, DST-Centre for Interdisciplinary Mathematical Sciences, Banaras Hindu University, Varanasi, U.P.

^[2](Department of Computer Science, M.P. Bhoj (Open) University Kolar Road Bhopal, M.P) India.

B.T. Institute of Research and Technology, Seronja, Sagar, M.P.

^[3](Department of Computer Science, M.P. Bhoj (Open) University, Kolar Road, Bhopal, M. P.) India.

ABSTRACT

There are many browsers available for internet surfing and user has options to choose anyone providing the maximum facility. Every browser has popularity and limitations. The popularity is related to number of users who prefer a browser over others. Similarly, the limitation relates to excess delay in searching websites, which is browser failure. The browser sharing is a phenomenon which relates to the number of users attracted for using a particular browser besides its limitations. This paper presents an analysis of browser sharing when limitations of two browsers are rated as equal value. The term iso-failure appears for equality of browsers failure probability. An attempt has been made to obtain the approximate linear relationship between find browser sharing and initial share. A straight line is fitted on the generated data using the method of least square. The coefficient of determination and confidence interval support the theoretical facts.

Keywords – Transition Probability Matrix (TPM), Markov Chain Model (MCM), Coefficient of Determination (COD), Confidence Interval, Iso-Failure.

I. INTRODUCTION

A browser is used for accessing the different sites of internet. If a user takes into application only two browsers then he may has a favor for anyone depending upon the market popularity or the failure probability. If b_1 and b_2 are the two probabilities related to browser failure then both are suppose to be different. The notation iso-failure means the equality of failure level probability for both the browsers. If two browsers are in competitions then it is a matter of interest to know which one is having better share than others. This paper introduces the concept of iso-failure in the web browsing phenomenon. A stochastic model is proposed and analysis is performed. The basic model is proposed by Naldi (2002) and extended by Shukla and Gadewar (2007). Deshpande and Karpis (2004) discussed the Markov model application over web page access computing the prediction. A similar useful contribution is due to Pirolli (1996). A Markov chain model helps to establish interrelationship between process variables. Shukla and Jain (2007) have suggested stochastic model for multilevel queue scheduling and further extended by Shukla *et al.* (2010). In a useful contribution Shukla and Singhai (2011) discussed analysis of user web browsing behavior with the help of Markov chain model. This paper extends the same in light of iso-failure probability and establishes the linear relationship.

2. A REVIEW

Medhi (1991, 1992) presented a detailed discussion on the stochastic process and their applications. Chen and Mark (1993) discussed the fast packet switch shared concentration and output queueing for a busy channel. Humbali and Ramani (2002) evaluated multicast switch with a variety of traffic patterns. Newby and Dagg (2002) have a useful contribution on the optical inspection and maintenance for stochastically deteriorating system. Dorea *et al.* (2004) used Markov chain for the modeling of a system and derived some useful approximations. Yeian and Lygeres (2005) presented a work on stabilization of class of stochastic different equations with Markovian switching. Shukla *et al.* (2007 a) advocated for model based study for space division switches in computer network. Francini and Chiussi (2002) discussed some interesting features for QoS guarantees to the unicast and multicast flow in multistage packet switch. On the reliability analysis of network a useful contribution is by Agarwal and Lakhwinder (2008) whereas Paxson (2004) introduced some of their critical experiences while measuring the internet traffic. Shukla *et al.* (2009 a, b & c) presented different dimensions of internet traffic sharing in the light of share loss analysis. Shukla *et al.* (2010 a, b, c & d) have given some Markov chain model applications in view to disconnectivity factor, multi marketing and crime based analysis. Shukla *et al.* (2011 a, b, c, d, e & f) discussed the elasticity property and its impact on parameters of internet traffic sharing in presence blocking probability of computer network specially when two operators are in business competitions with each other in a market.

3. OBJECTIVES:

The contents of this paper is for

1. To examine the browser sharing when there exist iso failure of browsers.
2. To establish linear relationship using procedure of least square.

4. MODEL: Let $\{X_n, n \geq 0\}$ be a Markov chain on state space $\{C, Q, B_1, B_2, S\}$ as per Shukla and Singhai (2011) where

State C: represents connecting state.

State Q: user quitting from the process

State B₁: user attempts to surf through browser B₁.

State B₂: user attempts to surf through browser B₂.

State S: success for connectivity and surfing.

The $X^{(n)}$ denotes the position of random variable X in the state space at the nth browser connectivity attempt made by a web user.

5. ASSUMPTIONS FOR USER BROWSING BEHAVIOR [see Shukla and Singhai (2011)]

- (1) The user attempts for dial up connection to use Internet. If the connection is not established, user quits with the probability P_c.
- (2) When connection is made user chooses any one of browsers B₁, B₂ with the probability p and 1-p respectively.
- (3) User navigates to any one browser at a time when successfully opened.
- (4) Browser B_i (i=1, 2) failure occurs due to non-opening of any site through browser B_i. Then user either quits (with probability p_q) or switches to the next browser.
- (5) Switching between browsers is on attempt by attempt basis (n=1, 2, 3....).
- (6) Initial preference for a browser is based on quality of services and variety of facility features are contained in both browsers.
- (7) Failure probability of a browser B₁ is b₁ and of B₂ is b₂.
- (8) Transition probability of surfing through B₁, being completed in a single attempt is (1 - b₁).
- (9) Absorbing state (transition from a state to itself) probability is 1. No further transition from this state occurs.

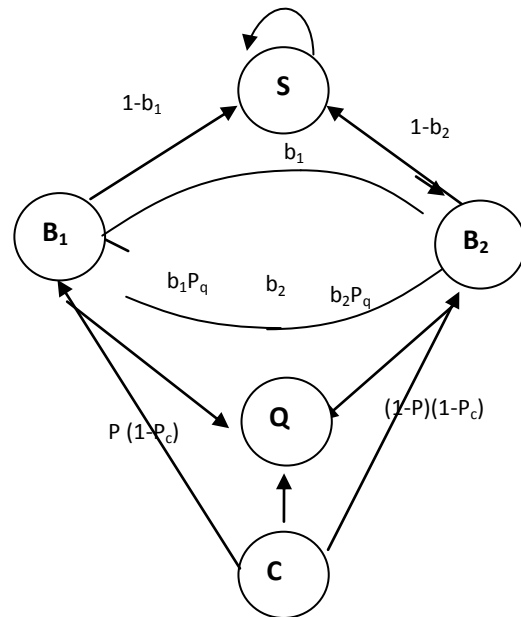


Fig.5.1 [Transition diagram of user browsing]

The initial conditions n=0, (state probability before the first surf attempt) are:

$$\left. \begin{aligned} P[X^{(0)} = C] &= 1 \\ P[X^{(0)} = B_1] &= 0 \\ P[X^{(0)} = B_2] &= 0 \\ P[X^{(0)} = S] &= 0 \\ P[X^{(0)} = Q] &= 0 \end{aligned} \right\} \quad (5.1)$$

The unit-step transition probability matrix is:

	B ₁	B ₂	S	Q	C
B ₁	0	b ₁ (1-b ₁)	(1-b ₁)	b ₁ P _q	0
B ₂	b ₂ (1-b ₂)	0	(1-b ₂)	b ₂ P _q	0
S	0	0	1	0	0
Q	0	0	0	1	0
C	P(1-P _c)	(1-P)(1-P _c)	0	P _c	0

Table: 5.1 [Transition Probability Matrix]

Under these assumptions user's browsing behavior has a Markov Chain Model (see fig.5.1) in which the transition probabilities are on the arcs connecting the circles and representing the chain states.

By using Shukla and Singhai (2011) we write

$$P[X^{(2n)} = B_1] = b_1^{n-1} b_2^n (1-p)(1-pc)(1-pq)^{2n-1}; n > 0 \dots (5.1)$$

$$P[X^{(2n+1)} = B_1] = (b_1 b_2)^n P(1-P_c)(1-P_q)^{2n}; n > 0 \dots (5.2)$$

Similarly, for browser B₂

$$P[X^{(2n)} = B_2] = b_1^n b_2^{n-1} P(1-P_c)(1-P_q)^{(2n-1)}; n > 0 \dots (5.3)$$

When n is odd

$$P[X^{(2n+1)} = B_2] = (b_1 b_2)^n (1-P)(1-P_c)(1-P_q)^{2n}; n > 0 \dots (5.4)$$

6. BROWSER SHARING: As per Shukla and Singhai (2011) browser sharing by B₁ is

$$P_1 = \lim_{n \rightarrow \infty} \bar{P}_1^{(2n)} = (1-b_1)(1-P_c) \left[\frac{P + (1-P)(1-P_q)b_2}{1-b_1 b_2 (1-P_q)^2} \right] \dots (6.1)$$

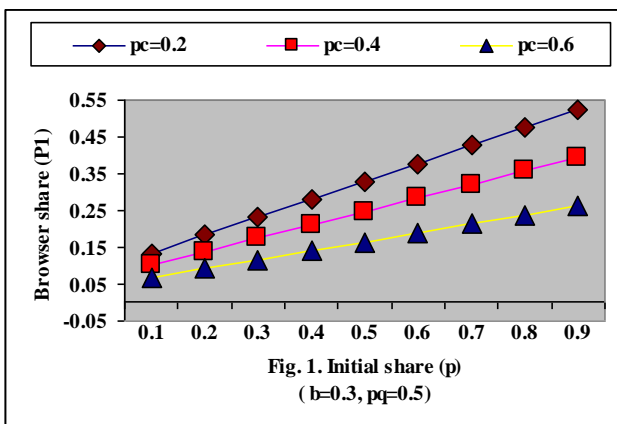
7. ISO-FAILURE: The failure probability of first browser B₁ is b₁ and second browser B₂ is b₂.

Let us define b₁=b₂=b then this condition constitute the iso-failure browser probability and iso-failure curves.

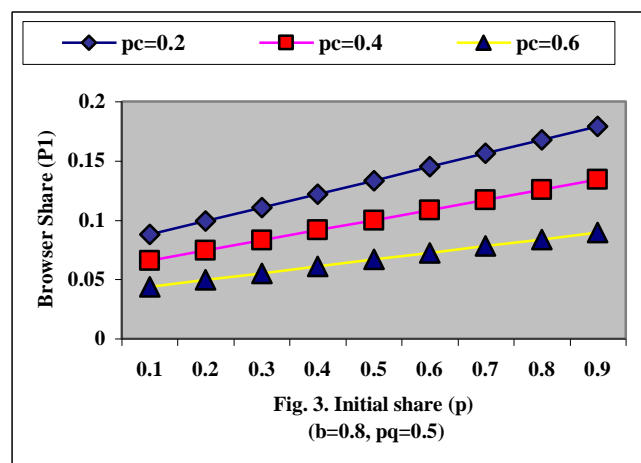
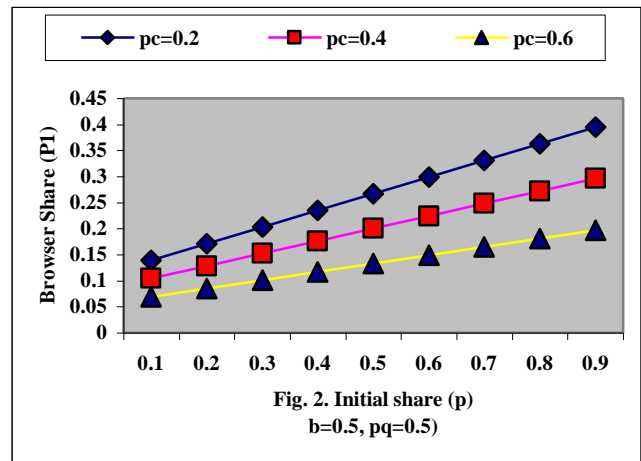
Now the (6.1) expression will be

$$P_1 = (1-b)(1-pc) \left[\frac{p + (1-p)(1-pq)b}{1-b^2(1-pq)^2} \right] \dots (7.1)$$

8. ISO-FAILURES CURVES: According to fig. 1 the browser share and initial share are linearly related when the condition of Iso-failure is imposed on the expressions. The quitting probability p_c if high the browser share reduces but the linear relationship between p and P₁ remains maintained.



In fig. 2 and fig. 3 the similar pattern is observed when the Iso-failure level is kept high the browser share reduces.



9. FITTING THE STRAIGHT LINE: We are to approximate the relationship between parameter P and p through a straight line $\hat{P}_1 = a + b.p$ where a and b are constants to be obtained by the method of least square. For the ith observation p_i we write the relationship as $\hat{P}_{1i} = a + b.p_i$ (i=1, 2, 3, ..., n). The normal equations are

$$\left. \begin{aligned} \sum_{i=1}^n P_{1i} &= n.a + b \sum_{i=1}^n p_i \\ \sum_{i=1}^n P_{1i} \cdot p_i &= a \sum_{i=1}^n p_i + b \sum_{i=1}^n p_i^2 \end{aligned} \right\} \dots (9.1)$$

By solving the normal equations (9.1), the least square estimates of a and b are as \hat{a}, \hat{b} :

$$\hat{b} = \left\{ \frac{n \sum_{i=1}^n P_{1i} p_i - (\sum_{i=1}^n P_{1i})(\sum_{i=1}^n p_i)}{n \sum_{i=1}^n p_i^2 - (\sum_{i=1}^n p_i)^2} \right\} \dots (9.2)$$

$$\hat{a} = \left\{ \frac{1}{n} \sum_{i=1}^n P_{1i} - \hat{b} \sum_{i=1}^n p_i \right\} \dots (9.3)$$

Where n is the number of observations in sample of size n, the resultant straight line is

$$\hat{P}_1 = \left\{ \hat{a} + \hat{b} \cdot p \right\} \dots (9.4)$$

The coefficient of determination (COD) as a measure of good curve fitting is

$$COD = \frac{\sum (P_{1i} - \bar{P}_1)^2}{\sum (P_{1i} - \bar{P}_1)^2} \dots (9.5)$$

Where $\bar{P} = \frac{1}{n} \sum P_{1i}$ is mean of original data of variable P_1 obtained through Markov chain model. The term $\hat{P}_{1i} = \hat{a} + \hat{b} \cdot p_i$ is the estimated by values of P_{1i} given observation p_i . The COD lies between 0 to 1. If the line is good fit then it is near to 1. We generate pair of values (p, P_1) in tables (9.1, 9.2, and 9.3) by providing few fixed input parameters.

Table 9.1 (P_1 by expression (6.1), \hat{P}_1 by (9.4) with known p_c, b, p_q , (9.4.1))

Fixed parameter	P	0.1	0.2	0.3	0.4	0.5	0.6	0.7	0.8	0.9	COD
$p_c=0.4$ $b=0.3$ $p_q=0.5$	P_1	0.1009	0.1374	0.1740	0.2105	0.2470	0.2835	0.3201	0.3566	0.3931	1.000
	\hat{P}_1	0.1009	0.1374	0.1740	0.2105	0.2470	0.2835	0.3201	0.3566	0.3931	
$\hat{a} = 0.06445; \hat{b} = 0.365217; \hat{P}_1 = \hat{a} + \hat{b} \cdot p; \hat{P}_1 = 0.06445 + 0.365217(p) \dots (9.4.1)$											

Table 9.2 (P_1 by expression (6.1), \hat{P}_1 by (9.4) with known p_c, b, p_q , (9.4.2))

Fixed parameter	P	0.1	0.2	0.3	0.4	0.5	0.6	0.7	0.8	0.9	COD
$p_c=0.4$ $b=0.5$ $p_q=0.5$	P_1	0.1041	0.1281	0.1520	0.1761	0.2110	0.2240	0.2481	0.2721	0.2961	1.000
	\hat{P}_1	0.1041	0.1281	0.1521	0.1761	0.2110	0.2240	0.2481	0.2720	0.2961	
$\hat{a} = 0.081271; \hat{b} = 0.241254; \hat{P}_1 = \hat{a} + \hat{b} \cdot p; \hat{P}_1 = 0.081271 + 0.241254(p) \dots (9.4.2)$											

Table 9.3 (P_1 by expression (6.1), \hat{P}_1 by (9.4) with known p_c, b, p_q , (9.4.3))

Fixed parameter	P	0.1	0.2	0.3	0.4	0.5	0.6	0.7	0.8	0.9	COD
$p_c=0.4$ $b=0.7$ $p_q=0.5$	P_1	0.0851	0.0984	0.1117	0.1251	0.1384	0.1517	0.1651	0.1784	0.191	1.000
	\hat{P}_1	0.0851	0.0984	0.1117	0.1251	0.1384	0.1517	0.1651	0.1784	0.191	
$\hat{a} = 0.071791; \hat{b} = 0.133333; \hat{P}_1 = \hat{a} + \hat{b} \cdot p; \hat{P}_1 = 0.071791 + 0.133333(p) \dots (9.4.3)$											

10. CONFIDENCE INTERVAL: The $100(1 - \alpha)$ percent confidence interval for a and b are

$$\hat{a} \pm \left\{ t_{(n-2)} \frac{\alpha}{2} \right\} .s. \left[\sqrt{\frac{1}{n} + \frac{\bar{p}}{\sum_{i=1}^n (p_i - \bar{p})^2}} \right] \quad \dots(10.1)$$

$$\hat{b} \pm \left\{ t_{(n-2)} \frac{\alpha}{2} \right\} .s. \left[\sqrt{\sum_{i=1}^n (p_i - \bar{p})^2} \right] \quad \dots(10.2)$$

Where $s = \sqrt{\frac{\sum (P_{li} - \hat{P}_{li})^2}{n - 2}}$

Table: 10.1 Calculation of Confidence interval for a and b

Fixed parameter $P_c = 0.4, b = 0.3, p_q = 0.5$	$\hat{a} = 0.06445$	$\hat{b} = 0.365217$	(a=0.06445, a=0.06445) (b= 0.365217 , b=0.365217)
$P_c = 0.4, b = 0.5, p_q = 0.5$	$\hat{a} = 0.081271$	$\hat{b} = 0.241254$	(a=0.081271, a=0.081271) (b=0.241254 , b=0.241254)
$P_c = 0.4, b = 0.7, p_q = 0.5$	$\hat{a} = 0.071791$	$\hat{b} = 0.133331$	(a=0.07179 , a=0.07179), (b=0.13333 , b=0.013333)
Average Estimate	$\bar{a} = 0.072504$	$\bar{b} = 0.2465983$	$\hat{P}_1 = \bar{a} + \bar{b}(p)$ $\hat{P}_1 = 0.072504 + 0.2465983(p)$

11. DISCUSSIONS:

While considering fig. 1 we observe that there is a linear trend exists between final browser share and initial share using (6.1). This trend increases with the increase of initial share. If p_c probability is high then browser share level is low. It seems final browser share is inversely proportional to the quitting probability p_c which is usual also. The same pattern appears in fig. 2 and fig. 3. The linear pattern between p and \bar{p}_1 is replaced by a direct equation of a straight line in the form $\hat{P}_1 = \hat{a} + \hat{b}.p$. The least square estimates of \hat{a} are 0.06445, 0.081271, 0.07179 and \hat{b} are 0.365217, 0.241254, 0.13333 respectively. The three possible equations of linear relationship between p and \hat{P}_1 are $\hat{P}_1 = (0.06445 + 0.365217.p)$, $\hat{P}_1 = (0.081271 + 0.241254.p)$, $\hat{P}_1 = (0.071791 + 0.13333.p)$

The coefficients of determination (COD) in each case are exactly 1 therefore the estimated values of a and b are very close to the real values. The confidence intervals are

For \hat{a} : (0.06445, 0.06445), (0.08271, 0.081271), (0.071791, 0.071791)

For \hat{b} : (0.365217, 0.365217), (0.241254, 0.241254), (0.13333, 0.13333)

The average equation of linear relationship is

$$\hat{P}_1 = \bar{a} + \bar{b}(p); \hat{P}_1 = 0.72504 + 0.2465983(p).$$

12. CONCLUSION:

The least square based line fitting between P_{li} and \hat{p}_1 is accurate because of high values of COD which is nearly equal to unity. The confidence interval for \hat{a} and \hat{b} are overlapping with the true values showing the robustness of the estimates. It seems the fittings of straight lines are good approximations of the complicated relationships between final browser share probability and initial browser share probability. The resultant relationship is

$$\hat{P}_1 = \bar{a} + \bar{b}(p); \hat{P}_1 = 0.072504 + 0.2465983(p)$$

which could be used us a rule for quick calculations

REFERENCES

- [1] **Medhi, J. (1991):** Stochastic models in queuing theory, Academic Press Professional, Inc., San Diego, CA.
- [2]. **Medhi, J. (1992):** Stochastic Processes, Ed.4, Wiley Eastern Limited (Fourth reprint), New Delhi.
- [3]. **Chen, D.X. and Mark, J.W. (1993):** A fast packet switch shared concentration and output queuing,

- IEEE Transactions on Networking, vol. 1, no. 1, pp. 142-151.
- [4]. **Hambali, H. and Ramani, A. K., (2002):** A performance study of at multicast switch with different traffics, Malaysian Journal of Computer Science. Vol. 15, Issue No. 02, Pp. 34-42.
- [5]. **Naldi, M. (2002):** Internet access traffic sharing in a multi-user environment, Computer Networks. Vol. 38, pp. 809-824.
- [6]. **Newby, M. and Dagg, R. (2002):** Optical inspection and maintenance for stochastically deteriorating systems: average cost criteria, Jour. Ind. Statistical Associations. Vol. 40, Issue No. 02, pp. 169-198.
- [7]. **Francini, A. and Chiussi, F.M. (2002):** Providing QoS guarantees to unicast and multicast flows in multistage packet switches, IEEE Selected Areas in Communications, vol. 20, no. 8, pp. 1589-1601.
- [8]. **Dorea, C.C.Y., Cruz and Rojas, J. A. (2004):** Approximation results for non-homogeneous Markov chains and some applications, Sankhya. Vol. 66, Issue No. 02, pp. 243-252.
- [9]. **Paxson, Vern, (2004):** Experiences with internet traffic measurement and analysis, ICSI Center for Internet Research International Computer Science Institute and Lawrence Berkeley **National Laboratory**.
- [10]. **Yeian, C. and Lygeres, J. (2005):** Stabilization of class of stochastic differential equations with Markovian switching, System and Control Letters. Issue 09, pp. 819-833.
- [11]. **Shukla, D., Gadewar, S. and Pathak, R.K. (2007 a):** A stochastic model for space division switches in computer networks, International Journal of Applied Mathematics and Computation, Elsevier Journals, Vol. 184, Issue No. 02, pp235-269.
- [12]. **Shukla, D. and Thakur, Sanjay, (2007 b)** Crime based user analysis in internet traffic sharing under cyber crime, Proceedings of National Conference on Network Security and Management (NCSM-07), pp. 155-165, 2007.
- [13]. **Agarwal, Rinkle and Kaur, Lakhwinder (2008):** On reliability analysis of fault-tolerant multistage interconnection networks, International Journal of Computer Science and Security (IJCSS) Vol. 02, Issue No. 04, pp. 1-8.
- [14]. **Shukla, D., Tiwari, Virendra, Thakur, S. and Deshmukh, A. (2009 a):**Share loss analysis of internet traffic distribution in computer networks, International Journal of Computer Science and Security (IJCSS), Malaysia, Vol. 03, issue No. 05, pp. 414-426.
- [15]. **Shukla, D., Tiwari, Virendra, Thakur, S. and Tiwari, M. (2009 b) :**A comparison of methods for internet traffic sharing in computer network, International Journal of Advanced Networking and Applications (IJANA).Vol. 01, Issue No.03, pp.164-169.
- [16]. **Shukla, D., Tiwari, V. and Kareem, Abdul, (2009 c)** All comparison analysis in internet traffic sharing using markov chain model in computer networks, Georgian Electronic Scientific Journal: Computer Science and Telecommunications. Vol. 06, Issue No. 23, pp. 108-115.
- [17]. **Shukla, D., Tiwari, Virendra, and Thakur, S. (2010 a):** Effects of disconnectivity analysis for congestion control in internet traffic sharing, National Conference on Research and Development Trends in ICT (RDTICT-2010), Lucknow University, Lucknow.
- [18]. **Shukla, D., Gangele, Sharad and Verma, Kapil, (2010 b):** Internet traffic sharing under multi-market situations, Published in Proceedings of 2nd National conference on Software Engineering and Information Security, Acropolis Institute of Technology and Research, Indore, MP, (Dec. 23-24,2010), pp 49-55.
- [19]. **Shukla, D., and Thakur, S. (2010 c):** Stochastic Analysis of Marketing Strategies in internet Traffic, INTERSTAT (June 2010).
- [20]. **Shukla, D., Tiwari, V., and Thakur, S., (2010 d):** Cyber Crime Analysis for Multi-dimensional Effect in Computer Network, Journal of Global Research in Computer Science(JGRCS), Vol. 01, Issue 04, pp.31-36.
- [21]. **Shukla, D., Gangele, Sharad, Verma, Kapil and Singh, Pankaja (2011 a):** Elasticity of Internet Traffic Distribution Computer Network in two Market Environment, Journal of Global research in Computer Science (JGRCS) Vol.2, No. 6, pp.6-12.
- [22]. **Shukla, D., Gangele, Sharad, Verma, Kapil and Singh, Pankaja (2011 b):** Elasticities and Index Analysis of Usual Internet Browser share Problem, International Journal of Advanced Research in Computer Science (IJARCS),Vol. 02, No. 04, pp.473-478.
- [23]. **Shukla, D., Gangele, Sharad, Verma, Kapil and Thakur, Sanjay, (2011 c):** A Study on Index Based Analysis of Users of Internet Traffic Sharing in Computer Networking, World Applied Programming (WAP), Vol. 01, No. 04, pp. 278-287.
- [24]. **Shukla, D., Gangele, Sharad, Singhai, Rahul and Verma, Kapil, (2011 d):** Elasticity Analysis of Web Browsing Behavior of Users, International Journal of Advanced Networking and Applications (IJANA), Vol. 03, No. 03, pp.1162-1168.
- [25]. **Shukla, D., Verma, Kapil and Gangele, Sharad, (2011 e):** Re-Attempt Connectivity to Internet Analysis of User by Markov Chain Model, International Journal of Research in Computer Application and Management (IJRCM) Vol. 01, Issue No. 09, pp. 94-99.
- [26]. **Shukla, D., Gangele, Sharad, Verma, Kapil and Trivedi, Manish, (2011 f):** Elasticity variation under Rest State Environment In case of Internet Traffic Sharing in Computer Network, International Journal of Computer Technology and Application (IJCTA) Vol. 02, Issue No. 06, pp. 2052-2060.
- [27]. **Shukla, D., Singhai, Rahul [2011]:** Analysis of User Web Browsing Using Markov chain Model, International Journal of Advanced Networking and Application (IJANA), Vol. 02, Issue No. 05, pp. 824-830.

Transportation Study on Road Network and Programming for Identified Transport Infrastructure Projects In Salem, Tamilnadu, India

T. SUBRAMANI¹, R. ELANGO VAN², P. K. KUMARES AN³

¹Professor & Dean, Department of Civil Engineering, VMKV Engg College, Vinayaka Missions University, Salem, India

²Professor & Principal, Sri Balaji Chockalingam Engg College, Arni, India

³Professor & Dean, Examination, VMKV Engg. College, Vinayaka Missions University, Salem, India

ABSTRACT

Salem is the fifth largest city with a population of 7.54 lakhs (2011) in Tamil Nadu. Local Authorities faced with great difficulties to identify required various road improvement projects. Local authorities have inadequate funds to improve these road networks from all angles at any point of time. Repair or improvement works may have to be under taken on a basis which has to be decided based on socio-economic, administrative, technical, political factors etc., The identified road network selected for the study comprises 162 road links in Salem Corporation. Existing traffic condition, surface condition of carriageway, street lighting, footpath condition and drainage condition in the Salem Corporation area has been studied in detail. Traffic volume count survey was conducted on the identified 162 road links in Salem Corporation. Identify the type of transport facilities required for the road links. In programming process, priorities are set for project implementation. Even in cases where a formal process of priority setting does not exist, the allocation of organizational and financial resources for the development of some projects over others is an implicit setting of priorities. In programming process, priorities are set for project implementation. Even in cases where a formal process of priority setting does not exist, the allocation of organizational and financial resources for the development of some projects over others is an implicit setting of priorities. The important technique devised in this study is working out priority indices based on measures of current conditions of the facilities. There are two approaches for fixing the priorities to select road links to improve existing conditions. In the first approach priorities are fixed mainly based on hierarchy of road network and considering location of road links with weightages assigned to the road links In the second approach priorities are fixed mainly based on location of road links and considering hierarchy of road network with weightages assigned to the road links.

Keywords – Transportation, Roadnetwork, Programming, Infrastructure, Projects

1. INTRODUCTION - IMPORTANCE OF TRANSPORTATION IN URBAN DEVELOPMENT

Transportation contributes to the economic, industrial, social and cultural development of any country. It is well recognized that transport performs a key role in achieving fast economic growth of developing countries. Export and import, industry agriculture defence, social services (health, education), general administration, maintenance of law and order, exploitation of untapped resources, mobility of persons etc., are some of the many areas of activity which are very closely linked to the availability of adequate transportation.

Growth of urban areas and nature extent of availability of various classes of labour force are influenced by the extent of development of transport facilities. This growth in turn has a cause and effect impact on transport services. Since increase in urban population demands better transportation facilities and services. It may be necessary in the case of a country of India's vastness to provide transportation facilities in anticipation of demand, so that the transportation acts as a catalytic agent in development of different sectors.

2. DEFINITION FOR PROGRAMMING

Programming is a technical and political process that established priorities for projects by assessing current and future resource availability in order to stage projects over time. Technical analysis and political considerations are elements of programming that are closely interrelated, with the relative impact of each on any one project decision varying greatly as decision makers seek to satisfy both the relevant transportation policies and the many interest groups involved. There are two tasks which play an important role in the programming process and which are critical to its success – setting priorities for project selection and determining the availability of funds (Meyer M.D., Miller E.J. 1984).

3. NEED FOR PROGRAMMING

With limited resources available for improvements to the transportation network, much of the interest of decision makers is focused on the programming and budgeting process. The specifics of this process vary from one city or governmental structure to another. In some cases, political decision makers may be interested in the progress of specific projects because these projects are important politically. In other cases decision makers may not be interested in specific projects, but rather in the overall policy that represents. If there were unlimited resources for transportation projects in an urban centre, there would not be much problem in prioritising the activities.

However, the financial and organized resources available for transportation investment are always limited and in some instances even be shrinking. In addition to the constraint of declining funding levels, the small number of construction firms in an urban area and the limited ability of government agencies to supervise project construction also limit the number of projects that can be implemented in any one year. Further the limited capacity of government agencies to design facilities or to monitor the design process constrains the number of projects that can reach the programming stage. Given these circumstances, it becomes necessary to establish priorities for project implementation that is to determine which projects require immediate attention and would receive funding.

4. OBJECTIVES OF THE PRESENT STUDY

1. To examine the existing transport infrastructure facility like roads in the selected Salem urban centre.
2. To conduct Traffic volume survey on the selected 162 road links in Salem Corporation
3. To identify the required road improvement projects in the selected urban centre.
4. To identify the traffic congested road links in Salem Corporation.
5. To find the extra widening required for the different road links to carry existing traffic volume.
6. To find the roads which require Traffic management measures with widening of carriageway.
7. To Rank the problems for prioritization in the order of their magnitude and complexity by using rating values.
8. Prepare the order of priority for taking up road improvement projects with respect to the hierarchy of road net work & location of road links.

5. METHODOLOGY

1. Summarize the findings and recommendations of various previous studies.
2. Identify and collect an relevant information required from local agencies such as demographic trends, map showing the existing land-use and growth trends, income and expenditure, road network details – physical condition, traffic information.
3. Critically evaluate the data to understand the overall conditions of existing infrastructural facilities in the Salem urban centre.
4. Conduct traffic volume survey on identified 162 road links.
5. Analysis the data to identify the magnitude and complexity of the problems, using computer programs
6. Identify the type of road improvement projects require to meet the existing traffic.
7. Prepare a questionnaire and conduct survey to assign ratings to various road attributes.
8. Ranking the problems for prioritization in the order of their magnitude and complexity by using rating values.

9. Find the order of priority for taking up road improvement projects with respect to the hierarchy of road net work & location of road links

6. STUDY OF PAST AND PRESENT CONDITIONS IN SALEM CITY

6.1 SALEM – GENERAL

Salem is the fifth largest city in Tamil Nadu over an area of 91.34 Sq.kms. Salem city is located at distance of 350 kms from a Chennai on the west, and 160 kms from Coimbatore and it got the fifth largest population of 7.54 lakhs as per 2011 census in Tamil Nadu.. It is situated at the trijunction of Bangalore, Trichirappalli and Chennai roads. The City is located at 11 40’ North and 78 10’ on the East. The general topography is plain The city is surrounded by the hills viz. the shervarous and Nagarmalai on the North, The Kanjamalai on the west, the Goodamalai on the East.

6.2 POPULATION GROWTH

The population in Salem has grown at a rate of 23 percent per decade between 1951 and 1971, the rate has been lower for the decade 1971 – 1981 at 17 percent and 14 percent per decade between 1991 and 2011. Table.1 gives the growth of population within the Salem town. Population growth of Salem City Corporation given in Table 1.

Table 1. Population growth of Salem City Corporation

Year	Salem town / corporation* population	Decade variation	% of decade variation
1901	70621	-	-
1911	59153	(-) 11468	(-) 16.24
1921	52244	(-) 6909	(-) 11.68
1931	102149	(-) 49935	95.58
1941	129702	27523	26.94
1951	202335	72633	56
1961	249145	46810	23.13
1971	308716	59571	23.9
1981	361394	52678	17.06
1991*	579951	218557	60.47
2001*	672330	92379	15.92
2011*	754000	81670	12.15

6.3. EXISTING LAND-USE STRUCTURES

The extent of Salem town is 91.34 Sq.km of this the developed area is 4648 Hectares i.e. 48.71 percent of the total area and undeveloped area is 4894 hectares i.e. 51.29 per cent of the total area. The Table 2. gives the existing land use details of Salem City Corporation area & Figure. 1. is showing the existing land use details of Salem City Corporation area.

6.4 EXISTING TRAFFIC SITUATION

The traffic in Salem town is heterogeneous in nature comprising of slow moving vehicles such as hand carts, animal drawn vehicles, bicycle and fast moving vehicles such as mini cargo vans, Passenger vans Lorries, buses etc. In the absence of separate lanes for slow moving vehicles and cyclists all the

vehicles are found to use the available narrow carriageway. The pedestrian side walks have been provided only near Collectorate. In almost all the main roads vendors occupy the road margins and side walks. Hence the pedestrians are deprived of the use of road margins and side walks and use the carriage way, causing hindrance to the free vehicle movement. This may be noticed more in the central area of the old town comprising of Collectorate and Bus stand complex the main private companies.

Table 2. Existing land use details of Salem city area

Sl. No	Use	Area in hectares	% to developed area	% to total area
	Developed area			
1	Residential	3091	66.50	32.39
2	Commercial	461	9.92	4.83
3	Industrial	465	10.00	4.88
4	Education	316	6.80	3.31
5	Public and semi-public	315	6.78	3.30
	Total developed area	4648	100	48.71
	Undeveloped area			
6	Agricultural area			
	A. Wet	1240	25.33	13.00
	B. Dry	2465	50.36	25.83
	C. Hillocks	728	14.89	7.63
7	Reserved forest	461	9.42	4.83
	Total undeveloped area	4894	100	51.29
	Net total	9542		100.00

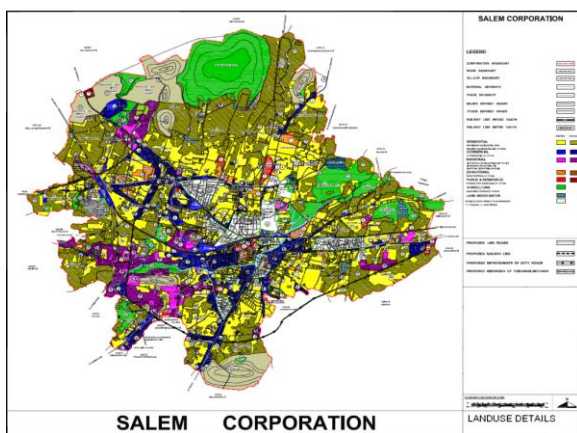


Figure.1. Existing land-use details of salem city corporation

7. IDENTIFIED ROAD NETWORK FOR THE PRESENT STUDY

Salem district as a whole has only 10,133.7 km. of road, out of which 214.6 km are cement concrete roads, 5098.1 kms. are bituminous surfaced road and the remaining 4821 kms. are water Bound Macadam roads. The unsurfaced road of 2352.7 kms. also exist in the district.

Salem Corporation has about 748.13kms. of surfaced roads under its control and maintenance as detailed below. The width of road ranges from 3.5 m to 14.0m in the major road network excluding the lanes and small roads. The details of the various categories of roads with their lengths in the town is show in Table. 3

Table.3 Types of roads with their length in Salem Corporation

Sl. No	Category	Road length (km)
1	Cement Concrete Super Roads	54.47
2	Black Topped Roads	628.17
3	Wbm Roads	17.04
4	Earthern Road	23.46
5	Others	24.66
	Total Length of Municipal Roads	748.13

The arterial road network of Salem Chosen for the study consists of four major radial corridors originating from the city bus stand. These roads are Attur road in the east, Trichy road and Coimbatore road in the South and Omalur road in the North west. In addition to these, there are a few secondary radial roads. One orbital corridor is identified and it consists of Shandipet road pallapatti main road and court road. Fig.2. shows the identified road network selected for the present study.

8. FIELD STUDIES TRAFFIC VOLUME SURVEY

One of the fundamental measures of traffic on a road system is the volume of traffic using the road in a given interval of time. It is also termed as flow and is expressed in vehicles per hour.

When the traffic is composed of number of types of vehicles, it is the normal practice to convert the flow into equivalent passenger car units (PCU), by using certain equivalence factors. The flow is then expressed as PCU per hour.

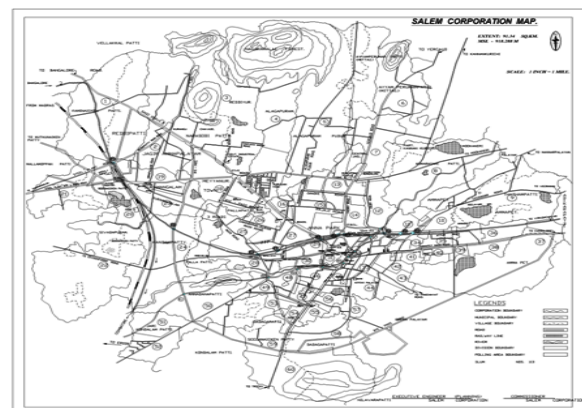


Figure.2. Identified road network of Salem city Corporation

A knowledge of the vehicular volume using a road network is important for understanding the efficiency at which the system works at present and the general quality of service offered to the road users knowing the flow characteristics, one can easily determine whether a particular section of a road is handling traffic much above or below its capacity. If the traffic is heavy, the road suffers from congestion with consequent loss in journey speeds. Lower speeds cause economic loss to the community due to time lost by the occupants of the vehicles and the higher operational cost of vehicles. Congestion also leads to traffic hazards. Volume counts are, therefore, indicators of the need to improve the transport facilities and are in an invaluable tool in the hands of transport planner.

In order to update the data base of the present existing traffic conditions, Traffic volume counts on selected road links in the urban centre were conducted. The detailed field survey programme was organized for 14 hours between 6 AM -8 PM. The block period is 15 minutes. Traffic volume count survey was conducted on the 162 road links and shown in Figure 3. With the help of these data the peak hour of traffic flow on each road link has been identified.

9. PHYSICAL CHARACTERISTICS

Physical Characteristics of road links in the network studied by field visits during the study and updated to the present existing condition. The study of physical characteristics comprises of surface condition, lighting condition footpath condition and drainage condition.

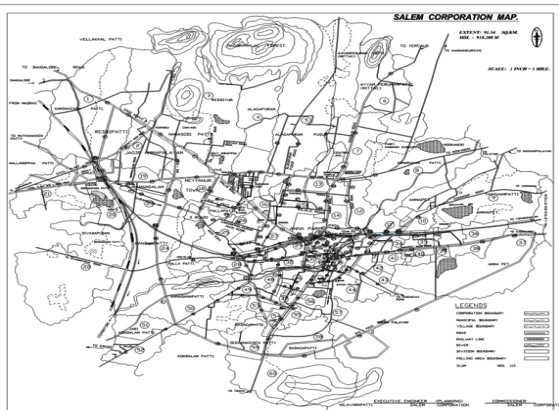


Figure 3. Traffic volume count survey points on the 162 road links

10. ROAD NETWORK DETAILS

Road network details collected from directorate of Town and Country Planning, Salem Corporation & Salem Local Planning Authority.

10.1 List Of Data Collected

The following data have been collected for Salem city

- i. Linkwise – road name details

The arterial road network which has been studied is broken into number of links. A link is defined as one-way part of the route between two intersections. The number of road links analyzed in the study is 162. The road links studied in the urban centres are given in Fig.3.

- ii. Linkwise – Physical informations. Following Physical information are collected for 162 road links. The following details of overall road links were collected for the study
 - Length of road links
 - Carriageway width
 - Footpath width
 - Right of way
 - Onstreet parking and width covered
 - Encroached area.
- iii. Linkwise Traffic Informations
 - Linkwise peak hour traffic flow in road links are calculated from the Traffic volume count survey
- iv. Linkwise – Existing physical conditions
 - Linkwise existing physical conditions, surface condition, lighting condition, footpath condition and drainage condition in 162 road links are collected. Surface condition, lighting condition, drainage condition and footpath conditions are graded as very poor, poor and fair. Details of existing landuse along the roadside, type of encroachment and onstreet parking on all road links are observed.

11. PROCEDURE ADOPTED TO IDENTIFY THE CONJESTED ROAD LINKS

The extent of the traffic volume on the road links determined from the traffic volume survey conducted at different locations. The equivalent PCU value of the peak hour traffic volume on the road links has been calculated. The equivalent PCU factors adopted for various vehicles are shown in Table.4

12. ROAD LINK CAPACITY

The step by step procedure adopted for calculating road link capacity is as follows.

Table.4 The Equivalent PCU Factors Adopted For Various Vehicles

Vehicle	PCU
Bus, Lorry/Truck	3
Car / Van	1
Two wheeler	0.5
Auto rickshaw	0.6
Cycle	0.4
Cycle rickshaw	1.5
HD cart	4.5
BD cart	8

1. The absolute capacity of a road link is assumed to be between 1300 and 1500 PCU Per hour per lane. Adopting the average of 1400 PCU per land width of 3.5 m, the absolute capacity is taken as 400 PCU per hour per metre width of carriageway.
2. The absolute capacity (400 PCU per metre) multiplied by the “effective” carriageway width gives the actual capacity of the road link. The effective carriageway width has been calculated by reducing the actual width of the carriageway due to different factors affecting the capacity.
3. The factors affecting the capacity are parking, encroachment and landuse. The reduction due to parking and encroachment is shown in Table .5. Predominant land use along the road link affects the capacity and the reduction in capacity due to this factor is shown in Table.6.

Calculated the effective width of carriageway considering the above three factors (Parking, encroachment, landuse). The capacity of each road link has been calculated by using the physical information’s (width of carriageway, parking space, encroachment) is follows.

$$\text{Effective width of of carriageway} = \text{Actual width of carriageway} \times (1 - \text{landuse} / 100) - \text{Parking space} - \text{Encroachment}.$$

$$\text{Capacity of road link} = \frac{\text{Effective width of carriageway} \times 400 \text{ PCU}}{400 \text{ PCU}}$$

Table.5 The Reduction Due To Parking And Encroachment

Type of parking \ Severity of Encroachment	Reduction (m)
Parking prohibited on either side	0
Parking permitted on one side	2.5
Parking permitted on either side	5
No Encroachment	0
Marginal Encroachment	1
Substantial Encroachment	2

Table.6. Reduction in capacity due to land use

Predominant land use	Reduction (per cent)
Open space	0
Residential	5
Institutional	10
Industrial	15
Commercial	30

13. LEVEL OF SERVICE OF ROAD LINKS

Comparison of updated traffic volume and capacity of road link give a volume capacity ratio. According to the volume capacity ratio the level of service of the road links are identified. It led to the identification of the degree of congestion in each road link.

Table 7. Level of service adopted in this study

Volume capacity ratio	Level of service
< 0.6	A
0.6 - 0.7	B
0.7 - 0.8	C
0.8 - 0.9	D
0.9 - 1.0	E
1.0 <	F

Table.8. Shows the Level of Service adopted corresponding to the volume capacity ratio. For design purpose Level of Service “C” is suitable for urban streets (Kadiyali L.R 2007).

The road link with Volume Capacity ratio more than 0.8 are classified as congested links. The effective width of carriageway, capacity, volume capacity ratio and Level of Service of all road links in Salem City corporation area calculated

Identify the type of improvements required for road links to carry existing traffic flow

Road links which are having volume capacity ratio more than 0.8 are considered as a congested links and these road links required improvements to carry existing traffic volume. The following procedure is adopted to identify the required improvement.

Road links which are having volume capacity ratio more than 0.8 reflect that road link will have insufficient width of carriageway to carry existing traffic. Instead of providing extra widening of carriageway it has been assumed that to prohibit the existing on street parking and remove the encroachment. After removing on street parking and encroachment the effective width of carriageway, capacity and volume capacity ratio have been calculated. If the volume capacity ratio is less than 0.8 then that road link required only removal of on street parking and encroachment to carry existing traffic flow.

If the volume capacity ratio after removing the on street parking and encroachment is more than 0.8 then that road links required a widening of carriageway. For providing extra widening the available extra width has been calculated from right-of- way. If the right of way is not available to widen the carriageway then that road link required traffic management measure.

If right of way have space then widen the carriageway up to its full width leaving one metre on each side for pedestrian movements. Again the effective width of carriageway and volume capacity ratio has been calculated. If the volume capacity ratio more than 0.8 then that road link required traffic management measure with extra widening. If the volume capacity ratio less than 0.7 than it reflect that extra widening width has been calculated by assuming average volume capacity ratio of 0.75.

14. TECHNOLOGIES USED FOR FIXING PRIORITY TO IMPLEMENT ROAD IMPROVEMENT PROJECTS.

Several efforts have been made to develop comparative analysis techniques to rank project along various dimension. The most popular approach is the use of priority indices based on current condition of the facility. In this study the points assumed to the various grades of attributes are shown in Table.8. The points assumed to the various grades of the attributes are varied from 0.75 to 3. The rating for each attribute like improving surface condition of carriageway, street lighting, footpath condition drainage condition and widening of carriageway are assigned from the experts view.

15. EXPERT SYSTEM

Questionnaire has been prepared for the purpose of collecting experts view on various road improvements to fix the rating to each. Survey has been conducted with experts and their views on various road attributes has been collected. Average value of each road attribute from the survey has been assumed as a rating to each road attribute. The rating assigned to each road attribute is shown in Table.9.

The weightage of the each road link has been calculated by using points allotted to various grades of road attributes and rating assigned to the each road attributes from the survey.

Table.8. Points assumed to the various grades of each road attributes

S. No	Item	Grade	Points	Variable
1	Surface condition	Very poor	1	X11
		Poor	2	X12
		Fair	3	X13
2	Lighting Condition	Very poor	1	X21
		Poor	2	X22
		Fair	3	X23
3	Drainage Condition	Very poor	1	X31
		Poor	2	X32
		Fair	3	X33
4	Foot path Condition	Very poor	1	X41
		Poor	2	X42
		Fair	3	X43
5	Level of service	F	3	X51
		E	3	X52
		D	3	X53
		C	2.25	X54
		B	1.5	X55
		A	0.75	X56

Weightage of each road link has been calculated as follows.

$$\text{Weightage} = (X_{11} \setminus X_{12} \setminus X_{13})W_1 + (X_{21} \setminus X_{22} \setminus X_{23})W_2 + (X_{31} \setminus X_{32} \setminus X_{33})W_3 + (X_{41} \setminus X_{42} \setminus X_{43})W_4 + (X_{51} \setminus X_{52} \setminus X_{53})W_5$$

Where

$X_{11}, X_{12}, X_{13}, \dots, X_{55}$ = Points allotted to various grades of each road attributes

w_1, w_2, w_3, w_4, w_5 = Ratings assigned to the various attributes from the survey

Table.9. Ratings assigned to each road attribute

S. No	Item	Rating	Variables
1	Improving the road surface condition	37.4	w1
2	Improving the street lighting	10.9	w2
3	Widening of carriage way for the given traffic volume	15.5	w5
4	Improving the footpath for pedestrian	14.3	w4
5	Improving the drainage condition	21.9	w3

If the the road link have all road attributes with very poor or poor grade, the the weightage of the road link should be very low of 96.125. If the road link have all road attributes with fair grade, the weightage should be very high of 300.

16. METHODS ADOPTED FOR FIXING PRIORITY TO IMPLEMENT ROAD IMPROVEMENT PROJECTS

In this study two approaches are considered to fix the priority for implementing road improvement projects.

PRIORITY BASED ON HIERARCHY OF ROAD NETWORK

In this approach the priority for selecting road links to implement road improvement projects are fixed on the basis of hierarchy of road network. According to the hierarchy of road network following priority is assumed.

- Priority 1. Radial roads in CBD area with low weightage.
- Priority 2. Radial roads in Fringe area with low weightage.
- Priority 3. Orbital roads in CBD area with low weightage.
- Priority 4. Orbital roads in Fringe area with low weightage.
- Priority 5. Other roads in CBD area with low weightage.
- Priority 6. Other roads in Fringe area with low weightage.

As per above priority basis the priority has been fixed to the road improvement projects of road links in Salem corporation area. The of priority for selecting road links to implement the road improvement projects as per hierarchy of road network is given in Table.10.

Table.10 Order of priority for implementing road improvement projects in Salem based on hierarchy of road network

Priority No	Link No.	Type	Location Type	Total weightage
1	140	Radial	CBD	135.625
2	146	Radial	CBD	147.1
3	139	Radial	CBD	147.25
4	52	Radial	CBD	157.525
5	55	Radial	CBD	157.525
6	79	Radial	CBD	162.125
7	85	Radial	CBD	180.625
8	145	Radial	CBD	181.975
9	86	Radial	CBD	184.025
10	2	Radial	CBD	191.525
11	67	Radial	CBD	191.525
12	123	Radial	CBD	191.525
13	124	Radial	CBD	191.525
14	43	Radial	CBD	194.2
15	44	Radial	CBD	194.2
16	138	Radial	CBD	196.275
17	1	Radial	CBD	203.15
18	122	Radial	CBD	205.825
19	60	Radial	CBD	206.55
20	61	Radial	CBD	206.55
21	66	Radial	CBD	214.775
22	100	Radial	CBD	217.3
23	125	Radial	CBD	217.3
24	126	Radial	CBD	217.3
25	127	Radial	CBD	217.3
26	45	Radial	CBD	217.45
27	97	Radial	CBD	217.45
28	121	Radial	CBD	217.45
29	115	Radial	CBD	227.725
30	154	Radial	CBD	228.925
31	46	Radial	CBD	229.075
32	47	Radial	CBD	229.075
33	42	Radial	CBD	231.6
34	49	Radial	CBD	231.6
35	128	Radial	CBD	231.6
36	129	Radial	CBD	231.6
37	131	Radial	CBD	231.6

38	149	Radial	CBD	231.6
39	53	Radial	CBD	232.325
40	133	Radial	CBD	233.05
41	65	Radial	CBD	240.55
42	3	Radial	CBD	243.225
43	152	Radial	CBD	243.225
44	153	Radial	CBD	243.225
45	4	Radial	CBD	250.825
46	6	Radial	CBD	250.825
47	118	Radial	CBD	250.825
48	151	Radial	CBD	254.85
49	114	Radial	CBD	262.45
50	116	Radial	CBD	265.125
51	117	Radial	CBD	265.125
52	48	Radial	CBD	266.475
53	130	Radial	CBD	266.475
54	132	Radial	CBD	266.475
55	147	Radial	CBD	266.475
56	148	Radial	CBD	266.475
57	150	Radial	CBD	266.475
58	5	Radial	CBD	274.075
59	110	Radial	CBD	274.075
60	111	Radial	CBD	288.375
61	112	Radial	CBD	288.375
62	113	Radial	CBD	288.375
63	29	Radial	Fringe	124.725
64	143	Radial	Fringe	147.1
65	144	Radial	Fringe	147.1
66	137	Radial	Fringe	147.975
67	51	Radial	Fringe	169.725
68	69	Radial	Fringe	169.725
69	28	Radial	Fringe	173.025
70	141	Radial	Fringe	173.025
71	70	Radial	Fringe	179.9
72	50	Radial	Fringe	180.625
73	142	Radial	Fringe	181.975
74	71	Radial	Fringe	183.3
75	68	Radial	Fringe	191.525
76	62	Radial	Fringe	194.925
77	63	Radial	Fringe	194.925
78	72	Radial	Fringe	203.875
79	12	Radial	Fringe	205.825
80	27	Radial	Fringe	205.825

81	9	Radial	Fringe	217.45
82	10	Radial	Fringe	217.45
83	134	Radial	Fringe	221.425
84	135	Radial	Fringe	221.425
85	155	Radial	Fringe	221.425
86	7	Radial	Fringe	227.725
87	13	Radial	Fringe	227.725
88	15	Radial	Fringe	228.45
89	136	Radial	Fringe	233.05
90	8	Radial	Fringe	243.225
91	25	Radial	Fringe	243.225
92	26	Radial	Fringe	243.225
93	108	Radial	Fringe	262.45
94	14	Radial	Fringe	274.075
95	109	Radial	Fringe	274.075
96	56	Orbital	CBD	157.525
97	57	Orbital	CBD	157.525
98	78	Orbital	CBD	162.125
99	91	Orbital	CBD	180.625
100	90	Orbital	CBD	184.025
101	58	Orbital	CBD	194.925
102	59	Orbital	CBD	194.925
103	159	Orbital	CBD	194.925
104	160	Orbital	CBD	194.925
105	87	Orbital	CBD	205.825
106	88	Orbital	CBD	205.825
107	89	Orbital	CBD	205.825
108	158	Orbital	CBD	206.55
109	157	Orbital	CBD	218.175
110	156	Orbital	CBD	255.575
111	74	Orbital	Fringe	124.725
112	73	Orbital	Fringe	136.35
113	76	Orbital	Fringe	136.35
114	77	Orbital	Fringe	136.35
115	75	Orbital	Fringe	147.975
116	31	Orbital	Fringe	154.85
117	32	Orbital	Fringe	169.15
118	17	Orbital	Fringe	183.3
119	39	Orbital	Fringe	190.325
120	40	Orbital	Fringe	190.325
121	41	Orbital	Fringe	201.95
122	11	Orbital	Fringe	205.825
123	16	Orbital	Fringe	206.55

124	30	Orbital	Fringe	206.55
125	33	Orbital	Fringe	206.55
126	19	Orbital	Fringe	216.1
127	64	Orbital	Fringe	218.175
128	18	Orbital	Fringe	253.5
129	20	Orbital	Fringe	253.5
130	21	Orbital	Fringe	253.5
131	22	Orbital	Fringe	253.5
132	34	Orbital	Fringe	276.75
133	35	Orbital	Fringe	276.75
134	36	Orbital	Fringe	288.375
135	37	Orbital	Fringe	288.375
136	38	Orbital	Fringe	288.375
137	54	Others	CBD	157.525
138	84	Others	CBD	169.725
139	92	Others	CBD	180.625
140	81	Others	CBD	184.025
141	83	Others	CBD	184.025
142	80	Others	CBD	194.925
143	94	Others	CBD	194.925
144	98	Others	CBD	203.15
145	93	Others	CBD	203.875
146	95	Others	CBD	205.825
147	96	Others	CBD	205.825
148	82	Others	CBD	207.275
149	120	Others	CBD	229.075
150	99	Others	CBD	254.85
151	119	Others	CBD	288.375
152	161	Others	Fringe	157.525
153	162	Others	Fringe	157.525
154	23	Others	Fringe	205.825
155	24	Others	Fringe	205.825
156	101	Others	Fringe	218.025
157	102	Others	Fringe	218.025
158	103	Others	Fringe	232.325
159	106	Others	Fringe	254.225
160	107	Others	Fringe	254.225
161	105	Others	Fringe	265.85
162	104	Others	Fringe	277.475

17. PRIORITY BASED ON LOCATION OF ROAD LINKS

In this approach the priority for selecting road links to implement road improvement projects are fixed on the basis of location of road link. According to the location of road link following priority is assumed.

- Priority 1. Radial roads in CBD area with low weightage.
- Priority 2. Orbital roads in CBD area with low weightage
- Priority 3. Other roads in CBD area with low weightage.
- Priority 4. Radial roads in Fringe area with low weightage.
- Priority 5. Orbital roads in Fringe area with low weightage.
- Priority 6. Other roads in Fringe area with low weightage.

As per above priority basis the priority has been fixed to the road improvement projects of road links in Salem corporation area. The of priority for selecting road links to implement the road improvement projects as per location of road link is given in Table.11.

Table.11. Order of priority for implementing road improvement projects in Salem based on location of road link

Priori ty no	Link number	Location	Type	Total weightage
1	140	CBD	Radial	135.625
2	146	CBD	Radial	147.1
3	139	CBD	Radial	147.25
4	52	CBD	Radial	157.525
5	55	CBD	Radial	157.525
6	79	CBD	Radial	162.125
7	85	CBD	Radial	180.625
8	145	CBD	Radial	181.975
9	86	CBD	Radial	184.025
10	2	CBD	Radial	191.525
11	67	CBD	Radial	191.525
12	123	CBD	Radial	191.525
13	124	CBD	Radial	191.525
14	43	CBD	Radial	194.2
15	44	CBD	Radial	194.2
16	138	CBD	Radial	196.275
17	1	CBD	Radial	203.15
18	122	CBD	Radial	205.825
19	60	CBD	Radial	206.55
20	61	CBD	Radial	206.55
21	66	CBD	Radial	214.775

22	100	CBD	Radial	217.3
23	125	CBD	Radial	217.3
24	126	CBD	Radial	217.3
25	127	CBD	Radial	217.3
26	45	CBD	Radial	217.45
27	97	CBD	Radial	217.45
28	121	CBD	Radial	217.45
29	115	CBD	Radial	227.725
30	154	CBD	Radial	228.925
31	46	CBD	Radial	229.075
32	47	CBD	Radial	229.075
33	42	CBD	Radial	231.6
34	49	CBD	Radial	231.6
35	128	CBD	Radial	231.6
36	129	CBD	Radial	231.6
37	131	CBD	Radial	231.6
38	149	CBD	Radial	231.6
39	53	CBD	Radial	232.325
40	133	CBD	Radial	233.05
41	65	CBD	Radial	240.55
42	3	CBD	Radial	243.225
43	152	CBD	Radial	243.225
44	153	CBD	Radial	243.225
45	4	CBD	Radial	250.825
46	6	CBD	Radial	250.825
47	118	CBD	Radial	250.825
48	151	CBD	Radial	254.85
49	114	CBD	Radial	262.45
50	116	CBD	Radial	265.125
51	117	CBD	Radial	265.125
52	48	CBD	Radial	266.475
53	130	CBD	Radial	266.475
54	132	CBD	Radial	266.475
55	147	CBD	Radial	266.475
56	148	CBD	Radial	266.475
57	150	CBD	Radial	266.475
58	5	CBD	Radial	274.075
59	110	CBD	Radial	274.075
60	111	CBD	Radial	288.375
61	112	CBD	Radial	288.375
62	113	CBD	Radial	288.375
63	56	CBD	Orbital	157.525
64	57	CBD	Orbital	157.525

65	78	CBD	Orbital	162.125
66	91	CBD	Orbital	180.625
67	90	CBD	Orbital	184.025
68	58	CBD	Orbital	194.925
69	59	CBD	Orbital	194.925
70	159	CBD	Orbital	194.925
71	160	CBD	Orbital	194.925
72	87	CBD	Orbital	205.825
73	88	CBD	Orbital	205.825
74	89	CBD	Orbital	205.825
75	158	CBD	Orbital	206.55
76	157	CBD	Orbital	218.175
77	156	CBD	Orbital	255.575
78	54	CBD	Others	157.525
79	84	CBD	Others	169.725
80	92	CBD	Others	180.625
81	81	CBD	Others	184.025
82	83	CBD	Others	184.025
83	80	CBD	Others	194.925
84	94	CBD	Others	194.925
85	98	CBD	Others	203.15
86	93	CBD	Others	203.875
87	95	CBD	Others	205.825
88	96	CBD	Others	205.825
89	82	CBD	Others	207.275
90	120	CBD	Others	229.075
91	99	CBD	Others	254.85
92	119	CBD	Others	288.375
93	29	Fringe	Radial	124.725
94	143	Fringe	Radial	147.1
95	144	Fringe	Radial	147.1
96	137	Fringe	Radial	147.975
97	51	Fringe	Radial	169.725
98	69	Fringe	Radial	169.725
99	28	Fringe	Radial	173.025
100	141	Fringe	Radial	173.025
101	70	Fringe	Radial	179.9
102	50	Fringe	Radial	180.625
103	142	Fringe	Radial	181.975
104	71	Fringe	Radial	183.3
105	68	Fringe	Radial	191.525
106	62	Fringe	Radial	194.925
107	63	Fringe	Radial	194.925

108	72	Fringe	Radial	203.875
109	12	Fringe	Radial	205.825
110	27	Fringe	Radial	205.825
111	9	Fringe	Radial	217.45
112	10	Fringe	Radial	217.45
113	134	Fringe	Radial	221.425
114	135	Fringe	Radial	221.425
115	155	Fringe	Radial	221.425
116	7	Fringe	Radial	227.725
117	13	Fringe	Radial	227.725
118	15	Fringe	Radial	228.45
119	136	Fringe	Radial	233.05
120	8	Fringe	Radial	243.225
121	25	Fringe	Radial	243.225
122	26	Fringe	Radial	243.225
123	108	Fringe	Radial	262.45
124	14	Fringe	Radial	274.075
125	109	Fringe	Radial	274.075
126	74	Fringe	Orbital	124.725
127	73	Fringe	Orbital	136.35
128	76	Fringe	Orbital	136.35
129	77	Fringe	Orbital	136.35
130	75	Fringe	Orbital	147.975
131	31	Fringe	Orbital	154.85
132	32	Fringe	Orbital	169.15
133	17	Fringe	Orbital	183.3
134	39	Fringe	Orbital	190.325
135	40	Fringe	Orbital	190.325
136	41	Fringe	Orbital	201.95
137	11	Fringe	Orbital	205.825
138	16	Fringe	Orbital	206.55
139	30	Fringe	Orbital	206.55
140	33	Fringe	Orbital	206.55
141	19	Fringe	Orbital	216.1
142	64	Fringe	Orbital	218.175
143	18	Fringe	Orbital	253.5
144	20	Fringe	Orbital	253.5
145	21	Fringe	Orbital	253.5
146	22	Fringe	Orbital	253.5
147	34	Fringe	Orbital	276.75
148	35	Fringe	Orbital	276.75
149	36	Fringe	Orbital	288.375
150	37	Fringe	Orbital	288.375

151	38	Fringe	Orbital	288.375
152	161	Fringe	Others	157.525
153	162	Fringe	Others	157.525
154	23	Fringe	Others	205.825
155	24	Fringe	Others	205.825
156	101	Fringe	Others	218.025
157	102	Fringe	Others	218.025
158	103	Fringe	Others	232.325
159	106	Fringe	Others	254.225
160	107	Fringe	Others	254.225
161	105	Fringe	Others	265.85
162	104	Fringe	Others	277.475

18. CONCLUSION

An important product of the analysis is the development of a program which outlines the improvements to be carried out. From the study made, the type of improvement required to the road links to carry the existing traffic flow has been identified. Total number of road links requiring various types of improvements in Salem city corporation area to carry existing traffic flow is shown in Table.10.

Table.10. Types of improvements required to carry existing traffic flow

Sl. No	Type of Improvement Required	Total Number of Road links
1.	Removal of onstreet parking and encroachment	44
2.	Widening of carriageway	52
3.	Traffic Management Measure required with extrawidening of carriageway	23

In programming process, priorities are set for project implementation. Even in cases where a formal process of priority setting does not exist, the allocation of organizational and financial resources for the development of some projects over others is an implicit setting of priorities. The important technique devised in this study is working out priority indices based on measures of current conditions of the facilities. There are two approaches for fixing the priorities to select road links to improve existing conditions.

In the first approach priorities are fixed mainly based on hierarchy of road network and considering location of road links with weightages assigned to the road links. In the second approach priorities are fixed mainly based on location of road links and considering hierarchy of road network with weightages assigned to the road links.

19. REFERENCES

- [1]. DTCP (1986), 'Short term improvement program ME – Traffic and Transportation study for Coimbatore, Madurai, Trichy and Salem', DTCP, Tamil Nadu
- [2]. Hanspeter Georgi (1973), 'Cost- Benefit Analysis and Public Investments in Transport: A Survey', First Edition, Butter Worths (Publishers), London.
- [3]. Kadiyali.L.R.(2007), 'Traffic Engineering and Transport Planning', 7th edition, Khanna publishers, Delhi.
- [4]. Khanna S.K – Justo C.E.G (2010), 'Highway Engineering', 9th edition, Nem Chand and Bros. publishers, Roorkee(U.P) Lindsay R. Peat (1982), 'Practical Guide to DBMS selection', Walter de Grawyter, New York.
- [5]. Meyer M.d.Miller E.J (1984), 'Urban Transportation Planning', Mcgraw – Hill series, New Delhi.
- [6]. Subramanian P. (1990), 'Capacity restrained trip assignment model for Madras City', ME Urban Engineering Thesis, Madras – 600025.
- [7]. V.N.Vazirani & S.P.Chandola, 'Transportation Engineering Vol.I', 5th edition, Khanna Publishers, New Delhi
- [8]. Dr.L.R.Kadyali & Dr.N.B.Lal, 'Principles and Practices of Highway Engineering', 5th edition, Khanna Publishers, New Delhi
- [9]. B.L.Gupta & Amit Gupta 'Highway and bridge Engineering' 3rd edition Standard Publishers Distributers, New Delhi
- [10]. C.Jotin Khisty & B.Kent Lall, 'Transportation Engineering' 3rd edition, PHI Learning Private Limited, New Delhi
- [11]. Gurcharan Singh, 'Highway Engineering' 5rd edition Standard Publishers Distributers, New Delhi
- [12]. R.K. Khitoliya, 'Principles of Highway Engineering' 1st edition, Dhanpat Rai Publishing Company, New Delhi.
- [13]. DTCP (1999), 'Comprehensive Traffic and Transportation Study for Salem', Pallavan Transport Consultancy Services Ltd., Chennai, Tamil Nadu.

ANAMBRA STATE, SCALING UP URBAN WATER SUPPLY AND SANITATION DELIVERY: THE PERSPECTIVE OF WATER SUPPLY AND SANITATION SECTOR REFORM PROGRAMME

Otti Victor Ifeanyichukwu*
Ejikeme Romanus Ifeanyichukwu**
Nwajuaku Afam Ifeanyichukwu***

(*, ** Federal Polytechnic, Oko; *** Nnamdi Azikiwe University, Awka)

Abstract

The provision of water to majority of Nigerians has always been at the discretion of the Government without any say whatsoever by the beneficiary communities. Of course this anomaly has led many communities to be without access to this essential commodity, because the reasons were more political than social-economical. The present democratically elected government has gone a long way to reverse the deprivation of potable water to the majority of Nigerians, through the introduction of progressive policies, legislation and procedures in federal ministry of water resources (FMWR). This paper is intended to discuss practical strategies of maximizing the benefits of such policies to the beneficiary communities through development facilitation, Anambra state ministry of Bureau of utilities and water resources in partnership with World Bank through water supply and sanitation reform programme (WSSSRP) as reference.

KEYWORDS: Water and Sanitation, essential commodity, socio-economical, community, policy, strategy.

Introduction

Water is a source of life and researchers over the years have pointed to the fact that fresh water resources are not unlimited. Although desert encroachment has left some communities homeless in the North and gully erosion is a permanent threat in south eastern part of the country destroying pipe borne water and upturning overhead and ground tanks. Urban communities need to use these scarce resources with care so that future generation will be able to benefit from good quality water. Moreover, correct utilization of water does not mean merely consuming it without thinking what happens to it after words, but means that care should also be taken of the waste water in order to avoid pollution and alleviate the spread of dangerous diseases.[3]

High population growth rates, rapid urbanisation, unsustainable exploitation of water resources for domestic, industrial and agricultural purposes, as well as the continue degradation of freshwater resources through waste discharge in Niger Delta region, are but some of the factors which have in the past led to improper water resources management in many developing countries. Therefore, water supply and sanitation are considered human rights and they are basic priorities of the development programme in Nigeria. More so, experience in developing countries has shown that provision of water and sanitation facilities should go hand in hand with education and training in their proper use before good results in improving the quality of life in the urban communities can be achieved.[5][7]

Consequently, the beneficiaries of water and sanitation projects should learn where the water comes from, where the wastes go to, why these services should be paid for and how to take responsibility for and ownership over the infrastructures provided.

In realizing the complexity of the above issues and the nature of expertise in various organisations, Anambra State Government formed a working agreement with World Bank, through an agency, Water Supply and Sanitation Sector Reform Programme (WSSSRP). Based on the needs of infrastructural development projects in Nigeria, Anambra State Government and World Bank partnership designed a framework for education, training and operation processes in urban and rural community water supply and sanitation projects.[5]

Objective

The aim of the programme is to identify the more promising approaches in order to disseminate these into the rest of the sector for consideration where applicable. The approaches are based on a refined set of internationally acceptable water reformed principles which have emerged over the years.[6] These principles are listed as follows:

- Water sources and catchment protection are essential
- Adequate water allocation needs to be agreed upon between stake holders within a national frame work
- Efficient water use is essential and often an important water sources
- Management needs to be taken care of at lowest appropriate levels

- Involvement of all stake holders is required
- Striking a gender balance is needed as activities related to different roles of men and women
- Skill development are the key to sustainability
- Water is treated as having an economic and socio values.

Methodology

The basic priorities of Anambra State are the empowerment of urban community by providing them with the knowledge to make their own decision and to take ownership of development projects. This programme of education, training and operation is vital part of every urban community water supply and sanitation projects should be an inseparable part of the whole development process, from the pre-project phase through monitoring and evaluation, implementation and finally to the operation and maintenance after a project has been completed.[2]

The programme framework was developed by team of specialist in different fields; engineering, social science, education and training. The framework must be tested with the beneficiaries of various water supply and sanitation projects before making it available for use in infrastructural development projects.[4]

The framework consists of light phases namely;

- i. Pre-project
- ii. Feasibility
- iii. Detailed survey
- iv. Project planning
- v. Monitoring and Evaluation
- vi. Pre contract
- vii. Construction
- viii. Operation and maintenance

Framework table

Technical Issues	Socio-Economic Issues
Pre-Project <ul style="list-style-type: none"> • Initial approach • Organisation of community • Health Education • Hygiene Education • Payment principles • Vandalising 	<ul style="list-style-type: none"> - Entering a community - Community mobilization - Development Programme Principles/financing State Government - Gender issues - Community participation - Communication
Feasibility <ul style="list-style-type: none"> • Needs analysis • Feasibility study • Technologies/Technical aspects • Cost • Appoint technical consultant 	<ul style="list-style-type: none"> - Project Process - Committee management - Resources - Agriculture - Introduction to technology
Detailed survey <ul style="list-style-type: none"> • Water & Sanitation committee • Site/terrain features • Ability to pay • Population • Characteristic • Responsibility/payment for services 	<ul style="list-style-type: none"> - Leadership skill - Introduction to engineering - Cost - Available Technology
Project Planning <ul style="list-style-type: none"> • Technology choice/cost • Project proposal • Fund raising • Project management • Decision making 	<ul style="list-style-type: none"> - Management procedures - Conflict/stress management - Financial management - Operation and maintenance - Entrepreneurship - Institutional aspects in management skills
Monitoring & Evaluation	On-going – takes place after each phase

(Pre- contract - Design - Training • Tenderers • Project management • Labour/work - Tender period - Tender award	- Specification - Business skill - Contracts - Legal aspects - Risk in business
Construction - Quality - Programme - Budget - Variation orders/ claims - Defects liability period	- Specification - Construction - Management - Contracts - Legal aspects - Risk in business
Operation & maintenance - technical - Routine - Problem solving - Collection of money - Responsibility/vandalism	- Leisure time activities - Diversification skills - Payment collection/control /auditing

Viewing from above table, testing of the whole framework step by step will be a time consuming and expensive process because it requires following implementation of a whole project, which in some cases may continue for a number of years. Four phases have therefore been identified for testing and evaluation namely;

- Pre project
- Monitoring and Evaluation
- Construction
- Operation and Maintenance

Each one of the above phases of framework will be tested under the condition of actual infrastructural development projects with different types of urban communities. Anambra State Government in conjunction with World Bank has already developed various educational tools such as posters, booklets, a scale model of a settlement manuals etc. which will be used to convey the information to the communities involved in water supply and sanitation projects. The training will be done by facilitators (NGOs) already engaged with on-going or planned projects, who will use the available tools and follows the steps and requirement of the framework.[8]

The process of training, education and operation will be monitored by social scientists and engineers from the Government as well as specialist in education, training and construction from World Bank. The facilitators and urban community members who will be receiving the training will also provide a valuable feedback on the sustainability and applicability of the framework. The results of the evaluation will then be used for final revision of the framework and the production of guidelines for using the framework in water supply and sanitation projects.[1]

Results

The basic needs approach requires an intervention of Anambra State in the creation of access to essential service. These services include portable water, employment, sanitation, health, education, security, food and others. The provision of these services by the State Government on the other hand, depends on the resources of Federal Government, and the economic policies that are pursued by the government. Obviously a country whose policies are not geared towards sustainable growth and development often fails to afford these services, especially as Federal Government has poor social welfare programme, which is found to lack in the adequate provision of these basic needs, even if she has high level of growth. These policies are, however, only enabling mechanism but cannot deliver and create capacity to have a community facilitation mechanism that will ensure the creation of absorption capacity in the urban communities.[6][7]

Conclusion

The provision of portable water to urban communities is a broad process that requires the coordination of needs, resources and institutional framework. This coordination needs to be underpinned by effective facilitation. The process is often time consuming and depends on the level of development of the urban communities and their institutions. Its success should be judged according to how equitable the power balances turn out to be as well as socio-economic, political and environmental sustainability.[1] It is worth noting that urban community driven development has been in existence but a new experience in water and sanitation is coming up in Nigeria and its success will be determined by how the relationship within resource institutions and communities are managed.

References

- [1] BEBBINGTON, A et al “Of Texts and practices:Empowerment and organisational culture in World Bank Funded Rural Development Programme” Journal of Development Studies Vol 43 no 4 [2007] pp597-621
- [2] CASLEY, D.J. et al : The collection analysis and use of Monitoring and Evaluation Data: World Bank Publication.[1988] pp 101-119
- [3] CLEAVER, F Tet al “Water Governance andpoverty:What works for the poor?” Bradford:University of Bradford [2005] pp 53-67
- [4] KADER, A.:Water supply and sanitation policy: Department of Water Affair and Foresting Cape Town.[1994] pp91-111
- [5] RIVERA, D.:Private Sector Participation in the water supply and waste water Sector Directions in Development Series. World Bank Washington DC.[1996] pp 195-207
- [6] SALLY, B.:Practical Strategies for involving women as well as men in water and sanitation activities: Institute of Development Studies, University of Sussex, Brighton (save land).[1993] pp99-121
- [7] World Bank, : Proceeding of Seminar on Water Resources Management in Tanzania.[1994] pp87-103
- [8] World Bank,:Toolkits for Private Sector participation in water and sanitation: World Bank, Washington DC.[1996] pp 29-45

A posteriori error estimation for incompressible flow problem

Samy Alami¹, Abdeslam Elakkad², and Ahmed Elkhalfi¹

¹Laboratoire Génie Mécanique - Faculté des Sciences et Techniques B.P. 2202 - Route d'Imouzzer - Fès Maroc

²Mathématiques, Centre de Formation des Instituteurs Sefrou, B.P: 243 Sefrou Maroc

ABSTRACT

This paper describes numerical solutions of incompressible Navier-Stokes equations. It includes algorithms for discretization by finite element methods and a posteriori error estimation of the computed solutions.

A numerical experiment on the driven cavity flow is given to demonstrate the effectiveness of the error estimate. We compare the result with the solution from ADINA system as well as with values from other simulations.

Keywords - Navier-Stokes Equations, Finite Element Method, A posteriori error estimation, Adina system.

I. INTRODUCTION

This paper describes a numerical solution of partial differential equations (PDEs) that are used to model steady incompressible fluid flow. For the equations, we offer a choice of two-dimensional domains on which the problem can be posed, along with boundary conditions and other aspects of the problem, and a choice of finite element discretizations on a quadrilateral element mesh.

The plan of the paper is as follows. The model problem is described in section II, followed by a posteriori error bounds of the computed solution in section III and numerical experiments are carried out in section VI.

II. INCOMPRESSIBLE NAVIER-STOKES EQUATIONS

We consider the steady-state Navier-Stokes equations for the flow of a Newtonian incompressible viscous fluid with constant viscosity:

$$\begin{cases} -\nu \nabla^2 \vec{u} + \vec{u} \cdot \nabla \vec{u} + \nabla p = \vec{f}, & \text{sur } \Omega \\ \nabla \cdot \vec{u} = 0, & \text{sur } \Omega \\ \vec{u} = \vec{0}, & \text{sur } \Gamma \end{cases} \quad (1)$$

Where $\nu > 0$ is a given constant called the kinematic viscosity.

\vec{u} is the fluid velocity, p is the pressure field, ∇ is the gradient and $\nabla \cdot$ is the divergence operator.

The boundary value problem that is considered is the system (1) posed on two or three-dimensional domain Ω .

We define the spaces:

$$V = H_0^1(\Omega) \times H_0^1(\Omega), \quad (2)$$

and

$$W = \left\{ q \in L^2(\Omega) : \int_{\Omega} q(x) dx = 0 \right\}, \quad (3)$$

Let the bilinear forms $a : V \times V \rightarrow \mathbb{R}$, $b : V \times W \rightarrow \mathbb{R}$, $d : W \times W \rightarrow \mathbb{R}$, and the trilinear form $c : V \times V \times V \rightarrow \mathbb{R}$

$$a(u, v) = \nu \int_{\Omega} \nabla u \cdot \nabla v dx, \quad b(v, q) = - \int_{\Omega} (q \nabla \cdot v) dx, \quad d(p, q) = \int_{\Omega} p q dx, \quad (4)$$

$$c(z, u, v) = \int_{\Omega} (z \cdot \nabla u) \cdot v. \quad (5)$$

These inner products induce norms on V and W denoted by $\|v\|_V$ and $\|q\|_W$ respectively.

$$\|v\|_V = a(v, v)^{\frac{1}{2}} \quad \forall v \in V, \quad (6)$$

$$\|q\|_W = d(q, q)^{\frac{1}{2}} \quad \forall q \in W. \quad (7)$$

Given the continuous functional $l : V \rightarrow \mathbb{R}$

$$l(v) = \int_{\Omega} f \cdot v dx, \quad (8)$$

Then the standard weak formulation of the Navier-Stokes flow problem (1) is the following:

Find $(u, p) \in V \times W$ such that

$$a(u, v) + b(v, p) + c(u, u, v) + b(u, q) = l(q), \quad \text{for all } (v, q) \in V \times W. \quad (9)$$

Let the subspace of divergence-free velocities be given by

$$V_{E_0} = \{z \in V; z \cdot n = 0 \text{ sur } \partial\Omega \text{ et } \nabla \cdot z = 0 \text{ sur } \Omega\}. \quad (10)$$

The convection term is skew-symmetric: $c(z, u, v) = -c(z, v, u)$; over V_{E_0} , this mean that

$$c(z, u, u) = 0 \quad \forall z \in V_{E_0} \quad (11)$$

The problem (9) is known [4] to possess a unique solution whenever the data is sufficiently small. In particular, if

$$l(v) \leq \theta \frac{V^2}{C} |v|_{H^1(\Omega)} \quad \forall v \in V, \quad (12)$$

For some fixed $\theta \in [0,1)$ then there is a unique solution $u \in V$ satisfying

$$|u|_{H^1(\Omega)} \leq \theta \frac{V}{C}. \quad (13)$$

Let P be a regular partitioning of the domain Ω into the union of N subdomains K such that

- $N < \infty$,
- $\bar{\Omega} = \bigcup_{K \in P} \bar{K}$,
- $K \cap J$ is empty whenever $K \neq J$,
- Each K is a convex Lipschitzian domain with piecewise smooth boundary ∂K .

The common boundary between subdomains K and J is denoted by

$$\Gamma_{KJ} = \partial K \cap \partial J. \quad (14)$$

The finite element subspaces X and M are constructed in the usual manner so that the inclusion $X \times M \subset V \times W$ holds.

The finite element approximation to (9) is then

Find (u^X, p^M) such that

$$a(u^X, v^X) + b(v^X, p^M) + c(u^X, u^X, v^X) + b(u^X, q^M) = l(q^M) \quad (15)$$

For all $(v^X, q^M) \in V \times W$.

Let $(e, E) \in V \times W$ be the error in the finite element approximation, $e = u - u^X$ and $E = p - p^M$ and define $(\phi, \psi) \in V \times W$ to be the Ritz projection of the modified residuals

$$a(\phi, v) + d(\psi, q) = a(e, v) + b(v, E) + b(e, q) + D(u^X, v), \quad (16)$$

for all $(v, q) \in V \times W$,

where

$$D(u, u^X, v) = c(u, u, v) - c(u^X, u^X, v).$$

Theorem 2.1. Let (13) hold. Then there exist positive constants K_1 and K_2 such that

$$K_1 \left(\|\phi\|_V^2 + \|\psi\|_W^2 \right) \leq \|u - u^X\|_V^2 + \|p - p^M\|_W^2 \leq K_2 \left(\|\phi\|_V^2 + \|\psi\|_W^2 \right) \quad (17)$$

Proof. See T.J. Oden, W. Wu, and M. Ainsworth [16].

III. A POSTERIORI ERROR ANALYSIS

The local velocity space on each subdomain $K \in P$ is

$$V_K = \{v \in H^1(K) \times H^1(K) : v = 0 \text{ sur } \partial\Omega \cap \partial K\} \quad (18)$$

And the pressure space is

$$W_K = L^2(K) \quad (19)$$

Let the bilinear forms

$$a_K : V_K \times V_K \rightarrow \mathbb{R}, \quad b_K : V_K \times W_K \rightarrow \mathbb{R}, \\ d_K : W_K \times W_K \rightarrow \mathbb{R},$$

and the trilinear form $c_K : V_K \times V_K \times V_K \rightarrow \mathbb{R}$

$$a_K(u, v) = \nu \int_K \nabla u \cdot \nabla v, \quad b_K(v, q) = - \int_K q (\nabla \cdot v),$$

$$d_K(p, q) = - \int_K pq \quad (20)$$

$$c_K(z; u, v) = \int_K (z \cdot \nabla u) \cdot v \quad (21)$$

Given the continuous functional $l_K : V_K \rightarrow \mathbb{R}$

$$l_K(v) = \int_K f \cdot v \, dx \quad (22)$$

Hence for $v, w \in V$ and $q \in W$ we have

$$a(v, w) = \sum_{K \in P} a_K(v_K, w_K) \quad (23)$$

$$b(v, q) = \sum_{K \in P} b_K(v_K, q_K) \quad (24)$$

$$c(z, u, v) = \sum_{K \in P} c_K(z_K, u_K, v_K) \quad (25)$$

$$l(v) = \sum_{K \in P} l_K(v_K) \quad (26)$$

The broken velocity space $V(P)$ is defined by

$$V(P) = \prod_{K \in P} V_K \quad (27)$$

And the broken pressure space is defined by

$$W(P) = \left\{ q \in \prod_{K \in P} W_K : \int_{\Omega} q(x) \, dx = 0 \right\} \quad (28)$$

Examining the previous notations reveals that

$$W(P) = W \quad (29)$$

We consider the space of continuous linear functional τ on $V(P) \times W(P)$ that vanish on the space $V \times W$ Therefore, let $H(div, \Omega)$ denote the space

$$H(div, \Omega) = \{A \in L^2(\Omega)^{2 \times 2} : div A \in L^2(\Omega)^2\} \quad (30)$$

Equipped with norm

$$\|A\|_{H(div, \Omega)} = \left\{ \|A\|_{L^2(\Omega)}^2 + \|div A\|_{L^2(\Omega)}^2 \right\}^{\frac{1}{2}} \quad (31)$$

Theorem 3.1. A continuous linear functional τ on the space $V(P) \times W(P)$ vanishes on the space $V \times W$ if and only if there exists $A \in H(div, \Omega)$ such that

$$\tau[(v, q)] = \sum_{K \in P} \int_{\partial K} n_K \cdot Av_K ds, \quad (32)$$

Where n_K denotes the unit outward normal vector on the boundary of K .

Proof. See M. Ainsworth and J. Oden [5].

It will be useful to introduce the stress like tensor $\sigma(v, q)$ formally defined to be

$$\sigma_{ij} = v \frac{\partial v_i}{\partial x_j} - q \delta_{ij} \quad (33)$$

where δ_{ij} is the Kronecker symbol.

In order to define the value of the normal component of the stress on the interelement boundaries it is convenient to introduce notations for the jump on Γ_{KJ} :

$$[[n \cdot \sigma(v^x, q^M)]] = n_K \cdot \sigma(v_K^x, q_K^M) + n_J \cdot \sigma(v_J^x, q_J^M) \quad (34)$$

Furthermore, an averaged normal stress on is defined as

$$\langle n_K \cdot \sigma(v^x, q^M) \rangle = \begin{bmatrix} \alpha_{KJ}^{(1)} & 0 \\ 0 & \alpha_{KJ}^{(2)} \end{bmatrix} n_K \cdot \sigma(v_K^x, q_K^M) + \begin{bmatrix} \alpha_{JK}^{(1)} & 0 \\ 0 & \alpha_{JK}^{(2)} \end{bmatrix} n_K \cdot \sigma(v_J^x, q_J^M) \quad (35)$$

where $\alpha_{KJ}^{(i)} : \Gamma_{KJ} \rightarrow \mathbb{R}$ are smooth (polynomial) functions. Naturally, should the stress be continuous then it is required that the averaged stress coincide with this value.

Therefore, on Γ_{KJ} ,

$$\begin{bmatrix} \alpha_{KJ}^{(1)} & 0 \\ 0 & \alpha_{KJ}^{(2)} \end{bmatrix} + \begin{bmatrix} \alpha_{JK}^{(1)} & 0 \\ 0 & \alpha_{JK}^{(2)} \end{bmatrix} = \begin{bmatrix} 1 & 0 \\ 0 & 1 \end{bmatrix} \quad (36)$$

The notation $[[.]]$ is also used to define jumps in the elements of $V(P)$ between subdomains.

Define

and

$$[[v]] = \begin{cases} v_K - v_J, & K > J, \\ v_J - v_K, & K < J, \end{cases} \quad (37)$$

$$[[n]] = \begin{cases} n_K - n_J, & K > J, \\ n_J - n_K, & K < J. \end{cases} \quad (38)$$

The following identity, valid for $v \in V(P)$ is readily verified:

$$\sum_{K \in P} \int_{\partial K} \langle n_K \cdot \sigma(u^x, p^M) \rangle \cdot v ds = \sum_{\Gamma_{KJ}} \int_{\Gamma_{KJ}} \langle n_K \cdot \sigma(u^x, p^M) \rangle \cdot [[v]] ds \quad (39)$$

Lemma 3.1. Under the above notations and conventions, there exists $\bar{\mu} \in H(div, \Omega)$ such that for all $(w, q) \in V(P) \times W(P)$

$$\bar{\mu}[(w, q)] = \sum_{\Gamma_{KJ}} \int_{\Gamma_{KJ}} \langle n_K \cdot \sigma(u^x, p^M) \rangle \cdot [[w]] ds \quad (40)$$

Proof. See M. Ainsworth and J. Oden [14].

Summarizing, we have shown the following :

Theorem 3.2. Let $J_K : V_K \rightarrow \mathbb{R}$ be a quadratic functional

$$J_K(w_K) = \frac{1}{2} a_K(w_K, w_K) - l_K(w) + a_K(u^x, w_K) + b_K(w_K, p^M) + C_K(u^x, u^x, w_K) - \int_{\partial K} \langle n_K \cdot \sigma(u^x, p^M) \rangle \cdot w_K ds. \quad (41)$$

Then

$$\|\phi\|_V^2 + \|\psi\|_W^2 \leq \sum_{K \in P} \left(-2 \inf_{w_K \in V_K} J_K(w_K) + d_K(\nabla \cdot u_K^x, \nabla \cdot u_K^x) \right). \quad (42)$$

The analysis has leads to problems on each subdomain of the form

$$\inf_{w_K \in V_K} J_K(w_K).$$

Suppose for a moment that the minimum exists, then the minimizing element is characterized by finding $\phi_K \in V_K$ such that

$$d(\phi_K, v) = l_K(v) - a_K(u^x, v) - b_K(v, p^M) - C_K(u^x, u^x, v) + \int_{\partial K} \langle n_K \cdot \sigma(u^x, p^M) \rangle \cdot v ds \quad (43)$$

for all $v \in V_K$.

The necessary and sufficient conditions for the existence of a minimum are that the data satisfy the following compatibility for equilibration condition:

$$0 = l_K(\theta) - a_K(u^x, \theta) - b_K(\theta, p^M) - C_K(u^x, u^x, \theta) + \int_{\partial K} \langle n_K \cdot \sigma(u^x, p^M) \rangle \cdot \theta ds \quad (44)$$

For all $\theta \in Ker[a, V_K]$,

where

$$Ker[a, V_K] = \{\theta \in V_K : a_K(w, \theta) = 0 \quad \forall w \in V_K\}. \quad (45)$$

When the subdomain K lies on the boundary $\partial\Omega$ the local problem (43) will be subject to a homogeneous Dirichlet condition on a portion of their boundaries and thus will be automatically well posed. However, elements away from the boundary are subject to pure Neumann conditions and the null space of the operator $a(\cdot, \cdot)$ will contain the rigid motions

$$Ker[a, V_K] = Span\{\theta_1, \theta_2\}, \quad (46)$$

and

$$\theta_1 = \begin{bmatrix} 1 \\ 0 \end{bmatrix}, \quad \theta_2 = \begin{bmatrix} 0 \\ 1 \end{bmatrix} \quad (47)$$

We shall be able to construct data which satisfy the equilibration condition (44). First we define

$$\begin{bmatrix} \lambda_{KJ}^{(1)} & 0 \\ 0 & \lambda_{KJ}^{(2)} \end{bmatrix} = \begin{bmatrix} \alpha_{KJ}^{(1)} & 0 \\ 0 & \alpha_{KJ}^{(2)} \end{bmatrix} - \frac{1}{2} \begin{bmatrix} 1 & 0 \\ 0 & 1 \end{bmatrix}, \quad (48)$$

So that consistency condition (36) becomes

$$\begin{bmatrix} \lambda_{KJ}^{(1)} & 0 \\ 0 & \lambda_{KJ}^{(2)} \end{bmatrix} + \begin{bmatrix} \lambda_{JK}^{(1)} & 0 \\ 0 & \lambda_{JK}^{(2)} \end{bmatrix} = \begin{bmatrix} 0 & 0 \\ 0 & 0 \end{bmatrix}, \quad (49)$$

The averaged interelement stress may be rewritten

$$\langle n_K \cdot \sigma(v^x, q^M) \rangle = \langle n_K \cdot \sigma(v^x, q^M) \rangle_{\frac{1}{2}} + \llbracket n \cdot \sigma(v^x, q^M) \rrbracket \begin{bmatrix} \lambda_{KJ}^{(1)} & 0 \\ 0 & \lambda_{KJ}^{(2)} \end{bmatrix} \quad (50)$$

Where $\langle n_K \cdot \sigma(v^x, q^M) \rangle_{\frac{1}{2}}$ denotes the interelement averaged stress obtained using the symmetrical weighting corresponding to $\alpha = \frac{1}{2}$. The equilibration condition then becomes

$$\begin{aligned} l_K(\theta) - a_K(u^x, \theta) - b_K(\theta, p^M) - C_K(u^x, u^x, \theta) + \int_{\partial K} \langle n_K \cdot \sigma(u^x, p^M) \rangle \cdot \theta ds \\ = - \sum_{J \in P} \llbracket n \cdot \sigma(u^x, p^M) \rrbracket \begin{bmatrix} \lambda_{KJ}^{(1)} & 0 \\ 0 & \lambda_{KJ}^{(2)} \end{bmatrix} \cdot \theta ds, \end{aligned} \quad (51)$$

For all $\theta \in Ker[a, V_K]$.

Let $\{V_A\}$ be chosen so that $Span\{V_A\} \times Span\{V_A\} \subset V$ and scaled so that

$$\sum_A V_A(x) \equiv 1. \quad (52)$$

The relation (52) must hold at all points x contained in elements which do not interest the boundary of the domain.

The functions $\lambda_{KJ}^{(k)} : \Gamma_{KJ} \rightarrow \mathbb{R}$ are chosen to be of the form

$$\lambda_{KJ}^{(k)}(s) = \sum_A \lambda_{KJ,A}^{(k)} V_A(s), \quad (53)$$

Where $\lambda_{KJ,A}^{(k)}$ are constants to be determined. Owing the constraint (49), it is required that

$$\lambda_{KJ,A}^{(k)} + \lambda_{JK,A}^{(k)} = 0, \quad (54)$$

for each A.

Lemma 3.2. Suppose that for each V_A the constants $\lambda_{KJ,A}^{(k)}$ can be chosen to satisfy

$$- \sum_{J \in P} \lambda_{KJ,A}^{(k)} \rho_{KJ,A}^{(k)} = b_{K,A}^{(k)} \quad (55)$$

for $k=1, 2$, where

$$\begin{aligned} b_{K,A}^{(k)} = l_K(V_A, \theta_k) - a_K(u^x, V_A, \theta_k) - b_K(V_A, \theta_k, p^M) - C_K(u^x, u^x, V_A, \theta_k) \\ + \int_{\partial K} V_A(s) \langle n_K \cdot \sigma(u^x, p^M) \rangle \cdot \theta_k ds, \end{aligned} \quad (56)$$

and

$$\rho_{KJ,A}^{(k)} = \int_{\Gamma_{KJ}} \llbracket n \cdot \sigma(v^x, q^M) \rrbracket \cdot \theta_k ds \quad (57)$$

Then

$$0 = l_K(\theta) - a_K(u^x, \theta) - b_K(\theta, p^M) - C_K(u^x, u^x, V_A, \theta) + \int_{\partial K} \langle n_K \cdot \sigma(u^x, p^M) \rangle \cdot \theta ds, \quad (58)$$

for all $\partial\Omega = \partial\Omega_D \cup \partial\Omega_N$.

Proof. The result follows immediately by forming appropriate linear combination of (55), and using (53) and (49). Summarizing and incorporating the results of section 3 we have

Theorem 3.3. Let the conditions of Theorem 2.1 hold. Then there exists a constant C such that

$$\|(e, E)\|_*^2 \leq C \sum_{K \in P} \eta_K^2 \quad (59)$$

Where

$$\eta_K = \{a_K(\phi_K, \phi_K) + d_K(\nabla \cdot u^x, \nabla \cdot u^x)\}^{\frac{1}{2}}, \quad (60)$$

We define the global error estimator

$$\eta = \left(\sum_{K \in P} \eta_K^2 \right)^{\frac{1}{2}} \quad (61)$$

IV. NUMERICAL SIMULATIONS

In this section some numerical results of calculations with finite element Method and ADINA system will be presented. Using our solver, we run the test problem driven cavity flow [1, 6, 7, 8, 9, 10].

$$\left\{ y = 1; -1 \leq x \leq 1 \mid u_x = 1 - x^4 \right\} \text{a leaky cavity.}$$

The streamlines are computed from the velocity solution by solving the Poisson equation numerically subject to a zero Dirichlet boundary condition.

The solution shown in figure 1 corresponds to a Reynolds number of 100. The particles in the body of the fluid move in a circular trajectory.

The profiles of the u-velocity component along the vertical centerline and the v-velocity component along the

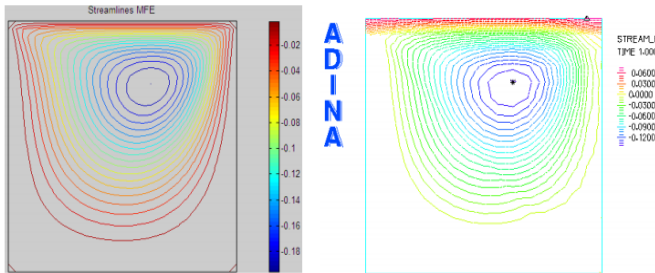


Fig.1. Uniform streamline plot with FE (left), and uniform streamline plot computed with ADINA system (right) using $Q_1 - P_0$ approximation, a 32×32 square grid and Reynolds number $Re=100$.

This is a classic test problem used in fluid dynamics, known as driven-cavity flow. It is a model of the flow in a square cavity with the lid moving from left to right. Let the computational model:

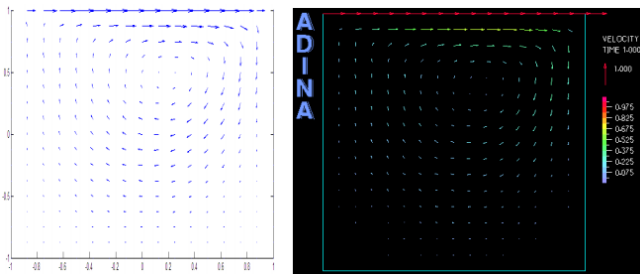


Fig.2. Velocity vectors solution by FE (left) and velocity vectors solution (right) computed with ADINA system with a 32×32 square grid and $Re= 100$.

horizontal centerline are shown in Figure 2 for $Re=1000$. In this figure, we have also included numerical predictions from [6] and ADINA system. There is excellent agreement between the computed results, those published in [6] and the results computed with ADINA system.

Table 1. Estimated errors for leaky driven cavity for the flow with Reynolds number $Re =100$.

	$\ u - u^X\ _V$	η
8×8	8.704739×10^{-2}	1.720480×10^0
16×16	3.115002×10^{-2}	1.084737×10^0
32×32	9.545524×10^{-3}	5.919904×10^{-1}
64×64	2.676623×10^{-3}	3.160964×10^{-1}

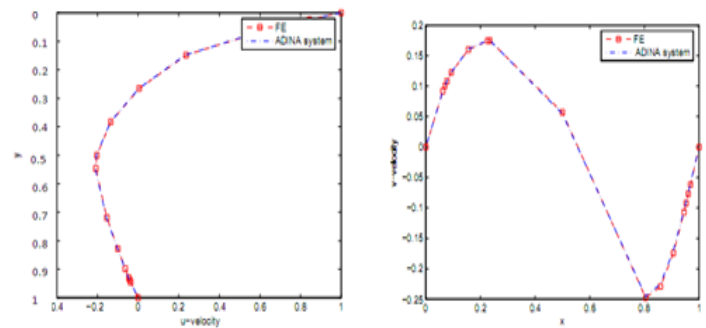


Fig.3. Velocity component u at vertical centerline (left plot), and the velocity component v at horizontal centerline (right plot) with a 129×129 square grid and Reynolds number $Re=1000$.

Figure 3 shows the velocity profiles for lines passing through the geometric center of the cavity.

These features clearly demonstrate the high accuracy achieved by the proposed finite element method for solving the Navier-Stokes equations in the lid-driven squared cavity.

V. CONCLUSION

We were interested in this work in the numeric solution for two dimensional partial differential equations modeling (or arising from) steady incompressible fluid flow. It includes algorithms for discretization by finite element methods and a posteriori error estimation of the computed solutions.

Our results agree with Adina system.

Numerical experiments were carried out and compared with satisfaction with other numerical results, either resulting from the literature, or resulting from calculation with commercial software like Adina system.

ACKNOWLEDGEMENTS

The authors would like to appreciate the referees for giving us the several corrections.

REFERENCES

- [1] U. Ghia, K. Ghia, and C. Shin, High Re solution for incompressible viscous flow using the Navier-Stokes equations and a multigrid method, *Journal of Computational Physics*, 48(3), 1982, 387–395.
- [2] H.C. Elman, D.J. Silvester and A.J. Wathen, *Finite Elements and Fast Iterative Solvers with Applications in Incompressible Fluid Dynamics*, Oxford University Press, 2005.
- [3] G.O.C. Zienkiewicz, R.L. Taylor and P. Nithiarasu, *The Finite Element Method for Fluid Dynamics*, Sixth edition. Elsevier Butterworth-Heinemann, 2005.
- [4] V. Girault and P.A. Raviart, *Finite Element Methods for Navier-Stokes Equations*, Springer-Verlag, Berlin, 1986.
- [5] M. Ainsworth and J. Oden, *A Posteriori Error Estimation in Finite Element Analysis*, wiley, New York, [264, 266, 330, 334, 335], 2000..
- [6] H.C. Elman, D.J. Silvester and A.J. Wathen, *Finite Elements and Fast Iterative Solvers with Applications in Incompressible Fluid Dynamics*, Oxford University Press, 2005.
- [7] E. Erturk, T.C. Corke and C. Gokcol, Numerical solutions of 2-D steady incompressible driven cavity flow at high Reynolds numbers, *International Journal for Numerical Methods in Fluids*, 48 (7), 2005, 747-774.
- [8] Salvador Garcia, *The Lid-Driven Square Cavity Flow: from Stationary to Time Periodic and Chaotic*, Communications in Computational Physics, 2 (5), 2007, 900-932.
- [9] E. Barragy and G.F. Carey, Stream function-vorticity driven cavity solution using p finite elements, *Computers & Fluids*, 26 (5), 1997, 453-468.
- [10] M. Li, T. Tang and B. Fornberg, A compact fourth-order finite difference scheme for the steady incompressible Navier-Stokes equations, *International Journal for Numerical Methods in Fluids*, 20(10), 1995, 1137–1151.
- [11] P.M. Gresho and R.L. Sani, *Incompressible Flow and The finite element Method*, John Wiley and Sons, 1998.
- [12] D. Kay and D. Silvester, A posteriori error estimation for stabilized mixed approximations of the Stokes equations, *SIAM J. Scientific Computing*, 21(4), 1999, 1321-1336.
- [13] R. Verfurth, *A Review of a posteriori Error Estimation and Adaptive Mesh-Refinement Techniques*, Wiley-Teubner, Chichester, 1996.
- [14] M. Ainsworth and J. Oden, A posteriori error estimates for Stokes and Oseen equations, *SIAM Journal on Numerical Analysis*, 34(1), 1997, 228-245.
- [15] A. Gauthier, F. Saleri, and A. Veneziani, A fast preconditioner for the incompressible Navier–Stokes equations, *Computing and Visualization in science*, 6(2-3), 2004, 105–112.
- [16] T.J. Oden, W. Wu, and M. Ainsworth, An a posteriori error estimate for finite element approximations of the Navier-Stokes equations, *Computer Methods in Applied Mechanics and Engineering*, 111(1-2), 1994, 185-202.
- [17] K.W. Morton and D.F. Mayers, *Numerical Solution of Partial Differential Equations. An Introduction*, Second Edition, Cambridge University Press, 2005.

OPTIMIZATION OF MACHINING PARAMETERS IN CNC TURNING OF MARTENSITIC STAINLESS STEEL USING RSM AND GA

Poornima*¹, Sukumar*²

¹(SECOND M.E (INDUSTRIAL ENGINEERING), KUMARAGURU COLLEGE OF TECHNOLOGY, COIMBATORE)INDIA

²(FACULTY OF MECHANICAL ENGINEERING, KUMARAGURU COLLEGE OF TECHNOLOGY, COIMBATORE)INDIA

ABSTRACT

Metal cutting process is one of the complex process which has numerous factors contributing towards the quality of the finished product. CNC turning is one among the metal cutting process in which quality of the finished product depends mainly upon the machining parameters such as feed, speed, depth of cut, type of coolant used, types of inserts used etc. Similarly the work piece material plays an important role in metal cutting process. Hard materials such as stainless steel grades, Nickel alloys, Titanium alloys are very difficult to machine due to their high hardness. While machining these hard materials, optimized machining parameters results in good surface finish, low tool wear, etc. This study involves in identifying the optimized parameters in CNC turning of martensitic stainless steel. The optimization technique used in this study are Response surface methodology, and Genetic algorithm. These optimization techniques are very helpful in identifying the optimized control factors with high level of accuracy.

Key words: Turning, machining, response surface methodology, genetic algorithm.

I. INTRODUCTION

Hard turning is a process, in which materials in the hardened state (50–70 HRC) are machined with the single point cutting tools. This has become possible with the availability of the new cutting tool materials. Since a large number of operations are required to produce the finished product, if some of the operations can be combined, or eliminated, or can be substituted by the new process, product cycle time can be reduced and productivity can be improved. The traditional method of machining the hardened materials includes rough turning, heat treatment, and then grinding process. Hard turning eliminates the series of operations required to produce the component and thereby reducing the cycle time and hence resulting in productivity improvement. The various advantages of hard turning are the higher productivity, reduced set up times, surface finish closer to grinding and ability to machine the complex parts. Various work materials which can be machined by the hard turning process include high speed steels, die steels, bearing steels, alloy steels, case hardened steels, white cast iron and alloy cast iron. Rigid machine tools with adequate power, very hard and tough tool materials with appropriate tool geometry, tool holders with high stiffness and appropriate cutting conditions are some of the prerequisites for hard turning.

Surface roughness plays an important role as it influences the fatigue strength, wear rate, coefficient of friction, and corrosion resistance of the machined components. In actual practice, there are many factors which affect the surface roughness, i.e. tool variables, work piece variables and cutting conditions. Tool variables include tool material, nose radius, rake angle, cutting

edge geometry, tool vibration, tool overhang, tool point angle, etc. Work piece variables include material, hardness and other mechanical properties. Cutting conditions include speed, feed and depth of cut. As the hard turning process involves large number of parameters, the process control becomes complex and it would be difficult to select the appropriate cutting conditions and tool geometry for achieving the required surface quality. Various researchers have developed the surface roughness predictive models for the conventional turning, but these models may not be useful for hard turning because hard turning differs from that of the conventional turning process. So, it would be necessary to study the effects of speed, feed, effective rake angle and nose radius on the surface roughness so as to develop the predictive models for hard turning. In hard turning process, the cutting inserts are always provided with the negative chamfer angle in order to increase the edge strength of the cutting tools. This negative chamfer angle acts as a negative rake angle to the insert. The total effective rake then becomes the sum of the negative rake angle provided by the chamfer angle of the inserts and the negative rake angle provided by the tool holder to the cutting inserts.

II. LITERATURE REVIEW

The performance of hard turning is measured in terms of surface finish, cutting forces, power consumed and tool wear. Surface finish influences functional properties of machined components. Surface finish, in hard turning, has been found to be influenced by a number of factors such as feed rate, cutting speed, work material characteristics, work hardness, cutting time, tool nose radius and tool geometry, stability of the machine tool and the work piece set-up, the use of cutting fluids, etc. König et al. [1] have reported that CBN and ceramic cutting tools are widely used in industries for the machining of the various hard materials. In many applications, the cutting of ferrous materials in their hardened condition can replace grinding to give significant savings in cost and increase in productivity. Cutting tool geometry plays a very important role in hard turning process. The rake angle and the nose radius of the turning inserts directly affect the cutting forces, power and surface finish. The edge strength of the cutting inserts depends upon edge preparation, i.e. by the honing radius, chamfer angles. Some investigations related to the effect of tool geometry have been reported by the researchers. Thiele and Melkote [2] have investigated the cutting edge geometry and the workpieces hardness on surface generation in the finish hard turning of AISI 52100 steel. CBN inserts, with various representative cutting edge preparations, were used as the cutting tool materials. This study shows that the effect of edge geometry on surface roughness and cutting forces is statistically significant. Specifically, large edge hones produce higher average surface roughness values than small edge hones. The effect of two factor interactions of the edge geometry and the work piece hardness on the surface roughness is also found to be important. Also large edge hones generate higher forces in the axial, radial and tangential directions than small edge hones. Dahlman et al. [3] have conducted the study on the influence of

rake angle, cutting speed and cutting depth on residual stresses in hard turning. Results show that a greater negative rake angle gives higher compressive stresses as well as a deeper affected zone below surface. The compressive stresses increase with the increased feed rate. Zhou et al. [4] have investigated the effect of chamfer angle on the wear of PCBN cutting tool. Results show that chamfer angle has a great influence on the cutting force and tool life. All the three force components increase with an increase of the chamfer angle. The optimized chamfer angle, for the maximum tool life as suggested by this study, is 15°. In this study, cutting conditions were kept constant. Chou and Song [5] have investigated the effects of tool nose radius on finish hard turning with ceramic tools. In this study, surface finish, tool wear, cutting forces, and, particularly, white layers were evaluated at different machining conditions. Results show that large tool nose radii not only give finer surface finish, but also considerable tool wear compared to small nose radius tools. Specific cutting energy also increases slightly with tool nose radius. Large nose radius tools generate shallower white layers when cutting by worn tools. For new tools, small nose radius results in larger uncut chip thickness, and thus, induces deeper white layers. Endres and Kountanya [6] have reported the effects of corner radius and edge radius on tool flank wear. Results show the interaction of corner radius and edge radius and their effects on process performance, measured in terms of tool flank wear and forces. The general conclusion is that an advantage exists in using a larger corner radius when using a larger edge radius. Mital and Mehta rate and cutting speed on surface roughness and tool wear were experimentally

process. Response surface designs are employed to investigate and predict the following conditions of a process. RSM methodology is practical, economical and relatively easy for use. They are the effect on a particular response by a given set of input variables over some specified region of interest. The required values of variables to obtain desirable or acceptable levels of a response. The required values of variables to achieve a minimum or maximum response and the mature response surface near this minimal or maximal value. To describe the response surface method by second order polynomials, the factor in the experimental design should have atleast three levels. A three level factorial experiment in which all possible combinations of k factors at all the levels are used is called 3k full factorial design which is employed

III.METHODOLOGY

A. Design of experiments

Design of experiments is a standard tool to conduct the experiment in an optimum way to investigate the effects of process parameters on the response or output parameter. The various steps involved in the design of experiments are identifying the important process parameter, finding the upper and lower limit of selected process parameter and developing the box benhen design matrix. The design matrix for three factors involves three blocks in which each of two factors are varied through the four possible combinations of higher and lower limits. In each block a certain number of factors are put through all combinations for the three factorial design, while the other factors are kept at central values.

C. ANOVA

Since there are a large number of variables controlling the process, some mathematical models are required to represent the process. However, these models are to be developed using only the significant parameters influencing the process rather than including all the parameters. In order to achieve this, statistical analysis of the experimental results will have to be processed using the analysis of variance (ANOVA). ANOVA is a computational technique that enables the estimation of the relative contributions of each of the control factors to the overall measured response. In the present work, only the significant parameters will be used to develop mathematical models using response surface methodology (RSM). These models would be of great use during the optimization of the process variables. RSM methodology is practical, economical and relatively easy for use. Regression equation obtained as follows:

$$\text{SurfaceRoughness} = 1.51539 - 0.01518 * A - 1.30442 * B - 0.47976 * C - 0.00002A^2 - 6.80272B^2 - 0.02333C^2 + 0.07857 * A * B + 0.00575 * A * C + 2.142 * B * C$$

Where A- speed, B-Feed, C-Depth of cut

TABLE 1 MACHINING PARAMETER LEVELS

Parameters	Unit	Levels		
		-1	0	1
Speed	m/min	80	100	120
Feed	m/min	0.150	0.185	0.220
Depth of cut	mm	0.5	1.0	1.5

B. RESPONSE SURFACE METHODOLOGY

Response surface designs are employed in the empirical study of relationship between one or more measured response variables and a number of independent or controllable variables of a

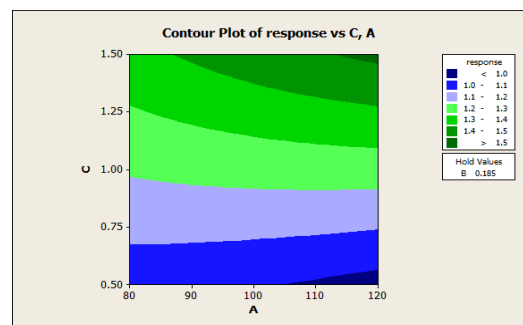


Fig.1 contour plot for speed vs feed

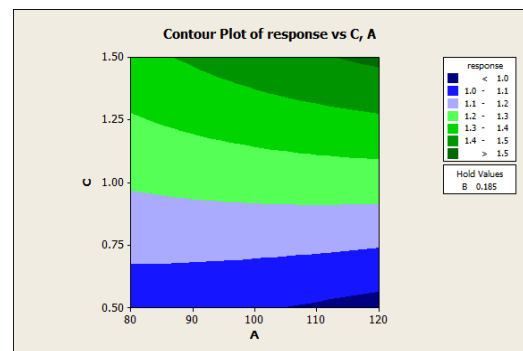


Fig. 2 contour plot for speed vs depth of cut

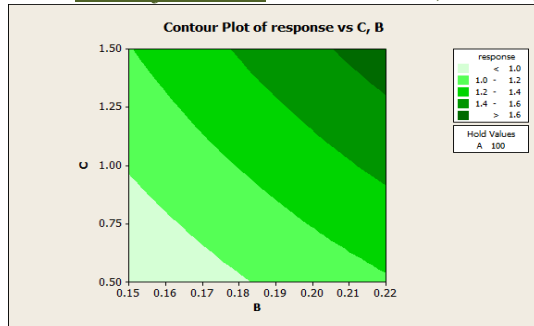


Fig.3 contour plot for feed vs depth of cut

D. GENETIC ALGORITHM

Genetic algorithm is a heuristic search technique used in computing to find exact or approximate solutions to optimization and search problems. They are categorised as global search heuristics and are particular class of evolutionary algorithms that use techniques inspired by evolutionary biology such as inheritance, mutation, selection and cross over. The key issues such as chromosome encoding, selection process and evolution methodology. In addition a local search mechanism is proposed for selecting the initial population to improve the performance of GA. Genetic algorithm in general is a purpose search algorithm suitable for optimization problems due to its processing approach and due to its structure and it is able to return a set of optimal solutions. MATLAB is a high performance language for technical computing which is used to optimize the objective function of different materials in genetic algorithm.

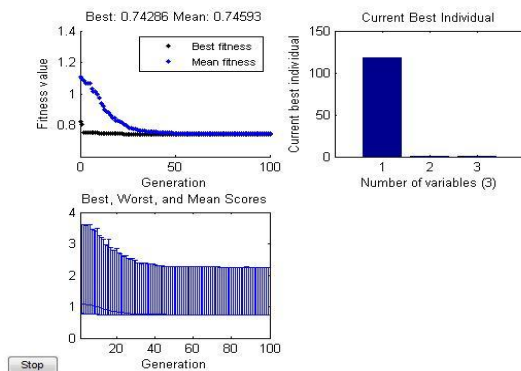


Fig 4 Genetic algorithm results

IV. ANALYSIS AND DISCUSSION

The surface quality of the machined parts is the value of surface roughness or the waviness are mainly decided by the three factors speed, feed and depth of cut beyond the levels influenced by the other factors. The surface roughness is mainly a result of three controllable factors and hence it is easier to attain the physical dimensions. A detailed study could give the effect of speed, feed, depth of cut, nose radius and other factors on the surface roughness. These studies and effects of factors on surface roughness have been evaluated and models are developed to address the requirements of the end operator, who decides the input parameters based on the specified requirements. The goal of this study is to obtain a mathematical model that relates the surface roughness to three machining parameters in turning operation, precisely to the speed, feed and depth of cut. Therefore two approaches have been used such as response surface methodology (RSM) and analysis of variance (ANOVA). Genetic algorithm approach can be used for the fine tuning of the results obtained to get the optimized solution.

VII. CONCLUSION

This paper provides a detailed study on the surface roughness of the martensitic stainless steel (SS40). The detailed study and the optimization procedure has been made to study the effect of speed, feed and depth of cut while machining which would help in real practice. The machining parameter ranges were analyzed and then the experimentation was carried out according to the optimization approaches. The results obtained from RSM are R-Sq obtained was 99.9% which indicates that selected parameters (speed, feed, depth of cut) significantly affect the response (surface roughness). The Best ranges obtained by using the genetic algorithm approach are Cutting velocity (speed) -119.93 m/min, Feed-0.15 m/min and Depth of cut -0.5mm. Hence the Optimal surface roughness from GA is 0.74 microns.

VI. REFERENCES

- [1] Abdul Jalil, Adeel H. Suhail, S.V. Wong (2010) "Optimization of Cutting Parameters Based on Surface Roughness and Assistance of Workpiece Surface Temperature in Turning Process" American J. of Engineering and Applied Sciences 3 (1): 102-108, 2010 ISSN 1941-7020
- [2] Dilbag Singh, P. Venkateswara Rao (2006) "A surface roughness prediction model for hard turning process" Published online: Springer-Verlag London Limited
- [3] N.R. Dharb, M.M.A. Khan, M.A.H. Mithu (2009) "Effects of minimum quantity lubrication on turning AISI 9310 alloy steel using vegetable oil-based cutting fluid" Journal of Materials Processing Technology 209 5573-5583
- [4] Babur Ozelik, Emel Kuram, Erhan Demirbas, M. Huseyin Cetin (2009) "Evaluation of vegetable based cutting fluids with extreme pressure and cutting parameters in turning of AISI 304L by Taguchi method" Journal of Materials Processing Technology 209 5573-5583
- [5] M.D.Abad, M.M.Abdelhameed, M.A. ElHakim, M.A.Shalaby, S.C.Veldhuis (2011) Wear behavior of some cutting tool materials in hard turning of HSS "Tribology International 44 1174-1181
- [6] M.Sortino G. Totis(2011) "Development of a modular dynamometer for triaxial cutting force measurement in turning" International Journal of Machine Tools & Manufacture
- [7] Anselmo Eduardo Diniz, Vitor Augusto A. de Godoy (2011) "Turning of interrupted and continuous hardened steel surfaces using ceramic and CBN cutting tools" Journal of Materials Processing Technology 211 1014-1025
- [8] M. Dix, R. Neugebauer, B. Reichmann, A. Schubert (2011) "Influence exerted by tool properties on the energy efficiency during drilling and turning operations" CIRP Journal of Manufacturing Science and Technology
- [9] B. Dilip Jerold, M. Pradeep Kumar (2011) "Experimental investigation of turning AISI 1045 steel using cryogenic carbon dioxide as the cutting fluid" Journal of Manufacturing Processes

- [10] C.Y.Chan, C.F.Cheung, W.B.Lee, S.Ton, H. Wang (2011) "Dynamic modelling of shear band formation and tool-tip vibration in ultra-precision diamond turning" International Journal of Machine Tools & Manufacture 51 512–519
- [11] A. Attanasio, C. Cappellini, G. Rotella, R. M'Saoubi, D. Umbrello (2011) "Tool wear effects on white and dark layer formation in hard turning of AISI 52100 steel" ScienceDirect Wear
- [12] Ilhan Asilturk, Harun Akkus (2011) "Determining the effect of cutting parameters on surface roughness in hard turning using the Taguchi method " published on ScienceDirect Measurement
- [13] Chandra Nath, Kui Liu, Mustafizur Rahman, Xinquan Zhang (2011) "Experimental study on ultrasonic elliptical vibration cutting of hardened steel using PCD tools" Journal of Materials Processing Technology 211 1701– 1709
- [14] Harpreet Singh, Jagdev Singh, Rupinder Singh, Simran preet, Singh (2011) " Investigation on wear behaviour of cryogenically treated TiAlN coated tungsten carbide inserts in turning" Gill International Journal of Machine Tools & Manufacture 51 25–33
- [15] K.S. Al-Athel, M.S.Gadala" The use of volume of solid (VOS) approach in simulating metal cutting with chamfered and blunt tools" International Journal of Mechanical Sciences 53 (2011) 23–30
- [16] M.P. Johansson, L. Karlsson, Knutsson, M. Oden (2011) "Machining performance and decomposition of TiAlN/TiN multilayer coated metal cutting inserts" Surface & Coatings Technology 205 4005–4010
- [17] G. Buza, Z. Kalazi, G. Kaptay A. Sytcheva, N.V. Verezub, A. Fedorov, O. Verezu (2011) (2011) "Performance of a cutting tool made of steel matrix surface nano-composite produced by in situ laser melt injection technology" Journal of Materials Processing Technology 211 750–758
- [18] Yi-Chi Wang, Yi-CheChiu, Yu-PengHung (2011) "Optimization of multi-task turning operations under minimal tool waste consideration" Robotics and Computer-Integrated Manufacturing 27 674–680
- [19] Aman Aggarwal, Anil Gupta, Hari Singh (2011) "Taguchi-fuzzy multi output optimization (MOO) in high speed CNC turning of AISI P-20 tool steel" Expert Systems with Applications 38 6822–6828
- [20] E.Altus, J. Saffury (2010) "Chatter resistance of non-uniform turning bars with attached dynamic absorbers— Analytical approach" Journal of Sound and Vibration 329 2029–2043
- [21] Asif Iqbal, Naeem Ullah Dar (2010)"Optimal formation of fuzzy rule-base for predicting process's performance measures" Expert Systems with Applications 38 4802–4808
- [22] Erol Turkes, Suleyman Nes eli, Suleyman Yald (2011) "Optimization of tool geometry parameters for turning operations based on the response surface methodology" published on ScienceDirect Measurement 44 580–587
- [23] A. Aramcharoen, P.T. Mativenga, M.F. Rajemi (2010) "Sustainable machining: selection of optimum turning conditions based on minimum energy considerations" Journal of Cleaner Production 18 1059–1065
- [24] M. Anthony Xavier, M. Adithan (2009) "Determining the influence of cutting fluids on tool wear and surface roughness during turning of AISI 304 austenitic stainless steel" journal of materials processing technology 2 0 9 900–909
- [25] E. Daniel Kirby, Julie Z. Zhang, Joseph C Chen (2007) "The development of an in-process surface roughness adaptive control system in turning operations" Springer Science Business Media, LLC

Assembly Line Balancing of Watch Movement Assembly

Vignasathya*¹, Bhaskar*²

¹(FIRST M.E (INDUSTRIAL ENGINEERING), KUMARAGURU COLLEGE OF TECHNOLOGY
COIMBATORE, INDIA)

²(FACULTY OF MECHANICAL ENGINEERING, KUMARAGURU COLLEGE OF TECHNOLOGY
COIMBATORE, INDIA)

*TITAN WATCH INDUSTRIES, HOSUR, TAMILNADU, INDIA

ABSTRACT

The assembly line of watches at titan industry (calibre 5000 auto line) contains larger inventory and non value added activities leading to increased cycle time and cost of operation. Thus assembly line balancing is done by using lean tools heijunka and redesign in line layouts . Assembly Line Balancing, or simply Line Balancing (LB), is the problem of assigning operations to workstations along an assembly line, in such a way that the assignment be optimal in some sense. Thus the project deals with studying the existing manufacturing configuration at the movement assembly and implementation of lean system resulting in shortening of cycle time, set up time, production quantity and overall equipment efficiency.

Key words: line balancing, line layouts, cycle time.

I. INTRODUCTION

Customisation demands variants with unique characteristics. Producing a range of variants often means that the time to complete a task at a work station differs between variants, resulting in difficulty keeping a high and constant utilisation. Different cycle times means that certain stations requires more time then is available, "peaks", and it leads to operators having to work faster on oncoming models to compensate for this. Therefore, one should avoid sequencing "peakmodels" after one another. Work load distribution is referred to as line balancing or the Japanese term heijunka . Balancing and sequencing activities attempt to evenly divide time over stations to achieve high utilisation and using available cycle time as efficiently as possible.

II. METHODOLOGY

A comprehensive literature review was completed and current theories studied to gain an in-depth understanding.

A. Heijunka

The production needed to be increased in order to meet demand. A shortage of parts meant nothing was obtained in correct quantity or on time. Two weeks of the month was spent gathering materials arriving in no particular order and assembly took place during the next two weeks, which would not work if production levels increased. Hence, like many other components of the Toyota Production System (TPS) heijunka was born out of necessity. "The simple definition of heijunka is production leveling" (Toyota imports forum, 2008). Heijunka is one of the cornerstones of Toyota's production. It is a vital part

enabling Toyota to achieve highest quality, lowest cost and shortest lead time. It evens out workload over available production time both by product mix and volume. Heijunka sequence production uniformly, involving both workload leveling and line balancing (Liker, 2004) and consequently carries dual intentions (Coleman and Vaghefi, 1994):

- Reduction in inventories due to very small batches, mixed production.
 - The associated ability to equate work loads in each production process to each other and capacity.
- Associated with heijunka are the three M's (Figure 2);
- Muda – non value added.
 - Muri – overburdening people or machines.
 - Mura – unevenness.
- . Effects of heijunka (Coleman and Vagehefi, 1994):
- Reduction in overall inventories.
 - Reduction of required productive capacity.
 - Reduction of lead times to the customer.
 - Heijunka's line-balancing aspect implies that employees are not encouraged by dissimilar work loads to migrate toward easier tasks and away from those jobs which need most improvement.

B. Line layouts

Different line design layouts are all associated with an assembly line balancing (ALB) problem. Balancing distributes tasks to work stations and work content per station and variant. Line balancing is divided in areas depending on layout of the assembly line. To minimise work overload sequencing is carried out (Boysenet al., 2008). The sequence determines spreading of material demand and labour utilisation at workstations. Two objectives are central (Boysen et al., 2007):

- Work overload: Work overload can be avoided if a sequence is found, where variants causing high station times alternate with less work-intensive ones.
- Just in time objectives: Different models are composed of different options and thus require different parts, so that the model sequence influences the progression of material demands over time. The two objectives are done through mixed-model sequencing .

III. MANUFACTURE AND PRODUCT DESCRIPTION

The product is a electronic watch. This paper deals with the movement assembly process of the hand setting assembly. The major process steps in manufacturing are sketched in Fig. 1. Finally, 11 stations with a continuous materials flow compose the assembly line.

IV. INITIAL LAYOUT

A single-model assembly line of watch calibre 5000 is used that is limited to producing one variant and is mainly used for mass production of one homogeneous product. In unpaced lines, workpieces are transferred whenever the required operations are

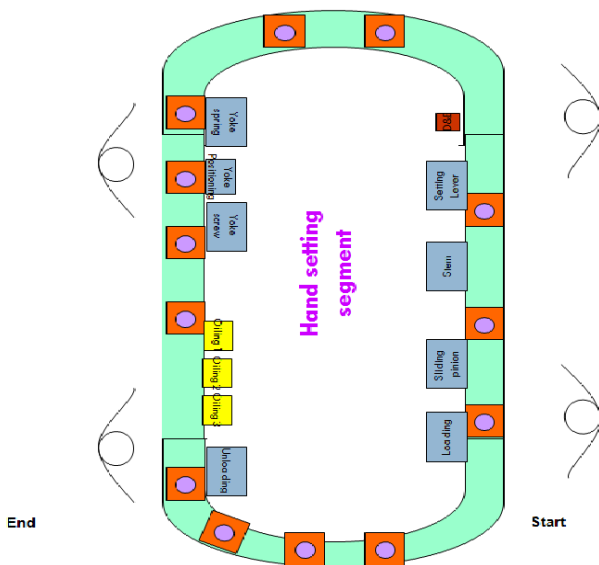


Fig 1 Initial layout

completed, rather than being bound to a given time span ($\beta_1 = \text{unpac}$). Further distinguish as to whether all stations pass on their work pieces simultaneously (synchronous) or whether each station decides on transference individually (asynchronous). Under asynchronous movement, a work piece is always moved as soon as all required operations at a station are completed and the successive station is not blocked anymore by another work piece. After transference the station continues to work on a new work piece, unless the preceding station is unable to deliver (starving). In order to minimize waiting times, buffers are installed in-between stations, which can temporarily store work pieces ($\beta_6 = \text{buffer}$). Thereby, a trade-off between work-in-progress, which can be reduced by using few buffers, and throughput, which is increased by installing more and larger buffers, has to be observed. Buffers can only be used to compensate for temporary deviations in task times.

Sliding pinion and yoke positioning stations are faster than loading and yoke spring stations respectively, the buffer storage will soon be filled to capacity and lose its function. In addition unnecessary travelling time at setting lever, detect and eject, sp oiling, final inspection adds up to the increase in cycle time.

Stochastic task times ($\alpha_3 = \text{tsto}$) are caused by (i) deviations in manual labour, (ii) default of machinery and/or (iii) by a model-mix ($\alpha_1 = \text{mix}$), which cannot be anticipated upfront.

Thus in this line, the production rate is no longer given by a fixed cycle time, but is rather dependent on the realised task times. These can be estimated as long as the distribution functions are known which are, however, considerably influenced by buffer allocation. Thus, the configuration planning of assembly system needs to: (1) determine a line balance, (2) allocate buffer storages, (3) estimate throughput (and/or further measures of efficiency).



Fig 2 Existing layout

V. MODIFICATIONS AND LAYOUT PROPOSAL

Slight changes in the work content at a station might lead to a more efficient buffer allocation and improve the system's overall performance. Optimal buffer allocations could thus be determined repetitively for varying line balances or both problems might be solved simultaneously.

Once resources are allotted to stations, heavy machinery might not be reallocated. In this case, all tasks which require this resource need to remain at their previous station, which can be enforced by assignment restrictions ($\alpha_5 = \text{fix}$). Often, the movement of a machine is, however, not technically impossible, but rather associated with movement costs. In this case, movement costs might need to be considered explicitly. Additionally, space constraints need to be observed whenever a machine is moved. The space at a station might be limited, so that two tasks each of which requires a large machine cannot be assigned to the same station ($\alpha_5 = \text{inc}$).

TABEL 1 PROPOSED LAYOUT CHANGES

Station	Existing distance cm	Proposed distance cm	Reasons
Loading to Sliding pinion	135	135	
Sliding pinion to Stem	76	96	Changeover from 2.19s to 2.64s, small distance to accommodate pallets will lead to ideal time of machines in previous stations
Stem to Setting lever	37	25	2.64s to 1.94s thus the station will process quickly no pallets are to be accommodated
Setting lever to D&E	51	35	1.97s to 1.98s thus they will be processed in same

			speed
D&E to Yoke spring	144	144	Circular path of conveyor
Yoke spring to Yoke positioning	18	18	2.23s to 1.4s thus speed of processing is higher
Yoke Positioning to Yoke Screw	57	110	1.4s to 2.96s hence more distance to accommodate will reduce ideal time of previous stations
Yoke screw to SP Oiling	53	32	2.96s to 2.95s thus both stations will process in same speed
SP Oiling to Yoke oiling	31	31	2.95s to 2.96s same processing time
Yoke Oiling to SL Oiling	18	18	2.96s to 1.58s thus it be processed quickly
SL Oiling to Final inspection	50	18	1.58 to 0.88 thus processed quickly

TABEL 2 BENIFITS OF THE PROPOSED LAYOUT

	Envisaged	Existing
Production quantity	9700	7000
Production rate	2.69	3.72

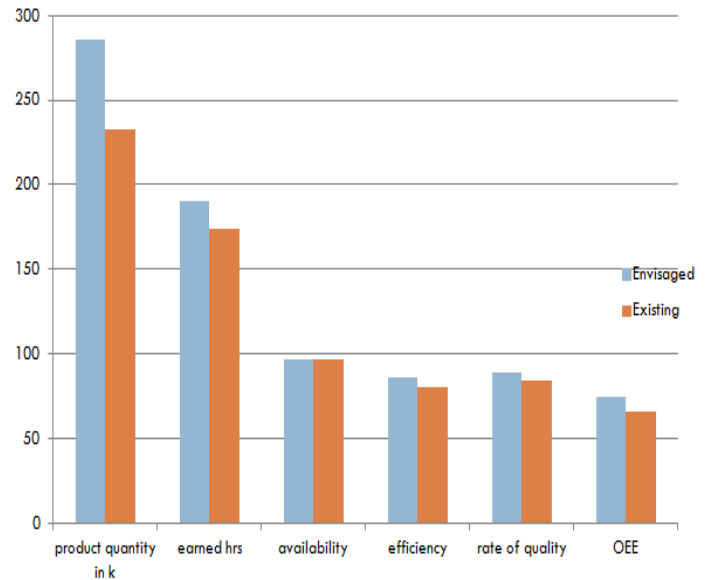


Fig 2 Result of proposed layout

VI. ANALYSIS AND DISCUSSION

The analysis of asynchronous lines revealed an interesting attribute, generally referred to as „bowl phenomenon“ according to which the throughput of a line can be improved by assigning smaller station loads to central stations than to those located at the beginning or end of the line. This effect is the stronger, the higher the stochastic deviations of processing times . The same concept applies to buffer allocation, if buffer storages in the centre (or at bottle-neck stations) are increased in size . In this context, the use of a global cycle time seems inappropriate, and should thus be replaced by station-specific local cycle times to account for this phenomenon, which assign a lower work content to central stations or alternatively enforce a higher probability of regarding the cycle time in case of a stochastic model.

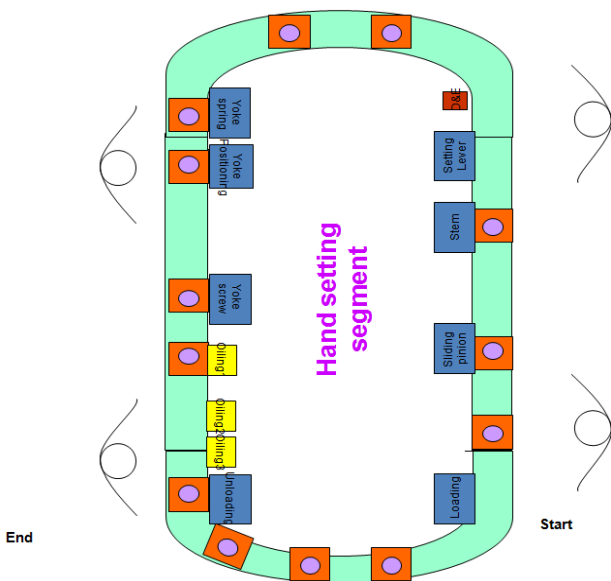


Fig 3 Proposed Layout

VII. CONCLUSION

This paper provides a case study of the titan watch industry movement assembly layout by means of assembly line balancing and heijunka, which connects manufacturing system design objectives to operational objectives. It focuses the assembly line balancing of operations by eliminating nonvalue-added time and decreasing the intermediate stocks and eliminate inefficiencies. Results explain that the design of layout without buffer space and unnecessary transportation reduces the waste in terms of unnecessary inventories, excessive transportation, and idle times applicable to every production and layout designs. the application of these skills of production help to enhance the materials flow in the assembly line in a short time and under particular conditions of small storage space and requirements of flexibility. The empirical results drawn from the case implementation serve to demonstrate that an operative decision has helped to improve the metrics lean, in particular to reduce the production time and increase overall equipment efficiency shows the transformation of a former line manufacturing organization into a better lean organization that has set a lowest cycle time.

REFERENCES

- [1]. Ahlem zayati and frédérique biennier (2005), “Towards lean service bus architecture for industrial integration Infrastructure and pull manufacturing strategies”, IEEE, Vol. 8, No. 4, pp. 137-148.
- [2]. Aiyong rong and attila (2007), “Problem of a pcb assembly line with modular Placement machines”, IEEE , Vol. 3, No. 6, pp. 156-168.
- [3]. Ajit kumar sahu and Singh (2006), “Lean philosophy: implementation in a forging company”, IEEE, Vol. 2, No. 9, pp. 267-278.
- [4]. Babak javadi and alireza rahimi-vahed (2007), “Solving a multi-objective mixed-model assembly line Sequencing problem by a fuzzy goal programming approach”, IEEE, Vol. 13, No. 14, pp. 18-31.
- [5]. Bagher and Zandieh (2006), “Line balancing of stochastic u-type assembly lines: an imperialist Competitive algorithm”, IEEE, Vol. 4, No. 9, pp. 348-378.
- [6]. Barroso and Machado (2008) , “Identifying Vulnerabilities in the Supply Chain”, IEEE, Vol. 8, No. 4, pp. 137-148.
- [7]. Bowen D.E and Youngdahl M.E (2006), "Lean service : in defense of a production-line approach", International Industry Management, Vol. 9, No. 3, pp. 207-225.
- [8]. Brunt and Taylor (1998) , "Valse stream management", The International Journal of Logistics Management, Vol. 9, No. 1, pp. 25-42.
- [9]. Cagliano. R and Caniato. F (2004), “Lean, agile and traditional supply: how do they impact manufacturing performance”, IEEE., Vol. 1, No. 7, pp. 276-288.
- [10]. Carrie Steinlicht and Andrew Neary (2006), “Program Development Work in Progress: Value Stream Mapping the Educational Process Outcomes”, IEEE, Vol. 8, No. 4, pp. 137-148.
- [11]. Cruz Machado (2009), “How Lean Supply Chain Effects Product Cost and Quality - A Case Study of the Ford Motor Company”, IEEE, Vol. 3, No. 9, pp. 547-558.
- [12]. Guo-qiang pan and ding-zhong feng (2009), “Application research of shortening delivery time through value stream”, IEEE, Vol. 6, No. 24, pp. 295-308.
- [13]. Hino.S (2006), “Inside the Mind of Toyota: Management Principles for Enduring Growth”, IEEE , Vol. 5, No. 7, pp. 358-375.
- [14]. Ip and Yung (2008), “Conwip based control of a lamp assembly production line”, IEEE, Vol. 8, No. 4, pp. 137-148.
- [15]. Johannes Cottyn and Hendrik Van Landegh (2005), “ The Combined Adoption of Production IT and Strategic Initiatives – Initial Considerations for a Lean MES Analysis”, springerlink, , Vol. 2, No. 9, pp. 267-278.
- [16]. Karwan.K.R and Markland R.E (2003), "Integrating design principles and information technology to improve delivery and productivity in public sector operation", Journal of Operations Management, Vol. 24, No.5, pp. 347-362.
- [17]. L. N. Pattanaik and b. P. Sharma (2008), “Implementing lean manufacturing with cellular layout:A case study Modeling the machine configuration and line-balancing”, IEEE Vol. 8, No. 4, pp. 356-368.
- [18]. Linton and Cha(2005), Singapore institute of manufacturing technology “E-based inter-enterprise supply chain kanban for demand and order Fulfilment management”, springerlink, Vol. 16, No. 8, pp. 444-458.
- [19]. Machado, and Cruz (2009), “ Research on Value Stream Analysis and Optimization Methods”, IEEE, Vol. 1, No. 8, pp. 17-32.
- [20]. Magali Bosch-Mauchand and Ali Siadat em (2007), “VCS: value chains simulator, a tool for value analysis of manufacturing enterprise processes (a value-based decision support tool)”, IEEE, Vol. 4, No. 8, pp. 543-556.
- [21]. Pavnaskar .S.J, Gershenson .J.K and et al., (2003), “Classification scheme for lean manufacturing tools”, IEEE, Vol. 17, No. 28, pp. 1262-1278.
- [22]. Pegden, C. D and Shannon, R. E. et al.,(1995), “ Introduction to Simulation Using SIMAN” Second Edition. McGraw-Hill, Inc. New York. USA.
- [23]. Roberto álvarez and roque (2006) , “Redesigning an assembly line through leanManufacturing tools”, IEEE, Vol. 1, No. 8, pp. 17-32.
- [24]. Shah. R and Ward.P (2003), “Lean manufacturing: context, practice bundles, and performance”, IEEE, Vol. 5, No. 5, pp. 374-386.
- [25]. Silvestro.N and Silvestro,K.S (2007) , "New service design in the NHS: an evaluation of the strategic alignment", International Journal of Operations & Production Management, vol. 23, no. 4, pp. 401-417.
- [26]. Simon and wee (2006), “how lean supply chain effects product cost and Quality - a case study of the ford motor company”, IEEE, Vol. 17, No. 34, pp. 1137-1481.
- [27]. Sullivan and McDonald (2002), “Equipment replacement decisions and lean manufacturing”, IEEE, Vol. 2, No. 9, pp. 745-761.
- [28]. Synthia Xin Shen and Chuan Feng Ha (2009), “China electrical manufacturing services industry value stream mapping collaboration”, springerlink, , Vol. 4, No. 7, pp. 186-202.
- [29]. Toth and olli et al.,(2010), “ An application of design space for assembly process reasoning to utilize current assembly plant resources for new product Family members”, springerlink, , Vol. 2, No. 9, pp. 691-717.
- [30]. Tuangyot Supeekit and Kanokwan Kingphadung (2009) , “Service process redesign applying value stream analysis: the case of a patient discharging process” , IEEE, Vol. 13, No. 2, pp. 100-113.
- [31]. Wang and Liu (2007), “Assembly sequences merging based on assembly Unit partitioning”, springerlink, Vol. 8, No. 4, pp. 137-148.

Object Oriented Association (OOA) Mining Based Classification in Storage Cloud

V.Naresh Kumar¹ Ramesh nallamalli² Gorantla praveen³

I.Pavan Kumar⁴ K Subrahmanyam⁵

M.Tech[CSE] M.Tech[CSE] M.Tech[CSE] M.Tech[CSE] Professor
^{1,2,3,4,5}Dept of computer Science and Engineering, KL University, Vaddeswaram, Guntur (District), AP.

Abstract: Cloud Storage provides whatever amount of storage you require, on an immediate basis. It is persistent. It can be accessed in a variety of ways, both in the data center where the cloud is housed, as well as via the Internet. If you obtain this from an external provider, it is purchased on a pay as you go basis. You do not manage it, you use it, and the service provider manages it." Cloud systems should be geographically dispersed to reduce their vulnerability due to earthquakes and other catastrophes, which increase technical challenge on a great level of distributed data interpretability and mobility. Data interoperability is even more essential in the future as one component of a multi-faceted approach to many applications; many open challenges still remain such as cloud data security and the efficiency of query processing in the cloud. The proliferation of malware in recent years has presented a serious threat to the security of computer systems. Polymorphic computer viruses, which adopt obfuscation technique, are more complex and difficult than their original versions to detect, as well as new, previously unseen viruses, often making antivirus companies ineffective when using the classic signature-based virus detection technique. In this paper, we rest on the analysis of Win API calling sequences of PE files and propose a new approach for detecting polymorphic or even unknown malware in the Windows platform based on data mining technique, namely OOA Mining algorithm. Our approach rests on an analysis based on the Win API calling sequence that reflects the behavior of a piece of particular code. we develop the Intelligent Malware Detection System (IMDS) using Objective- Oriented Association (OOA) mining based classification. IMDS is an integrated system consisting of three major modules: PE parser, OOA rule generator, and rule based classifier. An OOA Fast FP- Growth algorithm is adapted to efficiently generate OOA rules for classification. A comprehensive experimental study on a large collection of PE files obtained from the anti-virus laboratory of King- Soft Corporation is performed to compare various malware detection approaches.

Keywords: OOA Mining, Windows API Sequence, PE File, Malware

I. Introduction

The proliferation of malware in recent years has presented a serious threat to the security of computer systems. Polymorphic computer viruses, which adopt obfuscation

technique, are more complex and difficult than their original versions to detect, as well as new, previously unseen viruses, often making antivirus companies ineffective when using the classic signature-based virus detection technique. In this paper, we rest on the analysis of Win API calling sequences of PE files and propose a new approach for detecting polymorphic or even unknown malware in the Windows platform based on data mining technique, namely OOA Mining algorithm[21]. Our approach rests on an analysis based on the Win API calling sequence that reflects the behavior of a piece of particular code. The analysis is carried out directly on the PE code. It is achieved in three major steps: construct the API calling sequences for both training set and testing set; and then extract the OOA rules from the training set using OOA Mining algorithm; at last, detect the testing set according to the OOA rules created by the OOA rules generator. We implement a malware detection system, DMAV system, to evaluate the effectiveness of our proposed approach, mainly three major modules included: 1. PE Parser: considering that virus scanner is a speed sensitive application, and, in order to improve the system performance, we develop a PE parser to construct the API calling sequences of a PE file instead of using a third party disassembler. In advance, in order to make convenience for our DMAV system's further analysis, we also implement three other functions: function calls' extraction from a PE file's export table, the extraction of a PE file's section information and the disassembler of a PE file. 2. OOA Rules Generator: after extracting the Win API sequences of the training set by our PE parse, we store these Win API sequences into the database as signatures, then pass them through the OOA Rules generator to mine the rules satisfying the specific objective, and thus store such rules into the OOA Rules database. In addition, we implement three distinguishing algorithms for our OOA mining, and they are as follows: OOA_Apriori, OOA_FPgrowth, OOA_DMAV_FPgrowth. 3. Malware Detection Module: in order to determine whether a PE file in the testing set is a malware or not, we pass this PE file's API sequence constructed by our PE parser, together with each OOA Rule in OOA Rules database created by our OOA rule generator, through a malware detection module. In this paper, we make contribution to optimize the signature creation using OOA mining algorithm, and, the experiment results illustrate that, compared to the other two OOA mining algorithms, our OOA_DMAV_FPgrowth algorithm performs the highest

efficiency. Thus, encouraging experimental results demonstrate the robustness and intelligence of our DMAV system: compared with several popular anti-virus software's, our DMAV system can detect not only known viruses, but also polymorphic and new previously unseen malware effectively and efficiently.

II. Related Work

Besides the traditional signature-based malware detection methods, there is some work to improve the signature-based detection [15, 3, 12] and also a few attempts to apply data mining and machine learning techniques to detect new malicious executables. Sung et al. [15] developed a signature based malware detection system called SAVE (Static Analyzer of Vicious Executables) which emphasized on detecting polymorphic malware. The basic idea of this approach is to extract the signatures from the original malware with the hypothesis that all versions of the same malware share a common core signature. Schultz et al. [13] applied Naive Bayes method to detect previously unknown malicious code. Decision Tree was studied in [18, 9]. Kolter et al. [9] gathered 1971 benign executables and 1651 malicious executables in Windows PE format, and examined the performance of different classifiers such as Naive Bayes, support vector machine (SVM) and Decision Tree using 10-fold cross validation and plotting ROC curves [16]. Their results also showed that the ROC curve of the Decision Tree method dominated all others. Different from earlier studies, our work is based on a large collection of malicious executables collected at KingSoft Anti-Virus Laboratory. In addition, we apply OOA mining technique to extract the characterizing frequent patterns to achieve accurate malware detection since frequent patterns found by association mining carry the underlying semantics of the data

III. The System Architecture

Our IMDS system is performed directly on Windows PE code. PE is designed as a common file format for all flavors of Windows operating system, and PE viruses are in the majority of the viruses rising in recent years. Some famous viruses such as CIH, CodeRed, CodeBlue, Nimda, Sircam, Killonce, Sobig, and LoveGate all aim at PE les. The system consists of three major components: PE parser, OOA rule generator, and malware detection module, as illustrated in Figure 1.

The functionality of the PE parser is to generate the Windows API execution sequence for each benign/malicious executable. Since a virus scanner is usually a speed sensitive application, in order to improve the system performance, we developed a PE parser to construct the API execution sequences of PE les instead of using a third party disassembler. If a PE file is previously compressed by a third party binary compress toll, it needs to be decompressed before being passed to the PE parser. Through the API query database, the API execution sequence generated by the PE parser can be converted to a group of 32-bit global IDs which represents the static execution sequence of the corresponding API functions.

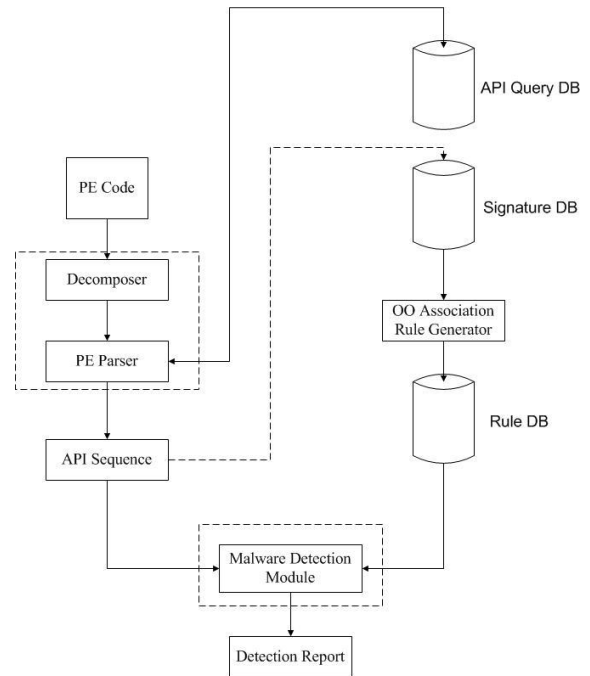


Figure 1. IMDS system architecture.

Then we use the API calls as the signatures of the PE les and store them in the signature database, which contains 6 fields: record ID, PE file name, file type ("0" represents benign file while "1" is for malicious file), called API sequence name, called API ID, and the total number of called API functions. After that, an OOA mining algorithm is applied to generate class association rules which are recorded in the rule database. To finally determine whether a PE file is malicious or not, we pass the selected API calls together with the rules generated to the malware detection module to perform the association rule based classification.

IV. CLASSIFICATION BASED ON OOA MINING

Both classification and association mining play important roles in data mining techniques. Classification is "the task of learning a target function that maps each feature set to one of the predefined class labels" [17]. For association rule mining, there is no predetermined target. Given a set of transactions in the database, all the rules that satisfied the support and confidence thresholds will be discovered [1]. As a matter of fact, classification and association rule mining can be integrated to association rule based classification [10, 2]. This technique utilizes the properties of frequent patterns to solve the scalability and over fitting issues in classification and achieves excellent accuracy [2]. In our IMDS system, we adapted OOA mining techniques [14] to generate the rules.

A. OOA Definitions

In our IMDS system, the goal is to find out how a set of API calls supports the specific objectives:

$$Obj_1 = (Group = Malicious), \text{ and } Obj_2 = (Group = Benign).$$

1) Definition1: (Support and confidence) $I = \{I_1, \dots, I_m\}$

be an itemset and $I \rightarrow Obj(os\%, oc\%)$ be an association rule in OOA mining. The support and confidence of the rule are defined as:

$$os\% = supp(I, Obj) = \frac{count(I \cup Obj, DB)}{|DB|} \times 100$$

$$oc\% = conf(I, Obj) = \frac{count(I \cup Obj, DB)}{count(I, DB)} \times 100 \quad \text{where}$$

the function count returns the number of records in the dataset DB where holds.

2) Definition 2: (OOA frequent itemset) Given $mos\%$ as a user-specified minimum support. I is OOA frequent item set/pattern in DB if $os\% \geq mos\%$.

3) Definition 3: (OOA rule) Given $moc\%$ as a user-specified confidence. Let $I = \{I_1, \dots, I_m\}$ be an OOA frequent itemset. $I \rightarrow Obj(os\%, oc\%)$ is an OOA rule if $oc\% \geq moc\%$.

B. OOA Fast FP-Growth Algorithm

Although Apriori algorithm can be extended to OOA mining, it requires many iterations to generate all of the frequent itemsets before generating the association rules. An alternative OOA mining algorithm called OOA FP-Growth is designed based on FP-Growth algorithm [6, 5]. In general, OOA FP-Growth algorithm is much faster than OOA Apriori for mining frequent itemsets. However, when the minimum support is small, OOA FP-Growth generates a huge number of conditional FP-trees recursively, which is time and space consuming. Our malware detection relies on finding frequent patterns from large collections of data, therefore, the efficiency is an essential issue to our system. In our IMDS system, we extend a modified FP-Growth algorithm proposed in [4] to conduct the OOA mining. This algorithm greatly reduces the costs of processing time and memory space, and we call it OOA Fast FP-Growth algorithm. Similar to OOA FP-Growth algorithm, there are also two steps in OOA Fast FP-Growth algorithm: constructing an OOA Fast FPtree and generating frequent patterns from the tree. But the structure of an OOA Fast FP-tree is different from that of an OOA FPtree in the following way: (1) The paths of an OOA Fast FP-tree are directed, and there is no path from the root to leaves. Thus, fewer pointers are needed and less memory space is required. (2) In an OOA FP-tree, each node is the name of an item, but in an OOA Fast FP-

tree, each node is the sequence number of an item, which is determined by the support count of the item. The detailed description can be referenced in [4].

C. An Illustrating Example

At the beginning of this section, we state that frequent patterns are essential to accurate classification. To demonstrate the effectiveness of the frequent patterns, we show an example rule generated by OOA Fast FP-Growth algorithm. We sample 5611 records from our signature database, of which 3394 records are malicious executables and 2217 records are benign executables. One of the rules we generated is:

$$(2230,398,145,138,115,77) \rightarrow Obj_1 = (Group = Malicious)(os = 0.296739, oc = 0.993437),$$

where os and oc represent the support and confidence, respectively. After converting the API IDs to API names via our API query database, this rule becomes:

(KERNEL32.DLL,OpenProcess;CopyFileA;CloseHandle;GetVersionExA;GetModuleFileNameA;WriteFile)→
 $obj_1 = (Group = Malicious)(os = 0.296739, oc = 0.993437)$

After analyzing the API sequence in this rule, we know that the program actually executes the following functions: (i) returns a handle to an existing process object; (ii) copies an existing file to a new file; (iii) closes the handle of the open object; (iv) obtains extended information about the version of the currently running operating system; (v) retrieves the complete path of the file that contains the specified module of current process; and (vi) writes data to the file. with the os and oc values, we know that this sequence of API appears in 1665 malware, while only in 11 benign files. Obviously, it is one of the essential rules for determining whether an executable is malicious or not. In the experiments section, we perform a comprehensive experimental study to evaluate the efficiency of different OOA mining algorithms.

D. Associative Classifier

For OOA rule generation, we use the OOA Fast FP-Growth algorithm to obtain all the association rules with certain support and confidence thresholds, and two objectives:

$$Obj_1 = (Group = Malicious), \text{ and } Obj_2 = (Group = Benign).$$

Then we apply the technique of classification based on association rules (CBA) to build a CBA classifier [10] as our malware detection module. The CBA classifier is built on rules with high support and confidence and uses the association between frequent patterns and the type of _les for prediction. So, our malware detection module takes the input of generated OOA rules and outputs the prediction of whether an executable is malicious or not.

V. DATA COLLECTION

As stated previously, we obtained 29580 Windows PE _les of which 12214 were recognized as benign executables while 17366 were malicious executables. The malicious executables mainly consisted of backdoors, worms, and Trojan horses and all of them were provided by the Anti-virus laboratory of KingSoft Corporation. The benign executables were gathered from the system _les of Windows 2000/NT and XP operating system.

VI. EXPERIMENTAL RESULTS AND ANALYSIS

We conduct three sets of experiments using our collected data. In the first set of experiments, we evaluate the efficiency of different OOA mining algorithms. The second set of experiments is to compare the abilities to detect polymorphic and unknown malware of our IMDS system with current widely-used anti-virus software.

The efficiency and false positives by using different scanners have also been examined. Finally, we compare our IMDS system with other classification based methods. All the experiments are conducted under the environment of Windows 2000 operating system plus Intel P4 1Ghz CPU and 1Gb of RAM.

A. Evaluation of Different OOA Mining Algorithms

In the first set of experiments, we implement OOA Apriori, OOA FP-Growth, and OOA Fast FP-Growth algorithms under Microsoft Visual C++ environment. We sample 5611 records from our signature database, which includes 3394 records of malicious executables and 2217 records of benign executables. By using different support and confidence thresholds, we compare the efficiency of the three algorithms, we observe that the time complexity increases exponentially as the minimum support threshold decreases. However, it shows obviously that the OOA Fast FP-Growth algorithm is much more efficient than the other two algorithms, and it even doubles the speed of performing OOA FP-Growth algorithm.

B. Comparisons of Different Anti-virus Scanners

In this section, we examine the abilities of detecting polymorphic malware and unknown malware of our system in comparison with some of the popular software tools such as Norton AntiVirus 2006, Dr.Web, McAfee VirusScan and Kaspersky Anti-Virus. The efficiency and the number of false positives are also evaluated.

1) Polymorphic Virus Detection

In this experiment, we sample 3000 malicious _les and 2000 benign _les in the training data set, then we use 1500 malware and 500 benign executables as the test data set. Several recent Win32 PE viruses are included in the test data set for analysis such as Lovedoor, My doom, Blaster, and Beagle. For each virus, we apply the obfuscation techniques described in [15] to create a set of polymorphic versions. Then we compare our system with current

most widely-used anti-virus software. The results shown in Table 4 demonstrate that our IMDS system achieves better accuracy than other software in polymorphic malware detection.

2) Unknown Malware Detection

In order to examine the ability of identifying new and previously unknown malware of our IMDS system, in the test data set, we use 1000 malware analyzed by the experts in KingSoft Anti-virus laboratory, while the signatures of the malware have not been recorded into the virus signature database. Comparing with other anti-virus software, our IMDS system performs most accurate detection. The results are listed in Table 5.

3) System Efficiency and False Positives

In malware detection, a false positive occurs when the scanner marks a benign file as a malicious one by error. False positives can be costly nuisances due to the waste of time and resources to deal with those falsely reported files. In this set of experiments, in order to examine the system efficiency and the number of false positives of the IMDS system, we sample 2000 executables in the test data set, which contains 500 malicious executables and 1500 benign ones. First, we compare the efficiency of our system with different scanners including the scanner named. SAVE. [15, 20] described in related work and some widely-used anti-virus software. The results illustrate that our IMDS system achieves much higher efficiency than other scanners when being executed in the same environment. The number of false positives by using different scanners are also examined. By scanning 1500 benign executables

whose signatures have not been recorded in the signature database, the obtained results clearly shows that the false positives by using our IMDS system are much fewer than other scanners.

C. Comparisons of Different Classification Methods

In this set of experiments, we compare our system with Naïve Bayes, Support Vector Machine (SVM) and Decision tree methods. We randomly select 2843 executables from our data collection, in which 1207 files are benign and 1636 executables are malicious. Then we convert the transactional sample data in our signature database into a relational table, in which each column corresponds to an API and each row is an executable. This transformation makes it easy to apply feature selection methods and other classification approaches. First, we rank each API using Max-relevance algorithm [11], classification. In the experiments, we use the Naive Bayes classifier and J4.8 version of Decision Tree implemented in WEKA [19], and also the SVM implemented in LIBSVM package [7]. For the OOA Fast FP-Growth mining, we select thresholds based on two criteria: setting as close to 1 as possible; and selecting a big without exceeding the maximum support in the data set. Then, in the experiment, we set to 0.294 and to 0.98. Ten-fold cross validation is used to evaluate the accuracy of each classifier.

VII. CONCLUSIONS

In this paper, we describe our research effort on malware detection based on window API sequence. In summary, our main contributions are: (1) We develop an integrated IMDS system based on analysis of Windows API execution sequences. The system consists of three components: PE parser, rule generator and classifier; (2) We adapt existing association based classification techniques our system on a large collection of executables including 12214 benign

samples and 17366 malicious ones; (4) We provide a comprehensive experimental study on various anti-virus software as well as various data mining techniques for malware detection using our data collection; (5) Our system has been already incorporated into the scanning tool of KingSoft's AntiVirus software.

VIII. REFERENCES

- [1] R. Agrawal and R. Srikant. Fast algorithms for association rule mining. In *Proceedings of VLDB-94*, 1994.
- [2] H. Cheng, X. Yan, J. Han, and C. Hsu. Discriminative frequent pattern analysis for effective classification. In *ICDE-07*, 2007.
- [3] M. Christodorescu and S. Jha. Static analysis of executables to detect malicious patterns. In *Proceedings of the 12th USENIX Security Symposium*, 2003.
- [4] M. Fan and C. Li. Mining frequent patterns in an fp-tree without conditional fp-tree generation. *Journal of Computer Research and Development*, 40:1216.1222, 2003.
- [5] J. Han and M. Kamber. *Data mining: Concepts and techniques, 2nd edition*. Morgan Kaufmann, 2006.
- [6] J. Han, J. Pei, and Y. Yin. Mining frequent patterns without candidate generation. In *Proceedings of SIGMOD*, pages 1.12, May 2000.
- [7] C. Hsu and C. Lin. A comparison of methods for multiclass support vector machines. *IEEE Trans. Neural Networks*, 13:415.425, 2002.
- [8] J. Kephart and W. Arnold. Automatic extraction of computer virus signatures. In *Proceedings of 4th Virus Bulletin International Conference*, pages 178.184, 1994.
- [9] J. Kolter and M. Maloof. Learning to detect malicious executables in the wild. In *Proceedings of KDD'04*, 2004.
- [10] B. Liu, W. Hsu, and Y. Ma. Integrating classification and association rule mining. In *Proceedings of KDD'98*, 1998.
- [11] H. Peng, F. Long, and C. Ding. Feature selection based on mutual information: Criteria of max-dependency, max-relevance, and min-redundancy. *IEEE Trans. Pattern Analysis and Machine Intelligence*, 27, 2005.
- [12] J. Rabek, R. Khazan, S. Lewandowski, and R. Cunningham. Detection of injected, dynamically generated, and obfuscated malicious code. In *Proceedings of the 2003 ACM workshop on Rapid malware*, pages 76.82, 2003.
- [13] M. Schultz, E. Eskin, and E. Zadok. Data mining methods for detection of new malicious executables. In *Proceedings of IEEE International Conference on Data Mining*, 2001.
- [14] Y. Shen, Q. Yang, and Z. Zhang. Objective-oriented utility-based association mining. In *Proceedings of IEEE International Conference on Data Mining*, 2002.
- [15] A. Sung, J. Xu, P. Chavez, and S. Mukkamala. Static analyzer of vicious executables (save). In *Proceedings of the 20th Annual Computer Security Applications Conference*, 2004.
- [16] J. Swets and R. Pickett. *Evaluation of diagnostic system: Methods from signal detection theory*. Academic Press, 1982.
- [17] P. Tan, M. Steinbach, and V. Kumar. *Introduction to data mining*. Addison Wesley, 2005.
- [18] J. Wang, P. Deng, Y. Fan, L. Jaw, and Y. Liu. Virus detection using data mining techniques. In *Proceedings of IEEE International Conference on Data Mining*, 2003.
- [19] H. Witten and E. Frank. *Data mining: Practical machine learning tools with Java implementations*. Morgan Kaufmann, 2005.
- [20] J. Xu, A. Sung, P. Chavez, and S. Mukkamala. Polymorphic malicious executable sanner by api sequence analysis. In *Proceedings of the International Conference on Hybrid Intelligent Systems*, 2004.
- [21] Yanfang Ye*, Dingding Wang, Dongyi Ye, "Intelligent Malware Detection System" in *proceedings of Industrial and Government Track Short Paper*, 2007.

Performance and Analysis of Edge detection using FPGA Implementation

R. Ponneela Vignesh¹, R. Rajendran²

¹PG Student/VLSI Design, SNS College of Technology, Coimbatore, Tamilnadu.

²Dept.of ECE, SNS College of Technology, Coimbatore, Tamilnadu.

Abstract

Edge detection serves as a pre-processing step for many image processing algorithms such as image enhancement, image segmentation, tracking and image/video coding. The edge detection is one of the key stages in image processing and object recognition. This paper present a Canny edge detection algorithm that results in significantly reduced memory requirements, decreased latency and increased throughput with no loss in edge detection performance. This edge detection algorithm is based on MATLAB simulation and FPGA implementation.

Keywords: Canny edge detector, MATLAB and FPGA

I. Introduction

Edge detection is a basic operation in image processing, it refers to the process identifying and locating sharp discontinuities in an image, the discontinuities are abrupt changes in pixel intensity which characterize boundaries of objects in a scene. It is a very important first step in many algorithms used for segmentation, tracking and object recognition [1].

There are an extremely large number of edge detection operators available, each designed to be sensitive to edges, typically it reduces the memory size and the computation cost[2] the edge detection algorithms are implemented using software, with advance in very large scale integration(VLSI) technology, their hardware implementation become an attractive alternative, especially for real-time applications, Many edge detection algorithms such as Robert detector, Prewitt detector, Kirsch detector, Gauss-Laplace detector and Canny edge detector have been proposed[3], among these algorithms has be widely used in the field of image processing because of its good performance[3]. It operates on two rows of pixels at a time this reduces the memory requirement at the expense of a decrease in the throughput [2]. In order to reduce memory requirements, decrease latency and increased throughput is proposed in [1]. An absolute different mask edge detection algorithm and its pipelined VLSI architecture for real-time application. But the edge detector in offers a trade-off between precision, cost and speed, and its capability to detect edges is not as good as the Canny algorithm [4].

In this paper, a method based on non-uniform and coarse quantization of the gradient magnitude histogram is proposed. In addition, the proposed algorithm is mapped onto reconfigurable hardware architecture. The original Canny edge detection algorithm computes the high and low thresholds for edge detection based on the entire image statistics which prevents the processing on individual block independently.

II. Canny edge detection algorithm

The Canny edge detection algorithm is known to many as the optimal edge detector. The first and most obvious is low error rate. It is the important that edges occurring in images should not be missed and that there are no responses to non-edges. The second criterion is that the edge points be well localized. A third criterion is to have only one response to a single edge.

This was implemented because the first two were not substantial enough to completely eliminate the possibility of multiple responses to an edge. Based on these criteria, the canny edge detector first smoothes the image to eliminate and noise. It then finds the image gradient to highlight regions with high spatial derivatives After the edge directions are known, non maximum suppression now has to be applied Non-maximum suppression is used to trace along the edge in the edge direction and suppress any pixel value that is not considered to be an edge. This will give a thin line in the output image.

The algorithm then tracks along these regions and suppresses any pixel that is not at the maximum (non maximum suppression). The gradient array is now further reduced by hysteresis. Hysteresis is used to track along the remaining pixels that have not been suppressed Hysteresis uses two thresholds and if the magnitude is below the first threshold, it is set to zero (made a non edge). To avoid this hysteresis uses 2 thresholds, a high and a low. If the magnitude is above the high threshold, it is made an edge. This model was based on a step edge corrupted by additive white Gaussian noise. Canny edge detection developed an approach to derive an optimal edge detector based on three criteria related to the detection performance. The Canny edge detection algorithm block diagram is shown in below.

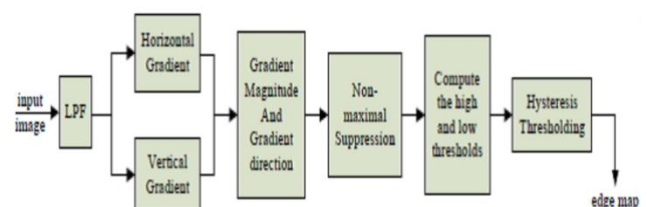


Fig 1 : Block of Canny edge detection

The Canny edge detection algorithm consists of the following steps:

- Calculating the horizontal gradient and vertical gradient at each pixel location by convolving the image with partial derivatives of a 2D Gaussian function.

- Smoothing the input image by Gaussian mask. The output smoothed the image.
- Computing the gradient magnitude and direction at each pixel location.
- Applying non-maximum suppression (NMS) to thin edge.
- Computing the hysteresis high and low thresholds based on the histogram of the magnitudes of the gradients of the entire image.
- Performing hysteresis thresholding to determine the edge map.
- The low pass filtering is achieved by taking the average pixel values.

It can be shown that convolving an image with a symmetric 2D Gaussian and then differentiating in the direction of the gradient forms simple and effective directional operator, which meets the three criteria mentioned above
 Suppose the $G(x, y)$ is a 2D Gaussian and $I(x, y)$ is the image, then the smoothed image $H(x, y)$ as

$$H(x, y) = G(x, y) * I(x, y)$$

Where the $H(x, y)$ is denoted as horizontal gradient, the $G(x, y)$ is denoted as gradient magnitude and $I(x, y)$ as smoothed image.

The data obtains usually contains some spurious responses in the non maximal suppression (NMS). This is called the streaking problem and is quite common in the edge detection problem. These streaking can be eliminated by using a threshold with hysteresis.

The Canny edge detector will be carried out in following four steps:

1. Image smoothing
 2. Gradient calculation and directional Non-Maximum suppression
 3. Calculating thresholds
 4. Thresholding with hysteresis.
1. Smooth the image with a two dimensional Gaussian. In most cases the computation of a two dimensional Gaussian is costly, so it is approximated by two one dimensional Gaussians, one in the x direction and the other in the y direction.
 2. Take the gradient of the image. This shows changes in intensity, which indicates the presence of edges. This actually gives two results, the gradient in the x direction and the gradient in the y direction.
 3. Non-maximal suppression. Edges will occur at points the where the gradient is at a maximum. Therefore, all points not at a maximum should be suppressed. In order to do this, the magnitude and direction of the gradient is computed at each pixel. Then for each pixel check if the magnitude of the gradient is greater at one pixel's distance away in either the positive or the negative direction perpendicular to the gradient. If the pixel is not greater than both, suppress it.
 4. Edge Thresholding. The method of thresholding used by the Canny Edge Detector is referred to as "hysteresis". It makes use of both a high threshold and a low threshold. If a pixel has a value above the high threshold, it is

set as an edge pixel. If a pixel has a value above the low threshold and is the neighbour of an edge pixel, it is set as an edge pixel as well. If a pixel has a value above the low threshold but is not the neighbour of an edge pixel, it is not set as an edge pixel. If a pixel has a value below the low threshold, it is never set as an edge pixel.

First the edge detection algorithm is implemented by applying a Gaussian filter on the whole image. Then the processed image data are used as the input to calculate the gradient at each pixel level and these gradient values are used to calculate the direction and the magnitude at a certain pixel.

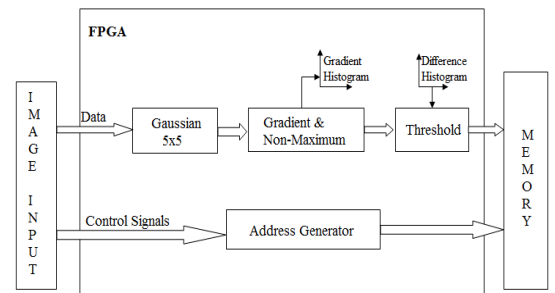


Fig 2 : Design flow of Canny edge detection

In order to implement the Canny edge detector algorithm, some steps must be followed. The following steps are executed sequentially:

- The first step is to filter out any noise in the original image before trying to locate and detect any edges.
- The Gaussian filter mask is used exclusively in Canny edge detection algorithm.
- The Gaussian smoothing can be performed using standard convolution methods. a convolution mask is much smaller than the actual image
- The larger width is the Gaussian mask and the lower is the detector sensitivity.
- The localization error in the detected edges also increases slightly as the Gaussian width is increased. The Gaussian in implementation is shown below.

	2	4	5	4	2
	4	9	12	9	4
1	5	12	15	12	5
115	4	9	12	9	4
	2	4	5	4	2

Fig 3: Discrete approximation to Gaussian function

- The second step is to find the edge strength by taking the gradient of the image.
- Then, the approximate absolute gradient magnitude (edge strength) at each point can be found.
- It uses a pair of 3x3 convolution masks, one estimating the gradient in the x-direction (columns).
- The other convolution masks estimating the gradient in the y-direction (rows). They are shown below:

-1	0	+1
-2	0	+2
-1	0	+1

Gx

+1	+2	+1
0	0	0
-1	-2	-1

Gy

The magnitude or edge strength of gradient is then approximated using the formula:

$$|G| = |G_x| + |G_y|$$

The direction of the edge is computed using the gradient in the x and y directions. Whenever the gradient in the x direction is equal to zero, the edge direction has to be equal to 90 degrees or 0 degrees, Formula for finding edge direction:

$$\theta = \tan^{-1} (G_y / G_x)$$

If GY has a value of zero, the edge direction will equal to 0 degrees. Otherwise the edge direction is equal to 90 degrees.

III Simulation results

The algorithm performance was tested using a variety of images. The simulations results are obtained in MATLAB. Here the results are tested by two images.

(a). Finger print and

(b). Eye

Simulation output:

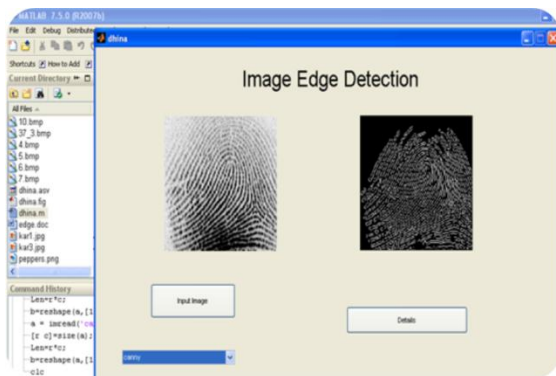


Fig 4: Matlab simulation result for Finger print image

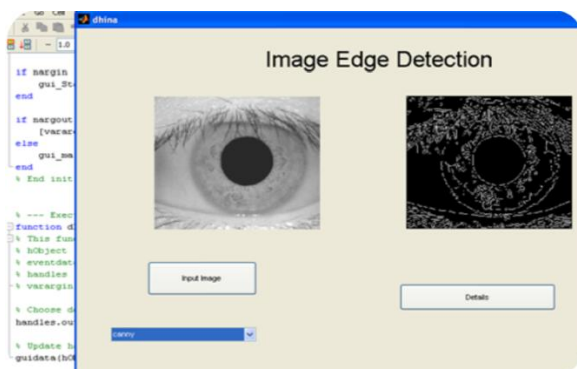


Fig 5: Matlab simulation result for Eye image

CONCLUSION

The result of the image can be obtained by using MATLAB. Thus compared to other edge detection algorithm, Canny edge detection algorithm use probability for finding error rate localization and response in various images. Thus even blurred image and images with noise can be detected accurately using this Canny edge detection algorithm as there is a specification of improving signal to noise ratio. It results in a significant speedup and successfully detects the edges of the images.

FUTURE WORK

Thus as a future enhancement, the implementation of Canny edge detection algorithm can be perform on FPGA platform and tested in system C. Thus tested in system C which can overcome the major disadvantage of canny edge detection algorithm of complex computation and time consuming. It is capable of supporting fast real time edge detection for images and videos.

REFERENCES

- [1] S. Varadarajan, C. Chakrabarti, L. J. Karam, and J. M. Bauza, "A distributed psycho-visually motivated Canny edge detector," IEEE ICASSP, pp.882-825, Mar.2010.
- [2] D. V. Rao and M. Venkatesan, "An efficient reconfigurable architecture and implementation of edge detection algorithm using Handle-C," ITCC, vol. 2, pp. 843 – 847, Apr. 2004.
- [3] W. He and K. Yuan, "An improved Canny edge detector and its realization on FPGA," WCICA, pp. 6561 –6564, Jun. 2008.
- [4] F. M. Alzahrani and T. Chen, "A real-time edge detector algorithm and VLSI architecture," *Real-Time Imaging*, vol. 3, no. 5, pp. 363 – 78, 1997.
- [5] J.F. Canny, "A computation approach to edge detection," IEEE Transactions on Pattern Analysis and Machine Intelligence, vol. 8, no.6, pp. 769-798, Nov 1986.
- [6] D. Marr and E. Hildreth, "Theory of edge Detection," Proc. Royal Soc. of London, series B, vol. 207, pp. 187-217, 1980.
- [7] D. Demigny, and T. Kamle, "A discrete expression of Canny's criteria for step edge detector performances evaluation", IEEE Transactions on Pattern Analysis and Machine Intelligence, 19(6), pp. 1199-1211, 1997.
- [8] L. Torres, M. Robert, E. Bourennane, and M. Paidavoine, "Implementation of a recursive real time edgedetector using retiming techniques," *VLSI*, pp. 811 –816, Aug. 1995.

Design and Simulation of Level Shifted Cascaded H-Bridge Multilevel Inverter Based DSTATCOM

P. SURENDRA BABU

Associate Prof in EEE
VRS & YRN COLLEGE OF ENGG & TECH,
CHIRALA, A.P, INDIA

Dr. BV. SANKER RAM

Prof in EEE & Director of Evaluation,
JNTU College of Engineering Hyderabad, A.P,
India.

Abstract- This paper presents an investigation of five-Level Cascaded H – bridge (CHB) Inverter as Distribution Static Compensator (DSTATCOM) in Power System (PS) for compensation of reactive power and harmonics. The advantages of CHB inverter are low harmonic distortion, reduced number of switches and suppression of switching losses. The DSTATCOM helps to improve the power factor and eliminate the Total Harmonics Distortion (THD) drawn from a Non-Liner Diode Rectifier Load (NLDRL). The D-Q reference frame theory is used to generate the reference compensating currents for DSTATCOM while Proportional and Integral (PI) control is used for capacitor dc voltage regulation. A CHB Inverter is considered for shunt compensation of a 11 kV distribution system. Finally a level shifted PWM (LSPWM) and phase shifted PWM (PSPWM) techniques are adopted to investigate the performance of CHB Inverter. The results are obtained through Matlab/Simulink software package.

Keywords- *DSTATCOM, Level shifted Pulse width modulation (LSPWM), Phase shifted Pulse width modulation (PSPWM), Proportional-Integral (PI) control, CHB multilevel inverter, D-Q reference frame theory.*

I. INTRODUCTION

Modern power systems are of complex networks, where hundreds of generating stations and thousands of load centers are interconnected through long power transmission and distribution networks. Even though the power generation is fairly reliable, the quality of power is not always so reliable. Power distribution system should provide with an uninterrupted flow of energy at smooth sinusoidal voltage at the contracted magnitude level and frequency to their customers. PS especially distribution systems, have numerous non linear loads, which significantly affect the quality of power. Apart from non linear loads, events like capacitor switching, motor starting and unusual faults could also inflict power quality (PQ) problems. PQ problem is defined as any manifested problem in voltage /current or leading to frequency deviations that result in failure or maloperation of customer equipment. Voltage sags and swells are among the many PQ problems the industrial processes have to face. Voltage sags are more severe. During the past few decades, power industries have proved that the adverse impacts on the PQ can be mitigated or avoided by conventional means, and that techniques using fast controlled force commutated power electronics (PE) are

even more effective. PQ compensators can be categorized into two main types. One is shunt connected compensation device that effectively eliminates harmonics. The other is the series connected device, which has an edge over the shunt type for correcting the distorted system side voltages and voltage sags caused by power transmission system faults.

The STATCOM used in distribution systems is called DSTACOM (Distribution-STACOM) and its configuration is the same, but with small modifications. It can exchange both active and reactive power with the distribution system by varying the amplitude and phase angle of the converter voltage with respect to the line terminal voltage.

A multilevel inverter can reduce the device voltage and the output harmonics by increasing the number of output voltage levels. There are several types of multilevel inverters: cascaded H-bridge (CHB), neutral point clamped, flying capacitor [2-5]. In particular, among these topologies, CHB inverters are being widely used because of their modularity and simplicity. Various modulation methods can be applied to CHB inverters. CHB inverters can also increase the number of output voltage levels easily by increasing the number of H-bridges. This paper presents a DSTATCOM with a proportional integral controller based CHB multilevel inverter for the harmonics and reactive power mitigation of the nonlinear loads. This type of arrangements have been widely used for PQ applications due to increase in the number of voltage levels, low switching losses, low electromagnetic compatibility for hybrid filters and higher order harmonic elimination.

II. DESIGN OF MULTILEVEL BASED DSTATCOM

A. Principle of DSTATCOM

A D-STATCOM (Distribution Static Compensator), which is schematically depicted in Figure-1, consists of a two-level Voltage Source Converter (VSC), a dc energy storage device, a coupling transformer connected in shunt to the distribution network through a coupling transformer. The VSC converts the dc voltage across the storage device into a set of three-phase ac output voltages. These voltages are in phase and coupled with the ac system through the reactance of the coupling transformer. Suitable adjustment of the phase and magnitude of the D-STATCOM output voltages allows effective control of active and reactive power exchanges between the DSTATCOM and the ac system. Such

configuration allows the device to absorb or generate controllable active and reactive power.

on the efficiency of the converter, without incurring significant switching losses.

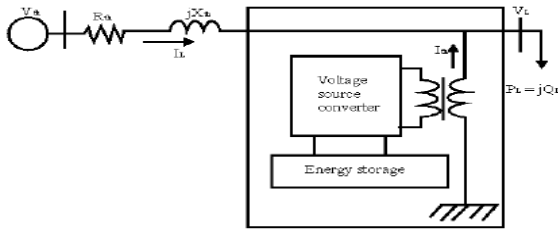


Figure – 1 Schematic Diagram of a DSTATCOM

The VSC connected in shunt with the ac system provides a multifunctional topology which can be used for up to three quite distinct purposes:

1. Voltage regulation and compensation of reactive power;
2. Correction of power factor
3. Elimination of current harmonics.

Here, such device is employed to provide continuous voltage regulation using an indirectly controlled converter. As shown in Figure-1 the shunt injected current I_{sh} corrects the voltage sag by adjusting the voltage drop across the system impedance Z_{th} . The value of I_{sh} can be controlled by adjusting the output voltage of the converter. The shunt injected current I_{sh} can be written as,

$$I_{sh} = I_L - I_S = I_L - (V_{th} - V_L) / Z_{th} \quad (1)$$

$$I_{sh} / _ \eta = I_L / _ - \theta \quad (2)$$

The complex power injection of the D-STATCOM can be expressed as,

$$S_{sh} = V_L I_{sh}^* \quad (3)$$

It may be mentioned that the effectiveness of the DSTATCOM in correcting voltage sag depends on the value of Z_{th} or fault level of the load bus. When the shunt injected current I_{sh} is kept in quadrature with V_L , the desired voltage correction can be achieved without injecting any active power into the system. On the other hand, when the value of I_{sh} is minimized, the same voltage correction can be achieved with minimum apparent power injection into the system.

B. Control for Reactive Power Compensation

The aim of the control scheme is to maintain constant voltage magnitude at the point where a sensitive load under system disturbances is connected. The control system only measures the rms voltage at the load point, i.e., no reactive power measurements are required. The VSC switching strategy is based on a sinusoidal PWM technique which offers simplicity and good response. Since custom power is a relatively low-power application, PWM methods offer a more flexible option than the fundamental frequency switching methods favored in FACTS applications. Apart from this, high switching frequencies can be used to improve

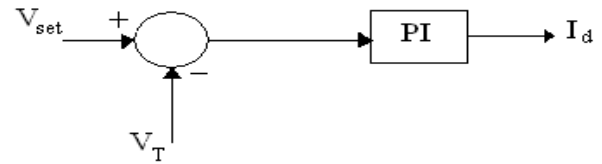


Figure-2 PI control for reactive power compensation

The controller input is an error signal obtained from the reference voltage and the rms terminal voltage measured. Such error is processed by a PI controller; the output is the angle δ , which is provided to the PWM signal generator. It is important to note that in this case, of indirectly controlled converter, there is active and reactive power exchange with the network simultaneously. The PI controller processes the error signal and generates the required angle to drive the error to zero, i.e. the load rms voltage is brought back to the reference voltage.

C. Control for Harmonics Compensation

The Modified Synchronous Frame method is presented in [7]. It is called the instantaneous current component (i_d - i_q) method. This is similar to the Synchronous Reference Frame theory (SRF) method. The transformation angle is now obtained with the voltages of the ac network. The major difference is that, due to voltage harmonics and imbalance, the speed of the reference frame is no longer constant. It varies instantaneously depending of the waveform of the 3-phase voltage system. In this method the compensating currents are obtained from the instantaneous active and reactive current components of the nonlinear load. In the same way, the mains voltages $V_{(a,b,c)}$ and the available currents $i_{l(a,b,c)}$ in α - β components must be calculated as given by (4), where C is Clarke Transformation Matrix. However, the load current components are derived from a SRF based on the Park transformation, where ‘ θ ’ represents the instantaneous voltage vector angle (5).

$$\begin{bmatrix} I_{l\alpha} \\ I_{l\beta} \end{bmatrix} = [C] \begin{bmatrix} I_{la} \\ I_{lb} \\ I_{lc} \end{bmatrix} \quad (4)$$

$$\begin{bmatrix} I_{ld} \\ I_{lq} \end{bmatrix} = \begin{bmatrix} \cos\theta & \sin\theta \\ -\sin\theta & \cos\theta \end{bmatrix} \begin{bmatrix} I_{l\alpha} \\ I_{l\beta} \end{bmatrix}, \theta = \tan^{-1} \frac{V_{\beta}}{V_{\alpha}} \quad (5)$$

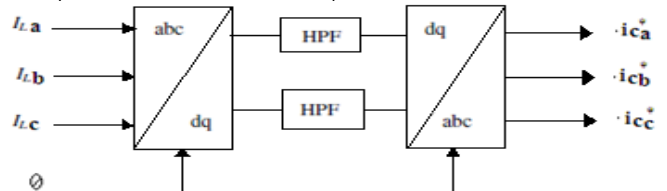


Figure-3 Block diagram of SRF method

Fig. 3 shows the block diagram SRF method. Under balanced and sinusoidal voltage conditions angle θ is a uniformly increasing function of time. This transformation angle is sensitive to voltage harmonics and unbalance; therefore $d\theta/dt$ may not be constant over a mains period.

With transformation given below the direct voltage component is

$$\begin{bmatrix} i_{ld} \\ i_{lq} \end{bmatrix} = \frac{1}{\sqrt{V_\alpha^2 + V_\beta^2}} \begin{bmatrix} V_\alpha & V_\beta \\ -V_\beta & V_\alpha \end{bmatrix} \quad (6)$$

$$\begin{bmatrix} i_{c\alpha} \\ i_{c\beta} \end{bmatrix} = \frac{1}{\sqrt{V_\alpha^2 + V_\beta^2}} \begin{bmatrix} V_\alpha & -V_\beta \\ V_\beta & V_\alpha \end{bmatrix} \begin{bmatrix} i_{cd} \\ i_{cq} \end{bmatrix} \quad (7)$$

$$\begin{bmatrix} I_{Comp,a} \\ I_{Comp,b} \\ I_{Comp,c} \end{bmatrix} = [C]^T \begin{bmatrix} i_{c\alpha} \\ i_{c\beta} \end{bmatrix} \quad (8)$$

D. Cascaded H-Bridge Multilevel Inverter

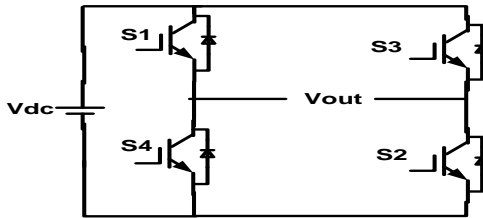


Figure-4 Circuit of the single cascaded H-Bridge Inverter

Fig.4 shows the circuit model of a single CHB inverter configuration. By using single H-Bridge we can get 3 voltage levels. The number of output voltage levels of CHB is given by 2n+1 and voltage step of each level is given by Vdc/2n, where n is number of H-bridges connected in cascaded. The switching table is given in Table 1.

Table-1 Switching table of single CHB inverter

Switches Turn ON	Voltage Level
S1,S2	Vdc
S3,S4	-Vdc
S4,D2	0

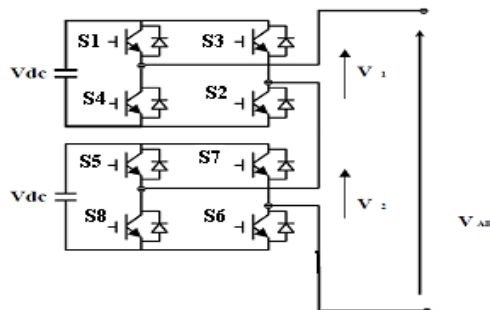


Figure-5 Block diagram of 5-level CHB inverter model

The switching mechanism for 5-level CHB inverter is shown in table-2.

Table 2. Switching table for 5-level CHB Inverter

Switches Turn On	Voltage Level
S1, S2	Vdc
S1,S2,S5,S6	2Vdc
S4,D2,S8,D6	0
S3,S4	-Vdc
S3,S4,S7,S8	-2Vdc

E. Design of Single H-Bridge Cell

1. Device Current

The IGBT and DIODE currents can be obtained from the load current by multiplying with the corresponding duty cycles. Duty cycle, $d = \frac{1}{2}(1+K\sin\omega t)$, Where, m = modulation index $K = +1$ for IGBT, -1 for Diode. For a load current given by

$$I_{ph} = \sqrt{2} I \sin(\omega t - \phi) \quad (9)$$

Then the device current can be written as follows.

$$\therefore i_{device} = \frac{\sqrt{2}}{2} I \sin(\omega t - \phi) x (1 + km \sin \omega t) \quad (10)$$

The average value of the device current over a cycle is calculated as

$$i_{avg} = \frac{1}{2\pi} \int_{\phi}^{\pi+\phi} \frac{\sqrt{2}}{2} I \sin(\omega t - \phi) x (1 + km \sin \omega t) d\omega t$$

$$= \sqrt{2} I \left[\frac{1}{2\pi} + \frac{k m}{g} \cos \phi \right] \quad (11)$$

The device RMS current can be written as

$$i_{rms} = \sqrt{\int_{\phi}^{\pi+\phi} \frac{1}{2\pi} (\sqrt{2} I \sin(\omega t - \phi))^2 x \frac{1}{2} x ((1 + km \sin \omega t) d\omega t)}$$

$$= \sqrt{2} I \sqrt{\frac{1}{g} + \frac{km}{3\pi} \cos \phi} \quad (12)$$

B IGBT Loss Calculation

IGBT loss can be calculated by the sum of switching loss and conduction loss. The conduction loss can be calculated by,

$$P_{on(IGBT)} = V_{ceo} * I_{avg(igbt)} + I_{rms(igbt)}^2 * r_{ceo} \quad (13)$$

$$I_{avg(igbt)} = \sqrt{2} I \left[\frac{1}{2\pi} + \frac{m}{g} \cos \phi \right] \quad (14)$$

$$I_{rms(igbt)} = \sqrt{2} I \sqrt{\left[\frac{1}{g} + \frac{m}{3\pi} \cos \phi \right]} \quad (15)$$

Values of V_{ceo} and r_{ceo} at any junction temperature can be obtained from the output characteristics (I_c vs. V_{ce}) of the IGBT as shown in Fig .6.

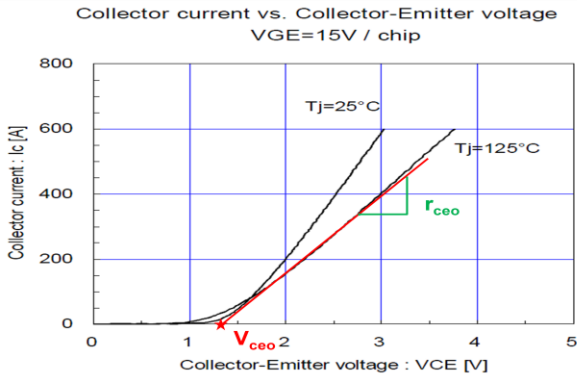


Figure 6 IGBT output characteristics

The switching losses are the sum of all turn-on and turn-off energies at the switching events

$$E_{sw} = E_{on} + E_{off} = a + bI + cI^2 \quad (16)$$

Assuming the linear dependence, switching energy

$$E_{sw} = (a + bI + cI^2) * \frac{V_{DC}}{V_{nom}} \quad (17)$$

Here V_{DC} is the actual DC-Link voltage and V_{nom} is the DC-Link Voltage at which E_{sw} is given. Switching losses are calculated by summing up the switching energies.

$$P_{sw} = \frac{1}{T_0} \sum_n E_{sw}(i) \quad (18)$$

Here 'n' depends on the switching frequency.

$$P_{sw} = \frac{1}{T_0} \sum_n (a + bI + cI^2) = \frac{1}{T_0} \left[\frac{a}{2} + \frac{bI}{\pi} + \frac{cI^2}{4} \right] \quad (19)$$

After considering the DC-Link voltage variations, switching losses of the IGBT can be written as follows.

$$P_{sw(IGBT)} = f_{sw} \left[\frac{a}{2} + \frac{bI}{\pi} + \frac{cI^2}{4} \right] * \frac{V_{DC}}{V_{nor}} \quad (20)$$

So, the sum of conduction and switching losses is the total losses given by

$$P_{T(IGBT)} = P_{on(IGBT)} + P_{sw(IGBT)} \quad (21)$$

C Diode Loss Calculation

The DIODE switching losses consist of its reverse recovery losses; the turn-on losses are negligible.

$$E_{rec} = a + bI + cI^2 \quad (22)$$

$$P_{sw(DIODE)} = f_{sw} \left[\frac{a}{2} + \frac{bI}{\pi} + \frac{cI^2}{4} \right] * \frac{V_{DC}}{V_{nor}} \quad (23)$$

So, the sum of conduction and switching losses gives the total DIODE losses.

$$P_{T(DIODE)} = P_{on(DIODE)} + P_{sw(DIODE)} \quad (24)$$

The total loss per one switch (IGBT+DIODE) is the sum of one IGBT and DIODE loss.

$$P_T = P_{T(IGBT)} + P_{sw(DIODE)} \quad (25)$$

D. Thermal Calculations

The junction temperatures of the IGBT and DIODE are calculated based on the device power losses and thermal resistances. The thermal resistance equivalent circuit for a module is shown in Fig 5. In this design the thermal calculations are started with heat sink temperature as the reference temperature. So, the case temperature from the model can be written as follows.

$$T_c = P_T R_{th(c-h)} + T_h \quad (26)$$

Here $R_{th(c-h)}$ = Thermal resistance between case and heat sink

$$P_T = \text{Total Power Loss (IGBT + DIODE)} \quad (27)$$

IGBT junction temperature is the sum of the case temperature and temperature raise due to the power losses in the IGBT.

$$T_{j(IGBT)} = P_{T(IGBT)} R_{th(j-c)IGBT} + T_c \quad (28)$$

The DIODE junction temperature is the sum of the case temperature and temperature raise due to the power losses in the DIODE.

$$T_{j(DIODE)} = P_{T(DIODE)} R_{th(j-c)DIODE} + T_c \quad (29)$$

The above calculations are done based on the average power losses computed over a cycle. So, the corresponding thermal calculation gives the average junction temperature. In order to make the calculated values close to the actual values, transient temperature values are to be added to the average junction temperatures.

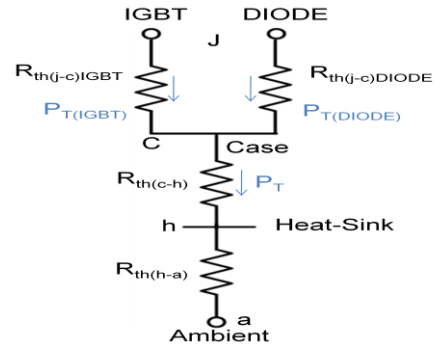


Figure. 5 Thermal resistance equivalent circuit

E. DC-Capacitor Selection

The required capacitance for each cell depends on the allowable ripple voltage and the load current. The rms ripple current flowing into the capacitor can be written as follows and the ripple current frequency is double the load current frequency.

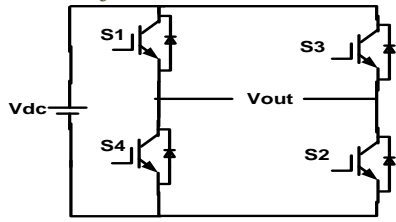


Fig. 6 H-Bridge converter

$$I_c = -\frac{1}{V_{dc}} \frac{1}{2} (|U_{ac}| * k + I_w L) \sin(2\omega t) \quad (30)$$

Since the value of 'L' is very small, the above equation can be simplified to

$$I_c = -\frac{1}{V_{dc}} \frac{1}{2} (|U_{ac}| * k) \sin(2\omega t) \quad (31)$$

$$I_c = -k \frac{1}{2} \frac{|U_{ac}|}{V_{dc}} * \sin(2\omega t) = -k \frac{m}{2} \sin(2\omega t) \quad (32)$$

Here 'm' is the modulation index and

$$I_{cp} = C \frac{du_{pp}}{dt}; \frac{m}{2} I \sqrt{2} = C 2\omega * \Delta V V_{dc} \quad (33)$$

$$C = \frac{m}{4\omega \Delta V * V_{dc}} \sqrt{2} I$$

F. PWM Techniques for CHB Inverter

The most popular PWM techniques for CHB inverter are 1. Phase Shifted Carrier PWM (PSCPWM), 2. Level Shifted Carrier PWM (LSCPWM).

1. Phase Shifted Carrier PWM (PSCPWM)

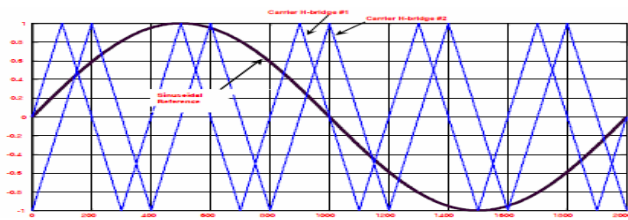


Fig. 7 phase shifted carrier PWM

Fig.7 shows the Phase shifted carrier pulse width modulation. Each cell is modulated independently using sinusoidal unipolar pulse width modulation and bipolar pulse width modulation respectively, providing an even power distribution among the cells. A carrier phase shift of 180°/m (No. of levels) for cascaded inverter is introduced across the cells to generate the stepped multilevel output waveform with lower distortion.

2. Level Shifted Carrier PWM (LSCPWM)

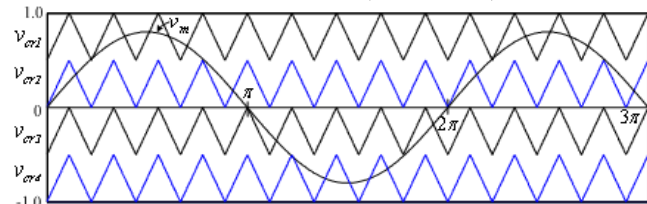


Fig. 8 Level shifted carrier PWM

Fig.8 shows the Level shifted carrier pulse width modulation. Each cell is modulated independently using sinusoidal unipolar pulse width modulation and bipolar pulse

width modulation respectively, providing an even power distribution among the cells. A carrier Level shift by 1/m (No. of levels) for cascaded inverter is introduced across the cells to generate the stepped multilevel output waveform with lower distortion.

IV. MATLAB/SIMULINK MODELING AND SIMULATION RESULTS

Fig. 9 shows the Matab/Simulink power circuit model of DSTATCOM. It consists of five blocks named as source block, non linear load block, control block, APF block and measurements block. The system parameters for simulation study are source voltage of 11kv, 50 hz AC supply, DC bus capacitance 1550e-6 F, Inverter series inductance 10 mH, Source resistance of 0.1 ohm and inductance of 0.9 mH. Load resistance and inductance are chosen as 30mH and 60 ohms respectively.

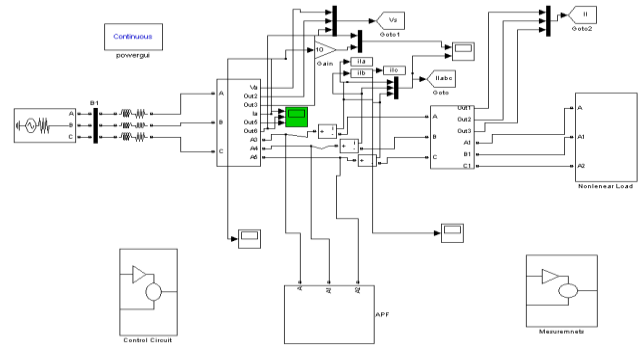


Fig. 9 Matlab/Simulink power circuit model of DSTATCOM

Fig. 10 shows the phase-A voltage of five level output of phase shifted carrier PWM inverter.

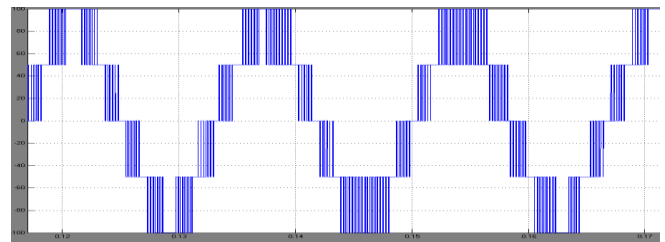


Fig. 10 five level PSCPWM output

Fig. 11 shows the three phase source voltages, three phase source currents and load currents respectively without DSTATCOM. It is clear that without DSTATCOM load current and source currents are same.

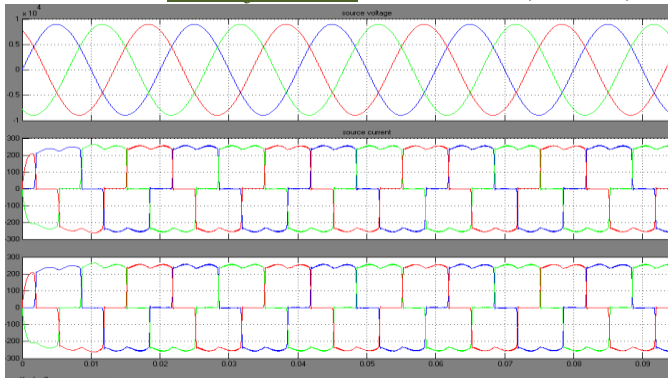


Fig. 11 Source voltage, current and load current without DSTATCOM

Fig. 12 shows the three phase source voltages, three phase source currents and load currents respectively with DSTATCOM. It is clear that with DSTATCOM even though load current is non sinusoidal source currents are sinusoidal.

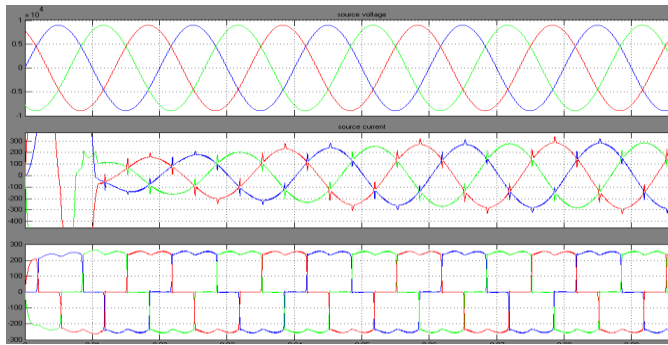


Fig. 12 Source voltage, current and load current with DSTATCOM

Fig. 13 shows the DC bus voltage. The DC bus voltage is regulated to 11kv by using PI regulator.

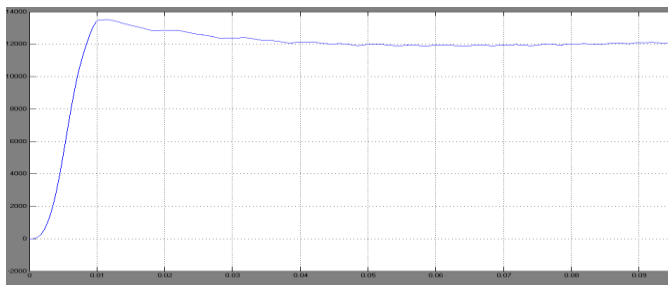


Fig. 13 DC Bus Voltage

Fig. 14 shows the phase-A source voltage and current, even though the load is non linear RL load the source power factor is unity.

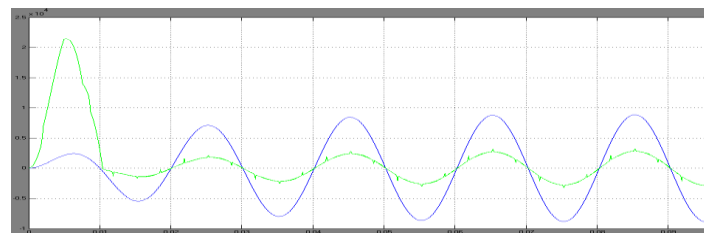


Fig. 14 Phase-A source voltage and current

Fig. 15 shows the harmonic spectrum of Phase –A Source current without DSTATCOM. The THD of source current without DSTATCOM is 36.89%.

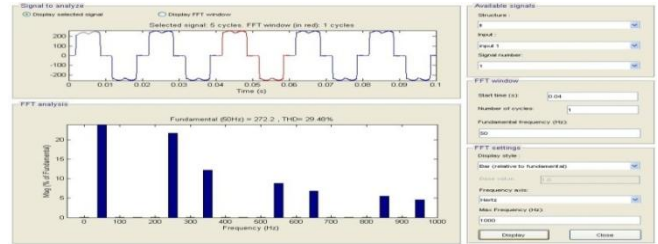


Fig. 15 Harmonic spectrum of Phase-A Source current without DSTATCOM

Fig. 16 shows the harmonic spectrum of Phase –A Source current with DSTATCOM. The THD of source current without DSTATCOM is 5.05%.

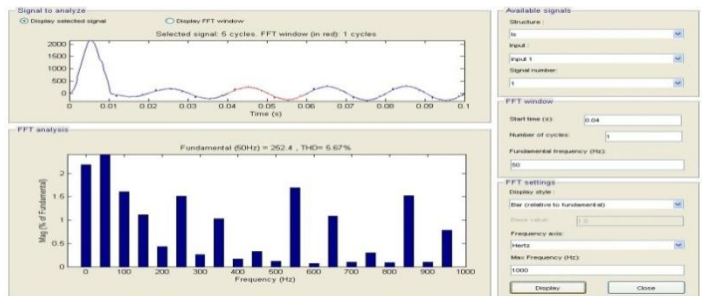


Fig. 16 Harmonic spectrum of Phase-A Source current with DSTATCOM

VI. CONCLUSION

A DSTATCOM with five level CHB inverter is investigated. Mathematical model for single H-Bridge inverter is developed which can be extended to multi H-Bridge. The source voltage , load voltage , source current, load current, power factor simulation results under non-linear loads are presented. Finally Matlab/Simulink based model is developed and simulation results are presented.

References

- [1] K.A Corzine, and Y.L Familiant, "A New Cascaded Multi-level H-Bridge Drive," IEEE Trans. Power.Electron., vol.17, no.1, pp.125-131. Jan 2002.
- [2] J.S.Lai, and F.Z.Peng "Multilevel converters – A new breed of converters," IEEE Trans. Ind.Appl., vol.32, no.3, pp.509-517. May/ Jun. 1996.
- [3] T.A.Maynard, M.Fadel and N.Aouda, "Modelling of multilevel converter," IEEE Trans. Ind.Electron., vol.44, pp.356-364. Jun.1997.
- [4] P.Bhagwat, and V.R.Stefanovic, "Generalized structure of a multilevel PWM Inverter," IEEE Trans. Ind. Appln, Vol.1A-19, no.6, pp.1057-1069, Nov./Dec..1983.
- [5] J.Rodriguez, Jih-sheng Lai, and F Zheng peng, "Multilevel Inverters; A Survey of Topologies,

- Controls, and Applications,” *IEEE Trans. Ind. Electron.*, vol.49 , no4., pp.724-738. Aug.2002.
- [6] Roozbeh Naderi, and Abdolreza rahmati, “Phase-shifted carrier PWM technique for general cascaded inverters,” *IEEE Trans. Power.Electron.*, vol.23, no.3, pp.1257-1269. May.2008.
- [7] Bhim Singh, Kamal AlHaddad & Ambrish Chandra, 1999, A Review of Active Filter for Power Quality Improvements, *IEEE Trans on Industrial Electronics*, 46(5), pp.960970
- [8] Mauricio Angulo, Pablo Lezana, Samir Kouro, Jos´e Rodr´ıguez and Bin Wu, ”Level-shifted PWM for Cascaded Multilevel Inverters with Even Power Distribution” *IEEE Power Electronics specialist conference*, 17-21 june 2007, pp.2373-2378.
- [9] B. P. McGrath and D. G. Holmes, “Multicarrier PWM strategies for multilevel inverters,” *IEEE Trans. Ind. Electron.*, vol. 49, no. 4, pp. 858–867, August 2002.